Studying Conformational Changes of Biomolecules with Spatiotemporal Resolution and *in cell* using Pulsed Dipolar EPR Spectroscopy

Dissertation

zur

Erlangung des Doktorgrades (Dr. rer. nat.)

der

Mathematisch-Naturwissenschaftlichen Fakultät

der

Rheinischen Friedrich-Wilhelms-Universität Bonn

vorgelegt von

Patrick Tobias Hett

aus

Bonn

Bonn 2023

Angefertigt mit Genehmigung der Mathematisch-Naturwissenschaftlichen Fakultät
der Rheinischen Friedrich-Wilhelms-Universität Bonn.

1. Gutachter: Prof. Dr. Olav Schiemann

2. Gutachter: Prof. Dr. Ulrich Kubitscheck

Tag der Promotion: 01.08.2023

Erscheinungsjahr: 2023

List of Publications

Parts of this thesis have been published in peer-reviewed journals:

[P1] **T. Hett**, O. Schiemann*, "PELDOR Measurements on Nitroxide-Labeled Oligonucleotides" in *Methods Mol. Biol.*, Vol. *2439,* (Eds.: G. Steger, H. Rosenbach, I. Span), Humana New York, **2022**, pp. 241-274. DOI: 10.1007/978-1-0716-2047-2_16

[P2] M. F. Vicino†, **T. Hett**†, O. Schiemann*, "Spin Labeling of RNA Using "Click" Chemistry for Coarse-grained Structure Determination *via* Pulsed Electron-electron Double Resonance Spectroscopy", *Bio-protoc.* **2021**, *11*, e4004. DOI: 10.21769/BioProtoc.4004

[P3] **T. Hett**†, T. Zbik†, S. Mukherjee, H. Matsuoka, W. Bönigk, D. Klose, C. Rouillon, N. Brenner, S. Peuker, R. Klement, H.-J. Steinhoff, H. Grubmüller, R. Seifert, O. Schiemann*, U. B. Kaupp*, "Spatiotemporal Resolution of Conformational Changes in Biomolecules by Combining Pulsed Electron-Electron Double Resonance Spectroscopy with Microsecond Freeze-Hyperquenching", *J. Am. Chem. Soc.* **2021**, *143*, 6981-6989. DOI: 10.1021/jacs.1c01081

[P4] J. J. Jassoy†, C. A. Heubach†, **T. Hett**, F. Bernhard; F. R. Haege, G. Hagelueken, O. Schiemann*, "Site Selective and Efficient Spin Labeling of Proteins with a Maleimide-Functionalized Trityl Radical for Pulsed Dipolar EPR Spectroscopy", *Molecules* **2019**, *24*, 2735. DOI: 10.3390/molecules24152735

[P5] N. Fleck, C. A. Heubach, **T. Hett**, F. R. Haege, P. P. Bawol, H. Baltruschat, O. Schiemann*, "SLIM: A Short-Linked, Highly Redox-Stable Trityl Label for High-Sensitivity In-Cell EPR Distance Measurements", *Angew. Chem. Int. Ed.* **2020**, *59*, 9767-9772. DOI: 10.1002/anie.202004452

[P6] N. Fleck, C. Heubach, **T. Hett**, S. Spicher, S. Grimme, O. Schiemann*, "Ox-SLIM: Synthesis of and Site-Specific Labelling with a Highly Hydrophilic Trityl Spin Label", *Chem. Eur. J.* **2021**, *27*, 5292-5297. DOI: 10.1002/chem.202100013

[P7] N. Fleck, **T. Hett**, J. Brode, A. Meyer, S. Richert, O. Schiemann*, "C–C Cross-Coupling Reactions of Trityl Radicals: Spin Density Delocalization, Exchange Coupling, and a Spin Label", *J. Org. Chem.* **2019**, *84*, 3293-3303. DOI: 10.1021/acs.joc.8b03229

[P8] D. Abdullin, **T. Hett**, N. Fleck, K. Kopp, S. Cassidy, S. Richert, O. Schiemann*, "Magneto-Structural Correlations in a Mixed Porphyrin(Cu^{2+})/Trityl Spin System: Magnitude, Sign and Distribution of the Exchange Coupling Constant", *Chem. Eur. J.* **2023**, e202203148. DOI: 10.1002/chem.202203148

Further Publications

O. Schiemann*, C. A Heubach, D. Abdullin, K. Ackermann, M. Azarkh, E. G Bagryanskaya, M. Drescher, B. Endeward, J. H Freed, L. Galazzo, D. Goldfarb, **T. Hett**, L. Esteban-Hofer, L. Fábregas Ibáñez, E. J. Hustedt, S. Kucher, I. Kuprov, J. E. Lovett, A. Meyer, S. Ruthstein, S. Saxena, S. Stoll, C. R Timmel, M. Di Valentin, H. S. Mchaourab*, T. F. Prisner*, B. E. Bode*, E. Bordignon*, M. Bennati*, G. Jeschke*, "Benchmark Test and Guidelines for DEER/PELDOR Experiments on Nitroxide-Labeled Biomolecules", *J. Am. Chem. Soc.* **2021**, *143*, 17875-17890. DOI: 10.1021/jacs.1c07371

E. Schubert†, **T. Hett**†, O. Schiemann*, Y. NejatyJahromy, "EPR studies on the kinetics of the α-hydroxyethyl radical generated by Fenton-like chemistry", *J. Magn. Reson.* **2016**, *265*, 10-15. DOI: 10.1016/j.jmr.2016.01.003

† These authors contributed equally.
* Corresponding author.

Conference Presentations

2017 Poster presentation at 39th FGMR Annual Discussion Meeting, Bayreuth.
Title of the poster: “Time Resolution in EPR Spectroscopy using Microsecond Hyperquenching”.

2018 Poster prize at 40th FGMR Annual Discussion Meeting, Leipzig.
Title of the poster: “Conformational Changes in a Cyclic Nucleotide-Binding Domain Studied by PELDOR Spectroscopy”.

2019 Poster presentation at EUROISMAR 2019, Berlin.
Title of the poster: “Performance of a Maleimide-Functionalized Trityl Spin Label in Pulsed Dipolar EPR Spectroscopy”.

Poster prize at 8th EFEPR School, Brno, Czech Republic.
Title of the poster: “Conformational Changes in a Cyclic Nucleotide-Binding Domain Studied by PELDOR Spectroscopy”.

2021 Research talk at 42nd FGMR Annual Discussion Meeting, Online.
Title of the talk: “Spatiotemporal Resolution of Conformational Changes in Biomolecules by Pulsed Electron-Electron Double Resonance Spectroscopy”.

Sigrid-Peyerimhoff-Forschungspreis of the Bonner Universitätsstiftung, prize talk in the colloquium of the GDCh Ortsverband Bonn.
Title of the talk: “Spatiotemporal Resolution of Conformational Changes in Biomolecules”.

Invited talk at the IES virtual EPR meeting (IVEM) of the international EPR society.
Title of the talk: “Spatiotemporal Resolution of Conformational Changes in Biomolecules by Pulsed Electron-Electron Double Resonance Spectroscopy”.

2022 Poster prize at EUROMAR 2022, Utrecht, The Netherlands.
Title of the poster: “Spatiotemporal Resolution of Conformational Changes in Biomolecules by Microsecond Freeze-Hyperquenching and PELDOR Spectroscopy”.

Ernst Prize of the GDCh Fachgruppe Magnetische Resonanz, prize talk at 43rd FGMR Annual Discussion Meeting, Karlsruhe.
Title of the talk: “Spatiotemporal Resolution of Conformational Changes in Biomolecules”.

Research talk at 5th NMR Meets Biology Meeting, Hospet, India.
Title of the talk: “Spatiotemporal Resolution of Conformational Changes in Biomolecules by Pulsed Electron-Electron Double Resonance Spectroscopy”.

Acknowledgements

First and foremost, I would like to express my deep gratitude to my supervisor and mentor, Prof. Dr. Olav Schiemann, for his continuous support throughout my time as a PhD student. Always open for discussions, he provided valuable feedback and stimulating ideas that encouraged me to dig deeper into science. I would also like to thank him for the opportunity to present my research at several international conferences and to contribute to scientific publications.

Furthermore, I would like to thank Prof. Dr. Ulrich Kubitscheck for acting as the second reviewer of my thesis and Prof. Dr. Connie Lu and Prof. Dr. U. Benjamin Kaupp for being part of my doctoral committee.

Most results presented in this thesis are the outcome of teamwork, and I would like to thank all my collaborators for their valuable contributions. In the project on time-resolved PELDOR, I had the pleasure to collaborate with Prof. Dr. U. Benjamin Kaupp and his group at the Max Planck Institute for Neurobiology of Behavior – caesar, Dr. Reinhard Seifert, Dr. Tobias Zbik, and Norbert Brenner. Furthermore, I would like to thank Prof. Dr. Helmut Grubmüller and Dr. Reinhard Klement from the Max Planck Institute for Multidisciplinary Sciences in Göttingen for introducing me to the field of molecular dynamics simulations and their helpful advice.

The EPR measurements on trityls were done in collaboration with Dr. Nico Fleck, Jean-Jacques Jassoy, and Caspar Heubach and I would like to thank them for synthesizing the trityl spin labels and for labelling the proteins.

Special thanks go to Dr. Dinar Abdullin for his advice on spectrometer operation and our enlightening discussions on various topics such as spin physics, programming, and data fitting. Likewise, I would like to thank Hamed Alaei for his technical support and for his cooperation in conducting the students' practical courses. Beyond, I would like to express my gratitude to all present and previous members of the research group for the nice working atmosphere and for fruitful discussions – especially my office mates, Catrin Allar, Olivia Kendall, Kevin Kopp, and Maria Vicino, shall be mentioned here.

The computation centre of the University of Bonn is acknowledged for granting access to the Bonna cluster and the Deutsche Forschungsgemeinschaft (DFG, project number 420322655, Koselleck grant to U. B. Kaupp) for funding my research.

Finally, I would like to thank my friends and family, especially my parents and my brother, for supporting me during my studies.

Abstract

The function of biomolecules is closely linked with their structure and dynamics. Furthermore, the interconversion of different conformations of a biomolecule determines its activity and is vital for biomolecular processes. Thus, for a thorough understanding of biomolecular function, it is crucial to monitor conformational changes over space and time. Here, the ligand-induced helix movement in a cyclic nucleotide-binding domain (CNBD) was studied with spatiotemporal resolution using pulsed electron-electron double resonance (PELDOR) spectroscopy and microsecond freeze-hyperquenching (MHQ). The PELDOR-derived distance distributions distinguished between the ligand-free *apo* state and the *holo* state, which was obtained upon binding of cyclic adenosine monophosphate (cAMP). By freezing a mixture of the CNBD and cAMP in the MHQ device at ageing times between 82 µs and 668 µs, the *apo*-to-*holo* transition could be monitored with Angstrom and microsecond spatiotemporal resolution. The PELDOR data revealed a gradual depletion of the *apo* state population and a simultaneous build-up of the *holo* state population, but no intermediates between the two states could be detected. This observation suggested that the helix movement occurred on a sub-microsecond time scale and thus could not be monitored by MHQ/PELDOR. Molecular dynamics (MD) simulation confirmed this notion by showing that the helix movement proceeds within a few nanoseconds. Saturation experiments revealed that cAMP binding was accomplished within the dead time of the MHQ device at cAMP-to-CNBD ratios above 67; therefore, ligand binding could be excluded as a potential cause of the population shift, as MHQ/PELDOR experiments were performed with 100-fold excess of cAMP. A mechanism was proposed to interpret these experimental and theoretical results based on dwell times: In a mechanistic picture, the *apo*-to-*holo* transition involves two free-energy barriers, ligand binding and the conformational change, which are both crossed within nanoseconds. Upon ligand binding, an *apo*-ligand-complex is formed in which the protein is structurally in the *apo* state but with the ligand settled in the binding pocket. The two barriers are separated by a dwell time, in which the *apo*-ligand-complex acquires thermal energy to cross the second barrier and to transit to the *holo* state. This dwell time is in the microsecond range and is thus the rate-limiting step on the trajectory from *apo* to *holo*. Since the dwell time is individual for each protein molecule and as PELDOR monitors a protein ensemble, MHQ/PELDOR could resolve the dwell-time distribution of the CNBD upon cAMP binding.

The structure of a biomolecule may depend on its environment, i.e. the physiologically active conformation *in cell* may differ from the one observed *in vitro*. While X-ray crystallography, nuclear magnetic resonance spectroscopy, and electron microscopy provide a high-resolution structure *in vitro*, electron paramagnetic resonance (EPR) pulsed dipolar spectroscopy (PDS) allows studying biomolecules *in cell*. Performing a PDS experiment *in cell* requires spin labels that are stable in the reductive cellular environment. While the commonly-used nitroxide labels such as MTSL are reduced quickly, (tris)-tetrathiatriarylmethyl (trityl)-based spin labels (TSLs) are stable under cellular conditions. Moreover, they have a narrow EPR spectrum, which allows for highly sensitive single-frequency PDS experiments at nanomolar concentrations. The performance of PDS in combination with TSLs was assessed on a construct of the *Yersinia* outer protein O (YopO) labelled with Mal-TSL, a label obtained by esterification of the so-called Finland trityl radical. It was found that the double-quantum coherence (DQC) experiment outperforms PELDOR and the single-frequency technique for refocusing dipolar couplings (SIFTER) in terms of the modulation depth and the signal-to-noise ratio. This was attributed to the more efficient phase cycle in DQC, which extracts the dipolar signal by double-quantum filtering. The distance distribution obtained with Mal-TSL was broader than the one obtained with MTSL, which is related to the long and flexible linker in Mal-TSL.

To narrow the distribution and to increase the distance resolution, the ester moiety in Mal-TSL was replaced by a single methylene group, giving rise to the short-linked maleimide trityl label SLIM. Shortening the linker from five rotatable bonds in Mal-TSL to two bonds in SLIM reduced the flexibility and thus the conformational freedom of the label. As a result, SLIM lead to a narrower distance distribution than Mal-TSL. This experimental finding was confirmed by *in silico* spin labelling, showing that the volume sampled by SLIM is more than twofold lower compared with Mal-TSL. The sensitivity of PDS with trityls was illustrated by a DQC experiment on SLIM-labelled YopO at 90 nM protein concentration. Exploiting the high sensitivity and the stability of SLIM, DQC could be performed upon injecting YopO into oocytes of the African clawed frog (*Xenopus laevis*). Of note, a conformational change could be observed upon translocating YopO into cells, which illustrates the need to study biomolecular structures in the native environment. The sensitivity was enhanced further by replacing the methyl groups in SLIM with hydroxyethyl groups, giving rise to a trityl label called Ox-SLIM. The absence of methyl substituents in the vicinity of the electron spin increased the phase-memory time and thus allowed for a DQC experiment at only 45 nM protein concentration. Additionally, the hydroxyethyl groups increased the hydrophilicity of the label and thus reduced aggregation and unspecific interactions with the biomolecule.

Beyond distance measurements on biomolecules, two trityl-based model compounds were used to study the electron-spin exchange interaction by continuous wave EPR, DQC, and density functional theory (DFT). Strong antiferromagnetic coupling was observed in a biphenyl-linked trityl biradical; the exchange-coupling constant was determined from the temperature dependence of the half-field signal and the interspin distance distribution was obtained by DQC. Taking spin-density delocalization into account, the experimental distance distribution could be confirmed by MD simulation. Furthermore, DFT was used to study the exchange coupling in a trityl radical connected by a phenyl bridge with copper(II) tetraphenyl porphyrin (TPP). The bridge dynamics were shown to modulate the exchange interaction: In the energy minimum with the phenyl ring almost perpendicular to the planes of TPP and trityl, weak ferromagnetic exchange was observed. Upon rotating the phenyl ring about the connection axis, strong antiferromagnetic coupling was observed if the phenyl ring was in-plane with TPP and the trityl, thus demonstrating that the exchange interaction sensitively depends on the orientation of the phenyl bridge.

Table of Contents

1 Introduction

Electron paramagnetic resonance (EPR), also called electron spin resonance (ESR), is a magnetic resonance technique to study atoms and molecules that carry at least one unpaired electron. In EPR spectroscopy, the electron spin states are split by an external magnetic field and transitions between the spin states are induced by microwave radiation.[1] Methodologically, EPR is closely related to nuclear magnetic resonance (NMR) spectroscopy, in which nuclear-spin transitions are induced by irradiation with radio waves.[2]

Spin is an intrinsic quantum-mechanical property of electrons and atomic nuclei and it has no classical analogue.[3(p.456)] The spin quantum number of a single electron is $S = 1/2$. In the EPR literature, the part of the molecule that carries the unpaired electron(s) is often referred to as the "paramagnetic centre" [1,4–8] or the "spin centre",[9] with examples of spin centres being radicals and paramagnetic metal ions. For paramagnetic centres with more than one unpaired electron, the individual spin quantum numbers add up to a higher group spin S if the spins strongly interact with each other,[10(p.33)] e.g. $S = 5/2$ in the case of the five unpaired electrons of the *high*-spin Fe(III) ion (electron configuration: [Ar] $3d^5$).[11] Depending on the ligands coordinating the metal ion, spin pairing can occur, which converts the *high*-spin state into the *low*-spin state and thereby decreases the group spin: The Fe(III) ion in the *low*-spin state, for example, has only one unpaired electron and therefore corresponds to a system of $S = 1/2$.

Requiring unpaired electrons, one might think that EPR spectroscopy is limited to a rather small number of naturally occurring open-shell molecules, which are often characterized by a short lifetime.[12] However, redox-chemistry, photoexcitation, or exogenous paramagnetic tags can introduce unpaired electrons into a diamagnetic molecule, thus rendering it EPR-active.[12] Further, short-lived paramagnetic intermediates in (bio)chemical reactions can be investigated using continuous or stopped flow,[13] freeze-quench,[14,15] or spin-trapping techniques,[12] which either stabilize the transient species or continuously generate it at a sufficient concentration to allow EPR detection.

Various disciplines benefit from insights obtained with EPR spectroscopy, e.g. physics, chemistry, material science, and biosciences, where EPR serves to detect, identify, and study the properties of paramagnetic centres. One field of application is site-directed spin labelling (SDSL) combined with pulsed dipolar EPR spectroscopy (PDS) to investigate the structure and dynamics of biomacromolecules such as proteins and oligonucleotides. In this regard, EPR can complement other techniques for biomolecular structure elucidation such as NMR spectroscopy, electron microscopy, and X-ray crystallography. As shown in this thesis, combining SDSL and PDS allows studying proteins in their native cellular environment and following structural changes with spatiotemporal resolution in the Angstrom distance range and on the microsecond time scale.

This cumulative dissertation is structured as follows: First, a brief introduction to the spin physics of EPR spectroscopy is given (section 1.1). Next, the experimental techniques used in this work are reviewed, namely continuous wave (*cw*) and pulsed EPR spectroscopy with a focus on PDS (section 1.2). The introduction closes with a section on biomolecular PDS including spin labels, site-directed spin labelling, and a comparison of PDS and further techniques for biomolecular structure elucidation. In section 2, the aim of this work is defined, followed by a discussion of the results of the publications (section 3). The publications themselves are collected in appendices [P1]-[P8].

1.1 Spin Physics of EPR Spectroscopy

1.1.1 Historical Background

In the year 1922, Stern and Gerlach observed a splitting of a beam of silver atoms in an inhomogeneous magnetic field.[16] This finding lead to the conclusion that the electron magnetic moment is restricted to certain discrete orientations in the magnetic field, formally known as the quantization of angular momentum.[3(p.3),16,17] In 1925, Uhlenbeck und Goudsmit [17,18] postulated that this quantization is due to the angular momentum of the unpaired electron in the 5s-orbital of the silver atom (electron configuration:[19(p.1304)] [Kr] $4d^{10}5s^1$) that they called the electron spin. In addition to this spin angular momentum, the electron also has an orbital angular momentum since it moves around the atomic nucleus.[20]

After the discovery of the electron spin, it took another 20 years until the first EPR experiment was performed in 1945 by Zavoisky [17] on $CuCl_2 \cdot 2\,H_2O$ at a radiofrequency of 133 MHz and a magnetic field of 4.76 mT.[3(p.3),21] Technological progress increased the achievable magnetic field strength and the frequency of electromagnetic radiation so that EPR experiments are nowadays performed with microwaves in the gigahertz range and at magnetic fields above 100 mT.[3(p.3)]

1.1.2 The Resonance Condition

For EPR investigation, the atom or molecule must have spin angular momentum and therefore at least one unpaired electron, i.e. $S > 1/2$. The electron spin can be described by a vector [21]

$$\vec{S} = \begin{pmatrix} S_x \\ S_y \\ S_z \end{pmatrix} = (S_x \quad S_y \quad S_z)^T \tag{1}$$

with the components S_x, S_y, S_z along the axes x, y, and z of the Cartesian grid. Here and in all following equations, the superscript *T* denotes the transposition of a row vector into a column vector and *vice versa*. Due to Heisenberg's uncertainty principle, only one component of $\vec{S}$ can be determined at a time (S_z, by convention), while the two remaining components are undetermined. The z-component is given by [20]

$$S_z = m_s \hbar \tag{2}$$

where m_s is the magnetic quantum number [3(p.93)]

$$m_s = -S, -S+1, \ldots, +S \tag{3}$$

This leads to

$$M = 2S + 1 \tag{4}$$

possible values for m_s,[3(p.13)] with *M* being the multiplicity [3(p.13)] that governs the nomenclature of the respective spin state (e.g. $S = 1/2$ leads to $M = 2$ describing a doublet state; $S = 1$ corresponds to a triplet state, etc.).[3(p.13)] The magnitude of $\vec{S}$ is given by [21]

$$\left|\vec{S}\right| = \hbar\sqrt{S(S+1)} \tag{5}$$

with the reduced Planck constant $\hbar = h/2\pi$.

Figure 1 shows m_s and $\left|\vec{S}\right|$ for systems with a total spin $S = 1/2$, $S = 1$, and $S = 3/2$.

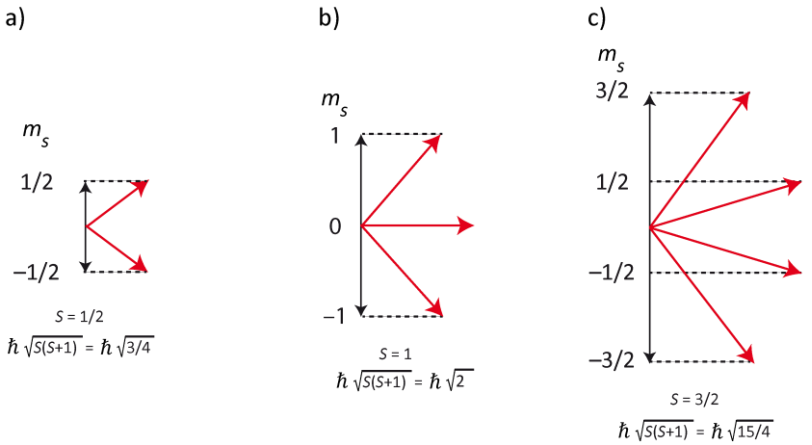

Figure 1: Graphical representation of the magnetic quantum number m_s and the magnitude of the spin vector $|\vec{S}| = \hbar\sqrt{S\,(S+1)}$ (red arrows) for a) S = 1/2, b) S = 1, c) S = 3/2. Adapted from [3(p.13)].

According to classical physics, particles with the angular momentum $\vec{l}$, the mass m, and the electric charge q are associated with the magnetic moment $\vec{\mu}$ [3(p.15)]

$$\vec{\mu} = \frac{q}{2m}\vec{l} \tag{6}$$

As the electron is an elementary particle that cannot be described accurately by classical physics, a quantum-mechanical treatment is mandatory, in which the electron magnetic moment reads [10(p.16)]

$$\vec{\mu}_e = g_e \frac{-e}{2m_e}\hbar\vec{S} \tag{7}$$

with the *g*-factor of the free electron g_e, the elementary charge *-e*, and the electron mass m_e.[10(p.16)] The *g*-value of the free electron (precise value: g_e=2.0023193043737) [10(p.17)] stems from quantum electrodynamics and bridges the gap between classical physics and a rigorous quantum-physical treatment.[10(p.17)] If the unpaired electron is bound to an atom, its *g*-value deviates from g_e due to the coupling of spin angular momentum and orbital angular momentum (spin-orbit coupling, SOC), an effect that is relevant especially in the case of heavy atoms such as transition metal ions.[10(p.28–29)] Organic radicals, by contrast, usually have a *g*-value close to g_e.[1] The *g*-value may thus be regarded as a "fingerprint" [1,10(p.29)] analogous to the chemical shift in NMR spectroscopy that allows identifying a paramagnetic centre and characterizing, e.g., its ligands and coordination symmetry.[10(p.29)]

Eq. (7) can be simplified by introducing Bohr's magneton β_e [10(p.16)]

$$\beta_e = \frac{|e|\hbar}{2m_e} = 9.274 \cdot 10^{-24}\,\frac{\mathrm{J}}{\mathrm{T}} \tag{8}$$

and the gyromagnetic ratio of the electron γ_e [3(p.15)]

$$\gamma_e = \frac{-eg_e}{2m_e} = -1.761 \cdot 10^{11}\,\frac{\mathrm{C}}{\mathrm{kg}} \tag{9}$$

This leads to [3(p.15),10(p.16)]

$$\vec{\mu}_e = -g_e\beta_e\,\vec{S} = \gamma_e\hbar\vec{S} \tag{10}$$

Note that $\vec{\mu}_e$ is antiparallel to $\vec{S}$ due to the negative charge of the electron.[20] In the absence of a magnetic field, the magnetic moments $\vec{\mu}_e$ are oriented randomly and their energy levels are degenerate.[20] Upon applying an external magnetic field $\overrightarrow{B_0} = (B_{0,x} \quad B_{0,y} \quad B_{0,z})^T$, the magnetic moments align either parallel or antiparallel with $\overrightarrow{B_0}$ and their energy is given by [3(p.18)]

$$E = -\vec{\mu}_e \cdot \overrightarrow{B_0} = g_e\beta_e\vec{S}\,\overrightarrow{B_0} \tag{11}$$

Due to the electron-Zeeman effect, the energy levels of the electron spin are split in a magnetic field and the degeneracy is lifted. Assuming that the magnetic field is applied along the z-axis, $\overrightarrow{B_0} = (0 \quad 0 \quad B_{0,z})^T = B_{0,z}$, and considering only the z-component of the magnetic moment [3(p.15)]

$$\mu_{e,z} = -g_e \beta_e m_s \tag{12}$$

eq. (11) simplifies to [3(p.20)]

$$E = g_e \beta_e m_s B_{0,z} \tag{13}$$

For a single unpaired electron (m_s = ± 1/2), the energy of the Zeeman levels reads

$$\begin{aligned} E_\alpha &= E\left(m_s = +\frac{1}{2}\right) = +\frac{1}{2} g_e \beta_e B_{0,z} \\ E_\beta &= E\left(m_s = -\frac{1}{2}\right) = -\frac{1}{2} g_e \beta_e B_{0,z} \end{aligned} \tag{14}$$

The upper Zeeman level (m_s = +1/2) corresponds to the magnetic moment antiparallel to $B_{0,z}$ and is called the α-state, whereas the lower level (m_s = -1/2) with the magnetic moment parallel to $B_{0,z}$ is the β-state.[21]

Analogous to the electron spin $\vec{S}$, the nuclear spin $\vec{I}$ is associated with the magnetic quantum number m_I

$$m_I = -I, -I+1, \ldots, +I \tag{15}$$

and its energy levels are split in a magnetic field due to the nuclear-Zeeman effect. In EPR spectroscopy, spin transitions are quantum-mechanically allowed if they fulfil the selection rule [22]

$$\Delta m_s = \pm 1 \text{ and } \Delta m_I = 0, \tag{16}$$

which is related to the conservation of angular momentum.[3(p.21)] As the microwave photon that triggers the EPR transition carries "one unit of [spin] angular momentum"[3(p.21)] (±ħ),[23(p.112)] the spin transition must also change the spin angular momentum by ±1 to conserve the total angular momentum.[3(p.21),23(p.112)] Thus, for S = 1/2, spin transitions can be triggered between the α- and β-Zeeman levels with the energy difference given by [21]

$$\Delta E = E_\alpha - E_\beta = g_e \beta_e B_{0,z} \tag{17}$$

Substituting ΔE in eq. (17) by the relation of the energy E and the frequency ν (or equivalently the angular frequency $\omega = 2\pi\nu$) of an electromagnetic wave

$$E = h\nu = \hbar\omega \tag{18}$$

leads to the resonance condition of EPR spectroscopy [21]

$$\Delta E = h\nu = g_e \beta_e B_{0,z} \tag{19}$$

If the resonance condition is fulfilled, i.e. if the energy of the incident electromagnetic radiation matches the energy difference between the Zeeman levels, spin transitions from the lower to the upper state and *vice versa* can occur. In EPR spectroscopy, these transitions are driven by the interaction of the magnetic field component of microwave radiation with the magnetic moment of the electron spin.[1] By contrast, most other spectroscopic techniques are based on the interaction of an electric dipole moment with the electric field component of electromagnetic radiation.[20] Equation (19) indicates that the resonance frequency and the magnetic field strength are proportional to each other, implying that resonance occurs at various combinations of ν and $B_{0,z}$ for a given g-value. Note that in EPR spectroscopy, $B_{0,z}$ is often given in the unit Gauss (G) with 1 G = 10^{-4} T.

The ratio of spins populating the α- and β-Zeeman states is given by Boltzmann statistics [20]

$$\frac{N_\alpha}{N_\beta} = \frac{N\left(m_s = +\frac{1}{2}\right)}{N\left(m_s = -\frac{1}{2}\right)} = \exp\left(-\frac{\Delta E}{k_B T}\right) = \exp\left(-\frac{g_e \beta_e B_{0,z}}{k_B T}\right) \tag{20}$$

where T is the temperature and k_B is the Boltzmann constant. For $g = g_e$, $B_0 = 3000$ G, and $T = 300$ K, it follows $N_\alpha/N_\beta = 0.9986$, i.e. the Zeeman states are almost equally populated.[20] When the resonance condition is fulfilled, microwave radiation is absorbed by the spin system, which leads to an EPR signal and increases the population ratio N_α/N_β. Spin relaxation, on the other hand, describes the return from the upper to the lower Zeeman state and thus a decrease of N_α/N_β. If excitation exceeds relaxation, the population of both levels may be equalized, i.e. $N_\alpha/N_\beta = 1$, which results in saturation of the spin system.[20] In this case, no further excitation from the lower to the upper state is possible and the EPR signal decreases.

1.1.3 The Vector Picture

In a sample containing typically about 10^{14} spin centres,[24] the individual magnetic moments $\overrightarrow{\mu_i}$ of the N electron spins add up to a macroscopic magnetization $\overrightarrow{M_0}$ given by [10(p.17)]

$$\overrightarrow{M_0} = \frac{1}{V}\sum_{i=1}^{N} \overrightarrow{\mu_i} \tag{21}$$

with V being the volume of the sample.[10(p.17)] By contrast to a single electron spin or a single magnetic moment, macroscopic magnetization is a bulk property giving rise to an EPR signal.[10(p.17–18)] In the thermal equilibrium and if the external magnetic field is applied along the z-axis, $\overrightarrow{M_0}$ is aligned with the z-axis (Figure 2a):

$$\overrightarrow{M_0} = \frac{1}{V}\sum_{i=1}^{N} \overrightarrow{\mu_{i,z}} = \overrightarrow{M_z} \tag{22}$$

The x- and y-components of the magnetic moments, by contrast, add up to zero [3(p.14)]

$$\begin{aligned} \overrightarrow{M_x} &= \frac{1}{V}\sum_{i=1}^{N} \overrightarrow{\mu_{i,x}} = 0 \\ \overrightarrow{M_y} &= \frac{1}{V}\sum_{i=1}^{N} \overrightarrow{\mu_{i,y}} = 0 \end{aligned} \tag{23}$$

By irradiating the sample with microwaves at a frequency that fulfils the resonance condition, $\overrightarrow{M_0}$ is moved out of the equilibrium and precesses on a cone about the z-axis at the Larmor frequency [10(p.18),21]

$$\omega_L = \frac{g_e \beta_e B_0}{\hbar} \tag{24}$$

Figure 2b shows this precession in the so-called laboratory frame, a Cartesian grid with the axes x, y, and z.[10(p.17–18),21] To follow the evolution of the macroscopic magnetization in an EPR experiment more easily, it is convenient to introduce a reference frame whose axes x' and y' rotate around z at ω_L, i.e. at the angular frequency of the magnetization vector.[21] In this so-called rotating frame (Figure 2c), the magnetization appears stationary, and this concept will prove useful later when discussing the effects of pulse sequences.[10(p.18),21]

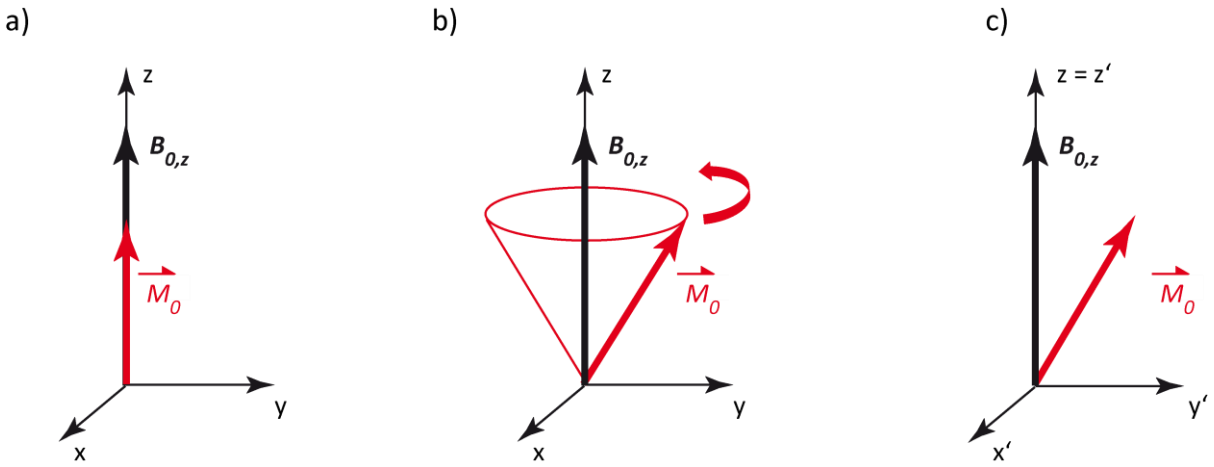

Figure 2: Representation of the macroscopic magnetization vector $\overrightarrow{M_0}$ in the Cartesian frame. a) In the thermal equilibrium, $\overrightarrow{M_0}$ is aligned with the magnetic field along the z-axis. b) Upon irradiation with microwaves, $\overrightarrow{M_0}$ is tilted away from the z-axis. In the laboratory frame, $\overrightarrow{M_0}$ precesses on a cone about the magnetic field $B_{0,z}$ at the Larmor frequency ω_L. c) In the rotating frame, $\overrightarrow{M_0}$ appears stationary. Adapted from [21].

1.1.4 The Spin Hamiltonian

In quantum mechanics, the total energy of a system of quantum particles is given by the Hamilton operator $\hat{H}$,[3(p.42)] usually abbreviated as Hamiltonian.[10(p.16)] In the following, spin operator vectors will be marked with a circumflex ($\hat{}$) and matrices will be printed in bold letters. The part of the Hamiltonian that contains only the operators of the electron spin ($\hat{S}$), the nuclear spin ($\hat{I}$), and fundamental constants is called the static spin Hamiltonian $\hat{H}_0$.[10(p.26)] For a single paramagnetic centre of total electron spin *S* with *m* nuclei of spin quantum number *I*, $\hat{H}_0$ reads in units of angular frequency [10(p.26)]

$$\begin{aligned}\hat{H}_0 &= \hat{H}_{EZ} + \hat{H}_{NZ} + \hat{H}_{HF} + \hat{H}_{NQ} + \hat{H}_{NN} + \hat{H}_{ZFS} \\ &= \frac{\beta_e}{\hbar}\overrightarrow{B_0}^T \boldsymbol{g_e}\hat{\vec{S}} - \frac{\beta_n}{\hbar}\sum_{k=1}^{m} g_{n,k}\overrightarrow{B_0}^T\hat{\vec{I}}_k + \sum_{k=1}^{m}\hat{\vec{S}}^T\boldsymbol{A_k}\hat{\vec{I}}_k + \sum_{I_k>\frac{1}{2}}\hat{\vec{I}}_k^T\boldsymbol{P_k}\hat{\vec{I}}_k + \sum_{i\neq k}\hat{\vec{I}}_i^T\boldsymbol{d}^{(i,k)}\hat{\vec{I}}_k + \hat{\vec{S}}^T\boldsymbol{D}\hat{\vec{S}}\end{aligned} \quad (25)$$

Therein, $\hat{H}_{EZ}$ describes the electron-Zeeman interaction with the external magnetic field $\overrightarrow{B_0}$ and $\hat{H}_{NZ}$ the nuclear-Zeeman interaction of the *m* nuclei. $\hat{H}_{HF}$ is the hyperfine interaction between the electron spin and the nuclear spins. The next two terms focus exclusively on nuclei: $\hat{H}_{NQ}$ describes the interaction of the nuclear quadrupole moment with the electric field gradient of surrounding electrons and nuclei, which is relevant for nuclear spins with $I \geq 1$.[10(p.32)] $\hat{H}_{NN}$ represents pairwise spin-spin dipolar interactions between nuclei.[10(p.34)] Finally, $\hat{H}_{ZFS}$ is the zero-field splitting term, which results from SOC and dipolar spin-spin coupling of unpaired electrons in systems with $S > 1/2$.[4,10(p.33)]

All parameters of the spin Hamiltonian can be determined by fitting experimental spectra or by quantum-chemical methods such as density functional theory (DFT).[25] The following sections focus on the components of the spin Hamiltonian in detail.

1.1.4.1 Electron-Zeeman Interaction

The electron-Zeeman term [1,10(p.28)]

$$\hat{H}_{EZ} = \frac{\beta_e}{\hbar} \overrightarrow{B_0}^T \boldsymbol{g_e} \hat{\vec{S}} = \frac{\beta_e}{\hbar} \begin{pmatrix} B_{0,x} & B_{0,y} & B_{0,z} \end{pmatrix} \begin{pmatrix} g_x & 0 & 0 \\ 0 & g_y & 0 \\ 0 & 0 & g_z \end{pmatrix} \begin{pmatrix} \hat{S}_x \\ \hat{S}_y \\ \hat{S}_z \end{pmatrix} \tag{26}$$

describes the interaction of the electron spin with the external magnetic field $\overrightarrow{B_0}$ and typically dominates $\hat{H}_0$ for systems of $S = 1/2$.[10(p.28)] The *g*-value, so far treated as the scalar g_e when deriving the resonance condition (eq. (19)), has been replaced by the *g*-matrix $\boldsymbol{g}$ (also called *g*-tensor) to account for *g*-anisotropy, i.e. the dependence of the *g*-value on the orientation of the molecule with respect to the magnetic field.[20] Like the deviation of the *g*-value from g_e, this orientation-dependence results from SOC.[10(p.28)] As can be inferred from eq. (26), the magnitude of the electron-Zeeman splitting scales with the magnetic field strength $\overrightarrow{B_0}$. Therefore, peaks that overlap at a lower magnetic field can be disentangled using high-field EPR, e.g. by separating signals from species with similar *g*-values or resolving the components of the *g*-tensor in the case of weak *g*-anisotropy.[10(p.29)] As an example, the *g*-tensor of a tetrathiatriarylmethyl (trityl) radical ($g_x = g_y = 2.0034$, $g_z = 2.0023$) [26] can be resolved at G-band (180 GHz / 6.4 T), whereas the spectrum displays a single isotropic line at X-band (9 GHz / 0.3 T; section 1.2.1).[26]

The *g*-matrix is usually given in its principal axis system (PAS), in which $\boldsymbol{g}$ contains the diagonal elements g_x, g_y, and g_z that indicate the *g*-values along the axes of the PAS.[27] As shown in Figure 3, the orientation of $\overrightarrow{B_0}$ with respect to the PAS is described by the zenith angle θ (between $\overrightarrow{B_0}$ and the z-axis) and the azimuth angle φ (between the projection of $\overrightarrow{B_0}$ onto the xy-plane and the x-axis).[28(p.94)]

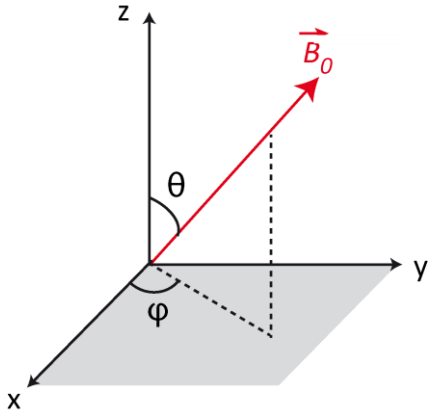

Figure 3: Principal axis system x, y, z of the *g*-matrix. The vector $\overrightarrow{B_0}$ shown in red indicates the direction of the magnetic field and the grey shaded area marks the xy-plane. Adapted from [27].

In disordered samples such as a frozen solution or a powder, the paramagnetic centres are randomly oriented with respect to $\overrightarrow{B_0}$ (arbitrary combinations of θ and φ), and all orientations are equally probable.[1,27] The EPR spectrum then corresponds to a superposition of the individual spectra at the respective angles θ and φ, where each spectrum is weighted with $\sin(\theta)$.[27] The factor $\sin(\theta)$ leads to a higher weighting of spectra with $\overrightarrow{B_0}$ in the xy-plane of the PAS (i.e. $\theta = 90°$ and $\sin(\theta) = 1$) compared to spectra with $\overrightarrow{B_0}$ parallel to the z-axis (i.e. $\theta = 0°$ and $\sin(\theta) = 0$). This can be rationalized by considering a unit sphere (Figure 4): As there is exactly one orientation in which $\overrightarrow{B_0}$ is parallel to the z-axis, only few molecules whose symmetry axis coincides with the direction of $\overrightarrow{B_0}$ will contribute to the spectrum, and the signal intensity will be concomitantly low.[27] The number of possible orientations of $\overrightarrow{B_0}$ and hence the signal intensity increases with θ, reaching a maximum when $\overrightarrow{B_0}$ lies within the xy-plane perpendicular to the z-axis ($\theta = 90°$).[27]

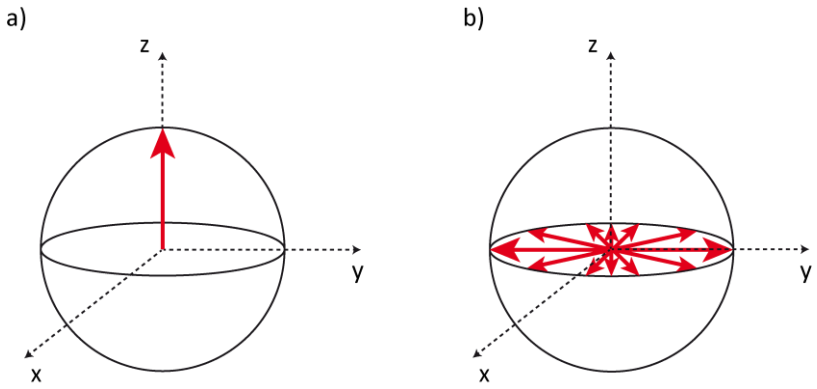

Figure 4: Orientation of the magnetic field vector (red arrow) in the principal axis system. a) Exactly one orientation is possible if the magnetic field vector is along the z-axis (θ = 0°). b) The number of orientations is maximal if the magnetic field vector is in the xy-plane (θ = 90°). Adapted from [27,29(p.17)].

The local molecular and orbital symmetry of the paramagnetic centre can lead to coinciding principal values of the *g*-matrix. If all three principal values are equal ($g_x = g_y = g_z$) [1] as encountered for paramagnetic centres of spherical symmetry,[21] the *g*-matrix is called isotropic. In the absence of hyperfine coupling, isotropic *g*-matrices give rise to a single-line EPR spectrum (Figure 5a).[20]

In the case of axial symmetry, the paramagnetic centre exhibits a unique rotation axis that by convention corresponds to the z-axis of the PAS. This results in a unique *g*-value along the z-axis, which differs from the *g*-value corresponding to the plane perpendicular to the z-axis ($g_x = g_y \neq g_z$).[1] In systems of axial symmetry, g_x and g_y are therefore called the perpendicular component ($g_x = g_y = g_\perp$) and g_z the parallel component ($g_z = g_{||}$) of the *g*-matrix.[10(p.28)] Owing to the intensity weighting discussed above, the EPR signal corresponding to $g_\perp$ will be larger than the one arising from $g_{||}$.[22] This results in two distinct signal patterns for EPR spectra with axial symmetry, depending on whether $g_\perp$ is smaller or larger than $g_{||}$ (Figure 5b,c).[22]

If the principal *g*-values differ ($g_x \neq g_y \neq g_z$), the *g*-matrix is called rhombic (Figure 5d).[10(p.28),20]

These three cases (isotropic, axial, rhombic) each give rise to a characteristic signal pattern in the EPR spectrum, which allows identifying the symmetry of the *g*-matrix and of the paramagnetic centre.[1] Figure 5 shows simulated EPR spectra of isotropic, axial, and rhombic g-matrices as absorption spectra (red) and as the first derivative (black) obtained experimentally by field-modulated *cw* EPR spectroscopy (section 1.2.1).

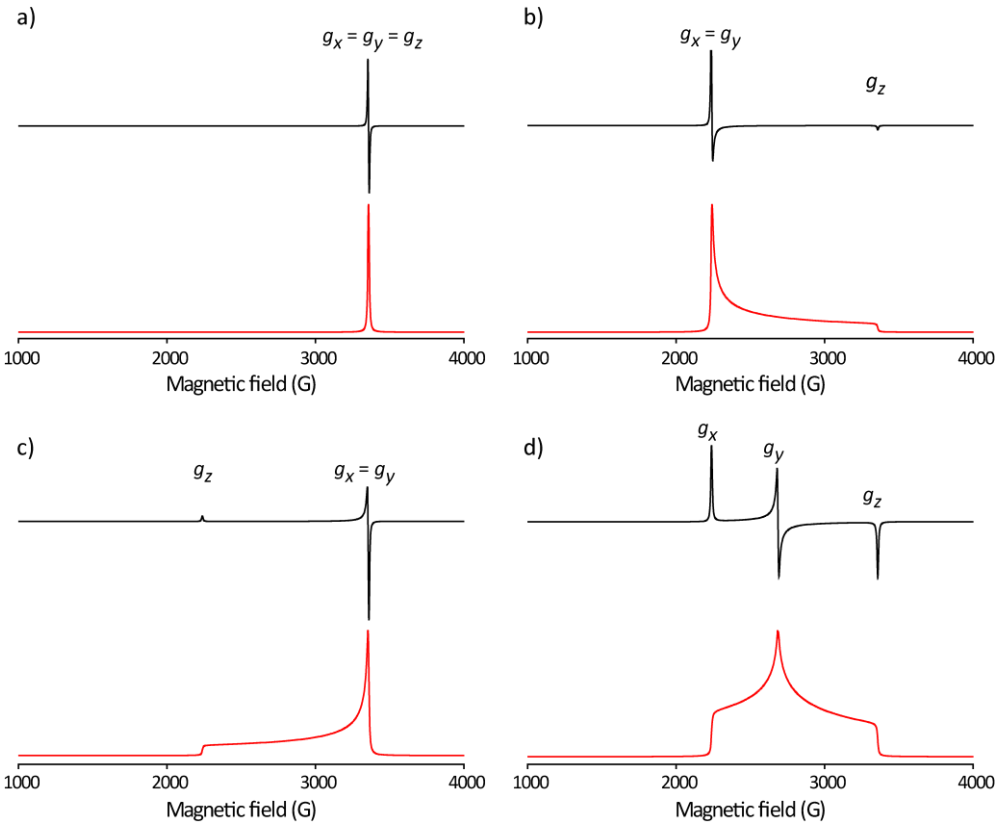

Figure 5: Manifestation of *g*-anisotropy in X-band (9.4 GHz) *cw* EPR spectra simulated with EasySpin.[30] The absorption spectrum is shown in red and its first derivative obtained from the experiment in black. a) Isotropic *g*-matrix ($g_x = g_y = g_z = 2.0$); b) Axial *g*-matrix ($g_x = g_y = 3.0$, $g_z = 2.0$); c) Axial *g*-matrix ($g_x = g_y = 2.0$, $g_z = 3.0$); d) Rhombic *g*-matrix ($g_x = 3.0$, $g_y = 2.5$, $g_z = 2.0$).

One example of axial and rhombic EPR spectra from this thesis are the aqua-complex and the azido-complex of metmyoglobin. The aqua-complex contains an Fe(III) ion in the *high*-spin state ($S = 5/2$) and leads to an axial spectrum, whereas the azido-complex contains *low*-spin Fe(III) ($S = 1/2$) and gives rise to a rhombic spectrum. Further details can be found in publication [P3].[15]

The effect of *g*-anisotropy on the EPR spectrum can be observed only if the paramagnetic species is either completely immobilized or if it rotates slowly on the timescale of the EPR experiment.[3(p.11)] If the molecule tumbles rapidly as is often the case for small molecules in solution, the *g*-matrix is averaged to the isotropic *g*-value [1,10(p.28)]

$$g_{iso} = \frac{1}{3}(g_x + g_y + g_z) \tag{27}$$

and an isotropic EPR spectrum will be obtained. In intermediate cases where the *g*-anisotropy is partially averaged, the tumbling of the paramagnetic molecule can be described by a rotational correlation time τ_{corr}.[1] For details, refer to section 1.2.1 and Figure 17.

1.1.4.2 Nuclear-Zeeman Interaction

Similar to electrons and in analogy to eq. (7), nuclei with a spin quantum number $I > 0$ (e.g. $I = 1/2$ for ^{1}H and $I = 1$ for ^{14}N) have a magnetic moment [20]

$$\vec{\mu}_n = g_n \frac{+e_p}{2m_p} \hbar \vec{I} = g_n \beta_n \vec{I} \tag{28}$$

Therein, g_n is the nuclear g-value, e_p the proton charge, m_p the proton mass, and β_n the nuclear magneton. The interaction of $\vec{\mu}_n$ with the external magnetic field is called the nuclear-Zeeman effect, and the corresponding Hamiltonian $\hat{H}_{NZ}$ reads [10(p.29)]

$$\hat{H}_{NZ} = -\frac{\beta_n}{\hbar} \overrightarrow{B_0}^T \boldsymbol{g_n} \hat{\vec{I}} \tag{29}$$

with the nuclear g-matrix $\boldsymbol{g_n}$, which is in principle anisotropic like the electron g-matrix $\boldsymbol{g_e}$ (eq. (26)). However, as the anisotropy of $\boldsymbol{g_n}$ is often negligible in EPR spectroscopy, it is commonly treated as isotropic and replaced by a scalar g_n.[10(p.29)] Being dimensionless and element-specific, g_n can be positive or negative and takes absolute values ranging from 0.097 (^{191}Ir) to 5.58 (^{1}H).[10(p.29)] Since the proton mass ($m_p = 1.673 \cdot 10^{-27}$ kg) is larger than the electron mass ($m_e = 9.109 \cdot 10^{-31}$ kg),[10(p.XXII)] the nuclear magneton [3(p.578)]

$$\beta_n = \frac{|e|\hbar}{2m_p} = 5.051 \cdot 10^{-27} \frac{J}{T} \tag{30}$$

is by a factor of 1836 smaller than Bohr's magneton β_e. Considering eq. (26) and eq. (29), it follows that the electron-Zeeman interaction is stronger than the nuclear-Zeeman interaction at the same magnetic field strength. For this reason, the nuclear-Zeeman effect is comparatively weak and often has no visible effect on the EPR spectrum.[10(p.29)]

1.1.4.3 Hyperfine Interaction

The magnetic moments of electrons and nuclei interact not only with the external magnetic field but also with each other if they are closer than approx. 1 nm.[6] This phenomenon is called hyperfine coupling. The corresponding hyperfine Hamiltonian [10(p.29)]

$$\hat{H}_{HF} = \hat{\vec{S}}^T \boldsymbol{A} \hat{\vec{I}} \tag{31}$$

with the hyperfine tensor $\boldsymbol{A}$ encompasses the isotropic Fermi-contact ($\hat{H}_{FC}$) and the anisotropic spin-dipolar interaction ($\hat{H}_{SD}$). The Fermi-contact term [6,10(p.29)]

$$\hat{H}_{FC} = a_{iso} \hat{\vec{S}}^T \hat{\vec{I}} \tag{32}$$

with the isotropic hyperfine coupling constant in angular frequency units [6,10(p.30)]

$$a_{\text{iso}} = \frac{2}{3} \frac{\mu_0}{\hbar} g_e \beta_e g_n \beta_n |\Psi_0(0)|^2 \tag{33}$$

results from the interaction of the electron-spin density at the position of the nucleus with the nuclear spin.[10(p.30),21] In eq. (33), μ_0 is the magnetic vacuum permeability and $|\Psi_0(0)|^2$, the absolute square of the electron wave function, represents the electron-spin density at the nucleus.[6] Isotropic hyperfine coupling requires spin density in an s-orbital, as this is the only type of orbital with a finite probability density at the nucleus.[6] As s-orbitals are spherical, the Fermi-contact interaction $\hat{H}_{FC}$ is isotropic [3(p.39)] and thus, it is not averaged out if the spin-bearing molecule tumbles rapidly, e.g. in solution.[27]

The spin-dipolar term [3(p.120),10(p.30)]

$$\hat{H}_{SD} = \frac{\mu_0}{4\pi\hbar} g_e \beta_e g_n \beta_n \left[\frac{3\left(\hat{\vec{S}}^T \vec{r}\right)\left(\vec{r}^T \hat{\vec{I}}\right)}{r^5} - \frac{\hat{\vec{S}}^T \hat{\vec{I}}}{r^3} \right] \tag{34}$$

describes the dipole-dipole interaction between $\overrightarrow{\mu_e}$ and $\overrightarrow{\mu_n}$, which are connected by the vector $\vec{r} = (r_x \quad r_y \quad r_z)^T$ of magnitude $r = |\vec{r}|$. As $\vec{r}$ takes the orientation of the dipole moments into account, the dipole-dipole interaction is anisotropic.[21]

Expanding eq. (34) by calculating the scalar product yields [3(p.121)]

$$\begin{aligned}\widehat{H}_{SD} = \frac{\mu_0}{4\pi\hbar} g_e\beta_e g_n\beta_n \\ \cdot \left\{\frac{3}{r^5}\left[\hat{S}_x\hat{I}_x\left(r_x{}^2 - \frac{r^2}{3}\right) + \hat{S}_x\hat{I}_y r_x r_y + \hat{S}_x\hat{I}_z r_x r_z + \hat{S}_y\hat{I}_x r_x r_y + \hat{S}_y\hat{I}_y\left(r_y{}^2 - \frac{r^2}{3}\right)\right.\right. \\ \left.\left. + \hat{S}_y\hat{I}_z r_y r_z + \hat{S}_z\hat{I}_x r_x r_z + \hat{S}_z\hat{I}_y r_y r_z + \hat{S}_z\hat{I}_z\left(r_z{}^2 - \frac{r^2}{3}\right)\right]\right\}\end{aligned} \tag{35}$$

Excluding $\hat{S}$ and $\hat{I}$, the nine summands in eq. (35) can be collected in the hyperfine dipolar interaction tensor $\boldsymbol{T}$ [3(p.121),21]

$$\boldsymbol{T} = \frac{\mu_0}{4\pi\hbar} g_e\beta_e g_n\beta_n \begin{pmatrix} \frac{3r_x{}^2 - r^2}{r^5} & \frac{3r_x r_y}{r^5} & \frac{3r_x r_z}{r^5} \\ \frac{3r_y r_x}{r^5} & \frac{3r_y{}^2 - r^2}{r^5} & \frac{3r_y r_z}{r^5} \\ \frac{3r_z r_x}{r^5} & \frac{3r_z r_y}{r^5} & \frac{3r_z{}^2 - r^2}{r^5} \end{pmatrix} = \frac{\mu_0}{4\pi\hbar} g_e\beta_e g_n\beta_n \begin{pmatrix} T_{xx} & T_{xy} & T_{xz} \\ T_{yx} & T_{yy} & T_{yz} \\ T_{zx} & T_{zy} & T_{zz} \end{pmatrix} \tag{36}$$

so that the spin-dipolar Hamiltonian transforms into [3(p.121),10(p.30)]

$$\widehat{H}_{SD} = \hat{\vec{S}}^T \boldsymbol{T} \hat{\vec{I}} \tag{37}$$

As discussed in the context of the *g*-tensor, $\boldsymbol{T}$ can be expressed in its principal axis system such that the off-diagonal elements vanish.[21] Eq. (36) reveals that $\boldsymbol{T}$ is symmetrical about its main diagonal $(\boldsymbol{T_{ij}} = \boldsymbol{T_{ji}})$ and traceless,[3(p.121),21] i.e. the sum of the diagonal elements equals zero:

$$\begin{aligned} T_{xx} + T_{yy} + T_{zz} &= \frac{\mu_0}{4\pi\hbar} g_e\beta_e g_n\beta_n \cdot \left[\left(\frac{3r_x{}^2 - r^2}{r^5}\right) + \left(\frac{3r_y{}^2 - r^2}{r^5}\right) + \left(\frac{3r_z{}^2 - r^2}{r^5}\right)\right] \\ &= \frac{\mu_0}{4\pi\hbar} g_e\beta_e g_n\beta_n \cdot \frac{1}{r^5}\left[\underbrace{3r_x{}^2 + 3r_y{}^2 + 3r_z{}^2}_{3r^2} - 3r^2\right] \\ &= 0 \end{aligned} \tag{38}$$

The fact that $\boldsymbol{T}$ is traceless implies that the anisotropic part of the dipolar interaction averages to zero if the paramagnetic species tumbles rapidly, e.g. in solution, so that $\widehat{H}_{SD}$ does not contribute to the EPR spectrum in this case.

Hyperfine interaction leads to a splitting of the signals in the EPR spectrum, which provides information on the local environment of the electron spin such as the identity and the number of nearby nuclei. In an isotropic EPR spectrum, the number of equidistant peaks that arise from hyperfine coupling is given by the multiplicity *M* [22]

$$M = 2nI + 1 \tag{39}$$

where n is the number of equivalent nuclei and *I* the nuclear-spin quantum number.

Figure 6a shows an energy level diagram of a spin system with *S* = 1/2 and *I* = 1, e.g. a nitroxide radical, including the electron-Zeeman (EZI), nuclear-Zeeman (NZI), and hyperfine (HFI) interactions yielding six energy levels (E_1-E_6) in total. Considering the selection rule of EPR spectroscopy (eq. (16)), three transitions are allowed, marked by coloured arrows in Figure 6a. These transitions lead to three lines in the EPR spectrum (Figure 6b), as confirmed by eq. (39).

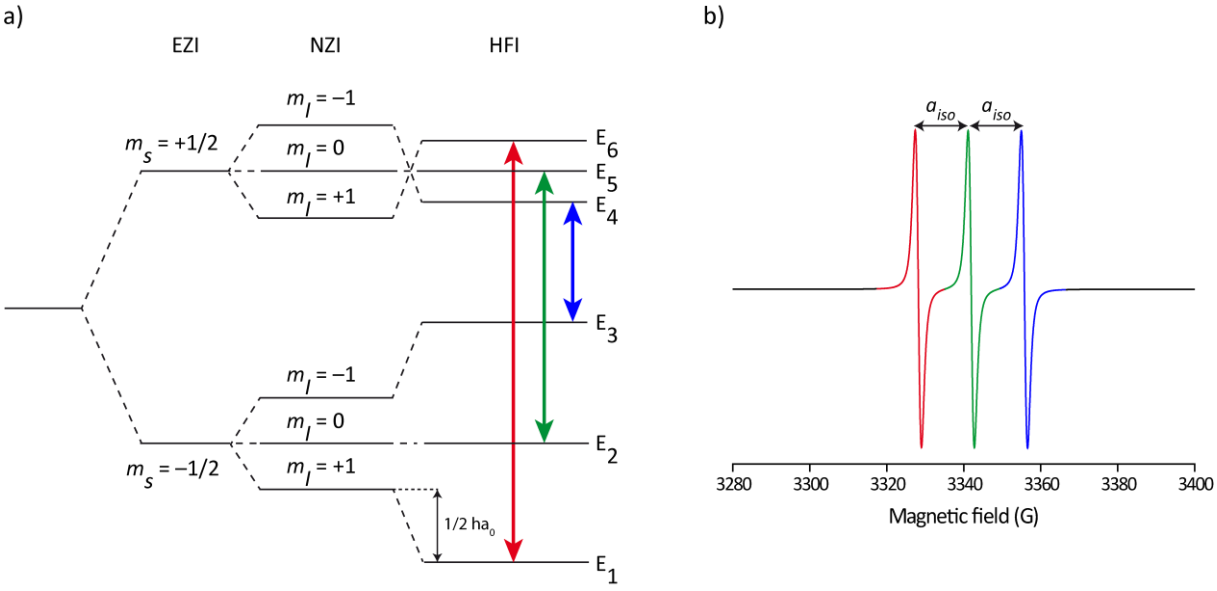

Figure 6: a) Schematic energy level diagram for a spin system with S = 1/2 and I = 1 including the electron-Zeeman (EZI), nuclear-Zeeman (NZI), and the hyperfine (HFI) interaction with a hyperfine-coupling constant $a_{iso} > 0$ and $|1/2\ ha_{iso}| > |g_n\beta_n B_0|$. Coloured arrows indicate the transitions allowed according to the selection rule of EPR spectroscopy ($\Delta m_s = \pm 1$; $\Delta m_I = 0$). b) EPR spectrum resulting from the transitions in (a) as simulated with EasySpin;[30] the peaks corresponding to the transitions in (a) are displayed in the same colour. Simulation parameters: g = 2.0055, a_{iso}= 38.7 MHz ≙ 13.8 G, peak-to-peak linewidth = [1 G, 1 G], given in the form of Gaussian and Lorentzian contributions. Adapted from [3(p.51),31(p.19),32].

Considering the electron-Zeeman splitting, the nuclear-Zeeman splitting, and the hyperfine interaction, the energy levels are given by [3(p.47),33]

$$E = g_e\beta_e m_s B_0 - g_n\beta_n m_I B_0 + h a_{iso} m_s m_I \tag{40}$$

This leads to the following expressions for the energy levels E_1 to E_6 shown in Figure 6a:[3(p.51)]

$$\begin{aligned}
E_1 &= -\frac{1}{2} g_e\beta_e B_0 - g_n\beta_n B_0 - \frac{1}{2} h a_{iso} & E_4 &= +\frac{1}{2} g_e\beta_e B_0 + g_n\beta_n B_0 - \frac{1}{2} h a_{iso} \\
E_2 &= -\frac{1}{2} g_e\beta_e B_0 & E_5 &= +\frac{1}{2} g_e\beta_e B_0 \\
E_3 &= -\frac{1}{2} g\beta_e B_0 + g_n\beta_n B_0 + \frac{1}{2} h a_{iso} & E_6 &= +\frac{1}{2} g_e\beta_e B_0 - g_n\beta_n B_0 + \frac{1}{2} h a_{iso}
\end{aligned} \tag{41}$$

The allowed transitions are associated with the energy differences $\Delta E_{red,\ green,\ blue} = h\nu$ and the resonance fields $B_{red,\ green,\ blue}$ (colours refer to Figure 6) [3(p.51)]

$$\begin{aligned}
\Delta E_{red} &= E_6 - E_1 = g_e\beta_e B_0 + h a_{iso} & \rightarrow \quad B_{red} &= \frac{h\nu}{g_e\beta_e} - \frac{a_{iso} h}{g\beta_e} \\
\Delta E_{green} &= E_5 - E_2 = g_e\beta_e B_0 & \rightarrow B_{green} &= \frac{h\nu}{g_e\beta_e} \\
\Delta E_{blue} &= E_4 - E_3 = g_e\beta_e B_0 - h a_{iso} & \rightarrow \quad B_{blue} &= \frac{h\nu}{g_e\beta_e} + \frac{a_{iso} h}{g_e\beta_e}
\end{aligned} \tag{42}$$

Figure 6 and eq. (41)-(42) reveal that the three lines in the isotropic nitroxide spectrum are separated by the hyperfine coupling constant a_{iso}. Importantly, as a constant, a_{iso} is independent of the field/frequency combination used for recording the EPR spectrum.

Hyperfine coupling constants can be interpreted in terms of molecular structures and properties: Isotropic hyperfine coupling permits drawing conclusions on the spin-density distribution in a molecule.[27] The anisotropic part encodes the distance between the unpaired electron and the coupled nucleus:[27] By measuring the hyperfine coupling using electron-nuclear double resonance (ENDOR) spectroscopy,[34] distances of up to 15 Å between electron and nuclear spins could be determined at a precision of 0.1 Å.[35] Especially for studying the active sites of proteins or nucleic acids, the distance range below 15 Å is of particular interest.[35] Further, hyperfine coupling constants report on physicochemical properties such as the polarity of the microenvironment surrounding the electron spin.[36]

1.1.4.4 Nuclear-quadrupole interaction and nuclear spin-spin interaction

Nuclei with a spin quantum number $I \geq 1$ have a non-spherical charge distribution, which gives rise to an isotope-specific nuclear electric quadrupole moment.[10(p.32)] The nuclear quadrupole moment interacts with the electric field gradient caused by the surrounding electrons and nuclei,[10(p.32)] with the nuclear-quadrupole Hamiltonian $\widehat{H}_{NQ}$ given by [10(p.32)]

$$\widehat{H}_{NQ} = \widehat{\vec{I}}^{T} \boldsymbol{P} \widehat{\vec{I}} \tag{43}$$

Therein, $\boldsymbol{P}$ is the nuclear-quadrupole tensor, which is traceless in its PAS, i.e. the nuclear-quadrupole interaction averages to zero if the molecule tumbles.[37] Nuclear quadrupole coupling has only minor effects on the EPR spectrum, as it often vanishes below the inhomogeneous linewidth.[37] If it is observable, though, it manifests itself by equally shifting all lines of a spectrum, but it does not cause additional splitting of EPR lines.[37]

The dipolar interaction between the nuclear spins I_i and I_k is described by the Hamiltonian [10(p.34)]

$$\widehat{H}_{NN} = \widehat{\vec{I}_i}^{T} \boldsymbol{d}^{(i,k)} \widehat{\vec{I}_k} \tag{44}$$

where $\boldsymbol{d}^{(i,k)}$ is the nuclear dipole coupling tensor. As the nuclear dipolar interaction is much smaller than all other interactions in the spin Hamiltonian, it usually cannot be resolved in EPR spectroscopy, but it is routinely used in NMR to determine molecular structures.[10(p.34)]

1.1.4.5 Zero-Field Splitting

In paramagnetic centres with more than one unpaired electron, e.g. molecules in triplet states and *high*-spin metal ions, the spins interact with each other. If the coupling between the magnetic moments of the electron spins is strong, the spins can no longer be treated separately, but rather add up to a total spin $S > 1/2$.[27] In such systems, the ground state has a multiplicity of $M = 2S+1$,[10(p.33)] e.g. a triplet state for $S = 1$. Due to zero-field splitting (ZFS), which is based on the dipolar coupling between the electron spins and on SOC, the three sublevels of the triplet state are not degenerate even in the absence of a magnetic field.[10(p.33)]

The ZFS-Hamiltonian [4,10(p.33)]

$$\widehat{H}_{ZFS} = \widehat{\vec{S}}^{T} \boldsymbol{D} \widehat{\vec{S}} \tag{45}$$

contains the symmetric and traceless zero-field interaction tensor $\boldsymbol{D}$.[10(p.33)]

1.1.4.6 Electron-Spin Dipolar Coupling

For the following discussion, it is assumed that two spin centres (S = 1/2), referred to as spin 1 and spin 2, are located at the Cartesian coordinates (x_1, y_1, z_1) and (x_2, y_2, z_2) in an external magnetic field $\overrightarrow{B_0}$. The direction of $\overrightarrow{B_0}$ shall coincide with the z-axis of the Cartesian grid. The orientation of spin 2 relative to spin 1 is given by the polar coordinates ($\vec{r}$, θ, φ),[8,38(p.67)] where $\vec{r}$ is the distance vector connecting spins 1 and 2, θ the zenith angle between $\vec{r}$ and the z-axis, and φ the azimuth angle between the x-axis and the projection of $\vec{r}$ onto the xy-plane (Figure 7).[28(p.94),38(p.67),39]

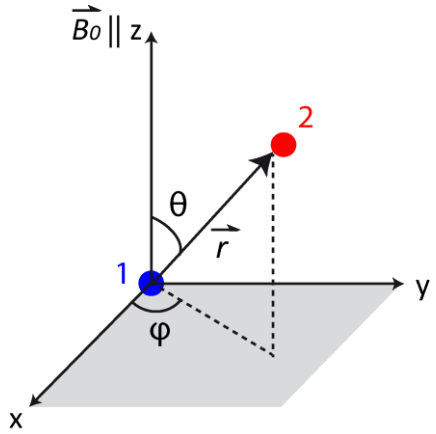

Figure 7: Schematic representation of two electron spins 1 and 2 (blue and red spheres) connected by the distance vector $\vec{r}$. The zenith angle θ and the azimuth angle φ describe the orientation of $\vec{r}$ with respect to the external magnetic field $\overrightarrow{B_0}$.[28(p.94)] The shaded area indicates the xy-plane. Adapted from [38(p.67),40].

Both electrons will be treated as point dipoles (point-dipole approximation), which is a valid assumption for interspin distances larger than approx. 2 nm if spin delocalization is negligible.[41]

As given by classical physics, a magnetic moment $\vec{\mu}$ induces a magnetic field $\vec{B}(\vec{r},\vec{\mu})$, whose strength at a point $\vec{r}$ is given by [41]

$$\vec{B}(\vec{r},\vec{\mu}) = -\frac{\mu_0}{4\pi}\frac{1}{r^3}\left[\vec{\mu} - \frac{3}{r^2}(\vec{\mu}^T \cdot \vec{r})\,\vec{r}\right] \tag{46}$$

with $r = |\vec{r}|$. The magnetic moment $\overrightarrow{\mu_1}$ associated with spin 1 interacts with the magnetic field induced by $\overrightarrow{\mu_2}$, with the interaction energy of the two magnetic dipoles being [41]

$$E_{DD} = -\overrightarrow{\mu_1}^T \cdot \vec{B}(\vec{r},\overrightarrow{\mu_2}) = -\overrightarrow{\mu_2}^T \cdot \vec{B}(\vec{r},\overrightarrow{\mu_1}) \tag{47}$$

Substituting $\vec{B}(\vec{r},\vec{\mu})$ in eq. (47) by eq. (46) yields [8,41]

$$E_{DD} = \frac{\mu_0}{4\pi}\cdot\frac{1}{r^3}\left[\overrightarrow{\mu_1}^T\,\overrightarrow{\mu_2} - \frac{3}{r^2}\left(\overrightarrow{\mu_1}^T\,\vec{r}\right)\left(\overrightarrow{\mu_2}^T\,\vec{r}\right)\right] \tag{48}$$

Based on the correspondence principle,[41] this classical expression for the interaction energy between $\overrightarrow{\mu_1}$ and $\overrightarrow{\mu_2}$ can be translated into the quantum-mechanical dipole-dipole Hamiltonian $\hat{H}_{DD}$. Substituting $\overrightarrow{\mu_1}$ and $\overrightarrow{\mu_2}$ using eq. (10) yields [8]

$$\hat{H}_{DD} = \frac{\mu_0}{4\pi}\cdot\frac{1}{r^3}\cdot\gamma_1\gamma_2\hbar^2\left[\widehat{\vec{S}_1}^T\,\widehat{\vec{S}_2} - \frac{3}{r^2}\left(\widehat{\vec{S}_1}^T\,\vec{r}\right)\left(\widehat{\vec{S}_2}^T\,\vec{r}\right)\right] \tag{49}$$

The gyromagnetic ratios γ_1 and γ_2 of the two electrons can be substituted by [41]

$$\gamma_1 = g_1\frac{\beta_e}{\hbar} \text{ and } \gamma_2 = g_2\frac{\beta_e}{\hbar} \tag{50}$$

which leads to the Hamiltonian for the dipolar coupling of two electron spins in energy units

$$\widehat{H}_{DD} = \frac{\mu_0}{4\pi} \cdot \frac{1}{r^3} \cdot g_1 g_2 \beta_e^2 \left[\widehat{\vec{S}_1}^T \widehat{\vec{S}_2} - \frac{3}{r^2} \left(\widehat{\vec{S}_1}^T \vec{r} \right) \left(\widehat{\vec{S}_2}^T \vec{r} \right) \right] \tag{51}$$

According to eq. (18), division by $\hbar$ yields $\widehat{H}_{DD}$ in angular frequency units [10(p.34)]

$$\widehat{H}_{DD} = \frac{\mu_0}{4\pi\hbar} \cdot \frac{1}{r^3} \cdot g_1 g_2 \beta_e^2 \left[\widehat{\vec{S}_1}^T \widehat{\vec{S}_2} - \frac{3}{r^2} \left(\widehat{\vec{S}_1}^T \vec{r} \right) \left(\widehat{\vec{S}_2}^T \vec{r} \right) \right] \tag{52}$$

If the point-dipole approximation is fulfilled for both electron spins and if their magnetic moments are aligned parallel to $\overrightarrow{B_0}$,[41] the dipolar Hamiltonian can be split into the operators $\hat{A} - \hat{F}$, which constitute the so-called dipolar alphabet [8,38(p.66),41]

$$\widehat{H}_{DD} = \frac{\mu_0}{4\pi\hbar} \cdot \frac{1}{r^3} \cdot g_1 g_2 \beta_e^2 \left(\hat{A} + \hat{B} + \hat{C} + \hat{D} + \hat{E} + \hat{F} \right) \tag{53}$$

with [8,38(p.66),41]

$$\begin{aligned}
\hat{A} &= \hat{S}_1^z \hat{S}_2^z \left(1 - 3\cos^2\theta\right) \\
\hat{B} &= -\frac{1}{4} \left(\hat{S}_1^+ \hat{S}_2^- + \hat{S}_1^- \hat{S}_2^+ \right) \left(1 - 3\cos^2\theta\right) \\
\hat{C} &= -\frac{3}{2} \left(\hat{S}_1^+ \hat{S}_2^z + \hat{S}_1^z \hat{S}_2^+ \right) \sin\theta \cos\theta \, e^{-i\varphi} \\
\hat{D} &= -\frac{3}{2} \left(\hat{S}_1^- \hat{S}_2^z + \hat{S}_1^z \hat{S}_2^- \right) \sin\theta \cos\theta \, e^{i\varphi} \\
\hat{E} &= -\frac{3}{4} \hat{S}_1^+ \hat{S}_2^+ \sin^2\theta \, e^{-2i\varphi} \\
\hat{F} &= -\frac{3}{4} \hat{S}_1^- \hat{S}_2^- \sin^2\theta \, e^{2i\varphi}
\end{aligned} \tag{54}$$

The terms $\hat{A} - \hat{F}$ are products of a spin-operator part that contains $\hat{S}^+$, $\hat{S}^-$, and $\hat{S}_z$ and an angular part involving θ and φ.[42(p.36),43(p.279)] As angular contributions are present in all terms $\hat{A} - \hat{F}$, the dipolar interaction is purely anisotropic.[44(p.113)] $\hat{S}^+$ and $\hat{S}^-$ are the raising and lowering operators [41]

$$\begin{aligned}
\hat{S}^+ &= \hat{S}_x + i\hat{S}_y \\
\hat{S}^- &= \hat{S}_x - i\hat{S}_y
\end{aligned} \tag{55}$$

that change m_s by ±1.[10(p.75),42(p.37)] A derivation of the expressions $\hat{A} - \hat{F}$ starting from classical physics is given in appendix 7.1. For discussing the effect of the operators $\hat{A} - \hat{F}$ on the two-spin system, it is convenient to introduce a total magnetic quantum number M_S, which is the sum of the individual magnetic quantum numbers of spins 1 and 2:[38(p.69)]

$$M_S = m_{s,1} + m_{s,2} \tag{56}$$

Figure 8 illustrates the transitions between the different combinations of m_s-levels and indicates the effect of the operators $\hat{A} - \hat{F}$ on M_S.

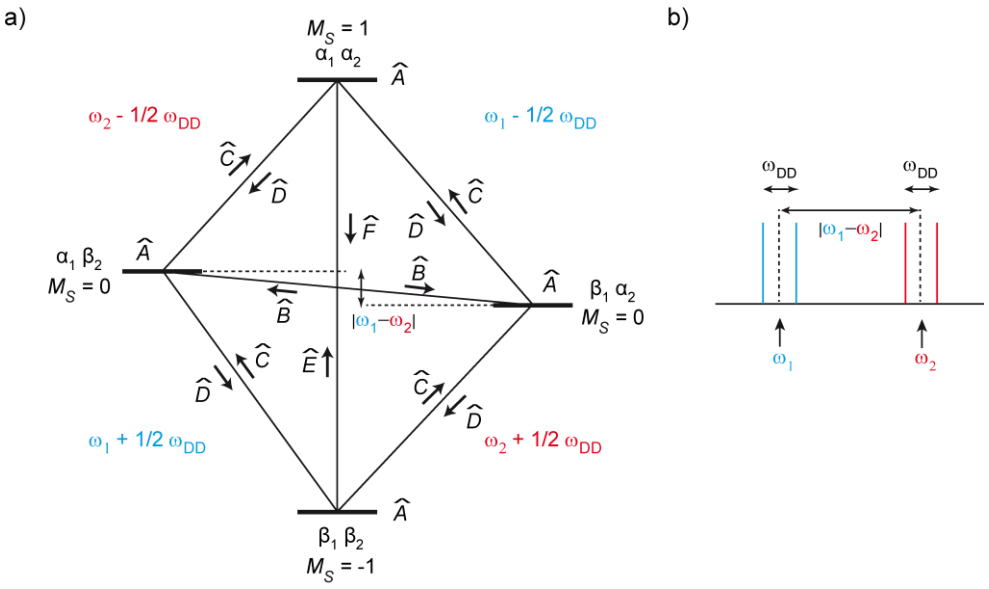

Figure 8: Dipolar coupling of two electron spins. a) Energy level diagram for a system of two dipolar-coupled electron spins 1 and 2. The subscript letters (1, 2) denote the electron spin; α and β refer to the magnetic quantum numbers m_s = +1/2 ("spin up") and m_s = -1/2 ("spin down"), respectively. M_S denotes the total magnetic quantum number of the respective energy level. $\hat{A} - \hat{F}$ are the operators of the dipolar alphabet. b) Schematic stick spectrum. The resonance lines of the spins centred at the frequencies ω_1 and ω_2 are split by the dipolar coupling frequency ω_{DD}. Adapted from [41,45,46].

Figure 8a reveals that $\hat{A}$ and $\hat{B}$ correspond to zero-quantum transitions ($\Delta M_S = 0$):[43(p.147),45] While $\hat{A}$ does not change the magnetic quantum number of either spin (it contains no raising or lowering operator),[47(p.659)] $\hat{B}$ is called the "flip-flop"-term [45] that alters the magnetic quantum number of both spins ($\alpha_1\beta_2 \leftrightarrow \beta_1\alpha_2$). As spins 1 and 2 are flipped in reverse direction, M_S = 1 for both states connected by $\hat{B}$. $\hat{C}$ and $\hat{D}$ correspond to single-quantum transitions ($\Delta M_S = \pm 1$) [43(p.147)] in which only one spin is flipped (e.g. $\beta_1\beta_2 \leftrightarrow \beta_1\alpha_2$). Note that the angular parts of $\hat{C}$ and $\hat{D}$ are complex conjugates of each other (eq. (54)).[29(p.170),42(p.37)] $\hat{E}$ and $\hat{F}$ correspond to double-quantum transitions ($\Delta M_S = \pm 2$),[43(p.147)] i.e. both spins are flipped into the same direction ("flip-flip", e.g. $\beta_1\beta_2 \leftrightarrow \alpha_1\alpha_2$).[45,48] As with $\hat{C}$ and $\hat{D}$, the angular parts of $\hat{E}$ and $\hat{F}$ are complex conjugates of each other (eq. (54)).[42(p.37)]

As shown by eq. (17), the electron-Zeeman splitting E_{EZI} scales with $B_{0,z}$, whereas the dipolar interaction E_{DD} (eq. (48)) is independent of the external magnetic field.[17] Consequently, at high magnetic fields (> 1 T),[41] the Zeeman interaction exceeds all other interactions of the electron spin [17] including the dipolar coupling ($E_{EZI} >> E_{DD}$ or equivalently $\omega_1 >> \omega_{DD}$, $\omega_2 >> \omega_{DD}$),[41] a situation that is called the high-field approximation.[17] Depending on the magnitude of the dipolar coupling frequency ω_{DD} relative to the Larmor frequencies ω_1 and ω_2 in the absence of dipolar coupling, some terms of the dipolar alphabet become negligible.[41]

One can classify the operators $\hat{A} - \hat{F}$ as *secular*, *non-secular*, and *pseudo-secular*.[41] In this context, *secular* means that the operator is time-independent in the rotating frame [44(p.155)] ("secular" originates from the Latin word *saeculum*, which means "generations ago" [49] in the sense of a long period of time), while *non-secular* implies a time-dependence. *Pseudo-secular* terms *can* have a time dependence, depending on whether "like" or "unlike" spins are considered. The dipolar-coupled spins 1 and 2 are called "like" spins if ω_{DD} is much larger than the difference in their Larmor frequencies [41,45]

$$\omega_{DD} \gg \Delta\omega_{1,2} = |\omega_1 - \omega_2| \tag{57}$$

and "unlike" spins if [45]

$$\omega_{DD} \ll \Delta\omega_{1,2} = |\omega_1 - \omega_2| \tag{58}$$

The case of "like" spins may occur in single-frequency PDS experiments (sections 1.2.3.3-1.2.3.4), where pulses at one microwave frequency simultaneously excite spins 1 and 2.[41] By contrast, in double-frequency experiments like PELDOR (section 1.2.3.1) where spin 1 and spin 2 are addressed by two different microwave frequencies, the spins are classified as "unlike".[41,50]

In the framework of the secular approximation, only those operators $\hat{A} - \hat{F}$ that are time-independent in the rotating frame are relevant and have to be retained for further consideration.[51(p.37–39)] Non-secular operators, on the other hand, contain rapidly oscillating terms that average to zero and can thus be neglected.[51(p.37–39)] The transformation of the operators $\hat{A} - \hat{F}$ from the laboratory frame into the rotating frame and their time (in)dependence is shown in appendix 7.2.

As can be inferred from eq. (54), the $\hat{A}$-term of the dipolar alphabet contains only spin operators that act along the z-axis, i.e. the quantization axis of the electron spin. Being time-independent in the rotating frame, $\hat{A}$ is referred to as the *secular* term that must always be retained.[41]

The $\hat{B}$-term is called *pseudo-secular*, as it can be secular or non-secular depending on whether "like" spins or "unlike" spins are considered.[41] Thus, a case distinction is necessary here: For "like" spins with identical Larmor frequencies ($\omega_1 = \omega_2$), it can be shown that the time-dependent terms vanish so that $\hat{B}$ is classified as secular (appendix 7.2) and has to be retained in the dipolar Hamiltonian.[52] An exception to this rule occurs if the width of the EPR spectrum and the excitation bandwidth of the microwave pulses both exceed ω_{dd}.[41,53] This holds true for single-frequency PDS experiments with trityl radicals and an interspin distance above approx. 2.5 nm,[54] provided that the microwave pulses excite the whole spectrum (30 MHz at Q-band [26]) and that exchange coupling (section 1.1.4.7) is smaller than the dipolar coupling.[53] For "unlike" spins ($\omega_1 \neq \omega_2$), by contrast, the time dependence persists, i.e. $\hat{B}$ is non-secular and can be neglected.[52] This situation applies to PELDOR experiments with nitroxide spin labels.[41]

The terms $\hat{C}$ and $\hat{D}$ are negligible if the high-field approximation is fulfilled for both spins [41,55]

$$\omega_{DD} \ll \omega_1 \textbf{ and } \omega_{DD} \ll \omega_2 \tag{59}$$

Relations (59) typically hold true at microwave frequencies above 9 GHz and for distances above 1.5-2 nm.[28(p.95),56] The double-quantum transitions described by the operators $\hat{E}$ and $\hat{F}$ are negligible if at least one of the Larmor frequencies exceeds ω_{DD} [41]

$$\omega_{DD} \ll \omega_1 \textbf{ or } \omega_{DD} \ll \omega_2 \tag{60}$$

Note that relations (60) are trivial whenever relations (59) are fulfilled. For the reasons discussed above, the terms $\hat{C} - \hat{F}$ are called *non-secular*. Considering only the secular part $\hat{A}$, $\hat{H}_{DD}$ reads

$$\hat{H}_{DD} = \frac{\mu_0}{4\pi\hbar} \cdot \frac{1}{r^3} \cdot g_1 g_2 \beta_e^2 \cdot \hat{S}_1^z \hat{S}_2^z \, (1 - 3\cos^2\theta) = \omega_{DD} \hat{S}_1^z \hat{S}_2^z \tag{61}$$

with the dipolar coupling frequency ω_{DD} [40]

$$\omega_{DD}(\theta, r) = \frac{\mu_0}{4\pi\hbar} \cdot \frac{1}{r^3} \cdot g_1 g_2 \beta_e^2 \cdot (1 - 3\cos^2\theta) \tag{62}$$

Using $\hbar = h/2\pi$ and by assuming $g_1 = g_2 = 2$, eq. (62) simplifies to

$$\omega_{DD}(\theta, r) = \underbrace{\frac{4\mu_0 \beta_e^2}{4\pi \cdot h}}_{52 \text{ MHz nm}^3} \cdot 2\pi \cdot \frac{1}{r^3} \cdot (1 - 3\cos^2\theta) = D_{Dip} \cdot \frac{1}{r^3} \cdot (1 - 3\cos^2\theta) \tag{63}$$

with the dipolar coupling constant $D_{Dip} = 2\pi \cdot 52$ MHz nm^3.[8]

Equation (63) reveals that ω_{DD} ranges between

$$\omega_{DD,\perp} = \omega_{DD}(\theta = 90°, r) = \frac{D_{Dip}}{r^3} \tag{64}$$

If the interspin vector is perpendicular to the magnetic field and

$$\omega_{DD,||} = \omega_{DD}(\theta = 0°, r) = -2\frac{D_{Dip}}{r^3} \tag{65}$$

for the parallel orientation. Eq. (62)-(65) also show that ω_{DD} is inversely proportional to the cube of the interspin distance; e.g., at r = 1 nm, $\omega_{DD,\perp} = 326\ \mathrm{MHz}$ and at r = 10 nm, $\omega_{DD,\perp} = 326\ \mathrm{kHz}$. Notably, at the magic angle $\theta = \arccos\left(\sqrt{1/3}\right) \approx 54.74°$, the dipolar coupling vanishes as $(1 - 3\cos^2\theta) = 0$. This fact is exploited by the so-called magic angle spinning (MAS) in solid-state NMR spectroscopy: By quickly spinning a sample tube at the magic angle with respect to $\overrightarrow{B_0}$, the time average of θ corresponds to the magic angle for all dipolar-coupled spins. Thus, under MAS, the dipolar coupling is averaged out and the dipolar broadening vanishes, which increases the spectral resolution and the sensitivity.[48]

If the molecule tumbles rapidly, e.g. in solution, the orientation of $\vec{r}$ with respect to $\overrightarrow{B_0}$ changes continuously and the angle θ can take any value between 0 and 360°. The probability $P(\theta)$ of a particular value θ is proportional to $\sin(\theta)$.[57] Thus, by weighting ω_{DD} with $P(\theta)$ and integrating over $\theta = [0, 2\pi]$, it can be shown that ω_{DD} is averaged to zero if the molecule tumbles:

$$\begin{aligned}\int_0^{2\pi} \omega_{DD}(\theta, r) \cdot P(\theta)\, d\theta &= D_{Dip} \cdot \frac{1}{r^3} \int_0^{2\pi} (1 - 3\cos^2\theta) \cdot \sin\theta\ d\theta \\ &= \left[D_{Dip} \cdot \frac{1}{r^3} \cdot \sin^2\theta \cdot (-\cos\theta) \right]_0^{2\pi} = 0\end{aligned} \tag{66}$$

This implies that no dipolar coupling can be measured in solution unless the molecule is immobilized. The dipolar Hamiltonian (eq. (49)) can be given in tensorial form, which reads

$$\hat{H}_{DD} = \widehat{\overrightarrow{S_1}}^T \boldsymbol{D}\, \widehat{\overrightarrow{S_2}} \tag{67}$$

under the secular approximation.[10(p.34)] Herein, $\boldsymbol{D}$ is the dipolar coupling tensor [10(p.34)]

$$\boldsymbol{D} = \frac{\mu_0}{4\pi\hbar} \cdot \frac{1}{r^3} g_1 g_2 \beta_e^2 \begin{pmatrix} -1 & & \\ & -1 & \\ & & 2 \end{pmatrix} = \begin{pmatrix} -\omega_{DD} & & \\ & -\omega_{DD} & \\ & & 2\omega_{DD} \end{pmatrix} \tag{68}$$

As the dipolar coupling vanishes if the molecule rotates, $\boldsymbol{D}$ is traceless.[41]

In disordered solids like a frozen solution or a powder, the paramagnetic molecules are oriented randomly. For such a situation, the intensity $I\left(\omega_{DD}(r,\theta)\right)$ of the dipolar spectrum reads [29(p.171)]

$$I\left(\omega_{DD}(r,\theta)\right) = \frac{\sin\theta}{\left(\frac{d\omega_{DD}(r,\theta)}{d\theta}\right)} = \frac{1}{\frac{6\ D_{Dip}}{r^3}\cos\theta} \tag{69}$$

where the denominator is given by the derivative of eq. (63)

$$\frac{d}{d\theta}\omega_{DD}(r,\theta) = \frac{6\ D_{Dip}}{r^3}\cos\theta\sin\theta \tag{70}$$

Re-arranging eq. (63) for $\cos\theta$ yields

$$\cos\theta = \frac{1}{\sqrt{3}}\sqrt{1 - \frac{\omega_{DD}}{D_{Dip}/r^3}} \tag{71}$$

Inserting eq. (71) into eq. (69) leads to

$$I\left(\omega_{DD}(r,\theta)\right) = \frac{1}{\frac{6D_{Dip}}{r^3}\frac{1}{\sqrt{3}}\sqrt{1-\frac{\omega_{DD}}{D_{Dip}/r^3}}} \tag{72}$$

Eq. (72) describes one half of the dipolar powder spectrum of a two-spin system (S = 1/2), the second half is obtained by inverting the sign of $\omega_{DD}(r,\theta)$.[29(p.171)] Summing both halves yields the whole dipolar powder spectrum, which is called a Pake Pattern after its discoverer G. Pake.[58] Figure 9a shows the correlation between θ and ω_{dd} and Figure 9b the Pake Pattern.

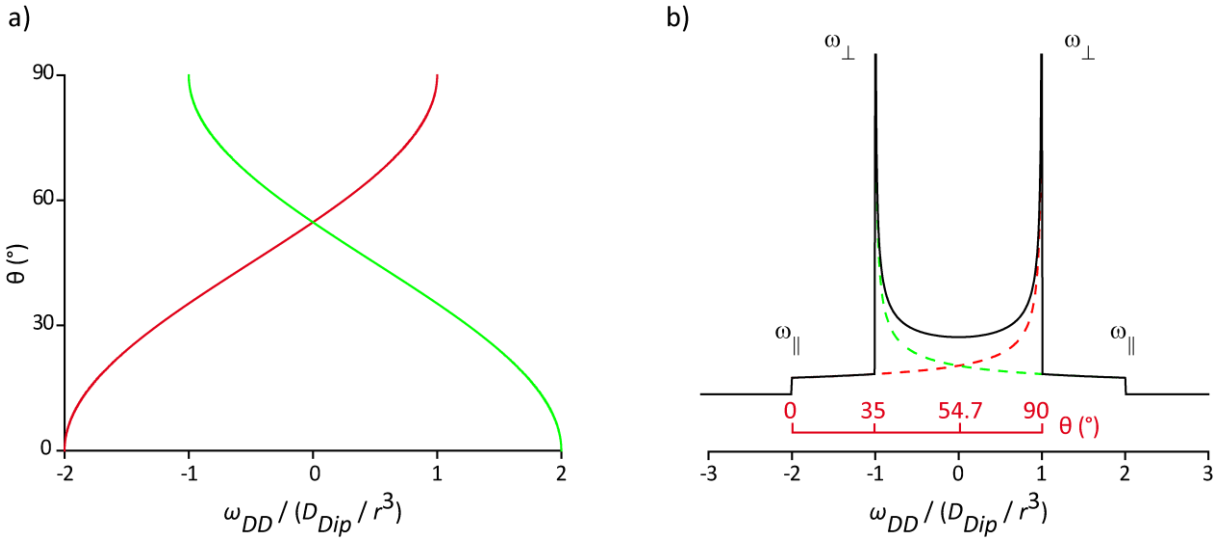

Figure 9: Electron-spin dipolar coupling. a) Relation between the dipolar coupling frequency $\omega_{DD}/(D_{Dip}/r^3)$ and the angle θ according to eq. (71) (red) and its mirror image (green). b) Construction of the Pake Pattern: The red line corresponds to eq. (72), the green line is its mirror image. The spectrum shown in black is the Pake Pattern obtained as the sum of the red and green lines.

As can be gleaned from Figure 9a, the dipolar coupling frequency (red line) ranges from $\omega_{DD} = -2\frac{D_{Dip}}{r^3}$ at $\theta = 0°$ to $\omega_{DD} = +1\frac{D_{Dip}}{r^3}$ at $\theta = 90°$. The green line is obtained by mirroring the red one at zero frequency. The Pake pattern (Figure 9b) has singularities at $\omega_{DD,||} = \pm 2\frac{D_{Dip}}{r^3}$ corresponding to the parallel orientation ($\theta = 0°$) of $\vec{r}$ with respect to $\overrightarrow{B_0}$ and at $\omega_{DD,\perp} = \pm\frac{D_{Dip}}{r^3}$ for the perpendicular orientation ($\theta = 90°$).

This shows that the interspin distance can be calculated from the dipolar coupling frequency ω_{DD}, provided that the angles θ are sampled homogeneously and that the Pake pattern is experimentally accessible. For the distance range encountered in biological samples (typically 1.5-16 nm),[40,59] the dipolar coupling is measured using PDS (section 1.2.3).

1.1.4.7 Electron-Spin Exchange Coupling

In addition to the dipolar coupling introduced in section 1.1.4.6, exchange coupling occurs between electron spins if the orbitals of the unpaired electrons overlap.[10(p.32)] In the liquid state, collisions of spin centres can lead to orbital overlap.[10(p.34)] In the solid state, orbitals overlap if the interspin distance is below approx. 1.5 nm [10(p.34)] or if the spins are delocalized,[10(p.34)] e.g. as a result of conjugated molecular bridges connecting the two spin centres.[60]

The Heisenberg-Dirac-van Vleck (HDvV) [61(p.106)] Hamiltonian for exchange coupling is given by [5]

$$\widehat{H}_{ex} = -2J\,\widehat{\vec{S}_1}^{T} \cdot \widehat{\vec{S}_2} \tag{73}$$

with the exchange coupling constant *J*. Although *J* can in principle be anisotropic and would then be a tensor, it is common for organic radicals to treat the exchange interaction as isotropic and *J* as a scalar.[3(p.160),10(p.34)] As a result, the exchange interaction can be observed in solution, by contrast to the dipolar interaction that is averaged out if the molecule tumbles (section 1.1.4.6).[5] Note that there are different variants of the exchange Hamiltonian, e.g. $\widehat{H}_{ex} = -J\,\widehat{\vec{S}_1}^{T}\,\widehat{\vec{S}_2}$ and $\widehat{H}_{ex} = +J\,\widehat{\vec{S}_1}^{T}\,\widehat{\vec{S}_2}$.[5] Thus, care needs to be taken when comparing different values of *J*. Throughout this thesis, the convention defined in eq. (73) will be used.

Exchange interaction leads to a situation where the spins of the two electrons can no longer be treated separately (e.g. S_1 and S_2 for electrons 1 and 2).[5,61(p.103)] Instead and similar to the spin-spin interactions discussed with respect to zero-field splitting, the system is characterized by a total spin quantum number *S*, which can take the values [5]

$$S_1 + S_2, S_1 + S_2 - 1, \ldots, |S_1 - S_2| \tag{74}$$

For two unpaired electrons with $S_1 = 1/2$, $S_2 = 1/2$, this leads to $S = 1$ and $S = 0$, where the former is called a triplet state and the latter is a singlet state.[3(p.160)] The energy of the spin states is given by [5]

$$E(S, S_1, S_2) = -J[S(S+1) - S_1(S_1+1) - S_2(S_2+1)] \tag{75}$$

and consequently, $E = +1.5\,J$ for the singlet state and $E = -0.5\,J$ for the triplet state. The energy gap $\Delta E = 2J$ typically ranges between 0 cm^{-1} and approx. 1000 cm^{-1} (0-30,000 GHz).[5]

The nomenclature of the exchange coupling depends on the sign of *J*: If $J > 0$, the higher spin state ($S = 1$) is the ground state and the exchange coupling is called *ferromagnetic*.[5,61(p.26)] This corresponds to a "weak antibonding situation".[10(p.34)] Conversely, if $J < 0$, the lower spin state ($S = 0$) is the ground state and the exchange coupling is called *antiferromagnetic*,[5,61(p.26)] which corresponds to a "weak bonding situation".[10(p.34)]

Figure 10 shows the energy levels for ferromagnetic and antiferromagnetic exchange coupling.

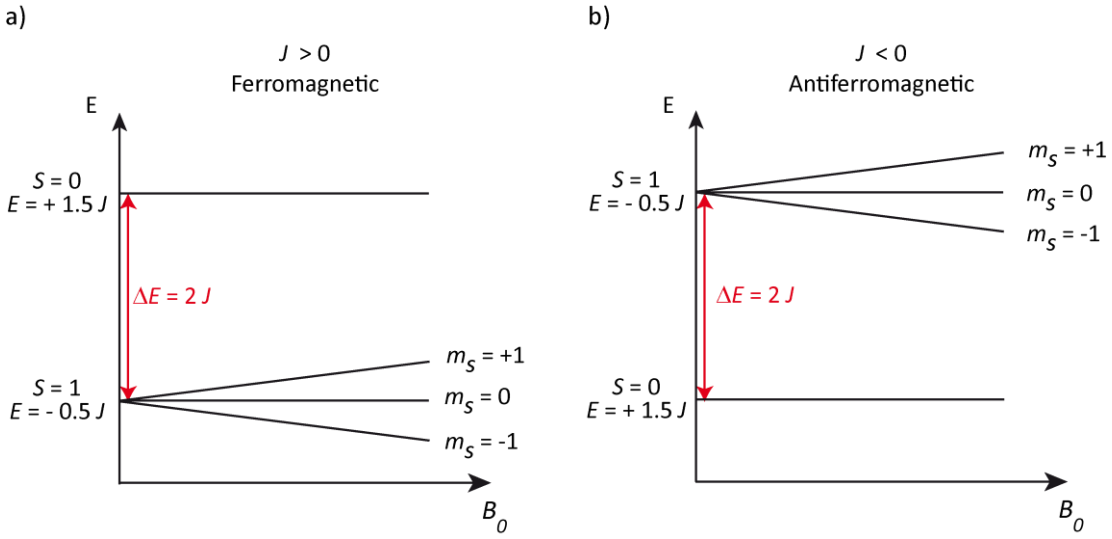

Figure 10: Exchange coupling of two electron spins (S = 1/2) leads to splitting into a singlet (S = 0) and a triplet (S = 1) state separated by the energy gap $\Delta E = 2J$. a) Energy scheme for *ferromagnetic* coupling, i.e. the ground state has the maximum total spin (S = 1, triplet). The degeneracy of the triplet state is lifted due to the Zeeman interaction. b) Energy scheme for *antiferromagnetic* coupling, i.e. the ground state has the minimum total spin (S = 0, singlet). The degeneracy of the triplet state is lifted due to the Zeeman interaction. Adapted from [3(p.161),5].

Note that the degeneracy of the state triplet is lifted by the Zeeman interaction and that the energy levels are therefore split, whereas the singlet state remains unchanged.[61(p.104)] Considering both J and the Zeeman splitting, the Hamiltonian reads [5]

$$\hat{H} = -2J\,\widehat{\vec{S}_1}^{T} \cdot \widehat{\vec{S}_2} + \sum_{i=1}^{2} \beta_e \widehat{\vec{B}_0}^{T} g_i \widehat{\vec{S}_i} \tag{76}$$

which gives rise to the following energy levels [5]

$$\begin{aligned} E(S=0) &= +1.5\,J & E(S=1, m_s=-1) &= -0.5\,J - \frac{1}{2}\beta_e B_0 (g_1 + g_2) \\ E(S=1, m_s=0) &= -0.5\,J & E(S=1, m_s=+1) &= -0.5\,J + \frac{1}{2}\beta_e B_0 (g_1 + g_2) \end{aligned} \tag{77}$$

If $g_1 = g_2 = g_e$, this simplifies to

$$\begin{aligned} E(S=0) &= +1.5\,J & E(S=1, m_s=-1) &= -0.5\,J - g_e \beta_e B_0 \\ E(S=1, m_s=0) &= -0.5\,J & E(S=1, m_s=+1) &= -0.5\,J + g_e \beta_e B_0 \end{aligned} \tag{78}$$

Due to the selection rule $\Delta S = 0$ that dictates the conservation of the total spin,[5] transitions between the singlet and the triplet state are quantum-mechanically forbidden. The only transitions in Figure 10 that strictly conform with the selection rule of EPR spectroscopy (eq. (16)) correspond to $\Delta m_s = \pm 1$ within the triplet state,[5] and they give rise to the so-called *main-field* signal.[62]

In addition to this allowed $\Delta m_s = \pm 1$ transition, a formally forbidden double-quantum ($\Delta m_s = \pm 2$) transition between the levels $m_s = -1$ and $m_s = +1$ of the triplet manifold can occur.[63(p.217)] As the transition probability scales inversely with the square of the microwave frequency,[64] the $\Delta m_s = \pm 2$ transition may be partially allowed and thus observable at X-band or lower frequencies.[64,65] It is triggered if the energy difference ΔE between the $m_s = +1$ and $m_s = -1$ levels matches the energy of either one or two microwave photons.[3(p.196),63(p.217)]

According to eq. (78), ΔE is given by

$$\Delta E = E(S = 1, m_s = +1) - E(S = 1, m_s = -1) = 2g_e\beta_e B_0 \tag{79}$$

If this energy gap is bridged by one photon ($E = h\nu$), the resonance field B_0' corresponds to

$$B_0' = \frac{h\nu}{2g_e\beta_e} = \frac{1}{2}\frac{h\nu}{\underbrace{g_e\beta_e}_{B_0}} = \frac{1}{2}B_0 \tag{80}$$

This single-photon double-quantum transition leads to a so-called *half-field signal*, which occurs at half the field of the allowed $\Delta m_s = \pm 1$ transition $\left(B_0' = \frac{1}{2}B_0\right)$.[5,66] If present, the half-field signal is clear evidence of a triplet state [67] and its intensity change with the temperature reports on the population of the singlet and triplet state.[3(p.184),5] This in turn permits determining *J*.[5] Note that the half-field signal is generally weak in intensity [67] and, depending on the magnitude of *J*, it requires liquid helium temperatures and high microwave power to be observable.[68]

If two microwave photons ($E = 2\ h\nu$) are involved in the double-quantum transition, the resonance field B_0 is given by

$$B_0 = \frac{2h\nu}{2g_e\beta_e} = \frac{h\nu}{g_e\beta_e} \tag{81}$$

which, for organic radicals, is in the range of a magnetic field corresponding to g ≈ 2.[3(p.196)] Like the half-field signal, this transition can only be observed at high microwave power.[3(p.217),63(p.217),69]

The magnitude of *J* compared with other contributors to the spin Hamiltonian (e.g. hyperfine interaction or the difference in the Zeeman energies of S_1 and S_2, generically summarized as ΔE) [5] allows classifying the exchange interaction into three regimes, namely strong ($|J| >> \Delta E$), intermediate ($|J| \approx \Delta E$), and weak ($|J| << \Delta E$) exchange coupling.[31(p.278)] The shape of an EPR spectrum depends on this coupling regime, and even simple spectra can change remarkably with *J*. Further, the interplay of *J* and the remaining terms of the spin Hamiltonian can lead to a mixing of the singlet and the triplet state, thus partially allowing the forbidden $\Delta S = 1$ transitions.[5]

Figure 11a shows the *cw* EPR spectrum of a two-spin system (isotropic *g*-values $g_1 = 2.0$, $g_2 = 2.1$) at various levels of exchange coupling. The magnitude of *J* is given with respect to the difference in the Zeeman splitting ($|J|/\Delta g\beta_e B_0$). Energy diagrams with the transitions leading to the EPR spectra are provided in Figure 11b.

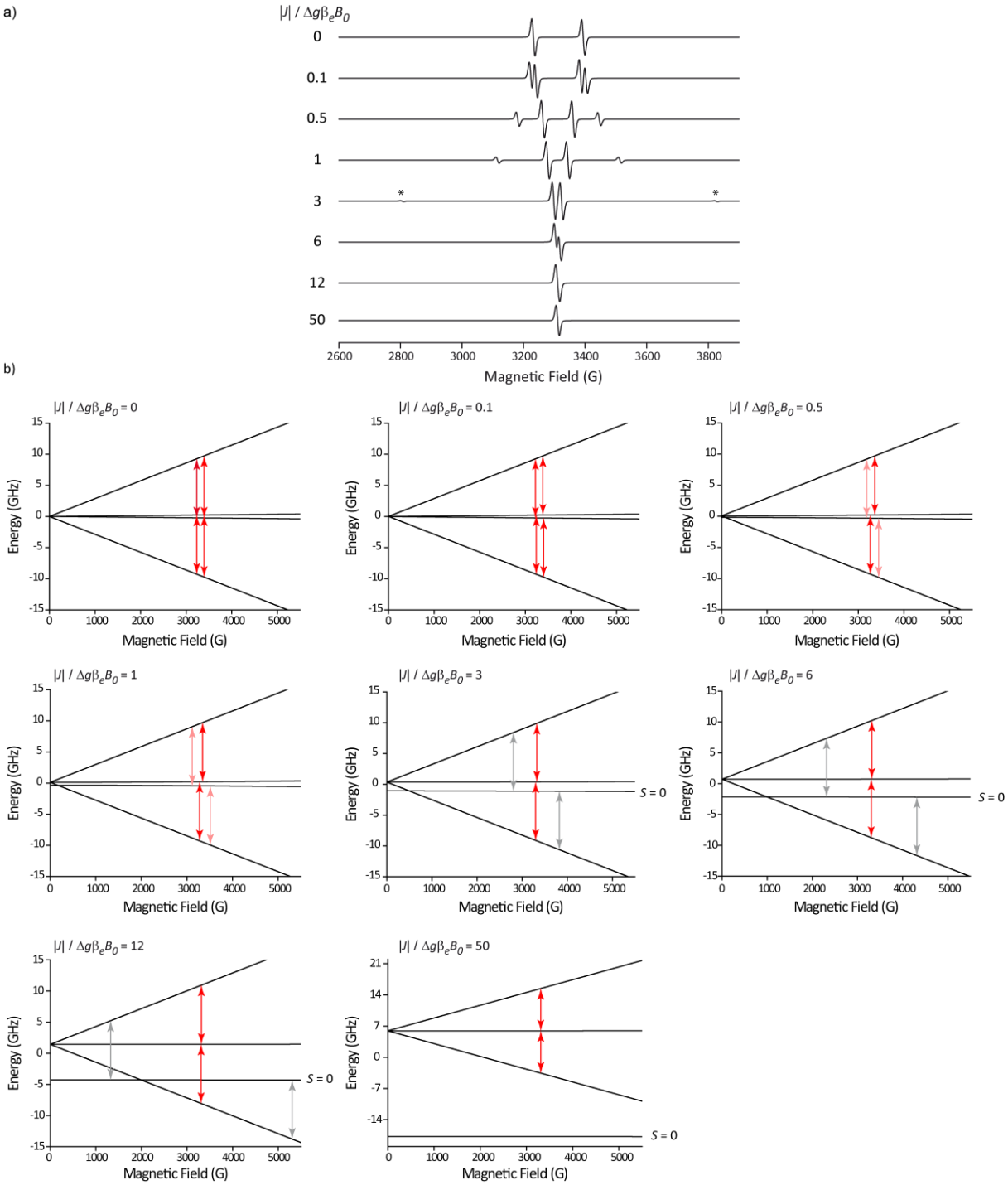

Figure 11: Effect of exchange coupling on the powder *cw* EPR spectrum of a two-spin system (g_1 = 2.0, g_2 = 2.1). a) *cw* EPR spectra simulated with EasySpin [30] (microwave frequency = 9.5 GHz; peak-to-peak linewidth = [10 G, 1 G], given in the form of Gaussian and Lorentzian broadening; no hyperfine coupling). $|J|/\Delta g\beta_e B_0$ is the ratio of the exchange coupling and the difference in the Zeeman energies of the two spins; the asterisks in the spectrum at $|J|/\Delta g\beta_e B_0 = 3$ indicate weak ΔS = ±1 transitions. Adapted from [5]. b) Plot of the energy levels and the transitions that lead to the EPR signals as obtained from the "levelsplot" function in EasySpin.[30] S = 0 denotes the singlet state. Allowed transitions are shown in red, ΔS = ±1 transitions partially allowed due to state mixing in grey.

In the absence of exchange coupling ($|J|/\Delta g\beta_e B_0 = 0$), the two spins can be treated in the "uncoupled basis",[5] where the four spin states $\beta_1\beta_2$, $\beta_1\alpha_2$, $\alpha_1\beta_2$, and $\alpha_1\alpha_2$ [5] arise by combining the magnetic quantum numbers m_s of spin 1 and spin 2. In total, four partially degenerate Δm_s = ±1 transitions

are allowed, where two of them have discrete energies and lead to two signals centred at g_1 and g_2.[5] Figure 12a shows the energy level diagram and a schematic spectrum for this situation.

In the weak-coupling regime ($|J|/\Delta g\beta_e B_0 = 0.1$), the exchange interaction can be treated as a perturbation of the Zeeman splitting and the energy levels are shifted by J.[5] This lifts the degeneracy and the four transitions have different energies, leading to four peaks in the spectrum, i.e. the lines at g_1 and g_2 split into doublets.[5] Figure 12b shows the energy level diagram and a schematic spectrum for this situation.

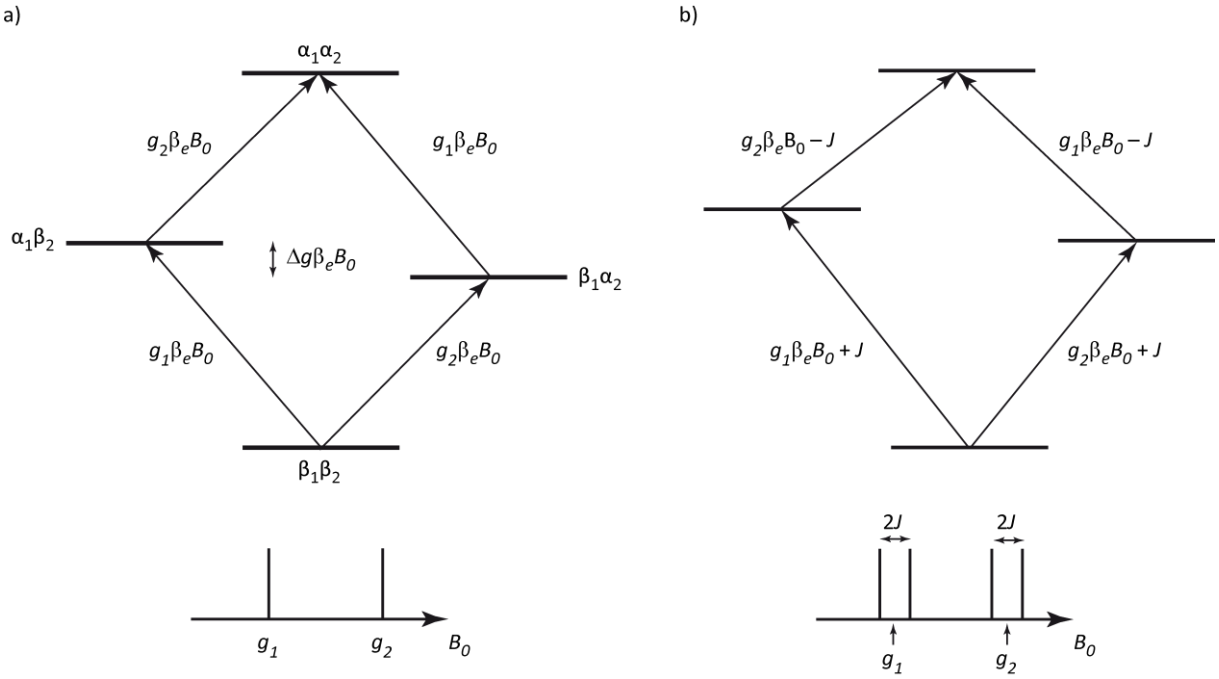

Figure 12: Energy level diagrams and schematic spectra for a two-spin system ($g_1 > g_2$). a) Absence of exchange coupling and b) Presence of weak exchange coupling. Adapted from [5].

With increasing $|J|/\Delta g\beta_e B_0$, the spin system enters the regime of intermediate coupling, which can lead to complicated peak patterns.[5] At $|J|/\Delta g\beta_e B_0$ equal to 0.5 and 1, four peaks are observed, where the inner two peaks shift towards each other with increasing J and the outer peaks move to the sides of the spectrum and decrease in intensity. As $|J|/\Delta g\beta_e B_0$ grows further, the exchange coupling can no longer be treated as a perturbation of the Zeeman interaction; the spin system is now described by a singlet and a triplet state. The mixing of the singlet and the triplet state can partially allow the forbidden ΔS = ±1 transitions (e.g. at $|J|/\Delta g\beta_e B_0 = 3$, Figure 11b), which may be observed as weak signals in the periphery of the spectrum (marked with asterisks in Figure 11a). Due to the low transition probability, however, these peaks are not always resolved.

Finally, as the strong coupling regime is entered ($|J|/\Delta g\beta_e B_0 = 50$), only transitions within the triplet state are observed. These are degenerate and give rise to a single EPR line. Notably, as can be seen from Figure 11b, the energy gap between singlet and triplet is so large that the states do not mix any longer, i.e. no ΔS = ±1 transition occurs.

Apart from shifting the Zeeman levels and thus the peak positions, exchange coupling can also impact the hyperfine splitting in the *cw* EPR spectrum. Figure 13 illustrates this fact on example of a nitroxide in different coupling regimes. If the two electron spins are weakly coupled ($|J| \ll |a_{iso}|$), the isotropic hyperfine splitting a_{iso} is identical to the one observed in the absence of exchange coupling (Figure 13a).[5] In the intermediate coupling regime ($|J| \approx |a_{iso}|$), complicated peak patterns with several asymmetric signals arise (Figure 13b).[5] In the limit of strong exchange interaction ($|J| \gg |a_{iso}|$), the

splitting observed in the spectrum is halved ($a_{iso}/2$) compared with the uncoupled spin system (Figure 13c).[3(p.190),5]

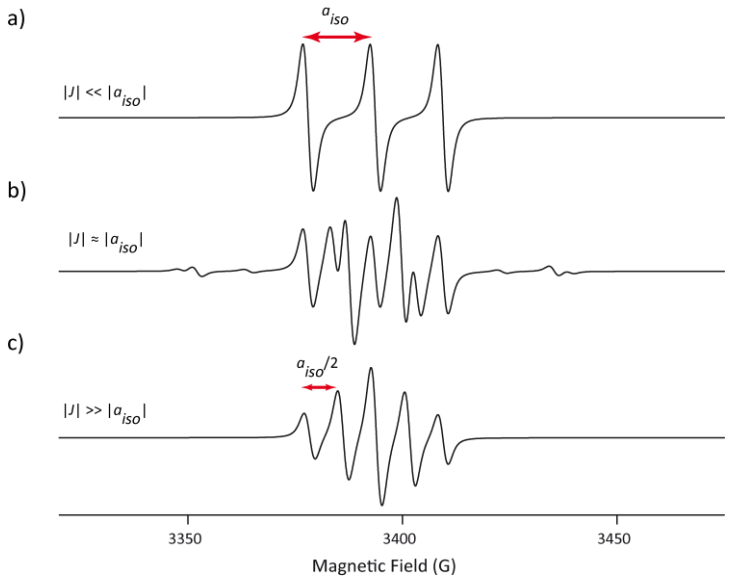

Figure 13: Isotropic EPR spectrum of a two-spin system with S_1 = 1/2, S_2 = 1/2, and a single ^{14}N nucleus (I = 1) in different exchange-coupling regimes. The spectra were simulated with EasySpin [30] based on the following parameters: $g_1 = g_2$ = 2.0; $|a_{iso}|$ = 44 MHz; peak-to-peak linewidth = [1.5, 1.5] G corresponding to Gaussian and Lorentzian broadening; exchange coupling a) $|J|$ = 0, b) $|J|$ = 100 MHz, c) $|J|$ = 10 GHz. Parameters taken from [5].

Exchange coupling also affects the dipolar spectrum as it modifies the frequencies of the singularities corresponding to the perpendicular and the parallel orientations. Figure 14 shows the dipolar spectra of a two-spin system in the absence of exchange coupling (Figure 14a), in the weak-coupling regime (Figure 14b), and in the strong-coupling regime (Figure 14c).

Weak exchange coupling is defined by $\left|J - \frac{\omega_{DD}}{2}\right| \ll |\omega_1 - \omega_2|$ with ω_1 and ω_2 being the Larmor frequencies of the uncoupled electron spins.[60] For a pair of weakly exchange-coupled spins, the exchange coupling constant J adds to the dipolar coupling constant ω_{DD} and the dipolar spectra exhibit the electron-electron splitting ω_{ee} [60,70,71]

$$\omega_{ee} = \omega_{DD} + J = \frac{D_{Dip}}{r^3} \cdot (1 - 3\cos^2\theta) + J. \tag{82}$$

This leads to singularities at the positions $\omega_\perp = \pm |D_{Dip} + J|$ and $\omega_{||} = \pm \left|2D_{Dip} - J\right|$.[72(p.9),73] As the spectrum depends on both D_{Dip} and J, the dipolar and the exchange coupling constant can be determined simultaneously.[73,74] Figure 14b illustrates the changes in the dipolar spectrum when exchange coupling (J < 0) is present: Compared to the uncoupled case (J = 0, Figure 14a), the singularities of the Pake pattern (perpendicular component) move towards each other and approach the zero frequency, while the edges (parallel component) diverge to the sides of the spectrum.[72(p.9)]

In the strong-coupling regime, i.e. $\left|J - \frac{\omega_{dd}}{2}\right| \gg |\omega_1 - \omega_2|$, the dipolar spectrum corresponds to an undistorted [73] Pake pattern (Figure 14c), but the frequencies of the singularities are augmented by a factor of 1.5 compared to the uncoupled case.[60,73] The dipolar coupling frequency then reads [52,60,75]

$$\omega_{DD}(\theta, r) = \frac{3}{2} \cdot \frac{D_{Dip}}{r^3} \cdot (1 - 3\cos^2\theta)\,. \tag{83}$$

The singularities in the Pake pattern occur at ± 1.5 D_{Dip} (perpendicular component) and ± 3 D_{Dip} (parallel component).[73] Of note, in the strong-coupling regime, the dipolar spectrum is independent of J, i.e. unlike D_{Dip}, J cannot be determined from the spectrum.[60,73]

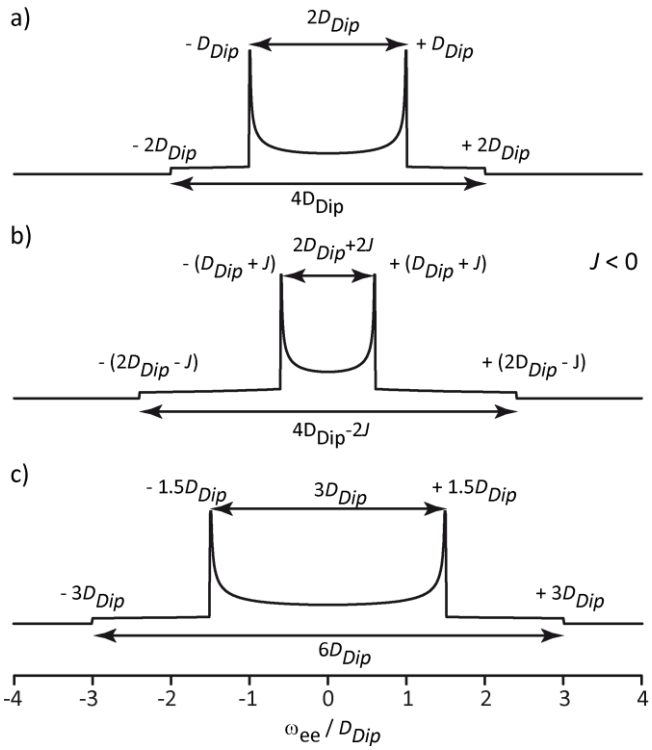

Figure 14: Influence of exchange coupling on the dipolar spectra of a two-spin system ($S_1 = 1/2$, $S_2 = 1/2$). a) No exchange coupling, the Pake Pattern has singularities at $\omega_{ee} = \pm D_{Dip}$ (perpendicular component) and $\omega_{ee} = \pm 2D_{Dip}$ (parallel component). b) In the regime of weak exchange coupling, J adds to ω_{DD}, leading to a shift of the singularities to $\omega_{ee} = \pm|D_{Dip} + J|$ (perpendicular component) and $\omega_{ee} = \pm|2D_{Dip} - J|$ (parallel component). The example shown here corresponds to $J < 0$, i.e. the singularities of the Pake pattern approach each other, whereas the edges move towards the outer sides. c) In the case of strong exchange coupling, the singularities occur at $\pm 1.5\ D_{Dip}$ (perpendicular orientation) and at $\pm 3\ D_{Dip}$ (parallel orientation). Adapted from [60].

The influence of J on the dipolar spectrum has to be taken into account when determining interspin distances *via* PDS. In the absence of exchange interaction, the interspin distance can be computed *via*

$$r_{\text{no exch.}} = \sqrt[3]{\frac{D_{Dip}}{\omega_\perp}} \tag{84}$$

and in the case of strong exchange coupling, it is given by

$$r_{\text{strong exch.}} = \sqrt[3]{\frac{3}{2} \cdot \frac{D_{Dip}}{\omega_\perp}} = \sqrt[3]{\frac{3}{2}} \cdot r_{\text{no exch.}} \tag{85}$$

Equation (85) reveals that the interspin distance would be underestimated by a factor of $\sqrt[3]{3/2} = 1.145$ if the exchange interaction was neglected.[29(p.173),45] This corresponds to a distance error of up to 15%,[60] e.g. approx. 2 Å for r ≈ 15 Å.[45,60]

1.2 Experimental Techniques

1.2.1 Continuous Wave EPR Spectroscopy

Continuous wave (*cw*) EPR spectroscopy is often the starting point of an EPR study. It reports on the identity and the dynamics of a paramagnetic species, e.g. in terms of the *g*-tensor and its anisotropy, the hyperfine splitting, and the linewidth. In *cw* EPR spectroscopy, the sample is continuously irradiated with microwaves of a constant frequency, while the external magnetic field B_0 is swept in the range where EPR transitions are expected.[22] If the resonance condition (eq. (19)) is fulfilled, microwaves will be absorbed by the spin system, which results in an EPR signal.

Experimentally, *cw* EPR spectra are recorded using field modulation, i.e. a magnetic field B_{mod} oscillating at a frequency ν_{mod} is applied parallel to the main magnetic field B_0. As a result, the resonance condition and thus the EPR signal is modulated by ν_{mod}.[76] By using a lock-in detector that selectively records EPR signals oscillating at ν_{mod}, noise that occurs at other frequencies is efficiently suppressed, thus improving the sensitivity and the signal-to-noise ratio (SNR).[76] Thus, for X-band *cw* EPR, spin concentrations in the low micromolar range are required for organic radicals (e.g. 5 µL of a 10 µM solution) [77] and in the higher micromolar to millimolar range for transition metal ions.[77] Of note, due to field modulation, *cw* EPR spectra are obtained as the first derivative (Figure 15a) of the absorption spectrum (Figure 15b).[22,76]

In spectroscopy, the integral of the absorption spectrum is proportional to the number of molecules that evoke the signal.[76] Thus, the double integral of a *cw* EPR spectrum (Figure 15c) permits determining the number of spins in a sample, either by comparing with a standard of known concentration or by using a so-called "spin counting" routine.[78(p.15–24)] The latter is often implemented in the spectrometer software and allows estimating the number of spins without a reference sample.[78(p.15–24)]

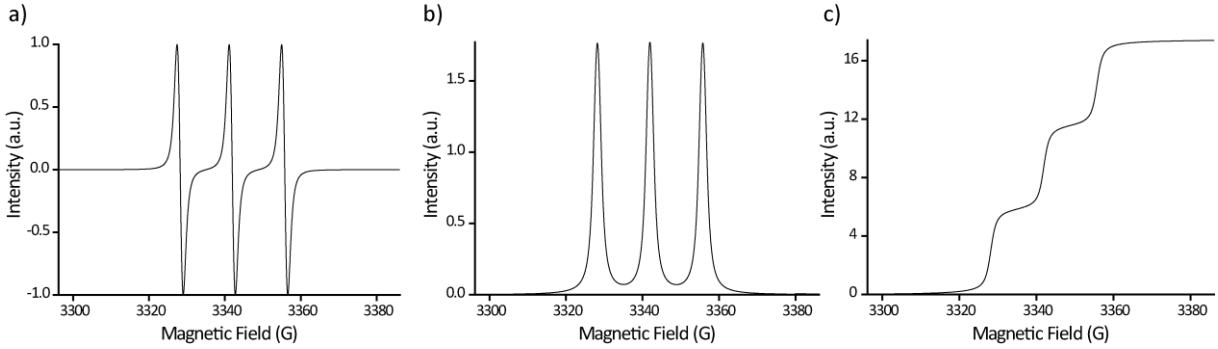

Figure 15: Simulated isotropic X-band (9.4 GHz) *cw* EPR spectrum of a nitroxide radical with g_{iso} = 2.0055 and $a_{iso}(^{14}N)$ = 40 MHz.[36] The Gaussian and Lorentzian contributions to the peak-to-peak linewidth were both set to 1 G. a) First derivative as obtained experimentally by *cw* EPR spectroscopy. b) Absorption spectrum obtained by integrating the spectrum in (a). c) Double integral trace of the spectrum in (a).

The linewidth of an EPR signal is determined by homogeneous and inhomogeneous broadening [3(p.339)] and can be determined by least-squares fitting of the experimental *cw* EPR spectrum.[30] In terms of mathematical functions, the homogeneous broadening is described by a Lorentzian line shape and inhomogeneous broadening by a Gaussian line shape.[3(p.339),10(p.40)]

Homogeneous line broadening is governed by spin relaxation, i.e. the return of the electron spin from the upper into the lower Zeeman state. According to Heisenberg's uncertainty principle, the lifetime Δt of an excited state dictates the uncertainty in the energy of that state ($\Delta E \cdot \Delta t \sim \hbar$).[23] By substituting *E* with the resonance condition (eq. (19)), it can be shown that the resonance field *B* is dispersed across a range ΔB, which constitutes the homogeneous linewidth:[23]

$$g\beta_e \Delta B \cdot \Delta t \sim \hbar \rightarrow \Delta B \sim \frac{\hbar}{g\beta_e \Delta t} \tag{86}$$

Equation (86) reveals that the EPR line narrows at a longer lifetime Δt (slow relaxation) and broadens if Δt is short (fast relaxation). For this reason, the homogeneous line broadening is also called "lifetime broadening".[23(p.81)] Note that the minimal width of an EPR line is governed by homogeneous broadening, i.e. interactions vanishing in the homogeneous linewidth cannot be resolved by any EPR technique.[10(p.40)] Inhomogeneous line broadening results from overlapping homogeneously broadened lines, with each of them having a slightly different resonance field.[10(p.40),23(p.81)] Main contributors to inhomogeneous broadening are unresolved hyperfine splitting, unresolved *g*-anisotropy, and dipolar interactions.[8,23] Of note, interactions obscured in *cw* EPR spectra by inhomogeneous broadening can be extracted by pulsed EPR experiments (section 1.2.2).

Cw EPR spectroscopy allows studying samples in all three states of matter, with the liquid and the solid state being the most common for EPR experiments.[3(p.19)] In the liquid state and if the spin centre rotates fast, anisotropic contributions to the spin Hamiltonian are averaged out and the *cw* EPR spectrum is isotropic. EPR spectra obtained in the solid state, by contrast, contain both the isotropic and the anisotropic interactions. If the anisotropy is large enough, it can be resolved in the spectrum and provides insight into the respective tensor of the spin Hamiltonian (section 1.1.4); otherwise, it contributes to the inhomogeneous linewidth.

Multi-frequency *cw* EPR spectroscopy is a means to disentangle the field-dependent *g*-anisotropy from field-independent interactions such as hyperfine anisotropy.[2] Due to a larger Zeeman splitting, *g*-anisotropy is resolved better at higher magnetic fields and microwave frequencies: Spectra from species with weak *g*-anisotropy, for example, may appear isotropic at low microwave frequency (X-band, 9.4 GHz), but anisotropic at higher frequency bands (J-band, 260 GHz). Figure 16 shows simulated EPR spectra of a trityl radical with a weakly anisotropic *g*-tensor (g_x = 2.0034, g_y = 2.0032, g_z = 2.0023),[26] illustrating that microwave frequencies of W-band (94 GHz) or higher are required to resolve the *g*-anisotropy.

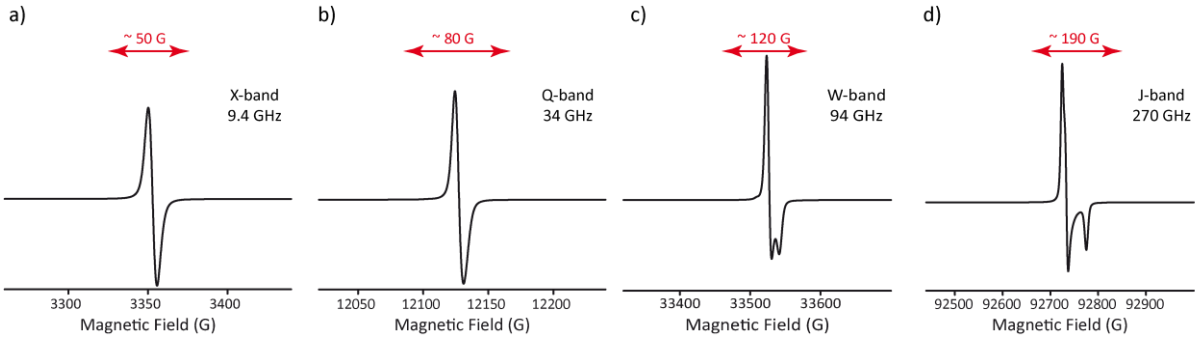

Figure 16: Simulated *cw* EPR spectra of a trityl radical at different microwave frequencies. Simulation parameters taken from [26]: g_x = 2.0034, g_y = 2.0032, g_z = 2.0023; Hstrain_x =10 MHz, Hstrain_y = 12 MHz, Hstrain_z = 16 MHz;[1] $A_x(^{13}C)$ = 20.6 MHz, $A_y(^{13}C)$ = 20.6 MHz, $A_z(^{13}C)$ = 160.1 MHz; Peak-to-peak linewidth = 2 G for the Gaussian and the Lorentzian contribution. While the spectrum is isotropic at low microwave frequencies such as X-band (a) or Q-band (b), the *g*-anisotropy is resolved at higher frequencies (W-band (c) or J-band (d). The red arrows indicate that the spectral width increases at higher fields upon resolving the *g*-anisotropy.[36]

In solution, the *cw* EPR spectrum reports on the dynamics of a paramagnetic species, provided it has an anisotropic *g*- or *A*-tensor.[36] If the spin-bearing molecule tumbles, the anisotropy is (partially) averaged out, which leads to a characteristic line shape depending on the tumbling rate. The degree of immobilization and hence the extent of anisotropy observable in the spectrum is expressed by the

[1] Hstrain denotes a broadening due to unresolved hyperfine splitting.[79].

rotational correlation time τ_{corr}, which is the average time it takes the molecule to rotate by one radian.[22,80] Figure 17 shows simulated X-band *cw* EPR spectra of a nitroxide radical at different rotational correlation times. In spin-labelling EPR studies, these characteristic changes of the line shape allow distinguishing free and bound spin label, which correspond to the isotropic and the slow-motion regime, respectively.

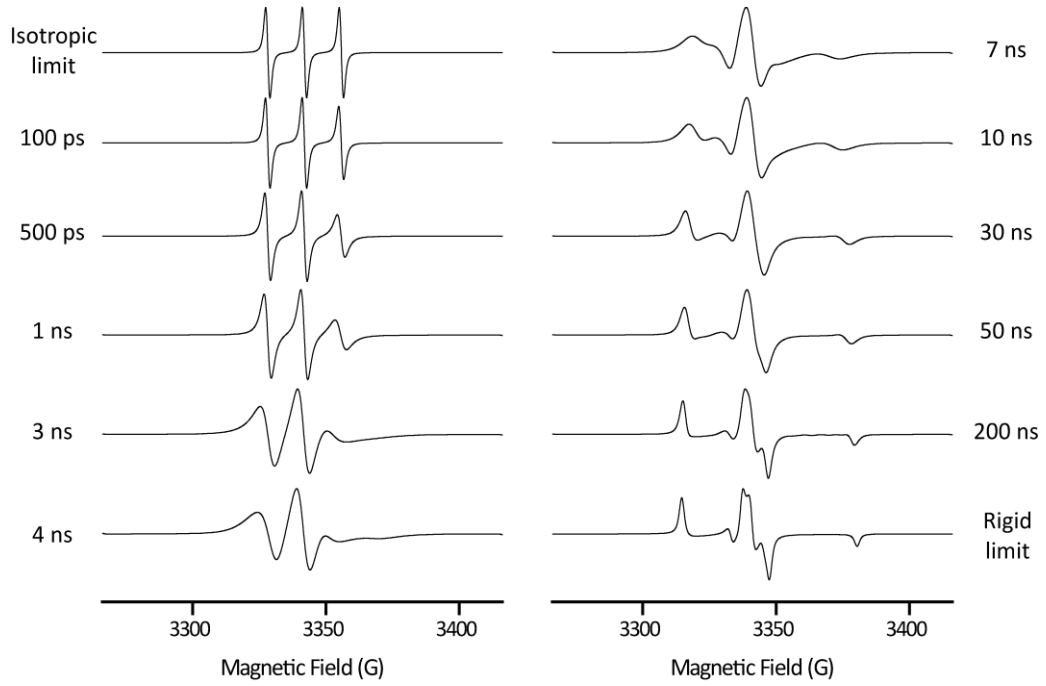

Figure 17: X-band (9.4 GHz) *cw* EPR spectra of a nitroxide radical as a function of the rotational correlation time simulated with EasySpin.[30] Simulation parameters: g_x = 2.008, g_y = 2.006, g_z = 2.002; $A_x(^{14}N)$ = 12 MHz, $A_y(^{14}N)$ = 12 MHz, $A_z(^{14}N)$ = 92 MHz.[36] The Gaussian and Lorentzian contributions to the peak-to-peak linewidth were both set to 1 G.

1.2.2 Pulsed EPR Spectroscopy

Pulsed EPR spectroscopy is a means to investigate electron-spin interactions that are unresolved in the *cw* EPR spectrum due to inhomogeneous line broadening.[10(p.41),81] It uses high-power microwave pulses to flip the electron spin, thereby rotating the macroscopic magnetization vector by a tip angle α. The value of α depends on the amplitude (i.e. the microwave power) and the length of the pulse;[29(p.292)] a pulse that rotates the magnetization vector by α = 90° is referred to as a π/2-pulse, a π-pulse rotates the magnetization vector by α = 180°. Applying a π/2-pulse to the equilibrium state creates transverse magnetization that can be detected as an EPR signal.[81] Longitudinal magnetization, by contrast, is not detectable in pulsed EPR spectroscopy.[10(p.21)]

The versatility of pulsed EPR experiments stems from the opportunity to vary pulse lengths, interpulse delays, the number of pulses, and to apply pulses at different microwave frequencies within one experiment.[81] Various pulse sequences have been developed that selectively address different spin interactions, e.g. the electron-nuclear hyperfine coupling (hyperfine spectroscopy),[82–84] the electron-electron dipolar coupling (pulsed dipolar spectroscopy),[8,9,57] and electron-spin relaxation (relaxometry).[85] The effect of microwave pulses on the macroscopic magnetization of a spin ensemble will be discussed in the following.

1.2.2.1 The Free Induction Decay and the Spin Echo

By applying a π/2-pulse to a spin system in thermal equilibrium (Figure 18a), the magnetization vector is rotated into the transverse plane; if the π/2-pulse is of +y-phase, it rotates the magnetization vector along the +x-axis (Figure 18b).[81] Spins packets, i.e. spins that have identical resonance frequencies,[81] precess about the z-axis at their individual rotation frequencies, which can be thought of as the magnetization vector splitting into sub-vectors (Figure 18c).[81] Owing to the different rotation frequencies, the spin packets dephase over time and the net magnetization in the transverse plane decreases. This phenomenon is called free induction decay (FID), which is routinely detected in NMR spectroscopy but often hidden within the dead time of the EPR spectrometer.[81]

By applying a π-pulse at a delay τ after the π/2-pulse, the spin packets are inverted around the y-axis (Figure 18d), but they keep their sense and speed of precession. At another time delay τ after the π-pulse, all spins refocus and create macroscopic magnetization along the -x-axis (Figure 18e), which gives rise to a spin echo named after its discoverer E. Hahn.[81,86] The Hahn echo can be thought of as a reverse FID in which the spin packets reunite, followed by a forward FID in which the spin packets dephase again.[3(p.369),81]

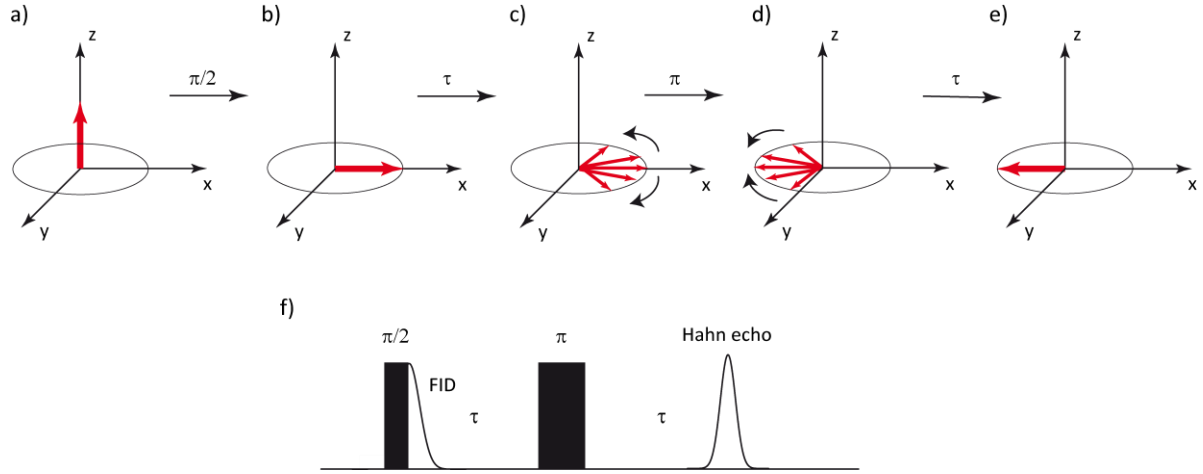

Figure 18: Vector model of the Hahn echo. Bold red arrows symbolize macroscopic magnetization, light red arrows indicate spin packets. a) In the thermal equilibrium, the macroscopic magnetization is oriented along the z-axis (longitudinal magnetization). b) By applying a π/2-pulse, the magnetization vector is tilted by 90° into the transverse plane. c) The spin packets precess around the z-axis at their individual rotation speed, which gives rise to the free induction decay (FID). d) The spin packets are inverted by a π-pulse, but they keep their sense and speed of rotation. e) The spin packets refocus along the -x-axis and give rise to macroscopic magnetization referred to as the Hahn echo. f) Schematic representation of the Hahn echo sequence.

In Figure 18, it was shown that a Hahn echo sequence with a π/2-pulse of +y-phase eventually leads to an echo with -x-phase. If the phase of the π/2-pulse is inverted to -y, the phase of the echo will equally invert to +x.[81] By using a phase-sensitive detector, the phase of the echo can be read out in addition to its intensity. This allows for a technique called phase cycling, in which the pulse sequence is executed multiple times with the pulse phases varied in a defined manner. Appropriately adding or subtracting the recorded signals suppresses unwanted echoes and FIDs that may overlap with the desired echo.[81] Thus, phase cycling prevents artefacts that would impede data analysis.

As outlined above, pulse sequences create transverse magnetization and thereby move the spin system out of equilibrium. If the spins did not interact with their environment and with each other, they would remain in the transverse plane and keep their phase coherence. However, spin relaxation drives the spin system back into the thermal equilibrium and further leads to a loss of phase coherence within the spin packets.[85] The two mechanisms of electron spin relaxation, namely the energy-driven longitudinal relaxation and the entropy-driven transverse relaxation, are discussed in the following two sections.

1.2.2.2 Longitudinal Electron Spin Relaxation

Longitudinal relaxation, also termed spin-lattice relaxation, describes the return of the magnetization back into the thermal equilibrium due to energy transfer from the spin system to its surrounding ("lattice").[81] Longitudinal relaxation is characterized by the time constant T_1 that can be measured by an inversion recovery experiment.[81]

In the inversion recovery experiment (Figure 19a), a π-pulse inverts the equilibrium magnetization from the +z to the -z-axis. Due to longitudinal relaxation within the interpulse delay *T*, the magnetization along -z declines and +z magnetization builds up. After the interval *T*, a Hahn echo experiment follows to read out the longitudinal magnetization. Recording the Hahn echo amplitude as a function of *T* yields an inversion recovery trace (Figure 19b), which can be described by a monoexponential function [87]

$$y(T) = A_0 \cdot \exp\left(-\frac{T}{T_1}\right) \tag{87}$$

Therein, $y(T)$ is the echo amplitude as a function of *T*, A_0 is the echo amplitude at $T = 0$, and T_1 is the spin-lattice relaxation time.

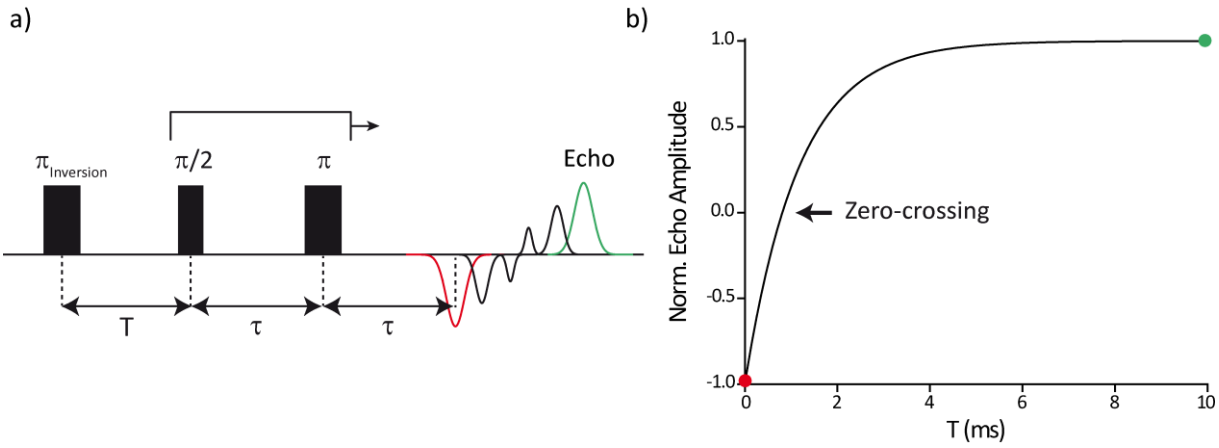

Figure 19: The inversion recovery sequence. a) Scheme of the pulse sequence. As the interpulse delay *T* is incremented, the magnetization gradually returns to the +z-axis and the echo amplitude increases (red: maximal inversion; green: full relaxation). The interpulse delay τ is kept constant throughout the experiment. b) Inversion recovery curve. The red and green dots mark the points of maximal inversion and full relaxation, respectively.

The return of the magnetization into the thermal equilibrium dictates the minimal time between two cycles of a pulse sequence (shot repetition time, SRT) that is required to prevent saturation of the spin system.

1.2.2.3 Transverse Electron Spin Relaxation

Transverse relaxation, also called spin-spin relaxation, describes the loss of phase coherence of the magnetic moments within a spin packet.[81] Once the magnetic moments have lost phase coherence, they cannot be refocused anymore to form a spin echo.[81,85] Phase coherence decays over time due to spin-spin interactions, with stronger interactions resulting in less coherence. The characteristic time constant of spin-spin relaxation is T_2, which can be determined by fitting a monoexponential function to the FID.[85]

Experimentally, transverse spin relaxation is studied by recording the Hahn echo amplitude as a function of the interpulse delay τ (Figure 20a).[81] Note that the amplitude is by convention shown as a function of 2τ (Figure 20b),[40] as the interpulse delay τ and hence spin-spin relaxation occurs twice in the Hahn echo sequence.[81] The time constant of the echo decay is called the phase memory time T_M, which encompasses T_2 and the effects of other decoherence mechanisms such as nuclear spin diffusion.[81,88] T_M is obtained by fitting a stretched exponential decay function [81]

$$y(2\tau) = y_0 \cdot \exp\left[\left(-\frac{2\tau}{T_M}\right)^x\right] \tag{88}$$

to the Hahn echo decay curve with y_0 being the echo intensity at $\tau = 0$ and x a stretch exponent that ranges between 0.5 and 3.[88] T_M, which usually is in the range of microseconds [89] for organic radicals, limits the length of interpulse delays with transverse magnetization such as the dipolar evolution time in PDS (section 1.2.3).[81] Careful optimization of the sample conditions is a means to prolong T_M, e.g. by reducing the spin concentration,[40] by adding cryoprotective glass-forming agents such as ethylene glycol or glycerol,[8] by submillisecond freezing,[90] and by deuterating the solvent [40,91,92] or even the whole (bio)molecule.[59,93,94]

If the electron spin interacts with the surrounding nuclear spins, the Hahn echo decay curve will exhibit oscillations at the Larmor frequency of the coupled nucleus (Figure 20b), a phenomenon referred to as electron spin echo envelope modulation (ESEEM).[81] For this reason, the experiment for recording the Hahn echo decay is also called the two-pulse ESEEM experiment.

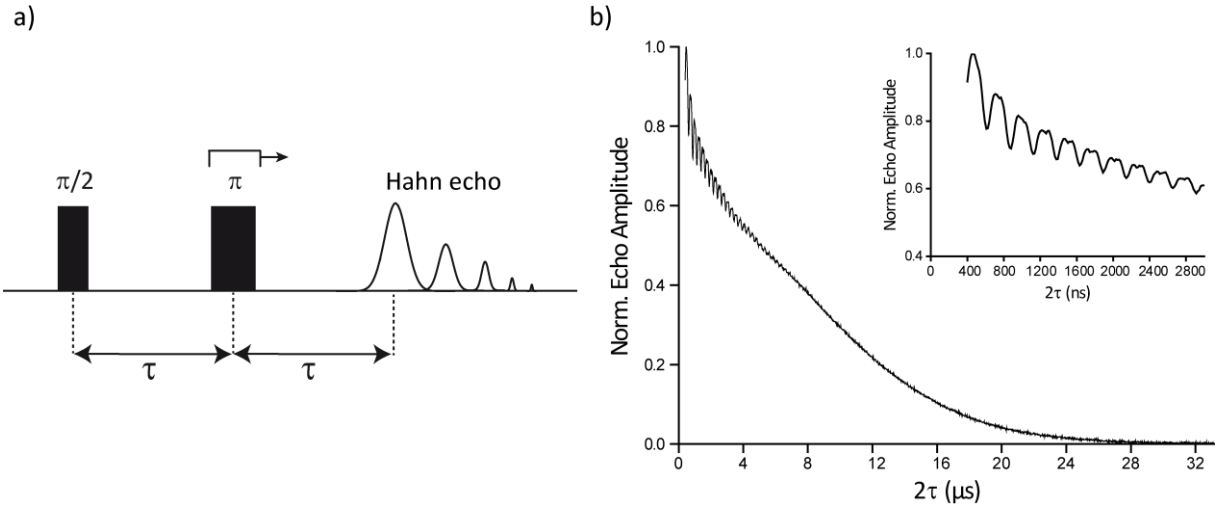

Figure 20: The two-pulse ESEEM sequence. a) Scheme of the pulse sequence. As the interpulse delay τ is incremented, the amplitude of the Hahn echo decreases due to loss of coherence. b) Hahn echo decay curve that exhibits oscillations from deuterium ESEEM (see inset).

1.2.3 Pulsed Dipolar EPR Spectroscopy

Pulsed dipolar EPR spectroscopy (PDS) is a generic term for pulsed EPR experiments that measure the dipolar coupling frequency ω_{DD} between the spins of unpaired electrons. While the theory of magnetic dipolar coupling has been outlined in section 1.1.4.6, this chapter will first focus on experimental aspects of PDS in general and then discuss the specificities of the different PDS pulse sequences.

As shown by eq. (63), ω_{DD} is proportional to the inverse cube of the interspin distance. At short distances, ω_{DD} can exceed the inhomogeneous linewidth of the spin centres so that the dipolar coupling may be observable as a splitting in the *cw* EPR spectrum.[8,95] For nitroxides, this applies to distances below approx. 2 nm.[60,95] At larger distances, however, the dipolar splitting generally vanishes below the inhomogeneous linewidth and cannot be resolved anymore in the *cw* EPR spectrum.[8] At this point, PDS methods become useful: By refocusing all interactions that lead to inhomogeneous line broadening, it recovers the homogeneous linewidth and thereby increases the spectral resolution.[8,96] As a result, PDS allows determining interspin distances between 1.5 nm and an upper limit of up to 16 nm,[59] which is governed by transverse relaxation.[8] The lower limit of 1.5 nm arises from the need to uniformly excite the dipolar spectrum, which is possible only if the excitation bandwidth of the microwave pulses is larger than ω_{DD}.[56,89] As the nanometre range is the relevant length scale in biomolecules, PDS combined with site-directed spin labelling [97–99] has been used as a "molecular ruler" [100] in studying structures and conformational changes of large proteins,[7,101,102] oligonucleotides,[103–105] and their complexes.[106–110]

PDS pulse sequences give rise to a spin echo, which is modulated by the dipolar coupling frequency ω_{DD} upon incrementing or decrementing interpulse delays in a specified way. Recording the echo intensity as a function of the so-called dipolar evolution time yields dipolar traces (time traces) as primary data, which encode ω_{DD} in the form of oscillations.[53] For reliable data analysis, it is crucial to record at least two oscillation periods corresponding to the longest mean distance $\langle r \rangle$.[40,53] To ensure a sufficient resolution of the dipolar oscillations, the step width of the data points on the trace is usually set to 8-12 ns.[40]

Fourier transformation of the time trace yields the dipolar spectrum in the frequency domain, which has the shape of a Pake pattern (section 1.1.4.6). If different distances occur within an ensemble of spins, the corresponding dipolar frequencies all contribute to the time trace; this permits inferring the distribution of interspin distances from the time trace. The distance distribution in turn reports on the conformational ensemble of the biomolecule and the spin label.[7]

Time traces differ in terms of the frequency and the damping of the dipolar oscillations, depending on the interspin distance, the width, and the modality of the distribution. Figure 21 shows simulated time traces and the corresponding dipolar spectra for Gaussian-shaped distance distributions

$$P(r) = \frac{1}{\sigma\sqrt{2\pi}} \cdot \exp\left(-\frac{(r - \langle r \rangle)^2}{2\sigma^2}\right) \tag{89}$$

where the standard deviation σ represents the distribution width and $\langle r \rangle$ is the mean distance. Three cases are illustrated, namely the influence of the mean distance $\langle r \rangle$ (Figure 21a), of the distribution width σ (Figure 21b), and of bimodality (Figure 21c) on the shape of the time trace.

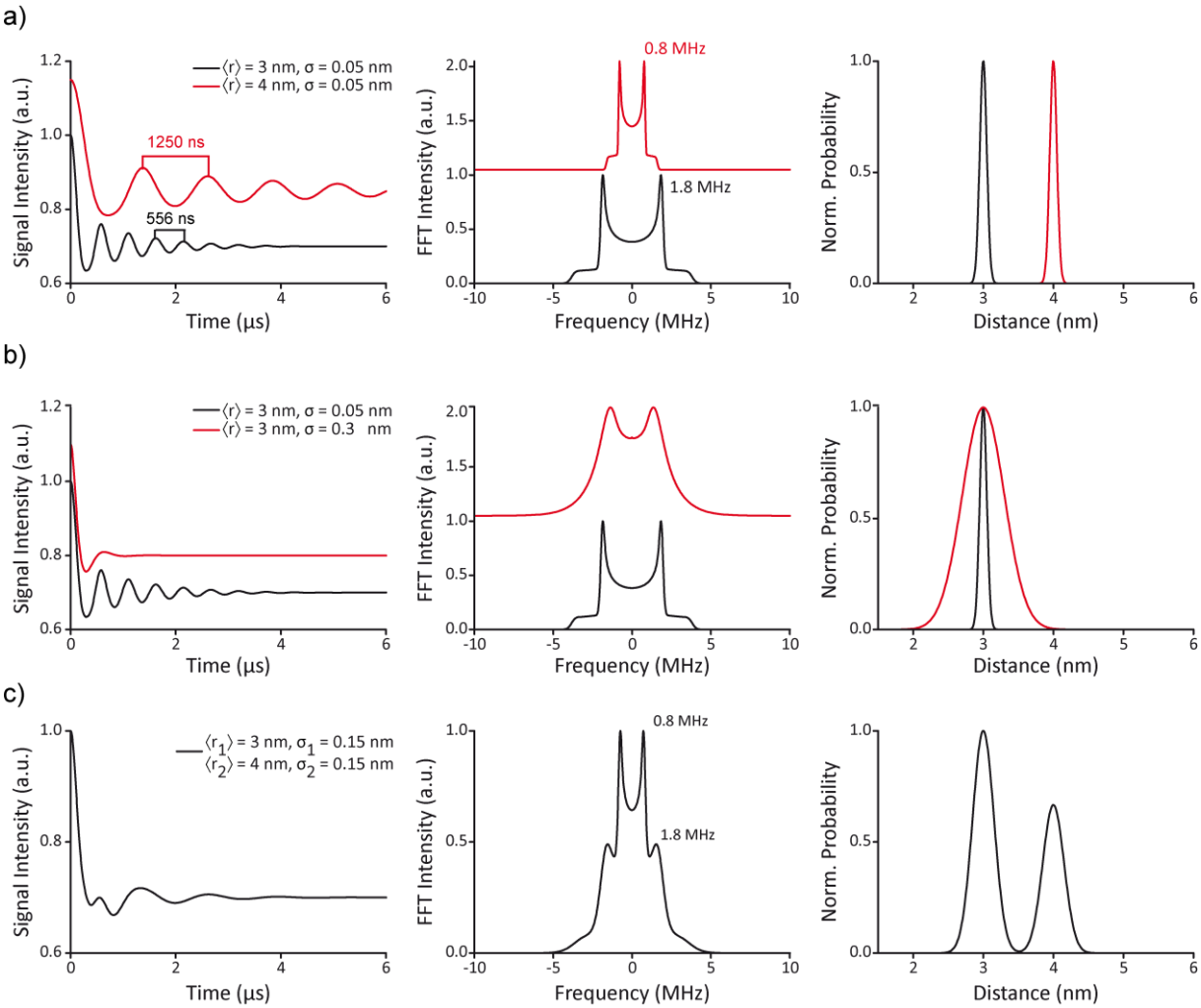

Figure 21: Correlation between the shape of the PDS time trace (first column), the dipolar spectrum (second column), and the distance distribution (third column). The time traces corresponding to Gaussian distance distributions were simulated with EasySpin,[30] the frequency spectra were obtained from DeerAnalysis [111] as the fast Fourier transform (FFT) of the time trace. a) Unimodal distributions, $\langle r \rangle$ = 3 nm, σ = 0.05 nm (black) and $\langle r \rangle$ = 4 nm, σ = 0.05 nm (red). b) Unimodal distributions, $\langle r \rangle$ = 3 nm, σ = 0.05 nm (black) and $\langle r \rangle$ = 3 nm, σ = 0.3 nm (red). c) Bimodal distribution with $\langle r_1 \rangle$ = 3 nm, σ_1 = 0.15 nm and $\langle r_2 \rangle$ = 4 nm, σ_2 = 0.15 nm, modes weighted as 3:2.

Figure 21a compares the time traces and the dipolar spectra for Gaussian distributions of 0.05 nm width and a mean distance of 3 nm and 4 nm. The shorter distance evokes a shorter oscillation period (556 ns at $\langle r \rangle$ = 3 nm; 1250 ns at $\langle r \rangle$ = 4 nm), which reflects the higher dipolar coupling frequency (1.8 MHz at $\langle r \rangle$ = 3 nm; 0.8 MHz at $\langle r \rangle$ = 4 nm). As a rule of thumb, the steeper the initial decay in the time trace is, the shorter is the interspin distance.

Figure 21b illustrates the influence of the distribution width at a constant mean distance of 3 nm: While the narrow distribution (σ = 0.05 nm) gives rise to prominent oscillations along the whole time trace, the oscillations are strongly damped for the broad distribution (σ = 0.3 nm). Owing to the larger number of discrete interspin distances in the broader distribution, more dipolar frequencies contribute to the trace and their oscillations with (slightly) different periods will cancel due to destructive interference.[112] This also washes out the dipolar spectrum, where especially the parallel component is not resolved anymore.

Figure 21c demonstrates the changes in the time trace and the dipolar spectrum upon introducing a second mode into the distance distribution. While (narrow) unimodal distributions yield time traces

with periodic oscillations (Figure 21a,b), the traces of multimodal distributions contain largely different dipolar frequencies and thus an irregular oscillation pattern. Notably, if the modes of the distribution and thus the dipolar frequencies are sufficiently separated from each other, they can be recognized as individual peaks in the dipolar spectrum (Figure 21c).

Dipolar coupling occurs between the electron spins within the same molecule (intramolecular coupling) and between the spins on different molecules in close proximity (intermolecular coupling). As a result, the experimental dipolar signal $V(t)$ is the product of the intramolecular and the intermolecular contribution to the dipolar coupling:[40]

$$V(t) = V_{intra}(t) \cdot V_{inter}(t) \tag{90}$$

Therein, $V_{intra}(t)$ is called the form factor that represents the oscillating dipolar signal and encodes the distance distribution.[57,113] $V_{inter}(t)$ is the non-modulated background of the time trace, the form of which depends on the concentration and the spatial distribution of the spins.[111] To infer the distance distribution, both contributions to $V(t)$ have to be disentangled, which is achieved by approximating $V_{inter}(t)$ with an exponential or polynomial background function $B(t)$ (Figure 22a) and then dividing $V(t)$ by $B(t)$.[111] In that context, longer time traces ease fitting of $B(t)$ to $V_{inter}(t)$ and thereby increase the accuracy of $B(t)$ and of the distance distribution. A way to scrutinize the impact of the background removal on the distance distribution is to systematically vary the fitting range of $V_{inter}(t)$ and to compute the distance distribution for each background fit (background validation).[114] Only those features of the distance distribution that are independent of the background fitting and thus prevail in the background validation can be regarded as reliable.

$V_{intra}(t)$ permits inferring the modulation depth Δ (Figure 22b), a parameter that reflects the fraction of the dipolar spectrum excited by microwave pulses.[89,115,116] Exciting a larger fraction of the spectrum results in a deeper modulation of the trace.[8] The modulation depth depends on the inversion efficiency λ and thus on the excitation bandwidth (i.e. the length, power,[117] and shape [118]) of the microwave pulses in relation to the width of the EPR spectrum. In the case of biomolecular samples prepared by site-directed spin labelling, the labelling efficiency *f* needs to be taken into account, so that the modulation depth of a two-spin system is given by [40,119]

$$\Delta = \lambda \cdot f \tag{91}$$

If f = 1 and in the limit that the whole EPR spectrum is excited in a PDS experiment ($\lambda = 1$), Δ equals 100%.[120] On the other hand, Δ is zero in the absence of intramolecular dipolar coupling, e.g. if a biomolecule carries only one spin label. In this case, the time trace would correspond to the intermolecular background. For Pulsed Electron-Electron Double Resonance (PELDOR, section 1.2.3.1) in particular, the modulation depth scales with the number of dipolar-coupled spins.[96,121,122] Exploiting this fact, it could be shown that Δ allows counting the number of dipolar-coupled spins in model systems,[73,123] a methodology that has been used to determine the oligomerization state of a multimeric protein.[101,124,125] Another approach for spin counting *via* PDS are multi-quantum coherence experiments combined with an appropriate phase cycle, which selectively filters out the dipolar signal arising from a system with *n* dipolar-coupled spins ($1 \leq n \leq 4$).[126]

The signal-to-noise ratio (SNR) of a PDS trace is given by [40]

$$SNR = \frac{\Delta}{\sigma(\mathrm{noise})} \tag{92}$$

with $\sigma(\mathrm{noise})$ being the standard deviation of the noise in the trace. The SNR depends on the spin concentration (typically 20-50 µM [40]) and the loss of coherence due to transverse relaxation during the dipolar evolution in the PDS experiment; thus, for a given phase-memory time T_M, the SNR will

decrease with increasing trace length. Signal averaging improves the SNR with the square root of the acquisition time [127] and it should ideally be larger than 20 to permit reliable data analysis.[40]

Various software packages have been released to compute a probability distribution of distances $P(r)$ (Figure 22c) from $V_{intra}(t)$, e.g. DeerAnalysis,[111] DeerLab,[128] DeerNet,[129] GLADD/DD,[130] and PeldorFit.[131] Transforming $V_{intra}(t)$ into $P(r)$ is an ill-posed mathematical problem, i.e. introducing small imperfections in $V_{intra}(t)$ such as noise and uncertainties from background removal can lead to large errors in $P(r)$.[111] A method to solve this ill-posed problem is Tikhonov regularization.[111,122]

In PDS data analysis, the experimental form factor $V_{intra}(t)$ is to be reproduced by a simulated form factor given by the product of a so-called kernel matrix $K(t,r)$ and the distribution $P(r)$:[111]

$$V_{intra}(t) = K(t,r) \cdot P(r) \tag{93}$$

Therein, $K(t,r)$ describes the correlation between $V_{intra}(t)$ and $P(r)$. Conventional least-squares fitting of the time trace minimizes the root-mean-square deviation of $K(t,r) \cdot P(r)$ and $V_{intra}(t)$; this, however, would lead to "overfitting" with the simulation reproducing noise in the experimental data.[111] The resulting distance distribution would be "spiky" and contain numerous narrow peaks, the positions and amplitudes of which vary with the SNR.[111] To circumvent this issue, Tikhonov regularization, also referred to as penalized least-squares fitting,[132] imposes a certain degree of smoothness on the distance distribution.[133] By introducing a penalty on distribution roughness, the target function to be minimized turns into [111]

$$G_\alpha(P) = \underbrace{\|K(t,r) \cdot P(r) - V_{intra}(t)\|^2}_{\rho\ (\text{time-domain misfit})} + \alpha \underbrace{\left\| \frac{d^2}{dr^2} P(r) \right\|^2}_{\eta\ (\text{roughness})} \tag{94}$$

The first term, $\rho = \left\|K(t,r) \cdot P(r) - V_{intra}(t)\right\|^2$, describes the mean-square deviation of the simulated and the experimental form factor called the time-domain misfit,[133] where ρ decreases as the simulation improves. The second term contains the roughness η of the distance distribution, mathematically given by the square norm of the second derivative of $P(r)$ with respect to r.[111] Large values of η indicate a steep change and thus a rough ("spiky") distribution. The regularization parameter α is the scaling factor of the roughness penalty,[133] which weights the smoothness of the distribution and the goodness-of-fit. [111] Thus, choosing an appropriate value for α provides a trade-off between the goodness-of-fit to the time trace and the smoothness of the distance distribution.

An aid in finding the optimal regularization parameter is the so-called L-curve, which is a plot of $\ln(\eta)$ against $\ln(\rho)$ for a range of regularization parameters α (Figure 22d).[111] Small values of α (left-hand side of the L-curve) tend to overfit and undersmooth,[132] i.e. they yield a good fit to the time trace (small $\ln(\rho)$) but produce a spiky distance distribution (large $\ln(\eta)$). By slightly increasing α, the distance distribution smoothens considerably and $\ln(\eta)$ decreases steeply, whereas $\ln(\rho)$ is affected only weakly.[111] This constitutes the left branch of the L-curve in Figure 22d. Large values of α in the right branch, by contrast, produce poor fits in the time domain (large $\ln(\rho)$) and oversmooth the distance distribution (small $\ln(\eta)$).[111] The regularization parameter that appropriately balances $\ln(\rho)$ and $\ln(\eta)$ corresponds to the intersection of both branches and it is defined by the L-curve corner criterion.[111]

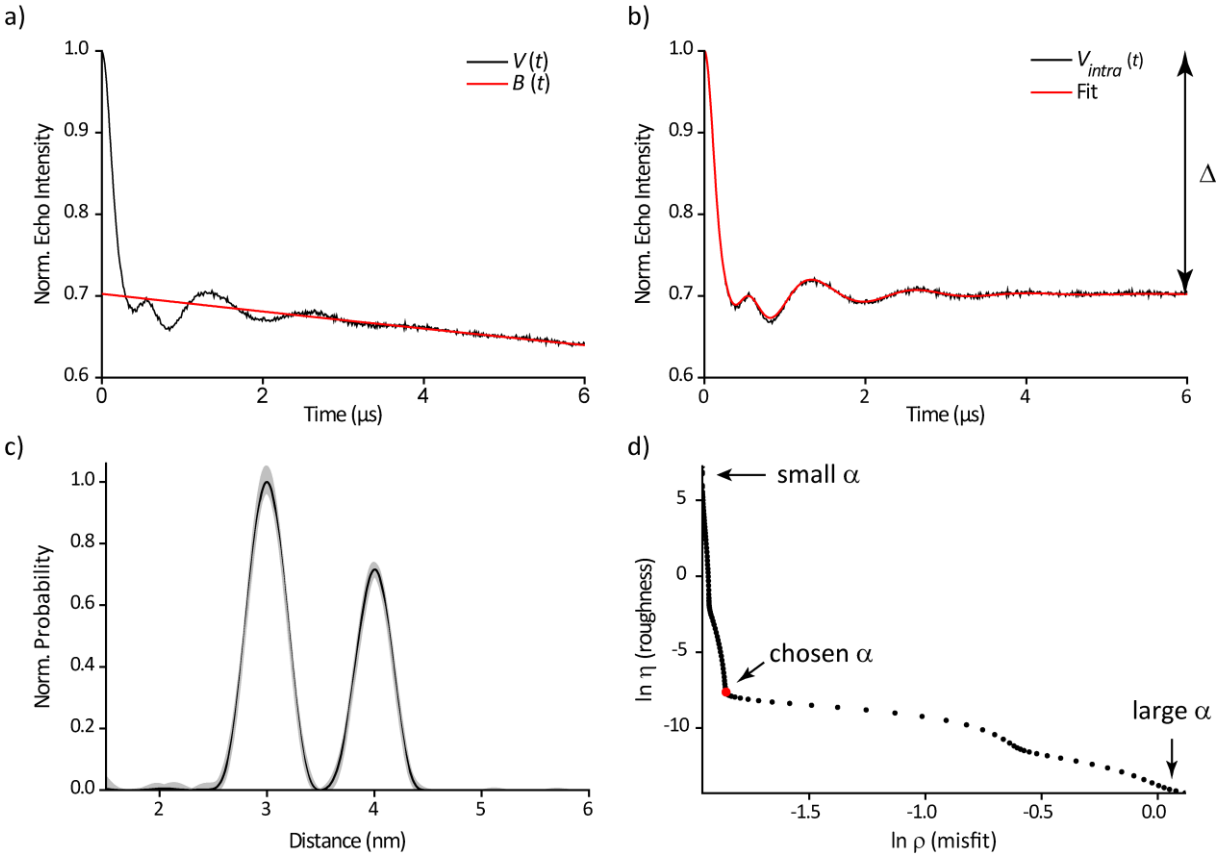

Figure 22: Transformation of PDS data into a distance distribution using Tikhonov regularization. a) Primary data $V(t)$ in black with a background fit $B(t)$ approximating $V_{inter}(t)$ in red. b) Background-corrected time trace $V_{intra}(t)$ in black and the fit obtained by Tikhonov regularization in red. The arrow marks the modulation depth Δ. c) Distance distribution. The uncertainty estimate from a background validation is shaded in grey. d) L-curve for Tikhonov regularization. The red dot marks the regularization parameter α chosen to compute the distance distribution.

An alternative and fully automatic approach for PDS data analysis called DEERNet uses artificial intelligence based on deep neural networks.[129] DEERNet directly converts $V(t)$ into $P(r)$ using solely its training database, i.e. no manual background fitting or choosing a regularization parameter are required.[114] The key benefit of this approach is its independence from (at least partially) subjective decisions such as background fitting and choosing the regularization parameter, thus rendering the data analysis more reproducible and less biased by user interference.[40,114]

The PDS experiment of choice depends on the spectral width and the relaxation properties of the two dipolar-coupled spins. In the case of a moderately broad spectrum (50 MHz ≙ 18 G) [89] and similar relaxation rates of both spins, Pulsed Electron-Electron Double Resonance (PELDOR) is applicable. This situation is encountered, e.g., for nitroxide-labelled biomolecules. If the dipolar-coupled spins have vastly different longitudinal relaxation times and spectral widths, e.g. a slowly-relaxing organic spin label with a narrow EPR spectrum and a fast-relaxing metal centre with a broad EPR spectrum, the experiment of choice would be Relaxation-Induced Dipolar Modulation Enhancement (RIDME). Finally, for spin centres with a narrow EPR spectrum like trityls, single-frequency experiments such as the Single Frequency Technique for Refocusing Dipolar Couplings (SIFTER) and Double-Quantum Coherence (DQC) are well-suited. The following sub-chapters give an overview of these methods.

1.2.3.1 PELDOR / DEER

Pulsed **El**ectron-Electron **Do**uble **R**esonance (PELDOR), also called **D**ouble **E**lectron-**E**lectron **R**esonance (DEER), is a PDS technique introduced in 1981 by Milov *et al.*[121,134] as a three-pulse sequence, which was extended in 1998 by Spiess [135] and Jeschke [136] to a four-pulse sequence.

PELDOR is a "pump-probe" experiment [137] that selectively addresses the dipolar-coupled spins A and B with two microwave frequencies, namely an observer frequency $\omega_{\mathrm{Observe}}$ resonant with spin A and a pump frequency ω_{Pump} resonant with spin B. To selectively address spins A and B, the frequency offset

$$\Delta\omega = \left|\omega_{Pump} - \omega_{Observe}\right| \tag{95}$$

should be large enough so that the excitation profiles of the microwave pulses do not overlap. Strongly overlapping excitation profiles would lead to artefacts in the time trace and reduce the modulation depth.[138]

In the original three-pulse PELDOR experiment (Figure 23), the observer sequence generates a Hahn echo (HE) on spin A and the pump pulse selectively flips spin B.[8] Inverting spin B changes the local magnetic field at spin A and thus shifts its Larmor frequency by the dipolar coupling frequency ω_{DD}.[40] This leads to a phase shift of $\pm\omega_{DD}T$ [40] and therefore imperfect refocusing of spin A by the π-pulse,[8] with *T* being the dipolar evolution time from the beginning of the sequence to the position of the pump pulse (Figure 23). Upon incrementing *T*, the intensity $V(T)$ of the Hahn echo oscillates periodically at ω_{DD} according to [8]

$$V(T) = V_0 \cos(\omega_{DD}T) \tag{96}$$

where V_0 is the intensity at $T = 0$. Recording the echo intensity as a function of *T* yields the PELDOR time trace.

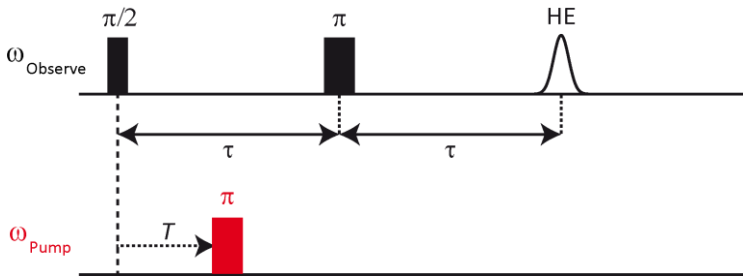

Figure 23: Schematic representation of the three-pulse PELDOR sequence. The intensity of the Hahn echo (HE) generated on spin A is recorded as a function of the dipolar evolution time *T*, which corresponds to the interval between the first observer pulse ($\pi/2$) and the pump pulse shown in red. Adapted from [8].

At small values of *T*, the pump pulse and the first observer pulse overlap, leading to artefacts in the trace that impede determining the zero-time of the dipolar evolution.[8] The acquisition of useful data is thus restricted to the dipolar evolution after the initial dead time, which complicates data analysis. This limitation has been removed by the dead-time free four-pulse PELDOR sequence (Figure 24a), which is nowadays the most widely used PDS experiment.[7,40]

Four-pulse PELDOR differs from its predecessor in that the observer sequence contains an additional refocusing pulse at a delay τ_2 after the HE (Figure 24a). Keeping the length of the interpulse delays τ_1 and τ_2 constant and incrementing the position of the pump pulse within the first interval τ_2 leads to a refocused echo (RE) that oscillates at $\cos(\omega_{DD}T)$.[40] The zero-time of the dipolar evolution and thus the maximum of the trace occurs when the position of the pump pulse coincides with the Hahn echo.[139] As there is no pulse overlap at short dipolar evolution times, the experiment does not suffer from a dead time and the beginning of the trace is artefact-free.

To invert as many spins as possible and to maximize the sensitivity, the pump pulse is commonly set to the maximum of the EPR spectrum and the observer pulse is applied at the offset $\Delta\omega$.[40] Figure 24b illustrates the positions of the pump and observer pulse in the nitroxide spectrum at Q-band, highlighting that a frequency offset of 80-100 MHz [40] provides a good trade-off between minimizing the bandwidth overlap and retaining a sufficient spectral intensity at the observer position.

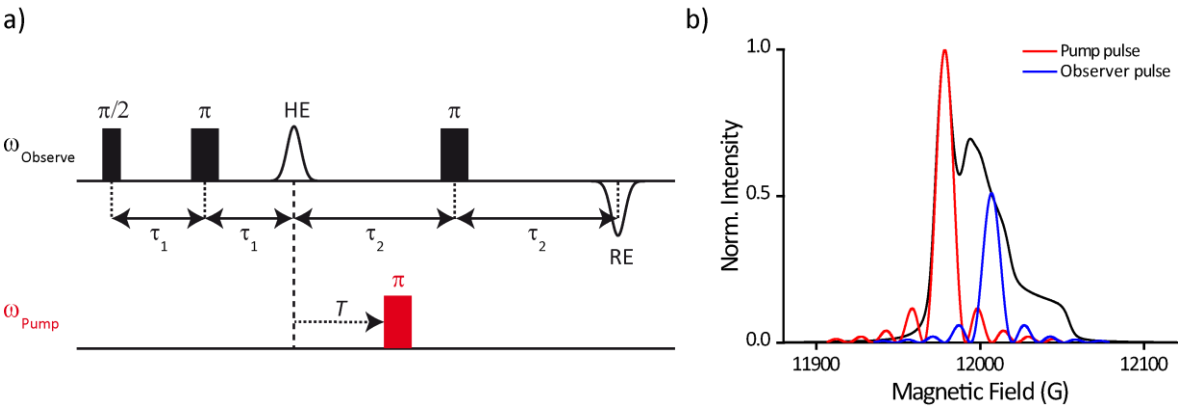

Figure 24: a) Pulse sequence of four-pulse PELDOR. The observer sequence (black) acting on spin A creates a Hahn echo (HE) and a refocused echo (RE). The position of the pump pulse (red) relative to the HE is given by the dipolar evolution time *T*, with *T* being incremented during the PELDOR experiment. When the pump pulse inverts spin B, the local magnetic field and thus the Larmor frequency of spin A changes, which shifts the phase of spin A by $\omega_{DD}T$. Consequently, the intensity of the RE oscillates at $\cos(\omega_{DD}T)$ upon incrementing *T*. Recording the intensity of the RE as a function of T yields the PELDOR time trace. b) Excitation profiles of rectangular pump and observer pulses (pulse lengths: 24 ns) simulated with EasySpin.[30] The pump pulse (red) is set to the maximum of the nitroxide spectrum (Q-band, black) and the observer pulse (blue) is applied at a frequency offset of $\Delta\omega = 80$ MHz. Adapted from [40].

As the spectrum is broader than the excitation bandwidth of the microwave pulses, the pulses excite only a fraction of spins A and B.[140] Assuming that the excited spins correspond to all possible values of θ (Figure 7), the PELDOR time trace encodes the whole Pake pattern.[100] However, if sampling of all angles θ is not achieved, a phenomenon called orientation selection can occur, which is often the case for rigid biomolecules and rigid spin labels.[8,136,141] If orientation selection is present, the pulses excite only those spin pairs that have a certain orientation θ, which depends on the positions of the pump and probe pulses in the EPR spectrum. The time trace then no longer encodes the whole Pake pattern and the resulting distance distribution would be biased. Averaging the time traces recorded at different spectral positions of pump and probe pulses is a means to suppress orientation selection.[40] Further, by simulating the time traces, angular information can be obtained in addition to the distance.[131]

Guidelines on the acquisition and analysis of PELDOR data have been defined in the community White Paper.[40] A detailed step-by-step workflow on setting up a PELDOR experiment and on data analysis developed in the context of this thesis can be found in references [142] and [143].

1.2.3.2 RIDME

Relaxation-**I**nduced **D**ipolar **M**odulation **E**nhancement (RIDME) [144–146] is well-suited if the dipolar-coupled spins A and B have largely different longitudinal relaxation times, where $T_1(A) \gg T_1(B)$ is assumed in the following discussion. This situation is encountered for spin systems that consist of, e.g., a slowly-relaxing organic spin label and a fast-relaxing metal centre.[147] In contrast to the two-frequency technique PELDOR, RIDME is a single-frequency experiment that generates an echo on the slowly-relaxing spin A. Spin B, which is selectively inverted in PELDOR by the pump pulse, flips spontaneously in RIDME due to longitudinal relaxation; this corresponds to changing its magnetic quantum number m_s.[148] Random flips of spin B alter the resonance frequency of spin A by $\Delta m_s \cdot \omega_{DD}$, leading to a modulation of the echo.[147] If spin B has $S = 1/2$, $|\Delta m_s| = \pm 1$, i.e. the RIDME trace is modulated only at the base frequency ω_{DD} of the dipolar coupling. For spin systems of $S > 1/2$, however, $|\Delta m_s|$ takes any integer value between $-2S$ and $+2S$, which leads to the admixture of higher harmonics of ω_{DD} to the time trace (e.g. $2\omega_{DD}$, $3\omega_{DD}$).[148]

While the excitation bandwidth is limited in PELDOR by the length of the pump pulse, the spontaneous spin flips in RIDME act like an inversion pulse of "virtually infinite […] bandwidth".[149] Thus, in contrast to PELDOR, RIDME allows measuring the dipolar coupling if the EPR spectrum of the B-spin exceeds the excitation bandwidth of the microwave pulses. This situation occurs, e.g., for metal ions with a large *g*-anisotropy such as Fe(III).[147,150,151]

Figure 25 shows the sequence of the five-pulse RIDME experiment. It starts with the equilibrium magnetization of spin A given by the vector $(0, 0, -M_0)$. The first $\pi/2$-pulse applied in x-direction tilts the magnetization to the y-axis, i.e. $(0, -M_0, 0)$. Within the delay τ_1, the magnetization precesses in the transverse plane and is described by $(-M_0\sin(\omega\tau), -M_0\cos(\omega\tau), 0)$ with ω being the off-resonance frequency of the spin packet.[145] The following π-pulse refocuses the magnetization and creates a Hahn echo at the time $2\tau_1$. During the interval *t* after the Hahn echo, the spin packets start to defocus again.[149] Next, a $\pi/2$-pulse applied in x-direction rotates the y-component of the transverse magnetization to the z-axis,[148,149] resulting in $\big(-M_0\sin(\omega\tau), 0, +M_0\cos(\omega\tau)\big)$,[145] where it is stored during the mixing time T_{mix}.[149] Since T_{mix} is longer than the phase-memory time of spin A, the x-component of the magnetization decays, eventually leading to $\big(0, 0, +M_0\cos(\omega\tau)\big)$.[145] If T_{mix} is of the order of the longitudinal relaxation time of spin B, the latter will flip spontaneously during T_{mix} and thereby change the Larmor frequency of spin A by the dipolar coupling frequency.[149] Another $\pi/2$-pulse rotates the magnetization to the y-axis, i.e. $(0, +M_0\cos(\omega\tau), 0)$, which can be expressed as the sum of the vectors $(-M_0/2\,\sin(\omega\tau), +M_0/2\,\cos(\omega\tau), 0)$ and $(+M_0/2\,\sin(\omega\tau), +M_0/2\,\cos(\omega\tau), 0)$.[145] The first vector corresponds to a stimulated echo (SE), the latter can be refocused by the final π-pulse to form a refocused virtual echo (RVE).[145,148,149] In addition to generating the RVE, the π-pulse also refocuses the SE to a refocused stimulated echo (RSE).
Both the RSE and the RVE are modulated by the dipolar coupling.[145] While the RVE occurs at a constant point in time ($t_{\mathrm{RVE}} = 2\tau_1 + 2\tau_2 + T_{mix}$) at a delay τ_2 after the last π-pulse, the temporal position of the RSE changes as it depends on *t*. The RSE occurs at $t_{\mathrm{RSE}} = 2\tau_1 + T_{mix} + 2\tau_2 - 2t$, i.e. at a delay $\tau_2 - 2t$ after the last π-pulse.

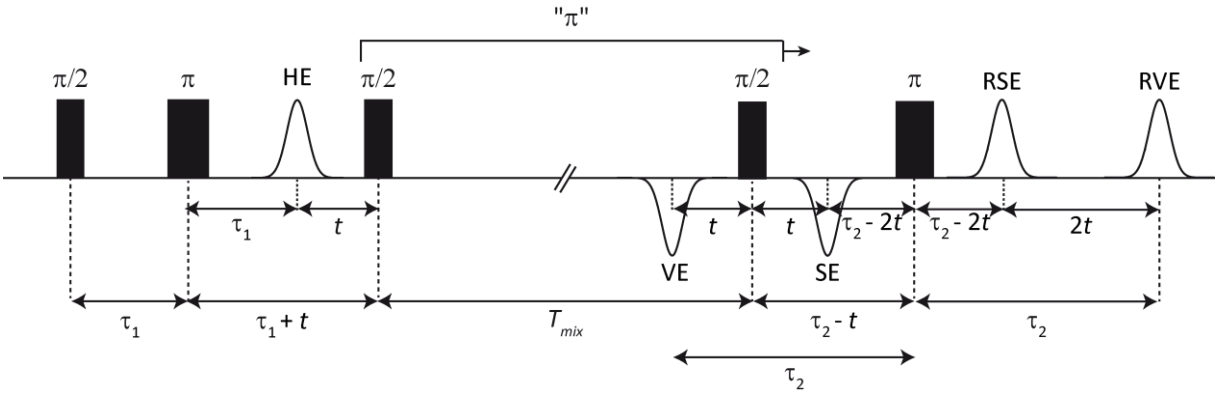

Figure 25: Pulse sequence of the five-pulse RIDME experiment; HE abbreviates "Hahn echo", VE "virtual echo", SE "stimulated echo", RSE "refocused stimulated echo", and RVE "refocused virtual echo". The magnetization of a slowly-relaxing spin A is monitored *via* the RSE or the RVE, while spin B spontaneously flips during the mixing time T_{mix} and thus modulates the echo. Recording the echo intensity as a function of t while incrementing $\tau_1 + t$ and decrementing $\tau_2 - t$ yields a RIDME time trace that encodes the dipolar coupling. Adapted from [145,146].

In RIDME, the interval $\tau_1 + t$ is incremented and $\tau_2 - t$ is decremented. The intensity of either the RSE or the RVE is recorded as a function of t to obtain a RIDME time trace that encodes the dipolar coupling.[147] In practice, one often prefers the RVE over the RSE:[145,152] Detecting the RSE at any delay t requires the interval $\tau_2 - 2t$ to be longer than the spectrometer dead time ($\tau_2 > 2t + t_{dead}$). Thus, for long RIDME traces (long t), large values of τ_2 are required, which would lead to a concomitantly low signal intensity due to dephasing.[145] For the RVE, by contrast, the relation $\tau_2 > t_{dead}$ needs to be fulfilled, i.e. less dephasing will occur and the signal intensity will be higher. This increases the sensitivity and the SNR.[153] Beyond these aspects, RIDME traces recorded using the RVE have been reported to contain a lower contribution of higher harmonics of the dipolar coupling and more prominent oscillations.[153]

The modulation depth Δ in a RIDME experiment depends only on the length of T_{mix}, the spin state S of spin of B, and the longitudinal relaxation of spin B, but not on its spectral width.[147,148] In RIDME [148]

$$\Delta(\Delta m_s \neq 0) = 1 - \frac{1}{2S+1} \tag{97}$$

can be up to 50% for spin systems of S = 1/2 and even larger for systems of S > 1/2.

Orientation selection can be present in RIDME for two reasons, the first being the incomplete excitation of the spectrum of spin A. It occurs if the EPR spectrum is broader than the excitation bandwidth of the microwave pulses and can be identified by performing RIDME at different magnetic field values. Secondly, relaxation anisotropy of spin B can induce orientation selection.[154,155] Comparing RIDME traces acquired with different mixing times is a means to check for orientation selection from relaxation anisotropy.[154]

1.2.3.3 DQC

Double **Q**uantum **C**oherence (DQC) is a single-frequency PDS technique introduced in 1996 by Freed *et al*.[9,45,46,156–158] By contrast to PELDOR and RIDME, the DQC experiment cannot be considered as a typical pump-probe experiment. Therefore, the working principle of DQC is usually described using the concept of coherence order.[45] For the following discussion, the coherence orders p = 0 (zero-quantum coherence, ZQC), p = ± 1 (single-quantum coherence, SQC), and p = ± 2 (double-quantum coherence, DQC) are relevant.[45] Zero-quantum coherence (p = 0) describes the longitudinal magnetization in the thermal equilibrium.[159,160] Single-quantum coherence (p = ±1) corresponds to transverse magnetization,[159] with p = -1 called *in-phase* coherence and p = +1 called *anti-phase* coherence.[45] Only *in-phase*

coherence is detectable in EPR spectroscopy.[45] Coherence of higher order such as double-quantum coherence (DQC, p = ±2) corresponds to zero net magnetization and is thus not directly observable.[45] Nevertheless, it can be converted to single-quantum *in-phase* coherence, which corresponds to a detectable spin echo.[45]

Coherence is generated and interconverted by microwave pulses: A $\pi/2$-pulse creates coherence (e.g. $p = 0 \rightarrow p = +1$, i.e. $\Delta p = 1$) [45] or changes the coherence order by an uneven number (e.g. $p = -1 \rightarrow p = +2$, i.e. $\Delta p = 3$) [161] and a π-pulse inverts the coherence order (e.g. $p = +1 \rightarrow p = -1$, i.e. $\Delta p = 2$).[161] The free evolution in the interpulse delays, by contrast, does not change the coherence order ($\Delta p = 0$). A coherence transfer map (Figure 26b) is a graphical representation of the coherence order and its changes during the experiment.[159,160]

Spin echoes arise when the system has been equally long on the p = +1 and p = -1 coherence order.[159,162] This fact can be rationalized by considering the difference in the resonance frequency ω_s of a spin and the microwave frequency ω_{MW} [159]

$$\Omega_s = \omega_s - \omega_{MW} \tag{98}$$

If $\Omega_s \neq 0$, the spins acquire a phase offset $\exp(-ip\Omega_s t)$ during free evolution,[159] with i being the imaginary unit, p the coherence order, and t the time of free evolution. By spending the time t at both coherence orders, p = +1 and p = -1, the phase offsets cancel. If all spins with their individual Ω_s are in phase and refocus, a spin echo will occur.[159,162]

The six-pulse DQC sequence shown in Figure 26a consists of $\pi/2$- and π-pulses separated by the interpulse delays τ_1, τ_2, and T. It can be subdivided into three sections: (i) The preparation block $(\pi/2 - \tau_1 - \pi - \tau_1 - \pi/2)$ that creates DQC, (ii) the evolution block $(T - \pi - T)$ in which DQC is refocused, and (iii) the mixing and detection block $(\pi/2 - \tau_2 - \pi - \tau_2)$ that generates *in-phase* SQC and thus a detectable spin echo.[9,45,157]

In the preparation block, a $\pi/2$-pulse (pulse 1) creates SQC (p = ± 1), which evolves during the interval τ_1 and in the presence of the dipolar coupling ω_{DD} [45] as *in-phase* (p = -1) and *anti-phase* (p = +1) coherence.[45] A π-pulse (pulse 2) refocuses the coherences and thereby inverts the coherence order from p = ±1 to $p = \mp 1$.[81] At the time τ_1 after this π-pulse, the coherence has been equally long at p = +1 and p = -1 (or equally at p = -1 and p = +1), a situation in which the *in-phase* SQC (p = -1) leads to a Hahn echo that is modulated by ω_{DD}.[45,159] Applying a $\pi/2$-pulse (pulse 3) at the time of the Hahn echo transforms *anti-phase* SQC (p = +1) into DQC (p = ±2), which is refocused by the π-pulse (pulse 4) in the evolution block.[45] This refocusing maximizes the echo intensity at the end of the pulse sequence.[45] Of note, DQC will arise only for dipolar-coupled spins,[163] i.e. molecules with a single spin will not contribute to the final signal, provided that the intermolecular dipolar coupling is weak.[9,45] Recalling that DQC corresponds to zero net magnetization,[45] it is obvious that it needs to be converted into SQC for detection. This is accomplished by the $\pi/2$-pulse (pulse 5) in the mixing and detection block, which transforms the previously refocused DQC (p = ±2) into *anti-phase* SQC (p = +1).[45] The final π-pulse (pulse 6) refocuses ("mixes") the *anti-phase* SQC (p = +1) into in-phase SQC (p = -1), which is detected as a spin echo.[45]

As can be seen from Figure 26b, four coherence transfer pathways involving DQC occur, namely: (i) p: 0 → +1 → -1 → +2 → -2 → +1 → -1; (ii) p: 0 → +1 → -1 → -2 → +2 → +1 → -1; (iii) p: 0 → -1 → +1 → -2 → +2 → +1 → -1; (iv) p: 0 → -1 → +1 → +2 → -2 → +1 → -1.[164] Applying a 64-step [45] phase cycle extracts these four pathways and efficiently suppresses contributions from all other (undesired) coherence pathways that do not involve DQC.[50] In that regard, the sequence $(\pi/2 - T - \pi - T - \pi/2)$ that generates, refocuses, and converts DQC acts as a so-called double-quantum filter (DQF).

Note that this DQF only "labels"[9] the DQC pathways to be retained, while the filtering itself is accomplished by the phase cycle.[9]

In the DQC experiment, τ_1 is incremented and τ_2 is simultaneously decremented, i.e. the temporal position of the echo $\left(t_{\mathrm{DQC}} = 2\tau_1 + 2T + 2\tau_2\right)$ does not change. The delay *T* is kept constant throughout the sequence, i.e. the DQF is shifted along the time axis. Recording the echo intensity as a function of $\tau_1 - \tau_2$ yields the DQC time trace (Figure 26c), which is symmetric about its maximum at the refocusing position [8] ($\tau_1 = \tau_2$). For data analysis, the trace is mirrored about its maximum, which increases the signal-to-noise ratio by a factor of $\sqrt{2}$.

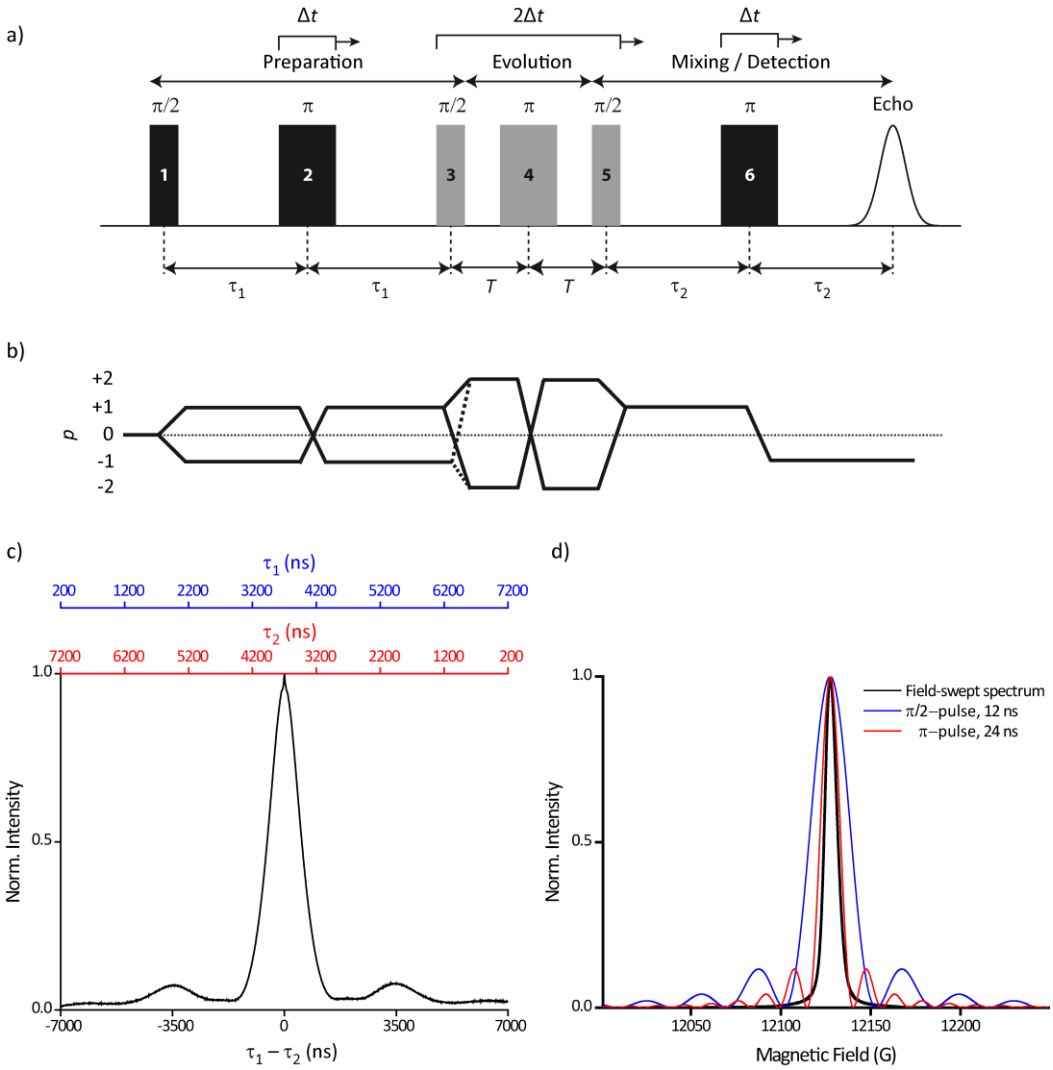

Figure 26: The DQC experiment. a) Pulse sequence of the six-pulse DQC experiment. The interpulse delay τ_1 is incremented by Δt and τ_2 is simultaneously decremented by Δt; this corresponds to shifting pulses 2 and 6 by Δt and pulses 3, 4, and 5 by $2\Delta t$. The echo intensity is recorded as a function of $\tau_1 - \tau_2$. Adapted from [9]. b) Coherence transfer map showing the pathways of quantum coherence order *p* in the DQC experiment. Adapted from [9]. Starting at p = 0, the initial $\pi/2$-pulse (pulse 1) generates *in-phase* and *anti-phase* SQC (*p* = ± 1). The π-pulse (pulse 2) inverts the sign of the coherence order to *p* = ∓1. The following $\pi/2$-pulse (pulse 3) generates DQC (*p* = ± 2), which is refocused (*p* = ∓ 2) by a π-pulse (pulse 4). A $\pi/2$-pulse (pulse 5) converts the DQC into *anti*-phase SQC (*p* = +1), which is refocused to *in-phase* SQC (*p* = -1) by the final π-pulse (pulse 6) and thus gives rise to a spin echo. The segment $\pi/2 - T - \pi - T - \pi/2$, which generates DQC and converts it back to SQC, is called the "double-quantum filter". c) DQC trace as a function of τ_1, τ_2, and $\tau_1 - \tau_2$. Note that the maximum of the trace is obtained at $\tau_1 = \tau_2$. d) Excitation profiles of rectangular microwave pulses ($\pi/2$ = 12 ns, blue; π = 24 ns, red) simulated with EasySpin.[30] The field-swept spectrum of a trityl radical at Q-band is shown in black. As the excitation bandwidth of the microwave pulses exceeds the trityl spectrum, it is fully excited in the DQC experiment.

As a single-frequency PDS technique, DQC performs well on spin centres with a narrow EPR spectrum such as trityl radicals.[120,147] Provided that the width of the spectrum is equal to or smaller than the pulse bandwidth, it can be fully excited with rectangular microwave pulses (Figure 26d).[26,73,165] This leads to a high sensitivity even at low concentrations,[45] a modulation depth of up to 100%, and an accordingly high signal-to-noise ratio (eq. (92)).[45,73,163] Furthermore, full excitation excludes orientation selection [8,9,45,50] and it may allow determining interspin distances below 15 Å.[8,45,50,166] In that regard, care has to be taken that the excitation bandwidth of the pulses still exceeds the dipolar coupling frequency ω_{DD}; otherwise, the pseudo-secular contribution to the dipolar Hamiltonian needs to be taken into account in data analysis (section 1.1.4.6).[53] By combining DQC with shaped pulses,[167] the whole EPR spectrum of paramagnetic species with a larger spectral width can be excited, which makes the technique very promising.[168]

Compared with PELDOR, RIDME, and SIFTER (section 1.2.3.4), time traces obtained from the DQC experiment usually have a small contribution from the non-modulated intermolecular background.[9] Nevertheless, as demonstrated on singly-labelled biomolecules,[169] they are not entirely background-free so that background removal is still important.[7] Note that the background function of the DQC experiment cannot be described analytically and it depends on the shape of the EPR spectrum, the excitation profile of the pulses,[7] the spin concentration, and the dipolar evolution time.[9]

A detailed workflow on setting up a DQC experiment and on DQC data analysis has been developed in the context of publications [P4], [P5], [P6], and [P7] and is provided in appendix 7.3.

1.2.3.4 SIFTER

The **Si**ngle-**F**requency **T**echniq**e** for **R**efocusing Dipolar Couplings (SIFTER) was developed in 2000 by Spiess and Jeschke.[75] Like DQC, it uses a single microwave frequency and thus has optimal performance when applied to spin centres with a narrow EPR spectrum or in combination with shaped pulses.[116,170]

SIFTER is based on the solid-echo sequence $\left((\pi/2)_x - \tau - (\pi/2)_y - \tau - \mathrm{Echo}\right)$ known from NMR spectroscopy [8,171] to refocus the dipolar coupling between *like* spins, but not between unlike spins.[41,75,171] For optimal performance in PDS, a π-pulse has been introduced into each of the delays τ,[60,75] which yields the SIFTER sequence shown in Figure 27a.

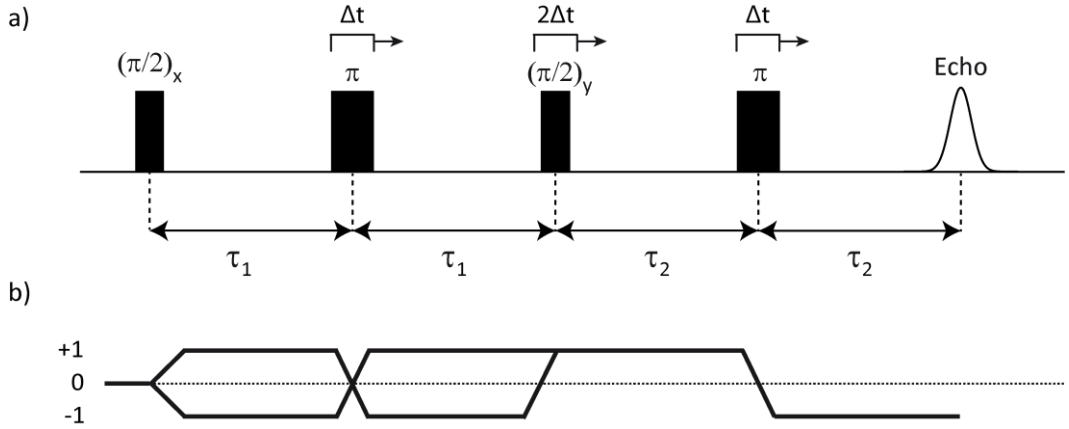

Figure 27: The SIFTER experiment. a) Pulse sequence of the SIFTER experiment. The interpulse delay τ_1 is incremented by Δt and τ_2 is simultaneously decremented by Δt; this corresponds to shifting the π-pulses by Δt and the $(\pi/2)_y$-pulse by $2\Delta t$. The echo intensity is recorded as a function of $\tau_1 - \tau_2$. b) Coherence transfer map showing the pathways of quantum coherence order *p* in the SIFTER experiment. Adapted from [9].

As shown for the DQC experiment, coherence orders are a means to describe the effect of microwave pulses in SIFTER (Figure 27b): Starting at p = 0, the first $(\pi/2)_x$ -pulse generates SQC (p = ±1), which is refocused by the following π-pulse (p = ∓1). Next, a $(\pi/2)_y$-pulse, whose phase is shifted by 90° compared to the $(\pi/2)_x$-pulse,[170] produces *anti-phase* coherence and thereby refocuses the dipolar coupling.[170] The last π-pulse converts the *anti-phase* coherence (p = +1) into *in-phase* coherence (p = -1), i.e. a detectable (refocused) spin echo, which oscillates at the dipolar coupling frequency.[9,75]

Comparing the pulse sequences of SIFTER (Figure 27) and DQC (Figure 26), it becomes obvious that both selectively generate *anti-phase* coherence (p = +1) in the last-but-one step, which is finally converted into detectable *in-phase* coherence (p = -1). However, the origin of the *anti-phase* coherence differs between the two pulse sequences: Whereas the DQC experiment generates *anti-phase* coherence *via* the double-quantum filter, SIFTER uses a $(\pi/2)_y$-pulse for that purpose. Thus, and by contrast to the DQC experiment, SIFTER is purely based on SQC and does not involve double-quantum coherence (Figure 27b).

The pulse timing in DQC and SIFTER is the same, i.e. τ_1 and τ_2 are incremented and decremented, respectively, and the echo intensity is recorded as a function of $\tau_1 - \tau_2$. The dipolar coupling is fully refocused at $\tau_1 = \tau_2$ so that the SIFTER trace peaks at $\tau_1 - \tau_2 = 0$.[8] Like DQC, SIFTER is a constant-time experiment, i.e. the length of the pulse sequence and thus the position of the echo on the time axis ($t_{\mathrm{SIFTER}} = 2\tau_1 + 2\tau_2$) does not change.[75] Compared with DQC, SIFTER has a stronger background contribution.[73,169]

1.2.4 Pulsed Dipolar EPR Spectroscopy for Biomolecular Structure Elucidation

1.2.4.1 Spin Labels and Spin Labelling for Pulsed Dipolar EPR spectroscopy

Distance distributions from PDS measurements provide coarse-grained information on the structure of biomolecules. They report on the structural (dis)order,[172] can be used to determine the position of metal ions *via* trilateration,[173] and permit inferring conformational changes upon ligand binding [15,174,175] or the translocation from *in vitro* into cells.[165,176,177] For a PDS experiment, the biomolecule needs to carry at least two unpaired electrons.[8,147] Some biomolecules are paramagnetic by their very nature, e.g. metalloproteins that contain paramagnetic ions like Fe(III) and Cu(II),[115,147] or intermediates in biochemical processes such as the tyrosyl radical.[178,179] Most biomolecules, however, lack unpaired electrons and are thus diamagnetic, which renders them EPR-silent.[180,181] This changed with the advent of site-directed spin labelling (SDSL), a technique to attach paramagnetic reporter molecules called spin labels to selected sites of the biomolecule. Spin labels convey paramagnetism either through open-shell metal ions like Cu(II) [182–185] and Gd(III) [186–190] or *via* stable organic radicals like nitroxides [29,97,191–193] and tetrathiatriarylmethyl (trityl, TAM) [120,165,169,194–197] radicals. They have a bioconjugation group that reacts with the labelling site of the biomolecule, e.g. a cysteine residue of a protein or an alkyne substituent of a modified oligonucleotide.

In nitroxides, the spin density is (de)localized in the N–O bond with approx. 60% residing on the oxygen atom and 40% on the nitrogen atom.[181] Methyl or more bulky substituents adjacent to the N-O-bond sterically shield the radical and thus stabilize it.[181] Figure 28 shows a selection of nitroxide spin labels with different bioconjugation groups for proteins and oligonucleotides and exemplarily indicates the labelling reaction. For clarity, the bioconjugation group of the label is shown in blue and the reacting fragment on the biomolecule in red.

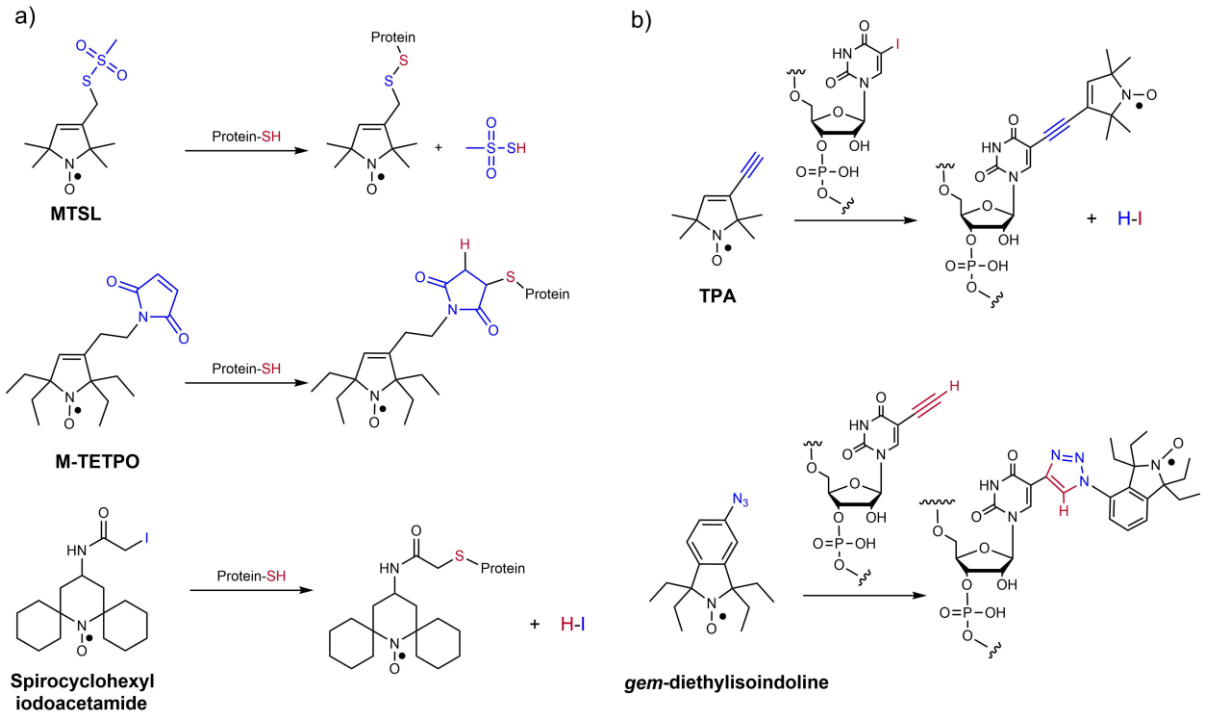

Figure 28: Nitroxide spin labels. a) Cysteine-selective nitroxide labels for proteins. The most commonly used **m**ethane**thio**sulfonate-functionalized label MTSL [97] forms a disulphide bond (R–S–S–R) with the cysteine residue. Maleimides such as the **t**etra**et**hylpi**p**eridinyl**o**xy-based M-TETPO [192,193] and iodoacetamide such as spirocyclohexyl iodoacetamide [198] form thioether (C–S–C) bonds. b) Nitroxide labels for oligonucleotides. 2,2,5,5-**t**etramethyl-**p**yrrolin-1-oxyl-3-**a**cetylene (TPA) links with the unnatural nucleotide 5-iodouridine in a Sonogashira cross-coupling reaction,[199] the azide-functionalized *gem*-diethylisoindoline [200] nitroxide undergoes a "click"-reaction with the alkyne-functionalized nucleotide.

By far most common for protein labelling is the commercially available methanethiosulfonate-functionalized nitroxide MTSL (also called MTSSL),[97] which forms a disulphide bond with a cysteine residue (R–S–S–R, Figure 28a). Well-established procedures for labelling with MTSL have been developed and the disulphide bond is principally strong enough for stable bioconjugation, but it cleaves under reducing conditions as found in cells.[192,201]

Another functional group often used for protein labelling is maleimide as in M-TETPO [192] (Figure 28a), which targets cysteine residues and forms a thioether bond (C–S–C) by a Michael addition.[202] In contrast to the disulphide-linkage of MTSL, the thioether bond is stable in the reducing environment of living cells.[201,203] For this reason, the maleimide moiety has found widespread application not only for the bioconjugation of nitroxides and other spin labels such as trityls [165,169,195,196] (*vide infra*) but also for labelling with fluorescent dyes in microscopy.[204] Challenges encountered with maleimide labels include their higher steric demand compared with MTSL,[201] their propensity to unspecifically label amino acids other than cysteine (e.g. lysine), and the hydrolysis of the maleimide group.[201] Note that the two latter phenomena occur only under basic conditions and can therefore be alleviated by controlling the pH-value during the labelling reaction (pH ≈ 7).[169,201] If labelling at a neutral pH is not feasible, exchanging the maleimide by the less pH-sensitive iodoacetamide group (e.g. spirocyclohexyl iodoacetamide,[127] Figure 28a) may be worth trying.[201]

Spin labels for oligonucleotides (Figure 28b) include 2,2,5,5-tetramethyl-pyrrolin-1-oxyl-3-acetylene (TPA) [199] and the azide-functionalized *gem*-diethylisoindoline nitroxide,[200] which react with the chemically modified oligonucleotide *via* Sonogashira cross-coupling and “click”-chemistry, respectively.

Commonly, PDS measurements are conducted in dilute frozen solution at cryogenic temperatures (< 80 K),[205] i.e. under a condition that is markedly different from the native environment of the biomolecule in a living cell. Since the measurement conditions can tremendously influence the distance distribution and thus the structure derived from it, the ultimate goal would be to perform the PDS experiment *in cell* and at room temperature. As demonstrated by injection into oocytes of *Xenopus laevis* (African clawed frog), maleimide-linked nitroxides like M-TETPO (Figure 28a) can in principle be used for *in cell* PDS experiments.[192] Further, the spirocyclohexyl iodoacetamide label (Figure 28a) allowed PELDOR measurements at room temperature.[127] Nevertheless, these experiments suffer from two limitations imposed by nitroxides: Firstly, their lifetime in the cellular environment is relatively short, as they are reduced to diamagnetic hydroxylamines within minutes.[192,206] Secondly, their phase-memory time T_M is short at room temperature, which limits the dipolar evolution time in PDS experiments.[127]

An alternative class of spin labels that addresses these limitations are (tris)-tetrathiatriarylmethyl radicals (trityls, TAM).[207,208] They are based on the triphenylmethyl radical, the first organic radical ever discovered, which was identified by Gomberg in 1900.[207] Trityl spin labels with different bioconjugation groups have been developed, most of them are ester or amide derivatives of the so-called Finland trityl (FTAM) radical.[209] Figure 29a shows the structural formulae of FTAM and various trityl spin labels (TSLs).

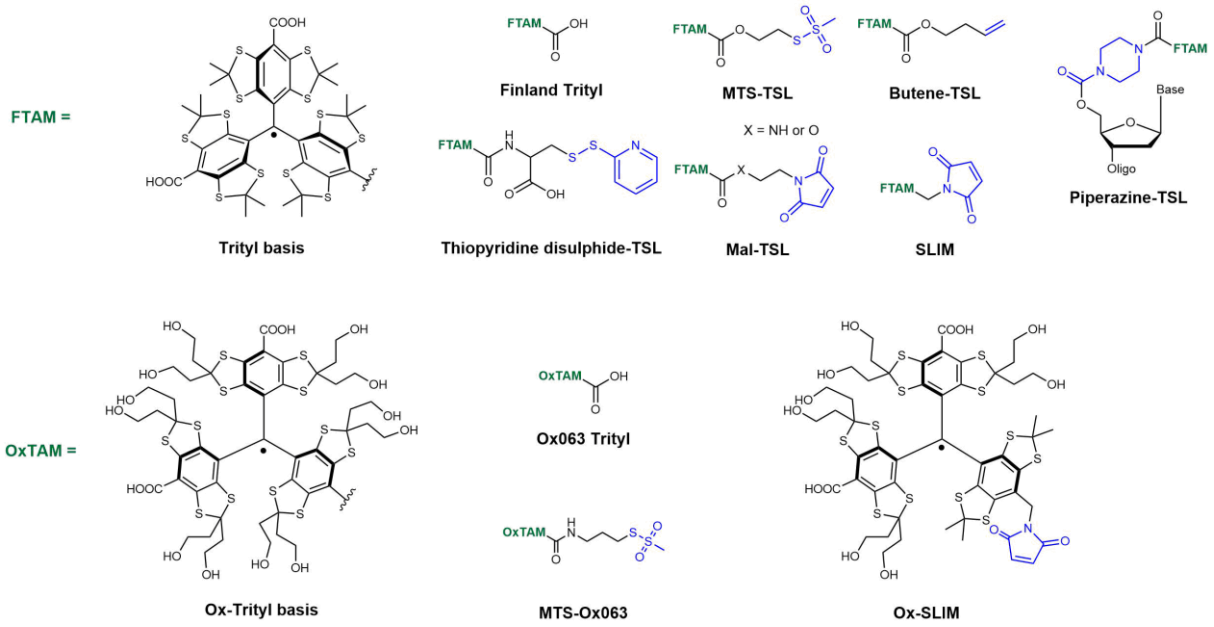

Figure 29: Structures of Finland trityl (FTAM) and trityl spin labels (TSLs). Most TSLs arise from esterification [169,194] or amidation [196,210,211] of FTAM, whereas the maleimide groups of the **s**hort-**li**nked **m**aleimide (SLIM) [165] and Ox-SLIM [195] are connected to the trityl basis by a single methylene group. Replacing the methyl groups at the thioketals of FTAM by hydroxyethyl substituents (OxTAM) increases the hydrophilicity as in MTS-Ox063 [208] and Ox-SLIM.[195]

Bioconjugation groups used for trityls include methanethiosulfonate,[194,208] butene,[194] piperazine,[211–213] thiopyridine disulphide,[210] and maleimide.[165,169,195,196] They are linked to the trityl basis *via* esterification [169,194] or amidation [196,210,211] of Finland trityl, or *via* C-C cross-coupling.[165,195] Owing to their large nonpolar basis, Finland-type trityl labels are hydrophobic, which can trigger aggregation of the label with itself [214,215] or with hydrophobic regions of the biomolecule.[169,194,196,216] A means to increase the hydrophilicity, mediate water solubility,[217] and thereby counteract aggregation is replacing the methyl groups in Finland-type trityls by hydroxyethyl substituents. This leads to the so-called Ox-type trityls, with Ox063 [217] being the parent compound and MTS-Ox063 [208] and Ox-SLIM [195] labels derived from it.

In contrast to nitroxides, trityls are highly biopersistent, i.e. they can withstand the reductive conditions *in cell* for several hours.[165,197,218] This allows studying the structure of a biomolecule in its native cellular environment.[165,194,197] Further, trityls have a phase-memory time of up to 10 µs at room temperature [219] and therefore allow PDS under almost physiological conditions.[212,213]

In the absence of hyperfine coupling and due to their small *g*-anisotropy, trityls exhibit a narrow EPR spectrum even at higher magnetic fields. This allows exciting the whole spectrum with rectangular microwave pulses.[26,196] Therefore, combining trityls with single-frequency techniques provides high sensitivity, a good signal-to-noise ratio, and allows PDS measurements at spin concentrations as low as 45 nM.[195] An important aspect concerning PDS on trityls is the delocalization of the spin across the aromatic system, with approx. 70% of the spin density located at the central carbon atom and the remaining 30% distributed across the phenyl rings.[52,220] This needs to be taken into account when analysing PDS data at interspin distances below 2.5 nm, where it may invalidate the point-dipole approximation.[52,72(p.96),172] At larger distances, however, trityls behave like an effective point-dipole with respect to the partner spin, i.e. spin-density delocalization can be neglected in that case.[72(p.96)] Despite their advantageous properties, trityl labels have a downside in that their relatively large size compared to nitroxide spin labels may interfere with the biomolecule and thus impede its structure and function.[175,216]

Apart from stable organic radicals, spin labels can be based on paramagnetic metal ions or light-induced triplet states. Figure 30 shows examples of Gd(III),[186,190] Cu(II),[184,185] and photoactivatable [221–223] spin labels.

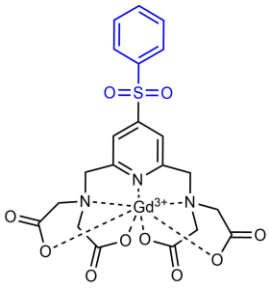

4PS-PyMTA-Gd(III)

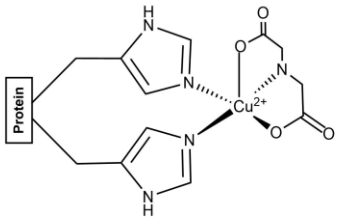

Cu(II) double histidine Cu(dHis)-IDA

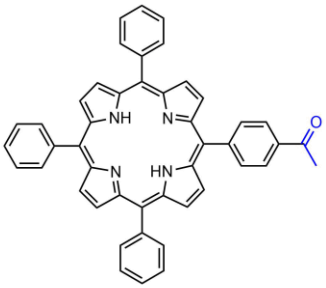

Tetraphenyl porphyrin (TPP)

Figure 30: Spin labels based on Gd(III) and Cu(II) ions and the photoactivatable tetraphenyl porphyrin (TPP). In **4**-**p**henyl**s**ulfonyl-(**py**ridin-2,6-diyl)bis**m**ethylenenitrilo **t**etrakis-(**a**cetic acid) (4PS-PyMTA-Gd(III)) [190], nitrogen and oxygen atoms of the ligand chelate the Gd(III) ion. The copper(II) double histidine motive is formed by histidine residues at the i^{th} and $(i+4)^{th}$ positions of a protein and **i**mino**di**a**c**etate (IDA). Photoactivatable labels like **t**etra-**p**henyl **p**orphyrin can be excited into an EPR-active triplet state by laser irradiation.

In Gd(III) and Cu(II)-based labels, the nitrogen and oxygen atoms of organic ligands chelate the metal ion and thereby stabilize the complex.[184,190] Gadolinium(III) labels such as 4PS-PyMTA-Gd(III) [190] are stable under reducing conditions and have therefore been used for *in cell* PDS experiments.[186,190] Depending on the particular chelate ligand, however, Gd(III) may be released from the complex and exchanged by Mn(II) endogenous to the cell.[190] The broad spectrum of Gd(III) and the spin state of $S = 7/2$ [147] can make data acquisition and analysis challenging: PELDOR time traces from the spin pair Gd(III)/Gd(III) usually exhibit a modulation depth below 5%,[147,148,188] as only a small fraction of the spectrum can be excited with rectangular pulses.[147] In RIDME, the modulation depth is larger; however, owing to $S = 7/2$, higher harmonics of the dipolar coupling contribute and have to be included in the data analysis.[147,148]

Another metal-based spin label for proteins is the copper double histidine motive (Cu(dHis)), which is formed by Cu(II), iminodiacetate (IDA), and two histidine residues located at the positions *i* and *i+4*.[184] Cu(dHis) is a highly rigid label and therefore produces narrow distance distributions.[184]

Finally, photoactivatable spin labels like tetraphenyl porphyrin (TPP) can be excited into a triplet state by laser irradiation, which allows measuring distances *via* light-induced DEER experiments.[221–223]

1.2.4.2 In Silico Spin Labelling

To interpret the PDS-derived distance distribution in terms of a biomolecular structure, it is crucial to take the dynamics of the label and its influence on the distribution into account.[224] *In silico* spin labelling is a method to translate the distance distribution into structural information. It requires a high-resolution structure of the biomolecule obtained by, e.g., X-ray crystallography, NMR spectroscopy, or electron microscopy. Modelling the label into the biomolecular structure and computing its dynamics yields a conformer ensemble that represents the mobility of the label at the bioconjugation site (Figure 31).[172] Techniques to compute the conformer ensemble and the corresponding distance distribution include the accessible-volume approach,[225–227] the rotamer-library approach,[224,228–230] molecular dynamics (MD) simulation,[100,104,231–233] and MD simulations with dummy spin labels (MDDS).[234]

The accessible-volume approach as implemented in mtsslWizard [225–227] engineers the spin label into the biomolecule (Figure 31a) and explores its flexibility by rotating it around all rotatable bonds.[225] During this procedure, label conformers that clash neither with themselves nor with the biomolecule are collected and form a conformer ensemble that represents the volume accessible to the label (Figure 31b).[225] Solely geometry-based, the accessible-volume approach neglects interactions of the label with the solvent and the biomolecule except for steric clashes. MtsslWizard performs no energy weighting, i.e. it considers all label conformers equally probable, irrespective of their particular energy.[225] Nevertheless, the overall agreement of the experimental and the *in silico* distribution is good and the experimental distance can be predicted at an accuracy of approx. 3 Å (Figure 31c).[225–227]

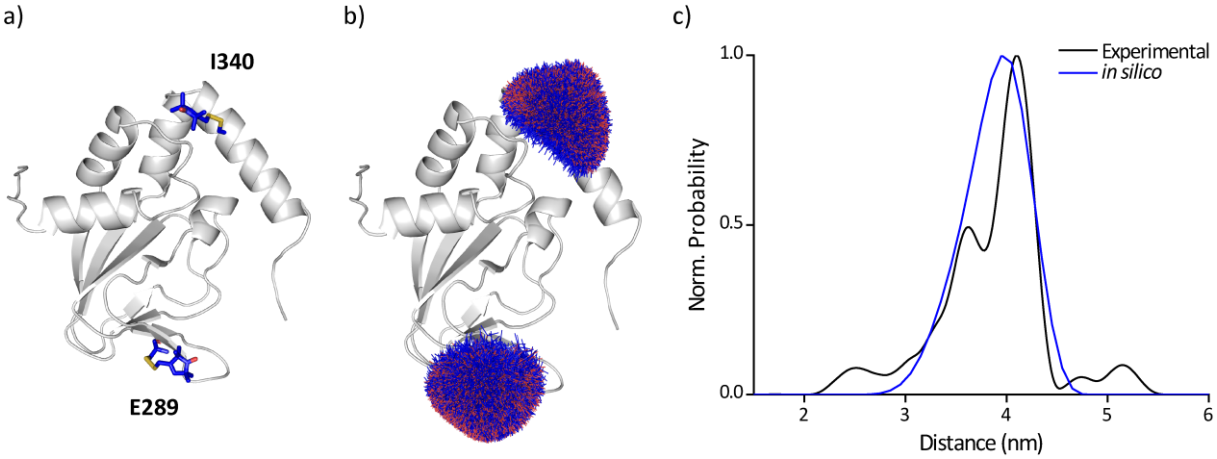

Figure 31: *In silico* spin labelling of a protein with mtsslWizard. a) Structure of the cyclic nucleotide-binding domain (CNBD, PDB-ID: 2kxl,[235] grey) from *Mesorhizobium loti* with MTSSL attached to residues E289 and I340. b) Ensembles of label conformers obtained for the construct shown in (a). c) Experimental distance distribution (black) and the *in silico* distribution (blue) obtained from the ensembles shown in (b). Adapted from [15].

In contrast to mtsslWizard, the toolbox for Multiscale Modeling of Macromolecules (MMM) [224,228–230] is based on the rotamer-library approach and takes interactions between the label and the biomolecule into account. Briefly, MMM uses pre-computed rotamer libraries that include the free energy f_i of each rotamer *i*. It successively attaches the *i* rotamers to the biomolecule and computes the interaction energy Δu_i, considering attractive and repulsive interactions.[224] With the total free energy given by $f_i + \Delta u_i$, MMM assigns a weight p_i to each label rotamer according to a Boltzmann distribution. Collecting all rotamers and considering their respective weights p_i yields the conformer ensemble.[224] As with mtsslWizard, the accuracy of the predicted distance is up to 3 Å.[236] Both mtsslWizard and MMM are computationally efficient and provide the *in silico* distance distribution within seconds.[226,227,236] They can be applied to every biomolecule irrespective of its size,[224] because only the flexibility of the label is considered, whereas the structure of the biomolecule itself is kept fixed. However, considering

only the flexibility of the label and neglecting protein dynamics and interactions with the solvent is also a major limitation of these two approaches.[224]

All-atom MD simulations [100,104,231–233] include the dynamics of both, the biomolecule and the label, and are therefore computationally more demanding. Replacing the spin label by dummy atoms as in MDDS decreases the computational cost; nevertheless, MD simulations rarely outperform mtsslWizard and MMM in terms of accuracy.[237] Recently, a combination of the Conformer-Rotamer Ensemble Sampling Tool (CREST) [238] and molecular dynamics (CREST/MD) [239] has been introduced, which searches for label conformers, ranks them according to their energy, and performs MD simulations on those conformers of protein and label that were identified as relevant *via* Boltzmann weighting. CREST/MD can predict the most probable distance at an error below 1 Å (deviation between experiment and simulation),[239] which allows disentangling the influence of label conformers and of the biomolecule itself on the distance distribution.

Finally, *in silico* labelling is a valuable tool to find labelling sites for SDSL/PDS. Generally, a labelling site should fulfil a few conditions: (i) it should be located on the surface of the biomolecule and thus be well accessible to the label, (ii) it should not be located in the active site of a biomolecule, where modifications may disturb biomolecular function, and (iii) it should be located in well-defined secondary structure elements such as α-helices and β-sheets of a protein, as this likely gives rise to narrow distance distributions. Especially for tracking conformational changes in biomolecules, a so-called difference-distance map [225] helps to find labelling sites that are expected to show a large distance change and non-overlapping distance distributions.

1.2.4.3 Comparison of PDS and further methods for biomolecular structure elucidation

Structural biology has established several methods to study biomolecules and their complexes. High-resolution techniques like NMR spectroscopy, X-ray crystallography, and cryogenic electron microscopy (cryo-EM) can determine the three-dimensional molecular structure at an atomistic level.[240] Further biophysical techniques that provide coarse-grained structural information include small-angle X-ray/neutron scattering (SAXS/SANS), Förster resonance energy transfer (FRET), and PDS. All these methods have their unique strengths and limitations and therefore complement each other.[240] This fact is exploited by integrative structural biology, which aims at deriving a holistic structure and the conformational dynamics of a biomolecule by combining results from different techniques.[172,241] This section discusses their advantages and shortcomings.

To date, about 200,600 structures[2] have been deposited in the Protein data Bank (PDB), most of them stemming from X-ray crystallography (86% of all structures), followed by NMR spectroscopy (≈7%) and cryo-EM (≈7%). Figure 32 shows the total number of structures the three techniques have contributed to the PDB between 1980 and 2022.

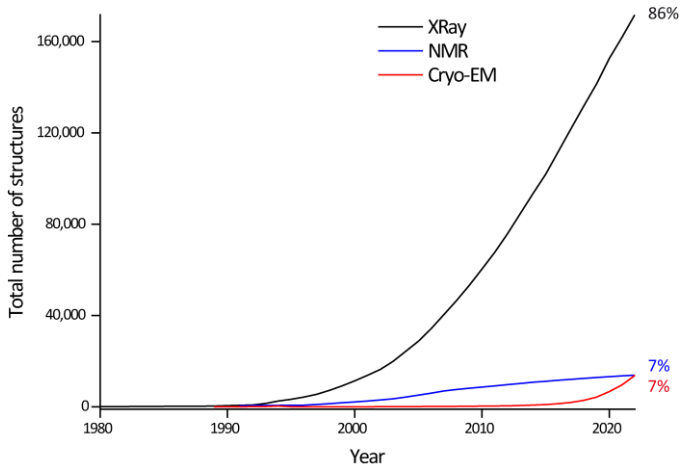

Figure 32: Cumulative number of structures solved by X-ray crystallography, NMR spectroscopy, and cryo-EM available in the PDB between 1980 and 2022. Source of Data: Research Collaboratory for Structural Bioinformatics Protein Databank (RCSB PDB), www.rcsb.org, accessed 31.01.2023.

Biomolecular NMR spectroscopy is performed under near-native conditions in solution at room temperature. By monitoring the dynamics and flexibility of the biomolecule, it yields a conformer ensemble and provides access to thermodynamic and kinetic parameters.[242] Further, time-resolved NMR allows following conformational changes such as folding processes with millisecond time resolution.[243,244] From a technical point of view, most biomolecular NMR experiments exploit the nuclear Overhauser effect (NOE) to collect a large set of short-range distance (< 6 Å) and angular constraints, which define the three-dimensional structure with atomic resolution.[245] While NMR spectroscopy was originally confined to biomolecules lighter than approx. 30 kDa,[246] the continuous development of hardware, pulse sequences, and schemes for isotope labelling has extended the limit to approx. 100 kDa nowadays.[240,247] The size-restriction originates from the decreased tumbling rate of large biomolecules, which enhances nuclear spin relaxation and thus reduces the spectral resolution.[247]

X-ray crystallography also provides structural information with atomic resolution, but unlike NMR spectroscopy, it imposes no limit on the molecular size.[240] As a diffraction technique, it requires crystallization, which can be challenging especially for biomolecules of poorly defined structure such as intrinsically disordered proteins.[240] Since the crystal lattice is an artificial environment in which crystal

[2] Obtained from www.rcsb.org/stats/ on 31.01.2023.

packing effects may alter the biomolecular fold, the structure derived by crystallography does not necessarily coincide with the solution structure.[240]

In recent years, cryo-EM has increased its importance in structural biology and is about to surpass NMR spectroscopy in terms of the total number of structures (Figure 32). Like X-ray crystallography, cryo-EM is free from a size-limitation and yields a high-resolution structure, but it does not require crystals and is applicable on a single-molecule basis.[240] It therefore permits studying a wide range of biomolecules and benefits from the low sample consumption, even though the sample preparation is challenging.[240]

Small-angle X-ray scattering (SAXS) and small-angle neutron scattering (SANS) are low-resolution (> 10 Å) techniques to elucidate the overall shape of a biomolecule.[240] SAXS and SANS are complementary to each other, with SAXS being based on X-ray scattering by electrons and SANS on neutron scattering by nuclei. As both techniques are applied in solution, they do not require crystallization of the biomolecule,[240] but their results become difficult to interpret as the size of the system grows.[60]

Förster Resonance energy transfer (FRET) is a technique to measure distances between fluorescence labels. Regarding its information content, FRET is similar to PDS and therefore, the two methods deserve a more detailed comparison. Both techniques require introducing reporter groups into the biomolecule, namely spin labels for PDS and chromophores for FRET.[248,249] Spin labels are usually smaller and have a shorter and more rigid linker than chromophores, this decreases the likelihood of perturbing the local structure and the dynamics of the biomolecule.[199,250,251] A rigid linker further constrains the conformational freedom of the label, which eases correlating the measured distance with the biomolecular structure.[199] While PDS typically uses two labels of the same type, e.g. nitroxides, FRET requires orthogonal labelling with two different dye molecules called a donor and an acceptor. As a result, fluorescence labelling is often more challenging than spin labelling.[60,175,231,251]

PDS measures the *magnetic* dipolar coupling between electron spins, whereas FRET is based on the interaction between the *electric* dipole moments of the donor and acceptor chromophores.[248,252,253] Briefly, exciting the donor at an appropriate wavelength in the absence of an acceptor creates fluorescence of intensity F_D, which decays *via* radiative and non-radiative mechanisms.[252] If the donor is close to an acceptor and if the emission spectrum of the donor and the absorption spectrum of the acceptor overlap, a non-radiative resonance energy transfer occurs between the two dyes.[231,252] This phenomenon called Förster resonance energy transfer (FRET) enhances the depopulation of the excited state of the donor, which now fluoresces at the intensity $F_{DA} < F_D$.[252] Of note, as the energy transfer from the donor to the acceptor occurs *via* radiationless dipole-dipole coupling and does *not* involve photon emission, the expression "fluorescence resonance energy transfer" widely used in the literature is, strictly speaking, incorrect.[254(p.443),255] Measuring F_D in the absence and F_{DA} in the presence of an acceptor chromophore permits calculating the FRET efficiency E:[252,254(p.446)]

$$E = 1 - \frac{F_{DA}}{F_D} = \frac{R_0^6}{R_0^6 + r^6} \tag{99}$$

with the Förster distance R_0 that depends, *inter alia*, on the overlap of the donor and the acceptor spectrum and the relative orientation of the dipoles to each other.[252] At $r = R_0$, the FRET efficiency is 50%, i.e. half of all fluorophores undergo FRET.[252] Equation (99) shows that the electric dipole-dipole interaction in FRET scales with the inverse sixth power of the distance ($E \sim r^{-6}$), whereas for the magnetic dipole-dipole interaction in PDS, the relation is $\omega_{DD} \sim r^{-3}$. As a result, a spin label can access a larger distance range than a given FRET pair,[175] which is most sensitive if $0.5R_0 < r < 2R_0$.[254(p.446)] PDS can measure the whole Pake pattern and thus reports on the dipolar coupling ω_{DD} and the exchange interaction *J* in a single measurement.[199] Resonance energy transfer, by contrast, has to be

disentangled from other mechanisms that lead to fluorescence quenching by reference measurements.[199] A further distinction between FRET and PDS arises from the orientation-dependency of the dipolar interaction: Provided that the whole Pake pattern is resolved, PDS allows inferring the distance without taking the orientation θ of the interspin vector into account.[100,199] In FRET, assumptions are required on the parameter κ^2, which describes the mutual orientation of the electric dipoles.[252]

PDS and FRET differ in terms of sensitivity and measurement conditions: While PDS is performed at cryogenic temperatures in frozen solution, FRET works at room temperature and in the liquid state, i.e. under the native conditions of biomolecules. In this regard, time-resolved FRET permits tracking conformational changes in real-time with nanosecond resolution.[249] By contrast, resolving a conformational change with PDS requires freeze-quenching.[15,90,199] In terms of sensitivity, FRET outperforms PDS, as it can be performed on a single-molecule level.[50] On the other hand, PDS as an ensemble measurement technique requires a spin concentration in the low micromolar range.[40,199] FRET and PDS can both investigate a biomolecule in the cellular environment, particularly benefitting from their high specificity in the sense that they are blind to the diamagnetic or non-fluorescent “background”. Nevertheless, interpreting FRET and PDS data with regard to a particular scientific problem often requires reference structures from high-resolution techniques.

Finally, apart from complementary experimental techniques, a range of computational methods such as MD simulation and DFT calculations can help to interpret experimental data. In this context, a tool called AlphaFold should be mentioned, which predicts the protein structure based on the amino-acid sequence and its similarity with other proteins using artificial intelligence.[256]

2. Motivation

The first part of this work focuses on a PELDOR-based methodology to track conformational changes of biomolecules like proteins and oligonucleotides. PELDOR provides an interspin distance distribution that can be interpreted with regard to the conformation of the biomolecule. Excellent theoretical reviews on PELDOR have been published, but well-established workflows on running a PELDOR experiment and data analysis are rare. Thus, the publications discussed in section 3.1.1 provide step-by-step protocols on setting up PELDOR and on analysing and interpreting PELDOR data with a special emphasis on pitfalls and how to avoid them.

Biomolecules are highly dynamic and adopt different conformations, which are often associated with a particular function. External events such as ligand binding can trigger the conversion between conformational states. Resolving conformational changes over space and time is of particular interest for a thorough understanding of biomolecular function, and one may want to investigate e.g. the length and time scale or the mechanistic pathway of a conformational change. PELDOR can detect conformational changes with Angstrom precision as a change of the distance distribution, but it cannot *per se* resolve the time course. In section 3.1.2, the combination of microsecond-freeze hyperquenching (MHQ) and PELDOR will be introduced to monitor the ligand-induced conformational change of a protein with spatiotemporal resolution. Corroborated by MD simulation, MHQ/PELDOR will be used to propose a functional mechanism of this conformational change.

Ligand binding is one example of physical cues that can affect the conformation of a biomolecule. Generally, biomolecular structure sensitively depends on the surrounding, and it can differ between a buffer solution *in vitro* and the native cellular environment, where the biomolecule interacts with further cell components. Consequently, obtaining a structure of the physiologically active state would require studying the biomolecule *in cell*. Combined with the stable trityl spin labels, single-frequency PDS experiments permit studying biomolecules in the cellular environment. However, the intricacies of trityl labelling and single-frequency PDS techniques have led to a rather low data quality in the past. Three publications discussed in the second part of this thesis (sections 3.2.1-3.2.3) address these issues and assess the potential of maleimide-linked trityl labels and PDS to study proteins *in vitro* and *in cell*.

Apart from spin labelling, trityls can be assembled to model compounds to investigate the electron-spin exchange interaction, which is of interest to disciplines such as materials science, quantum computing, and spintronic applications. In section 3.2.4-3.2.5, two exchange-coupled model systems will be studied: First, a biphenyl-bridged trityl biradical will be used to examine the effect of strong exchange coupling and of spin density delocalization on *cw* EPR and DQC experiments. The experimental results will be interpreted using MD simulations and DFT calculations. Second, the exchange interaction will be studied in a model system that consists of copper (II) tetraphenyl porphyrin linked with a trityl radical *via* a phenyl bridge. Here, the influence of the bridge dynamics on the exchange coupling will be assessed by DFT calculations.

3. Results and Discussion

3.1 Pulsed Electron-Electron Double Resonance with Nitroxide Labels

3.1.1 Setting up and analysing a PELDOR Experiment

The experimental protocol discussed in this chapter has been published in *Methods in Molecular Biology* and in *bio-protocol*. The publications are reproduced in appendices [P1] and [P2].

PELDOR is the most widely used PDS technique. As shown in Figure 33, the number of scientific publications containing the terms “Pulsed Electron-Electron Double Resonance” or “Double Electron-Electron Resonance” increased particularly during the past 15 years (2007-2022), which mirrors the growing importance of PELDOR to the scientific community.

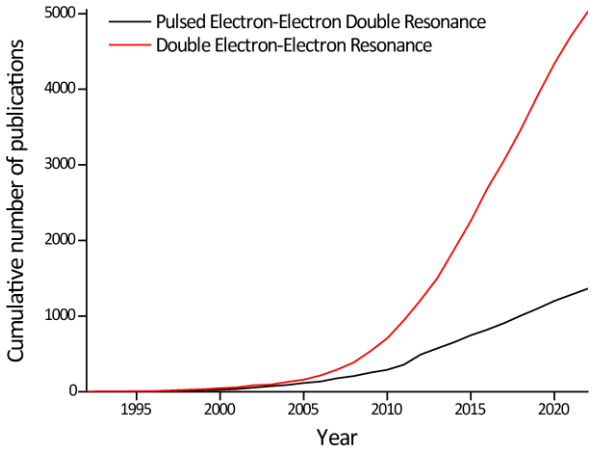

Figure 33: Cumulative number of hits in Google Scholar for the search terms “Pulsed Electron-Electron Double Resonance” and “Double Electron-Electron Resonance” between 1992 and 2022.
Source of data: https://scholar.google.de, accessed 31.01.2023.

Running a PELDOR experiment can be a daunting and confusing task for EPR novices. This illustrates the need for a comprehensive and detailed guide on how to set up the experiment and how to analyse and interpret the data. For this reason, publications [P1] and [P2] provide hands-on protocols with step-by-step instructions on four-pulse PELDOR, including data analysis and interpretation. The publications further highlight potential pitfalls and give advice on how to avoid them.

The procedure of setting up a PELDOR experiment consists of several consecutive steps that serve to optimize the measurement parameters such as pulse lengths and interpulse delays. First, the echo-detected field-swept spectrum is recorded and the magnetic field is set to the value of the maximum signal. Second, inversion recovery and two-pulse ESEEM experiments are performed to obtain estimates on longitudinal and transverse electron-spin relaxation, respectively. Third, a transient nutation experiment is conducted to determine the pump pulse length that maximally inverts the magnetization. After these set-up experiments, PELDOR itself is launched. Signal averaging for typically 1-72 h [40] increases the SNR and thus makes data analysis more reliable in terms of background fitting and computing the distance distribution. For remote-monitoring of the acquisition progress and for saving backup files, the application “Scanstate” has been developed.[257]

Translating the time trace into a distance distribution is an ill-posed problem (section 1.2.3), which can be solved using, e.g., Tikhonov regularization [111] or artificial intelligence such as trained neural networks.[129] The distance distribution can be analysed in terms of the most probable distance, the mean distance, and the distribution width; this gives insight into the structure and dynamics of the biomolecule. *In silico* spin labelling software like mtsslWizard,[225–227] MMM,[224,229] and CREST/MD [239] can help to interpret the experimental distance distribution in terms of a structural model of the biomolecule. Additional complimentary techniques (section 1.2.4.3) support this procedure.

3.1.2 Adding Microsecond Time Resolution to PELDOR

The results discussed in this chapter have been published in the *Journal of the American Chemical Society*. The publication and its supporting information are reproduced in appendix [P3].

Biomolecules are highly dynamic and the interconversion of their different conformations is key to biomolecular function (structure-function-relationship). Therefore, resolving conformational changes over space and time is of particular interest for an in-depth understanding of biomolecular processes. If the distance distributions of the initial and the final state differ, PELDOR can detect a conformational change with Angstrom precision. Performed in frozen solution, it provides a static picture of the biomolecule in its different conformations, but dynamical information such as the time scale and the exact pathway of the structural change is not accessible.[199] However, coupling PELDOR with fast freeze-quench techniques such as MHQ [258] offers the opportunity to follow biomolecular conformational changes with high spatiotemporal resolution.

In this project, the combination MHQ/PELDOR was used to resolve a ligand-induced conformational change of the cyclic nucleotide-binding domain (CNBD) of a bacterial ion channel.[259,260] Triggered by the binding of cyclic adenosine monophosphate (cAMP), a terminal α-helix undergoes a sliding movement (Figure 34a), which has been observed by NMR spectroscopy [235,261] and X-ray crystallography.[262] Using SDSL and PELDOR, a doubly-labelled construct was identified that can track the helix movement from the ligand-free *apo* state to the ligand-bound *holo* state; the distance change was -1.9 nm (Figure 34b).

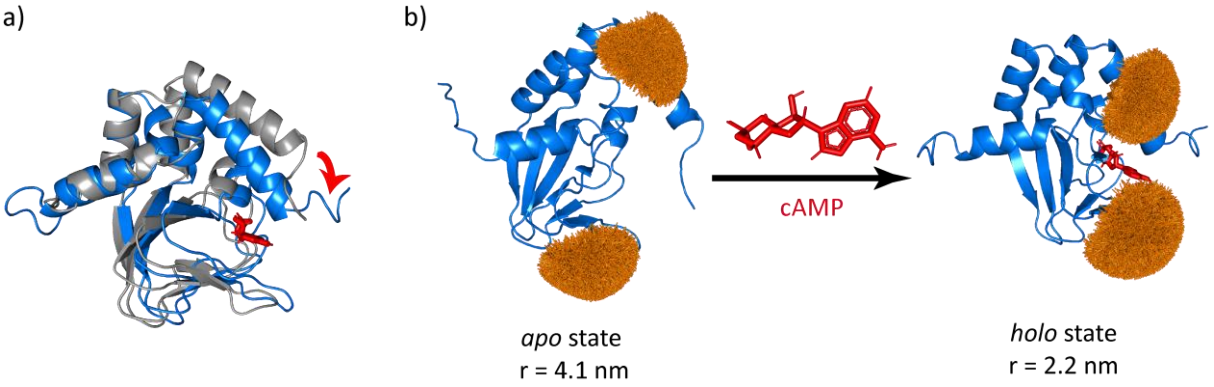

Figure 34: Conformational change of the CNBD from *Mesorhizobium loti* upon cAMP binding as inferred from the NMR structures of the ligand-free *apo* (PDB-ID: 2kxl) and the cAMP-bound *holo* (PDB-ID: 2k0g) state. a) Overlay of the *apo* (grey) and *holo* state (blue), highlighting the movement of the terminal α-helix (red arrow). b) NMR structures of the CNBD (blue) with spin-label conformers from mtsslWizard (orange). The most probable inter-spin distance changes by -1.9 nm upon cAMP binding. Adapted from [15].

The trajectory from the *apo* to the *holo* state was sampled by mixing the CNBD (150 µM) with cAMP (15 mM) in the MHQ device and freezing the mixture after different ageing times. As shown in Figure 35a/b, MHQ/PELDOR resolved the gradual depletion of the *apo* state population and a concomitant build-up of the *holo* state. Of note, neither a gradual shift of the distribution along the distance axis could be observed, as expected for monitoring the helix movement, nor peaks that would indicate intermediates (Figure 35b). This suggests that the helix movement occurs on a sub-microsecond time scale, which is below the time resolution of the MHQ device. MD simulation of the *apo*-to-*holo* transition corroborates this notion, as it revealed a switch of the α-helix within a few nanoseconds. The fractions of the *apo* and the *holo* at each time point (Figure 35c) were determined by deconvolution of the PELDOR traces.

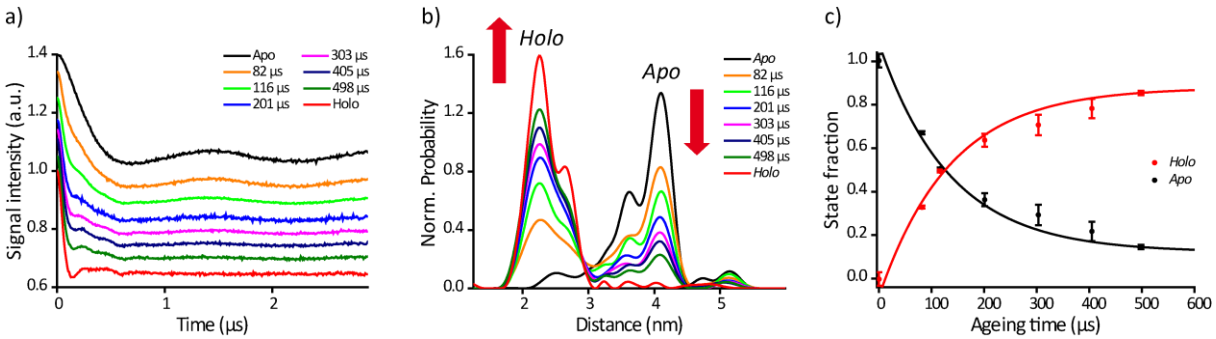

Figure 35: Time-resolved PELDOR data of the CNBD construct E289R1/I340R1. a) PELDOR time traces obtained from MHQ samples at different ageing times with the corresponding distance distributions shown in (b). The post-mixing concentrations were [CNBD] = 150 µM and [cAMP] = 15 mM. c) Fractions of the *apo* and *holo* state as a function of the ageing time. Data points represent the mean, the error bars the standard deviation (n = 3). Adapted from [15].

To assess whether the population shift from the *apo* to the *holo* state reflects ligand binding, saturation experiments were performed, i.e. MHQ samples were prepared at different cAMP concentrations while keeping the ageing time and the CNBD concentration constant. For ratios [cAMP]/[CNBD] exceeding 67, the fractions of *apo* and *holo* remained constant, indicating complete saturation of the CNBD within the dead time of the MHQ device. As the time-resolved PELDOR experiments had been conducted at a 100-fold excess of cAMP, ligand binding could be ruled out as a possible explanation for the population shift. This finding suggests that the rate-limiting step resolved by MHQ/PELDOR must be located on the reaction coordinate between ligand binding and the conformational change.

Mechanistically, these experimental and computational results were interpreted with the schematic free-energy diagram shown in Figure 36. It contains two barriers, namely ligand binding and the conformational change, which are both crossed within nanoseconds if the cAMP concentration is high enough to rapidly saturate the CNBD.

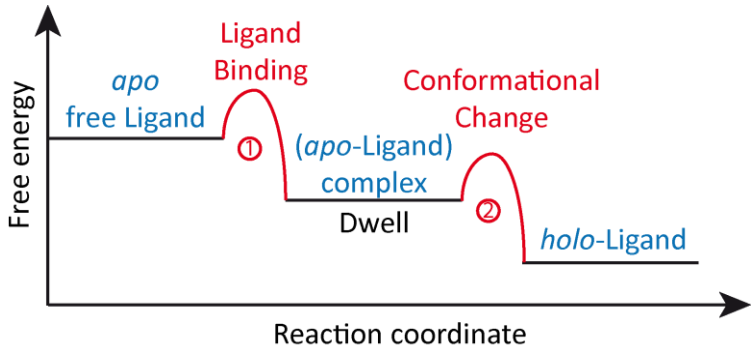

Figure 36: Schematic free-energy profile of a ligand-induced conformational change. The energy barriers marked in red are crossed within nanoseconds, the length of the dwell time between the barriers is in the microsecond range and individual for each protein molecule. Adapted from [15].

After passing the first barrier, protein and ligand form an *apo*-ligand complex, in which the CNBD is structurally in the *apo* state with the ligand attached to the binding site. During a dwell time, the *apo*-ligand complex accumulates the thermal energy needed to cross the second free-energy barrier and to transit to the *holo* state. This dwell time is in the microsecond range and therefore the rate-limiting step on the trajectory from *apo* to *holo*. As it is individually long for each protein molecule, the dwell time is statistically distributed, with longer ageing times permitting a larger number of protein molecules to undergo the conformational change. Thus, MHQ/PELDOR could resolve the dwell-time distribution of the *apo*-ligand complex and shed light on the mechanism of ligand-induced conformational changes.

3.2 EPR Spectroscopy on Trityl Radicals

3.2.1 PDS on a Maleimide-Functionalized Trityl Spin label

The results of this project have been published in *Molecules*. The publication and its supporting information are reproduced in appendix [P4].

As discussed in section 1.2.4.1, key advantages of trityl labels include their high stability in the reductive cellular environment, their narrow EPR line allowing for single-frequency PDS experiments, and their long T_M relaxation times at room temperature. However, the previously-used labels such as the methanethiosulfonate-linked MTS-TSL or butene-TSL [194] (Figure 37) suffered from unspecific labelling, low labelling efficiency, and aggregation with themselves and the protein. This was largely related to the high hydrophobicity of trityls and, in the case of MTS-TSL, also to the methanethiosulfonate group. To address these shortcomings, a maleimide-functionalized trityl label called Mal-TSL was synthesized, which is characterized by its reduction stability and its selectivity for cysteine residues.

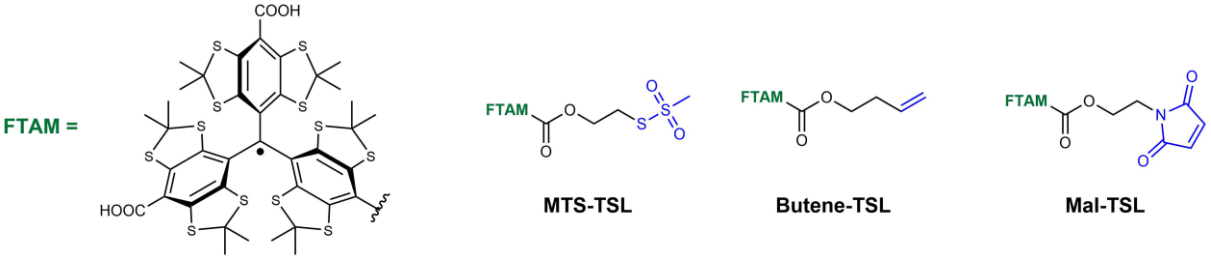

Figure 37: Structures of spin labels based on the Finland trityl (FTAM) with methanethiosulfonate (MTS-TSL), butene (Butene-TSL), and maleimide (Mal-TSL) as bioconjugation group.

Combined with an elaborate labelling procedure that carefully controls the pH-value and the label concentration, Mal-TSL diminished aggregation and unspecific labelling. Free in dilute solution, the *cw* EPR spectrum displays a single narrow line. Interestingly and despite the small *g*-anisotropy, immobilization of Mal-TSL upon bioconjugation broadens the *cw* EPR spectrum, which can be used to verify successful labelling and the absence of unbound spin label. To explore the performance of Mal-TSL in PDS, two double-cysteine constructs of the *Yersinia* outer protein O (YopO) [263,264] were labelled and subjected to DQC, SIFTER, and PELDOR experiments. As a benchmark, PELDOR experiments were also performed on the same protein construct labelled with the nitroxide MTSL.

The DQC traces showed a modulation depth of more than 80%, which is larger than the 20-50% formerly reported for trityl-labelled proteins.[196,210] The deep modulation reflects the high labelling efficiency and site-selectivity of Mal-TSL, and it further illustrates the performance of the label in combination with the DQC experiment. SIFTER, by contrast, lead to a modulation depth of only 25%. In this regard, DQC benefits from its 64-step phase cycle, which allows for double-quantum filtering and thereby suppresses unwanted pathways more efficiently than the 16-step phase cycle in SIFTER. This increases the modulation depth and minimizes the unmodulated background of the time trace, thereby reducing ambiguity in the background fitting.[73] Nevertheless and as herein demonstrated on a singly-labelled YopO construct, the DQC experiment is not entirely background-free;[7] PDS traces from singly-labelled constructs served as experimental background.

Owing to its higher modulation depth, DQC outperforms SIFTER in terms of SNR (eq. (92); DQC: 8 $min^{-1/2}$, SIFTER: 5.9 $min^{-1/2}$). This contrasts a previous report of SIFTER being more sensitive and yielding a two-fold higher SNR than DQC on bistrityl model compounds.[73] In that study, however, DQC and SIFTER provided comparable modulation depths (DQC: 100%, SIFTER: 70-80%),[73] whereas here, the DQC trace has a more than threefold deeper modulation than the SIFTER trace. Thus, particularly due to its smaller intermolecular background, DQC is superior to SIFTER when performed on trityl-labelled proteins.

PELDOR experiments on trityl-labelled YopO yielded a time trace with 20% modulation depth and an SNR of 1.4 $min^{-1/2}$, indicating that PELDOR is inferior to DQC and SIFTER in determining trityl-trityl distances. Owing to the narrow trityl spectrum, the frequency offset $\Delta\upsilon$ (eq. (95)) between the pump and observer pulses needs to be as small as 15 MHz. At such a small offset, long ($\pi/2$ = 32 ns, π = 64 ns) and therefore selective microwave pulses are required to prevent overlap of their excitation bandwidths. This limits the fraction of excited spins and comes at the expense of the modulation depth. For these reasons, PELDOR is not the experiment of choice for trityl-trityl distance measurements at Q-band, but it has shown its potential at higher microwave frequencies such as G-band.[26]

PELDOR on the MTSL-labelled construct yielded a time trace with the 35% modulation depth typical of nitroxides at Q-band, and an SNR of approx. 8 $min^{-1/2}$, which is on par with the values obtained by DQC with Mal-TSL. At the temperature of 50 K chosen here to allow direct comparison, the trityl label loses its sensitivity advantage for two reasons: First, the longer shot-repetition time required to prevent saturation (15 ms for trityls, 3 ms for nitroxides) increases the acquisition time. Second, Mal-TSL has a shorter phase-memory time than MTSL at 50 K and thus a reduced signal intensity. Therefore, optimizing the measurement temperature for trityl-trityl PDS experiments to find a trade-off between a long T_M and a short T_1 time may increase the SNR further.

Regarding the distribution widths, both *in silico* labelling with mtsslWizard and the PDS data indicate a broader distribution for Mal-TSL than for MTSL. The overall shape of the distributions, however, is the same for both labels. The broadening in the case of Mal-TSL likely originates from its longer and more flexible linker, which increases the conformational freedom of the label. Shortening the linker group might reduce its flexibility and thus narrow the distance distribution, which would in turn ease correlating it with a biomolecular structure. This question will be addressed in section 3.2.2.

3.2.2 SLIM: A Short-Linked Trityl Label for In-Cell EPR Distance Measurements

The results of this project have been published in *Angewandte Chemie International Edition*. The publication and its supporting information are reproduced in appendix [P5].

As demonstrated in section 1.2.4.1 on example of Mal-TSL, a long linker gives rise to a broad and potentially ambiguous distance distribution, which can complicate the correlation with a biomolecular structure. Consequently, this project aimed at shortening the linker, reducing its flexibility, and thus narrowing the distance distribution. The new **s**hort-**li**nked **m**aleimide (SLIM) label connects the trityl core and the maleimide by a single methylene group (Figure 38) and thereby shortens the linker from five rotatable bonds in Mal-TSL to two rotatable bonds in SLIM.

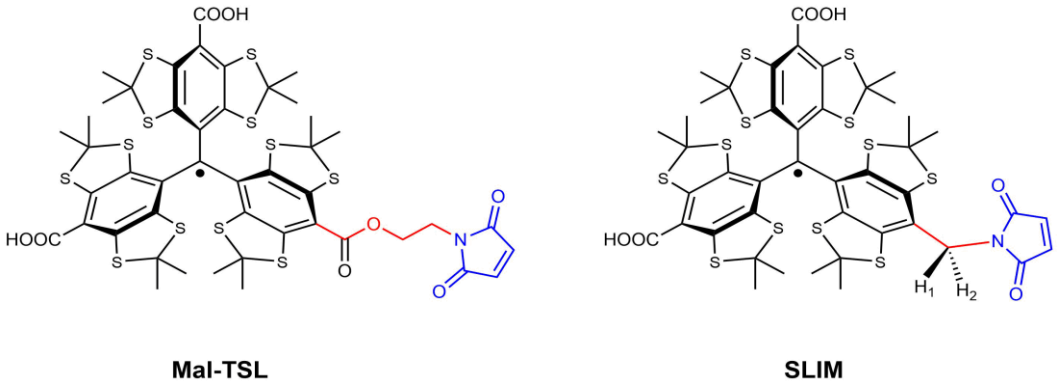

Figure 38: Structures of the maleimide-linked trityl spin label Mal-TSL and the short-linked maleimide trityl spin label SLIM. For clarity, the bioconjugation group is shown in blue and the rotatable bonds of the linker in red.

Devoid of the ester functionality, SLIM features not only a shorter linker but is also more stable than Mal-TSL under reducing conditions. While the EPR signal of Mal-TSL gradually decayed over 15 hours in ascorbate solution, no decrease in signal intensity was observed for SLIM. In Mal-TSL, the electron-withdrawing effect of the ester group stabilizes the negative charge upon reduction. SLIM, by contrast, does not have an electron-withdrawing substituent conjugated to the trityl core and, therefore, the reduction is disfavoured. Furthermore, the methylene linker in SLIM is biocompatible, i.e. by contrast to the ester group in Mal-TSL, it is not cleaved in the cell. These facts make SLIM suitable for studying the conformation of biomolecules in their native cellular environment.

Contrary to the single-line *cw* EPR spectrum of Mal-TSL, SLIM shows nine peaks at room temperature. The spectrum is governed by hyperfine coupling to the nitrogen atom of the maleimide (A_N = 1.71 MHz) and the two magnetically inequivalent benzylic protons (H_1 and H_2 in Figure 38; A_{H1} = 6.00 MHz and A_{H2} = 2.96 MHz), which mirror the helical chirality of trityls.[165] The experimentally observed hyperfine splitting could be confirmed by a DFT calculation of the coupling constants. In frozen solution, SLIM gives rise to a doublet spectrum, which is dominated by the hyperfine coupling to H_1. Interestingly, immobilization upon spin labelling yields a similar spectrum at room temperature, which permits distinguishing free from bound label and can therefore confirm successful bioconjugation.

The performance of SLIM in DQC and PELDOR was assessed on a YopO construct with the labelling sites on a rigid α-helix (Figure 39a). DQC yielded a 4 µs-long dipolar trace with 87% modulation depth and an SNR of 674 $h^{-1/2}$; the PELDOR time trace had a modulation depth of 20% and an SNR of 155 $h^{-1/2}$. The PDS traces of both experiments displayed prominent oscillations and yielded a bimodal distance distribution. Interestingly, PELDOR on the same construct labelled with MTSL (modulation depth: 32%; SNR: 248 $h^{-1/2}$) also resolved this bimodality, indicating that it is independent of the label and suggesting that the α-helix adopts two different conformations. By contrast, DQC on YopO labelled with Mal-TSL (modulation depth: 80%; SNR: 503 $h^{-1/2}$) revealed a broad and trimodal distance distribution, which could be confirmed by a PELDOR experiment on the same sample. Resulting from the long and flexible linker of TSL-Mal, the trimodality demonstrates the need for a short linker group. The volumes of the *in silico* conformer ensembles from mtsslWizard support this notion, with Mal-TSL sampling a space (15,200 Å³) more than twice as large as SLIM (6490 Å³). Regarding the SNR of the dipolar traces, the combination SLIM/DQC outperforms MTSL/PELDOR and also Mal-TSL/DQC.

SLIM has a longer phase-memory time than Mal-TSL and thus increases the sensitivity and the SNR in PDS experiments. Exploiting the high sensitivity, a DQC trace with a dipolar evolution time of 2.5 µs could be recorded at the physiologically relevant protein concentration of 90 nM. To prove its suitability for *in cell* EPR measurements, SLIM-labelled YopO was injected into oocytes of the African clawed frog *Xenopus laevis*. In addition to background signals stemming from manganese and presumably a radical endogenous to oocytes, the trityl peak could be unambiguously identified by its T_1 relaxation time, which is one order of magnitude longer than the T_1 times of the other signals. Upon injecting the protein into oocytes, the phase-memory time decreased due to molecular crowding and the presence of Mn(II) ions.[265] Nevertheless, it was still long enough to record a DQC trace of 3.5 µs length (Figure 39b). Compared with the distance distribution obtained *in vitro*, the *in cell* distribution showed only one peak (Figure 39c), indicating that one helix conformer is preferred in the cellular environment. Thus, SLIM allowed tracking a conformational change of YopO upon translocation into cells.

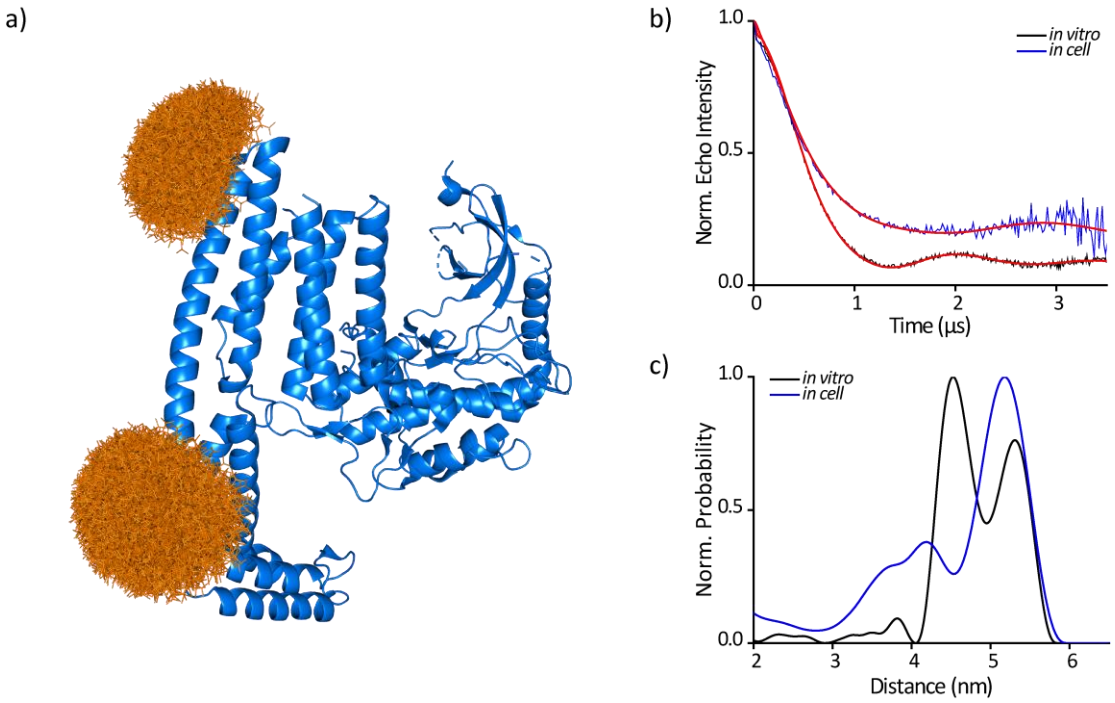

Figure 39: a) Cartoon representation of YopO (PDB-ID: 4ci6, blue) with spin labels (orange) attached to an α-helix. b) DQC time traces recorded *in vitro* (black) and *in cell* (blue); the fits to the experimental traces are shown in red. c) Distance distributions obtained from the time traces in (b), same colour code. Adapted from [165].

3.2.3 Ox-SLIM: A Highly Hydrophilic Trityl Spin Label

The results discussed in this chapter have been published in *Chemistry – A European Journal*. The publication and its supporting information are reproduced in appendix [P6].

One drawback of trityl labels is their hydrophobicity, which decreases the water solubility and may trigger self-aggregation or unspecific adhesion to hydrophobic regions of the biomolecule. One way to increase the hydrophilicity is substituting the methyl groups on the thioketals by hydroxyethyl groups, which leads to the so-called Ox063-type [208,217] trityls (Figure 40). In this project, a trityl label named Ox-SLIM (Figure 40) has been introduced, which combines the beneficial properties of Ox063 and SLIM, namely high hydrophilicity, a short linker, and high redox-stability. Ox-SLIM has eight hydroxyethyl substituents on two bis(thioketal)aryl units to convey hydrophilicity; the third bis(thioketal)aryl unit that carries the maleimide bioconjugation group, by contrast, remains methyl-functionalized to ensure high accessibility for the protein.

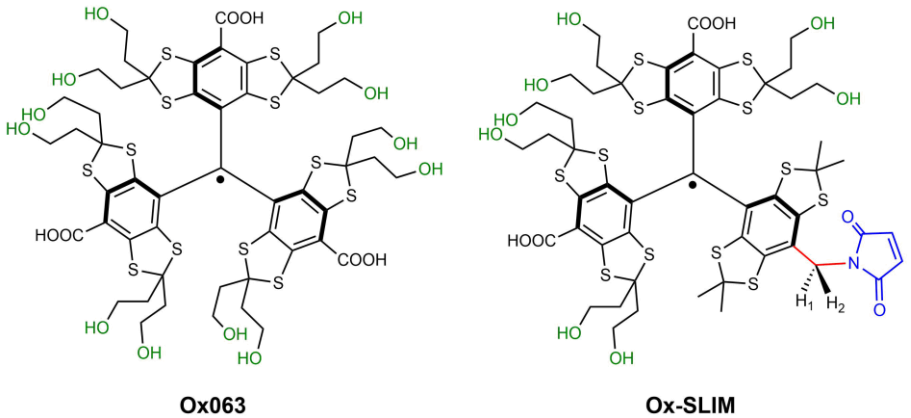

Figure 40: Structure of the hydrophilic trityl compounds Ox063 and Ox-SLIM. For clarity, the maleimide group for bioconjugation is shown in blue, the methylene linker in red, and the hydroxyl groups conveying hydrophilicity in green.

The *cw* EPR spectrum of Ox-SLIM in aqueous solution displays nine peaks, as already observed for SLIM, and the hyperfine coupling constants of SLIM and Ox-SLIM (A_N = 1.48 MHz, A_{H1} = 6.09 MHz, A_{H2} = 3.02 MHz) coincide well.[195] As expected, Ox-SLIM shows a doublet spectrum in frozen solution, which is further superimposed by a dipolar splitting (Pake pattern). Fitting the Pake pattern with EasySpin [30] (Figure 41a) reveals a dipolar coupling constant of 54 MHz, which corresponds to an inter-spin distance of 9.9 Å. The dipolar splitting originates from Ox-SLIM molecules that form a non-covalent dimer, which is stabilized by hydrogen bonds involving the maleimide groups. Adding glycerol suppresses the dimerization by competitive hydrogen bonding and the dipolar splitting vanishes. Notably, no dimerization has been observed for Ox-SLIM-labelled proteins.

The performance of Ox-SLIM in DQC experiments has been assessed on the double-cysteine mutant of YopO that was also used with SLIM (Figure 39a). A time trace of 7 µs length could be recorded at a modulation depth of 95% and an SNR of 133 $h^{-1/2}$ (Figure 41b), thereby outperforming a DQC measurement on the same construct labelled with SLIM (87% modulation depth; SNR = 46 $h^{-1/2}$). Note that the SNR given here for SLIM differs from the value reported in section 3.2.2 due to the different dipolar evolution times (7 µs *vs.* 4 µs). The higher SNR obtained with Ox-SLIM is mostly related to its longer phase-memory time (T_M = 4 µs) compared with SLIM (T_M = 1.4 µs). In this context, Ox-SLIM benefits from the absence of methyl groups in the vicinity of the spin, as methyl-group rotation leads to loss of coherence and thus shortens the phase-memory time.[85,189,266] The distance distribution obtained with Ox-SLIM is bimodal (Figure 41c) and resembles the one obtained with SLIM, further supporting the idea of the α-helix (Figure 39a) existing in two conformations.

The long phase-memory time of Ox-SLIM results in an outstanding sensitivity, as demonstrated by a DQC measurement at a protein concentration of 45 nM (Figure 41b). This is half the concentration used for the DQC experiment with SLIM-labelled YopO (section 3.2.2) and so far represents the bottom limit for trityl-trityl distance measurements. Notably, the DQC trace of 4.5 µs length displays clear dipolar oscillations and even allows resolving the bimodality (Figure 41c).

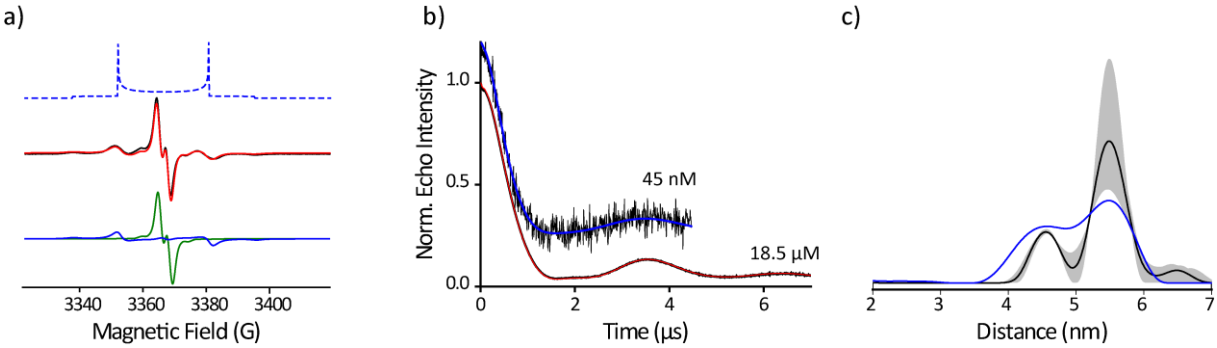

Figure 41: a) *Cw* EPR spectrum of Ox-SLIM in frozen aqueous solution (middle row, black) and the EasySpin [30] fit (middle row, red) consisting of a doublet spectrum (bottom row, green) governed by hyperfine coupling and a dipolar spectrum (bottom row, blue). The integrated dipolar spectrum (Pake Pattern) is shown in the top row. b) Background-corrected DQC time traces of YopO labelled with Ox-SLIM at protein concentrations of 18.5 µM and 45 nM (black). The corresponding fits are shown in red and blue. For clarity, the trace recorded at 45 nM has been shifted by 0.2 on the ordinate axis. c) Distance distribution obtained from the DQC experiment at 18.5 µM (black) and the background validation (grey). The distribution obtained at 45 nM is overlaid in blue. Adapted from [195].

3.2.4 Exchange and Dipolar Coupling in a Biphenyl-bridged Trityl Biradical

The results discussed in this chapter have been published in the *Journal of Organic Chemistry*. The publication and its supporting information are reproduced in appendix [P7].

Apart from their application as spin labels, trityls can be assembled to a variety of so-called model compounds, i.e. organic molecules that serve for testing EPR experiments such as PDS sequences. In this project, the influence of exchange coupling on the *cw* EPR spectrum and the DQC time trace has been studied using the biphenyl-bridged trityl biradical shown in Figure 42.

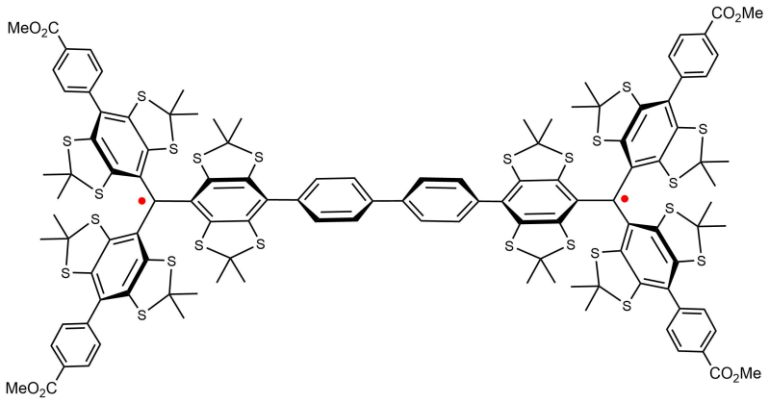

Figure 42: Structure of a biphenyl-bridged trityl biradical. For clarity, the unpaired electrons are marked in red.

This biradical features a fully conjugated π-electron system that leads to strong exchange coupling. In the solution-state *cw* EPR spectrum, the exchange interaction manifests itself in the hyperfine splitting of ^{13}C nuclei, which is half as large as for the trityl monoradical.[5] The exchange interaction further leads to a half-field signal, which could be detected in frozen solution at temperatures below 20 K. Recording the peak-to-peak intensity I_{p2p} of the half-field signal as a function of the temperature *T* and analysing it with a Bleaney-Bowers type equation [65,267,268]

$$I_{p2p}T = C \cdot \left(\frac{1}{3 + \exp(-2J/k_BT)}\right) \tag{100}$$

revealed a strong antiferromagnetic exchange with the coupling constant J = -2.8 cm^{-1} = -83.9 GHz ($-2J\overrightarrow{S_1}\overrightarrow{S_2}$ convention). In eq. (100), *C* is a spectrometer constant [267] and k_B the Boltzmann constant.

In addition to the exchange coupling, the close proximity of the electron spins leads to a strong dipolar interaction that can be observed as a Pake pattern in the main-field region of the low-temperature *cw* EPR spectrum. Analysing this Pake pattern and inferring the interspin distance requires caution: Due to the narrow trityl spectrum, the Larmor frequencies of both spins are similar ($\omega_1 \approx \omega_2$, "like"-spins) and the spin system is in the strong-coupling regime according to $\left|J - \frac{\omega_{dd}}{2}\right| \gg |\omega_1 - \omega_2|$.[60] As shown in eq. (83), the simultaneous presence of strong exchange and dipolar coupling increases the observed dipolar-coupling frequency by a factor of 1.5.[60,73] Taking this fact into account when fitting the Pake pattern with EasySpin [30] reveals a dipolar coupling constant of 11 MHz, which corresponds to an interspin distance of 16.7 Å.

A DQC experiment yielded a time trace with several oscillations, indicating a narrow distance distribution, as expected for a rigid model compound. In line with eq. (62) and (83), the distance axis obtained from DeerAnalysis [111] was multiplied by $\sqrt[3]{1.5}$, thus taking the effect of strong exchange coupling into account. The distance distribution shows a maximum at 16.6 Å, which coincides well with the value from *cw* EPR. Molecular dynamics simulation with GFN-xTB [269] on a DFT-optimized structure provided a distance distribution peaking at 18.7 Å. Taking the spin density delocalization into account shifts the most probable distance to 17.2 Å, which falls into the error margin of the DQC experiment (± 1 Å).

3.2.5 Exchange Coupling in a Copper(II) Porphyrin/Trityl Spin System

The results discussed in this chapter have been published in *Chemistry – A European Journal*. The publication and its supporting information are reproduced in appendix [P8].

Exchange coupling can occur not only in biradicals (section 3.2.4) but also in molecules that contain a radical and a paramagnetic metal ion. In this project, the exchange interaction in a phenyl-bridged copper(II) tetraphenyl porphyrin (CuTPP)/trityl model system (Figure 43a) was studied by *cw* EPR spectroscopy and DFT calculations.

Continuous wave EPR spectroscopy at X-, Q-, and W-band revealed a weak ferromagnetic exchange interaction (J = +0.15 cm^{-1} = +4.5 GHz, $-2J\overrightarrow{S_1}\overrightarrow{S_2}$ convention). The sign and magnitude of *J* were confirmed by a DFT calculation on the PBE0-D3/def2-TZVP [270] level of theory using a DFT-optimized structure of the molecule. DFT was further used to explore the influence of the bridge dynamics on *J*: In the optimized structure, the atoms of CuTPP and trityl were constrained to their positions and the phenyl ring was rotated about the connecting axis; this corresponds to varying the dihedral angle X, which is defined by the atoms C1, C2, C3, and C4 (Figure 43a), between 0° and 360°. For each orientation of the phenyl bridge, the energy *E* and the exchange coupling constant *J* were calculated. Figure 43b shows the relative energy ΔE with respect to the energy minimum and *J* as a function of X.

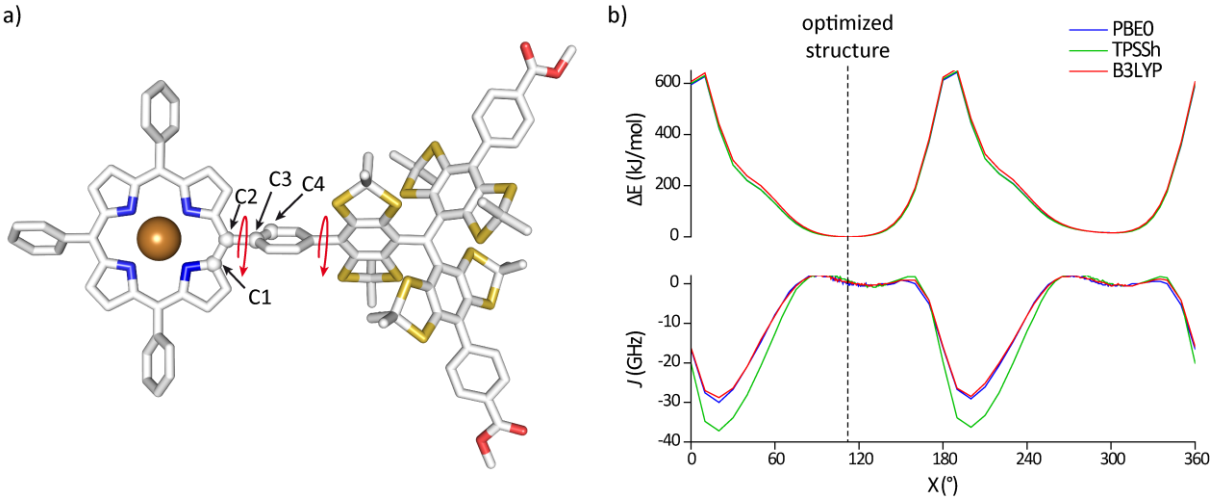

Figure 43: a) Structure of CuTPP/trityl optimized by DFT on the PBE0-D3/def2-TZVP level of theory. Atoms C1-C5 define the dihedral angle X. The red arrows indicate the rotation of the phenyl linker. b) Profiles of the relative energy ΔE (top) and *J* (bottom) obtained by DFT (PBE0-D3/def2-TZVP, TPSSh-D3/def2-TZVP, B3LYP-D3/def2-TZVP) as a function of the dihedral angle X. The dashed line marks $X = 109°$ corresponding to the optimized structure.

Figure 43b reveals that ΔE and *J* sensitively depend on X and that *J* changes between antiferromagnetic ($J < 0$) and ferromagnetic ($J > 0$) coupling. If the phenyl ring is in plane with CuTPP and the trityl ($X = 20°$), π-conjugation occurs, which results in antiferromagnetic exchange coupling. Ferromagnetic exchange coupling occurs close to the energy minimum ($X = 109°$), where the connecting phenyl ring is perpendicular to CuTPP. This orientation results in a low overlap of the p_z-orbitals of the phenyl bridge and the orbitals of CuTPP and trityl. Of note, this finding is independent of the DFT functional. According to the Boltzmann distribution, only conformers with $95° < X < 130°$ are populated at the freezing point of the solvent (178 K for toluene), which explains the weak ferromagnetic exchange coupling observed experimentally.

This example shows that including the dynamics of the linker is crucial for understanding the exchange interaction in para-phenyl bridged model compounds of a trityl radical and a metal ion.

4 Summary and Outlook

In this thesis, PDS EPR has been used to study the conformation and conformational changes of biomolecules with spatiotemporal resolution and *in cell*. Furthermore, two exchange-coupled model systems were investigated using EPR spectroscopy and DFT calculations.

The first part of this thesis (section 3.1) focused on PELDOR. Two hands-on protocols (section 3.1.1) were published, which describe setting up a PELDOR experiment and the data analysis in a detailed step-by-step fashion. They highlight potential pitfalls one may encounter during the acquisition, analysis, and interpretation of PELDOR data and give advice on how to circumvent them. Thus, these protocols will aid particularly novices to the field of EPR in performing PELDOR and they may further increase the reproducibility of measurements by providing established workflows.

In section 3.1.2, the combination of MHQ and PELDOR was introduced to monitor ligand-induced conformational changes of biomolecules with spatiotemporal resolution in the Angstrom distance range and on the microsecond time scale. Herein, the *apo*-to-*holo* transition of a transmembrane protein was monitored upon ligand binding and the results were interpreted in the framework of a dwell time. Molecular dynamics simulation underpinned this interpretation of the PELDOR data. In a mechanistic picture, two free-energy barriers – ligand binding and conformational change – occur on the pathway from the *apo* to the *holo* state. In between these barriers, the protein forms an *apo*-ligand-complex in which it accumulates thermal energy to change its conformation. At high ligand excess, both barriers are crossed within nanoseconds, which is below the time resolution of the MHQ device. The dwell time of the *apo*-ligand-complex, by contrast, is in the microsecond range and could be resolved. Thus, in this project, MHQ/PELDOR helped to unravel the mechanism and the time scale of a biomolecular conformational change. As an outlook, implementing a light source like a laser into the MHQ device may allow studying photo-triggered biochemical reactions such as light-induced conformational changes in the visual pigment rhodopsin.[271]

The second topic of this thesis was EPR spectroscopy on trityl radicals (section 3.2) with emphasis on PDS on trityl-labelled proteins. In section 3.2.1, the maleimide-linked spin label Mal-TSL was shown to outperform previous trityl labels in single-frequency PDS experiments on proteins, yielding time traces with a modulation depth of more than 80%. Compared with the nitroxide MTSL that served as a benchmark, Mal-TSL lead to a broader distance distribution and thus a lower resolution, which was mostly related to the long and flexible linker.

The short-linked maleimide trityl spin label SLIM introduced in section 3.2.2 addressed this shortcoming by reducing the linker length and thus narrowing the distance distribution. Its high stability under reducing conditions allowed for DQC experiments on the *Yersinia* outer protein O (YopO) in *X. laevis* oocytes. Comparing the distance distribution *in cell* with the one obtained *in vitro* on the same protein construct revealed a conformational change upon translocation into cells. This finding highlights the need to study biomolecules in their native cellular environment to obtain a realistic picture of the physiologically active conformation. By exploiting the high sensitivity of single-frequency PDS experiments with trityl radicals, a DQC trace at a protein concentration of 90 nM could be recorded.

The advantageous properties of SLIM were further complemented by replacing the methyl by hydroxyethyl groups, yielding the hydrophilic trityl label Ox-SLIM (section 3.2.3). Apart from its increased water solubility, Ox-SLIM has a longer phase-memory time than SLIM and thus shows a higher sensitivity in PDS. This allowed performing DQC at a protein concentration of 45 nM, which so far is the lower limit for trityl-trityl distance measurements. Notably, the data quality of the DQC trace was high enough to reproduce the distance distribution obtained at micromolar concentration. The opportunity

to perform PDS experiments at nanomolar concentrations not only reduces protein consumption but also allows measurements at physiologically relevant concentrations of biomolecules.

As a perspective, the trityl labels SLIM and Ox-SLIM may be used for PDS experiments in cell types other than oocytes, e.g. HeLa[3],[187] HEK[4],[272] or *E. Coli*.[273] In this respect, it would be interesting to see whether the conformational change observed upon introducing YopO into cells is specific to *X. laevis* oocytes or if it occurs regardless of the cell type. Another potential application of trityl labels is PDS at room temperature, which might allow monitoring physiological processes under *in vivo* conditions. Finally, the ultimate goal would be to combine MHQ and *in cell* PDS experiments using trityls to study ligand-induced conformational changes of biomolecules within cells and with spatiotemporal resolution. Exploiting the high sensitivity of DQC experiments on trityl labelled proteins, the sample consumption of MHQ may be decreased further.

Apart from these biophysical applications, EPR spectroscopy complemented by DFT calculations and MD simulations was used to study two exchange-coupled model systems. A biphenyl-linked bistrityl model compound served to demonstrate the influence of exchange coupling and spin-density delocalization on *cw* EPR spectra and DQC time traces. Using the temperature dependence of the half-field signal, strong antiferromagnetic exchange coupling was observed. The distance distribution obtained by DQC could be confirmed with Angstrom accuracy using DFT and MD, thereby highlighting the need to include both the exchange interaction and the spin-density delocalization in the data analysis (section 3.2.4). Future studies may explore how the exchange interaction of bistrityl biradicals changes with the length and the chemical properties of the bridge (e.g. monophenyl, acetylene, etc.) connecting the two spin centres. Profound knowledge of the correlation between *J* and the bridge may allow designing molecules with a specific size of the exchange interaction.

Furthermore, the exchange coupling in a phenyl-bridged copper(II) porphyrin/trityl model system has been investigated (section 3.2.5) by *cw* EPR and DFT. The weak ferromagnetic exchange coupling observed by *cw* EPR spectroscopy could be confirmed by DFT calculations. Moreover, DFT was used to investigate the influence of the bridge dynamics on the exchange coupling constant *J*. A change between weak ferromagnetic and strong antiferromagnetic exchange was found, depending on the orientation of the phenyl ring with respect to the planes of porphyrin and trityl. Of note, weighting the conformers with a Boltzmann distribution could reproduce the experimental value of *J*. These findings revealed that the exchange interaction in phenyl-bridged porphyrin/trityl model compounds sensitively depends on the conformation and the dynamics of the linker group. The investigations presented in sections 3.2.4 and 3.2.5 may be relevant for disciplines like quantum information science and material science.

[3] Human cervical cancer cells, originally from Henrietta Lacks

[4] Human embryonic kidney

5 References

[1] P. Gast, E. J. J. Groenen, *eMagRes* **2016**, *5*, 1435-1444.

[2] K. Möbius, W. Lubitz, N. Cox, A. Savitsky, *Magnetochemistry* **2018**, *4*, 50.

[3] J. A. Weil, J. R. Bolton, *Electron Paramagnetic Resonance*: *Elementary Theory and Practical Applications*, John Wiley & Sons Inc., Hoboken, **2007**.

[4] J. Telser, *eMagRes* **2017**, *6*, 207-234.

[5] E. J. L. McInnes, D. Collison, *eMagRes* **2016**, *5*, 1445-1458.

[6] M. Bennati, *eMagRes* **2017**, *6*, 271-282.

[7] G. Jeschke, *Annu. Rev. Phys. Chem.* **2012**, *63*, 419-446.

[8] O. Schiemann, T. F. Prisner, *Q. Rev. Biophys.* **2007**, *40*, 1-53.

[9] P. P. Borbat, J. H. Freed, *eMagRes* **2017**, *6*, 465-494.

[10] A. Schweiger, G. Jeschke, *Principles of Pulse Electron Paramagnetic Resonance*, Oxford University Press, Oxford/New York, **2001**.

[11] Daniella Goldfarb, Electron Paramagnetic Resonance Applications to Catalytic and Porous Materials in *Electron Paramagnetic Resonance: A Practitioner's Toolkit* (Eds. M. Brustolon, E. Giamello), John Wiley & Sons Inc. Hoboken, **2009**, pp. 451-487.

[12] M. M. Roessler, E. Salvadori, *Chem. Soc. Rev.* **2018**, *47*, 2534-2553.

[13] E. Schubert, T. Hett, O. Schiemann, Y. NejatyJahromy, *J. Magn. Reson.* **2016**, *265*, 10-15.

[14] A. Collauto, H. A. DeBerg, R. Kaufmann, W. N. Zagotta, S. Stoll, D. Goldfarb, *Phys. Chem. Chem. Phys.* **2017**, *19*, 15324-15334.

[15] T. Hett, T. Zbik, S. Mukherjee, H. Matsuoka, W. Bönigk, D. Klose, C. Rouillon, N. Brenner, S. Peuker, R. Klement et al., *J. Am. Chem. Soc.* **2021**, *143*, 6981-6989.

[16] W. Gerlach, O. Stern, *Z. Physik* **1922**, *9*, 349-352.

[17] G. Jeschke, Electron Paramagnetic Resonance Spectroscopy in *Ullmann's Encyclopedia of Industrial Chemistry*, Wiley-VCH Verlag GmbH & Co. KGaA, **2013**.

[18] G. E. Uhlenbeck, S. Goudsmit, *Naturwissenschaften* **1925**, *13*, 953-954.

[19] E. Wiberg, N. Wiberg, G. Fischer, *Lehrbuch der Anorganischen Chemie*, De Gruyter, Berlin/New York, **2007**.

[20] D. M. Murphy, EPR (Electron Paramagnetic Resonance) Spectroscopy of Polycrystalline Oxide Systems in *Metal Oxide Catalysis* (Eds. S. D. Jackson, J. S. J. Hargreaves), Wiley-VCH Verlag GmbH & Co. KGaA Weinheim, Germany, **2008**, pp. 1-50.

[21] C. Corvaja, Introduction to Electron Paramagnetic Resonance in *Electron Paramagnetic Resonance: A Practitioner's Toolkit* (Eds. M. Brustolon, E. Giamello), John Wiley & Sons Inc. Hoboken, **2009**, pp. 1-36.

[22] A. van der Est, *eMagRes* **2016**, *5*, 1411-1422.

[23] D. T. Petasis, *EPR Spectroscopy*, De Gruyter, Berlin/Boston, **2022**.

[24] Y. E. Nesmelov, A. Gopinath, D. D. Thomas, *J. Magn. Reson.* **2004**, *167*, 138-146.

[25] F. Neese, *eMagRes* **2017**, *6*, 1-22.

[26] D. Akhmetzyanov, P. Schöps, A. Marko, N. C. Kunjir, S. T. Sigurdsson, T. F. Prisner, *Phys. Chem. Chem. Phys.* **2015**, *17*, 24446-24451.

[27] M. Bennati, D. M. Murphy, Electron Paramagnetic Resonance Spectra in the Solid State in *Electron Paramagnetic Resonance: A Practitioner's Toolkit* (Eds. M. Brustolon, E. Giamello), John Wiley & Sons Inc. Hoboken, **2009**, pp. 195-250.

[28] K. Möbius, A. Savitsky, *High-Field EPR Spectroscopy on Proteins and their Model Systems: Characterization of Transient Paramagnetic States*, Royal Society of Chemistry, Cambridge, **2008**.

[29] D. Marsh, *Spin-Label Electron Paramagnetic Resonance Spectroscopy*, CRC Press LLC, Boca Raton/London/New York, **2020**.

[30] S. Stoll, A. Schweiger, *J. Magn. Reson.* **2006**, *178*, 42-55.
[31] G. Hanson, L. Berliner, *High Resolution EPR*: *Applications to Metalloenzymes and Metals in Medicine*, Springer, Dordrecht/Heidelberg/London/New York, **2009**.
[32] C. Karunakaran, M. Balamurugan, Advances in Electron Paramagnetic Resonance in *Spin Resonance Spectroscopy: Principles and Applications* (Ed. C. Karunakaran), Elsevier Amsterdam/Oxford/Cambridge, **2018**, pp. 229-280.
[33] D. M. Murphy, R. D. Farley, *Chem. Soc. Rev.* **2006**, *35*, 249-268.
[34] S. Pribitzer, D. Mannikko, S. Stoll, *Phys. Chem. Chem. Phys.* **2021**, *23*, 8326-8335.
[35] A. Meyer, S. Dechert, S. Dey, C. Höbartner, M. Bennati, *Angew. Chem. Int. Ed.* **2020**, *59*, 373-379.
[36] E. Bordignon, *eMagRes* **2017**, *6*, 235-254.
[37] S. Stoll, D. Goldfarb, *eMagRes* **2017**, *6*, 495-510.
[38] C. P. Slichter, *Principles of Magnetic Resonance*, Springer, Berlin/Heidelberg/New York/London/Paris/Tokyo/Hongkong, **1990**.
[39] S. S. Eaton, G. R. Eaton, Distance Determination in *Distance Measurements in Biological Systems by EPR* (Eds. L. J. Berliner, G. R. Eaton, S. S. Eaton), Springer New York, **2002**, pp. 347-381.
[40] O. Schiemann, C. A. Heubach, D. Abdullin, K. Ackermann, M. Azarkh, E. G. Bagryanskaya, M. Drescher, B. Endeward, J. H. Freed, L. Galazzo et al., *J. Am. Chem. Soc.* **2021**, *143*, 17875-17890.
[41] G. Jeschke, H. W. Spiess, Distance Measurements in Solid-State NMR and EPR Spectroscopy in *Novel NMR and EPR Techniques* (Eds. J. Dolinšek, M. Vilfan, S. Žumer), Springer Berlin/Heidelberg, **2006**, pp. 21-63.
[42] J. Kowalewski, L. Mäler, *Nuclear Spin Relaxation in Liquids*: *Theory, Experiments, and Applications*, CRC Press, Boca Raton/London/New York, **2018**.
[43] R. V. Hosur, V. M. R. Kakita, *A Graduate Course in NMR Spectroscopy*, Springer, Cham, **2022**.
[44] K. Müller, M. Geppi, *Solid State NMR*: *Principles, Methods, and Applications*, Wiley-VCH, Weinheim, **2021**.
[45] P. P. Borbat, J. H. Freed, Pulse Dipolar Electron Spin Resonance: Distance Measurements in *Structural Information from Spin-Labels and Intrinsic Paramagnetic Centres in the Biosciences* (Eds. C. R. Timmel, J. R. Harmer), Springer Berlin/Heidelberg, **2013**, pp. 1-82.
[46] P. P. Borbat, J. H. Freed, Double-Quantum ESR and Distance Measurements in *Distance Measurements in Biological Systems by EPR* (Eds. L. J. Berliner, G. R. Eaton, S. S. Eaton), Springer New York, **2002**, pp. 383-459.
[47] K. C. Brown, *Essential Mathematics for NMR and MRI Spectroscopists*, Royal Society of Chemistry, Cambridge, **2020**.
[48] M. Weingarth, M. Baldus, Introduction to Biological Solid-State NMR in *Advances in Biological Solid-State NMR: Proteins and Membrane-active Peptides* (Eds. F. Separovic, A. Naito), Royal Society of Chemistry Cambridge, **2014**, pp. 1-17.
[49] B. R. Masters, The History of Perturbation Theory from Astronomy to Quantum Mechanics in *Handbook of Biomedical Nonlinear Optical Microscopy* (Eds. B. R. Masters, P. So), Oxford University Press Oxford/New York, **2008**, pp. 36-41.
[50] S. K. Misra, J. H. Freed, Distance Measurements: Continuous-Wave (CW)- and Pulsed Dipolar EPR in *Multifrequency Electron Paramagnetic Resonance: Theory and Applications* (Ed. S. K. Misra), Wiley-VCH Weinheim, **2011**, pp. 545-588.
[51] K. J. D. MacKenzie, M. E. Smith, *Multinuclear Solid-State NMR of Inorganic Materials*, Pergamon, Amsterdam/Boston/London/New York/Oxford/Paris/San Diego/San Francisco/Singapore/Sydney/Tokyo, **2002**.
[52] N. C. Kunjir, G. W. Reginsson, O. Schiemann, S. T. Sigurdsson, *Phys. Chem. Chem. Phys.* **2013**, *15*, 19673-19685.
[53] G. Jeschke, Y. Polyhach, *Phys. Chem. Chem. Phys.* **2007**, *9*, 1895-1910.

[54] E. G. Bagryanskaya, O. A. Krumkacheva, M. V. Fedin, S. R. A. Marque, *Methods Enzymol.* **2015**, *563*, 365-396.
[55] A. M. Bowen, C. E. Tait, C. R. Timmel, J. R. Harmer, Orientation-Selective DEER Using Rigid Spin Labels, Cofactors, Metals, and Clusters in *Structural Information from Spin-Labels and Intrinsic Paramagnetic Centres in the Biosciences* (Eds. C. R. Timmel, J. R. Harmer), Springer Berlin/Heidelberg, **2013**, pp. 283-327.
[56] J. E. Banham, C. M. Baker, S. Ceola, I. J. Day, G. H. Grant, E. J. J. Groenen, C. T. Rodgers, G. Jeschke, C. R. Timmel, *J. Magn. Reson.* **2008**, *191*, 202-218.
[57] G. Jeschke, *eMagRes* **2016**, *5*, 1459-1476.
[58] G. E. Pake, *J. Chem. Phys.* **1948**, *16*, 327-336.
[59] T. Schmidt, M. A. Wälti, J. L. Baber, E. J. Hustedt, G. M. Clore, *Angew. Chem. Int. Ed.* **2016**, *55*, 15905-15909.
[60] G. Jeschke, *Macromol. Rapid Commun.* **2002**, *23*, 227-246.
[61] O. Kahn, *Molecular Magnetism*, VCH Verlagsgesellschaft, Weinheim, **1993**.
[62] C. Elschenbroich, G. Heikenfeld, M. Wünsch, W. Massa, G. Baum, *Angew. Chem. Int. Ed.* **1988**, *27*, 414-416.
[63] A. Bencini, D. Gatteschi, *EPR of Exchange Coupled Systems*, Dover Publications Inc., Mineola, **2012**.
[64] W. E. Antholine, Low Frequency EPR of Cu^{2+} in Proteins in *Biomedical EPR, Part A: Free Radicals, Metals, Medicine, and Physiology* (Eds. S. R. Eaton, G. R. Eaton, L. J. Berliner), Springer New York/Boston/Dordrecht/London/Moscow, **2005**, pp. 417-454.
[65] N. Fleck, T. Hett, J. Brode, A. Meyer, S. Richert, O. Schiemann, *J. Org. Chem.* **2019**, *84*, 3293-3303.
[66] J. Svorec, M. Valko, J. Moncol, M. Mazúr, M. Melník, J. Telser, *Transition Met. Chem.* **2009**, *34*, 129-134.
[67] E. Goovaerts, *eMagRes* **2017**, *6*, 343-358.
[68] S. S. Eaton, K. M. More, B. M. Sawant, G. R. Eaton, *J. Am. Chem. Soc.* **1983**, *105*, 6560-6567.
[69] W. A. Yager, E. Wasserman, R. M. R. Cramer, *J. Chem. Phys.* **1962**, *37*, 1148-1149.
[70] A. Weber, O. Schiemann, B. Bode, T. F. Prisner, *J. Magn. Reson.* **2002**, *157*, 277-285.
[71] D. Margraf, P. Cekan, T. F. Prisner, S. T. Sigurdsson, O. Schiemann, *Phys. Chem. Chem. Phys.* **2009**, *11*, 6708-6714.
[72] Y. D. Tsvetkov, M. K. Bowman, Y. A. Grishin, *Pulsed Electron-Electron Double Resonance: Nanoscale Distance Measurement in the Biological, Materials and Chemical Sciences*, Springer, Cham, **2019**.
[73] A. Meyer, J. J. Jassoy, S. Spicher, A. Berndhäuser, O. Schiemann, *Phys. Chem. Chem. Phys.* **2018**, *20*, 13858-13869.
[74] A. G. Maryasov, Y. D. Tsvetkov, J. Raap, *Appl. Magn. Reson.* **1998**, *14*, 101-113.
[75] G. Jeschke, M. Pannier, A. Godt, H. W. Spiess, *Chem. Phys. Lett.* **2000**, *331*, 243-252.
[76] Peter Höfer, Basic Experimental Methods in Continuous Wave Electron Paramagnetic Resonance in *Electron Paramagnetic Resonance: A Practitioner's Toolkit* (Eds. M. Brustolon, E. Giamello), John Wiley & Sons Inc. Hoboken, **2009**, pp. 37-82.
[77] G. Jeschke, Electron Paramagnetic Resonance Spectroscopy in *Encyclopedia of Supramolecular Chemistry* (Eds. J. L. Atwood, J. W. Steed), CRC Press Boca Raton, **2004**, pp. 520-527.
[78] G. R. Eaton, S. S. Eaton, D. P. Barr, R. T. Weber, *Quantitative EPR*, Springer, Wien/New York, **2010**.
[79] S. Stoll, A. Schweiger, EasySpin: Simulating cw ESR Spectra in *ESR Spectroscopy in Membrane Biophysics* (Ed. M. A. Hemminga, L. J. Berliner), Springer New York, **2007**, pp. 299-321.

[80] T. I. Smirnova, A. I. Smirnov, High-Field ESR Spectroscopy in Membrane and Protein Biophysics in *ESR Spectroscopy in Membrane Biophysics* (Ed. M. A. Hemminga, L. J. Berliner), Springer New York, **2007**, pp. 165-251.
[81] S. Stoll, *eMagRes* **2017**, *6*, 23-38.
[82] J. R. Harmer, *eMagRes* **2016**, *5*, 1493-1514.
[83] D. Goldfarb, *eMagRes* **2017**, *6*, 101-114.
[84] S. van Doorslaer, *eMagRes* **2017**, *6*, 51-70.
[85] S. S. Eaton, G. R. Eaton, *eMagRes* **2016**, *5*, 1543-1556.
[86] E. L. Hahn, *Phys. Rev.* **1950**, *80*, 580-594.
[87] J. R. Biller, J. E. McPeak, S. S. Eaton, G. R. Eaton, *Appl. Magn. Reson.* **2018**, *49*, 1235-1251.
[88] S. S. Eaton, G. R. Eaton, Relaxation Times of Organic Radicals and Transition Metal Ions in *Distance Measurements in Biological Systems by EPR* (Eds. L. J. Berliner, G. R. Eaton, S. S. Eaton), Springer New York, **2002**, pp. 29-154.
[89] G. Jeschke, *ChemPhysChem* **2002**, *3*, 927-932.
[90] T. Schmidt, J. Jeon, Y. Okuno, S. C. Chiliveri, G. M. Clore, *ChemPhysChem* **2020**, *21*, 1224-1229.
[91] R. Dastvan, B. E. Bode, M. P. R. Karuppiah, A. Marko, S. Lyubenova, H. Schwalbe, T. F. Prisner, *J. Phys. Chem. B* **2010**, *114*, 13507-13516.
[92] E. R. Canarie, S. M. Jahn, S. Stoll, *J. Phys. Chem. Lett.* **2020**, *11*, 3396-3400.
[93] H. El Mkami, R. Ward, A. Bowman, T. Owen-Hughes, D. G. Norman, *J. Magn. Reson.* **2014**, *248*, 36-41.
[94] R. Ward, A. Bowman, E. Sozudogru, H. El Mkami, T. Owen-Hughes, D. G. Norman, *J. Magn. Reson.* **2010**, *207*, 164-167.
[95] R. Ward, O. Schiemann, Interspin Distance Determination by EPR in *Encyclopedia of Biophysics* (Ed. G. C. K. Roberts), Springer Berlin/Heidelberg, **2013**, pp. 1116-1123.
[96] A. D. Milov, A. G. Maryasov, Y. D. Tsvetkov, *Appl. Magn. Reson.* **1998**, *15*, 107-143.
[97] L. J. Berliner, J. Grunwald, H. Hankovszky, K. Hideg, *Anal. Biochem.* **1982**, *119*, 450-455.
[98] W. L. Hubbell, C. J. López, C. Altenbach, Z. Yang, *Curr. Opin. Struct. Biol.* **2013**, *23*, 725-733.
[99] S. A. Shelke, S. T. Sigurdsson, Site-Directed Nitroxide Spin Labeling of Biopolymers in *Structural Information from Spin-Labels and Intrinsic Paramagnetic Centres in the Biosciences* (Eds. C. R. Timmel, J. R. Harmer), Springer Berlin/Heidelberg, **2013**, pp. 121-162.
[100] O. Schiemann, N. Piton, Y. Mu, G. Stock, J. W. Engels, T. F. Prisner, *J. Am. Chem. Soc.* **2004**, *126*, 5722-5729.
[101] G. Hagelueken, W. J. Ingledew, H. Huang, B. Petrovic-Stojanovska, C. Whitfield, H. El Mkami, O. Schiemann, J. H. Naismith, *Angew. Chem. Int. Ed.* **2009**, *48*, 2904-2906.
[102] C. Pliotas, R. Ward, E. Branigan, A. Rasmussen, G. Hagelueken, H. Huang, S. S. Black, I. R. Booth, O. Schiemann, J. H. Naismith, *Proc. Natl. Acad. Sci. U.S.A.* **2012**, *109*, E2675-E2682.
[103] K. Halbmair, J. Seikowski, I. Tkach, C. Höbartner, D. Sezer, M. Bennati, *Chem. Sci.* **2016**, *7*, 3172-3180.
[104] M. Heinz, N. Erlenbach, L. S. Stelzl, G. Thierolf, N. R. Kamble, S. T. Sigurdsson, T. F. Prisner, G. Hummer, *Nucleic Acids Res.* **2020**, *48*, 924-933.
[105] C. Wuebben, M. F. Vicino, M. Mueller, O. Schiemann, *Nucleic Acids Res.* **2020**, *48*, 10518-10526.
[106] D. Constantinescu-Aruxandei, B. Petrovic-Stojanovska, O. Schiemann, J. H. Naismith, M. F. White, *Nucleic Acids Res.* **2016**, *44*, 954-968.
[107] O. Duss, E. Michel, M. Yulikov, M. Schubert, G. Jeschke, F. H.-T. Allain, *Nature* **2014**, *509*, 588-592.
[108] O. Duss, M. Yulikov, G. Jeschke, F. H.-T. Allain, *Nat. Commun.* **2014**, *5*, 3669.
[109] C. Vazquez Reyes, N. S. Tangprasertchai, S. D. Yogesha, R. H. Nguyen, X. Zhang, R. Rajan, P. Z. Qin, *Cell Biochem. Biophys.* **2017**, *75*, 203-210.

[110] Z. Wu, A. Feintuch, A. Collauto, L. A. Adams, L. Aurelio, B. Graham, G. Otting, D. Goldfarb, *J. Phys. Chem. Lett.* **2017**, *8*, 5277-5282.
[111] G. Jeschke, V. Chechik, P. Ionita, A. Godt, H. Zimmermann, J. Banham, C. R. Timmel, D. Hilger, H. Jung, *Appl. Magn. Reson.* **2006**, *30*, 473-498.
[112] S. Rein, P. Lewe, S. L. Andrade, S. Kacprzak, S. Weber, *J. Magn. Reson.* **2018**, *295*, 17-26.
[113] G. Jeschke, Interpretation of Dipolar EPR Data in Terms of Protein Structure in *Structural Information from Spin-Labels and Intrinsic Paramagnetic Centres in the Biosciences* (Eds. C. R. Timmel, J. R. Harmer), Springer Berlin/Heidelberg, **2013**, pp. 83-120.
[114] H. Russell, R. Cura, J. E. Lovett, *Front. Mol. Biosci.* **2022**, *9*, 915167.
[115] M. Ji, S. Ruthstein, S. Saxena, *Acc. Chem. Res.* **2014**, *47*, 688-695.
[116] P. Schöps, P. E. Spindler, A. Marko, T. F. Prisner, *J. Magn. Reson.* **2015**, *250*, 55-62.
[117] M. Teucher, J. W. Sidabras, A. Schnegg, *Phys. Chem. Chem. Phys.* **2022**, *24*, 12528-12540.
[118] A. Doll, S. Pribitzer, R. Tschaggelar, G. Jeschke, *J. Magn. Reson.* **2013**, *230*, 27-39.
[119] G. Jeschke, M. Sajid, M. Schulte, A. Godt, *Phys. Chem. Chem. Phys.* **2009**, *11*, 6580-6591.
[120] G. W. Reginsson, N. C. Kunjir, S. T. Sigurdsson, O. Schiemann, *Chem. Eur. J.* **2012**, *18*, 13580-13584.
[121] A. D. Milov, A. B. Ponomarev, Y. Tsvetkov, *Chem. Phys. Lett.* **1984**, *110*, 67-72.
[122] G. Jeschke, G. Panek, A. Godt, A. Bender, H. Paulsen, *Appl. Magn. Reson.* **2004**, *26*, 223-244.
[123] B. E. Bode, D. Margraf, J. Plackmeyer, G. Dürner, T. F. Prisner, O. Schiemann, *J. Am. Chem. Soc.* **2007**, *129*, 6736-6745.
[124] D. Hilger, H. Jung, E. Padan, C. Wegener, K.-P. Vogel, H.-J. Steinhoff, G. Jeschke, *Biophys. J.* **2005**, *89*, 1328-1338.
[125] S. Valera, K. Ackermann, C. Pliotas, H. Huang, J. H. Naismith, B. E. Bode, *Chem. Eur. J.* **2016**, *22*, 4700-4703.
[126] M. Bretschneider, P. E. Spindler, O. Y. Rogozhnikova, D. V. Trukhin, B. Endeward, A. A. Kuzhelev, E. Bagryanskaya, V. M. Tormyshev, T. F. Prisner, *J. Phys. Chem. Lett.* **2020**, *11*, 6286-6290.
[127] V. Meyer, M. A. Swanson, L. J. Clouston, P. J. Boratyński, R. A. Stein, H. S. Mchaourab, A. Rajca, S. S. Eaton, G. R. Eaton, *Biophys. J.* **2015**, *108*, 1213-1219.
[128] L. Fábregas Ibáñez, G. Jeschke, S. Stoll, *Magn. Reson.* **2020**, *1*, 209-224.
[129] S. G. Worswick, J. A. Spencer, G. Jeschke, I. Kuprov, *Sci. Adv.* **2018**, *4*, eaat5218.
[130] R. A. Stein, A. H. Beth, E. J. Hustedt, *Methods Enzymol.* **2015**, *563*, 531-567.
[131] D. Abdullin, G. Hagelueken, R. I. Hunter, G. M. Smith, O. Schiemann, *Molecular Physics* **2015**, *113*, 544-560.
[132] T. H. Edwards, S. Stoll, *J. Magn. Reson.* **2018**, *288*, 58-68.
[133] T. H. Edwards, S. Stoll, *J. Magn. Reson.* **2016**, *270*, 87-97.
[134] A. D. Milov, K. M. Salikhov, M. D. Shirov, *Sov. Phys. Solid State* **1981**, 565-569.
[135] R. E. Martin, M. Pannier, F. Diederich, V. Gramlich, M. Hubrich, H. W. Spiess, *Angew. Chem. Int. Ed.* **1998**, *37*, 2834-2837.
[136] M. Pannier, S. Veit, A. Godt, G. Jeschke, H. W. Spiess, *J. Magn. Reson.* **2000**, *142*, 331-340.
[137] O. Schiemann, *Methods Enzymol.*, *469*, 329-351.
[138] K. M. Salikhov, I. T. Khairuzhdinov, *Appl. Magn. Reson.* **2015**, *46*, 67-83.
[139] G. W. Reginsson, O. Schiemann, *Biochem. J.* **2011**, *434*, 353-363.
[140] J. E. Lovett, A. M. Bowen, C. R. Timmel, M. W. Jones, J. R. Dilworth, D. Caprotti, S. G. Bell, L. L. Wong, J. Harmer, *Phys. Chem. Chem. Phys.* **2009**, *11*, 6840-6848.
[141] R. G. Larsen, D. J. Singel, *J. Chem. Phys.* **1993**, *98*, 5134-5146.
[142] M. F. Vicino, T. Hett, O. Schiemann, *Bio-protocol* **2021**, *11*, e4004.

[143] T. Hett, O. Schiemann, PELDOR Measurements on Nitroxide-Labeled Oligonucleotides in *DNAzymes: Methods and Protocols* (Ed. G. Steger, H. Rosenbach, I. Span), Humana New York, **2022**, pp. 241-274.
[144] L. V. Kulik, S. A. Dzuba, I. A. Grigoryev, Y. Tsvetkov, *Chem. Phys. Lett.* **2001**, *343*, 315-324.
[145] S. Milikisyants, F. Scarpelli, M. G. Finiguerra, M. Ubbink, M. Huber, *J. Magn. Reson.* **2009**, *201*, 48-56.
[146] D. Abdullin, M. Suchatzki, O. Schiemann, *Appl. Magn. Reson.* **2022**, *53*, 539-554.
[147] D. Abdullin, O. Schiemann, *ChemPlusChem* **2020**, *85*, 353-372.
[148] S. Razzaghi, M. Qi, A. I. Nalepa, A. Godt, G. Jeschke, A. Savitsky, M. Yulikov, *J. Phys. Chem. Lett.* **2014**, *5*, 3970-3975.
[149] K. Keller, A. Doll, M. Qi, A. Godt, G. Jeschke, M. Yulikov, *J. Magn. Reson.* **2016**, *272*, 108-113.
[150] D. Abdullin, P. Brehm, N. Fleck, S. Spicher, S. Grimme, O. Schiemann, *Chem. Eur. J.* **2019**, *25*, 14388-14398.
[151] D. Abdullin, H. Matsuoka, M. Yulikov, N. Fleck, C. Klein, S. Spicher, G. Hagelueken, S. Grimme, A. Lützen, O. Schiemann, *Chem. Eur. J.* **2019**, *25*, 8820-8828.
[152] I. Ritsch, H. Hintz, G. Jeschke, A. Godt, M. Yulikov, *Phys. Chem. Chem. Phys.* **2019**, *21*, 9810-9830.
[153] A. Meyer, O. Schiemann, *J. Phys. Chem. A* **2016**, *120*, 3463-3472.
[154] F. D. Breitgoff, K. Keller, M. Qi, D. Klose, M. Yulikov, A. Godt, G. Jeschke, *J. Magn. Reson.* **2019**, *308*, 106560.
[155] J. L. Wort, K. Ackermann, D. G. Norman, B. E. Bode, *Phys. Chem. Chem. Phys.* **2021**, *23*, 3810-3819.
[156] S. Saxena, J. H. Freed, *Chem. Phys. Lett.* **1996**, *251*, 102-110.
[157] S. Saxena, J. H. Freed, *J. Chem. Phys.* **1997**, *107*, 1317-1340.
[158] P. P. Borbat, J. H. Freed, *Chem. Phys. Lett.* **1999**, *313*, 145-154.
[159] S. Stoll, B. Kasumaj, *Appl. Magn. Reson.* **2008**, *35*, 15-32.
[160] G. Bodenhausen, H. Kogler, R. R. Ernst, *J. Magn. Reson.* **1984**, *58*, 370-388.
[161] S. K. Misra, P. P. Borbat, J. H. Freed, *Appl. Magn. Reson.* **2009**, *36*, 237-258.
[162] S. Stoll, R. D. Britt, *Phys. Chem. Chem. Phys.* **2009**, *11*, 6614-6625.
[163] P. P. Borbat, H. S. Mchaourab, J. H. Freed, *J. Am. Chem. Soc.* **2002**, *124*, 5304-5314.
[164] S. K. Misra, H. R. Salahi, *Magn. Reson. Solids* **2021**, *23*, 21101.
[165] N. Fleck, C. A. Heubach, T. Hett, F. R. Haege, P. P. Bawol, H. Baltruschat, O. Schiemann, *Angew. Chem. Int. Ed.* **2020**, *59*, 9767-9772.
[166] J. H. Freed, *Annu. Rev. Phys. Chem.* **2000**, *51*, 655-689.
[167] P. E. Spindler, P. Schöps, W. Kallies, S. J. Glaser, T. F. Prisner, *J. Magn. Reson.* **2017**, *280*, 30-45.
[168] T. Kaufmann, T. J. Keller, J. M. Franck, R. P. Barnes, S. J. Glaser, J. M. Martinis, S. Han, *J. Magn. Reson.* **2013**, *235*, 95-108.
[169] J. J. Jassoy, C. A. Heubach, T. Hett, F. Bernhard, F. R. Haege, G. Hagelueken, O. Schiemann, *Molecules* **2019**, *24*, 2735.
[170] A. Doll, G. Jeschke, *Phys. Chem. Chem. Phys.* **2016**, *18*, 23111-23120.
[171] J. G. Powles, P. Mansfield, *Phys. Lett.* **1962**, *2*, 58-59.
[172] G. Jeschke, *Emerging Top. Life Sci.* **2018**, *2*, 9-18.
[173] D. Abdullin, N. Florin, G. Hagelueken, O. Schiemann, *Angew. Chem. Int. Ed.* **2015**, *54*, 1827-1831.
[174] D. Nguyen, D. Abdullin, C. A. Heubach, T. Pfaffeneder, A. Nguyen, A. Heine, K. Reuter, F. Diederich, O. Schiemann, G. Klebe, *Angew. Chem. Int. Ed.* **2021**, *60*, 23419-23426.
[175] B. Joseph, E. A. Jaumann, A. Sikora, K. Barth, T. F. Prisner, D. S. Cafiso, *Nat. Protoc.* **2019**, *14*, 2344-2369.
[176] A. Collauto, S. von Bülow, D. B. Gophane, S. Saha, L. S. Stelzl, G. Hummer, S. T. Sigurdsson, T. F. Prisner, *Angew. Chem. Int. Ed.* **2020**, *59*, 23025-23029.

[177] B. Joseph, A. Sikora, D. S. Cafiso, *J. Am. Chem. Soc.* **2016**, *138*, 1844-1847.
[178] M. Bennati, A. Weber, J. Antonic, D. L. Perlstein, J. Robblee, J. Stubbe, *J. Am. Chem. Soc.* **2003**, *125*, 14988-14989.
[179] V. P. Denysenkov, D. Biglino, W. Lubitz, T. F. Prisner, M. Bennati, *Angew. Chem. Int. Ed.* **2008**, *47*, 1224-1227.
[180] P. Widder, J. Schuck, D. Summerer, M. Drescher, *Phys. Chem. Chem. Phys.* **2020**, *22*, 4875-4879.
[181] M. Drescher, *Top. Curr. Chem.* **2012**, *321*, 91-119.
[182] A. Gamble Jarvi, X. Bogetti, K. Singewald, S. Ghosh, S. Saxena, *Acc. Chem. Res.* **2021**, *54*, 1481-1491.
[183] A. Gamble Jarvi, T. F. Cunningham, S. Saxena, *Phys. Chem. Chem. Phys.* **2019**, *21*, 10238-10243.
[184] T. F. Cunningham, M. R. Putterman, A. Desai, W. S. Horne, S. Saxena, *Angew. Chem. Int. Ed.* **2015**, *54*, 6330-6334.
[185] J. L. Wort, S. Arya, K. Ackermann, A. J. Stewart, B. E. Bode, *J. Phys. Chem. Lett.* **2021**, *12*, 2815-2819.
[186] M. Qi, A. Groß, G. Jeschke, A. Godt, M. Drescher, *J. Am. Chem. Soc.* **2014**, *136*, 15366-15378.
[187] Y. Yang, F. Yang, Y.-J. Gong, J.-L. Chen, D. Goldfarb, X.-C. Su, *Angew. Chem. Int. Ed.* **2017**, *56*, 2914-2918.
[188] D. Goldfarb, *Phys. Chem. Chem. Phys.* **2014**, *16*, 9685-9699.
[189] Y. Yang, F. Yang, Y.-J. Gong, T. Bahrenberg, A. Feintuch, X.-C. Su, D. Goldfarb, *J. Phys. Chem. Lett.* **2018**, *9*, 6119-6123.
[190] Y. Yang, F. Yang, X.-Y. Li, X.-C. Su, D. Goldfarb, *J. Phys. Chem. B* **2019**, *123*, 1050-1059.
[191] F. Torricella, A. Pierro, E. Mileo, V. Belle, A. Bonucci, *Biochim. Biophys. Acta, Proteins Proteomics* **2021**, *1869*, 140653.
[192] G. Karthikeyan, A. Bonucci, G. Casano, G. Gerbaud, S. Abel, V. Thomé, L. Kodjabachian, A. Magalon, B. Guigliarelli, V. Belle et al., *Angew. Chem. Int. Ed.* **2018**, *57*, 1366-1370.
[193] C. S. Klug, M. T. Lerch, J. B. Feix, Applications of Nitroxide Spin Labels to Structural Biology in *Nitroxides* (Eds. O. Ouari, D. Gigmes), Royal Society of Chemistry Cambridge, **2021**, pp. 392-419.
[194] J. J. Jassoy, A. Berndhäuser, F. Duthie, S. P. Kühn, G. Hagelueken, O. Schiemann, *Angew. Chem. Int. Ed.* **2017**, *56*, 177-181.
[195] N. Fleck, C. Heubach, T. Hett, S. Spicher, S. Grimme, O. Schiemann, *Chem. Eur. J.* **2021**, *27*, 5292-5297.
[196] A. Giannoulis, Y. Yang, Y.-J. Gong, X. Tan, A. Feintuch, R. Carmieli, T. Bahrenberg, Y. Liu, X.-C. Su, D. Goldfarb, *Phys. Chem. Chem. Phys.* **2019**, *21*, 10217-10227.
[197] Y. Yang, B.-B. Pan, X. Tan, F. Yang, Y. Liu, X.-C. Su, D. Goldfarb, *J. Phys. Chem. Lett.* **2020**, *11*, 1141-1147.
[198] A. Rajca, V. Kathirvelu, S. K. Roy, M. Pink, S. Rajca, S. Sarkar, S. S. Eaton, G. R. Eaton, *Chem. Eur. J.* **2010**, *16*, 5778-5782.
[199] O. Schiemann, N. Piton, J. Plackmeyer, B. E. Bode, T. F. Prisner, J. W. Engels, *Nat. Protoc.* **2007**, *2*, 904-923.
[200] C. Wuebben, S. Blume, D. Abdullin, D. Brajtenbach, F. Haege, S. Kath-Schorr, O. Schiemann, *Molecules* **2019**, *24*, 4482.
[201] J. P. Klare, Chemistry of Spin Labeling in *Encyclopedia of Biophysics* (Ed. G. C. K. Roberts), Springer Berlin/Heidelberg, **2013**, pp. 287-293.
[202] T. S. Braun, P. Widder, U. Osswald, L. Groß, L. Williams, M. Schmidt, I. Helmle, D. Summerer, M. Drescher, *ChemBioChem* **2020**, *21*, 958-962.
[203] L. Hofmann, S. Ruthstein, *J. Phys. Chem. B* **2022**, *126*, 7486-7494.
[204] C. K. Ellison, T. N. Dalia, A. B. Dalia, Y. V. Brun, *Nat. Protoc.* **2019**, *14*, 1803-1819.
[205] O. Krumkacheva, E. Bagryanskaya, *J. Magn. Reson.* **2017**, *280*, 117-126.

[206] A. Bonucci, O. Ouari, B. Guigliarelli, V. Belle, E. Mileo, *ChemBioChem* **2020**, *21*, 451-460.
[207] T. T. Tidwell, Triarylmethyl and Related Radicals in *Stable Radicals* (Ed. R. G. Hicks), John Wiley & Sons Ltd. Chichester, **2010**, pp. 1-31.
[208] V. M. Tormyshev, A. S. Chubarov, O. A. Krumkacheva, D. V. Trukhin, O. Y. Rogozhnikova, A. S. Spitsyna, A. A. Kuzhelev, V. V. Koval, M. V. Fedin, T. S. Godovikova et al., *Chem. Eur. J.* **2020**, *26*, 2705-2712.
[209] I. Dhimitruka, M. Velayutham, A. A. Bobko, V. V. Khramtsov, F. A. Villamena, C. M. Hadad, J. L. Zweier, *Bioorg. Med. Chem. Lett.* **2007**, *17*, 6801-6805.
[210] Z. Yang, Y. Liu, P. Borbat, J. L. Zweier, J. H. Freed, W. L. Hubbell, *J. Am. Chem. Soc.* **2012**, *134*, 9950-9952.
[211] G. Y. Shevelev, O. A. Krumkacheva, A. A. Lomzov, A. A. Kuzhelev, D. V. Trukhin, O. Y. Rogozhnikova, V. M. Tormyshev, D. V. Pyshnyi, M. V. Fedin, E. G. Bagryanskaya, *J. Phys. Chem. B* **2015**, *119*, 13641-13648.
[212] G. Y. Shevelev, O. A. Krumkacheva, A. A. Lomzov, A. A. Kuzhelev, O. Y. Rogozhnikova, D. V. Trukhin, T. I. Troitskaya, V. M. Tormyshev, M. V. Fedin, D. V. Pyshnyi et al., *J. Am. Chem. Soc.* **2014**, *136*, 9874-9877.
[213] A. A. Kuzhelev, O. A. Krumkacheva, G. Y. Shevelev, M. Yulikov, M. V. Fedin, E. G. Bagryanskaya, *Phys. Chem. Chem. Phys.* **2018**, *20*, 10224-10230.
[214] I. Marin-Montesinos, J. C. Paniagua, M. Vilaseca, A. Urtizberea, F. Luis, M. Feliz, F. Lin, S. van Doorslaer, M. Pons, *Phys. Chem. Chem. Phys.* **2015**, *17*, 5785-5794.
[215] I. Marin-Montesinos, J. C. Paniagua, A. Peman, M. Vilaseca, F. Luis, S. van Doorslaer, M. Pons, *Phys. Chem. Chem. Phys.* **2016**, *18*, 3151-3158.
[216] B. Joseph, V. M. Tormyshev, O. Y. Rogozhnikova, D. Akhmetzyanov, E. G. Bagryanskaya, T. F. Prisner, *Angew. Chem. Int. Ed.* **2016**, *55*, 11538-11542.
[217] M. Poncelet, J. L. Huffman, V. V. Khramtsov, I. Dhimitruka, B. Driesschaert, *RSC Adv.* **2019**, *9*, 35073-35076.
[218] A. P. Jagtap, I. Krstic, N. C. Kunjir, R. Hänsel, T. F. Prisner, S. T. Sigurdsson, *Free Radical Res.* **2015**, *49*, 78-85.
[219] A. A. Kuzhelev, D. V. Trukhin, O. A. Krumkacheva, R. K. Strizhakov, O. Y. Rogozhnikova, T. I. Troitskaya, M. V. Fedin, V. M. Tormyshev, E. G. Bagryanskaya, *J. Phys. Chem. B* **2015**, *119*, 13630-13640.
[220] M. K. Bowman, C. Mailer, H. J. Halpern, *J. Magn. Reson.* **2005**, *172*, 254-267.
[221] M. G. Dal Farra, S. Ciuti, M. Gobbo, D. Carbonera, M. Di Valentin, *Molecular Physics* **2019**, *117*, 2673-2687.
[222] M. Di Valentin, M. Albertini, M. G. Dal Farra, E. Zurlo, L. Orian, A. Polimeno, M. Gobbo, D. Carbonera, *Chem. Eur. J.* **2016**, *22*, 17204-17214.
[223] A. Bertran, A. Barbon, A. M. Bowen, M. Di Valentin, *Methods Enzymol.* **2022**, *666*, 171-231.
[224] G. Jeschke, *Protein Science* **2018**, *27*, 76-85.
[225] G. Hagelueken, D. Abdullin, O. Schiemann, *Methods Enzymol.* **2015**, *563*, 595-622.
[226] G. Hagelueken, D. Abdullin, R. Ward, O. Schiemann, *Molecular Physics* **2013**, *111*, 2757-2766.
[227] G. Hagelueken, R. Ward, J. H. Naismith, O. Schiemann, *Appl. Magn. Reson.* **2012**, *42*, 377-391.
[228] Y. Polyhach, E. Bordignon, G. Jeschke, *Phys. Chem. Chem. Phys.* **2011**, *13*, 2356-2366.
[229] G. Jeschke, *Protein Science* **2021**, *30*, 125-135.
[230] G. Jeschke, L. Esteban-Hofer, *Methods Enzymol.* **2022**, *666*, 145-169.
[231] D. Klose, J. P. Klare, D. Grohmann, C. W. M. Kay, F. Werner, H.-J. Steinhoff, *PloS one* **2012**, *7*, e39492.
[232] K. Sale, L. Song, Y.-S. Liu, E. Perozo, P. Fajer, *J. Am. Chem. Soc.* **2005**, *127*, 9334-9335.
[233] D. Sezer, J. H. Freed, B. Roux, *J. Am. Chem. Soc.* **2009**, *131*, 2597-2605.

[234] S. M. Islam, B. Roux, *J. Phys. Chem. B* **2015**, *119*, 3901-3911.
[235] S. Schünke, M. Stoldt, J. Lecher, U. B. Kaupp, D. Willbold, *Proc. Natl. Acad. Sci. U.S.A.* **2011**, *108*, 6121-6126.
[236] G. Jeschke, *Prog. Nucl. Magn. Reson. Spectrosc.* **2013**, *72*, 42-60.
[237] D. Abdullin, G. Hagelueken, O. Schiemann, *Phys. Chem. Chem. Phys.* **2016**, *18*, 10428-10437.
[238] P. Pracht, F. Bohle, S. Grimme, *Phys. Chem. Chem. Phys.* **2020**, *22*, 7169-7192.
[239] S. Spicher, D. Abdullin, S. Grimme, O. Schiemann, *Phys. Chem. Chem. Phys.* **2020**, *22*, 24282-24290.
[240] A. Schlundt, J.-N. Tants, M. Sattler, *Methods* **2017**, *118-119*, 119-136.
[241] A. C. Steven, W. Baumeister, *J. Struct. Biol.* **2008**, *163*, 186-195.
[242] A. Zhuravleva, D. M. Korzhnev, *Prog. Nucl. Magn. Reson. Spectrosc.* **2017**, *100*, 52-77.
[243] M. Cammarata, M. Levantino, F. Schotte, P. A. Anfinrud, F. Ewald, J. Choi, A. Cupane, M. Wulff, H. Ihee, *Nat. Methods* **2008**, *5*, 881-886.
[244] S. K. Misra, J. H. Freed, Molecular Motions in *Multifrequency Electron Paramagnetic Resonance: Theory and Applications* (Ed. S. K. Misra), Wiley-VCH Weinheim, **2011**, pp. 497-544.
[245] Y. Hu, K. Cheng, L. He, X. Zhang, B. Jiang, L. Jiang, C. Li, G. Wang, Y. Yang, M. Liu, *Anal. Chem.* **2021**, *93*, 1866-1879.
[246] M. Billeter, G. Wagner, K. Wüthrich, *J. Biomol. NMR* **2008**, *42*, 155-158.
[247] S. Schütz, R. Sprangers, *Prog. Nucl. Magn. Reson. Spectrosc.* **2020**, *116*, 56-84.
[248] M. Burger, S. Rein, S. Weber, P. Gräber, S. Kacprzak, *Eur. Biophys. J.* **2020**, *49*, 1-10.
[249] M. F. Peter, C. Gebhardt, R. Mächtel, G. G. M. Muñoz, J. Glaenzer, A. Narducci, G. H. Thomas, T. Cordes, G. Hagelueken, *Nat. Commun.* **2022**, *13*, 4396.
[250] J. W. Engels, C. Grünewald, L. Wicke, Site-Directed Spin Labeling of RNA for Distance Measurements by EPR in *Chemical Biology of Nucleic Acids: Fundamentals and Clinical Applications* (Eds. V. A. Erdmann, W. T. Markiewicz, J. Barciszewski), Springer Berlin/Heidelberg, **2014**, pp. 385-407.
[251] Y.-W. Chiang, P. P. Borbat, J. H. Freed, *J. Magn. Reson.* **2005**, *172*, 279-295.
[252] F. S. Wouters, Förster Resonance Energy Transfer and Fluorescence Lifetime Imaging in *Fluorescence Microscopy* (Ed. U. Kubitscheck), Wiley-VCH Verlag GmbH & Co. KGaA Weinheim, **2017**, pp. 405-451.
[253] D. Margraf, B. E. Bode, A. Marko, O. Schiemann, T. F. Prisner, *Molecular Physics* **2007**, *105*, 2153-2160.
[254] J. R. Lakowicz, *Principles of Fluorescence Spectroscopy*, Springer, New York, **2006**.
[255] S. E. Braslavsky, *Pure Appl. Chem.* **2007**, *79*, 293-465.
[256] J. Jumper, R. Evans, A. Pritzel, T. Green, M. Figurnov, O. Ronneberger, K. Tunyasuvunakool, R. Bates, A. Žídek, A. Potapenko et al., *Nature* **2021**, *596*, 583-589.
[257] Tobias Hett, "ScanState", can be found under https://github.com/TobiasHett/ScanState, accessed 20.11.2022.
[258] A. V. Cherepanov, S. de Vries, *Biochim. Biophys Acta* **2004**, *1656*, 1-31.
[259] J. Kowal, N. Biyani, M. Chami, S. Scherer, A. J. Rzepiela, P. Baumgartner, V. Upadhyay, C. M. Nimigean, H. Stahlberg, *Structure* **2018**, *26*, 20-27.
[260] C. M. Nimigean, T. Shane, C. Miller, *J. Gen. Physiol.* **2004**, *124*, 203-210.
[261] S. Schünke, M. Stoldt, K. Novak, U. B. Kaupp, D. Willbold, *EMBO Rep.* **2009**, *10*, 729-735.
[262] G. M. Clayton, W. R. Silverman, L. Heginbotham, J. H. Morais-Cabral, *Cell* **2004**, *119*, 615-627.
[263] E. E. Galyov, S. Håkansson, A. Forsberg, H. Wolf-Watz, *Nature* **1993**, *361*, 730-732.
[264] W. L. Lee, J. M. Grimes, R. C. Robinson, *Nat. Struct. Mol. Biol.* **2015**, *22*, 248-255.
[265] F. Wojciechowski, A. Groß, I. T. Holder, L. Knörr, M. Drescher, J. S. Hartig, *Chem. Commun.* **2015**, *51*, 13850-13853.

[266] A. A. Kuzhelev, O. A. Krumkacheva, I. O. Timofeev, V. M. Tormyshev, M. V. Fedin, E. G. Bagryanskaya, *Appl. Magn. Reson.* **2018**, *49*, 1171-1180.
[267] J. Fritscher, M. Beyer, O. Schiemann, *Chem. Phys. Lett.* **2002**, *364*, 393-401.
[268] B. Bleaney, K. D. Bowers, *Proc. R. Soc. Lond. A* **1952**, *214*, 451-465.
[269] S. Grimme, C. Bannwarth, P. Shushkov, *J. Chem. Theory Comput.* **2017**, *13*, 1989-2009.
[270] F. Weigend, R. Ahlrichs, *Phys. Chem. Chem. Phys.* **2005**, *7*, 3297-3305.
[271] O. P. Ernst, F. J. Bartl, *ChemBioChem* **2002**, *3*, 968-974.
[272] S. Kucher, C. Elsner, M. Safonova, S. Maffini, E. Bordignon, *J. Phys. Chem. Lett.* **2021**, *12*, 3679-3684.
[273] B. Joseph, A. Sikora, E. Bordignon, G. Jeschke, D. S. Cafiso, T. F. Prisner, *Angew. Chem. Int. Ed.* **2015**, *54*, 6196-6199.

6 Glossary

cAMP Cyclic Adenosine Monophosphate
CNBD Cyclic Nucleotide-Binding Domain
CREST Conformer-Rotamer Ensemble Sampling Tool
cryo-EM Cryogenic Electron Microscopy
CuTPP Copper(II) Tetraphenyl Porphyrin
cw *Continuous Wave*
D_{Dip} Dipolar Coupling constant
DEER Double Electron-Electron Resonance
DFT Density Functional Theory
DQC Double-Quantum Coherence
DQF Double-Quantum Filter
ENDOR Electron-Nuclear Double Resonance
EPR Electron Paramagnetic Resonance
ESEEM Electron Spin Echo Envelope Modulation
ESR Electron Spin Resonance
EZI Electron-Zeeman Interaction
FFT Fast Fourier Transform
FID Free Induction Decay
FRET Förster resonance Energy Transfer
FTAM Finland Trityl (Finland Tetrathiatriarylmethyl)
g_e, g_n electron *g*-factor, nuclear *g*-factor
HDvV Heisenberg-Dirac-van Vleck
HE Hahn Echo
HEK Human Embryonic Kidney Cells
HeLa Human cervical cancer cells, originally from Henrietta Lacks
HFI Hyperfine Interaction
I Nuclear Spin Quantum Number
IDA Iminodiacetate
J Electron-Spin Exchange Coupling Constant
MAS Magic Angle Spinning
MD Molecular Dynamics
MDDS Molecular Dynamics with Dummy Spin Labels
MHQ Microsecond Freeze-Hyperquenching
m_I Nuclear-Spin Magnetic Quantum Number
MMM Multiscale Modeling of Macromolecules
m_s Electron-Spin Magnetic Quantum Number
MTSL Methanethiosulfonate Nitroxide Spin Label
NMR Nuclear Magnetic Resonance
NOE Nuclear Overhauser Effect
NZI Nuclear-Zeeman Interaction
Ox-SLIM Hydroxylated Short-Linked Maleimide Trityl Label
OxTAM Hydroxylated Trityl

PAS Principal Axis System
PDB Protein Data Bank (www.rcsb.org)
PDS Pulsed Dipolar EPR Spectroscopy
PELDOR Pulsed Electron-Electron Double Resonance
RE Refocused Echo
RIDME Relaxation-Induced Dipolar Modulation Enhancement
RSE Refocused Stimulated Echo
RVE Refocused Virtual Echo
S Electron Spin Quantum Number
SANS Small-Angle Neutron Scattering
SAXS Small-Angle X-Ray Scattering
SDSL Site-directed Spin Labelling
SE Stimulated Echo
SIFTER Single-Frequency Technique for Refocusing Dipolar Couplings
SLIM Short-Linked Maleimide Trityl Label
SNR Signal-to-Noise Ratio
SOC Spin-Orbit Coupling
SQC Single-Quantum Coherence
SRT Shot Repetition Time
T_1 Spin-Lattice Relaxation Time / Longitudinal Relaxation Time
T_2 Spin-Spin Relaxation Time / Transverse Relaxation Time
TAM Trityl (Tetrathiatriarylmethyl)
τ_{corr} Rotational Correlation Time
TETPO Tetraethyl piperidinyloxy nitroxide label
T_M Phase-Memory Time
TPA 2,2,5,5-tetramethyl-pyrrolin-1-oxyl-3-acetylene nitroxide label
TPP Tetraphenyl Porphyrin
Trityl Tetrathiatriarylmethyl
TSL Trityl Spin Label
ZQC Zero-Quantum Coherence

7 Appendix

7.1 Derivation of the Dipolar Alphabet

For the following derivation of the dipolar alphabet, it is assumed that the magnetic moment $\vec{\mu}_1$ is located in the magnetic field $\vec{B}$ induced by a second magnetic moment $\vec{\mu}_2$. The magnetic moments $\vec{\mu}_1$ and $\vec{\mu}_2$ are connected by the distance vector $\vec{r}$ of the length $r = |\vec{r}|$.

The classical equation for the energy E of $\vec{\mu}_1$ in the magnetic field $\vec{B}$ of $\vec{\mu}_2$ reads [A1]

$$E = -\vec{\mu}_1^T \vec{B}(\vec{r}, \vec{\mu}_2) \tag{A1}$$

The magnetic field induced by a magnetic dipole moment is given by [A1]

$$\vec{B}(\vec{r}, \vec{\mu}) = -\frac{\mu_0}{4\pi}\frac{1}{r^3}\left[\vec{\mu} - \frac{3}{r^2}(\vec{\mu}^T\,\vec{r})\vec{r}\right] \tag{A2}$$

where $\vec{\mu}^T\,\vec{r}$ is the scalar product

$$\begin{pmatrix}\mu_x\\ \mu_y\\ \mu_z\end{pmatrix}^T \cdot \begin{pmatrix}r_x\\ r_y\\ r_z\end{pmatrix} = (\mu_x \quad \mu_y \quad \mu_z) \cdot \begin{pmatrix}r_x\\ r_y\\ r_z\end{pmatrix} = \mu_x r_x + \mu_y r_y + \mu_z r_z \tag{A3}$$

For simplicity, the exponent T indicating the transposition is omitted in the following (i.e. $\mu^T = \mu$). Inserting eq. (A2) into eq. (A1) yields the interaction energy of two magnetic dipoles

$$\begin{aligned} E &= -\vec{\mu}_1\left(-\frac{\mu_0}{4\pi}\cdot\frac{1}{r^3}\left[\vec{\mu}_2 - \frac{3}{r^2}(\vec{\mu}_2\,\vec{r})\vec{r}\right]\right) \\ &= \frac{\mu_0}{4\pi}\cdot\frac{1}{r^3}\left[\vec{\mu}_1\vec{\mu}_2 - \frac{3}{r^2}(\vec{\mu}_1\vec{r})(\vec{\mu}_2\,\vec{r})\right] \end{aligned} \tag{A4}$$

Using the correspondence principle [A1] ($\vec{\mu} \rightarrow \hat{S};\ E \rightarrow \hat{H}$) and $\vec{\mu} = -\gamma\hbar\hat{S}$ with $\hat{S} = \begin{pmatrix}S_x\\ S_y\\ S_z\end{pmatrix}$, the expression of the interaction energy can be transformed into the dipolar Hamilton operator $\hat{H}_{dd}$ [A1]

$$\begin{aligned} \hat{H}_{dd} &= \frac{\mu_0}{4\pi}\cdot\frac{1}{r^3}\cdot\left[\gamma_1\gamma_2\hbar^2\hat{S}_1\hat{S}_2 - \frac{3}{r^2}\left(\gamma_1\hbar\hat{S}_1\vec{r}\right)\left(\gamma_2\hbar\hat{S}_2\vec{r}\right)\right] \\ &= \frac{\mu_0}{4\pi}\cdot\frac{1}{r^3}\gamma_1\gamma_2\hbar^2\cdot\left[\hat{S}_1\hat{S}_2 - \frac{3}{r^2}\left(\hat{S}_1\vec{r}\right)\left(\hat{S}_2\vec{r}\right)\right] \end{aligned} \tag{A5}$$

With $\gamma_1 = g_1\frac{\beta_e}{\hbar}$ and $\gamma_2 = g_2\frac{\beta_e}{\hbar}$ follows [A1]

$$\hat{H}_{dd} = \frac{\mu_0}{4\pi}\cdot\frac{1}{r^3}g_1g_2\frac{\beta_e^2}{\cancel{\hbar^2}}\cancel{\hbar^2}\cdot\left[\hat{S}_1\hat{S}_2 - \frac{3}{r^2}\left(\hat{S}_1\vec{r}\right)\left(\hat{S}_2\vec{r}\right)\right] \tag{A6}$$

Since $E = h\nu = \hbar\omega$, dividing eq. (A6) by $\hbar$ transfers the Hamiltonian into angular frequency units [A2(p.34)]

$$\hat{H}_{dd} = \frac{\mu_0}{4\pi\hbar}\cdot\frac{1}{r^3}g_1g_2\beta_e^2\cdot\left[\hat{S}_1\hat{S}_2 - \frac{3}{r^2}\left(\hat{S}_1\vec{r}\right)\left(\hat{S}_2\vec{r}\right)\right] \tag{A7}$$

By inserting the spin-operator vectors $\hat{S}_1 = \begin{pmatrix}\hat{S}_{1,x}\\ \hat{S}_{1,y}\\ \hat{S}_{1,z}\end{pmatrix}$ and $\hat{S}_2 = \begin{pmatrix}\hat{S}_{2,x}\\ \hat{S}_{2,y}\\ \hat{S}_{2,z}\end{pmatrix}$ and transforming the Cartesian coordinates into spherical coordinates,[A3,A4(p.113)] $\vec{r} = \begin{pmatrix}r_x\\ r_y\\ r_z\end{pmatrix} = \begin{pmatrix}r\sin\theta\cos\varphi\\ r\sin\theta\sin\varphi\\ r\cos\theta\end{pmatrix}$, one obtains

$$\hat{H}_{dd} = \frac{\mu_0}{4\pi\hbar} \cdot \frac{1}{r^3} g_1 g_2 \beta_e^2 \cdot \left[\begin{pmatrix} \hat{S}_{1,x} \\ \hat{S}_{1,y} \\ \hat{S}_{1,z} \end{pmatrix} \begin{pmatrix} \hat{S}_{2,x} \\ \hat{S}_{2,y} \\ \hat{S}_{2,z} \end{pmatrix} - \frac{3}{r^2} \left(\begin{pmatrix} \hat{S}_{1,x} \\ \hat{S}_{1,y} \\ \hat{S}_{1,z} \end{pmatrix} \begin{pmatrix} r\sin\theta\cos\varphi \\ r\sin\theta\sin\varphi \\ r\cos\theta \end{pmatrix} \right) \cdot \left(\begin{pmatrix} \hat{S}_{2,x} \\ \hat{S}_{2,y} \\ \hat{S}_{2,z} \end{pmatrix} \begin{pmatrix} r\sin\theta\cos\varphi \\ r\sin\theta\sin\varphi \\ r\cos\theta \end{pmatrix} \right) \right] \tag{A8}$$

which extends to

$$\begin{aligned}
&\hat{H}_{dd} = \frac{\mu_0}{4\pi\hbar} \cdot \frac{1}{r^3} g_1 g_2 \beta_e^2 \cdot \left[\hat{S}_{1,x}\hat{S}_{2,x} + \hat{S}_{1,y}\hat{S}_{2,y} + \hat{S}_{1,z}\hat{S}_{2,z} \right. \\
&\left. - \frac{3}{r^2} \{ (\hat{S}_{1,x} r\sin\theta\cos\varphi + \hat{S}_{1,y} r\sin\theta\sin\varphi + \hat{S}_{1,z} r\cos\theta) \cdot (\hat{S}_{2,x} r\sin\theta\cos\varphi + \hat{S}_{2,y} r\sin\theta\sin\varphi + \hat{S}_{2,z} r\cos\theta) \} \right] \\
&= \frac{\mu_0}{4\pi\hbar} \cdot \frac{1}{r^3} g_1 g_2 \beta_e^2 \cdot \left[\hat{S}_{1,x}\hat{S}_{2,x} + \hat{S}_{1,y}\hat{S}_{2,y} + \hat{S}_{1,z}\hat{S}_{2,z} \right. \\
&\left. - \frac{3 \cdot r^2}{r^2} \{ (\hat{S}_{1,x}\sin\theta\cos\varphi + \hat{S}_{1,y}\sin\theta\sin\varphi + \hat{S}_{1,z}\cos\theta) \cdot (\hat{S}_{2,x}\sin\theta\cos\varphi + \hat{S}_{2,y}\sin\theta\sin\varphi + \hat{S}_{2,z}\cos\theta) \} \right] \\
&= \underbrace{\frac{\mu_0}{4\pi\hbar} \cdot \frac{1}{r^3} g_1 g_2 \beta_e^2}_{const} \cdot \left[\hat{S}_{1,x}\hat{S}_{2,x} + \hat{S}_{1,y}\hat{S}_{2,y} + \hat{S}_{1,z}\hat{S}_{2,z} \right. \\
&\left. - 3\{ (\hat{S}_{1,x}\sin\theta\cos\varphi + \hat{S}_{1,y}\sin\theta\sin\varphi + \hat{S}_{1,z}\cos\theta) \cdot (\hat{S}_{2,x}\sin\theta\cos\varphi + \hat{S}_{2,y}\sin\theta\sin\varphi + \hat{S}_{2,z}\cos\theta) \} \right]
\end{aligned} \tag{A9}$$

In the following, only the expression in square brackets of eq. (A9) is evaluated, i.e. the constant prefactor $\frac{\mu_0}{4\pi\hbar} \cdot \frac{1}{r^3} g_1 g_2 \beta_e^2$ is neglected. For the sake of clarity, the angular expressions in the square brackets are substituted as follows:

$$\begin{aligned}
u &= \hat{S}_{1,x}\sin\theta\cos\varphi & x &= \hat{S}_{2,x}\sin\theta\cos\varphi \\
v &= \hat{S}_{1,y}\sin\theta\sin\varphi & y &= \hat{S}_{2,y}\sin\theta\sin\varphi \\
w &= \hat{S}_{1,z}\cos\theta & z &= \hat{S}_{2,z}\cos\theta
\end{aligned} \tag{A10}$$

which leads to

$$\begin{aligned}
&\hat{S}_{1,x}\hat{S}_{2,x} + \hat{S}_{1,y}\hat{S}_{2,y} + \hat{S}_{1,z}\hat{S}_{2,z} - 3(u+v+w)(x+y+z) \\
&= \hat{S}_{1,x}\hat{S}_{2,x} + \hat{S}_{1,y}\hat{S}_{2,y} + \hat{S}_{1,z}\hat{S}_{2,z} + 3(ux + uy + uz + vx + vy + vz + wx + wy + wz) \\
&= \hat{S}_{1,x}\hat{S}_{2,x} + \hat{S}_{1,y}\hat{S}_{2,y} + \hat{S}_{1,z}\hat{S}_{2,z} \\
&- 3 \left(\hat{S}_{1,x}\hat{S}_{2,x} \underbrace{\sin^2\theta\cos^2\varphi}_{a} + \hat{S}_{1,x}\hat{S}_{2,y} \underbrace{\sin^2\theta\sin\varphi\cos\varphi}_{b} + \hat{S}_{1,x}\hat{S}_{2,z} \underbrace{\sin\theta\cos\theta\cos\varphi}_{c} \right. \\
&\quad + \hat{S}_{1,y}\hat{S}_{2,x} \underbrace{\sin^2\theta\sin\varphi\cos\varphi}_{b} + \hat{S}_{1,y}\hat{S}_{2,y} \underbrace{\sin^2\theta\sin^2\varphi}_{d} + \hat{S}_{1,y}\hat{S}_{2,z} \underbrace{\sin\theta\cos\theta\sin\varphi}_{e} \\
&\quad \left. + \hat{S}_{1,z}\hat{S}_{2,x} \underbrace{\sin\theta\cos\theta\cos\varphi}_{c} + \hat{S}_{1,z}\hat{S}_{2,y} \underbrace{\sin\theta\cos\theta\sin\varphi}_{e} + \hat{S}_{1,z}\hat{S}_{2,z} \underbrace{\cos^2\theta}_{f} \right)
\end{aligned} \tag{A11}$$

With the angular expressions

$$\begin{aligned}
a &= \sin^2\theta\cos^2\varphi & d &= \sin^2\theta\sin^2\varphi \\
b &= \sin^2\theta\sin\varphi\cos\varphi & e &= \sin\theta\cos\theta\sin\varphi \\
c &= \sin\theta\cos\theta\cos\varphi & f &= \cos^2\theta
\end{aligned} \tag{A12}$$

Next, $\hat{S}_x$ and $\hat{S}_y$ are substituted as follows using the ladder operators [A1]

$$\hat{S}^+ = \hat{S}_x + i\hat{S}_y \qquad \text{and} \qquad \hat{S}^- = \hat{S}_x - i\hat{S}_y \tag{A13}$$

which can be re-arranged in the following form:

$$\begin{aligned}
\hat{S}_{1,x} &= \frac{1}{2}(\hat{S}_1^+ + \hat{S}_1^-) & \hat{S}_{1,y} &= \frac{1}{2i}(\hat{S}_1^+ - \hat{S}_1^-) \\
\hat{S}_{2,x} &= \frac{1}{2}(\hat{S}_2^+ + \hat{S}_2^-) & \hat{S}_{2,y} &= \frac{1}{2i}(\hat{S}_2^+ - \hat{S}_2^-)
\end{aligned} \tag{A14}$$

This transforms eq. (A11) into:

$$
\begin{aligned}
&\frac{1}{4}(\hat{S}_1^+ + \hat{S}_1^-)(\hat{S}_2^+ + \hat{S}_2^-) + \frac{1}{4i^2}(\hat{S}_1^+ - \hat{S}_1^-)(\hat{S}_2^+ - \hat{S}_2^-) + \hat{S}_{1,z}\hat{S}_{2,z} \\
&- 3\left[\frac{1}{4}a(\hat{S}_1^+ + \hat{S}_1^-)(\hat{S}_2^+ + \hat{S}_2^-) + \frac{1}{4i}b(\hat{S}_1^+ + \hat{S}_1^-)(\hat{S}_2^+ - \hat{S}_2^-) + \frac{1}{2}c\hat{S}_{2,z}(\hat{S}_1^+ + \hat{S}_1^-)\right. \\
&+ \frac{1}{4i}b(\hat{S}_1^+ - \hat{S}_1^-)(\hat{S}_2^+ + \hat{S}_2^-) + \frac{1}{4i^2}d(\hat{S}_1^+ - \hat{S}_1^-)(\hat{S}_2^+ - \hat{S}_2^-) + \frac{1}{2i}e\hat{S}_{2,z}(\hat{S}_1^+ - \hat{S}_1^-) \\
&\left.+ \frac{1}{2}c\hat{S}_{1,z}(\hat{S}_2^+ + \hat{S}_2^-) + \frac{1}{2i}e\hat{S}_{1,z}(\hat{S}_2^+ - \hat{S}_2^-) + f\hat{S}_{1,z}\hat{S}_{2,z}\right] \\
&= \cancel{\frac{1}{4}\hat{S}_1^+\hat{S}_2^+} + \frac{1}{4}\hat{S}_1^+\hat{S}_2^- + \frac{1}{4}\hat{S}_1^-\hat{S}_2^+ + \cancel{\frac{1}{4}\hat{S}_1^-\hat{S}_2^-} - \cancel{\frac{1}{4}\hat{S}_1^+\hat{S}_2^+} + \frac{1}{4}\hat{S}_1^+\hat{S}_2^- + \frac{1}{4}\hat{S}_1^-\hat{S}_2^+ - \cancel{\frac{1}{4}\hat{S}_1^-\hat{S}_2^-} + \hat{S}_{1,z}\hat{S}_{2,z} \\
&\quad -3\left[\frac{1}{4}a\hat{S}_1^+\hat{S}_2^+ + \frac{1}{4}a\hat{S}_1^+\hat{S}_2^- + \frac{1}{4}a\hat{S}_1^-\hat{S}_2^+ + \frac{1}{4}a\hat{S}_1^-\hat{S}_2^-\right. \\
&\quad + \frac{1}{4i}b\hat{S}_1^+\hat{S}_2^+ - \frac{1}{4i}b\hat{S}_1^+\hat{S}_2^- + \frac{1}{4i}b\hat{S}_1^-\hat{S}_2^+ - \frac{1}{4i}b\hat{S}_1^-\hat{S}_2^- \\
&\quad + \frac{1}{2}c\hat{S}_1^+\hat{S}_{2,z} + \frac{1}{2}c\hat{S}_1^-\hat{S}_{2,z} \\
&\quad + \frac{1}{4i}b\hat{S}_1^+\hat{S}_2^+ + \frac{1}{4i}b\hat{S}_1^+\hat{S}_2^- - \frac{1}{4i}b\hat{S}_1^-\hat{S}_2^+ - \frac{1}{4i}b\hat{S}_1^-\hat{S}_2^- \\
&\quad + \frac{1}{4i^2}d\hat{S}_1^+\hat{S}_2^+ - \frac{1}{4i^2}d\hat{S}_1^+\hat{S}_2^- - \frac{1}{4i^2}d\hat{S}_1^-\hat{S}_2^+ + \frac{1}{4i^2}d\hat{S}_1^-\hat{S}_2^- \\
&\quad + \frac{1}{2i}e\hat{S}_1^+\hat{S}_{2,z} - \frac{1}{2i}e\hat{S}_1^-\hat{S}_{2,z} \\
&\quad + \frac{1}{2}c\hat{S}_2^+\hat{S}_{1,z} + \frac{1}{2}c\hat{S}_2^-\hat{S}_{1,z} \\
&\quad + \frac{1}{2i}e\hat{S}_2^+\hat{S}_{1,z} - \frac{1}{2i}e\hat{S}_2^-\hat{S}_{1,z} \\
&\quad \left. + f\hat{S}_{1,z}\hat{S}_{2,z}\right]
\end{aligned}
\tag{A15}
$$

In the following, eq. (A15) is sorted according to the spin operators to obtain the operators $\hat{A} - \hat{F}$ of the dipolar alphabet. Apart from the ladder operators, the Euler relations of the trigonometric functions will be used for rearranging and simplifying the equations:

$$
\begin{aligned}
\sin\theta &= \frac{1}{2i}\left(e^{i\theta} - e^{-i\theta}\right) & \cos\theta &= \frac{1}{2}\left(e^{i\theta} + e^{-i\theta}\right) \\
\sin^2\theta &= \frac{1}{4i^2}\left(e^{2i\theta} - 2e^0 + e^{-2i\theta}\right) & \cos^2\theta &= \frac{1}{4}\left(e^{2i\theta} + 2e^0 + e^{-2i\theta}\right)
\end{aligned}
\tag{A16}
$$

Further, the addition theorem of trigonometric functions

$$\sin^2\theta + \cos^2\theta = 1 \tag{A17}$$

and the imaginary identity

$$i^2 = -1 \tag{A18}$$

will be used.

Collecting the combination $\hat{S}_{1,z}\hat{S}_{2,z}$

$$
\begin{aligned}
&\hat{S}_{1,z}\hat{S}_{2,z} - 3f\hat{S}_{1,z}\hat{S}_{2,z} \\
&= \hat{S}_{1,z}\hat{S}_{2,z} - 3\hat{S}_{1,z}\hat{S}_{2,z}\cos^2\theta \\
&= \underline{\underline{\hat{S}_{1,z}\hat{S}_{2,z}(1 - 3\cos^2\theta) = \hat{A}}}
\end{aligned}
\tag{A19}
$$

Collecting the combination $\hat{S}_1^+\hat{S}_2^+$ (double-quantum transition)

$$
\begin{aligned}
&-3\left(\frac{1}{4}a\hat{S}_1^+\hat{S}_2^+ + \frac{1}{4i}b\hat{S}_1^+\hat{S}_2^+ + \frac{1}{4i}b\hat{S}_1^+\hat{S}_2^+ + \frac{1}{4i^2}d\hat{S}_1^+\hat{S}_2^+\right)\\
&= -\frac{3}{4}\hat{S}_1^+\hat{S}_2^+\left(a + \frac{1}{i}b + \frac{1}{i}b + \frac{1}{i^2}d\right)\\
&= -\frac{3}{4}\hat{S}_1^+\hat{S}_2^+\left(a + \frac{2}{i}b - d\right)\\
&= -\frac{3}{4}\hat{S}_1^+\hat{S}_2^+\left(\sin^2\theta\cos^2\varphi + \frac{2}{i}\sin^2\theta\sin\varphi\cos\varphi - \sin^2\theta\sin^2\varphi\right)\\
&= -\frac{3}{4}\hat{S}_1^+\hat{S}_2^+\sin^2\theta\left(\cos^2\varphi + \frac{2}{i}\sin\varphi\cos\varphi - \sin^2\varphi\right)\\
&= -\frac{3}{4}\hat{S}_1^+\hat{S}_2^+\sin^2\theta\left[\frac{1}{4}\left(e^{2i\varphi} + 2e^0 + e^{-2i\varphi}\right) + \frac{2}{i}\cdot\frac{1}{2i}\left(e^{i\varphi} - e^{-i\varphi}\right)\cdot\frac{1}{2}\left(e^{i\varphi} + e^{-i\varphi}\right)\right.\\
&\qquad\qquad \left. - \frac{1}{4i^2}\left(e^{2i\varphi} - 2e^0 + e^{-2i\varphi}\right)\right]\\
&= -\frac{3}{4}\hat{S}_1^+\hat{S}_2^+\sin^2\theta\left[\frac{1}{4}e^{2i\varphi} + \cancel{\frac{2}{4}} + \frac{1}{4}e^{-2i\varphi} - \frac{1}{2}\left(e^{2i\varphi} - e^{-2i\varphi}\right) + \frac{1}{4}e^{2i\varphi} - \cancel{\frac{2}{4}} + \frac{1}{4}e^{-2i\varphi}\right]\\
&= -\frac{3}{4}\hat{S}_1^+\hat{S}_2^+\sin^2\theta\left[\cancel{\frac{1}{4}e^{2i\varphi}} + \frac{1}{4}e^{-2i\varphi} - \cancel{\frac{1}{2}e^{2i\varphi}} + \frac{1}{2}e^{-2i\varphi} + \cancel{\frac{1}{4}e^{2i\varphi}} + \frac{1}{4}e^{-2i\varphi}\right]\\
&= \underline{\underline{-\frac{3}{4}\hat{S}_1^+\hat{S}_2^+\sin^2\theta\, e^{-2i\varphi} = \hat{E}}}
\end{aligned}
\tag{A20}
$$

Collecting the combination $\hat{S}_1^-\hat{S}_2^-$ (double-quantum transition)

$$
\begin{aligned}
&-3\left(\frac{1}{4}a\hat{S}_1^-\hat{S}_2^- - \frac{1}{4i}b\hat{S}_1^-\hat{S}_2^- - \frac{1}{4i}b\hat{S}_1^-\hat{S}_2^- + \frac{1}{4i^2}d\hat{S}_1^-\hat{S}_2^-\right)\\
&= -\frac{3}{4}\hat{S}_1^-\hat{S}_2^-\left(a - \frac{1}{i}b - \frac{1}{i}b + \frac{1}{i^2}d\right)\\
&= -\frac{3}{4}\hat{S}_1^-\hat{S}_2^-\left(a - \frac{2}{i}b - d\right)\\
&= -\frac{3}{4}\hat{S}_1^-\hat{S}_2^-\left(\sin^2\theta\cos^2\varphi - \frac{2}{i}\sin^2\theta\sin\varphi\cos\varphi - \sin^2\theta\sin^2\varphi\right)\\
&= -\frac{3}{4}\hat{S}_1^-\hat{S}_2^-\sin^2\theta\left(\cos^2\varphi - \frac{2}{i}\sin\varphi\cos\varphi - \sin^2\varphi\right)\\
&= -\frac{3}{4}\hat{S}_1^-\hat{S}_2^-\sin^2\theta\left[\frac{1}{4}\left(e^{2i\varphi} + 2e^0 + e^{-2i\varphi}\right) - \frac{2}{i}\cdot\frac{1}{2i}\left(e^{i\varphi} - e^{-i\varphi}\right)\cdot\frac{1}{2}\left(e^{i\varphi} + e^{-i\varphi}\right)\right.\\
&\qquad\qquad \left. - \frac{1}{4i^2}\left(e^{2i\varphi} - 2e^0 + e^{-2i\varphi}\right)\right]\\
&= -\frac{3}{4}\hat{S}_1^-\hat{S}_2^-\sin^2\theta\left[\frac{1}{4}e^{2i\varphi} + \cancel{\frac{2}{4}} + \frac{1}{4}e^{-2i\varphi} - \frac{1}{2i^2}\left(e^{2i\varphi} - e^{-2i\varphi}\right) + \frac{1}{4}e^{2i\varphi} - \cancel{\frac{2}{4}} + \frac{1}{4}e^{-2i\varphi}\right]\\
&= -\frac{3}{4}\hat{S}_1^-\hat{S}_2^-\sin^2\theta\left[\frac{1}{4}e^{2i\varphi} + \cancel{\frac{1}{4}e^{-2i\varphi}} + \frac{1}{2}e^{2i\varphi} - \cancel{\frac{1}{2}e^{-2i\varphi}} + \frac{1}{4}e^{2i\varphi} + \cancel{\frac{1}{4}e^{-2i\varphi}}\right]\\
&= \underline{\underline{-\frac{3}{4}\hat{S}_1^-\hat{S}_2^-\sin^2\theta\, e^{2i\varphi} = \hat{F}}}
\end{aligned}
\tag{A21}
$$

Collecting the combinations $\hat{S}^+\hat{S}^-$ and $\hat{S}^-\hat{S}^+$ (flip-flop-terms)

$$
\begin{aligned}
&\frac{1}{4}\hat{S}_1^+\hat{S}_2^- + \frac{1}{4}\hat{S}_1^-\hat{S}_2^+ + \frac{1}{4}\hat{S}_1^+\hat{S}_2^- + \frac{1}{4}\hat{S}_1^-\hat{S}_2^+ \\
&- 3\left(\frac{1}{4}a\hat{S}_1^+\hat{S}_2^- + \frac{1}{4}a\hat{S}_1^-\hat{S}_2^+ - \frac{1}{4i}b\hat{S}_1^+\hat{S}_2^- + \frac{1}{4i}b\hat{S}_1^-\hat{S}_2^+ + \frac{1}{4i}b\hat{S}_1^+\hat{S}_2^- - \frac{1}{4i}b\hat{S}_1^-\hat{S}_2^+ - \frac{1}{4i^2}d\hat{S}_1^+\hat{S}_2^- \right. \\
&\qquad \left. - \frac{1}{4i^2}d\hat{S}_1^-\hat{S}_2^+\right) \\
&= \left(\hat{S}_1^+\hat{S}_2^- + \hat{S}_1^-\hat{S}_2^+\right)\left[\frac{1}{4} + \frac{1}{4} - 3\left(\frac{1}{4}a - \frac{1}{\cancel{4i}}b + \frac{1}{\cancel{4i}}b - \frac{1}{4i^2}d\right)\right] \\
&= \left(\hat{S}_1^+\hat{S}_2^- + \hat{S}_1^-\hat{S}_2^+\right)\left[\frac{1}{2} - \frac{3}{4}a - \frac{3}{4}d\right] \\
&= \left(\hat{S}_1^+\hat{S}_2^- + \hat{S}_1^-\hat{S}_2^+\right)\left[\frac{1}{2} - \frac{3}{4}\sin^2\theta\cos^2\varphi - \frac{3}{4}\sin^2\theta\sin^2\varphi\right] \\
&= \left(\hat{S}_1^+\hat{S}_2^- + \hat{S}_1^-\hat{S}_2^+\right)\left[\frac{1}{2} - \frac{3}{4}\sin^2\theta\underbrace{(\cos^2\varphi + \sin^2\varphi)}_{1}\right] \\
&= \left(\hat{S}_1^+\hat{S}_2^- + \hat{S}_1^-\hat{S}_2^+\right)\left[\frac{1}{2} - \frac{3}{4}\cdot\frac{1}{4i^2}\left(e^{2i\theta} - 2e^0 + e^{-2i\theta}\right)\cdot 1\right] \\
&= \left(\hat{S}_1^+\hat{S}_2^- + \hat{S}_1^-\hat{S}_2^+\right)\left[\frac{1}{2} + \frac{3}{4}\cdot\frac{1}{4}\left(e^{2i\theta} - 2 + e^{-2i\theta}\right)\right] \\
&= \left(\hat{S}_1^+\hat{S}_2^- + \hat{S}_1^-\hat{S}_2^+\right)\left[\frac{1}{2} + \frac{3}{4}\cdot\frac{1}{4}\left(e^{2i\theta} - 2 + 4 + e^{-2i\theta}\right) - \frac{3}{4}\cdot\frac{1}{4}\cdot 4\right] \\
&= \left(\hat{S}_1^+\hat{S}_2^- + \hat{S}_1^-\hat{S}_2^+\right)\left[\frac{1}{2} + \frac{3}{4}\cdot\underbrace{\frac{1}{4}\left(e^{2i\theta} + 2 + e^{-2i\theta}\right)}_{\cos^2\theta} - \frac{3}{4}\right] \\
&= \left(\hat{S}_1^+\hat{S}_2^- + \hat{S}_1^-\hat{S}_2^+\right)\left[\frac{1}{2} + \frac{3}{4}\cos^2\theta - \frac{3}{4}\right] \\
&= \left(\hat{S}_1^+\hat{S}_2^- + \hat{S}_1^-\hat{S}_2^+\right)\left[-\frac{1}{4} + \frac{3}{4}\cos^2\theta\right] \\
&= \underline{\underline{-\frac{1}{4}\left(\hat{S}_1^+\hat{S}_2^- + \hat{S}_1^-\hat{S}_2^+\right)(1 - 3\cos^2\theta) = \hat{B}}}
\end{aligned}
\tag{A22}
$$

Collecting the combination $\hat{S}^+\hat{S}_z$

$$
\begin{aligned}
&-3\left(\frac{1}{2}c\hat{S}_1^+\hat{S}_{2,z} + \frac{1}{2i}e\hat{S}_1^+\hat{S}_{2,z} + \frac{1}{2}c\hat{S}_2^+\hat{S}_{1,z} + \frac{1}{2i}e\hat{S}_2^+\hat{S}_{1,z}\right) \\
&= -\frac{3}{2}\left(\hat{S}_1^+\hat{S}_{2,z} + \hat{S}_2^+\hat{S}_{1,z}\right)\left(c + \frac{1}{i}e\right) \\
&= -\frac{3}{2}\left(\hat{S}_1^+\hat{S}_{2,z} + \hat{S}_2^+\hat{S}_{1,z}\right)\left(\sin\theta\cos\theta\cos\varphi + \frac{1}{i}\sin\theta\cos\theta\sin\varphi\right) \\
&= -\frac{3}{2}\left(\hat{S}_1^+\hat{S}_{2,z} + \hat{S}_2^+\hat{S}_{1,z}\right)\sin\theta\cos\theta\left(\cos\varphi + \frac{1}{i}\sin\varphi\right) \\
&= -\frac{3}{2}\left(\hat{S}_1^+\hat{S}_{2,z} + \hat{S}_2^+\hat{S}_{1,z}\right)\sin\theta\cos\theta\left[\frac{1}{2}\left(e^{i\varphi} + e^{-i\varphi}\right) + \frac{1}{i}\cdot\frac{1}{2i}\left(e^{i\varphi} - e^{-i\varphi}\right)\right] \\
&= -\frac{3}{2}\left(\hat{S}_1^+\hat{S}_{2,z} + \hat{S}_2^+\hat{S}_{1,z}\right)\sin\theta\cos\theta\left[\frac{1}{2}\cancel{e^{i\varphi}} + \frac{1}{2}e^{-i\varphi} - \frac{1}{2}\cancel{e^{i\varphi}} + \frac{1}{2}e^{-i\varphi}\right] \\
&= \underline{\underline{-\frac{3}{2}\left(\hat{S}_1^+\hat{S}_{2,z} + \hat{S}_2^+\hat{S}_{1,z}\right)\sin\theta\cos\theta\cdot e^{-i\varphi} = \hat{C}}}
\end{aligned}
\tag{A23}
$$

Collecting the combination $\hat{S}^{-}\hat{S}_z$

$$
\begin{aligned}
&-3\left(\frac{1}{2}c\hat{S}_1^{-}\hat{S}_{2,z}-\frac{1}{2i}e\hat{S}_1^{-}\hat{S}_{2,z}+\frac{1}{2}c\hat{S}_2^{-}\hat{S}_{1,z}-\frac{1}{2i}e\hat{S}_2^{-}\hat{S}_{1,z}\right)\\
&=-\frac{3}{2}\left(\hat{S}_1^{-}\hat{S}_{2,z}+\hat{S}_2^{-}\hat{S}_{1,z}\right)\left(c-\frac{1}{i}e\right)\\
&=-\frac{3}{2}\left(\hat{S}_1^{-}\hat{S}_{2,z}+\hat{S}_2^{-}\hat{S}_{1,z}\right)\left(\sin\theta\cos\theta\cos\varphi-\frac{1}{i}\sin\theta\cos\theta\sin\varphi\right)\\
&=-\frac{3}{2}\left(\hat{S}_1^{-}\hat{S}_{2,z}+\hat{S}_2^{-}\hat{S}_{1,z}\right)\sin\theta\cos\theta\left(\cos\varphi-\frac{1}{i}\sin\varphi\right)\\
&=-\frac{3}{2}\left(\hat{S}_1^{-}\hat{S}_{2,z}+\hat{S}_2^{-}\hat{S}_{1,z}\right)\sin\theta\cos\theta\cdot\left[\frac{1}{2}\left(e^{i\varphi}+e^{-i\varphi}\right)-\frac{1}{i}\cdot\frac{1}{2i}\left(e^{i\varphi}-e^{-i\varphi}\right)\right]\\
&=-\frac{3}{2}\left(\hat{S}_1^{-}\hat{S}_{2,z}+\hat{S}_2^{-}\hat{S}_{1,z}\right)\sin\theta\cos\theta\cdot\left[\frac{1}{2}e^{i\varphi}+\cancel{\frac{1}{2}e^{-i\varphi}}+\frac{1}{2}e^{i\varphi}-\cancel{\frac{1}{2}e^{-i\varphi}}\right]\\
&=\underline{\underline{-\frac{3}{2}\left(\hat{S}_1^{-}\hat{S}_{2,z}+\hat{S}_2^{-}\hat{S}_{1,z}\right)\sin\theta\cos\theta\cdot e^{i\varphi}=\hat{D}}}
\end{aligned}
\tag{A24}
$$

Considering eq. (A9), one obtains

$$
\hat{H}_{DD}=\frac{\mu_0}{4\pi\hbar}\cdot\frac{1}{r^3}\cdot g_1g_2\beta_e^2\left(\hat{A}+\hat{B}+\hat{C}+\hat{D}+\hat{E}+\hat{F}\right) \tag{A25}
$$

with the operators $\hat{A}-\hat{F}$ called the "dipolar alphabet"[A1,A5]

$$
\begin{aligned}
\hat{A}&=\hat{S}_{1,z}\hat{S}_{2,z}\left(1-3\cos^2\theta\right)\\
\hat{B}&=-\frac{1}{4}\left(\hat{S}_1^{+}\hat{S}_2^{-}+\hat{S}_1^{-}\hat{S}_2^{+}\right)\left(1-3\cos^2\theta\right)\\
\hat{C}&=-\frac{3}{2}\left(\hat{S}_1^{+}\hat{S}_{2,z}+\hat{S}_2^{+}\hat{S}_{1,z}\right)\sin\theta\cos\theta\,e^{-i\varphi}\\
\hat{D}&=-\frac{3}{2}\left(\hat{S}_1^{-}\hat{S}_{2,z}+\hat{S}_2^{-}\hat{S}_{1,z}\right)\sin\theta\cos\theta\,e^{i\varphi}\\
\hat{E}&=-\frac{3}{4}\hat{S}_1^{+}\hat{S}_2^{+}\sin^2\theta\,e^{-2i\varphi}\\
\hat{F}&=-\frac{3}{4}\hat{S}_1^{-}\hat{S}_2^{-}\sin^2\theta\,e^{2i\varphi}
\end{aligned}
\tag{A26}
$$

Note that the operators $\hat{C}$ and $\hat{D}$ are complex conjugates $\left(\hat{C}=\hat{D}^{*}\right)$ of each other. The same holds true for the operators $\hat{E}$ and $\hat{F}$, i.e. $\hat{E}=\hat{F}^{*}$.

7.2 Derivation of the Secular Approximation of the Dipolar Hamiltonian

The secular approximation of the dipolar Hamiltonian can be derived upon transforming the equations into the rotating frame. "Secular" implies that the expressions are time-independent in the rotating frame (in the following, denoted by the superscript "rot"). The occasional use of colour helps to identify the respective terms throughout the mathematical operations.

The relations to interconvert the operators between the laboratory frame and the rotating frame are:[A6]

$$\begin{aligned} \hat{S}_x &= \hat{S}_x^{rot}\cos(\omega^{rot}t) + \hat{S}_y^{rot}\sin(\omega^{rot}t) \\ \hat{S}_y &= \hat{S}_y^{rot}\cos(\omega^{rot}t) - \hat{S}_x^{rot}\sin(\omega^{rot}t) \\ \hat{S}_z &= \hat{S}_z^{rot} \end{aligned} \tag{A27}$$

Operator $\hat{A}$

Transforming the operator $\hat{A}$ into the rotating frame immediately shows its time independence and thus proves that it is secular; it contains only the $\hat{S}_z$-operator and no trigonometric expressions that would involve *t*.

$$\begin{aligned} \hat{A} &= \hat{S}_{1,z}\hat{S}_{2,z}\,(1 - 3\cos^2\theta) \\ \hat{A} &= \hat{S}_{1,z}^{rot}\,\hat{S}_{2,z}^{rot}(1 - 3\cos^2\theta) \end{aligned} \tag{A28}$$

Operator $\hat{B}$

The secular approximation for the operator $\hat{B}$

$$\hat{B} = -\frac{1}{4}\left(\hat{S}_1^+\hat{S}_2^- + \hat{S}_1^-\hat{S}_2^+\right)(1 - 3\cos^2\theta) \tag{A29}$$

can be derived by substituting the ladder operators $\hat{S}^+$ and $\hat{S}^-$ according to eq. (A13) and by considering eq. (A18):

$$\begin{aligned} \hat{B} &= -\frac{1}{4}\,(1 - 3\cos^2\theta)\left(\hat{S}_1^+\hat{S}_2^- + \hat{S}_1^-\hat{S}_2^+\right) \\ &= -\frac{1}{4}(1 - 3\cos^2\theta)\left[\left(\hat{S}_{1,x} + i\hat{S}_{1,y}\right)\left(\hat{S}_{2,x} - i\hat{S}_{2,y}\right) + \left(\hat{S}_{1,x} - i\hat{S}_{1,y}\right)\left(\hat{S}_{2,x} + i\hat{S}_{2,y}\right)\right] \\ &= -\frac{1}{4}(1 - 3\cos^2\theta)\left[\hat{S}_{1,x}\hat{S}_{2,x} - \cancel{i\hat{S}_{1,x}\hat{S}_{2,y}} + \cancel{i\hat{S}_{1,y}\hat{S}_{2,x}} - i^2\hat{S}_{1,y}\hat{S}_{2,y}\right. \\ &\qquad\qquad \left. + \hat{S}_{1,x}\hat{S}_{2,x} + \cancel{i\hat{S}_{1,x}\hat{S}_{2,y}} - \cancel{i\hat{S}_{1,y}\hat{S}_{2,x}} - i^2\hat{S}_{1,y}\hat{S}_{2,y}\right] \\ &= -\frac{1}{4}(1 - 3\cos^2\theta)\left[2\hat{S}_{1,x}\hat{S}_{2,x} + 2\hat{S}_{1,y}\hat{S}_{2,y}\right] \end{aligned} \tag{A30}$$

The transformation into the rotating frame reads:

$$\begin{aligned} \hat{B} &= -\frac{1}{4}(1 - 3\cos^2\theta) \\ &\quad \cdot 2\left[\left(\hat{S}_{1,x}^{rot}\cos(\omega_1^{rot}t) + \hat{S}_{1,y}^{rot}\sin(\omega_1^{rot}t)\right)\cdot\left(\hat{S}_{2,x}^{rot}\cos(\omega_2^{rot}t) + \hat{S}_{2,y}^{rot}\sin(\omega_2^{rot}t)\right)\right. \\ &\quad \left. + \left(\hat{S}_{1,y}^{rot}\cos(\omega_1^{rot}t) - \hat{S}_{1,x}^{rot}\sin(\omega_1^{rot}t)\right)\cdot\left(\hat{S}_{2,y}^{rot}\cos(\omega_2^{rot}t) - \hat{S}_{2,x}^{rot}\sin(\omega_2^{rot}t)\right)\right] \\ &= -\frac{1}{4}(1 - 3\cos^2\theta) \\ &\quad \cdot 2\left[\hat{S}_{1,x}^{rot}\,\hat{S}_{2,x}^{rot}\cos(\omega_1^{rot}t)\cos(\omega_2^{rot}t) + \hat{S}_{1,x}^{rot}\,\hat{S}_{2,y}^{rot}\cos(\omega_1^{rot}t)\sin(\omega_2^{rot}t)\right. \\ &\quad + \hat{S}_{1,y}^{rot}\,\hat{S}_{2,x}^{rot}\sin(\omega_1^{rot}t)\cos(\omega_2^{rot}t) + \hat{S}_{1,y}^{rot}\,\hat{S}_{2,y}^{rot}\sin(\omega_1^{rot}t)\sin(\omega_2^{rot}t) \\ &\quad + \hat{S}_{1,y}^{rot}\,\hat{S}_{2,y}^{rot}\cos(\omega_1^{rot}t)\cos(\omega_2^{rot}t) - \hat{S}_{1,y}^{rot}\,\hat{S}_{2,x}^{rot}\cos(\omega_1^{rot}t)\sin(\omega_2^{rot}t) \\ &\quad \left. - \hat{S}_{1,x}^{rot}\,\hat{S}_{2,y}^{rot}\sin(\omega_1^{rot}t)\cos(\omega_2^{rot}t) + \hat{S}_{1,x}^{rot}\,\hat{S}_{2,x}^{rot}\sin(\omega_1^{rot}t)\sin(\omega_2^{rot}t)\right] \end{aligned} \tag{A31}$$

For “unlike”-spins, i.e. $\omega_1 \neq \omega_2$, this expression cannot be simplified further and the time dependence in the rotating frame persists. Being time-dependent for “unlike”-spins, $\hat{B}$ is non-secular and can thus be neglected in the context of the secular approximation.

For “like”-spins, $\omega_1^{rot} = \omega_2^{rot} = \omega^{rot}$ and it follows

$$\begin{aligned}
\hat{B} = &-\frac{1}{4}(1-3\cos^2\theta) \\
&\cdot 2\big[\hat{S}_{1,x}^{rot}\,\hat{S}_{2,x}^{rot}\cos(\omega^{rot}t)\cos(\omega^{rot}t) + \hat{S}_{1,x}^{rot}\,\hat{S}_{2,y}^{rot}\cos(\omega^{rot}t)\sin(\omega^{rot}t) \\
&+ \hat{S}_{1,y}^{rot}\,\hat{S}_{2,x}^{rot}\sin(\omega^{rot}t)\cos(\omega^{rot}t) + \hat{S}_{1,y}^{rot}\,\hat{S}_{2,y}^{rot}\sin(\omega^{rot}t)\sin(\omega^{rot}t) \\
&+ \hat{S}_{1,y}^{rot}\,\hat{S}_{2,y}^{rot}\cos(\omega^{rot}t)\cos(\omega^{rot}t) - \hat{S}_{1,y}^{rot}\,\hat{S}_{2,x}^{rot}\cos(\omega^{rot}t)\sin(\omega^{rot}t) \\
&- \hat{S}_{1,x}^{rot}\,\hat{S}_{2,y}^{rot}\sin(\omega^{rot}t)\cos(\omega^{rot}t) + \hat{S}_{1,x}^{rot}\,\hat{S}_{2,x}^{rot}\sin(\omega^{rot}t)\sin(\omega^{rot}t)\big] \\
= &-\frac{1}{4}(1-3\cos^2\theta) \\
&\cdot 2\big[\hat{S}_{1,x}^{rot}\,\hat{S}_{2,x}^{rot}\cos^2(\omega^{rot}t) + \hat{S}_{1,y}^{rot}\,\hat{S}_{2,y}^{rot}\sin^2(\omega^{rot}t) \\
&+ \hat{S}_{1,y}^{rot}\,\hat{S}_{2,y}^{rot}\cos^2(\omega^{rot}t) + \hat{S}_{1,x}^{rot}\,\hat{S}_{2,x}^{rot}\sin^2(\omega^{rot}t)\big] \\
= &-\frac{1}{4}(1-3\cos^2\theta) \\
&\cdot 2\Big[\hat{S}_{1,x}^{rot}\,\hat{S}_{2,x}^{rot}[\sin^2(\omega^{rot}t)+\cos^2(\omega^{rot}t)] \\
&+ \hat{S}_{1,y}^{rot}\,\hat{S}_{2,y}^{rot}[\sin^2(\omega^{rot}t)+\cos^2(\omega^{rot}t)]\Big] \\
= &-\frac{1}{4}(1-3\cos^2\theta)\cdot 2\big[\hat{S}_{1,x}^{rot}\,\hat{S}_{2,x}^{rot} + \hat{S}_{1,y}^{rot}\,\hat{S}_{2,y}^{rot}\big]
\end{aligned} \tag{A32}$$

The last transformation uses the addition theorem of trigonometric functions given by eq. (A17). This shows that $\hat{B}$ is time-independent for “like”-spins, i.e. it is secular and thus has to be retained in the secular approximation of the dipolar Hamiltonian. To conclude, it could be shown that $\hat{B}$ is pseudo-secular, i.e. it is secular for “like” spins and non-secular for “unlike” spins.

Operators $\hat{C}$ and $\hat{D}$

In the following, it will be shown that the operators $\hat{C}$ and $\hat{D}$ are non-secular.

$$\begin{aligned}
\hat{C} &= -\frac{3}{2}\big(\hat{S}_1^+\hat{S}_{2,z} + \hat{S}_2^+\hat{S}_{1,z}\big)\sin\theta\cos\theta\, e^{-i\varphi} \\
&= -\frac{3}{2}\big[(\hat{S}_{1,x}+i\hat{S}_{1,y})\hat{S}_{2,z} + (\hat{S}_{2,x}+i\hat{S}_{2,y})\hat{S}_{1,z}\big]\sin\theta\cos\theta\, e^{-i\varphi}
\end{aligned} \tag{A33}$$

Transformation into the rotating frame yields

$$\begin{aligned}
\hat{C} = &-\frac{3}{2}\sin\theta\cos\theta\, e^{-i\varphi}\cdot \\
&\Big[\Big(\hat{S}_{1,x}^{rot}\cos(\omega_1^{rot}t) + \hat{S}_{1,y}^{rot}\sin(\omega_1^{rot}t) + i\hat{S}_{y}^{rot}\cos(\omega_1^{rot}t) - i\hat{S}_{x}^{rot}\sin(\omega_1^{rot}t)\Big)\hat{S}_{2,z} \\
&+ \Big(\hat{S}_{2,x}^{rot}\cos(\omega_2^{rot}t) + \hat{S}_{2,y}^{rot}\sin(\omega_2^{rot}t) + i\hat{S}_{2,y}^{rot}\cos(\omega_2^{rot}t) - i\hat{S}_{2,x}^{rot}\sin(\omega_2^{rot}t)\Big)\hat{S}_{1,z}\Big]
\end{aligned} \tag{A34}$$

As the angular expressions in eq. (A34) do not cancel and as the addition theorem of trigonometric functions (eq. (A17)) is not applicable here, this expression cannot be simplified further and the time dependence persists. $\hat{C}$ is thus non-secular for “like” and “unlike” spins. As the operators $\hat{C}$ and $\hat{D}$ are complex conjugates of each other, $\hat{D}$ is non-secular, as well.

Operators $\hat{E}$ and $\hat{F}$

In the following, it will be shown that the operators $\hat{E}$ and $\hat{F}$ are non-secular.

$$\begin{aligned}\hat{E} &= -\frac{3}{4}\hat{S}_1^+\hat{S}_2^+ \sin^2\theta\, e^{-2i\varphi} \\ &= -\frac{3}{4}\left(\hat{S}_{1,x} + i\hat{S}_{1,y}\right)\left(\hat{S}_{2,x} + i\hat{S}_{2,y}\right)\sin^2\theta\, e^{-2i\varphi}\end{aligned} \tag{A35}$$

Transformation into the rotating frame yields

$$\begin{aligned}\hat{E} = -\frac{3}{4}\sin^2\theta\, e^{-2i\varphi} &\left(\hat{S}_{1,x}^{rot}\cos(\omega_1^{rot}t) + \hat{S}_{1,y}^{rot}\sin(\omega_1^{rot}t) + i\hat{S}_{1,y}^{rot}\cos(\omega_1^{rot}t)\right. \\ &\left. - i\hat{S}_{1,x}^{rot}\sin(\omega_1^{rot}t)\right)\left(\hat{S}_{2,x}^{rot}\cos(\omega_2^{rot}t) + \hat{S}_{2,y}^{rot}\sin(\omega_2^{rot}t) + i\hat{S}_{2,y}^{rot}\cos(\omega_2^{rot}t)\right. \\ &\left. - i\hat{S}_{2,x}^{rot}\sin(\omega_2^{rot}t)\right)\end{aligned} \tag{A36}$$

For "like"-spins, it follows

$$\begin{aligned}\hat{E} &= -\frac{3}{4}\sin^2\theta\, e^{-2i\varphi}\left(\hat{S}_{1,x}^{rot}\cos(\omega^{rot}t) + \hat{S}_{1,y}^{rot}\sin(\omega^{rot}t) + i\hat{S}_{1,y}^{rot}\cos(\omega^{rot}t) - i\hat{S}_{1,x}^{rot}\sin(\omega^{rot}t)\right) \\ &\quad\cdot\left(\hat{S}_{2,x}^{rot}\cos(\omega^{rot}t) + \hat{S}_{2,y}^{rot}\sin(\omega^{rot}t) + i\hat{S}_{2,y}^{rot}\cos(\omega^{rot}t) - i\hat{S}_{2,x}^{rot}\sin(\omega^{rot}t)\right) \\ &= -\frac{3}{4}\sin^2\theta\, e^{-2i\varphi} \\ &\cdot\left(\hat{S}_{1,x}^{rot}\hat{S}_{2,x}^{rot}\cos^2(\omega^{rot}t) + \hat{S}_{1,x}^{rot}\hat{S}_{2,y}^{rot}\cos(\omega^{rot}t)\sin(\omega^{rot}t) + i\hat{S}_{1,x}^{rot}\hat{S}_{2,y}^{rot}\cos^2(\omega^{rot}t) - i\hat{S}_{1,x}^{rot}\hat{S}_{2,x}^{rot}\cos(\omega^{rot}t)\sin(\omega^{rot}t)\right. \\ &+ \hat{S}_{1,y}^{rot}\hat{S}_{2,x}^{rot}\sin(\omega^{rot}t)\cos(\omega^{rot}t) + \hat{S}_{1,y}^{rot}\hat{S}_{2,y}^{rot}\sin^2(\omega^{rot}t) + i\hat{S}_{1,y}^{rot}\hat{S}_{2,y}^{rot}\sin(\omega^{rot}t)\cos(\omega^{rot}t) - i\hat{S}_{1,y}^{rot}\hat{S}_{2,x}^{rot}\sin^2(\omega^{rot}t) \\ &+ i\hat{S}_{1,y}^{rot}\hat{S}_{2,x}^{rot}\cos^2(\omega^{rot}t) + i\hat{S}_{1,y}^{rot}\hat{S}_{2,y}^{rot}\cos(\omega^{rot}t)\sin(\omega^{rot}t) + i^2\hat{S}_{1,y}^{rot}\hat{S}_{2,y}^{rot}\cos^{2(\omega^{rot}t)} - i^2\hat{S}_{1,y}^{rot}\hat{S}_{2,x}^{rot}\cos(\omega^{rot}t)\sin(\omega^{rot}t) \\ &\left.- i\hat{S}_{1,x}^{rot}\hat{S}_{2,x}^{rot}\sin(\omega^{rot}t)\cos(\omega^{rot}t) - i\hat{S}_{1,x}^{rot}\hat{S}_{2,y}^{rot}\sin^2(\omega^{rot}t) - i^2\hat{S}_{1,x}^{rot}\hat{S}_{2,y}^{rot}\sin(\omega^{rot}t)\cos(\omega^{rot}t) + i^2\hat{S}_{1,x}^{rot}\hat{S}_{2,x}^{rot}\sin^2(\omega^{rot}t)\right)\end{aligned} \tag{A37}$$

This expression cannot be simplified further even for "like" spins. As it is time-dependent, it is non-secular and can be neglected in the secular approximation. The same applies to "unlike" spins.

As the operators $\hat{E}$ and $\hat{F}$ are complex conjugates of each other, $\hat{F}$ is non-secular, as well.

7.3 Protocol for Setting up a DQC Experiment

The following section describes the DQC experiment on trityl-labelled protein samples using a Bruker (Bruker BioSpin, Rheinstetten, Germany) ELEXSYS E580 pulsed EPR spectrometer operated at Q-band with an ER5106QT2 resonator and a 150 W TWT amplifier (model 187 Ka, Applied Systems Engineering, Fort Worth, USA). For details on how to operate the spectrometer and the Xepr (Bruker BioSpin) software, refer to the instrument manual and publications [P1] and [P2].

Step 1 Power up the spectrometer and cool down the cryostat to a temperature of 70 K using a constant flow of cold helium gas. The temperature of 70 K provides a good trade-off between a long phase-memory time T_M and a short shot-repetition time (SRT).

Step 2 Insert the EPR sample tube into the sample rod so that the centre of the sample is located in the EPR-active zone of the resonator. For resonator-specific details, refer to the user manual of the spectrometer. Place the EPR sample tube in the resonator and over-couple the cavity as described in [P1] and [P2].

Step 3 Make sure that the temperature is stable at 70 K and does not fluctuate (± 0.1 K). Wait at least 20 minutes until the temperature of the sample has stabilized before you continue. The resonator and the sample need to be thermally well-equilibrated before starting the measurement since temperature changes can result in phase and frequency instabilities. As trityl radicals have a narrow EPR spectrum, phase and frequency drifts can lead to a tremendous decrease in sensitivity.

Step 4 Perform the safety test of the detection system as described in the user manual and switch the TWT amplifier into Operate mode.

Step 5 Set the magnetic field B_0 to the value which corresponds to $g \approx 2.0038$ at the given MW frequency ν (e.g. B_0 = 12016 G at ν = 33.7 GHz).

Step 6 Program the Hahn echo sequence $\pi/2–\tau–\pi–\tau–$Echo using the pulse tables. Set $\pi/2$ = 12 ns and π = 24 ns as a first guess, use an interpulse delay of τ = 200 ns, an SRT of 6.5 ms, and accumulate 10 shots per point. Start SpecJet to monitor the Hahn echo and lower the MW attenuation to maximize the echo intensity, i.e. to obtain $\pi/2$- and π-pulses at the given pulse lengths. In our hands, $\pi/2$- and π-pulses are obtained at ~3-5 dB attenuation when using pulse lengths of 12 ns and 24 ns for $\pi/2$ and π, respectively.
Alternatively, set the MW attenuation to 0 dB and determine the optimal pulse lengths by a transient nutation experiment.

Step 7 Optimize the phase of the MW pulses such that the entire signal will be detected in the real channel of the quadrature detector. Slightly changing the magnetic field (usually < 3 G) may be helpful in this step to fully bring the sample on resonance. Optimize the video gain amplification such that the echo fills the entire SpecJet display without clipping; set the number of averages in SpecJet to 1 for this purpose. Check again the attenuation and make sure that the echo is still maximized.

Step 8 Record the echo-detected field-swept EPR spectrum. To this end, set the integration gate symmetrically around the echo maximum and adjust the gate width such that the entire echo is covered. For the field-swept EPR spectrum, integrating the whole echo is crucial to obtain

a sufficiently high field resolution.[A7] Set the sweep width to 200 G, the number of points on the abscissa to 400, and start the experiment. As the experiment runs, adjust the number of scans to be accumulated; depending on the spin concentration, a few scans (e.g. n = 3) should be sufficient to obtain a good SNR. Save the spectrum and read off the magnetic field value that yields the maximum signal intensity. Set the centre field to this value.

Step 9 Perform the inversion recovery (IR, π_{inv}–T–π/2–τ–π–τ–Echo) experiment as described in the instrument manual to determine the longitudinal electron spin relaxation time. In the IR experiment, the Interval T is incremented and the echo amplitude is monitored as a function of T. Running the IR experiment from PulseSPEL, the following values proved to be appropriate for trityls at the temperature of 70 K: π/2 = 12 ns, π = 24 ns, τ = 200 ns, T = 400 ns, ΔT = 80 µs, SRT = 7,000 * srtu, h = 1, 626 points on the trace. Read off the time when the signal intensity has recovered to ~80% of its maximal value; this yields an appropriate value for the SRT.
If set up correctly, the IR trace should smoothly transition into a plateau (Figure A1a, at T > 20 ms). However, if the trace shows a kink and abruptly transitions into the plateau (Figure A1b), the detector is saturated and the signal is clipped. In this case, reduce the video gain amplification.

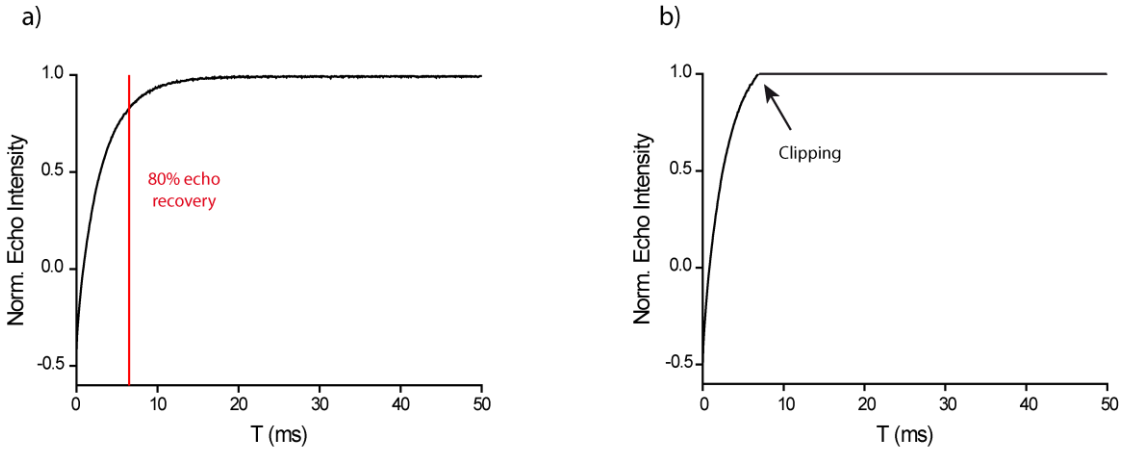

Figure A1: IR traces recorded with different video gain settings. a) 18 dB video gain, no clipping; the red line marks the value T = 6.5 ms when the echo has recovered to ~80% of its maximal intensity. b) 21 dB video gain, clipping can be seen from the absence of noise in the horizontal part of the trace and the kink indicated by the arrow.

Step 10 Perform the two-pulse electron spin echo envelope modulation (two-pulse ESEEM) experiment to obtain information on transverse electron spin relaxation. This experiment monitors the Hahn echo decay upon increasing the interpulse delay τ and permits inferring the maximally feasible dipolar evolution time in the DQC sequence. As detailed in the instrument manual, the two-pulse ESEEM experiment can be run conveniently from PulseSPEL using the following parameters: π/2 = 12 ns, π = 24 ns, τ = 200 ns, Δ τ = 8 ns, SRT = 6500 * srtu, h = 10, 2048-4096 points on the trace, depending on how quickly the echo decays (Figure A2).
Read off the time when the echo intensity has vanished to ≤ 5% of the initial amplitude. Note that the PulseSPEL program by default records the Hahn echo decay as a function of τ, whereas it is usually shown as a function of 2τ in the literature.[A8]

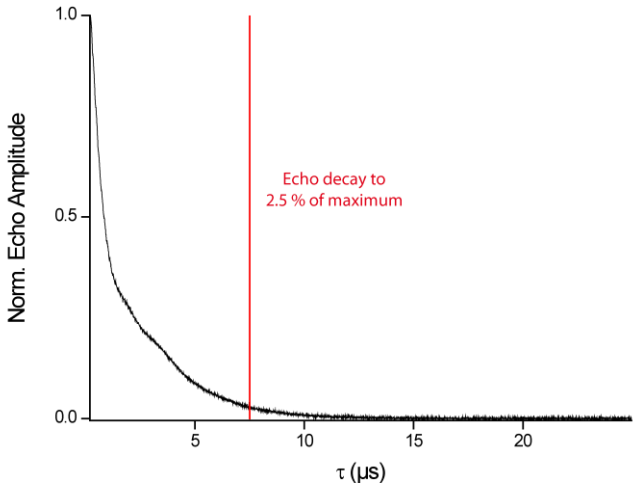

Figure A2: Hahn echo decay curve. Here, a dipolar evolution window of 7.5 µs (2.5 % of the maximum echo amplitude, marked by the red line) would be appropriate for the DQC experiment.

Step 11 Load the PulseSPEL file for setting up the DQC experiment,[5] which contains programs for the standing Hahn echo ("2P ESE Setup"), the standing DQC echo ("DQ ESE Setup"), and the DQC sequence ("ESE DQ-EPR"). Also, load the variable definition file,[5] which sets the acquisition parameters (pulse lengths, delays, etc.), into PulseSPEL. Table A1 lists the parameters of the DQC experiment with their conventional names and the corresponding PulseSPEL variables. Suggestions on values for the parameters are provided as well; however, one should always set the parameters (e.g. pulse lengths, SRT, trace length, etc.) to the optimal values determined in the previous steps. The meaning of the PulseSPEL variables d4 and d30 and the pulse timing of the DQC sequence are described in further detail in step 13.

Table A1: Parameters for the DQC experiment.

Conventional Variable	PulseSPEL Variable	Typical Value / Comment
π/2-pulse	p0	12 ns
π-pulse	p1	24 ns
Initial value of interpulse delay τ_1	d1	200 ns, must be longer than the spectrometer dead time
Initial value of interpulse delay τ_2	d2	d2 = d1 + d4
Interpulse delay T	d3	50 ns
–	d4	Time to start before axis = 0, equals the desired trace length
Increment Δt/2	d30	Even numbers between e.g. 2 ns and 8 ns, depending on the period of the dipolar oscillation to be resolved. The increment on the time trace will be Δt.
Increment for nuclear modulation averaging	d31	16 ns (to suppress ^{2}H-ESEEM)
Steps for nuclear modulation averaging	m	8 (to suppress ^{2}H-ESEEM)
Shot repetition time	SRT	e.g. 6,500 * 1.02 µs
Number of shots per point	h	e.g. 3
Number of scans	n	n ≥ 1

[5] Can be found at https://github.com/TobiasHett/DQC_PulseSPEL

Step 12 Select the“2P ESE Setup” experiment from the dropdown menu, select the “+x none” phase cycling option, and monitor the Hahn echo in SpecJet. Note that only the variables p0, p1, d1, and SRT are relevant for the Hahn echo. Check the phase settings. To attain maximum efficiency of the phase cycle in the DQC experiment, careful adjustment of the MW phase is crucial, which can be done at the stage of the Hahn echo. If the MW phase has been adjusted properly at step 7, summing the Hahn echo obtained from $\pi/2_{+x}$ / π_{+x} and $\pi/2_{-x}$ / π_{-x}-pulses should cancel the signal in the real and the imaginary channel of the quadrature detector. The same holds for $\pi/2_{+y}$ / π_{+y} and $\pi/2_{-y}$ / π_{-y}-pulses.

The “2P ESE Setup” experiment with the phase cycling options “sumx” and “sumy” records the Hahn echo with the respective phase settings (+x/-x or +y/-y), sums up the echoes, and thus permits checking proper phase adjustment (Figure A3). If a substantial signal remains in the real or imaginary channel with either of the phase cycling options, consider (usually slight) adjustments of the MW phase.

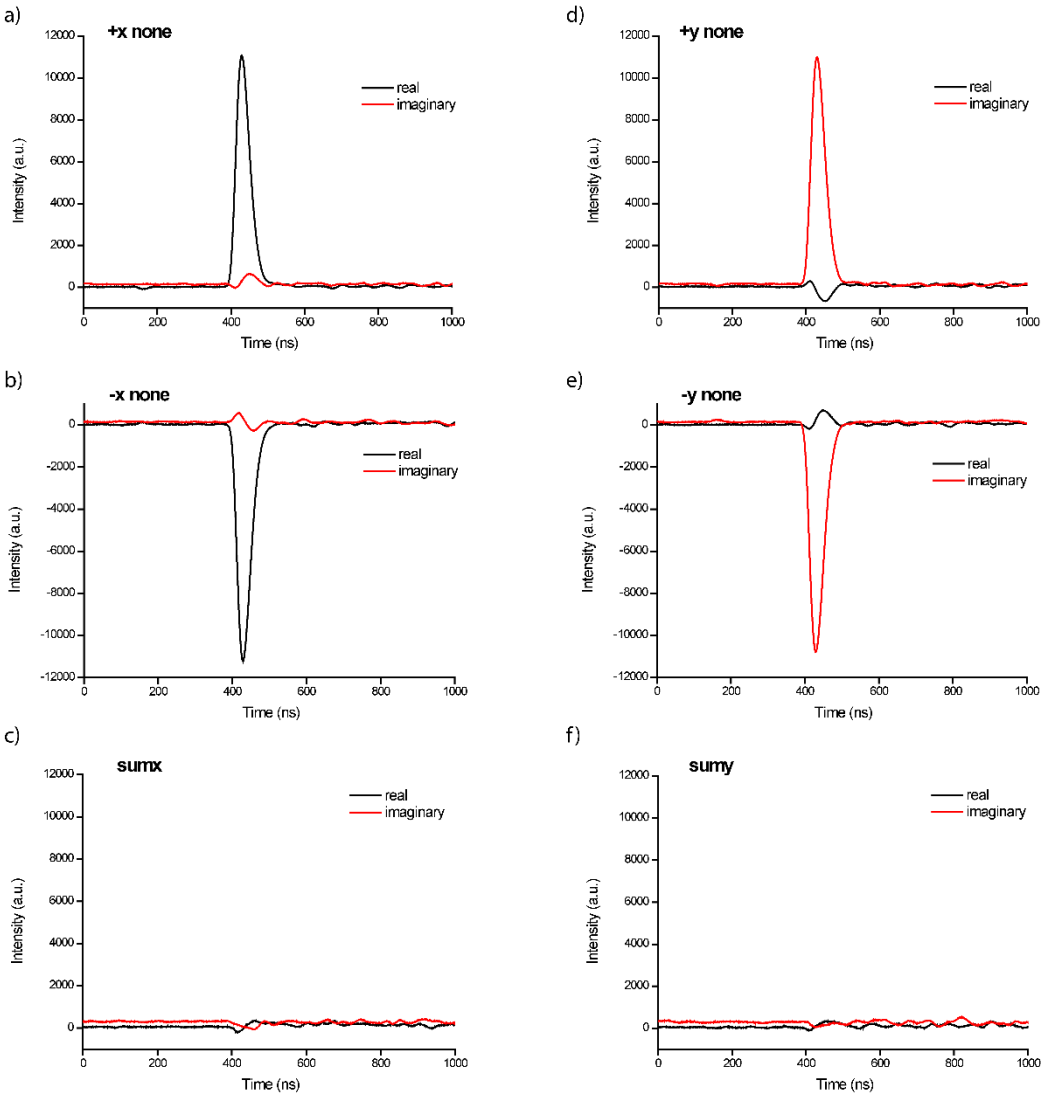

Figure A3: Hahn echoes recorded with different phase cycling options. a,b) Recording the Hahn echo with phase settings “+x none” and “–x none” inverts the signal by 180°, with “none” referring to the fact that no phase cycle is executed. c) Summing the signals from (a) and (b) with the phase cycle option “sumx” cancels the echo if the MW phase has been adjusted correctly. d-f) Analogous set-up experiment as in (a-c) with y-phase.

Once the MW phase has been adjusted, **do not change it anymore**. Imbalances in the phase will decrease the efficiency of the phase cycle in the DQC experiment and thus lead to artefacts in the time trace.

Step 13 For the following steps of setting up the DQC experiment, it is crucial to understand the timing conventions of the PulseSPEL program. As described in section 1.2.3.3, the DQC trace is recorded as a function of τ_1–τ_2. At the start of the program, the interpulse delay τ_2 is set to the value τ_1 + d4, where d4 determines the length of the time trace. Upon integrating the DQC echo obtained with τ_1 and $\tau_2 = \tau_1$ + d4 (shown at the x-value τ_1–τ_2 = –d4, i.e. as the leftmost point on the trace), τ_1 and τ_2 are incremented and decremented, respectively, by d30. The next time point on the trace is thus τ_1–$\tau_2 = (\tau_1 + d30) – (\tau_1 + d4 – d30) = –d4 + 2d30$. This is the reason why the time step on the DQC trace (Δt = 2d30) is doubled compared to the setting d30 in PulseSPEL. Continuing this incrementation and decrementation scheme leads to a time trace symmetric about the maximum at the zero-time, i.e. when the condition $\tau_1 = \tau_2$ is fulfilled (Figure A4).

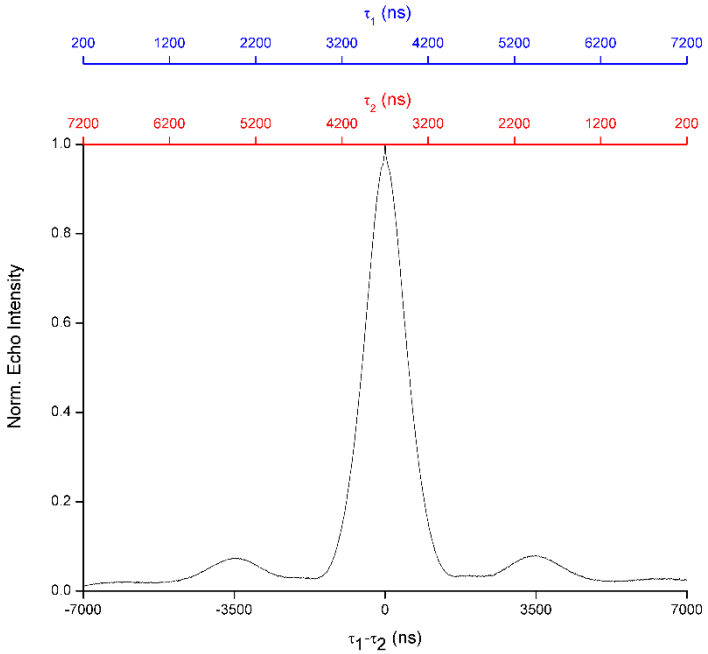

Figure A4: DQC time trace obtained with the interpulse delay parameters d1 = 200 ns, d2 = 200 ns, d3 = 50 ns, d4 = 7000 ns. The three x-axes show (from top to bottom) the interpulse delays τ_1 (blue), τ_2 (red), and the common representation of the trace as a function of τ_1–τ_2 (black). The DQC trace peaks at $\tau_1 = \tau_2$ = 3700 ns. Of note, the temporal position of the DQC echo does not change, as the sum of τ_1 and τ_2 is the same at every point on the trace ($\tau_1 + \tau_2$ = 7400 ns in this example).

Step 14 Decide on the length of the DQC trace (parameter d4). On the one hand, the maximum feasible length is governed by the echo decay observed in the two-pulse ESEEM experiment (step 10). On the other hand, at least two dipolar oscillations corresponding to the most probable distance in the distribution have to be resolved for reliable data analysis.[A8,A9] If there is prior knowledge on the expected interspin distance, calculate the oscillation period and thus the required trace length. Otherwise, determine a feasible value for the trace length from the Hahn echo decay curve (step 10). If you later realize that a longer DQC time trace is required to resolve at least two oscillations, abort the scan, increase the trace length, and restart the experiment. With the delay d1 and the trace length d4 for the DQC run, calculate the interpulse delays that fulfil the condition $\tau_1 = \tau_2$, i.e. that yield the maximum of the DQC time trace:

$$\tau_1 = \tau_2 = \frac{d4}{2} + d1 \tag{A38}$$

At this point of maximum echo intensity, the video gain amplification has to be adjusted such that the echo amplitude is maximized without clipping. Table A2 exemplarily summarizes the settings for the DQC run and the corresponding settings for the DQC setup.

Table A2: Exemplary interpulse delay settings for the DQC run and the DQC setup experiment.

DQC Run	DQC Setup
d0 = 404 ns	d0 = 0 ns
d1 = 200 ns	d1 = 3700 ns
d2 = d1 = 200 ns	d2 = d1 = 3700 ns
d3 = 50 ns	d3 = 50 ns
d4 = 7000 ns	d4 = 0 ns

Step 15 Set the values $\tau_1 = \tau_2$ calculated at step 14 for d1 and d2; set d4 = 0 ns, and the number of transient averages a = 1. Run the "DQ ESE Setup" experiment from PulseSPEL with the phase cycling option "+x none". Start SpecJet to observe the echo and preliminarily adjust the video gain such that no clipping occurs. The intensity of the DQC echo varies depending on the individual phase cycle step; this implies that the signal should be checked for clipping at each of the 64 steps of the phase cycle. To this end, uncheck the "On-Board Phase Cycling" option in the Xepr software (FT-EPR-Parameters → Options → On-Board Phase Cycling), select the "64-step" phase cycle from the dropdown list, and press the "Run" button. Each of the 64 separate phase cycling steps (Figure A5) will now be executed and the respective echo will show up in SpecJet so that clipping can be checked for.

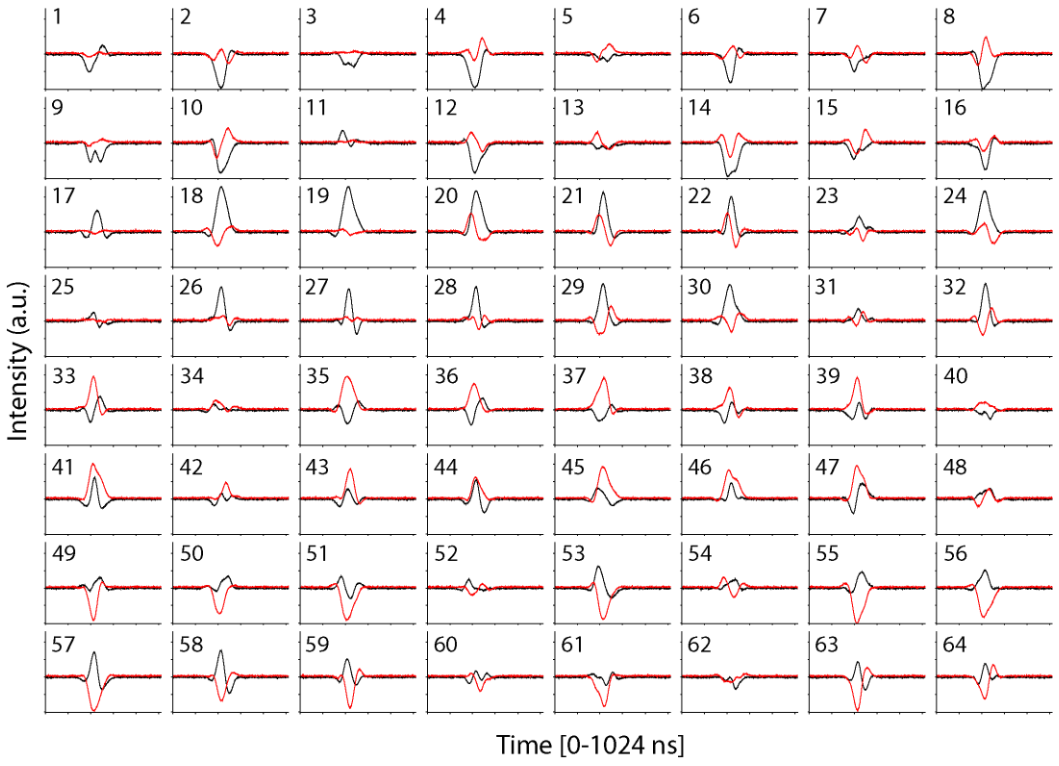

Figure A5: Representation of the individual 64 DQC echoes in the 64-step phase cycling procedure (see supplementary information of [A10]). The black traces show the real channel of the quadrature detector and the red traces the imaginary channel. Note the different echo intensities depending on the step of the phase cycle.

Step 16 If clipping occurs in any of the phase cycling steps, decrease the video gain amplification, abort the experiment, and run it again. If the program execution crashes with an error message ("Time out while waiting for data from SpecJet II"), restart it. Note that the filtered DQC echo cannot be shown directly in SpecJet as it requires the 64-step phase cycle. However, after recording all phase cycling steps, the DQC echo will be shown in the viewport of Xepr. Clipping has to be prevented as it leads to distortion of the DQC echo, which manifests itself by a broadening and splitting of the signal when summing up all 64 phase-cycling steps (Figure A6). Properly setting the video gain and optimizing the echo is thus crucial for unbiased measurements.

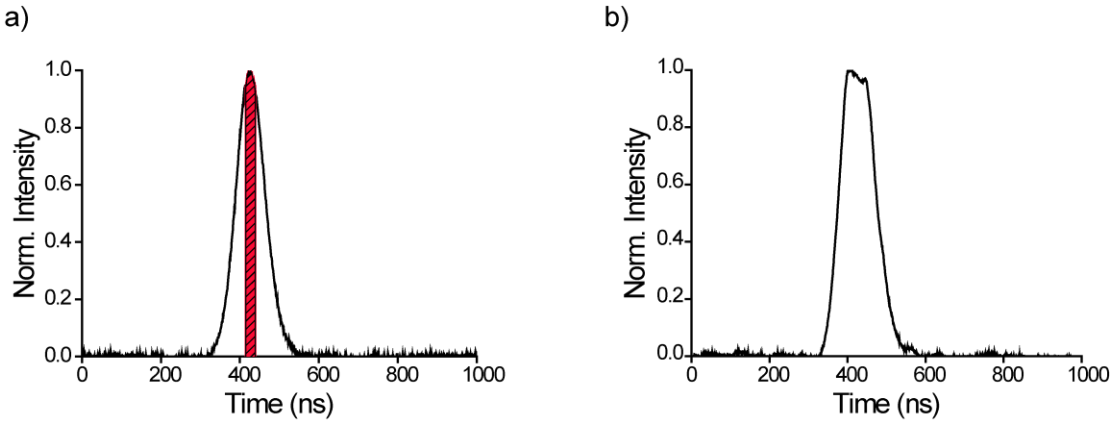

Figure A6: The DQC echo recorded at different settings of video gain amplification. The signal intensity has been normalized. a) 12 dB video gain, no clipping. The red area indicates the integration gate of 24 ns length around the echo maximum. b) 21 dB video gain, clipping. Note the broadening and distortion of the echo.

Step 17 Re-activate the "On-Board Phase Cycling" option. Press the "Run" button to record the DQC echo again with the 64-step phase cycle and read off the position of the echo maximum on the time axis. Set the integrator gate width (variable pg in PulseSPEL) to the length of the longest pulse in the sequence and adjust the acquisition trigger offset (variable d0 in PulseSPEL) such that the echo is centred within the acquisition gate.[A7] This maximizes the SNR of the DQC trace.

Step 18 Decide on the time step Δt on the DQC trace: On the one hand, the time step should be chosen small enough to allow for a sufficient resolution of the dipolar oscillations. On the other hand, setting the time step too small will unnecessarily increase the acquisition time without providing additional information. Depending on the oscillation period, time steps of Δt = 4 ns to 16 ns are most common; especially in the case of short interspin distances, the time step should not exceed 4 ns to resolve the steep initial decay. Note that for the reasons discussed at point 13, the increment d30 to be set in PulseSPEL equals Δt/2.

Step 19 Set the parameters d1, d2, d4, and d30 for the DQC run (Table A2). Calculate the number of points (NoP) to be recorded on the trace using eq. (A39):

$$NoP = \frac{d4}{d30} + 1 \tag{A39}$$

Set this value as the dimension of the abscissa for the "ESE DQ-EPR" experiment (dim2) in the PulseSPEL program.

Step 20 Select the "ESE DQ-EPR" experiment with the 64-step phase cycle from the dropdown list and press the "Run" button. The spectrometer will now perform the DQC experiment including the phase cycling and nuclear modulation averaging procedures. The approximate runtime can be calculated by

$$Runtime = h \cdot m \cdot n \cdot NoP \cdot PC \cdot SRT \tag{A40}$$

Herein, PC is the number of phase-cycling steps (64); the other variables are explained in Table A1. Note that the calculated runtime is to be understood as a lower limit of the acquisition time, as it does not include the overhead of the pulse programmer.[A11] Thus, the actual runtime can be longer than the value given by eq. (A40).

Step 21 When the DQC experiment has finished, save the data to the hard disk in the Bruker BES3T format (.DSC / .DTA-files).

Step 22 Convert the .DSC / .DTA-files into ASCII format (.dat) and mirror the DQC trace at the maximum, i.e. average the $+i^{th}$ and $-i^{th}$ data point next to the maximum. Data conversion and mirroring of the time trace can be done automatically in a single step using a Matlab script.[A12]

Step 23 Analyse the mirrored DQC trace. In the following, the analysis of DQC data using the DeerAnalysis [A13] toolbox for Matlab will be outlined.

I. Import DeerAnalysis into Matlab as described in the user manual of the program. Load the time trace into DeerAnalysis 2022 using ASCII as the input data format.

II. As the modulation depth of the time trace usually amounts to > 90%, the program will issue the message "Data decay to less than 2% of initial amplitude. Background correction switched off", i.e. background correction is by default disabled. Compared to other PDS techniques such as PELDOR or RIDME, the background contribution is considerably smaller in DQC as the phase cycle efficiently suppresses any signal which does not stem from the double quantum coherence pathway.[A14] In some cases, however, especially for higher spin concentrations, the intermolecular dipolar coupling becomes significant and the background of the trace cannot be neglected anymore. To still process those traces with DeerAnalysis, changes may be made in the program code to suppress the error message and thus allow background correction. For DeerAnalysis 2022, the following procedure proved to be successful: In the file "update_DA.m" within the DeerAnalysis folder, locate the code "if min(td_fit)<0.2". Replace 0.2 by 0.0 and restart DeerAnalysis; this enables background correction.

III. The background in the DQC experiment is not analytically known and depends on the profiles of the MW pulses and the EPR spectrum,[A15] i.e. assumptions on the background model have to be made. The most rigorous way of handling the DQC background is to record a DQC time trace on a singly TSL-labelled biomolecule and use this data as an experimental background.[A16] However, this approach is only feasible if non-covalent interactions between the monomeric biomolecules can be excluded. For details on how to use an experimental background, refer to the documentation of DeerAnalysis. Another option is to fit the background using a homogeneous n-dimensional model or polynomials in such a way that the background-corrected time trace is flat at long dipolar evolution times, i.e. the last quarter of the time trace.[A17] The quality of the background removal can be assessed by inspecting the Fourier transform of the time trace (i.e. the Pake pattern).

DeerNet, which transforms the time trace into a distance distribution using neural networks, should only be used with caution as it has not been trained with DQC traces. Thus, errors in the background fitting may occur.

IV. Use Tikhonov regularization to translate the dipolar trace into a distance distribution. With DQC traces, DeerAnalysis often yields well-shaped L-curves and choosing a regularization parameter in the corner of the L-curve is usually appropriate. Use the validation routine of DeerAnalysis to inspect the influence of the background correction on the distance distribution. Figure A7 illustrates the procedure of DQC data analysis.

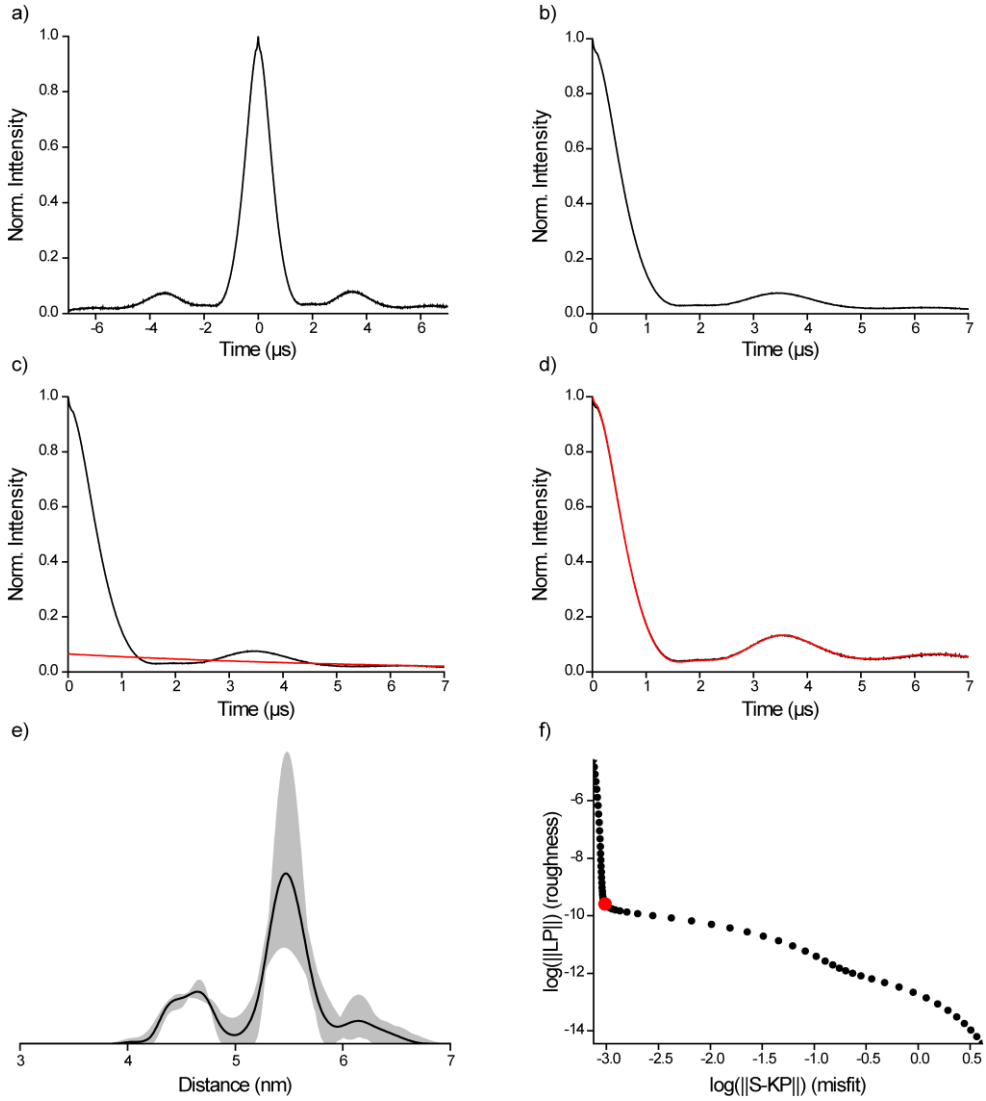

Figure A7: Analysis of DQC time traces. a) Normalized DQC time trace as obtained from the spectrometer. b) DQC time trace from (a), mirrored at the zero-time. c) DQC time trace from (b) with a background fit indicated in red. d) Background-corrected time trace obtained by dividing the time trace in (c) by the background fit in (c); the red line indicates a fit to the time trace from Tikhonov regularization. e) Distance distribution (black line) with the uncertainty analysis from the DeerAnalysis validation routine shown as a grey-shaded area. f) L-curve for setting the regularization parameter; the red dot marks the regularization parameter chosen in this example.

Step 24 Interpret the distance distribution using *in silico* spin labelling software like mtsslWizard,[A18,A19] MMM,[A20] or CREST/MD.[A21] Translate the results into a structural model of the biomolecule or answer a specific biochemical question in the framework of integrative structural biology.

7.4 References

[A1] G. Jeschke, H. W. Spiess, Distance Measurements in Solid-State NMR and EPR Spectroscopy in *Novel NMR and EPR Techniques* (Eds. J. Dolinšek, M. Vilfan, S. Žumer), Springer Berlin/Heidelberg, **2006**, pp. 21-63.

[A2] A. Schweiger, G. Jeschke, *Principles of Pulse Electron Paramagnetic Resonance*, Oxford University Press, Oxford/New York, **2001**.

[A3] S. J. Blundell, *Muon Spectroscopy*: *An Introduction*, Oxford University Press Inc., Oxford, **2022**.

[A4] K. Müller, M. Geppi, *Solid State NMR*: *Principles, Methods, and Applications*, Wiley-VCH, Weinheim, **2021**.

[A5] O. Schiemann, T. F. Prisner, *Q. Rev. Biophys.* **2007**, *40*, 1-53.

[A6] R. A. Wind, Solid-State NMR of Spin-1/2 Nuclei in *Modern NMR Techniques and their Application in Chemistry* (Eds. A. I. Popov, K. Hallenga), Marcel Dekker New York/Basel/Hongkong, **1991**, pp. 125-216.

[A7] G. Jeschke, Instrumentation and Experimental Setup in *ESR Spectroscopy in Membrane Biophysics* (Ed. M. A. Hemminga, L. J. Berliner), Springer New York, **2007**, pp. 17-47.

[A8] O. Schiemann, C. A. Heubach, D. Abdullin, K. Ackermann, M. Azarkh, E. G. Bagryanskaya, M. Drescher, B. Endeward, J. H. Freed, L. Galazzo et al., *J. Am. Chem. Soc.* **2021**, *143*, 17875-17890.

[A9] G. Jeschke, Y. Polyhach, *Phys. Chem. Chem. Phys.* **2007**, *9*, 1895-1910.

[A10] H. H. Haeri, P. Spindler, J. Plackmeyer, T. Prisner, *Phys. Chem. Chem. Phys.* **2016**, *18*, 29164-29169.

[A11] E. Reijerse, A. Savitsky, *eMagRes* **2017**, *6*, 187-206.

[A12] Tobias Hett, "DTA2dat", can be found under https://github.com/TobiasHett/DTA2dat, accessed 20.11.2022.

[A13] G. Jeschke, V. Chechik, P. Ionita, A. Godt, H. Zimmermann, J. Banham, C. R. Timmel, D. Hilger, H. Jung, *Appl. Magn. Reson.* **2006**, *30*, 473-498.

[A14] P. P. Borbat, J. H. Freed, *eMagRes* **2017**, *6*, 465-494.

[A15] G. Jeschke, *Annu. Rev. Phys. Chem.* **2012**, *63*, 419-446.

[A16] J. J. Jassoy, C. A. Heubach, T. Hett, F. Bernhard, F. R. Haege, G. Hagelueken, O. Schiemann, *Molecules* **2019**, *24*, 2735.

[A17] N. Fleck, C. A. Heubach, T. Hett, F. R. Haege, P. P. Bawol, H. Baltruschat, O. Schiemann, *Angew. Chem. Int. Ed.* **2020**, *59*, 9767-9772.

[A18] G. Hagelueken, D. Abdullin, O. Schiemann, *Methods Enzymol.* **2015**, *563*, 595-622.

[A19] G. Hagelueken, R. Ward, J. H. Naismith, O. Schiemann, *Appl. Magn. Reson.* **2012**, *42*, 377-391.

[A20] Y. Polyhach, E. Bordignon, G. Jeschke, *Phys. Chem. Chem. Phys.* **2011**, *13*, 2356-2366.

[A21] S. Spicher, D. Abdullin, S. Grimme, O. Schiemann, *Phys. Chem. Chem. Phys.* **2020**, *22*, 24282-24290.

7.5 Reproduction of Publications

[P1]: PELDOR Measurements on Nitroxide-Labeled Oligonucleotides

Reproduced with permission from

Tobias Hett, Olav Schiemann*, in: G. Steger, H. Rosenbach, I. Span, (eds) DNAzymes: Methods and Protocols, *Meth. Mol. Biol.* **2022**, *2439*, Humana New York, pp. 241-274.
DOI: https://doi.org/10.1007/978-1-0716-2047-2_16

* Corresponding author.

Published by Humana (New York, USA).

Contributions

- Compiling a workflow for setting up the PELDOR experiment and analysing PELDOR data.
- Writing the manuscript.

Chapter 16

PELDOR Measurements on Nitroxide-Labeled Oligonucleotides

Tobias Hett and Olav Schiemann

Abstract

In the past decades, pulsed dipolar electron paramagnetic resonance spectroscopy (PDS) has emerged as a powerful tool in biophysical chemistry to study the structure, dynamics, and function of biomolecules like oligonucleotides and proteins. Structural information is obtained from PDS methods in form of a distribution of distances between spin centers. Such spin centers can either be intrinsically present paramagnetic metal ions and organic radicals or may be attached to the biomolecule by means of site-directed spin labeling. The most common PDS experiment for probing interspin distances in the nanometer range is pulsed electron–electron double resonance (PELDOR or DEER). In the protocol presented here, we provide a step-by-step workflow on how to set up a PELDOR experiment on a commercially available pulsed EPR spectrometer, outline the data analysis, and highlight potential pitfalls. We suggest PELDOR measurements on nitroxide-labeled oligonucleotides to study the structure of either RNA-cleaving DNAzymes in complex with their RNA targets or modified DNAzymes with different functions and targets, in which deoxynucleotides are substituted by nitroxide-labeled nucleotides.

Key words Double electron–electron resonance (DEER), Electron paramagnetic resonance (EPR), Electron spin resonance (ESR), Pulsed electron–electron double resonance (PELDOR), Pulsed dipolar spectroscopy (PDS), Spin label

1 Introduction

Electron paramagnetic resonance (EPR) spectroscopy provides various methods for studying the structure and dynamics of biomolecules [1, 2]. In order to be applicable, EPR requires the presence of at least one unpaired electron in the biomolecule, for example, in the form of paramagnetic metal ions or cofactor radicals. If the biomolecule does not contain unpaired electrons, these may be introduced via site-directed spin labeling (SDSL) with stable organic radicals [3] like nitroxides [4] and trityls [5–8], or with paramagnetic metal ions like gadolinium(III) [9, 10] or copper(II)-based complexes [11, 12]. EPR-based hyperfine spectroscopy methods allow then to probe the surrounding up to about 8 Å

Gerhard Steger et al. (eds.), *DNAzymes: Methods and Protocols*,
Methods in Molecular Biology, vol. 2439, https://doi.org/10.1007/978-1-0716-2047-2_16,

around the electron spin center with atomic resolution [13]. Pulsed dipolar EPR spectroscopy (PDS) provides access to structures on the nanometer range by measuring the distance-dependent dipolar coupling between electron spin centers. The most frequently used PDS method is Pulsed Electron–electron Double Resonance (PELDOR or DEER) [14–16], which has been applied with Angstrom precision in the distance range of 1.5–16 nm [17].

There are several reviews on the theoretical principles, advantages, and limits of PDS spectroscopy in general [18] and PELDOR [16, 19, 20] in particular. Briefly, PELDOR is a pump-probe EPR experiment: In a coupled two-spin system (A–B), a refocused Hahn echo (RE) is recorded on spin A via the probe sequence $\pi/2$–τ_1–π–$(\tau_1 + \tau_2)$–π–τ_2–RE, which is applied at the probe-frequency ν_{probe} (Fig. 1a). Within the first interval τ_2, spin B is flipped by a π-pulse at the pump-frequency ν_{pump}. Moving the pump pulse within this interval τ_2 in incremental steps yields a modulated time trace, with the frequencies of this modulation encoding the dipolar electron–electron coupling between spins A and B. Usually, the recorded time trace is directly translated into a probability distribution of interspin distances by computational procedures as included in, for example, DeerAnalysis [21], GLADD/DD [22], or DeerLab [23] (Fig. 1b–e). The resulting distance distribution can be analyzed with respect to the most probable and mean distance, the distribution width, and the modality of the distribution. With the help of computational methods like, for example, mtsslWizard [24], MMM [25], or the GFN-FF based CREST/MD [26], these distributions can be translated into structural and dynamical information. PELDOR is thus complementary to other biophysical methods like nuclear magnetic resonance (NMR) spectroscopy [27, 28], X-ray crystallography [29, 30], Electron Microscopy (EM) [31, 32], and Förster resonance energy transfer (FRET) spectroscopy [33, 34]. Importantly, PELDOR has the following advantages:

1. It has no restriction with respect to the size of the biomolecule, the largest complex studied by PELDOR is the ribosome [35].
2. In the case of nitroxides, it requires biomolecular concentrations of ~20 μM, but concentrations down to ~45 nM have been measured with PDS [8].
3. It can be applied to the biomolecule free in solution [35–39], in membranes [40, 41], or in whole cells [5, 10].
4. Usually, the measurements are conducted on frozen solutions of the biomolecule, but measurements on immobilized samples at room temperature have been performed [42, 43].
5. The two spin labels do not need to be different, thus orthogonal labeling is obsolete.

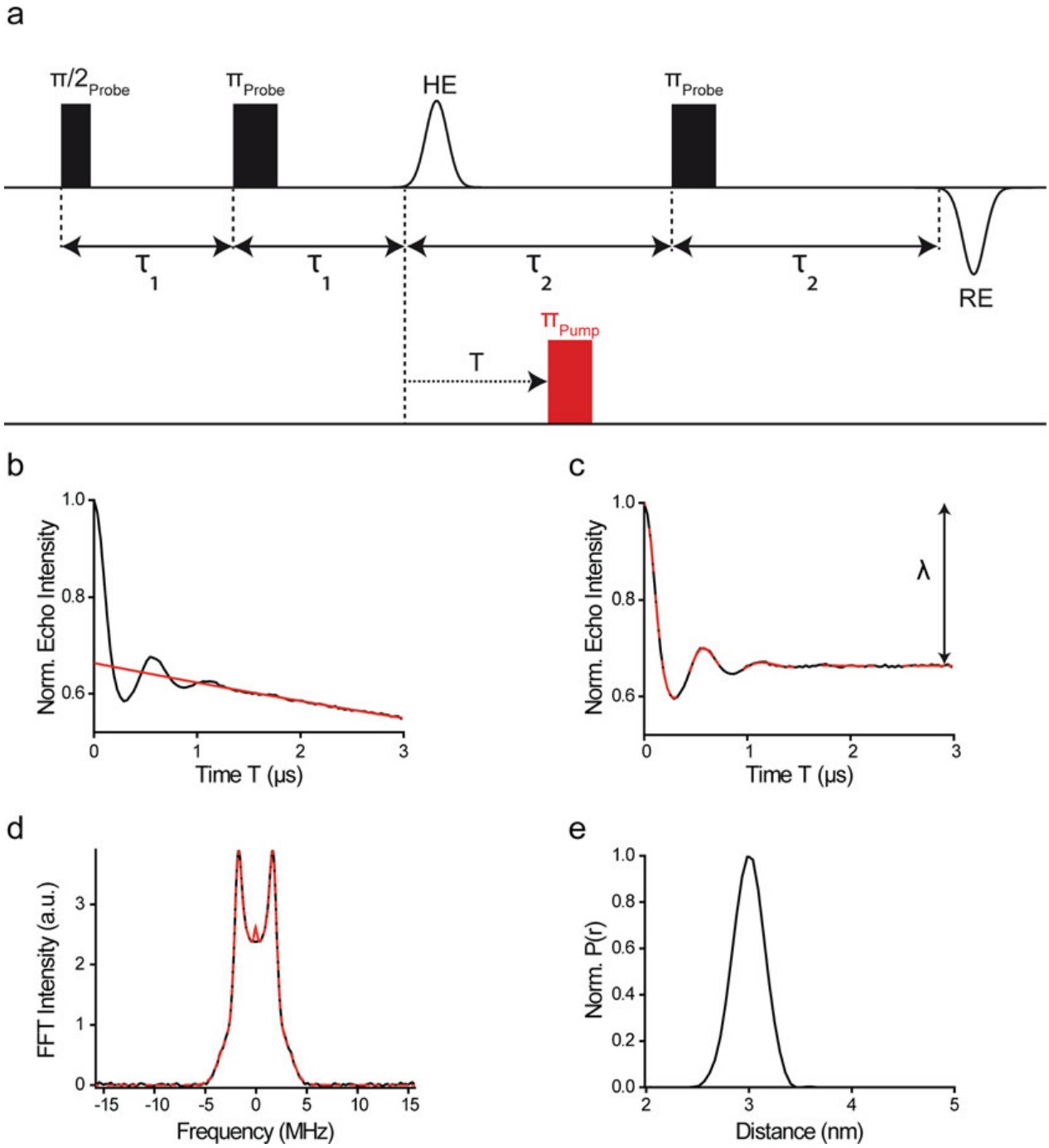

Fig. 1 The PELDOR experiment. (**a**) Pulse sequence of the PELDOR experiment. The probe sequence is shown in black, the pump pulse in red. HE abbreviates the Hahn echo, RE the refocused echo. In the PELDOR experiment, the position of the pump pulse is incremented within the interval τ_2, and the integrated intensity of the RE is plotted as a function of the dipolar evolution time *T*. (**b**) Original PELDOR time trace with a background fit indicated as a red line. (**c**) Background-corrected PELDOR time trace (form factor) with a fit indicated in red. The arrow denotes the modulation depth λ. (**d**) Fourier transformation of (**b**) yields the so-called Pake pattern. (**e**) Probability distribution of distances as obtained from transformation of the time trace (**c**)

6. The labels are small and have short linkers, thus making distance-to-structure translation easier and minimizing the impact of the label on the structure of the biomolecule.
7. The distance distributions are obtained without the need for a reference and with Angstrom precision [44].
8. Beyond distance distributions, PELDOR also yields angular information [45], can be used to count the monomers in multimers [46, 47], and allows spatiotemporal resolution in the Angstrom and microsecond range when coupled with fast freeze-quench techniques [48].

The protocol presented here guides the reader through the procedure of setting up a PELDOR experiment and highlights the key steps of data transformation from the primary time-domain signal into distance distributions. It focuses on Q-band PELDOR measurements on nitroxide-labeled RNA, for example to investigate RNA–DNAzyme complexes of RNA-cleaving DNAzymes or DNAzymes in which selected deoxynucleotides have been mutated to nitroxide-labeled ribonucleotides, as nitroxides are the most frequently used spin labels and Q-band (34 GHz) the most suitable frequency for a PELDOR experiment on nitroxide-bilabeled biomolecules. General guidelines on good practice regarding the set-up of the PELDOR experiment, the analysis of the time trace, and the interpretation of the distance distribution have also been defined in the white paper of the PELDOR/DEER community [49].

2 Materials

1. Biomolecule (1.6 nmol) spin-labeled with two nitroxide tags at a sufficiently high labeling efficiency (>80%), corresponding to 80 μL of a 20 μM solution of the biomolecule.
2. Deuterated ethylene glycol (EG-d_6) or deuterated glycerol (glycerol-d_8) as cryoprotectant, deuterated water (D_2O) as solvent.
3. Eppendorf pipette and elongated pipette tips to transfer the sample into the EPR tube.
4. Dewar vessels of different sizes and volumes to shock-freeze the prepared oligonucleotide samples in EPR tubes (for example with 40 mm inner width, 90 mm inner height; 57 mm inner width, 210 mm inner height).
5. 100 L Liquid helium tank.
6. Liquid nitrogen for freezing the sample and liquid helium for cooling the sample in the resonator.
7. Safety goggles and cold protection gloves.

8. EPR sample tubes made from clear fused quartz (CFQ) (Q-band, 3 mm outer diameter (o. d.), 159 mm length).
9. Light duty tissue wipers.
10. Pulsed EPR Spectrometer (e.g., ELEXSYS E580, Bruker, Rheinstetten, Germany) equipped with a Q-band bridge and a 150 W travelling wave tube amplifier (TWT, model 187 Ka from Applied Systems Engineering, Fort Worth, USA), an ER 5106QT–2 resonator (Bruker), and the corresponding accessory devices required for low-temperature operation, that is, a CF935 liquid Helium cryostat (Oxford Instruments, Abingdon, UK), an iTC503S temperature controller (Oxford Instruments), a helium transfer line (Oxford Instruments NanoScience, Abingdon, UK; model LLT600 or LLT650), a turbomolecular pump for evacuating the cryostat (e.g., from Pfeiffer Vacuum, Aßlar, Germany; HiCUBE 80 Eco), and a membrane pump (e.g., from KNF Neuberger GmbH, Freiburg, Germany; Type: PM26962-026.1.2) for maintaining a constant stream of cold helium gas.
11. Computer with MATLAB installed and the DeerAnalysis [21] toolbox imported into MATLAB. DeerAnalysis can be downloaded free of charge [50]. For DeerNet [51], installation of the Deep Learning Toolbox and the Signal Processing Toolbox for MATLAB are required.

The reader is advised to refer to the manual of the particular spectrometer, especially with regard to safety of the operator and the instrument. For clarity, references to control buttons and windows in the operating software are highlighted by quotation marks in the text.

3 Methods

3.1 Sample Preparation

Dissolve 1.6 nmol of spin-labeled RNA [52] in 64 µL D_2O and mix with 16 µL of EG-d_6 or glycerol-d_8 (*see* **Note 1**). Transfer the 80 µL into a 3 mm o.d. Q-band EPR tube using an Eppendorf pipette with an elongated pipette tip. Freeze the sample by immersing the EPR tube carefully into liquid nitrogen; after freezing, the sample height should be ~1 cm. Safety precaution: Whenever handling EPR tubes with samples frozen in liquid nitrogen, wear safety goggles (*see* **Note 2**).

3.2 Switching on the Spectrometer

Switch on the heat exchanger of the spectrometer and check the inward and return flow temperature. The former should be around 10–15 °C and the latter should not exceed 25–30 °C. If your spectrometer is equipped with a closed cooling circuit, make sure that there is enough cooling water in the system. Next, switch on

the spectrometer console, the magnet power supply, and the traveling-wave tube (TWT) amplifier. Keep the latter in **Standby** mode (**important!**). When the console has started up as indicated by a permanent green light of the status LED on the microwave (MW) bridge, connect the operating Xepr software to the spectrometer by selecting the "Connect to Spectrometer" option in the "Acquisition" menu bar. Before starting measurements, the spectrometer, especially the MW bridge, should have warmed up for at least 1 h to ensure sufficient stability of the electric components.

3.3 Cooling down the Cryostat and Inserting the Sample

Switch on the temperature controller of the cryostat and set the target temperature to 50 K. Connect the turbomolecular pump system with the cryostat and switch it on. Make sure that the cryostat has reached a pressure of ~10^{-4} mbar before proceeding with the following steps.

Connect the overflow valve of the liquid helium tank to the helium recovery system, if available, and make sure that the gas flow within the tubing is not blocked (e.g., due to bending). Ensure that the overflow valve is open so that no overpressure can build up in the tank. Open the needle valve on the helium transfer line and **slowly** (~ 2 min) insert the line into the helium tank, then fix it with a spanner. Check for gas flow by immersing the outlet of the transfer line into ethanol, wipe it, and connect the transfer line to the cryostat of the spectrometer. Connect the membrane pump with the transfer line. Close the cryostat with a stopper (Fig. 2a) or a sample rod to prevent condensation of air when cooling down. Open the needle valve at the transfer line approximately ¼ turn and switch on the membrane pump. It usually takes up to 20–30 min to cool the cryostat from room temperature to 50 K (*see* **Note 3**).

In the meantime, mount the EPR tube into the sample holder and screw the holder into the sample rod. The position of the sample holder is to be adjusted in such a way that the center of the frozen sample is 38 mm [53] below the lower end of the tube holder to ensure optimal positioning of the sample in the resonator (Fig. 2b). Quickly wipe the tube with a light duty tissue wiper to remove potential contaminants from the exterior of the tube. Before inserting the tube into the cryostat, ensure that the high power "Attenuation" is set to 60 dB and that the spectrometer is in the "Standby" mode.

When a temperature of approximately 50 K has been reached, stop the membrane pump and wait until the needle of the gas flow controller (Fig. 3) has dropped to zero. Remove the stopper from the cryostat, gently shake the sample rod to brush off liquid nitrogen, and quickly insert it into the cryostat. Do not keep the cryostat open unnecessarily long to prevent condensation of air in it (*see* **Note 4**). Give the sample and the cryostat at least 15 min to reach a thermal equilibrium before proceeding. If sample and cryostat are not in equilibrium, frequency and phase drifts might occur during the measurement.

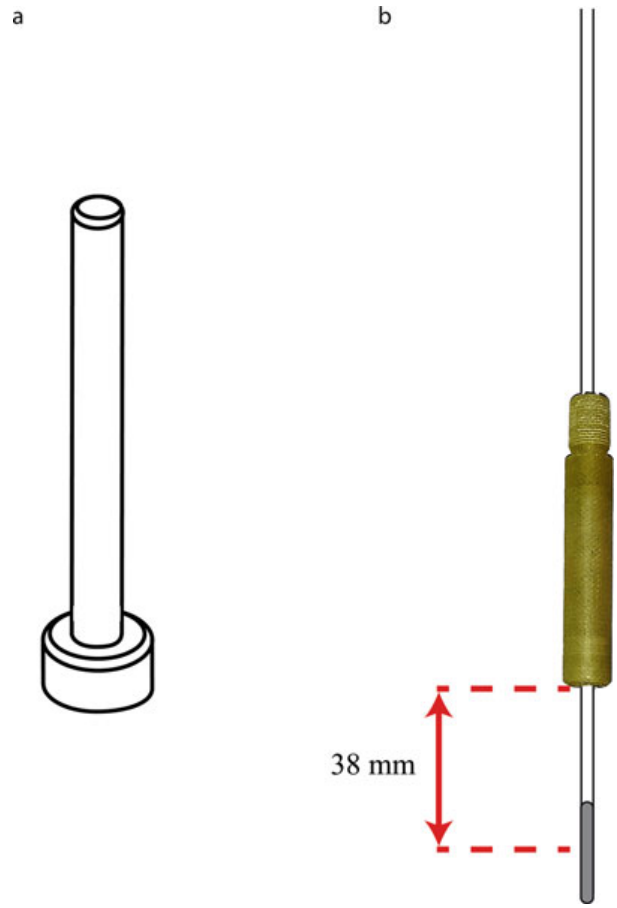

Fig. 2 Sample holder. (**a**) Stopper to close the cryostat and thus prevent condensation of air when cooling down. (**b**) Sample holder with an EPR tube mounted. The red arrows indicate the distance from the lower end of the holder to the center of the sample (38 mm)

Fig. 3 Gas flow controller

3.4 General Remarks on the Xepr Software

The following section describes the basic functions and windows of the Xepr software used for setting up pulsed EPR experiments. Screenshots of the respective program windows are shown in Figs. 4 and 5.

1. Viewport and main window (Fig. 4a, b): The toolbars in the main window permit calling various functions of the software (e.g., for saving and processing data, "Spectrometer Configuration") and opening further subwindows (e.g., "MW Bridge Tuning" panel, "FT EPR Parameters"). Figure 4b shows a close-up view of the most important icons used throughout the experiments. In the viewport, the recorded data and the current number of averages are displayed.
2. "FT Bridge" (Fig. 4c): Permits controlling parameters related to the MW Bridge (e.g., "CW Mode" and "Pulse Mode" in the "Bridge Configuration" tab, Fig. 4c-1), parameters regarding the detection system (e.g., "Video Gain," "Video Bandwidth," "Attenuation," "Signal Phase" in the "Receiver Unit" tab, Fig. 4c-2), and phase and amplitude settings of the Microwave Pulse Forming Unit (MPFU) channels ("MPFU Control" tab, Fig. 4c-3).
3. "SpecJet" (Fig. 4d) is a digital oscilloscope displaying the echo(es) generated by the pulse sequence currently executed from the Pulse Tables (see below). The real channel of the quadrature detection system is displayed in green, the imaginary channel in yellow.
4. "FT EPR Parameters" (Fig. 4e): Permits adjusting various spectroscopic variables, for example, the pulse sequence via the Pulse Tables ("Patterns" tab, Fig. 4e-1), the magnetic field (e.g., "Center Field" and "Sweep Width" in the "Field" tab, Fig. 4e-2), parameters regarding the MW bridge (e.g., "Attenuation," "Video Gain," "Current ELDOR Frequency," "ELDOR Attenuation" in the "Microwave" tab, Fig. 4e-3), and interfaces for data acquisition control (e.g., axis quantities and sizes, acquisition from the Pulse Tables and PulseSPEL in the "Acquisition" tab, Fig. 4e-4). It also includes a button for calling PulseSPEL (see below).
5. "Pulse Tables" (Fig. 4e-1): Option for manually programming pulse sequences by directly providing the pulse lengths, interpulse delays, and incrementation schemes. It is recommended for quickly setting up preliminary experiments, for example, the echo-detected field-swept EPR spectrum. The "Pulse Tables" are located in the "Patterns" tab in the "FT EPR Parameters" window (Fig. 4e-1). For experiments conducted using the Pulse Tables, *absolute* timing with respect to the beginning of the whole pulse sequence is used (*see* **Note 5**).

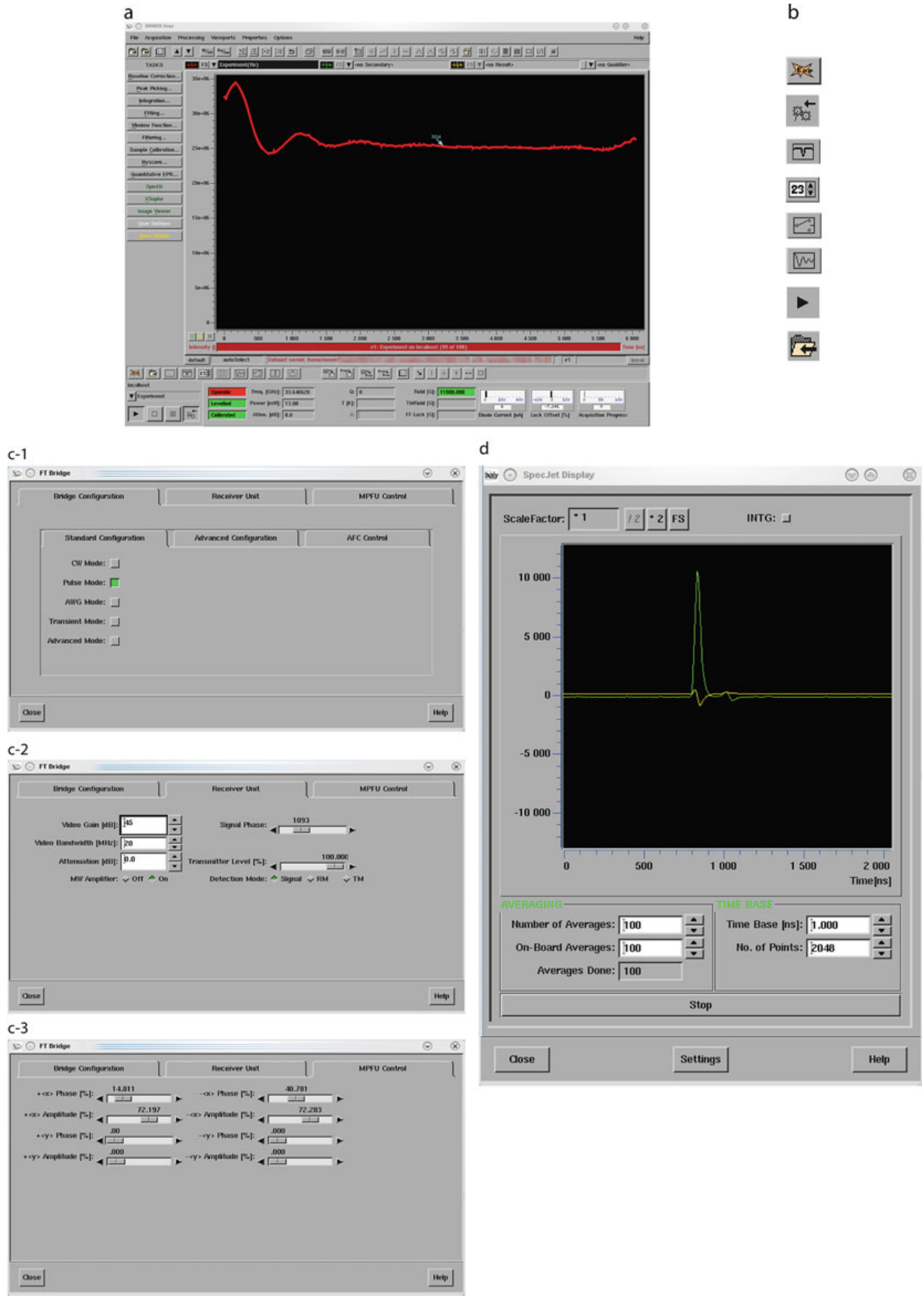

Fig. 4 Program windows of the Xepr software. (**a**) Main window with viewport. (**b**) Close-up view of relevant control buttons of the software (top to bottom): "Create new experiment," "Activate button," "MW Tuning Panel," "FT EPR Parameters," "FT Bridge," "SpecJet," "Run button," "Save Data to Disk." (**c**) FT Bridge and its subpanels (**c-1**) "Bridge Configuration," (**c-2**) "Receiver Unit," (**c-3**) "MPFU Control." (**d**) SpecJet. (**e**) FT EPR Parameters with its subpanels (**e-1**) "Patterns," (**e-2**) "Field," (**e-3**) "Microwave," (**e-4**) "Acquisition"

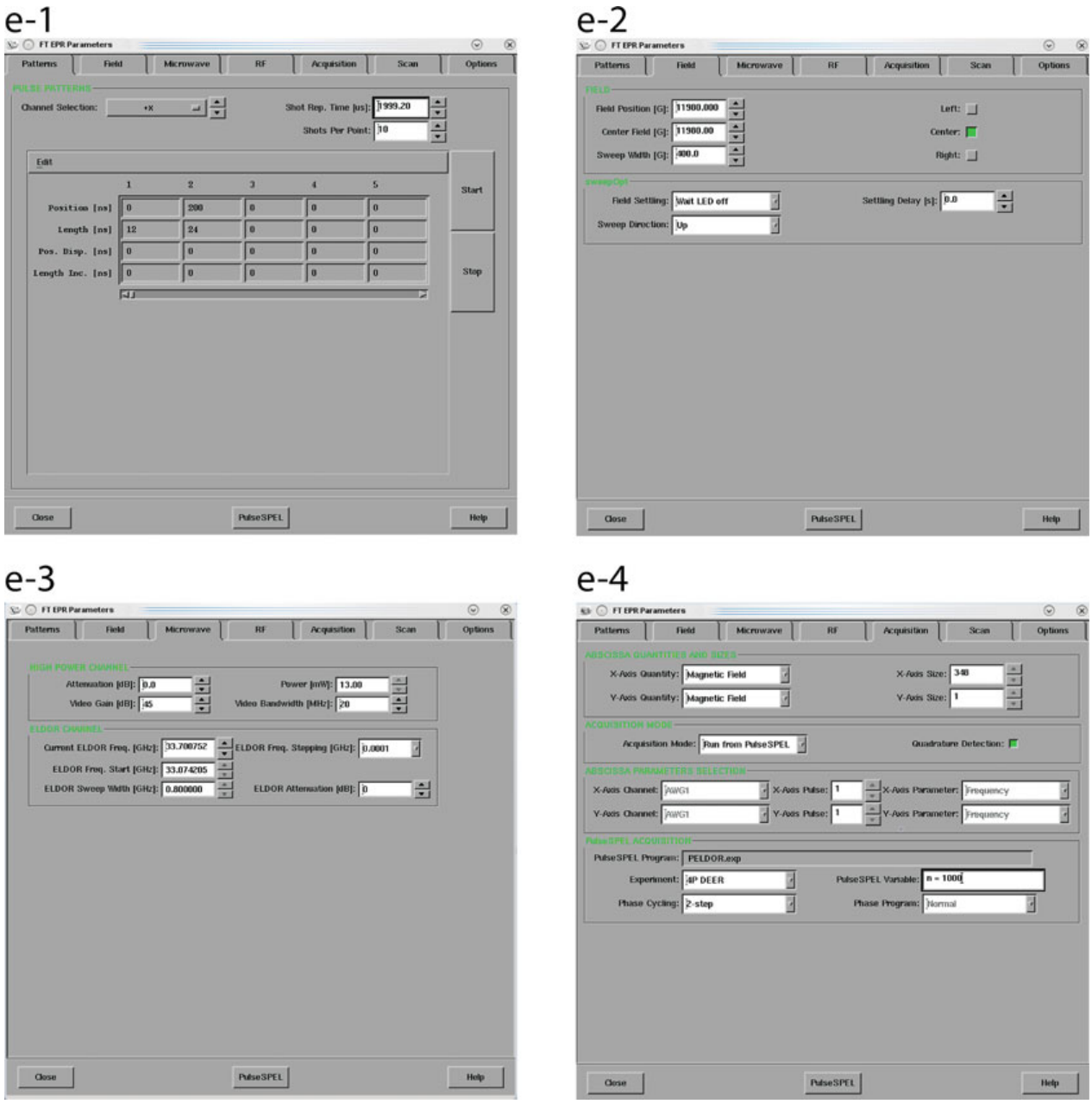

Fig. 4 (continued)

6. "PulseSPEL" (Bruker **Pulse SPE**ctroscopy **L**anguage) is a programming language for interacting with the spectrometer, which permits to easily set up also more sophisticated sequences with numerous pulses. By contrast to the pulse tables, it allows to implement phase cycling and modulation averaging procedures. PulseSPEL variables and programs have to be compiled and validated, respectively, by clicking the "Compile" and "Validate" buttons before execution. Afterward, the experiment can be started by clicking the "Run" button in the main window (Fig. 4b). Changes to PulseSPEL variables can be conveniently made using the variable box ("FT EPR Parameters"/"Acquisition," Fig. 4e-4) without explicitly

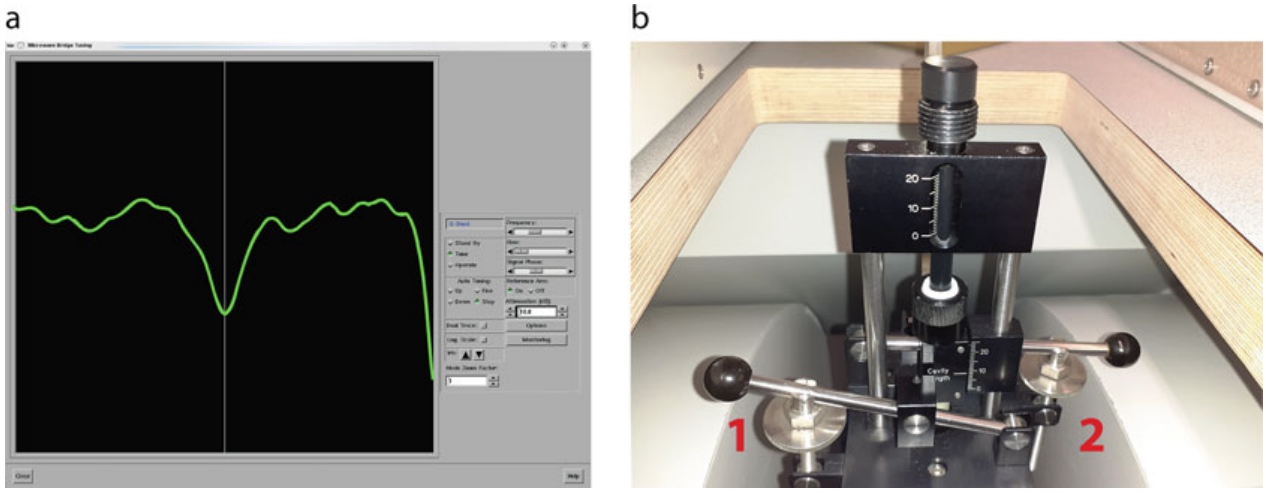

Fig. 5 (**a**) Screenshot of the MW bridge tuning panel. The dip in the center of the window corresponds to the "real" resonator dip, and the dip on the right is the "fake" dip. (**b**) Screws to adjust the resonator coupling (1) and the cavity length (2)

compiling them, partially even during the running experiment (e. g. number of scans n).

By contrast to the Pulse Tables, PulseSPEL uses *relative* timing of the pulse sequence and refers to the previous interpulse delay in the sequence. For a comparison of the timing in the Pulse Tables and PulseSPEL, refer to **Note 5**.

7. "MW Bridge Tuning" panel (Fig. 5a): Permits setting parameters related to the MW Bridge (e.g., MW frequency and phase) and to set the MW Bridge into "Standby," "Tune," and "Operate" mode.

3.5 Tuning the Spectrometer and Safety Check

Before running PELDOR experiments, the resonator has to be overcoupled such that its bandwidth is large enough to accommodate the pulses of both the pump and the probe frequency. The ER 5106QT-2 resonator used herein has two adjustment arms, one for the coupling and another one for the length of the cavity. By rotating the respective screw on the resonator (Fig. 5b), the cavity coupling (left screw, **1** in Fig. 5b) and the cavity length (right screw, **2** in Fig. 5b) can be altered. The resonance frequency of the ER 5106-QT2 is 34 GHz [53], and it can be fine-adjusted by the cavity length.

Open the "MW Bridge Tuning" panel. Go into the "Tune" mode, set the attenuation to 10 dB, and adjust the MW frequency to 33.7 GHz with the frequency slider. Next, adjust the cavity length (right screw, **2** in Fig. 5b) so that the resonator tuning dip becomes visible in the "MW Bridge Tuning" window (Fig. 5a). Note that there is a "real" and a "fake" dip for the ER 5106QT-2: The "fake" dip can be identified as it moves markedly when the cavity coupling (left screw, **1** in Fig. 5b) is changed, whereas the "real" dip stays in place. Adjust the cavity length so that the "real"

dip is centered and the "fake" dip on the right of the tuning window. This corresponds to the overcoupling condition (Fig. 5a). Usually, it is achieved at a cavity length of around 9 mm (*see* **Note 6**).

Create a new experiment by clicking the "Exp" button and choose the option "Pulse/Advanced." Click the "Activate" button and perform the safety check of the detection system as described in the instrument manual before switching the TWT into the Operate mode. Never (**!**) attempt to switch the TWT amplifier into the Operate mode without having observed the defense pulses, otherwise the detection system may get damaged. Never return into the "CW" mode without having switched the TWT to Standby. Make sure that the dead time set in the spectrometer configuration files is long enough so that no ringdown of the MW pulses occurs during signal detection. If in doubt, consult the instrument manual or your spectrometer administrator (*see* **Note 7**).

3.6 Preliminary Experiments

3.6.1 Standing Hahn Echo and Echo-Detected Field-Swept EPR Spectrum

Set the "Center Field" to a value corresponding to g ≈ 2.00 at the given MW frequency (e.g., ≈ 11,980 G at 33.7 GHz). Program the Hahn echo sequence ($\pi/2$–τ–π–τ–echo, Fig. 6) using the Pulse Tables: Choose the "+x" Channel in the "Channel Selection" menu, set a $\pi/2$-pulse of 12 ns length at the position 0 ns and a π-pulse of 24 ns length at the position 200 ns. (Fig. 4e-1). Confirm each entry in the Pulse Tables by pressing "enter" on the keyboard.

Next, select the "Acquisition Trigger" channel and adjust the acquisition trigger length to 4 ns at the position 0 ns. Set the "Integrator Time Base" to 1.0 ns, the number of "Shots Per Point" to 10 and the shot repetition time ("Shot Rep. Time") to 3000 μs, which is usually a good starting point for nitroxides at 50 K. Set the "Video Bandwidth" ("FT Bridge"\ "Receiver Unit") to 20 MHz. Next, click the "Start" buttons in the Pulse Tables window and in "SpecJet," and decrease the MW attenuation to observe the Hahn echo. The exact temporal position of the echo depends on the dead time of the spectrometer, refer to the manual of the particular instrument for details (*see* **Note 5**).

Find the attenuation at which the echo amplitude is maximized and adjust the video gain so that no clipping occurs; for this

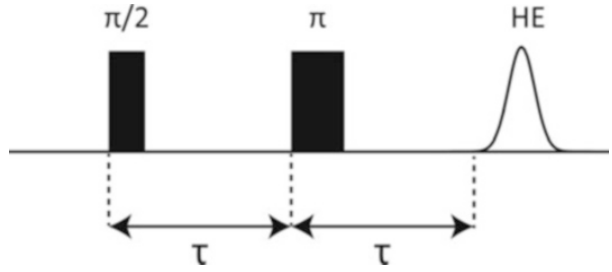

Fig. 6 Hahn echo (HE) pulse sequence. For the two-pulse ESEEM experiment, the interpulse delays τ are incremented and the HE amplitude is monitored

purpose, set "Number of Averages" = 1 in "SpecJet." At the microwave power level, which maximizes the echo amplitude, the applied pulses correspond to $\pi/2$ and π-pulses, which tilt the magnetization vector by 90° and 180°, respectively. If the echo amplitude does not go through a maximum when lowering the attenuation to 0 dB, increase the pulse lengths (e.g., $\pi/2 = 16$ ns, $\pi = 32$ ns; *see* **Note 8**). Adjust the "Signal Phase" to maximize the amplitude in the real signal channel and to bring it close to zero in the imaginary channel. Slight adjustments of the "Center Field" may be helpful in this step to fully bring the sample on resonance.

Next, record the echo-detected field-swept EPR spectrum, which is the integral of the Hahn echo plotted as a function of the magnetic field strength. In the Pulse Tables window, adjust the "Acquisition Trigger" position so that the echo starts on the left side of the "SpecJet" window and set the "Acquisition Trigger" length such that the whole echo is integrated (~120 ns). For the field-swept EPR experiment, integrating the whole echo is crucial to obtain a distortion-free spectrum and to maximize the spectral resolution [34]. Set the "Sweep Width" to 400 G and the number of points ("FT EPR Parameters"/ "Acquisition"/"X-Axis Size") to 800. Press the "Run" button in the main window to record the echo-detected field-swept EPR spectrum and save it to disk. Usually, a small number of scans (e.g., $n = 3$) is sufficient to obtain a good signal-to-noise ratio (SNR).

3.6.2 Two-Pulse Electron Spin Echo Envelope Modulation (ESEEM)

The Two-Pulse ESEEM experiment monitors the Hahn echo (Fig. 6) amplitude (y-quantity) as a function of the interpulse delay τ (x-quantity) and thus provides information on the transverse electron spin relaxation. Knowledge of this is relevant for choosing a proper value for the dipolar evolution time window in the PELDOR experiment. Note that the default PulseSPEL program for Two-Pulse ESEEM plots the Hahn echo amplitude as a function of τ; in the literature, however, the echo decay curves are occasionally shown as a function of 2τ.

Read off the magnetic field position at which the maximal signal intensity has been obtained in the field-swept spectrum and set the "Center Field" to this value. Open PulseSPEL ("FT EPR Parameters"\ "Acquisition"\ "PulseSPEL"). Load the PulseSPEL program "2p_ESEEM.exp" and the corresponding variable definitions "descrESEEM.def" located in the folder xeprFiles/PulseSPEL/sharedPulseSPEL/Standard/Spel2009/ESEEM (*see* **Note 9**).

After loading the experiment and the variable definitions file, click the buttons "Compile," "Show Program," "Validate," in the "PulseSPEL" window in the given order. Select "Run from PulseSPEL" ("FT EPR Parameters"/"Acquisition") and the experiment "2P ESE Setup." Click the "Run" button in the main window to record the Hahn echo. In the viewport, read off the time at which

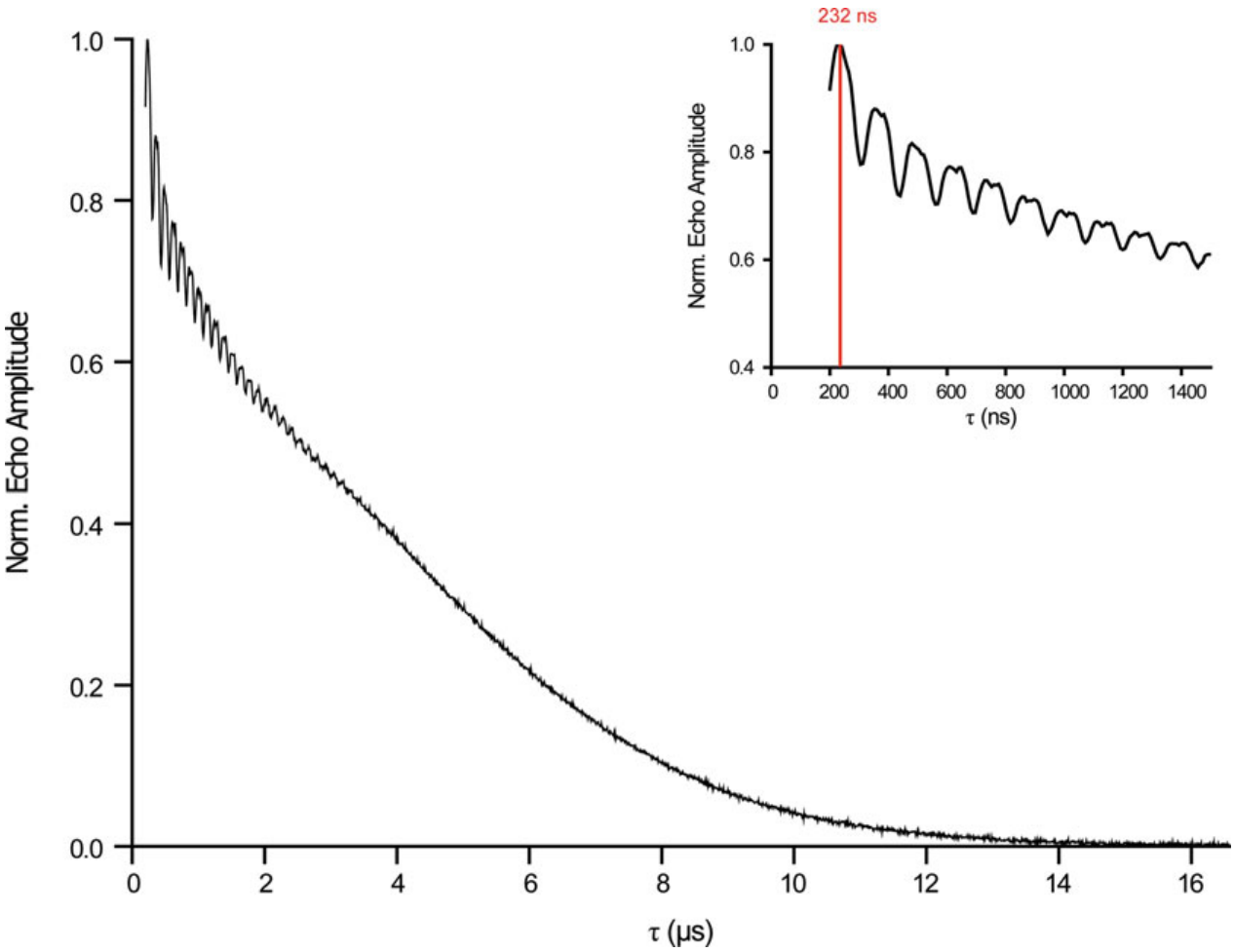

Fig. 7 Two-pulse electron spin echo envelope modulation (ESEEM) experiment. The Hahn echo amplitude is plotted as a function of the interpulse delay τ (Fig. 6). The inset shows a zoom-in on the first 1400 ns of the trace with the maximum at 232 ns indicated by a red line

the maximum of the echo occurs and set this value as the instrument-related acquisition delay parameter *d*0 in PulseSPEL (e.g., *d*0 = 432 ns, *see* **Notes 5** and **9**). Set the number of points for the Two-Pulse ESEEM program (dim2 in the PulseSPEL program) to 1024. Then, select the "2P ESEEM" experiment from the dropdown list with a two-step phase cycle and execute it by clicking "Run" in the main window. If the signal amplitude of the acquired Hahn echo decay curve does not reach the zero level, increase the number of points and/or the time increment *d*30 in the PulseSPEL program. In order to obtain a sufficient SNR, average multiple scans (e.g., $n = 3$) and save the trace to disk afterward (Fig. 7).

3.7 Setting up the PELDOR Experiment

As the PELDOR experiment requires phase cycling and nuclear modulation averaging to remove unwanted echoes and ESEEM, it is commonly run from a PulseSPEL program. Pulsed EPR spectrometers distributed by Bruker contain a default PulseSPEL program for the PELDOR experiment; however, many research groups

modified this program, developing their own syntax and conventions. Herein, we present the PELDOR setup using our modified version of the standard program; for reference, our PELDOR program can be found on GitHub [54].

3.7.1 Choice of Variables for the Hahn Echo

Load the PELDOR program and the corresponding variable definitions into PulseSPEL and click the "Compile," "Show Program," "Validate" buttons in the given order. For clarity, the variable definitions used in the PulseSPEL program are shown in Fig. 8.

For the $\pi/2$ and π-pulses of the probe sequence (variables *p*0 and *p*1 in the PulseSPEL program), set the pulse lengths which you identified as optimal for the Hahn echo.

The proper choice of the interpulse delay τ_1 (*d*1 in PulseSPEL) is governed by two aspects: (a) The loss of echo intensity due to transverse relaxation with increasing τ_1 and (b) the time interval the PELDOR trace is recorded prior to its maximum. In order to fulfil aspect (a), it would be desirable to set τ_1 as short as possible. However, for clear identification of the maximum in the PELDOR trace, which arises when the positions of the pump pulse and the Hahn echo coincide, the initial position of π_{pump} is set before the Hahn echo (Fig. 8). As the spectrometer has an instrument-based dead time delay (*d*3, 100 ns in this case) between the first π_{probe}-pulse and the pump pulse, τ_1 has a lower limit. In the literature, values of τ_1 ranging between 200 ns [55] and 400 ns [56] have been reported. As a guideline, τ_1 may be set to the value which yields the global maximum in the Two-Pulse ESEEM experiment, in this case 232 ns (Fig. 7).

3.7.2 Optimization of the Hahn Echo at the Pump Frequency

Set the MW attenuation to 0 dB, select the "2P ESE Setup" program (a PulseSPEL program for the Hahn echo), and press the "Run" button in the main window. Press "Start" in the Pulse Tables window, "Run" in "SpecJet," and open the "MPFU Control" tab in the "FT Bridge" window. Adjust the "+<x> Amplitude" such that the pulses correspond to $\pi/2$ and π, thus maximizing the Hahn echo observed in "SpecJet"; with a pulse length of $\pi/2 = 12$ ns, the channel amplitude slider bar should show a value of around 68%. Use the *global* "Signal Phase" shifter (e.g., in "FT Bridge"/"Receiver Unit") to adjust the MW phase such that the entire signal is detected in the real channel. The imaginary channel should be zero on average (Fig. 4d).

3.7.3 Inversion of the Hahn Echo

Select the "3P ELDOR Setup" experiment (Fig. 9). In this experiment, the inversion pulse π_{pump} (*p*2 in the PulseSPEL program) is applied before the Hahn echo sequence, thus inverting the echo amplitude. In "FT EPR Parameters"/"Microwave," set the "Current ELDOR Frequency," that is, the frequency of the pump pulse ν_{pump}, to the current MW frequency (~33.7 GHz). The pump frequency is later needed for computing the probe frequency, thus

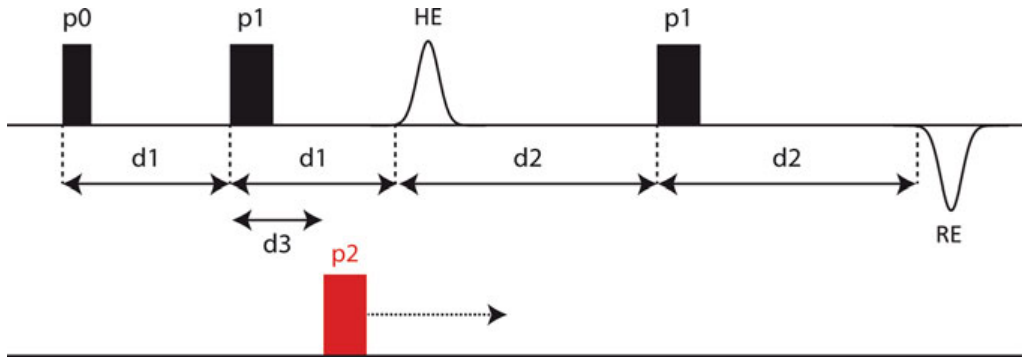

Fig. 8 Pulse sequence of the PELDOR experiment with the pulses and interpulse delays labeled according to the nomenclature in the "4P DEER" PulseSPEL program. HE abbreviates the Hahn echo, RE the refocused echo. The detection sequence is shown in black, the pump pulse in red. Note that the initial position of the pump pulse is set before the Hahn echo, which permits proper determination of the zero-time in the PELDOR trace. The following correlation between the PulseSPEL variable definitions shown here and the conventional variables applies: $d1 = \tau_1$; $d2 = \tau_2$; $d3$ = spectrometer dead time delay; $p0 = \pi/2_{probe}$; $p1 = \pi_{probe}$; $p2 = \pi_{pump}$

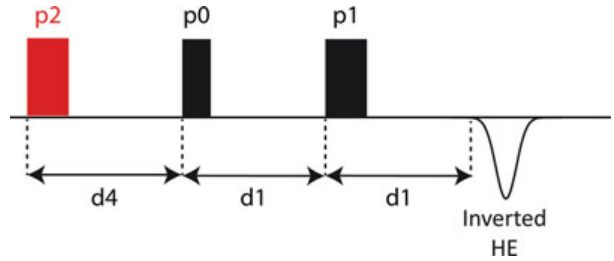

Fig. 9 Pulse sequence of the Three-Pulse ELDOR Setup experiment. In this experiment, all three pulses are applied at the pump frequency (33.7 GHz). For the Three-Pulse ELDOR Nutation experiment, the length of the pump pulse $p2$ is incremented and the amplitude of the inverted HE is monitored. The following correlation of the PulseSPEL variable definitions as shown in the figure and the conventional variables applies: $d1 = \tau$; $d4 = T$; $p0 = \pi/2_{probe}$; $p1 = \pi_{probe}$; $p2 = \pi_{pump}$

write it down. Press the "Run" button in the main window. Read off the time position of the echo maximum in the viewport, add it to the current value of $d0$ in PulseSPEL, and update $d0$ to this new value, for example, via the "PulseSPEL Variable" box in the "FT EPR Parameters"/"Acquisition" tab. Press "Run" again and check that the echo maximum is located on the left of the viewport. Start "SpecJet" and stepwise decrease the "ELDOR Attenuation" to 0 dB, which should lead to the inversion of the echo amplitude (*see* **Note 10**).

3.7.4 Optimization of the Pump Pulse Length

Press the "Stop" buttons in the Pulse Tables and in "SpecJet", select the "3P ELDOR Nutation" experiment from the dropdown menu, and press the "Run" button in the main window. In this experiment, the Hahn echo amplitude is recorded as a function of the pump pulse length π_{pump} (Fig. 9).

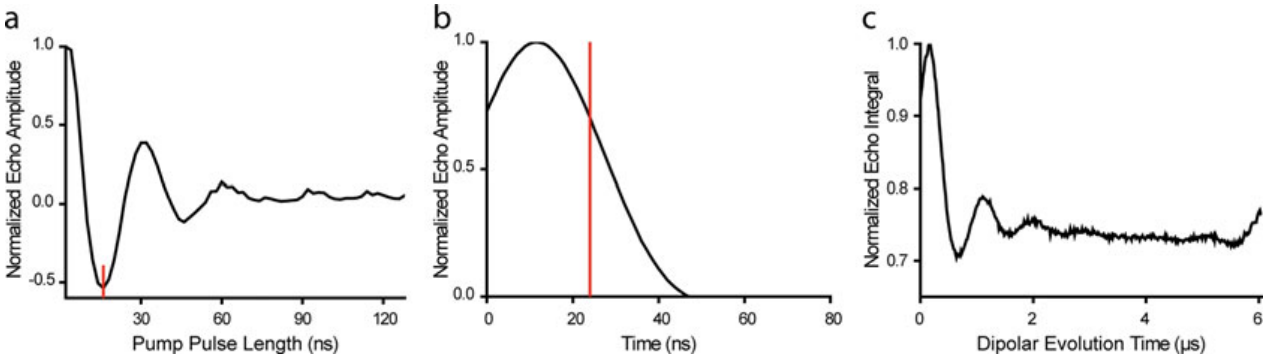

Fig. 10 Key steps in setting up the PELDOR experiment. (**a**) Transient nutation experiment ("3P ELDOR Nutation") to determine the optimal pump pulse length, 16 ns in this case as marked by the red bar. (**b**) Plot of the refocused echo ("4 P DEER Setup"); the acquisition delay offset *d*0 has been adjusted so that the maximal echo amplitude is located at 12 ns. The red bar indicates the integration gate with a length of 24 ns. (**c**) PELDOR time trace as obtained from the spectrometer prior to shifting of the zero-time and cutting of the pulse overlap artefact at the end of the trace

Read off the optimal pump pulse length which permits full inversion of the echo, that is, which yields the global minimum in the nutation trace (Fig. 10a), and set it as variable *p*2. Ideally, this value should be between ~12 ns and ~18 ns (*see* **Note 11**). If two pump pulse lengths lead to a comparable inversion of the echo (e.g., 16 ns and 14 ns), choose the shorter one, which is associated with a larger excitation bandwidth.

3.7.5 Changing the MW Frequency to the Probe Position and Safety Check

In the next step, change the MW frequency to the probe position: Set the "Attenuation" to 60 dB, the "ELDOR Attenuation" to 30 dB, and switch the TWT amplifier into the Standby mode. As the cathode voltage of the TWT has dropped to 0 V, switch the spectrometer into "CW" mode ("FT Bridge"). Change the MW frequency in the "MW Bridge Tuning" panel to the probe frequency, for example, 80 MHz lower than ν_{pump}, depending on the desired frequency offset $\Delta\nu$ (*see* Fig. 11 and **Note 12**).

Perform again the safety check of the detection system. If the defense pulses are present, switch the TWT into the Operate mode.

3.7.6 Optimization of the Hahn Echo at the Probe Frequency

In the next step, the Hahn echo will be optimized at the probe frequency. Set the "PulseSPEL" variable *d*0 = 360 ns, select the "2P ESE Setup" experiment with the phase cycle option "+<x> none", and press the "Run" button in the main window. Press "Start" in the Pulse Tables window, "Run" in "SpecJet," and decrease the attenuation stepwise to 0 dB. Adjust the video gain to prevent clipping. Then, adjust the "+<x> Amplitude" slider bar in the "MPFU Control" panel such that the echo in the real signal channel is maximized (~72% in the slider bar) and set the "+<x> Phase" such that the real part of the signal becomes maximally negative. Next, select the "–<x> none" phase cycle option and press "Run" again. Adjust the "–<x> Amplitude" slider bar such that the echo in

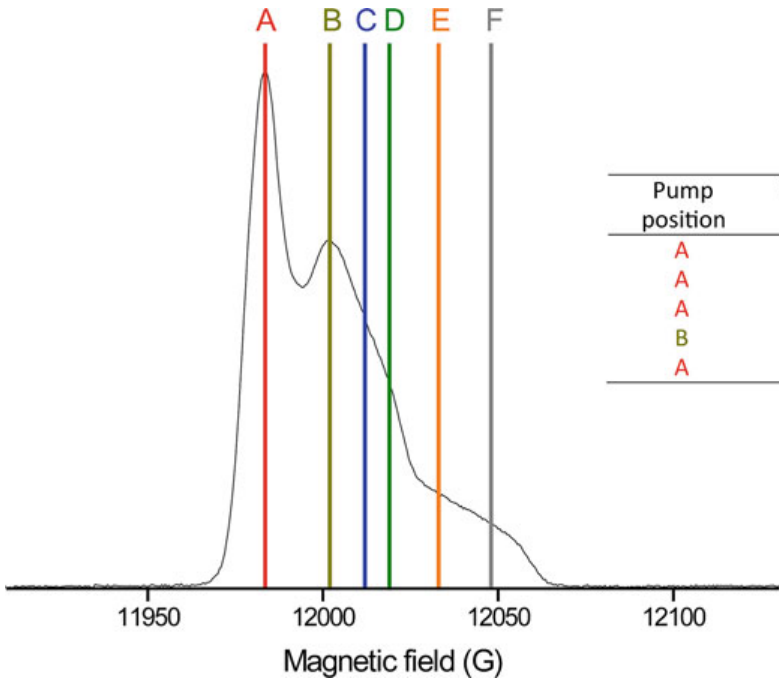

Pump position	Detection position	Δν (MHz)
A	B	60
A	C	80
A	D	100
B	E	120
A	F	180

Fig. 11 Echo-detected field-swept EPR spectrum with the positions of the pump pulse and the observer pulses indicated for different frequency offsets $\Delta\nu$

the real signal channel is maximized (~72% in the slider bar), and adjust the "−<x> Phase" slider bar such that the echo amplitude is maximally positive. For both phase cycling options, the imaginary signal channel should be zero on average. Finally, check that the echoes of the phase cycling options "+<x> none" and "−<x> none" have equal absolute amplitudes (*see* **Note 13**).

3.7.7 Choice of the Dipolar Evolution Window τ_2

Set the PulseSPEL variable *d2*, that is, the length of the dipolar evolution window τ_2 (Fig. 1a) of the PELDOR time trace, to a value appropriate for the specific case. Generally, longer dipolar evolution windows result in more reliable data and ease background fitting, but come at the expense of longer acquisition times. Thus, the dipolar evolution window should on the one hand not be shorter than at least 1.5 periods of the oscillation [26]. On the other hand, its upper limit is determined by the transverse electron spin relaxation, that is, the maximal length of *d2* is given by the time value at which the intensity has almost completely vanished in the Two-Pulse ESEEM experiment (e.g., ~11 μs in Fig. 7). If there is no prior knowledge on the expected interspin distance, start a PELDOR experiment with an intermediate length of the dipolar evolution window; a suitable value for *d2* may be determined in this case from the echo decay in the Two-Pulse ESEEM experiment. If you realize that a longer time window is needed for resolving at

least 1.5 oscillation periods, abort the experiment and change the PulseSPEL variable *d*2 accordingly.

3.7.8 Optimization of the Refocused Echo

Select the PulseSPEL program "4P DEER Setup," the phase cycling option "2-step", and press the "Run" button in the main window to execute the standing PELDOR experiment.

Press "Start" in the Pulse Tables tab, "Run" in "SpecJet", and set the "Number of Averages" to 1 in "SpecJet". Adjust the video gain such that no clipping of the refocused echo occurs; usually, a video gain between 36 dB and 48 dB is a good choice. Set the number of averages in "SpecJet" to a sufficiently high value to obtain a clear image of the refocused echo (100–1000 averages) and press "Run" in the main window. Read off the time value at which the maximum of the refocused echo occurs. Set the integration gate width (PulseSPEL variable pg) to the length of the longest pulse in the PELDOR sequence; this is most likely the π-pulse of the probe sequence (e.g., 24 ns). Adjust the acquisition trigger offset *d*0 such that the echo maximum is located at the center of the integration gate (e.g., at 12 ns, Fig. 10b). Adjusting the integration gate width to the length of the longest pulse in the sequence and centering the echo within the gate maximizes the SNR for PDS experiments [57].

3.7.9 Setting Parameters for Nuclear Modulation Averaging

Adjust the parameters for modulation averaging to suppress deuterium ESEEM in the PELDOR time trace. Averaging 8 steps (variable *m* in the PulseSPEL program) over one ESEEM oscillation period usually leads to an almost complete suppression of ESEEM in the PELDOR experiment. The time increment for modulation averaging (*d*31 in the PulseSPEL program) can be computed by $(1/\nu_{\mathrm{Larmor}})/\mathrm{m}$, where ν_{Larmor} is the Larmor frequency of ^{2}H at the given field. At Q-band, this results in $d31 = 16$ ns for $m = 8$ [35].

3.7.10 Setting the Time Resolution for the PELDOR Experiment

Decide on the temporal resolution of the PELDOR trace, that is, the time increment between two data points on the trace (PulseSPEL variable *d*30). As a rule of thumb, the shorter the period of the dipolar oscillation is, the shorter *d*30 should be to obtain a sufficiently high resolution. However, a too high resolution in combination with a long dipolar evolution time window (PulseSPEL variable *d*2) will result in excessively long acquisition times. For instance, the interspin distance of 1.5 nm corresponds to a dipolar frequency of ~15 MHz, that is, the oscillation period is ~66 ns; in this case, a time step of 4 ns is recommended, especially to resolve the fast initial decay in the time trace. A trace length of 1 μs would be enough to cover several oscillations.

At a distance of 3.5 nm, the dipolar coupling frequency is ~1.2 MHz and the oscillation period ~800 ns. Thus, a time step of 8 ns or 16 ns would be appropriate and the length of the time

trace should be ~3–4 μs, so that the intermolecular background can be fitted reasonably.

Next, compute the number of points ("dim5" in the PulseSPEL program) to be recorded on the PELDOR time trace, which is given by the equation

$$\mathrm{dim5} = \frac{d1 + d2 - 2 \times d3}{d30}$$

wherein $d1$, $d2$ = lengths of the interpulse delays τ_1 and τ_2 in the PELDOR sequence; $d3$ = dead time delay of the spectrometer (Fig. 8); $d30$ = time step of the PELDOR trace; all of these values can be found in the PulseSPEL program. Set the calculated value for *dim*5 in the PulseSPEL program. Select the "4P DEER" (Fig. 8) experiment and press the "Run" button. Click the "Re/Im" button in the main window to display the imaginary channel in the viewport, which should fluctuate around zero if the MW phase has been adjusted properly. If there is an appreciable amount of signal in the imaginary channel, adjust the "Signal Phase" in the "FT Bridge"/ "Receiver Unit" window, abort, and restart the "4P DEER" program.

Set the number of scans to a sufficiently high value (e.g., $n = 1000$, depending on the sample and your parameter settings) and let the measurement run. The SNR of the time trace will improve with the square root of the acquisition time; depending on the spin concentration and the time trace length, acquisition times of 4–24 h are common (*see* **Note 14**). After stopping the measurement, save the recorded trace to disk (*see* Fig. 10c, **Note 15**).

For remote monitoring of the current measurement status and for optionally saving intermediate states of the measurement, the MATLAB-application "ScanState.m" may be used, which is freely available [58]. The option to continuously save the traces is especially advantageous if software or hardware errors occur during the measurement, which may lead to deterioration of the data quality (temperature increase due to liquid helium shortage, frequency and phase drifts, TWT faults, software crash, etc.).

3.8 Removing the Sample

Drag all MPFU channel slider bars to zero ("MPFU Control"). Set the high power "Attenuation" to 60 dB, the "ELDOR Attenuation" to 30 dB, and switch the TWT into the Standby mode. Go into the "CW" mode ("FT Bridge"/"Bridge Configuration"), readjust the MW frequency to 33.7 GHz with the slider bar, and set the MW Bridge to "Standby" ("MW Bridge Tuning" panel). Switch off the membrane pump and wait until the needle of the gas flow controller has dropped to zero before removing the sample rod from the cryostat (*see* **Note 16**).

At this point, another measurement on a different sample can be started by following this protocol from Subheading 3.3.

Otherwise, the spectrometer should be switched off as described in Subheading 3.9.

3.9 Switching off the Spectrometer

First, switch off the TWT by pressing the On/Off-button. It will take a few minutes to cool down and turn off. Close all subwindows of the Xepr-software, but leave the main window open. Disconnect from the EPR spectrometer by clicking "Acquisition"\ "Disconnect from Spectrometer" and then close the main window. Switch off the magnet power supply, the console, and the heat exchanger in the given order. Close the needle valve of the helium transfer line.

3.10 Data Analysis

3.10.1 Data Formats and Data Conversion

The Xepr software saves the data in the Bruker BES3T® format generating .DSC and .DTA-files, with the former containing experiment-related acquisition parameters such as the code of a PulseSPEL program and the latter the spectral data in binary format. DTA-files can be conveniently converted into ASCII files (.dat) using the MATLAB-application "DTA2dat" [59], which is based on the eprload-function provided with the EasySpin package [60]. Optionally, exporting the data directly in the ASCII format is also possible in the Xepr software.

3.10.2 Analysis of PELDOR Data

For analyzing PELDOR time traces, various programs have been established, for example, LongDistances [61], DIPFIT [62], GLADD/DD [22], DeerAnalysis [21], and DeerLab [23]. The following section is dedicated to the analysis of PELDOR time traces by means of the MATLAB-based DeerAnalysis program, which can be downloaded free of charge [50].

Time traces saved in the BES3T® format can be directly imported into DeerAnalysis. Analysis of PELDOR traces is commonly subdivided into two steps: (a) the separation of intermolecular and intramolecular contributions to the time trace by fitting the background, and (b) the translation of the background-corrected time trace into a distance distribution. DeerAnalysis provides different computational approaches to fulfil this task, a selection of these is briefly discussed here.

1. Data preprocessing and background removal

   The first step in data analysis is to shift the time axis so that the maximum of the dipolar trace is at the zero time. Additionally, artefacts possibly occurring at the end of the trace due to overlapping of the refocusing pulse and the pump pulse should be cut off (Fig. 10c). Next, the intramolecular dipolar coupling has to be separated from the background, the latter resulting from intermolecular dipolar interactions. Usually, a good starting point is to assume a 3D-homogeneous background and to use the autooptimize function (**!**-button in the software) for the background start. The quality of the background correction can be judged by inspecting the Fourier transform of the

time domain data. The so-called Pake pattern should neither show a deep hole, nor a spike at the zero frequency [41].

2. Transformation of the time trace into the distance distribution

   DeerAnalysis provides different methods for solving the ill-posed problem of translating the background-corrected time trace, also called form factor, into a distance distribution. Approximate Pake Transformation (APT) is a comparatively fast approach and can provide an initial guess of the distance distribution [21]. Regularization techniques such as model-free Tikhonov regularization can be used to find a more stable solution to the ill-posed problem [21]. After computing the distance distribution, the influence of background correction should be examined by the validation tool in DeerAnalysis, which systematically varies the background correction parameters within given ranges, and statistically evaluates the resulting distance distributions. Uncertainty estimates will be shown as grey shaded areas. Apart from APT and Tikhonov regularization, parametrized models such as Gaussian distance distributions can be used to fit the time traces [21, 63]. This also permits to generate user-defined models.

   All of the approaches mentioned above require crucial input from the user, for example, regarding background correction or the choice of the regularization parameter α. In order to circumvent this user interference and potential biasing of distance distributions, data analysis can also be done by trained neural networks with the DeerNet [51] feature in DeerAnalysis. Within this option, user input is limited to setting the zero-time and the time trace cutoff; background correction and transformation of the form factor into a distance distribution is done by the program automatically. Note that DeerNet requires the Deep Learning Toolbox and the Signal Processing Toolbox to be installed and licensed in MATLAB.

3. Data interpretation

   The distance information extracted from the PELDOR data can be translated into structural models by means of in silico spin labeling software, for example, the mtsslWizard toolbox [24] for PyMOL, the MMM [25] program for MATLAB, and the GFN-FF based CREST/MD approach [26]. These programs calculate distance distributions based on the structure of the spin label and the structure of the biomolecule, where the latter can often be obtained from the protein data bank [64]. The error of these in silico methods is up to 3.5 Å for mtsslWizard [65], down to 2 Å for CREST/MD [26].

   As said above, distance distributions can be interpreted in terms of the most probable distance, the mean distance, and the modality. However, especially when it comes to the

modality and shoulders of the distribution, one should beware of overinterpretation. These features should only be interpreted if the underlying time trace is of high quality; if these features are interpreted, they must not vanish in the validation of the PELDOR data and further evidence should be gained from other biophysical methods that supports the interpretation [49]. When analyzing distance distributions, one should also keep in mind that shoulders or peaks may be associated either with different conformations of biomolecules or of the label. One should also consider possible changes of the structure and function of the biomolecule upon spin labeling. If there are biochemical assays which can be used to prove the proper function of the labeled biomolecule, these should be performed [49].

3.10.3 Data Quality and Reproducibility

The quality of PELDOR data can be judged in terms of the modulation depth λ (Fig. 1) and the SNR of the time trace. It thus serves as a control of the sample quality and the measurement set-up.

For a two-spin system, the modulation depth achievable in the Q-band with rectangular pulses and a 150 W TWT amplifier amounts to 30–35%. The modulation depth decreases if the sample contains simply labeled biomolecules, either due to a low labeling efficiency (<80%) or due to partial degradation of the spin label. Free label remaining in the sample can also affect the modulation depth adversely. In terms of setting up the PELDOR measurement, double-checking the chosen acquisition parameters can help to exclude technical pitfalls (*see* **Note 15**).

The SNR of a PELDOR time trace can be given as the modulation depth divided by the standard deviation of the noise in the trace. Separation of the dipolar signal and the noise is achieved by polynomial fitting. The SNR can be determined using, for example, the program SnrCalculator, which is freely available [66]. As a rule of thumb, meaningful data analysis is possible if the absolute SNR is >20, with good data having an SNR larger than 100.

In general, the SNR depends linearly on the spin concentration of the sample and on the square root of the measurement time. However, it should also be considered that the intermolecular background decay in the PELDOR trace correlates with the spin concentration, and background fitting can become difficult at high spin concentrations. Finally, it should be noted that it is good practice to repeat a PELDOR measurement on independent samples prepared in the same manner, for example, in triplicate, to verify the results.

4 Notes

1. Cryoprotectants and their influence on the biomolecule

   The cryoprotectant acts as a glass-forming agent and prevents clustering of the biomolecules [67]. Choose the cryoprotectant which has the least impact on the structure and function of the biomolecule, and keep in mind that some biomolecules can bind and interact with EG-d_6 or glycerol-d_8. In the literature, different amounts of cryoprotectant have been reported, ranging from ~20% v/v [68] up to 50% v/v [69]. The optimal ratio of the cryoprotectant and the biomolecule has to be determined experimentally for each case.

2. Freezing samples in the EPR tube

   Tubes may crack during shock-freezing or upon rapid warming of the frozen tube, and possibly condensed liquid nitrogen may evaporate. This can result in uncontrolled ejection of the sample and in rupture of the tube. When working with larger amounts of liquid nitrogen, wear cold protection gloves in addition to the safety goggles.

3. Problems in cooling down and reaching a stable temperature of 50 K.

   If the cryostat cannot be cooled down at all, check the following points in the given order: Is the filling level of the helium tank sufficient? Has all tubing been connected tightly and to the correct ports of the gas flow controller and the helium pump? Double-check the inscription of the respective ports. If existing, is the helium recovery port open? Is the transfer line permeable and not blocked, and is it tightly screwed into the cryostat?

   If the temperature does not stabilize at 50 K, make sure that the flow of cold helium gas amounts to ca. 1 L/h. If the flow is far off, it is difficult to reach a stable temperature. Also, ensure that the vacuum within the transfer line insulation is properly maintained and, if necessary, evacuate the transfer line overnight.

4. Sample insertion

   Avoid transferring drops of liquid nitrogen sticking to the sample rod by gently shaking it before insertion into the cryostat. In this context, it is convenient to use a *small* Dewar vessel (40 mm inner width, 90 mm inner height) so that the EPR tube and the lower part of the sample holder can be immersed into liquid nitrogen, but not the rod itself. Use a ring stand to prevent the sample rod from falling over.

5. Comparison of the Pulse Tables and PulseSPEL

   Timing of the pulse sequence differs between the Pulse Tables and PulseSPEL. Whereas the Pulse Tables use absolute

timing with respect to the beginning of the pulse sequence to define pulses, interpulse delays, and echo positions, PulseSPEL refers to the previous event in the sequence. This difference is exemplified by means of the Hahn echo sequence (12 ns–200 ns–24 ns–200 ns), and the timing is given for the Pulse Tables and PulseSPEL (Fig. 12).

Running the Hahn echo from the Pulse Tables (Fig. 12a, b), detection starts at the beginning of the sequence and the echo will occur at ~800 ns, reaching its maximum at 832 ns. As shown in Fig. 12a, the exact echo position depends on the instrument delay, which is ~400 ns in this case. For recording the echo-detected field-swept EPR spectrum, the acquisition trigger should thus be set to the position ~790 ns with a length of ~120 ns. Note: Even though the time axis starts with the first pulse, the pulses themselves are not recorded as the detector is "closed" to protect it from the high-power MW radiation.

If the Hahn echo sequence is run from PulseSPEL (Fig. 12c,d), detection starts at the end of the second interpulse delay τ. Thus, the offset between the origin of the time axis and the echo start is ~400 ns, corresponding to the instrument delay.

Pulse Tables and PulseSPEL have in common that the interpulse delays always start at the leading edge of a pulse [70].

6. It is difficult to achieve a stable tuning condition

   Unstable tuning can have several reasons. Check and try to address the following points:

   (a) The MW frequency is unstable. Possible reasons are as follows: (1) The MW Bridge was not warmed up long enough. Give the instrument a longer period of time to warm up before starting experiments, at least 1 h (2). The cooling water entering the MW Bridge is too warm, possibly due to chiller faults or insufficient cooling water in the system. Check the cooling water level and check if the cooling aggregate has turned off.

   (b) Sample and cryostat are not in the thermal equilibrium. Give the sample at least 15 min to reach and stabilize at the temperature of 50 K.

   (c) If the tuning dips start moving even without any changes being made to the spectrometer, this might indicate condensation of liquid nitrogen in the cryostat. That often comes along with an unusual tuning picture different from the one shown in Fig. 5a. Remove the sample as described in Subheading 3.8, warm up the spectrometer to at least 120 K for at least 20 min, and start from the beginning. If this does not help in resolving the problem,

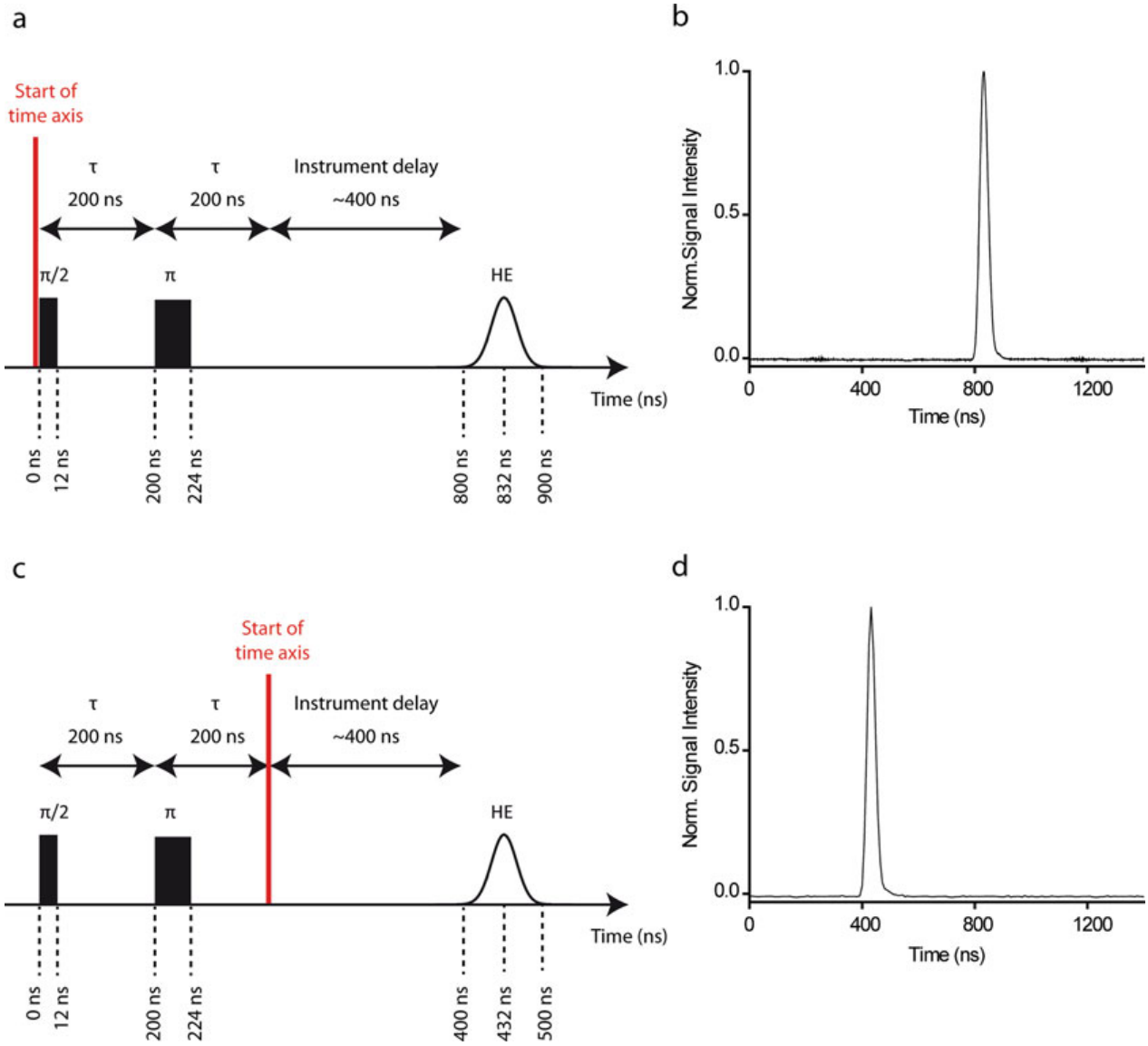

Fig. 12 Timing of pulse sequences exemplified by the Hahn echo. (**a**) *Absolute* timing with respect to the beginning of the pulse sequence as used by the pulse tables. The time axis starts at the beginning of the pulse sequence; in consideration of the instrument delay, the echo arises at ~800 ns. (**b**) Hahn echo recorded from the pulse tables. (**c**) *Relative* timing with respect to the end of the last interpulse delay of the pulse sequence as used by PulseSPEL. The time axis starts at the end of the last interpulse delay; in consideration of the instrument delay, the echo arises at ~400 ns. (**d**) Hahn echo recorded from PulseSPEL

warm up the spectrometer to room temperature and blow a stream of nitrogen gas through the resonator overnight.

7. Safety check

   As a warning reminder, never switch the TWT into the Operate mode if the defense pulses have not been displayed in "SpecJet" as this would damage the detection system. Try the following steps if you cannot see the defense pulses: Make sure that a valid pulse sequence is being executed from the Pulse Tables and that "SpecJet" is running with enough points being displayed. Make sure that the "Video Gain" has been set

to 45 dB and that the "MW Amplifier" button has been switched to "On" ("FT Bridge"/ "Receiver Unit"). Occasionally, even though the defense pulses actually are present, they cannot be seen due to the phase settings. Drag the shifter of the "Signal Phase" (e.g., in "FT Bridge"/"Receiver Unit") to change the phase settings a bit and see whether the defense pulses become visible. If you are still unsuccessful in checking the defense pulses, contact your spectrometer administrator as some basic settings in the software or hardware might be faulty.

8. Finding and optimizing the Hahn echo

   If no echo can be observed at all, firstly ensure that the pulse sequence has been programmed properly and check that "SpecJet" displays enough points to detect a signal up to the time where the echo is expected. This can vary depending on the individual dead time of the spectrometer (*see* **Note 5**). If necessary, increase the "Number of Points" in "SpecJet." Make sure that the TWT has been switched into the Operate mode. Double-check the combination of magnetic field position and MW frequency.

   Next, check proper tuning (Subheading 3.5) and proper sample positioning in the resonator. Refer to Subheading 3.8 for safe sample removal from the spectrometer. Make sure that the EPR tube has not been pushed into the sample rod during insertion. This may occur if the cavity is blocked by ice (frozen nitrogen or air moisture). In that case, warm up and completely defrost the spectrometer (*see* **Notes 4** and **6c**).

   If the resonator has been properly overcoupled, the maximal echo amplitude should be obtained at an attenuation of approximately 3–5 dB when using pulse lengths of $\pi/2 = 12$ ns and $\pi = 24$ ns. If the echo amplitude keeps growing when decreasing the attenuation <3 dB, go back to Subheading 3.5 and check the tuning. If the amplitude of the Hahn echo still cannot be maximized, the transmitted power is insufficient to achieve $\pi/2$ and π-pulses at the given pulse lengths. In this case, increase the pulse lengths (e.g., to $\pi/2 = 14$ ns and $\pi = 28$ ns or $\pi/2 = 16$ ns and $\pi = 32$ ns) and try again.

   If the echo shows a low signal-to-noise ratio and requires a rather high "Video Gain" setting, the spin concentration in the sample may not be sufficient. Perform a *cw*-EPR spin counting experiment; the spin concentration in the sample should amount to at least ~20 μM to obtain a decent signal.

9. Two-Pulse ESEEM

   Use the pulse lengths for $\pi/2$ and π which you identified as optimal for the standing Hahn echo. The following variable settings for the Two-Pulse ESEEM experiment should work if the Hahn echo has been optimized with pulse lengths of 12 ns and 24 ns for $\pi/2$ and π, respectively: $p0 = 12$ ns; $p1 = 24$ ns;

$d0 = 0$ ns (for setup) and $d0 = 432$ ns (for experiment); $d1 = 200$ ns; $d30 = 8$ ns; $h = 10$; $n = 1$.

Herein, $p0$ and $p1$ is the length of the $\pi/2$ and π-pulses, respectively; $d0$ is a constant instrument-related acquisition trigger delay; $d1$ is the interpulse delay denoted τ in the Hahn echo sequence (Fig. 6); $d30$ is the time step by which $d1$ is incremented; h is the number of shots per point; SRT is the shot repetition time, and n is the number of scans to accumulate.

10. Inversion of the Hahn echo

    If no inversion of the echo is observed, make sure that the "Current ELDOR Frequency" has been set to the correct value, that is, the current spectrometer frequency at which the pump pulse should be applied. Ensure that the pump pulse length (variable $p2$ in PulseSPEL) is between 12 and 18 ns. If the echo still does not invert upon reducing the "ELDOR Attenuation," a power loss in the ELDOR channel may have occurred. Contact your spectrometer administrator.

11. The nutation experiment reports a full inversion of the echo at pump pulse lengths >18 ns:

    (a) Make sure that the "ELDOR Attenuation" has been set to 0 dB.

    (b) Check proper tuning (*see* Subheading 3.5 and **Note 6**). Make sure that the resonator dip has been centered in the in the "MW Bridge Tuning" panel.

    (c) Unusually long pump pulse lengths may be indicative of liquid nitrogen condensation in the cryostat (*see* **Note 6c**).

12. Choice of the frequency offset $\Delta\nu$

    Generally, a smaller offset $\Delta\nu$ between the pump and observer frequency leads to a higher signal intensity and thus an improved SNR. However, choosing a too small $\Delta\nu$ ($\Delta\nu < 50$ MHz) will lead to overlapping excitation bandwidths of the probe and pump pulses and thus deteriorate the modulation depth. As a first attempt, use an offset of $\Delta\nu = 80$ MHz or 100 MHz.

    Regarding the choice of the frequency offset, it should be kept in mind that orientation selection can occur, especially when rigid spin labels are used [15, 71]. Orientation selection means that spins on resonance at a given combination of magnetic field and MW frequency correspond to a certain selected orientation. It implies that not all orientations of the distance vector with respect to the magnetic field direction are excited [72] and manifests itself in the oscillation periods of the time traces depending on the used frequency offset [73–75]. Orientation selection can be recognized best from the Fourier

transform (FFT) of the time traces which, in the presence of orientation selection, often lacks the parallel component of the Pake pattern [15]. It is good practice to check the presence of orientation selection by recording PELDOR traces at different frequency offsets (e.g., 60 MHz; 80 MHz; 100 MHz; 120 MHz; 180 MHz, Fig. 11). If orientation selection occurs, the PELDOR traces as such can no longer be analyzed individually. In order to minimize orientational selectivity, divide the signal intensity values of the traces by the respective number of scans and sum up all individual traces. The resulting time trace can then be processed by, for example, DeerAnalysis to obtain the distance distribution.

Apart from this method of analyzing orientation-selective PELDOR traces, there are programs such as PeldorFit [45] which can also extract angular information from the time trace in addition to the distance.

13. No echo is seen

    If no echo is seen at this stage of the experiment setup, check that the parameters set in PulseSPEL (interpulse delays *d*1 and *d*2; pulse lengths *p*0, *p*1, *p*2; acquisition trigger delay *d*0) are correct and ensure that enough points are shown in "SpecJet" to monitor the echo. Make sure not to mix up the units of the timing (e.g., *SRT* is given in μs; pulse lengths and delays are mostly given in ns in PulseSPEL; *d*2 in the PulseSPEL variable box is given in μs, however).

14. Acquisition time:

    In general, the approximate acquisition time for a given number of scans *n* can be determined by

$$\text{Acquisition time} = \text{dim5} \times \text{PC} \times m \times \text{SRT} \times h \times n$$

    Herein, dim5 = number of points on the trace as set in the PulseSPEL program; PC = number of phase cycling steps (usually 2 for PELDOR); *m* = number of modulation averaging steps (usually 8 for PELDOR); SRT = shot repetition time, *h* = number of shots per point, *n* = number of scans. Note, however, that the herein computed duration should be understood as a lower limit since overhead occurs due to reprogramming of the pulse programmer (called "PatternJet" in the Bruker instruments) during the pulse sequence [76]. Depending on the version of the PatternJet and especially for long experiments, deviations of up to several minutes between the predicted and the true acquisition time can occur.

15. The modulation depth of the PELDOR time trace and the SNR are lower than expected:

    (a) Double-check the attenuation (high power "Attenuation" and "ELDOR Attenuation" should have been set

to 0 dB), PulseSPEL variable settings (especially pump pulse length *p*2), amplitude and phase settings ("MPFU Control"), frequencies (probe and "Current ELDOR Frequency"), and the magnetic field position ("Center Field").

(b) It is possible that the MW Bridge was not sufficiently warmed up and/or the sample and cryostat were not in the thermal equilibrium before starting the experiment. Concomitant phase and frequency drifts might have led to deterioration of the data quality.

(c) The sample was not optimally prepared and contains, for example, simply labeled biomolecules or free spin label. Verify proper spin labeling by a *cw*-EPR spin counting experiment.

16. The sample cannot be removed from the cryostat

It may occur that the sample tube freezes and gets stuck in the cryostat, especially after opening and closing the cryostat many times when changing the sample, as this will inevitably lead to condensation of air. If the sample rod cannot be removed at all from the spectrometer, warm up the cryostat to a temperature above 77 K and try again to remove the rod. If only the EPR tube has got stuck in the cryostat, carefully reinsert the sample rod and warm up the cryostat to a temperature above 77 K. Then, try again to remove the tube. If this does not help, warm up the spectrometer to room temperature. However, keep in mind that the tube may burst when warming up and would thus contaminate the resonator. In this case, careful cleaning as described in the spectrometer manual is mandatory.

In order to prevent sample tubes from getting stuck in the cryostat, try to avoid transferring drops of liquid nitrogen into it by using a small Dewar vessel as described in **Note 4**. Also, minimize the time the resonator is opened to prevent condensation of air.

References

1. Goldfarb D, Stoll S (eds) (2018) EPR spectroscopy: fundamentals and methods. eMagRes books. Wiley, Chichester, West Sussex
2. Schweiger A, Jeschke G (2001) Principles of pulse electron paramagnetic resonance. Oxford University Press, Oxford
3. Timmel CR, Harmer JR (2013) Structural information from spin-labels and intrinsic paramagnetic centres in the biosciences. In: Structure and bonding, vol 152. Springer, Berlin
4. Marsh D (2020) Spin-label electron paramagnetic resonance spectroscopy. CRC Press, Taylor & Francis Group, Boca Raton
5. Fleck N, Heubach CA, Hett T et al (2020) SLIM: a short-linked, highly redox-stable trityl label for high-sensitivity in-cell EPR distance measurements. Angew Chem Int Ed Engl 59(24):9767–9772. https://doi.org/10.1002/anie.202004452
6. Jassoy JJ, Heubach CA, Hett T et al (2019) Site selective and efficient spin labeling of proteins with a maleimide-functionalized trityl radical

for pulsed dipolar EPR spectroscopy. Molecules 24(15):2735. https://doi.org/10.3390/molecules24152735

7. Yang Y, Pan B-B, Tan X et al (2020) In-cell trityl-trityl distance measurements on proteins. J Phys Chem Lett 11(3):1141–1147. https://doi.org/10.1021/acs.jpclett.9b03208
8. Fleck N, Heubach C, Hett T, Spicher S, Grimme S, Schiemann O (2021) Ox-SLIM: synthesis of and site-specific labelling with ahighly hydrophilic trityl spin label. Chem Eur J 27(16):5292-5297. https://doi.org/10.1002/chem.202100013
9. Qi M, Gross A, Jeschke G et al (2014) Gd(III)-PyMTA label is suitable for in-cell EPR. J Am Chem Soc 136(43):15366–15378. https://doi.org/10.1021/ja508274d
10. Yang Y, Yang F, Gong Y-J et al (2018) High sensitivity in-cell EPR distance measurements on proteins using an optimized Gd(III) spin label. J Phys Chem Lett 9(20):6119–6123. https://doi.org/10.1021/acs.jpclett.8b02663
11. Singewald K, Bogetti X, Sinha K et al (2020) Double histidine based EPR measurements at physiological temperatures permit site-specific elucidation of hidden dynamics in enzymes. Angew Chem Int Ed Engl 59(51):23040–23044. https://doi.org/10.1002/anie.202009982
12. Cunningham TF, Putterman MR, Desai A et al (2015) The double-histidine Cu^{2+}-binding motif: a highly rigid, site-specific spin probe for electron spin resonance distance measurements. Angew Chem Int Ed Engl 54(21):6330–6334. https://doi.org/10.1002/anie.201501968
13. Sahu ID, McCarrick RM, Lorigan GA (2013) Use of electron paramagnetic resonance to solve biochemical problems. Biochemistry 52(35):5967–5984. https://doi.org/10.1021/bi400834a
14. Milov AD, Salikhov KM, Schirov MD (1981) Application of ELDOR in electron-spin echo for paramagnetic center space distribution in solids. Fiz Tverd Tela 23:975–982
15. Pannier M, Veit S, Godt A et al (2000) Dead-time free measurement of dipole-dipole interactions between electron spins. J Magn Reson 142(2):331–340. https://doi.org/10.1006/jmre.1999.1944
16. Jeschke G (2012) DEER distance measurements on proteins. Annu Rev Phys Chem 63:419–446. https://doi.org/10.1146/annurev-physchem-032511-143716
17. Schmidt T, Wälti MA, Baber JL et al (2016) Long distance measurements up to 160 Å in the GroEL Tetradecamer using Q-band DEER EPR spectroscopy. Angew Chem Int Ed Engl 55(51):15905–15909. https://doi.org/10.1002/anie.201609617
18. Schiemann O, Prisner TF (2007) Long-range distance determinations in biomacromolecules by EPR spectroscopy. Q Rev Biophys 40(1):1–53. https://doi.org/10.1017/S003358350700460X
19. Reginsson GW, Schiemann O (2011) Pulsed electron-electron double resonance: beyond nanometre distance measurements on biomacromolecules. Biochem J 434(3):353–363. https://doi.org/10.1042/BJ20101871
20. Borbat PP, Freed JH (2013) Pulse dipolar electron spin resonance: distance measurements. In: Timmel CR, Harmer JR (eds) Structural information from spin-labels and intrinsic paramagnetic centres in the biosciences, vol 152. Springer, Berlin, pp 1–82
21. Jeschke G, Chechik V, Ionita P et al (2006) DeerAnalysis2006—a comprehensive software package for analyzing pulsed ELDOR data. Appl Magn Reson 30(3–4):473–498. https://doi.org/10.1007/BF03166213
22. Brandon S, Beth AH, Hustedt EJ (2012) The global analysis of DEER data. J Magn Reson 218:93–104. https://doi.org/10.1016/j.jmr.2012.03.006
23. Fábregas Ibáñez L, Jeschke G, Stoll S (2020) DeerLab: a comprehensive software package for analyzing dipolar electron paramagnetic resonance spectroscopy data. Magn Reson 1(2):209–224. https://doi.org/10.5194/mr-1-209-2020
24. Hagelueken G, Abdullin D, Schiemann O (2015) mtsslSuite: probing biomolecular conformation by spin-labeling studies. Methods Enzymol 563:595–622. https://doi.org/10.1016/bs.mie.2015.06.006
25. Polyhach Y, Bordignon E, Jeschke G (2011) Rotamer libraries of spin labelled cysteines for protein studies. Phys Chem Chem Phys 13(6):2356–2366. https://doi.org/10.1039/C0CP01865A
26. Spicher S, Abdullin D, Grimme S et al (2020) Modeling of spin-spin distance distributions for nitroxide labeled biomacromolecules. Phys Chem Chem Phys 22(42):24282–24290. https://doi.org/10.1039/D0CP04920D
27. Reckel S, Gottstein D, Stehle J et al (2011) Solution NMR structure of Proteorhodopsin. Angew Chem 123(50):12148–12152. https://doi.org/10.1002/ange.201105648
28. Fürtig B, Richter C, Wöhnert J et al (2003) NMR spectroscopy of RNA. Chembiochem

4(10):936–962. https://doi.org/10.1002/cbic.200300700
29. Westhof E (2015) Twenty years of RNA crystallography. RNA 21(4):486–487. https://doi.org/10.1261/rna.049726.115
30. Cate JH, Doudna JA (2000) Solving large RNA structures by X-ray crystallography. Methods Enzymol 317:169–180. https://doi.org/10.1016/s0076-6879(00)17014-4
31. Khatter H, Myasnikov AG, Natchiar SK et al (2015) Structure of the human 80S ribosome. Nature 520(7549):640–645. https://doi.org/10.1038/nature14427
32. Wrapp D, Wang N, Corbett KS et al (2020) Cryo-EM structure of the 2019-nCoV spike in the prefusion conformation. Science 367(6483):1260–1263. https://doi.org/10.1126/science.abb2507
33. Stephenson JD, Kenyon JC, Symmons MF et al (2016) Characterizing 3D RNA structure by single molecule FRET. Methods 103:57–67. https://doi.org/10.1016/j.ymeth.2016.02.004
34. Lakowicz JR (2006) Principles of fluorescence spectroscopy, 3rd edn. Springer, New York, NY
35. Malygin AA, Krumkacheva OA, Graifer DM et al (2019) Exploring the interactions of short RNAs with the human 40S ribosomal subunit near the mRNA entry site by EPR spectroscopy. Nucleic Acids Res 47(22):11850–11860. https://doi.org/10.1093/nar/gkz1039
36. Pliotas C, Ward R, Branigan E et al (2012) Conformational state of the MscS mechanosensitive channel in solution revealed by pulsed electron-electron double resonance (PELDOR) spectroscopy. Proc Natl Acad Sci U S A 109(40):E2675–E2682. https://doi.org/10.1073/pnas.1202286109
37. Constantinescu-Aruxandei D, Petrovic-Stojanovska B, Schiemann O et al (2016) Taking a molecular motor for a spin: helicase mechanism studied by spin labeling and PELDOR. Nucleic Acids Res 44(2):954–968. https://doi.org/10.1093/nar/gkv1373
38. Duss O, Michel E, Yulikov M et al (2014) Structural basis of the non-coding RNA RsmZ acting as a protein sponge. Nature 509(7502):588–592. https://doi.org/10.1038/nature13271
39. Duss O, Yulikov M, Jeschke G et al (2014) EPR-aided approach for solution structure determination of large RNAs or protein-RNA complexes. Nat Commun 5:3669. https://doi.org/10.1038/ncomms4669
40. Ward R, Pliotas C, Branigan E et al (2014) Probing the structure of the mechanosensitive channel of small conductance in lipid bilayers with pulsed electron-electron double resonance. Biophys J 106(4):834–842. https://doi.org/10.1016/j.bpj.2014.01.008
41. Joseph B, Tormyshev VM, Rogozhnikova OY et al (2016) Selective high-resolution detection of membrane protein-ligand interaction in native membranes using trityl-nitroxide PELDOR. Angew Chem Int Ed Engl 55(38):11538–11542. https://doi.org/10.1002/anie.201606335
42. Meyer V, Swanson MA, Clouston LJ et al (2015) Room-temperature distance measurements of immobilized spin-labeled protein by DEER/PELDOR. Biophys J 108(5):1213–1219. https://doi.org/10.1016/j.bpj.2015.01.015
43. Gränz M, Erlenbach N, Spindler P et al (2018) Dynamics of nucleic acids at room temperature revealed by pulsed EPR spectroscopy. Angew Chem Int Ed Engl 57(33):10540–10543. https://doi.org/10.1002/anie.201803682
44. Stelzl LS, Erlenbach N, Heinz M et al (2017) Resolving the conformational dynamics of DNA with Ångstrom resolution by pulsed electron-electron double resonance and molecular dynamics. J Am Chem Soc 139(34):11674–11677. https://doi.org/10.1021/jacs.7b05363
45. Abdullin D, Hagelueken G, Hunter RI et al (2015) Geometric model-based fitting algorithm for orientation-selective PELDOR data. Mol Phys 113(6):544–560. https://doi.org/10.1080/00268976.2014.960494
46. Hagelueken G, Ingledew WJ, Huang H et al (2009) PELDOR spectroscopy distance fingerprinting of the octameric outer-membrane protein Wza from Escherichia coli. Angew Chem Int Ed Engl 48(16):2904–2906. https://doi.org/10.1002/anie.200805758
47. Valera S, Ackermann K, Pliotas C et al (2016) Accurate extraction of nanometer distances in multimers by pulse EPR. Chemistry 22(14):4700–4703. https://doi.org/10.1002/chem.201505143
48. Hett T, Zbik T, Mukherjee S, Matsuoka H, Bönigk W, Klose D, Rouillon C, Brenner N, Peuker S, Klement R, Steinhoff H-J, Grubmüller H, Seifert R, Schiemann O, Kaupp UB (2021) Spatiotemporal resolution of conformational changes in biomolecules by combining pulsed electron–electron double resonance spectroscopy with microsecond freeze-hyperquenching.. J Am Chem Soc 143(18):6981-6989. https://doi.org/10.1021/jacs.1c01081
49. Schiemann O, Heubach CA, Abdullin D, Ackermann K, Azarkh M, Bagryanskaya EG,

Drescher M, Endeward B, Freed JH, Galazzo L, Goldfarb D, Hett T, Esteban Hofer L, Fábregas Ibáñez L, Hustedt EJ, Kucher S, Kuprov I, Lovett JE, Meyer A, Ruthstein S, Saxena S, Stoll S, Timmel CR, Di Valentin M, Mchaourab HS, Prisner TF, Bode BE, Bordignon E, Bennati M, Jeschke G (2021) Benchmark test and guidelines for DEER/PELDOR experiments on nitroxide-labeled biomolecules. J Am Chem Soc 143 (43):17875–17890. https://doi.org/10.1021/jacs.1c07371

50. Jeschke G (2019) DeerAnalysis 2019. https://epr.ethz.ch/software.html. Accessed 11 Jan 2021
51. Worswick SG, Spencer JA, Jeschke G et al (2018) Deep neural network processing of DEER data. Sci Adv 4(8):eaat5218. https://doi.org/10.1126/sciadv.aat5218
52. Vicino MF, Wuebben C, Kerzhner M, Famulok M, Schiemann O. Spin labeling of long RNAs via click reaction and enzymatic ligation. Methods Mol Biol
53. Bruker BioSpin GmbH, EPR Division (2014) Product description: ER 5106QT-2 Q-Band Probehead
54. Hett T (2020) PELDOR_PulseSPEL. https://github.com/TobiasHett/PELDOR_PulseSPEL. Accessed 11 Jan 2021
55. Ghimire H, McCarrick RM, Budil DE et al (2009) Significantly improved sensitivity of Q-band PELDOR/DEER experiments relative to X-band is observed in measuring the intercoil distance of a leucine zipper motif peptide (GCN4-LZ). Biochemistry 48(25): 5782–5784. https://doi.org/10.1021/bi900781u
56. Endeward B, Butterwick JA, MacKinnon R et al (2009) Pulsed electron-electron double-resonance determination of spin-label distances and orientations on the tetrameric potassium ion channel KcsA. J Am Chem Soc 131(42): 15246–15250. https://doi.org/10.1021/ja904808n
57. Jeschke G (2007) Instrumentation and experimental setup. In: ESR spectroscopy in membrane biophysics, vol 27. Springer US, Boston, MA, pp 17–47
58. Hett T (2020) ScanState. https://github.com/TobiasHett/ScanState. Accessed 11 Jan 2021
59. Hett T (2020) DTA2dat. https://github.com/TobiasHett/DTA2dat. Accessed 11 Jan 2021
60. Stoll S, Schweiger A (2006) EasySpin, a comprehensive software package for spectral simulation and analysis in EPR. J Magn Reson 178(1):42–55. https://doi.org/10.1016/j.jmr.2005.08.013
61. Altenbach C (2020) LongDistances. https://sites.google.com/site/altenbach/labview-programs/epr-programs/long-distances. Accessed 22 Jan 2021
62. Steinhoff HJ, Radzwill N, Thevis W et al (1997) Determination of interspin distances between spin labels attached to insulin: comparison of electron paramagnetic resonance data with the X-ray structure. Biophys J 73(6):3287–3298. https://doi.org/10.1016/S0006-3495(97)78353-X
63. Jeschke G, Stoll S (2019) DeerAnalysis User Manual - Version 2019. http://www.epr.ethz.ch/software/index. Accessed 11 Jan 2021
64. Berman HM, Westbrook J, Feng Z, Gilliland G, Bhat TN, Weissig H, Shindyalov IN, Bourne PE (2000) The Protein Data Bank. Nucleic Acids Res 28:235–242. https://www.rcsb.org
65. Hagelueken G, Ward R, Naismith JH et al (2012) MtsslWizard: in silico spin-labeling and generation of distance distributions in PyMOL. Appl Magn Reson 42(3):377–391. https://doi.org/10.1007/s00723-012-0314-0
66. Abdullin D, Brehm P, Fleck N, Spicher S, Grimme S, Schiemann O (2019) Pulsed EPR dipolar spectroscopy on spin pairs with one highly anisotropic spin center: the low-spin Fe (III) case. Chem Eur J 25:14388–14398. https://github.com/dinarabdullin/SnrCalculator
67. Schmidt T, Jeon J, Okuno Y et al (2020) Sub-millisecond freezing permits cryoprotectant-free EPR double electron-electron resonance spectroscopy. ChemPhysChem 21(12): 1224–1229. https://doi.org/10.1002/cphc.202000312
68. Wuebben C, Vicino MF, Mueller M et al (2020) Do the P1 and P2 hairpins of the guanidine-II riboswitch interact? Nucleic Acids Res 48(18):10518–10526. https://doi.org/10.1093/nar/gkaa703
69. Abdullin D, Florin N, Hagelueken G et al (2015) EPR-based approach for the localization of paramagnetic metal ions in biomolecules. Angew Chem Int Ed Engl 54(6): 1827–1831. https://doi.org/10.1002/anie.201410396
70. Weber RT (2005) ELEXSYS E580 User's Manual. Bruker BioSpin Corporation, Manual Version 2.0
71. Larsen RG, Singel DJ (1993) Double electron–electron resonance spin–echo modulation: spectroscopic measurement of electron spin

pair separations in orientationally disordered solids. J Chem Phys 98(7):5134–5146. https://doi.org/10.1063/1.464916

72. Ward R, Schiemann O (2013) Interspin distance determination by EPR. In: Roberts GCK (ed) Encyclopedia of biophysics. Springer, Berlin, pp 1116–1123
73. Marko A, Margraf D, Yu H et al (2009) Molecular orientation studies by pulsed electron-electron double resonance experiments. J Chem Phys 130(6):64102. https://doi.org/10.1063/1.3073040
74. Prisner TF, Marko A, Sigurdsson ST (2015) Conformational dynamics of nucleic acid molecules studied by PELDOR spectroscopy with rigid spin labels. J Magn Reson 252:187–198. https://doi.org/10.1016/j.jmr.2014.12.008
75. Jeschke G (2007) Dipolar spectroscopy - double-resonance methods. In: Harris RK, Wasylishen RL (eds) eMagRes. Wiley, Chichester, pp 1459–1476
76. Reijerse E, Savitsky A (2007) Electron paramagnetic resonance instrumentation. In: Harris RK, Wasylishen RL (eds) eMagRes. Wiley, Chichester, pp 187–206

[P2]: Spin Labeling of RNA Using “Click” Chemistry for Coarse-grained Structure Determination *via* Pulsed Electron Electron-electron Double Resonance Spectroscopy

Reproduced with permission from

Maria F. Vicino†, Tobias Hett†, Olav Schiemann*, *Bio-protoc.* **2021**, *11,* e4004.
DOI: https://doi.org/10.21769/BioProtoc.4004

† These authors contributed equally.
* Corresponding author.

Published by bio-protocol (Sunnyvale, USA).

Contributions

- Compiling a workflow for setting up the PELDOR experiment and analysing PELDOR data.
- Writing the manuscript in parts.

Please cite this article as: Vicino *et al*., (2021). Spin Labeling of RNA Using "Click" Chemistry for Coarse-grained Structure Determination via Pulsed Electron-electron Double Resonance Spectroscopy. *Bio-protocol* 11(9): e4004. DOI: 10.21769/BioProtoc.4004.

bio-protocol www.bio-protocol.org/e4004 Bio-protocol 11(09): e4004. DOI:10.21769/BioProtoc.4004

Spin Labeling of RNA Using "Click" Chemistry for Coarse-grained Structure Determination via Pulsed Electron-electron Double Resonance Spectroscopy

Maria F. Vicino[#], Tobias Hett[#] and Olav Schiemann*

Institute of Physical and Theoretical Chemistry, Rheinische Friedrich-Wilhelms-University, Bonn, Germany

*For correspondence: schiemann@pc.uni-bonn.de

[#]Contributed equally to this work

[Abstract] Understanding the function of oligonucleotides on a molecular level requires methods for studying their structure, conformational changes, and internal dynamics. Various biophysical methods exist to achieve this, including the whole toolbox of Electron Paramagnetic Resonance (EPR or ESR) spectroscopy. An EPR method widely used in this regard is Pulsed Electron-Electron Double Resonance (PELDOR or DEER), which provides distances in the nanometer range between electron spins in biomolecules with Angstrom precision, without restriction to the size of the biomolecule, and in solution. Since oligonucleotides inherently do not contain unpaired electrons, these have to be introduced in the form of so-called spin labels. Firstly, this protocol describes how nitroxide spin labels can be site-specifically attached to oligonucleotides using "Click" chemistry. The reaction provides little byproducts, high yields, and is conveniently performed in aqueous solution. Secondly, the protocol details how to run the PELDOR experiment, analyze the data, and derive a coarse-grained structure. Here, emphasis is placed on the pitfalls, requirements for a good dataset, and limits of interpretation; thus, the protocol gives the user a guideline for the whole experiment *i.e.*, from spin labeling, via the PELDOR measurement and data analysis, to the final coarse-grained structure.

Graphical abstract:

Please cite this article as: Vicino *et al.*, (2021). Spin Labeling of RNA Using "Click" Chemistry for Coarse-grained Structure Determination via Pulsed Electron-electron Double Resonance Spectroscopy. *Bio-protocol* 11(9): e4004. DOI: 10.21769/BioProtoc.4004.

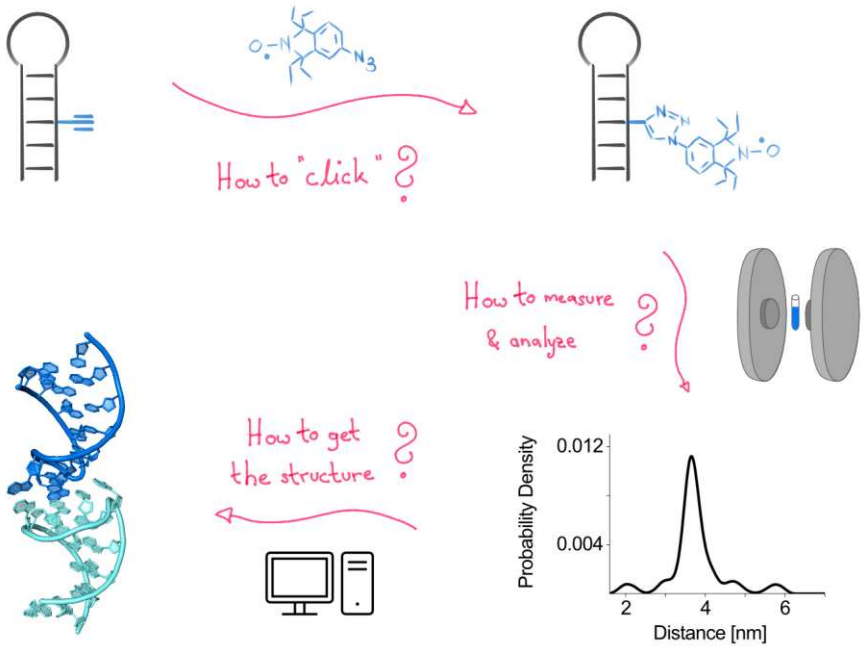

Schematic overview of the workflow described in this protocol: First, the spin-labeling of RNA is described, which is performed as a "Click"-reaction between the alkyne-functionalized RNA strand and the azide group of the spin label. Next, step-by-step instructions are given for setting up PELDOR/DEER distance measurements on the labeled RNA, and for data analysis. Finally, guidelines are provided for building a structural model from the previously analyzed data.

Keywords: Oligonucleotides, "Click" Chemistry, Spin Labeling, EPR, ESR, PELDOR, DEER

[Background] The function of biomolecules is rooted in their three-dimensional structure, dynamics, and interaction with other molecules. For example, proteins and oligonucleotides adopt structures that provide interaction sites or binding pockets for metal ions, organic ligands, and other oligonucleotides or proteins. Upon complex formation, the structure of the biomacromolecule may change, and it is this structural change that is the basis for function; thus, methods are needed that enable resolution of the structures along the trajectory of the conformational change. X-ray crystallography, nuclear magnetic resonance (NMR) spectroscopy, electron microscopy (EM), small-angle X-ray scattering (SAXS), atomic force microscopy (AFM), optical trap, and magnetic tweezers are powerful methods for obtaining the structures of biomolecules at atomic resolution (Salas *et al.*, 2015; Lottspeich and Engels, 2018; Geffroy *et al.*, 2018); yet, they also have their limitations. X-ray crystallography requires the biomolecule to be crystallized and is, as EM, limited in providing information on dynamics and conformational intermediates. NMR spectroscopy can follow the dynamics of biomolecules since it is performed in liquid solution, but is limited with respect to the size of the biomolecule. Complementary to these techniques, fluorescence microscopy (FM), Förster resonance energy transfer (FRET), and electron paramagnetic resonance (EPR) spectroscopy are biophysical methods that allow resolution of the dynamics of structural changes without size restriction and in solution (Yang *et al.*, 2012; Lottspeich and Engels,

2018; Kuzhelev *et al*., 2018). In the toolbox of EPR spectroscopy (Schweiger *et al*., 2001; Goldfarb *et al*., 2018), a set of pulse sequences summarized under the term Pulsed Dipolar EPR Spectroscopy (PDS; Schiemann *et al*., 2007) measures the dipolar coupling between the spins of unpaired electrons. This coupling encodes the inter-spin distance, from which structural and dynamic information can be derived. Owing to the high sensitivity of PDS, measurements at biomolecular concentrations down to the nanomolar range are feasible (Fleck *et al*., 2020). Out of all PDS techniques, Pulsed Electron-Electron Double Resonance (PELDOR or DEER) is the most prominent and works in a distance range from 1.5 to 16 nm upon deuteration of the buffer and the whole protein (Schmidt *et al*., 2016) with Angstrom precision (Jeschke, 2012; Tsvetkov *et al*., 2019). PELDOR imposes no size restriction (Malygin *et al*., 2019), and can be performed on biomolecules in liquid (Yang *et al*., 2012) or frozen solution (Duss *et al*., 2014), in membranes (Dastvan *et al*., 2019), and within cells (Theillet *et al*., 2016). However, since PELDOR requires unpaired electrons and biomolecules are usually diamagnetic, techniques are needed for site-directed spin labeling (Shelke and Sigurdsson, 2014). Focusing on RNA oligonucleotides, there are two principal strategies for spin labeling (Ward and Schiemann, 2014): the first is the phosphoramidite approach, where a spin-labeled phosphoramidite is incorporated into the RNA strand during solid-phase synthesis (Beaucage *et al*., 1992; Lottspeich and Engels, 2018) and the second is the post-synthetic method, where a functionalized RNA strand is labeled after synthesis (Kerzhner *et al.,* 2016). The major drawbacks of the phosphoramidite approach are the rather laborious synthesis of the spin-labeled phosphoramidite and the easy reduction of the label during RNA synthesis, leading to an EPR-silent state. For the post-synthetic strategy, RNA strands modified with a unique functional group can be obtained commercially and are then reacted with a spin label carrying the complementary functional group. However, labeling with high yields and efficient purification with minimal product loss can be challenging. Even though the length of commercially available RNA oligonucleotides is limited, there are well-established methods for obtaining longer RNA strands, *e.g.*, via enzymatic ligation (Duss *et al*., 2014; Kerzhner *et al*., 2018).

In this protocol, built on the publications Kerzhner *et al*., 2018, Wuebben *et al*., 2019 and 2020, we first introduce a workflow for the post-synthetic spin labeling of RNA oligonucleotides based on the "Click" reaction. Here, the "Click" reaction is performed as a copper-(I)-catalyzed [2+3] cycloaddition between an alkyne-substituted 5'-uridine in the RNA strand and an azide group on a nitroxide label (Figure 1). The reaction is usually quantitative and fast, and the purification of the labeled RNA can be easily performed via reversed-phase High Performance Liquid Chromatography (HPLC). Secondly, the protocol outlines how to set up and perform the PELDOR measurement. Thirdly, it provides a workflow for data analysis and the transformation of the distances into structures. Importantly, possible pitfalls are highlighted and tips provided on how to overcome experimental difficulties, which are rarely found in the literature.

Please cite this article as: Vicino *et al.*, (2021). Spin Labeling of RNA Using "Click" Chemistry for Coarse-grained Structure Determination via Pulsed Electron-electron Double Resonance Spectroscopy. *Bio-protocol* 11(9): e4004. DOI: 10.21769/BioProtoc.4004.

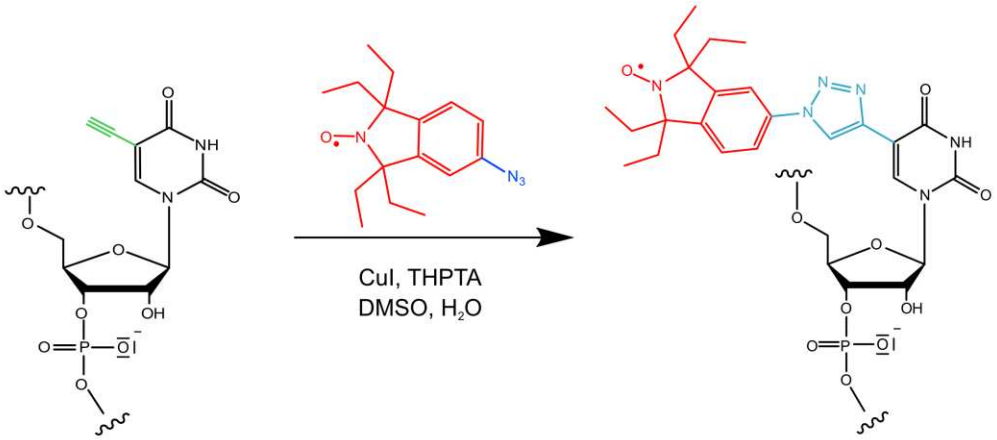

Figure 1. Reaction scheme of the "Click" reaction used in this protocol. The azide-functionalized spin label (azide group in blue; nitroxide moiety and 1,1,3,3-tetraethyl-5-azoisoindolin-2-oxyl backbone in red) is attached to a 5-ethynyl-2′-deoxyuridine nucleotide (ethynyl group in green) in the RNA strand (black). Copper, in its oxidation state (I), forms a complex with tris ((1-hydroxy-propyl-1H-1,2,3-triazol-4-yl) methyl) amine (THPTA), catalyzing this reaction in aqueous solution, which leads to the formation of a triazol linker (cyan) covalently connecting the nitroxide moiety to the RNA.

Beyond this application, labeling via "Click" chemistry is restricted neither to RNA nor to nitroxides or spin labels in general. It can be applied to *e.g.*, DNA (El-Sagheer and Brown, 2010) and proteins (Nikić *et al.*, 2015) and can be used for fluorescent labels (Liang *et al.*, 2019). For protein labeling, one would make use of unnatural amino acids *e.g.*, 4-ethynyl-L-phenylalanine (Widder *et al.*, 2019). Note, however, that the reaction conditions will have to be adapted to the particular system under study. The workflow for the Q-band PELDOR experiment is universally applicable to measurements of nitroxide-labeled biomolecules. Likewise, the data analysis and distance-to-structure transformation can be adapted for other PDS techniques or other types of spin labels.

Materials and Reagents

Note: It is very important to set up an RNase-free environment. Therefore, use only autoclaved pipette tips, clean your bench and tools with 70% ethanol or RNase Away, and wear protective gloves.

1. RNase Away (Thermo Fisher, catalog number: 7003PK) or 70% Ethanol (Julius Hoesch GmbH, catalog number: 125900)
2. 1.5 ml and 2 ml Eppendorf tubes
3. 2.5 nmol dried RNA oligonucleotide with one or more 5-ethynyl-2'-deoxyuridine modifications (commercially synthesized and delivered in dried form *e.g.*, from Metabion or Biomers, see procedure for more details), stored at -20°C (Note 1)
4. Diethylpyrocarbonate (DEPC, Carl Roth, catalog number: K028.3)-treated water

5. Copper(I)-iodide (Cu(I); Carl Roth, catalog number: 0305.1), stored at room temperature under ambient conditions in a regular container, as received
6. Dimethyl sulfoxide (DMSO, Carl Roth, catalog number: A994.2), stored at room temperature
7. 3.6 µl 250 mM tris ((1-hydroxy-propyl-1H-1,2,3-triazol-4-yl) methyl) amine (THPTA, Sigma, catalog number: 762342-100MG) solution in DMSO, stored at -20°C, vortex the solution prior to use
8. 2 µl 100 mM 1,1,3,3-tetraethyl-5-azoisoindolin-2-oxyl (Wuebben *et al.*, 2019) or 1,1,3,3-tetramethyl-5-azoisoindolin-2-oxyl (Kerzhner *et al.*, 2018) solution in DMSO, stored at -20°C, vortex the solution prior to use
9. Hamilton syringe, 50 µl
10. Buffer A, acetonitrile (Carl Roth, catalog number: 8825.2), stored at room temperature
11. Buffer B, 0.1 M triethylammonium acetate (TEAA) (1 M solution, Labomedic, catalog number: 2001741), stored at room temperature
12. For Liquid Chromatography-Mass Spectrometry (LC-MS): Buffer C, 10 mM triethylamine (Merck, catalog number: 90340-2.5L), stored at room temperature
13. For LC-MS, Buffer D, 0.1 M hexafluoroisopropanol (Merck, catalog number: 18127-50ML), stored at room temperature
14. For spin counting and determination of labeling efficiency: 10 µl capillaries (Hirschmann Laborgeräte, catalog number: L925.1)
15. Deuterated ethylene glycol (EG-d_6) as a cryoprotectant (Merck, catalog number: 530549), stored at room temperature
16. Deuterated water (D_2O) as a solvent (Deutero, order number: 00506), stored at room temperature
17. Pipette and matching elongated pipette tips (Sorenson BioScience, 200 µl MµltiFlex Round, catalog number: # 28480) to transfer the sample into the EPR tube
18. For PELDOR measurement: Q-band EPR sample tubes with 3 mm outer diameter made from clear-fused quartz (CFQ) (Wilmad LabGlass, catalog number: G542PN000001470)
19. Light-duty tissue wipers (VWR, European catalog number: 115-0202)
20. Liquid nitrogen (Air Liquide) for freezing the sample and liquid helium (Air Liquide) for cooling the sample in the resonator
21. DEPC-treated water (see Recipes)

Equipment

1. SpeedVac vacuum concentrator: Eppendorf Concentrator plus (Eppendorf, Rotor: F-45-48-11) or freeze dryer: Alpha 3-4 LSC basic (Martin Christ Gefriertrocknungsanlagen)
2. Thermomixer (Eppendorf)
3. Table-top centrifuge (Eppendorf)
4. Milli-Q Ultrapure Water System (Merck Millipore)

5. NanoDrop Spectrophotometer (Thermo Fisher)
6. High-Performance Liquid Chromatography (HPLC) system (Agilent, Series 1,200)
7. Reversed-phase C18 column, heatable (Zorbax 300SB-C18, 4.6 × 150 mm for RNA sequences shorter than 50 nucleotides or Zorbax 300SB-C18, 9.4 × 250 mm column for RNA sequences exceeding 50 nucleotides)
8. Amicon® Ultra-0.5 centrifugal filter device with a nominal molecular weight limit (NMWL) of 3,000 Da (Merck, catalog number: UFC500396)
9. Liquid Chromatography-Mass Spectrometry (LC-MS) system (HTC esquire from Bruker Daltonics in combination with an HPLC system). If you have no access to an LC-MS system, you can perform an analytical HPLC run and subsequently determine the exact mass via matrix-assisted laser desorption/ionization (MALDI) mass spectrometry or electrospray ionization (ESI) mass spectrometry
10. For spin counting and determination of labeling efficiency: continuous wave (*cw*) EPR spectrometer (Bruker BioSpin, model: EMXnano)
11. Pulsed EPR spectrometer (Bruker BioSpin, model: ELEXSYS E580) equipped with a Q-band microwave bridge (Bruker) and an ER5106-QT2 resonator (Bruker) for PELDOR measurements. When using an X-band resonator for continuous wave operation (*e.g.*, Bruker ER4119HS), spin counting experiments can also be performed on this spectrometer
12. 150 W travelling wave tube amplifier (TWT, Applied Systems Engineering, model: 187 Ka)
13. Liquid helium cryostat (Oxford Instruments, model: CF935)
14. Temperature controller (Oxford Instruments, model: iTC503S)
15. Helium transfer line (Oxford Instruments NanoScience, model: LLT600 or LLT650) and gas flow controller (Oxford Instruments)
16. Turbomolecular pump for evacuating the cryostat (Pfeiffer Vacuum, model: HiCUBE 80 Eco)
17. Membrane pump for maintaining a constant stream of cold helium gas (KNF Neuberger, model: PM26962–026.1.2)
18. Dewar vessels for shock-freezing and handling the EPR sample tubes at liquid nitrogen temperatures (KGW Isotherm, Type 00C, 13.5 cm in height; Type 3C, 26 cm in height)
19. 100 L liquid helium tank (Cryo Anlagenbau, model CS 100 H)
20. Safety goggles and cold protection gloves
21. PC with Linux, as delivered with the spectrometer

Software

1. Matlab Version R2018a or later (The MathWorks Inc., www.mathworks.com). For DeerNet, the Deep Learning Toolbox and the Signal Processing Toolbox for Matlab should be installed
2. DeerAnalysis (*e.g.*, DeerAnalysis 2019) toolbox for Matlab, available free of charge (G. Jeschke, https://epr.ethz.ch/software.html)
3. Software for data analysis and graphing, *e.g.*, Origin (OriginLab Corporation,

www.originlab.com), SciDAVIS (http://scidavis.sourceforge.net), or Excel (Microsoft Corporation, https://products.office.com/excel)

4. Xepr-software, as delivered with the EPR spectrometer, for hardware control and data acquisition (Bruker)
5. *In silico* spin labeling software, *e.g.*, mtsslSuite (G. Hagelueken, www.mtsslsuite.isb.ukbonn.de; Hagelueken *et al.*, 2015), MMM (G. Jeschke, https://epr.ethz.ch/software.html; Polyhach *et al.*, 2011) or the GFN/FF-based CREST/MD (S. Grimme, https://github.com/grimme-lab; Spicher *et al.*, 2020)
6. IDT OligoAnalyzer Tool (IDT, www.idtdna.com/pages/tools/oligoanalyzer)
7. SnrCalculator (D. Abdullin, https://github.com/dinarabdullin/SnrCalculator)

Procedure

A. RNA Labeling

1. Order your modified RNA oligonucleotide. For this protocol, the following sequence is used: 5′-GCG GGG ACG ACC C**X**G C-3′, with **X** = 5-ethynyl-2′-deoxyuridine

   The labeling position should not disturb the overall RNA structure or its function; thus, avoid labeling at catalytically active sites or binding pockets. To minimize possible perturbations, design the modified oligonucleotide strands by exchanging a naturally occurring uridine nucleotide with the modified 5-ethynyl-2′-deoxyuridine. Moreover, where possible, it is preferable to integrate the modification into a double-stranded RNA region since this promotes narrow distance distributions.

   Note: Establish an RNase-free environment: Clean your bench and tools e.g., pipettes with 70% ethanol or RNase Away. Wear protective gloves throughout this workflow.
2. Aliquot the RNA
   a. Dissolve the RNA oligonucleotide in DEPC-treated water (see Recipes).
   b. Aliquot 2.5 nmol RNA into 1.5-ml Eppendorf tubes (Note 1).
   c. Dry the RNA oligonucleotide aliquots in a SpeedVac vacuum concentrator or a freeze dryer. Store the dried RNA oligonucleotide aliquots at -20°C.
3. Set up the RNA labeling reaction
   a. Pre-heat the Thermomixer to 60°C.
   b. Dissolve the dried RNA oligonucleotide in 4.4 µl DEPC-treated water (see Recipes).
   c. Weigh 1-2 mg CuI (X) into a 2-ml Eppendorf tube and calculate the volume of DMSO (Y), to obtain a 50 mM Cu^+ solution:

$$\frac{X\,[\mathrm{mg}] \cdot 100}{0.952\left[\frac{\mathrm{g}}{\mathrm{L}}\right]} = \mathbf{Y}\,[\mu\mathrm{l}]$$

Read Note 2 before you continue!

d. Dissolve CuI in Y µl DMSO and immediately prepare the Cu^+-complex by mixing together:
20 µl DMSO
8 µl 50 mM Cu^+ solution from the previous step
3.6 µl 250 mM THPTA/DMSO solution
Vortex the mixture and incubate for 5 min at room temperature

e. Set up the labeling reaction by pipetting the following solutions into the 1.5-ml Eppendorf tube containing the dissolved RNA (Step A3b):
2 µl spin label/DMSO solution, taken from the 100 mM stock solution
4.6 µl THPTA-Cu^+ solution (Step A3d)
Shortly vortex the reaction mixture and incubate the reaction at 300 rpm and 60°C for 30 min (Note 3)

4. Desalt the RNA oligonucleotide and remove Cu^+ via an Amicon Ultra centrifugal filter device
   a. Add 480 µl DEPC-treated water to each reaction tube and transfer each solution to an Amicon Ultra-0.5 filter, previously inserted into an Amicon collection tube.
   b. Spin and concentrate for 30 min at 14,000 × *g* and room temperature.
   c. Add 500 µl DEPC-treated water to the Amicon filter device and spin again for 30 min at room temperature and 14,000 × *g*, discard the flowthrough.
   d. Repeat Step A4c one more time.
   e. For RNA recovery, turn the Amicon filter device around and insert it into a clean Amicon collection tube. Spin for 2 min at room temperature and 14,000 × *g*.
   f. Pipette 50 µl Milli-Q water into the Amicon filter device and wash the membrane by pipetting up and down or by vortexing. Then, place the filter device again upside down and spin for 2 min at room temperature and 14,000 × *g*.
   g. Wash the filter membrane again, as described in Step A4f, two more times. The sample volume should now be around 200 µl.
   h. Determine the amount of RNA oligonucleotide (n_{RNA}) using the NanoDrop: Clean the NanoDrop measurement pedestal with 70% ethanol using a light-duty tissue wiper. Using a pipette, transfer 1 µl DEPC-treated water onto the measurement pedestal and run a blank measurement as a reference. Clean the pedestal with a light-duty tissue wiper, pipette 1 µl RNA solution onto the measurement pedestal and measure the absorbance at 260 nm (Abs_{260nm}). Then, calculate n_{RNA} with the extinction coefficient (ε_{RNA}), either provided by the vendor or calculated using an online tool such as the IDT *OligoAnalizer Tool* and the volume of your RNA oligonucleotide sample (V_{RNA}) using:

$$\frac{Abs_{260nm}\left[\frac{1}{cm}\right]}{\varepsilon_{RNA}\left[\frac{L}{cm \cdot mol}\right]} \cdot V_{RNA}[L] = n_{RNA}\ [mol]$$

Evaporate the excess water from your RNA oligonucleotide sample, either with the

SpeedVac vacuum concentrator or the freeze dryer, until you obtain a volume that does not exceed half of your HPLC-loop capacity. If using a 100 µl injection loop, *e.g.*, inject a volume of 30-50 µl.

5. Reversed-phase HPLC purification
   a. Start with the equilibration of your reversed-phase column. Therefore, re-buffer the column to 8% buffer A (acetonitrile) and 92% buffer B (0.1 M triethylammonium acetate).
   b. Perform a blank run to check the purity of your column before you purify your sample: Load 30-50 µl Milli-Q water with a Hamilton syringe into the injection loop and start the HPLC run. The blank run uses the same operation parameters as the purification run of your RNA sample. In general, you will need to fine-tune the HPLC run for each new RNA sequence. However, you can use the following settings as a starting point for RNA sequences shorter than 50 nucleotides: Elute with a gradient of 8% → 25% buffer A for 20 min with a flow rate of 1.5 ml/min. Then, equilibrate your column back to 8% buffer A. For short RNA sequences, use the analytical Zorbax 300SB-C18, 4.6 × 150 mm column, but for sequences exceeding 50 nucleotides, use the preparative Zorbax 300SB-C18, 9.4 x 250 mm column. The elution profile for the preparative column is: Elute with 8% acetonitrile for 10 min and then apply a gradient of 8% → 23% buffer A for 55 min with a constant flow rate of 2 ml/min. Finally, equilibrate your column back to 8% buffer A. It is important to heat your HPLC column to avoid the formation of tertiary RNA structures (Figure 2). Heat the column to 60°C, also during the blank run, to ensure the same conditions.

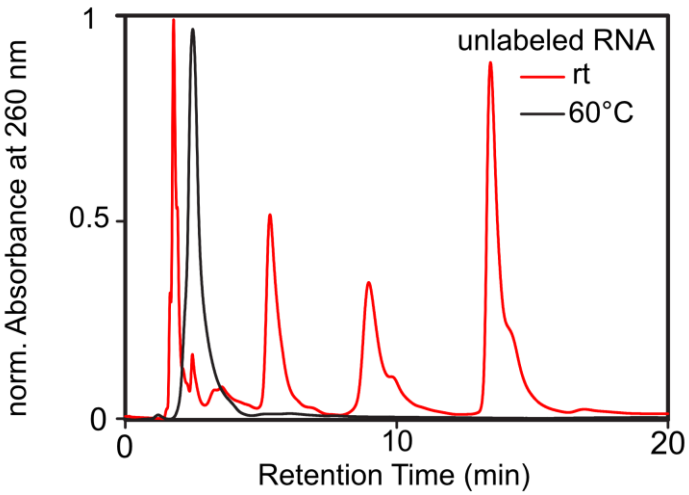

Figure 2. Exemplary normalized HPLC chromatograms of unlabeled RNA at different column temperatures. Upon column heating, the formation of tertiary structures is inhibited, which leads to a single peak (black chromatogram).

   c. Inject your RNA sample into the loop. Do not inject more than 2.5 nmol RNA to avoid column overloading. However, you should check the capacity and properties in the manufacturer's instructions of the particular column you use.

d. Run the HPLC method.

e. Separately collect the fractions of unlabeled and labeled RNA. The collection can be performed manually or, if your HPLC is equipped with a fraction collector, automatically. If you use a fraction collector, you can set a constraint to collect everything that exceeds an absorbance of *e.g.*, 15 mAU.

f. Pool each HPLC peak separately and concentrate the solutions in the SpeedVac vacuum concentrator until you obtain a volume of about 500 µl for each peak.

g. After the HPLC run has finished, proceed with the purification of your next sample or store the HPLC column. The storage of your column is achieved by rebuffering it to 80% buffer A.

6. Desalt the labeled RNA with an Amicon Ultra centrifugal filter device

a. Desalt the RNA samples using an Amicon Ultra centrifugal filter device, as already described above in Steps A4a-A4h.

b. After desalting your RNA samples, concentrate them in the SpeedVac vacuum concentrator until you reach the desired concentration. Yields of 50-70% with respect to the starting amount of RNA are usually obtained; the losses largely originate from the purification steps. The labeling itself is quantitative, as shown in the HPLC chromatograms (Figure 3).

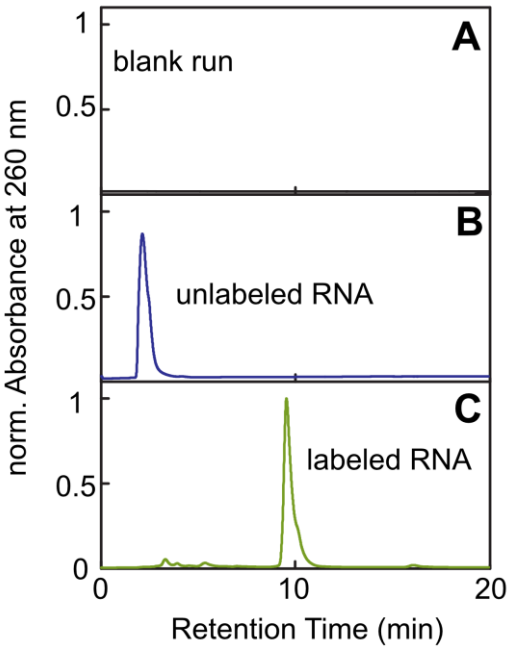

Figure 3. Normalized chromatograms of different HPLC runs. A. Chromatogram obtained by injection of water (blank run). B. Chromatogram obtained by injection of unlabeled RNA. C. Chromatogram obtained by injection of RNA from a labeling reaction. From the chromatogram of the labeled RNA (C), it can be inferred that there is almost no unlabeled RNA left in the reaction mixture, as only a negligible peak at a retention time of ~2 min is obtained. For further purification, only the peak at a retention time of 10 min has been collected and used.

7. Determine the purity of your labeled RNA sequence via LC-MS (or HPLC and mass spectrometry separately)
   a. Perform an LC-MS measurement of the unlabeled RNA, as a reference. The procedure is analogous to that of an HPLC run (equilibration of the column with buffer C, injection, run, and storage). Use a gradient of 5% → 20% buffer D for 20 min with a constant flow rate of 0.4 ml/min.
   b. Perform an LC-MS measurement of the labeled RNA sample; use the gradient specified in Step A7a. Successful labeling can be checked by determining the exact mass of the species present in a specific LC peak.
   c. If you do not have access to an LC-MS system, perform an analytical HPLC run and subject the fractions containing RNA to ESI-MS or MALDI-MS to determine the exact mass.
8. Determine the spin labeling efficiency
   a. Determine the concentration of labeled RNA (c_{RNA}) using the NanoDrop (Step A4h).
   b. Prepare 10 µl 25 µM RNA solution, if each RNA strand is singly labeled. If the RNA strand is doubly labeled, halve the RNA concentration.
   c. Fill the solution into a 10 µl capillary.
   d. Perform a *cw* EPR measurement as described in the user's manual of the EMXnano spectrometer. Use the "spin count" routine from Bruker to determine the spin concentration (c_{spin}). Another way to determine the spin concentration is to doubly integrate the *cw* EPR spectrum and to relate this double integral value to that of a reference sample of known spin concentration. The error margin of both spin quantitation methods is 10-20%.
   e. Calculate the labeling efficiency. For singly labeled RNA sequences, the efficiency is given by:

$$\frac{c_{spin}}{c_{RNA}} \cdot 100 = \text{labeling efficiency [\%]}$$

   For doubly labeled sequences, use:

$$\frac{c_{spin}}{2c_{RNA}} \cdot 100 = \text{labeling efficiency [\%]}$$

   f. Keep in mind that although LC-MS reveals almost quantitative labeling, the yield of labeled RNA with respect to the starting RNA is 50-70% due to losses during purification.
9. Prepare the PELDOR sample
   a. For singly labeled RNA, transfer 2.0 nmol into an Eppendorf tube and dry it in the SpeedVac vacuum concentrator or freeze-dryer. Halve the amount for doubly labeled RNA.
   b. Dissolve the RNA in 64 µl D_2O. Add 16 µl EG-d_6 as a cryoprotectant and mix the solution carefully in an Eppendorf tube. This yields a sample of 80 µl with a spin concentration of 25 µM containing 20% v/v EG-d_6 (Note 4). During PELDOR measurements, the resonator should be completely filled with your sample; thus, even if your RNA amount is scarce, avoid

preparing samples with a volume less than 60 µl.

c. Fill the entire 80 µl into a 3 mm outer diameter Q-band EPR tube with the Eppendorf pipette using the elongated pipette tips. Carefully shake the EPR tube such that the sample collects at the bottom.

d. Freeze the sample by carefully immersing the EPR tube into a Dewar vessel with liquid nitrogen. As EPR tubes may crack during freezing, wear safety goggles and use cold-protection gloves when handling liquid nitrogen. Keep the tube in the Dewar vessel with liquid nitrogen.

B. PELDOR Measurements

1. Prepare the ELEXSYS E580 Q-Band EPR spectrometer (Bruker BioSpin) for the PELDOR measurement:

   As EPR spectrometers are sensitive devices that can be damaged upon operator errors, stick to this protocol and the instructions in the user manual of the instrument. In case of doubt, seek advice from a more experienced colleague.

   a. Connect the turbomolecular pump to the cryostat, switch on the pump, and evacuate the cryostat to a reduced pressure of ~10^{-4} mbar. Evacuating overnight may be helpful to reach the required vacuum conditions.

   b. Switch on the heat exchanger of the spectrometer and check the temperature of the inward and return flow. Depending on the ambient temperature, the former should be around 10-15°C and the latter should not surpass 25-30°C. If the spectrometer has a closed cooling circuit, check the water level in this system and refill if necessary.

   c. Switch on the spectrometer console, the magnet power supply, and the TWT amplifier. It is important to keep the TWT in the **Standby** mode to prevent damage of the detection system. Give the system ~1 h to warm-up before starting measurements as this ensures electronic stability of the spectrometer.

   d. Connect the overflow valve of the helium tank to the helium recovery system, if available in your facility. Make sure that the gasflow through the tubing is not blocked (*e.g.*, due to bending) and open the overflow valve on the helium tank to prevent pressure build-up.

   e. From this step on, wear cold protection gloves and safety goggles! Open the needle valve on the helium transfer line. **Slowly** (~3 min for the whole procedure) insert the transfer line into the helium tank. As the transfer line enters the liquid helium, the gas meter will indicate a gasflow and occasionally, a hiss-sound can be perceived. If helium gas exits the tank directly from the upper opening, first screw the nut encircling the transfer line hand-tight and then fix it with a spanner as soon as the transfer line is fully inserted into the tank.

   f. Immerse the lance of the transfer line into ethanol and check for gasflow. Wipe the gas outlet with a tissue and connect the lance to the cryostat of the spectrometer.

   g. Close the cryostat with an empty sample rod to prevent condensation of air within the cryostat.

h. Connect the membrane pump to the port on the transfer line. Open the needle valve on the transfer line approximately ¼ turn and switch on the membrane pump to maintain a stream of cold helium gas. Using the gasflow controller of the cryostat, adjust the helium gasflow to ~1 L/h. Switch on the iTC503S temperature controller and set the target temperature to 50K. Cooling down the cryostat from ambient temperatures to 50K usually takes 20-30 min (Note 5).

i. Take the EPR tube out of the liquid nitrogen Dewar vessel and quickly wipe it with a tissue to remove potential contaminants and ice. However, make sure not to keep the EPR tube outside the liquid nitrogen for too long to prevent the sample from warming up. If liquid nitrogen has condensed within the tube, warming up the tube might lead to ejection of the sample or even rupture of the tube.

j. Insert the EPR tube into a tightly fitting sample holder and adjust its position such that the sample will be located in the EPR-active zone of the resonator. For the ER5106-QT2 resonator, the center of the sample should be 38 mm below the lower end of the tube holder.

k. Screw the sample holder, with the EPR tube inserted, into a sample rod.

l. Ensure that the spectrometer is in the **Standby** mode. Stop the membrane pump, wait until the needle of the gasflow controller has dropped to zero, and remove the empty sample rod from the cryostat. Quickly, but also carefully and straight, insert the sample rod, with the EPR tube mounted, as far as it will go. Do not leave the cryostat open for a longer period to prevent air condensation (Note 6). Wait at least 20 min before you proceed to the next steps so that the sample is thermally equilibrated.

2. Spectrometer tuning and safety check

a. Familiarize yourself with the basic functions and operation windows of the Xepr-software by means of the spectrometer manual. In particular, look up keywords such as "Pulse Tables," "PulseSPEL," "SpecJet," "FT EPR Parameters," "FT Bridge," "Microwave Bridge Tuning Dialog Box," and "Acquisition Trigger." If you need further explanations, ask a more experienced EPR colleague for advice. In the following steps, the buttons, input boxes, and menu bars in the Xepr-software that you should use at a particular step are set in quotation marks.

b. Connect the Xepr-software to the spectrometer by selecting "Connect to Spectrometer" in the "Acquisition"-menu and open the "Microwave Bridge Tuning Dialog Box." Go into the "Tune"-mode and set the "Attenuation" to 10 dB. Set the microwave (MW) frequency to ~33.7 GHz.

c. Over-couple the resonator (Note 7). The ER5106-QT2 resonator has two screws to adjust the cavity length (right screw) and the cavity coupling (left screw). Adjust the cavity length such that the resonator tuning dip becomes visible in the MW Bridge Tuning Dialog Box. Note that there are two tuning dips for the ER5106-QT2 resonator, a "real" dip and a "fake" dip. These can be distinguished as the "fake" dip moves markedly when the coupling screw is rotated, whereas the "real" dip stays in place. Changing the cavity length moves both dips

simultaneously.

Adjust the cavity coupling and the cavity length such that the "real" dip is centered in the Tuning Dialog Box and that the minimum of the "fake" dip is on the right side of the window.

d. Perform the safety check of the spectrometer's detection system as described in the instrument manual. Attention: Do not attempt to switch the TWT into the Operate mode, if the defense pulses are absent, as this would damage the detection circuitry. In case of doubt, consult your spectrometer administrator.

3. Optimize a standing Hahn echo (Weber, 2005)
   a. Adjust the "Center Field" B_0 to the value corresponding to g ~2.00 at the current MW frequency v (*e.g.*, B_0 ~11,980 G at v ~33.7 GHz).
   b. In the Pulse Tables, program the Hahn echo sequence (π/2–τ–π–τ–Echo) into the "+x"-channel using pulse lengths of 12 ns and 24 ns for π/2 and π-pulses, respectively. Use τ = 200 ns for the interpulse delay. After entering pulse lengths and delays into the Pulse Tables, confirm each entry by pressing "Enter" on the keyboard.
   c. Select the "Acquisition Trigger"-channel from the dropdown menu and set the acquisition trigger "Length" to 4 ns at the "Position" 0 ns. Set the "Integrator Time Base" to 1.0 ns, the "Shot Rep. Time" to 3,000 µs, and the number of "Shots Per Point" to 10.
   d. Click "Start" in the Patterns window, "Run" in SpecJet, and decrease the MW "Attenuation" to observe the Hahn echo in SpecJet. Adjust the "Attenuation" to maximize the Hahn echo amplitude *i.e.*, to obtain π/2 and π-pulses at the given pulse lengths (Note 8).
   e. Set the "No. of Averages" in SpecJet to 1. Set the "Video Bandwidth" to 20 MHz and adjust the "Video Gain" amplification such that the echo is not clipped. Fine-adjust the MW phase such that the echo is fully detected in the real channel of the quadrature detector (green trace in SpecJet); the signal in the imaginary channel (yellow trace in SpecJet) should be zero on average. Slight changes in the "Center Field" may be helpful in this context to fully bring the sample on resonance.
4. Record the echo-detected field-swept EPR spectrum
   a. Adjust the acquisition trigger "Position" in the Pulse Tables in such a way that the echo starts at the left of the SpecJet window and increase the acquisition trigger "Length" to ~120 ns, in order to cover the whole echo (Figure 4A). This maximizes the spectral resolution of the field-swept spectrum (Figure 4B).

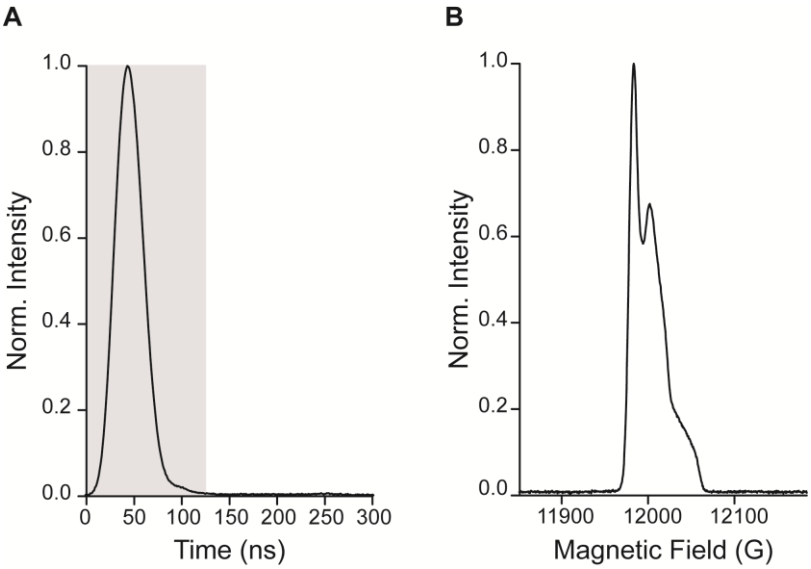

Figure 4. Initial steps for setting up pulsed EPR experiments. A. Hahn echo. B. Echo-detected field-swept EPR spectrum. The grey area in (A) marks the integration region to obtain the field-swept spectrum.

b. In the "Field"-tab within the FT EPR Parameters window, set the "Sweep Width" to 400 G.
c. Switch to the "Acquisition"-tab to set the "X-Axis Size", *i.e.*, the number of points in the spectrum. Usually, 800 is an appropriate value, corresponding to a resolution of 0.5 G/point.
d. Press the "Run" button in the main window to record the spectrum (Figure 4B). Depending on the spin concentration, average multiple scans to obtain a good signal-to-noise ratio (SNR) and save the data to disk.
e. Read off the magnetic field value that yields the maximum signal intensity in the field-swept spectrum and **write it down**, you will need it later.

5. Perform the Two-Pulse Electron Spin Echo Envelope Modulation (Two-Pulse ESEEM) experiment to obtain information on transverse electron spin relaxation, which limits the dipolar evolution window in the PELDOR experiment. In the Two-Pulse ESEEM experiment, the Hahn echo amplitude is monitored as a function of the interpulse delay τ. The default PulseSPEL program provided by Bruker records it as a function of τ. Note, however, that some literature references show these Hahn echo decay curves as a function of 2τ.
   a. Set the "Center Field" to the magnetic field value of the signal maximum in the field-swept spectrum.
   b. In the "Acquisition"-tab, open "PulseSPEL" by clicking the corresponding button.
   c. Load the standard PulseSPEL program for the Two-Pulse ESEEM experiment, which is by default located in the folder:
   `"xeprFiles/PulseSPEL/sharedPulseSPEL/Standard/Spel2009/ESEEM"`, and the corresponding variable definitions `"descrESEEM.def"`.
   d. Set the variables to the values shown in Table 1.

Please cite this article as: Vicino *et al*., (2021). Spin Labeling of RNA Using "Click" Chemistry for Coarse-grained Structure Determination via Pulsed Electron-electron Double Resonance Spectroscopy. *Bio-protocol* 11(9): e4004. DOI: 10.21769/BioProtoc.4004.

Table 1. Parameters for the Two-Pulse ESEEM experiment

Parameter	Description	Value
p0	Length of π/2-pulse	Use the values which you identified as optimal in section B, step 3d.
p1	Length of π-pulse	
d1	Initial interpulse delay τ	200 ns
d0	Acquisition trigger offset	0 ns (for setup) Usually ~432 ns (for experiment)
SRT	Shot-Repetition-Time	3,000 * srtu (with srtu = 1.02 µs).
h	Number of Shots per Point	10
d30	Time increment	8 ns

e. Click the buttons "Compile," "Show Program," and "Validate" in this order.

f. In the "Acquisition"-toolbar, choose the option "Run from PulseSPEL," select the experiment "2P ESE Setup," and press the "Run"-button in the main program window. Read off the time value at which the echo amplitude is maximal and set this value as the acquisition trigger delay parameter d0. Usually, this value amounts to d0 = 432 ns.

g. Select the "2P ESEEM" experiment with a two-step phase cycle, set the number of points for this experiment (parameter dim2 in the PulseSPEL program) to 1,024, and click the "Run" button in the main window to record the Hahn echo decay curve (Figure 5B).

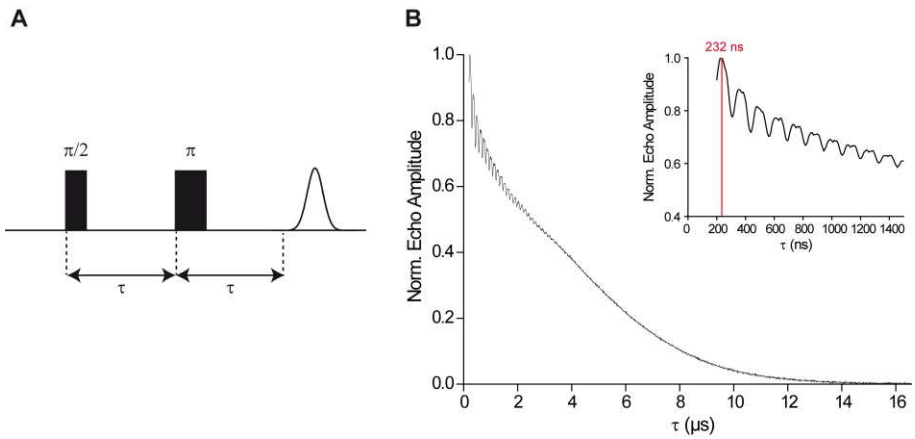

Figure 5. The Two-Pulse ESEEM experiment. A. Schematic representation of the Hahn-echo sequence. In the Two-Pulse ESEEM experiment, the interpulse delay τ is incremented and the echo amplitude is measured as a function of τ. B. Typical Hahn echo decay curve. The inset shows the initial 1.5 µs of the trace, the maximum at 232 ns is highlighted by a red line.

h. If the curve does not reach the zero level at long interpulse delays τ, increase the number of points and/or the time step d30. Read off the time value at which the echo intensity has dropped to almost zero and **write it down**.

6. Setting up the PELDOR experiment

   PELDOR is a double-frequency experiment that uses the probe frequency ν_{probe} to create a signal on a spin A in a molecule and flips a spin B in the same molecule with the pump frequency ν_{pump}. The four-pulse PELDOR sequence is shown in Figure 6. Firstly, a Hahn echo (HE) is created by a π/2 and a π-pulse applied at ν_{probe} and affecting spin A. Next, a pump pulse π_{pump} at the frequency ν_{pump} inverts spin B. Finally, a refocusing π-pulse at ν_{probe} is applied, refocusing the Hahn echo from spin A. In the PELDOR experiment, the position of the pump pulse is incremented within the interval τ_2 and the integrated intensity of the refocused echo (RE) is measured as a function of the delay T. This yields the so-called PELDOR time trace. If intramolecular dipolar coupling between spins A and B occurs, the coupling frequency will be encoded in the oscillations of the time trace. The overall exponential decay refers to the intermolecular dipolar interactions.

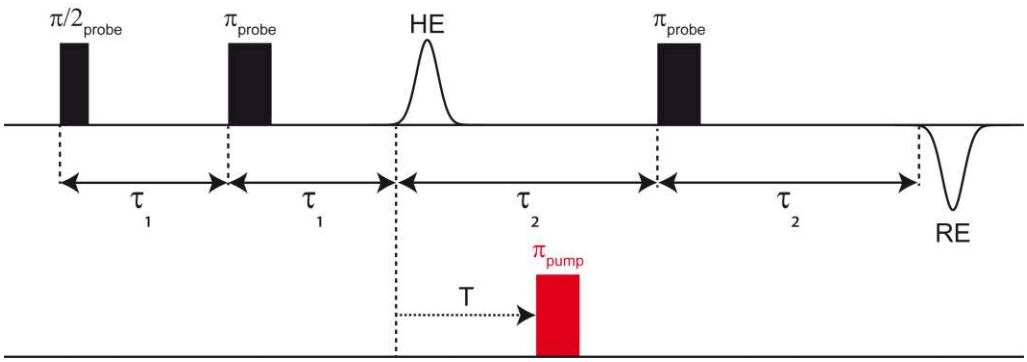

Figure 6. Schematic representation of the PELDOR sequence. Microwave pulses at the probe frequency are shown in black, the pump pulse is displayed in red. "HE" abbreviates the Hahn echo, "RE" the refocused echo. In the PELDOR experiment, the position of the pump pulse is incremented within the first interval τ_2 and the integrated intensity of the RE is measured as a function of T.

The set-up of the PELDOR experiment consists of various steps, and as PELDOR requires phase cycling and nuclear modulation averaging, it is commonly run from a PulseSPEL program. The Bruker EPR spectrometers are by default equipped with a PulseSPEL program for PELDOR; however, many research groups have developed their own programs featuring custom variable definitions and conventions. Herein, we describe how to set up the PELDOR experiment with our version of the PulseSPEL program, which is available in the Appendix.

a. Set the variables for the Hahn echo and optimize it at the pump frequency, which is applied in the center of the resonator dip (33.7 GHz).
   i. Load the PELDOR program and the variable definition file into PulseSPEL.
   ii. Set the following parameters in PulseSPEL (Table 2):

Table 2. Parameters for setting up the PELDOR experiment. The given parameters are starting values that will be optimized during the course of experimental setup

Parameter	Description	Value
p0	Length of π/2-pulse	Use the values which you identified as optimal in Step B3d.
p1	Length of π-pulse	
p2	Length of pump pulse	16 ns as a first guess.
d0	Acquisition trigger offset	~360 ns
d1	Interpulse delay τ_1	Time of the first maximum in the Two-Pulse ESEEM trace, herein 232 ns.
d2	Interpulse delay τ_2	Set it to a length with enough signal intensity, ~3,000-4,000 ns in this case.
SRT	Shot-Repetition-Time	3,000 * srtu (with srtu = 1.02 µs).
h	Number of Shots per Point	10
m	Number of steps for nuclear modulation averaging	8
d30	Time increment for the trace	8 ns
d31	Time increment for nuclear modulation averaging	16 ns
d3	Instrument-related dead time delay	Typically ~100 ns

Note that the PELDOR experiment is tolerant toward variation of these parameters within certain ranges. However, setting completely improper parameters will result in a poor SNR, a low modulation depth, and data distortion.

iii. Click "Compile," "Show Program," and "Validate" in this order.

iv. Select the "2P ESE Setup" experiment. Press the "Run" button in the main window, click "Start" in SpecJet and in the Pulse Tables, and lower the "Attenuation" to 0 dB.

v. Open the "MPFU control"-tab. Drag the "< +x > Amplitude" slider bar to a level of ~60-70% to maximize the Hahn echo amplitude in SpecJet.

vi. Adjust the global MW phase using the "Signal Phase" slider bar in the FT bridge window. The MW phase should be adjusted such that the signal appears in the real channel of SpecJet and the imaginary channel should be zero on average.

b. Apply the pump pulse to invert the echo and determine the optimal pump pulse length.

i. Click "Stop" in the Pulse Tables and in SpecJet.

ii. Select the "3P ELDOR Setup" experiment, set the "Current ELDOR Frequency" to the current spectrometer frequency (~33.7 GHz), and press the "Run"-button in the main window. **Write down** the "Current ELDOR Frequency" for later use.

iii. Read off the time at which the maximum of the echo occurs in the viewport (Figure 7A, *e.g.*, 72 ns), add it to d0, and set the new value of d0 (*e.g.*, 432 ns) in PulseSPEL. Press "Run" in the main window; the echo should now be maximal at the zero-time on the abscissa in the view port (Figure 7B).

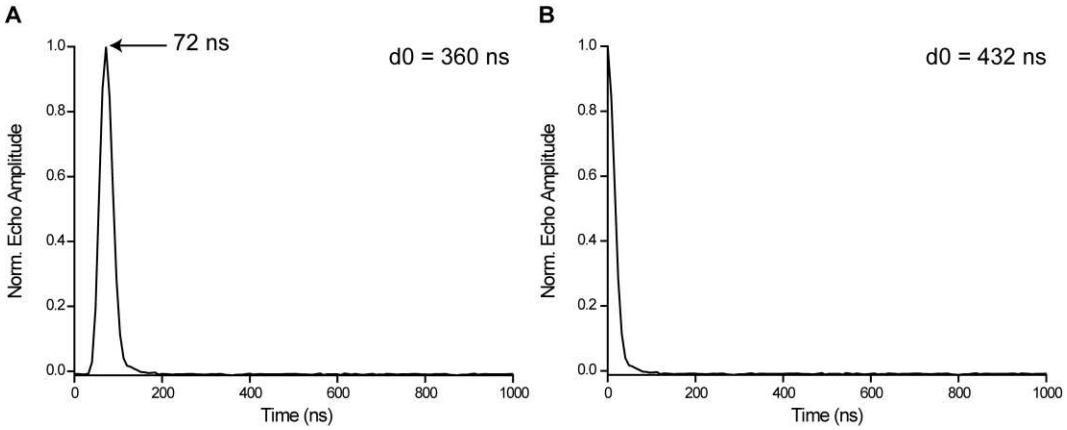

Figure 7. Adjustment of the echo position on the time axis by changing the PulseSPEL variable d0. A. d0 = 360 ns, the echo maximum is located at 72 ns. B. d0 = 432 ns, the echo maximum coincides with the origin of the abscissa.

iv. Start SpecJet. Decrease the "ELDOR Attenuation" to 0 dB, which should invert the Hahn echo (Note 9a-d).

v. Click "Stop" in SpecJet and in the Pulse Tables window. Select the "3P ELDOR Nutation" experiment and press "Run" in the main window; this experiment increments the pump pulse length and measures the amplitude of the Hahn echo. Read off the pump pulse length that leads to the global minimum of the nutation trace and set this value as the parameter p2. Typically, and depending on the sample, optimal pump pulse lengths between 12 ns and 18 ns are obtained (Note 9e).

vi. Set the "Attenuation" to 60 dB, the "ELDOR Attenuation" to 30 dB, and switch the TWT amplifier into the **Standby** mode. Set the MW Bridge into the "CW"-mode.

c. Change the MW frequency and optimize the Hahn echo at the probe frequency.

i. Open the "MW Bridge Tuning Dialog Box" and change the spectrometer frequency by the desired offset (*e.g.*, -80 MHz with respect to the pump frequency) using the "Frequency Slider."

ii. Perform the safety check as described in the instrument manual and switch the TWT into the Operate mode.

iii. Select the "2P ESE Setup" experiment, the phase cycle option "< + x > none", and press "Run" in the main window.

iv. Click "Start" in the Pulse Tables window, "Run" in SpecJet, and decrease the "Attenuation" to 0 dB in steps of 10 dB.

v. Drag the "< + x > Amplitude" slider bar in the MPFU control window to maximize the echo amplitude. Adjust the "< + x > Phase" such that the signal has a negative sign in the real channel. The imaginary channel should be zero on average.

vi. Select the "< - x > none" phase cycle option and again click "Run" in the main window. Adjust the "< - x > Amplitude" slider bar to maximize the Hahn echo. Drag the "< - x > Phase" slider such that the signal has a positive sign in the real channel. The imaginary part of the signal should be zero on average.

vii. Make sure that the *absolute* echo amplitudes obtained with the phase cycle options "< + x > none" and "< - x > none" are equal.

d. Choose the length of the dipolar evolution window τ_2.

i. The length of the interval τ_2, *i.e.*, the length of the PELDOR time trace, is governed by two aspects, namely transverse electron spin relaxation and the inter-spin distance to be resolved. Transverse electron spin relaxation dictates the maximum of the dipolar evolution window, this can be read off the Hahn echo decay curve recorded in Step B5. The minimal length of τ_2 is given by the need to resolve at least 1.5 dipolar oscillations encoding the most probable distance in the sample for reliable data analysis.

ii. If you have prior knowledge of the expected inter-spin distance (*e.g.*, from *in silico* spin labeling), compute the expected oscillation period and set τ_2 accordingly to resolve at least 1.5 oscillations in the time trace.

iii. If there is no information available on the expected distance, choose a value for τ_2 according to the Hahn echo decay curve. Set τ_2 to a value at which sufficient signal intensity is still left in the Two-Pulse ESEEM-trace. If you later realize that a longer dipolar evolution time window is needed to resolve 1.5 oscillations, abort the PELDOR run, increase τ_2, and re-start the measurement. Note that artefacts may occur at the end of the time trace, which have to be cut off later (see section on Data analysis). Take this into account and hence increase τ_2 sufficiently.

iv. Set the chosen value for τ_2 in PulseSPEL and activate it by clicking "Compile," "Show Program," and "Validate." Depending on the length of the time trace, consider increasing or decreasing the time increment d30. Find a trade-off between a sufficiently high resolution of the dipolar oscillations and acceptable measurement times (Note 10).

e. Optimize the refocused Hahn echo.

i. Set the "ELDOR Attenuation" to 0 dB.

ii. Select the "4P DEER Setup" program with the phase cycle option "2-step". Click "Run" in the main window, "Start" in the Pulse Tables window, and "Run" in SpecJet.

iii. Set the "No. of Averages" in SpecJet to 1.

iv. Increase the "Video Gain" amplification such that the echo fills the whole display of SpecJet without clipping at the top or bottom edge.

v. In SpecJet, set the "No. of Averages" to a higher value (100-1,000) such that the echo can be recognized clearly. Depending on the number of transient averages to accumulate, this may take a while.

vi. Press "Run" in the main window to transfer the echo from SpecJet into the viewport. Read off the time position at which the echo is maximal.

vii. Set the integration gate width (parameter pg in PulseSPEL) to the length of the longest pulse in the PELDOR sequence, most likely the π-pulse at the probe frequency.

viii. Adjust the acquisition trigger offset d0 such that the echo maximum is located at the center of the integration gate. Example: Assume that the refocused echo, recorded with d0 = 360 ns, peaks at 72 ns (Figure 8A). The integration gate length should be 24 ns starting at the zero-point of the time axis (grey rectangle in Figure 8B). Thus, in order to transfer the echo maximum to the position of 12 ns, set the acquisition delay d0 = 360 ns + (72 - 12) ns = 420 ns.

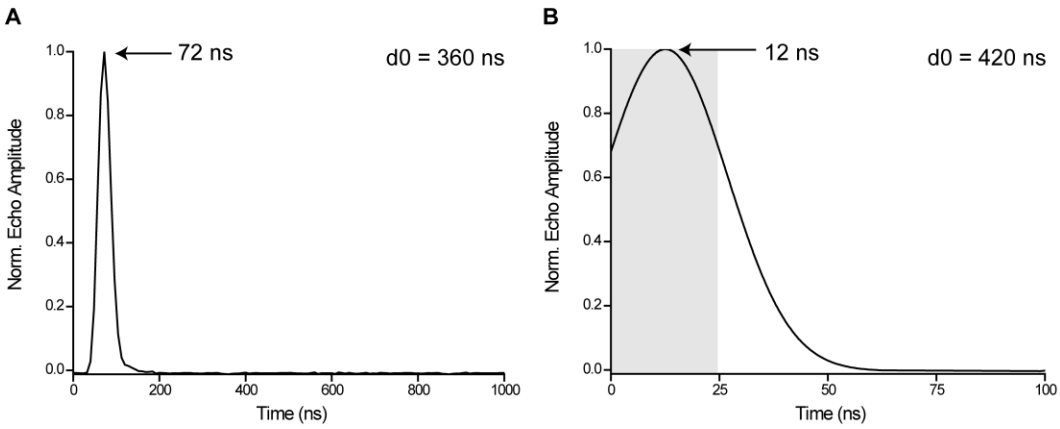

Figure 8. Adjustment of the echo position by changing the PulseSPEL variable d0. A. d0 = 360 ns, the echo maximum is located at 72 ns. B. d0 = 420 ns, the echo peaks at 12 ns. The grey rectangle indicates the integration gate width of 24 ns for the PELDOR experiment.

ix. Click "Run" in the main window and check proper positioning of the echo.

f. Run the PELDOR experiment.

i. Calculate the number of points to be recorded on the PELDOR time trace and set it as the parameter dim5 in the PulseSPEL program. It is given by:

$$\text{dim5} = \frac{\text{d1+d2-2d3}}{\text{d30}}$$

with the interpulse delays d1 and d2 of the PELDOR sequence (τ_1 and τ_2 in Figure 6), the dead-time delay of the spectrometer d3, and the time increment d30.

ii. Select the "4P DEER" experiment and the 2-step phase cycle from the dropdown menu and click "Run" in the main window. Click the "Re/Im"-button in the main window toolbar

Please cite this article as: Vicino *et al.*, (2021). Spin Labeling of RNA Using "Click" Chemistry for Coarse-grained Structure Determination via Pulsed Electron-electron Double Resonance Spectroscopy. *Bio-protocol* 11(9): e4004. DOI: 10.21769/BioProtoc.4004.

to display the imaginary channel and make sure that it is flat and around the zero level. Change the MW phase accordingly, if there is an appreciable amount of signal in the imaginary channel.

iii. Set a sufficiently high number of scans (50-1,500) to achieve a good SNR. The SNR can be defined as the modulation depth divided by the standard deviation of the noise and should amount to at least 20 or better 100 to permit reliable data analysis. Determination of the SNR can be achieved using *e.g.*, the program SnrCalculator. Depending on the spin concentration, the length of the time trace, and the chosen frequency offset, acquisition times between 4 h and 48 h are usual (Note 10).

iv. As the measurement has finished, save the data on disk in the standard Bruker BES3T-format (.DTA / .DSC-files).

A summary of all key steps described above is shown in Figure 9.

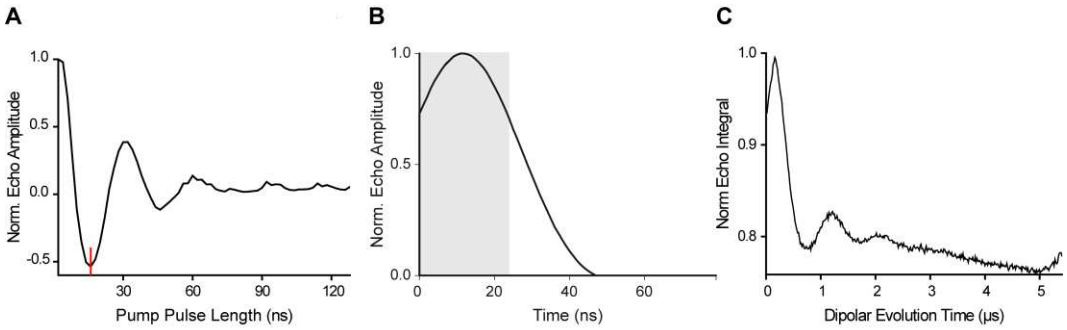

Figure 9. Synopsis of the key steps for setting up a PELDOR experiment. A. Transient nutation experiment. The optimal pump pulse length that leads to a maximal inversion of the echo is given at the global minimum of the trace and marked by a red line. B. Refocused Hahn echo. The integration gate has a length of 24 ns and is indicated by the grey shaded area. C. Raw PELDOR time trace as obtained from the spectrometer prior to data processing.

7. Switch the TWT into the **Standby** mode. Set the "Attenuation" to 60 dB and the "ELDOR Attenuation" to 30 dB. Switch the microwave bridge into the "CW"-mode and then to "**Standby**".
8. If the RNA strand and the spin label are rigid, as is the case here and in Wuebben *et al.*, 2020, orientation selection can occur, *i.e.*, not all orientations of the inter-spin vector with respect to the external magnetic field are sampled in one pair of pump and probe frequency. Orientation selection manifests itself in the PELDOR time traces by the dipolar oscillations becoming dependent on the microwave frequency offset Δv. Moreover, the Fourier-transform of the time traces no longer displays the whole Pake pattern.

   Regarding data acquisition, two approaches exist to cope with orientation selection. Firstly, the PELDOR experiment can be performed at the frequency offset with minimal orientation selection; in our hands, this is achieved by applying the pump pulse at the maximum of the nitroxide spectrum and the probe pulses at an offset of -80 MHz with respect to ν_{pump}.

   Secondly, PELDOR measurements can be performed at different combinations of ν_{pump} and

ν_{probe}. This approach also offers the possibility to take the orientational selectivity explicitly into account during data analysis (see section on Data analysis; Wuebben *et al.*, 2019).

If you opt for the latter approach, repeat this protocol from Step B6c, now using another offset between ν_{pump} and ν_{probe} (Figure 10). It is recommended to perform orientation-selective measurements on a particular sample directly one after another and not to remove the sample in between. Thus, the tuning and the sample positioning within the resonator will be equal for all offsets and no changes in spectrometer sensitivity will affect the data quality.

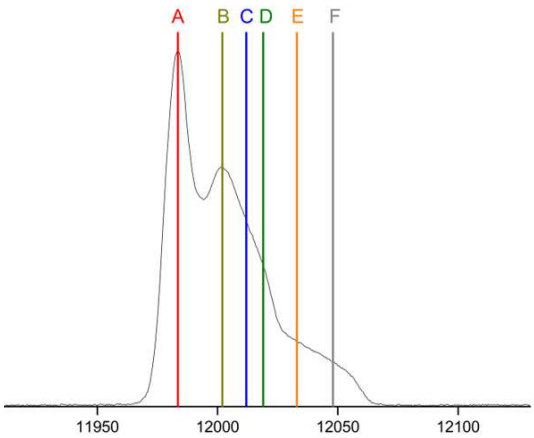

Pump position	Probe position	Δν (MHz)
A	B	60
A	C	80
A	D	100
B	E	120
A	F	180

Figure 10. Echo-detected field-swept EPR spectrum with the positions of the pump pulse and the probe pulses indicated for different frequency offsets Δv

9. If all measurements on a particular sample have been performed, switch off the membrane pump, wait for the needle of the gasflow controller to drop to zero, and remove the sample rod.
10. At this point, one can either perform PELDOR measurements on another sample, or completely switch off the spectrometer as described in the instrument manual.
    Note: It is good practice to perform the PELDOR experiment on two to three independently prepared samples to ensure data reliability and reproducibility.

Data analysis

1. If a single PELDOR time trace has been recorded at the frequency offset showing the least orientational selectivity (Δv = 80 MHz, in our hands), perform data analysis starting at point 3.
2. If PELDOR data have been collected at different combinations of pump and probe positions (Figure 11A), pre-process the time traces in the following way: Divide the raw data recorded at the different offsets by the respective number of scans. Afterwards, sum up all traces and save the result for further processing (Figure 11B). In this way, orientation selection is minimized. This step can be performed either with the data processing tools in the Xepr-software or, more

Please cite this article as: Vicino *et al*., (2021). Spin Labeling of RNA Using "Click" Chemistry for Coarse-grained Structure Determination via Pulsed Electron-electron Double Resonance Spectroscopy. *Bio-protocol* 11(9): e4004. DOI: 10.21769/BioProtoc.4004.

conveniently if many traces are to be processed, a home-written Matlab-script.

Alternatively, and to obtain additional angular information on the orientation of the spin label with respect to the external magnetic field, the program PeldorFit can be used (Abdullin *et al*., 2015).

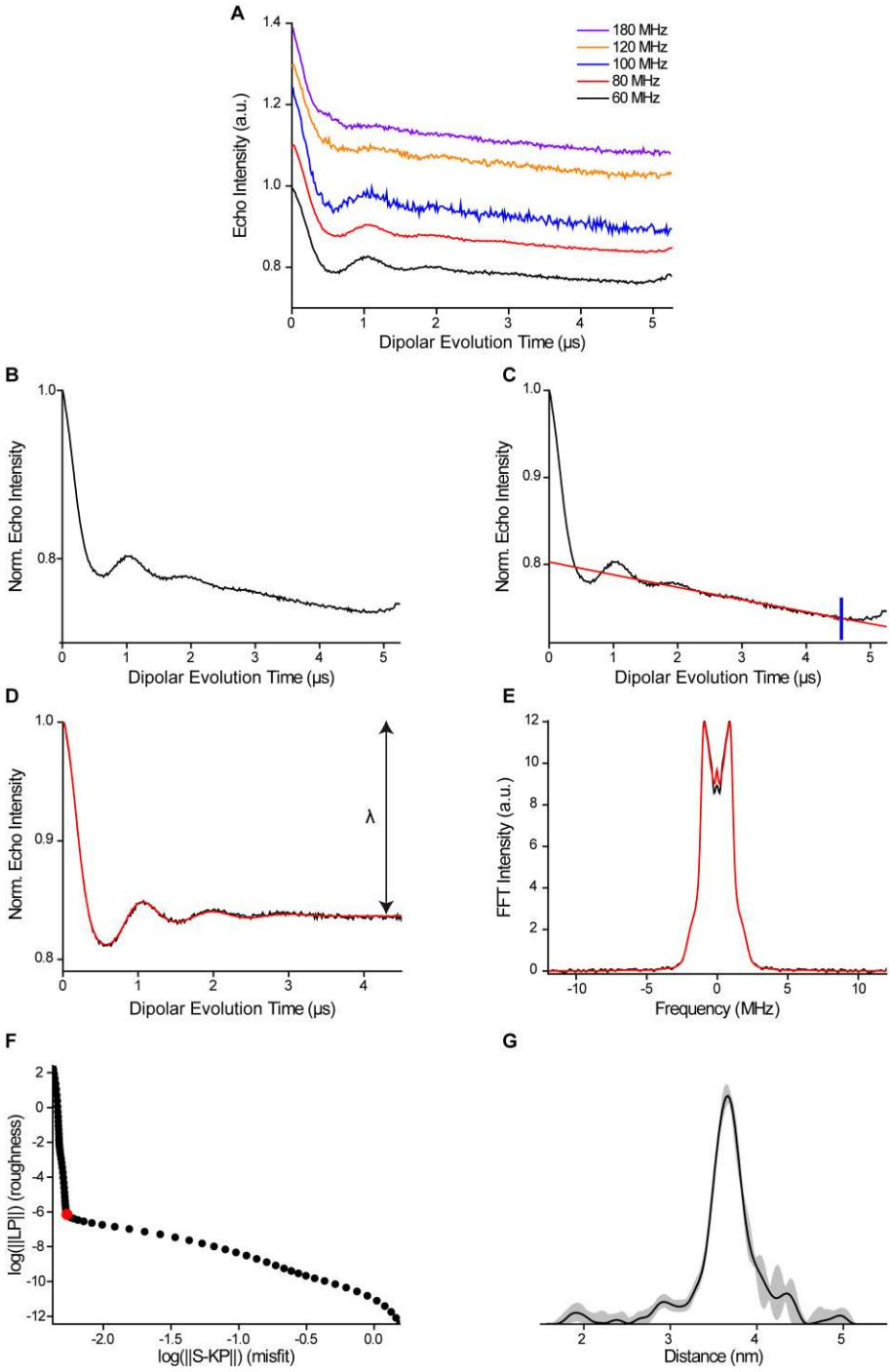

Figure 11. Analysis of orientation-selective PELDOR data. A. Time traces obtained at different offsets between the pump and observer frequency. B. Time trace obtained by summation of the traces shown in (A). C. Time trace from (B) with a background fit indicated as a red line. The cut-off to remove the artefact at the end of the trace is shown in blue. D.

Background-corrected time trace with a fit obtained by Tikhonov regularization in red. The arrow indicates the modulation depth λ. E. Pake pattern obtained by Fourier transformation of (D). F. L-curve with the regularization parameter used for computing the distance distribution highlighted in red. G. Distance distribution with the background validation shown as grey shading.

3. Start Matlab. In Matlab, click the "Set Path" button and import the DeerAnalysis folder including its subfolders into Matlab. Click "Save," "Close," and then start DeerAnalysis via the command line by entering "DeerAnalysis." For more detailed instructions, consult the manual and the original publication on DeerAnalysis (Jeschke *et al.*, 2006).
4. In DeerAnalysis, click the "Load" button, which is located on the right of the window. Select the file containing the PELDOR time trace without orientation selection (either .dat in ASCII-format or .DTA/.DSC in BES3T-format). If you use the BES3T-format, make sure that the .DTA and .DSC-files are both located in the same folder.
5. Adjust the parameters for raw data processing using the interfaces in the top left corner of the graphical user interface (GUI). Set the zero-time to the maximum of the time trace by clicking the "+" and "-" -buttons or by directly entering a value. Perform a phase correction such that the imaginary part of the dataset is flat and approximately zero. As a starting point, click the "!"-button associated with the phase-correction option.
6. Set the cut-off parameter to remove artefacts at the end of the time trace (Figure 11C). These artefacts, mostly related to overlap of the pump pulse and the refocusing pulse, manifest themselves by a sudden rise in signal at the end of the trace.
7. Apply a background fit to remove the intermolecular part of the dipolar coupling. Select the 3D-homogeneous background model in the center panel of the GUI. This background model is based on the function $B(t) = e^{-kt^{d/3}}$ with the density of spins, k, and the dimensionality of the homogeneous distribution, d (Jeschke *et al.*, 2006). Click the "!"-button to auto-optimize the time value for the background start. Inspect the quality of the background correction in the time and frequency domain: In the time domain, the trace should be flat at long dipolar evolution times (Figure 11D). In the frequency domain, the Fourier-transform should have the shape of a Pake pattern and should neither show a deep hole nor a sharp spike at the zero-frequency (Figure 11E). If you identify any of these deficits, change the value for the background start to improve background correction. If you are still unsuccessful, consider changing the background model, *e.g.*, by altering the dimensionality or by selecting a polynomial background.
8. After background correction, select the "Tikhonov" option in the "Distance analysis"-panel on the right in the GUI and tick the "L-curve" checkbox. Click the "Compute"-button and wait for the L-curve to appear in the GUI (Figure 11F). The L-curve provides a method for solving the ill-posed problem of translating the PELDOR time trace into a distance distribution and permits choosing the regularization parameter for Tikhonov regularization. In the L-curve plot, the abscissa represents the deviation of the fitted time trace from the experimental data and the

ordinate indicates the roughness of the resulting distance distribution, both shown on a logarithmic scale. Various criteria can be applied to determine the optimal regularization parameter, *e.g.*, the L-curve corner criterion (Lc), the Generalized Cross Validation criterion (GCV), and the Akaike Information Criterion (AIC). Usually, selecting a regularization parameter close to the corner of the L-curve is a good choice. Uncheck the "L-curve" tick-box above the plot to display the distance distribution.

9. In order to test for the influence of background removal on the distance distribution (Figure 11G), call the validation routine of DeerAnalysis by clicking the "Validation"-button. Adjust the validation range for the selected parameters and press the "Compute"-button. As the computation has finished, the ensemble of background fits, background-corrected time traces with their respective fits, and distance distributions will be shown. The background-corrected time trace that has the best fit at the selected regularization parameter can be displayed by clicking the "!"-button in the "Parameter set selection" in the center of the GUI. Choose one of the provided parameter sets and click the "Close"-button to quit the validation window. The selected dataset is then transferred into the main window with the distance distribution shown as a bold black line. The uncertainty analysis as obtained from the validation routine is shown as a grey shaded area.
10. Save the results by clicking the "Save" button. This generates ASCII-files containing the raw data with the background fit ("*_bckg.dat"), the background-corrected trace and its fit ("*_fit.dat"), the dipolar spectrum ("*_spc.dat"), the distance distribution ("*_distr.dat"), and the L-curve ("*_Lcurve.dat"). A summary of data processing including all parameters specified above will be written to the file ("*_res.txt").
11. Apart from Tikhonov regularization, DeerAnalysis provides further methods for transforming the dipolar trace into a distance distribution. A rather fast but less elaborate approach is Approximate Pake Transformation (APT), which is used to obtain a first guess of the distance distribution upon loading the time trace. Distance distributions obtained from APT should be regarded as preliminary results only. The DeerNet (Worswick *et al.*, 2018) feature analyzes the time trace using trained neural networks and performs background-correction and translation from the time domain into the distance domain in one step. An advantage of DeerNet is the lack of user interference, *i.e.*, no manual background correction and no choice of a regularization parameter is required. This increases reproducibility of data analysis and prevents data bias, especially in terms of background uncertainty. In addition to these generic analysis methods, parametrized models assuming, *e.g.*, a Gaussian-shaped distance distribution or a random coil, can be used. In this context, DeerAnalysis also permits constructing and implementing user-defined models. For other programs for data analysis, see Note 11.
12. Plot the results in your preferred data visualization program (*e.g.*, Origin, SciDAVIS, Matlab, Excel, *etc.*).
13. Apart from the inter-spin distance, the time trace provides further information on the sample, which should be taken into account for data interpretation: The time trace can be analyzed with

respect to the modulation depth (number of coupled spins in a molecule), the background decay (sample concentration and homogeneity), and the signal-to-noise ratio (quality of sample/measurement). The distance distribution can be analyzed in terms of the most probable and mean distances, the width, the modality, and the shape of the distribution. Any features of the distribution to be interpreted must not vanish in the validation. Especially if the shape of the distribution and, *e.g.*, shoulders are to be interpreted, the PELDOR data should be of high quality, should be reproducible, and additional evidence obtained from independent techniques should be taken into account.

14. Transform your PELDOR-derived distance distribution into a coarse-grained structural model. From the PELDOR measurement, the distance between the spins of the two unpaired electrons is obtained. In order to transform this inter-spin distance into structural information, *in silico* spin labeling programs such as, *e.g.*, mtsslWizard, MMM, or the GFN/FF-based CREST-MD, can be used. Based on the structure of the biomolecule, which can either be taken from databases or modeled *in silico*, these programs generate rotamer ensembles of the spin label and further compute an inter-spin distance distribution. Comparing this *in silico* distribution with the PELDOR-derived one, permits, *e.g.*, refining an existing structural model, monitoring conformational changes, and docking subunits or parts of biomolecular complexes (Duss *et al.*, 2014; Peter *et al.*, 2019). In this regard, it is advisable to record PELDOR data on several constructs of a biomolecule using different labeling positions. Alternatively, the distance between an anchor point, *e.g.,* a spatially fixed metal ion, and various labeling sites can be measured, thus permitting location of the metal ion within the fold of the biomolecule by trilateration (Abdullin *et al.*, 2014). Moreover, the geometry of multimeric biomolecular complexes, and thus the assembly of the subunits, has been reconstructed from distance measurements (Hagelueken *et al.*, 2009; Pilotas *et al.*, 2012; Valera *et al.*, 2016).

    Especially for challenging systems, integrated structural biology has turned into a powerful tool: The combination of *e.g.*, FRET, cryo-EM, NMR, X-ray, SAXS, and EPR allows a comprehensive view of the structure. These methods are complementary to each other, each providing pieces of information that can be assembled into a more detailed structural model. Figure 12 summarizes the approach of integrated structural biology and highlights the contribution of EPR spectroscopy.

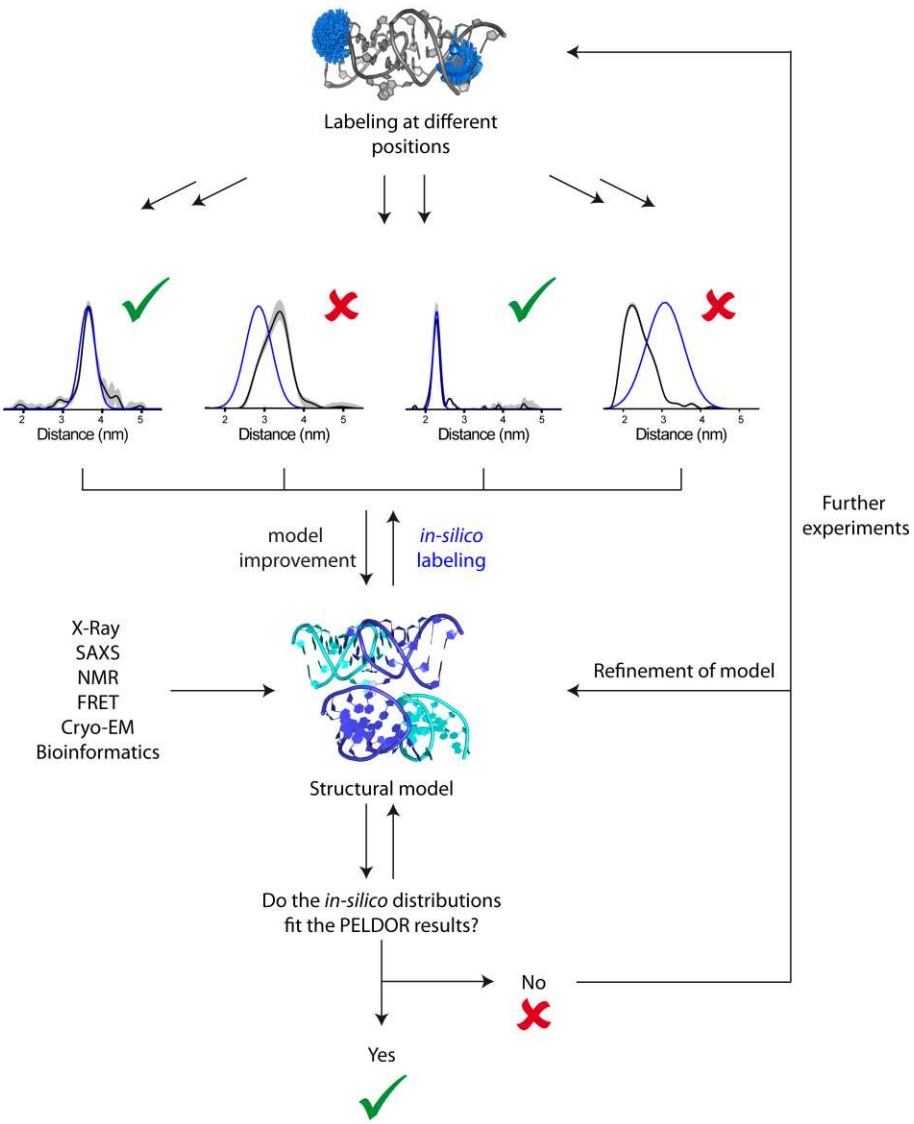

Figure 12. Integrative structural biology. Information from different biophysical methods is combined to a structural model of the biomolecule. Distance distributions derived *in-silico* from this model are compared with the experimental (PELDOR) ones. They can either match or deviate from each other: if the distributions match, the model is confirmed; if they deviate, further experiments are needed as well as refinement of the model.

Notes

1. Usually, two labeling reactions can be performed in parallel (in separate Eppendorf tubes), each containing 2.5 nmol RNA. The reaction can be scaled-up to 5 nmol RNA in one Eppendorf tube and in principle, more than 5 nmol RNA (in one Eppendorf tube) should also work. However, when scaling up, you may need to adjust the reaction conditions, *e.g.*, reaction temperature and time. This is also important for each new RNA oligonucleotide sequence you start working with.
2. It is very important that the complexation of Cu^{+} with THPTA takes place immediately after

dissolving CuI in DMSO, when the solution still has a yellow color. Cu^{+} is very prone to oxidation by atmospheric oxygen (Hein and Fokin, 2010; Chandrasekaran, 2016) and the formation of Cu^{2+} in solution can be monitored by the solution's color: It changes from light to dark yellow when CuI is completely dissolved and turns dark green and finally brown within 5 to 10 min. At this stage, the solution should not be used.

3. The reaction time needs to be determined individually for each new RNA oligonucleotide. For this, it is recommended to perform a labeling reaction and take samples of 1 or 2 µl every 5 to 10 min. After desalting these samples via an Amicon Ultra centrifugal filter device, you can analyze the reaction progress via HPLC, as described in the procedure Step A5.
4. EG-d_6 acts as a glass-forming agent, *i.e.*, the frozen sample is homogenous. The glass state and the deuterated matrix prolong the phase-memory time of the electron spins, permitting longer dipolar evolution time windows in the PELDOR experiment. Note that some biomolecules can bind or interact with the cryoprotectant (Vagenende *et al*., 2009; Schmidt *et al*., 2020). Both the cryoprotectant itself and the ratio of the cryoprotectant and the biomolecule have to be optimized for each individual case. As an alternative to EG-d_6, deuterated glycerol (glycerol-d_8) or trehalose can be used.
5. If the temperature does not stabilize at 50K or does not drop at all, address the following points in the given order:
   a. Check the fill level of the helium tank.
   b. Check that all tubing has been connected tightly to the right ports of the membrane pump, the gasflow controller, and the transfer line. Make sure that the helium recovery port is open.
   c. Make sure that the transfer line is permeable and not blocked *e.g.*, with ice.
   d. If the temperature is unstable, make sure that the gasflow amounts to ~1 L/h; much higher or lower flow rates can lead to temperature instabilities. Moreover, check the vacuum within the transfer line insulation and, if necessary, evacuate the transfer line.
6. Use a small Dewar vessel to cool the EPR tube. In this way, the lower part of the tube can be immersed in the liquid nitrogen, whereas the upper part of the sample rod is outside the coolant. This minimizes the transfer of liquid nitrogen into the cryostat and can prevent difficulties when overcoupling the resonator and removing the EPR tube after the measurement.
7. If the tuning is unstable, check the following points:
   a. Is the microwave frequency stable? MW frequency instabilities can occur if the electric components were not given enough time to warm up. Moreover, make sure that the cooling water entering the microwave bridge is not too warm (<15°C).
   b. Are the sample and the cryostat in thermal equilibrium and is the temperature stable? After inserting the EPR tube, wait at least 20 min before starting the measurement.
   c. If the resonator tuning dip starts moving without any changes being made to the spectrometer, nitrogen may have condensed in the cryostat. In this case, remove the sample, warm up the cryostat to ~120K for at least 20 min, and re-start from Step B1l. If the problem cannot be solved, warm up the cryostat to room temperature and blow a stream of

nitrogen gas through the resonator overnight.

8. If no echo is seen, try the following steps:
   a. Double-check the parameters such as MW frequency, Center Field, and pulse lengths *etc.*
   b. Make sure that SpecJet displays enough points to detect the echo at all.
      If the Hahn echo amplitude does not cross a maximum when stepwise reducing the attenuation to 0 dB, consider the following aspects:
      i. Check the over-coupling of the resonator. Make sure that the "real" resonator tuning dip is in the center of the MW Bridge Tuning Dialog Box. Especially, make sure to center the "real" dip in the window and not the "fake" dip.
      ii. The MW power may not be sufficient to achieve π/2 and π-pulses at the given pulse lengths. Increase the pulse lengths (*e.g.*, to π/2 = 16 ns and π = 32 ns) and again try to optimize the Hahn echo.
9. If no inversion of the echo can be observed or if the transient nutation experiment reports an optimal pump pulse length greater than 18 ns, address the following points:
   a. Make sure that the "Current ELDOR Frequency" has been properly set, *i.e.*, to the current spectrometer frequency.
   b. Check that the pump pulse length (p2 in the PulseSPEL program) is between 12 ns and 18 ns.
   c. Make sure that the "ELDOR Attenuation" has been set to 0 dB.
   d. Check the tuning and make sure that the tuning dip is centered in the "MW Bridge Tuning Dialog Box" *i.e.*, that the MW frequency coincides with the resonance frequency of the cavity.
   e. Unexpectedly long pump pulse lengths determined from the transient nutation experiment may indicate condensation of liquid nitrogen in the cryostat. See Notes 6 and 7c.
10. The approximate duration of a PELDOR measurement is given by:

$$\text{Duration} = \text{SRT} \cdot \text{PC} \cdot \text{m} \cdot \text{h} \cdot \text{n} \cdot \text{dim5}$$

    with the shot-repetition-time SRT, the number of phase cycling steps PC (usually 2), the number of nuclear modulation averaging steps m (usually 8), the number of shots per point h, the number of scans to accumulate n, and the number of points to record on the trace dim5.
11. Apart from the commonly used DeerAnalysis software for translating the PELDOR time trace into a distance distribution, further programs for this task have been published. A selection of these is given below:
    DeerLab (Fábregas Ibáñez *et al.*, 2020)
    LongDistances (Altenbach, C.; https://sites.google.com/site/altenbach/labview-programs/epr-programs/long-distances)
    GLADD/DD (Brandon *et al.*, 2012)
    DIPFIT (Steinhoff *et al.*, 1997)

Recipes

1. DEPC-treated water
   Add 0.1-0.2 ml DEPC to 100 ml Milli-Q water, incubate overnight in the fume hood
   Due to CO_2-formation, the bottle should not be tightly closed
   Finally, autoclave the solution to remove the remaining DEPC

Acknowledgments

Funding via the University of Bonn (TRA-2) and the DFG (Reinhart Koselleck grant, Projektnummer 420322655) is gratefully acknowledged.
The protocol is based on the following original research papers:
Wuebben, C., Vicino, M. F., Mueller, M. and Schiemann, O. (2020). Do the P1 and P2 hairpins of the Guanidine-II riboswitch interact? *Nucleic Acids Res.* 48(18): 10518-10526.
Wuebben, C., Blume, S., Abdullin, D., Brajtenbach, D., Haege, F., Kath-Schorr, S. and Schiemann, O. (2019). Site-Directed Spin Labeling of RNA with a Gem-Diethylisoindoline Spin Label: PELDOR, Relaxation, and Reduction Stability. *Molecules* 24(24): 4882.
Kerzhner, M., Matsuoka, H., Wuebben, C., Famulok, M. and Schiemann, O. (2018). High-Yield Spin Labeling of Long RNAs for Electron Paramagnetic Resonance Spectroscopy. *Biochemistry* 57(20): 2923-2931.

Competing interests

No competing interests to declare.

References

1. Abdullin, D., Florin, N., Hagelueken, G. and Schiemann, O. (2014). EPR-Based Approach for the Localization of Paramagnetic Metal Ions in Biomolecules. *Angew Chem Int Ed* 54: 1827-1831.
2. Abdullin, D., Hagelueken, G., Hunter, R. I., Smith, G. M. and Schiemann, O. (2015). Geometric model-based fitting algorithm for orientation-selective PELDOR data. *Mol Phys* 113(6): 644-560.
3. Beaucage, S. L. and Radhakrishman, P. I. (1992). Advances in the Synthesis of Oligonucleotides by the Phosphoramidite Approach. *Tetrahedron* 48: 2223-2311.
4. Brandon, S., Beth, A. H. and Hustedt, E. J. (2012). The global analysis of DEER data. *J Magn Reson* 218: 93-104.
5. Chandrasekaran, S. (Ed.) (2016). Click Reactions in Organic Synthesis. ISBN: 978-3-527-33916-7. John Wiley & Sons, Inc, Weinheim, Germany.
6. Dastvan, R., Mishra, S., Peskova, Y., Nakamoto, R. K. and Mchaourab, H. S. (2019).

Mechanism of allosteric modulation of P-glycoprotein by transport substrates and inhibitors. *Science* 364(6441): 689-692.

7. Duss, O., Michel, E., Yulikov, M., Schubert, M., Jeschke, G. and Allain, F. H.-T. (2014). Structural basis of the non-coding RNA RsmZ acting as a protein sponge. *Nature* 509(7502): 588-592.
8. Fábregas Ibáñez, L., Jeschke, G. and Stoll, S. (2020). DeerLab: a comprehensive software package for analyzing dipolar electron paramagnetic resonance spectroscopy data. *Magn Reson* 1(2): 209-224.
9. Fleck, N., Heubach, C. A., Hett, T., Haege, F. R., Bawol, P. P., Baltruschat, H. and Schiemann, O. (2020). SLIM: A Short-Linked, Highly Redox-Stable Trityl Label for High-Sensitivity In-Cell EPR Distance Measurements. *Angew Chem Int Ed* 59(24): 9767-9772.
10. Geffroy, L., Mangeol, P., Bizebard, T. and Bockelmann, U. (2018). RNA Unzipping and Force Measurements with a Dual Optical Trap. In: Peterman, E. (Ed.) Single Molecule Analysis. Methods in Molecular Biology, vol. 1665, pp. 25-41, Humana Press, New York.
11. Goldfarb, D. and Stoll, S. (Eds.) (2018). EPR spectroscopy: Fundamentals and methods. EMagRes Books. ISBN: 978-1-119-16298-8. John Wiley & Sons Ltd, Chichester, West Sussex.
12. Hagelueken, G., Ingledew, W. J., Huang, H., Petrovic-Stojanovska, B., Whitfield, C., El Mkami, H., Schiemann, O. and Naismith, J. H. (2009). PELDOR Spectroscopy Distance Fingerprinting of the Octameric Outer-Membrane Protein Wza from *Escherichia coli*. *Angew Chem Int Ed* 48: 2904-2906.
13. Hagelueken, G., Abdullin, D. and Schiemann, O. (2015). mtsslSuite: Probing Biomolecular Conformation by Spin-Labeling Studies. *Methods Enzymol* 563: 595-622.
14. Hein, J. E. and Fokin, V. V. (2010). Copper-catalyzed azide-alkyne cycloaddition (CuAAC) and beyond: new reactivity of copper(I) acetylides. *Chem Soc Rev* 39(4): 1302-1315.
15. Jeschke, G. (2012). DEER distance measurements on proteins. *Annu Rev Phys Chem* 63: 419-446.
16. Jeschke, G., Chechik, V., Ionita, P., Godt, A., Zimmermann, H., Banham, J., Timmel, C. R., Hilger, D. and Jung, H. (2006). DeerAnalysis2006 – a comprehensive software package for analyzing pulsed ELDOR data. *Appl Magn Reson* 30 (3-4): 473-498.
17. Kerzhner, M., Abdullin, D., Więcek, J., Matsuoka, H., Hagelueken, G., Schiemann, O. and Famulok, M. (2016). Post-synthetic Spin-Labeling of RNA through Click Chemistry for PELDOR Measurements. *Chem Eur J* 22: 12113-12121.
18. Kerzhner, M., Matsuoka, H., Wuebben, C., Famulok, M. and Schiemann, O. (2018). High-Yield Spin Labeling of Long RNAs for Electron Paramagnetic Resonance Spectroscopy. *Biochemistry* 57(20): 2923-2931.
19. Kuzhelev, A. A., Krumkacheva, O. A., Shevelev, G. Y., Yulikov, M., Fedin, M. V. and Bagryanskaya, E. G. (2018). Room-temperature distance measurements using RIDME and the orthogonal spin labels trityl/nitroxide. *Phys Chem Chem Phys* 20(15): 10224-10230.
20. Liang, D., Wu, K., Tei, R., Bumpus, T. W., Ye, J. and Baskin, J. M. (2019). A real-time, click chemistry imaging approach reveals stimulus-specific subcellular locations of phospholipase D

activity. *PNAS* 116: 15453-15462.

21. Lottspeich, F. and Engels J. W. (Eds.) (2018). Bioanalytics: Analytical Methods and Concepts in Biochemistry and Molecular Biology. ISBN: 978-3-527-33919-8. Wiley-VCH, Weinheim, Germany.
22. Malygin, A. A., Krumkacheva, O. A., Graifer, D. M., Timofeev, I. O., Ochkasova, A. S., Meschaninova, M. I., Venyaminova, A. G., Fedin, M. V., Bowman, M., Karpova, G. G. and Bagryanskaya, E. G. (2019). Exploring the interactions of short RNAs with the human 40S ribosomal subunit near the mRNA entry site by EPR spectroscopy. *Nucleic Acids Res* 47(22): 11850-11860.
23. Nikić, I., Kang, J. H., Girona, G. E., Aramburu, I. V. and Lemke, E. A. (2015). Labeling proteins on live mammalian cells using click chemistry. *Nat Protoc* 10: 780-791.
24. Peter, M. F., Tuukkanen, A. T., Heubach, C. A., Selsam, A., Duthie, F. G., Svergun, D. I., Schiemann, O. and Hagelueken, G. (2019). Studying Conformational Changes of the Yersinia Type-III-Secretion Effector YopO in Solution by Integrative Structural Biology. *Structure* 27 (9): 1416-1426.
25. Pilotas, C., Ward, R., Branigan, E., Rasmussen, A., Hagelueken, G., Huang, H., Black, S. S., Booth, I. R., Schiemann, O. and Naismith, J. H. (2012). Conformational state of the MscS mechanosensitive channel in solution revealed by pulsed electron-electron double resonance (PELDOR) spectroscopy. *PNAS* 109 (40): E2675-E2682.
26. Polyhach, Y., Bordignon, E. and Jeschke, G. (2011). Rotamer libraries of spin labelled cysteines for protein studies. *Phys Chem Chem Phys* 13(6): 2356-2366.
27. El-Sagheer, A. H. and Brown, T. (2010). Click chemistry with DNA. *Chem Soc Rev* 39: 1388-1405.
28. Salas, D., Gocheva, V. and Nöllmann, M. (2015). Constructing a Magnetic Tweezers to Monitor RNA Translocation at the Single-Molecule Level. In: Boudvillain, M. (Ed.). RNA Remodeling Proteins. Methods in Molecular Biology, vol. 1259, pp. 257-273, Humana Press, New York.
29. Schiemann, O. and Prisner, T. F. (2007). Applications of electron paramagnetic resonance to distance measurements in biomolecules. *Quart Rev Biophys* 40: 1-53.
30. Schmidt, T., Wälti, M. A., Baber, J. L., Hustedt, E. J. and Clore, G. M. (2016). Long Distance Measurements up to 160 Å in the GroEL Tetradecamer Using Q-Band DEER EPR Spectroscopy. *Angew Chem Int Ed* 55: 15905-15909.
31. Schmidt, T., Jeon, J., Okuno, Y., Chiliveri, S. C. and Clore, G. M. (2020). Submillisecond Freezing Permits Cryoprotectant-Free EPR Double Electron-Electron Resonance Spectroscopy. *ChemPhysChem* 21: 1224-1229.
32. Schweiger, A. and Jeschke, G. (Eds.). (2001). Principles of pulse electron paramagnetic resonance. ISBN: 9780198506348. Oxford University Press, Oxford.
33. Shelke, S. A. and Sigurdsson, S. T. (2014). Site-Directed Nitroxide Spin Labeling of Biopolymers. *Struct Bond* 152: 121-162.
34. Spicher, S., Abdullin, D., Grimme, S. and Schiemann, O. (2020). Modeling of spin-spin distance

distributions for nitroxide labeled biomacromolecules. *Phys Chem Chem Phys* 22: 24282-24290.

35. Steinhoff, H. J., Radzwill, N., Thevis, W., Lenz, V., Brandenburg, D., Antson, A., Dodson, D. and Wollmer, A. (1997). Determination of interspin distances between spin labels attached to insulin: comparison of electron paramagnetic resonance data with the X-ray structure. *Biophys J* 73(6): 3287-3298.
36. Theillet, F.-X., Binolfi, A., Bekei, B., Martorana, A., Rose, H. M., Stuiver, M., Verzini, S., Lorenz, D., van Rossum, M., Goldfarb, D. and Selenko, P. (2016). Structural disorder of monomeric A-synuclein persists in mammalian cells. *Nature* 534: 45-50.
37. Tsvetkov, Y. D., Bowman and M., Grishin, Y. (Eds.). (2019). Pulsed Electron-Electron Double Resonance. Nanoscale Distance Measurements in the Biological, Materials and Chemical Sciences. Springer, Berlin, Germany.
38. Vagenende, V., Yap, M. G. S. and Trout, B. L. (2009). Mechanisms of Protein Stabilization and Prevention of Protein Aggregation by Glycerol. *Biochemistry* 48(46): 11084-11096.
39. Valera, S., Ackermann, K., Pilotas, C., Huang, H., Naismith, J. H. and Bode, B. E. (2016). Accurate Extraction of Nanometer Distances in Multimers by Pulse EPR. *Chem Eur J* 22: 4700-4703.
40. Ward, R. J. and Schiemann, O. (2014). EPR-based Distance Measurements in Oligonucleotides. *Struct Bond* 152: 249-282.
41. Weber, R. T. (2005). ELEXSYS E580 user's manual. Bruker BioSpin Corporation, Billerica, USA.
42. Widder, P., Berner, F., Summerer, D. and Drescher, M. (2019). Double Nitroxide Labeling by Copper-Catalyzed Azide-Alkyne Cycloadditions with Noncanonical Amino Acids for Electron Paramagnetic Resonance Spectroscopy. *ACS Chem Biol* 14 (5): 839-844.
43. Worswick, S. G., Spencer, J. A., Jeschke, G. and Kuprov, I. (2018). Deep neural network processing of DEER data. *Sci Adv* 4: eaat5218.
44. Wuebben, C., Blume, S., Abdullin, D., Brajtenbach, D., Haege, F., Kath-Schorr, S. and Schiemann, O. (2019). Site-Directed Spin Labeling of RNA with a Gem-Diethylisoindoline Spin Label: PELDOR, Relaxation, and Reduction Stability. *Molecules* 24(24): 4882.
45. Wuebben, C., Vicino, M. F., Mueller, M. and Schiemann, O. (2020). Do the P1 and P2 hairpins of the Guanidine-II riboswitch interact? *Nucleic Acids Res* 48(18): 10518-10526.
46. Yang, Z., Liu, Y., Borbat, P., Zweier, J. L., Freed, J. H. and Hubbell, W. L. (2012). Pulsed ESR dipolar spectroscopy for distance measurements in immobilized spin labeled proteins in liquid solution. *J Am Chem Soc* 134(24): 9950-9952.

[P3]: Spatiotemporal resolution of conformational changes in biomolecules by combining pulsed electron-electron double resonance spectroscopy with microsecond freeze-hyperquenching

Reproduced with permission from

Tobias Hett†, Tobias Zbik†, Shatanik Mukherjee, Hideto Matsuoka, Wolfgang Bönigk, Daniel Klose, Christophe Rouillon, Norbert Brenner, Sebastian Peuker, Reinhard Klement, Heinz-Jürgen Steinhoff, Helmut Grubmüller, Reinhard Seifert, Olav Schiemann*, U. Benjamin Kaupp*, *J. Am. Chem. Soc.* **2021**, *143*, 6981-6989.
DOI: https://doi.org/10.1021/jacs.1c01081

† These authors contributed equally.
* Corresponding authors.

Contributions

- Performing all *cw* EPR and pulsed EPR experiments.
- Proposition of labelling sites *via in silico* labelling.
- Analysis and interpretation of EPR data including the deconvolution of PELDOR traces.
- Performing, analysing, and interpreting MD simulations.
- Interpretation of EPR and MD data in the framework of dwell times.
- Writing the first draft of the manuscript and major contributions in all steps of reviewing and editing the manuscript.

JACS
JOURNAL OF THE AMERICAN CHEMICAL SOCIETY

pubs.acs.org/JACS

Article

Spatiotemporal Resolution of Conformational Changes in Biomolecules by Combining Pulsed Electron−Electron Double Resonance Spectroscopy with Microsecond Freeze-Hyperquenching

Tobias Hett,[‡] Tobias Zbik,[‡] Shatanik Mukherjee, Hideto Matsuoka, Wolfgang Bönigk, Daniel Klose, Christophe Rouillon, Norbert Brenner, Sebastian Peuker, Reinhard Klement, Heinz-Jürgen Steinhoff, Helmut Grubmüller, Reinhard Seifert, Olav Schiemann,* and U. Benjamin Kaupp*

Cite This: *J. Am. Chem. Soc.* 2021, 143, 6981−6989

Read Online

ACCESS | Metrics & More | Article Recommendations | Supporting Information

ABSTRACT: The function of proteins is linked to their conformations that can be resolved with several high-resolution methods. However, only a few methods can provide the temporal order of intermediates and conformational changes, with each having its limitations. Here, we combine pulsed electron−electron double resonance spectroscopy with a microsecond freeze-hyperquenching setup to achieve spatiotemporal resolution in the angstrom range and lower microsecond time scale. We show that the conformational change of the C_α-helix in the cyclic nucleotide-binding domain of the *Mesorhizobium loti* potassium channel occurs within about 150 μs and can be resolved with angstrom precision. Thus, this approach holds great promise for obtaining 4D landscapes of conformational changes in biomolecules.

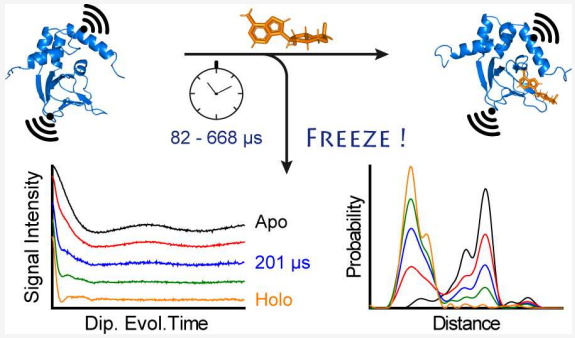

INTRODUCTION

The function of biomolecules is intimately linked to their structure and dynamics. Often, effector-triggered conformational changes are key to protein function. Membrane-spanning proteins such as G protein-coupled receptors or ion channels, which are particularly challenging for structural biology,[1,2] exist in active and inactive conformations. The transition between active and inactive form is triggered by ligand binding[3−6] or physical cues such as changes in membrane voltage,[7] absorption of light,[8,9] or mechanical forces.[10] These conformational changes happen on different length and time scales ranging from angstrom to nanometers, and picoseconds to seconds.[11] X-ray crystallography, NMR spectroscopy, and electron microscopy greatly advanced our knowledge about structures and their dynamics. Here, we introduce a combination of pulsed electron−electron double resonance spectroscopy (PELDOR or DEER)[12−14] with so-called microsecond freeze-hyperquenching (MHQ) as a complementary technique (MHQ/PELDOR) to achieve a 4D conformational landscape from the initial to the final conformational state with high spatiotemporal resolution.

PELDOR yields ensemble distributions of distances between electron-spin centers in frozen samples in the range of 1.5 to 16 nm with angstrom precision.[15] In biomolecules, spin centers can be introduced via site-directed spin labeling (SDSL) of, for example, cysteine residues in proteins by means of nitroxide spin labels.[16] Combining SDSL and PELDOR, the structures and conformational changes of large proteins,[12,17,18] oligonucleotides,[19−21] and protein/oligonucleotide complexes[22−26] have been studied in solution,[27,28] in membranes,[29−32] or even whole cells.[33−36] Although PELDOR provides information on the conformational ensemble present at the freezing point,[37,38] it is blind to the time scales and sequence of conformational events.

However, coupling SDSL/PELDOR with fast freeze-quench techniques[39] may permit taking snapshots along the trajectory of a conformational change and provide access to the time domain with temporal resolution only limited by the mixing and freezing kinetics. The time scale of protein dynamics ranges from femtoseconds for bond vibrations via nano- and microseconds for movements of α-helices and β-sheets, up to seconds or even hours for folding and assembly of multisubunit proteins.[11] Ligand-induced conformational changes are of particular interest, as they trigger important cellular reactions, and the rate-limiting steps are often unknown. To follow such movements in proteins, mixing and freeze-quenching should be completed within microseconds. While

Received: February 5, 2021
Published: April 27, 2021

typical freeze-quench setups operate on a millisecond time scale,[40,41] an MHQ device can reach minimal aging times of roughly 100 μs.[39] MHQ combined with continuous wave (CW) electron paramagnetic resonance (EPR) has been used to examine the binding kinetics of the azide/metmyoglobin system,[39] the lifetime of catalytic intermediates,[42−44] the refolding of cytochrome oxidases,[45] and the electron-transfer rates in the respiratory complex I.[46] Two previous studies have employed freeze-quench/PELDOR to test the distance distribution width with respect to the freezing time.[37,38] Ligand-activated conformational motions, however, have so far not been studied by MHQ, which extends the time scale from milli- to microseconds.

Here we study the ligand-induced conformational dynamics of the bacterial cyclic nucleotide-gated (CNG) K^+ channel from *Mesorhizobium loti* (MloK1), which opens by binding of cyclic adenosine monophosphate (cAMP) to a cyclic nucleotide-binding domain (CNBD).[47,48] Upon binding, the CNBD undergoes a conformational change, including a movement of the C-terminal C_α-helix (Figure 1). This

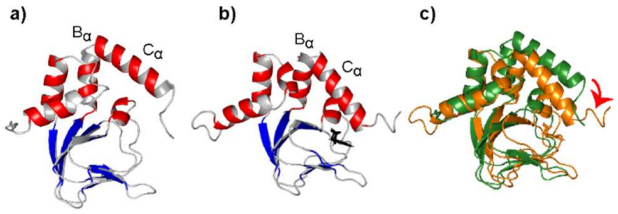

Figure 1. Structure of the CNBD of the MloK1 channel. (a) Structure of the ligand-free *apo* state (PDB-ID: 2kxl) and (b) the cAMP-bound *holo* state (PDB-ID: 2k0g). (c) Overlay of both structures (*apo* in green, *holo* in orange) illustrating the C_α-helix movement upon ligand binding (red arrow).

movement has been inferred from X-ray[49] and NMR[50,51] structures of the CNBD in its *apo* and *holo* states and has also been predicted by atomistic simulations.[52] A similar movement has been detected with PELDOR in a related hyperpolarization-activated and cyclic nucleotide-gated channel (HCN2)[53] and the bacterial CNG channel SthK.[54]

We will show that MHQ/PELDOR can resolve conformational changes of the MloK1 CNBD on the angstrom and low-microsecond time scale. In addition, placing spin labels at different sites in the CNBD can provide a 4D picture of a conformational change with amino-acid resolution.

EXPERIMENTAL SECTION

The MHQ device is based on a prototype reported by de Vries' group (Figure S1).[39] It consists of a rotating aluminum cold-plate, a vacuum hood, and two syringes connected by tubing to a four-jet tangential micromixer. The protein and ligand solutions are injected from syringes via tubing into the micromixer. The mixture is ejected from the micromixer as a free-flowing thin jet (diameter: 20 μm) that is freeze-quenched within microseconds on a rotating cold-plate. The micromixer is mounted on a robotic swivel arm that allows vertical and horizontal movements. Vertical movement ascertains that the entire cold-plate surface is optimally used for freezing; horizontal movement sets the distance between micromixer and cold-plate and, thereby, the aging time, t_a.

The aging time t_a consists of three components: the mixing time t_m (residence time in the micromixer), the transport time t_t (time-of-flight in the jet), and the quenching or freezing time t_q (SI Section 1.1).[39,41]

$$t_a = t_m + t_t + t_q$$

The time t_m is determined by the mixer volume and the flow rate during mixing. The time t_q depends on the jet diameter as well as the heat conductivity of the aqueous sample and the cold-plate material.[37,39] The diameter of the jet, known from the orifice diameter, and the volumetric flow rate yield a t_m of 1 μs and a t_q of approximately 40 μs.[39] The transport time t_t is set by the jet velocity and the distance between the mixer orifice and the cold-plate.[39] Its lower limit is given by a safe minimal distance between the orifice and the cold-plate of about >2 mm (SI Section 1.1). Microsecond quenching requires high linear flow rates (up to 200 m s^{-1}) achieved by HPLC pumps. Small uniform jet diameters are obtained by operating the mixer and the cold-plate under a vacuum hood. The vacuum prevents jet breakup and ensures that experimental and theoretically expected transport times match. The actual transport time t_t, as demonstrated by laser Doppler anemometry, is only <10% shorter than the value calculated from flow rates.[39] The shortest aging time t_a achieved was 82 μs (Table S1).

RESULTS

Calibration of the MHQ Device. The reaction kinetics between equine heart metmyoglobin (MetMb) and sodium azide (NaN_3)[55] was employed to calibrate the MHQ aging times. In the *apo* state, the Fe(III) ion in the heme group is in the *high*-spin state ($S = 5/2$, abbreviated *hs*), and binding of azide switches it to the *low*-spin state ($S = 1/2$, abbreviated *ls*). *Hs*- and *ls* Fe(III) give rise to an apparent axial ($g_{xx} = g_{yy} = 5.8$, $g_{zz} = 2.0$) and orthorhombic EPR spectrum ($g_{zz} = 2.8$, $g_{yy} = 2.2$, $g_{xx} = 1.8$),[56,57] respectively, which allows following the progression of the reaction by CW EPR spectroscopy (Figure 2).

The reaction gradually progressed with the aging time (Figure 2c,d, Extended Data Figure 1, SI Section 9.1). The signal intensities of *hs* Fe(III) at $g_{xx} = g_{yy} = 5.8$ decreased with t_a, whereas the intensities of the *ls* state ($g_{zz} = 2.8$ and $g_{yy} = 2.2$) concomitantly increased (Figure 2c). The fraction of *hs* and *ls* state trapped in the frozen sample at an aging time t_a can be deduced from the peak-to-peak intensities of the respective signals in the CW EPR spectra (Figure 2c and SI Section 4.5). These fractions were fitted by two exponentials $y = ae^{-k_1't} + be^{-k_2't}$ with pseudo-first-order rate constants $k_1' = 19\,669 \pm 5406$ s^{-1} and $k_2' = 1358 \pm 189$ s^{-1} (Figure 2d). These rate constants k′ translate into second-order rate constants $k_1 = 26\,225 \pm 7208$ M^{-1} s^{-1} and $k_2 = 1811 \pm 253$ M^{-1} s^{-1}, which are in good agreement with previous accounts (Table S2).[39]

The biphasic behavior may be attributed to different reactions occurring in parallel, e.g., binding of N_3^- and HN_3, or temperature drifts depending on the length of the jet.[39] The dispersion of the *y*-values (coefficient of variation = SD/mean) (Figure 2d) was maximally 17% for $t_a = 82$ μs and ranged between 0.6% and 8.0% for all other data points. Thus, for our purpose, reliable aging times as short as 82 μs and up to 668 μs can be obtained with the MHQ device, yet the operational range is much larger (<20 ms).

MHQ/PELDOR Can Resolve Movements in the CNBD of the MloK1 Channel. The *apo* state of the MloK1 CNBD undergoes a cAMP-induced conformational change (Figure 1), the most prominent being a movement of the C_α-helix[49−51] (NMR structures: PBD-IDs: 2kxl, *apo* and 2k0g, *holo*[50] and crystal structures: PDB-IDs: 1u12, *apo* and 1vp6, *holo*[49]).

Based on the *apo* and *holo* state structures, sites for labeling with the nitroxide spin label *S*-(1-oxyl-2,2,5,5-tetramethylpyrroline-3-methyl)methanethiosulfonate (MTSSL) were chosen

https://doi.org/10.1021/jacs.1c01081
J. Am. Chem. Soc. 2021, 143, 6981−6989

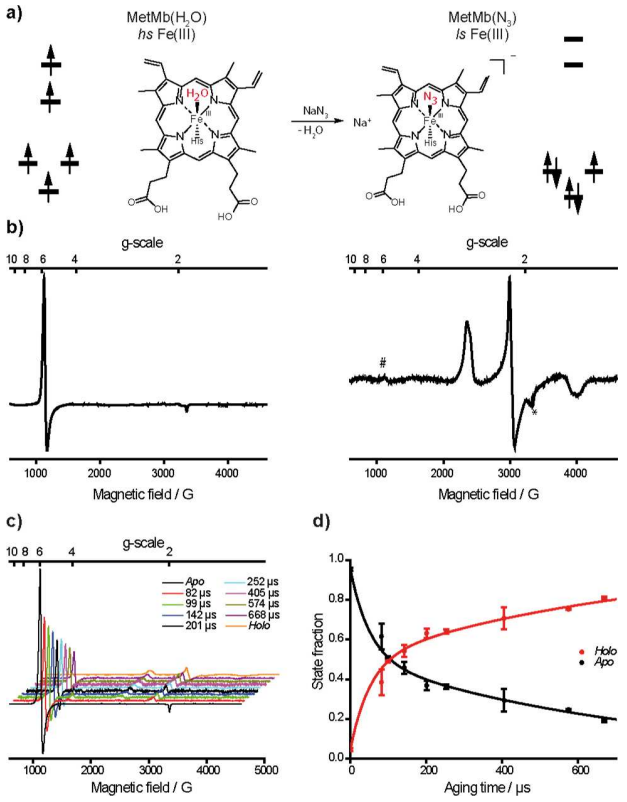

Figure 2. Reaction between MetMb and NaN_3 converting Fe(III) from the *hs* to the *ls* state. (a) Lewis structures of the *hs* and *ls* states. For clarity, only the porphyrin ring of MetMb is shown. Orbital diagrams indicate the occupation of t_{2g} and e_g orbitals in the octahedral ligand field for either the *hs* or *ls* state. (b) Continuous-wave X-band (9.4 GHz) EPR spectra recorded at 20 K of MetMb in the *hs* state (left) and the *ls* state (right). In the spectrum of the *ls* state, a residual of the *hs* Fe(III) state due to incomplete conversion is marked by (#); a resonator background signal is marked by an asterisk (*). (c) Stack plot of CW X-band EPR spectra recorded from samples undergoing different aging times t_a. (d) Fraction of the *apo* and *holo* state as a function of t_a. The fractions have been derived from the signal amplitudes of *hs* Fe(III) and *ls* Fe(III) in the CW EPR spectra (SI Section 4.5) and are given as mean (full circle) ± SD (error bars) of triplicates. Solid lines: fit using two exponentials ($y = ae^{-k_1't} + be^{-k_2't}$) to experimental data. To ascertain pseudo-first-order kinetics, NaN_3 was used in 1000-fold excess. Postmixing concentrations: [MetMb] = 0.75 mM, [NaN_3] = 0.75 M. Note that at $t_a = 0$, about 5% *ls* Fe(III) MetMb is present.

using difference-distance maps generated with the *in-silico* spin-labeling program mtsslWizard (SI Section 5 and Figure S6).[58] The selection was based on three criteria: (1) one labeling site is on the C_α-helix; (2) the distance distributions of *apo* and *holo* states range between 2 and 8 nm to facilitate high-quality PELDOR data; and (3) the distance distributions should be narrow (<1 nm full width at half-height, fwhh) and well separated (Δr > 0.6 nm) to facilitate the identification of distance changes. The amino-acid pair E289R1/I340R1 (where R1 refers to the nitroxide-labeled cysteine) was particularly promising due to its large Δr of −1.8 nm and its narrow distribution widths. In addition, the pair R254R1/E336R1 with a Δr of only −0.3 nm was selected to gauge the limitations of the method.

Controls. We subjected these constructs to several controls to assess whether the spin label and the EPR sample preparation significantly affect the protein structure, the ligand binding, or the conformational change. First, we studied whether two native cysteine residues (C263, C331) of the CNBD were accessible for cysteine-reactive reagents and would interfere with distance determinations between exogenous spin labels. In the *apo* state, incubation of wild-type (wt) CNBD with Ellman's reagent modified approximately one cysteine per CNBD monomer, and the resulting protein was no longer able to bind cAMP. Therefore, we decided to remove the endogenous cysteines by site-directed mutagenesis. Of the different constructs, C263S/C331L, which was suggested by the software CUPSAT (Cologne University Protein Stability Analysis Tool),[59] displayed the lowest K_D value for 8-(2-[7-nitro-4-benzofurazanyl]aminoethylthio)-adenosine-3′,5′-cyclic monophosphate (8-NBD-cAMP) (103 ± 27 mM). All mutants studied here are based on this cysteine-free C263S/C331L mutant.

Second, as spin labeling in high yields and quantitative cAMP removal required unfolding and refolding of the protein, we assessed the potential impact of unfolding/refolding on the distance distribution by also purifying and labeling the CNBD without unfolding (SI Section 2.8). The most probable distances and distribution widths of the *apo* and *holo* state of construct E289R1/I340R1 prepared via unfolding/refolding or in the native state agree well (Figure S8). Moreover, CW EPR spectra recorded at room temperature suggest that the local flexibility of the spin labels is similar for the two protein samples (Figure S9). This result indicates that the protein structure is not altered by unfolding and refolding.

Third, we probed how the R1 side chain affects binding of cAMP and 8-NBD-cAMP to the CNBD by independent techniques: the dissociation constants K_D were determined either in a stopped-flow setup using the NBD fluorescence or by isothermal calorimetry (SI Section 3). Although the K_D constants were altered, values were <10 μM, similar to the binding constants of cAMP and cGMP for the CNG channels in olfactory neurons and photoreceptors, respectively[5] (Table S5).

Fourth, we tested whether the structures of the *apo* and *holo* states are preserved upon labeling and freezing in the MHQ by comparing the experimental (PELDOR) distance distributions of the *apo* and *holo* states with those predicted by mtsslWizard or MMM on the basis of the NMR structures.[51] We have chosen the NMR structures instead of the crystal structures because crystal packing effects may have altered the structure and some of the amino-acid residues are not resolved in the crystal structure. The experimental distance distributions of the mutated and labeled CNBD are highly similar compared to the distance distributions generated *in silico* by means of mtsslWizard or MMM from the NMR structures of the native CNBD (Table S4). This comparison shows that the global protein structure has not been disturbed significantly.

Fifth, we compared the distance distributions of samples that were rapidly quenched in the MHQ (t_a = 82 μs) with samples slowly immersed in liquid nitrogen (freezing time ~1.5 s).[37] Rapid freezing by MHQ does not allow for sufficient time to relax to the thermodynamic energy minimum at the freezing point, and, compared to slow freezing, a broader conformational ensemble may be trapped. This can lead to differences in the shape and width of the distance distributions depending on the freezing conditions.[37,38] Here, we find that distributions

https://doi.org/10.1021/jacs.1c01081
J. Am. Chem. Soc. 2021, 143, 6981−6989

broaden in fast-frozen samples, apart from the *apo* state of E289R1/I340R1, where the intensity ratios of the peaks at 4 nm are altered (Figure S10).

Finally, we examined whether the addition of 20% deuterated ethylene glycol (EG-d_6) as cryoprotectant affects the EPR properties of the spin system. We observed that the phase-memory time T_M of the spin label increases from 2.5 to 3.2 μs upon adding EG-d_6, which enables longer time windows for the dipolar evolution in the PELDOR experiment and improves the signal-to-noise ratio[12] (Figure S11 and Table S6). In addition, the background correction of PELDOR time traces is improved, and thus more reliable distance distributions are obtained. Beyond this, the distance distributions with and without EG-d_6 are very similar, from which we conclude that the protein structure is not affected by the cryoprotectant.

In conclusion, these controls show that the label and rapid MHQ freezing does not alter the global structure or the function of the protein.

Assessing the Conformational Change. The *apo* state sample of the MloK1 CNBD was mixed in the MHQ with buffer only. The *holo* state, which is the cAMP/CNBD complex, was first formed outside of the MHQ by adding cAMP and then mixed with buffer in the MHQ. The final protein and cAMP concentrations after 1:1 mixing at t_a = 82 μs were 150 μM and 15 mM, respectively. The background-corrected time traces and the corresponding distance distributions are shown in Figure 3 (SI Section 9.2).

The *apo* and *holo* state of E289R1/I340R1 display a bimodal distance distribution with both modes falling within the envelope predicted by mtsslWizard (Figure 3). We reason that the bimodality is caused by interactions of the label rotamers with the protein, which are difficult to predict by *in-silico* methods[60] (Figure S7). The change in the most probable distances, Δr = −1.9 nm, between *apo* and *holo* state agrees with the mtsslWizard prediction. For the R254R1/E336R1 construct, experimental and predicted distance distributions for the *apo* and *holo* state also match within the error margin of mtsslWizard (0.4 nm). Based on the PELDOR background validation (Figure 3), the peak for the *apo* state at 2.5 and 2.8 nm for constructs E289R1/I340R1 and R254R1/E336R1, respectively, may indicate a small contribution of the *holo* state, whereas the minor peaks at longer distances are artifacts. Overall, the distance change of Δr = −0.4 nm between the *apo* and *holo* state of R254R1/E336R1 is in good agreement with the mtsslWizard prediction. Due to the particularly small distance change and large overlap between the distance distributions of *apo* and *holo*, this construct indeed illustrates the resolution of our method.

Next, we examined the kinetics of the conformational change during the transition from the *apo* to the *holo* state by varying t_a from 82 to 498 μs. After 1:1 mixing the protein sample (200 μL) in the MHQ with cAMP-containing buffer (500 μL), final protein and cAMP concentrations were 150 μM and 15 mM, respectively. Of note, the mixer had been first conditioned with an excess of cAMP-containing buffer (300 μL) before the *apo* protein entered the mixer. This precaution ascertains that the protein sample was not partially mixed with buffer that did not contain cAMP.

As can be gleaned from Figure 4a,d, the time traces and the distance distributions change with t_a. The time-resolved changes in the distance distributions for E289R1/I340R1 show that with increasing t_a, the *apo* and *holo* state populations

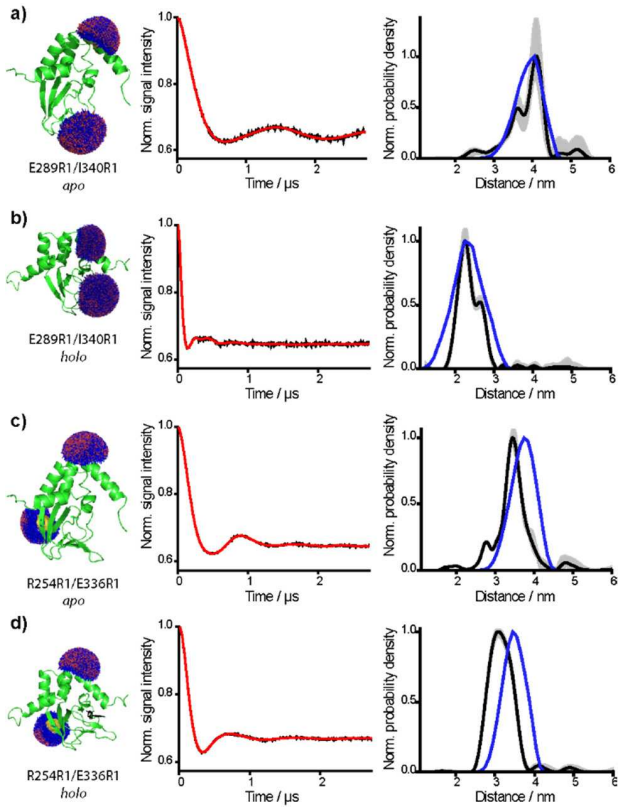

Figure 3. PELDOR data for *apo* and *holo* states of E289R1/I340R1 and R254R1/E336R1. Rotamer distribution of R1 (blue) based on the NMR structure (green) (PDB IDs: 2kxl, *apo* and 2k0g, *holo*) (left panels). Background-corrected time traces (black lines) for the *apo* and *holo* state and the respective fits (red lines) (middle panels). Distance distributions of the *apo* and *holo* state corresponding to the respective time traces in middle panels. The *y*-axis is normalized to the maximum of the probability density of the best fit (black line). Background validation is shown as gray-shaded areas. The distance distributions predicted by mtsslWizard are shown as blue lines (right panels). (a) E289R1/I340R1 *apo* state. (b) E289R1/I340R1 *holo* state. (c) R254R1/E336R1 *apo* state. (d) R254R1/E336R1 *holo* state. Both, the *apo* and *holo* samples of R254R1/E336R1 and E289R1/I340R1 were prepared at MHQ aging times t_a of 82 μs. For the *apo* state, the postmixing concentration was [CNBD] = 150 μM. The *holo* form was produced by adding cAMP to the *apo* form outside the MHQ, before mixing with buffer in the MHQ, yielding final concentrations of [CNBD] = 150 μM and [cAMP] = 15 mM.

respectively decreased and increased stoichiometrically (Figure 4b,c and Extended Data Figure 2, SI Section 9.2). However, neither a gradual shift of the most probable distance from the *apo* to the *holo* state nor additional peaks along the reaction coordinate were observed, suggesting that structural intermediates are not detected.

The fraction of *apo* and *holo* state was quantified by deconvolution of the PELDOR time traces (SI Section 4.7). A plot of the fractions of *apo* and *holo* state versus t_a was fitted by a monoexponential function:

$$y = y_0 + A\, e^{-kt}$$

yielding a rate constant k of 7398 ± 1179 s^{-1} for E289R1/I340R1 and of 7508 ± 867 s^{-1} for R254R1/E336R1. All regression parameters are collected in Table S3. Interestingly, the k values are highly similar, indicating that the underlying

https://doi.org/10.1021/jacs.1c01081
J. Am. Chem. Soc. 2021, 143, 6981−6989

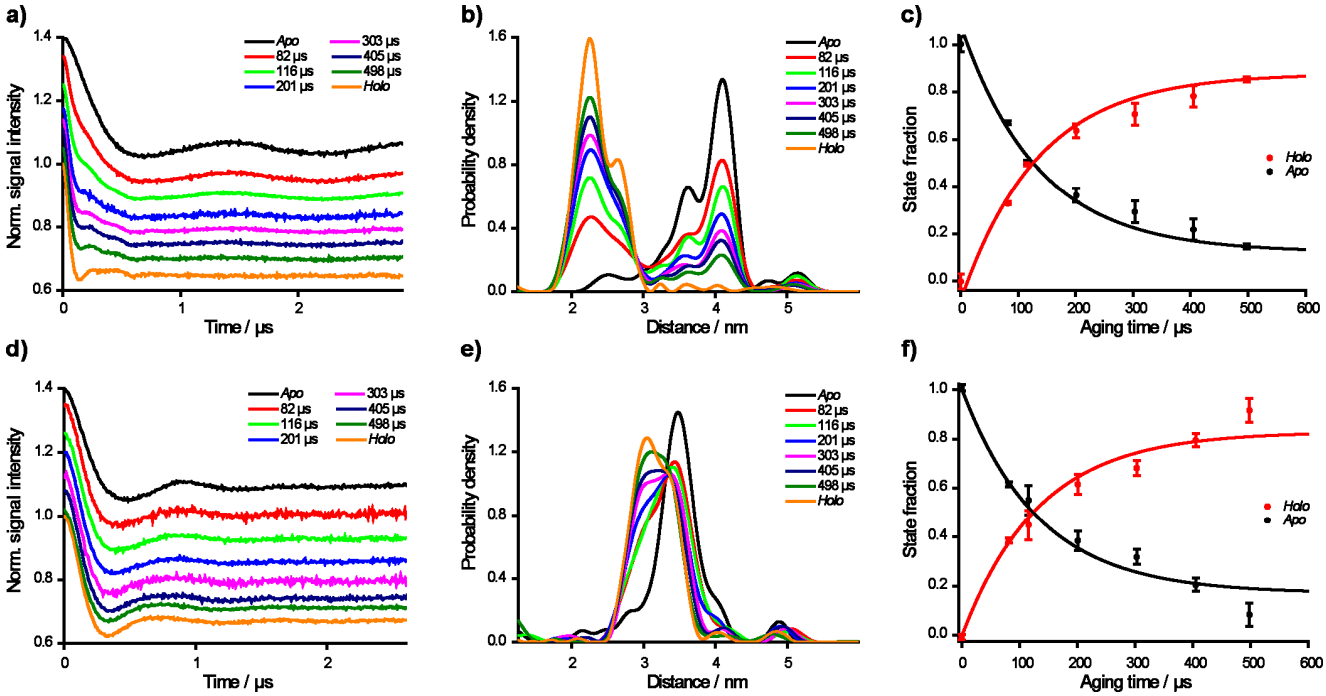

Figure 4. Time-resolved PELDOR data. The background-corrected PELDOR time traces obtained for aging times t_a ranging from 82 to 498 μs (color code see legend) for (a) E289R1/I340R1 and (d) R254R1/E336R1. Note that the time traces were normalized but shifted on the *y*-axis for the sake of clarity. The postmixing concentrations were [CNBD] = 150 μM and [cAMP] = 15 mM, respectively. The corresponding distance distributions are shown in (b) for E289R1/I340R1 and in (e) for R254R1/E336R1. In (c) and (f), the fractions of *apo* and *holo* state are plotted against t_a. Data points represent the mean; the error bars, the standard deviation (n = 3 experiments). Data have been fitted with a monoexponential function, indicated by red and black lines (R289R1/I340R1: R^2 = 0.982; R254R1/E336R1: R^2 = 0.993).

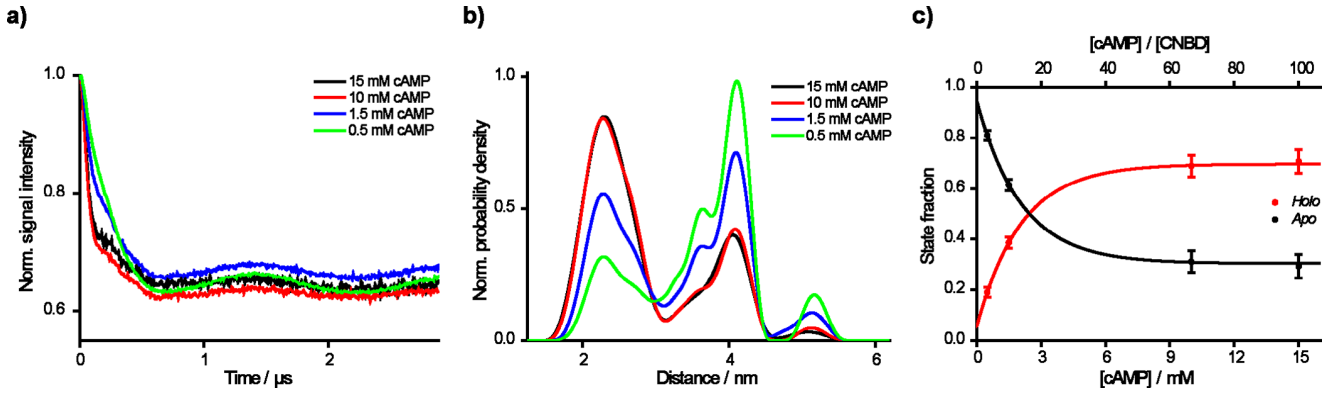

Figure 5. cAMP concentration series for E289R1/I340R1 at t_a = 303 μs. (a) Background-corrected PELDOR time traces for final [cAMP] = 0.5 mM (green), 1.5 mM (blue), 10 mM (red), and 15 mM (black). (b) Corresponding distance distributions using the same color code as in (a). (c) Plot of the fractions of *apo* and *holo* state against cAMP concentration. Data represent the mean ± SD (n = 3 experiments).

process monitored by MHQ/PELDOR is independent of the labeling site on the C_α-helix. In addition, construct R254R1/E336R1 illustrates that even changes as small as 0.4 nm of strongly overlapping distance distributions can be resolved.

Because our experiments monitor ensemble averages, the C_α-helix movement of individual molecules, which supposedly is rapid and stochastic, is not resolved in the MHQ/PELDOR experiment. Indeed, molecular dynamics (MD) simulation suggests that the helix movement takes only a few nanoseconds, which is much faster than the experimental rate constant k (Figure S13 and Extended Data Figure 5, SI Section 9.3). Therefore, we scrutinized whether the kinetics reflects rate-limiting cAMP binding. To this end, MHQ samples were prepared at a t_a of 303 μs. The protein concentration after 1:1 mixing in the MHQ was in each case 150 μM, whereas the final cAMP concentration varied between 0.5 and 15 mM, equivalent to a CNBD/cAMP ratio ranging from 1:3 to 1:100. The background-corrected PELDOR time traces, the corresponding distance distributions, and the calculated fraction of *apo* and *holo* state versus cAMP concentration are shown in Figure 5 (Extended Data Figure 3, SI Section 9.2).

At cAMP concentrations larger than 10 mM ([cAMP]/[CNBD] ~67), the fractions are independent of the cAMP concentration, confirming saturation of the CNBD with cAMP. This demonstrates that diffusion-controlled ligand binding under the MHQ/PELDOR conditions is not rate-limiting and that the rate-limiting step occurs further down the *apo*-to-*holo* pathway. This conclusion was confirmed by measuring the

https://doi.org/10.1021/jacs.1c01081
J. Am. Chem. Soc. 2021, 143, 6981−6989

ligand-binding kinetics in a stopped-flow device using fluorescence spectroscopy (Table S5).

DISCUSSION

Here we combined PELDOR with the rapid-freezing technique MHQ to follow changes in protein conformation on a time scale of >82 μs with high precision. Labels at two different sites in the C_α-helix of a CNBD report distance changes of 0.4 and 1.9 nm, respectively, yet the rate constants for the conformational change are virtually identical. In addition, amino acids E336 and I340 are only three residues apart, yet display very different Δr values. For a linear movement around the hinge between B_α and C_α (Figure 1), a similar Δr is expected for both residues. Our data thus suggest that upon ligand binding, C_α not only moves closer to the β-sheet domain but also rotates, which is also observed in the NMR structures. Finally, the data set for R254R1/E336R1 illustrates the strength of the MHQ/PELDOR combination for monitoring local conformational changes in proteins, even if the distance changes are as small as 0.4 nm.

We observed a gradual transition from the *apo* to the *holo* state, but detected no distinct population that would indicate a conformational intermediate (Figure 4). This result can be interpreted in light of the concept of dwell or waiting times.[61] In this concept, ligand binding and conformational change are both thermally driven processes. A free-energy profile for a simplified case involves only three distinct states: (1) the protein in the *apo* state plus unbound ligand; (2) the ligand complexed to the protein, but the protein still being in the *apo* state; and (3) the ligand bound to the protein in the final *holo* structure (Figure 6).

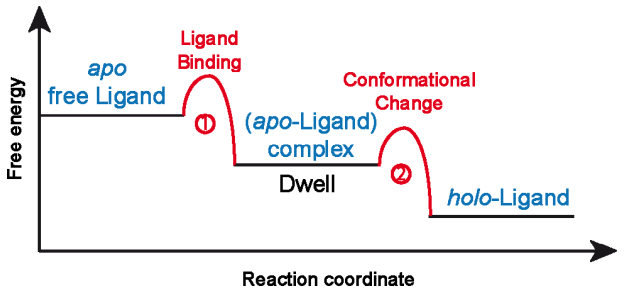

Figure 6. Schematic free-energy profile of a ligand-induced conformational change in a protein. The transition events are marked in red. The length of the dwell time is individual for every individual molecule. Depending on the spectroscopic technique used, i.e., whether the ligand or the protein is observed, the method will report on different states of this landscape (see text).

The crossings of the two free-energy barriers, that is, the complexation of ligand to the *apo* structure and the subsequent conformational transition to the final *holo* structure, both occur in the nanosecond to low microsecond range. Thus, they exceed the time resolution of the MHQ device (<80 μs). However, the dwell time of the system in the ligand-complexed *apo* state can be considerably longer, spanning the range from a few to hundreds of microseconds. Thus, binding at high ligand concentrations and conformational transition happen on time scales that are largely different from the dwell time of the *apo*-ligand complex. At lower ligand concentrations, the binding event becomes rate limiting (Figure 5).

The dwell time of the *apo*-ligand complex is different for each individual protein molecule, resulting macroscopically in a distribution of dwell times. Such a distribution of dwell times is also compatible with MD simulations, which show that dwell times of the *apo*-ligand complex derived from MD trajectories are exponentially distributed (Figure S14 and SI Section 9.3). For short aging times t_a in relation to the individual dwell time, only a small number of protein molecules can undergo the conformational transition. For longer aging times, the probability increases that protein molecules populate the *holo* state. Thus, the time constants determined for E289R1/I340R1 and R254R1/E336R1 reflect the average dwell times for the cAMP-induced conformational change rather than the C_α-helix movement or the binding kinetics themselves. This picture agrees with recent atomistic simulations, which revealed "prebinding" of the ligand to different surface sites, followed by induced-fit conformational motions of the binding pocket and entropic barriers to ligand binding as the rate-limiting steps.[52] We note that this concept neither rules out conformational motions during the first ligand binding steps that, however, are below the PELDOR resolution, nor claims that, for the *apo*-ligand complex, the ligand is already positioned at its final binding site. It does imply, though, that the second step is independent of concentration. Thus, MHQ/PELDOR is able to extract dwell times from conformational rearrangements, further illustrating the power of this technique to study ligand-triggered protein kinetics. Comparing the PELDOR-derived dwell times with those inferred from MD reveals an 18-fold difference (Figure S14). This discrepancy may be attributed to two factors. First, the temperature of the solution jet is not precisely known, but likely below room temperature, and may decrease gradually over the jet length. By contrast, the MD simulation temperature was 300 K. Thus, the experimentally determined dwell times are expected to be longer. Second, because the entire conformational change is a stochastic multistage process whose duration exceeds the simulation time of 3.5 μs, only the first step(s) en route to the *holo* state is monitored in the MD simulation. Thus, the MD simulation probably underestimates the overall dwell time. This combination of overestimation of dwell times in the experiment and underestimation in the MD simulation may explain the discrepancy.

For this proof-of-concept study, we used high concentrations and larger volumes to obtain high-quality data at short measurement times (60 nmol protein, 200 μL, i.e., 300 μM per time point at a signal-to-noise ratio (SNR) between 70 and 100 $h^{-1/2}$ and a time trace length of 2.8 μs). To demonstrate the sensitivity of MHQ/PELDOR, we also used protein amounts as small as 7.5 nmol (75 μM, 100 μL) per time point, which still yielded a good SNR of 25 for a measurement time of 8 h (SI Section 8). Thus, the protein amount, measurement time, and SNR can be similar to that of typical Q-band PELDOR measurements. Sample consumption can be reduced even further when working at higher EPR frequencies such as W-band.[40,62]

Spatiotemporal resolution has also been achieved with other methods, each having its own strengths and limitations and often being complementary to each other. For example, a fluorescently labeled ligand, such as 8-NBD-cAMP,[63,64] versus a spin label addresses two different observables: fluorescence spectroscopy probes the environment of the cAMP ligand and thus reports on the crossing of barrier 1 in Figure 6 (aqueous solution vs complexation in the hydrophobic protein), whereas

https://doi.org/10.1021/jacs.1c01081
J. Am. Chem. Soc. 2021, 143, 6981−6989

PELDOR reports on the *apo*-to-*holo* transition, which is rate-limited by the dwell time of the ligand-complexed *apo* state. A further example is time-resolved Förster resonance energy transfer (trFRET). It is measured in solution at ambient temperatures,[65] whereas MHQ/PELDOR is measured in the frozen state. Yet, MHQ/PELDOR has the advantages that (1) the two sites carry the same label, and orthogonal labeling with two different labels as in FRET is obsolete; (2) due to the small size of spin labels, the alteration of the native protein structure is likely less severe and distance measurements are more precise; (3) the circumvention of the κ^2-problem by measuring the whole Pake pattern makes the data analysis parameter-free; and (4) the accessible distance range is larger than for a single FRET pair.[66] Another example is time-resolved solution NMR at room temperature.[67] NMR spectroscopy, like MHQ/PELDOR, requires substantial amounts of protein sample, yet MHQ/PELDOR has no limitation with respect to the size of the biomolecule.

CONCLUSION

In conclusion, the MHQ/PELDOR approach holds great potential for following conformational changes in large biomolecules with spatiotemporal resolution on the angstrom and microsecond time scale. In our proof-of-concept study, we have determined the mean dwell time for a helix movement triggered by a small ligand. MHQ/PELDOR holds promise to temporally resolve both dwell times and slower conformational transitions that happen in the >100 μs range. On a final note, MHQ/PELDOR is by no means restricted to proteins: It might be useful to follow conformational changes in any biomolecule, provided that these changes can be triggered by an external event such as ligand binding and that they proceed on a time scale of >82 μs. As the MHQ device is operated under a vacuum hood, quick changes of pressure or temperature are presumably difficult to implement. However, we envision to use the MHQ as a fast-freezing device and trigger folding events or conformational changes by light using photolysis of caged compounds, photoswitches, or photo-triggers.

ASSOCIATED CONTENT

Supporting Information

The Supporting Information is available free of charge at https://pubs.acs.org/doi/10.1021/jacs.1c01081.

Instrumentation, detailed experimental procedures (protein preparation, EPR sample preparation), details on data analysis, details on MD simulations (PDF)

AUTHOR INFORMATION

Corresponding Authors

Olav Schiemann − *Institute of Physical and Theoretical Chemistry, University of Bonn, 53115 Bonn, Germany;* orcid.org/0000-0001-6346-9779; Email: schiemann@pc.uni-bonn.de

U. Benjamin Kaupp − *Center of Advanced European Studies and Research (caesar), 53175 Bonn, Germany; Life & Medical Sciences Institute (LIMES), University of Bonn, 53115 Bonn, Germany;* orcid.org/0000-0002-0696-6397; Email: u.b.kaupp@caesar.de

Authors

Tobias Hett − *Institute of Physical and Theoretical Chemistry, University of Bonn, 53115 Bonn, Germany;* orcid.org/0000-0003-3821-5165

Tobias Zbik − *Center of Advanced European Studies and Research (caesar), 53175 Bonn, Germany*

Shatanik Mukherjee − *Center of Advanced European Studies and Research (caesar), 53175 Bonn, Germany*

Hideto Matsuoka − *Institute of Physical and Theoretical Chemistry, University of Bonn, 53115 Bonn, Germany;* Present Address: H.M.: Graduate School of Science, Osaka City University, 3-3-138 Sugimoto, Sumiyoshi-ku, Osaka, 558-8585, Japan.

Wolfgang Bönigk − *Center of Advanced European Studies and Research (caesar), 53175 Bonn, Germany*

Daniel Klose − *Fachbereich Physik, Universität Osnabrück, 49076 Osnabrück, Germany;* Present Address: D.K.: Departement Chemie and Angewandte Biowissenschaften, Lab. Für Physikalische Chemie, ETH Zürich, Vladimir-Prelog-Weg 1-5/10, 8093 Zürich, Switzerland.; orcid.org/0000-0002-3597-0889

Christophe Rouillon − *Center of Advanced European Studies and Research (caesar), 53175 Bonn, Germany*

Norbert Brenner − *Center of Advanced European Studies and Research (caesar), 53175 Bonn, Germany*

Sebastian Peuker − *Center of Advanced European Studies and Research (caesar), 53175 Bonn, Germany*

Reinhard Klement − *Department of Theoretical and Computational Biophysics, Max Planck Institute for Biophysical Chemistry, 37077 Göttingen, Germany*

Heinz-Jürgen Steinhoff − *Fachbereich Physik, Universität Osnabrück, 49076 Osnabrück, Germany*

Helmut Grubmüller − *Department of Theoretical and Computational Biophysics, Max Planck Institute for Biophysical Chemistry, 37077 Göttingen, Germany;* orcid.org/0000-0002-3270-3144

Reinhard Seifert − *Center of Advanced European Studies and Research (caesar), 53175 Bonn, Germany*

Complete contact information is available at: https://pubs.acs.org/10.1021/jacs.1c01081

Author Contributions

‡T.H. and T.Z. contributed equally.

Notes

The authors declare no competing financial interest.

ACKNOWLEDGMENTS

Funding by the DFG via a Reinhart Koselleck Grant (Projektnummer 420322655) to U.B.K. and the University of Bonn via TRA-2 (Building Blocks of Matter and Fundamental Interactions) is gratefully acknowledged.

REFERENCES

(1) Hilger, D.; Masureel, M.; Kobilka, B. K. Structure and dynamics of GPCR signaling complexes. *Nat. Struct. Mol. Biol.* **2018**, *25* (1), 4−12.

(2) Rosenbaum, D. M.; Rasmussen, S. G. F.; Kobilka, B. K. The structure and function of G-protein-coupled receptors. *Nature* **2009**, *459* (7245), 356−363.

(3) Kaupp, U. B. Olfactory signalling in vertebrates and insects: differences and commonalities. *Nat. Rev. Neurosci.* **2010**, *11* (3), 188−200.

(4) Kaupp, U. B.; Seifert, R. Molecular Diversity of Pacemaker Ion Channels. *Annu. Rev. Physiol.* **2001**, *63* (1), 235−257.
(5) Kaupp, U. B.; Seifert, R. Cyclic Nucleotide-Gated Ion Channels. *Physiol. Rev.* **2002**, *82* (3), 769−824.
(6) Weis, W. I.; Kobilka, B. K. The Molecular Basis of G Protein-Coupled Receptor Activation. *Annu. Rev. Biochem.* **2018**, *87* (1), 897−919.
(7) Bezanilla, F. How membrane proteins sense voltage. *Nat. Rev. Mol. Cell Biol.* **2008**, *9* (4), 323−332.
(8) Hofmann, K. P.; Scheerer, P.; Hildebrand, P. W.; Choe, H.-W.; Park, J. H.; Heck, M.; Ernst, O. P. A G protein-coupled receptor at work: the rhodopsin model. *Trends Biochem. Sci.* **2009**, *34* (11), 540−552.
(9) Sattig, T.; Rickert, C.; Bamberg, E.; Steinhoff, H.-J.; Bamann, C. Light-Induced Movement of the Transmembrane Helix B in Channelrhodopsin-2. *Angew. Chem., Int. Ed.* **2013**, *52* (37), 9705−9708.
(10) Jin, P.; Jan, L. Y.; Jan, Y.-N. Mechanosensitive Ion Channels: Structural Features Relevant to Mechanotransduction Mechanisms. *Annu. Rev. Neurosci.* **2020**, *43* (1), 207−229.
(11) Klostermeier, D.; Rudolph, M. G. *Biophysical Chemistry*; CRC Press, 2017.
(12) Jeschke, G. DEER Distance Measurements on Proteins. *Annu. Rev. Phys. Chem.* **2012**, *63* (1), 419−446.
(13) Milov, A. D.; Salikhov, K. M.; Schirov, M. D. Application of ELDOR in electron-spin echo for paramagnetic center space distribution in solids. *Fiz. Tverd. Tela (Leningrad)* **1981**, *23*, 975−982.
(14) Pannier, M.; Veit, S.; Godt, A.; Jeschke, G.; Spiess, H. Dead-Time Free Measurement of Dipole-Dipole Interactions between Electron Spins. *J. Magn. Reson.* **2000**, *142* (2), 331−340.
(15) Schmidt, T.; Wälti, M. A.; Baber, J. L.; Hustedt, E. J.; Clore, G. M. Long Distance Measurements up to 160 Å in the GroEL Tetradecamer Using Q-Band DEER EPR Spectroscopy. *Angew. Chem., Int. Ed.* **2016**, *55* (51), 15905−15909.
(16) Timmel, C. R.; Harmer, J. R., Eds. *Structural Information from Spin-Labels and Intrinsic Paramagnetic Centres in the Biosciences*; Structure and Bonding, Vol. *152*; Springer: Berlin Heidelberg, 2013; DOI: 10.1007/978-3-642-39125-5.
(17) Hagelueken, G.; Ingledew, W. J.; Huang, H.; Petrovic-Stojanovska, B.; Whitfield, C.; ElMkami, H.; Schiemann, O.; Naismith, J. H. PELDOR Spectroscopy Distance Fingerprinting of the Octameric Outer-Membrane Protein Wza from Escherichia coli. *Angew. Chem., Int. Ed.* **2009**, *48* (16), 2904−2906.
(18) Pliotas, C.; Ward, R.; Branigan, E.; Rasmussen, A.; Hagelueken, G.; Huang, H.; Black, S. S.; Booth, I. R.; Schiemann, O.; Naismith, J. H. Conformational state of the MscS mechanosensitive channel in solution revealed by pulsed electron-electron double resonance (PELDOR) spectroscopy. *Proc. Natl. Acad. Sci. U. S. A.* **2012**, *109* (40), E2675−E2682.
(19) Halbmair, K.; Seikowski, J.; Tkach, I.; Höbartner, C.; Sezer, D.; Bennati, M. High-resolution measurement of long-range distances in RNA: pulse EPR spectroscopy with TEMPO-labeled nucleotides. *Chemical Science* **2016**, *7* (5), 3172−3180.
(20) Heinz, M.; Erlenbach, N.; Stelzl, L. S.; Thierolf, G.; Kamble, N. R.; Sigurdsson, S. T.; Prisner, T. F.; Hummer, G. High-resolution EPR distance measurements on RNA and DNA with the non-covalent G spin label. *Nucleic Acids Res.* **2020**, *48* (2), 924−933.
(21) Wuebben, C.; Vicino, M. F.; Mueller, M.; Schiemann, O. Do the P1 and P2 hairpins of the Guanidine-II riboswitch interact? *Nucleic Acids Res.* **2020**, *48* (18), 10518−10526.
(22) Constantinescu-Aruxandei, D.; Petrovic-Stojanovska, B.; Schiemann, O.; Naismith, J. H.; White, M. F. Taking a molecular motor for a spin: helicase mechanism studied by spin labeling and PELDOR. *Nucleic Acids Res.* **2016**, *44* (2), 954−968.
(23) Duss, O.; Michel, E.; Yulikov, M.; Schubert, M.; Jeschke, G.; Allain, F. H.-T. Structural basis of the non-coding RNA RsmZ acting as a protein sponge. *Nature* **2014**, *509* (7502), 588−592.
(24) Duss, O.; Yulikov, M.; Jeschke, G.; Allain, F. H.-T. EPR-aided approach for solution structure determination of large RNAs or protein-RNA complexes. *Nat. Commun.* **2014**, *5* (1), 3669.
(25) Vazquez Reyes, C.; Tangprasertchai, N. S.; Yogesha, S. D.; Nguyen, R. H.; Zhang, X.; Rajan, R.; Qin, P. Z. Nucleic Acid-Dependent Conformational Changes in CRISPR-Cas9 Revealed by Site-Directed Spin Labeling. *Cell Biochem. Biophys.* **2017**, *75* (2), 203−210.
(26) Wu, Z.; Feintuch, A.; Collauto, A.; Adams, L. A.; Aurelio, L.; Graham, B.; Otting, G.; Goldfarb, D. Selective Distance Measurements Using Triple Spin Labeling with Gd^{3+}, Mn^{2+}, and a Nitroxide. *J. Phys. Chem. Lett.* **2017**, *8* (21), 5277−5282.
(27) Borbat, P. P.; Mchaourab, H. S.; Freed, J. H. Protein Structure Determination Using Long-Distance Constraints from Double-Quantum Coherence ESR: Study of T4 Lysozyme. *J. Am. Chem. Soc.* **2002**, *124* (19), 5304−5314.
(28) Yang, Z.; Liu, Y.; Borbat, P.; Zweier, J. L.; Freed, J. H.; Hubbell, W. L. Pulsed ESR Dipolar Spectroscopy for Distance Measurements in Immobilized Spin Labeled Proteins in Liquid Solution. *J. Am. Chem. Soc.* **2012**, *134* (24), 9950−9952.
(29) Bleicken, S.; Jeschke, G.; Stegmueller, C.; Salvador-Gallego, R.; García-Sáez, A. J.; Bordignon, E. Structural Model of Active Bax at the Membrane. *Mol. Cell* **2014**, *56* (4), 496−505.
(30) Galazzo, L.; Meier, G.; Timachi, M. H.; Hutter, C. A. J.; Seeger, M. A.; Bordignon, E. Spin-labeled nanobodies as protein conformational reporters for electron paramagnetic resonance in cellular membranes. *Proc. Natl. Acad. Sci. U. S. A.* **2020**, *117* (5), 2441−2448.
(31) Joseph, B.; Sikora, A.; Bordignon, E.; Jeschke, G.; Cafiso, D. S.; Prisner, T. F. Distance Measurement on an Endogenous Membrane Transporter in E. coli Cells and Native Membranes Using EPR Spectroscopy. *Angew. Chem., Int. Ed.* **2015**, *54* (21), 6196−6199.
(32) Ward, R.; Pliotas, C.; Branigan, E.; Hacker, C.; Rasmussen, A.; Hagelueken, G.; Booth, I. R.; Miller, S.; Lucocq, J.; Naismith, J. H.; Schiemann, O. Probing the Structure of the Mechanosensitive Channel of Small Conductance in Lipid Bilayers with Pulsed Electron-Electron Double Resonance. *Biophys. J.* **2014**, *106* (4), 834−842.
(33) Fleck, N.; Heubach, C. A.; Hett, T.; Haege, F. R.; Bawol, P. P.; Baltruschat, H.; Schiemann, O. SLIM: A Short-Linked, Highly Redox-Stable Trityl Label for High-Sensitivity In-Cell EPR Distance Measurements. *Angew. Chem., Int. Ed.* **2020**, *59* (24), 9767−9772.
(34) Krstić, I.; Hänsel, R.; Romainczyk, O.; Engels, J. W.; Dötsch, V.; Prisner, T. F. Long-Range Distance Measurements on Nucleic Acids in Cells by Pulsed EPR Spectroscopy. *Angew. Chem., Int. Ed.* **2011**, *50* (22), 5070−5074.
(35) Qi, M.; Groß, A.; Jeschke, G.; Godt, A.; Drescher, M. Gd(III)-PyMTA Label Is Suitable for In-Cell EPR. *J. Am. Chem. Soc.* **2014**, *136* (43), 15366−15378.
(36) Yang, Y.; Pan, B.-B.; Tan, X.; Yang, F.; Liu, Y.; Su, X.-C.; Goldfarb, D. In-Cell Trityl-Trityl Distance Measurements on Proteins. *J. Phys. Chem. Lett.* **2020**, *11* (3), 1141−1147.
(37) Georgieva, E. R.; Roy, A. S.; Grigoryants, V. M.; Borbat, P. P.; Earle, K. A.; Scholes, C. P.; Freed, J. H. Effect of freezing conditions on distances and their distributions derived from Double Electron Electron Resonance (DEER): A study of doubly-spin-labeled T4 lysozyme. *J. Magn. Reson.* **2012**, *216*, 69−77.
(38) Schmidt, T.; Jeon, J.; Okuno, Y.; Chiliveri, S. C.; Clore, G. M. Submillisecond Freezing Permits Cryoprotectant-Free EPR Double Electron-Electron Resonance Spectroscopy. *ChemPhysChem* **2020**, *21* (12), 1224−1229.
(39) Cherepanov, A. V.; de Vries, S. Microsecond freeze-hyper-quenching: development of a new ultrafast micro-mixing and sampling technology and application to enzyme catalysis. *Biochim. Biophys. Acta, Bioenerg.* **2004**, *1656* (1), 1−31.
(40) Collauto, A.; DeBerg, H. A.; Kaufmann, R.; Zagotta, W. N.; Stoll, S.; Goldfarb, D. Rates and equilibrium constants of the ligand-induced conformational transition of an HCN ion channel protein domain determined by DEER spectroscopy. *Phys. Chem. Chem. Phys.* **2017**, *19* (23), 15324−15334.

(41) Pievo, R.; Angerstein, B.; Fielding, A. J.; Koch, C.; Feussner, I.; Bennati, M. A Rapid Freeze-Quench Setup for Multi-Frequency EPR Spectroscopy of Enzymatic Reactions. *ChemPhysChem* **2013**, *14* (18), 4094−4101.
(42) de Vries, S. The role of the conserved tryptophan272 of the Paracoccus denitrificans cytochrome c oxidase in proton pumping. *Biochim. Biophys. Acta, Bioenerg.* **2008**, *1777* (7−8), 925−928.
(43) Paulus, A.; Werner, C.; Ludwig, B.; de Vries, S. The cytochrome ba3 oxidase from Thermus thermophilus does not generate a tryptophan radical during turnover: Implications for the mechanism of proton pumping. *Biochim. Biophys. Acta, Bioenerg.* **2015**, *1847* (10), 1093−1100.
(44) Wiertz, F. G. M.; Richter, O.-M. H.; Ludwig, B.; de Vries, S. Kinetic Resolution of a Tryptophan-radical Intermediate in the Reaction Cycle of Paracoccus denitrificans Cytochrome c Oxidase. *J. Biol. Chem.* **2007**, *282* (43), 31580−31591.
(45) Srour, B.; Strampraad, M. J.; Hagen, W. R.; Hagedoorn, P.-L. Refolding kinetics of cytochrome c studied with microsecond timescale continuous-flow UV-vis spectroscopy and rapid freeze-quench EPR. *J. Inorg. Biochem.* **2018**, *184*, 42−49.
(46) de Vries, S.; Dörner, K.; Strampraad, M. J. F.; Friedrich, T. Electron Tunneling Rates in Respiratory Complex I Are Tuned for Efficient Energy Conversion. *Angew. Chem., Int. Ed.* **2015**, *54* (9), 2844−2848.
(47) Kowal, J.; Biyani, N.; Chami, M.; Scherer, S.; Rzepiela, A. J.; Baumgartner, P.; Upadhyay, V.; Nimigean, C. M.; Stahlberg, H. High-Resolution Cryoelectron Microscopy Structure of the Cyclic Nucleotide-Modulated Potassium Channel MloK1 in a Lipid Bilayer. *Structure* **2018**, *26* (1), 20−27 e3.
(48) Nimigean, C. M.; Shane, T.; Miller, C. A Cyclic Nucleotide Modulated Prokaryotic K^+ Channel. *J. Gen. Physiol.* **2004**, *124* (3), 203−210.
(49) Clayton, G. M.; Silverman, W. R.; Heginbotham, L.; Morais-Cabral, J. H. Structural Basis of Ligand Activation in a Cyclic Nucleotide Regulated Potassium Channel. *Cell* **2004**, *119* (5), 615−627.
(50) Schünke, S.; Stoldt, M.; Novak, K.; Kaupp, U. B.; Willbold, D. Solution structure of the Mesorhizobium loti K1 channel cyclic nucleotide-binding domain in complex with cAMP. *EMBO Rep.* **2009**, *10* (7), 729−735.
(51) Schünke, S.; Stoldt, M.; Lecher, J.; Kaupp, U. B.; Willbold, D. Structural insights into conformational changes of a cyclic nucleotide-binding domain in solution from Mesorhizobium loti K1 channel. *Proc. Natl. Acad. Sci. U. S. A.* **2011**, *108* (15), 6121−6126.
(52) Voß, B.; Seifert, R.; Kaupp, U. B.; Grubmüller, H. A Quantitative Model for cAMP Binding to the Binding Domain of MloK1. *Biophys. J.* **2016**, *111* (8), 1668−1678.
(53) Puljung, M. C.; DeBerg, H. A.; Zagotta, W. N.; Stoll, S. Double electron-electron resonance reveals cAMP-induced conformational change in HCN channels. *Proc. Natl. Acad. Sci. U. S. A.* **2014**, *111* (27), 9816−9821.
(54) Evans, E. G. B.; Morgan, J. L. W.; DiMaio, F.; Zagotta, W. N.; Stoll, S. Allosteric conformational change of a cyclic nucleotide-gated ion channel revealed by DEER spectroscopy. *Proc. Natl. Acad. Sci. U. S. A.* **2020**, *117* (20), 10839−10847.
(55) Panarelli, E. G.; van der Meer, H.; Gast, P.; Groenen, E. J. J.; Blanco, F. J. Effective coupling of rapid freeze-quench to high-frequency electron paramagnetic resonance. *PLoS One* **2020**, *15* (5), No. e0232555.
(56) Fittipaldi, M.; García-Rubio, I.; Trandafir, F.; Gromov, I.; Schweiger, A.; Bouwen, A.; van Doorslaer, S. A Multi-Frequency Pulse EPR and ENDOR Approach to Study Strongly Coupled Nuclei in Frozen Solutions of High-Spin Ferric Heme Proteins. *J. Phys. Chem. B* **2008**, *112* (12), 3859−3870.
(57) Maurus, R.; Bogumil, R.; Nguyen, N. T.; Mauk, A. G.; Brayer, G. Structural and spectroscopic studies of azide complexes of horse heart myoglobin and the His-64→Thr variant. *Biochem. J.* **1998**, *332* (1), 67−74.
(58) Hagelueken, G.; Abdullin, D.; Schiemann, O. mtsslSuite. Probing Biomolecular Conformation by Spin-Labeling Studies. *Methods Enzymol.* **2015**, *563*, 595−622.
(59) Parthiban, V.; Gromiha, M. M.; Schomburg, D. CUPSAT: prediction of protein stability upon point mutations. *Nucleic Acids Res.* **2006**, *34*, W239−W242.
(60) Polyhach, Y.; Bordignon, E.; Jeschke, G. Rotamer libraries of spin labelled cysteines for protein studies. *Phys. Chem. Chem. Phys.* **2011**, *13* (6), 2356−2366.
(61) Weikl, T. R.; Paul, F. Conformational selection in protein binding and function. *Protein Sci.* **2014**, *23* (11), 1508−1518.
(62) Cruickshank, P. A. S.; Bolton, D. R.; Robertson, D. A.; Hunter, R. I.; Wylde, R. J.; Smith, G. M. A kilowatt pulsed 94 GHz electron paramagnetic resonance spectrometer with high concentration sensitivity, high instantaneous bandwidth, and low dead time. *Rev. Sci. Instrum.* **2009**, *80* (10), 103102.
(63) Cukkemane, A.; Grüter, B.; Novak, K.; Gensch, T.; Bönigk, W.; Gerharz, T.; Kaupp, U. B.; Seifert, R. Subunits act independently in a cyclic nucleotide-activated K^+ channel. *EMBO Rep.* **2007**, *8* (8), 749−755.
(64) Peuker, S.; Cukkemane, A.; Held, M.; Noé, F.; Kaupp, U. B.; Seifert, R. Kinetics of Ligand-Receptor Interaction Reveals an Induced-Fit Mode of Binding in a Cyclic Nucleotide-Activated Protein. *Biophys. J.* **2013**, *104* (1), 63−74.
(65) Haran, G.; Haas, E.; Szpikowska, B. K.; Mas, M. T. Domain motions in phosphoglycerate kinase: determination of interdomain distance distributions by site-specific labeling and time-resolved fluorescence energy transfer. *Proc. Natl. Acad. Sci. U. S. A.* **1992**, *89* (24), 11764−11768.
(66) Joseph, B.; Jaumann, E. A.; Sikora, A.; Barth, K.; Prisner, T. F.; Cafiso, D. S. In situ observation of conformational dynamics and protein ligand-substrate interactions in outer-membrane proteins with DEER/PELDOR spectroscopy. *Nat. Protoc.* **2019**, *14* (8), 2344−2369.
(67) Fürtig, B.; Buck, J.; Manoharan, V.; Bermel, W.; Jäschke, A.; Wenter, P.; Pitsch, S.; Schwalbe, H. Time-resolved NMR studies of RNA folding. *Biopolymers* **2007**, *86* (5−6), 360−383.

NOTE ADDED AFTER ISSUE PUBLICATION

This article was initially published with an incorrect copyright statement and was corrected on or around May 28, 2021.

https://doi.org/10.1021/jacs.1c01081
J. Am. Chem. Soc. 2021, 143, 6981−6989

Supporting Information for

Spatio-Temporal Resolution of Conformational Changes in Biomolecules by Combining Pulsed Electron-Electron Double Resonance Spectroscopy with Microsecond Freeze-Hyperquenching

Tobias Hett[1‡], Tobias Zbik[2‡], Shatanik Mukherjee[2], Hideto Matsuoka[1$], Wolfgang Bönigk[2], Daniel Klose[3§], Christophe Rouillon[2], Norbert Brenner[2], Sebastian Peuker[2], Reinhard Klement[4], Heinz-Jürgen Steinhoff[3], Helmut Grubmüller[4], Reinhard Seifert[2], Olav Schiemann[1*], U. Benjamin Kaupp[2,5*]

[1] Institute of Physical and Theoretical Chemistry, University of Bonn, Wegelerstr. 12, 53115 Bonn, Germany.

[2] Center of Advanced European Studies and Research (caesar), Ludwig-Erhard-Allee 2, 53175 Bonn, Germany.

[3] Fachbereich Physik, Universität Osnabrück, Barbarastr. 7, 49076 Osnabrück, Germany.

[4] Department of Theoretical and Computational Biophysics, Max Planck Institute for Biophysical Chemistry, Am Fassberg 11, 37077 Göttingen, Germany.

[5] Life & Medical Sciences Institute (LIMES), University of Bonn, Carl-Troll-Str. 31, 53115 Bonn, Germany.

[‡] These authors contributed equally to this work.

* Email:
Schiemann@pc.uni-bonn.de
U.B.Kaupp@caesar.de

Contents

Methods

1. Practical considerations of MHQ device operation

1.1. Adjustment of aging times

The aging time t_a is determined by:

$$t_a = t_m + t_t + t_q$$

Due to the small mixer volume of ~ 10 pL,[1] the mixing time t_m is below 1 µs and is neglected here. The transport time t_t of the sample is determined by the flow rate of the reactants and the total jet length, i.e. the distance between the mixer orifice (OR) and the cold-plate (CP) surface. The orifice is attached to a screw-in cap (SC) (diameter 2 mm). Thus, the manually adjusted distance is the length SC-CP. The theoretical transport time t_t is:

$$t_t = \frac{Total\ Jet\ Length \cdot \pi r^2}{Flow\ Rate}$$

with r being the radius of the orifice and, therefore, also of the jet. The shortest t_t is limited by the minimal distance between cold-plate and orifice of about 2 mm. The t_t is multiplied by a factor 0.9 that accounts for the actual transport time, which is 10% shorter than the calculated value.[1] The quenching or freezing time t_q is about 40 µs.[1] This leads to:

$$t_a = 0.9 \cdot t_t + 40\ \mu s$$

Table S1 summarizes the settings used for the present study.
Table S1: Distances and times used for the calculation of t_a.

SC–CP / mm	OR–CP / mm	t_t / µs	t_a / µs
2	4	25	65
3	5	47	82
5	7	66	99
7	9	85	116
10	12	113	142
17	19	179	201
23	25	236	252
29	31	292	303
41	43	405	405
52	54	509	498
61	63	594	574
72	74	697	668

SC-CP is the distance between the screw-in cap and the cold-plate, OR–CP the total jet length, t_t the calculated transport time and t_a the aging time. Note that the total jet length is longer by 2 mm due to the thickness of the screw-in cap sitting on the orifice. All values shown in the table are valid for a total volumetric flow rate of 2 ml min^{-1}, except for t_a = 65 µs, which uses a flow rate of 3 ml min^{-1}. The shortest t_a of 65 µs was not further used due to contamination with copper abrasions.

At short aging times (t_a < 80 µs), the distance between the orifice and the cold-plate is reduced to values below 3 mm. This can result in occasional contact of the corners of the brass screw-in cap and the cold-plate, which leads to abrasion of the cap as proven by traces of copper (Cu^{2+}) found in *cw* EPR spectra of samples at the aging time of 65 µs.

1.2. Work flow

First, the horizontal distance between the mixer and the cold-plate that sets t_t is adjusted. Second, a heat gun preventing the motor axis from freezing is switched on (temperature: 300 °C). Next, the hollow cylindrical cold-plate is covered with a cloth to prevent water condensation and cooled with liquid nitrogen for 20 minutes. The reactants, usually protein sample and ligand solution, were loaded into Hamilton® gas-tight syringes (1700 series; 250 µl and 500 µl) and stored on ice prior to use. Volumes and concentrations were as follows: calibration of aging time: X-Band, 400 µl MetMb, 1.5 mM; 1000 µl NaN_3, 1.5 M; CNBD measurements: Q-Band, 200 µl protein, 300 µM; 500 µl cAMP up to 30 mM. In order to prevent the PEEK tubing (0.25 mm inner diameter, Upchurch) and the orifice from clogging, insoluble particles were removed from the solutions by syringe filters (0.45 µm filter, Merck).

When the cooling process has finished, the following steps must be completed within two minutes, otherwise the temperature of the cold-plate would rise above -140 °C, preventing efficient quenching of the reaction. The blanket is pulled away quickly and the remaining liquid nitrogen is removed from the cold-plate. Then, the robotic swivel arm is moved into its working position above the cold-plate (Figure S1) and the vacuum hood is put in place. The vacuum pump (XDS-10, Edwards) is switched on to establish the vacuum. When a pressure of 100 mbar has been reached, the motor (Servomotor IndraDyn A, Bosch Rexroth) controlled by the IndraWorks Ds software (Bosch Rexroth) is switched on (7,000 rpm). The remaining liquid nitrogen evaporates and the pressure drops further. Due to the low pressure, the air resistance and thus the probability of a jet break-up is reduced, which would ultimately lead to modified aging times.[1]

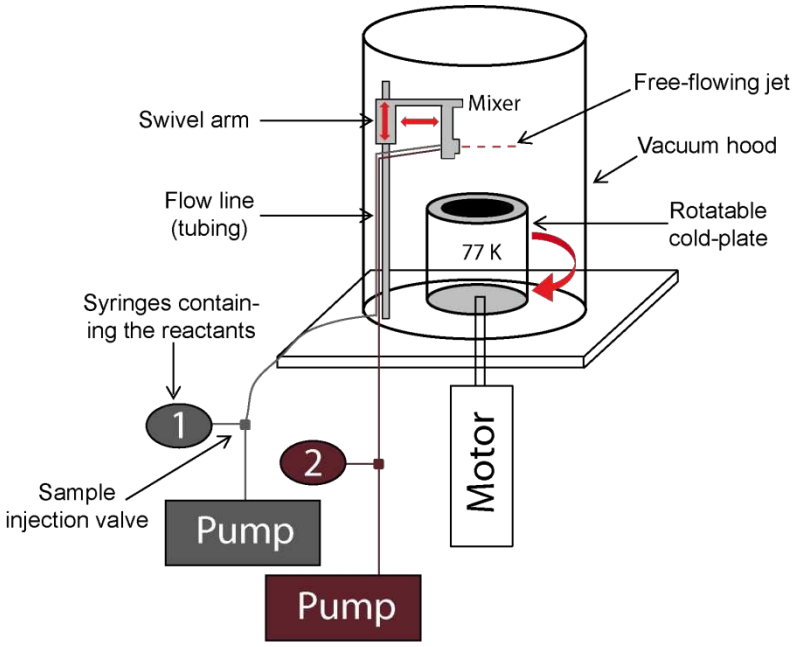

Figure S1: Schematic layout of the basic components of the MHQ device. Highlighted are the rotating cold-plate with motor, pumps, syringes 1 and 2, tubing, micromixer, swivel arm, and vacuum hood.

Protein and ligand are injected into the respective high-pressure injection valves (7725i, Rheodyne LLC) and as the pressure drops to 30 mbar, the reactants are loaded into the micromixer by the HPLC pumps. The ligand is injected first before the protein so that full saturation of the protein can be ensured. Controlled by the LinControl software (Lin Engineering), a stepping motor (Lineareinheit, A-Drive Technology) moves the robotic mixer arm vertically to the cold-plate, and the reactants are sprayed in a thin liquid jet (20 µm diameter) onto the surface of the rotating cold-plate. To ensure synchronous movement of the mixer arm and injection of the protein solution, the stepping motor is automatically triggered when injecting the protein. Finally, the cold-plate is stopped and the vacuum hood is re-ventilated with cold nitrogen gas (infused with tubing from a Dewar vessel with liquid nitrogen). Next, the interior of the cold-plate cylinder is quickly filled with liquid nitrogen to prevent the sample from warming up. Setting the cold-plate into slow rotation (50 rpm) permits to scratch the frozen sample from the walls of the plate.

1.3. Sample packing

The finely dispersed frozen sample is transferred to standard X-Band (o.d. 4 mm) or Q-Band (o.d. 3 mm) EPR tubes by means of a double-walled funnel (Figure S2).

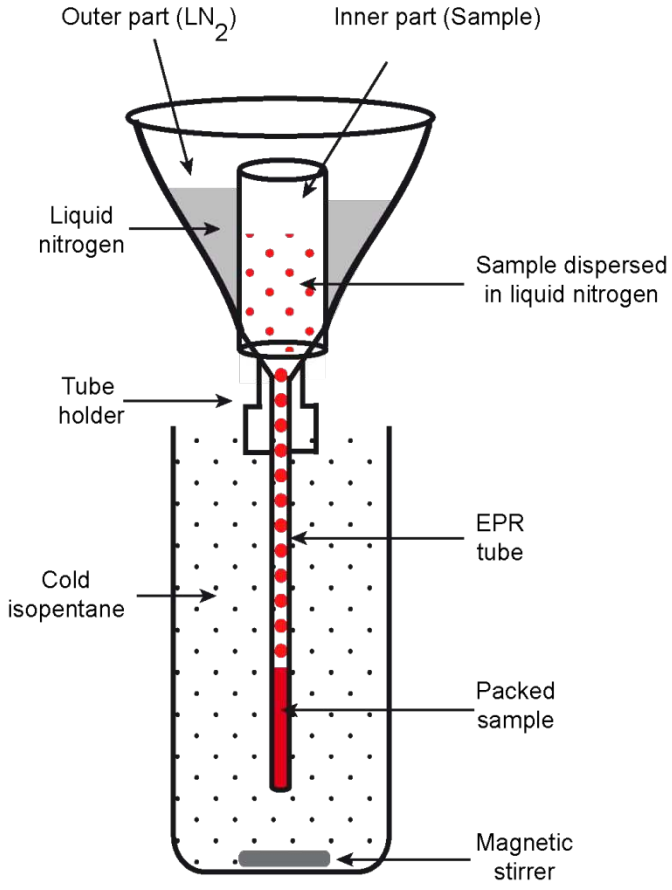

Figure S2: Schematic drawing of the sample packing setup. The sample-packing setup consists of a double-walled funnel, an isopentane cold bath, and a magnetic stirrer.

An EPR tube is mounted onto an opening of the inner part of the funnel. The tube is immersed into a cold bath (mixture of isopentane and liquid nitrogen) that is vigorously stirred to establish a homogeneous temperature distribution and prevent ice formation at the bottom of the vessel. By filling the inner and outer part of the funnel with liquid nitrogen, the entire tool is cooled before the sample suspension is poured into the inner part. While waiting for liquid nitrogen in the inner part of the funnel to evaporate, the outer part is regularly refilled with liquid nitrogen. When the sample is almost freed from liquid nitrogen, the powder is pushed into the EPR tube and compressed by a pre-cooled aluminum rod. Strongly compressing the sample optimizes the packing density and, thereby, enhances the spin concentration. Removing liquid nitrogen is crucial because liquid nitrogen trapped in the EPR tube will quickly evaporate upon removing the tube from the Dewar container, which can result in uncontrolled ejection of the sample from the tube or damage the tube itself.

2. Protein preparation, labeling, and characterization

2.1. Horse heart metmyoglobin

Horse heart metmyoglobin (MetMb) and sodium azide (NaN_3) used for the calibration of the MHQ device were obtained from Sigma-Aldrich. Prior to use, a MetMb solution (1.5 mM) and a NaN_3 solution (1.5 M) were freshly prepared in sodium citrate buffer (25 mM, pH 5).

2.2. Cloning of CNBD mutants

The introduction of cysteine residues into the cyclic nucleotide-binding domain (CNBD) of the MloK1 channel was performed by site-directed mutagenesis. The starting template was the cysteine-free CNBD mutant C263S/C331L, cloned into the pMalc2X vector, which links the CNBD to a maltose-binding protein tag (MBP) used for purification. Mutagenesis was accomplished by the polymerase chain reaction (PCR). PCR primers were designed using the home-written PCsuppWin software. The PCR products were digested by the restriction enzymes BamHI and EcoR1, ligated, and transformed into *E. coli* Top 10 cells. Single clones were picked and grown in LB medium. Plasmids were purified using the MilliPore kit (Merck) and checked by sequencing.

2.3. Transformation of plasmid DNA

A frozen aliquot of 50 µl competent *E. coli* BL21 (DE3) pLysE (Merck) cells was thawed on ice and 50 ng of plasmid DNA was added. The solution was incubated on ice for 30 min prior to a heat shock performed for 1 min at 42 °C in a water bath. Cells were cooled on ice for 2 min. Then, 200 µl of LB medium was added and incubated for 30 min at 37 °C/800 rpm in a shaking incubator. The suspension was plated on agar plates containing ampicillin (100 µg/ml) and incubated overnight at 37 °C.

2.4. Expression of recombinant proteins

A single colony of transformed *E. coli* cells was picked and grown overnight at 37 °C and 180 rpm in 50 ml LB medium (Roth) containing ampicillin. The overnight culture was used to inoculate 5 L of TB medium (Roth), resulting in an $OD_{600} \approx 0.2$. Cells were grown in a fermenter (Infors HT) at 37 °C and 1,500 rpm under constant air flow (7 ml/min). Cell growth was constantly monitored until an OD_{600} between 2.5 and 3 was obtained. At this point, the temperature was lowered to 20 °C and protein expression was induced by addition of isopropyl-β-D-thiogalactopyranosid (IPTG; Sigma) to a final concentration of 0.8 mM. Protein expression continued for 20 h. Cells were harvested by centrifugation (6,000 x g for 10 min at 4 °C); the supernatant was discarded, and cell pellets were collected and stored at -20 °C.

2.5. Protein purification

Frozen *E. coli* pellets were thawed and resuspended (3x volume/mass) in PBS containing (mM): 10 Na^+ phosphate, 150 NaCl, pH 7.4, 10 di-thiothreitol (DTT; Sigma), and protease inhibitor cocktail (Complete EDTA-free; Sigma). All following steps were performed on ice. Cells were lysed by sonication (Sonies Vibra Cell, 4 min, 40% max. amplitude) and insoluble debris was removed by centrifugation (40,000 x g, 60 min, 4 °C). The supernatant containing the soluble CNBD was collected.

2.6. Affinity purification

The supernatant of lysed cell pellets was incubated with amylose resin (NEB) (0.2 ml/g *E. coli* pellet) for 30 min at 4 °C under constant rotation. Resin was sedimented by centrifugation (4,000 x g, 10 min) and the supernatant was discarded. For washing, the resin was mixed with PBS, centrifuged (4,000 x g, 10 min), and the supernatant was discarded. This washing step was performed five times to remove *E. coli* proteins and excess DTT. Finally, instead of elution from the amylose resin by high sugar concentrations, the protein was eluted by denaturation in guanidine buffer containing (mM): 10 Na^+ phosphate, 150 NaCl, 6,000 guanidine, pH 7.4) (2.5 ml buffer/ml resin), which disrupts the tertiary structure of the CNBD/MBP protein. Unfolded MBP does not bind to the amylose resin and the protein is released. The amylose resin was sedimented by centrifugation and the CNBD-containing supernatant was collected. The denaturation step was used for two additional reasons: First, *E. coli* cells inherently contain cAMP that binds to the CNBD during expression and purification. Upon denaturation, cAMP can be washed away. Second, depending on the mutant, the yield of spin labeling was significantly higher in the unfolded compared to the native form.

2.7. Spin labelling of protein with unfolding/refolding

The nitroxide spin label S-(1-oxyl-2,2,5,5-tetramethylpyrroline-3-methyl)methanethiosulfonate (MTSSL) was attached via disulfide bond formation to cysteine residues. MTSSL was added to the solution of unfolded protein in a 5-fold molar excess and incubated overnight at 4 °C. Excess spin label was removed by size-exclusion chromatography. The labeling efficiency is given as molar protein-to-spin label ratio. The spin concentration was determined by *cw* X-Band EPR spin-counting experiments (see SI, section 4.2) and the protein concentration by UV-VIS spectroscopy (see SI, section 2.10). Of note, the *cw* EPR spectra of both constructs, E289R1/I340R1 and R254R1/E336R1, are diagnostic of immobilized nitroxide label and thus prove successful labeling of the protein (Figure S3).

Removal of cAMP and spin label. The unfolded CNBD was separated from free cAMP and spin label using Amicon spin columns (30 kDa cut-off). The protein solution was concentrated by centrifugation in the spin column at 4,000 x g (final volume 1 ml), followed by addition of 4 ml of guanidine buffer and subsequent centrifugation. This step was repeated three times. To ensure that cAMP removal was complete, cAMP remaining bound to the CNBD was determined photometrically using the absorption maxima of the CNBD and cAMP at 280 nm and 260 nm, respectively. The absorption ratio A260:A280 was determined to 0.8 for a cAMP-free CNBD-MBP solution.

Refolding of denatured proteins. To restore the native protein fold, 3 ml of a CNBD solution was added stepwise under slow stirring to 40 ml of ice-cold refolding buffer containing (mM): 7 Na_2HPO_4, 3 NaH_2PO_4, 150 NaCl, 500 L-arginine, and 10 EDTA at pH 7.4. Finally, the solution volume was reduced to 2-4 ml by centrifugation in an Amicon spin column (cut-off 30 kDa).

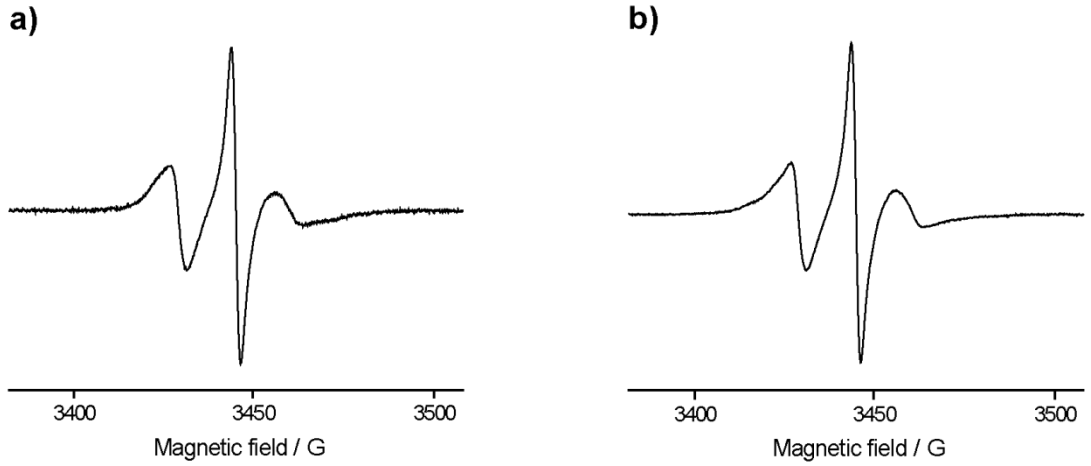

Figure S3: *cw* X-Band EPR spectra of the spin-labeled MloK1 CNBD constructs.
(a) E289R1/I340R1 at a protein concentration of 283 µM and a spin concentration of 468 µM, corresponding to a labeling efficiency of 83%. (b) R254R1/E336R1 at a protein concentration of 300 µM and a spin concentration of 453 µM, corresponding to a labeling efficiency of 76%. Both samples were prepared via the "unfolding/refolding" procedure.

2.8. Spin labelling of protein without unfolding/refolding

The protocol was identical up to binding of the MBP-tagged CNBD (E289C/I340C) to the amylose resin. Instead of eluting the protein from the resin by denaturation in guanidine buffer, the protein was first washed twice with PBS buffer/2 mM DTT containing 5 mM cGMP to release endogenous *E. coli* cAMP by competition. After another two washes with PBS buffer/2 mM DTT to remove cGMP, the protein was eluted with 20 ml PBS buffer/2 mM DTT containing 10 mM D-(+)-maltose (Sigma-Aldrich). The eluate was concentrated to 3 ml using a 30 kDa cutoff filter (Amicon Ultracel 30K) before loading to a PD10 column (GE Healthcare) to remove DTT prior to MTSSL labeling. The protein was eluted from the PD10 column with PBS. The spin label MTSSL was added to the eluate at a molar ratio of 20 per 1 free cysteine (40 per protein) and incubated overnight at 4 °C. The sample was concentrated to 3.5 ml and loaded onto column (HiLoad 16/60 Superdex 200) for size-exclusion chromatography. The fractions corresponding to the spin-labeled MBP-tagged CNBD (E289C/I340C) were pooled and concentrated to 83 µM protein. All other procedures were identical to those using unfolded/refolded protein samples.

2.9. Size-exclusion chromatography (SEC)

During refolding, a fraction of the protein aggregates. Refolded and aggregated protein fractions were separated by SEC using a HiLoad Superdex 200 column (16/60 Prep grade, GE Healthcare), equilibrated with two column volumes PBS using an Äkta chromatography system (Äkta Purifier, GE Healthcare). The refolded CNBD monomer eluted in a single peak at 84 ml. Fractions were pooled and concentrated in a spin column. The CNBD concentration was adjusted to 300 µM, and aliquots of 200 µl were frozen in liquid nitrogen and stored at -80 °C.

2.10. Determination of protein concentration

The concentration of purified CNBD-MBP fusion protein was determined by absorption measurements at 280 nm. The absorption coefficient ε_{280} for the CNBD-MBP protein (71,850 M^{-1} cm^{-1}) was calculated from the amino-acid sequence. The total protein content of cell homogenates was determined using the Bradford assay. The Bradford reagent was mixed 1:4 with distilled water and 1 µl of protein solution. The solution was incubated for 5 min, and the absorption was measured in a photometer at 595 nm. Bradford solution without protein was used as blank. The Bradford assay was calibrated using bovine serum albumin (BSA).

2.11. Analysis of protein samples by SDS-PAGE

Composition and purity of protein samples was analyzed by SDS-polyacrylamide gel electrophoresis (SDS-PAGE). The SDS-PAGE gels consisted of a 15% running gel and a 5% stacking gel. Samples containing 1-10 µg protein were mixed with 4x Laemmli buffer and heated to 95 °C for 5 min. A mix of molecular weight markers was loaded as reference. Electrophoresis was performed at 25 mA for 1 hour. SDS-PAGE gels were stained using Coomassie Brilliant Blue for 2 hours. Gels were destained overnight in destaining solution (30% v/v ethanol and 10% v/v acetic acid).

2.12. Time considerations

The preparation and labeling of the MHQ sample involve a 2-day protocol per batch. Set-up and execution of mixing in the MHQ takes about 2 h per time point.

3. Characterization of cAMP binding to wt and mutant CNBD

3.1. Equilibrium binding

The cAMP binding affinity of unlabeled and spin-labeled CNBD was determined by fluorescence spectroscopy and isothermal calorimetry (ITC). The CNBD (2 µM) was mixed with the fluorescent cAMP analogue 8-NBD-cAMP (Biolog) at concentrations ranging from 0.1 to 5 µM. All solutions were prepared in PBS. The emission spectrum of 8-NBD-cAMP was recorded in a spectrofluorometer (QM-4, PTI) by excitation at 470 nm and an emission scan between 500 nm and 600 nm. A reference titration without protein was recorded and subtracted from the data. The baseline-corrected emission at 530 nm was plotted against the 8-NBD-cAMP concentration. The data points were fitted with the equation

$$\Delta F = \left(\left(\frac{1}{2} * (C + L + K_D)\right) - \sqrt{\left(\frac{1}{4} * (C + L + K_D)^2 - C * L\right)}\right) * x$$

wherein ΔF is the change in fluorescence, C the protein concentration, L the ligand concentration, K_D the dissociation constant, and *x* a proportionality factor. From this fit, K_D was calculated. ITC was performed with a MicroCal iTC200 instrument (Malvern Panalytical) to measure cAMP binding to the CNBD. The protein and ligand solutions were prepared in the same buffer (PBS) to prevent heat signals resulting from buffer dilution. All titrations were performed at 25 °C. The syringe was loaded with a 1.5-mM cAMP solution and the sample cell with 150-µM solution of the CNBD. Ligand was injected into the cell in 1.66 µl-steps under constant stirring at 700 rpm. The differential power was set to 6 and the interval between injections was 180 s. Data was analyzed with the software delivered with the calorimeter.

3.2. Kinetic measurements using the stopped-flow apparatus

Stopped-flow experiments were performed in an SFM-400 (BioLogic). The principles and practical aspects of the technique are described elsewhere.[2,3]

4. EPR spectroscopy

4.1. *Cw* X-Band EPR spectrometer

Low-temperature *cw* EPR spectra of the MetMb samples were recorded at X-Band (~9 GHz) on an EMXmicro EPR spectrometer (Bruker BioSpin) equipped with an ER4122SHQE resonant cavity (Bruker), an ER4112HV liquid helium cryostat (Bruker), and a Mercury iTC503 temperature controller (sensor type ESR900, Oxford Instruments). All spectra were obtained at 20 K using the following parameters: 0.5 mW microwave power (25 dB attenuation), 10 G modulation amplitude, 85 ms conversion time, 81.92 ms time constant, 3,600 data points, 1.1 points per Gauss, 5 averages. Baseline drifts related to the electrostatic behavior of the sample powder[1] and packing inhomogeneity were corrected for by splining. Peak-to-peak amplitudes of the respective signals were analyzed to deduce the fractions of *hs* and *ls* Fe(III), for details see SI, section 4.5. Data acquisition and processing was done using the Xenon software (Bruker). Workload for measurement set-up and acquisition time: ~ 30 – 40 min per sample.

4.2. Spin counting

Cw EPR spin counting experiments to determine the labeling efficiency were performed at X-Band at RT on an EMXnano benchtop EPR spectrometer (Bruker). The aqueous protein solutions were filled into 10 µl capillaries (Disposable Capillaries, Hirschmann Laborgeräte) and then transferred into X-Band EPR tubes with an outer diameter of 4 mm (Wilmad LabGlass). Acquisition parameters were: 2.5 mW microwave power (16 dB attenuation), 1 G modulation amplitude, 20.48 ms conversion time, 20.94 ms time constant, 1,300 data points, 10 points per Gauss. Spin quantitation was performed by double integration of the first-derivative spectra and the on-board spin counting routine. Data acquisition and processing was done using the Xenon software (Bruker). Workload for measurement set-up and acquisition time: ~ 15 – 20 min per sample.

4.3. Pulsed Q-Band EPR spectrometer

Pulsed EPR experiments were performed at Q-Band (~33 GHz) on an ELEXSYS E580 spectrometer equipped with a Flexline probehead and an ER 5106 QTII resonator (Bruker). The temperature was adjusted to 50 K using a CF935 continuous-flow helium cryostat in combination with an iTC503S temperature controller (Oxford Instruments). For amplifying the microwave pulses, a 150 W travelling wave tube (TWT) pulse amplifier (model 187 Ka, Applied Systems Engineering) was used. All data was acquired using quadrature detection.

4.4. Pulsed Electron-Electron Double Resonance (PELDOR)

PELDOR experiments were carried out using the standard four-pulse sequence $\pi/2(\nu_A)–\tau_1–\pi(\nu_A)–(\tau_1+t)–\pi(\nu_B)–(\tau_2–t)–\pi(\nu_A)–\tau_2–$echo. The magnetic field was adjusted such that the pump pulse frequency ν_B (33.7 GHz) was in resonance with the maximum of the nitroxide spectrum; the detection frequency ν_A was 100 MHz lower. The length of $\pi/2$ and π detection pulses was set to 12 and 24 ns, respectively, and the length of the pump pulse was adjusted by a transient nutation experiment in such a way that a maximal inversion of the magnetization could be obtained (12 ns–18 ns). Two-step phase cycling was applied to the $\pi/2$ pulse to remove receiver baseline offsets and unwanted echoes. The initial value of τ_1 was set to 260 ns being incremented 8 times by 16 ns, thus removing deuterium ESEEM from the dipolar traces (nuclear modulation averaging). τ_2 was set to 3 µs. The position of the pump pulse with respect to the primary echo was incremented by 8 ns steps. Ten shots per point on the dipolar trace were recorded, and the shot repetition time was set to 2 ms. Data acquisition was

controlled using the XEPR software (Bruker) and transformation of the time-domain signal into interspin distance distributions was done using the DeerAnalysis 2019 software.[4] Background correction was done assuming a 3D-homogeneous distribution of nano-objects and distance distributions were computed by Tikhonov regularization with the optimal regularization parameter α determined according to the L-curve corner criterion. A statistical uncertainty analysis was done by the validation routine of DeerAnalysis. Workload for measurement set-up: ~ 30 – 45 min. Acquisition time: ~ 7 h per sample.

4.5. Analysis of *cw* X-Band EPR spectra from the MetMb/NaN_3 calibration reaction

First, *apo* MetMb (*hs* Fe(III)) and *holo* MetMb (*ls* Fe(III)) samples of identical concentrations and volumes (i.e. number of spins) were prepared and frozen by immersion of the EPR tubes into liquid nitrogen. In order to quantify the amount of *hs* and *ls* Fe(III), the peak-to-peak amplitude was used of the g = 5.8 (I(hs_{apo})) and the g = 2.2 signal (I(ls_{holo})) of *hs* and *ls* Fe(III), respectively. Double integration of the signals was dismissed because of baseline artefacts. It turned out that both samples yield different signal intensities despite having nominally the same number of spins, which is attributed to the largely different relaxation times and thus different saturation behaviors. Therefore, rather than the absolute values, the intensity ratios of the peak-to-peak amplitudes of the *hs* and *ls* Fe(III) signal were used. The normalization factor is:

$$\mathrm{NF} = \frac{hs_{apo}}{ls_{holo}} = \frac{\mathrm{I(hs}_{apo})}{\mathrm{I(ls}_{holo})} = \frac{68.50}{4.42} = 15.49$$

With this, the percentage of the *hs* state (% hs_{apo}) in a sample can be calculated by the fraction of the [hs_{apo}] concentration to the total spin concentration ([hs_{apo}] + [ls_{holo}]):

$$\%\, hs_{apo} = \frac{[hs_{apo}]}{[hs_{apo}] + [ls_{holo}]} \cdot 100$$

$$= \frac{\mathrm{I(hs}_{apo})}{\mathrm{I(hs}_{apo}) + \mathrm{NF} \cdot \mathrm{I(ls}_{holo})} \cdot 100$$

4.6. Comparison of the rate constants of the MetMb/NaN_3 reaction with the literature

In order to compare the reaction rate constants determined here to literature values, Figure 11 of Cherepanov and de Vries[1] has been digitized and the fractions of *apo* and *holo* state for [NaN_3] = 0.75 M have been estimated by extrapolation. The digitized data was re-analyzed by fitting with one or two exponential functions (Figure S4). Originally, Cherepanov and de Vries[1] used a single exponential fit to analyze their data. However, a two-exponential function does provide a much better fit to their data. The respective rate constants of Cherepanov and de Vries[1] and our data are compared in Table S2. In conclusion, the rate constants of the calibration reaction determined here and by Cherepanov and de Vries[1] are in excellent agreement.

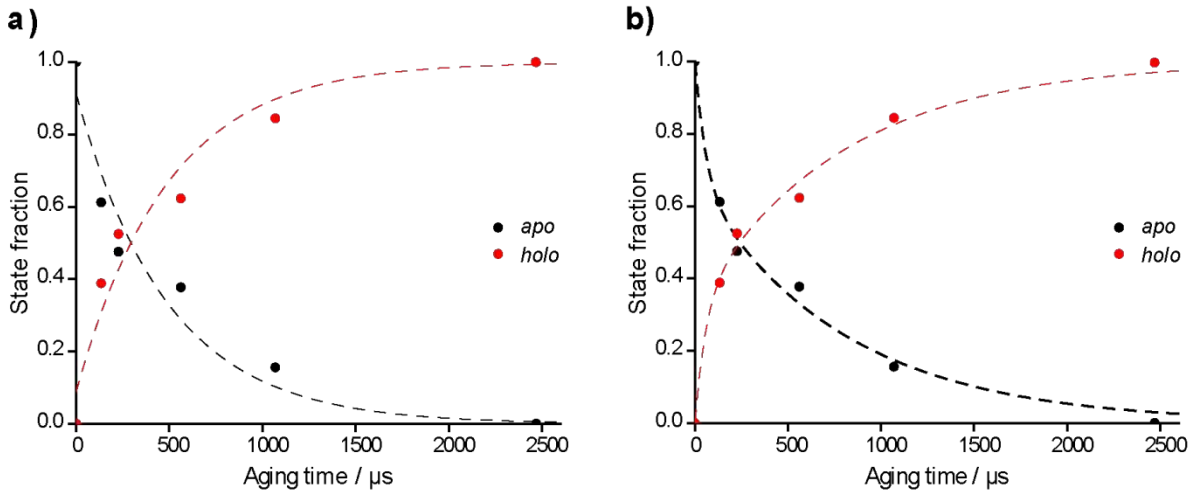

Figure S4: Re-analysis of the data from Cherepanov and de Vries 2004.[1] (a) The fraction of *apo* and *holo* states of the MetMb/NaN_3 reaction was fitted by a single exponential function ($y = Ae^{-k'_1 t}$). (b) Fit by a two-exponential function ($y = Ae^{-k'_1 t} + Be^{-k'_2 t}$). The resulting rate constants are given in Table S2.

Table S2: Fitting of the MetMb/NaN_3 kinetics to a two-exponential function[#].

	Cherepanov and de Vries[1]	This work
pre-exponential coefficients	A = 0.33 ± 0.15 B = 0.67 ± 0.14	A = 0.44 ± 0.06 B = 0.51 ± 0.05
pseudo-first order rate constants	k'_1 = 17,262 ± 24,889 s^{-1} k'_2 = 1,263 ± 363 s^{-1}	k'_1 = 19,669 ± 5,406 s^{-1} k'_2 = 1,358 ± 189 s^{-1}
second order rate constants	k_1 = 23,016 ± 33,185 M^{-1} s^{-1} k_2 = 1,684 ± 484 M^{-1} s^{-1}	k_1 = 26,225 ± 7,208 M^{-1} s^{-1} k_2 = 1,811 ± 252 M^{-1} s^{-1}
goodness of fit	R^2 = 0.99	R^2 = 0.99

[#] $y = A \cdot e^{-k'_1 t} + B \cdot e^{-k'_2 t}$

4.7. Deconvolution of PELDOR time traces

Time traces obtained from MHQ-shot samples were deconvolved to obtain the fraction of *apo* and *holo* state using a home-written MATLAB script, which solves the linear equation

$$\mathbf{MHQ} = A \cdot \boldsymbol{apo} + B \cdot \boldsymbol{holo}$$

Herein, "MHQ", "*apo*", and "*holo*" are vectors containing the time traces of the respective states with "MHQ" representing the trace of the sample quenched at a defined aging time. The scalars "A" and "B" denote the respective contributions of *apo* and *holo* traces to optimally reproduce the experimental trace ("MHQ"). In order to obtain a reliable deconvolution, it is necessary to compensate for occasional differences in the modulation-depth λ that result from slightly varying labeling efficiencies among different protein batches and from imperfections in setting up the PELDOR experiment. Therefore, modulation-depth scaling,[4,5] which computationally equalizes the modulation-depth of the three traces before solving the linear equation, has been implemented into the program. Herein, the modulation-depth of all traces has been scaled to λ of the *apo* time trace. The modulation-depth scaling factor f_λ is calculated as:[4,5]

$$f_\lambda = \frac{\sum_{k=1}^{N} [\ln V_{apo}(t_k)]^2}{\sum_{k=1}^{N} \ln V_{apo}(t_k) \ln V_{MHQ}(t_k)}$$

where V_{apo} is a vector representing the *apo* time trace in form of intensity versus discrete dipolar evolution times t_k, and V_{MHQ} is the vector for the MHQ-quenched sample for a defined aging time t_a. With this modulation-depth scaling factor, the original MHQ time trace V_{MHQ} can be scaled to the modulation-depth of the *apo* trace:

$$V_{MHQ}^{rescaled} = e^{f_\lambda \cdot \ln(V_{MHQ})} = \left(e^{\ln(V_{MHQ})}\right)^{f_\lambda} = V_{MHQ}^{f_\lambda}$$

The same procedure was applied to the time trace obtained from the *holo* state. Then, the linear equation above can be solved. Figure S5 shows the deconvolution for the time traces of construct E289R1/I340R1 at t_a = 303 µs.

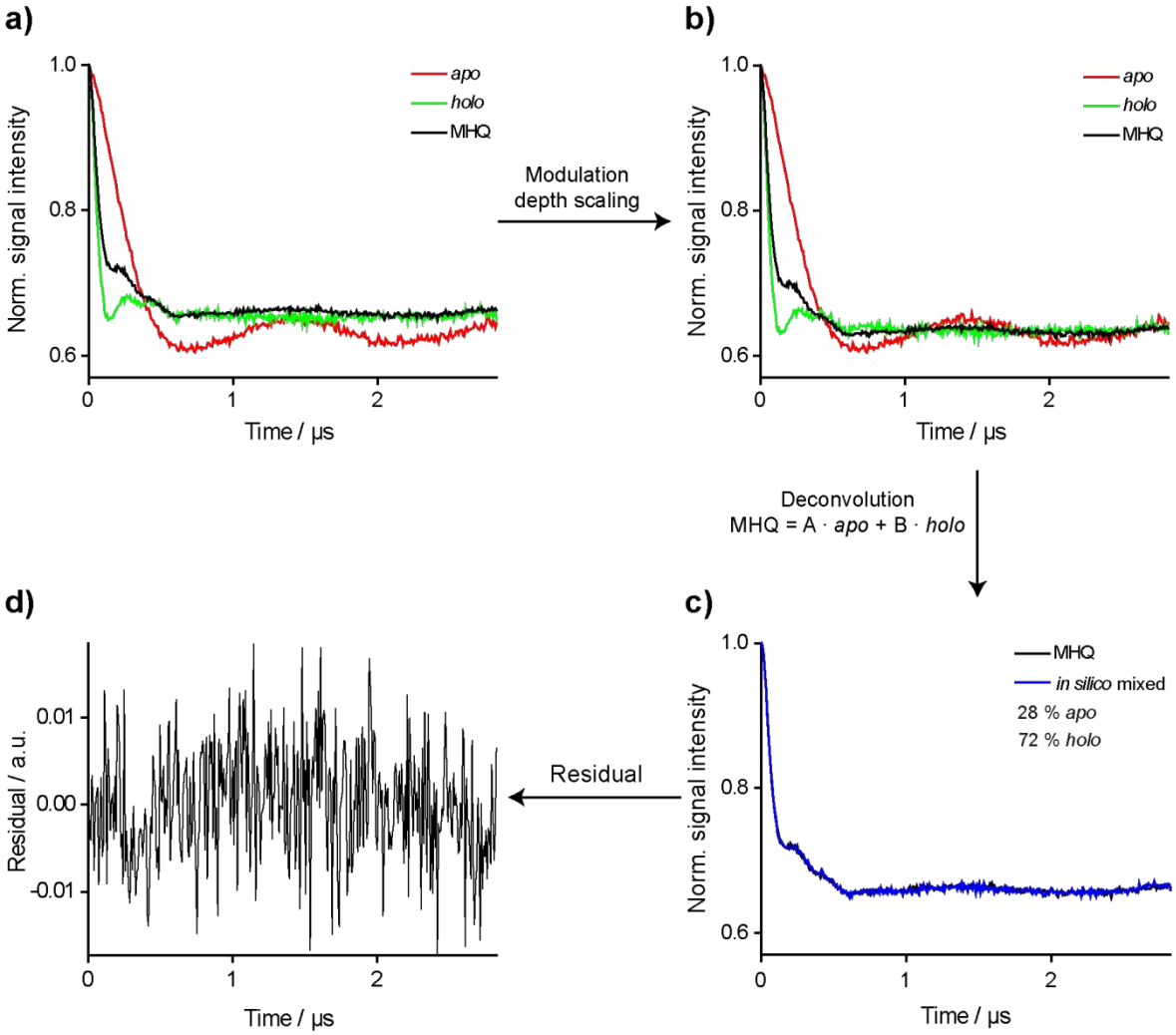

Figure S5: Deconvolution of PELDOR time traces. (a) Background-corrected time traces obtained from DeerAnalysis of construct E289R1/I340R1. (b) Time traces after modulation-depth scaling. The modulation depths of the *apo* state, the *holo* state, and the MHQ time trace have been normalized. (c) Deconvolution of the MHQ time trace to obtain the fractions of *apo* and *holo* state. Experimental trace (black); corresponding trace obtained by *in-silico* mixing of *apo* and *holo* traces with the respective weighting factors (blue). (d) The residual between experimental and *in-silico* time traces shown in (c) represents noise.

Table S3: **Fitting parameters for the time-resolved PELDOR data of constructs E289R1/I340R1 and R254R1/E336R1 in Figure 4 (see main text).**

Regression parameter	E289R1/I340R1	R254R1/E336R1
y_0 / a.u.	0.12 ± 0.04	0.17 ± 0.04
A / a.u.	0.96 ± 0.08	0.84 ± 0.05
k / s^{-1}	7,398 ± 1,179	7,508 ± 867

The data in Figure 4 was fitted by $y = y_0 + A \cdot e^{-kt}$.

5. *In-silico* spin labeling

5.1. Computing distance distributions with mtsslWizard

For computing distance distributions with mtsslWizard,[6] the NMR structures of the CNBD (PDB-IDs: 2kxl, *apo* and 2k0g, *holo*) were used. In mtsslWizard, the maximum number of conformers was set to 10,240 per labeling site ("painstaking" mode in the software), using a van-der-Waals cutoff of 2.5 Å and 5 allowed clashes ("loose" mode). In order to exclude possible influences from crystal packing effects, only NMR structures were used for computing distance distributions. Table S4 compares the most probable inter-spin distance r, the mean inter-spin distance ⟨r⟩, and the full width at half height FWHH for the mtsslWizard derived distributions and the experimental distance distribution.

Table S4: Parameters characterizing the PELDOR and mtsslWizard derived distance distributions of the MloK1 CNBD constructs E289R1/I340R1 and R254R1/E336R1. *In-silico* predictions are based on the NMR structures (PDB-ID: 2kxl, *apo*; 2k0g, *holo*).

		r / nm	⟨r⟩ / nm	FWHH / nm
E289R1/I340R1	PELDOR *apo*	4.1	3.9	0.4
	mtsslWizard *apo*	4.1	3.9	0.8
	PELDOR *holo*	2.2	2.4	0.5
	mtsslWizard *holo*	2.3	2.3	0.9
R254R1/E336R1	PELDOR *apo*	3.5	3.4	0.5
	mtsslWizard *apo*	3.8	3.7	0.8
	PELDOR *holo*	3.1	3.2	0.8
	mtsslWizard *holo*	3.5	3.5	0.8

r denotes the most probable interspin distance, ⟨r⟩ the mean distance, and FWHH the full-width at half height. PDB IDs used for labeling in mtsslWizard: *apo*: NMR 2kxl; *holo*: NMR 2k0g.

5.2. Difference-distance map (DDM)

The DDM (Figure S6) was computed based on the NMR structures (PDB-IDs: 2kxl/2k0g) and all distance changes larger than 6 Å were highlighted, which was evaluated to be the minimum requirement to obtain non-overlapping distributions for *apo* and *holo*. If both sites were additionally located in structurally ordered regions, i.e. α-helices or β-sheets, full *in-silico* distance distributions were computed. From these constructs, those that showed absolute distances between 1.5 and 8 nm were considered for experimental spin labeling.

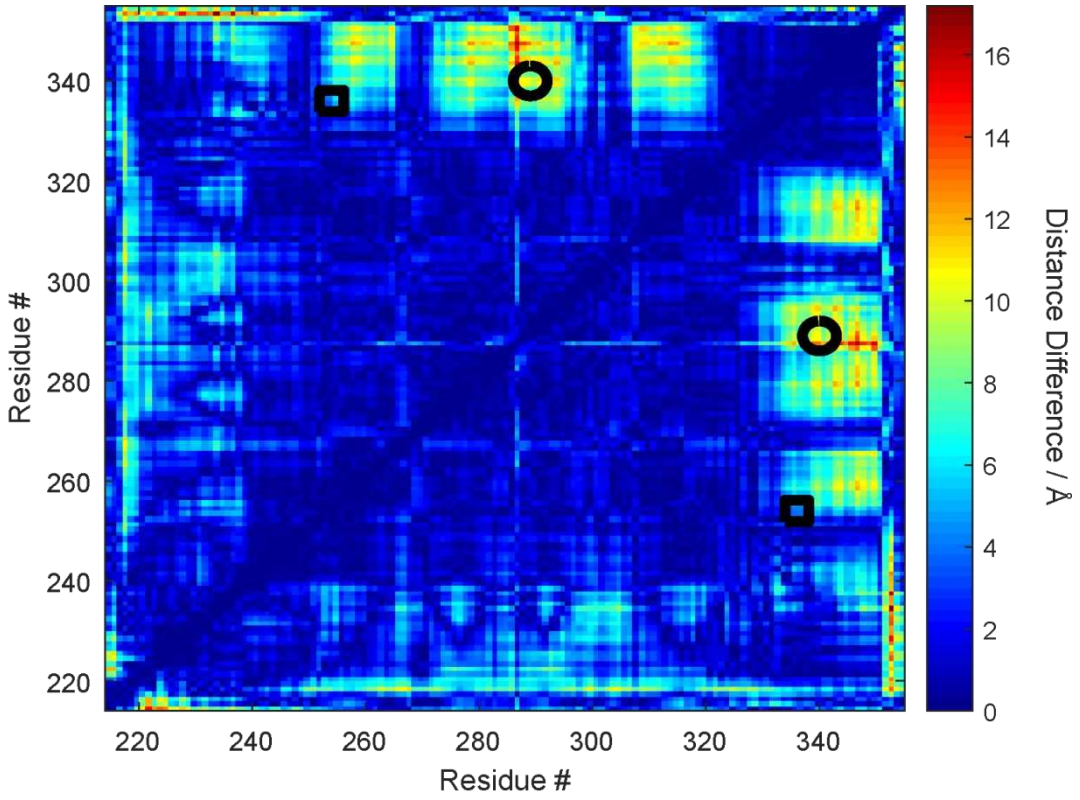

Figure S6: Difference-distance map (DDM). DDM obtained from mtsslWizard in combination with the NMR structures (PDB-IDs: 2kxl, *apo* and 2k0g, *holo*). The black circles and squares indicate constructs E289/I340 and R254/E336, respectively.

5.3. Computing distance distributions with MMM

For computing distance distributions within MMM,[7] the NMR structures of the CNBD (PDB-IDs: 2kxl, *apo* and 2k0g, *holo*) were used. In MMM, distance distributions were computed using the preset temperature selection "cryogenic" with the rotamer libraries being optimized for a temperature of 175 K, which roughly corresponds to the glass transition temperatures of the buffers used for PELDOR.

A comparison of distance distributions derived from MMM, mtsslWizard, and the PELDOR data is shown in Figure S7.

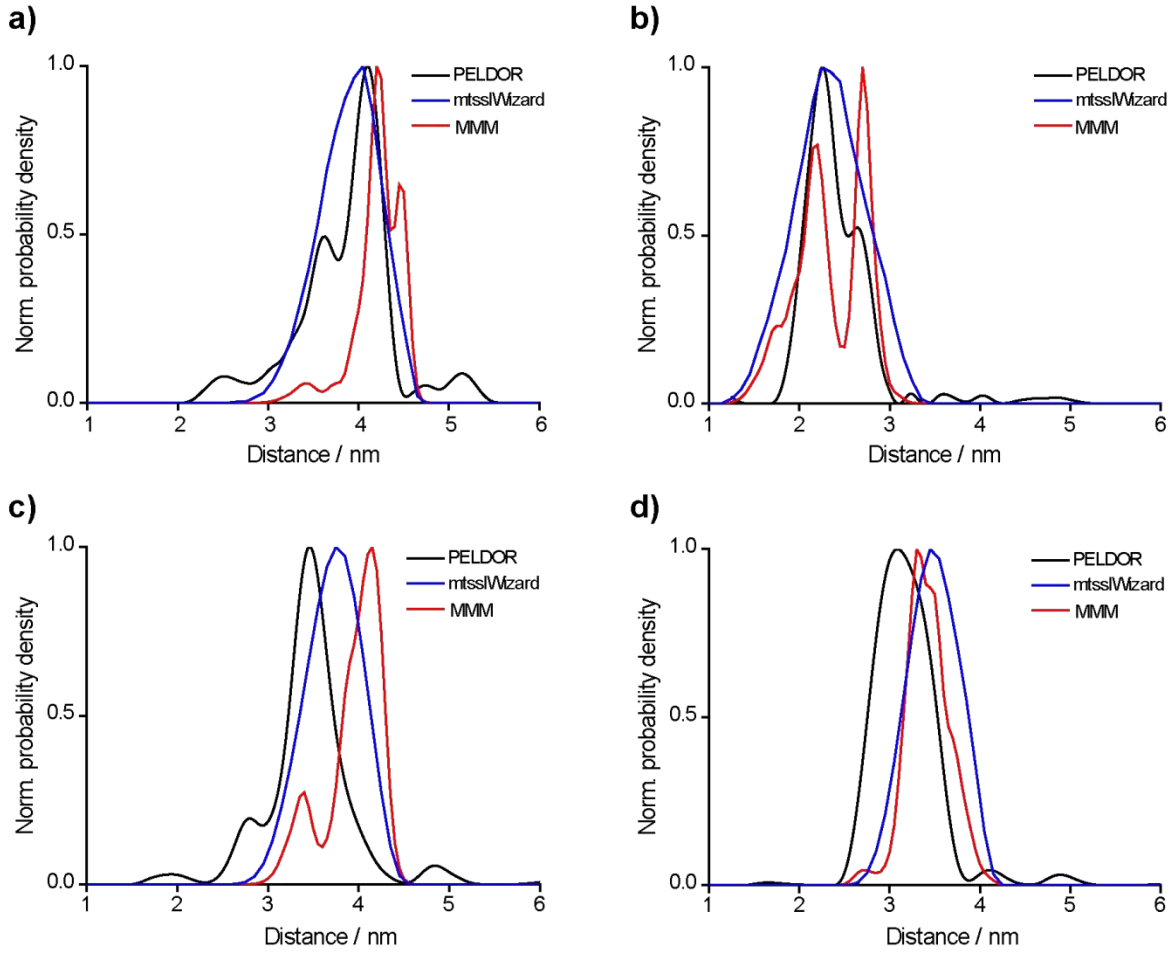

Figure S7: Comparison of mtsslWizard and MMM derived distance distributions with the experimental distance distributions. The distance distributions derived from mtsslWizard (blue), MMM (red), and the experiment (black) are overlaid. The *in-silico* predictions are based on the NMR structures of the MloK1 CNBD (PDB-IDs: 2kxl, *apo* and 2k0g, *holo*). (a) E289R1/I340R1 *apo*. (b) E289R1/I340R1 *holo*. (c) R254R1/E336R1 *apo*. (d) R254R1/E336R1 *holo*.

6. Assessing the effects of spin labelling and sample preparation on the protein structure and ligand binding

6.1. Influence of unfolding/refolding on the protein structure

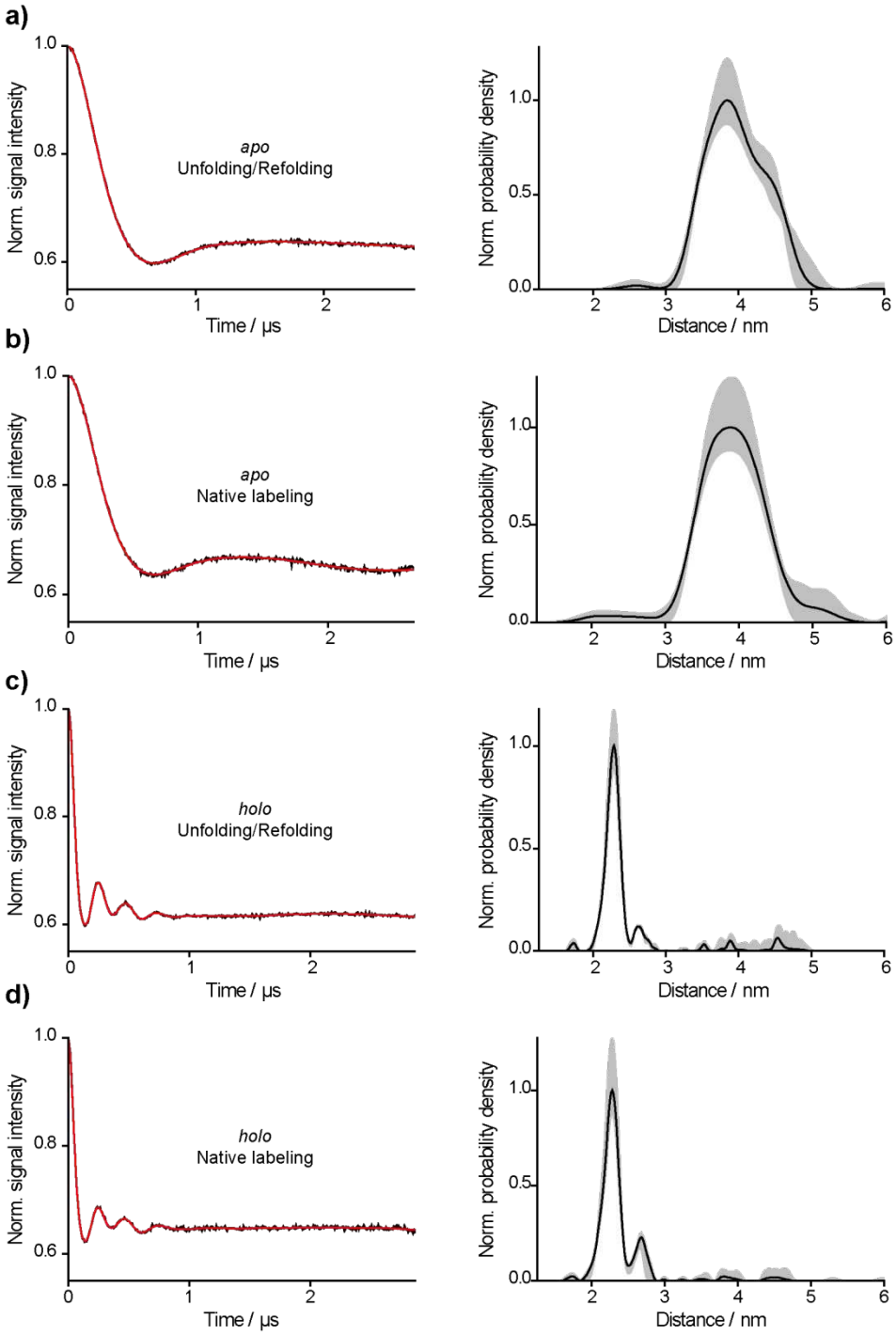

Figure S8: Influence of the labeling method on the PELDOR distance distributions of the *apo* and *holo* state of MloK1 construct E289R1/I340R1. The background-corrected PELDOR time traces (left panel) are shown together with the corresponding distance distributions (right panel). The red lines indicate a fit to the time traces subjected to Tikhonov regularization. The DeerAnalysis background validation is shown as grey shading in the distance distributions. (a) *apo* unfolding/refolding. (b) *apo* native labeling. (c) *holo* unfolding/refolding. (d) *holo* native labeling. All samples have been prepared via slow freezing.

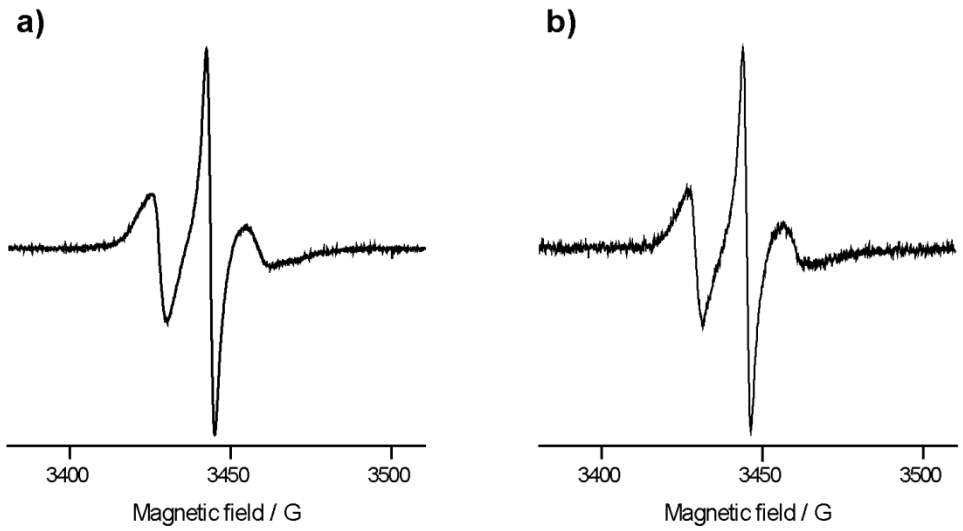

Figure S9: *cw* X-Band EPR spectra of construct E289R1/I340R1 at RT. (a) Sample involving unfolding and refolding steps. (b) Native sample that has not been subjected to unfolding.

6.2. Effect of the spin label on cAMP binding

Table S5: Summary of dissociation constants K_D of wt and mutant cyclic-nucleotide binding domains (CNBD) for cAMP and 8-NBD-cAMP.

CNBD	ligand	K_D / µM	K_D kinetics / µM	k_{on} / (10^7 M^{-1} s^{-1})	k_{off} / s^{-1}
WT [a]	8-NBD-cAMP	0.022	0.018	1.3 ± 0.02	0.23 ± 0.01
	cAMP	0.068	0.064	2.7 ± 0.4	1.7 ± 0.02
R254|E336 [b]	8-NBD-cAMP	0.28 ± 0.02	1.8	1.2 ± 0.4	16.4 ± 5.4
	cAMP [d]	9.53 ± 1.1	4.3	2.1 ± 1	86.9 ± 34.6
	8-NBD-cAMP 10% EG [c]	-	1.9	1.0 ± 0.04	18.7 ± 0.5
	cAMP 10% EG [c]	-	9.6	0.7 ± 0.1	69.6 ± 6.1
E289|I340 [b]	8-NBD-cAMP	-	0.6	2.3 ± 0.5	12.1 ± 4.6
	cAMP [d]	-	5.9	0.8 ± 0.1	45.9 ± 11.4
	8-NBD-cAMP 10% EG [c]	-	0.4	2.1 ± 0.4	8.2 ± 1.8
	cAMP 10% EG [c]	-	7.5	0.3 ± 0.01	19.6 ± 0.5

[a] from Peuker *et al.*[3] and Cukkemane *et al*[8]; [b] mean ± s.d. (n = 3); [c] ethylene glycol (EG); [d] data from isothermal calorimetry (ITC).

6.3. Effect of rapid vs. slow freezing on the distance distribution

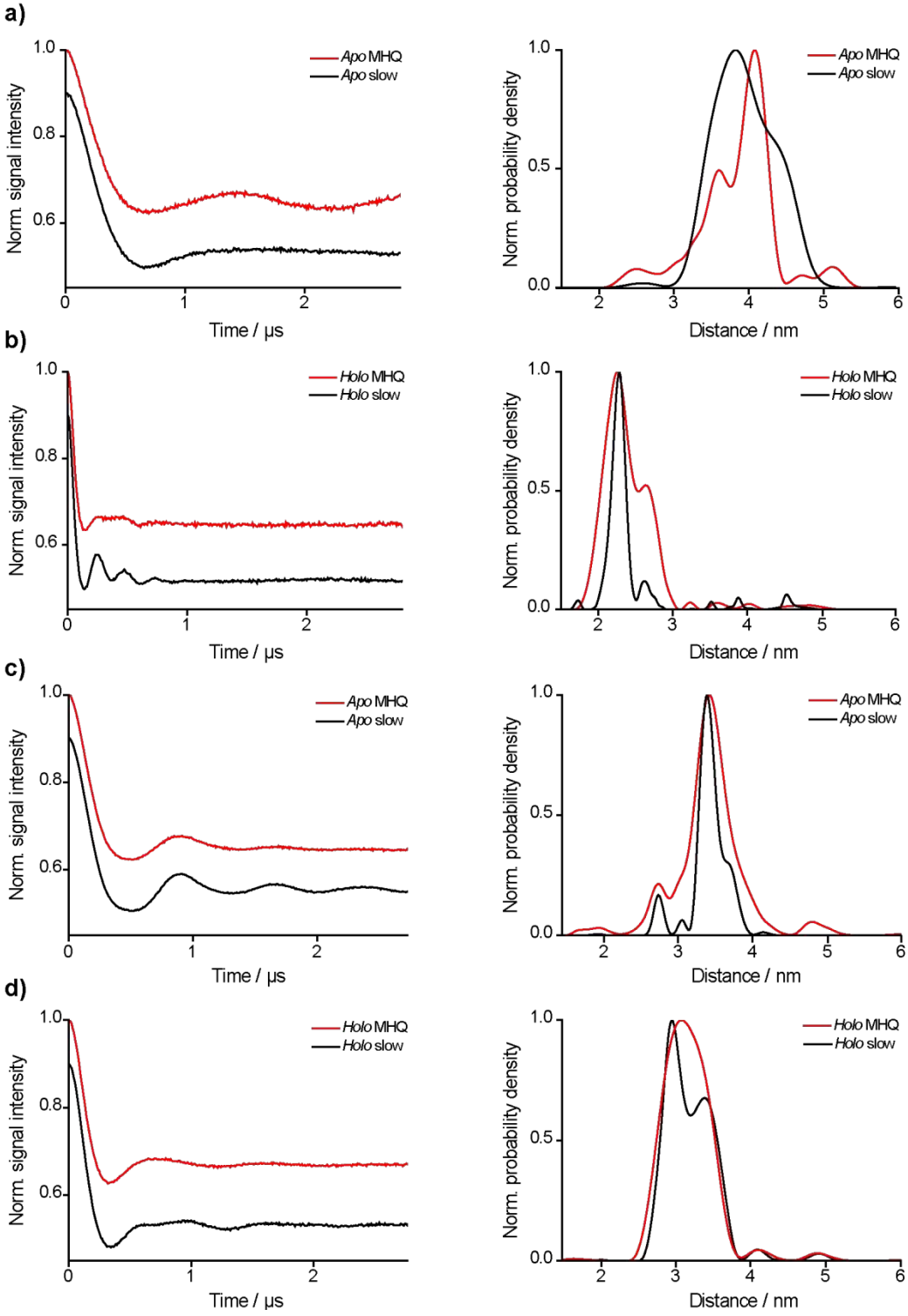

Figure S10: Influence of the freezing conditions on the PELDOR distance distributions of the *apo* and *holo* state of MloK1 constructs E289R1/I340R1 and R254R1/E336R1. The background-corrected PELDOR time traces (left panel) are shown together with the corresponding distance distributions (right panel). Note that the time traces were normalized but shifted on the y-axis for the sake of clarity. Red: MHQ freezing, t_a = 82 µs; black: slow freezing. (a) E289R1/I340R1 *apo*. (b) E289R1/I340R1 *holo*. (c) R254R1/E336R1 *apo*. (d) R254R1/E336R1 *holo*.

6.4. Influence of ethylene glycol

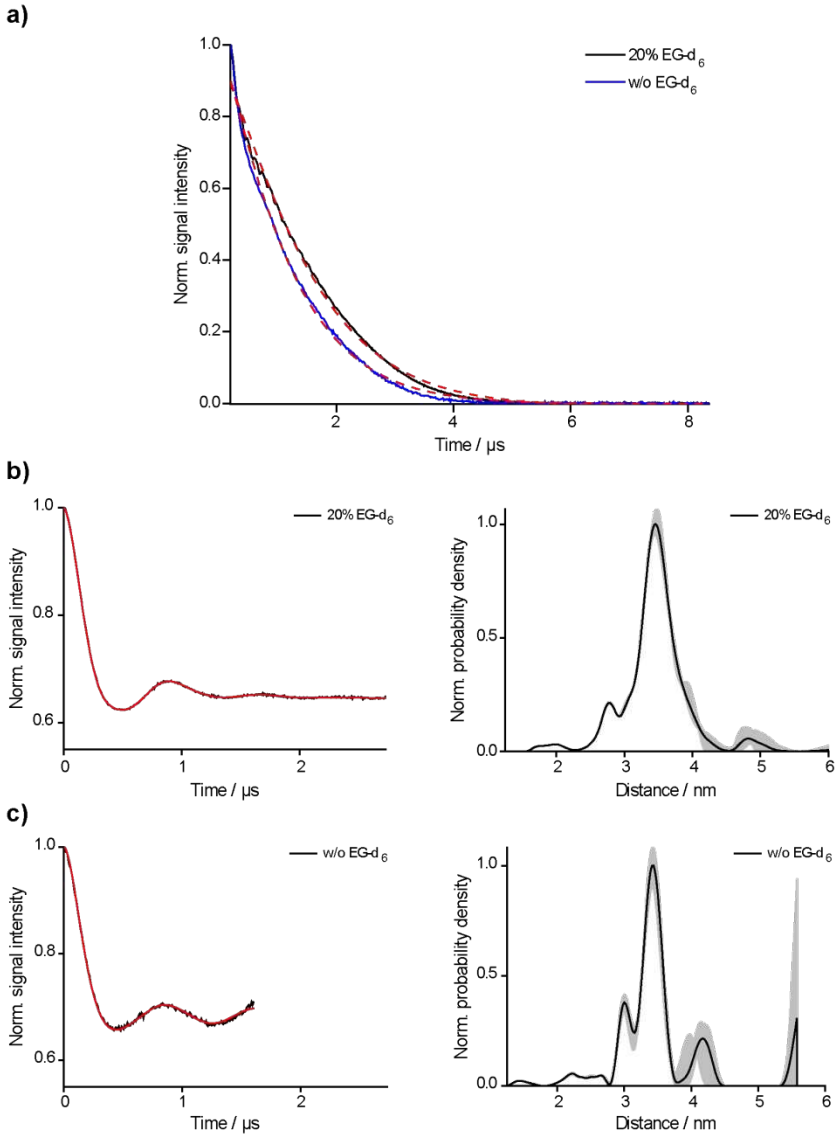

Figure S11: Influence of EG-d_6 on pulsed EPR data of MHQ-frozen MloK1 CNBD construct R254R1/E336R1 in the *apo* state for t_a = 82 µs. (a) 2-Pulse Hahn echo decay curves recorded on samples with (black) and without (blue) EG-d_6 (20%). The red dashed line indicates the fit by a stretched exponential decay. (b) PELDOR time trace and the corresponding distance distribution in the presence of 20% EG-d_6. The red line is the fit to the time trace. (c) PELDOR time trace and the corresponding distance distribution in the absence of EG-d_6. The red line is the fit to the time trace.

Table S6: Fitting parameters of the 2-Pulse Hahn echo decay curves in Figure S11.

Fit parameter[#]	w/o EG-d_6	with 20% EG-d_6
A	1.016	0.964
T_M / µs	2.5	3.2
B	1.151	1.242
C	$8.6 \cdot 10^{-4}$	$-7.0 \cdot 10^{-3}$

[#] The echo decay curves were fitted according to the stretched exponential function $y = A \cdot e^{\left(\frac{-2t}{T_M}\right)^B} + c$

Taken together, these controls support the notion that the overall structure and conformational changes are largely preserved in the labeled constructs under MHQ conditions.

7. Molecular Dynamics (MD) simulations

7.1. Simulation set-up and general parameters

MD simulations and data analysis were carried out with the molecular dynamics simulation package GROMACS[9–11] (Version 2018.1).

In total, four types of MD simulations were performed: (i) simulations on the *apo* state (PDB-ID: 2kxl), (ii) simulations on the *holo* state (PDB-ID: 2k0g), (iii) simulations on the *apo* state with the cAMP ligand positioned in the binding pocket of the *apo* state, and (iv) simulations on the *holo* state (PDB-ID: 2k0g) with the cAMP ligand removed. Parametrization of the cAMP ligand was taken from Voß et al.[12] Prior to MD production runs, the simulation systems were subjected to energy minimization and equilibration as detailed below.

For simulation-type (i) and (ii), the first NMR structure of the respective ensembles deposited in the PDB (2kxl, *apo* and 2k0g, *holo*) was extracted, energy minimization and equilibration were performed, and the systems were subjected to the MD production runs. For type (iii), the cAMP ligand was placed in the structure of the *apo* state (PDB-ID: 2kxl) at the position and in the orientation as described for the *holo* state (PDB-ID: 2k0g). After minimizing and equilibrating this simulation system, MD production runs were performed. For type (iv), the cAMP ligand was removed from the first NMR structure of the ensemble deposited in the PDB for the *holo* state (PDB-ID: 2k0g). After minimization and equilibration, MD production runs were performed.

For energy minimization, equilibration, and production runs, the AMBER99SB*-ILDN force field[13] and the TIP-3P water model[14] were used. Simulations were run in cubic simulation boxes using periodic boundary conditions; the distance between the solute and the walls was set to 1.1 nm. The salt concentration was set to 100 mM by adding Na^+ and Cl^- ions, and the system was electrostatically neutralized with the GROMACS genion tool. Throughout all simulations, long-range electrostatic interactions were computed with a particle-mesh Ewald (PME) summation using a maximal Fourier grid spacing of 0.13 nm and cubic interpolation. For neighbor-searching, the short-range electrostatic cutoff distance and the van-der-Waals cutoff were both set to 1.0 nm.

7.2. Energy minimization and equilibration

Energy minimization was done by the steepest-descent algorithm, as implemented in GROMACS, until the maximum force fell below a threshold of 1000 kJ mol^{-1} nm^{-1}. Subsequent equilibration was carried out at T = 300 K in the NVT ensemble for a total of 96 ps and at p = 1 bar in the NPT ensemble for 400 ps. Newton's equations of motion were integrated using the leap-frog algorithm with a time step of 2 fs. Initial random velocities were generated from a Maxwell-Boltzmann distribution. All atom bonds (including bonds between heavy atoms and hydrogen) were restrained by the LINCS algorithm using a harmonic force constant of 1000 kJ mol^{-1} nm^{-2}. Temperature coupling to a heat bath at a reference temperature of 300 K was achieved by the velocity-rescaling method and a coupling time constant of 0.1 ps. Pressure coupling was performed by means of the Parrinello-Rahman barostat with a reference pressure of 1 bar and a time constant of 20 ps.

7.3. Production runs

For MD production runs, Newton's equations of motion were integrated using the leap-frog algorithm with a time step of 2 fs. Temperature coupling, pressure coupling, and bond constraints were achieved using the same parameters as described above. Five trajectories of up to ~1.6 µs each were computed

for the *apo* and *holo* state structures (simulation types (i) and (ii)). For the conformational changes studied in simulation types (iii) and (iv), 24 trajectories were computed, respectively. Each trajectory was up to approximately 3.5 μs in length.

7.4. Analysis of production runs

MD trajectories were processed by the "trjconv" module of GROMACS. Periodic boundary effects were removed, the simulation system was centered within the box, and translational and rotational trajectories of protein molecules were fitted with the "progressive" option in GROMACS to obtain a continuous trajectory. Next, a cosine-shaped low-pass filter with a length of 5 ns was applied to the trajectories. For the *apo* and *holo* state simulations (simulation types (i) and (ii)), the C_α-distances of amino acids E289 and I340 were computed along the unfiltered trajectories (Extended Data Figure 4a, SI section 9.3). The magnitude of fluctuations in the C_α-distances in the *apo* and *holo* state trajectories served as a means to define distinct distance levels for the *apo* and *holo* state.

The root-mean-square deviation of atomic positions (RMSD) was computed relative to the average of the first 10 ns of the respective filtered trajectory (Extended Data Figure 4b, c, SI section 9.3). For calculation of the RMSD, only C_α-atoms of α-helices and β-sheets within structurally defined protein regions were considered (Figure S12). The *apo* and *holo* state trajectories which showed the smallest and most stable RMSD, respectively, were used for computing an average protein structure (first column of the trajectories shown in Extended Data Figure 4, SI section 9.3). These average structures were computed prior to trajectory filtering and leaving out the initial 50 ns. Thus, the system was allowed to equilibrate and adapt a stable conformation. The rationale behind this was to obtain equilibrated *apo*/*holo* structures from MD, which represent a refinement of the PDB-structures in the framework of the chosen MD parameters.

a)

b)

Figure S12: Representative average structures obtained from MD simulations. Structure averaging was performed across the unfiltered trajectories starting at a simulation time of 50 ns. The average *apo* state structure (simulation type i) is shown in (a) and the average *holo* state structure (simulation type ii) is shown in (b). These structures were used for computing the RMSD of the trajectories simulating the conformational changes (simulation types iii and iv) towards the respective target state. Note that for RMSD computation, only the C_α-atoms of the α-helices and β-sheets colored in red and yellow, respectively, were considered.

The conformational changes affecting amino acids E289/I340 were detected by monitoring the C_α-C_α distances along the unfiltered trajectories of simulation type (iii) (Figure S13, Extended Data Figure 5, SI section 9.3).

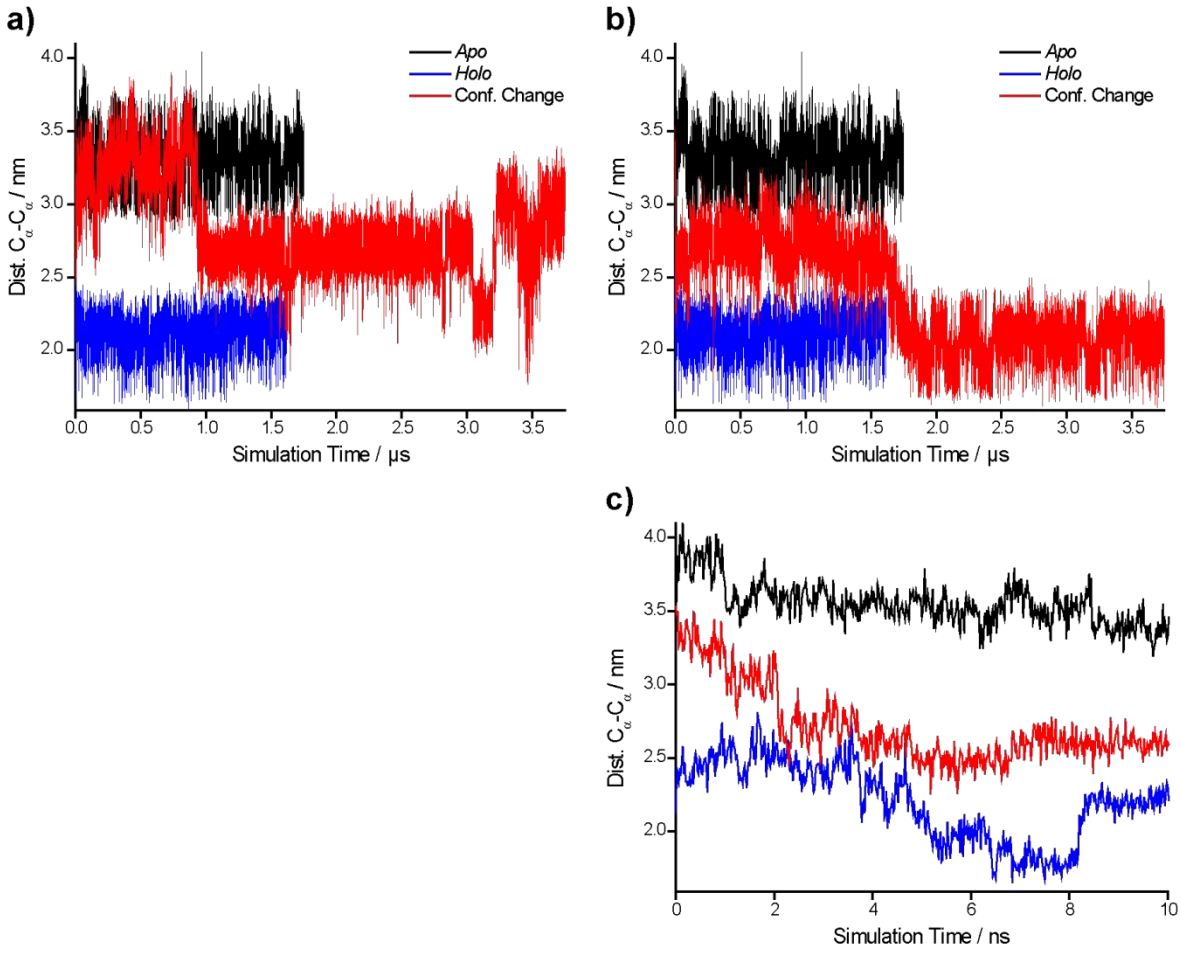

Figure S13: Molecular dynamics (MD) simulations. MD trajectories monitoring the C_α-distance of residues E289 and I340. "*apo*" refers to the *apo* state (PDB-ID: 2kxl), "*holo*" to the *holo* state (PDB-ID 2k0g), and "Conformational change" denotes the trajectory simulating the conformational change after placing the cAMP ligand into the binding pocket of the *apo* state. (a) and (b) show a selection of 24 trajectories (Extended Data Figure 4, 5, SI section 9.3), (c) shows a close-up view on the first 10 ns of (b). The trajectories obtained from the *apo* (black) and *holo* (blue) states are located on two distinct distance levels and do not cross each other. The trajectory simulating the conformational change (red) starts at the distance level of the *apo* state and then switches towards that of the *holo* state. The *apo*-to-*holo* transition occurs on the low microsecond timescale and involves nanosecond-lasting jumps. These jumps lead to intermediate distance levels that the system populates for some time before returning to the *apo* state (a) or proceeding to the *holo* state (b). The different time periods that the system stays at the distance level of the *apo* or intermediate state before switching to the *holo* state reflect differently long dwell times. Remarkably, as the conformational change has proceeded, no return to the distance level of the *apo* state can be observed within the simulation time.

Dwell times were determined manually from distance jumps observed in the trajectories and are shown as a cumulative histogram in Figure S14. Analyzing the C_α-C_α distance of a selected pair of amino acids resembled the MHQ/PELDOR approach in which the respective interspin distance was measured. Conformational changes towards the *holo* state structure were monitored by calculating the RMSD of the filtered trajectories with respect to the average *holo* state structure (Extended Data Figure 6, SI section 9.3).

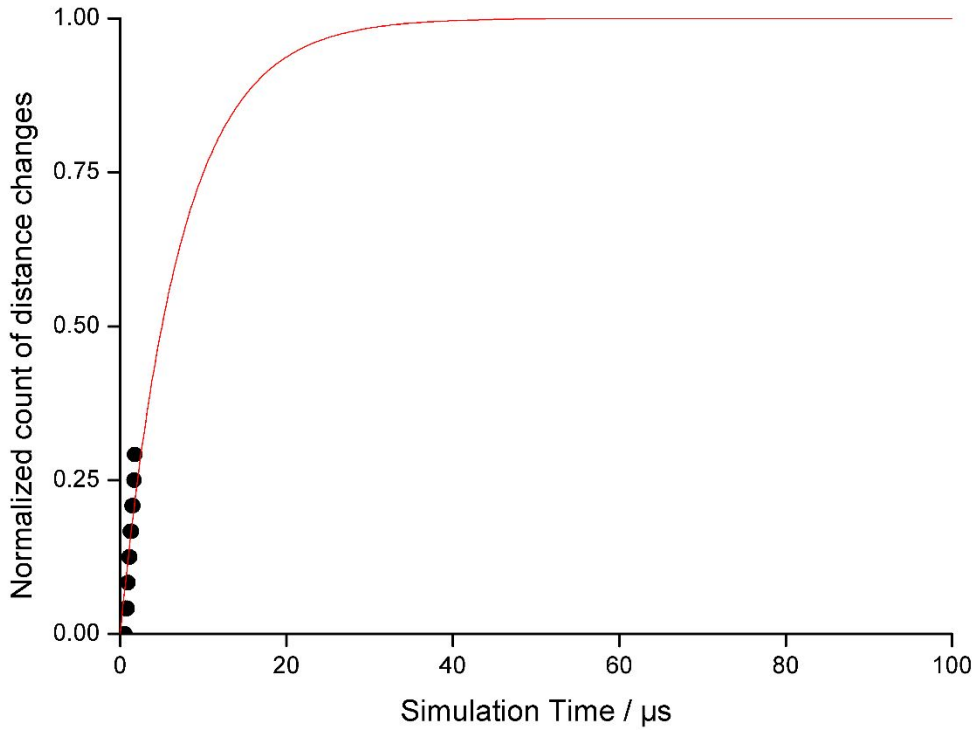

Figure S14: Cumulative histogram obtained from the MD-derived dwell times. The dwell times were determined from changes of the C_α-distances observed in simulations on the *apo* state structure with the ligand inserted into the binding pocket (simulation type iii; Extended Data Figure 5, SI section 9.3). The red line indicates an exponential fit $y = 24 \cdot (1 - e^{-t/\tau})$ to the data points with the time constant τ = 7.2 µs as fit parameter. τ is related to the rate constant k^{MD} via $k^{MD} = \tau^{-1}$ = 139,000 s^{-1}. Comparing k^{MD} with the average experimental rate constant k^{MHQ} = 7450 s^{-1} (see main text) reveals a deviation by a factor ~ 18. This deviation may be explained by two reasons: First, the MD trajectories at the given length most likely do not reflect the complete transition from the *apo* to the *holo* state in all cases, i.e. the dwell times would be underestimated. This leads to an overestimate of k^{MD}. Moreover, the stepwise nature of the conformational change introduces a large dispersion in the dwell times. Second, because the MHQ chamber engulfs a cold plate at liquid-nitrogen temperatures and is operated under low pressure, the jet temperature may drop and thus decrease k^{MHQ}. Taken together, over- and underestimation of k^{MD} and k^{MHQ}, respectively, enhance the difference between rate constants.

Simulations of type (iv) were analyzed by computing the RMSD of the filtered trajectory towards the average *apo* state structure obtained from type (i) (Extended Data Figure 7, SI section 9.3). Indeed, several of these simulations converged towards the average *apo* state structure, suggesting that the conformational changes observed in type (iii) were induced by the presence of the cAMP ligand.

8. Reduction of sample consumption for MHQ/PELDOR

Protein samples for MHQ/PELDOR experiments were prepared at a concentration of $[CNBD]_{pre\text{-}mixing}$ = 300 µM and a volume of V_{CNBD} = 200 µL i.e., 60 nmol or 2 µg per time point. This amount is approximately 15-fold higher than that normally required for PELDOR experiments (~ 80 µL, ~50 µM protein, i.e., 4 nmol). To assess whether MHQ/PELDOR can also provide data with a fair SNR using lower protein quantities, we reduced the protein concentration and the sample volume: The E289R1/I340R1 construct in the *apo* state was mixed 1:1 in the MHQ with buffer solution using $[CNBD]_{pre\text{-}mixing}$ = 75 µM and V_{CNBD} = 100 µL i.e., 7.5 nmol. The result of this experiment is shown in Figure S15.

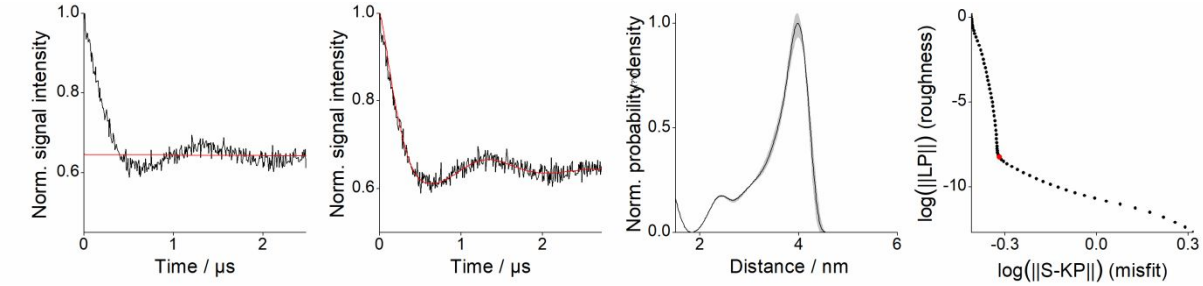

Figure S15: MHQ/PELDOR on the MloK1-CNBD construct E289R1/I340R1 at reduced amount of protein. $[CNBD]_{pre\text{-}mixing}$ = 75 µM, V_{CNBD} = 100 µL i.e., 7.5 nmol. An acquisition time of 8 h has been chosen to obtain an SNR of ~ 25. As a rule of thumb, a PELDOR time trace permits reliable analysis when the SNR is at least 25. The time trace in Figure S15 clearly shows dipolar oscillations. Although longer measurement times are required, MHQ/PELDOR can be performed with the generic volume and concentration regime of PELDOR. Note, however, that the acquisition time not only depends on the amount of protein injected into the MHQ, but also on the dilution due to condensation of air moisture and the packing density of the sample i.e., the spin concentration in the EPR-active zone of the resonator.

9. Extended Data

9.1. *cw* X-Band EPR spectra for the MetMb/NaN_3 calibration time series

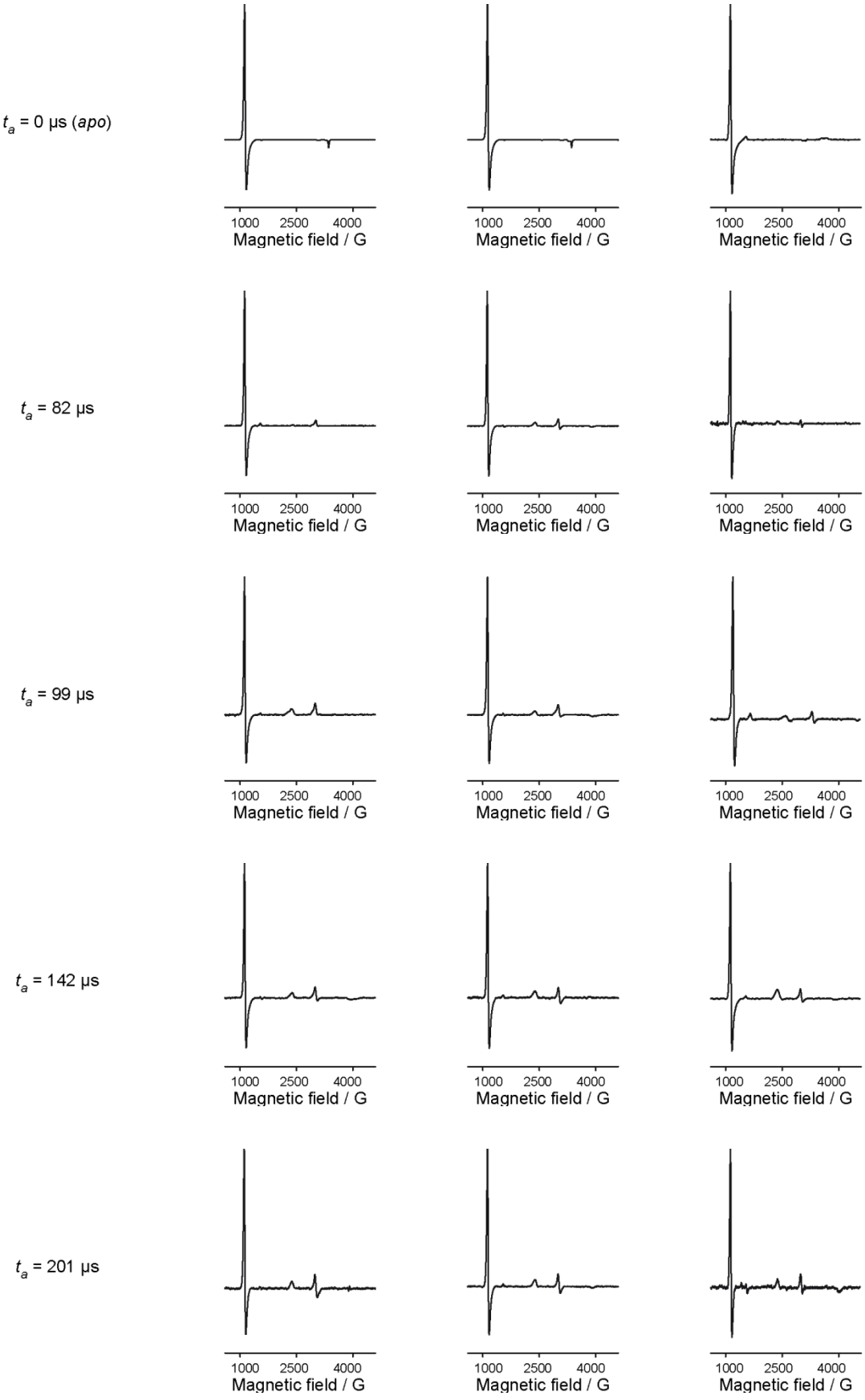

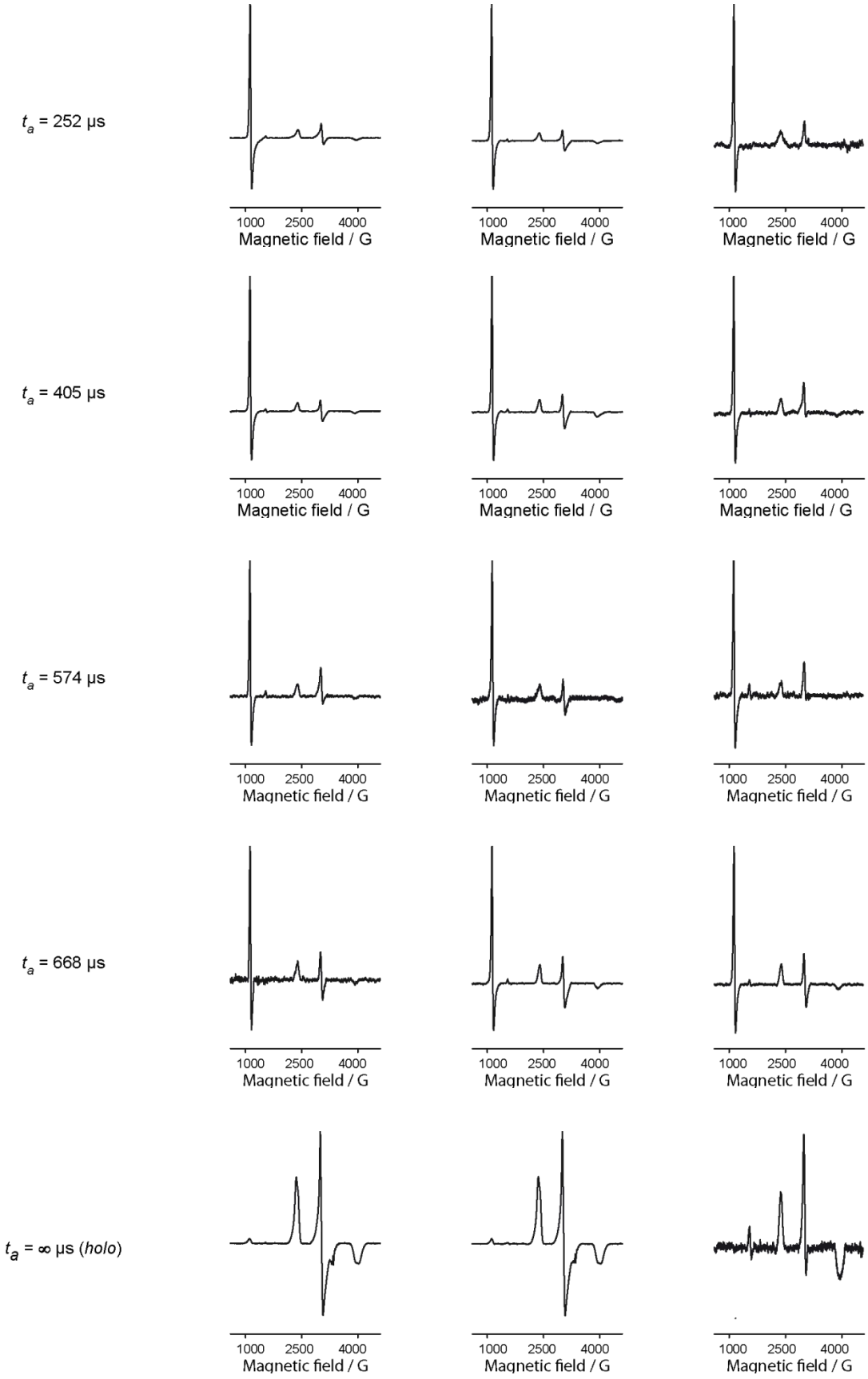

Extended Data Figure 1: Original *cw* X-Band EPR spectra for the MetMb/NaN_3 calibration time series ([MetMb] = 0.75 mM, [NaN_3] = 0.75 M), each time point t_a in triplicates.

9.2. Original PELDOR data and data analysis overview

a) E289R1/I340R1

t_a = 0 µs (*apo*)

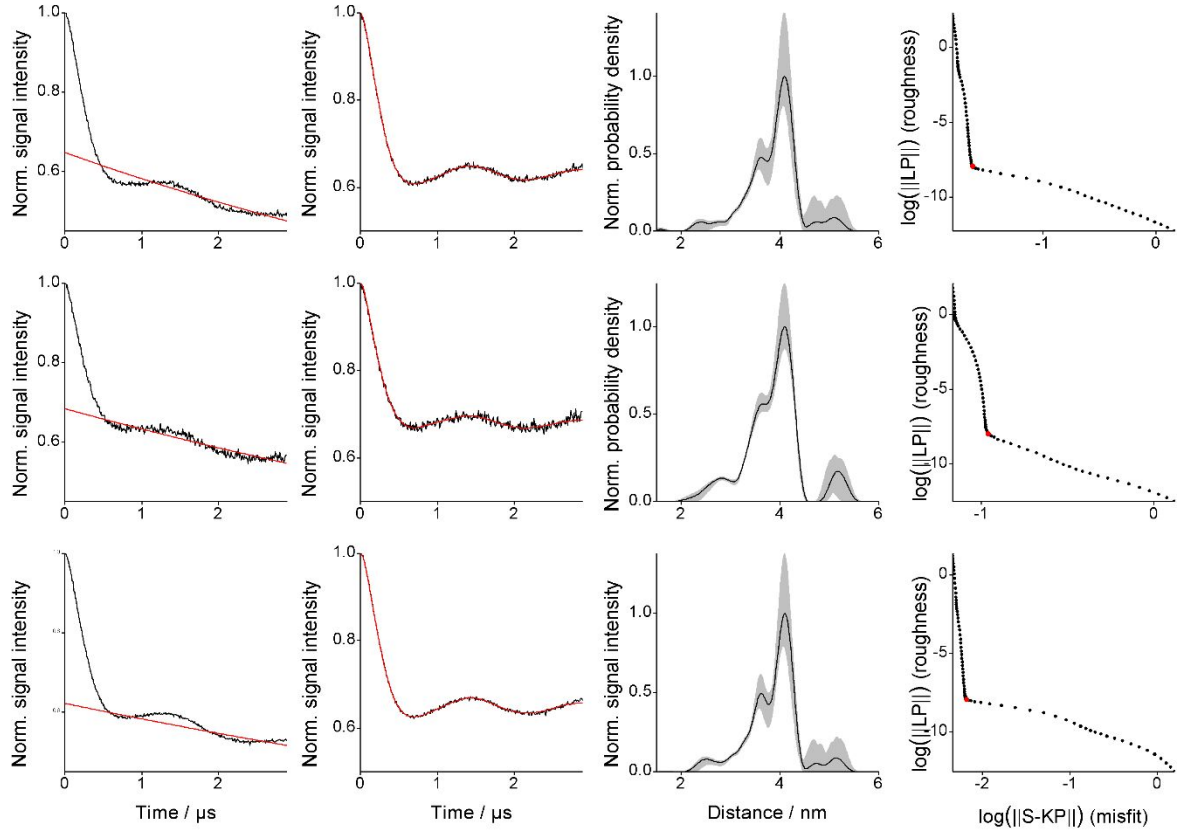

t_a = 82 µs

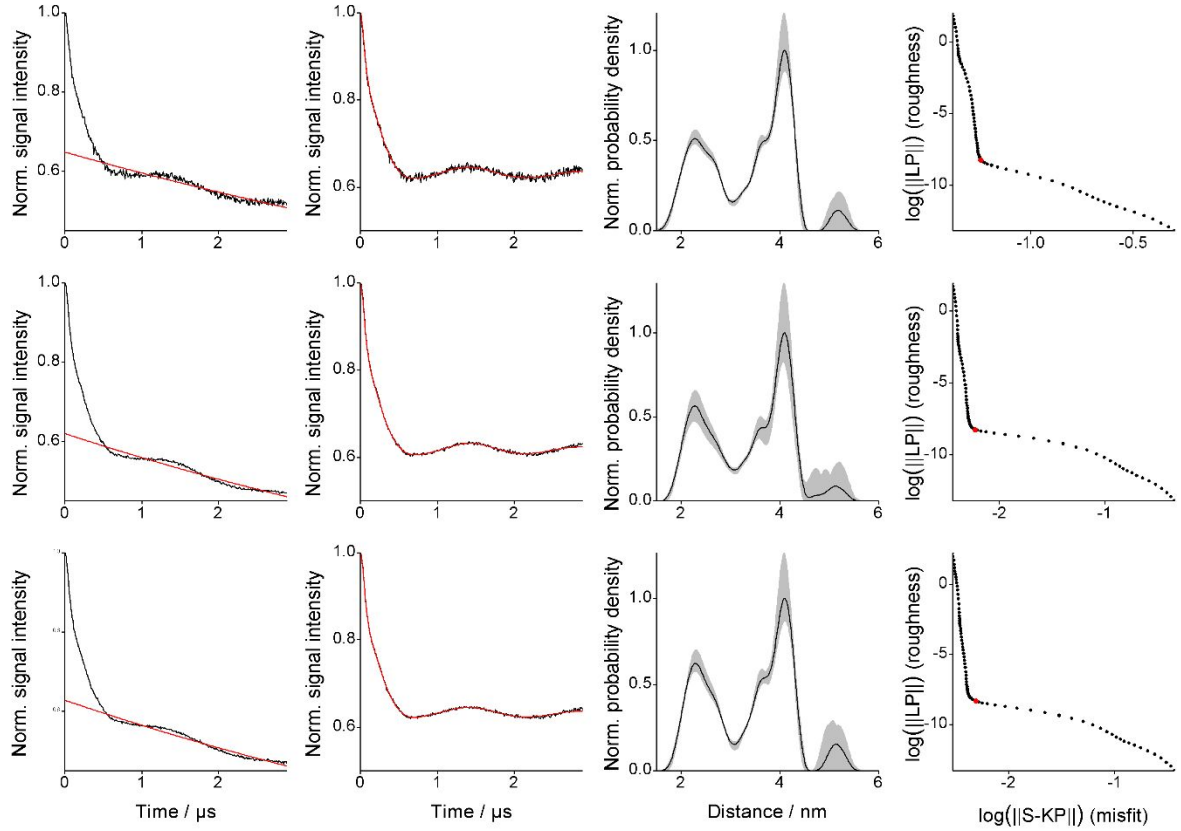

t_a = 116 µs

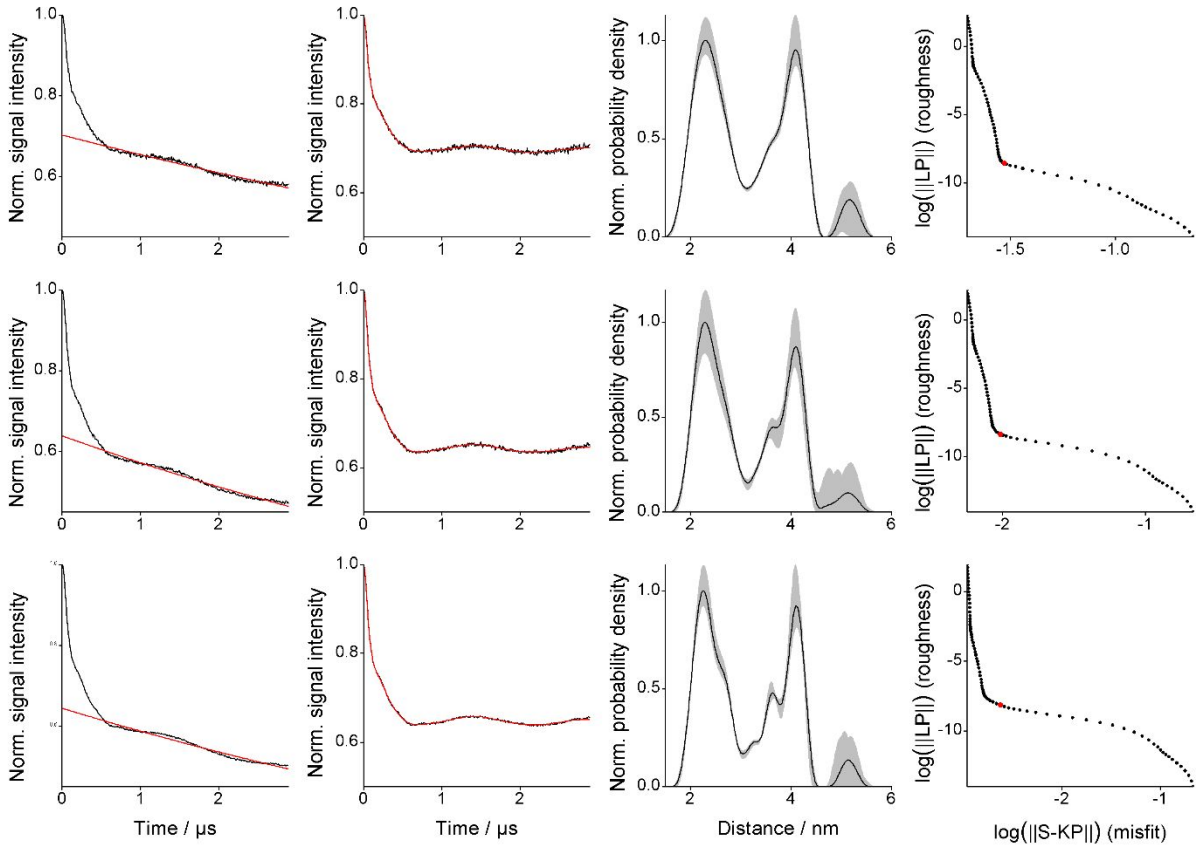

t_a = 201 µs

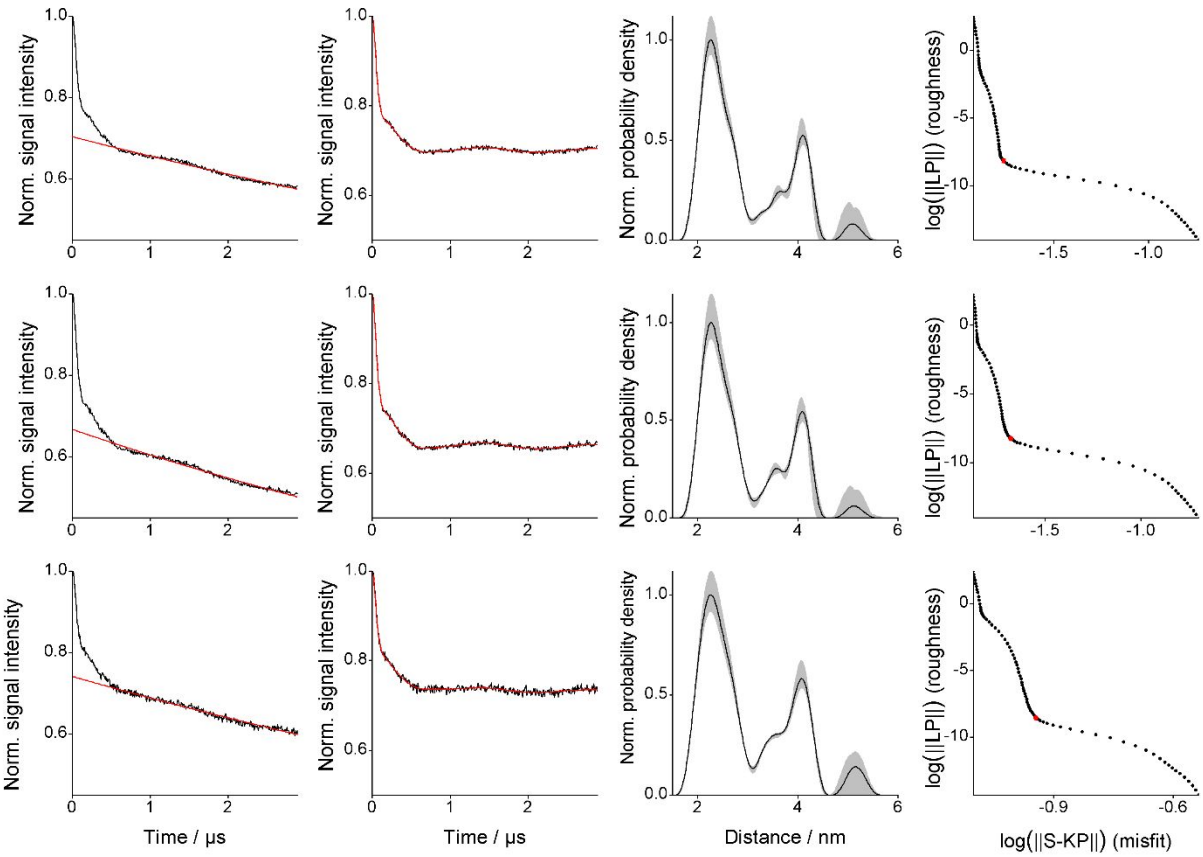

t_a = 303 µs

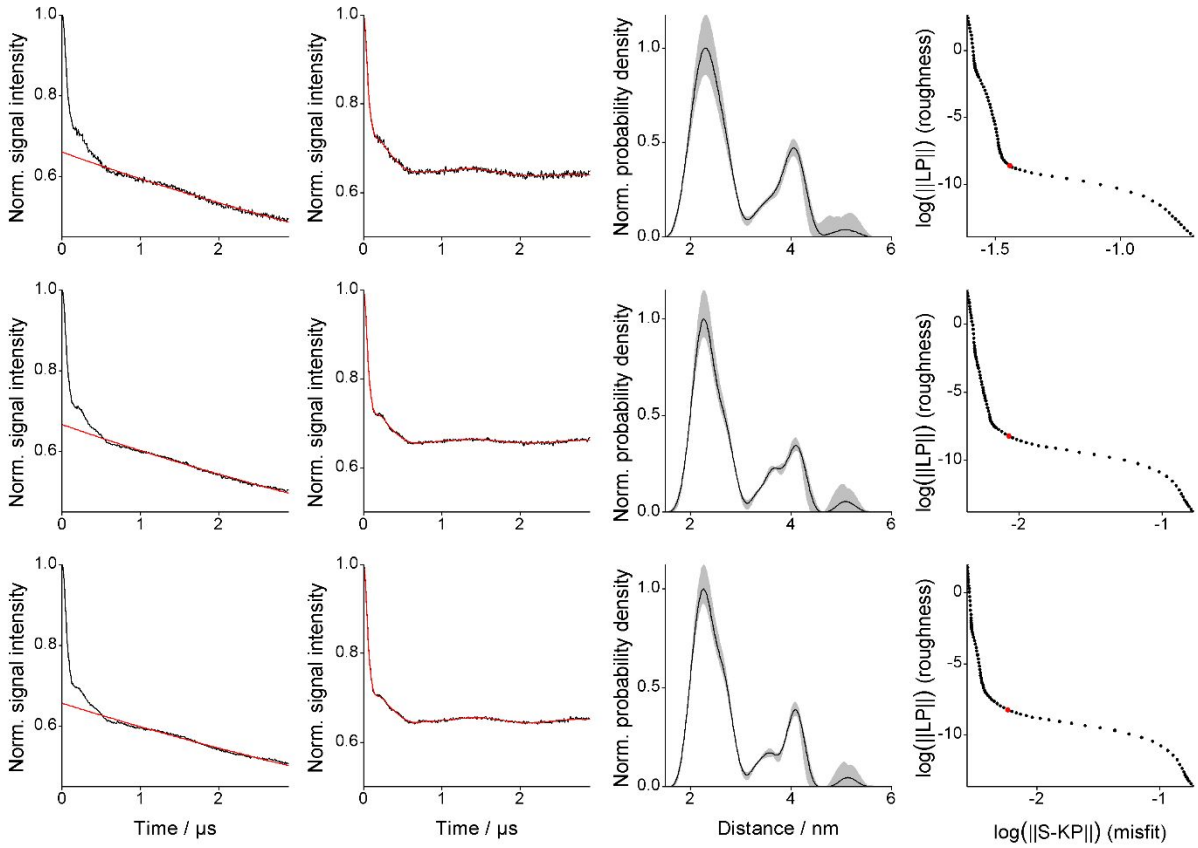

t_a = 405 µs

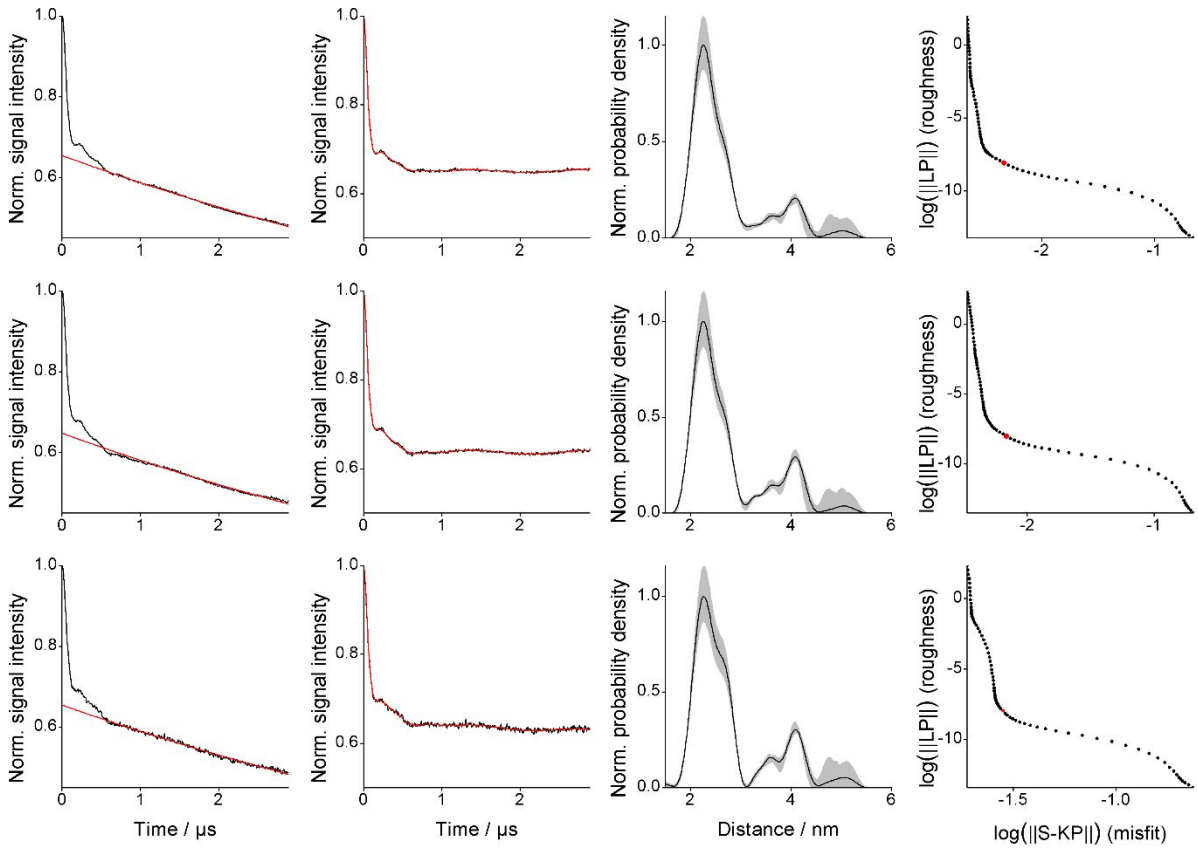

t_a = 498 µs

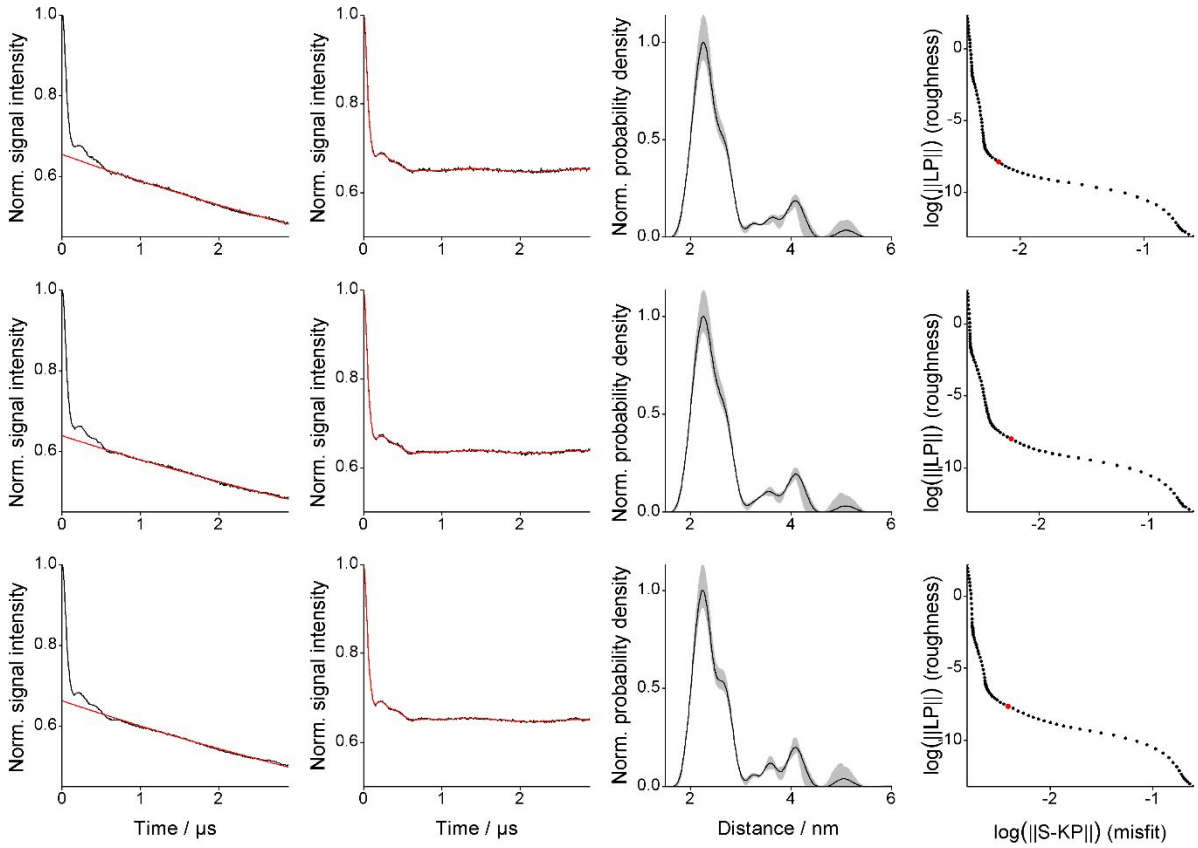

t_a = ∞ µs (*holo*)

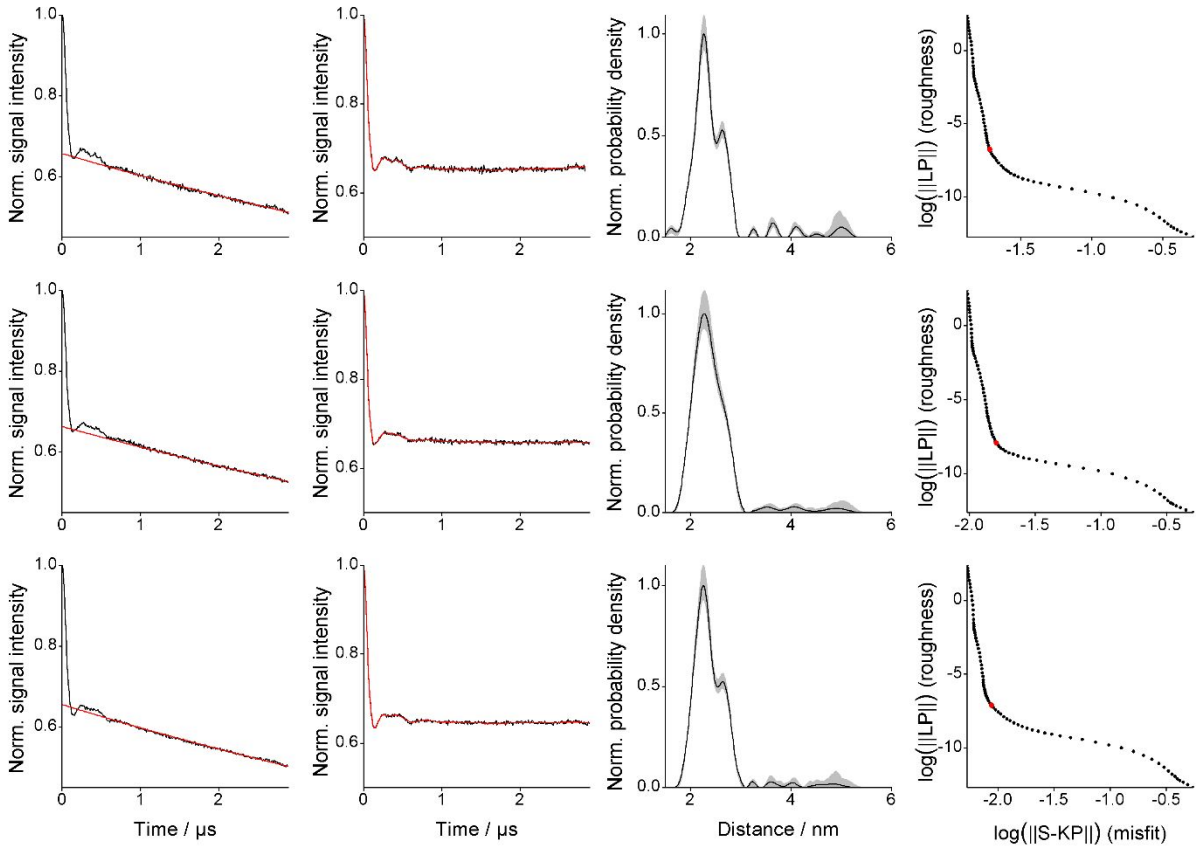

b) R254R1/E336R1

***t_a* = 0 µs (*apo*)**

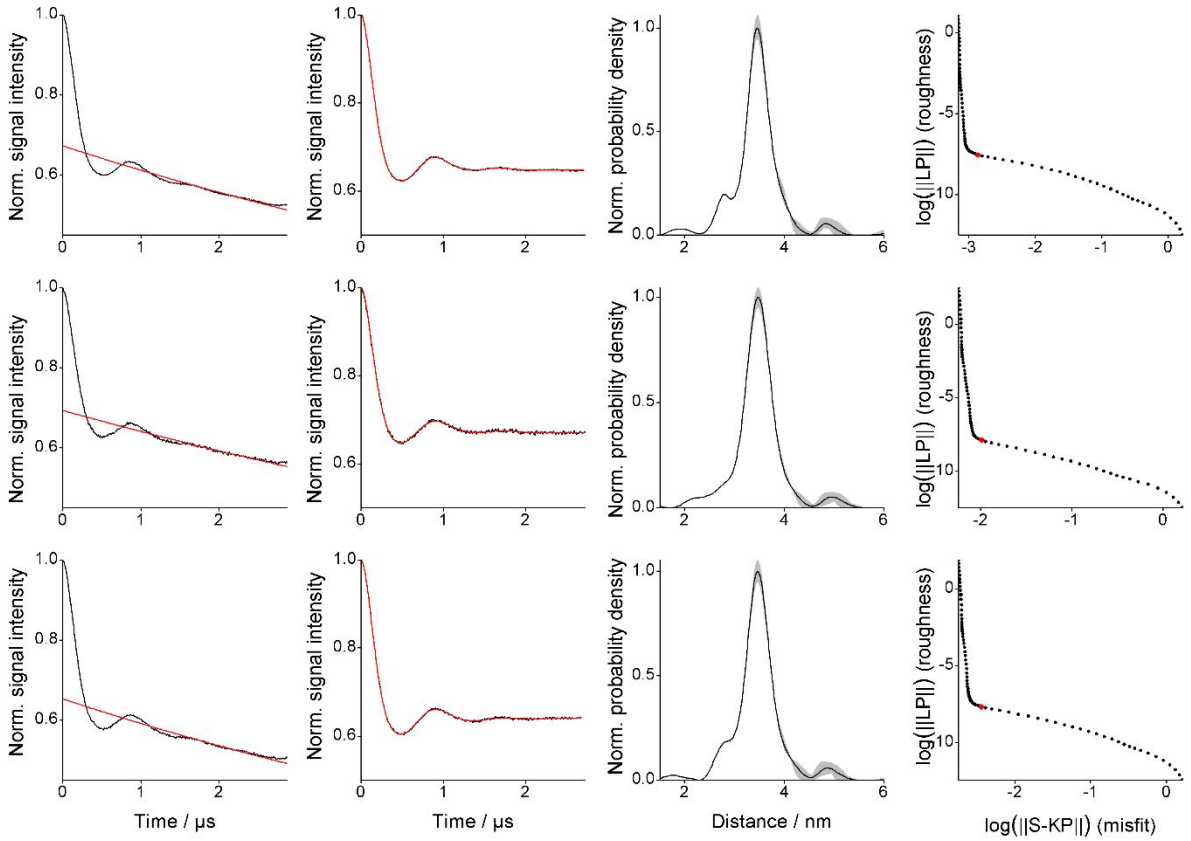

***t_a* = 82 µs**

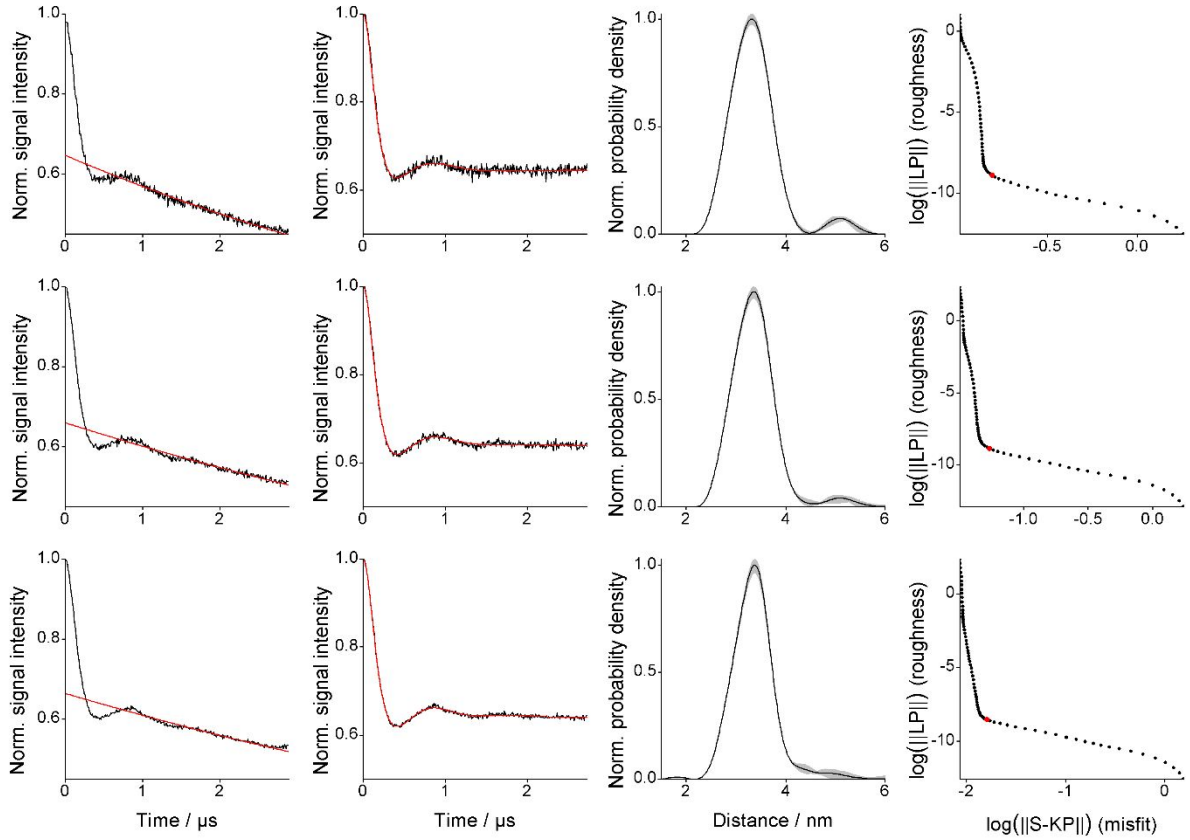

t_a = 116 µs

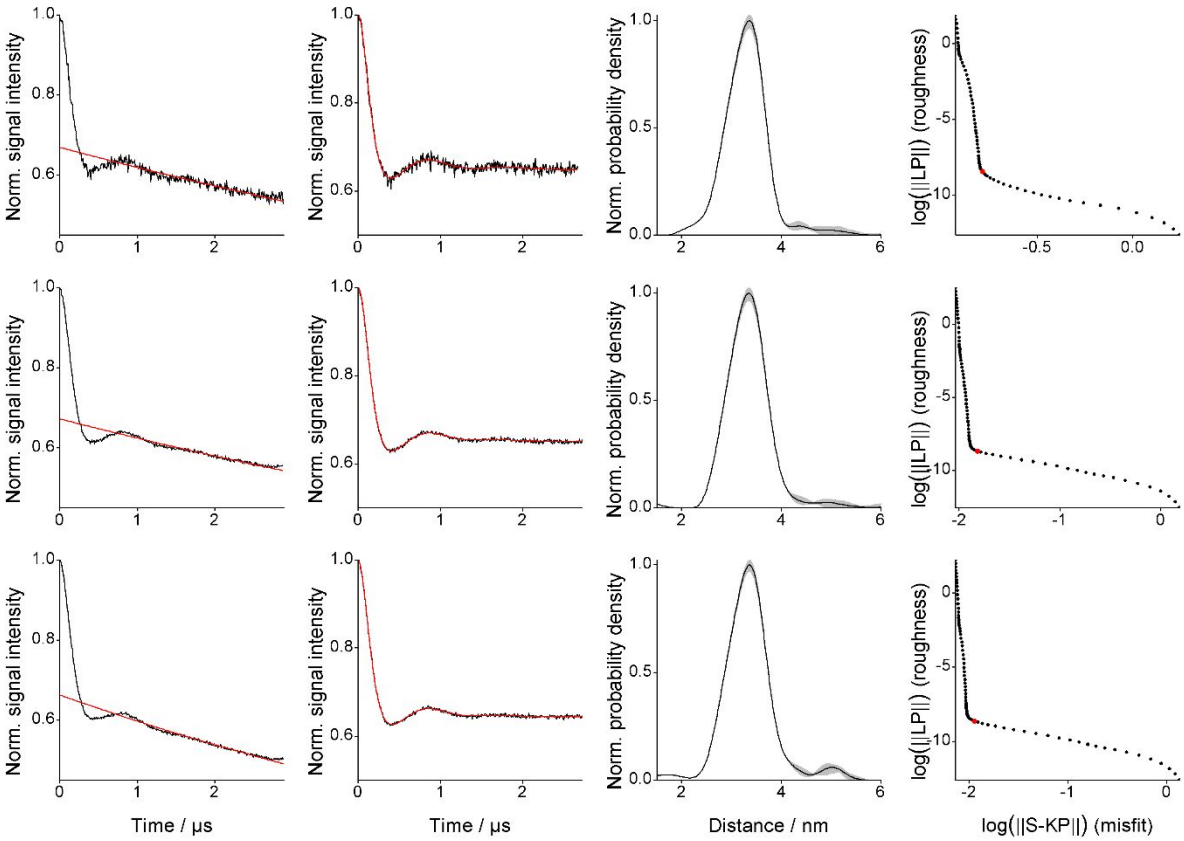

t_a = 201 µs

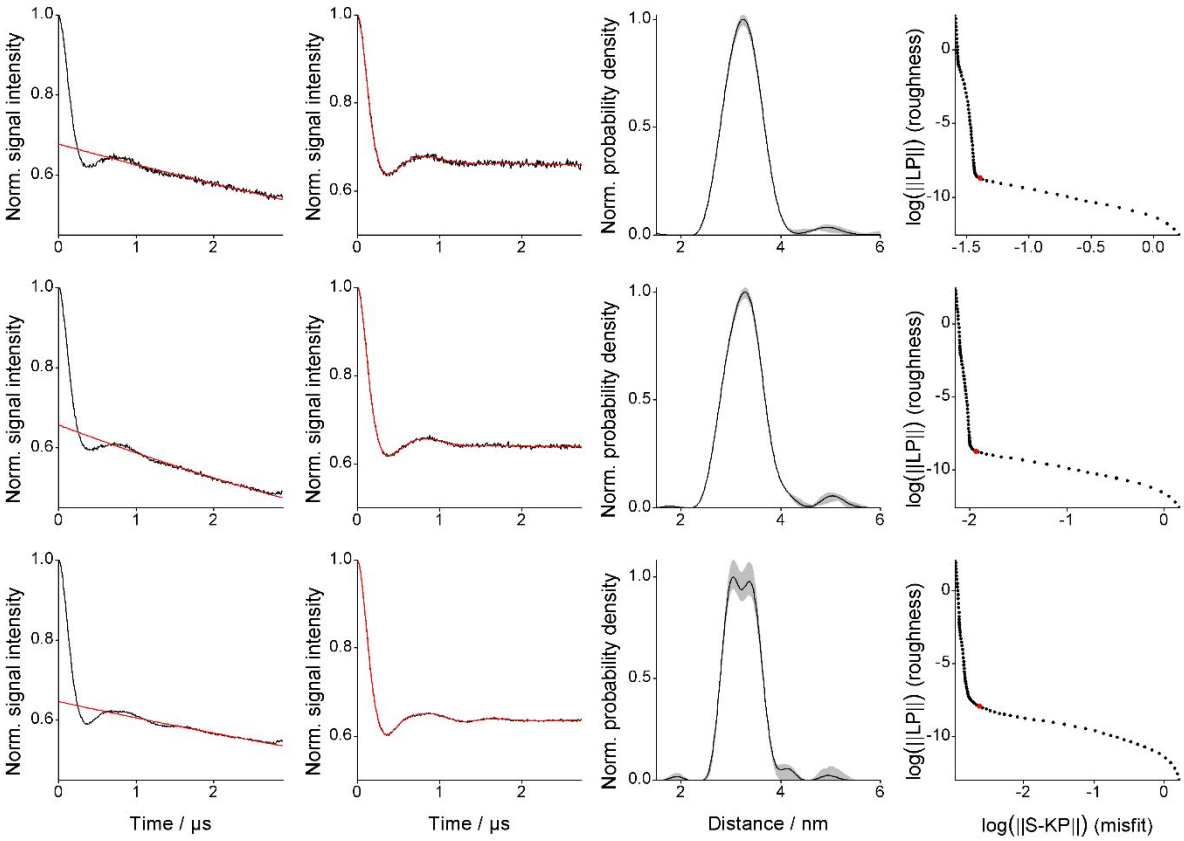

t_a = 303 µs

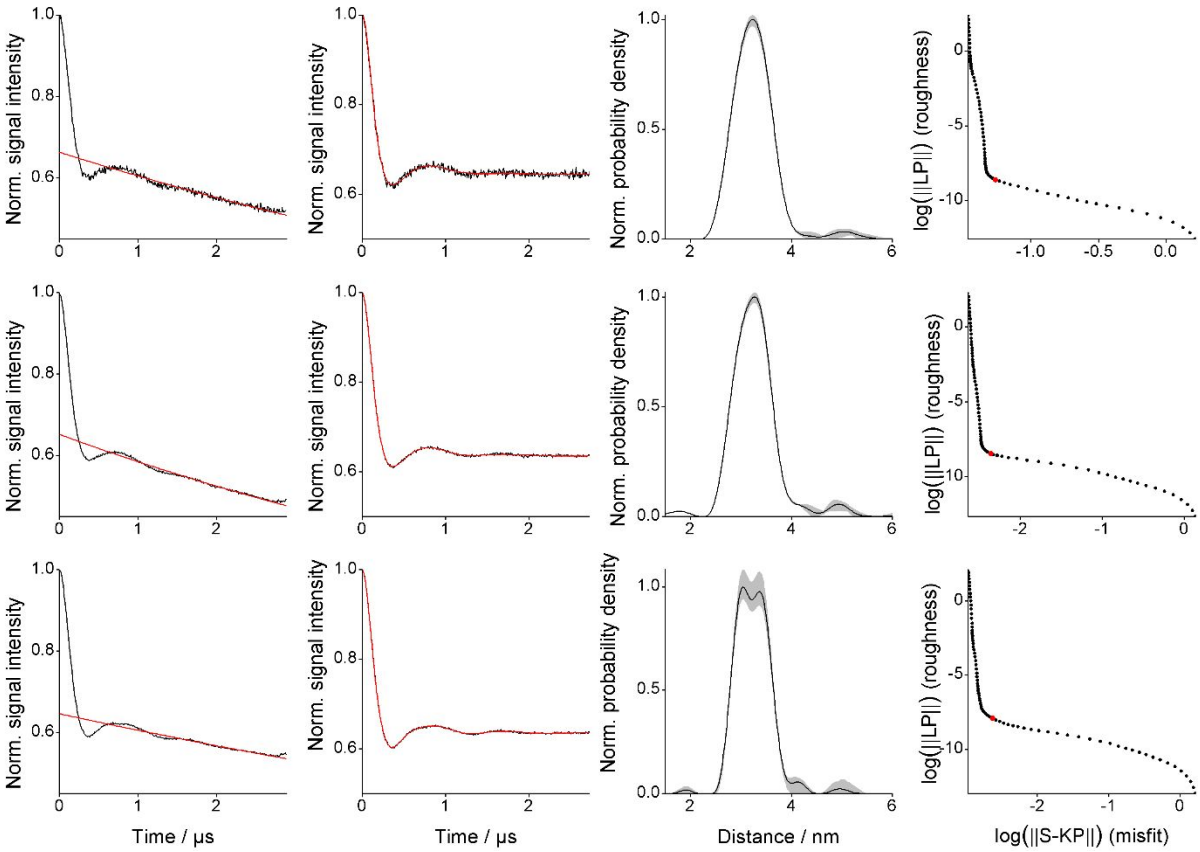

t_a = 405 µs

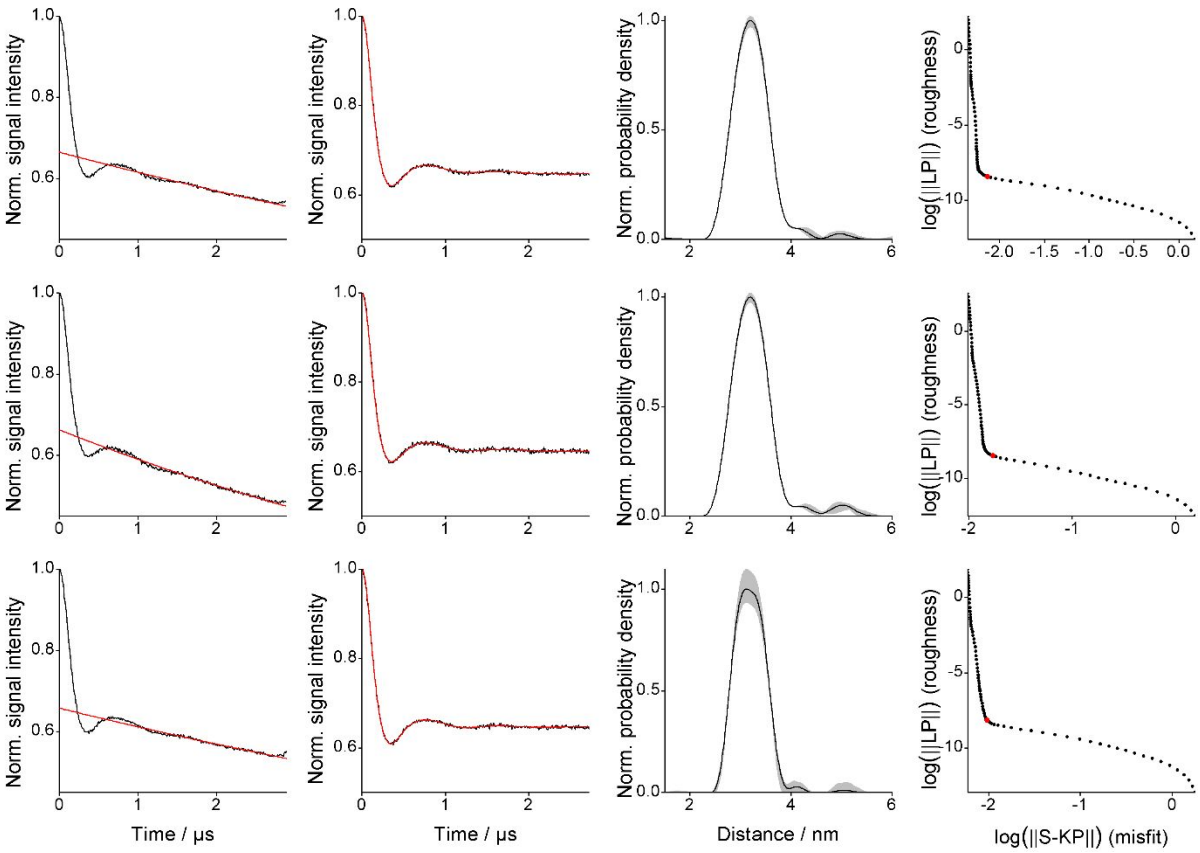

t_a = 498 µs

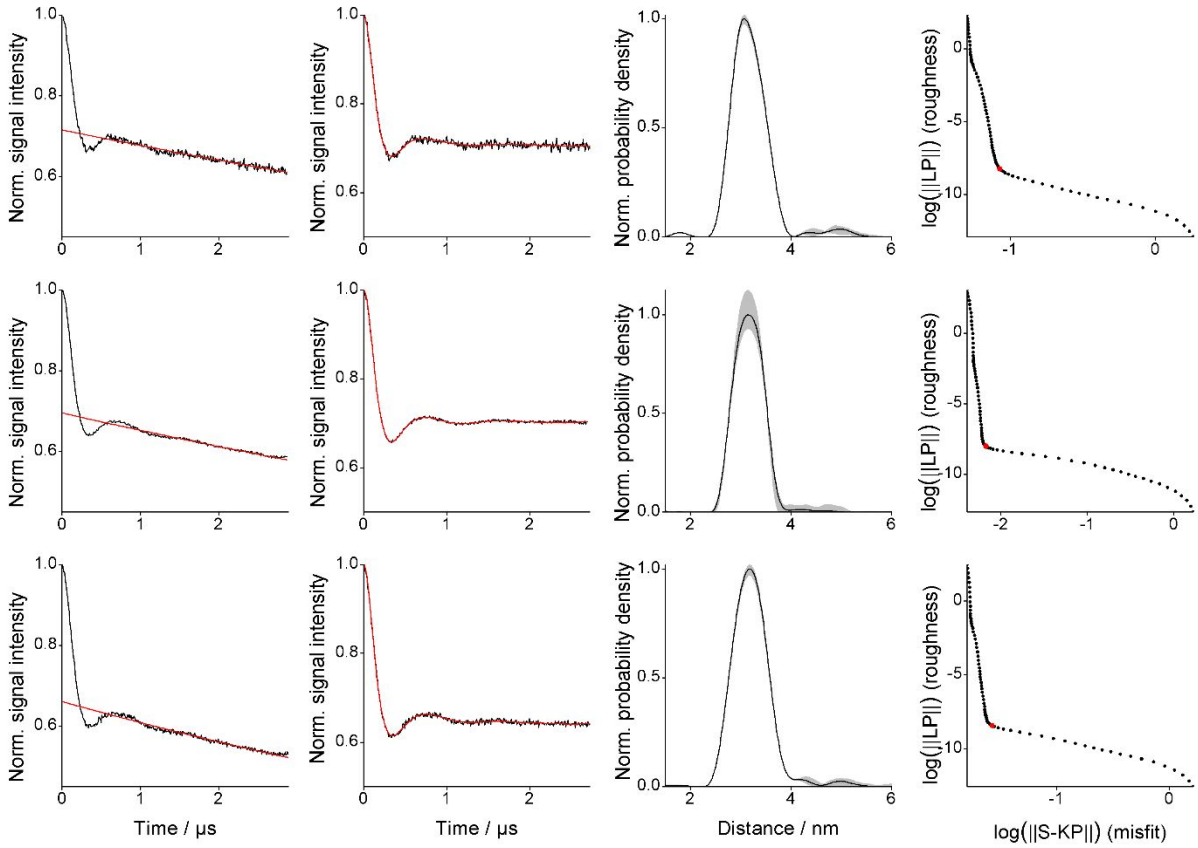

t_a = ∞ µs (*holo*)

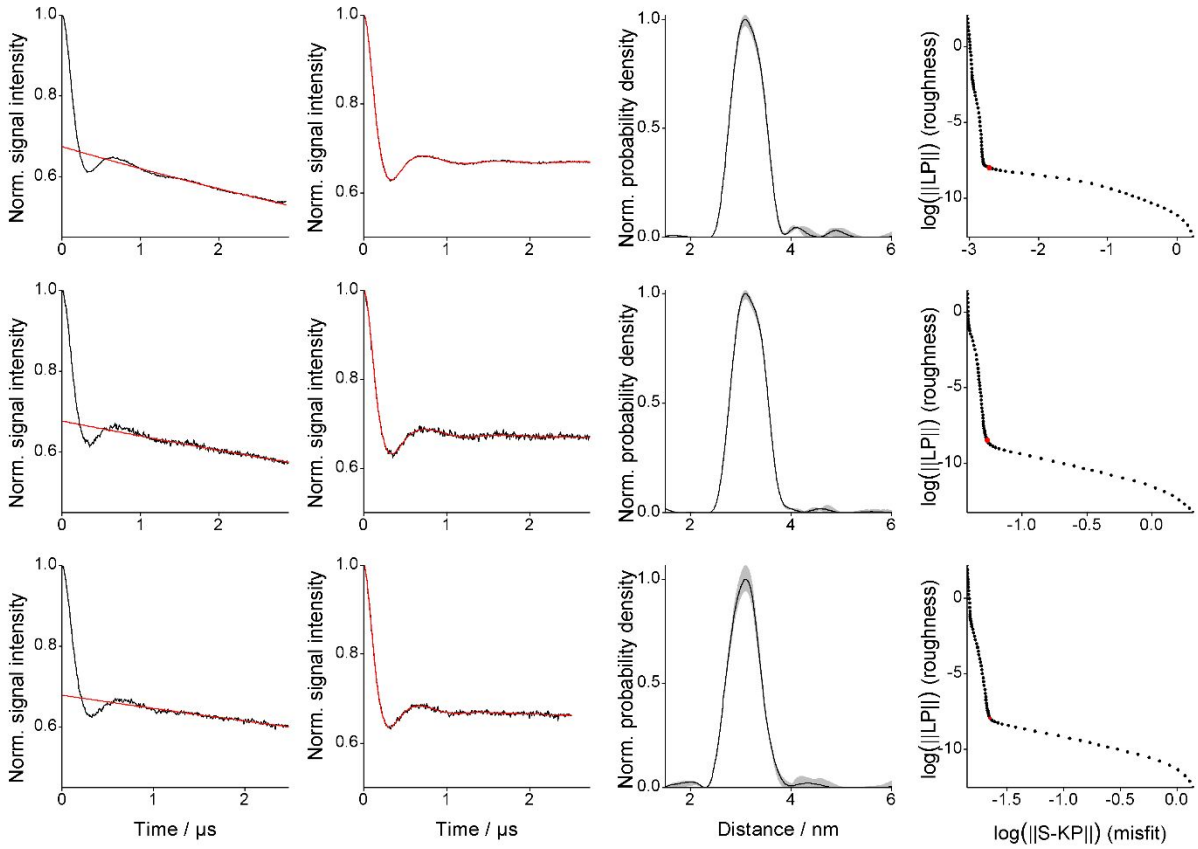

Extended Data Figure 2 Original PELDOR data and data analysis overview. The PELDOR data is shown for each of the triplicates for each time point t_a including (from left to right) the original time trace together with the background fit, the background-corrected time trace overlaid with the fit, the corresponding distance distribution plus data validation, and the L-curve for (a) E289R1/I340R1 – PELDOR time series ([CNBD] = 150 µM, [cAMP] = 15 mM) and (b) R254R1/E336R1 – PELDOR time series ([CNBD] = 150 µM; [cAMP] = 15 mM).

[cAMP] = 15 mM (taken from the time series above)

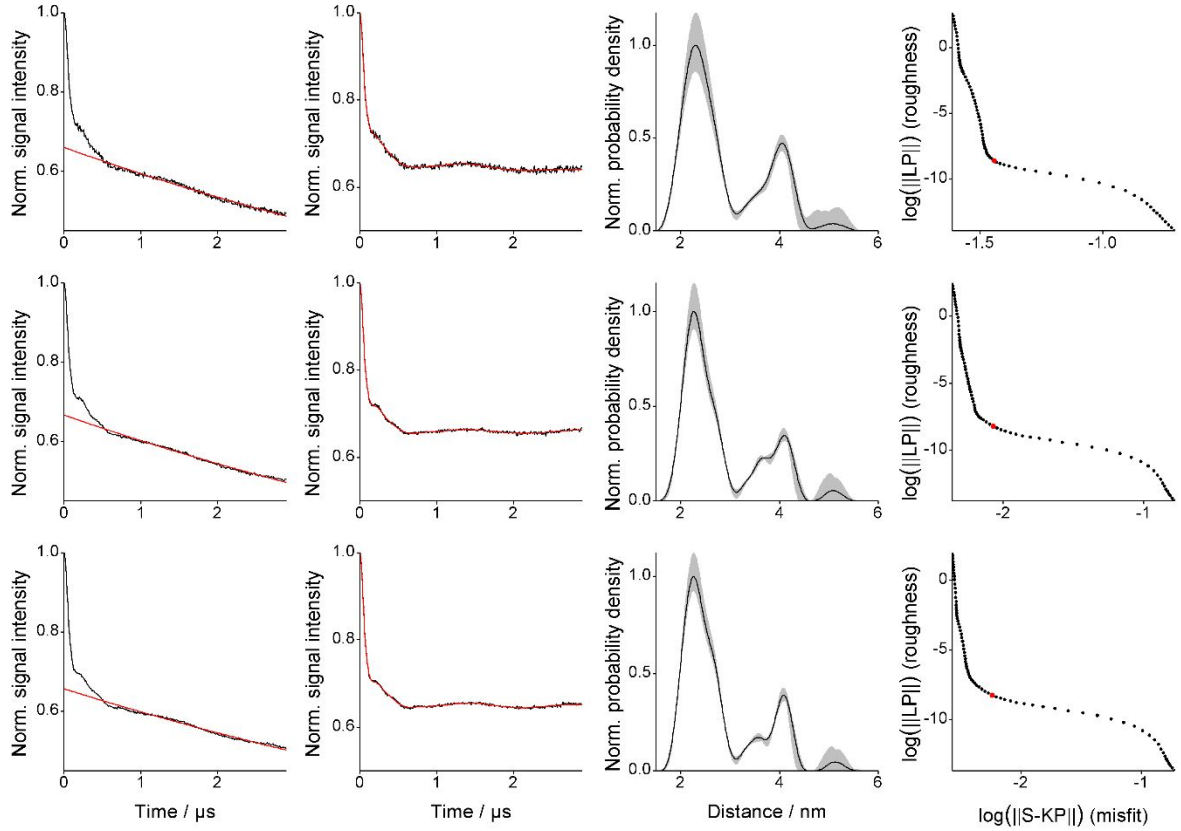

[cAMP] = 10 mM

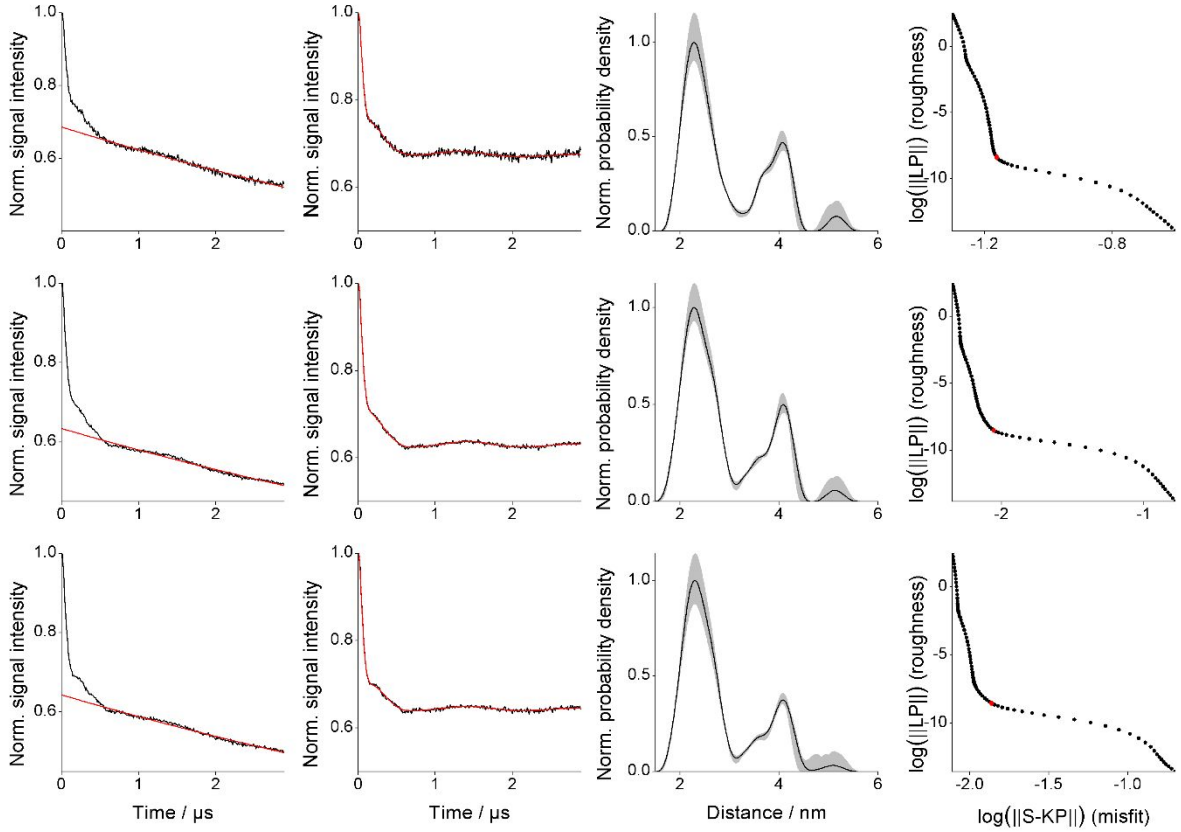

[cAMP] = 1.5 mM

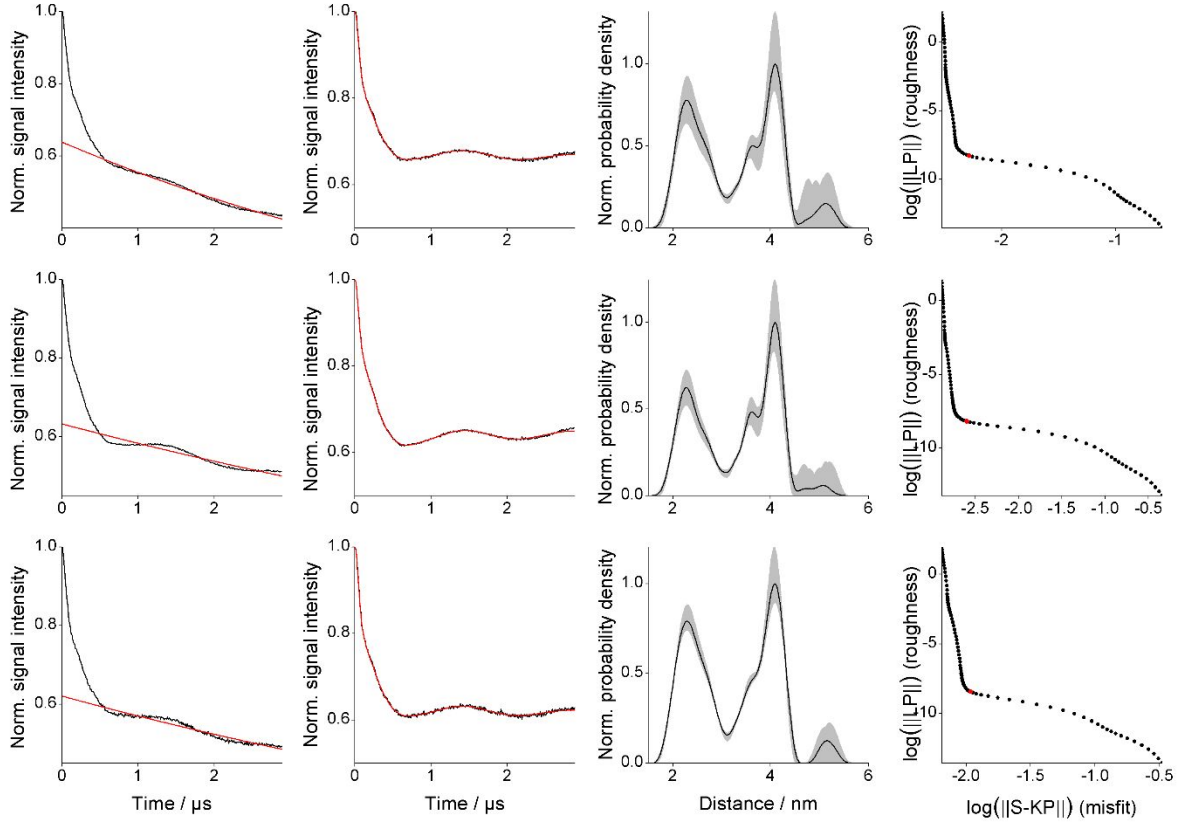

[cAMP] = 0.5 mM

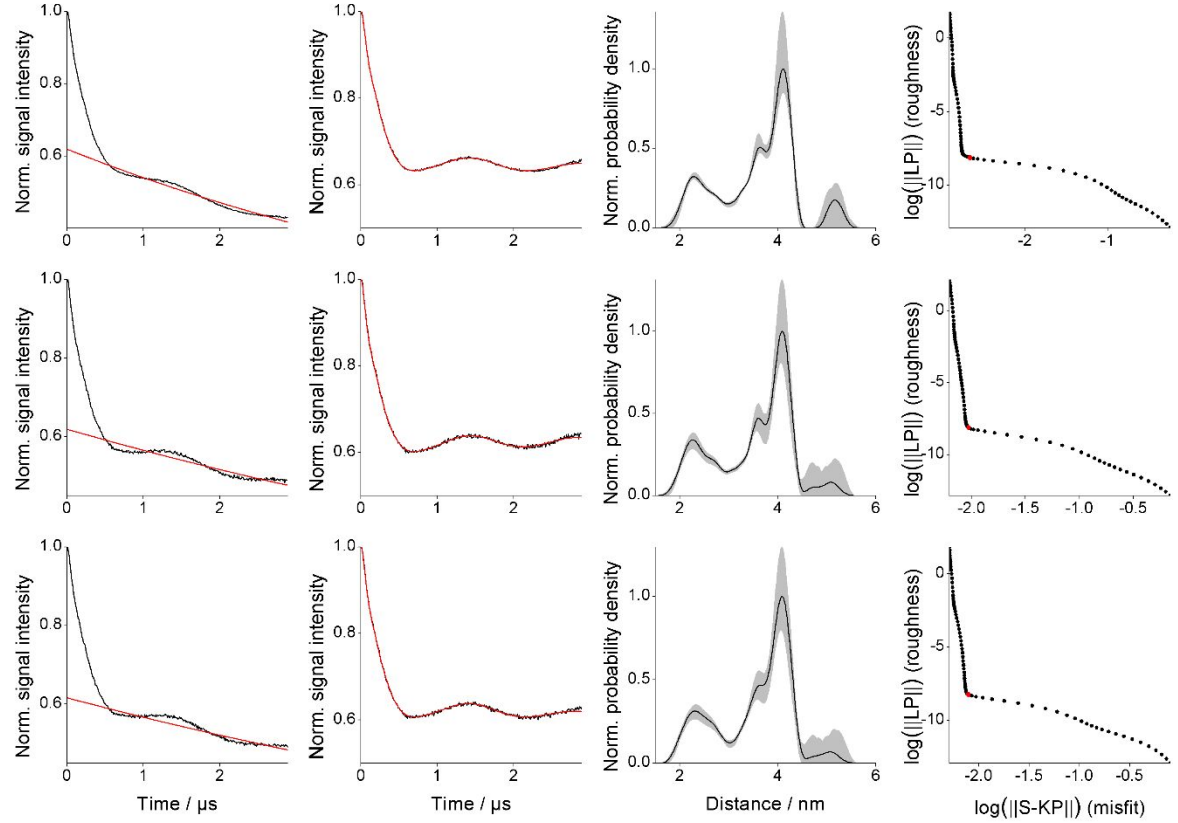

Extended Data Figure 3: Original PELDOR time traces and data analysis overview for the concentration series E289R1/I340R1 – ([CNBD] = 150 µM; t_a = 303 µs).

9.3. MD simulation data

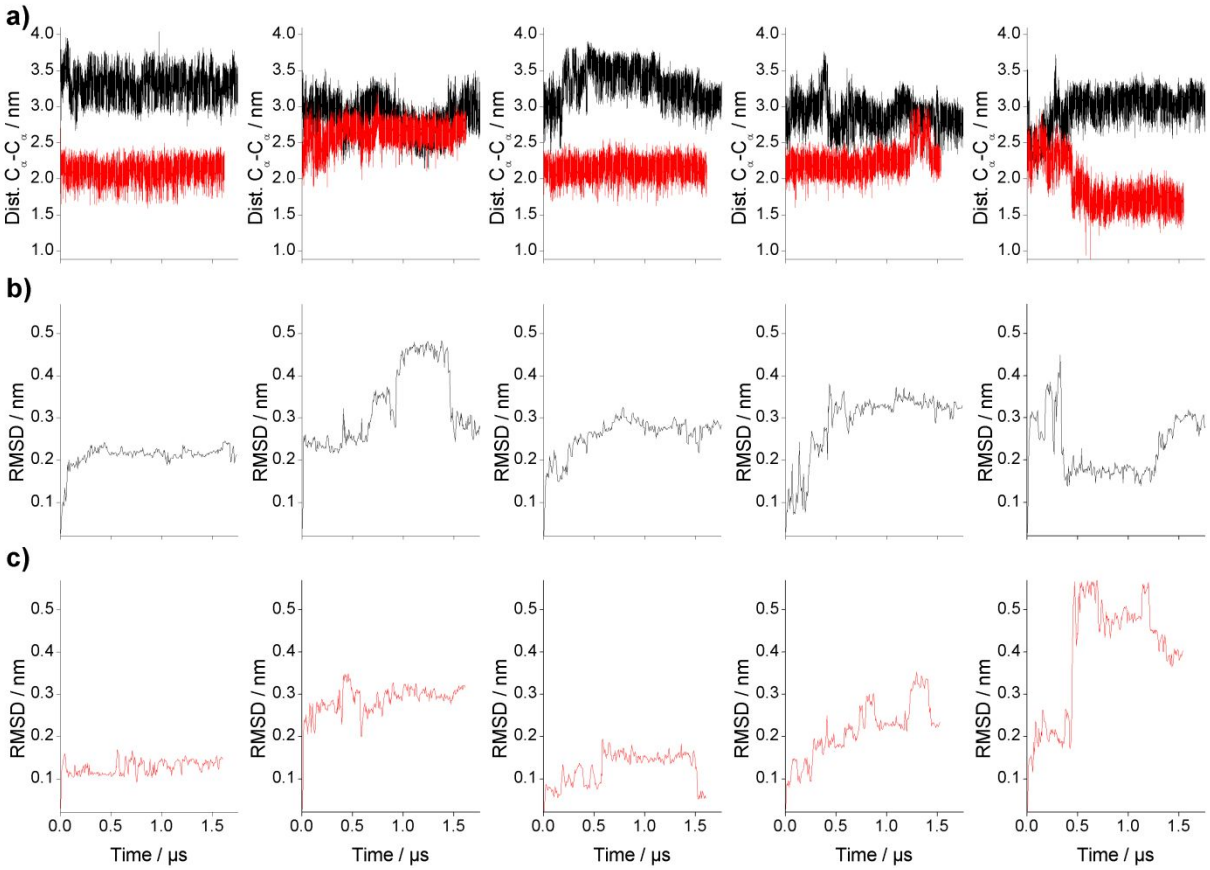

Extended Data Figure 4: Analysis of MD simulations of the *apo* and *holo* state. (a) C_α distances of amino-acid pair E289/I340 monitored along the five unfiltered MD trajectories for the *apo* (PDB-ID: 2kxl; simulation type i) and *holo* state (PDB-ID: 2k0g; simulation type ii). Black and red lines refer to the *apo* and *holo* state trajectories, respectively. (b) RMSD plots along the five filtered MD trajectories of the *apo* state structure (PDB-ID: 2kxl; simulation type i). (c) RMSD plots of the *holo* state structure (PDB-ID: 2k0g; simulation type ii). The RMSD has been calculated with regard to the average of the first 10 ns of a trajectory. Note that only C_α-atoms of α-helices and β-sheets (Figure S12) were used for RMSD calculation.

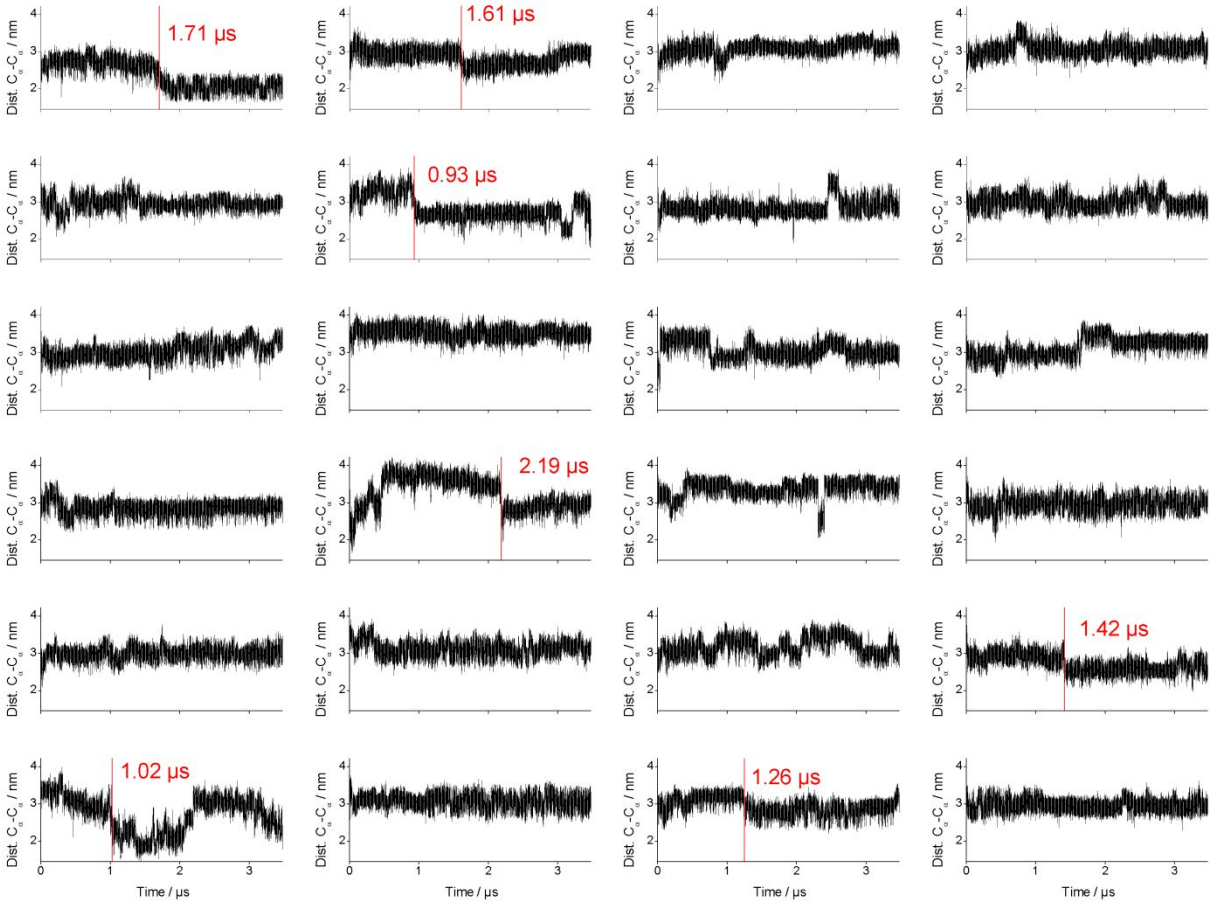

Extended Data Figure 5: C_α-C_α-distances for amino acid pair E289/I340 along unfiltered MD simulations on the transition from the *apo* state with the ligand inserted into the binding pocket to the *holo* state (simulation type iii). The abrupt distance changes are marked by red lines and the corresponding waiting times are indicated in red.

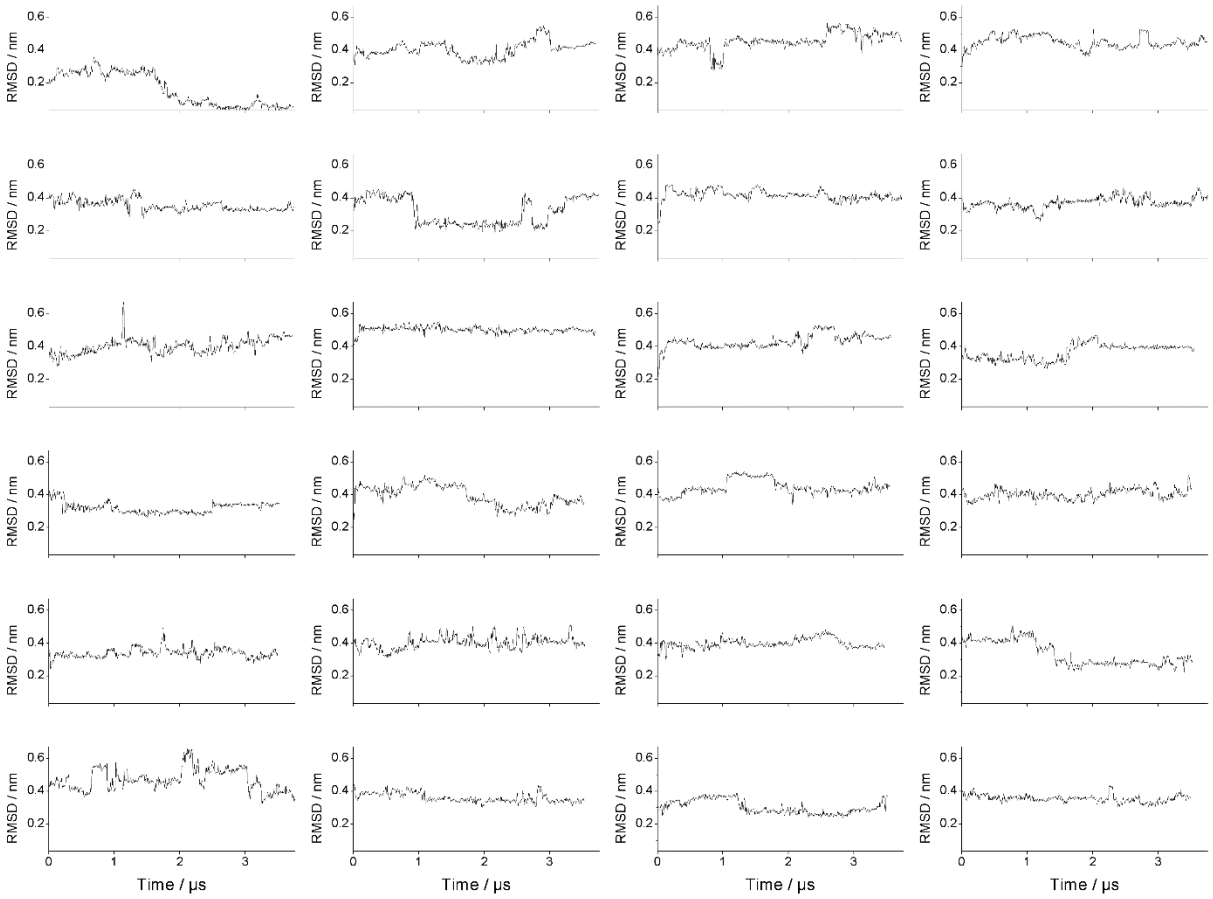

Extended Data Figure 6: RMSD of filtered MD simulations for the transition from the *apo* state with the ligand inserted into the binding pocket to the *holo* state (simulation type iii). The RMSD has been calculated with respect to the C_α-atoms of selected secondary structure elements in the equilibrated *holo* structure as shown in Figure S12b. The decreasing RMSD in several simulations indicates that, upon inserting the cAMP ligand into the *apo* state structure, the *apo* state is converted to the *holo* state structure.

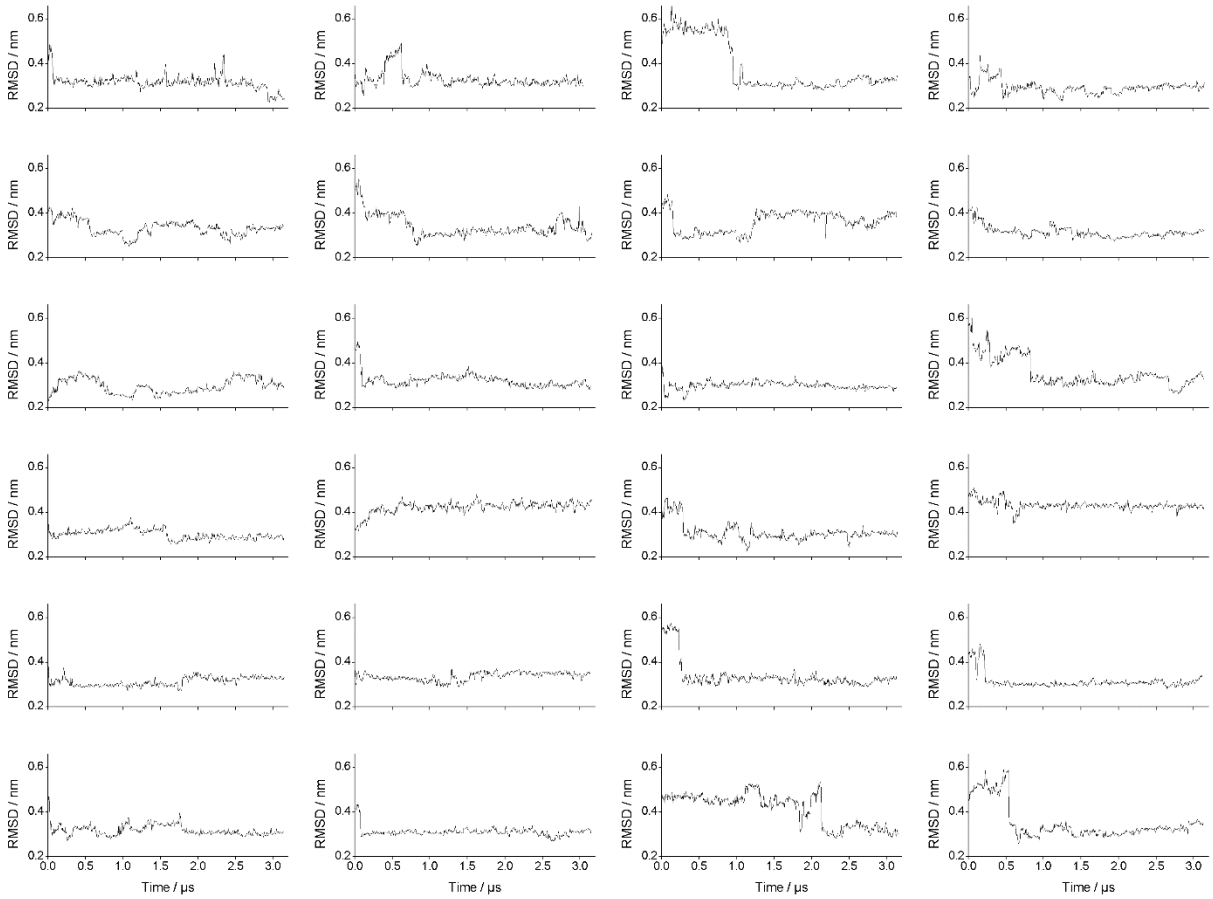

Extended Data Figure 7: RMSD of filtered MD simulations for the transition from the *holo* state back to the *apo* state (simulation type iv). The RMSD has been calculated with respect to the C_α atoms of selected secondary structure elements in the equilibrated *apo* structure as shown in Figure S12a. The decreasing RMSD in several simulations indicates that, when the cAMP ligand is erased, the *holo* state is converted back to the *apo* state structure. This confirms the assumption that the herein monitored structural changes are indeed related to the presence of the cAMP-ligand.

10. References

(1) Cherepanov, A. V.; Vries, S. de. Microsecond freeze-hyperquenching: development of a new ultrafast micro-mixing and sampling technology and application to enzyme catalysis. *Biochimica et Biophysica Acta (BBA) - Bioenergetics* **2004**, *1656* (1), 1–31. DOI: 10.1016/j.bbabio.2004.02.006.

(2) Hamzeh, H.; Alvarez, L.; Strünker, T.; Kierzek, M.; Brenker, C.; Deal, P. E.; Miller, E. W.; Seifert, R.; Kaupp, U. B. Kinetic and photonic techniques to study chemotactic signaling in sea urchin sperm. In *Methods Cell Biol*, **2019**, *151*, 487–517. DOI: 10.1016/bs.mcb.2018.12.001.

(3) Peuker, S.; Cukkemane, A.; Held, M.; Noé, F.; Kaupp, U. B.; Seifert, R. Kinetics of Ligand-Receptor Interaction Reveals an Induced-Fit Mode of Binding in a Cyclic Nucleotide-Activated Protein. *Biophysical Journal* **2013**, *104* (1), 63–74. DOI: 10.1016/j.bpj.2012.11.3816.

(4) Jeschke, G.; Chechik, V.; Ionita, P.; Godt, A.; Zimmermann, H.; Banham, J.; Timmel, C. R.; Hilger, D.; Jung, H. DeerAnalysis2006—a comprehensive software package for analyzing pulsed ELDOR data. *Applied Magnetic Resonance* **2006**, *30* (3-4), 473–498. DOI: 10.1007/BF03166213.

(5) Jeschke, G.; Panek, G.; Godt, A.; Bender, A.; Paulsen, H. Data analysis procedures for pulse ELDOR measurements of broad distance distributions. *Applied Magnetic Resonance* **2004**, *26* (1-2), 223–244. DOI: 10.1007/BF03166574.

(6) Hagelueken, G.; Abdullin, D.; Schiemann, O. mtsslSuite. Probing Biomolecular Conformation by Spin-Labeling Studies *Methods Enzymol*, **2015**; *563*, 595–622. DOI: 10.1016/bs.mie.2015.06.006.

(7) Polyhach, Y.; Bordignon, E.; Jeschke, G. Rotamer libraries of spin labelled cysteines for protein studies. *Phys. Chem. Chem. Phys.* **2011**, *13* (6), 2356–2366. DOI: 10.1039/CoCP01865A.

(8) Cukkemane, A.; Grüter, B.; Novak, K.; Gensch, T.; Bönigk, W.; Gerharz, T.; Kaupp, U. B.; Seifert, R. Subunits act independently in a cyclic nucleotide-activated K^+ channel. *EMBO reports* **2007**, *8* (8), 749–755. DOI: 10.1038/sj.embor.7401025.

(9) Abraham, M. J.; Murtola, T.; Schulz, R.; Páll, S.; Smith, J. C.; Hess, B.; Lindahl, E. GROMACS: High performance molecular simulations through multi-level parallelism from laptops to supercomputers. *SoftwareX* **2015**, *1-2*, 19–25. DOI: 10.1016/j.softx.2015.06.001.

(10) Berendsen, H.; van der Spoel, D.; van Drunen, R. GROMACS: A message-passing parallel molecular dynamics implementation. *Computer Physics Communications* **1995**, *91* (1-3), 43–56. DOI: 10.1016/0010-4655(95)00042-E.

(11) Páll, S.; Abraham, M. J.; Kutzner, C.; Hess, B.; Lindahl, E. Tackling Exascale Software Challenges in Molecular Dynamics Simulations with GROMACS. In: Markidis S., Laure E. (eds) Solving Software Challenges for Exascale. EASC 2014. Lecture Notes in Computer Science, vol 8759, **2015**, pp 3–27. Springer, Cham. DOI: 10.1007/978-3-319-15976-8_1.

(12) Voß, B.; Seifert, R.; Kaupp, U. B.; Grubmüller, H. A Quantitative Model for cAMP Binding to the Binding Domain of MloK1. *Biophysical Journal* **2016**, *111* (8), 1668–1678. DOI: 10.1016/j.bpj.2016.09.014.

(13) Aliev, A. E.; Kulke, M.; Khaneja, H. S.; Chudasama, V.; Sheppard, T. D.; Lanigan, R. M. Motional timescale predictions by molecular dynamics simulations: Case study using proline and hydroxyproline sidechain dynamics. *Proteins: Structure, Function, and Bioinformatics* **2014**, *82* (2), 195–215. DOI: 10.1002/prot.24350.

(14) Jorgensen, W. L.; Chandrasekhar, J.; Madura, J. D.; Impey, R. W.; Klein, M. L. Comparison of simple potential functions for simulating liquid water. *The Journal of Chemical Physics* **1983**, *79* (2), 926–935. DOI: 10.1063/1.445869.

[P4]: Site Selective and Efficient Spin Labeling of Proteins with a Maleimide-Functionalized Trityl Radical for Pulsed Dipolar EPR Spectroscopy

Reproduced with permission from

J. Jacques Jassoy†, Caspar A. Heubach†, Tobias Hett, Frédéric Bernhard, Florian R. Haege, Gregor Hagelueken, Olav Schiemann*, *Molecules* **2019**, *24*, 2735.
DOI: http://doi.org/10.3390/molecules24152735

† These authors contributed equally.
* Corresponding author.

Contributions

- *Cw* and pulsed EPR spectroscopy including data analysis.
- Writing of the manuscript in parts.

molecules

MDPI

Article

Site Selective and Efficient Spin Labeling of Proteins with a Maleimide-Functionalized Trityl Radical for Pulsed Dipolar EPR Spectroscopy

J. Jacques Jassoy †, Caspar A. Heubach †, Tobias Hett, Frédéric Bernhard, Florian R. Haege, Gregor Hagelueken and Olav Schiemann *

Institute of Physical and Theoretical Chemistry, Rheinische Friedrich-Wilhelms-University Bonn, Wegelerstr. 12, 53115 Bonn, Germany

* Correspondence: schiemann@pc.uni-bonn.de; Tel.: +49-(0)228732989; Fax: +49-(0)228732073

† These authors equally contributed to this work.

Received: 2 July 2019; Accepted: 25 July 2019; Published: 27 July 2019

Abstract: Pulsed dipolar electron paramagnetic resonance spectroscopy (PDS) in combination with site-directed spin labeling (SDSL) of proteins and oligonucleotides is a powerful tool in structural biology. Instead of using the commonly employed *gem*-dimethyl-nitroxide labels, triarylmethyl (trityl) spin labels enable such studies at room temperature, within the cells and with single-frequency electron paramagnetic resonance (EPR) experiments. However, it has been repeatedly reported that labeling of proteins with trityl radicals led to low labeling efficiencies, unspecific labeling and label aggregation. Therefore, this work introduces the synthesis and characterization of a maleimide-functionalized trityl spin label and its corresponding labeling protocol for cysteine residues in proteins. The label is highly cysteine-selective, provides high labeling efficiencies and outperforms the previously employed methanethiosulfonate-functionalized trityl label. Finally, the new label is successfully tested in PDS measurements on a set of doubly labeled *Yersinia* outer protein O (YopO) mutants.

Keywords: proteins; distance measurements; EPR; DQC; PELDOR; SIFTER

1. Introduction

The combination of site-directed spin labeling (SDSL) with electron paramagnetic resonance (EPR) spectroscopy has proven to be a valuable tool in structural biology [1–3]. In particular, the use of pulsed dipolar EPR spectroscopy (PDS) methods for measuring distances between spin centers in the range of 1.6–16 nm, like pulsed electron-electron double resonance (PELDOR or DEER) [4,5], the double quantum coherence experiment (DQC) [6–8], the single frequency technique for refocusing dipolar couplings (SIFTER) [9] or relaxation induced dipolar modulation enhancement (RIDME) [10,11] have been very successful in providing information on the structure, conformational changes and dynamics of proteins [12–18], oligonucleotides [19–23] and their complexes [24,25]. Most of these studies rely on spin labeling with nitroxides. For protein labeling, the most established spin label is the methanethiosulfonate-functionalized nitroxide MTSSL **1** (Figure 1), which reacts with cysteine residues to form the disulfide bonded side chain **R1** [26,27]. MTSSL provides high labeling yields and site selectivity through a combination with site-directed mutagenesis, which places the cysteines and thus the **R1** side chain at the desired positions in the protein.

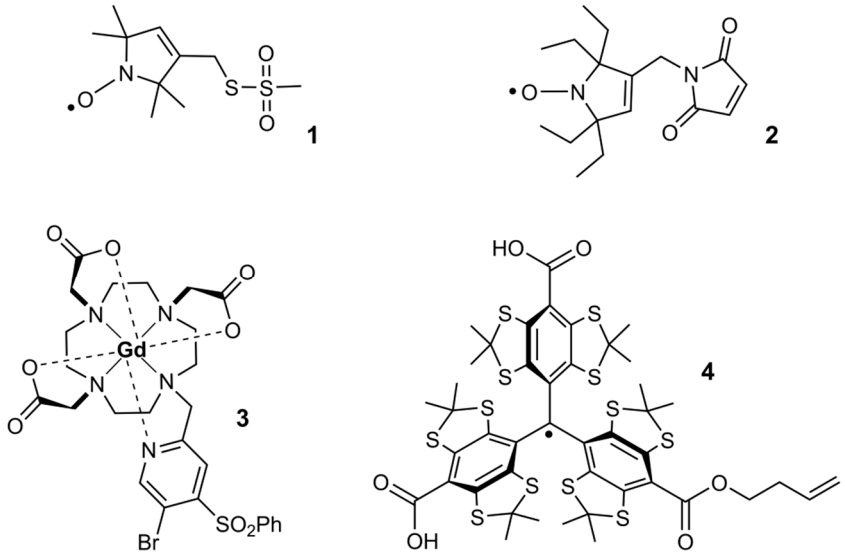

Figure 1. The molecular structures of selected spin labels: MTSSL **1**, M-TETPO **2**, BrPSPy-DO3A-Gd(III) **3**, TSL-BUTENE **4**.

In order to study biomolecules under physiological conditions, it would be highly desirable to perform such SDSL/PDS studies at room temperature in the liquid state and within the cells. However, such studies involving nitroxides as spin labels are usually limited to frozen buffer solutions due to the relaxation behavior of the nitroxides [27,28]. Furthermore, under *in cell* conditions, MTSSL, as well as all *gem*-dimethyl nitroxides, is quickly reduced to EPR-inactive hydroxylamine [29] and the bioconjugating MTSSL disulfide bond is reductively cleaved [30]. Thus, new cysteine targeting spin labels have been designed and tested *in cell* to address these issues: (a) Sterically shielded nitroxides such as **2** [31], (b) gadolinium(III)-based spin tags like **3** [32] and (c) triarylmethyl (trityl) radicals such as **4** (Figure 1) [33]. The compounds **2**–**4** are bioconjugated to cysteine residues via stable thioether bonds and show an increased in cell EPR signal persistency.

In particular, trityl spin labels hold great promise because they feature not only extended life times within the cells [34] but also several EPR spectroscopic distinctions from nitroxides and Gd-complexes, which can be advantageous in orthogonal spin labeling strategies [25,28,35–37]. Trityl spin labels based on the Finland Trityl **5** (Figure 2), display a single narrow line [38–40], which increases the EPR sensitivity and favors the use of single-frequency EPR experiments, such as SIFTER [9] or DQC [6–8]. Additionally, the carbon centered trityl spins show longer phase memory times T_m at room temperature in the liquid state than paramagnetic metal or nitroxide spin centers [41,42], enabling pulsed EPR distance measurements at physiological temperatures [28,35,43–45].

Since the introduction of **5** [46] many synthesis improvements [33,47–50] and derivatization strategies [44,49–59] as well as applications of trityl compounds in medicinal probing [60,61], imaging [62,63], as magnetic materials [64], and as spin labels in structural biology [28,33,35–37,43–45,65] have been reported. Recent examples for the trityl labeling of cysteine residues in proteins used butene (**4**, Figure 1) [33] or methanethiosulfonate (**6** and **7**, Figure 2) [33,35,36] derivatives of **5** to establish the bioconjugation via thioether bonds for *in cell* studies or via disulfide bonds for in vitro studies, respectively. However, both approaches revealed complications, namely a low labeling efficiency of 36% in the case of the butene derivative **4** [33] and unspecific, non-covalent protein-trityl aggregation in the case of **5**, **7**, and **8** [36,65,66].

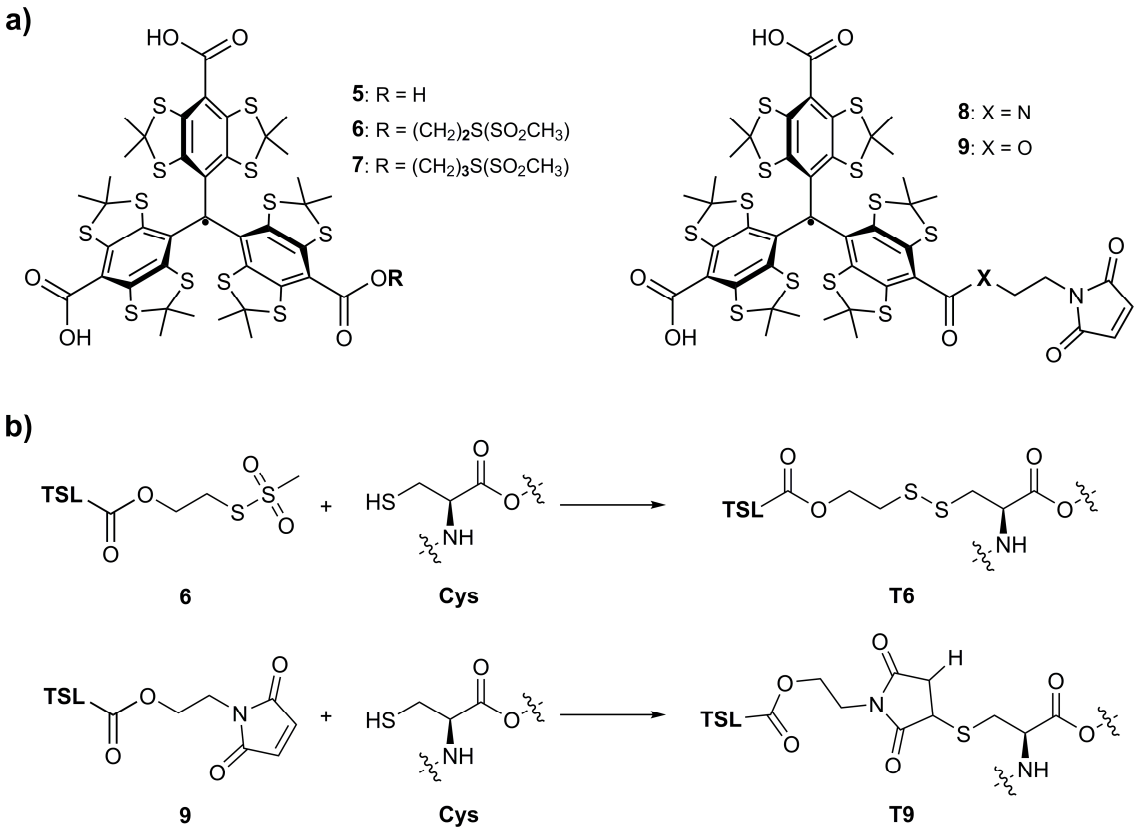

Figure 2. Lewis structures of Finland Trityl **5** and trityl spin labels **6**–**9** (**a**). Exemplary bioconjugation of trityl spin labels (TSL) **6** and **9** to cysteine residues resulting in the modified side chains **T6** and **T9** (**b**).

In order to further develop the scope of protein labeling with trityl radicals, this work presents the synthesis and characterization of the maleimide-derivatized trityl **9** (Figure 2) as well as a procedure for its selective bioconjugation to cysteine residues. Its labeling performance is meticulously assessed and compared to its predecessor **6** using *Yersinia* outer protein O mutants (YopO, ~72 kDa) [67,68] as a model system. The spin labels **8** and **9** differ with respect to the linker group, amide in the case of the former and ester for the latter. While the increased stability of amides against hydrolytic cleavage might be beneficial for *in cell* SDSL-EPR, the stronger electron withdrawing ester substituent in **9** was employed here to avert the reported EPR signal loss for **8**, due to oxidation of the trityl radical [49,65,69]. Finally, trityl label **9** is tested in trityl-trityl distance measurements by means of DQC, SIFTER and PELDOR experiments on doubly labeled YopO mutants and compared to the data obtained from the corresponding MTSSL-labeled protein.

2. Results and Discussion

2.1. Synthesis

The parent compound **5** was synthesized according to the literature [33,47–49] and esterified with the alcohol 2-hydroxyethyl maleimide using 2-chloro-1-methylpyridinium iodide (CMPI) as the activator [33,70]. After column chromatography, compound **9** was obtained as a brown solid in a yield of 21%. The identity of **9** was confirmed through ESI(+)-HRMS, UV/Vis, and *cw* EPR spectroscopy and its purity was assessed through MALDI-TOF mass spectrometry as well as medium pressure liquid chromatography (Figure S1–S7).

2.2. Redox-Stability of Trityls

The chemical stability of the previously used methanethiosulfonate-trityl label **6** and the new maleimide-functionalized trityl label **9** was compared by monitoring their *cw* EPR spectra in gas-tightly sealed aqueous buffer solutions with and without ascorbate over a period of 21 h (Figure 3). In the absence of ascorbate, it was found that the double integral of **6** reduced to 60% of the initial amplitude after ~6 h before reaching a plateau level. During the same period, the line width reduced from 0.30 to 0.24 G. This finding points towards the oxygen consuming generation of diamagnetic trityl anions and the eventual stop of this reaction after all oxygen has been consumed (Figure 3a) [69]. In contrast, **9** shows stable double integral values and line widths under the same conditions (Figure 3b). In the presence of a 25-fold molar excess of ascorbate as a reducing agent, the double integral value of **6** is halved after 5 h (Figure 3c) whereas label **9** (Figure 3d) decayed only by 10% within the same time. Both set-ups demonstrate that trityl label **9** is considerably more redox-stable than **6**, which is beneficial for EPR experiments under the reducing conditions of *in cell* studies.

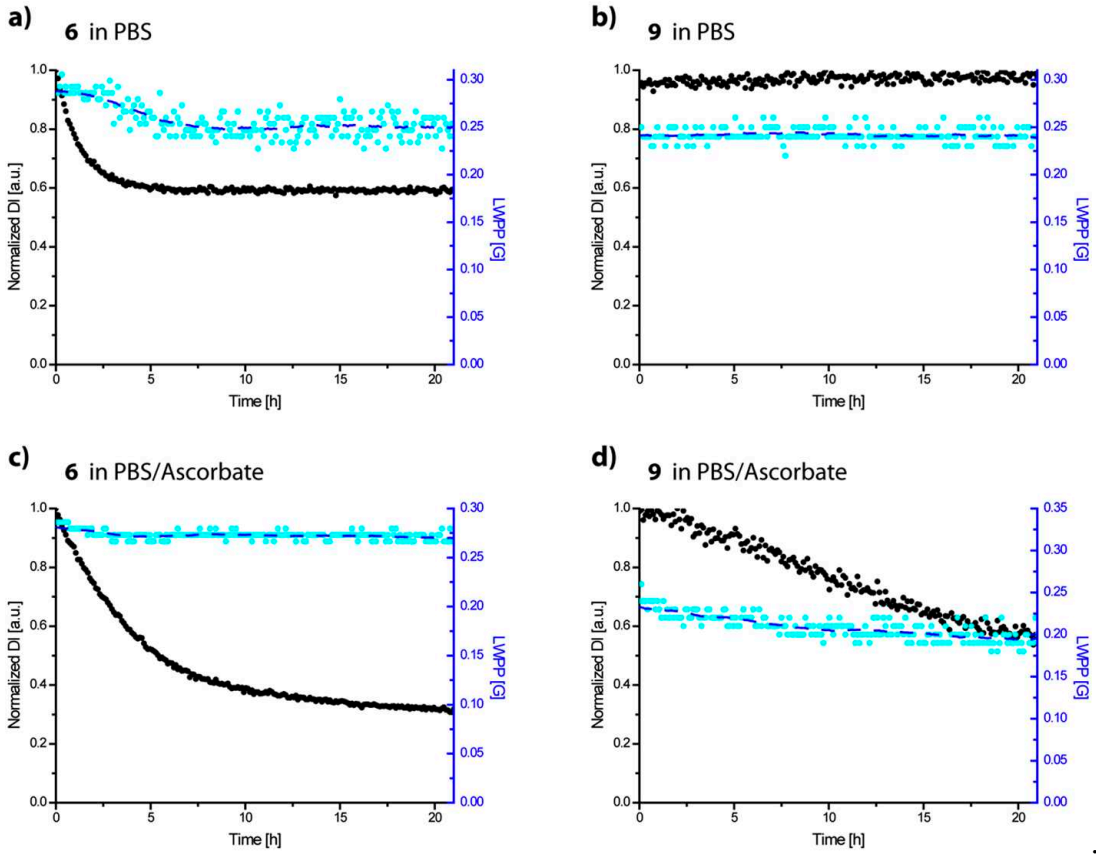

Figure 3. The stability of trityl labels **6** and **9**. The normalized double integral values (black), peak-to-peak line width values (cyan) of 200 µM gas tight incubations of **6** (**a**,**c**) and **9** (**b**,**d**) in PBS buffer and in PBS buffer with 5 mM ascorbate. EMXmicro acquisition parameters: modulation amplitude: 0.1 G, microwave power: 558 µW, time constant: 20.48 ms, sweep time: 69.02 s, resolution: 100 Pts/G for **6** and 154 Pts/G for **9**, sweep width: 20 G.

2.3. Labeling

In previous publications, it was found that trityl radicals derived from Finland Trityl **5** aggregate in aqueous solution above 60 µM [64] and that non-bioconjugated trityl remnants were often found next to trityl-labeled proteins even after separation attempts with size exclusion chromatography [36,65]. However, all reported trityl labeling procedures of the proteins used trityl concentrations in the range of 200–1500 µM [33,36,43,65], meaning that the formation of trityl aggregates was favored. Therefore, it was tested here, whether it is possible to suppress trityl aggregation and thus facilitate the separation of the excess label by working with free trityl label concentrations not far above the critical aggregation concentration during the bioconjugation and the subsequent purification steps.

In a first test, the cysteine free protein construct YopO C219A (further on referred to as YopO-WT) was incubated with maleimide trityl **9**, methanethiosulfonate trityl **6** and the parent trityl **5** as a non-bioconjugatable reference benchmark. Since YopO-WT has no cysteines, none of the samples should show a trityl signal after incubation and the separation of the excess label via size exclusion chromatography. All incubations were performed in phosphate buffer solutions at pH = 6.8 in order to disfavor competing reactions of **9** with the 35 lysine residues [71] within YopO-WT and to avoid the deactivating hydrolysis of the bioconjugating maleimide moiety [72]. The trityl labels were prepared as 84 µM solutions in the buffer (2.50 mL) and added to the protein solutions (3.50 mL), resulting in final incubation concentrations of 35 µM and 3.5 µM for label and protein, respectively. After size exclusion chromatography (PD-10), the protein solutions were concentrated to approximately 5 µM and analyzed by UV/Vis spectroscopy and *cw* EPR (Figure 4).

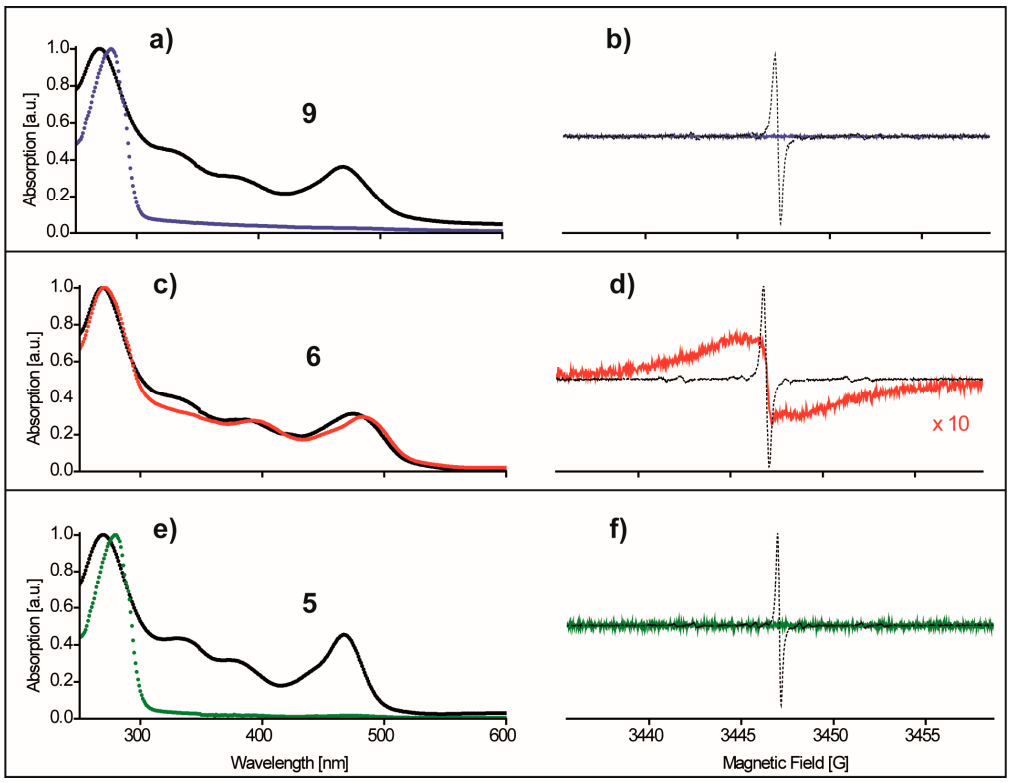

Figure 4. The incubations of **9** (blue), **6** (red) and **5** (green) with cysteine-free YopO-WT. The spectra shown have been recorded after size exclusion chromatography. Panels (**a**,**c**,**e**): normalized UV/Vis spectra of the protein solutions in juxtaposition with 20 µM buffer solutions of the pure trityl compounds **9**, **6**, and **5** (black). Panels (**b**,**d**,**f**): corresponding room temperature *cw* X-band EPR spectra overlaid with the spectrum of the free label (dashed black line) for the sake of comparison.

According to the obtained UV/Vis and EPR spectra, excess label **9** (Figure 4a,b, blue trace) and **5** (Figure 4e,f, green trace) were successfully separated from the cysteine-free YopO-WT protein as seen by the absence of the characteristic trityl UV/Vis band at ~467 nm (black traces in Figure 4a,e), the absence of an EPR signal from these samples and mass spectrometry only detecting unlabeled protein masses for the incubation with **9** (Figure S14). In contrast, the incubation of YopO-WT with **6** lead even at this low trityl concentration and after column chromatography to a UV/Vis absorption band at ~467 nm and a significantly broadened trityl signal in the *cw* EPR spectrum (Figure 4c,d, red trace). This does clearly indicate that trityl remnants could not be separated from the protein in this case. Interestingly, such a broadened *cw* EPR spectrum was also obtained upon prolonged incubations (16 h, 4 °C) of **6** without the protein (Figure S16a). As no comparable line broadening was found for protein free incubations of **9** (Figure S16b) and **5**, the deviant properties of **6** must be related to its methanethiosulfonate moiety. As it is known that MTSSL **1** forms a disulfide-bridged bisnitroxide in solution over time [27], it can be reasonably assumed that also **6** forms such a disulfide-bridged bistrityl compound leading to the observed broadening of the EPR signal. This hypothesis was tested by irradiation of the sample from Figure S16a with UV light of λ = 254 nm in order to cleave the disulfide bridge [73], and to recover the corresponding narrow line EPR spectrum, which is exactly what was observed (Figure S17). At the same time, the spin count before and after UV light irradiation did not change, indicating that the line does not narrow due to a light-induced depletion of trityl centers. The attempts to disfavor the dimerization of **6** by varying the incubation time and temperatures did not help, nor was it possible to separate the seemingly aggregated dimers by using other chromatography methods (AEKTA, size exclusion and hydrophobic interaction materials) or dialysis procedures (20 h, ×5 million volume dilution, 5000 MWCO membrane). Remarkably, no evidence for free label remnants were reported in the labeling of the solid support fixated T4 lysozyme protein with **7** [35] and with another disulfide trityl derivative CT02-TP [43]. Apparently, the aggregated label as well as possible dimerization products could be removed from the protein sample by repeated washing of the protein-loaded beads with buffer solution. In the present work on YopO, similar attempts using ^{6}His tag modified YopO mutants immobilized on nickel affinity beads did not lead to the separation of residual **6**.

Next, a general labeling procedure for the maleimide-derivatized label **9** was developed using YopO mutants S88C/L113C and YopO L113C/L353C with highly exposed cysteine residues under varied reaction conditions. In each case, the criterion in the evaluation of the labeling outcome was the resulting trityl/protein ratio after size exclusion chromatography as determined by UV/Vis spectroscopy (Supplementary Materials, Section 4.2). The following aspects turned out to be crucial for a successful labeling: (a) The trityl concentration in the labeling solution has to be kept below 35 μM until after the separation of the free label from the labeled protein. Otherwise, trityl aggregates were formed [64] that exceeded the molecular cut-off (MWCO = 5000) of the employed PD-10 size exclusion column and were eluted alongside the protein. (b) At the cost of prolonged reaction times (16 h), the labeling proceeded best in slightly acidic solutions (pH = 6.5–6.8) and at low temperatures (4 °C). In contrast, the attempt to increase the cysteine nucleophilicity through basic solution conditions (pH = 7.5–8.5) as usually done [65,74], resulted in excessive trityl/protein ratios that could indicate lysine labeling under alkaline conditions [71]. Increasing the temperature to room temperature led to lower labeling efficiencies, maybe due to the accelerated hydrolyzation of the maleimide group [72]. This competing process is conventionally countered by favoring the second order labeling reactions over the pseudo first order hydrolyzation reactions via high label concentrations, an option which is not possible in the present case. (c) The separation of the free label via PD-10 column worked best when the column was loaded with 2 mL of the incubation solution, i.e., 70 nmol of **9**, followed by 500 μL of buffer solution. The higher trityl amounts per loading apparently surpassed the column capacity and led to only partial removal of the free label.

Based on the findings made above, a labeling protocol was derived and then applied to the double cysteine YopO mutants S585C/Q603C and V559C/N624C. The introduced cysteine residues are located on the YopO GDI domain helix α14 [68] (Figure 5) whose rather rigid structure serves as a distance ruler that separates the labeling sites by five (S585C/Q603C) and seven (V599C/N624C) helix turns. According to the in silico predictions calculated with mtsslWizard [75], the expected mean distances between the trityl conformer clouds are 3.4 nm and 4.3 nm for YopO S585C/Q603C (red) and YopO V599C/N624C (mint), respectively.

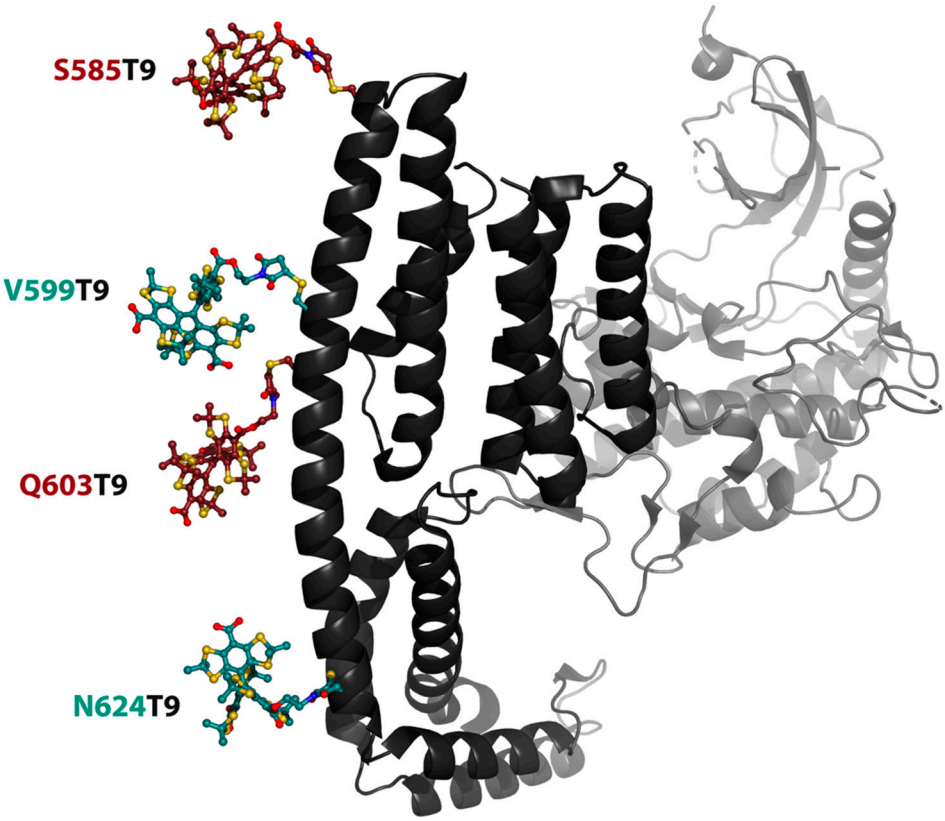

Figure 5. PyMOL cartoon representation of the GDI (front, black) and kinase domain (back, grey) of YopO (PDB-ID: 4ci6). The labeling positions on the GDI domain are indicated by color coded trityl pairs for the two studied mutants YopO S585C/Q603C (red) and YopO V559C/N624C (mint). For clarity reasons, only one conformer of **T9** is displayed for each labeling site.

After incubation with **9**, purification and concentrating, the resulting protein solutions were subjected to analytical size exclusion chromatography, UV/Vis spectroscopy, *cw* EPR spin count experiments and ESI(+) mass spectrometry (MS). In addition, the functional and thus structural integrity of the labeled protein was checked using an assay to detect the autophosphorylation capability of YopO in the presence of actin [68]. Exemplarily, the assessment results for the doubly labeled YopO mutant V599**T9**/N624T**9** are displayed in Figure 6 (For the S585**T9**/Q603**T9** data set see Figure S8).

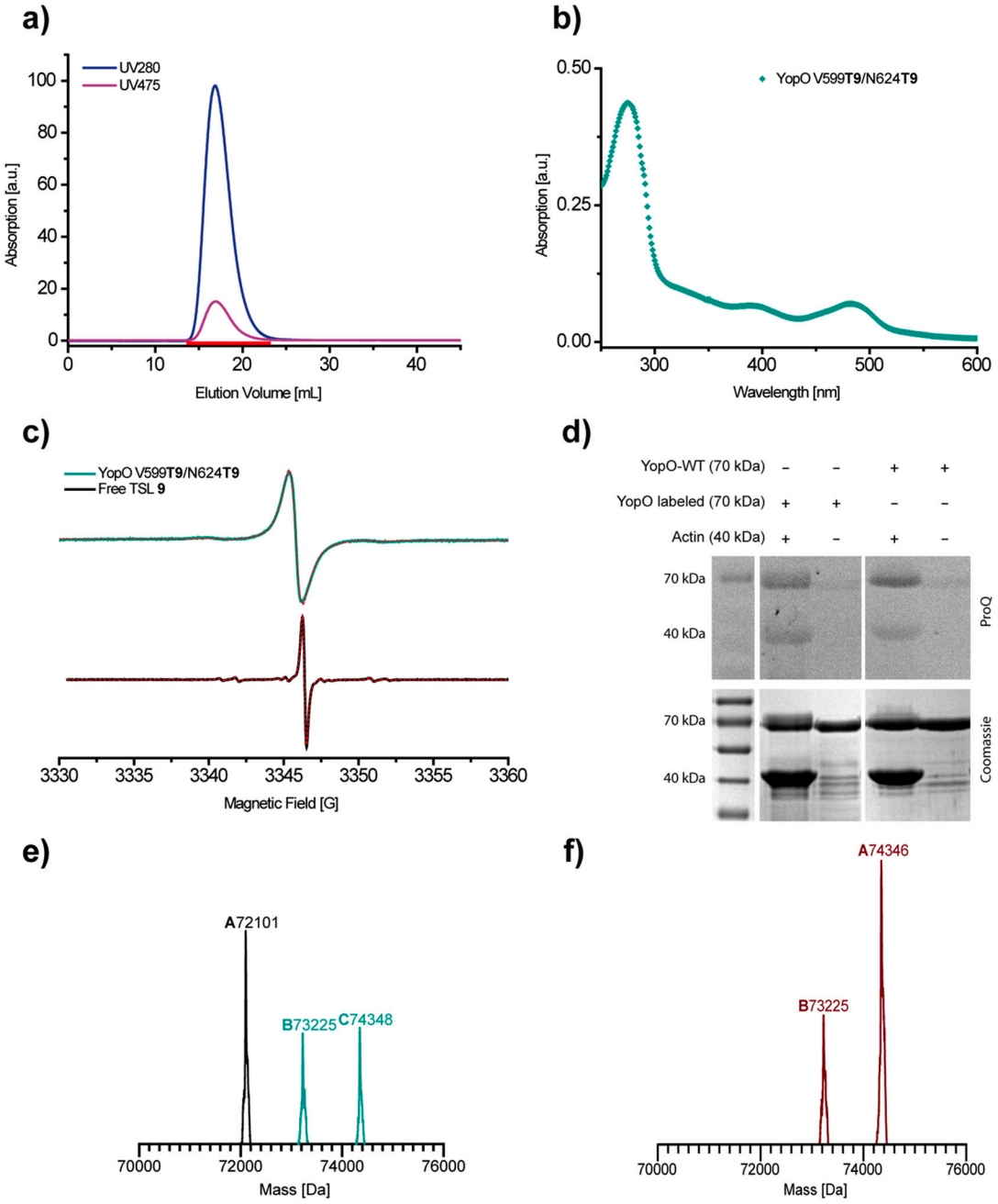

Figure 6. The labeling of YopO V599C/N624C with **9**. The analytics after the separation of the free label via PD-10 column. (**a**) HiPrep 26/10 size exclusion chromatogram of the labeled protein showing the trityl specific absorption at ~475 nm (red) and the absorption at 280 nm (blue). (**b**) UV/Vis spectrum of the labeled protein. The absorption maxima at ~475 nm and at ~280 nm are calculated to represent a concentration ratio of **9** to YopO of 1.8/1, i.e., 90% labeling efficiency. (**c**) The room temperature X-band *cw* EPR spectrum of the labeled protein YopO V599**T9**/N624**T9** (mint) as compared to the free label (black). The dashed red lines indicate spectral simulations obtained with EasySpin (Supplementary Materials, Section 8.2) [76]. EMXmicro acquisition parameters: modulation amplitude 0.15 G, microwave power 2.783 mW, time constant 20.48 ms, sweep time 42.04 s, resolution 67 pts/G. (**d**) The phosphorylation assay of labeled YopO V599**T9**/N624**T9** in comparison to YopO-WT. The phosphorylation is detected using ProQ Diamond stain and subsequent Coomassie staining. (**e**) ESI(+)-MS of the intact protein YopO V599**T9**/N624**T9**. The doubly labeled protein calculated: 74,347.6 Da, found: 74,348 Da (peak **C**). (**f**) ESI(+)-MS of the intact protein YopO S585**T9**/Q603**T9**. The doubly labeled protein calculated: 74,345.6 Da, found: 74,346 Da (peak **A**).

The size exclusion elugram (Figure 6a) shows that the trityl specific absorbance at ~475 nm is only detected in conjunction with the protein absorption band at ~280 nm. This finding rules out the presence of trityl aggregates and indicates the successful separation of free trityl. A trityl-protein ratio of 1.8/1 and thus a labeling efficiency of 90% was calculated from the UV/Vis absorbances at ~280 and ~475 nm (Figure 6b, for calculation see SI Section 4.2). The *cw* EPR spectrum of YopO V599**T9**/N624T**9** (mint trace in Figure 6c) is broadened as compared to free **9** (black trace in Figure 6c) but neither broader features indicative of aggregation nor narrow features indicative of free **9** are visible. As the observed line broadening is not accompanied by additional features and is straightforwardly simulated as a consequence of the trityl immobilization at the protein surface, the *cw* EPR spectrum corroborates the successful separation of the free label. Additionally, the *cw* EPR spin count reports a spin concentration of 87 µM at a protein concentration of 50 µM (Supplementary Materials, Section 8.1). Thus, the labeling efficiency as determined by UV/Vis (90%) matches within error the one determined by EPR (87%), which is much better than the 36% obtained previously for label **4**. The functional and thus structural integrity of the labeled YopO mutant is validated by a phosphorylation assay (Figure 6d). In accordance with the reported kinase activity of unlabeled YopO [67,68], both trityl-labeled mutants are phosphorylated in the presence but not in the absence of actin.

Finally, ESI(+) (Figure 6e) and MALDI(+) mass spectra (Figure S15a) of the protein sample reports the expected mass of 74348 Da (calculated: 74347.6 Da) for the doubly trityl-labeled sample (Figure 6e). In contrast to earlier reports [65], no threefold-labeled protein was detected, which points to the successful suppression of lysine labeling due to the chosen pH value of the labeling incubation. The additional mass peaks at 73225 Da and 72101 Da correspond to singly and unlabeled YopO, respectively. However, their intensities strongly vary for both YopO mutants and for the type of mass spectrometry used (Supplementary Materials, Section 5). This indicates that the non- and mono-labeled species are formed either during the mass spectrometry measurement and/or the preparation procedure for the mass spectrometry samples, which requires acidic conditions (trifluoracetic acid) and leads to the detachment of the label via retro-Michael reaction [77]. Several attempts to avoid the acidic MS-sample preparation failed. Consequently, the achieved labeling efficiencies are not reflected in the obtained MS spectra.

2.4. PDS Measurements

The doubly trityl labeled protein samples V599**T9**/N624**T9** and S585**T9**/Q603**T9** were measured with DQC and SIFTER [41], while the MTSSL labeled reference samples V599**R1**/N624**R1** and S585**R1**/Q603**R1**, were measured with PELDOR. The choice of the different pulse sequences is based on the different spectral width of the labels [2,6,9,11]. Figure 7 shows the background corrected time traces and the corresponding distance distributions (Figures S25 and S27, original time traces).

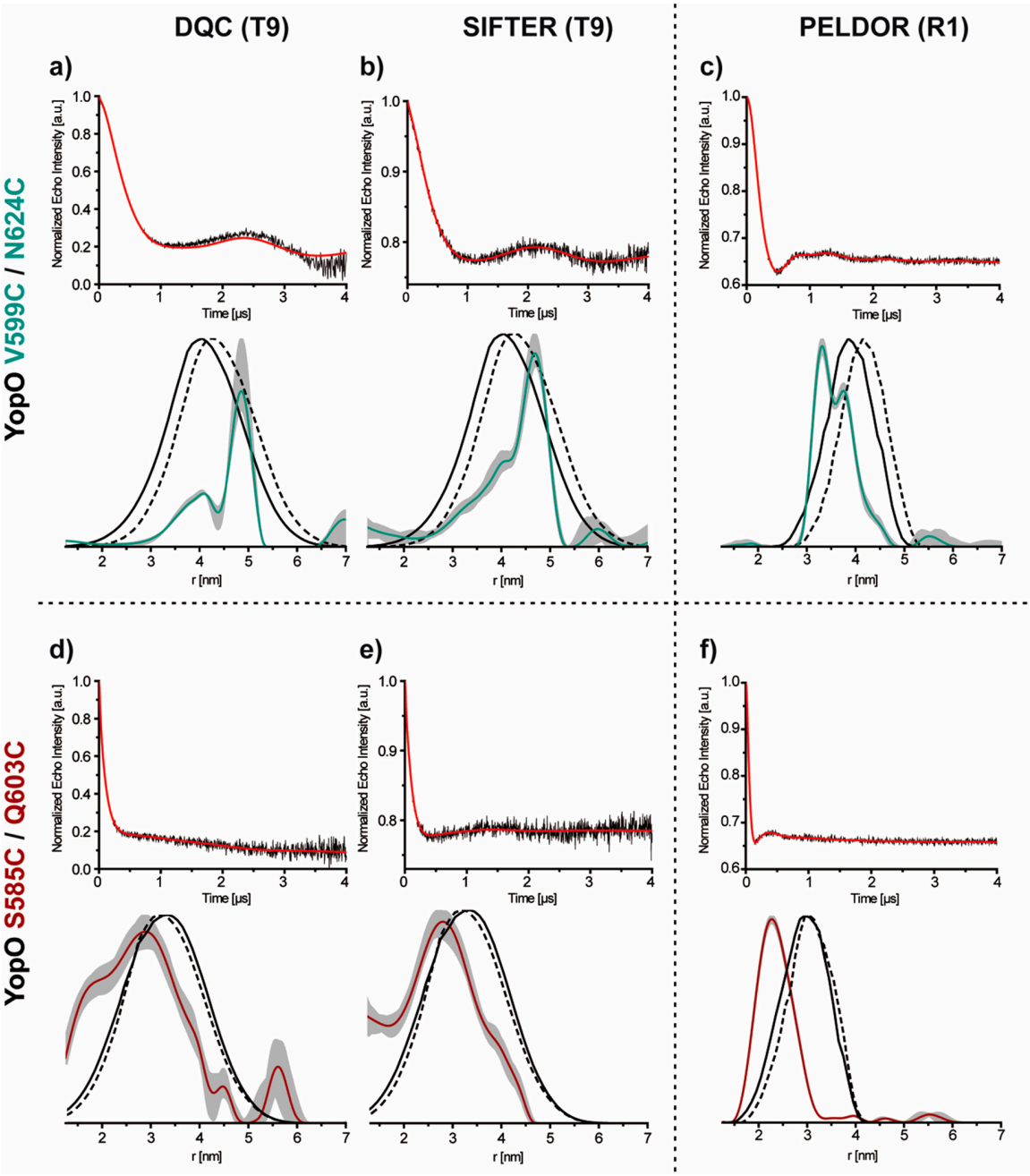

Figure 7. The PDS data of YopO V599C/N624C and S585C/Q603C. On the left, the background corrected DQC (**a**,**d**) and SIFTER (**b**,**e**) time traces (top) and their corresponding distance distributions (bottom) for YopO V599**T9**/N624**T9** and S585**T9**/Q603**T9**. On the right, the PELDOR (**c**,**f**) time traces (top) and the corresponding distance distributions (below) for YopO V599**R1**/N624**R1** (mint) and S585**R1**/Q603**R1** (red). In each case, the background corrected PDS time traces are shown in black, the corresponding fits from Tikhonov regularization in red. The distance distributions are shown in the respective color code while shaded grey areas indicate the error margins as obtained by the validation routine of DeerAnalysis [78]. The in silico predictions of the distance distributions were generated with mtsslWizard [75] and overlaid as dashed (PDB-ID 4ci6) and solid (PDB-ID 2h7o) black lines.

For the nitroxide- and trityl-labeled YopO mutant V599C/N624C, each time trace shows oscillations (Figure 7a–c, top) while mutant S585C/Q603C shows only strongly modulation damped time traces for both label types (Figure 7d–f, top). Regarding the modulation depths, both trityl-labeled mutants have modulation depths of 20–25% in the SIFTER [9,40,79] and of more than 80% in the DQC experiments.

The differences in the modulation depth are attributed to the specifics of the two pulse sequences, especially the highly effective 64 step phase cycle in the case of DQC [7,80]. Nevertheless, the obtained modulation depth in DQC parallels those found for quantitatively labeled oligonucleotide samples [81] and model compounds [39,79] reflecting the high labeling efficiency and sample purity achieved here. The previously reported DQC modulation depths on trityl labeled proteins varied between 20–50% [43,65].

The signal-to-noise-ratios (SNR) [40,79,82] show that the trityl-trityl DQC (8.9 $min^{-1/2}$ and 7.0 $min^{-1/2}$, Figure 7a,d, top) and SIFTER experiments (5.8 $min^{-1/2}$ and 5.9 $min^{-1/2}$, Figure 7b,e, top) are more sensitive than the corresponding trityl-trityl PELDOR experiment (1.4 $min^{-1/2}$ and 1.1 $min^{-1/2}$, Figure S26). However, at a modulation depth of 35%, the nitroxide-nitroxide PELDOR measurements gave similar SNRs (9.9 $min^{-1/2}$ and 7.3 $min^{-1/2}$, Figure 7c,f, top) as the trityl-trityl DQC and SIFTER experiments. Thus, the sensitivity advantage of the trityl based single frequency experiments over nitroxide-nitroxide PELDOR measurements [1,6,9,11] is lost here due to two reasons: (1) The fivefold longer shot repetition time of 15 ms for the trityl labeled samples as compared to 3 ms for the MTSSL labeled samples (both at 50 K, Figure S20a+c) [41]. (2) The phase memory time T_m for the trityl radicals (1.3 µs) is by a factor of 3.5 shorter than for the nitroxide radicals (4.6 µs, both at 50 K, Figure S20b+d) [42].

The corresponding distance distributions are shown in Figure 7a–f and are compared to the in silico labeling results. The in silico labeling was done with mtsslWizard in combination with the crystal structures of a $YopO_{89–729}$ complex with actin (PDB-ID 4ci6, dashed black line) and a homologous structure of the truncated (amino acids 434–732) actin-free YpkA GDI domain from *Yersinia pestis* (PDB-ID 2h7o, solid black line). In each case, the experimental distance distributions are a subset of the in silico derived distributions. However, the **R1**/PELDOR derived distance distributions show a large shift of the most probable distance of up to 1 nm. For the **T9**-labeled samples, this distance shift is also observed although less marked, probably due to the different linker length/flexibility. In addition, mutant V599**C**/N624**C** reveals at least bimodal distance distributions for both, **R1** and **T9**. Both effects, the distance shift and the bimodality, may either be caused by preferred label conformations [2,83–85] and/or by YopO conformers with different bending degrees of the labeled α14 helix. The latter would fit to recent observations that the structure of YopO in solution seems to partially deviate from the crystal structure [86]. In any case, the new trityl spin label reproduces the results obtained with MTSSL.

3. Conclusions

The trityl-based spin label **9** was successfully synthesized, and by careful control of the labeling conditions, a labeling protocol could be established which enabled the site-selective bioconjugation of **9** to cysteines in high yields and without aggregations. This enabled PDS measurements between two trityl labels on YopO with good quality. Although the sensitivity advantage of trityl labels over nitroxide labels is lost here because of a fast T_m relaxation, combining nitroxide and trityl labels with different functional groups enables orthogonal spin labeling. It could also be shown that the labeling of proteins with the methanethiosulfonate derivatized trityl compound **6** is compromised by the formation of a disulfide bridged bistrityl compound, which could not be separated from the protein. In order to improve the applicability and versatility of trityl labels in the future, new labels should display increased water solubility, e.g., by functionalizing the trityl OX063 instead of the Finland trityl. In addition, the linker group between trityl core and bioreactive moiety should be shortened and/or made more rigid to narrow the PDS-derived distance distributions.

4. Materials and Methods

4.1. Synthesis of **9**

Under an atmosphere of argon, compound **5** (98.0 mg, 98.0 µmol) was dissolved in dry tetrahydrofuran (6 mL) and dry triethylamine (68 µL, 490 µmol). The mixture was stirred at room

temperature for 30 min and then cooled to 0 °C. Consecutively, N(2-hydroxyethyl)maleimide (13.8 mg, 98.0 μmol), 2-chloromethylpyridinium iodide (CMPI, 33.2 mg, 130 μmol) and 4-dimethylaminopyridine (5.50 mg, 45.0 μmol) were given into the reaction which thereupon was allowed to warm to room temperature and stirred overnight. After 18 h, the reaction was quenched with aqueous HCl (0.36 M, 20 mL), the phases were separated, the aqueous layer was extracted with dichloromethane (2 × 10 mL) and the combined organic layers were concentrated under reduced pressure. According to MALDI-(+)-MS (Figure S1), this crude product mixture was composed of Finland trityl substrate, the one-fold and the two-fold 2-hydroxyethylmaleimide ester products. The crude product was coated onto silica gel (*w*/*w* = 1/3), packed into a cartridge which was mounted on a reversed phase column (Buechi FlasPure EcoFlex C18, 20 g, Büchi, Essen, Germany) and eluted with an acetonitrile gradient (10–100%) in deionized water (Figure S2). The product was isolated (Figures S3–S5) as a brown solid in a yield of 21% (22.7 mg, 20.2 μmol). Figure S6 shows UV/Vis and *cw* EPR spectra of the isolated compound **9** in buffer solutions. Figure S7 displays *cw* EPR spectra of compound **9** dissolved in organic solvents and revealing a $A(^1H)$ hyperfine coupling constant of 0.28 MHz and a g_{iso}-value of 2.0035.

4.2. Protocol for Labeling YopO with **9**

The protein (YopO, 20 nM in 2.5 mL) is incubated in the labeling buffer (20 mM POi, pH 6.8, 50 mM NaCl) with a five-fold molar excess of TCEP for 1.5 h at 4 °C in order to cleave disulfide bridged protein dimers. The remaining TCEP was removed using a PD-10 desalting column and the labeling reaction is set up immediately afterwards.

To the collected 3.5 mL protein solution is added a 5-fold molar excess per cystein of **9** (dissolved in 2.5 mL labeling buffer) resulting in a total volume of 6 mL containing 3.3 μM protein and 33 μM of **9**. The solution is incubated for 16 h at 4 °C. The free label excess was removed by loading fractions of 2 mL of the labeling solution onto a PD-10 size exclusion column (GE healthcare) followed by 500 μL of the labeling buffer and then eluting with 3.5 mL the labeling buffer. The total load of trityl on the PD10 should not exceed 70 nmol for maximum separation performance. The protein fraction was concentrated to 2.5 mL using a centrifugal concentrator (Vivaspin 6/10k MWCO, Sartorius, Goettingen, Germany).

4.3. UV-Vis Setup

For all UV/Vis experiments, 700 μL of the respective sample were loaded into a 0.7 mL Rotilabo®-precision quartz glass cuvette (Roth, Karlsruhe, Germany) and UV/Vis spectra were recorded from 600 to 200 nm at a rate of 0.3 s nm^{-1} using a Cary 100 UV-Vis (Agilent Technologies, Santa Clara, CA, USA).

4.4. Mass Spectrometry (MS) Setup

The ESI(+)-MS spectra were recorded on a LTQ Orbitrap Discovery spectrometer (Thermo Scientific, Waltham, MA, USA) while MALDI-MS spectra were obtained using an ultrafleXtreme TOF/TOF spectrometer (Bruker Daltonik, Bremen, Germany).

4.5. EPR Sample Preparation

The sample preparation for YopO labeled with **9**: After the UV/Vis concentration determination, all YopO-**T9** samples were spun down in a centrifugal concentrator (Vivaspin 6/10k MWCO) to volumes below 300 μL, rebuffered with 10 mL deuterated PELDOR buffer (100 mM TES pH 7.5, 100 mM NaCl) and concentrated to a final protein concentration of ~50 μM.

The sample preparation for YopO labeled with MTSSL: All YopO-R1 samples were rebuffered with 8 mL PELDOR buffer (100 mM TES pH 7.5, 100 mM NaCl). The samples were further concentrated to a final protein concentration > 50 μM.

cw EPR: The samples were loaded into a 10 µL glass capillary (Disposable Capillaries, Hirschmann® Laborgeräte, Eberstadt, Germany), sealed with super glue and placed in an X-band tube (O.D. 4 mm, Wilmad-LabGlass).

Pulsed EPR: The samples were diluted 1:1 in deuterated ethylene glycol, transferred into a Q-band EPR tube (O.D. 3 mm, Wilmad LabGlass, Vineland, NJ, USA) and flash-frozen in liquid nitrogen.

4.6. EPR Setup

The room temperature *cw* EPR measurements were performed at X-band frequencies (~9 GHz) either on a Bruker (Bruker BioSpin, Rheinstetten, Germany) EMXmicro spectrometer equipped with an ER 4122SHQ resonator or on a Bruker EMXnano spectrometer (Bruker BioSpin, Rheinstetten, Germany) as stated in the respective figure captions.

The pulsed EPR measurements were conducted at Q-band frequencies (33.7 GHz) on a Bruker (Bruker BioSpin, Rheinstetten, Germany) ELEXSYS E580 EPR spectrometer (equipped with an ER 5106QT-II resonator and a 150 W TWT-amplifier (Applied Systems Engineering, Fort Worth, TX, USA). All data was acquired using quadrature detection. The temperature was adjusted to the appropriate value (between 50 K and 80 K) using a CF935 helium gas-flow cryostat (Oxford Instruments, Abingdon, UK) in conjunction with an Oxford Instruments ITC 502 temperature controller.

More detailed description of all methods and procedures can be found in the Supporting Information.

Supplementary Materials: The following are available online at. It contains additional figures and experiments, full materials and methods including detailed and complete experimental procedures. EPR, UV/Vis, chromatography equipment, chemical synthesis and biosynthesis, EPR and MS sample preparations.

Author Contributions: Conceptualization, O.S.; methodology, J.J.J. and C.A.H.; software, T.H. and G.H.; validation and formal analysis, J.J.J., C.A.H. and T.H.; investigation, J.J.J., C.A.H., T.H., F.B. and F.R.H.; resources, O.S.; data curation, J.J.J., C.A.H. and T.H.; writing—original draft preparation, J.J.J., C.A.H., T.H. and O.S.; writing—review and editing, J.J.J., C.A.H., T.H., G.H. and O.S.; visualization, C.A.H. and T.H.; supervision, project administration and funding acquisition, O.S.

Funding: This research was funded by the Deutsche Forschungsgemeinschaft through SPP1601 (grant SCHI 531/6-2).

Acknowledgments: We thank Stefan Müller from CECAD Cologne and Marianne Engeser for the MS analysis of our protein samples.

Conflicts of Interest: The authors declare no competing financial interest.

References

1. Schiemann, O.; Prisner, T.F. Long-range distance determinations in biomacromolecules by EPR spectroscopy. *Q. Rev. Biophys.* **2007**, *40*, 1–53. [CrossRef] [PubMed]
2. Jeschke, G. DEER Distance Measurements on Proteins. *Annu. Rev. Phys. Chem.* **2012**, *63*, 419–446. [CrossRef]
3. Timmel, C.R.; Harmer, J.R. Structural Information from Spin-Labels and Intrinsic Paramagnetic Centres in the Biosciences. *Struct. Bond.* **2014**, *152*, 1–332.
4. Milov, A.D.; Salikhov, K.M.; Schirov, M.D. Application of ELDOR in electron-spin echo for paramagnetic center space distribution in solids. *Fiz. Tverd. Tela (Leningrad)* **1981**, *23*, 975–982.
5. Milov, A.; Ponomarev, A.; Tsvetkov, Y. Electron-electron double resonance in electron spin echo: Model biradical systems and the sensitized photolysis of decalin. *Chem. Phys. Lett.* **1984**, *110*, 67–72. [CrossRef]
6. Saxena, S.; Freed, J.H. Double quantum two-dimensional Fourier transform electron spin resonance: Distance measurements. *Chem. Phys. Lett.* **1996**, *251*, 102–110. [CrossRef]
7. Saxena, S.; Freed, J.H. Theory of double quantum two-dimensional electron spin resonance with application to distance measurements. *J. Chem. Phys.* **1997**, *107*, 1317–1340. [CrossRef]
8. Borbat, P.P.; Freed, J.H. Multiple-quantum ESR and distance measurements. *Chem. Phys. Lett.* **1999**, *313*, 145–154. [CrossRef]
9. Jeschke, G.; Pannier, M.; Godt, A.; Spiess, H. Dipolar spectroscopy and spin alignment in electron paramagnetic resonance. *Chem. Phys. Lett.* **2000**, *331*, 243–252. [CrossRef]

10. Kulik, L.; Dzuba, S.; Grigoryev, I.; Tsvetkov, Y. Electron dipole–dipole interaction in ESEEM of nitroxide biradicals. *Chem. Phys. Lett.* **2001**, *343*, 315–324. [CrossRef]
11. Milikisyants, S.; Scarpelli, F.; Finiguerra, M.G.; Ubbink, M.; Huber, M. A pulsed EPR method to determine distances between paramagnetic centers with strong spectral anisotropy and radicals: The dead-time free RIDME sequence. *J. Magn. Reson.* **2009**, *201*, 48–56. [CrossRef] [PubMed]
12. Park, S.-Y.; Borbat, P.P.; Gonzalez-Bonet, G.; Bhatnagar, J.; Pollard, A.M.; Freed, J.H.; Bilwes, A.M.; Crane, B.R. Reconstruction of the chemotaxis receptor–kinase assembly. *Nat. Struct. Mol. Boil.* **2006**, *13*, 400–407. [CrossRef] [PubMed]
13. Banham, J.E.; Timmel, C.R.; Abbott, R.J.M.; Lea, S.M.; Jeschke, G. The Characterization of Weak Protein–Protein Interactions: Evidence from DEER for the Trimerization of a von Willebrand Factor a Domain in Solution. *Angew. Chem. Int. Ed.* **2006**, *45*, 1058–1061. [CrossRef] [PubMed]
14. Denysenkov, V.P.; Prisner, T.F.; Stubbe, J.; Bennati, M. High-field pulsed electron–electron double resonance spectroscopy to determine the orientation of the tyrosyl radicals in ribonucleotide reductase. *Proc. Natl. Acad. Sci. USA* **2006**, *103*, 13386–13390. [CrossRef] [PubMed]
15. Pilotas, C.; Ward, R.; Branigan, E.; Rasmussen, A.; Hagelueken, G.; Huang, H.; Black, S.S.; Booth, I.R.; Schiemann, O.; Naismith, J.H. Conformational state of the MscS mechanoselective channel in solution revealed by pulsed electron-electron double resonance (PELDOR) spectroscopy. *Proc. Natl. Acad. Sci. USA* **2012**, *109*, E2675–E2682. [CrossRef] [PubMed]
16. Herget, M.; Baldauf, C.; Schölz, C.; Parcej, D.; Wiesmüller, K.-H.; Tampé, R.; Abele, R.; Bordignon, E. Conformation of peptides bound to the transporter associated with antigen processing (TAP). *Proc. Natl. Acad. Sci. USA* **2011**, *108*, 1349–1354. [CrossRef] [PubMed]
17. Glaenzer, J.; Peter, M.F.; Thomas, G.H.; Hagelueken, G. PELDOR Spectroscopy Reveals Two Defined States of a Sialic Acid TRAP Transporter SBP in Solution. *Biophys. J.* **2017**, *112*, 109–120. [CrossRef] [PubMed]
18. Abdullin, D.; Florin, N.; Hagelueken, G.; Schiemann, O. EPR-Based Approach for the Localization of Paramagnetic Metal Ions in Biomolecules. *Angew. Chem. Int. Ed.* **2015**, *54*, 1827–1831. [CrossRef] [PubMed]
19. Schiemann, O.; Cekan, P.; Margraf, D.; Prisner, T.F.; Sigurdsson, S.T. Relative Orientation of Rigid Nitroxides by PELDOR: Beyond Distance Measurements in Nucleic Acids. *Angew. Chem.* **2009**, *121*, 3342–3345. [CrossRef]
20. Marko, A.; Denysenkov, V.P.; Margraf, D.; Cekan, P.; Schiemann, O.; Sigurdsson, S.T.H.; Prisner, T.F. Conformational Flexibility of DNA. *J. Am. Chem. Soc.* **2011**, *133*, 13375–13379. [CrossRef]
21. Stelzl, L.S.; Erlenbach, N.; Heinz, M.; Prisner, T.F.; Hummer, G. Resolving the Conformational Dynamics of DNA with Ångstrom Resolution by Pulsed Electron–Electron Double Resonance and Molecular Dynamics. *J. Am. Chem. Soc.* **2017**, *139*, 11674–11677. [CrossRef] [PubMed]
22. Krstić, I.; Frolow, O.; Sezer, D.; Endeward, B.; Weigand, J.E.; Suess, B.; Engels, J.W.; Prisner, T.F. PELDOR Spectroscopy Reveals Preorganization of the Neomycin-Responsive Riboswitch Tertiary Structure. *J. Am. Chem. Soc.* **2010**, *132*, 1454–1455. [CrossRef] [PubMed]
23. Kerzhner, M.; Matsuoka, H.; Wuebben, C.; Famulok, M.; Schiemann, O. High-Yield Spin Labeling of Long RNAs for Electron Paramagnetic Resonance Spectroscopy. *Biochemistry* **2018**, *57*, 2923–2931. [CrossRef] [PubMed]
24. Duss, O.; Michel, E.; Yulikov, M.; Schubert, M.; Jeschke, G.; Allain, F.H.-T. Structural basis of the non-coding RNA RsmZ acting as a protein sponge. *Nature* **2014**, *509*, 588–592. [CrossRef] [PubMed]
25. Wu, Z.; Feintuch, A.; Collauto, A.; Adams, L.A.; Aurelio, L.; Graham, B.; Otting, G.; Goldfarb, D. Selective Distance Measurements Using Triple Spin Labeling with Gd3+, Mn2+, and a Nitroxide. *J. Phys. Chem. Lett.* **2017**, *8*, 5277–5282. [CrossRef]
26. Berliner, L.J.; Grunwald, J.; Hankovszky, H.; Hideg, K. A novel reversible thiol-specific spin label: Papain active site labeling and inhibition. *Anal. Biochem.* **1982**, *119*, 450–455. [CrossRef]
27. Likhtenshtein, G.I.; Yamauchi, J.; Nakatsuji, S.; Smirnov, A.I.; Tamura, R. *Nitroxides: Applications in Chemistry, Biomedicine, and Materials Science*, 1st ed.; Wiley-VCH Verlag GmbH & Co. KGaA: Weinheim, Germany, 2008; ISBN 978-3-527-31889-6.
28. Kuzhelev, A.A.; Krumkacheva, O.A.; Shevelev, G.Y.; Yulikov, M.; Fedin, M.V.; Bagryanskaya, E.G.; Shevelev, G.Y. Room-temperature distance measurements using RIDME and the orthogonal spin labels trityl/nitroxide. *Phys. Chem. Chem. Phys.* **2018**, *20*, 10224–10230. [CrossRef]

29. Azarkh, M.; Okle, O.; Eyring, P.; Dietrich, D.R.; Drescher, M. Evaluation of spin labels for in-cell EPR by analysis of nitroxide reduction in cell extract of Xenopus laevis oocytes. *J. Magn. Reson.* **2011**, *212*, 450–454. [CrossRef]
30. Lawless, M.J.; Shimshi, A.; Cunningham, T.F.; Kinde, M.N.; Tang, P.; Saxena, S. Analysis of Nitroxide-Based Distance Measurements in Cell Extracts and in Cells by Pulsed ESR Spectroscopy. *ChemPhysChem* **2017**, *18*, 1653–1660. [CrossRef]
31. Karthikeyan, G.; Bonucci, A.; Casano, G.; Gerbaud, G.; Abel, S.; Thomé, V.; Kodjabachian, L.; Magalon, A.; Guigliarelli, B.; Belle, V.; et al. A Bioresistant Nitroxide Spin Label for In-Cell EPR Spectroscopy: In Vitro and In Oocytes Protein Structural Dynamics Studies. *Angew. Chem. Int. Ed.* **2018**, *57*, 1366–1370. [CrossRef]
32. Yang, Y.; Yang, F.; Gong, Y.-J.; Bahrenberg, T.; Feintuch, A.; Su, X.-C.; Goldfarb, D. High Sensitivity In-Cell EPR Distance Measurements on Proteins Using an Optimized Gd(III) Spin Label. *J. Phys. Chem. Lett.* **2018**, *9*, 6119–6123. [CrossRef] [PubMed]
33. Jassoy, J.J.; Berndhaeuser, A.; Duthie, F.; Kuehn, S.P.; Hagelueken, G.; Schiemann, O. Versatile Trityl Spin Labels for Nanometer Distance Measurements on Biomolecules In Vitro and within Cells. *Angew. Chem. Int. Ed.* **2017**, *56*, 177–181. [CrossRef] [PubMed]
34. Jagtap, A.P.; Krstic, I.; Kunjir, N.C.; Hänsel, R.; Prisner, T.F.; Sigurdsson, S.T.H. Sterically shielded spin labels for in-cell EPR spectroscopy: Analysis of stability in reducing environment. *Free Radical Res.* **2015**, *49*, 78–85. [CrossRef] [PubMed]
35. Yang, Z.; Bridges, M.D.; López, C.J.; Rogozhnikova, O.Y.; Trukhin, D.V.; Brooks, E.K.; Tormyshev, V.; Halpern, H.J.; Hubbell, W.L. A Triarylmethyl Spin Label for Long-Range Distance Measurement at Physiological Temperatures Using T1 Relaxation Enhancement. *J. Magn. Reson.* **2016**, *269*, 50–54. [CrossRef] [PubMed]
36. Joseph, B.; Tormyshev, V.M.; Rogozhnikova, O.Y.; Akhmetzyanov, D.; Bagryanskaya, E.G.; Prisner, T.F. Selective High-Resolution Detection of Membrane Protein-Ligand Interaction in Native Membranes Using Trityl-Nitroxide PELDOR. *Angew. Chem.* **2016**, *128*, 11710–11714. [CrossRef]
37. Gmeiner, C.; Klose, D.; Mileo, E.; Belle, V.; Marque, S.R.A.; Dorn, G.; Allain, F.H.T.; Guigliarelli, B.; Jeschke, G.; Yulikov, M. Orthogonal Tyrosine and Cysteine Site-Directed Spin Labeling for Dipolar Pulse EPR Spectroscopy on Proteins. *J. Phys. Chem. Lett.* **2017**, *8*, 4852–4857. [CrossRef] [PubMed]
38. Reginsson, G.W.; Kunjir, N.C.; Sigurdsson, S.T.; Schiemann, O. Trityl Radicals: Spin Labels for Nanometer-Distance Measurements. *Chem. A Eur. J.* **2012**, *18*, 13580–13584. [CrossRef]
39. Kunjir, N.C.; Reginsson, G.W.; Schiemann, O.; Sigurdsson, S.T. Measurements of short distances between trityl spin labels with cw EPR, DQC and PELDOR. *Phys. Chem. Chem. Phys.* **2013**, *15*, 19673. [CrossRef]
40. Akhmetzyanov, D.; Schöps, P.; Kunjir, N.C.; Sigurdsson, S.T.; Marko, A.; Prisner, T.F. Pulsed EPR dipolar spectroscopy at Q- and G-band on a trityl biradical. *Phys. Chem. Chem. Phys.* **2015**, *17*, 24446–24451. [CrossRef]
41. Owenius, R.; Eaton, G.R.; Eaton, S.S. Frequency (250 MHz to 9.2 GHz) and viscosity dependence of electron spin relaxation of triarylmethyl radicals at room temperature. *J. Magn. Reson.* **2005**, *172*, 168–175. [CrossRef]
42. Kuzhelev, A.A.; Trukhin, D.V.; Krumkacheva, O.A.; Strizhakov, R.K.; Rogozhnikova, O.Y.; Troitskaya, T.I.; Fedin, M.V.; Tormyshev, V.M.; Bagryanskaya, E.G. Room—Temperature Electron Spin Relaxation of Triarylmethyl Radicals at the X- and Q-Bands. *J. Phys. Chem. B* **2015**, *119*, 13630–13640. [CrossRef] [PubMed]
43. Yang, Z.; Liu, Y.; Borbat, P.; Zweier, J.L.; Freed, J.H.; Hubbell, W.L. Pulsed ESR dipolar spectroscopy for distance measurements in immobilized spin labeled proteins in liquid solution. *J. Am. Chem. Soc.* **2012**, *134*, 9950–9952. [CrossRef] [PubMed]
44. Shevelev, G.Y.; Krumkacheva, O.A.; Lomzov, A.A.; Kuzhelev, A.A.; Rogozhnikova, O.Y.; Trukhin, D.V.; Troitskaya, T.I.; Tormyshev, V.M.; Fedin, M.V.; Pyshnyi, D.V.; et al. Physiological-Temperature Distance Measurement in Nucleic Acid using Triarylmethyl-Based Spin Labels and Pulsed Dipolar EPR Spectroscopy. *J. Am. Chem. Soc.* **2014**, *136*, 9874–9877. [CrossRef] [PubMed]
45. Krumkacheva, O.; Bagryanskaya, E. EPR-based distance measurements at ambient temperature. *J. Magn. Reson.* **2017**, *280*, 117–126. [CrossRef]
46. Andersson, S.; Rydbeck, A.; Mahno, R.S. Free Radicals. US Patent 5728370, 17 March 1998.
47. Reddy, T.J.; Iwama, T.; Halpern, H.J.; Rawal, V.H. General Synthesis of Persistent Trityl Radicals for EPR Imaging of Biological Systems. *J. Org. Chem.* **2002**, *67*, 4635–4639. [CrossRef]

48. Dhimitruka, I.; Velayutham, M.; Bobko, A.A.; Khramtsov, V.V.; Villamena, F.A.; Hadad, C.M.; Zweier, J.L. Large Scale Synthesis of a Persistent Trityl Radical for Use in Biomedical EPR Applications and Imaging. *Bioorganic Med. Chem. Lett.* **2007**, *17*, 6801–6805. [CrossRef]
49. Rogozhnikova, O.Y.; Vasiliev, V.G.; Troitskaya, T.I.; Trukhin, D.V.; Mikhalina, T.V.; Halpern, H.J.; Tormyshev, V.M. Generation of Trityl Radicals by Nucleophilic Quenching of Tris(2,3,5,6-tetrathiaaryl)methyl Cations and Practical and Convenient Large-Scale Synthesis of Persistent Tris(4-carboxy-2,3,5,6-tetrathiaaryl)methyl Radical. *Eur. J. Org. Chem.* **2013**, *2013*, 3347–3355. [CrossRef]
50. Hintz, H.; Vanas, A.; Klose, D.; Jeschke, G.; Godt, A. Trityl Radicals with a Combination of the Orthogonal Functional Groups Ethyne and Carboxyl: Synthesis without a Statistical Step and EPR Characterization. *J. Org. Chem.* **2019**, *84*, 3304–3320. [CrossRef]
51. Liu, Y.; Villamena, F.A.; Sun, J.; Xu, Y.; Dhimitruka, I.; Zweier, J.L. Synthesis and Characterization of Ester-Derivatized Tetrathiaarylmethyl Radicals as Intracellular Oxygen Probes. *J. Org. Chem.* **2008**, *73*, 1490–1497. [CrossRef]
52. Dhimitruka, I.; Bobko, A.A.; Hadad, C.M.; Zweier, J.L.; Khramtsov, V.V. Synthesis and Characterization of Amino Derivatives of Persistent Trityl Radicals as Dual Function pH and Oxygen Paramagnetic Probes. *J. Am. Chem. Soc.* **2008**, *130*, 10780–10787. [CrossRef]
53. Decroos, C.; Prangé, T.; Mansuy, D.; Boucher, J.-L.; Li, Y. Unprecedented ipso aromatic nucleophilic substitution upon oxidative decarboxylation of tris(pcarboxyltetrathiaaryl) methyl (TAM) radicals: A new access to diversely substituted TAM radicals. *Chem. Commun.* **2011**, *47*, 4805–4807. [CrossRef] [PubMed]
54. Driesschaert, B.; Marchand, V.; Leveque, P.; Gallez, B.; Marchand-Brynaert, J. A phosphonated triarylmethyl radical as a probe for measurement of pH by EPR. *Chem. Commun.* **2012**, *48*, 4049. [CrossRef] [PubMed]
55. Tormyshev, V.M.; Rogozhnikova, O.Y.; Bowman, M.K.; Trukhin, D.V.; Troitskaya, T.I.; Vasiliev, V.G.; Shundrin, L.A.; Halpern, H.J. Preparation of Diversely Substituted Triarylmethyl Radicals by the Quenching of Tris(2,3,5,6-tetrathiaaryl)methyl Cations with C-, N-, P-, and S-Nucleophiles. *Eur. J. Org. Chem.* **2014**, *2014*, 371–380. [CrossRef] [PubMed]
56. Driesschaert, B.; Bobko, A.A.; Khramtsov, V.V.; Zweier, J.L. Nitro-Triarylmethyl Radical as Dual Oxygen and Superoxide Probe. *Cell Biochem. Biophys.* **2017**, *75*, 241–246. [CrossRef] [PubMed]
57. Tan, X.; Tao, S.; Liu, W.; Rockenbauer, A.; Villamena, F.A.; Zweier, J.L.; Song, Y.; Liu, Y. Synthesis and Characterization of the Perthiatriarylmethyl Radical and Its Dendritic Derivatives with High Sensitivity and Selectivity to Superoxide Radical. *Chem. A Eur. J.* **2018**, *24*, 6958–6967. [CrossRef] [PubMed]
58. Fleck, N.; Hett, T.; Brode, J.; Meyer, A.; Richert, S.; Schiemann, O. C–C Cross Coupling of Trityl Radicals: Spin Density Delocalization, Exchange Coupling, and a Spin Label. *J. Org. Chem.* **2019**, *84*, 3293–3303. [CrossRef] [PubMed]
59. Qu, Y.; Li, Y.; Tan, X.; Zhai, W.; Han, G.; Hou, J.; Liu, G.; Song, Y.; Liu, Y. Synthesis and Characterization of Hydrophilic Trityl Radical TFO for Biomedical and Biophysical Applications. *Chem. A Eur. J.* **2019**, *25*, 7888–7895. [CrossRef] [PubMed]
60. Frank, J.; Elewa, M.; Said, M.M.; El Shihawy, H.A.; El-Sadek, M.; Muller, D.; Meister, A.; Hause, G.; Drescher, S.; Metz, H.; et al. Synthesis, Characterization, and Nanoencapsulation of Tetrathiatriarylmethyl and Tetrachlorotriarylmethyl (Trityl) Radical Derivatives—A Study To Advance Their Applicability as in Vivo EPR Oxygen Sensors. *J. Org. Chem.* **2015**, *80*, 6754–6766. [CrossRef]
61. Marchand, V.; Levêque, P.; Driesschaert, B.; Marchand-Brynaert, J.; Gallez, B.; Marchand-Brynaert, J. In vivo EPR extracellular pH-metry in tumors using a triphosphonated trityl radical. *Magn. Reson. Med.* **2016**, *77*, 2438–2443. [CrossRef]
62. Khramtsov, V.V.; Bobko, A.A.; Tseytlin, M.; Driesschaert, B. Exchange Phenomena in the Electron Paramagnetic Resonance Spectra of the Nitroxyl and Trityl Radicals: Multifunctional Spectroscopy and Imaging of Local Chemical Microenvironment. *Anal. Chem.* **2017**, *89*, 4758–4771. [CrossRef]
63. Kishimoto, S.; Krishna, M.C.; Khramtsov, V.V.; Utsumi, H.; Lurie, D.J. In Vivo Application of Proton-Electron Double-Resonance Imaging. *Antioxid. Redox Signal.* **2018**, *28*, 1345–1364. [CrossRef] [PubMed]
64. Peman, A.; Vilaseca, M.; Vitalla, F.L.; Van Doorslaer, S.; Marin-Montesinos, I.; Paniagua, J.C.; Pons, M. Paramagnetic spherical nanoparticles by the self-assembly of persistent trityl radicals. *Phys. Chem. Chem. Phys.* **2016**, *18*, 3151–3158.

65. Giannoulis, A.; Yang, Y.; Gong, Y.-J.; Tan, X.; Feintuch, A.; Carmieli, R.; Bahrenberg, T.; Liu, Y.; Su, X.-C.; Goldfarb, D. DEER distance measurements on trityl/trityl and Gd(iii)/trityl labelled proteins. *Phys. Chem. Chem. Phys.* **2019**, *21*, 10217–10227. [CrossRef] [PubMed]
66. Song, Y.; Liu, Y.; Liu, W.; Villamena, F.A.; Zweier, J.L. Characterization of the Binding of the Finland Trityl Radical with Bovine Serum Albumin. *RSC Adv.* **2014**, *4*, 47649–47656. [CrossRef] [PubMed]
67. Galyov, E.E.; Håkansson, S.; Forsberg, A.; Wolf-Watz, H. A secreted protein kinase of Yersinia pseudotuberculosis is an indispensable virulence determinant. *Nature* **1993**, *361*, 730–732. [CrossRef] [PubMed]
68. Lee, W.L.; Grimes, J.M.; Robinson, R.C. Yersinia effector YopO uses actin as bait to phosphorylate proteins that regulate actin polymerization. *Nat. Struct. Mol. Boil.* **2015**, *22*, 248–255. [CrossRef] [PubMed]
69. Tan, X.; Chen, L.; Song, Y.; Rockenbauer, A.; Villamena, F.A.; Zweier, J.L.; Liu, Y. Thiol-Dependent Reduction of the Triester and Triamide Derivatives of Finland Trityl Radical Triggers O2-Dependent Superoxide Production. *Chem. Res. Toxicol.* **2017**, *30*, 1664–1672. [CrossRef]
70. Jassoy, J.J.; Meyer, A.; Spicher, S.; Wuebben, C.; Schiemann, O. Synthesis of Nanometer Sized Bis- and Tris-trityl Model Compounds with Different Extent of Spin–Spin Coupling. *Molecules* **2018**, *23*, 682. [CrossRef]
71. Brewer, C.F.; Riehm, J.P. Evidence for possible nonspecific reactions between N-ethylmaleimide and proteins. *Anal. Biochem.* **1967**, *18*, 248–255. [CrossRef]
72. Machida, M.; Machida, M.I.; Kanaoka, Y. Hydrolysis of N-substituted maleimides: Stability of fluorescence thiol reagents in aqueous media. *Chem. Pharm. Bull.* **1977**, *25*, 2739–2743. [CrossRef]
73. Denes, F.; Pichowicz, M.; Povie, G.; Renaud, P. Thiyl Radicals in Organic Synthesis. *Chem. Rev.* **2014**, *114*, 2587–2693. [CrossRef] [PubMed]
74. Nair, D.P.; Podgórski, M.; Chatani, S.; Gong, T.; Xi, W.; Fenoli, C.R.; Bowman, C.N. ChemInform Abstract: The Thiol-Michael Addition Click Reaction: A Powerful and Widely Used Tool in Materials Chemistry. *Chem. Mater.* **2014**, *45*, 724–744. [CrossRef]
75. Hagelueken, G.; Ward, R.; Naismith, J.H.; Schiemann, O. MtsslWizard: In Silico Spin-Labeling and Generation of Distance Distributions in PyMOL. *Appl. Magn. Reson.* **2012**, *42*, 377–391. [CrossRef] [PubMed]
76. Stoll, S.; Schweiger, A. EasySpin, a comprehensive software package for spectral simulation and analysis in EPR. *J. Magn. Reson.* **2006**, *178*, 42–55. [CrossRef] [PubMed]
77. Baldwin, A.D.; Kiick, K.L. Tunable degradation of maleimide-thiol adducts in reducing environments. *Bioconjugate Chem.* **2011**, *22*, 1946–1953. [CrossRef] [PubMed]
78. Jeschke, G.; Chechik, V.; Ionita, P.; Godt, A.; Zimmermann, H.; Banham, J.; Timmel, C.R.; Hilger, D.; Jung, H. DeerAnalysis2006—A comprehensive software package for analyzing pulsed ELDOR data. *Appl. Magn. Reson.* **2006**, *30*, 473–498. [CrossRef]
79. Meyer, A.; Jassoy, J.J.; Spicher, S.; Berndhäuser, A.; Schiemann, O. Performance of PELDOR, RIDME, SIFTER, and DQC in measuring distances in trityl based bi- and triradicals: Exchange coupling, pseudosecular coupling and multi-spin effects. *Phys. Chem. Chem. Phys.* **2018**, *20*, 13858–13869. [CrossRef]
80. Borbat, P.P.; Freed, J.H. *EPR Spectroscopy: Fundamentals and Methods*; Goldfarb, D., Stoll, S., Eds.; John Wiley & Sons: Hoboken, NJ, USA, 2018; Chapter 20; pp. 425–462, ISBN 9781119162988.
81. Shevelev, G.Y.; Gulyak, E.L.; Lomzov, A.A.; Kuzhelev, A.A.; Krumkacheva, O.A.; Kupryushkin, M.S.; Tormyshev, V.M.; Fedin, M.V.; Bagryanskaya, E.G.; Pyshnyi, D.V. A Versatile Approach to Attachment of Triarylmethyl Labels to DNA for Nanoscale Structural EPR Studies at Physiological Temperatures. *J. Phys. Chem. B* **2018**, *122*, 137–143. [CrossRef]
82. Bahrenberg, T.; Yang, Y.; Goldfarb, D.; Feintuch, A. rDEER: A Modified DEER Sequence for Distance Measurements Using Shaped Pulses. *Magnetochemistry* **2019**, *5*, 20. [CrossRef]
83. Hagelueken, G.; Ingledew, W.J.; Huang, H.; Petrovic-Stojanovska, B.; Whitfield, C.; ElMkami, H.; Schiemann, O.; Naismith, J.H. PELDOR Spectroscopy Distance Fingerprinting of the Octameric Outer-Membrane Protein Wza fromEscherichia coli. *Angew. Chem.* **2009**, *121*, 2948–2950. [CrossRef]
84. Jeschke, G. Interpretation of Dipolar EPR Data in Terms of Protein Structure. *Struct. Bond.* **2014**, *152*, 83–120.
85. Abdullin, D.; Hagelueken, G.; Schiemann, O. Determination of nitroxide spin label conformations via PELDOR and X-ray crystallography. *Phys. Chem. Chem. Phys.* **2016**, *18*, 10428–10437. [CrossRef] [PubMed]

86. Peter, M.F.; Tuukkanen, A.T.; Heubach, C.A.; Selsam, A.; Duthie, F.G.; Svergun, D.I.; Schiemann, O.; Hagelueken, G. Studying Conformational Changes of the Yersinia Type-III-Secretion Effector YopO in Solution by Integrative Structural Biology. *Structure* **2019**, *27*, 1–11. [CrossRef] [PubMed]

Sample Availability: Samples of the compounds are not available from the authors.

Site Selective and Efficient Spin Labeling of Proteins with a Maleimide-Functionalized Trityl Radical for Pulsed Dipolar EPR Spectroscopy

*J. Jacques Jassoy‡, Caspar A. Heubach‡, Tobias Hett, Frédéric Bernhard, Florian R. Haege, Gregor Hagelueken, Olav Schiemann**

Institute of Physical and Theoretical Chemistry, Rheinische Friedrich-Wilhelms-University Bonn, Wegelerstr. 12, 53115 Bonn, Germany, email: schiemann@pc.uni-bonn.de, phone: +49(0)228732989, fax: +49(0)228732073

‡ These authors equally contributed to this work.

Supporting Information

Table of Contents

1. Synthesis and Characterization of 9

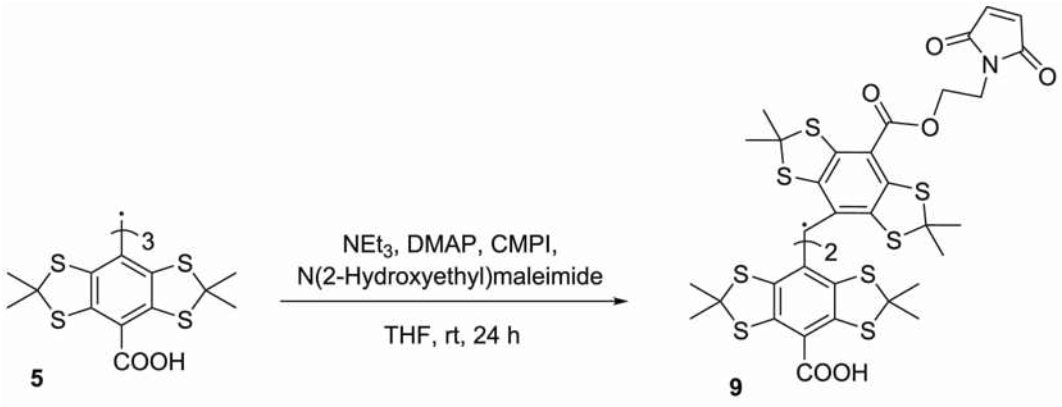

Scheme S1. Reaction leading to compound **9**. DMAP = dimethylaminopyridine, CMPI = 2-chloro-methylpyridinium iodide, THF = tetrahydrofuran.

MS (MALDI+) *m/z*: $[M]^{\bullet+}$ 1121.9 (100).

HRMS (ESI(+)) *m/z*: $[M]^{\bullet+}$ calcd for $[C_{46}H_{44}NO_8S_{12}]^{\bullet+}$: 1121.9710, found: 1121.9707.

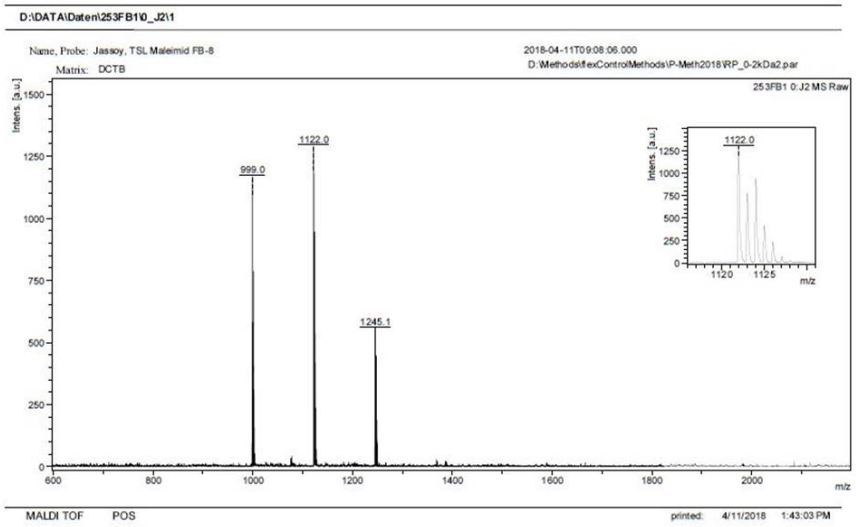

Figure S1. MALDI-(+)-MS of the crude product mixture after aqueous work-up. m/z 999.0 = Finland Trityl, m/z 1122.0 = [**9**], m/z = 1245.1 = [twofold ester product].

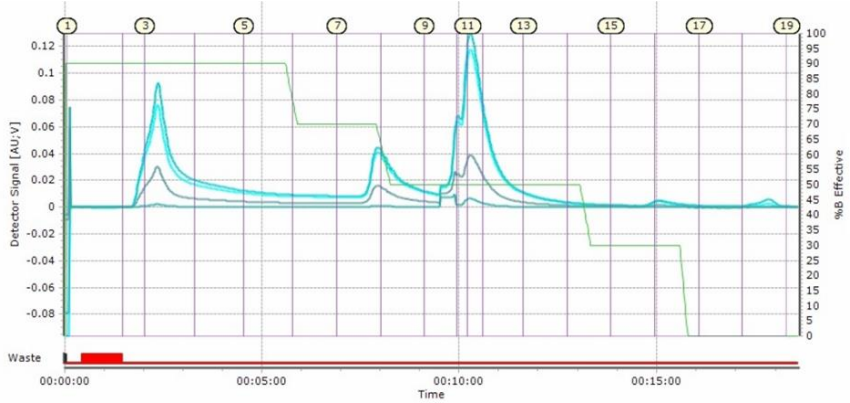

Figure S2. Elugram obtained during the reversed phase (C18) MPLC purification of the crude product mixture. A gradient of acetonitrile (10%-100%) in water was applied. Compound **9** was eluted in fractions 11 and 12.

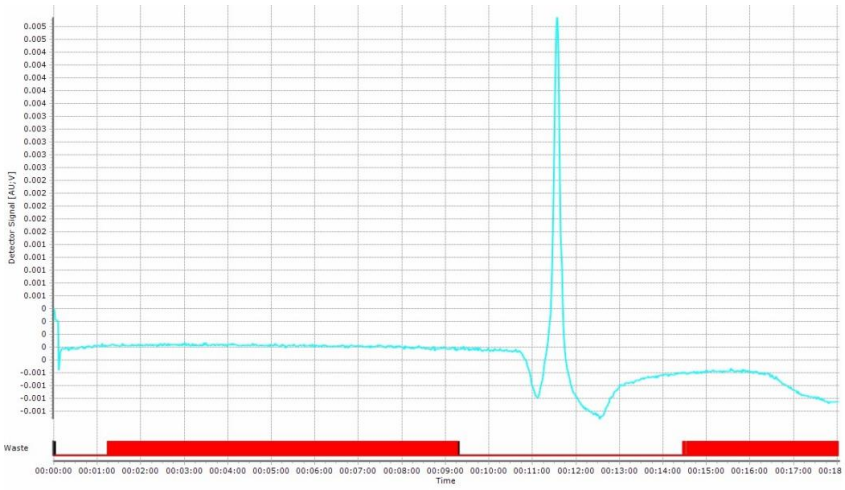

Figure S3. Reversed phase (C18) MPLC purity assessment elugram of **9**. A gradient of acetonitrile (10%-100%) in water was applied to elute a 1 mg sample of **9**.

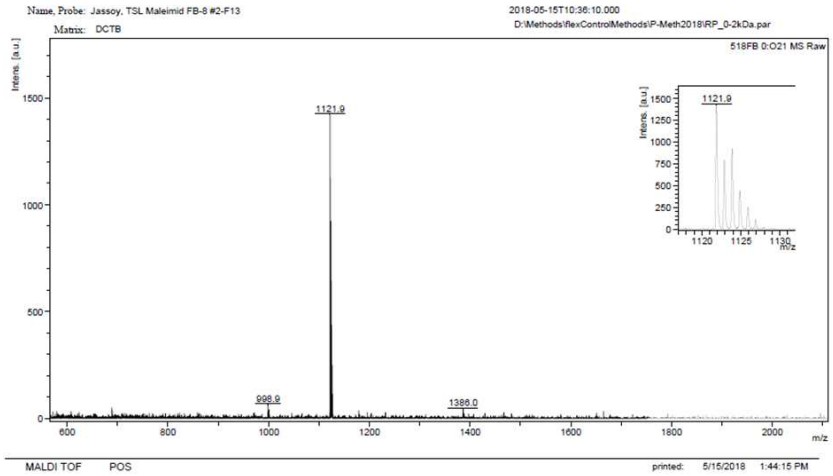

Figure S4. MALDI-(+)-MS of combined fractions 11 and 12 after MPLC purification. m/z: 999.9 (5) [Finland Trityl+H], 1121.9 (100) [**9**], 1380.0 (3) [unknown].

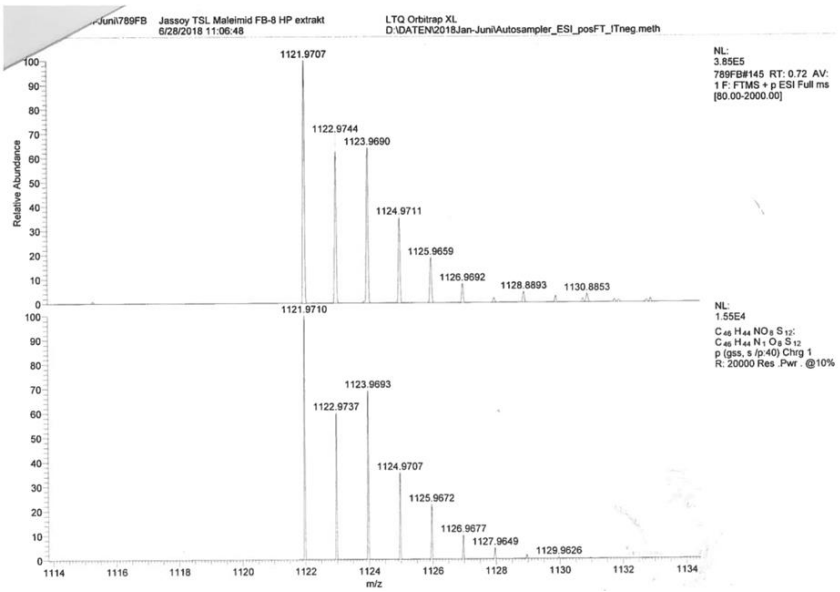

Figure S5. ESI-(+)-HRMS of **9**. Top panel: m/z = 1121.9707 found, bottom panel: m/z = 1121.9710 calculated.

256

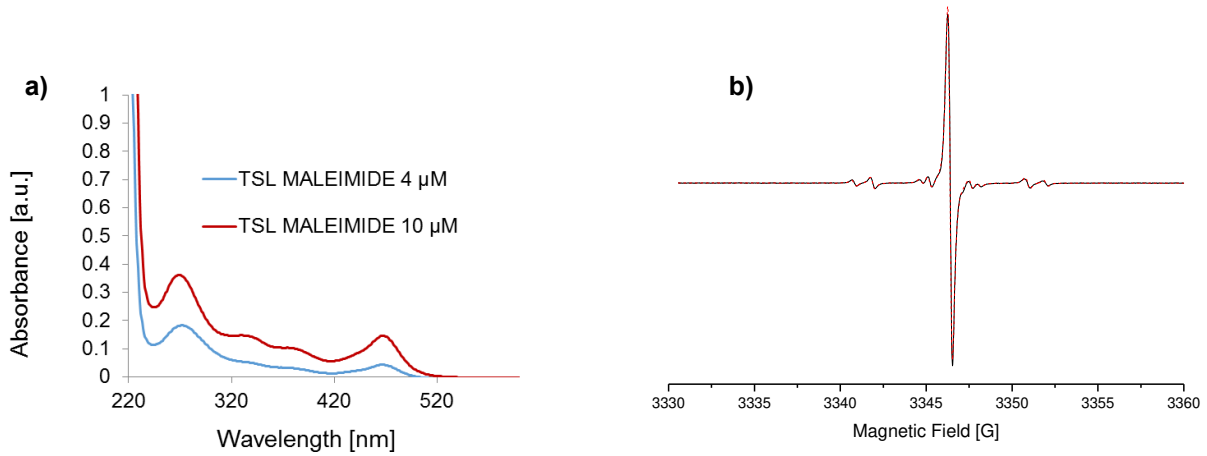

Figure S6. a) UV/Vis spectrum of **9** at 4 µM (blue) and at 10 µM (red) in TRIS buffer, pH 7.0. **b)** Room temperature *cw* EPR spectrum of **9** at 100 µM in 10 mM TES buffer (100 mM NaCl), pH 7.4 (black trace), superimposed with the corresponding EasySpin[3] simulation (red trace). EMXmicro, modulation amplitude: 0.150 G, microwave power: 2.756 mW, time constant: 20.48 ms, resolution: 67 pts/G. Simulation parameters are declared in Table S3, entry c.

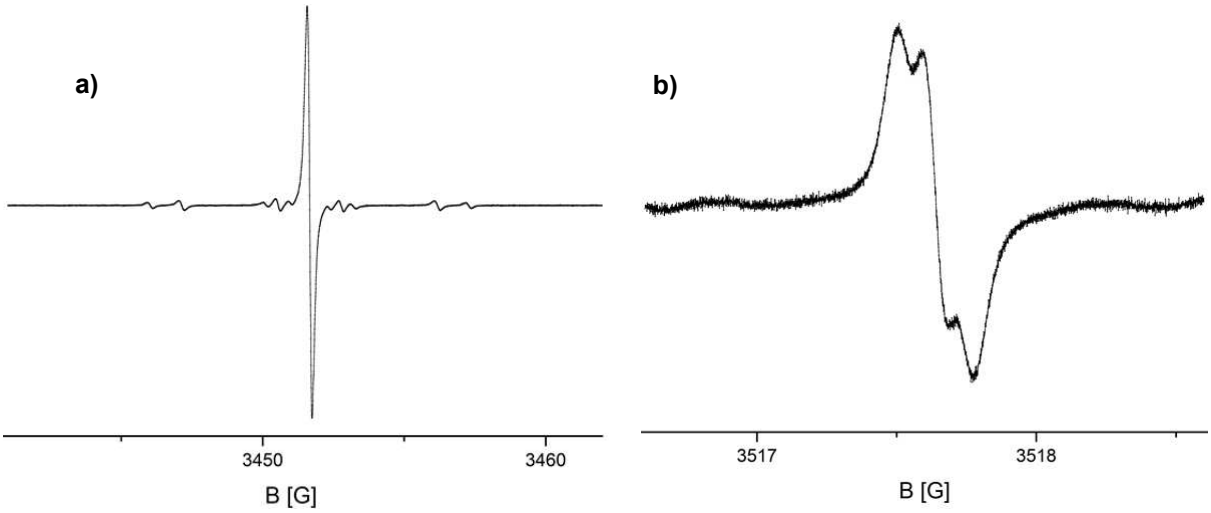

Figure S7. a) Room temperature *cw* EPR spectrum of **9** at 67 µM in degassed DMSO. EMXmicro, modulation amplitude: 0.008 G, microwave power: 794 µW, time constant: 5.12 ms, sweep time: 449.98 s, resolution: 250 pts/G, frequency: 9.637744 GHz, g-value = 1.9949637, ^{13}C coupling constants = 3.15 MHz, 12.68 MHz, 15.82 MHz. **b)** Room temperature *cw* EPR spectrum of TSL **9** at 67 µM in degassed DCM. EMXmicro, modulation amplitude: 0.030 G, microwave power: 929 µW, time constant: 10.24 ms, sweep time: 320 s, resolution: 2000 pts/G, frequency: 9.863920 GHz.

2. Analytical Data for YopO S585T9/Q603T9 and V599T9/N624T9

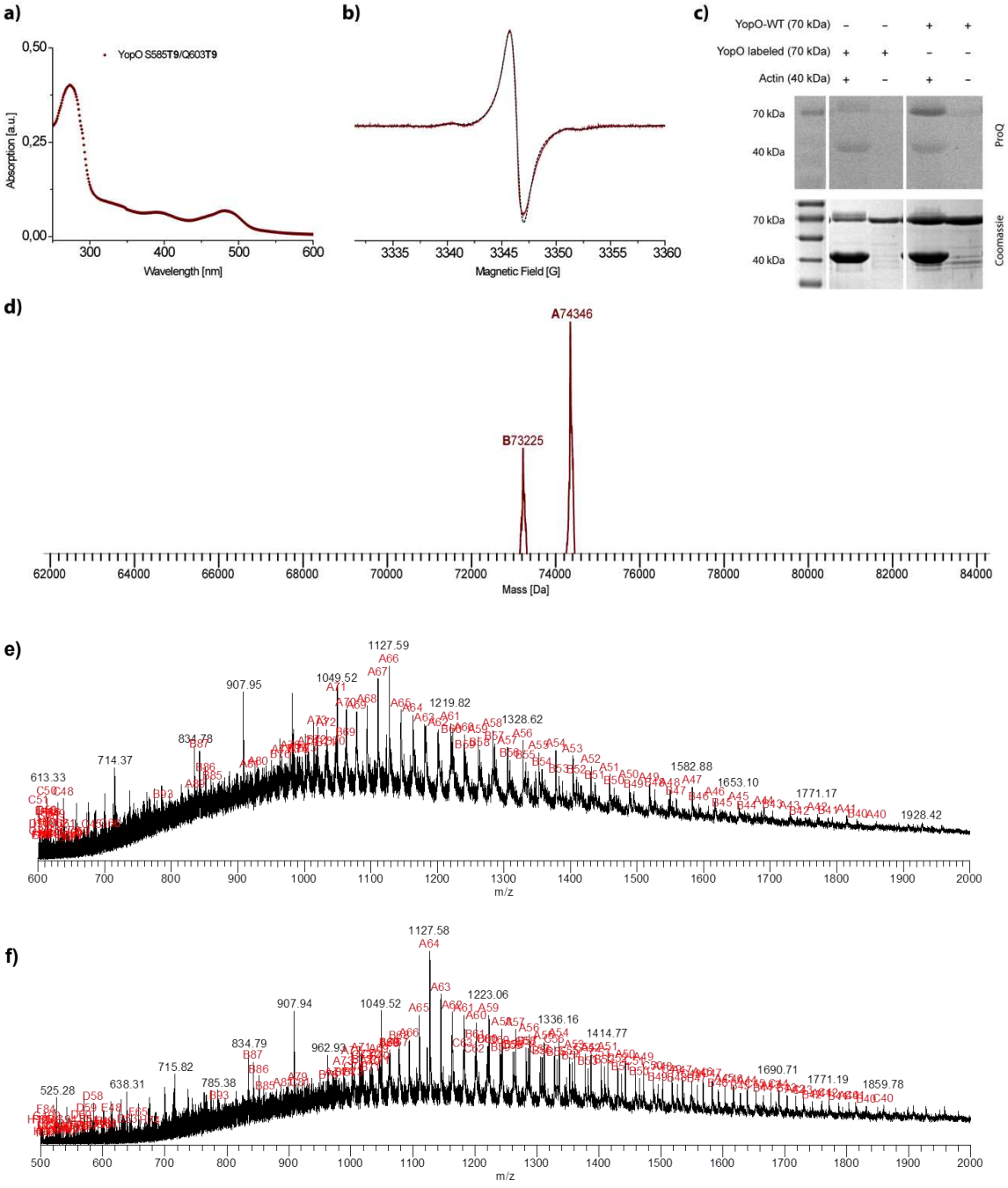

Figure S8. (a) UV/Vis absorption spectrum of YopO S585**T9**/Q603**T9**. Molar ratio of YopO to **9** yields quantitative labeling of both cysteines using equation (I) and (II) in SI section 4.2 (b) *cw* EPR spectrum recorded at an EMXmicro of YopO S585**T9**/Q603**T9** (~50 µM). Quantitative spin count via double integration against a 100 µM reference sample of free TSL **9** gave a relative spin concentration of 90 µM. A simulated spectrum is overlaid as a dashed black line. (c) Phosphorylation assay setup for YopO S585**T9**/Q603**T9** showing the catalytic activity of the protein. (d) Deconvoluted ESI(+)-MS of the sample. Doubly labeled protein calculated: 74345.6 Da, found: 74346 Da (Peak **A**); singly labeled protein calculated: 73222.6 Da, found: 73225 Da (Peak **B**). e) Raw ESI(+)-MS spectrum of YopO S585**T9**/Q603**T9**. f) Raw ESI(+)-MS spectrum of YopO V599**T9**/N624**T9** (supplement for deconvoluted ESI(+)-MS of maintext Figure 6e)**.**

258

3. Activity Assay

2 µM YopO-WT and YopO labeled with **9**, respectively, were incubated in the presence of 6 µM G-actin in phosphorylation buffer (50 mM Tris•HCl pH 8.0, 10 mM $MgCl_2$, 1 mM ATP, 2 mM $MnCl_2$) for 30 min. at 37 °C. A sample without G-actin in the incubation mixture served as a negative control. The assay was quenched by the addition of 8x SDS buffer and subsequent boiling of the sample at 95 °C for 5 min. SDS-PAGE gels were first fixed in 45% MeOH, 10% AcOH (2 times, 30 min, 100 mL), washed with MilliQ water (3 times, 10 min, 100 mL) and then stained in the dark with Pro-Q Phosphoprotein Diamond Stain (Thermo Fisher Scientific) for 90 min. Excess staining solution was removed in 20% Acetonitrile, 50 mM NaOAc pH 4.0 (3 times, 30 min, 100 mL) and gels were washed with MilliQ water (2 times, 5 min, 100 mL). Gels were imaged at a UV table using a 590 nm longpass emission filter. Subsequently, the gels were stained in Coomassie for visualization of total protein.

4. UV/Vis Quantification Methods

4.1 Dilution series

The following figures (Figure S9–S11) summarize the UV/Vis absorption of **5**, **6** and **9** at different concentrations and pH values in phosphate buffer solutions (20 mM PO_i, 50 mM NaCl).

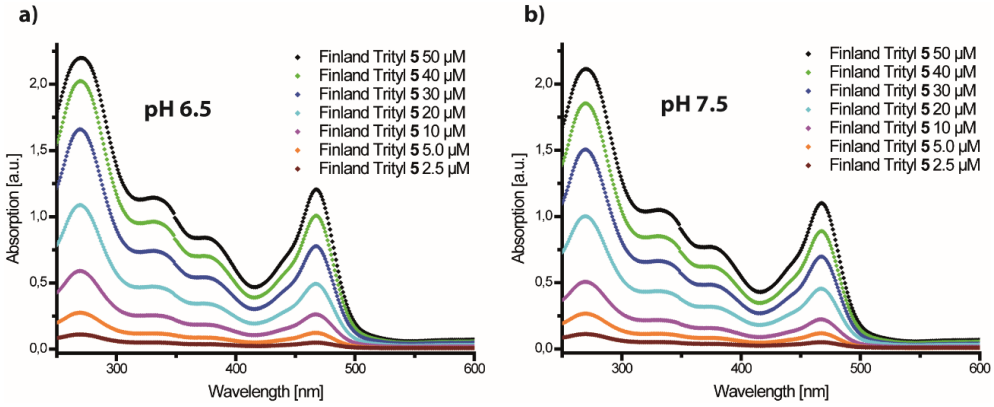

Figure S9. UV/Vis spectra of 2.5–50 µM **5** in PO_i buffer pH 6.5 (a) and pH 7.5 (b).

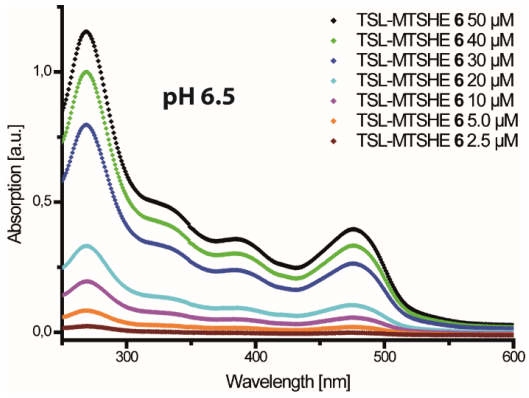

Figure S10. UV/Vis spectra of 2.5–50 µM **6** in PO_i buffer pH 6.5.

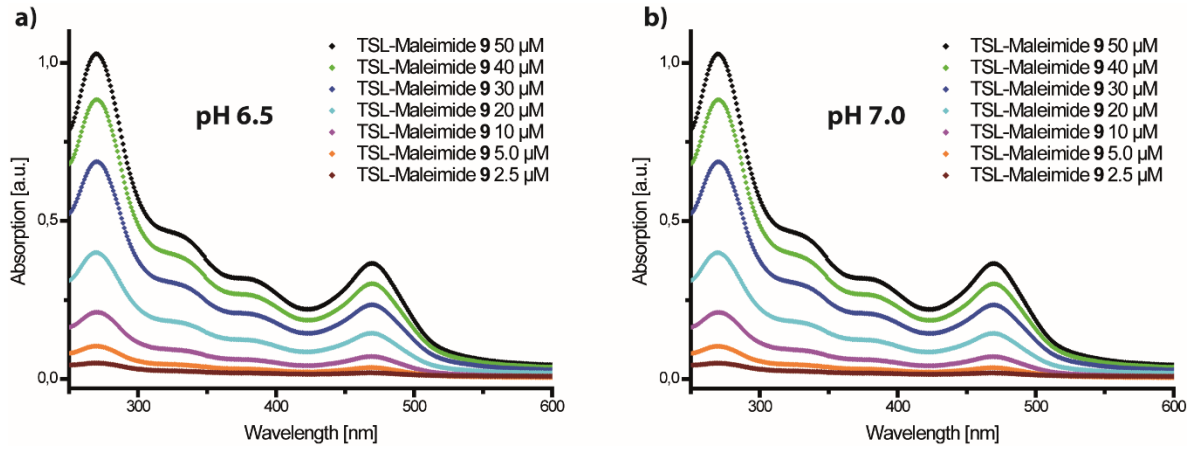

Figure S11. UV/Vis spectra of 2.5–50 µM **9** in POi buffer pH 6.5 (a) and pH 7.0 (b).

In the case of **5**, the absorbance of the trityl is slightly increased in an acidic buffer system (Figure S9a) as compared to alkaline conditions (Figure S9b). For **6**, the UV/Vis absorbance shows a strong decrease in the absorbance going from a 30 µM concentration to 20 µM (Figure S10). This may be related to the experimental findings in section 6 below. For **9**, the dilution series at pH 6.5 (Figure S11a) and pH 7.0 (Figure S11b) show no significant differences at a given concentration.

4.2 Calibration Curve for 9

For **9**, the concentration dependent absorbance at 467 nm and 280 nm is plotted in Figure S12 with the resulting linear equations displayed in Table S1.

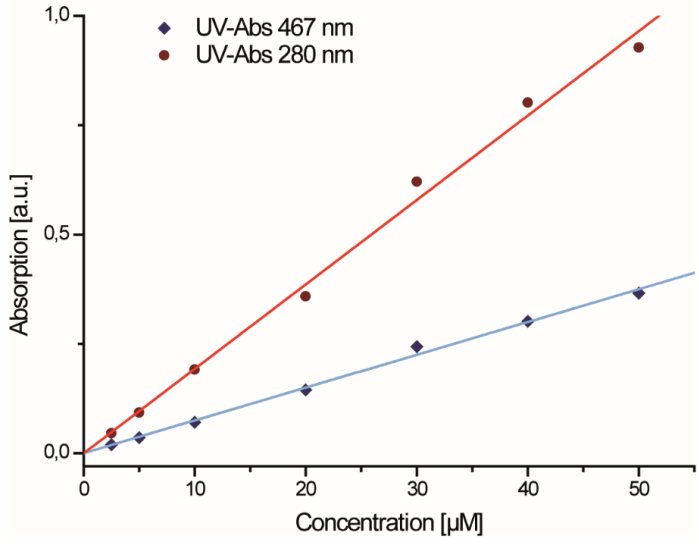

Figure S12. UV/Vis calibration curve of TSL **9** (in PO_i buffer pH 6.5) for the absorption at 467 nm and 280 nm. Linear regression parameters are summarized in Table S1.

Table S1. Linearized equations of the calibration curves shown in Figure S16.

Wavelength [nm]	Linear Equation
280	$(\mathbf{I})\ \mathrm{Abs}_{280} = 0.0193\,\frac{\mathrm{a.u.}}{\mu\mathrm{M}}\,[\mathrm{TSL}\ \mathbf{9}] - 1.725 \cdot 10^{-4}\ \mathrm{a.u.}$
467	$(\mathbf{II})\ \mathrm{Abs}_{467} = 0.0075\,\frac{\mathrm{a.u.}}{\mu\mathrm{M}}\,[\mathrm{TSL}\ \mathbf{9}] - 4.604 \cdot 10^{-4}\ \mathrm{a.u.}$

In order to evaluate the molar ratio between **9** and YopO in the labeling experiments, the absorbance peak of **9** at ~467 nm is used to determine the concentration of **9** in a labeled sample via equation (**II**). Knowing the concentration of **9**, the contribution of the label to the absorbance at ~280 nm can be estimated by means of the linear equation (**I**) and the remaining absorption is attributed to the protein fraction in the respective sample. Since a slight bathochromic shift of the local absorbance maximum at 467 nm of **9** and small spectral deviations after the labeling reactions were observed, concentrations were determined using the maximum absorbance peaks at ~467 nm and ~280 nm. For YopO, an extinction coefficient was obtained of $\varepsilon_{280} = 0.04939\,\frac{a.u.}{\mu M}$ using the web-based peptide parameter computing tool ProtParam.

4.3 Deconvolution of UV/Vis spectra

In order to evaluate the accuracy of the concentration determinations outlined above the following experiment was performed: UV/Vis spectra of an unlabeled 4.05 µM YopO solution and a 10 µM solution of **9** in labeling buffer (recorded at a Cary 100 UV-Vis) were fitted (Figure S13a) to the function

$$[\mathrm{Sample}] = (\mathrm{a} \cdot [\mathrm{YopO}] + (1 - \mathrm{a}) \cdot [\mathrm{TSL}\ \mathbf{9}]) \cdot \mathrm{b} + \mathrm{c}$$

where b denotes the scaling factor and c corresponds to an offset correction factor. These fits were then used to deconvolute the UV-vis spectra of labeled YopO mutants V599**T9**/N624**T9** (Figure S13b) and YopO S585**T9**/Q603**T9** (Figure S13c). Table S2 summarizes the quantification by both methods.

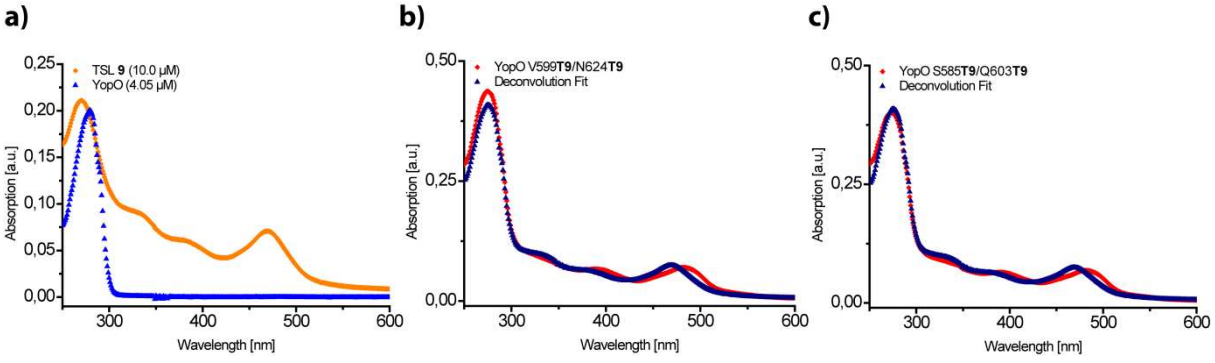

Figure S13. UV/Vis spectra of 4.05 µM YopO (blue) and 10 µM TSL **9** (red) in labeling buffer (a). Recorded UV/Vis spectra after the labeling reaction and excess label removal (marine) and the corresponding deconvolution fit (red) of YopO V599**T9**/N624**T9** (b) and YopO S585**T9**/Q603**T9** (c).

Table S2. Concentrations of YopO and **9** in the spectra of (Figure S13 b and c) determined using either the deconvolution or the maximum peak method.

Sample	Deconvolution	Maximum Peak
(a) YopO V599C/N624C	4.65 µM YopO 10.68 µM **9**	5.20 µM YopO 9.33 µM **9**
(b) YopO S585C/Q603C	3.90 µM YopO 10.94 µM **9**	4.56 µM YopO 9.13 µM **9**

Comparing the resulting concentrations of YopO and **9** using either the deconvolution or the maximum peak value method, the deconvolution method gives slightly lower concentrations of YopO and slightly higher concentrations of **9**. However, the deconvolution function is not able to correct for the bathochromic shift in the absorbance of **9**, leading to unsatisfactory fits in the region above 300 nm. Overall, both methods give sufficiently accurate results for the determination of the concentrations of YopO and **9**.

5. MS Analyses of Labeled YopO

5.1 MS Protein Sample Preparations

ESI(+)-MS: The protein solutions were desalted with an Amicon centricon by exchanging the buffer with a mixture of 0.1% formic acid and 20% acetonitrile in milliQ water. The exchange was performed adding 3x 500 µL to 50 µL of protein buffer solution. This solution was then injected into the ESI-MS instrument.

MALDI(+)-MS: The protein buffer solutions were mixed with matrix solution (2,5-dihydroxyacetophenon (DHAP) in ethanol with diammonium hydrogencitrate) and a 2% trifluoroacetic acid (TFA) solution in water. The resulting suspension was transferred to a stainless steel MALDI target and evaporated to dryness at room atmosphere conditions.

5.2 ESI(+)-MS on YopO-WT after labeling incubation with 9

In addition to UV/Vis and *cw* EPR (main text Figure 6) also the ESI(+)-MS spectra show only unlabeled YopO-WT (Figure S14).

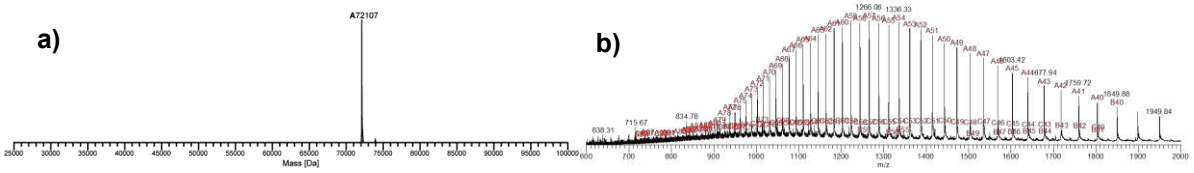

Figure S14. a) Deconvoluted ESI(+)-MS of 0-cysteine YopO-WT incubated with **9**, calculated: 72108 Da, found: 72107 Da. b) Raw ESI(+)-MS spectrum of YopO-WT incubated with **9**.

5.3 MALDI(+)-MS of YopO V599T9/N624T9 and S585T9/Q603T9

Both MALDI-MS analyses show masses of the respective non-, onefold- and twofold-labeled YopO mutants. This is inconsistent with the labeling degree distributions reported by ESI(+)-MS (Figure 6 of the main text). Also, *cw* EPR and UV/Vis report a high labeling efficiency, which is not reflected in these MS results. However, the MALDI as well as the ESI sample preparation required acidic conditions (2% trifluoroacetic acid for MALDI and 0.1% formic acid for ESI(+)), which promote partial label detachment via retro-Michael reactions before and during the MS measurements. Several attempts to skip the acidic sample preparation failed.

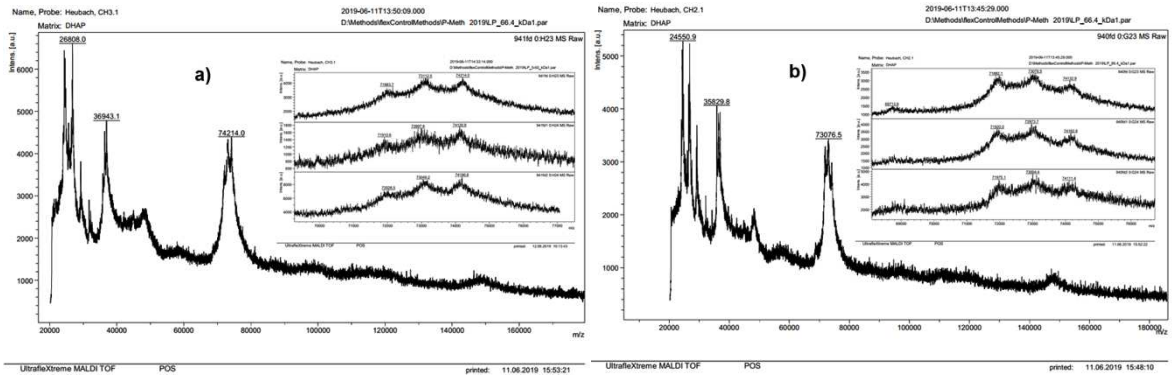

Figure S15. MALDI-MS of YopO V599**T9**/N624**T9** (a) and of YopO S585**T9**/Q603**T9** (b).

6. Dimer Formation of 6 and Cleavage

Two separated 25 µM solutions of **6** and **9** in labeling buffer (20 mM PO_i pH 6.8, 50 mM NaCl) were incubated for 16 h at 4 °C under the exclusion of light. The solutions were spun down to a final volume of 300 µL using VivaSpin 2/10k MWCO. From each solution a part was transferred into a 10 µL glass capillary and *cw* EPR spectra were recorded using a Bruker EMXnano spectrometer (Figure S16). Then the sample of **6** was irradiated with UV light (Figure S17).

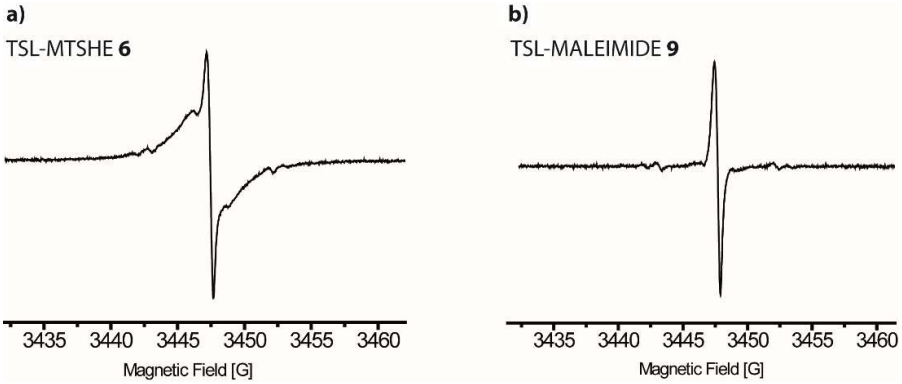

Figure S16. *cw* EPR spectrum of **6** (a) and **9** (b) after incubation of the trityls in PO_i buffer pH 6.8 for 16 h at 4 °C and subsequent centrifugation by means of a Vivaspin 2/10k MWCO centricon.

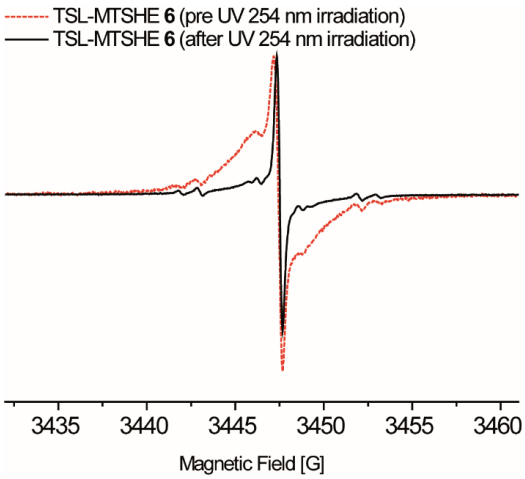

Figure S17. *cw* EPR spectra of **6** prior to (red, dashed) and after (black, solid) irradiation with UV light of 254 nm for 10 min.

The determined ratio of the double integrals before and after UV irradiation (Figure S17) is 1 **:** 0.92. Taking the error of the method into account (20%), this means that the number of spins does not change upon UV irradiation, which further supports the hypothesis of disulfide bridging between two molecules of **6** in prolonged incubations. In contrast to the case of **6**, the *cw* EPR of **9** does not display a similar line shape broadening (Figure S16b) after incubation, indicating that **9** remains unchanged under the labeling conditions.

7. MTSSL Labeling of YopO

For the MTSSL references, YopO V599C/N624C and YopO S585C/Q603C were incubated in 3 mM DTT for 30 min at room temperature. After reducing agent removal via PD10 size exclusion chromatography, the protein containing fraction was incubated with a 10-fold molar excess of MTSSL per cysteine in MTSSL labeling buffer (50 mM Tris•HCl pH 8.0, 50 mM NaCl) for 16 h at 4 °C. The excess free spin label was removed using a centrifugal concentrator (Vivaspin 2/10k MWCO).

8. EPR Measurements

8.1 Spin Count

The room temperature *cw* EPR spectra of both YopO mutants were used to derive the labeling efficiency in reference to the free TSL **9** buffer solution of known concentration (100 µM) (Figure S18).

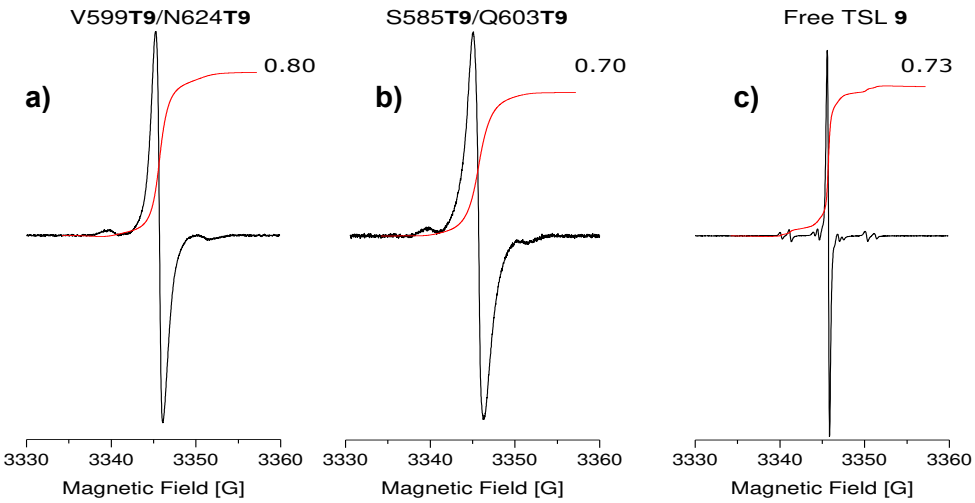

Figure S18. Room temperature *cw* EPR spectra obtained from YopO mutants (a) V599**T9**/N264**T9** (109% labeling efficiency) and (b) S585**T9**/Q603**T9** (95% labeling efficiency). The spin concentrations of the protein samples were determined in reference to the 100 µM **TSL 9** solution in buffer (c).

8.2 Simulation of cw EPR Spectra

The cw EPR spectra of YopO V599**T9**/N624**T9** (Table S3, entry a; Figure 6 in the main text) and S585**T9**/Q603**T9** (Table S3, entry b; Figure S8b) were simulated using the "chili" routine of EasySpin[1] taking into account g-anisotropy and a rotational correlation time τ. The hyperfine coupling tensor was assumed to be isotropic. The spectrum of free label **9** (Table S3, entry c; Figure S6b) was simulated using the "garlic" routine of EasySpin.[1] All simulation parameters are summarized in Table S3. The range of the fitted values is in accordance with the literature.[2,3] Assignments of hyperfine coupling constants to explicit ^{13}C nuclei in the case of **9** was done according to Bowman *et al*.[3]

Table S3. EasySpin simulation parameters.

Sample	Simulation Parameter
(a) YopO V599C/N624C	g = (2.0041, 2.0043, 2.0015) A = 30.8 MHz LWPP = (0, 0.035) mT τ = 15 ns
(b) YopO S585C/Q603C	g = (2.0036, 2.0058, 2.0005) A = 31.1 MHz LWPP = (0, 0.031) mT $\tau \approx 11$ ns
(c) free TSL 9	g = 2.0034 $A_{1Phenyl}$ = 31.3 MHz $A_{2,6Phenyl}$ = 25.3 MHz $A_{3,5Phenyl}$ = 6.8 MHz $A_{4Phenyl}$ = 9.4 MHz LWPP = (0.017, 0.018) mT

8.3 Relaxation Time Measurements

Relaxation times T_1 and T_m were measured with the Inversion Recovery (IR) pulse sequence (Figure S19a) and via a two-pulse Electron Spin Echo Envelope Modulation (2pESEEM) experiment (Figure S19b). The pulse sequences were applied at the maximum of the field sweep spectrum and the temperature was set to 50 K, 60 K, 70 K and 80 K. Both IR and 2pESEEM experiments included phase cycling, two steps for 2pESEEM and four steps for IR.[4] All parameters of the IR and 2PESEEM pulse sequences are given in Table S4.

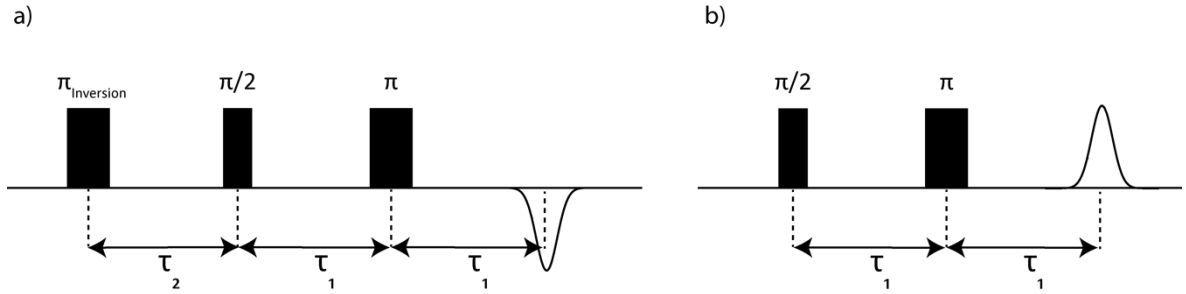

Figure S19. a) Inversion Recovery (IR) for T_1 measurements and b) two-Pulse ESEEM (2pESEEM) for T_m measurements.

Table S4. Pulse sequence parameters for the relaxation experiments.

Inversion Recovery		Two-Pulse ESEEM	
Variable	**Value**	**Variable**	**Value**
π/2	12 ns	π/2	12 ns
π	12 ns	π	24 ns
$\pi_{Inversion}$	22–24 ns	–	–
τ_1	300 ns	τ_1	200 ns
τ_2	400 ns	–	–
τ_2 increment	100 µs	τ_1 increment	8 ns
Shots per Point	10	Shots per Point	10
Shot Repetition Time	50 ms	Shot Repetition Time	40 ms

The T_1 relaxation times were extracted by multiplying the recorded IR curves by –1 and fitting a single exponential decay ($y = a \cdot \exp(-x/T_1) + c$).[12] The T_m relaxation times were obtained by fitting a stretched exponential decay ($y = a \cdot \exp((-x/T_m)^c) + d$) to the echo decay curves acquired by the 2pESEEM experiment.[4] The traces recorded from double mutant YopO V599**T9**/N624**T9** are displayed in Figure S20 and the fit values for T_1 and T_m are summarized in Table S5.

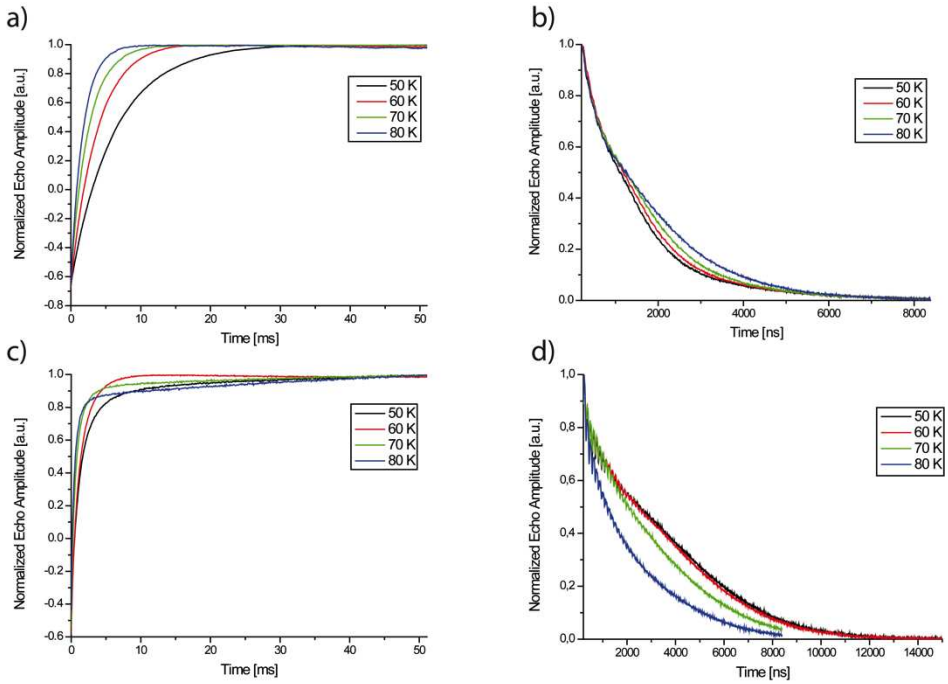

Figure S20. Inversion Recovery traces (a,c) and Two-Pulse ESEEM traces (b,d) recorded on V599**T9**/N624**T9** (a,b) and V599**R1**/N624**R1** (c,d) at different temperatures.

Table S5. Relaxation times of V599**T9**/N624**T9** and V599**R1**/N624**R1** at different temperatures.

	*V599**T9**/N624**T9***		*V599**R1**/N624**R1***	
T [K]	**T_1 [ms]**	**T_m [µs]**	**T_1 [ms]**	**T_m [µs]**
50	6.3	1.3	1.9	4.6
60	3.6	1.4	1.4	4.4
70	2.5	1.6	0.9	4.6
80	1.7	1.6	0.7	1.5

9. PDS Measurements

9.1 DQC

The six-pulse DQC sequence (Figure S21) was applied at the magnetic field position which yielded the maximal intensity in the field-swept EPR spectrum. The phase of the microwave radiation was adjusted such that the intensity of the DQC echo was maximal in the real channel. Pulse lengths and interpulse delays are given in Table S6. The shot repetition time (SRT) was set to 15.3 ms.[5] A 64–step phase cycle was applied to remove undesired echoes and thus extract the pure double quantum coherence pathway contributions.[6,7] In order to remove deuterium ESEEM from the dipolar traces, a modulation averaging procedure was applied (τ_1 and τ_2 in 8 steps of 16 ns).[2]

Table S6. Pulse sequence settings for DQC.

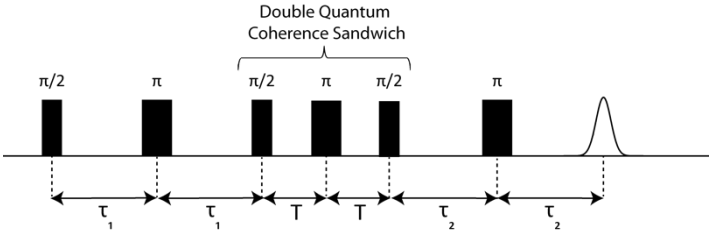

Figure S21. Schematic representation of the DQC pulse sequence. The employed sequence was adapted from literature procedures.[6]

Variable	Value
$(\pi/2)_x$	12 ns
$(\pi/2)_y$	12 ns
π	24 ns
τ_1	250 ns
τ_2	4500 ns
T	50 ns
Shots per Point	3
Shot Repetition Time	15.3 ms

9.2 SIFTER

The SIFTER sequence (Figure S22) in conjunction with a 16-step phase cycle[8] was applied at the magnetic field position yielding the highest signal amplitude in the field sweep spectra. Modulation averaging (τ_1 and τ_2 in 8 steps of 16 ns) was applied to remove deuterium ESEEM from the time traces. All pulse lengths, interpulse delay times and further parameters are given in Table S7.

Table S7. Pulse sequence settings for SIFTER.

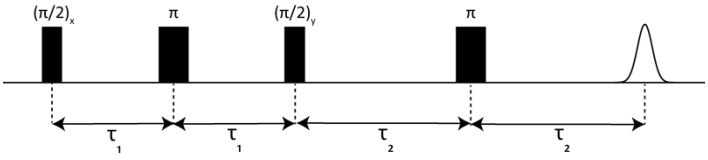

Figure S22. Schematic representation of the SIFTER pulse sequence. The employed sequence was adapted from literature procedures.[9]

Variable	Value
$(\pi/2)_x$	12 ns
$(\pi/2)_y$	12 ns
π	24 ns
τ_1	300 ns
τ_2	4500 ns
Shots per Point	3
Shot Repetition Time	15.3 ms

9.3 PELDOR

For the PELDOR experiment (Figure S23)[9] on **9** the settings in Table S8 were used. The length of the pump pulse $(\pi)_B$ was determined by a transient nutation experiment. The pump pulse $(\pi)_B$ was set to the maximum of the field sweep spectrum and the observer pulses were applied at a frequency offset of –15 MHz relative to the pump frequency. Regarding the suppression of deuterium ESEEM, an 8-step modulation averaging procedure was applied with a time increment of 16 ns. Additionally, a two-step phase cycle was used in order to remove undesired echoes and to correct for receiver baseline offsets.

Table S8. Pulse sequence settings for PELDOR.

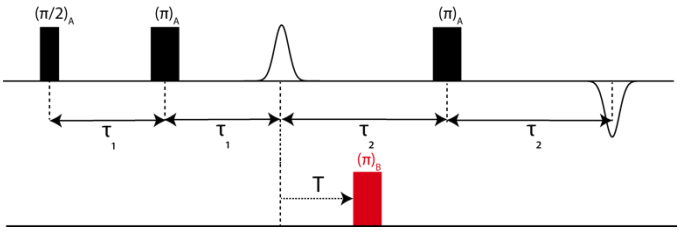

Figure S23. PELDOR pulse sequence.

Variable	Value
$(\pi/2)_A$	32 ns
$(\pi)_A$	64 ns
$(\pi)_B$	64 ns
τ_1	260 ns
τ_2	4500 ns
Shots per Point	3
Shot repetition time	15.3 ms

For the PELDOR experiment on **R1**-labeled YopO, the pump pulse was applied at the magnetic field position, which yields the maximal signal amplitude. The detection sequence was applied at a frequency offset of –100 MHz with respect to the pump frequency. The other parameters were set as given in Table S9. The optimal length of the $(\pi)_B$ pump pulse was determined by a transient nutation experiment. As mentioned above, a modulation averaging procedure and a two-step phase cycle was used to average out deuterium ESEEM and to remove unwanted echoes as well as baseline offsets.

Table S9. Pulse sequence settings for PELDOR on **R1**.

Variable	Value
$(\pi/2)_A$	12 ns
$(\pi)_A$	24 ns
$(\pi)_B$	16 ns
τ_1	300 ns
τ_2	4500 ns
Shots per Point	3
Shot Repetition Time	3.06 ms

9.4 Original PDS Time Traces, Background Removal and Validation

All PDS data was analyzed using the DeerAnalysis 2018 package for MATLAB.[10] In PDS, the resulting time trace is a convolution of the wanted dipolar interaction between the pair of spin labels within one protein molecule (intramolecular) and a background contribution between spins located on different macromolecules (intermolecular). The intramolecular dipolar interaction can be extracted by different procedures depending on the respective experiment: for PELDOR spectroscopy, the background is usually fitted directly to the time trace assuming a three-dimensional distribution of background nano-objects.[11,12] For the single-frequency experiments DQC and SIFTER, however, such an analytical treatment of the background is not applicable.[12,13] In this case, experimental background data obtained by performing DQC/SIFTER measurements on labeled single cysteine mutants have been used.[14-16] Then, an 8th order polynomial was fit to the thus obtained time traces (Figure S24) quantifying the experimental background. The DQC and SIFTER time traces were then

divided by these fits.[14-16] Figure S25-S26 display the datasets for PELDOR, DQC and SIFTER with background correction and validation for V599**T9**/N524**T9** and S585**T9**/Q603**T9**.

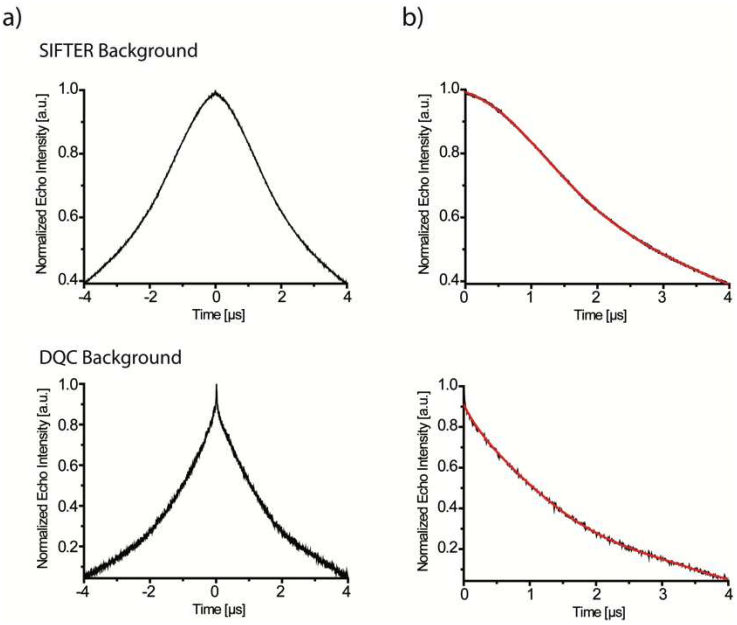

Figure S24. DQC and SIFTER time traces obtained from a YopO L113**T9** single mutant used for background correction. Subfigures (a) show the background traces prior to mirroring. In subfigure (b), the traces are mirrored at the zero-time origin and the red line indicates a polynomial fit of 8th order.

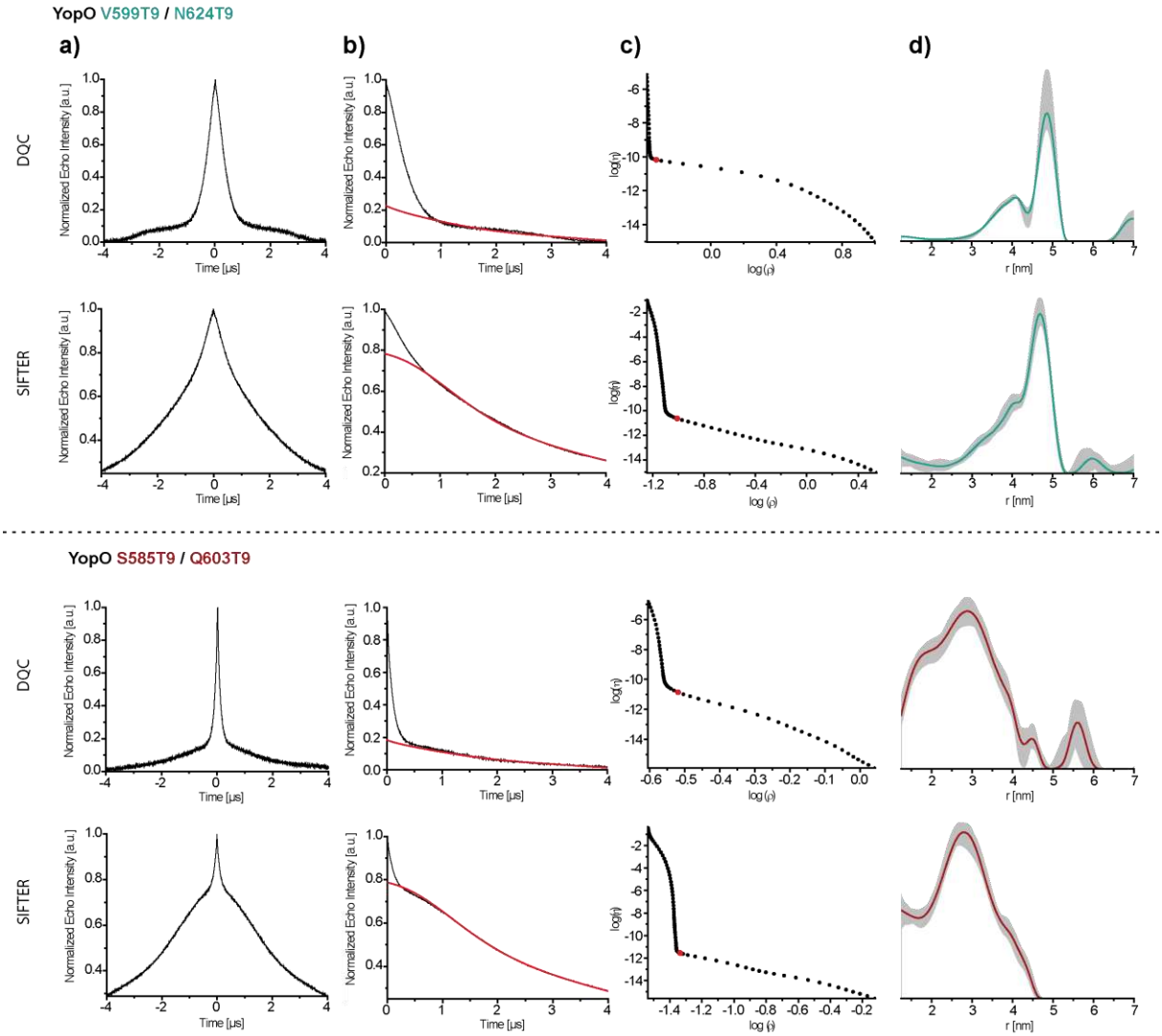

Figure S25. DQC and SIFTER time traces obtained from the YopO double mutants V599**T9**/N624**T9** and S585**T9**/Q603**T9**. Raw dipolar traces are shown prior to (a) and after (b) mirroring at the zero-time origin. The red line in panels (b) represents the experimental background fit obtained from the single cysteine mutant. Panels (c) show the L-curves generated by DeerAnalysis where the red dot marks the regularization parameter automatically chosen by DeerAnalysis for computing the distance distributions shown in panels (d).

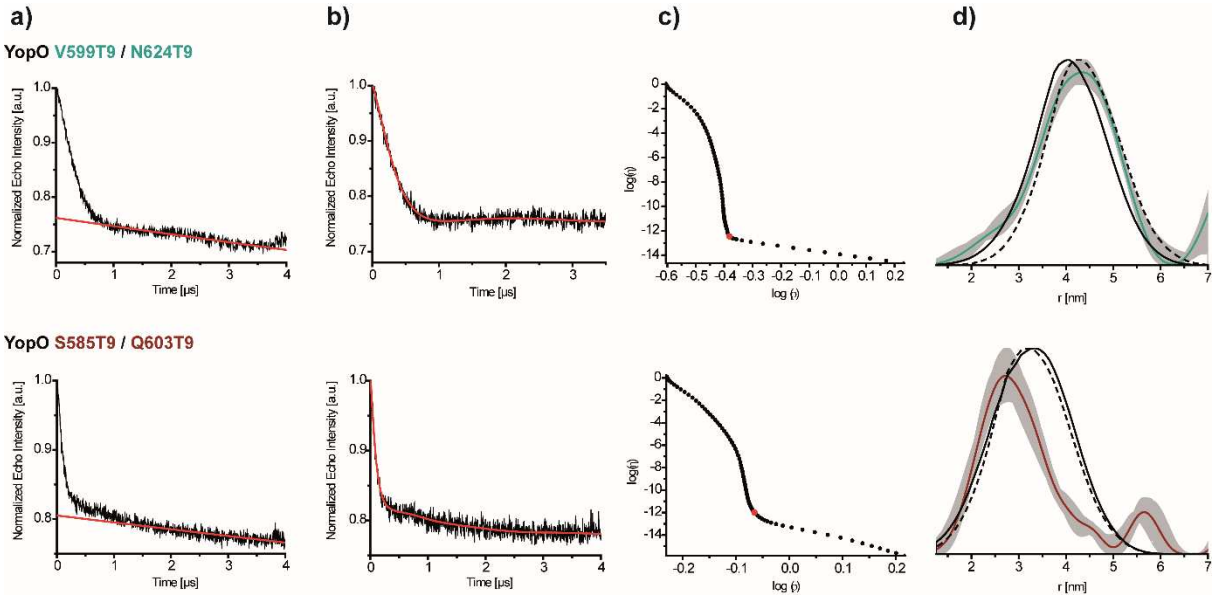

Figure S26. PELDOR time traces obtained from YopO double mutants V599**T9**/N624**T9** and S585**T9**/Q603**T9**. Panels (a) show the experimental time traces with a red line indicating the background fit assuming a three-dimensional homogeneous distribution of background objects. Column (b) displays the background-corrected dipolar traces with red lines indicating a fit used to compute distance distributions. Panel (c) shows the L-curves and the optimal regularization parameters determined by the L-curve criterion (c) which are used to compute the distance distributions shown in (d). The grey shaded areas in subfigures (d) indicate the uncertainty of the distance distributions as obtained by the Validation tool of DeerAnalysis and the black dashed and solid lines show the mtsslWizard predictions obtained from the PDB structures 4ci6 (dashed) and 2h7o (solid).

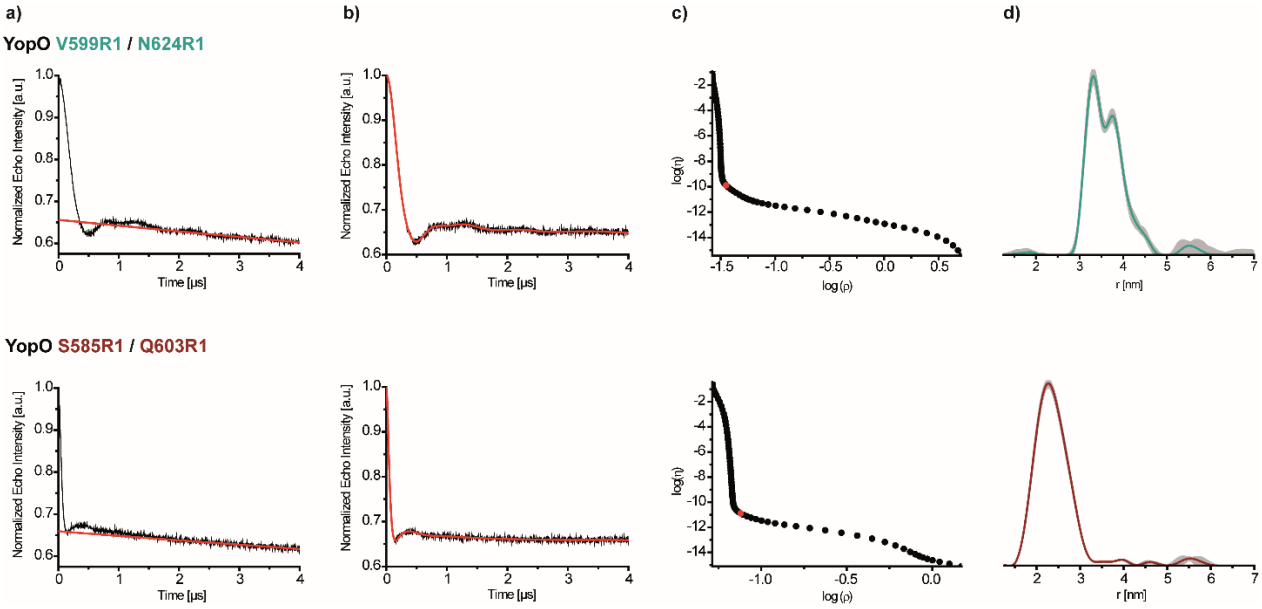

Figure S27. PELDOR data of YopO V599**R1**/N624**R1** (top) and S585**R1**/Q603**R1** (bottom). (a) Raw dipolar traces (black) and background fits (red). (b) Background-corrected time traces. (c) L-curves and the regularization parameter chosen for computing the distance distributions marked in red. (d) Distance distributions obtained by Tikhonov regularization.

9.5 Signal to Noise Ratio (SNR) determination

The quality of the recorded dipolar traces can be estimated by the signal-to-noise ratio (SNR) defined as

$$SNR = \frac{\lambda}{\sigma_N} \cdot \frac{1}{\sqrt{t}}$$

where λ is the modulation depth of the dipolar trace, t is the acquisition time of the respective experiment, and σ_N is the standard deviation of the noise of the trace. In order to deconvolve the noise from the wanted signal, the signal has been approximated by a polynomial fit (polynomial of second to 5th order). Subtracting this fit from the measured traces yields the pure noise contributions. The SNR has been calculated from the raw data prior to background-correction using the software SnrCalculator.[17] The thus obtained SNR values of all dipolar traces shown either in the main text or the supporting information are compiled in Table S10.

Table S10. Signal-to-Noise ratios obtained via different PDS measurements on trityl and nitroxide-labeled YopO double mutants.

	V599**Label**/N624**Label**	S585**Label**/Q603**Label**
DQC (**T9**)	8.9 $min^{-1/2}$	7.0 $min^{-1/2}$
SIFTER (**T9**)	5.8 $min^{-1/2}$	5.9 $min^{-1/2}$
PELDOR (**T9**)	1.4 $min^{-1/2}$	1.1 $min^{-1/2}$
PELDOR (**R1**)	9.9 $min^{-1/2}$	7.3 $min^{-1/2}$

10. Protein Work

10.1 Mutagenesis

Truncated $YopO_{89-729}$ C219A (YopO-WT) from *Yersinia enterocolitica* was cloned in frame into a pGex6p1 vector (GE) and amplified in *E. coli* DH5α cells. YopO V599C/N624C and YopO S585C/Q603C were constructed starting from YopO-WT by *QuickChange* mutagenesis[18] and subsequently transformed in *E. coli* DH5α cells. The employed primer pairs are declared in Table S11.

Table S11. Quick change mutagenesis primer pairs.

	Sequence
C219A *fwd*	5‘-GTGCTTCTGACACACTAAGAAGCCTCGCCGATAG-3‘
C219A *rev*	5‘-AGTGTGTCAGAAGCACGCCAACCATCCACCTC-3‘
V599C *fwd*	5‘-GCTTCCTGAATCGATTAGCTGAGGCTAAGTGCACCTTG-3‘
V599C *rev*	5‘-GGAGAGTATTCAATTGCTGCGACAAGGTGCACTTAGCC-3‘
N624C *fwd*	5‘-GAGAGTGCGAAAGCGCAACTATCTATTCTGATTTGTCGTTCAG-3‘
N624C *rev*	5‘-GAGCAACATCAGCCCAAGAACCTGAACGACAAATCAGAATAG-3‘
S585C *fwd*	5‘-CACAGCAAGGGCAGCCCGTGTCCTGTGAAACCT-3‘
S585C *rev*	5‘-CTAATCGATTCAGGAAGCTGTAGGTTTCACAGGACACG-3‘
Q603C *fwd*	5‘-CGATTAGCTGAGGCTAAGGTCACCTTGTCGTGTCAATTG-3‘
Q603C *rev*	5‘-CTGCTGCTGCTGGAGAGTATTCAATTGACACGACAAGG-3‘

After plasmid amplification, the mutagenesis was confirmed via Sanger sequencing (Figure S28).

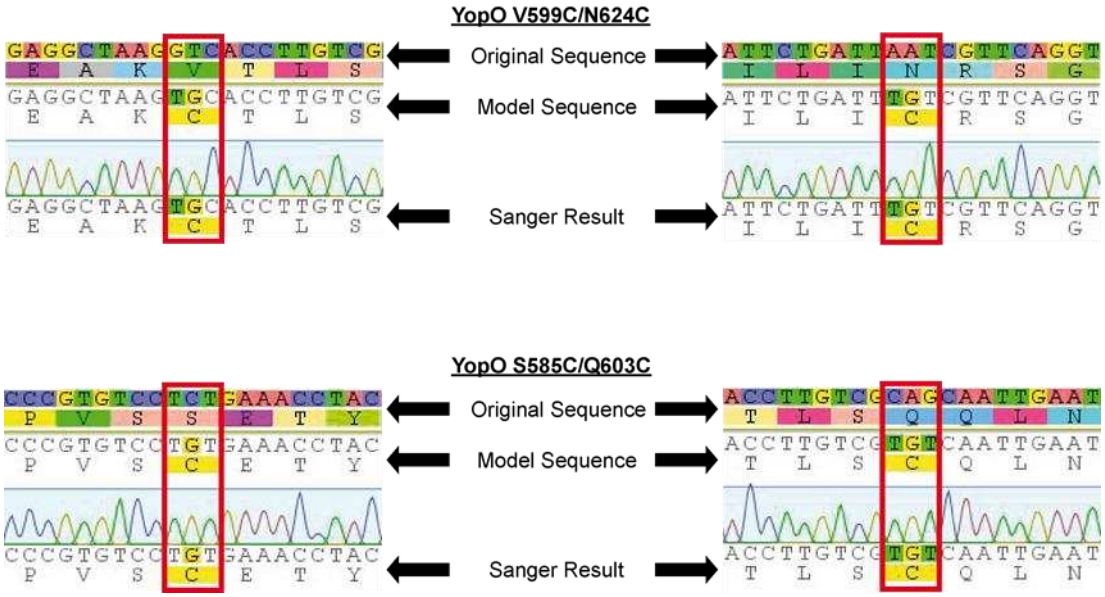

Figure S28. Sequencing results of YopO V509C/N624C and YopO S585C/Q603C.

10.2 Expression and Purification

All YopO constructs were expressed in *E. coli* Rosetta (DE3) cells. The cells were cultured in LB medium containing 0.3 mM ampicillin and 0.1 mM chloramphenicol for selection purposes. Cell cultures were incubated at 37 °C until an OD_{600} of ~0.8-1.0 was reached. Protein expression was induced with 0.1 mM IPTG (isopropyl β-D-1-thiogalactopyranoside), the culture was further incubated for ~16 h at 16 °C and then, the pellet was harvested after separation by centrifugation (4000 rcf, 20 min, 4 °C).

The cell pellet was re-suspended in five-times w/v lysis buffer (50 mM Tris•HCl pH 8.0, 150 mM NaCl and 3 mM DTT) and lysed twice at 30 kpsi in a cell disruptor (Constant Systems Limited) The lysate was spun down to remove insoluble cell debris (48,500 rcf, 20 min, 4 °C) and the supernatant was incubated with GST sepharose (GE) beads which were then equilibrated with lysis buffer for 1 h at room temperature under slight agitation. The GST-suspension was filled into a gravity column and the flowthrough was run over the column an additional time to increase the total protein yield. The beads were washed with 50 mL lysis buffer and the protein elution from the GST beads took place overnight in 20 mL elution buffer (50 mM Tris•HCl pH 8.0, 150 mM NaCl, 1 mM DTT, 1mM EDTA, 100 U PreScission protease) at 4 °C stimulated by gentle shaking. The flowthrough was diluted with 150 mL no-salt buffer (50 mM Tris•HCl pH 8.0) and 220 µL of a 2 M DTT stock were added. An ion-exchange chromatography against a linear gradient of high-salt buffer (50 mM Tris•HCl pH 8.0, 1 M NaCl) was performed using an EnrichQ 10/100 column (Bio-Rad) and the fractions containing pure YopO (based on SDS-PAGE and subsequent Coomassie stain) were pooled and concentrated below 3 mL using a centrifugal concentrator. The sample was further purified via size-exclusion chromatography in gel filtration buffer (50 mM Tris•HCl pH 8.0, 50 mM NaCl) on a HiLoad Superdex 200 16/600 (GE Healthcare), the fractions containing the target protein (Figure S29) were pooled and concentrated to ~100 µM YopO. The samples were flash frozen and stored in 50 µL aliquots at -80 °C. From 1 L cell culture, ~ 1.4 mg protein were obtained.

YopO-WT

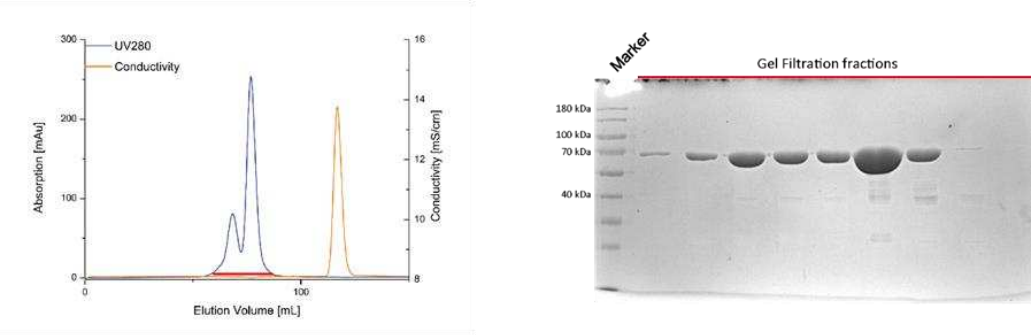

YopO-V599C/N624C

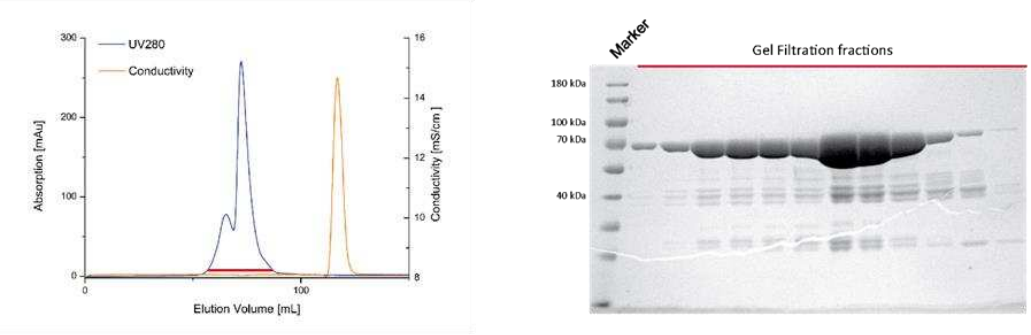

YopO-S585C/Q603C

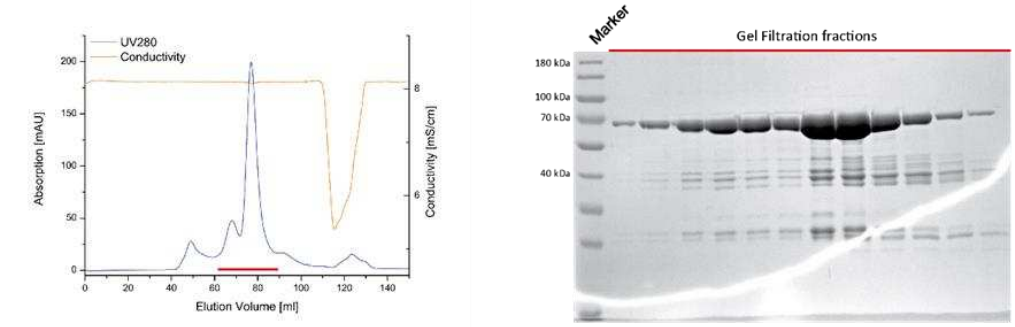

Figure S29. Chromatograms of the final HiLoad Superdex 16/600 200pg runs for all YopO constructs used (left). SDS-PAGE gels of the marked (red) elution fractions (right).

11. References

[1] Stoll, S., Schweiger, A. (2006), J. Magn. Reson. 178, 42–55.

[2] Akhmetzyanov, D., Schöps, P., Marko, A., Kunjir, N. C., Sigurdsson, S. Th., Prisner, T. F. (2015), Phys. Chem. Chem. Phys. 17, 24446–24451.

[3] Bowman, M. K. Mailer, C., Halpern, H. J. (2005), J. Magn. Reson. 172, 254–267.

[4] Weber, R. T. (2005) ELEXSYS E580 Pulse EPR Spectrometer User's Manual, Chapter 6, Bruker BioSpin Corporation, USA.

[5] Stoll, S. (2018) EPR Spectroscopy: Fundamentals and Methods (Goldfarb, D., Stoll, S., Eds.), Chapter 11, Wiley, UK.

[6] Borbat, P. P., Freed, J. H. (1999) Chem. Phys. Lett. 313, 145–154.

[7] Saxena, S., Freed, J. H. (1997) J. Chem. Phys. 107, 1317–1340.

[8] Jeschke, G., Pannier, M., Godt, A., Spiess H. W. (2000) Chem. Phys. Lett. 331, 243–252.

[9] Meyer, A., Jassoy, J. J., Spicher, S., Berndhäuser, A., Schiemann, O. (2018) Phys. Chem. Chem. Phys. 20, 13858-13869.

[10] Jeschke, G., Chechik, V., Ionita, P., Godt, A., Zimmermann, H., Banham, J., Timmel, C. R., Hilger, D., Jung, H. (2006) Appl. Magn. Reson. 30, 473–498.

[11] Milov, A. D., Maryasov, A. G., Tevetkov, Y. D. (1998) Appl. Magn. Reson. 15, 107–143.

[12] Jeschke, G. (2014) Struct. Bond. 152, 83–120.

[13] Borbat, P. P., Mchaourab, H. S., Freed, J. H. (2002) J. Am. Chem. Soc. 124, 5304–5314.

[14] Akhmetzyanov, D., Schöps, P., Marko, A., Kunjir, N., Sigurdsson, S. Th., Prisner, T. F. (2015) Phys. Chem. Chem. Phys. 17, 24446–24451.

[15] Yang, Z., Liu, Y., Borbat, P. P., Zweier, J. L., Freed, J. H., Hubbell, W. L. (2012) J. Am. Chem. Soc. 134, 9950–9952.

[16] Shevelev, G. Y., Krumkacheva, O. A., Lomzov, A. A., Kuzhelev, A. A., Rogozhnikova, O. Y., Trukhin, D. V., Troitskaya, T. I., Tormyshev, V. M., Fedin, M. V., Pyshnyi, D. V., Bagryanskaya, E. G. (2014) J. Am. Chem. Soc. 136, 9874–9877.

[17] https://github.com/dinarabdullin/SnrCalculator

[18] Liu, H., Naismith, J. H. (2008) BMC Biotechnol. 8, 91–101.

[P5]: SLIM: A Short-Linked, Highly Redox-Stable Trityl Label for High-Sensitivity In-Cell EPR Distance Measurements

Reproduced with permission from

Nico Fleck, Caspar A. Heubach, Tobias Hett, Florian R. Haege, Pawel P. Bawol, Helmut Baltruschat, Olav Schiemann*, *Angew. Chem. Int. Ed.* **2020**, *59*, 9767–9772.
DOI: https://doi.org/10.1002/anie.202004452

* Corresponding author.

Contributions

- Performing pulsed EPR experiments *in vitro* and *in cell*.
- Analysis of *cw* and pulsed EPR data.
- DFT calculations to obtain the structure and EPR parameters of SLIM.
- *In silico* spin labelling and calculation of the conformer cloud volume.
- Writing of the manuscript in parts.

How to cite: *Angew. Chem. Int. Ed.* **2020**, *59*, 9767–9772
International Edition: doi.org/10.1002/anie.202004452
German Edition: doi.org/10.1002/ange.202004452

Spin Labeling Hot Paper

SLIM: A Short-Linked, Highly Redox-Stable Trityl Label for High-Sensitivity In-Cell EPR Distance Measurements

*Nico Fleck, Caspar A. Heubach, Tobias Hett, Florian R. Haege, Pawel P. Bawol, Helmut Baltruschat, and Olav Schiemann**

Abstract: *The understanding of biomolecular function is coupled to knowledge about the structure and dynamics of these biomolecules, preferably acquired under native conditions. In this regard, pulsed dipolar EPR spectroscopy (PDS) in conjunction with site-directed spin labeling (SDSL) is an important method in the toolbox of biophysical chemistry. However, the currently available spin labels have diverse deficiencies for in-cell applications, for example, low radical stability or long bioconjugation linkers. In this work, a synthesis strategy is introduced for the derivatization of trityl radicals with a maleimide-functionalized methylene group. The resulting trityl spin label, called SLIM, yields narrow distance distributions, enables highly sensitive distance measurements down to concentrations of 90 nM, and shows high stability against reduction. Using this label, the guanine-nucleotide dissociation inhibitor (GDI) domain of Yersinia outer protein O (YopO) is shown to change its conformation within eukaryotic cells.*

Introduction

Carbon-centered trityl radicals have emerged as important molecules for in-vivo imaging,[1] oximetry,[2,3] pH-sensing.[3] and as polarizing agents in dynamic nuclear polarization (DNP)[4,5] experiments. Additionally, the so-called Finland trityl **1**•[6] (Figure 1) has been used for synthesizing trityl-based spin labels **2**•–**8**•[7–11] out of which **2**•[7] and **3**•[8] paved the way for biomolecular structure determination at physiological temperatures using pulsed dipolar electron-paramagnetic-resonance spectroscopy (PDS).[12,13] Furthermore, trityl labels **4**• and **7**• have been shown to be suitable for PDS measurements within cells.[9,14] Advantages of trityl labels are their long relaxation times T_M at room temperature,[15] their single-line EPR spectra yielding large signal-to-noise ratios (SNR),[16] their spin state of $S = {}^1/_2$, which makes data analysis simple,[17] and their increased reduction stability compared to *gem*-dimethylnitroxides allowing for in-cell measurements.[9,14] Although such in-cell measurements are possible, the currently used tritys are still reduced within cells.[18] In contrast, Gd^{III}-based spin labels are inert to reduction within cells, but, depending on the particular type of the complex, the Gd^{III} ion may be exchanged for metal ions present in the cell.[19] The relaxation times T_M of Gd^{III} can be shorter or longer than those of tritys, depending on the utilized ligand,[14,20] and the electron-spin state of $S = 7/2$ imposes challenges on data analysis.[21,22] Thus, in order to keep the trityl core but to make it more suitable for in-cell measurements, its redox properties have to be tuned, possibly by exchanging the electron-withdrawing carboxy substituents with electron-donating groups. Furthermore, the currently used synthesis strategy for introducing the bioconjugation group via esterification (**4**•–**6**•, **8**•)[9,11] or amidation (**2**•, **3**•, **7**•)[7,8,10] of the carboxylic groups (Figure 1) leads to long, flexible linkers that make the PDS-derived distance distributions broad and, in some cases, multimodal.[11] This, in turn, renders the interpretation of such distance distributions error-prone. Last but not least, the label

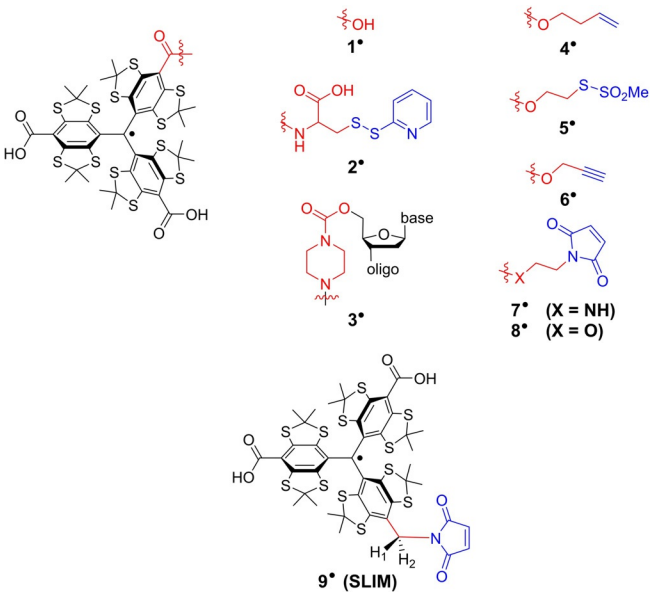

Figure 1. Finland trityl **1**•, various trityl labels (**2**•–**8**•) reported in the literature, and the new trityl label **9**• (SLIM). For the sake of clarity, the radical basis is depicted in black, the linker in red, and the bioconjugation site in blue.

[*] N. Fleck, C. A. Heubach, T. Hett, F. R. Haege, Prof. Dr. O. Schiemann
Institute of Physical and Theoretical Chemistry, University of Bonn
Wegelerstr. 12, 53115 Bonn (Germany)
E-mail: schiemann@pc.uni-bonn.de
P. P. Bawol, Prof. Dr. H. Baltruschat
Institute of Physical and Theoretical Chemistry, University of Bonn
Römerstr. 164, 53117 Bonn (Germany)
Supporting information and the ORCID identification number(s) for the author(s) of this article can be found under: https://doi.org/10.1002/anie.202004452.

should not be cleaved from the biomolecule under in-cell conditions, rendering the ester connectivity of the bioconjugation group to the trityl core[23] and the disulfide bridge forming a methanethiosulfonate group[24] unsuitable. With respect to the latter, the thioether-forming maleimide group has been confirmed to be advantageous.[25]

Therefore, the work presented herein introduces a synthesis by which the maleimide group is coupled to the trityl core via just one methylene group leading to the label **9**•, called SLIM (short-linked maleimide), which provides narrow distance distributions, increased stability against reduction, high labeling efficiencies, and large signal-to-noise ratios in PDS measurements.

Results and Discussion

Synthesis and Characterization

The synthesis of SLIM **9**• is shown in Scheme 1 and starts from trityl alcohol **10**, which can be obtained from 1,2,4,5-tetrachlorobenzene in three steps.[9] Subsequent deprotonation and treatment with activated Boc-anhydride afforded the threefold ester **11** by adapting a recent protocol of Hintz et al.[26] Statistical reduction of one ester moiety with $LiAlH_4$ broke the C_3 symmetry and lead to **12** in a yield of 42% (58% based on recovered starting material **11**).

In the next step, the required C–N bond on the way to **9**• was formed in a Mitsunobu reaction[27] between **12** and **13** leading to **14** in a yield of 70%. The excellent Michael-acceptor properties of maleimides required the protection of their C=C bond in form of the Diels–Alder adduct **13** in order to prevent side reactions with Ph_3P,[28] which is needed as a reagent in the Mitsunobu transformation. The *endo*-isomer of **13**[29] was chosen over the *exo*-isomer, because it provides sufficient retro-Diels–Alder reactivity already at 60 °C (see Supporting Information, Section 2.2.4) instead of 150 °C, which is necessary for the cleavage of the *exo*-adduct of **13**.[30,31] The deprotection at 60 °C is compatible with the thermal stability of the radical center,[32] which is crucial for the final deprotection to **9**•. However, first, the *t*-butyl esters in **14** are cleaved by trifluoroacetic acid concomitant to the abstraction of the hydroxyl group. This leads to tritylium ion **15**$^+$, which is then reduced in situ with tin(II) chloride to **15**•. Finally, **9**• was obtained by simply heating **15**• to 60 °C overnight leading to a quantitative deprotection of the maleimide. Relative to starting compound **10**, the overall yield of the five-step synthesis was 13%. The identity and purity of **9**• was confirmed by high-resolution mass spectrometry and HPLC (see Supporting Information, Sections 2.3.2–2.3.3). For further characterization, a continuous-wave (cw) X-band EPR spectrum of **9**• in a PBS buffer (PBS = phosphate-buffered saline) was recorded at room temperature (Figure 2a). The spectrum displays nine major lines due to hyperfine coupling of the electron spin to the imido nitrogen atom ($A_N = 1.71$ MHz) and the two benzylic hydrogen atoms ($A_{H1} = 6.00$ MHz, $A_{H2} = 2.96$ MHz). The fact that the hyperfine-coupling constants of H1 and H2 (Figure 1) differ from each other is also seen in DFT calculations and can be attributed to the helical chirality of the trityl scaffold (see Supporting Information, Section 8.1). Freezing the sample to 100 K resulted in the EPR spectrum shown in Figure 2b with a splitting between both lines of 7.44 MHz, which is, in large parts, governed by the hyperfine coupling to H1. Thus, and in contrast to the Finland trityl derivatives **2**•–**8**•, SLIM **9**• does not give rise to a single line in the frozen state. However, the spectral width of ≈10 G is still, on the one hand, narrow enough to permit full excitation with conventional rectangular pulses and, on the other hand, broad enough to also enable PELDOR experiments.

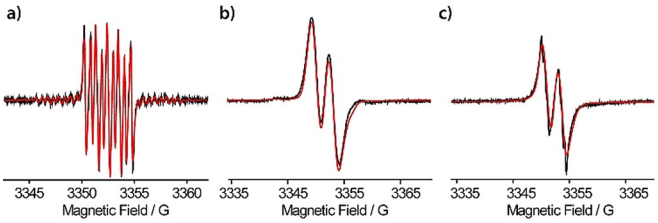

Figure 2. Cw X-band EPR spectra of **9**• in a PBS buffer a) at 298 K, b) at 100 K, and c) of **9**• bound to the single-cysteine mutant YopO N624C in a PBS buffer at 298 K.

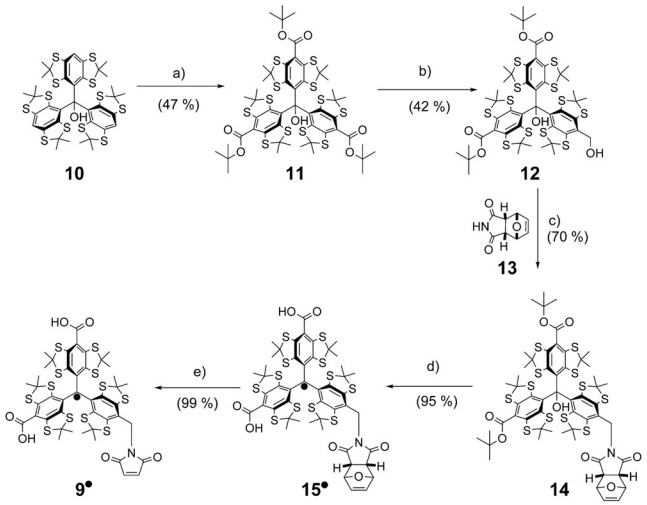

Scheme 1. Synthesis of SLIM **9**•. a) 1) *n*-BuLi, TMEDA, Et_2O, rt, 0.5 h; 2) *N-tert*-butoxycarbonylpyridinium *tert*-butanolate, Et_2O, 24 h. b) $LiAlH_4$, THF, rt, 1 h. c) Ph_3P, diethyl azodicarboxylate, THF, 0 °C, 0.5 h. d) 1) CF_3COOH, CH_2Cl_2, rt, 2 h; 2) $SnCl_2$, THF, 0.3 h. e) CH_3CN, 60 °C, 24 h.

Redox Stability

With respect to in-cell measurements, the stability of a spin label against reduction is important. As shown in the literature,[33–35] the *para*-substituents of trityl radicals hold a strong influence on the electrode potentials. Generally, the carbanion T^- is stabilized by electron withdrawing groups, such as esters or amides, resulting in an increase of the reduction potential. This implies that all spin labels obtained

by esterification or amidation of **1**• are more prone to reduction than **1**• itself. In contrast, the imidomethylene substituent in **9**• rather acts as an electron-donating group, destabilizing the corresponding carbanion and restraining the reduction compared to **1**•. Indeed, this behavior is seen in the cyclovoltammograms (Figure S28, Supporting Information). The reduction potential of **9**• is lowered by 46 mV compared to **1**•, furnishing it with an increased stability towards reduction. Due to the higher reactivity of the corresponding carbanion $\mathbf{9}^-$ towards H^+, its reduction is less reversible than for **1**•, as seen when using slower scan rates (see Supporting Information, Section 4.1). In contrast to the reduction, the oxidation of **9**• is slightly promoted by 26 mV compared to **1**•. Nonetheless, no oxidative degradation was observed under ambient conditions.

In order to probe the in-cell persistence of **9**•, its cw-EPR-signal intensity was monitored over time under several commonly used and in-cell-related conditions.[18,36,37] In a 4.75 mM ascorbate solution (Figure 3a), **9**• does not decay at all, whereas trityl label **8**• decays to 62% within 15 h, the *gem*-diethyl label **S5** bound to DNA (see Supporting Information, Section 3.1) is reduced to 18% in the same time and the *gem*-dimethyl label MTSL is completely reduced within 1.5 h.

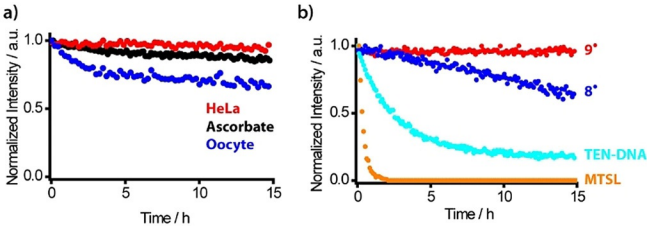

Figure 3. a) Plot of the EPR intensities (double integral) vs. time for 200 μM **9**• (red), **8**• (blue), tetraethyl nitroxide **S5** (cyan), and MTSL (orange) in a PBS buffer containing 4.75 mM sodium ascorbate, each corresponding to a 24-fold molar excess of ascorbate. b) Plot of the EPR intensities (double integral) against time for **9**• conjugated to YopO N624C (50 μM) in HeLa-lysate (red), 4.75 mM ascorbate (black), and *Xenopus laevis* oocyte lysate (blue). The initial intensities were comparable, and the dead time was below 6 min in each case. Label **S5** was conjugated to DNA to provide sufficient water solubility.

In another step, **9**• was conjugated to *Yersinia* outer protein O (YopO) mutant N624C and the labeled protein was added to a 4.75 mM solution of ascorbate, HeLa cell lysate, and oocyte lysate. As can be seen in Figure 3b, also under these conditions, **9**• is reduced only marginally in the case of ascorbate and HeLa lysate. Even within *Xenopus laevis* oocyte lysate, the most reducing cell lysate tested herein, only a decay to 71% is observed after 15 h. Label **9**• is thus considerably more stable than the *gem*-dimethyl nitroxides and at least on par with the best *gem*-diethyl nitroxides according to literature reports.[36,37]

Spin Labeling

Successful spin labeling requires high site-selectivity and high labeling efficiency. In order to probe for the first aspect, the cysteine-free mutant of YopO[38,39] was incubated with **9**• under typical labeling conditions.[11] MALDI-MS showed the mass for the unlabeled protein only, indicating that no other amino acid is covalently labeled by **9**• (see Supporting Information, Section 3.3.5). Non-covalent labeling and the presence of inseparable aggregates of **9**• were tested for by using UV/Vis spectroscopy. The UV/Vis spectrum after labeling shows a weak absorption band at 464 nm (see Supporting Information, Section 3.3.4) indicating that 6.9 ± 0.6% of non-bound **9**• are present in the sample relative to the protein. This behavior of trityls is known[10,11,40] and, in this case, actually quite effectively diminished by the labeling protocol.

The efficiency of the bioconjugation was subsequently examined using the single-cysteine YopO mutant N624C. ESI-MS (see Supporting Information, Section 3.3.5) confirmed that only one label is bound. The labeling efficiency was estimated to be quantitative based on ESI-MS and 94 ± 9% based on UV/Vis and EPR spin-counting experiments. Interestingly, **9**• covalently bound to YopO yields a room-temperature cw X-band EPR spectrum similar to that of **9**• free in the frozen state, which can be simulated by only slightly adjusting the EPR parameters of **9**• at 100 K (Figure 2 and Supporting Information, Section 5). Thus, the slow rotation of **9**• bound to a protein brings the label into the rigid limit and enables the distinction of bound label from unbound label.

Distance Measurements

In a next step, the effect of the reduced linker length on PDS derived distance distributions was assessed on the double-cysteine mutant YopO Y588C/N624C (see Supporting Information, Section 3.3.1) by labeling it with **9**•, **8**•, and MTSL. The resulting doubly labeled constructs YopO-**9**•, YopO-**8**•, and YopO-MTSL were characterized (see Supporting Information, Section 3.3.4) and subjected to double-quantum coherence (DQC)[41,42] and pulsed electron–electron double-resonance (PELDOR)[43–45] experiments whose background-corrected time traces are shown in Figure 4 for original time traces, see the Supporting Information, Section 7.5). The PELDOR time trace of YopO-MTSL (Figure 4a) exhibits the typical modulation depth of 32% for Q-band PELDOR and a SNR of 248 $h^{-1/2}$. The corresponding distance distribution shows a bimodal distribution, which was seen before for other MTSL-YopO mutants involving α-helix 14 in the guanine-nucleotide dissociation inhibitor (GDI) domain.[11] For YopO-**9**•, the narrow spectral width of the trityl signal called for a DQC experiment, which almost tripled the modulation depth to 87% and the SNR to 674 $h^{-1/2}$ (Figure 4c). This high SNR prompted us to reduce the YopO-**9**• concentration to 90 nM, which still gave an SNR of 2 $h^{-1/2}$ at a time window length of 2.5 μs (see Supporting Information, Section 7.7). Performing PELDOR measurements on YopO-

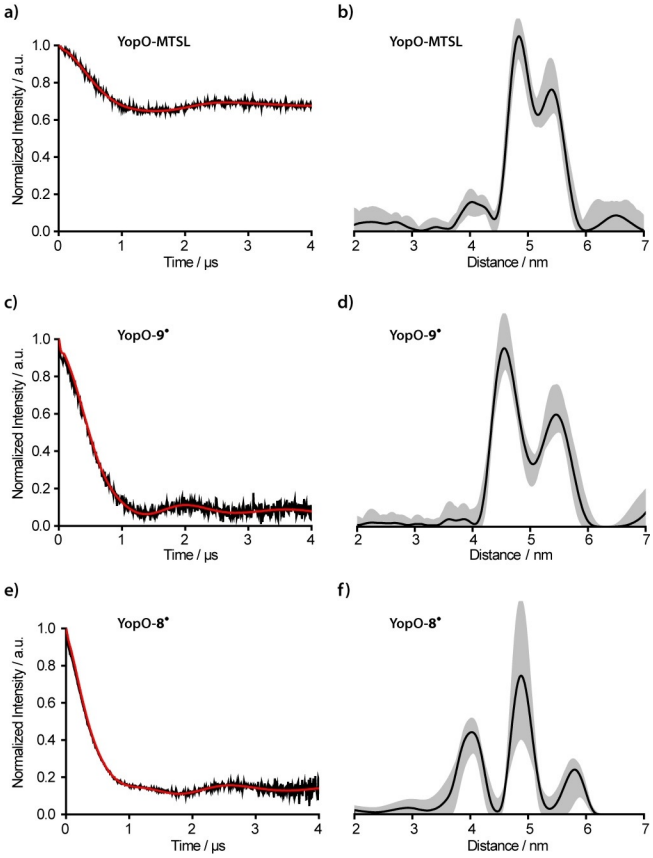

Figure 4. PDS experiments on mutant Y588C/N624C-YopO labeled with a), b) MTSL (PELDOR), c), d) **9•** (DQC), and e), f) **8•** (DQC). Background-corrected time traces (black) are given along with their fits (red) in (a,c,e), and the resulting distance distributions are provided in (b,d,f) in black with the corresponding DeerAnalysis validation shown as grey shaded areas.

9• provided a SNR of only 155 $h^{-1/2}$ (see Supporting Information, Section 7.5). This shows that the combination DQC/**9•** outperforms the PELDOR/MTSL combination.[11] Notably, the bimodality seen for YopO-MTSL is also resolved for YopO labeled with **9•**, and both the widths and weights of the two modes are very similar in both cases (see Supporting Information, Section 7.5).

Since the bimodality is observed for two different spin labels, MTSL and **9•**, and two PDS techniques, PELDOR and DQC, it can be related to two different conformers of the α-helix, as previously discussed.[11,39] The peak at 4.5 nm is assigned to the straight form of α-helix 14 (PDB-ID: 2h7o) and the peak at 5.3 nm to its bent form (PDB-ID: 4ci6).[11,39] In the crystal structures, the bent form is only found when actin is bound, whereas here, in frozen solution, both conformations of α-helix 14 seem to be present even in the absence of the actin ligand. Interestingly, the addition of human platelet actin did not change the obtained distance distribution, strongly indicating that the conformation of α-helix 14 is independent of the actin-binding process (see Supporting Information, Section 7.6).

In contrast, the DQC experiment on YopO-**8•** (SNR of 503 $h^{-1/2}$) provides a broad trimodal distance distribution (Figure 4e,f), which is attributed to the longer linker and thus a broader range of label conformers for **8•**, especially with shorter distances (see Supporting Information, Section 8.2.2). The differences in the conformer space of **8•** and **9•** can be quantified in silico[46] via the accessible volume both labels sample.[47,48] This yielded 15200 $Å^3$ and 6940 $Å^3$ for **8•** and **9•**, respectively, and thus, a reduction of the conformer space by 54% upon going from **8•** to **9•**. This example thus nicely highlights the importance of a short linker group as provided by the new SLIM label.

In-Cell Measurements

To test the feasibility of **9•** for in-cell structure elucidation, DQC measurements on the aforementioned Y588C/N624C-YopO mutant were performed within eukaryotic *Xenopus laevis* oocytes. The rationale behind the choice of this type of cells as model system is twofold: first, oocytes exhibit the highest reducing activity of all cell types under study[36] (Figure 3c) and do, thus, serve as a true in-cell benchmark test for **9•**. Second, although YopO is a prokaryotic protein, its full enzymatic function is only initiated upon translocation into eukaryotic immune cells through the *Yersinia* type-3 secretion system, a needle-like structure that penetrates the outer membrane of the innate immune cells.[49,50] Here, the oocytes serve as the eukaryotic species and their size enables mimicking this translocation process of YopO-**9•** using a microinjection system (see Supporting Information, Section 6). In this way, samples with a bulk spin concentration of 11 µM were obtained and subjected to Q-band DQC experiments.

Due to the presence of Mn^{II} in oocytes and spin-crowding effects, the phase-memory time T_M is shortened compared to in-vitro measurements (see Supporting Information, Section 7.8). However, an incubation of the injected oocytes over 2 h led to a more uniform distribution of the labeled protein within the oocytes enabling a dipolar-evolution-time window of 3.5 µs for the in-cell DQC experiment. The obtained time trace (Figure 5a) exhibits a SNR of 23 $h^{-1/2}$ (2 $h^{-1/2}$ $µM^{-1}$), which is considerably higher than previously reported for in-cell measurements with nitroxide-[36,51,52] and trityl-labeled[9] biomolecules. Even in comparison to W-band PELDOR/trityl

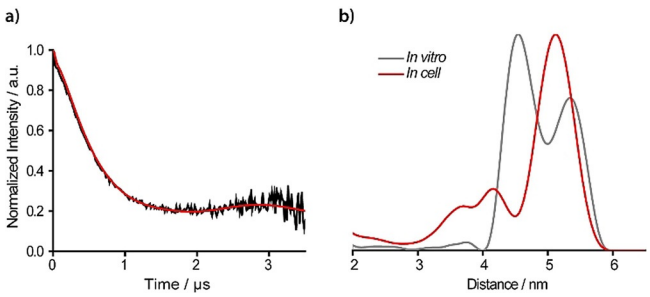

Figure 5. a) Background-corrected in-cell DQC time trace and the corresponding fit of YopO-**9•** after an incubation period of 2 h. b) Distance distribution of the in cell experiment (red) overlaid with the distance distribution obtained in vitro (3.5 µs trace length, grey).

and PELDOR/Gd^{III} measurements, the Q-band DQC/SLIM combination is at least on par.[14,53–56] Remarkably, the distance distribution from the in-cell measurement differs from the in-vitro-derived ones (Figures 4d and S38,S39). This can already be seen when comparing the time traces; the in-cell time trace has a considerably longer oscillation period (3 µs) than the in-vitro counterparts (2 µs). Accordingly, the long-distance peak at 5.1 nm prevails within oocytes and is now the dominating peak, whereas the peak at 4.5 nm is strongly diminished. This data thus indicates a preferred selection of the bent form of α-helix 14 of the GDI domain of YopO in the eukaryotic cytosol. The straight conformation of α-helix 14 leads to shorter inter-spin distances, which are well pronounced in the in-vitro experiments but are strongly diminished in the in-cell measurement (compare the Supporting Information, Section 7.8). This effect may be related to molecular crowding[57,58] and/or binding of regulatory proteins such as Rac1[59] in the eukaryotic cytosol. More in-depth studies on this will follow.

Conclusion

In this work, the trityl spin label SLIM was introduced and probed for its suitability in PDS experiments. Its synthesis involved a Mitsunobu-type transformation using a protected maleimide, which can be deprotected in a mild retro-Diels–Alder reaction. Bioconjugation of SLIM to cysteines proceeds in high yields and site-selectively. Its narrow spectral width enables high-sensitivity distance measurements down to low nanomolar protein concentrations, and the short linker leads to narrow and, thus, more reliable distance distributions. Additionally, SLIM features a high stability towards reduction, making in-cell PDS measurements at high SNRs feasible. In profit of this, it could be shown that the injection of YopO into a eukaryotic cell leads to a change in the conformational ensemble of the GDI domain. Thus, SLIM is a very promising label improving the capability to obtain structural information from biomolecules within their natural cellular environment.

Acknowledgements

Funding of the Deutsche Forschungsgemeinschaft (DFG) via SPP1601 is gratefully acknowledged.

Conflict of interest

The authors declare no conflict of interest.

Keywords: EPR spectroscopy · in-cell measurements · radicals · spin labeling · trityl radical

[1] B. B. Williams, H. J. Halpern, in *Biomedical EPR—Part A: Free Radicals, Metals, Medicine and Physiology* (Eds.: S. R. Eaton, G. R. Eaton, L. J. Berliner), Springer US, Boston, **2005**, pp. 283–319.
[2] B. Epel, C. R. Haney, D. Hleihel, C. Wardrip, *Med. Phys.* **2010**, *37*, 2553–2559.
[3] A. A. Bobko, I. Dhimitruka, J. L. Zweier, V. V. Khramtsov, *J. Am. Chem. Soc.* **2007**, *129*, 7240–7241.
[4] G. Mathies, M. A. Caporini, V. K. Michaelis, Y. Liu, K. N. Hu, D. Mance, J. L. Zweier, M. Rosay, M. Baldus, R. G. Griffin, *Angew. Chem. Int. Ed.* **2015**, *54*, 11770–11774; *Angew. Chem.* **2015**, *127*, 11936–11940.
[5] J. H. Ardenkjær-Larsen, B. Fridlund, A. Gram, G. Hansson, L. Hansson, M. H. Lerche, R. Servin, M. Thaning, K. Golman, *Proc. Natl. Acad. Sci. USA* **2003**, *100*, 10158–10163.
[6] S. Andersson, A. Rydbeck, R. S. Mahno, US Patent 5728370, **1999**.
[7] Z. Yang, Y. Liu, P. Borbat, J. L. Zweier, J. H. Freed, W. L. Hubbell, *J. Am. Chem. Soc.* **2012**, *134*, 9950–9952.
[8] G. Y. Shevelev, O. A. Krumkacheva, A. A. Lomzov, A. A. Kuzhelev, O. Y. Rogozhnikova, D. V. Trukhin, T. I. Troitskaya, V. M. Tormyshev, M. V. Fedin, D. V. Pyshnyi, et al., *J. Am. Chem. Soc.* **2014**, *136*, 9874–9877.
[9] J. J. Jassoy, A. Berndhäuser, F. Duthie, S. P. Kühn, G. Hagelueken, O. Schiemann, *Angew. Chem. Int. Ed.* **2017**, *56*, 177–181; *Angew. Chem.* **2017**, *129*, 183–187.
[10] A. Giannoulis, Y. Yang, Y.-J. Gong, X. Tan, A. Feintuch, R. Carmieli, T. Bahrenberg, Y. Liu, X.-C. Su, D. Goldfarb, *Phys. Chem. Chem. Phys.* **2019**, *21*, 10217–10227.
[11] J. J. Jassoy, C. A. Heubach, T. Hett, F. Bernhard, F. R. Haege, G. Hagelueken, O. Schiemann, *Molecules* **2019**, *24*, 2735.
[12] G. W. Reginsson, O. Schiemann, *Biochem. Soc. Trans.* **2011**, *39*, 128–139.
[13] G. Jeschke, *Annu. Rev. Phys. Chem.* **2012**, *63*, 419–446.
[14] Y. Yang, B. Pan, F. Yang, Y. Liu, X. Su, D. Goldfarb, *J. Phys. Chem. Lett.* **2020**, *11*, 1141–1147.
[15] A. A. Kuzhelev, D. V. Trukhin, O. A. Krumkacheva, R. K. Strizhakov, O. Y. Rogozhnikova, T. I. Troitskaya, M. V. Fedin, V. M. Tormyshev, E. G. Bagryanskaya, *J. Phys. Chem. B* **2015**, *119*, 13630–13640.
[16] G. W. Reginsson, N. C. Kunjir, S. T. Sigurdsson, O. Schiemann, *Chem. Eur. J.* **2012**, *18*, 13580–13584.
[17] N. C. Kunjir, G. W. Reginsson, O. Schiemann, S. T. Sigurdsson, *Phys. Chem. Chem. Phys.* **2013**, *15*, 19673–19685.
[18] A. P. Jagtap, I. Krstic, N. C. Kunjir, R. Hänsel, T. F. Prisner, S. T. Sigurdsson, *Free Radical Res.* **2015**, *49*, 78–85.
[19] M. Qi, A. Groß, G. Jeschke, A. Godt, M. Drescher, *J. Am. Chem. Soc.* **2014**, *136*, 15366–15378.
[20] M. Azarkh, A. Bieber, M. Qi, J. W. A. Fischer, M. Yulikov, A. Godt, M. Drescher, *J. Phys. Chem. Lett.* **2019**, *10*, 1477–1481.
[21] D. Goldfarb, *Phys. Chem. Chem. Phys.* **2014**, *16*, 9685–9699.
[22] D. Abdullin, O. Schiemann, *ChemPlusChem* **2020**, https://doi.org/10.10002/cplu.201900705.
[23] Z. Yang, M. D. Bridges, C. J. López, O. Y. Rogozhnikova, D. V. Trukhin, E. K. Brooks, V. Tormyshev, H. J. Halpern, W. L. Hubbell, *J. Magn. Reson.* **2016**, *269*, 50–54.
[24] R. Igarashi, T. Sakai, H. Hara, T. Tenno, T. Tanaka, H. Tochio, M. Shirakawa, *J. Am. Chem. Soc.* **2010**, *132*, 8228–8229.
[25] R. Roser, M. J. Schmidt, M. Drescher, D. Summerer, *Org. Biomol. Chem.* **2016**, *14*, 5468–5476.
[26] H. Hintz, A. Vanas, D. Klose, G. Jeschke, A. Godt, *J. Org. Chem.* **2019**, *84*, 3304–3320.
[27] K. C. K. Swamy, N. N. B. Kumar, E. Balaraman, K. V. P. P. Kumar, *Chem. Rev.* **2009**, *109*, 2551–2651.
[28] M. A. Walker, *J. Org. Chem.* **1995**, *60*, 5352–5355.
[29] E. H. Discekici, A. H. St. Amant, S. N. Nguyen, I. H. Lee, C. J. Hawker, J. Read De Alaniz, *J. Am. Chem. Soc.* **2018**, *140*, 5009–5013.

[30] O. K. Farha, R. L. Julius, M. F. Hawthorne, *Tetrahedron Lett.* **2006**, *47*, 2619 – 2622.
[31] Z. Lu, R. Weber, R. J. Twieg, *Tetrahedron Lett.* **2006**, *47*, 7213 – 7217.
[32] N. Fleck, T. Hett, J. Brode, A. Meyer, S. Richert, O. Schiemann, *J. Org. Chem.* **2019**, *84*, 3293 – 3303.
[33] X. Tan, L. Chen, Y. Song, A. Rockenbauer, F. A. Villamena, J. L. Zweier, Y. Liu, *Chem. Res. Toxicol.* **2017**, *30*, 1664 – 1672.
[34] C. Decroos, V. Balland, J. L. Boucher, G. Bertho, Y. Xu-Li, D. Mansuy, *Chem. Res. Toxicol.* **2013**, *26*, 1561 – 1569.
[35] B. Driesschaert, A. A. Bobko, T. D. Eubank, A. Samouilov, V. V. Khramtsov, J. L. Zweier, *Bioorg. Med. Chem. Lett.* **2016**, *26*, 1742 – 1744.
[36] G. Karthikeyan, A. Bonucci, G. Casano, G. Gerbaud, S. Abel, V. Thomé, L. Kodjabachian, A. Magalon, B. Guigliarelli, V. Belle, et al., *Angew. Chem. Int. Ed.* **2018**, *57*, 1366 – 1370; *Angew. Chem.* **2018**, *130*, 1380 – 1384.
[37] T. S. Braun, P. Widder, U. Osswald, L. Groß, L. Williams, M. Schmidt, I. Helmle, D. Summerer, M. Drescher, *ChemBioChem* **2020**, *21*, 958 – 962.
[38] E. E. Galyov, S. Håkansson, Å. Forsberg, H. Wolf-Watz, *Nature* **1993**, *361*, 730 – 732.
[39] M. F. Peter, A. T. Tuukkanen, C. A. Heubach, A. Selsam, F. G. Duthie, D. I. Svergun, O. Schiemann, G. Hagelueken, *Structure* **2019**, *27*, 1416 – 1426.
[40] I. Marin-Montesinos, J. C. Paniagua, A. Peman, M. Vilaseca, F. Luis, S. Van Doorslaer, M. Pons, *Phys. Chem. Chem. Phys.* **2016**, *18*, 3151 – 3158.
[41] S. Saxena, J. H. Freed, *Chem. Phys. Lett.* **1996**, *251*, 102 – 110.
[42] S. Saxena, J. H. Freed, *J. Chem. Phys.* **1997**, *107*, 1317 – 1340.
[43] A. D. Milov, K. M. Salikhov, M. D. Schirov, *Fiz. Tverd. Tela* **1981**, *23*, 975 – 982.
[44] A. Milov, A. Ponomarev, Y. Tsvetkov, *Chem. Phys. Lett.* **1984**, *110*, 67 – 72.
[45] M. Pannier, S. Veit, A. Godt, G. Jeschke, H. W. Spiess, *J. Magn. Reson.* **2000**, *142*, 331 – 340.
[46] G. Hagelueken, R. Ward, J. N. Naismith, O. Schiemann, *Appl. Magn. Reson.* **2012**, *42*, 377 – 391.
[47] K. Sale, L. Song, Y. Liu, E. Perozo, P. Fajer, *J. Am. Chem. Soc.* **2005**, *127*, 9334 – 9335.
[48] G. Hagelueken, D. Abdullin, O. Schiemann, *Methods Enzymol.* **2015**, *563*, 595 – 622.
[49] G. V. Plano, K. Schesser, *Immunol. Res.* **2013**, *57*, 237 – 245.
[50] W. L. Lee, J. M. Grimes, R. C. Robinson, *Nat. Struct. Mol. Biol.* **2015**, *22*, 248 – 255.
[51] I. Krstić, R. Hänsel, O. Romainczyk, J. W. Engels, V. Dötsch, T. F. Prisner, *Angew. Chem. Int. Ed.* **2011**, *50*, 5070 – 5074; *Angew. Chem.* **2011**, *123*, 5176 – 5180.
[52] P. Widder, J. Schuck, D. Summerer, M. Drescher, *Phys. Chem. Chem. Phys.* **2020**, *22*, 4875 – 4879.
[53] A. Martorana, G. Bellapadrona, A. Feintuch, E. Di Gregorio, S. Aime, D. Goldfarb, *J. Am. Chem. Soc.* **2014**, *136*, 13458 – 13465.
[54] Y. Yang, F. Yang, Y. Gong, J. Chen, D. Goldfarb, X. Su, *Angew. Chem. Int. Ed.* **2017**, *56*, 2914 – 2918; *Angew. Chem.* **2017**, *129*, 2960 – 2964.
[55] Y. Yang, F. Yang, Y. Gong, T. Bahrenberg, A. Feintuch, X. Su, D. Goldfarb, *J. Phys. Chem. Lett.* **2018**, *9*, 6119 – 6123.
[56] F. Wojciechowski, A. Groß, I. T. Holder, L. Knörr, M. Drescher, J. S. Hartig, *Chem. Commun.* **2015**, *51*, 13850 – 13853.
[57] H.-X. Zhou, *FEBS Lett.* **2013**, *587*, 1053 – 1061.
[58] Y. Wang, M. Sarkar, A. E. Smith, A. S. Krois, G. J. Pielak, *J. Am. Chem. Soc.* **2012**, *134*, 16614 – 16618.
[59] G. Prehna, M. I. Ivanov, J. B. Bliska, C. E. Stebbins, *Cell* **2006**, *126*, 869 – 880.

Manuscript received: March 26, 2020
Version of record online: April 30, 2020

Angewandte Chemie
Eine Zeitschrift der Gesellschaft Deutscher Chemiker

Supporting Information

SLIM: A Short-Linked, Highly Redox-Stable Trityl Label for High-Sensitivity In-Cell EPR Distance Measurements

*Nico Fleck, Caspar A. Heubach, Tobias Hett, Florian R. Haege, Pawel P. Bawol, Helmut Baltruschat, and Olav Schiemann**

anie_202004452_sm_miscellaneous_information.pdf

Author Contributions

N.F. Investigation: Lead; Writing—Original Draft: Lead
T.H. Formal analysis: Lead; Investigation: Supporting; Writing—Original Draft: Supporting
F.H. Investigation: Supporting
P.B. Investigation: Supporting
H.B. Writing—Review & Editing: Supporting.

Table of Contents

1. General Procedures and Instrumentation

NMR spectra were recorded on Avance I 300, Avance I 400, Avance III HD 500, or Avance III HD 700 spectrometers (Bruker BioSpin, Rheinstetten, Germany). Chemical shifts are reported referenced to hydrogen residual peaks of the NMR solvent.[5]

MALDI(+)-spectra were recorded in a Bruker Daltonics UltraFlex TOF/TOF spectrometer (Bruker, Rheinstetten, Germany). For organic compounds, DCTB was used as the matrix, whereas DHAP was used for protein samples. For ESI(+), a Synapt G2-Si spectrometer (Waters, Milford, USA) was employed. APCI-spectra were obtained on an Orbitrap XL spectrometer (Thermo Fisher Scientific, Bremen, Germany). Protein samples were subjected to mass spectrometric analysis in 20 mM PO_i buffer (pH = 6.8, 50 mM NaCl).

For analytical chromatography, an UHPLC system (PLATINblue-series, Knauer GmbH, Berlin, Germany) equipped with a Eurospher II 100-2 C18P, 2 µm, 2 x 100 mm column (Knauer GmbH, Berlin, Germany) and a UV detector working at 265 nm was used.

All continuous wave (*cw*) EPR measurements were performed at X-band frequencies (~9.4 GHz) either on an EMXmicro or EMXnano spectrometer (Bruker BioSpin, Rheinstetten, Germany). Measurements at room temperature were done on the EMXmicro using an ER 4122SHQ resonator. Measurements at 100 K were conducted using a Bruker 4119HS resonator in conjunction with a ER 4141VT temperature control system, which operates with a continuous flow of nitrogen gas. For all samples, X-band EPR-tubes with an outer diameter of 5 mm obtained from Wilmad Labglass (Brand of SP Industries, Warminster, USA) were used. Aqueous samples were, however, filled into 10 µL capillaries (Disposable Capillaries, Hirschmann Laborgeräte, Eberstadt, Germany), which were then transferred into the X-band tubes.

cw-EPR spectra of the pure SLIM label and after bioconjugation were recorded in frozen solution using a modulation amplitude of 0.2 G, a microwave power of 7.4 µW (44 dB attenuation), a time constant of 20.48 ms and a conversion time of 20.59 ms. 2000 data points were recorded, corresponding to a resolution of 25 points per G. Quantitative EPR measurements were conducted employing the on-board spin counting routine of the EMXnano spectrometer. *CW*-EPR measurements at room temperature were performed at an attenuation of 25 dB (603.1 µW) and a modulation amplitude of 0.1 G.

Pulsed EPR measurements were conducted at Q-band frequencies (~33.7 GHz) on a Bruker (Bruker BioSpin, Rheinstetten, Germany) ELEXSYS E580 EPR spectrometer equipped with an ER5106QT-II resonator and a 150 W TWT-amplifier (Applied Systems Engineering, Fort Worth, TX, USA). All data was acquired using quadrature detection. The temperature was adjusted to the appropriate value (between 10 K and 50 K) using a CF935 helium gas-flow cryostat (Oxford Instruments, Abingdon, UK) in conjunction with an Oxford Instruments iTC 503 temperature controller.

2. Synthesis

2.1 General Procedures Synthesis

Chemicals were purchased from commercial suppliers and used without further purification. Diethyl ether was dried over 4 Å molecular sieves, and THF was distilled over sodium wire with benzophenone. Where indicated, solvents were degassed by applying three freeze-pump-thaw cycles. Thin layer chromatography was conducted using 250 µm F254 silica plates provided by Merck, and spots were visualized with UV-light at 254 nm. Spots of trityl alcohols can be stained selectively by irradiating the TLC-plate for 5 min with UV-light at 254 nm (5 W). For column chromatography, silica gel (60 Å pore size, 40 – 63 µm particle size) purchased from Merck was used. Solvents were generally removed under reduced pressure by a rotary evaporator, products were further dried in oil-pump vacuum at 10^{-3} mbar. The concentration of *n*-butyl lithium solutions was determined prior to use by titration following the protocol of *Winkle et al.*[1] Trityl alcohol **10** was obtained following our previously published protocol.[2] 3aRS,4SR,7RS,7aSR-4,7-epoxy-3,3a,7,7a-tetrahydro-2H-isoindoli-1,3-dione (**13**) was prepared according to the literature.[3] Compound **S1** was obtained following the procedure of *Hintz et al.*[4] using DMF instead of N-formylpiperidine.

2.2 Synthetic Protocols

2.2.1 Synthesis of S2

2,2,6,6-tetramethyl-8-(hydroxymethyl)benzo[1,2-d;4,5-d]bis(1,3-dithiol)

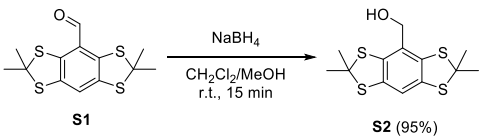

S1 **S2** (95%)

S1 (800 mg, 2.5 mmol) was dissolved in 15 mL dry dichloromethane and 20 mL dry methanol were added. Then, sodium borohydride (300 mg, 3.83 mmol, 1.50 eq.) was added, whereupon the yellow solution lost its color. After 15 minutes of stirring at room temperature, the solvents were removed under reduced pressure and water (30 mL) was added. The aqueous phase was extracted with ethyl acetate (3 x 20 mL) and the unified organic phases were dried over $MgSO_4$. After removal of the solvents, the crude product is obtained as an off-white solid, which was then purified by column chromatography on silica eluting with CyH/EtOAc (9:1) giving **S2** (R_f = 0.18) in a yield of 767 mg (95%).
^{1}H-NMR (400 MHz, $CDCl_3$, 298 K, δ in ppm): 7.01 (s, 1H), 4.56 (s, 2H), 1.89 (s, 12H).
$^{13}C\{^1H\}$-NMR (100 MHz, $CDCl_3$, 298 K, δ in ppm): 136.6, 136.0, 129.5, 116.5, 65.3, 65.2, 31.5.
HRMS (ESI+, *m/z,* $[M]^+$): calc. for $C_{13}H_{16}OS_4$, 316.0078; found 316.0077.

2.2.2 Synthesis of **S3**

2,2,6,6-tetramethyl-8-(1-methyl(3aRS,4SR,7RS,7aSR-4,7-epoxy-3,3a,7,7a-tetrahydro-2H-isoindoli-1,3-dione-2-yl)- benzo[1,2-d;4,5-d]bis(1,3-dithiol)

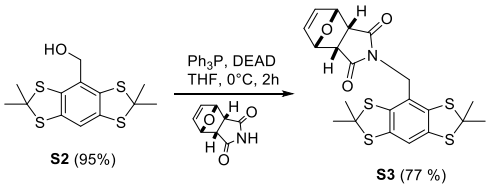

S2 (300 mg, 0.95 mmol, 1.25 eq.), **13** (125 mg, 0.76 mmol), and Ph_3P (200 mg, 0.76 mmol) were dissolved in 10 mL dry THF. Then, DEAD (132 mg, 120 µL, 0.76 mmol) was added and the reaction mixture was stirred for 1 h at 0°C. Subsequently, the reaction mixture was poured onto water (50 mL) and extracted with CH_2Cl_2 (2 x 30 mL). The unified organic phases were dried over $MgSO_4$ and solvents were removed under reduced pressure. The product (R_f = 0.3) was isolated by column chromatography on silica eluting with CyH/EtOAc (2:1) in a yield of 338 mg (77%).

^{1}H-NMR (500 MHz, $CDCl_3$, 298 K, δ in ppm): 6.99 (s, 1H), 6.44 (bs, 2H), 5.29 (m, 2H), 4.37 (s, 2H), 3.54 (m, 2H), 1.86 (s, 12H).

$^{13}C\{^1H\}$-NMR (125 MHz, $CDCl_3$, 298 K, δ in ppm): 173.9, 136.6, 136.6, 134.9, 124.1, 116.6, 79.4, 65.4, 46.1, 43.1, 31.2.

HRMS (APCI, *m/z,* $[M+H]^+$): calc. for $C_{21}H_{22}NO_3S_4$, 464.0477; found 464.0474.

2.2.3 Synthesis of **S4**

2,2,6,6-tetramethyl-8-(1-methyl(3,4-dehydropyrolidin-1,3-dione-2-yl)benzo[1,2-d;4,5-d]bis(1,3-dithiol)

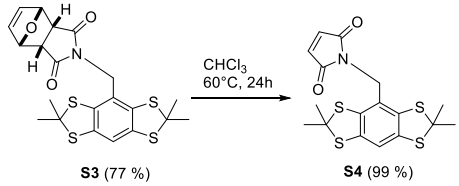

S3 (100 mg) was dissolved in 20 mL chloroform and stirred at 60 °C overnight and under an argon atmosphere. Afterwards, all volatiles were removed and **S4** was obtained in a quantitative yield of 85 mg as a colorless solid.

^{1}H-NMR (500 MHz, $CDCl_3$, 298 K, δ in ppm): 7.01 (s, 1H), 6.68 (s, 2H), 4.57 (s, 2H), 1.87 (s, 12H).

$^{13}C\{^1H\}$-NMR (125 MHz, $CDCl_3$, 298 K, δ in ppm): 169.73, 136.76, 136.16, 134.15, 124.94, 116.48, 65.62, 42.06, 31.25.

HRMS (ESI+, *m/z,* $[M+H]^+$): calc. for $C_{21}H_{22}NO_3S_4$, 316.0215; found 316.0213.

2.2.4 Retro Diels-Alder reaction: Kinetics

Since **15•** is paramagnetic and therefore not suitable for NMR-measurements, model compound **S3** was used in order to examine the Retro-Diels-Alder reaction leading to **9•**. For this, 100 mg of **S3** were dissolved in 5 mL $CDCl_3$ and heated to 60 °C under argon. Then, samples of 0.5 mL were drawn out of the reaction mixture with a syringe, cooled, and subjected to ^{1}H-NMR analysis immediately. Since **S3** and its Retro-Diels-Alder product **S4** can be differentiated by NMR, it was possible to extract the reaction kinetics, which follows a first order rate law as shown in Figure S1. After 1380 min (23 h), complete conversion to the free maleimide was observed.

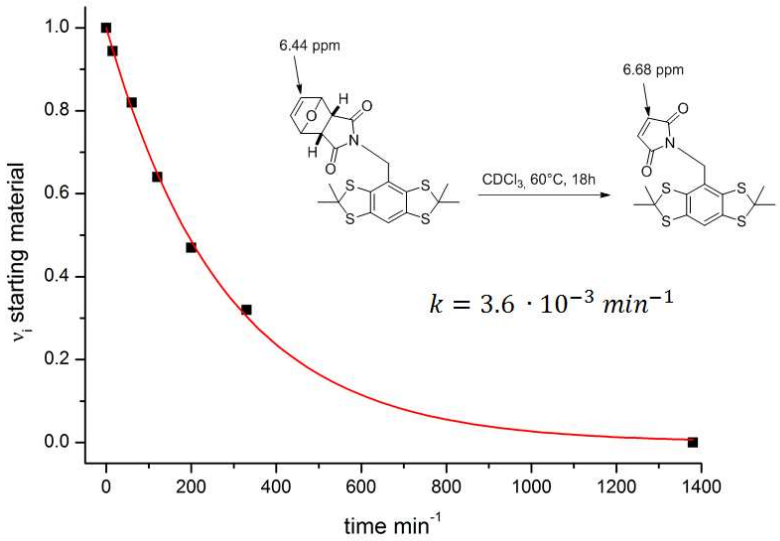

***Figure S1**: Kinetics for Retro-Diels-Alder reaction based on ^{1}H-NMR. Experimentally determined molar ratio of starting material (black dots) with exponential fit (red line).*

Based on a first-order rate law, a rate constant of 0.0036 min^{-1} was found by least-square fitting. This value compared well to rate constants obtained for similar furane-maleimide adducts.[6] From this, it was concluded that the tetrathioaryl-substituent does not influence the Retro-Diels-Alder reactivity. Therefore, the same conditions were applied in the synthesis of **9•**.

2.2.5 Synthesis of literature known compound **11**

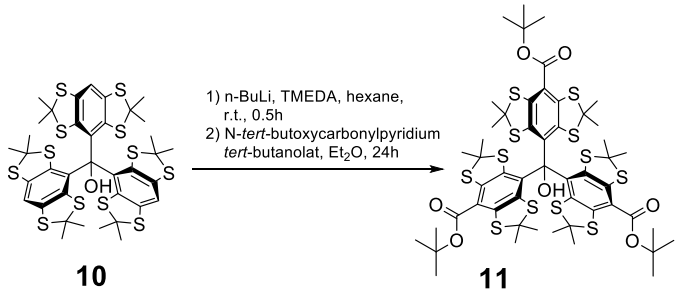

Tris[2,2,6,6-tetramethyl-8-(carboxy-tert-butyl)benzo[1,2-d;4,5-d]bis(1,3-dithiol)-4-yl]methanolTrityl alcohol **10** (3.00 g, 3.40 mmol) was dissolved in 100 mL dry Et_2O and N,N,N',N'-tetramethylethylendiamin (5.0 mL, 3.87 g, 34.0 mmol, 10 eq.) were added under argon. Then, the solution was cooled down to 0°C and *n*-butyl lithium (2.5 M in hexane, 13.6 mL, 34.0 mmol, 10 eq.) was added slowly. The yellowish solution obtained by this was stirred for 2 h at room temperature. In parallel, a solution of N,N-dimethylamino pyridine (12,44 g, 102.0 mmol, 30 eq.) and di-tert-butyl dicarbonate (18.42 g, 18.36 mL, 84.7 mmol, 25 eq.) in 300 mL dry Et_2O was prepared and stirred for 90 min at room temperature. Then, the solution of the lithiated trityl alcohol was transferred to the activated Boc_2O, whereupon the reaction mixture turned greenish and was stirred overnight in order to complete the carbonylation. After quenching with 300 mL water, the organic phase was separated and the aqueous one extracted with 100 mL Et_2O. The unified organic phases were dried over $MgSO_4$ and the solvent was removed. The yellow-orange crude product was purified by column chromatography on silica eluting with CyH/Et_2O (3:1, *v/v*) giving **11** as an orange solid (R_f = 0.38) in a yield of 1.88 g (16 mmol, 47 %). The analytical data is in accordance with the literature.[2]

2.2.6 Synthesis of **12**

Bis{[2,2,6,6-tetramethyl-8-(carboxy-tert-butyl)benzo[1,2-d;4,5-d]bis(1,3-dithiol)-4-yl]}-{[2,2,6,6-tetramethyl-8-(hydroxymethyl)benzo[1,2-d;4,5-d]bis(1,3-dithiol)-4-yl]}methanol

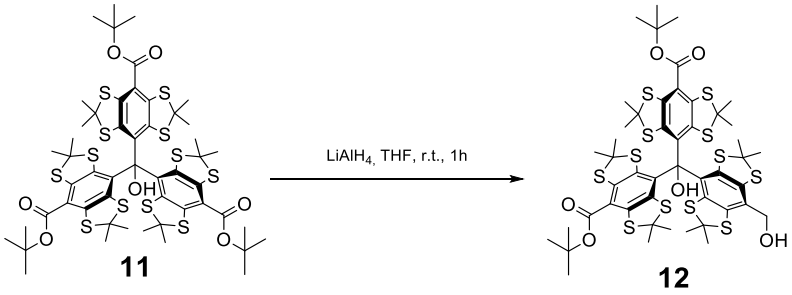

11 **12**

Trityl alcohol **11** (345 mg, 0.29 mmol) was dissolved in 15 mL THF, in parallel a solution of lithium aluminum hydride (170 mg, 4.47 mmol in 10 mL THF, 0.45 mmol mL^{-1}) was prepared. Then, the reduction was started by addition of 0.5 mL (0.23 mmol, 0.78 eq.) of the $LiAlH_4$ solution to the reaction mixture. After stirring for 5 min, the conversion was checked by TLC on SiO_2 eluting with CyH/EtOAc (2:1), where the product appears at $R_f = 0.78$ below the starting material. It was continued with a repetitive addition of 0.25 mL $LiAlH_4$-solution and evaluation by TLC after 5 min, until significant amounts of the twofold reduction product occur. Then, the reaction mixture was quenched by slow addition of 30 mL water and extracted with diethyl ether. The organic phase was separated and dried over $MgSO_4$, after removal of the solvents, an orange crude product was obtained, which was purified by column chromatography on silica eluting with CyH/EtOAc (2:1, *v/v)*. The product **12** was isolated as a yellow solid ($R_f = 0.78$) in a yield of 136 mg (42 %, 58 % brsm). Note, that the starting material (93 mg, 0.08 mmol, 27 mol%) could be recovered and used again in order to maximize the yield of this statistical transformation.

^{1}H-NMR (700 MHz, $CDCl_3$, 298 K, δ in ppm): 6.68 (s, 1H), 4.71 (d, $^{2}J_{H,H}$ = 12.4 Hz, 1H), 4.66 (d, $^{2}J_{H,H}$ = 12.4 Hz, 1H), 1.79 (s, 6H), 1.78 (s, 3H), 1.77 (s, 3H), 1.77 (s, 3H), 1.73 (s, 3H), 1.72 (s, 3H), 1.71 (s, 3H), 1.66 (s, 3H), 1.65 (s, 9H), 1.65 (s, 9H), 1.63 (s, 3H), 1.62 (s, 3H).

$^{13}C\{^{1}H\}$-NMR (176 MHz, $CDCl_3$, 298 K, δ in ppm): 165.58, 141.48, 141.43, 141.38, 141.05, 140.59, 140.50, 140.42, 140.20, 139.26, 138.53, 137.88, 137.72, 134.53, 134.42, 130.95, 130.56, 123.04, 122.98, 84.48, 84.39, 84.27, 66.04, 63.36, 62.57, 61.99, 61.07, 60.86, 60.83, 35.01, 34.86, 34.04, 33.36, 32.02, 31.17, 30.13, 29.69, 29.33, 28.55, 27.89, 27.86, 27.58.

HRMS (MALDI+, DCTB-matrix, *m/z,* $[M]^+$): calc. for $C_{48}H_{58}O_6S_{12}$, 1114.0876; found 1114.0884.

2.2.7 Synthesis of **14**

Bis{[2,2,6,6-tetramethyl-8-(carboxy-tert-butyl)benzo[1,2-d;4,5-d]bis(1,3-dithiol)-4-yl]}-{[2,2,6,6-tetramethyl-8-(1-methyl(3aRS,4SR,7RS,7aSR-4,7-epoxy-3,3a,7,7a-tetrahydro-2H-isoindoli-1,3-dione-2-yl)-(1[1,2-d;4,5-d]bis(1,3-dithiol)-4-yl]}methanol

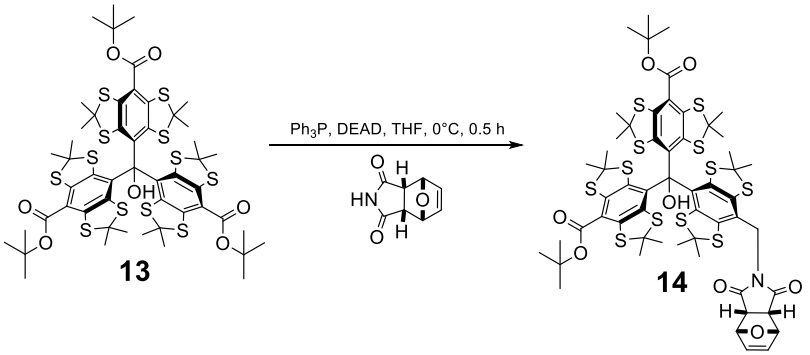

Trityl alcohol **12** (34 mg, 30.5 µmol), triphenyl phosphine (15 mg, 57.2 µmol, 1.87 eq.), and 3aRS,4SR,7RS,7aSR-4,7-epoxy-3,3a,7,7a-tetrahydro-2H-isoindoli-1,3-dione (10 mg, 60.6 µmol, 1.98 eq.) were dissolved in 1.5 mL dry THF under argon. Then, the reaction mixture was cooled down to 0 °C and 14 µL diethylazodicarboxylate (DEAD, 14 µL, 15.5 mg, 89.3 µmol, 2.92 eq.) were added, whereupon an immediate color change from orange to dark brown was observed. After stirring for 30 min at 0 °C, TLC (SiO_2, CyH/EtOAc 2:1, *v/v*) showed complete consumption of the starting material and water (10 mL) was added. The mixture was extracted with CH_2Cl_2 and the organic phase was separated and dried over $MgSO_4$. After removal of the solvents under reduced pressure, column chromatography on silica eluting with CyH/EtOAc (2:1 *v/v)* was performed in order to isolate the product (R_f = 0.43) as a yellow solid in a yield of 27 mg (70 %).

^{1}H-NMR (700 MHz, $CDCl_3$, 298 K, δ in ppm): 6.66 (s, 1H), 6.46 (dd, $^3J_{H,H}$ = 5.8, $^3J_{H,H}$ = 1.6 Hz, 1H), 6.43 (dd, $^3J_{H,H}$ = 5.9, $^3J_{H,H}$ = 1.6 Hz, 1H), 5.30 – 5.27 (m, 2H), 4.59 (d, $^2J_{H,H}$ = 14.6 Hz, 1H), 4.48 (d, $^2J_{H,H}$ = 14.6 Hz, 1H), 3.54 – 3.46 (m, 2H), 1.78 (s, 3H), 1.77 (s, 3H), 1.76 (s, 9H), 1.73 (s, 3H), 1.72 (s, 3H), 1.69 (s, 3H), 1.67 (s, 3H), 1.65 (s, 15H), 1.64 (s, 9H), 1.62 (s, 3H).

^{13}C{^{1}H}-NMR (176 MHz, $CDCl_3$, 298 K, δ in ppm): 173.90, 173.72, 165.60, 165.57, 141.51, 141.44, 141.36, 141.12, 140.72, 140.67, 140.53, 140.29, 139.33, 138.84, 138.57, 137.61, 134.97, 134.84, 134.50, 134.35, 130.65, 125.18, 123.02, 122.97, 84.47, 84.38, 84.28, 79.53, 63.39, 62.58, 62.14, 60.98, 60.88, 60.81, 46.15, 46.13, 44.00, 34.99, 34.92, 34.00, 33.27, 32.17, 31.41, 29.85, 29.81, 29.13, 28.55, 27.66, 27.54, 27.51.

HRMS (MALDI+, DCTB-matrix, *m/z,* [M-furane]$^+$): calc. for $C_{52}H_{59}NO_7S_{12}$, 1193.0935; found 1193.0922.

Note that **14** underwent Retro-Diels-Alder cleavage during mass-spectrometry, so that no M^+-peak was found neither in MALDI nor in ESI.

2.2.8 Synthesis of **15•**

Bis{[2,2,6,6-tetramethyl-8-carboxylbenzo[1,2-d;4,5-d]bis(1,3-dithiol)-4-yl]}-{[2,2,6,6-tetramethyl-8-(1-methyl(3aRS,4SR,7RS,7aSR-4,7-epoxy-3,3a,7,7a-tetrahydro-2H-isoindoli-1,3-dione-2-yl)-benzo[1,2-d;4,5-d]bis(1,3-dithiol)-4-yl]}methyl radical

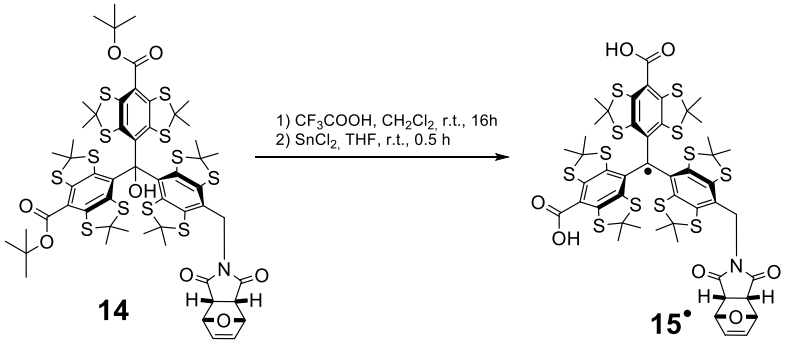

Trityl alcohol **14** (15 mg, 11.9 µmol) was dissolved in 100 µL dry CH_2Cl_2 under an argon atmosphere. Then, 2.0 mL CF_3COOH were added, whereupon the reaction mixture turned dark green. After stirring overnight, tin(II)-chloride (3.3 mg in 100 µL tetrahydrofurane, 17.8 mmol, 1.5 eq.) was added, whereupon a color change to brown was observable. After additional stirring for 15 min, all liquids were removed through high vacuum and the residue was taken up in 5 mL dichloromethane. The organic phase was washed with water, separated, and dried over $MgSO_4$. After removal of the solvents, a brown residue was obtained, which was purified by MPLC on RP-C18-silica eluting with CH_3CN/H_2O 4:1 (*v/v*). The first fraction was isolated and solvents were removed under reduced pressure obtaining **15** as a brown solid in a yield of 14 mg (95 %).
UHPLC (60 % CH_3CN, 40 % H_2O; each with 0.05 % CF_3COOH; t_r): 1.81 min
HRMS (MALDI+, DCTB-matrix, *m/z,* $[M]^+$): calc. for $C_{48}H_{46}NO_7S_{12}$, 1131.9917; found 1131.9906
cw-EPR (X-Band, DMSO, 200 µM, 298 K): g-value = 2.0034; A_N = 1.51 MHz, A_H = 3.39 MHz, A_H = 5.16 MHz, $A_{C,central}$ = 66.10 MHz, $A_{C,ipso}$ = 31.11 MHz, $A_{C,ortho}$ = 25.43 MHz, $A_{C,para}$ = 6.83 MHz, $A_{C,meta}$ = 3.51 MHz.

2.2.9 Synthesis of **9•**

Bis{[2,2,6,6-tetramethyl-8-carboxylbenzo[1,2-d;4,5-d]bis(1,3-dithiol)-4-yl]}-{[2,2,6,6-tetramethyl-8-(1-methyl(3,4-dehydropyrolidin-1,3-dione-2-yl)-benzo[1,2-d;4,5-d]bis(1,3-dithiol)-4-yl]}methyl radical

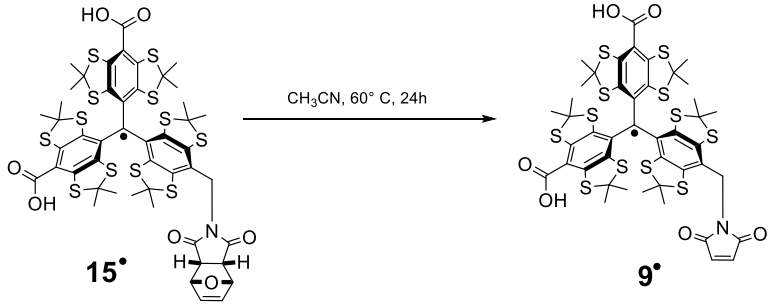

Trityl radical 15**•** (10 mg, 8.8 µmol) was suspended in 5 mL dry degassed acetronitrile and stirred at 60 °C for 24 h under argon atmosphere. All volatiles were removed in high vacuum and the product was obtained as a brown solid in quantitative yield of 9 mg.
UHPLC (60% CH_3CN, 40% H_2O; each with 0.05% CF_3COOH; t_r): 2.04 min
HRMS (MALDI+, DCTB-matrix, *m/z,* [M-furane]$^+$): calc. for $C_{44}H_{42}NO_6S_{12}$, 1063.966; found 1063.968
cw-EPR (X-Band, DMSO, 200 µM, 298 K): g-value = 2.0034; A_N = 1.48 MHz, A_H = 3.48 MHz, A_H = 6.06 MHz, $A_{C,central}$ = 66.16 MHz, $A_{C,ipso}$ = 31.22 MHz, $A_{C,ortho}$ = 25.45 MHz, $A_{C,para}$ = 6.86 MHz, $A_{C,meta}$ = 3.57 MHz.

2.3 Analytical Data Synthesis

2.3.1 NMR Spectra

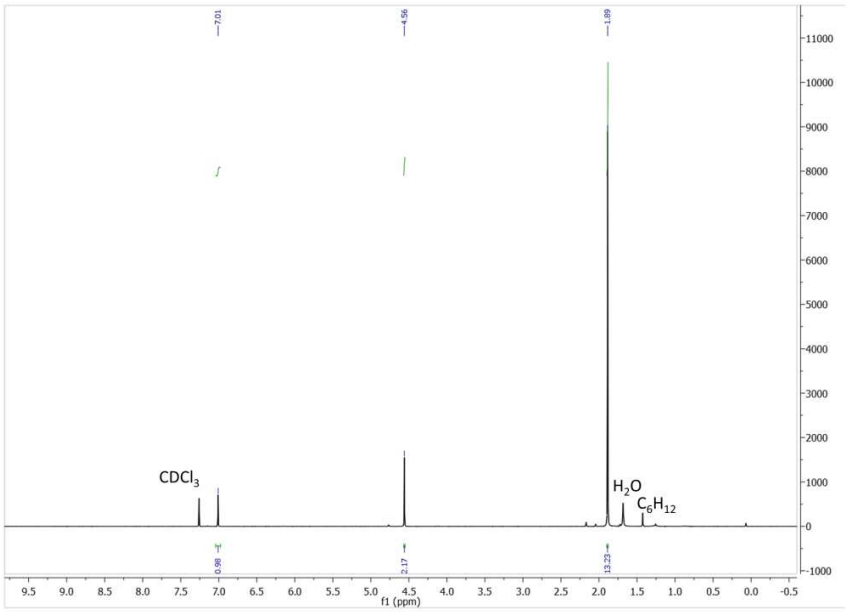

***Figure S2**: ^{1}H-NMR (500 MHz, 298 K, $CDCl_3$) of **S2**.*

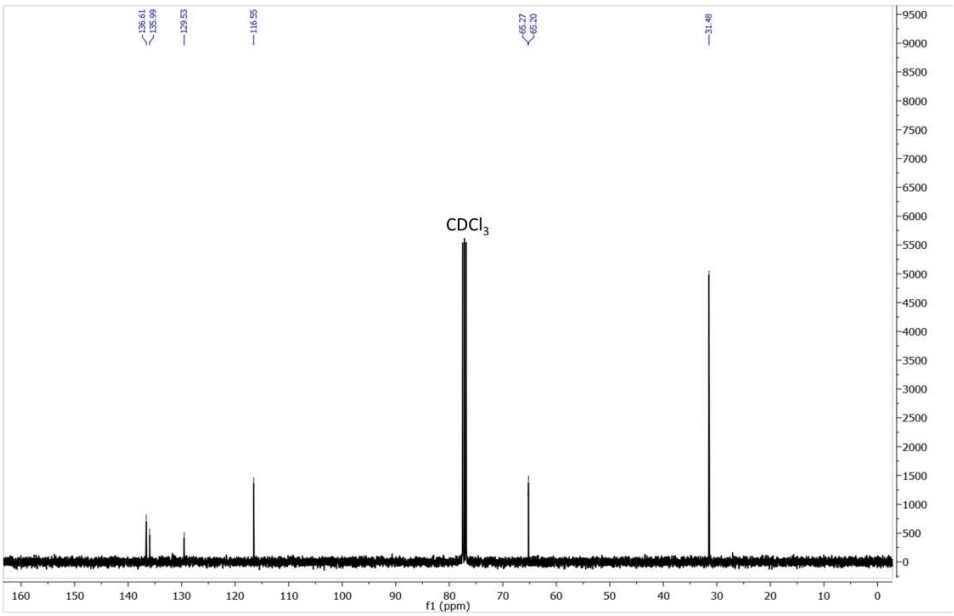

Figure S3**: $^{13}C\{^{1}H\}$-NMR (125 MHz, 298 K, $CDCl_3$) of **S2

298

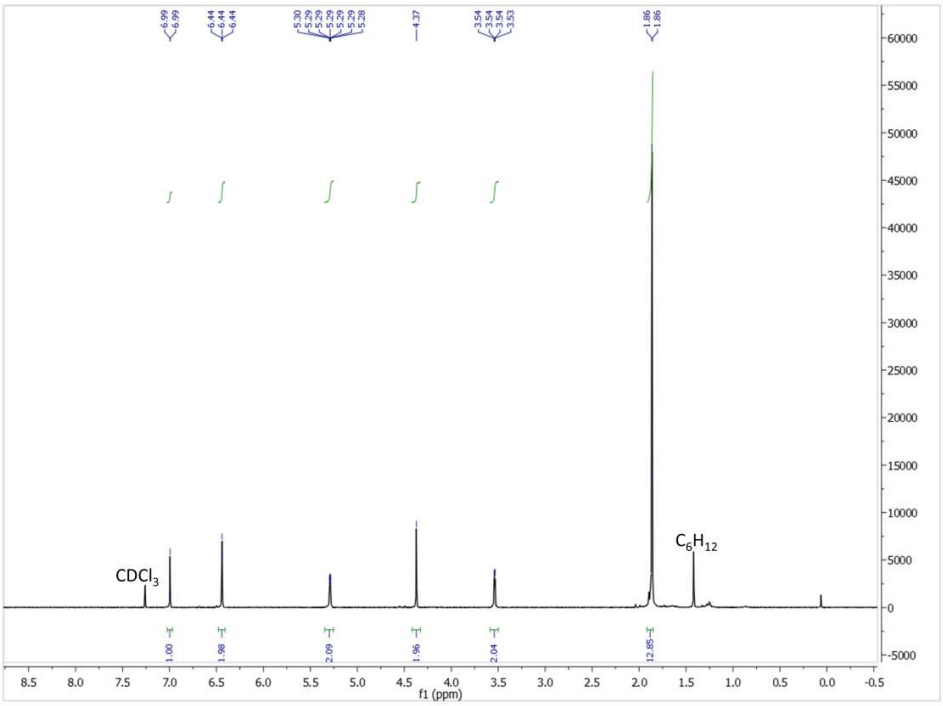

***Figure S4**: [1]H-NMR (500 MHz, 298 K, $CDCl_3$) of **S3**.*

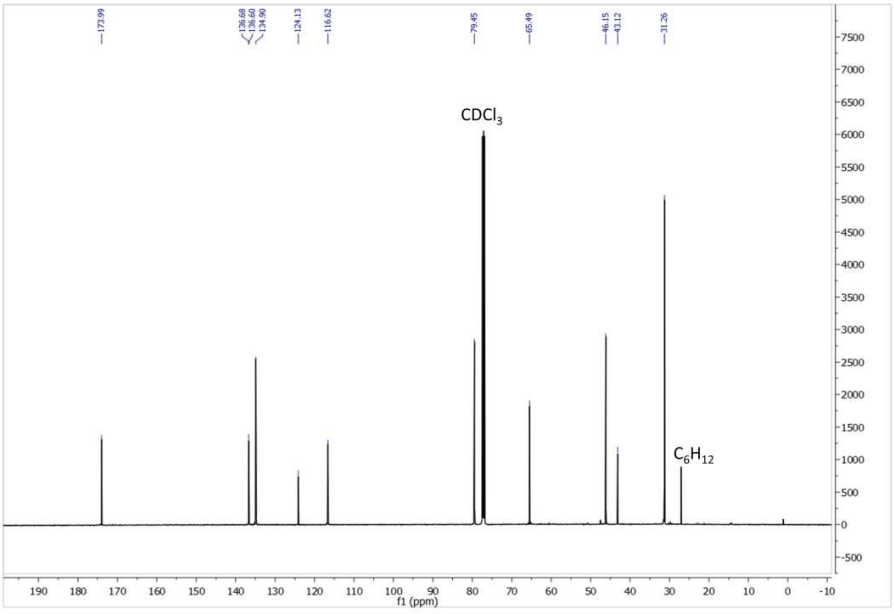

***Figure S5**: [13]C{[1]H}-NMR (125 MHz, 298 K, $CDCl_3$) of **S3**.*

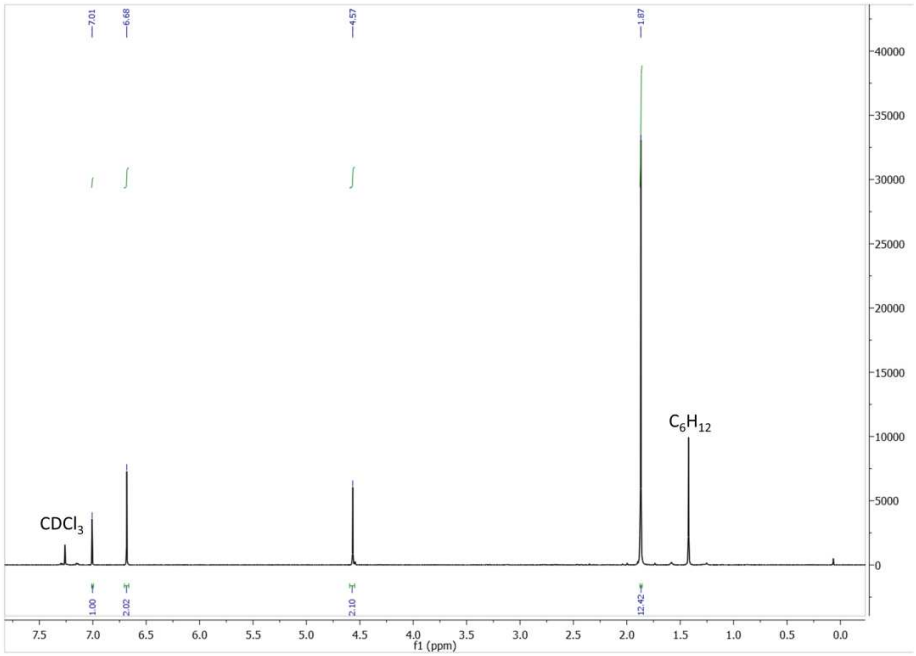

***Figure S6**: ^{1}H-NMR (500 MHz, 298 K, $CDCl_3$) of **S4**.*

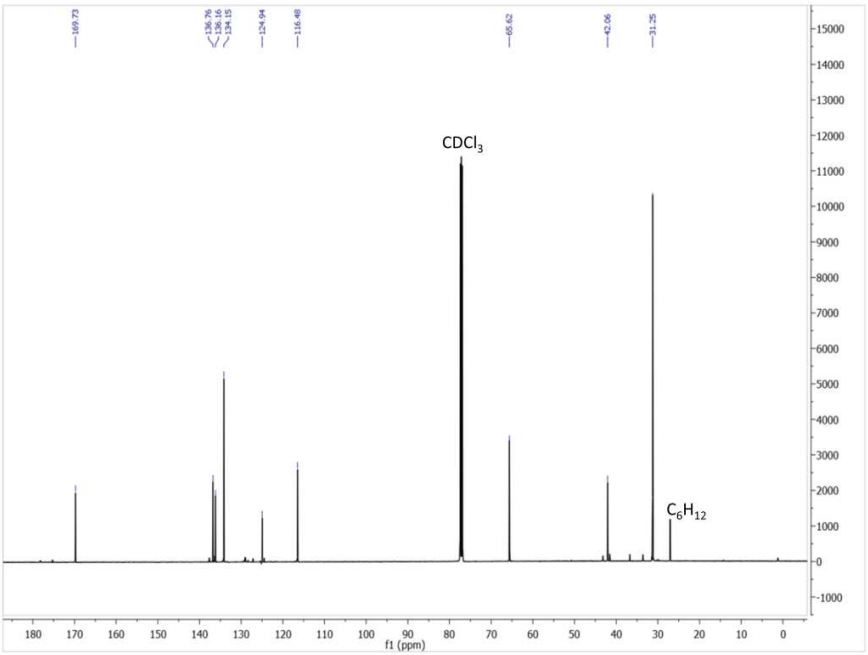

***Figure S7**: $^{13}C\{^{1}H\}$-NMR (125 MHz, 298 K, $CDCl_3$) of **S4**.*

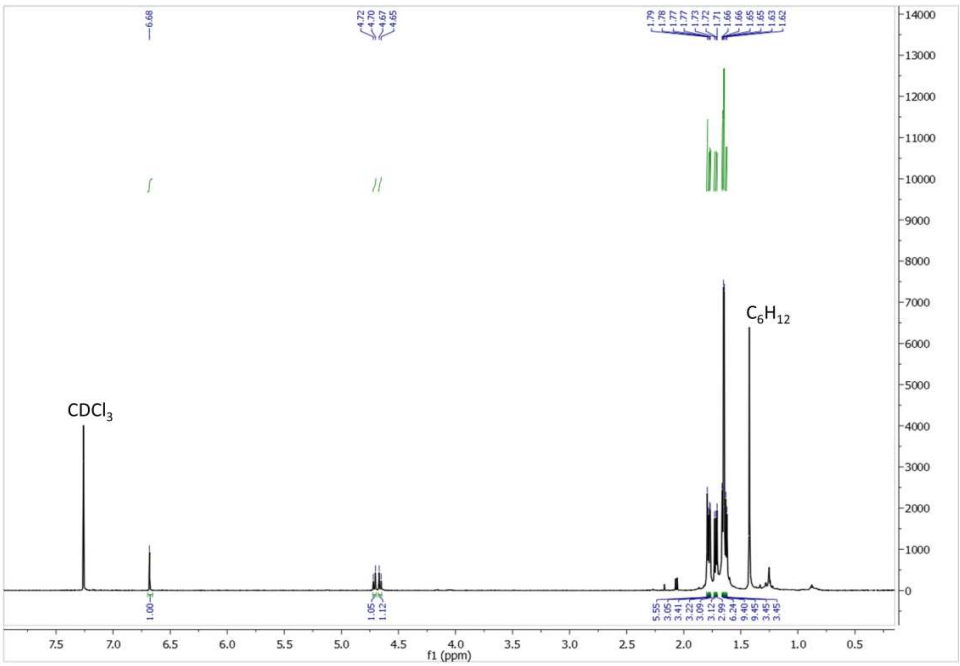

***Figure S8**: [1]H-NMR (700 MHz, 298 K, $CDCl_3$) of **12**.*

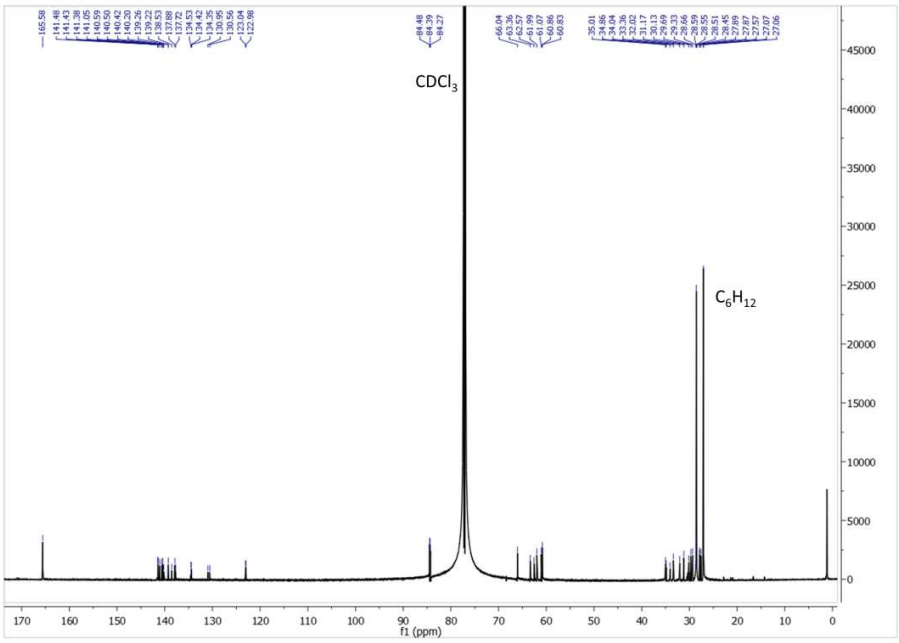

***Figure S9**: [13]C{[1]H}-NMR (176 MHz, 298 K, $CDCl_3$) of **12**.*

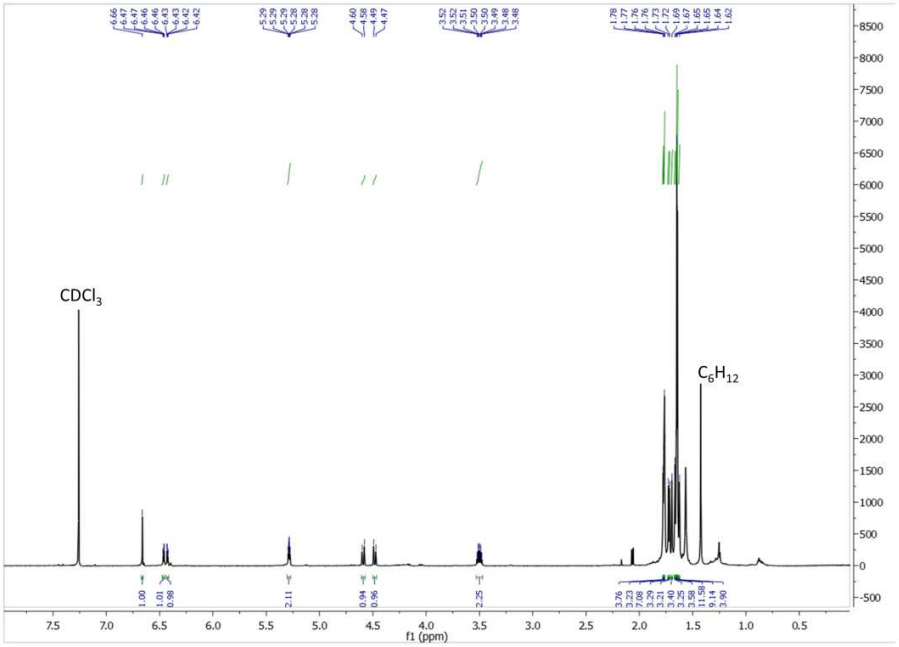

***Figure S10**: [1]H-NMR (700 MHz, 298 K, $CDCl_3$) of **14**.*

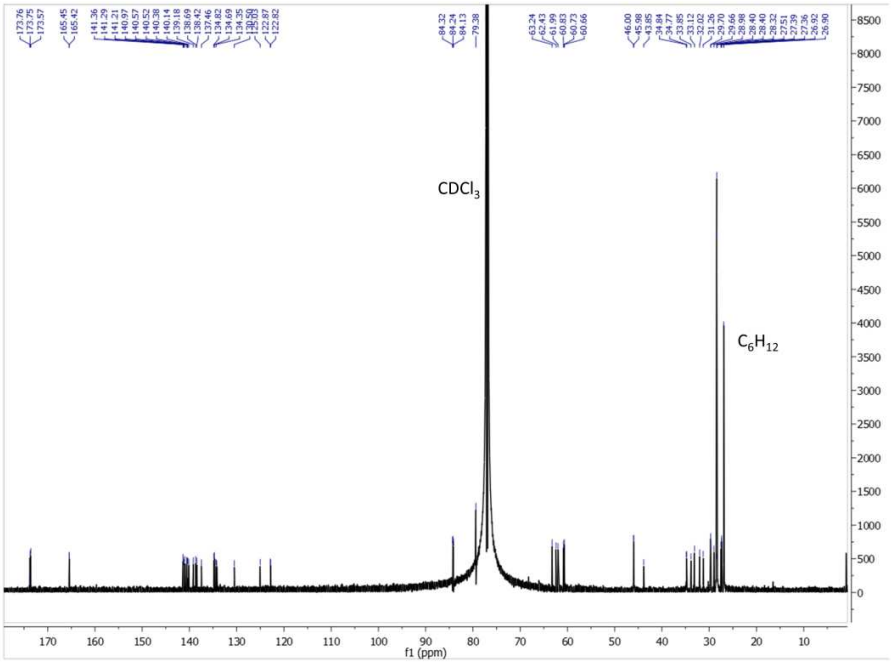

***Figure S11**: [13]C{[1]H}-NMR (176 MHz, 298 K, $CDCl_3$) of **14**.*

2.3.2 HRMS-Data

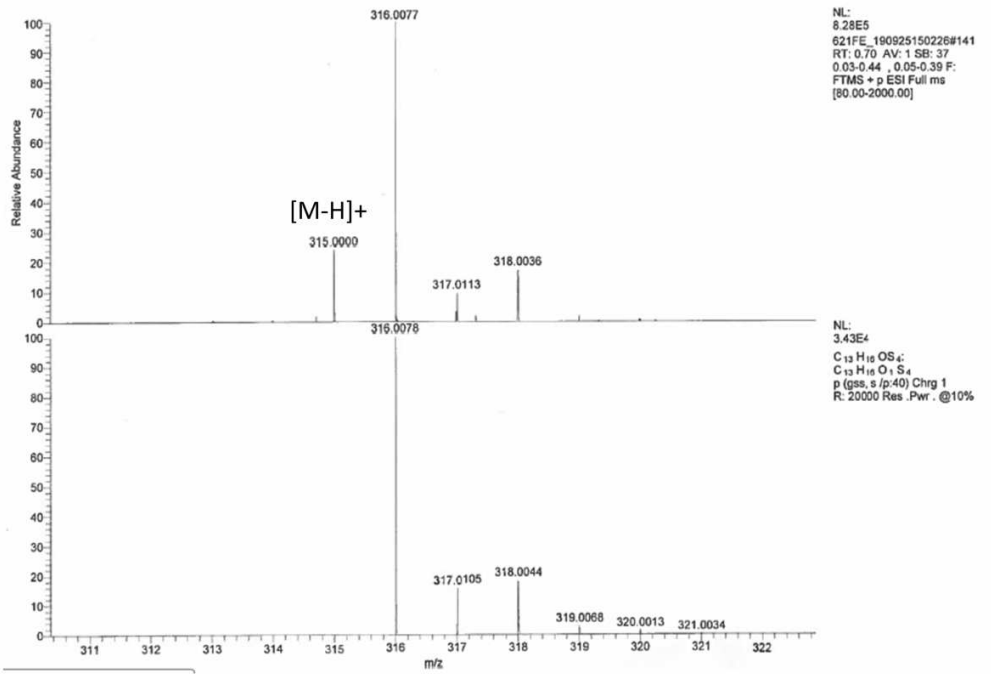

***Figure S12**: ESI(+)-HRMS (top) of **S2** and calculated isotope pattern for M^+ (bottom).*

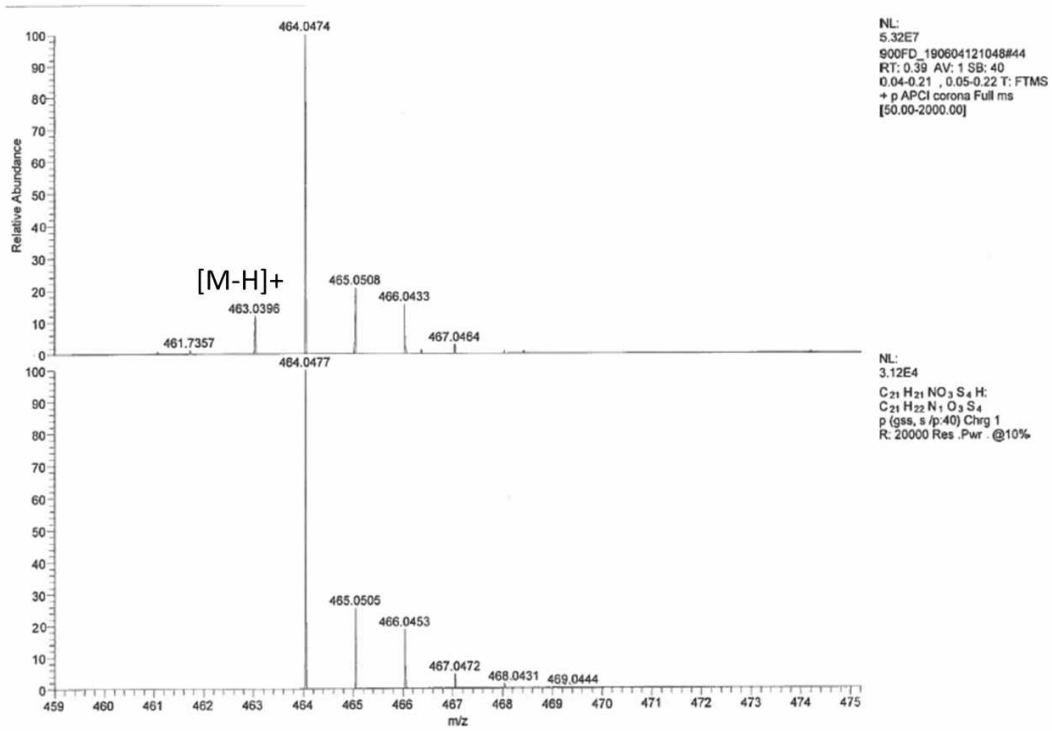

***Figure S13**: APCI-HRMS (top) of **S3** and calculated isotope pattern for $[M+H]^+$ (bottom).*

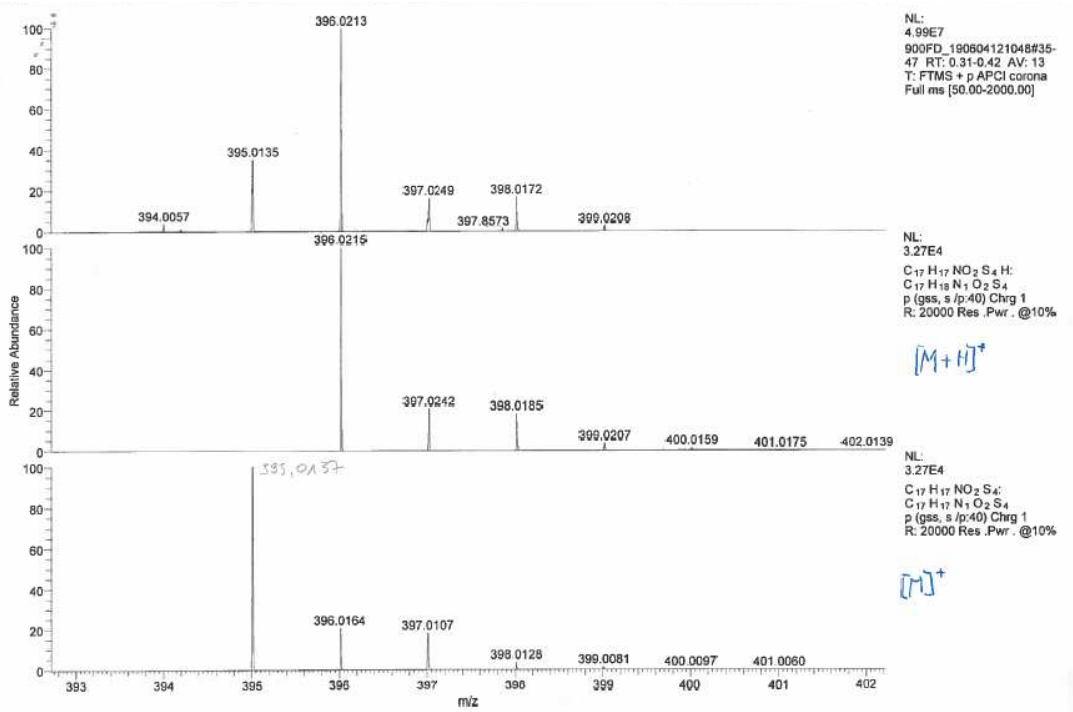

***Figure S14**: APCI-HRMS (top) of **S4** and calculated isotope patterns (bottom).*

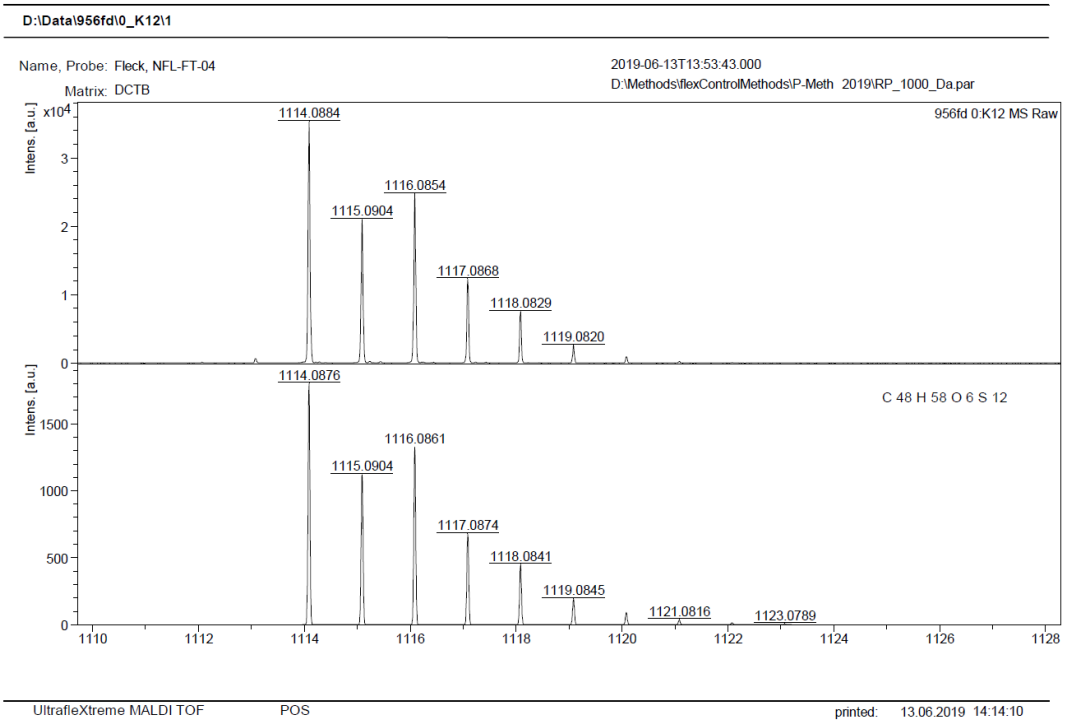

***Figure S15**: MALDI(+)-HRMS (top) of **12** and calculated isotope pattern for M^+ (bottom).*

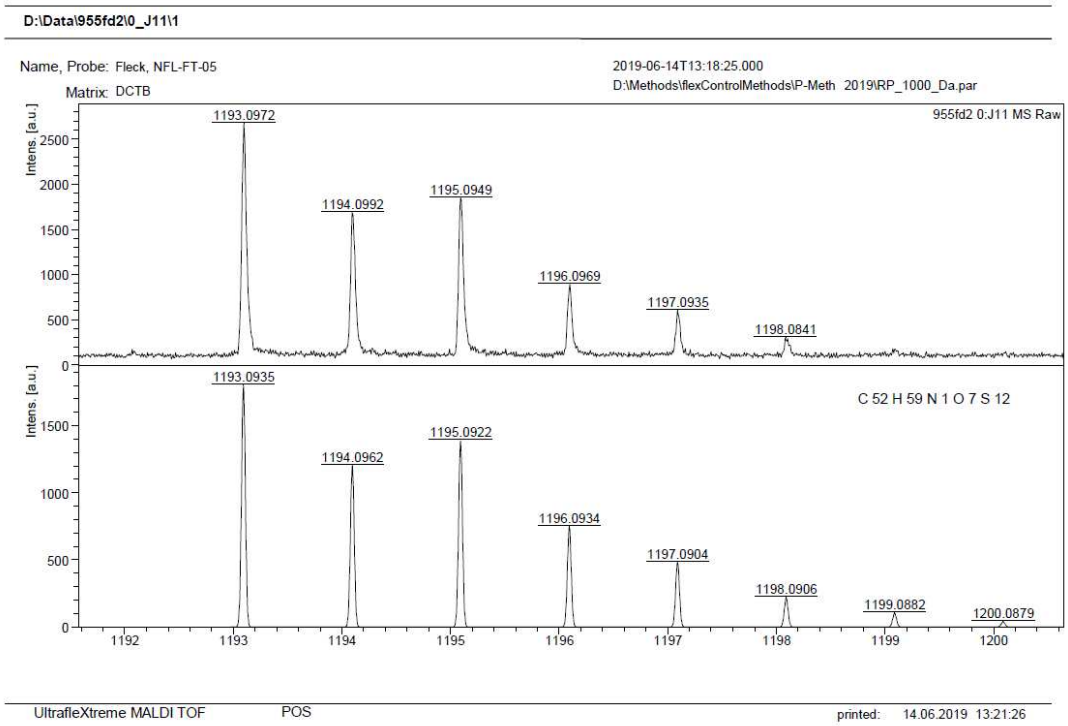

***Figure S16**: MALDI(+)-HRMS (top) of **14** and calculated isotope pattern for M^+ (bottom).*

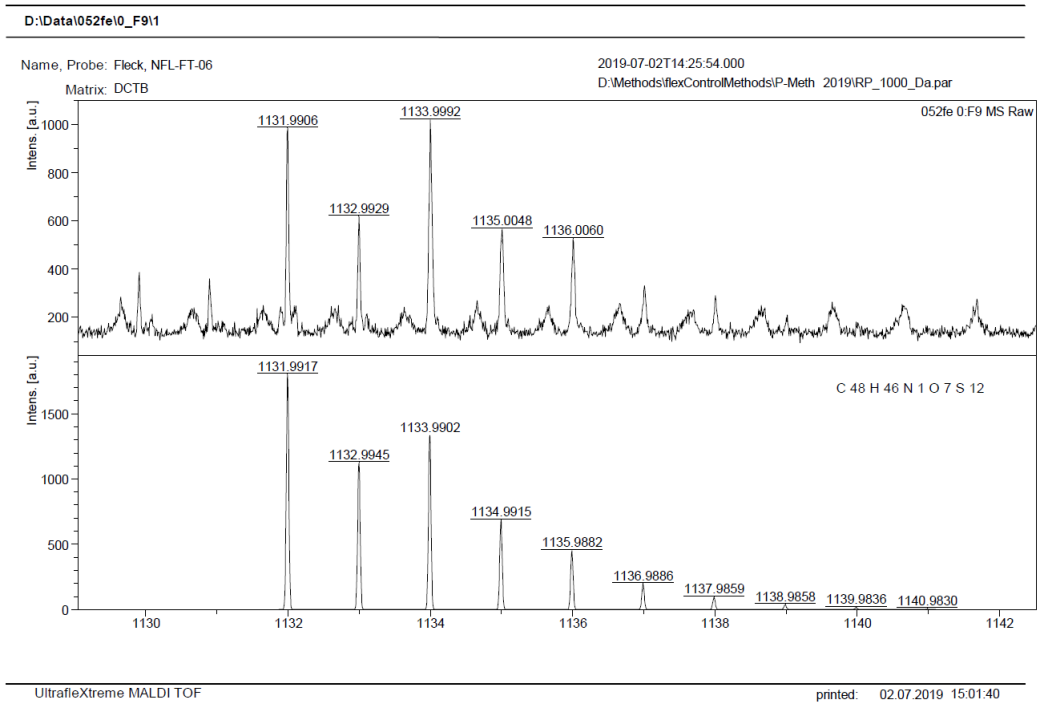

***Figure S17**: MALDI(+)-HRMS (top) of **15•** and calculated isotope pattern for M^+ (bottom). Note, that the $[M]^+$-peak shown here is not the base peak due to Retro-Diels-Alder fragmentation in the mass spectrometer and therefore suffers from low intensity. The regularly appearing noisy peaks belong to the spectrometer background.*

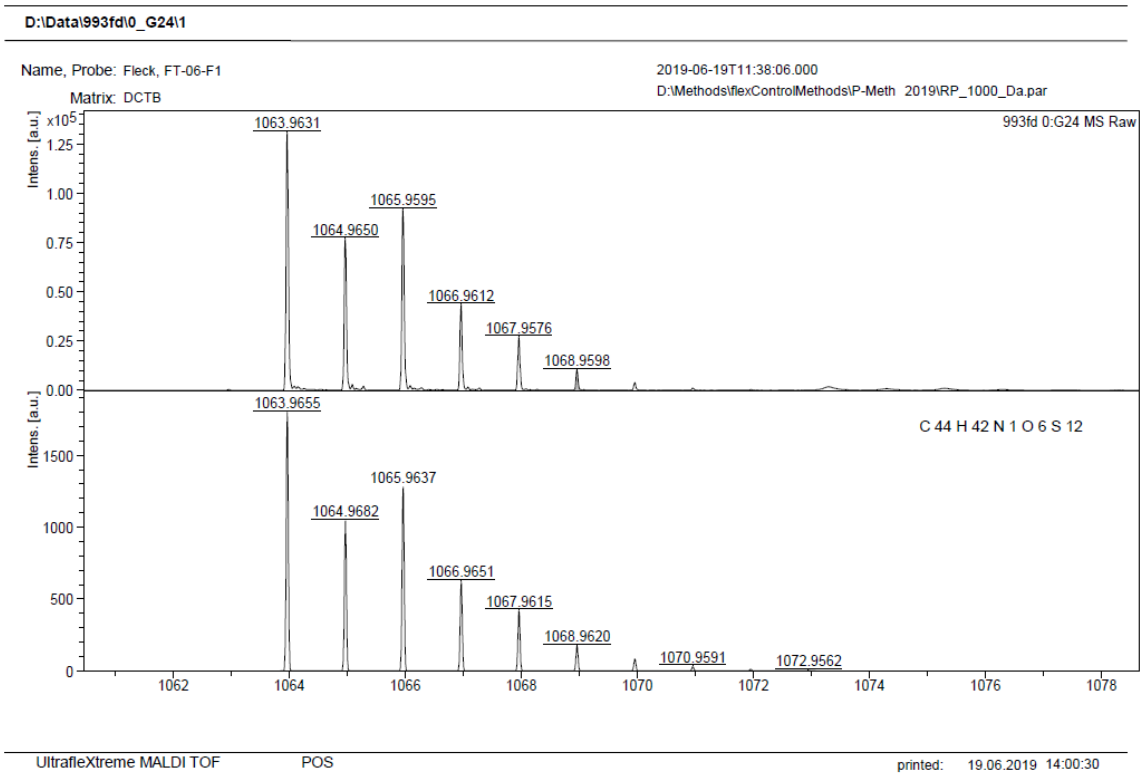

***Figure S18**: MALDI(+)-HRMS (top) of **9•** and calculated isotope pattern for M^+ (bottom).*

2.3.3 UHPLC Data

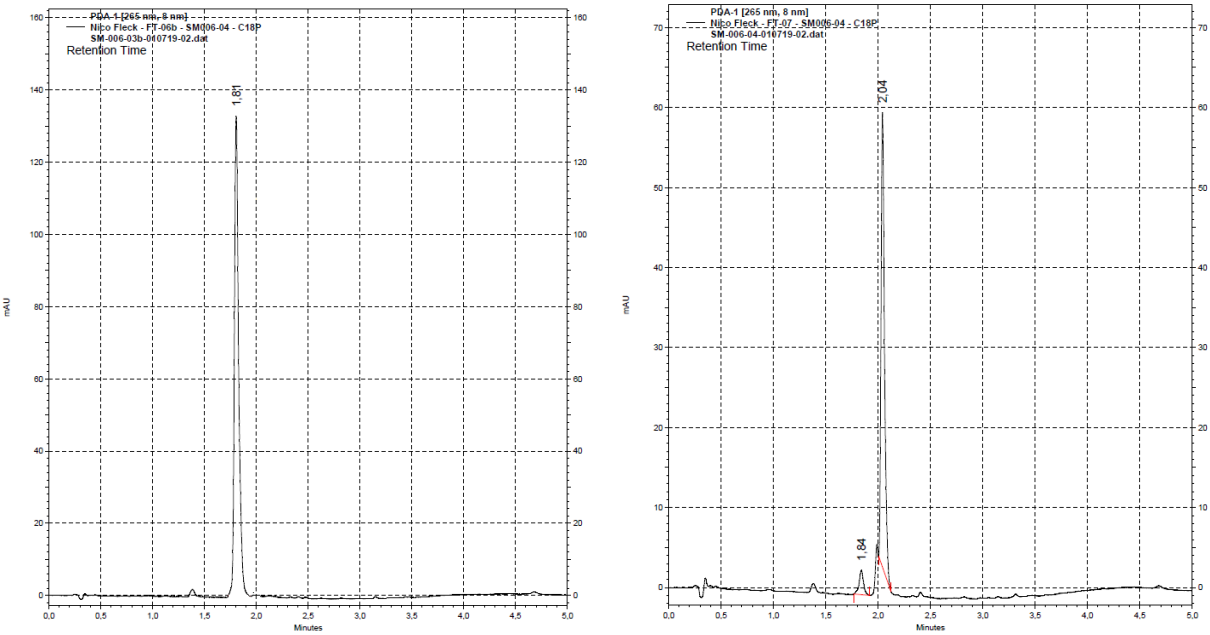

***Figure S19**: UHPLC chromatogram of **15•** (left) and of **9•** (right).*

3. Spin Labeling

3.1 Tetraethylnitroxide-DNA Construct

Since the isoindoline based tetraethylnitroxide **S5** does not possess sufficient solubility in aqueous environments, it was conjugated to a DNA strand. This yielded a water-soluble construct, which is suitable for stability measurements.

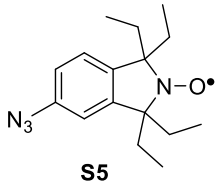

S5

For this, a DNA strand (5' GGG TGX CTG GTA CCC 3', obtained from *Metabion,* X = 5-ethynyl-2'dU) was labeled with **S5**[7] using our recently published protocol.[8] Annealing of the labeled strand with the complementary unmodified strand provided the singly labeled DNA duplex used for the stability studies.

3.2 SLIM Dilution Series and Calibration Curve

To create a stock solution of **9•** for subsequent protein labeling, the free label **9•** was dissolved in DMSO. Since potential weighing errors may have severe impact on the correctness of all following quantification routines, five independent EPR spin count experiments with the DMSO stock diluted 1:100 in POi buffer (20 mM POi pH 6.8, 50 mM NaCl) were performed on an EMXnano EPR spectrometer. The final concentration based on the mean value of these measurements accounted to 2.58 mM of **9•**.
A dilution series of **9•** in POi buffer was set up and measured on a Cary 100 UV-vis spectrometer (Agilent Technologies, Santa Clara, CA, USA) and the molar extinction coefficients of **9•** at 271 nm and 459 nm were determined via linearization according to the *Lambert-Beer law*.

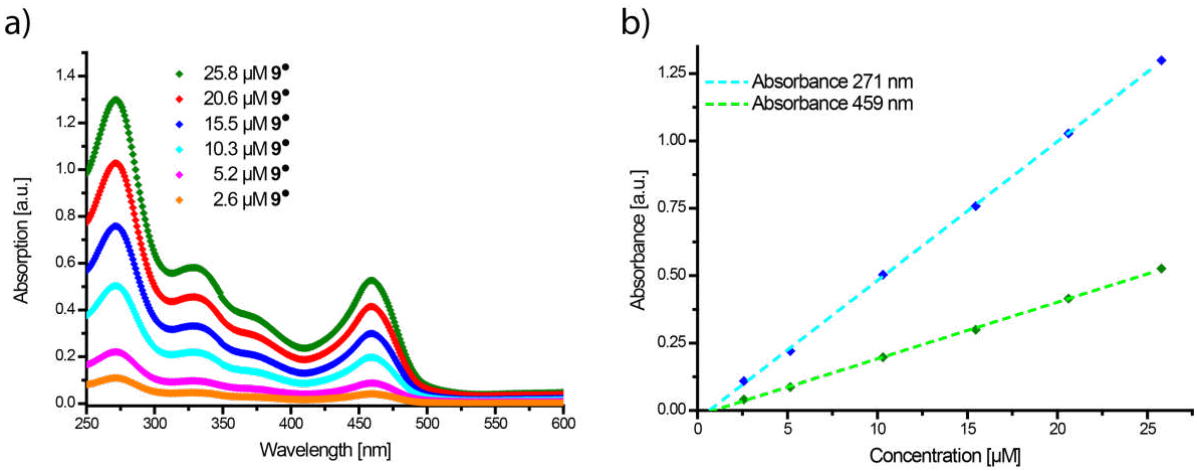

***Figure S20**: UV-vis dilution series of **9•** (a) and the linear fits of the absorbance at 271 nm (cyan) and 459 nm (green) (b).*

*Table S1: Extinction coefficients of **9•** at 271 nm and 471 nm.*

Wavelength [nm]	Extinction coefficient ε $\left[\frac{L}{\mu mol \cdot cm}\right]$
271	0.05152
459	0.02099

The labeling efficiencies of YopO in each labeling experiment using trityls **9•** or **8•** were determined using the previously implemented technique.[9] Since the protein itself only absorbs at ~280 nm and both trityl labels show a second absorption maximum at 459 nm (**9•**) or 467 nm (**8•**), the protein and respective trityl concentrations can be determined as follows:

$$c_{trityl} = \frac{A_{459/467}}{d \cdot \varepsilon_{trityl}}$$

$$c_{YopO} = \frac{A_{271} - c_{trityl} \cdot d \cdot \varepsilon_{271,trityl}}{d \cdot \varepsilon_{280,YopO}}$$

Although slight shifts in the absorption maxima wavelengths are seen for both trityl labels upon bioconjugation, the errors resulting from these shifts are negligible. The extinction coefficient of YopO was calculated using the computing tool ProtParam.[10] All utilized extinction coefficients are listed in Table S2.

*Table S2: Extinction coefficients of YopO, **8•** and **9•**.*

Protein/Trityl	ε $\left[\frac{L}{\mu mol \cdot cm}\right]$
YopO	ε_{280} = 0.04939
9•	ε_{271} = 0.05152 ε_{459} = 0.02099
8•	ε_{280} = 0.01930 ε_{467} = 0.00750

3.3 *Yersinia* outer protein O (YopO)

3.3.1 Construct Design

Truncated $YopO_{89\text{-}729}$ C219A (YopO-WT) from *Yersinia enterocolitica* was cloned in frame into the pGex6p1 vector (GE Healthcare, Chicago, IL, USA), transformed into *E.coli* DH5α cells and amplified. This construct served as the template for further mutagenesis and cysteine introduction via *QuickChange* mutagenesis[11] for YopO N624C and YopO Y588C/N624C. The primers are listed in Table S3.

Table S3: YopO primer pairs

	Sequence
Y588C *fwd*	5'-CAAGGGCAGCCCGTGTCCTCTGAAACCTGTAGCTTCC-3'
Y588C *rev*	5'-GACCTTAGCCTCAGCTAATCGATTCAGGAAGCTACAGGTTTCAG-3'
N624c *fwd*	5'-GAGAGTGCGAAAGCGCAACTATCTATTCTGATTTGTCGTTCAG-3'
N624C *rev*	5'-GAGCAACATCAGCCCAAGAACCTGAACGACAAATCAGAATAG-3'

After PCR, the new constructs were transformed into *E.coli* DH5α cells and the successful mutagenesis was confirmed *via* Sanger sequencing.

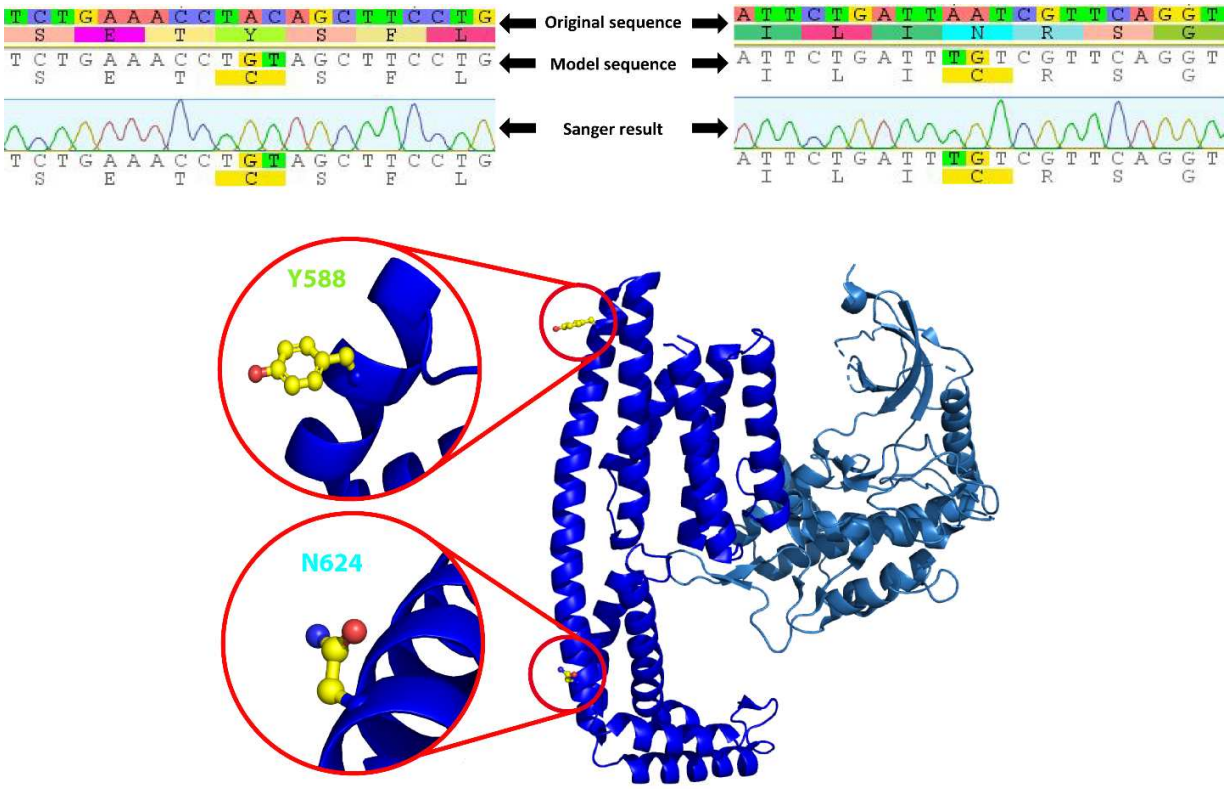

***Figure S21**: Sequencing results for YopO Y585C/N624C (top, excerpt taken from Geneious (Biomatters Ltd., Auckland, New Zealand)). PyMOL (Schrödinger, New York, NY, USA) representation showing the locations of the unmutated amino acid positions in YopO (PDB-ID: 4ci6) (bottom).*

3.3.2 YopO Expression

All YopO constructs were expressed in *E.coli* Rosetta (DE3) cells. From an agar plate, a single colony was picked and grown overnight at 37 °C / 180 rpm in 20 mL LB medium containing 0.3 mM ampicillin and 0.1 mM chloramphenicol. Main-cultures were set up in 1 L LB medium (0.3 mM ampicillin, 0.1 mM chloramphenicol) using 15 mL pre-culture and were incubated at 37 °C / 180 rpm until an OD_{600} of ~0.8 – 1.0 was reached. Protein expression was induced upon the addition of 0.1 mM IPTG (isopropyl β-D-1-thioglactopyranoside) and the cultures were incubated for ~16 h at 16 °C before being harvested after centrifugal separation (4000 rcf, 20 min, 4 °C).

3.3.3 YopO Purification

The cell pellet was re-suspended in 5 time v/w lysis buffer (50 mM Tris-Cl pH 8.0, 150 mM NaCl, 3 mM DTT), lysed twice in a cell disruptor (Constant Systems Limited, Northampton, UK) and the lysate was spun down to remove the insoluble cell debris (48,500 rcf, 20 min, 4 °C). GST sepharose beads were equilibrated with lysis buffer and incubated with the centrifugal supernatant for 1 h at room temperature under slight agitation. The GST-suspension was ran over a gravity column and the flow-through was passed over the settled beads an additional time to maximize the protein yield. The beads were washed with 50 mL of lysis buffer and then incubated in 20 mL elution buffer (50 mM Tris-Cl pH 8.0, 150 mM NaCl, 1 mM DTT, 100 U PreScission protease) overnight at 4 °C whilst slowly shaking. The suspension was filled back into the gravity column and the protein containing flow-through was diluted with 100 mL no-salt buffer (50 mM Tris-Cl pH 8.0) and 125 µL of a 2 M DTT stock were added. An ion-exchange chromatography on an EnrichQ 10/100

column (Bio-Rad Laboratories GmbH, Feldkirchen, Germany) was performed against a linear gradient of high-salt buffer (50 mM Tris-Cl pH 8.0, 1 M NaCl) and the protein containing fractions were pooled and concentrated down below 3.0 mL. The sample was loaded onto a HiLoad Superdex 200 16/600 (GE Healthcare, Chicago, IL, USA) and size-exclusion chromatography was performed in gel filtration buffer (50 mM Tris pH 8.0, 50 mM NaCl). Pure protein (based on SDS-PAGE) was pooled, flash frozen and stored in 100 µL aliquots at –80 °C.

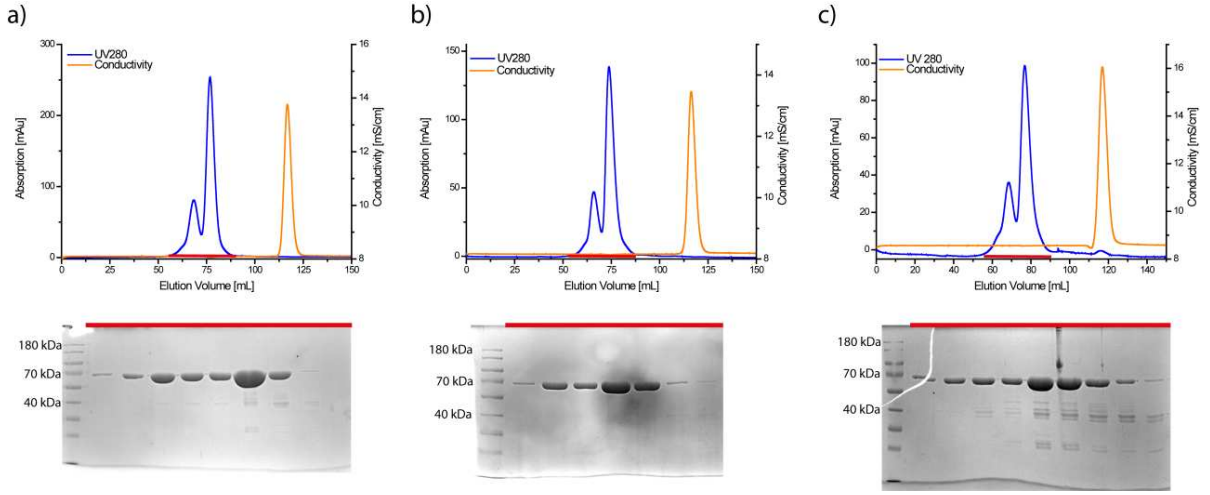

Figure S22: *HiLoad Superdex 200 16/600 gel filtration chromatographs of YopO 0-Cys (a), YopO N624C (b) and YopO Y588C/N624C (c) (top) and the corresponding SDS-PAGE gels of the indicated peaks (red) in the elugram. Note that in each gel filtration chromatograph two distinct absorption peaks are seen with the first one corresponding to non-covalent, homomeric YopO dimers (~140 kDa) and the latter to monomeric YopO proteins (~70 kDa) as also proven by non-reducing SDS-PAGE (not shown here).*

3.3.4 YopO Spin Labeling

Prior to each labeling experiment, 20 nmol of YopO were incubated for 1.5 h at 4 °C in 2.5 mL phosphate buffer (20 mM POi pH 6.8, 50 mM NaCl) containing a five-fold molar excess of TCEP to cleave any YopO multimers. The reducing agent was removed using a PD-10 desalting column and labeling reactions were set up immediately afterwards.

To the 3.5 mL PD-10 protein eluate, a 5-fold molar excess per cysteine (or 5-fold molar excess per YopO for the YopO-WT C219A construct) of SLIM **9•** pre-diluted in 3 mL POi buffer was added resulting in a final concentration of 3.1 µM YopO and 31 µM SLIM trityl respectively. The labeling reaction was incubated for 16 h at 4 °C. Next, the incubation solution was split into five equal fractions of 1.3 mL and passed successively over a PD-10 desalting column using the protocol for volumes less than 2.5 mL to remove any unbound free label remnants. All PD-10 eluate fractions were pooled and concentrated using a VivaSpin 6/50k MWCO (Sartorius, Göttingen, Germany) to less than 2.5 mL. For enhanced separation of any aggregation seeds or unbound label, the concentrated fractions were additionally purified using a HiPrep 26/10 desalting column (GE Healthcare, Chicago, IL, USA). Protein containing fractions were pooled, concentrated down to ~3.0 mL and a UV-vis spectrum was recorded on a Cary 100 UV-vis spectrometer. The labeling efficiencies were calculated as described in SI section 3.2.

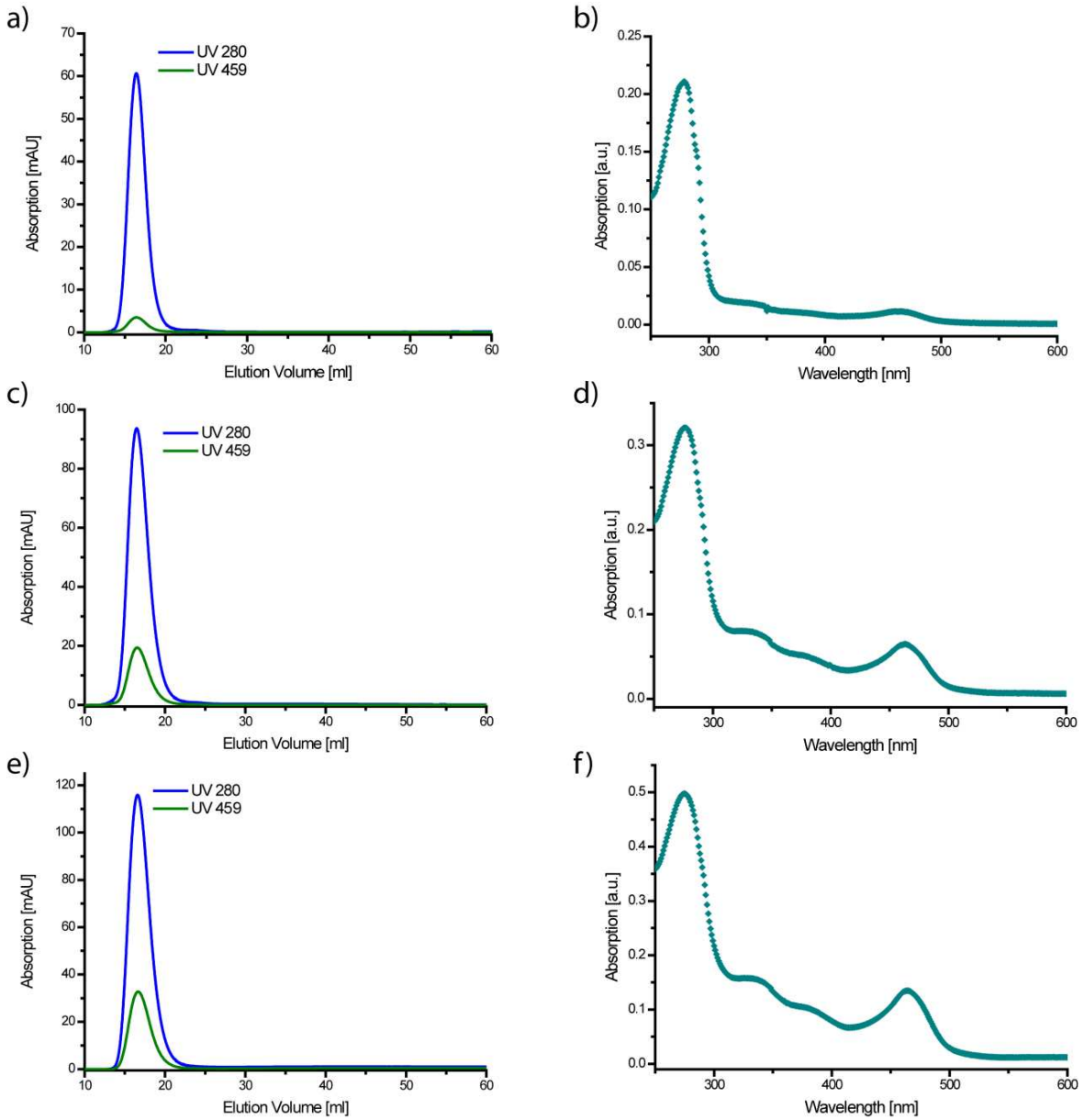

***Figure S23**: Elution chromatographs of the HiPrep 26/10 runs and UV-vis spectra for YopO 0-Cys (a+b), YopO N624C (c+d) and YopO Y588C/N624C (e+f).*

***Table S4**: Labeling efficiencies for YopO labeled with SLIM.*

Construct	Eq. SLIM per protein	Labeling efficiency [%]
YopO-WT	0.071 ± 0.006	7.1 ± 0.6
YopO N624C	0.955 ± 0.088	95.5 ± 8.8
YopO Y588C/N624C	1.916 ± 0.162	95.8 ± 8.8

The YopO Y588C/N624C reference sample labeled with **8•** were generated in exactly the same manner as the SLIM trityl samples, only using **8•** as the trityl species instead. For the **MTSL** reference sample, 20 nmol YopO were incubated with 3 mM DTT in 2.5 mL gel filtration buffer (50 mM Tris-Cl pH 8.0, 50 mM NaCl) for 2 h before removing the reducing agent via a PD-10 desalting column. Labeling reactions were set up

immediately afterwards by addition of a ten-fold molar excess of MTSL per cysteine. The labeling solution was incubated for 16 h at 4 °C. Excess free label was removed via a PD-10 desalting column and the pooled protein fractions were concentrated using a VivaSpin 6/10k MWCO.

All samples that were subjected to *in vitro* pulsed EPR experiments were rebuffered thrice in deuterated PDS buffer (100 mM TES pH 7.4, 100 mM NaCl) using a VivaSpin 6/50k MWCO.

3.3.5 YopO Mass Spectrometry

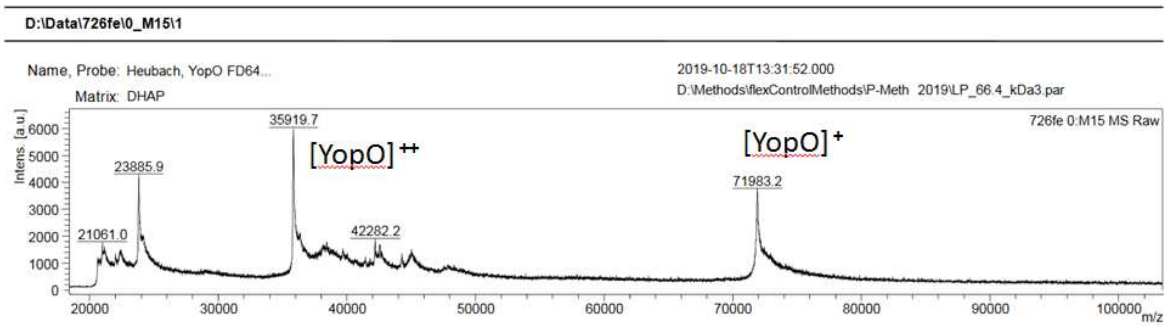

***Figure S24**: MALDI(+)-spectrum of YopO-WT after incubation with SLIM **9**•.*

Figure S24 shows the MALDI(+)-spectrum of YopO-WT after incubation with SLIM as described beforehand. While the peak for the unlabeled protein at 71,983 Da (calc. 72,108 for $C_{3176}H_{5085}N_{897}O_{989}S_{14}$) appears very clear, no signal of unspecifically labeled protein occurs, which would be at least 1,063 Da heavier.

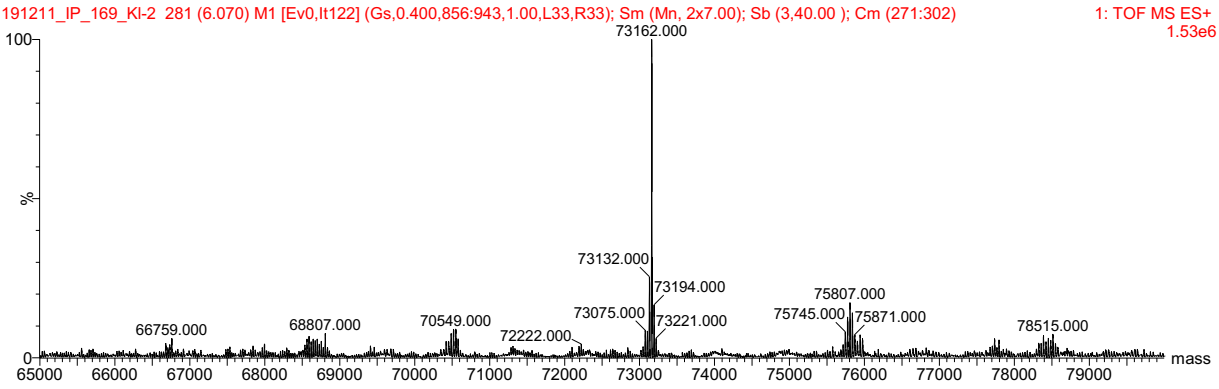

***Figure S25**: High-resolution ESI(+) of YopO N624C labeled with SLIM **9**•.*

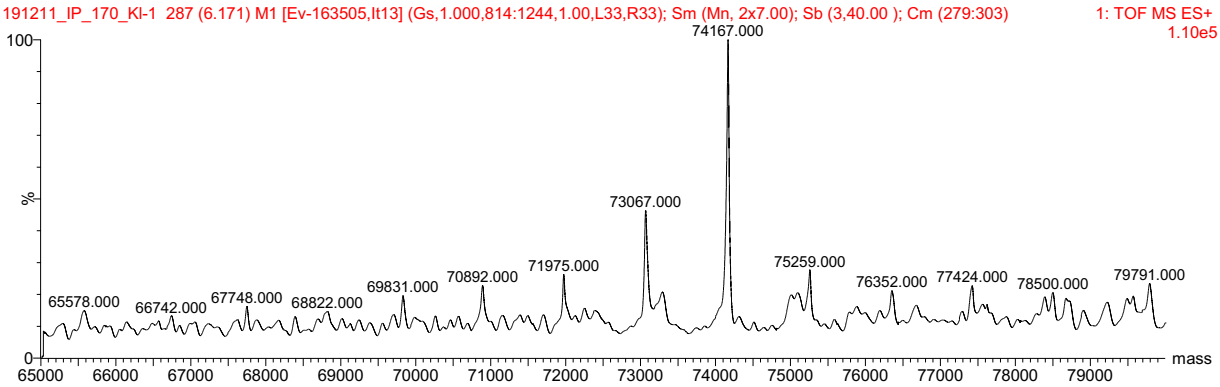

***Figure S26**: High-resolution ESI(+) of YopO Y588C/N624C labeled with SLIM **9•**.*

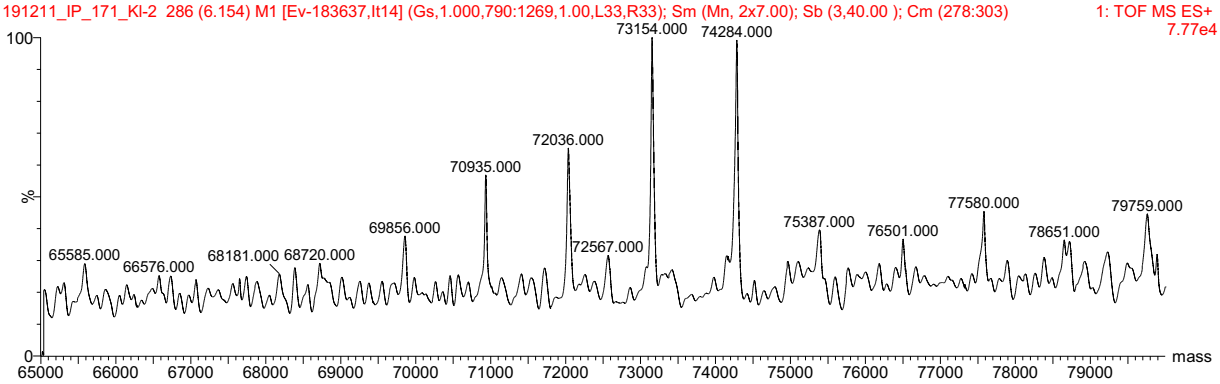

***Figure S27**: High-resolution ESI(+) of YopO Y588C/N624C labeled with **8•**.*

The identity of the labeled proteins was confirmed by high-resolution ESI(+) mass spectrometry as shown in Figures S25 – S27. These spectra clearly prove the chemoselective and successful labeling of the YopO mutants within in an accuracy exceeding 15 ppm.

***Table S5**: Calculated and measured masses for YopO mutants*

Mutant	Sum formula	Calc. mass [Da]	Exp. mass [Da]
YopO N624C /w **9•**	$C_{3219}H_{5126}N_{897}O_{994}S_{27}$	73,162	73,162
YopO Y588C/N624C /w **9•**	$C_{3257}H_{5164}N_{898}O_{999}S_{40}$	74,167	74,167
YopO Y588C/N624C /w **8•**	$C_{3261}H_{5168}N_{898}O_{1003}S_{40}$	74,283	74,284

4. Redox Stability

4.1 Cyclic Voltammetry

Cyclic voltammetry was carried out in a typical three electrode cell equipped with a Luggin capillary and a capacity of 30 mL. The working electrode was a glassy-carbon disc electrode with a surface area of 24.7 mm^2, and a gold sheet with an area of 50 mm^2 was used as the counter electrode. As the reference electrode, a reversible hydrogen electrode (RHE) was constructed from a platinum wire in PBS buffer by forming an H_2-bubble at the wire by electrolysis. For the measurement itself, a Bipotentiostat (Model AFCBP1, PINE research, Durham, NC, USA) and an AD converter connected to LabVIEW (National Instruments, Austin, TX, USA) were used. The cyclic voltammogram was also recorded via LabVIEW.

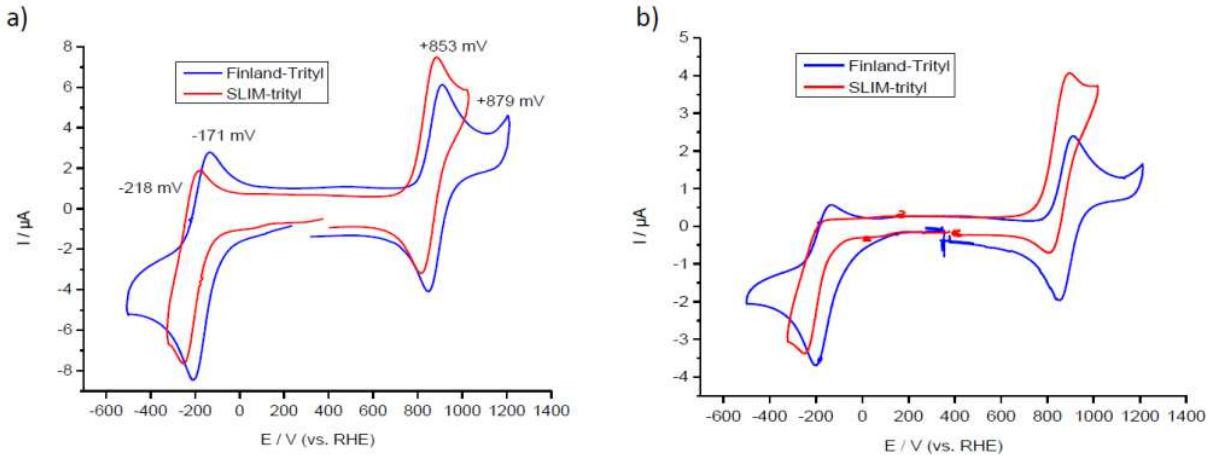

***Figure S28**: Cyclic voltammogram of SLIM **9•** (red) and Finland-Trityl **1•** (blue), each 500 µM in PBS buffer at pH 7.4 with a RHE at pH 7.4 as reference. A scan rate of a) 50 mV/s and b) 10 mV/s was applied in clockwise direction. Compared to the Finland-Trityl (blue), the reoxidation of the trityl-anion becomes less reversible, especially at 10 mV/s, for the SLIM-case (red), which means, that the quenching process with H^+ is faster in that case. The reason for this lies in the increased reactivity of the SLIM-anion, since it is thermodynamically less favored.*

4.2 Reduction Stability

4.2.1 Cell Lysates Preparation

Oocytes of the African claw frog *Xenopus laevis* were obtained from EcoCyte Bioscience (Dortmund, Germany) and lysate was prepared following a protocol of *Karthikeyan et al.*[13]. Within this procedure, the oocytes were mechanically disrupted and solid ingredients as well as the lipid layer was separated off by centrifugation. In total, 70 µL of lysate were obtained from 100 oocytes.

For HeLa cell lysate, HeLa S3 (ATCC® CCL-2.2, human cervical adenocarcinoma) were suspended in PBS buffer (600 µL per 10^8 cells) and the suspension was frozen in ethanol/$CO_{2(s)}$ for 5 min and subsequently thawed in and 37 °C water bath. This procedure was done three times, whereafter the cells were lysed with rapid oscillation within 5 minutes. Membranes were separated by centrifugation at 15000 rpm at 4 °C and the lysate was collected as the supernatant. It was separated into several aliquots and immediately shock frozen in liquid nitrogen and stored at –80 °C.

4.2.2. Stability Measurements

As outlined in the main text, the stability of SLIM **9•** and representatives of other spin label classes were assessed. For this, the respective label was diluted to a concentration of 200 µM in the corresponding medium and filled into a 10 µL capillary, which was then sealed with superglue and transferred into a 3 mm Q-band tube. In analogy to this, the labeled YopO N624C mutant was studied at 50 µM. The tube was then inserted into the spectrometer (EMXmicro) and the spectrometer was tuned properly. After this, a *cw*-EPR spectrum was recorded every 15 minutes over 15 hours. For reproducible results, it was crucial to warm up the spectrometer in advance to the measurement. Additionally, a home-written bash script was used to monitor the microwave frequency and power throughout the entire measurement. The signal intensities representing the spin concentration are obtained as the double integral over the spectrum for each time point. The dead time, measured from addition of the radical to the respective medium to the beginning of measurement, was kept below 6 minutes.

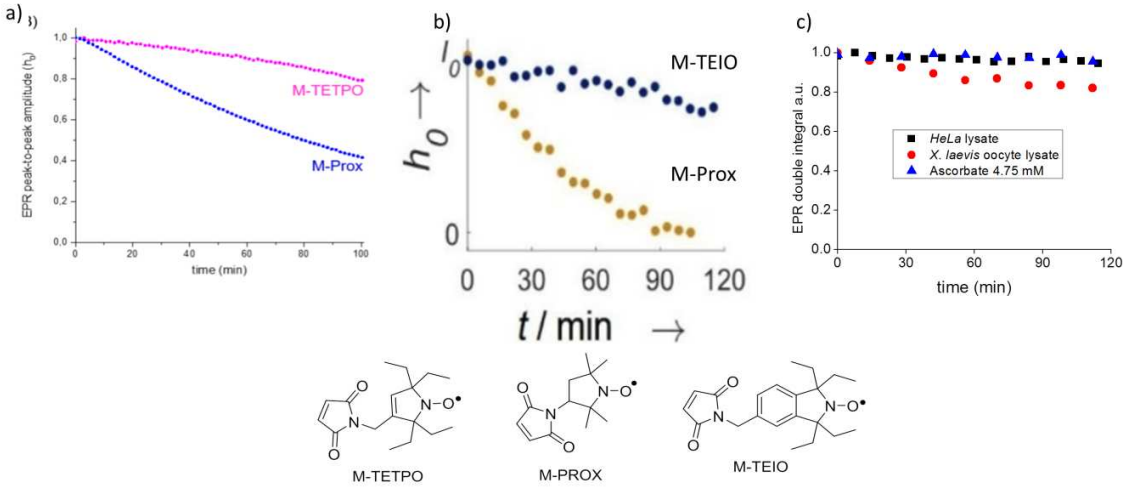

Figure S29: *Stability of various spin labels compared to* ***9•****. a) Spin labels M-TETPO and M-PROX in Xenopus laevis oocyte lysate. Excerpt from Karthikeyan et al., Angew. Chem.* ***2018****, 57, 1366 – 1370. © 2018 Wiley VCH Verlag GmbH & Co. KGaA, Weinheim, Germany. b) Spin labels M-TEIO and M-PROX in HEK (humane embryonal kidney cells) lysate. Excerpt from T. S. Braun et al., ChemBioChem* ***2019****, accepted manuscript, DOI: 10.1002/cbic.201900537. © to the authors, published by Wiley-VCH Verlag GmbH & Co. KGaA, Weinheim, Germany. c) Stability of* ***9•*** *in various media.*

5. Simulation of *cw*-EPR spectra

cw-EPR spectra were simulated using the EasySpin[14] toolbox for MATLAB (MathWorks, Natick, MA, USA). All obtained g-values, hyperfine coupling constants and peak-to-peak linewidths are summarized in Table S6. The spectra of the free (i.e. non-bioconjugated) trityl radicals in liquid solution (SLIM in PBS-buffer, Figure 2a in the main text; SLIM in DMSO, Figure S30a; **15•** in DMSO, Figure S30b) have been fitted using the "garlic" routine of EasySpin. Appropriate starting values for the "esfit" routine of EasySpin were taken from the study of *Bowman et al.*[15]

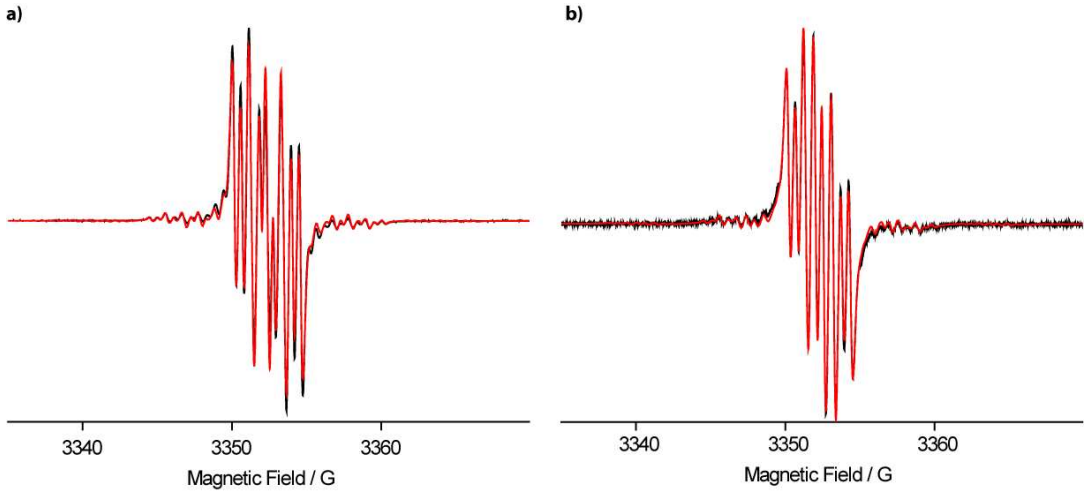

***Figure S30**: cw-EPR spectra of **9•** in DMSO (a) and of **15•** in DMSO (b) recorded at 298 K. The EasySpin simulation is overlaid as a red line.*

The spectrum of free SLIM in frozen solution at 100 K (Figure 2b in the main text) has been simulated with the "pepper" routine of EasySpin. The starting values of the anisotropic g- and A-tensors have been obtained as described in the following. To start, the percentage contributions pc_{xx}, pc_{yy}, pc_{zz} of g_{xx}, g_{yy} and g_{zz} to the isotropic g-value obtained from a DFT computation (SI, section 8.1) have been determined.

$$pc_{xx} = \frac{g_{XX}^{DFT}}{g_{iso}^{DFT}}; pc_{yy} = \frac{g_{YY}^{DFT}}{g_{iso}^{DFT}}; pc_{zz} = \frac{g_{ZZ}^{DFT}}{g_{iso}^{DFT}}$$

This procedure was also applied to DFT-derived hyperfine coupling constants A. With these percentages at hand, appropriate starting values (guesses) for the EasySpin fitting could be obtained by multiplying the percentage values with the isotropic g-value and hyperfine coupling constants extracted from the solution spectrum of free SLIM.

$$g_{XX}^{guess} = pc_{XX} \cdot g_{iso}^{fit} \cdot 3$$

The factor 3 in this equation is relevant to finally fulfill the following condition.

$$\frac{g_{xx} + g_{yy} + g_{zz}}{3} = g_{iso}$$

The spectrum of SLIM upon bioconjugation to YopO shown in Figure 2c the main text has been fitted with the "pepper" routine of EasySpin. The results obtained from the simulation of free SLIM in the frozen state were taken as starting values.

Table S6: cw X-band EPR Fitting Parameters

Sample	Fitting Results	
(a) **9•** 298 K, DMSO	g = 2.0034 A_N = 1.48 MHz A_{H1} = 3.48 MHz A_{H2} = 6.06 MHz LWPP = (0.007, 0.029) mT	$A_{C,central}$ = 66.16 MHz $A_{C,ipso}$ = 31.22 MHz $A_{C,ortho}$ = 25.45 MHz $A_{C,para}$ = 6.86 MHz $A_{C,meta}$ = 3.57 MHz
(b) **9•** 298 K, PBS	g = 2.0033 A_N = 1.71 MHz A_{H1} = 2.96 MHz A_{H2} = 6.00 MHz LWPP = (0.006, 0.018) mT	$A_{C,central}$ = 66.91 MHz $A_{C,ipso}$ = 31.63 MHz $A_{C,ortho}$ = 25.65 MHz $A_{C,para}$ = 7.27 MHz $A_{C,meta}$ = 3.90 MHz
(c) **15•** 298 K, DMSO	g = 2.0034 A_N = 1.51 MHz A_{H1} = 3.39 MHz A_{H2} = 5.16 MHz LWPP = (0.002, 0.034) mT	$A_{C,central}$ = 66.10 MHz $A_{C,ipso}$ = 31.11 MHz $A_{C,ortho}$ = 25.43 MHz $A_{C,para}$ = 6.83 MHz $A_{C,meta}$ = 3.51 MHz
(d) **9•** 100 K, PBS	g = (2.0028, 2.0036, 2.0040) A_N = (2.69, 0.64, 1.44) MHz A_{H1} = (4.14, 0.75, 2.86) MHz A_{H2} = (7.28, 7.55, 7.49) MHz LWPP = (0.089, 0.025) mT	$A_{C,central}$ = (3.45, 6.24, 185.27) MHz $A_{C,ipso}$ = (37.42, 37.64, 16.24) MHz $A_{C,ipso}$ = (38.11, 35.00, 21.01) MHz $A_{C,ipso}$ = (34.80, 34.87, 23.92) MHz
(e) YopO N624C /w **9•** 298 K, PBS	g = (2.0034, 2.0034, 2.0035) A_N = (2.19, 0.14,0.94) MHz A_{H1} = (3.64, 1.25, 2.36) MHz A_{H2} = (6.96, 5.05, 7.99) MHz LWPP = (0.051, 0.079) mT	$A_{C,central}$ = (3.92, 6.53, 184.78) MHz $A_{C,ipso}$ = (36.92, 37.14, 15.75) MHz $A_{C,ipso}$ = (37.61, 34.50, 21.49) MHz $A_{C,ipso}$ = (34.30, 34.37, 24.42) MHz

The observed ^{13}C-hyerfine coupling constants are similar to those reported for the Finland trityl[15].

6. *In Cell* Sample Preparation

Stage IV *Xenopus laevis* oocytes were purchased from EcoCyte Bioscience (Dortmund, Germany). All oocytes were visually checked for signs of apoptosis or other cell defects prior to use and only intact oocytes were used for subsequent experiments. Up to 30 oocytes were aligned on a plate with the darker animal hemisphere pointing towards the injection needle and kept moist using MBS buffer (5 mM HEPES pH 7.8, 88 mM NaCl, 1 mM KCl, 1 mM $MgSO_4$, 2.5 mM $NaHCO_3$, 0.7 mM $CaCl_2$). Injection needles were pulled over a Bunsen burner using glass capillaries with an outer diameter of 0.3 mm. Sufficiently thin needles were then filled with light silicone oil, mounted onto a Drummond Nanoject II microinjector (Broomall, PA, USA) and filled with SLIM-labeled YopO Y588C/N624C protein solution (~400 µM protein). For injection, oocytes were placed onto a homemade acryl glass plate with 1.5 mm x 1.5 mm grooves, which was covered with Parafilm (Bemis, Neenah, WI, USA) in advance. Each oocyte was carefully injected with 59.8 nL of protein solution, paying attention to not destroy the outer membrane. The injection itself was carried out into the dark animal hemisphere. If leakage occurred or the oocyte was damaged in other fashion during the injection process, it was discarded using a pipette. After injection of all oocytes, the oocytes were washed off the injection plate into a petri dish using MBS buffer where additional buffer was used to wash the oocyte's surface. Each oocyte was visually checked again for damage and then transferred into a Q-band tube filled to the top with MBS buffer. After up to 20 oocytes were transferred into the tube, excess buffer was removed using a syringe and the oocytes were incubated at 18° C for two hours to allow the protein to equilibrate and homogeneously distribute within the cell. After incubation, the sample was visually checked again and all oocytes appeared with intact spherical shape and the surrounding buffer was clear. Damaged oocytes can be recognized by loss of spherical shape and a nearby turbidity of the surrounding buffer caused by leaking cytosol. Subsequently, the Q-band tube was flash-frozen in liquid nitrogen. Key steps of the preparation and injection procedure are displayed in Figure S31.

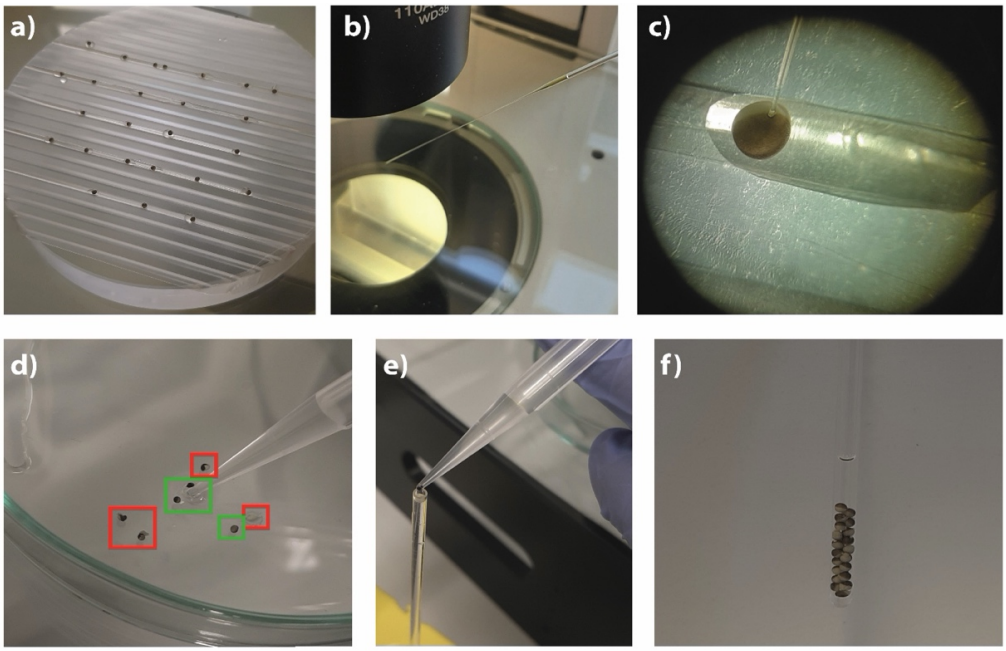

Figure S31*:* Preparation of *Xenopus laevis* oocytes for in-cell measurement. a) Alignment of the oocytes on the Parafilm-covered acryl glass plate. b) Injection needle with pulled up YopO protein. c) Penetration and injection process of an oocyte, picture taken with a smartphone through the lens of the microscope. d) Visual inspection of the oocytes after washing. Cells in the red square provide the instance of damage and were sorted-out subsequently whereas the ones in the green boxes were considered suitable for further experiments. e) Oocyte transfer into the Q-band tube with an Eppendorf pipette. f) Oocytes filled into the Q-band tube after incubation for 2h.

The maximum bulk concentration limit of spins was estimated using the following equation:

$$c_{\text{spin bulk}} = \frac{N_{\text{oocytes}} * c_{\text{Spin}} * 60\,nL}{V_{\text{Q-band tube}}} = \frac{20 * 800\,\mu M * 60\,nL}{70\mu L} = \mathbf{13.7\mu M}$$

Note that this estimation does not account for label degeneration during the two hours of incubation. The final spin concentration is estimated to be approximately 11 µM taking into account the findings of the label stabilities assessed by *cw*-EPR shown in Figure S29.

7. Pulsed EPR

7.1 EPR Sample Preparation

YopO samples were diluted 1:1 in ethylene glycol-d_6 to a final protein concentration of 25 µM, transferred into a Q-band EPR tube (O.D. 3 mm, Wilmad LabGlass, Vineland, NJ, USA) and flash-frozen in liquid nitrogen.

7.2 Relaxation Time Measurements

For the sake of comparison with other spin labels, the relaxation behavior of **9•** bound to the N624C YopO single cysteine mutant was evaluated with respect to T_1 and T_M obtained by inversion recovery (IR, Figure S32a) and two-pulse electron spin echo envelope modulation (2pESEEM, Figure S32b) experiments. The pulse sequences were applied at the maximum of the echo-detected field swept EPR spectrum and included phase cycling, two steps for 2pESEEM and four steps for IR. Acquisition parameters are given in Table S7.

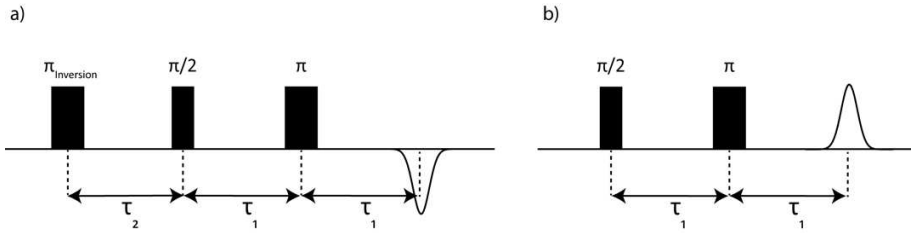

***Figure S32**: Pulse sequence applied for the inversion recovery (a) and the two-pulse ESEEM (b) experiment.*

***Table S7**: Pulse sequence parameters for relaxation time measurements.*

Inversion Recovery		Two-Pulse ESEEM	
Variable	**Value**	**Variable**	**Value**
π/2	12 ns	π/2	12 ns
π	24 ns	π	24 ns
$\pi_{\text{Inversion}}$	24 ns	–	–
τ_1	200 ns	τ_1	200 ns
τ_2	400 ns	–	–
τ_2 increment	1 ms	τ_1 increment	8 ns
Shots per Point	1	Shots per Point	1
Shot Repetition Time	1 s (10 K, 30 K) 500 ms (50 K)	Shot Repetition Time	500 ms

The results of the relaxation time measurements are summarized in Figure S33.

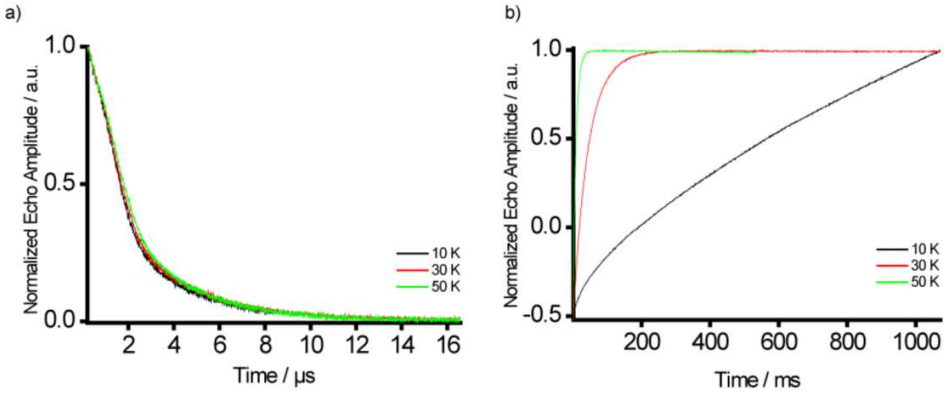

Figure S33: *Hahn echo decay curves (a) and inversion recovery traces (b) recorded on* **9•** *bound to the N624C YopO single cysteine mutant.*

7.3 Double Quantum Coherence (DQC) Experiments

The six-pulse Double Quantum Coherence (DQC) sequence (Figure S34) was applied at the magnetic field position corresponding to the maximum of the trityl field-swept EPR spectrum. The phase of the microwave radiation was adjusted on the Hahn echo sequence as to yield a maximally positive amplitude in the real signal channel of the quadrature detector. Proper phase adjustment was checked by summing amplitudes of the Hahn echo obtained from $(\pi/2)_{+x}/(\pi)_{+x}$ and $(\pi/2)_{-x}/(\pi)_{-x}$ pulses which averages out the signal. Pulse lengths and interpulse delays used for the DQC experiment are given in Table S8. The shot repetition time (SRT) was set to 15.3 ms.[16] A 64–step phase cycle was applied to remove undesired echoes and thus extract the pure double quantum coherence pathway contributions.[17,18] In order to eliminate deuterium ESEEM from the dipolar traces, a modulation averaging procedure was applied (τ_1 and τ_2 in 8 steps of 16 ns).[19] DQC measurements on YopO double cysteine mutants labeled with either SLIM or **8•** were performed at 50 K. In order to eliminate the background of the PDS time traces, a background correction[20] was performed. In the case of DQC (in cell and in vitro), polynomials of third order were used to fit the background contribution. Background correction was done using the DeerAnalysis package, and the "background start" value was chosen such that the corrected time trace was flat at long dipolar evolution times (last quarter of the time trace). In order to obtain an initial guess of the "background start" value, we used the "!" button in DeerAnalysis. The influence of the background on the distance distributions was checked by means of the validation tool in DeerAnalysis. In the present work, only the "background start" parameter was varied, and the variation ranges were set from the first local minimum of the time trace to the point when the oscillations were entirely damped.

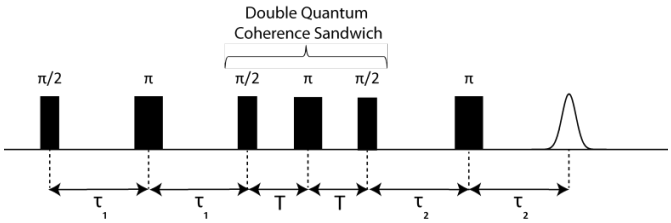

***Figure S34**: Pulse sequence applied for the DQC experiment.*

DQC data were mirrored at the zero-time origin. Next, background correction was performed by DeerAnalysis[21] using a third order polynomial. Subsequently, the background-corrected dipolar traces were translated into distance distributions via Tikhonov regularization with the optimal regularization parameter α determined according to the L-curve corner criterion. Finally, uncertainty estimations of the distance distributions were computed using the validation routine of DeerAnalysis.[21]

***Table S8**: Parameters of the DQC experiment.*

Variable	Value
π/2	12 ns
π	24 ns
τ_1	250 ns
τ_2	4000 ns
T	50 ns
Shots per Point	3
Shot Repetition Time	15.3 ms

7.4 Pulsed Electron-Electron Double Resonance (PELDOR) Experiments

Pulsed Electron-Electron Double Resonance (PELDOR, Figure S35) Spectroscopy was performed both on trityl- and nitroxide-labeled samples of YopO. Pulse lengths and interpulse delays are listed in Table S9. All PELDOR measurements were conducted at 50 K.

For the trityl-labeled YopO samples (**8•** and **9•**), the pump pulse $(\pi)_B$ was set to the maximum of the field-swept EPR spectrum and the observer pulses were applied at a frequency offset of –15 MHz relative to the pump frequency. The length of the pump pulse $(\pi)_B$ was determined by a transient nutation experiment. Regarding the suppression of deuterium ESEEM, an 8-step modulation averaging procedure was applied with a time increment of 16 ns. Additionally, a two-step phase cycle was used in order to remove undesired echoes and to correct for receiver baseline offsets.

For the PELDOR experiment on **R1**-labeled YopO, the pump pulse was applied at the magnetic field position which yields the maximal signal amplitude. The detection sequence was applied at a frequency offset of -100 MHz with respect to the pump frequency. The optimal length of the $(\pi)_B$ pump pulse was determined by a transient nutation experiment. As mentioned above, a modulation averaging procedure (8 steps with a 16 ns increment) and a two-step phase cycle was used to average out deuterium ESEEM and to remove unwanted echoes as well as baseline offsets. Background correction of the PELDOR time traces was done assuming a 3-dimensional homogeneous distribution. Validation of the background was done in the same way as described above for the DQC data.[22]

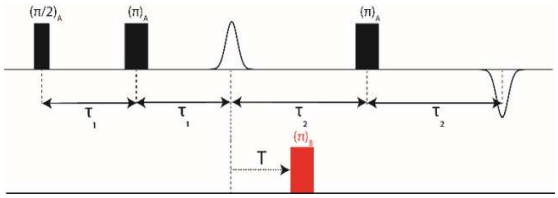

***Figure S35**: Pulse sequence applied for the PELDOR experiment.*

***Table S9**: Parameters of the PELDOR experiments*

Variable	8• / 9•	MTSL
$(\pi/2)_A$	32 ns	12 ns
$(\pi)_A$	64 ns	24 ns
$(\pi)_B$	60 ns	16 ns
τ_1	260 ns	260 ns
τ_2	4000 ns	4000 ns
Shots per Point	3	3
Shot Repetition Time	15.3 ms	1 ms

7.5 YopO PDS Results

Primary data of the YopO double mutant Y588C/N624C obtained by the different PDS techniques mentioned above are summarized in Figure S36.

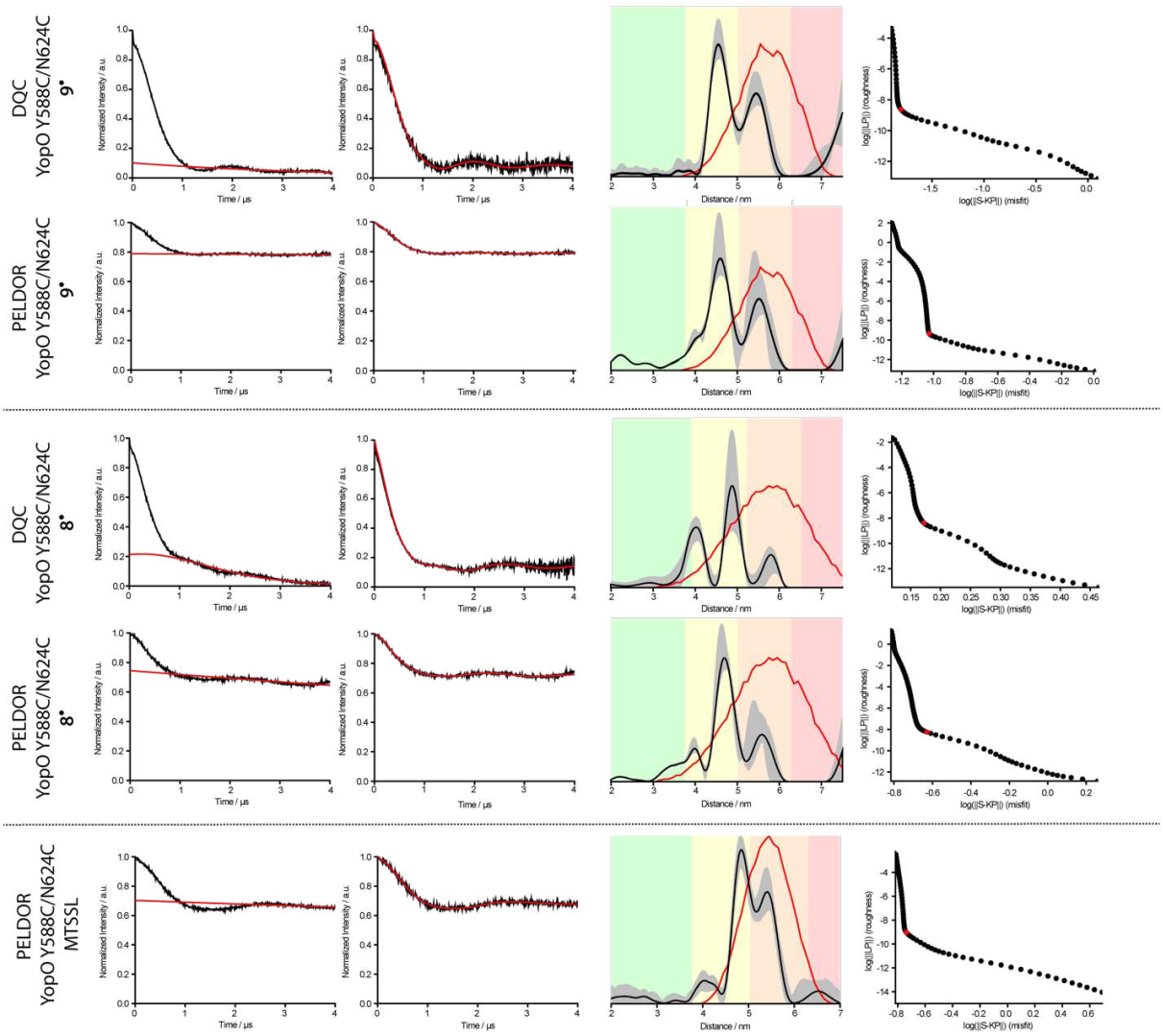

***Figure S36**: PDS data obtained for YopO Y588C/N624C. The red curves in the third column show the in silico predictions of the distance distributions computed by mtsslWizard using the PDB-ID 2h7o.*

It should be noted, that the DQC modulation depth should be 100 % according to theory. However, a in experiments the modulation depth is usually less (80% - 90%) as in the presents case and also as reported for model compounds. This can be attributed to the experimental conditions, where slight imperfections in the phase cycling reduce its efficiency as a double-quantum filter.[23]

The signal-to-noise ratio (SNR) of the dipolar traces can be defined as

$$SNR = \frac{\lambda}{\sigma_N} \cdot \frac{1}{\sqrt{t}}$$

with modulation depth of the trace λ, the acquisition time of the experiment t and the standard deviation of the noise of the trace σ_N. The noise has been deconvolved from the signal by fitting a polynomial of 8th order to the raw dipolar traces. The pure noise contributions have been obtained by subtracting the fit from the raw data. The SNR has been computed from the primary data prior to background correction by means of the software SnrCalculator.[24] The SNR values obtained by this method are summarized in Table S10.

***Table S10**: Signal-to-Noise Ratios obtained for the PDS Experiments on YopO Y588C/N624C.*

Experiment	YopO Y588C/N624C 9•	YopO Y588C/N624C 8•	YopO Y588C/N624C R1
DQC	674 $h^{-1/2}$	503 $h^{-1/2}$	–
PELDOR	155 $h^{-1/2}$	131 $h^{-1/2}$	248 $h^{-1/2}$

In order to quantify the widths of the bimodal distance distributions obtained using SLIM/DQC and MTSL/PELDOR, the distance distributions were fitted as a sum of two Gaussian functions:

$$y = y_0 + \frac{A}{w\sqrt{\pi/2}} exp\left(-2\left(\frac{x - x_c}{w}\right)^2\right)$$

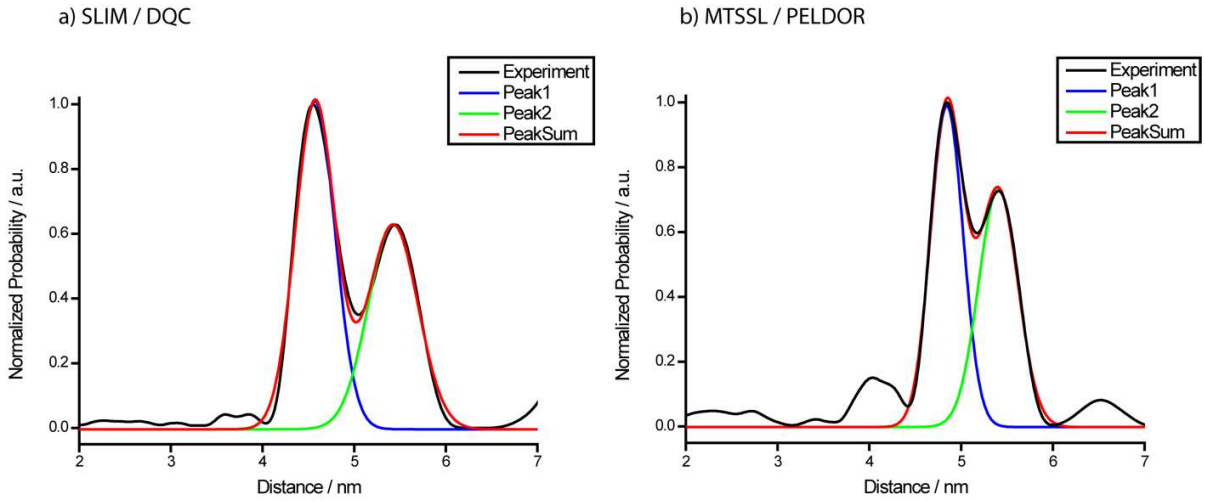

***Figure S37**: Analysis of the distance distribution bimodality with Gaussian functions.*

***Table S11**: Gaussian function parameters obtained for the fits shown in Figure S46.*

	SLIM / DQC	MTSL / PELDOR
Peak 1	Area: A = 0.55 Center: x_c = 4.57 nm Width: w = 0.43 nm Height: 1.01	Area: A = 0.44 Center: x_c = 4.84 nm Width: w = 0.35 nm Height: 0.99
Peak 2	Area: A = 0.43 Center: x_c = 5.42 nm Width: w = 0.54 nm Height: 0.63	Area: A = 0.39 Center: x_c = 5.41 nm Width: w = 0.43 nm Height: 0.73

7.6 PDS on YopO with human platelet actin

To validate the influence of actin binding to the α-helix 14 conformation, the YopO Y588C/N624C construct labeled with **9•** was incubated with human platelet actin. For this purpose, 1 mg human platelet actin (Cytoskeleton, Inc., Denver, CO, USA) was dissolved in 100 µL D_2O. Next, 50 µM **YopO-9•** was incubated with a 2-fold molar excess of actin and a 10-fold molar excess of the actin polymerization inhibitor latrunculin B (Merck KGaA, Darmstadt, Germany) in deuterated YopO-actin Buffer (4 mM TES pH 7.5, 0.4 mM ATP, 0.2 mM $CaCl_2$, 2 mM NaN_3) for 2 h on ice prior to the addition of 50 % deuterated ethylene glycol and flash freezing. Subsequently, the DQC experiment was performed as described in section 7.3 (Figure S38).

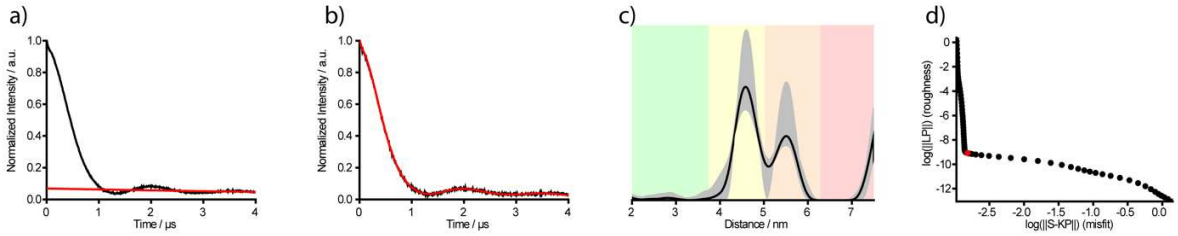

Figure S38: *a) Mirrored DQC time trace of YopO Y588C/N624C labeled with **9•** incubated with human platelet actin. The background function is indicated as a red line. b) Background-corrected time trace of (a) with the fit for Tikhonov regularization shown in red. c) Distance distribution obtained via Tikhonov regularization of (b) and the corresponding DeerAnalysis background validation shown in grey. d) L-curve with the chosen regularization parameter α shown in red.*

Interestingly, also in complex with human actin a bimodal distance distribution is obtained (Figure S38c). Overlaying both distance distributions obtained for **YopO-9•** in the absence and presence of actin shows that the conformation of α-helix 14 is independent of the actin binding process since both distributions are almost identical (Figure S39a). These data are in contrast to the two deposited crystal structures of YopO in the absence (PDB-ID: 2h7o) and presence (PDB-ID: 4ci6) of actin that show either a straight or bent conformation (Figure S39b+c). Here, we could demonstrate that in solution the α-helix 14 of YopO always resembles both, the straight and bent conformation, statistically and independently of the presence of actin.

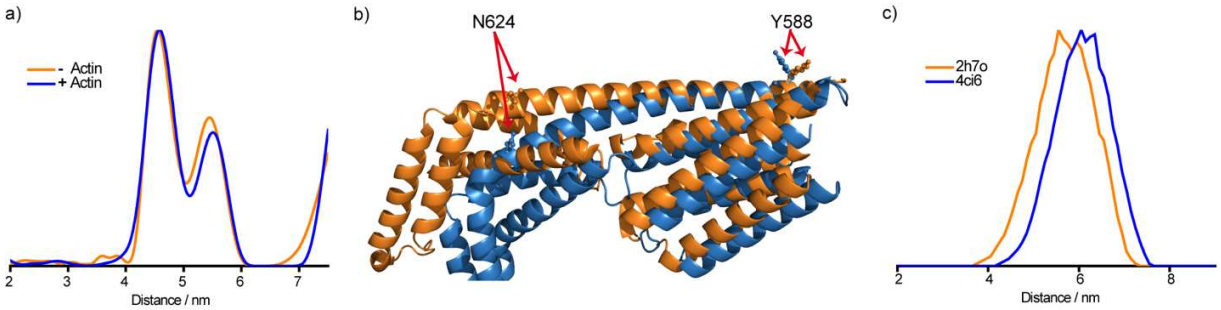

Figure S39: *a) Overlaid distance distributions of **YopO-9•** in the absence (orange) and presence (blue) of actin. b) Superposition of the GDI domains of the PDB-IDs 4ci6 (blue) and 2h7o (orange). b) Comparison of the in silico distance distributions of Y588C/N624C labeled with **9•** obtained for the different crystal structures of YopO (blue, PDB-ID: 4ci6) and YpkA (orange, PDB-ID: 2h7o).*

7.7 Evaluation of Concentration Limit for SLIM / DQC

In order to evaluate the lower concentration limit feasible for DQC experiments in combination with SLIM, YopO Y588C/N624C labeled with **9•** was diluted in PDS buffer. Q-band PDS samples were prepared with the

corresponding final protein concentrations in 30 % glycerol-d_8. The final spin concentration was verified by comparing the normalized amplitudes of the echo-detected field swept EPR spectra (Figure S40) of the nanomolar samples to the respective values obtained from the doubly labeled 25 µM YopO Y588C/N624C-**9•** reference sample.

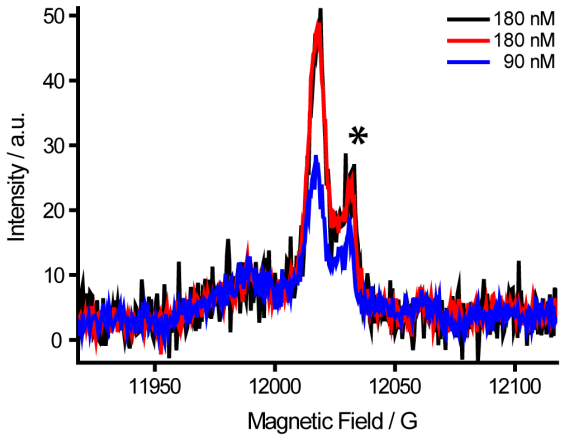

***Figure S40**: Field swept EPR spectra of nanomolar YopO Y588C/N624C-**9•** samples. The asterisk marks the E' signal stemming from the EPR tube.*

As can be seen in Figure S41, even at nanomolar concentration ranges, DQC experiments can be successfully performed, yielding time traces at a SNR of 2 $h^{-1/2}$ in both cases (note that the trace length at 90 nM was set to 2.5 µs instead of 4 µs). Both time traces recorded at nanomolar concentrations exhibit the same oscillation period as the 25 µM reference sample, thus underlining the reliability of the measurements and proving the possibility of DQC at nanomolar concentrations.

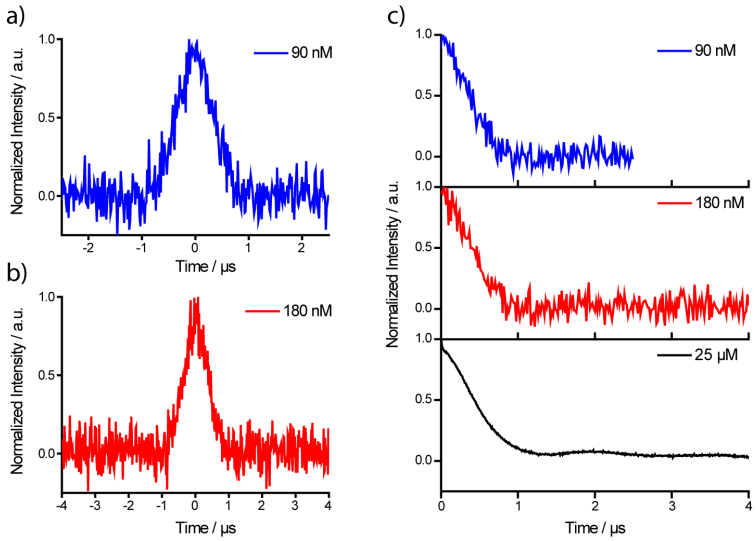

***Figure S41**: Original DQC time traces of YopO Y588C/N264C labeled with SLIM at a protein concentration of 90 nM (a) and 180 nm (b), respectively. c) Mirrored DQC time traces of the YopO samples at the given protein concentrations with the 25 µM reference sample (black, bottom) from section 7.5 as benchmark.*

7.8 *In Cell* Pulsed EPR Measurements

In order to check for the successful injection and the presence of trityl-labeled YopO within the oocytes, echo-detected field swept EPR spectra were recorded from untreated oocytes and after injection. Field swept spectra obtained from untreated oocytes show signals stemming from Mn(II) and an additional signal at g = 2.0054 which may stem from an organic radical endogenously present in oocytes (Figure S42a). After injection of SLIM-labeled protein, the trityl signal at g = 2.0037 dominates the spectrum and thus proves successful injection (Figure S42b).

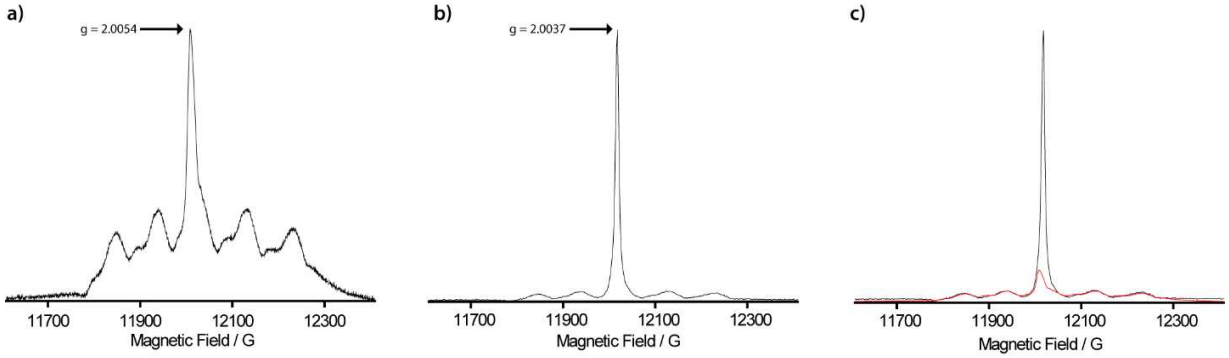

Figure S42*: a) Echo-detected field swept EPR Spectrum of pure oocytes prior to injection of spin-labeled protein. The spectrum clearly shows the presence of Mn(II) and of an organic radical giving rise to a signal at g = 2.0054. b) Echo-detected field swept EPR spectrum of oocytes after injection of trityl-labeled YopO with the spectrum being dominated by the trityl signal at g = 2.0037. c) Overlay of field swept EPR spectra before injection (red) and after injection (black) with the signal amplitude normalized to the Mn(II) signals.*

Longitudinal and transverse electron spin relaxation times (T_1, T_M) were studied for two reasons: Firstly, they provide insight into changes of the environment of the electron spin upon injection of the label into the oocyte cell, e.g. due to the presence of Mn(II) ions.[25] Secondly, especially the long T_1 relaxation time of trityl species unambiguously proves the presence of spin label within the cell. Therefore, T_1 and T_M were measured in untreated and injected oocytes at the magnetic field positions corresponding to the Mn(II) signal (11937 G), the dominant peak in the untreated oocytes (12009 G) and the trityl signal (12018 G). For details on relaxation measurement techniques, refer to SI section 7.2.

Figure S43 summarizes the results. Subfigures (S43a) and (S43b) contrast the relaxation behavior of SLIM bioconjugated to YopO *in vitro* and *in cell* after 120 minutes of incubation, showing that both longitudinal and transverse relaxation are enhanced in the cellular medium. This may be related to the endogenously present Mn(II) acting as a relaxation enhancer, but could as well be the result of crowding of spin-labeled protein in cell.[26]

Subfigures (S43c) and (S43d) show the relaxation behavior of the different species contributing to the field sweep spectrum. Comparing especially the longitudinal relaxation times at 12009 G pre- and post-injection shows clear differences related to the presence of trityl spins which are on resonance at this magnetic field. It also clearly points out that T_1 relaxation times can indicate the successful injection of labeled biomolecules into the cells. The fact that both T_1 and T_M are shorter at 12009 G (post injection) than at 12018 G shows the admixture of the fast-relaxing endogenous organic species to the trityl. This emphasizes that a careful inspection of the echo detected field swept EPR spectrum as well as the relaxation times associated with the different species is vital for choosing the correct magnetic field position for subsequent PDS experiments.

Subfigure (S43e) shows the effect of the incubation time of the oocytes after injection before flash-freezing on the transverse relaxation times. The Hahn echo decay curves clearly show that the phase memory time is extended with the incubation time, which is related to a more homogeneous distribution of the labeled biomolecule within the cell and thus reduced intermolecular dipolar coupling between electron spins.[27] However, when optimizing the incubation time, the optimal tradeoff between the beneficial homogeneous distribution of proteins in cell and the degeneration of the spin label has to be found.

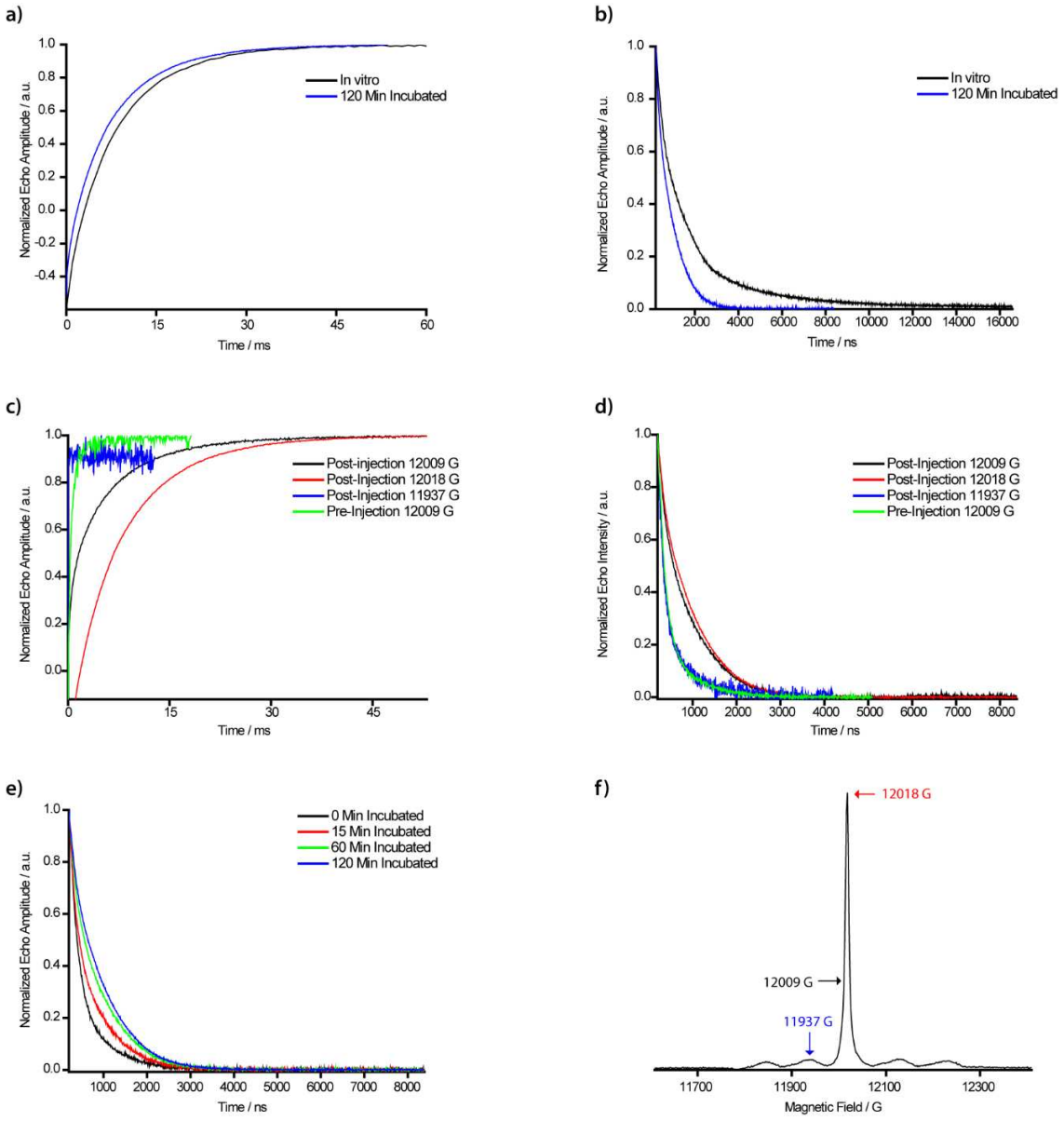

***Figure S43**: a, b) Comparison of inversion recovery traces (a) and Hahn echo decay curves (b) recorded on the trityl signal (12018 G) in vitro (black) and in oocytes after 120 minutes of incubation time. c,d) Comparison of inversion recovery traces (a) and Hahn echo decay curves at different field positions corresponding to the oocyte signal (12009 G), the trityl signal (12018 G) and the Mn(II) signal (11937 G). e) Hahn echo decay curved recorded on the trityl signal (12018 G) after different incubation times in oocytes. f) Echo-detected field swept EPR spectrum of SLIM-labeled YopO in oocytes with the relevant magnetic field positions marked by arrows.*

Due to the cellular environment and the non-deuterated buffer conditions, the acquisition parameter of the DQC experiment were adapted as summarized in Table S12 in order to optimize data acquisition. The thusly obtained *in cell* data are shown in Figure S44.

***Table S12**: Parameters of the in cell DQC experiment.*

Variable	Value
π/2	12 ns
π	24 ns
τ_1	200 ns
τ_2	3500 ns
T	50 ns
Shots per Point	20
Shot Repetition Time	15.3 ms

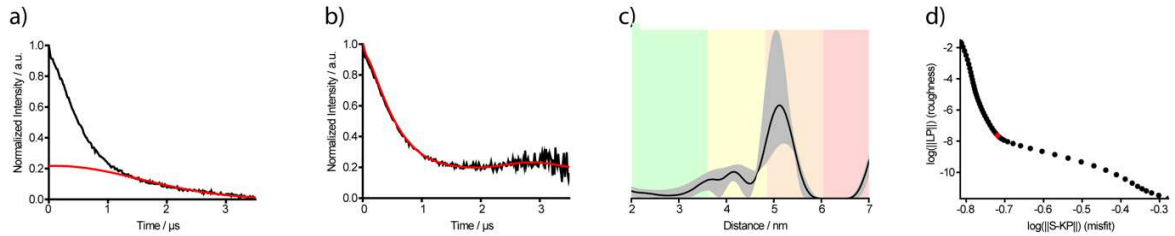

***Figure S44**: a) Mirrored DQC time trace of YopO Y588C/N624C labeled with **9•** and injected into oocytes with the background function indicated as a red line. b) Background-corrected time trace of (a) with the fit for Tikhonov regularization shown in red. c) Distance distribution obtained via Tikhonov regularization of (b) and the corresponding DeerAnalysis background validation shown in grey. d) L-curve with the chosen regularization parameter α shown in red.*

The *in cell* measurement (Figure S44) shows a monomodal distribution peaking at the position corresponding to the longer distance observed in the *in vitro* measurement (5.1 nm) (Figure S36). The marginal distance shift in the *in cell* sample by 0.2 nm as compared to the *in vitro* sample may be related to uncertainties in data analysis.

8. Theoretical Results

8.1 Density Functional Theory Computations

Density Functional Theory computations on the molecules were performed on a 64-core computer cluster using the ORCA quantum chemistry software package.[28] The structure of the SLIM label has been optimized on the B3LYP/def2-TZVP[29] level of theory using the RIJCOSX approximation (def2/J as auxiliary basis[30]) and the D3 dispersion correction.[31,32] Subsequent computations of the hyperfine coupling constants of the SLIM label **9•** were done using the eprnmr module of ORCA on the B3LYP/def2-TZVP level of theory. Again, the D3 correction was applied to account for dispersion interactions. The molecular coordinates of SLIM after geometry optimization are given in Table S13.

Table S13: Atomic coordinates obtained by the geometry optimization of the SLIM label ***9•*** *(B3LYP/def2-TZVP D3).*

Atom #	x	y	z
0C	0.822437	-4.468512	0.846234
1C	0.836906	-3.378944	-0.033744
2C	-0.277385	-2.513170	-0.122785
3C	-1.465085	-2.914959	0.518484
4C	-1.507815	-4.027049	1.359900
5C	-0.345252	-4.788269	1.572933
6S	2.365651	-5.290236	1.077728
7S	2.363681	-3.021817	-0.827466
8S	-3.066299	-4.385054	2.087791
9S	-2.999576	-2.146905	0.165851
10C	3.199071	-4.608758	-0.407731
11C	-3.839912	-2.756752	1.672734
12C	-3.637991	-1.758404	2.807972
13C	-5.315318	-2.985467	1.364753
14C	3.080261	-5.596215	-1.564262
15C	4.658581	-4.321717	-0.064033
16C	1.052094	-1.455055	-4.241579
17C	0.302897	-1.640030	-3.076607
18C	0.536094	-0.875037	-1.915668
19C	1.513713	0.146944	-1.990743
20C	2.320287	0.287510	-3.130385
21C	2.103083	-0.520609	-4.262503
22S	0.563319	-2.412574	-5.634332
23S	-1.039701	-2.764592	-3.193954
24S	3.615455	1.481568	-3.001868
25S	1.925037	1.188523	-0.634814
26C	-0.356778	-3.662932	-4.644912
27C	2.837734	2.418794	-1.633010
28C	1.878102	3.465694	-2.188782
29C	3.910655	3.054649	-0.757862
30C	0.597941	-4.754896	-4.172463
31C	-1.498490	-4.226462	-5.481646
32C	-0.456815	1.303197	2.177858
33C	-0.179045	0.121516	1.477338
34C	-0.656535	-0.055615	0.165471
35C	-1.534653	0.912754	-0.342675
36C	-1.903673	2.029597	0.410410
37C	-1.333478	2.263844	1.665453
38S	0.509321	1.577533	3.628031
39S	0.987282	-0.964955	2.223533
40S	-3.174283	3.036474	-0.289618
41S	-2.355277	0.696468	-1.876441
42C	0.950376	-0.184780	3.892194
43C	-2.954208	2.432386	-2.017966
44C	-1.928818	3.294730	-2.746032
45C	-4.304013	2.431863	-2.726321
46C	-0.090524	-0.870184	4.771318
47C	2.345594	-0.269754	4.504228
48C	-1.651454	3.513353	2.451517
49C	-0.182285	-1.167104	-0.679941
50N	-1.331366	4.738927	1.735103
51C	-0.108966	5.031568	1.139118
52C	-0.311418	6.319197	0.395878
53C	-1.567304	6.720862	0.567024
54C	-2.272457	5.728718	1.439150
55O	0.898963	4.371152	1.216331
56O	-3.410552	5.759731	1.832853
57C	-0.433515	-5.909518	2.523218
58O	-1.464673	-6.459360	2.838037
59O	0.753301	-6.275861	3.058266
60C	2.906121	-0.402151	-5.496115
61O	2.507925	-0.664279	-6.607399
62O	4.175983	0.011064	-5.277491
63H	-0.992139	3.324557	-2.195284
64H	-2.304475	4.314706	-2.852359
65H	-1.733415	2.885239	-3.739103
66H	-5.028164	1.825935	-2.185254
67H	-4.196559	2.032594	-3.736678
68H	-4.685154	3.451496	-2.807886
69H	-1.086391	-0.763576	4.346240
70H	-0.092883	-0.423299	5.767702
71H	0.135831	-1.935087	4.860390
72H	3.082504	0.210701	3.864096
73H	2.626662	-1.315373	4.645177
74H	2.357191	0.213327	5.483184
75H	-1.125465	3.500500	3.403873
76H	-2.719920	3.576766	2.668455
77H	0.581135	-7.044949	3.623056
78H	4.593132	0.104008	-6.148042
79H	-2.577131	-1.595014	2.990014
80H	-4.097248	-2.131301	3.726300
81H	-4.090710	-0.799500	2.545940
82H	-5.828978	-3.367062	2.249842
83H	-5.438609	-3.702948	0.555488
84H	-5.790928	-2.045798	1.076118
85H	2.037172	-5.817407	-1.780383
86H	3.584867	-6.530087	-1.305844
87H	3.543547	-5.185410	-2.464058
88H	4.734037	-3.606491	0.752264
89H	5.176816	-3.914816	-0.935154
90H	5.163910	-5.244581	0.229331

91H	1.123182	2.997107	-2.818803
92H	2.427607	4.191896	-2.792650
93H	1.384033	3.982716	-1.365307
94H	4.579778	2.300275	-0.346790
95H	3.436322	3.596418	0.062307
96H	4.495029	3.767811	-1.343944
97H	1.028552	-5.275478	-5.030951

98H	0.066827	-5.475829	-3.546476
99H	1.405871	-4.321608	-3.587487
100H	-2.171059	-3.438137	-5.815087
101H	-2.066678	-4.953913	-4.898135
102H	-1.097025	-4.741364	-6.356653
103H	0.486133	6.784077	-0.161815
104H	-2.065948	7.598343	0.186946

For implementing the new SLIM spin label into mtsslWizard, a geometry optimization (PBE/def2-SVP) on the SLIM label attached to a cysteine residue was performed in advance.

The hyperfine coupling constants obtained by DFT on the B3LYP/def-TZVP D3 level of theory are summarized in Table S14. Only hyperfine coupling constants to those nuclei which have also been observed experimentally are listed. For comparison, the isotropic coupling constants obtained by the EasySpin[14] fit of the *cw* EPR spectrum recorded in DMSO at 298 K are indicated. The numbering of the atoms within the structure is shown in Figure S45.

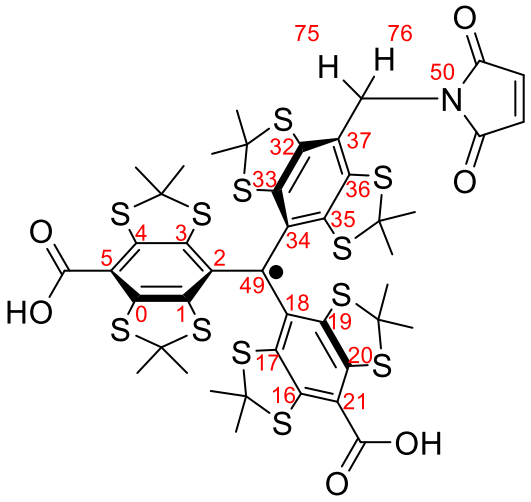

***Figure S45**: Structure of **9•** with atom enumeration applied for calculation of HFC-tensors.*

***Table S14**: Hyperfine coupling constants obtained by DFT (B3LYP/def-TZVP D3) computations and fitting of the cw-EPR spectrum recorded in DMSO at 298 K.*

	Atom #	DFT B3LYP/def-TZVP D3				Experimental
		A_{XX} / MHz	A_{YY} / MHz	A_{ZZ} / MHz	A_{iso} / MHz	A_{iso} / MHz
	50N	0.8868	0.9107	1.2518	1.0164	1.48
	75H	-0.1694	-0.2959	1.2142	0.2496	3.48
	76H	4.9565	5.1968	6.4721	5.5418	6.06
	49C	4.5936	4.7467	165.4203	58.2535	66.16
ipso	2C	-24.9686	-26.7889	-42.7462	-31.5012	31.22
ipso	18C	-24.5157	-26.3190	-42.0361	-30.9569	31.22
ipso	34C	-24.0005	-25.0611	-34.8107	-27.9575	31.22
ortho	1C	22.6342	24.0242	43.8507	30.1697	25.45
ortho	3C	11.4835	13.2499	33.6639	19.4658	25.45
ortho	17C	14.2218	15.7777	35.8105	21.9367	25.45
ortho	19C	19.5899	20.9609	43.1771	27.9093	25.45
ortho	33C	20.0554	21.6460	34.2153	25.3056	25.45
ortho	35C	15.3674	17.2719	28.6021	20.4138	25.45
para	5C	0.1572	1.0402	20.5164	7.2379	6.86
para	21C	0.1456	1.0618	22.5647	7.9240	6.86
para	37C	0.2124	0.9007	14.8309	5.3147	6.86
meta	0C	-1.9590	-2.9847	-12.0474	-5.6637	3.57
meta	4C	-4.8282	-5.7410	-13.6552	-8.0748	3.57
meta	16C	-4.1915	-5.1499	-14.3902	-7.9105	3.57
meta	20C	-2.8695	-3.9180	-12.8359	-6.5411	3.57
meta	32C	0.1930	-0.8838	-6.3693	-2.3534	3.57
meta	36C	-2.0127	-2.9963	-8.3120	-4.4403	3.57

8.2 *In Silico* Spin Labeling

Distance distributions were computed based on the two crystal structures of YopO deposited in the Protein Data Bank (PDB-IDs: YpkA 2h7o and YopO 4ci6) using the mtsslWizard[31] plugin for PyMOL. The maximal number of conformers to be found was 200 and the clashscore criteria were set to “loose”, implying that a *van-der-Waals* cutoff of 2.5 Å was set and 5 clashes were allowed.[32,33]

8.2.1 Conformer Cloud Volume

Conformer ensembles of **8•** and SLIM **9•** were generated on YopO N624C. The size of the conformer clouds was determined as described in the following paragraph and schematically shown in Figure S46. Basis of all computations was the prediction of the conformer cloud provided by mtsslWizard (Figure S46a+b). In order to obtain the ensemble of points in space describing the outer hull of the conformer cloud, the Cartesian coordinates of the atom which is the furthest away from the C_β-atom of the cysteine residue were extracted. Herein, the C_β-atom of cysteine serves as a fixed anchor point (Figure S46c).
Next, the overall point cloud containing the atomic coordinates of the carboxylic carbon atom and those of the hull atoms was collected (Figure S46d) which served as a basis for the computation of a so-called α-shape (Figure S46e). This α-shape obtained by the MATLAB command “alphaShape” encompasses the whole point cloud. The smallest possible alpha radius was determined automatically resulting in a tight fit of the 3D sphere to the data points. Finally, the volume of the α-shape was computed using the “volume” command of MATLAB providing a good approximation to the volume of the label conformer cloud.

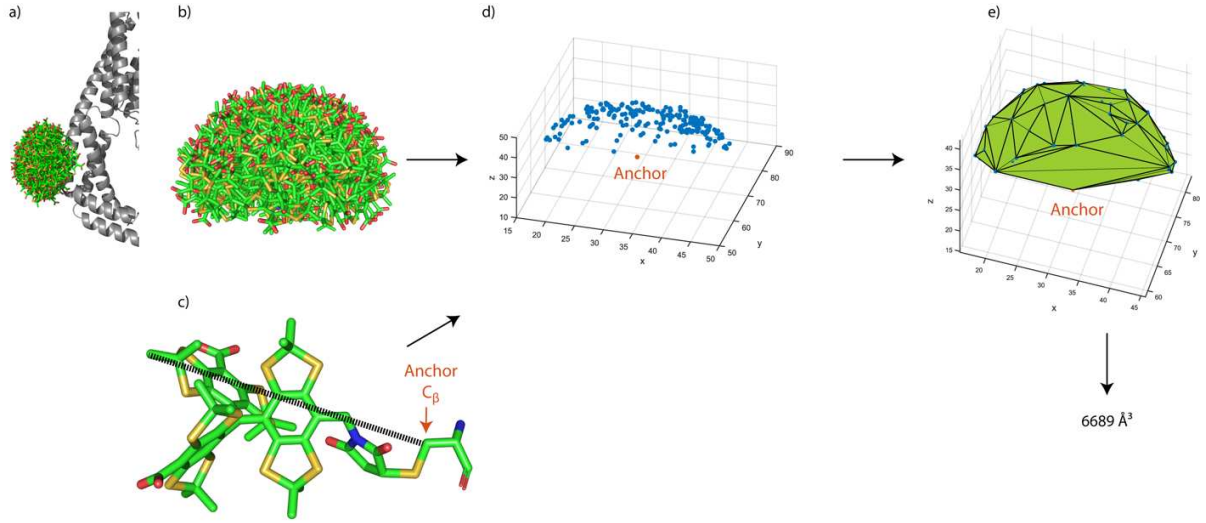

***Figure S46**: Computation of the volume of an in silico generated conformer cloud. a) YopO in silico labeled with SLIM at amino acid position N624. b) In silico generated conformer ensemble for SLIM. c) Structure of **9•** with the carboxylic carbon atom of cysteine shown as anchor point and the distance to the furthest atom indicated by a dashed line. d) Point cloud symbolizing the positions of the furthest atoms in blue and the anchor point in orange. e) Alpha-shape generated from the ensemble of coordinates shown in (d) with the resulting volume obtained by integration of the alpha-shape. The whole analysis was performed on 10 individually and independently generated conformer clouds of each of the labels SLIM and **8•**. Results are shown in Table S15.*

***Table S15**: Computed volumes of the conformer clouds obtained by in silico spin labeling of YopO with **9•** and **8•**.*

YopO N624C-9•		YopO N624C-8•	
Cloud #	Volume / Å³	Cloud #	Volume / Å³
1	6589	1	16232
2	6951	2	16637
3	6649	3	15081
4	7512	4	15316
5	7116	5	15986
6	7339	6	12855
7	6684	7	14415
8	7444	8	15539
9	6476	9	14272
10	6642	10	15669
Ø	**6940**	**Ø**	**15200**

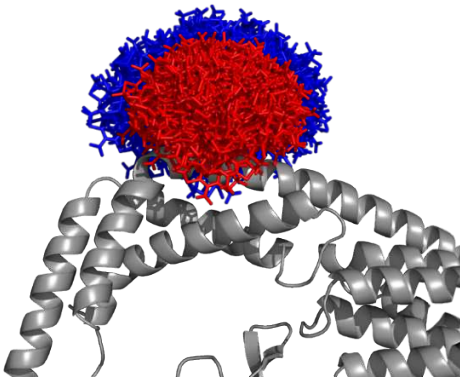

8.2.2 YopO **8•** Label Conformer Selection

As outlined in the main text, attractive interactions between the protein's α–helix and the hydrophobic surface of the trityl radical are conspicuous to cause the short-distance artefacts for **YopO-8•**. Label conformers representative for this are provided in Figure S47 below. It becomes evident that these conformers can only emerge due to the long linker of **8•**, which bends over into the propagation direction of the helix.

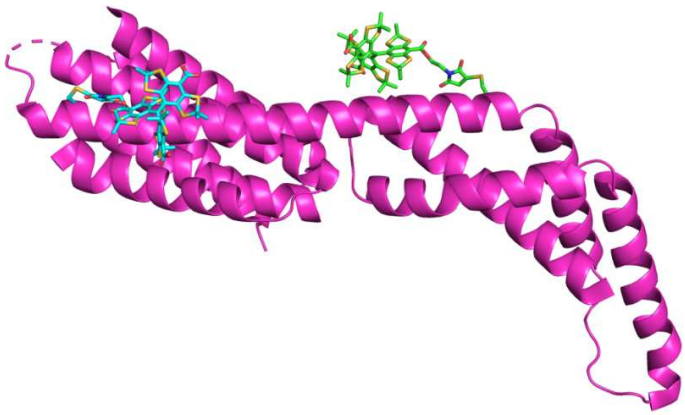

***Figure S47**: Selected label conformers for **YopO-8•**.*

9. Literature

[1] M. Winkle, J. Lansinger, R. C. Ronald, *J. Chem. Soc. Chem. Commun.* **1980**, 87–88.
[2] J. J. Jassoy, A. Berndhäuser, F. Duthie, S. P. Kühn, G. Hagelueken, O. Schiemann, *Angew. Chem. Int. Ed.* **2017**, *56*, 177–181.
[3] E. H. Discekici, A. H. St. Amant, S. N. Nguyen, I. H. Lee, C. J. Hawker, J. Read De Alaniz, *J. Am. Chem. Soc.* **2018**, *140*, 5009–5013.
[4] H. Hintz, A. Vanas, D. Klose, G. Jeschke, A. Godt, *J. Org. Chem.* **2019**, *84*, 3304–3320.
[5] G. R. Fulmer, A. J. M. Miller, N. H. Sherden, H. E. Gottlieb, A. Nudelman, B. M. Stoltz, J. E. Bercaw, K. I. Goldberg, *Organometallics* **2010**, *29*, 2176–2179.
[6] V. Froidevaux, M. Borne, E. Laborbe, R. Auvergne, A. Gandini, B. Boutevin, *RSC Adv.* **2015**, *5*, 37742–37754.
[7] M. M. Haugland, A. H. El-Sagheer, R. J. Porter, J. Peña, T. Brown, E. A. Anderson, J. E. Lovett, *J. Am. Chem. Soc.* **2016**, *138*, 9069–9072.
[8] C. Wuebben, S. Blume, D. Abdullin, D. Brajtenbach, F. Haege, S. Kath-Schorr, O. Schiemann, *Molecules* **2019**, *24*, 4482.
[9] J. J. Jassoy, C. A. Heubach, T. Hett, F. Bernhard, F. R. Haege, G. Hagelueken, O. Schiemann, *Molecules* **2019**, *24*, 2735.
[10] https://web.expasy.org/protparam/
[11] H. Liu, J. H. Naismith, *BMC Biotechnol.* **2008**, *8*, 91.
[12] M. Zehl, G. Allmaier, *Rapid Commun. Mass Spectrom.* **2004**, *18*, 1932–1938.
[13] G. Karthikeyan, A. Bonucci, G. Casano, G. Gerbaud, S. Abel, V. Thomé, L. Kodjabachian, A. Magalon, B. Guigliarelli, V. Belle, et al., *Angew. Chemie Int. Ed.* **2018**, *57*, 1366–1370.
[14] S. Stoll, A. Schweiger, *J. Magn. Reson.* **2006**, *178*, 42–55.
[15] M. K. Bowman, C. Mailer, H. J. Halpern, *J. Magn. Reson.* **2005**, *172*, 254–267.
[16] U. Stoll, S. (2018) (Goldfarb, D., Stoll, S., Eds.), Chapter 11, Wiley VCH
[17] P. P. Borbat, J. H. Freed, *Chem. Phys. Lett.* **1999**, *313*, 145–154.
[18] S. Saxena, J. H. Freed, *J. Chem. Phys.* **1997**, *107*, 1317–1340.
[19] D. Akhmetzyanov, P. Schöps, A. Marko, N. C. Kunjir, S. T. Sigurdsson, T. F. Prisner, *Phys. Chem. Chem. Phys.* **2015**, *17*, 24446–24451.
[20] P. P. Borbat, J. H. Freed in: *Methods in Enzymology*, Volume 423: Two-Component Systems, Part B. Eds: M. I. Simon, B. Crane, A. Crane, **2007**, Elsevier.
[21] G. Jeschke, V. Chechik, P. Ionita, A. Godt, H. Zimmermann, J. Banham, C. Timmel, D. Hilger, H. Jung, *Appl. Magn. Reson.* **2006**, *30*, 473–498.
[23] A.Meyer, J.J. Jassoy, S. Spicher, A. Berndhäuser, O. Schiemann, Phys. Chem. Chem. Phys., **2018**, *20*, 13858-13869
[23] https://github.com/dinarabdullin/SnrCalculator
[24] G.Jeschke, Y. Polyhach, *Phys. Chem. Chem. Phys*., **2007**, *9*, 1895–1910.
[25] F. Wojciechowski, A. Groß, I. T. Holder, L. Knörr, M. Drescher, J. S. Hartig, *Chem. Commun.* **2015**, *51*, 13850-13853.
[26] I. Krstic, R. Hänsel, O. Romainczyk, J. W. Engels, V. Dötsch, T. F. Prisner, *Angew. Chem. Int. Ed.* **2011**, *50*, 5070-5074.
[27] F. Neese, *WIREs Comput. Mol. Sci.* **2012**, *2*, 73–78.
[28] F. Weigend, R. Ahlrichs, *Phys. Chem. Chem. Phys.* **2005**, *7*, 3297–3305.
[29] F. Weigend, *Phys. Chem. Chem. Phys.* **2006**, *8*, 1057–1065.
[30] S. Grimme, S. Ehrlich, L. Goerigk, *J. Comput. Chem.* **2011**, *32*, 1456–1465.
[31] S. Grimme, J. Antony, S. Ehrlich, H. Krieg, *J. Chem. Phys.* **2010**, *132*, 154104.
[32] G. Hagelueken, R. Ward, J. H. Naismith, O. Schiemann, *Appl. Magn. Reson.* **2012**, *42*, 377–391.

[P6]: Ox-SLIM: Synthesis of and Site-Specific Labelling with a Highly Hydrophilic Trityl Spin Label

Reproduced with permission from

Nico Fleck, Caspar Heubach, Tobias Hett, Sebastian Spicher, Stefan Grimme, Olav Schiemann*, *Chem. Eur. J.* **2021**, *27*, 5292-5297.
DOI: https://doi.org/10.1002/chem.202100013

* Corresponding author.

Contributions

- Performing pulsed EPR experiments.
- Analysis of *cw* and pulsed EPR data.
- DFT calculations to obtain the structure and EPR parameters of Ox-SLIM.
- Writing of the manuscript in parts.

Full Paper
doi.org/10.1002/chem.202100013

Chemistry Europe
European Chemical Societies Publishing

Physical Organic Chemistry

Ox-SLIM: Synthesis of and Site-Specific Labelling with a Highly Hydrophilic Trityl Spin Label

Nico Fleck,[a] Caspar Heubach,[a] Tobias Hett,[a] Sebastian Spicher,[b] Stefan Grimme,[b] and Olav Schiemann*[a]

Abstract: The combination of pulsed dipolar electron paramagnetic resonance spectroscopy (PDS) with site-directed spin labelling is a powerful tool in structural biology. Rational design of trityl-based spin labels has enabled studying biomolecular structures at room temperature and within cells. However, most current trityl spin labels suffer either from aggregation with proteins due to their hydrophobicity, or from bioconjugation groups not suitable for in-cell measurements. Therefore, we introduce here the highly hydrophilic trityl spin label Ox-SLIM. Engineered as a short-linked maleimide, it combines the most recent developments in one single molecule, as it does not aggregate with proteins, exhibits high resistance under in-cell conditions, provides a short linker, and allows for selective and efficient spin labelling via cysteines. Beyond establishing synthetic access to Ox-SLIM, its suitability as a spin label is illustrated and ultimately, highly sensitive PDS measurements are presented down to protein concentrations as low as 45 nM resolving interspin distances of up to 5.5 nm.

Introduction

Since the discovery of the triphenylmethyl radical by Gomberg in 1900,[1] stable carbon-centred radicals received rising attention. This especially applies to trityl radicals of the tetrathioaryl-type (Scheme 1), derived from the so-called Finland trityl **1**•.[2,3] Within the past two decades, **1**• and its derivatives found widespread application in in vivo imaging,[4] oximetry,[5,6] pH-sensing,[7] viscosity measurements,[8] and as polarizing agents in dynamic nuclear polarization (DNP).[9,10] Moreover, trityl radicals emerged as spin labels[11–14] for pulsed dipolar electron paramagnetic resonance spectroscopy (PDS)[15–17] to elucidate structures of biomolecules.[18,19] Exploiting their long T_M relaxation times,[20] trityl radicals like **2**[13] paved the way to PDS measurements at physiological temperatures.[13,14,21] Recent trends in the development of trityl spin labels focused on their suitability for in-cell measurements, where the reductive intracellular environment presents additional challenges with respect to the stability of the radical centre. Initial studies with **3**•[18] proved the suitability of trityl radicals for this purpose in general, though the bioconjugation proceeded with low efficiency and inseparable aggregates. Trityl spin labels with functional groups for bioconjugation based on maleimides (**4**•, **5**•, **6**•)[22–24] coped with this challenge by providing highly selective and efficient linkage to cysteines. While **2**•–**5**• are simple esters/amides of **1**•, the benzylic CH_2-linker used to construct the so-called SLIM-trityl **6**• was shown to improve the stability towards intracellular reduction by shifting its redox potentials. Concomitantly, a short linker is introduced giving rise to narrow distance distributions.[24] Another inherent drawback caused by the lipophilic core of these first generation trityl spin labels is aggregation with themselves[25,26] and hydrophobic interactions with proteins.[18,19,22,23] This complicates the spin labelling of proteins and can adversely influence the PDS-derived dis-

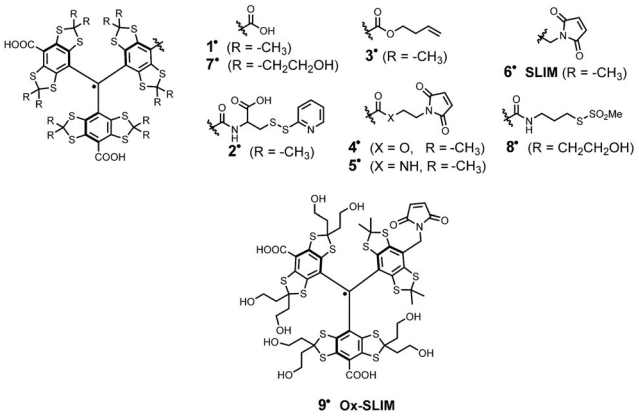

Scheme 1. Lewis structures of trityl spin labels and their parent compounds.

[a] N. Fleck, C. Heubach, T. Hett, Prof. Dr. O. Schiemann
University of Bonn, Institute of Physical and Theoretical Chemistry
Wegelerstr. 12, 53115 Bonn (Germany)
E-mail: schiemann@pc.uni-bonn.de

[b] S. Spicher, S. Grimme
University of Bonn, Institute of Physical and Theoretical Chemistry
Beringstr. 4, 53115 Bonn (Germany)

Supporting information and the ORCID identification number(s) for the author(s) of this article can be found under: https://doi.org/10.1002/chem.202100013.

tance distributions. With bovine serum albumin for instance, aggregation of **1**• occurred already at protein concentrations above 60 μM.[27] Therefore, efforts have been undertaken to increase the hydrophilicity of trityl radicals. For imaging and sensing purposes, conjugation of **1**• to dendritic PEG-esters,[28,29] dextrans,[30] or oligopeptides[31] addressed this issue. However, the resulting radicals become very large and are therefore not suitable as spin labels. Other approaches aimed for hydrophilic trityl cores by hydroxylation of the thioketal's methyl-substituents.[32] Accordingly, the Ox063 radical **7**• was reported early in patent literature but efficient synthetic access was disclosed only recently.[33] Based on this core, the hydrophilic spin label **8**• has been introduced,[34] and utilized for distance measurements on outer membranes of *E. coli* just recently.[35] Despite its high water-solubility, the methanethiosulfonate bioconjugation site is not suitable for in-cell applications[36] and such long linking groups lead to unnecessarily broad distance distributions.[22,35] Therefore, we report here the modular synthesis of the hydroxylated short linked maleimide trityl (Ox-SLIM) **9**• that combines the reduction resistance and short linkage of **6**• with the hydrophilicity of **7**•. The hydroxyl-groups on two of the bisthioketalaryl moieties provide the hydrophilicity, whereas the third, not hydroxylated bisthioketalaryl-unit carries the benzylic maleimide and ensures high accessibility for labelling. Finally, it is shown that Ox-SLIM **9**• enables highly sensitive PDS measurements down to protein concentrations as low as 45 nM at a distance of 5.5 nm.

Results and Discussion

The synthesis of Ox-SLIM **9**• needs aryl building block **10**, which can be obtained via two alternative routes from bisthioketal **11**[3,37] (Scheme 2). The first route starts with aromatic tri-

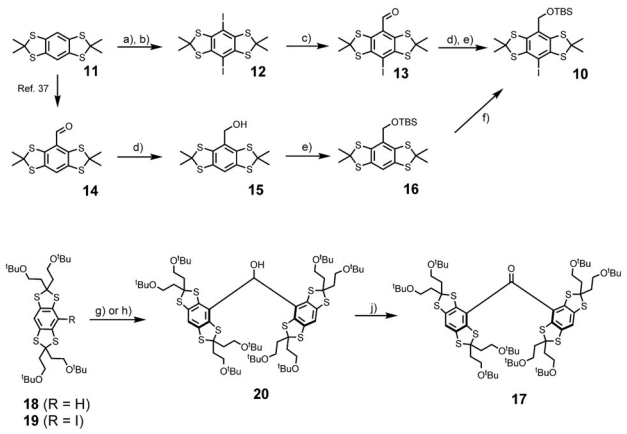

Scheme 2. Synthesis of building blocks **10** and **17**. a) 6.5 equiv. LiTMP, 0.1 equiv. Et_3NHCl, 12 equiv. Me_3SiCl, THF, −95 °C to r.t., 16 h. b) 3.0 equiv. ICl, CH_2Cl_2, r.t., 3 h, 86% over two steps. c) 1.1 equiv. *n*BuLi, THF, −95 °C, 45 min, then 15.0 equiv. DMF, to r.t., 16 h. 73% yield. d) 2.0 equiv. $NaBH_4$, CH_2Cl_2/MeOH 2:1, r.t., 30 min, 93% from **14**. e) 1.2 equiv. *t*BuMe$_2$SiCl, 2.5 equiv. Imidazole, DMF, r.t., 16 h, 82% over two steps from **13**, 91% from **15**. f) 1. LiTMP, THF, −78 °C, 2 h. 2. I_2, to r.t., 16 h, 56%. g) 0.95 equiv. *n*BuLi, THF, −95 °C, then 0.4 equiv. HCO_2Me, r.t., 16 h, 36%, for **12**. h) 1.95 equiv. *t*BuLi, 0.48 equiv., THF, −95 °C, 45 min, then 0.48 equiv. HCO_2Me, r.t., 16 h, 88%, for **13**. i) 1.25 equiv. Dess–Martin-periodinane, CH_2Cl_2, r.t., 60 min, 93%.

methylsilylation of **11** by reaction with lithium tetramethylpiperide (LiTMP) and in situ quenching with trimethylsilyl chloride. Noteworthy, the basicity of LiTMP ($pK_a = 37$)[38] is not sufficient for quantitative deprotonation of **11**, but it does not react with Me_3SiCl either due to its low nucleophilicity.[38] This transformation avoids the use of stronger yet more nucleophilic bases such as lithium alkyls, which were shown to cleave the carbon–sulfur bond in **11**.[32,40] An *ipso*-iododesilylation with ICl then afforded **12** in a yield of 86%. Lithium-halogen exchange with *n*BuLi at −95 °C runs cleanly without any evidence for thioketal-cleavage, and quenching with DMF gave aldehyde **13** in a yield of 73% after acidic workup. Subsequent carbonyl reduction with $NaBH_4$ and transformation of the benzylic alcohol to the TBS-ether with TBS-Cl under classical Corey conditions[41] provided **10** in a yield of 82% over the last two steps, and of 51% with respect to **11**. However, the poor solubility of aldehyde **13** in most organic solvents rendered a scale-up of this route cumbersome. Therefore, alternative access to **10** was sought for, and achieved via aldehyde **14**, the synthesis of which has been described recently.[40] Reduction of **14** with $NaBH_4$ gave alcohol **15** and subsequent silylation yielded TBS-ether **16**, both in yields of 93% and 95%, respectively. Next, **16** was iodinated adapting a recent procedure by Poncelet et al.[33] Though the iodination proceeded with a conversion of only 65% on a 2 gram scale, simple recrystallization from CH_3CN allowed for isolation of pure **10** in a yield of 56%, or 39% with respect to **11**.

In the second branch of the converging synthesis towards **9**•, ketone **17** was synthesized from thioketals **18** and **19**, which are available in three and four steps, respectively, following a recent protocol.[33] Deprotonation of **18** with *n*BuLi and reaction of the resulting anion with methyl formate provided diarylmethanol **20**, if performing the lithiation at −95 °C. However, the yield of 36% was fairly low. This was also the case when using MeLi.[40] By contrast, generating the lithiumaryl from **19** via lithium–halogen exchange with *t*BuLi at −95 °C increased the yield to 89%. In the final step of this branch, Dess–Martin-oxidation of **20** led to ketone **17** in a yield of 93%.

Within the further synthesis, the most critical step is the formation of the triarylmethanol scaffold in **21** (Scheme 3). Considering the DFT-optimized structure of ketone **17** (Figures S71 and 72), the Bürgi–Dunitz trajectory appears blocked by the bulky *tert*-butoxy substituents and this steric congestion requires tremendous structural reorganization during the transformation. Ultimately, side-reactions such as thioketal cleavage[32,40] or decomposition of lithium organyls through reaction with solvent molecules makes this transformation additionally cumbersome. To cope with these issues, the required nucleophile was generated from **10** by lithium-halogen exchange with exactly 2.0 equiv. *t*BuLi at −95 °C. While other lithium alkyls leave the corresponding alkyl halide behind, no electrophiles remain in the solution using *t*BuLi, so that the aryl lithium can only react with the ketone. In this way, **21** was obtained in an isolated yield of 83%, while the use of *s*BuLi[33] resulted in our hands in a yield of only 31%. Moreover, metal–halogen exchange performed superior compared to direct lith-

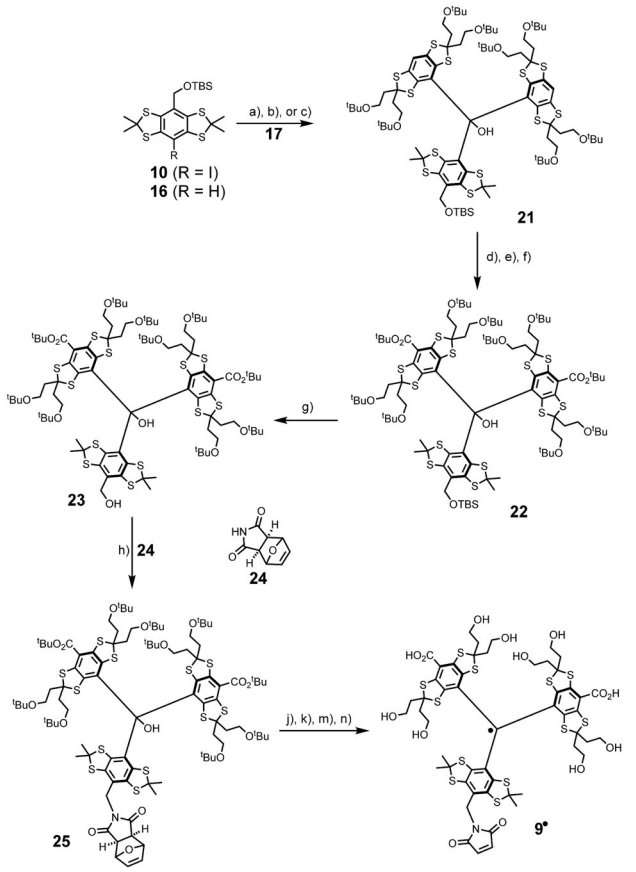

Scheme 3. Final steps for the synthesis of **9**•. a) *t*BuLi, −95 °C, Et_2O, 45 min, then **17**, to r.t., 16 h, 83%; b) *s*BuLi, −95 °C, Et_2O, 45 min, then **17**, to r.t., 16 h, 31%; c) MeLi, THF, r.t., 100 min, exchange for Et_2O, then **18**, 16 h, 11%. a, b) for **10**, c) for **16**. d) *s*BuLi, −20 °C, TMEDA, 120 min. e) CO_2, to r.t., 16 h. f) O-*tert*-butyl-N,N′-diisopropylisourea, PhMe, 60 °C, 4 h, 47% over three steps. g) nBu_4NF, THF, 45 °C, 3 h, 82%. h) ADDP, nBu_3P, **24**, THF, r.t., 5 h, 71%. i, 1) CF_3SO_3H, CH_3CN, r.t., 4 h. 2) $SnCl_2$, THF, r.t., 20 min. j) HCO_2H, 45 °C, 16 h. l) $NaHCO_3$, MeOH, r.t., 16 h. m) DMF, 100 °C, 16 h, 60% over four steps.

iation of **16** with conditions proposed by Hintz et al.,[40] where the yield dropped to 11%. Noteworthy, the choice of solvent seemed important: No conversion was observed within *n*-hexane, presumably related to lacking stabilization of the ionic intermediate of the nucleophilic addition, while diethyl ether proved suitable for this transformation. Advantageous of the benzylic TBS-ether in **10** and **21** is that it paves the way for the late-stage introduction of the concealed maleimide as outlined below. In addition, any functionality compliant with the metal–halogen exchange conditions (e.g. protected alkynes)[40] can be incorporated at this stage, highlighting the versatility of the approach chosen here for accessing asymmetric trityl radicals with high hydrophilicity.

Next, the carboxylation of trityl alcohol **21** was carried out by deprotonation with *s*BuLi in TMEDA/*n*-hexane using gaseous CO_2 as electrophile. Other frequently applied carboxylation reagents such as Boc_2O[16,24,40] more likely contain traces of water, severely diminishing the yield of the dicarboxylated product. The obtained dicarboxylic acid was then converted into the corresponding *tert*-butyl diester **22** using *O-tert*-butyl-diisopropylisourea,[42] since classical Steglich conditions[43] (DCC, DMAP) or the combination Boc_2O/DMAP[44] yielded only traces of product. Subsequently, the TBS-ether in **22** was cleaved with commercially available nBu_4NF (TBAF) in THF yielding **23**. Here, 10 equiv of TBAF and a slightly elevated temperature of 45 °C were required for sufficient reactivity. The C–N bond required for **9**• was introduced via a Mitsunobu reaction in analogy to our previous work, where the maleimide was concealed as a thermally labile tetrahydroisoindolinone.[24] However, since elevated temperatures are required in the later route, the *exo*-Diels–Alder adduct of furane and maleimide **24** was used, which does not undergo retro-Diels–Alder fragmentation up to 50 °C (Supporting Information section 3.3). Carrying out the transformation with the classical reagents Ph_3P and diethylazodicarboxylate (DEAD), **25** was obtained in a yield of only 32% among many unknown by-products (Supporting Information section 3.1). Using instead tri-*n*-butylphosphine and 1,1′-azodicarbonyldipiperidine (ADDP) increased the yield of the Mitsunobu-type C–N bond formation and afforded **25** in a yield of 71%. Both, the acceleration of the C–N bond formation owing to the higher pK_a of the intermediate betaine and steric factors avoiding interactions with the central OH-group are assumed to contribute to this improved yield. In the further course towards **9**•, the corresponding trityl radical was generated with CF_3SO_3H and reduction of the generated tritylium cation with $SnCl_2$ in situ.

The resulting product was immediately treated with neat formic acid at 45 °C for 16 h in order to convert the remaining *tert*-butyl ethers to formate esters and ensure the cleavage of the *tert*-butyl esters. The formate esters were then subjected to very mild hydrolysis with $NaHCO_3$ in methanol at room temperature. It should be noted that other hydrolysing conditions involving LiOH or $Ba(OH)_2$ endangered the integrity of the concealed maleimide (Supporting Information section 3.4). Finally, the maleimide group was deprotected by means of a retro-Diels–Alder reaction at 100 °C in degassed DMF giving the fully characterized (cw-EPR, HRMS, HPLC; cf. Supporting Information) and water-soluble spin label **9**•.

The room temperature continuous wave (cw) X-band EPR spectrum of **9**• is shown in Figure 1a. In analogy to the spectrum of **6**•,[24] it consists of nine resolved lines which arise from hyperfine coupling to the benzylic nitrogen (A_N = 1.48 MHz) and the two magnetically inequivalent benzylic hydrogen atoms (A_{H1} = 3.02 MHz; A_{H2} = 6.09 MHz). Interestingly, record-

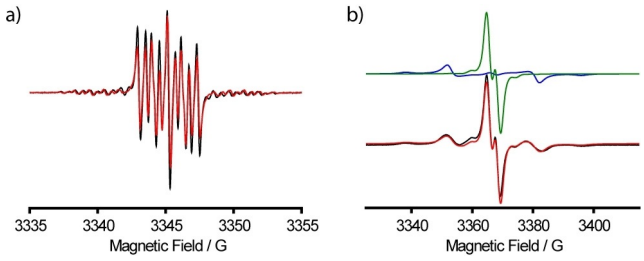

Figure 1. CW X-band EPR spectra of 50 μM **9**• in aqueous PBS buffer recorded at a) room temperature and at b) 100 K after addition of 20% glycerol; simulations are overlaid in red. For (b), the experimental spectrum was simulated as a sum of a monomer (green) and a dimer of **9**• (blue).

ing the spectrum in frozen solution does not only reveal the expected apparent doublet of **9**• (in analogy to **6**•), but also exhibits a superimposed Pake pattern (Figure 1b) in a ratio of 69:31. Analysis of the Pake pattern provides a dipolar coupling constant of 19.4 G corresponding to an interspin distance of 9.9 Å.[22] The Pake pattern is attributed to a noncovalent dimer $(\mathbf{9}^{\bullet})_2$, which was experimentally observed in ESI(−)-MS (Figure S51). Additional evidence for $(\mathbf{9}^{\bullet})_2$ was obtained through a computational study involving a conformer search by the CREST[45] algorithm at the GFN-FF[46] level of theory. The conformation of lowest energy found by CREST was further optimized by B97-3c[47] and is shown in Figure 2. Hybrid-DFT

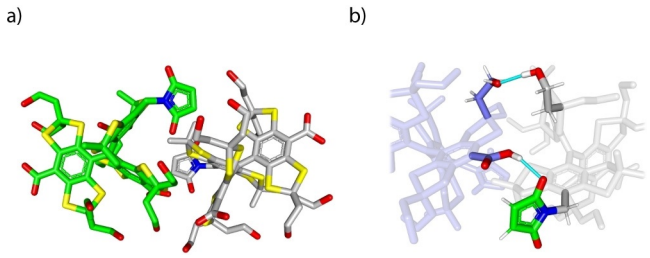

Figure 2. DFT structure of $(\mathbf{9}^{\bullet})_2$. a) Complete view, and b) close-up with hydrogen bonds highlighted in light blue.

single-point calculations (PBE0,[48] def2-TZVPP[49]) combined with GFN2-xTB[50] thermostatistical contributions and COSMO-RS(H_2O)[51] solvation free energies revealed that the homodimer is stabilized by $\Delta G = -14.8$ kcal mol^{-1} due to the formation of hydrogen bonds involving one maleimido substituent (SI section 8.1). For the Ox063-radical **7**•, a similar dimerization was shown to be facilitated by Me_4N^+ as a template,[25] a role fulfilled here by the maleimide moiety. Interestingly, high concentrations of glycerol suppressed dimerization to $(\mathbf{9}^{\bullet})_2$, presumably due to competitive hydrogen bonding, underpinning the non-covalent nature of the dimer (Supporting Information section 6.4). As mentioned above, the hydrophobicity of the first-generation trityl spin labels **2**•–**6**• leads to their aggregation with biomolecules. The concomitant immobilization triggers extensive line-broadening and consequently peak-to-peak amplitude reduction in the cw EPR spectra. This signal depletion has been implemented as a semi-quantitative measure of non-specific aggregation with proteins.[27,29,32] In order to test this, a cysteine-free construct (C219A) of yersinia outer protein O (YopO) was expressed, purified,[24] and added in increasing amounts to solutions of spin labels **4**•, **6**•, and **9**• (Figure 3a). For both **4**• and **6**•, significant signal depletion occurs, indicating aggregation with the protein. By contrast, virtually no signal depletion was encountered for **9**•, highlighting the hydrophilic nature of **9**• which impedes the aggregation.

Next, the performance of **9**• as a spin label was evaluated. Performing the labelling experiment on the cysteine-free YopO construct with 4 equivalents of **9**•, a minor extent of unspecific labelling (7%, Figure 3b and Supporting Information section 5.2) was observed. Applying the same labelling conditions to the double-cysteine mutant (Y588C/N624C), YopO could be doubly labelled with **9**• with a labelling efficiency of 85% (Figure 3b and Supporting Information section 5.3). Since the dimer $(\mathbf{9}^{\bullet})_2$ is only formed in appreciable amounts upon freezing it does not interfere with the labelling reaction, and once bound to a cysteine the maleimide group cannot be involved into the dimer formation anymore. In the following, the side chain generated by binding **9**• to a cysteine residue is called T^{ox}.

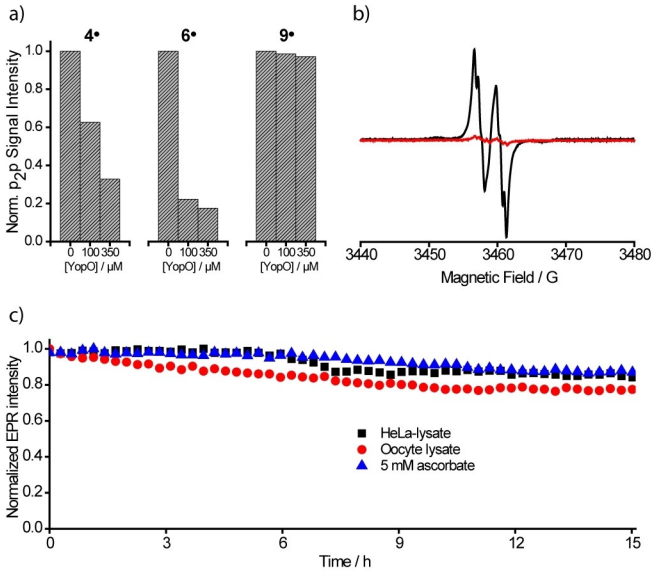

Figure 3. Properties of Ox-SLIM **9**•. a) CW X-band EPR peak-to-peak amplitude of trityl spin labels **4**•, **6**•, and **9**• (50 µM in PBS-buffer) at increasing concentration of cysteine-free YopO C219A. b) CW X-band EPR spectra of YopO Y588T^{ox}/N624T^{ox} (black) and YopO C219A (red) after labelling and workup. The spectra were recorded at 298 K in PBS-buffer. c) EPR double integral intensity of Y588T^{ox}/N624T^{ox} in HeLa lysate, *X. laevis* oocyte lysate, and 5 mM sodium ascorbate monitored over time.

In order to pave the way for future in-cell applications, the reduction stability of Y588T^{ox}/N624T^{ox} was assessed within aqueous solutions of 5 mM ascorbate and lysates of HeLa cells and *Xenopus laevis* oocytes. As shown in Figure 3c, YopO Y588T^{ox}/N624T^{ox} exhibits a high stability in these media, attributed to the imidomethylene-motif of **9**•, which destabilizes the anionic species resulting from reduction.[24]

Finally, a PDS measurement was performed on YopO Y588T^{ox}/N624T^{ox}. Exploiting the high sensitivity of the double quantum coherence (DQC) experiment,[24] the time trace shown in Figure 4a was obtained. It exhibits an SNR[52] of 133 h$^{-1/2}$, exceeding the value obtained with **6**• (46 h$^{-1/2}$) due to a longer T_M-relaxation time (Supporting Information chapter 7). The corresponding distance distribution shows a bimodal shape with most probable distances at 4.60 and 5.48 nm (Figure 4b), which coincide very well with the results obtained for **6**• on this mutant, and supports the idea that the reason for the bimodality are two different structure of the α-helix, at which the labels are bound.[24] Slight changes in the intensity distribution of the two peaks is attributed to different time trace lengths and different conformer clouds of the different labels. The high SNR prompted us to perform DQC measurements on a 45 nM sample of YopO Y588T^{ox}/N624T^{ox}, which still yielded an SNR of 1.24 h$^{-1/2}$ at a dipolar evolution time of

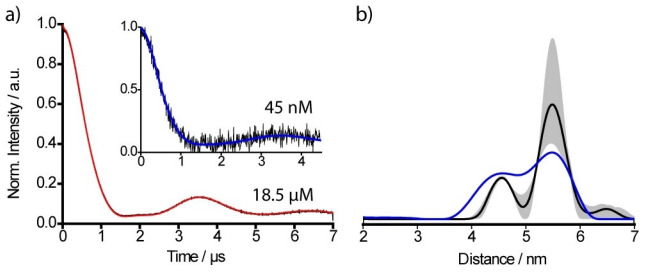

Figure 4. PDS measurements with **9**•. a) Background-corrected DQC time traces obtained for YopO Y588T^{ox}/N624T^{ox} (black), overlaid with their fits by DeerAnalysis (red/blue), shown at both 18.5 µM and 45 nM protein concentrations. b) Distance distribution derived from the time trace of the 18.5 µM sample with the background validation indicated in grey. The distance distribution obtained from the 45 nM samples is overlaid in blue.

4.5 µs (Supporting Information chapter 7). This implies a sensitivity improvement exceeding a factor of 2 compared to our recent publication.[24]

Conclusions

In this study, the highly hydrophilic trityl spin label Ox-SLIM **9**• was introduced through a streamlined synthesis without a statistical step. The chosen approach is highly versatile and the intermediates presented in this study can be utilized as precursors to various hydrophilic trityl radicals. Additionally, an improved Mitsunobu/retro-Diels–Alder sequence is used for the introduction of the maleimide. Overall, label **9**• combines most recent developments on trityl spin labels in a single molecule, i.e., a short linker, bioresistancy, and no aggregation with proteins. Demonstrated for the protein YopO, **9**• allows efficient labelling of cysteines in a selective fashion. Finally, distance measurements with protein concentrations down to 45 nM were viable, thus setting a new benchmark.

Acknowledgements

Funding by the DFG via SPP1601 is gratefully acknowledged. Open access funding enabled and organized by Projekt DEAL.

Conflict of interest

The authors declare no conflict of interest.

Keywords: biophysical chemistry · electron paramagnetic resonance · pulsed dipolar spectroscopy · spin labelling · trityl radicals

[1] M. Gomberg, *J. Am. Chem. Soc.* **1900**, *22*, 757–771.
[2] S. Andersson, A. Rydbeck, R. S. Mahno, US Patent 5728370, **1999**.
[3] T. J. Reddy, T. Iwama, H. J. Halpern, V. H. Rawal, *J. Org. Chem.* **2002**, *67*, 4635–4639.
[4] B. B. Williams, H. J. Halpern, *Biomed. EPR, Part A: Free Radicals, Metals, Medicine and Physiology* (Eds.: S. R. Eaton, G. R. Eaton, L. J. Berliner), Springer US, Boston, **2005**, pp. 283–319.
[5] B. Epel, C. R. Haney, D. Hleihel, C. Wardrip, *Med. Phys.* **2010**, *37*, 2553–2559.
[6] A. A. Bobko, I. Dhimitruka, T. D. Eubank, C. B. Marsh, J. L. Zweier, V. V. Khramtsov, *Free Radic. Biol. Med.* **2009**, *47*, 654–658.
[7] A. Boś-Liedke, M. Walawender, A. Woźniak, D. Flak, J. Gapiński, S. Jurga, M. Kucińska, A. Plewiński, M. Murias, M. Elewa, L. Lampp, P. Imming, K. Tadyszak, *Cell Biochem. Biophys.* **2018**, *76*, 19–28.
[8] M. Poncelet, B. Driesschaert, *Angew. Chem. Int. Ed.* **2020**, *59*, 16451–16454; *Angew. Chem.* **2020**, *132*, 16593–16596.
[9] G. Mathies, M. A. Caporini, V. K. Michaelis, Y. Liu, K. N. Hu, D. Mance, J. L. Zweier, M. Rosay, M. Baldus, R. G. Griffin, *Angew. Chem. Int. Ed.* **2015**, *54*, 11770–11774; *Angew. Chem.* **2015**, *127*, 11936–11940.
[10] J. H. Ardenkjær-Larsen, B. Fridlund, A. Gram, G. Hansson, L. Hansson, M. H. Lerche, R. Servin, M. Thaning, K. Golman, *Proc. Natl. Acad. Sci. USA* **2003**, *100*, 10158–10163.
[11] G. W. Reginsson, N. C. Kunjir, S. T. Sigurdsson, O. Schiemann, *Chem. Eur. J.* **2012**, *18*, 13580–13584.
[12] "*Trityl Radicals as Spin Labels*": O. Krumkacheva, B. Elena, in *Electron Paramagnetic Resonance,* The Royal Society of Chemistry, Cambridge, **2017**, pp. 35–60.
[13] Z. Yang, Y. Liu, P. Borbat, J. L. Zweier, J. H. Freed, W. L. Hubbell, *J. Am. Chem. Soc.* **2012**, *134*, 9950–9952.
[14] G. Y. Shevelev, O. A. Krumkacheva, A. A. Lomzov, A. A. Kuzhelev, O. Y. Rogozhnikova, D. V. Trukhin, T. I. Troitskaya, V. M. Tormyshev, M. V. Fedin, D. V. Pyshnyi, E. G. Bagryanskaya, *J. Am. Chem. Soc.* **2014**, *136*, 9874–9877.
[15] G. W. Reginsson, O. Schiemann, *Biochem. Soc. Trans.* **2011**, *39*, 128–139.
[16] G. Jeschke, *Annu. Rev. Phys. Chem.* **2012**, *63*, 419–446.
[17] P. P. Borbat, J. H. Freed, in *EMagRes*, Wiley, Chichester, **2017**, pp. 465–494.
[18] J. J. Jassoy, A. Berndhäuser, F. Duthie, S. P. Kühn, G. Hagelueken, O. Schiemann, *Angew. Chem. Int. Ed.* **2017**, *56*, 177–181; *Angew. Chem.* **2017**, *129*, 183–187.
[19] B. Joseph, V. M. Tormyshev, O. Y. Rogozhnikova, D. Akhmetzyanov, E. G. Bagryanskaya, T. F. Prisner, *Angew. Chem. Int. Ed.* **2016**, *55*, 11538–11542; *Angew. Chem.* **2016**, *128*, 11710–11714.
[20] A. A. Kuzhelev, D. V. Trukhin, O. A. Krumkacheva, R. K. Strizhakov, O. Y. Rogozhnikova, T. I. Troitskaya, M. V. Fedin, V. M. Tormyshev, E. G. Bagryanskaya, *J. Phys. Chem. B* **2015**, *119*, 13630–13640.
[21] Z. Yang, G. Jiménez-Osés, C. J. López, M. D. Bridges, K. N. Houk, W. L. Hubbell, *J. Am. Chem. Soc.* **2014**, *136*, 15356–15365.
[22] J. J. Jassoy, C. A. Heubach, T. Hett, F. Bernhard, F. R. Haege, G. Hagelueken, O. Schiemann, *Molecules* **2019**, *24*, 2735.
[23] A. Giannoulis, Y. Yang, Y.-J. Gong, X. Tan, A. Feintuch, R. Carmieli, T. Bahrenberg, Y. Liu, X.-C. Su, D. Goldfarb, *Phys. Chem. Chem. Phys.* **2019**, *21*, 10217–10227.
[24] N. Fleck, C. A. Heubach, T. Hett, F. R. Haege, P. P. Bawol, H. Baltruschat, O. Schiemann, *Angew. Chem. Int. Ed.* **2020**, *59*, 9767–9772; *Angew. Chem.* **2020**, *132*, 9854–9859.
[25] I. Marin-Montesinos, J. C. Paniagua, M. Vilaseca, A. Urtizberea, F. Luis, M. Feliz, F. Lin, S. Van Doorslaer, M. Pons, *Phys. Chem. Chem. Phys.* **2015**, *17*, 5785–5794.
[26] I. Marin-Montesinos, J. C. Paniagua, A. Peman, M. Vilaseca, F. Luis, S. Van Doorslaer, M. Pons, *Phys. Chem. Chem. Phys.* **2016**, *18*, 3151–3158.
[27] Y. Song, Y. Liu, W. Liu, F. A. Villamena, J. L. Zweier, *RSC Adv.* **2014**, *4*, 47649–47656.
[28] W. Liu, J. Nie, X. Tan, H. Liu, N. Yu, G. Han, Y. Zhu, F. A. Villamena, Y. Song, J. L. Zweier, Y. Liu, *J. Org. Chem.* **2017**, *82*, 588–596.
[29] Y. Song, Y. Liu, C. Hemann, F. A. Villamena, J. L. Zweier, *J. Org. Chem.* **2013**, *78*, 1371–1376.
[30] M. Poncelet, B. Driesschaert, O. Tseytlin, M. Tseytlin, T. D. Eubank, V. V. Khramtsov, *Bioorg. Med. Chem. Lett.* **2019**, *29*, 1756–1760.
[31] B. Driesschaert, P. Leveque, B. Gallez, J. Marchand-Brynaert, *Tetrahedron Lett.* **2013**, *54*, 5924–5926.
[32] Y. Qu, Y. Li, X. Tan, W. Zhai, G. Han, J. Hou, G. Liu, Y. Song, Y. Liu, *Chem. Eur. J.* **2019**, *25*, 7888–7895.
[33] M. Poncelet, J. L. Huffman, V. V. Khramtsov, I. Dhimitruka, B. Driesschaert, *RSC Adv.* **2019**, *9*, 35073–35076.
[34] V. M. Tormyshev, A. S. Chubarov, O. A. Krumkacheva, D. V. Trukhin, O. Y. Rogozhnikova, A. S. Spitsyna, A. A. Kuzhelev, V. V. Koval, M. V. Fedin, T. S. Godovikova, M. K. Bowman, E. G. Bagryanskaya, *Chem. Eur. J.* **2020**, *26*, 2705–2712.

[35] S. Ketter, A. Gopinath, O. Rogozhnikova, D. Trukhin, V. M. Tormyshev, E. G. Bagryanskaya, B. Joseph, *Chem. Eur. J.* **2021**, *27*, 2299 – 2304.
[36] R. Igarashi, T. Sakai, H. Hara, T. Tenno, T. Tanaka, H. Tochio, M. Shirakawa, *J. Am. Chem. Soc.* **2010**, *132*, 8228 – 8229.
[37] K. Kopp, O. Schiemann, N. Fleck, *Molecules* **2020**, *25*, 3666.
[38] M. Campbell, V. Snieckus, E. W. Baxter, in *e-EROS*, Wiley, **2008**, https://doi.org/10.1002/047084289X.rl143.pub2.
[39] T. D. Krizan, J. C. Martin, *J. Am. Chem. Soc.* **1983**, *105*, 6155 – 6157.
[40] H. Hintz, A. Vanas, D. Klose, G. Jeschke, A. Godt, *J. Org. Chem.* **2019**, *84*, 3304 – 3320.
[41] E. J. Corey, A. Venkateswarlu, *J. Am. Chem. Soc.* **1972**, *94*, 6190 – 6191.
[42] R. M. Burk, G. D. Berger, R. L. Bugianesi, N. N. Girotra, W. H. Parsons, M. M. Ponpipom, *Tetrahedron Lett.* **1993**, *34*, 975 – 978.
[43] B. Neises, W. Steglich, *Angew. Chem. Int. Ed. Engl.* **1978**, *17*, 522 – 524; *Angew. Chem.* **1978**, *90*, 556 – 557.
[44] K. Takeda, A. Akiyama, H. Nakamura, S. I. Takizawa, Y. Mizuno, H. Takayanagi, Y. Harigaya, *Synthesis* **1994**, *1994*, 1063 – 1066.
[45] P. Pracht, F. Bohle, S. Grimme, *Phys. Chem. Chem. Phys.* **2020**, *22*, 7169 – 7192.
[46] S. Spicher, S. Grimme, *Angew. Chem. Int. Ed.* **2020**, *59*, 15665 – 15673; *Angew. Chem.* **2020**, *132*, 15795 – 15803.
[47] J. G. Brandenburg, C. Bannwarth, A. Hansen, S. Grimme, *J. Chem. Phys.* **2018**, *148*, 064104.
[48] J. P. Perdew, M. Ernzerhof, K. Burke, *J. Chem. Phys.* **1996**, *105*, 9982 – 9985.
[49] A. Schäfer, C. Huber, R. Ahlrichs, *J. Chem. Phys.* **1994**, *100*, 5829 – 5835.
[50] C. Bannwarth, S. Ehlert, S. Grimme, *J. Chem. Theory Comput.* **2019**, *15*, 1652 – 1671.
[51] J. Reinisch, M. Diedenhofen, R. Wilcken, A. Udvarhelyi, A. Glöß, *J. Chem. Inf. Model.* **2019**, *59*, 4806 – 4813.
[52] D. Abdullin, P. Brehm, N. Fleck, S. Spicher, S. Grimme, O. Schiemann, *Chem. Eur. J.* **2019**, *25*, 14388 – 14398.

Manuscript received: January 3, 2021
Accepted manuscript online: January 6, 2021
Version of record online: February 17, 2021

Chemistry–A European Journal

Supporting Information

Ox-SLIM: Synthesis of and Site-Specific Labelling with a Highly Hydrophilic Trityl Spin Label

Nico Fleck,[a] Caspar Heubach,[a] Tobias Hett,[a] Sebastian Spicher,[b] Stefan Grimme,[b] and Olav Schiemann*[a]

Contents

1. General Procedures and Instrumentation

NMR-Spectroscopy: NMR spectra were recorded on Avance I 300, Avance I 400, Avance III HD 500, or Avance III HD 700 spectrometers (Bruker BioSpin, Rheinstetten, Germany). Chemical shifts are reported referenced to hydrogen residual peaks of the NMR solvent.[1]

Mass-Spectrometry: MALDI(+)-spectra were recorded in a Bruker Daltonics UltraFlex TOF/TOF spectrometer (Bruker, Rheinstetten, Germany). For organic compounds, DCTB was used as the matrix, whereas DHAP was used for protein samples. For ESI-MS of protein samples, a Synapt G2-Si spectrometer (Waters, Milford, USA) was employed. APCI-spectra and ESI-spectra of organic compounds were obtained on an Orbitrap XL spectrometer (Thermo Fisher Scientific, Bremen, Germany). Protein samples were subjected to mass spectrometric analysis in 20 mM PO_i buffer (pH = 6.8, 50 mM NaCl).

Chromatography: For analytical chromatography, an UHPLC system (PLATINblue-series, Knauer GmbH, Berlin, Germany) equipped with an Eurospher II 100-2 C18P, 2 µm, 2 x 100 mm column (Knauer GmbH, Berlin, Germany) and a UV detector working at 265 nm was used.

CW EPR: All continuous wave (*cw*) EPR spectra were recorded at X-band frequencies (~9.4 GHz) either on an EMXmicro or EMXnano spectrometer (Bruker BioSpin, Rheinstetten, Germany). On the EMXmicro, room temperature measurements were performed using an ER 4122SHQ (Bruker BioSpin, Rheinstetten, Germany) resonator, while measurements at 100 K were conducted with a 4119HS (Bruker) resonator in conjunction with an ER 4141VT temperature control system (Oxford cryogenics, UK). For all samples, X-band EPR-tubes with an outer diameter of 5 mm obtained from Wilmad Labglass (Brand of SP Industries, Warminster, USA) were used. Liquid aqueous samples were filled into 10 µL capillaries (Disposable Capillaries, Hirschmann Laborgeräte, Eberstadt, Germany) and these were placed in the X-band tubes. *CW* EPR measurements at room temperature were performed at an attenuation of 25 dB (603.1 µW) and a modulation amplitude of 0.1 G. CW EPR spectra at 100 K were recorded with an attenuation of 44 dB. Quantitative EPR measurements were conducted employing the on-board spin counting routine of the EMXnano spectrometer.

Pulsed EPR: Pulsed EPR measurements were conducted at Q-band frequencies (~33.7 GHz) on a ELEXSYS E580 EPR spectrometer equipped with an ER5106QT-II resonator (Bruker BioSpin, Rheinstetten, Germany) and a 150 W TWT-amplifier (Applied Systems Engineering, Fort Worth, TX, USA). All data was acquired using quadrature detection. The temperature was adjusted to 50 K using a CF935 helium gas-flow cryostat (Oxford Instruments, Abingdon, UK) and an Oxford Instruments iTC 503 temperature controller.

Synthesis: Chemicals purchased from commercial suppliers were used without further purification. Dry solvents were purchased from *Acros Organics* in sealed bottles containing molecular sieves. Where indicated, solvents were degassed by applying three freeze-pump-thaw cycles. Thin layer chromatography was conducted using 250 µm F254 silica plates provided by Merck, spots were visualized with UV-light at 254nm. Spots of trityl alcohols can be stained selectively by irradiating the TLC-plate for 5min with UV-light at 254nm (5W). For column chromatography, silica gel (60Å pore size, 40–63 µm particle size) purchased from Merck was used. Solvents for chromatography were purchased in analytical grade and used as received. The concentration of butyl lithium solutions was determined prior to use by titration against 2,5-dimethoxybenzylalcohol following the protocol of Winkle et al[2]. Compounds **11**[3], **14**[4], **18**[5], **19**[5], and **24**[6] were prepared according to literature protocols.

2. Synthetic Procedures

2.1 Thioketal **12**

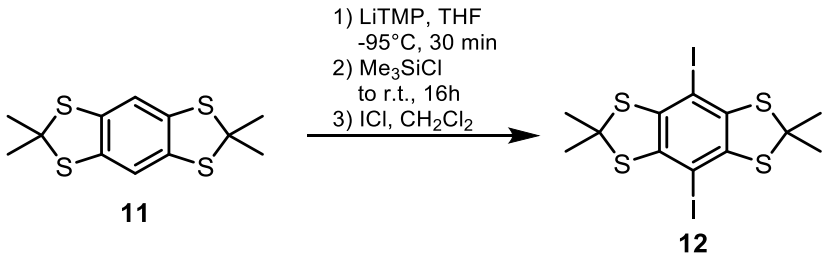

Et_3NHCl (96 mg, 0.7 mmol, 10 mol%) and 2,2,6,6-tetramethylpiperidin (6.92 g, 8.27 mL, 49.12 mmol, 7.00 eq.) were dissolved in 200 mL dry THF under argon. After cooling down to -95°C, *n*-butyl lithium (28.6 mL, 1.6 M in hexanes, 45.6 mmol, 6.50 eq.) was slowly added and the reaction mixture was stirred for 30 minutes to ensure complete formation of LiTMP. Then, **9** (2.00 g, 7.01 mmol) was added as a solid in an argon stream and the reaction mixture was stirred for further 45 min at -95°C. Afterwards, trimethylsilyl chloride (9.07 g, 10.60 mL, 84,1 mmol, 12 eq.) was added dropwise. After continuous stirring for 60 min, the mixture was allowed to warm up while stirred overnight.
50 mL 2M NaOH were slowly added and the organic phase was separated off. After extraction of the aqueous phase with 100 mL diethyl ether, the organic phases were unified and dried over $MgSO_4$. After removal of the solvents under reduced pressure, a yellow solid is obtained. To remove silanols and silylethers, the crude product was washed with cold acetone (3x15 mL), so that a white crystalline solid is obtained. The intermediate obtained, 2,2,6,6-Tetramethyl-4,8-bis(trimethylsilyl)-benzo[1,2-d;4,5-d]bis(1,3-dithiol) is used in the next step without further purification. For the *ipso*-iododesilylation, the obtained product is dissolved in 60 mL dry dichloromethane and cooled down to 0°C. Then, a solution of iodine monochloride (3.40 g, 1.10 mL, 21.03 mmol, 3.00 eq.) in 10 mL dichloromethane is added dropwise. After stirring for 1h under continuous cooling, the orange precipitate is collected and washed with cold acetone (3 x 20 mL) yielding the title compound as a bright yellow/greenish solid in a yield of 3.29 g (86 %).

^{1}H-NMR (500 MHz, $CDCl_3$, 298 K, δ in ppm): 1.91 (s, 12H)
$^{13}C\{^1H\}$-NMR (125 MHz, $CDCl_3$, 298 K, δ in ppm): 139.2, 81.3, 59.0, 32.2
HRMS (EI, *m/z,* $[M]^+$): calcd for $C_{12}H_{12}I_2S_4$, 537.7911; found 537.7911.

2.2 Aldehyde **13**

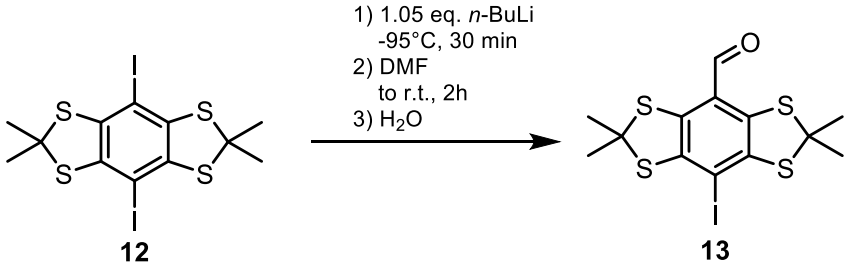

Compound **10** (3.22 g, 5.93 mmol) was dissolved in 250 mL dry THF and cooled down to -95 °C. Thereupon, *n*-butyl lithium (4.07 mL, 1.6 M in hexanes, 6.52 mmol, 1.1 eq.) was added dropwise resulting in a bright yellow color of the reaction mixture. After stirring at -95 °C for 30 min, dry DMF (7 mL, 6.65 g, 91.0 mmol, 15.3 eq.) was added and the reaction mixture was allowed to warm up overnight. Methanol (50

mL) was added carefully, whereupon the reaction mixture turned orange/yellow immediately. Solvents were removed under reduced pressure and the residue was taken up in 300 mL dichloromethane. After washing with water (50 mL) and brine (50 mL), the organic phase was dried over $MgSO_4$ and solvents were removed under reduced pressure yielding the orange title compound, which was subjected to column chromatography on SiO_2 eluting with cyclohexane/ethylacetate 2:1 (v/v). The title compound is obtained as an orange solid in a yield of 1.73 g (73%).
It should be noted, that using less THF results in precipitation of the starting material upon cooling. This leads to an effective excess of butyl lithium yielding the dialdehyde.

^{1}H-NMR (400 MHz, $CDCl_3$, 298 K, δ in ppm): 9.95 (s, 1H), 1.95 (s, 12H)
$^{13}C\{^1H\}$-NMR (100 MHz, $CDCl_3$, 298 K, δ in ppm): 188.5, 144.2, 136.3, 125.1, 88.9, 63.7, 32.2.
HRMS (APCI, *m/z,* $[M+H]^+$): calcd for $C_{13}H_{14}IOS_4$, 440.8965; found 440.8965.

2.3 Thioketal **10**

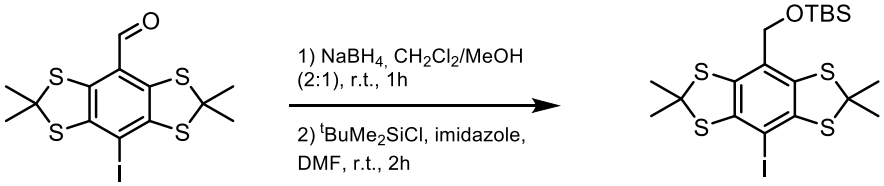

13 **10**

Compound **13** (1.56 g, 3.54 mmol) was dissolved in 80 mL dichloromethane and 40 mL methanol were added. Then, sodium borohydride (269 mg, 7.08 mmol, 2.0 eq.) was added, whereupon the reaction mixture lost its orange color quickly. After stirring for 1h, the solvents were evaporated and the residue was transferred into a Schlenk-flask and dried in high vacuum. Afterwards, imidazole (602 mg, 8.85 mmol, 2.5 eq.) was added and die mixture was dissolved in dry DMF. Upon complete dissolution, *tert*-butyldimethylsilyl chloride (640 mg, 4.25 mmol, 1.2 eq.) was added and the reaction mixture was stirred overnight. After dilution with 100 mL brine, the aqueous phase was extracted twice with dichloromethane and washed with brine several times in order to remove the DMF. The unified organic phases were dried over $MgSO_4$ and solvents were removed under reduced pressure. The yellow residue was suspended in 15 mL cyclohexane and filtered. Removal of the solvents from the filtrate and purification of the crude product by column chromatography on SiO_2 eluting with cyclohexane/ ethyl acetate 97:3 (v/v) yielded the title compound in a yield of 1.61 g (82 %) over two steps.

^{1}H-NMR (400 MHz, $CDCl_3$, 298 K, δ in ppm): 4.46 (s, 2H), 1.88 (s, 12H), 0.91 (s, 9H), 0.08 (s, 6H).
$^{13}C\{^1H\}$-NMR (100 MHz, $CDCl_3$, 298 K, δ in ppm): 142.5, 133.0, 129.8, 81.2, 65.1, 62.3, 31.7, 26.1, 18.6, -5.1.
HRMS (ACPCI, *m/z,* $[M]^+$): calcd for $C_{19}H_{29}IOS_4Si$, 555.9910; found 555.9902.

2.4 Alcohol **15**

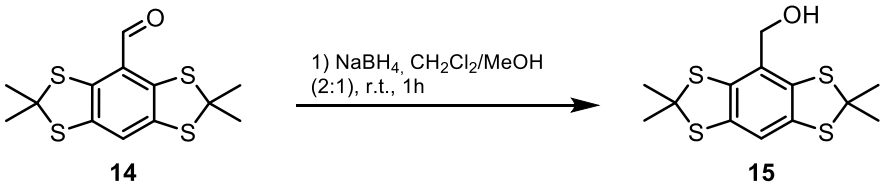

14 **15**

Aldehyde **14** (2.00 g, 6.39 mmol) was dissolved in 100 mL dichloromethane and 50 mL methanol were added. Sodium borohydride (486 mg, 12.78 mmol, 2.00 eq.) was added, whereupon the reaction mixture lost its orange color quickly. After stirring for 1h, the solvents were evaporated and the residue was taken up in 70 mL dichloromethane and the organic phase was washed with water, brine, and dried over $MgSO_4$. The solvents were removed under reduced pressure to yield the title compound as a colorless solid in a yield of 1.88 g (93 %).

^{1}H-NMR (500 MHz, $CDCl_3$, 298 K, δ in ppm): 7.01 (s, 1H), 4.56 (s, 2H), 1.89 (s, 12H)
$^{13}C\{^1H\}$-NMR (125 MHz, $CDCl_3$, 298 K, δ in ppm): 136.6, 136.0, 129.5, 116.6, 65.3, 65.2, 31.5.
HRMS (APCI, *m/z,* $[M]^+$): calcd for $C_{13}H_{16}OS_4$, 316.0078; found 316.0077.

2.5 Thioketal **16**

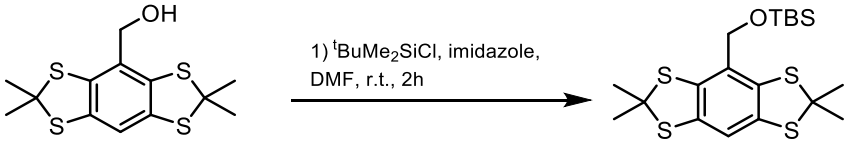

15 **16**

Alcohol **15** (1.71 g, 5.41 mmol) and imidazole (920 mg, 13.52 mmol, 2.50 eq.) were dissolved in 25 mL dry DMF and *tert*-butyldimethylsilyl chloride (974 mg, 6.49 mmol, 1.2 eq.) was added. The reaction mixture was stirred at room temperature over 2 h and quenched by addition of 100 mL water. Extraction was performed with 2 x 50 mL dichloromethane and the unified organic phases were washed with 3 x 100 mL brine. The organic phase was dried over $MgSO_4$ and solvents were removed under reduced pressure, giving a colorless oil. Purification was performed by column chromatography on silica eluting with cyclohexane/ethyl acetate 97:3 affording the title compound as a slowly crystallizing oil in a yield of 2.12 g (91 %).

^{1}H-NMR (500 MHz, $CDCl_3$, 298 K, δ in ppm): 6.99 (s, 1H), 4.55 (s, 2H), 1.87 (s, 12H), 0.91 (s, 9H), 0.08 (s, 6H).
$^{13}C\{^1H\}$-NMR (125 MHz, $CDCl_3$, 298 K, δ in ppm): 136.3, 135.6, 130.3, 116.2, 65.3, 64.9, 31.3, 26.1, 18.6, -5.1.
HRMS (APCI, *m/z,* $[M]^+$): calcd for $C_{19}H_{30}OS_4Si$, 430.0943; found 430.0940.

2.6 Thioketal **10**

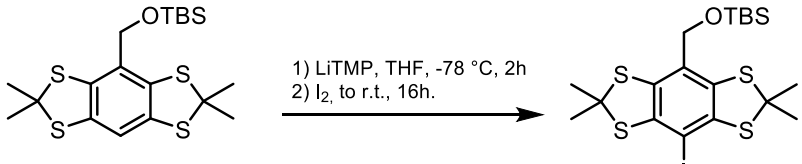

16 **10**

2,2,6,6-Tetramethylpiperidine (1.72 g, 2.07 mL, 12.2 mmol, 2.50 eq.) were dissolved in 50 mL dry THF and cooled to -96 °C. Then, n-butyl lithium (1.6 M in hexane, 7.63 mL, 12.2 mmol, 2.50 eq.) was added and the mixture was stirred for 45 min. Meanwhile, a solution of **16** (2.10 g, 4.88 mmol) in 20 mL dry THF is prepared and then added to the LiTMP solution. After stirring for 2 h at -96 °C, iodine (3.09 g, 12.2 mmol, 2.50 eq.) was added and reaction mixture was stirred for 16 h while warming up to room temperature. Then, 50 mL saturated $Na_2S_2O_3$ solution was added and the mixture was extracted with 3 x 40 mL diethyl ether. The organic phase was washed with water, brine, and dried over $MgSO_4$. After removal of the sol-

vents under reduced pressure, a yellowish crude product is obtained, which is recrystallized from acetonitrile to yield the pure title compound as a colorless solid in a yield of 1.52 g (56 %).
Analytical data of **10 is** provided above.

2.7 Diarylmethanol **20**

2.7.1 Method A

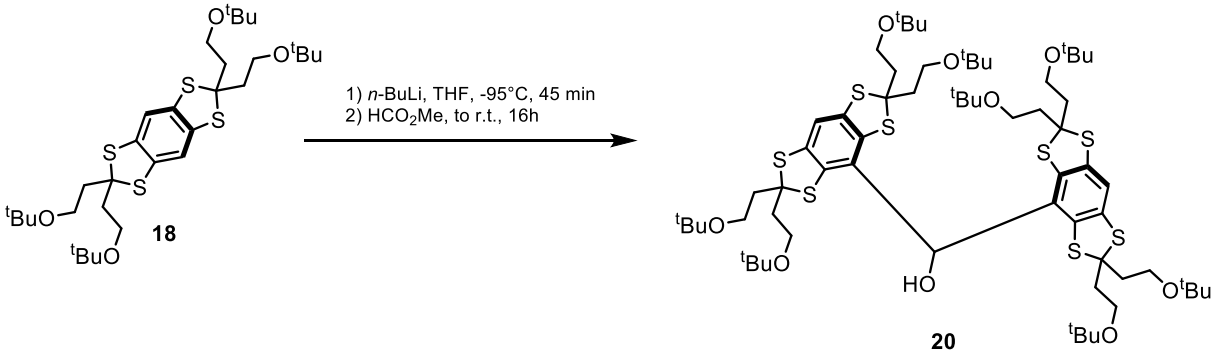

Compound **18** (2.00 g, 3.17 mmol) was dissolved in 50 mL dry THF and cooled to -95°C. Then, *n*-butyl lithium (2.5 M in hexanes, 1.2 mL, 3.00 mmol, 0.95 eq.) was added dropwise resulting in a bright yellow reaction mixture. After stirring for 45 min, methyl formiate (76 mg as a solution in 0.95 mL Et_2O, 1.27 mmol, 0.4 eq.) was added and the reaction mixture was allowed to reach room temperature overnight. Subsequently, THF was removed under reduced pressure and the residue was taken-up in 100 mL dichloromethane. After washing with water (50 mL) and brine (50 mL), the organic phase was dried over $MgSO_4$ and solvents were removed under reduced pressure. The crude product was subjected to column chromatography on silica eluting with cyclohexane/diethyl ether 3:1 (v/v) yielding the title compound as a pale-yellow foam in a yield of 736 mg, 36 % (71 % based on recovered **18** (985 mg)).

^{1}H-NMR (700 MHz, CD_2Cl_2, 298 K, δ in ppm): 7.03 (s, 2H), 3.49 (m, 16H), 2.28 (m, 16H), 1.15 (2x s, 72H)
^{13}C{^{1}H}-NMR (175 MHz, CD_2Cl_2, 298 K, δ in ppm): 138.2, 135.1 130.6, 116.8, 73.39, 73.38, 71.5, 59.2, 59.0, 41.4, 40.8, 27.9.
Note that due to the asymmetry of **20** for steric reasons, diastereotopic effects increase the number of ^{13}C-signals. As visible from figure S1, this asymmetry is reduced on the NMR-timescale with increasing temperature.
HRMS (ESI+, *m/z,* $[M]^+$): calcd for $C_{65}H_{108}O_9S_8$ 1288.5754, found 1288.5753

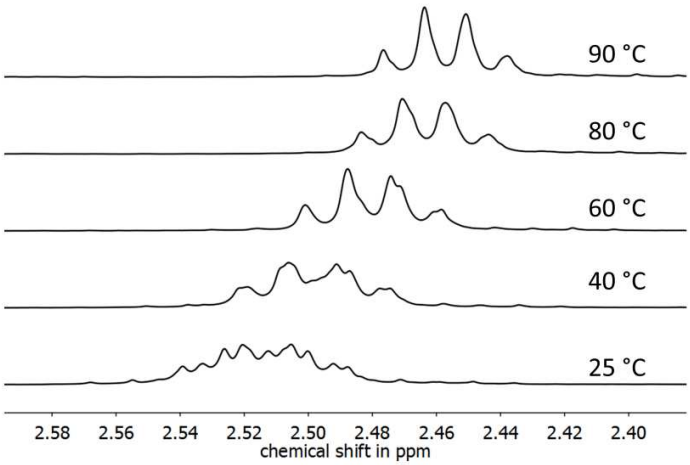

Figure S1: *^{1}H-NMR spectrum of **20** in toluene-d^{8} at variable temperatures.*

2.7.2 Method B

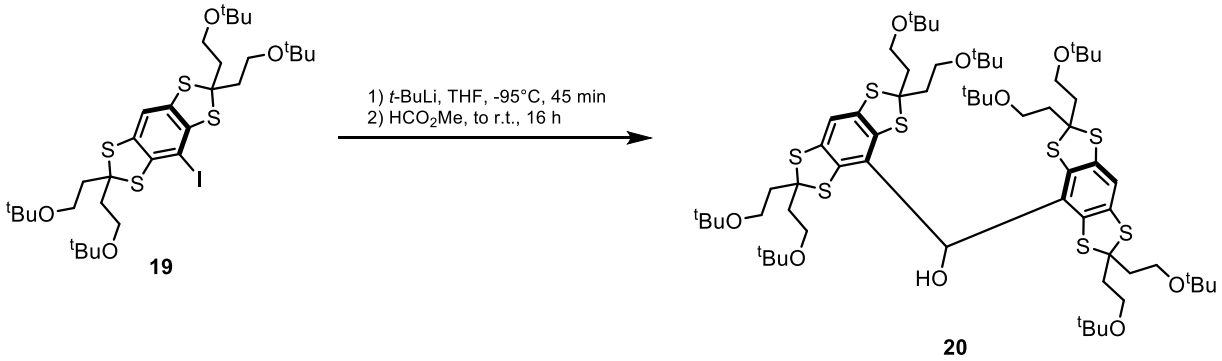

19 (2.87 g, 3.79 mmol) was dissolved in 60 mL dry THF and cooled down to -95°C, whereupon *tert*-butyl lithium (1.24 M in cyclohexane, 5.96 mL, 7.39 mol, 1.95 eq.) was added slowly. The reaction mixture was stirred for 45 min at -95°C and methyl formate (109 mg, 111 µL, 1.82 mmol, 0.48 eq.; dissolved in 0.9 mL dry THF) was added. The reaction mixture was stirred overnight while warming up to room temperature. The workup and the subsequent isolation of the title compound is carried out according to the aforementioned procedure involving direct lithiation of **18**. Yield 2.17 g (89%), based on **19**, and 66 % over two steps referring to **18**.

2.8 Diarylketone **17**

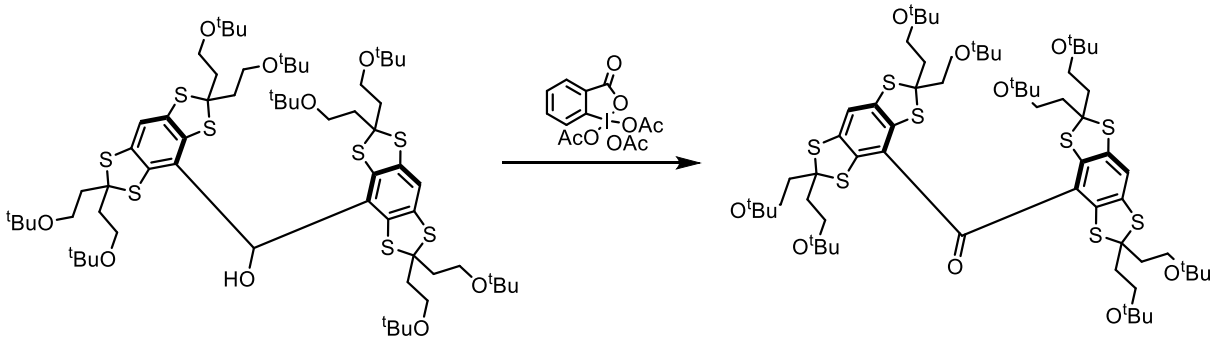

20 **17**

20 (2.96 g, 2.30 mmol) was dissolved in 50 mL dry dichloromethane. Then, *Dess-Martin-periodinane* (1.22 g, 2.87 mmol, 1.25 eq.) was added as a solid, whereupon the reaction mixture turned deep orange within 3 minutes of stirring. After further stirring at room temperature for 60 min, the reaction mixture was poured onto 50 mL ice-water and adjusted to pH 10 with 2M NaOH. The organic phase was separated and the aqueous layer extracted with 30 mL dichloromethane. The unified organic phases were dried over $MgSO_4$ and solvents were removed under reduced pressure to give the crude product as a dark orange oil. Subjecting it to column chromatography on silica and eluting with cyclohexane/diethyl ether 3:1 (v/v) yielded the title compound as an orange foam in a yield of 2.74 g (93 %).

^{1}H-NMR (700 MHz, CD_2Cl_2, 298 K, δ in ppm): 7.14 (s, 2H), 3.50 (t, 16, $^3J_{H,H}$ = 6.4 Hz), 2.32 (t, 16H,$^3J_{H,H}$ = 6.4 Hz), 1.14 (s, 72H).
$^{13}C\{^1H\}$-NMR (175 MHz, CD_2Cl_2, 298 K, δ in ppm): 194.2, 139.0, 136.7, 128.3, 119.3, 73.4, 72.5, 59.0, 41.0, 27.9.
HRMS (MALDI+, *m/z,* $[M]^+$): calcd for $C_{65}H_{106}O_9S_8$ 1286.5597, found 1286.5588

2.9 Trityl alcohol **21**

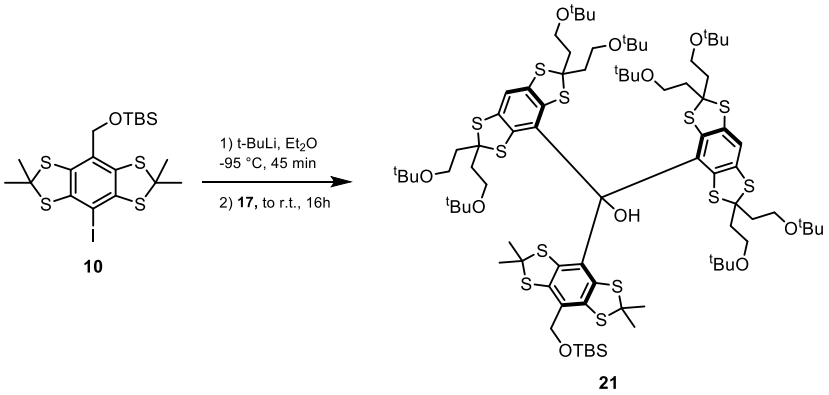

10 **21**

10 (1.173 g, 2.10 mmol) was dissolved in 25 mL dry diethyl ether and cooled down to -95°C. Then, *t*-butyl lithium (1.65 M in pentane, 2.55 mL, 4.21 mmol, 2.00 eq.) was added dropwise to the solution. After stirring for 45 min, **17** (1.68 g, 1.30 mmol, 0.62 eq., dissolved in 20 mL Et_2O) was added slowly and the cooling bath was removed. The reaction mixture was stirred overnight while warming up to room temperature. Afterwards, the reaction was quenched by addition of 50 mL brine, the etheric phase was separated and the aqueous layer was extracted twice with 30 mL Et_2O. The unified organic phases were dried over

$MgSO_4$ and subjected to column chromatography on silica eluting with cyclohexane/diethyl ether 9:1 (v/v) to provide the title compound as an off-white foam in a yield of 1.84 g (1.072 mmol, 83 % referred to **17**).

^{1}H-NMR (700 MHz, CD_2Cl_2, 298 K, δ in ppm): 7.15 (s, 1H), 7.10 (s, 1H), 6.48 (s, 1H), 4.69 (d, 1H, $^2J_{H,H}$ = 11.8 Hz), 4.59 (d, 1H, $^2J_{H,H}$ = 11.8 Hz), 3.59 – 3.16 (m, 16H), 2.50 – 2.00 (m, 16H), 1.82 (s, 3H), 1.80 (s, 3H), 1.77 (s, 3H), 1.70 (s, 3H), 1.18 (s, 9H), 1.15 (s, 18H), 1.13 (s, 9H), 1.11 (s, 9H), 1.11 (s, 9H), 1.06 (s, 9H), 1.03 (s, 9H), 0.94 (s, 9H), 0.13 (s, 3H), 0.10 (s, 3H).
^{13}C{^{1}H}-NMR (175 MHz, CD_2Cl_2, 298 K, δ in ppm): 139.77, 139.67, 139.46, 138.85, 138.77, 138.71, 138.60, 138.47, 138.43, 138.29, 137.50, 137.32, 132.86, 132.49, 131.90, 131.43, 118.43, 118.19, 84.17, 73.67, 73.39, 73.34, 73.32, 73.27, 73.26, 73.17, 73.11, 72.96, 71.10, 70.49, 69.52, 69.36, 66.39, 63.98, 63.05, 60.19, 59.65, 59.34, 59.32, 58.75, 58.71, 58.57, 58.27, 54.43, 54.22, 54.00, 53.78, 53.57, 45.41, 43.47, 40.87, 40.46, 39.77, 39.45, 38.90, 37.70, 34.61, 31.10, 30.78, 27.94, 27.92, 27.90, 27.88, 27.86, 27.81, 26.42, 18.93, -4.48, -4.76.
HRMS (MALDI+, *m/z,* [M]$^+$): calcd for $C_{84}H_{136}O_{10}S_{12}Si$ 1716.6546, found 1716.6621.

2.10 Trityl alcohol **22**

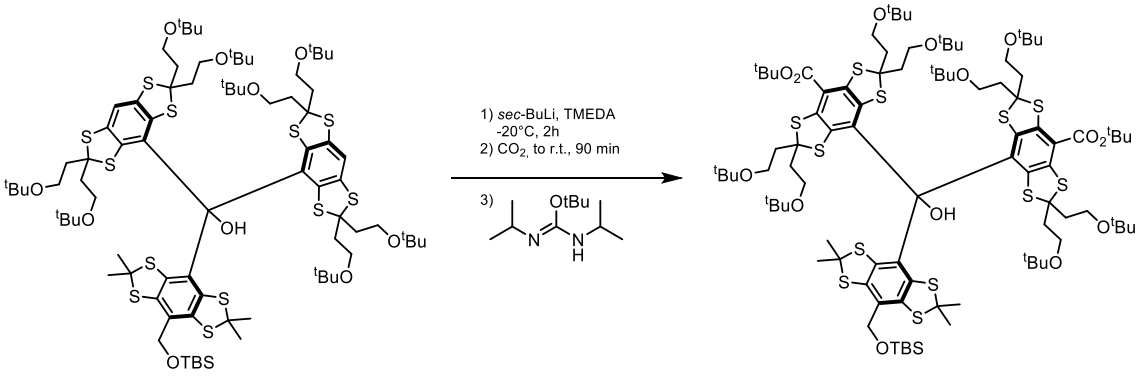

21 **22**

Trityl alcohol **21** (970 mg, 0.565 mmol) was dissolved in 20 mL dry TMEDA and cooled down to -20 °C. Then, *sec*-butyl lithium (6.83 mL, 1.24 M in cyclohexane, 8.47 mmol, 15.0 eq.) was added slowly. After 90 min, additional *sec*-butyl lithium (2.27 mL, 1.24 M in cyclohexane, 2.83 mmol, 5.0 eq.) was added and stirring at -20 °C was continued for further 30 min. The brown reaction mixture was diluted with 30 mL dry TMEDA and CO_2 (purity 4.5, 40 L gas volume) was bubbled through the solution for 4 hours, while the reaction mixture was warmed to room temperature after 2h. The solvents were removed under reduced pressure and the residue was taken-up in 50 mL diethyl ether. After washing with saturated 50 mL NH_4Cl solution, the organic phase was separated, dried over $MgSO_4$ and the solvents were removed under reduced pressure. The carboxylic acid product was dissolved in 20 mL dry toluene. In order to obtain the corresponding tert.-butyl ester, *O-tert*.-butyl-N,N'-diisopropylisourea (339 mg, 404 µL, 1.69 mmol, 3.0 eq.) was added and the reaction mixture heated to 60°C under inert atmosphere for 4h. After cooling down to room temperature, water (10 mL) and sat. NH_4Cl (10 mL) was added. The organic phase was separated, the aqueous layer extracted with 10 mL Et_2O, and the unified organic phases dried over $MgSO_4$. The solvents were removed under reduced pressure. Subjecting the crude product to column chromatography on silica and eluting with cyclohexane/diethyl ether 3:1 (v/v) afforded the title compound as a bright yellow foam in a yield of 508 mg (47.0 %).

^{1}H-NMR (500 MHz, CD_2Cl_2, 298 K, δ in ppm): 6.87 (s, 1H), 4.69 (d, 1H, $^2J_{H,H}$ = 11.7 Hz), 4.64 (d, 1H, $^2J_{H,H}$ = 11.7 Hz), 3.60 – 3.23 (m, 16H), 2.38 – 2.00 (m, 16H), 1.79 (s, 3H), 1.79 (s, 3H), 1.77 (s, 3H), 1.72 (s, 3H),

1.62 (s, 9H), 1.60 (s, 9H), 1.15 (s, 9H), 1.15 (s, 9H), 1.14 (s, 9H), 1.11 (s, 27H), 1.08 (s, 9H), 1.06 (s, 9H), 0.94 (s, 9H), 0.12 (s, 3H), 0.12 (s, 3H).
^{13}C-NMR (125 MHz, CD_2Cl_2, 298 K, δ in ppm): 165.76, 165.62, 141.39, 141.17, 141.12, 140.55, 140.33, 140.29, 139.89, 139.56, 139.33, 139.31, 138.82, 138.48, 135.46, 134.88, 131.51, 130.59, 123.95, 123.62, 84.66, 84.31, 84.12, 73.44, 73.40, 73.32, 73.31, 73.26, 73.25, 73.17, 73.16, 68.18, 68.16, 67.35, 66.97, 66.79, 63.36, 62.49, 59.84, 59.70, 59.32, 59.22, 58.58, 58.51, 58.41, 58.34, 54.43, 54.22, 54.00, 53.78, 53.57, 44.17, 43.97, 40.62, 40.38, 39.43, 38.90, 38.78, 34.97, 34.16, 28.67, 28.64, 28.03, 27.98, 27.96, 27.94, 27.92, 27.91, 27.90, 26.46, 19.01, -4.71, -4.77.
HRMS (MALDI+, *m/z,* $[M]^+$): calcd for $C_{94}H_{152}O_{14}S_{12}Si$ 1916.7594, found 1916.7604.

2.11 Trityl alcohol **23**

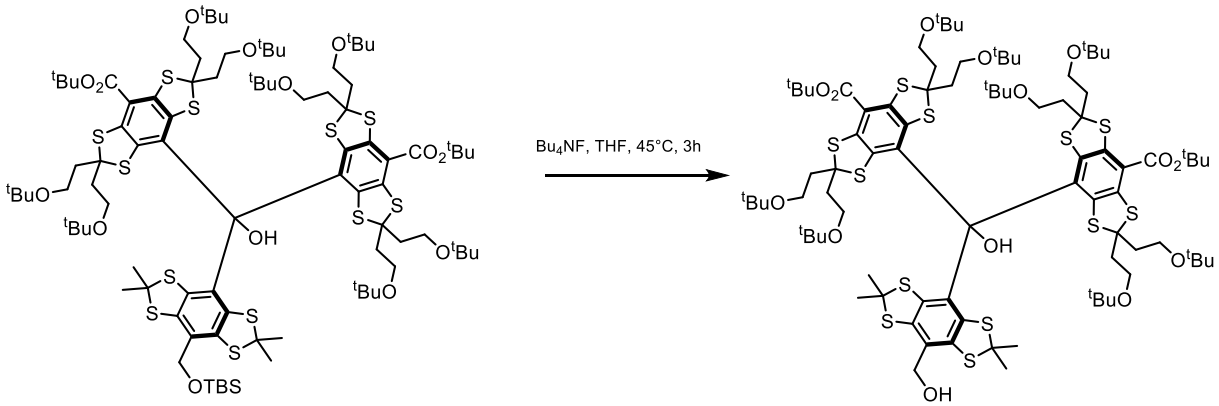

22 **23**

Trityl alcohol **22** (263 mg, 137.8 µmmol) were dissolved in 7 mL dry THF and tetra-*n*-butyl ammonium fluoride (1.38 mL, 1M in THF, 1.38 mmol, 10.0 eq.) was added. The reaction mixture was stirred at 45 °C under TLC control (cyclohexane/diethyl ether 1:1, SiO_2), which proved quantitative conversion after 5h. The solvent was removed under reduced pressure and the residue taken-up in 20 mL dichloromethane. Washing with 20 mL brine and removing the solvents after drying over $MgSO_4$ gave a dark orange oil, which was purified via column chromatography on silica eluting with a cyclohexane/diethyl ether gradient of 3:1 to 1:1 (v/v), providing the title compound as an orange foam in a yield of 203 mg (82%).
^{1}H-NMR (500 MHz, $CDCl_3$, 298 K, δ in ppm): 6.75 (s, 1H), 4.63 (d, 1H, $^2J_{H,H}$ = 12.4 Hz), 4.58 (d, 1H, $^2J_{H,H}$ = 12.4 Hz), 3.62 – 3.19 (m, 16H), 2.40 – 1.99 (m, 16H), 1.80 (s, 3H), 1.78 (s, 3H), 1.75 (s, 3H), 1.70 (s, 3H), 1.61 (s, 9H), 1.60 (s, 9H), 1.15 (s, 9H), 1.14 (s, 9H), 1.12 (s, 9H), 1.09 (s, 9H), 1.08 (s, 18H), 1.05 (s, 9H), 1.02 (s, 9H).
^{13}C-NMR (125 MHz, $CDCl_3$, 298 K, δ in ppm): ^{13}C NMR (126 MHz, $CDCl_3$) δ 165.52, 165.27, 141.38, 140.70, 140.63, 140.37, 140.34, 140.04, 139.60, 139.54, 138.64, 138.61, 137.76, 137.69, 135.55, 134.17, 130.36, 129.81, 123.32, 122.72, 84.15, 83.99, 83.84, 73.30, 73.12, 73.10, 72.98, 72.91, 72.84, 72.81, 72.79, 68.39, 67.01, 66.88, 66.29, 65.91, 63.16, 62.26, 59.54, 59.15, 58.95, 58.46, 58.44, 58.19, 57.92, 57.82, 43.54, 42.25, 41.11, 41.05, 39.47, 38.81, 38.10, 37.91, 35.17, 34.35, 28.46, 28.43, 27.77, 27.72, 27.71, 27.68, 27.65, 27.62, 27.60.
HRMS (MALDI+, *m/z,* $[M]^+$): calcd for $C_{88}H_{138}O_{14}S_{12}$ 1802.6730, found 1802.6734.

2.12 Trityl alcohol **25**

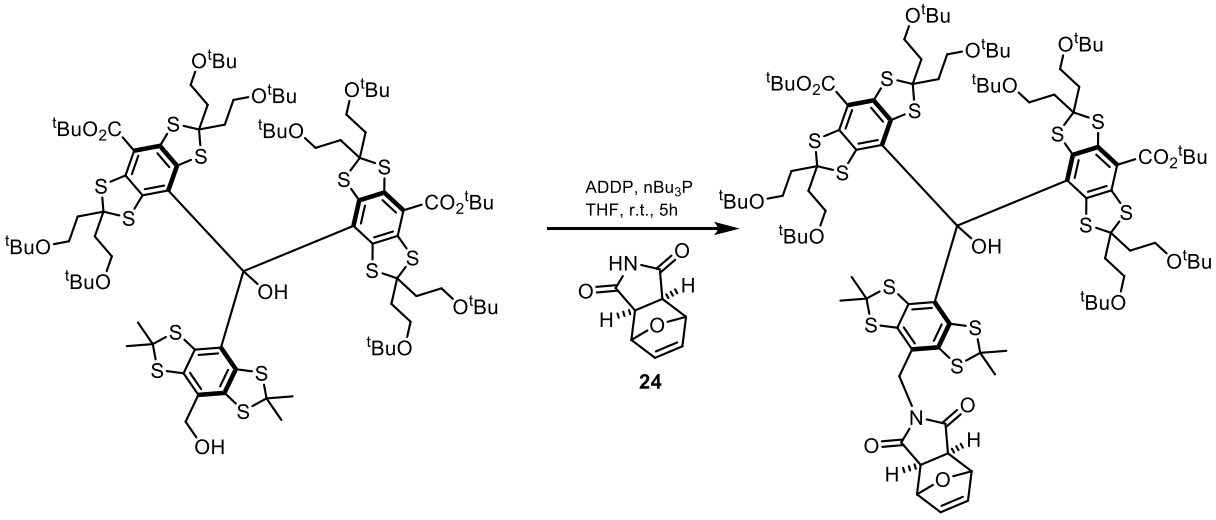

23 **25**

Trityl alcohol **23** (135 mg, 75 µmol) and compound **24** (34 mg, 210 µmol, 2.8 eq.) were placed in a Schlenk-tube and dissolved in 6 mL dry THF. Then, tri-*n*-butylphosphine (36 µL, 44 mg, 180 µmol, 2.4 eq., dissolved in 0.4 mL THF) and subsequently 1,1'-(azodicarbonyl)dipiperidine (46 mg, 180 µmol, 2.4 eq., dissolved in 1.0 mL THF) were added. The reaction mixture was stirred at room temperature under TLC control (CyH/Et_2O 1:1, SiO_2), until completion was observed after 4h. Then, water (10 mL) was added and the mixture was extracted with Et_2O (10 mL) twice. The organic phases were unified, washed with brine, dried over $MgSO_4$ and solvents were removed under reduced pressure to yield an orange oil, which was purified via column chromatographyon silica eluting with cyclohexane/diethyl ether 1:1 (v/v) to afford the title compound as an orange foam in a yield of 104 mg (71%).

^{1}H-NMR (500 MHz, $CDCl_3$, 298 K, δ in ppm): 6.76 (s, 1H), 6.49 (dd, 1H, $^3J_{H,H}$ = 6.0 Hz, $^3J_{H,H}$ = 1.5 Hz), 6.47 (dd, 1H, $^3J_{H,H}$ = 6.0 Hz, $^3J_{H,H}$ = 1.5 Hz), 5.29 (m, 1H), 5.27 (m, 1H), 4.63 (d, 1H, $^2J_{H,H}$ = 12.4 Hz), 4.54 (d, 1H, $^2J_{H,H}$ = 12.4 Hz), 3.59 – 3.26 (m, 16H), 2.91 (d, $^3J_{H,H}$ = 6.7 Hz), 2.85 (d, $^3J_{H,H}$ = 6.7 Hz), 2.42 – 2.02 (m, 16H), 1.79 (s, 6H), 1.77 (s, 3H), 1.69 (s, 3H), 1.62 (s, 18H), 1.17 (s, 9H), 1.14 (s, 9H), 1.13 (s, 9H), 1.11 (s, 9H), 1.10 (s, 9H), 1.10 (s, 9H), 1.05 (s, 9H), 1.04 (s, 9H).
^{13}C-NMR (125 MHz, $CDCl_3$, 298 K, δ in ppm): 2x 174.89*, 2x 165.44*, 141.17, 140.61, 140.55, 140.39, 139.99, 139.96, 139.85, 139.51, 138.88, 138.69, 138.62, 138.31, 136.74, 136.62, 135.00, 133.90, 130.55, 125.64, 124.75, 123.30, 122.85, 84.21, 83.92, 83.88, 80.99, 80.98, 73.11, 73.09, 73.01, 72.96, 72.88, 72.85, 72.75, 67.90, 66.81, 66.51, 66.40, 63.54, 63.48, 59.33, 59.21, 58.69, 58.35, 58.30, 58.20, 58.02, 47.56, 47.17, 43.73, 43.30, 42.27, 41.30, 40.25, 39.48, 39.16, 38.83, 38.30, 34.77, 32.51, 30.46, 29.14, 28.50, 28.46, 27.80, 27.77, 27.76, 27.72, 2x 27.67*.
*Note, that some signal splittings are not fully resolved in the spectrum.
HRMS (MALDI+, *m/z,* $[M]^+$): calcd for $C_{96}H_{143}NO_{16}S_{12}$ 1949.7050, found 1949.7060.

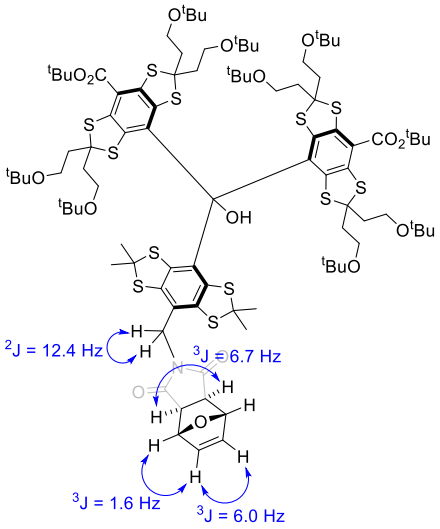

Figure S2: *Scalar $J_{H,H}$ coupling in* ***25*** *as derived from 2D-NMR experiments.*

2.13 Trityl radical **9•** (Ox-SLIM)

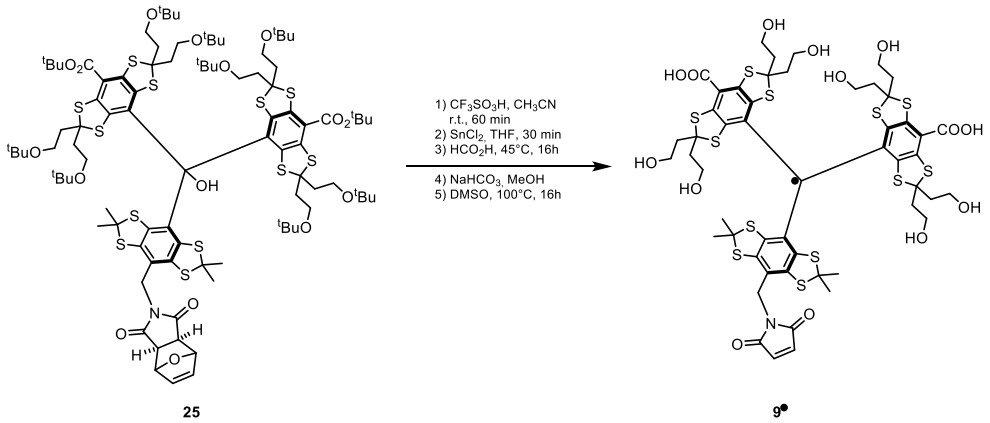

25 **9•**

25 (25 mg, 12.8 µmol) was dissolved in 2 mL dry acetonitrile and triflic acid (77 mg, 45 µL, 512 µmol, 40 eq.) were added whereupon the reaction mixture turned dark green. After stirring for 1h at room temperature, tin(II)-chloride (4.8 mg, 25.6 µmol, 2.0 eq.; dissolved in 200 µL THF) was added and stirring was continued for 30 min. Afterwards, solvents were removed under reduced pressure and 4 mL formic acid were added to the dark green residue. The reaction mixture was stirred at 45°C for 16h and all volatile compounds were removed in high-vacuum subsequently. Then, sodium bicarbonate (172 mg, 2.05 mmol, 160 eq.) and 4 mL methanol were added and the suspension was stirred at room temperature for 16 hours. The dark green suspension was filtered and the filtrate was loaded onto a 20g C18 cartridge (Flash-Pure EcoFlex by Büchi, Germany). Salts were removed by elution with 150 mL methanol/water (80:20 + 0.1 % HCO_2H), while the title compound was eluted by ramping the gradient to pure methanol (+0.1 % formic acid). The dark brown residue was dissolved in 2 mL dry DMF and the resulting brownish green solution was degassed by applying three freeze-pump-thaw cycles and then heated to 100°C for 16 hours. After removal of all volatiles in high vacuum at 45°C, the title compound was isolated via preparative HPLC as a brown solid in a yield of 10 mg (60%).

HRMS (MALDI+, *m/z,* $[M]^+$): calcd for $C_{52}H_{58}O_{14}S_{12}$ 1304.0500, found 1304.0528.
HRMS (ESI-, *m/z,* $[2M-H]^-$): calcd for $C_{104}H_{115}N_2O_{28}S_{24}$ 2609.094, found 2609.093 (base peak).

Preparative HPLC was performed using a Knauer Eurospher II 100-5 C18 column (250 x 16 mm; pre-column 30 x 16 mm). For each run, 9 mg of the crude product were injected as a solution in 100 µL methanol. The product was isolated as the fraction with a retention time of 12.69 min.
Gradient (A = CH_3CN + 0.1 % CF_3COOH; B = H_2O + 0.1 % CF_3COOH)
Start: 10% A + 90% B
05,0 min: 10% A + 90% B
20,0 min: 100% A
25,0 min: 100% A
25,5 min: 10% A + 90% B
30,0 min: 10% A + 90% B

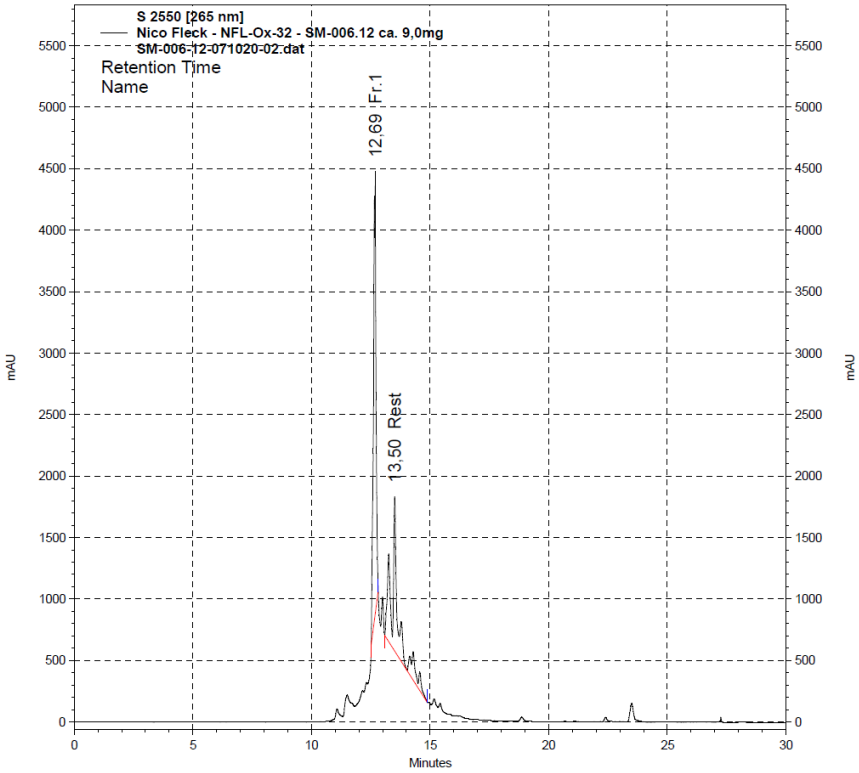

Figure S3: *Chromatogram of preparative HPLC @265 nm.*

3. Reaction Optimization

3.1 Mitsunobu Reaction

Performing the C-N bond formation from **23** to **25** under classical conditions using DEAD and Ph_3P, the product was obtained in a yield of only 31 %. The formation of several unknown byproduct was evident from TLC (Figure S4).

Figure S4: *TLC-analysis of the crude reaction mixture of the Mitsunobu-reaction of* ***23*** *to* ***25*** *using Ph_3P/DEAD. E = starting material, R = reaction mixture (product encircled), P = product.*

3.2 Formation of t-Butyl Esters for **22**

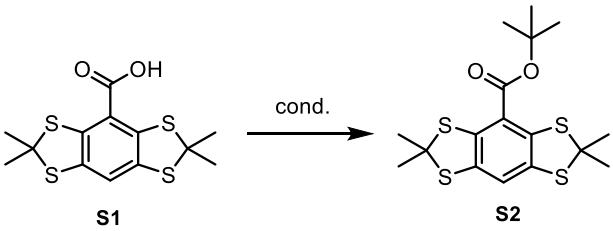

Scheme S1: *Model reaction for the formation of* ***22****.*

After carboxylation of **21** with CO_2, the formation of the *t*-butyl esters was required and the model reaction shown in scheme S1 was employed to seek for appropriate conditions. Compound **S1** was obtained by a protocol recently published by *Wessig* et al.[7] The esterifications were run at a 100 mg scale and 0.1 M with the conditions indicated in table S1 and the product was isolated via column chromatography on silica eluting with n-hexane/ethyl acetate 2:1.

Table S1: *Condition screening for the synthesis of tert.-butyl esters according to Scheme S1.*

entry	conditions	yield S2 (isolated)
1	*Steglich:* 1 eq. DCC, 1 eq. DMAP, 2 eq. t-BuOH, CH_2Cl_2, r.t. 16h	trace
2	1 eq. DMAP, 3 eq. Boc_2O, r.t., 16h	44 %
3	1.25 eq. O-*tert*.-butyl-N,N'-diisopropylisourea, toluene, 60°C, 2h.	95 %

Analytical data of **S2**:
^{1}H-NMR (400 MHz, $CDCl_3$, 298 K, δ in ppm): 7.11 (s, 1H), 1.84 (s, 12H), 1.67 (s, 9H).
^{13}C-NMR (100 MHz, CD_2Cl_2, 298 K, δ in ppm): 164.9, 139.3, 136.6, 122.2, 119.1, 84.4, 63.1, 31.5, 28.5.
MS (EI, *m/z*): 386.1 [24%, $M]^+$, 330.0 [51%, $M\text{-}C_4H_8]^+$, 315.0 [100%, $M\text{-}CH_3\text{-}C_4H_8]^+$.

3.3 Thermal stability of *exo*-Tetrahydroisoindolindione

While the thermal stability of the *endo*-tetrahydroisoindolindione moiety used to conceal the maleimide in our previous study on SLIM[8] is low, so that an unblocking temperature of 60°C is sufficient, this is not the case for the thermodynamically more favored *exo*-product. Seeking for unblocking conditions, compound **S3** was synthesized in analogy to its *endo*-derivative[8] and subjected to *Retro-Diels-Alder* reaction

through simple heating in DMF. As shown in Scheme S2 and Figure S5 the chemical shift of the vinylic protons differs remarkably in both compounds, so that the reaction can be tracked via ^{1}H-NMR.

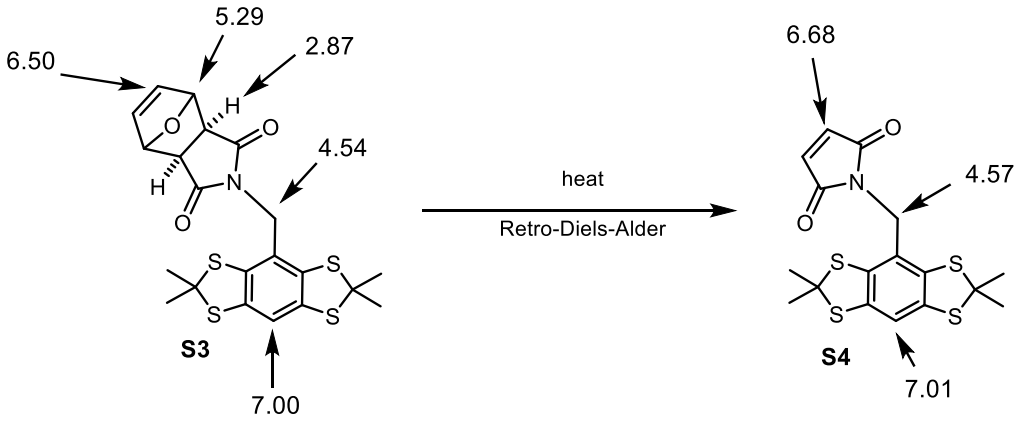

Scheme S2: *Retro-Diels-Alder fragmentation of exo-tetrahydroisoindolindione* ***S3*** *to maleimide* ***S3****. Chemical shifts in ^{1}H-NMR (in ppm, $CDCl_3$) are indicated to the respective proton-bearing positions with arrows.*

The analytical data of **S4** is provided in the Supporting Information of the study on SLIM.[8] The analytical data for **S3** is:
^{1}H-NMR (500 MHz, $CDCl_3$, 298 K, δ in ppm): 7.00 (s, 1H), 6.50 (m, 2H), 5.29 (s, 2H), 4.54 (s, 2H), 2.87 (s, 2H), 1.87 (s, 12H).
^{13}C-NMR (125 MHz, CD_2Cl_2, 298 K, δ in ppm): δ 175.2, 136.73, 136.70, 136.6, 124.3, 116.5, 81.0, 65.6, 47.5, 43.3, 31.3.
HRMS (ESI+, *m/z,* [M-furane]$^{+}$): calcd for $C_{17}H_{17}NO_2S_4$ 395.0137, found 395.0136.
Note, that compound ***S3*** *undergoes Retro-Diels-Alder fragmentation during MS.*

a) *b)*

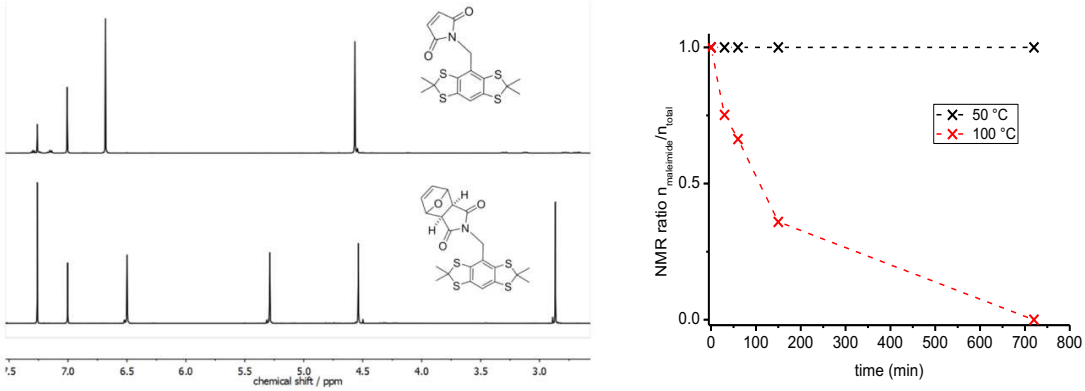

Figure S5: *a) ^{1}H-NMR spectra of* ***S3*** *and* ***S4****. b) Kinetics of the Retro-Diels-Alder cleavage of* ***S3****.*

Through integration of the ^{1}H-NMR spectra, the molar fraction of the maleimide was determined for several timepoints as shown in figure S5b. Clearly, no conversion is observed at 50°C, while slow unblocking occurs at 100°C yielding the free maleimide quantitatively after 12 hours.

3.4 Tests for conversion of **25•** to **9•**

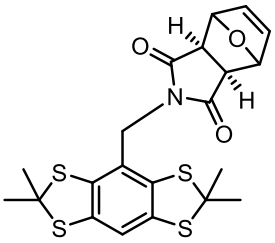

S3

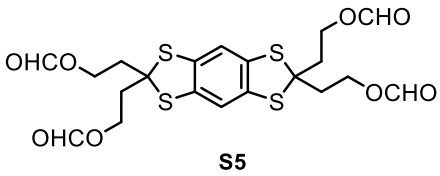

S5

Scheme S3: *Compounds **S3** and **S5***

Seeking for appropriate conditions to hydrolyze the formate ester intermediate occurring in the synthesis of **9•** from **25**, compounds **S3** and **S5** were synthesized (*vide supra* for **S3**) and subjected to various hydrolyzing conditions shown in table S2. The extent of hydrolysis was determined from ^{1}H-NMR spectra of the crude reaction mixture. As shown in Table S2, it turned out, that conditions typically applied for ester hydrolysis (LiOH/H_2O/THF, entry 1) led to a hydrolysis of the concealed maleimide. Even a milder surrogate, $Ba(OH)_2$/MeOH (entry 2) led to significant hydrolysis of the latter one. **S5** was obtained by heating **18** in neat formic acid at 45 °C for 2 h.

Table S2: *Screening for ester cleavage.*

No.	conditions / substrate conversion	Hydrolysis of **S5**	Hydrolysis of **S3**
1	10 eq. LiOH, 2h r.t., THF/MeOH/H_2O (5:5:1)	100 %	100 %
2	20 eq. $Ba(OH)_2$, MeOH/THF (5:3), 2h, r.t.	100 %	62 %
3	5 eq. $KOSiMe_3$, THF, r.t., 2 h	100 %	20 %
4	40 eq. K_2CO_3, MeOH, r.t., 16h	100 %	0 %
5	80 eq. $NaHCO_3$, MeOH, r.t., 16h	100 %	0 %

Analytical data for **S5**:
^{1}H-NMR (500 MHz, $CDCl_3$, 298 K, δ in ppm): 8.04 (s, 4H), 6.98 (s, 2H), 4.44 (t, 8H, $^{3}J_{H,H}$ = 7.4 Hz), 2.46 (t, 8H, $^{3}J_{H,H}$ = 7.4 Hz).
^{13}C-NMR (125 MHz, CD_2Cl_2, 298 K, δ in ppm): δ 160.7, 135.1, 116.6, 69.8, 60.8, 39.6.
HRMS (MALDI+,*m/z*): calcd for $[M]^+$ $C_{20}H_{22}O_8S_4$ 518.0192, found 518.0173.

4. Analytical data

4.1 NMR-Spectroscopy

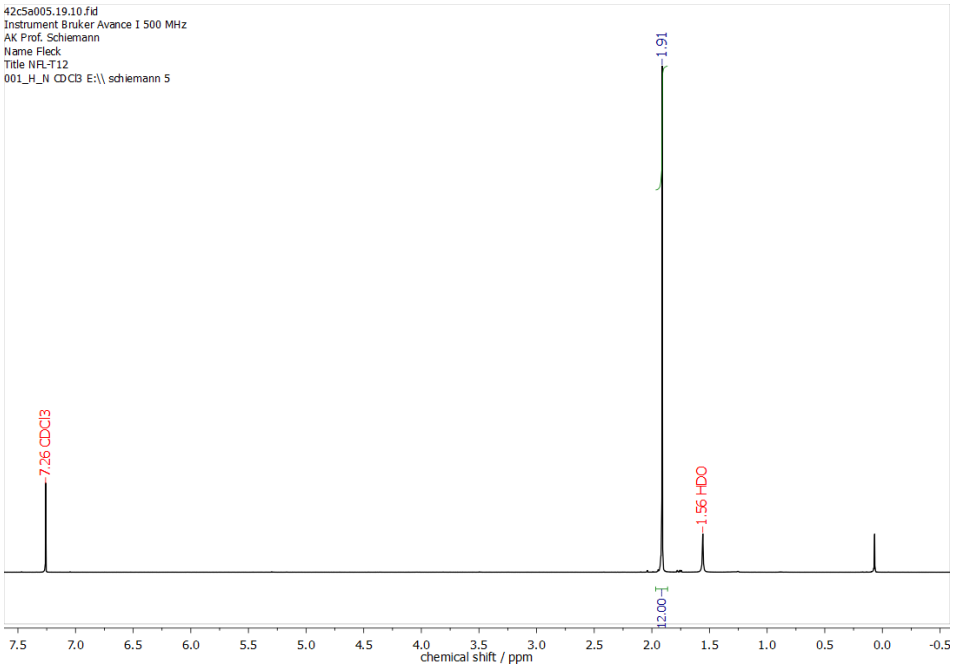

Figure S6: *^{1}H-NMR spectrum ($CDCl_3$, 500 MHz) of Thioketal* ***12***

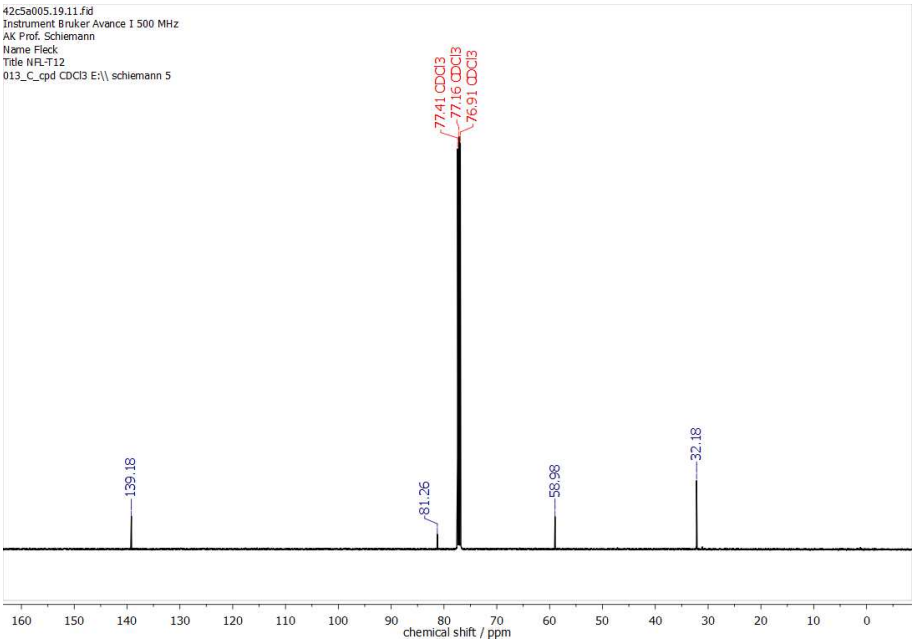

Figure S7: *^{13}C-NMR spectrum ($CDCl_3$, 125 MHz) of Thioketal* ***12***

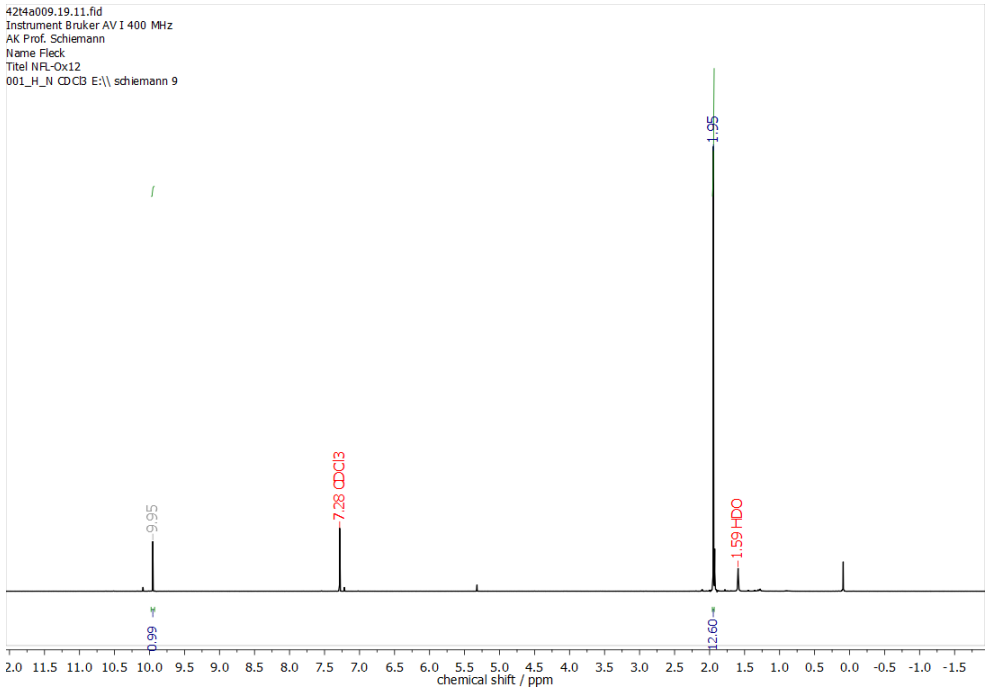

Figure S8: *^{1}H-NMR spectrum ($CDCl_3$, 400 MHz) of Aldehyde* ***13***

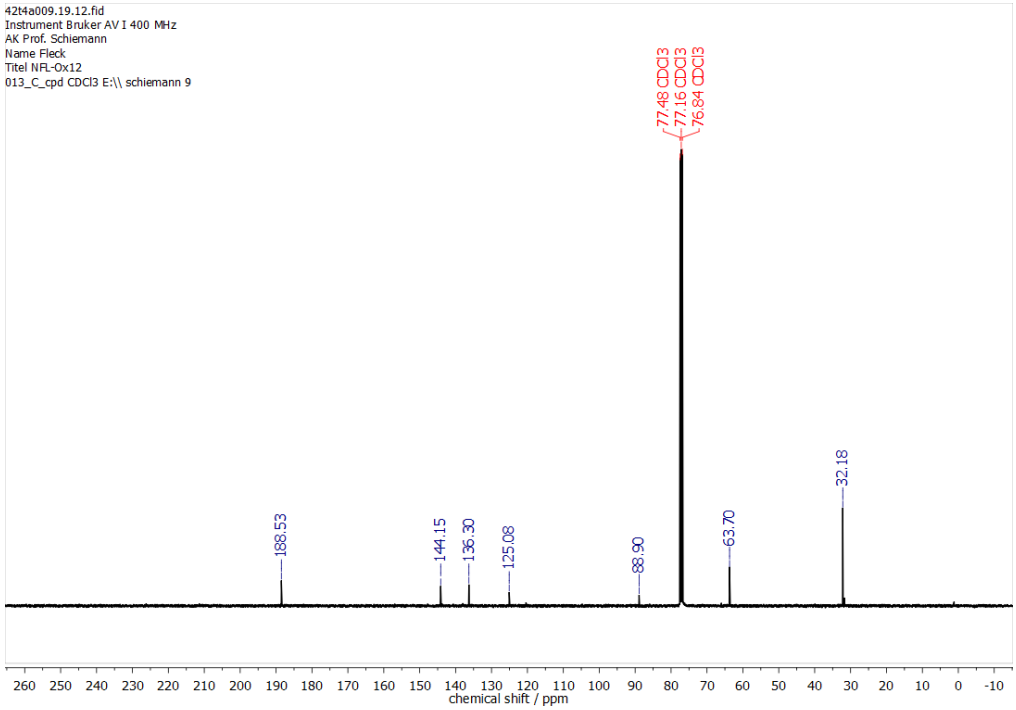

Figure S9: *^{13}C-NMR spectrum ($CDCl_3$, 100 MHz) of Aldehyde* ***13***

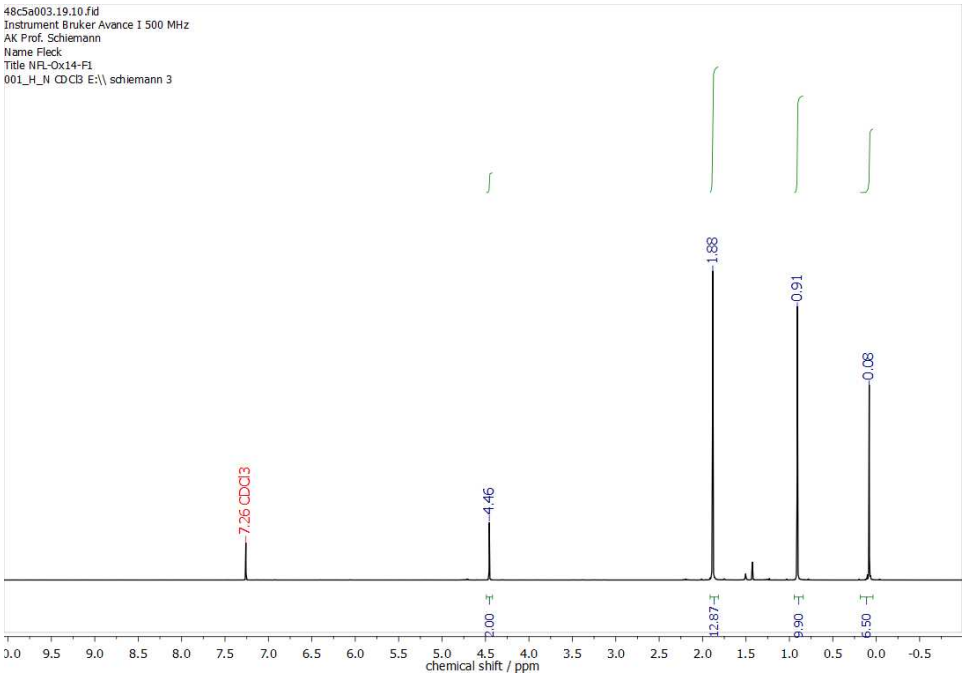

Figure S10: *^{1}H-NMR spectrum ($CDCl_3$, 500 MHz) of Thioketal* ***10***

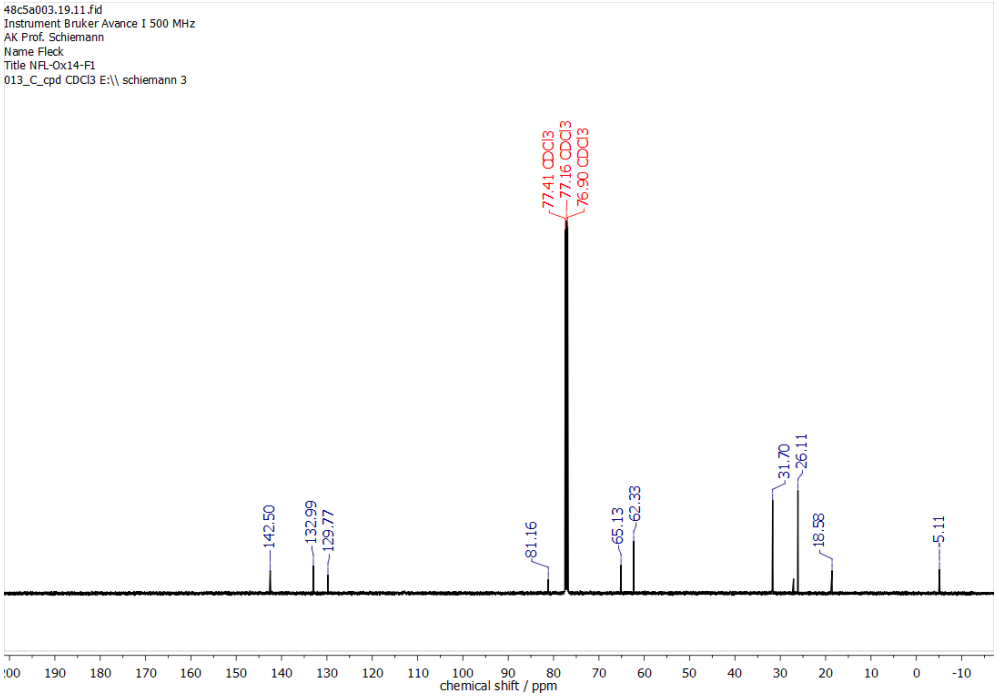

Figure S11: *^{13}C-NMR spectrum ($CDCl_3$, 125 MHz) of Thioketal* ***10***

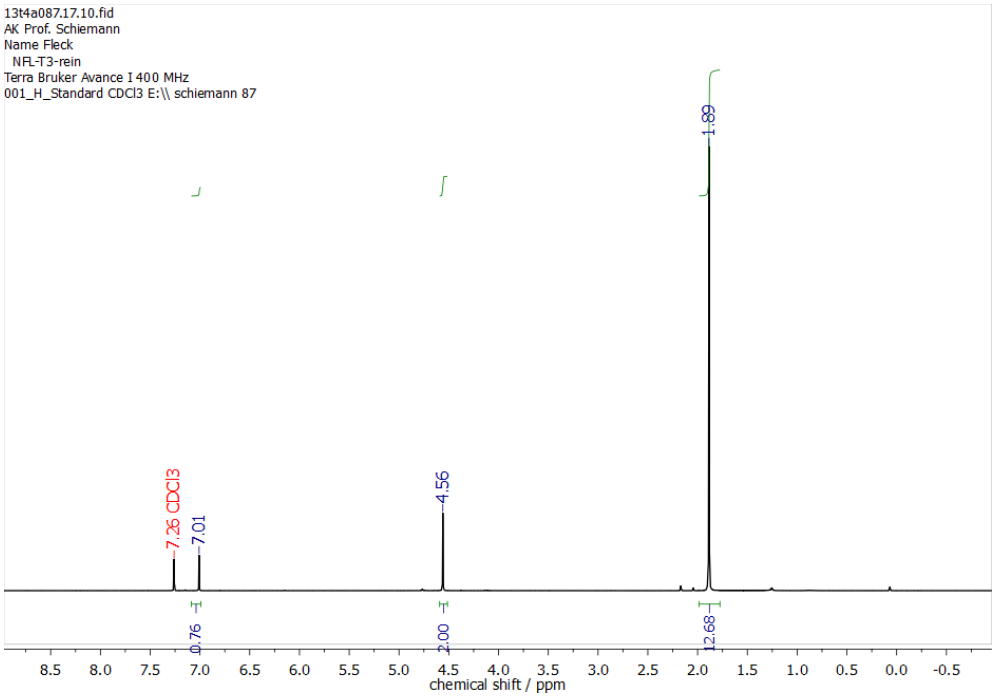

Figure S12: *^{1}H-NMR spectrum ($CDCl_3$, 400 MHz) of Alcohol* ***15****.*

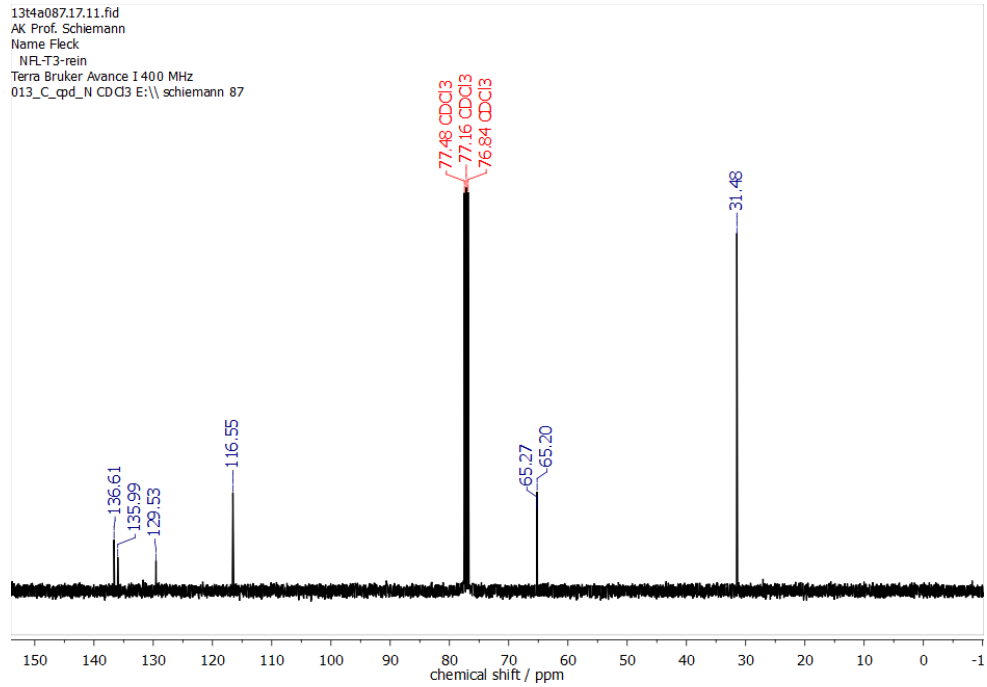

Figure S13: *^{13}C-NMR spectrum ($CDCl_3$, 100 MHz) of Alcohol* ***15****.*

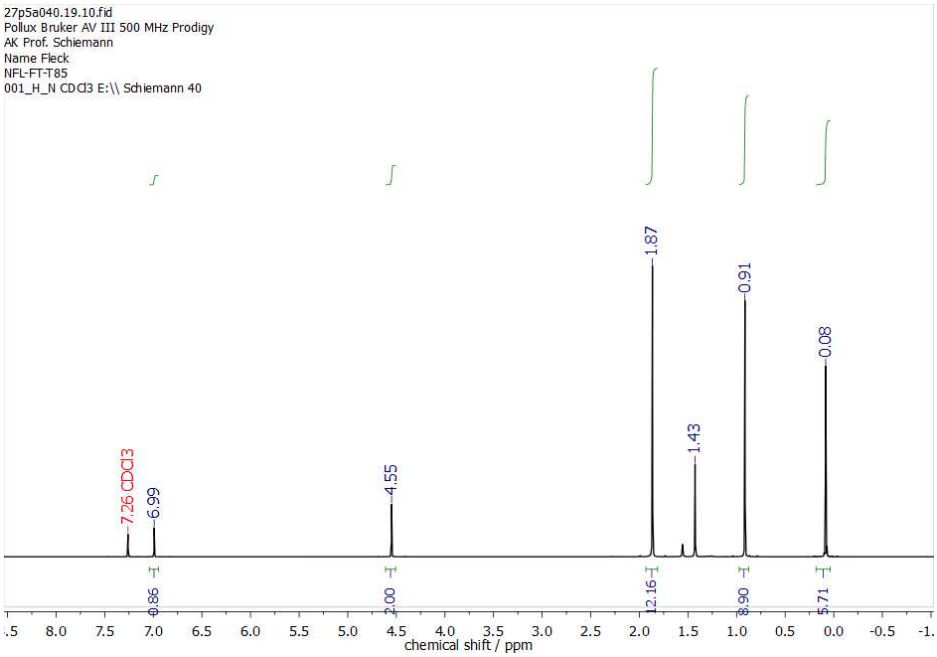

Figure S14: *^{1}H-NMR spectrum ($CDCl_3$, 500 MHz) of Thioketal* ***16****. The peak at 1.43 ppm is attributed to cyclohexane residues in the sample, present even after thorough drying at 10^{-3} mbar overnight.*

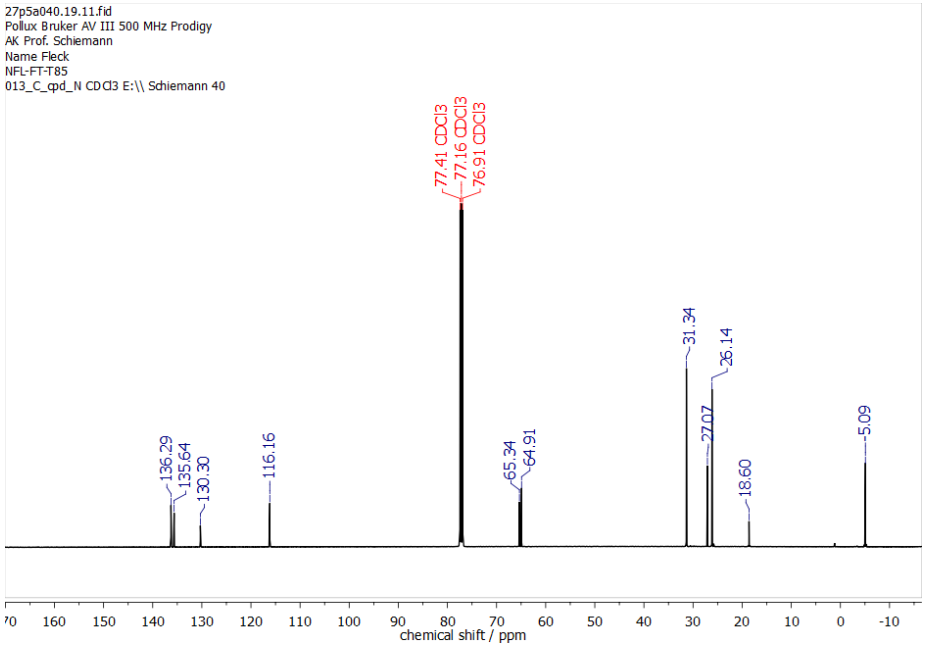

Figure S15: *^{13}C-NMR spectrum ($CDCl_3$, 125 MHz) of Thioketal* ***16****. The peak at 27.07 ppm belongs to cyclohexane (vide supra).*

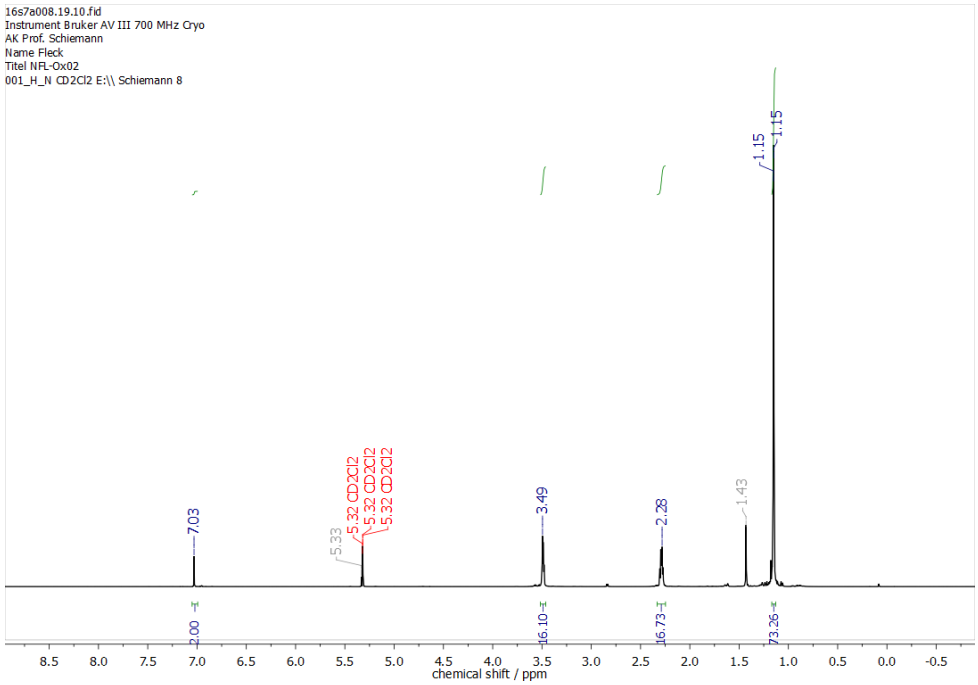

Figure S16: *^{1}H-NMR spectrum (CD_2Cl_2, 700 MHz) of Diarylmethanol* ***20****. The peak at 5.33 ppm belongs to non-deuterated dichloromethane and the one at 1.43 to a small impurity of cyclohexane.*

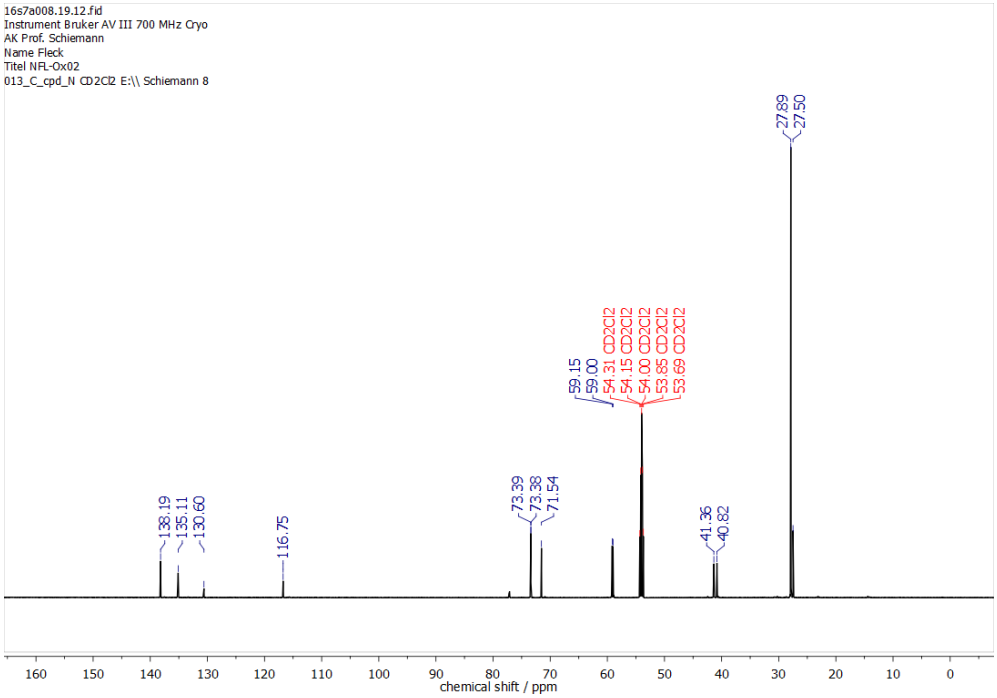

Figure S17: *^{13}C-NMR spectrum (CD_2Cl_2, 175 MHz) of Diarylmethanol* ***20****. The peak at 27.50 ppm belongs to a small impurity of cyclohexane.*

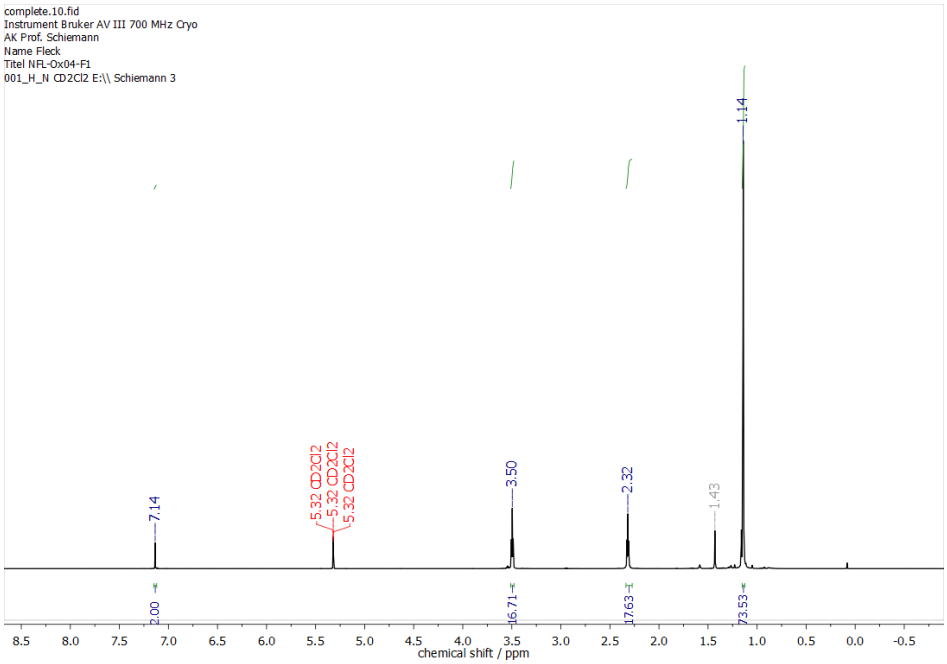

Figure S18: *^{1}H-NMR spectrum (CD_2Cl_2, 700 MHz) of Diarylketone* ***17****. The peak at 1.43 ppm belongs to a small impurity of cyclohexane.*

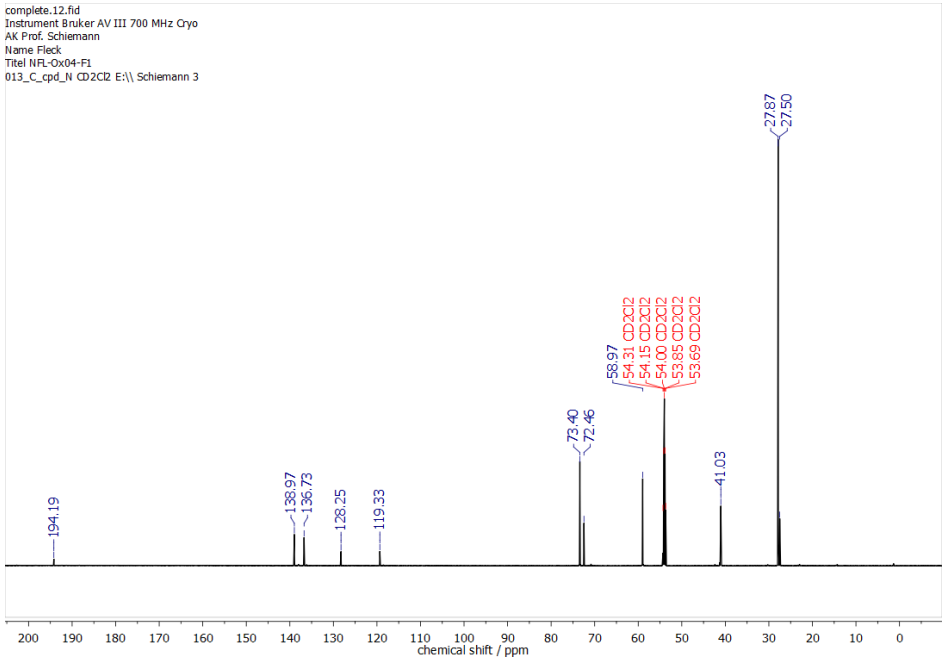

Figure S19: *^{13}C-NMR spectrum (CD_2Cl_2, 175 MHz) of Diarylketone* ***17****. The small peak at 27.5 ppm is attributed to an impurity by cyclohexane.*

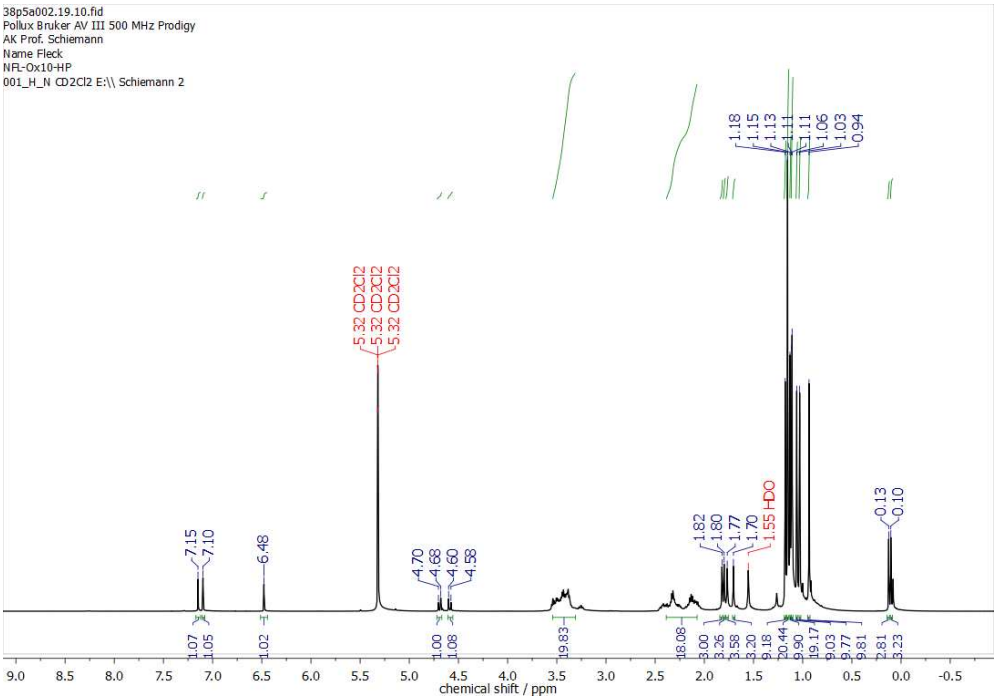

Figure S20: *^{1}H-NMR spectrum (CD_2Cl_2, 500 MHz) of Trityl alcohol* ***21.***

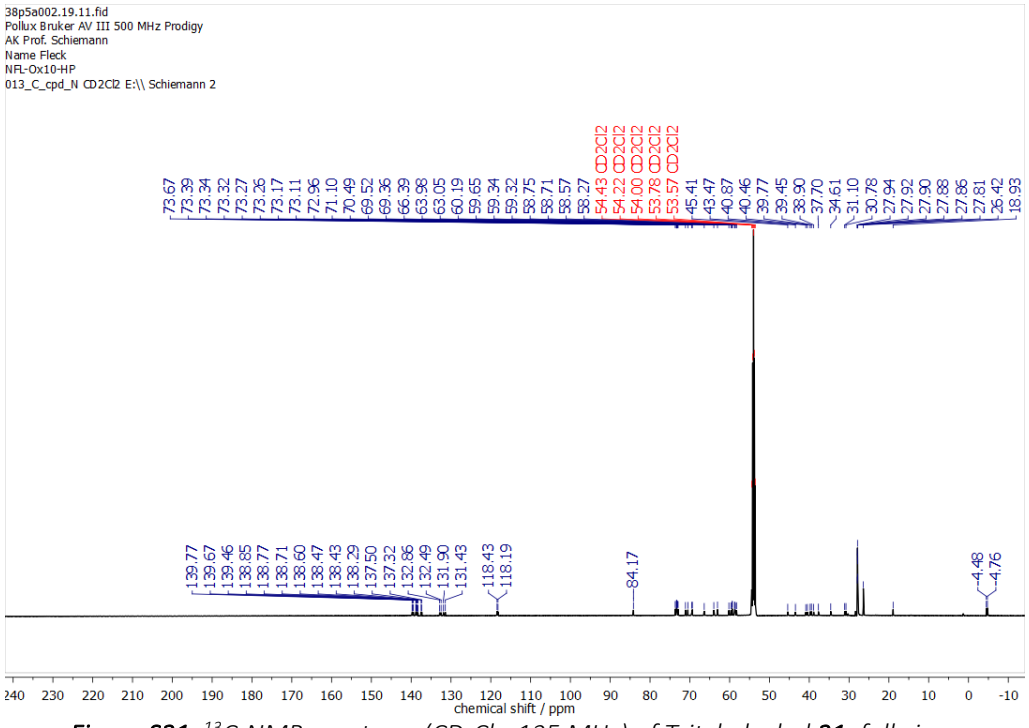

Figure S21: *^{13}C-NMR spectrum (CD_2Cl_2, 125 MHz) of Trityl alcohol* ***21****, full view.*

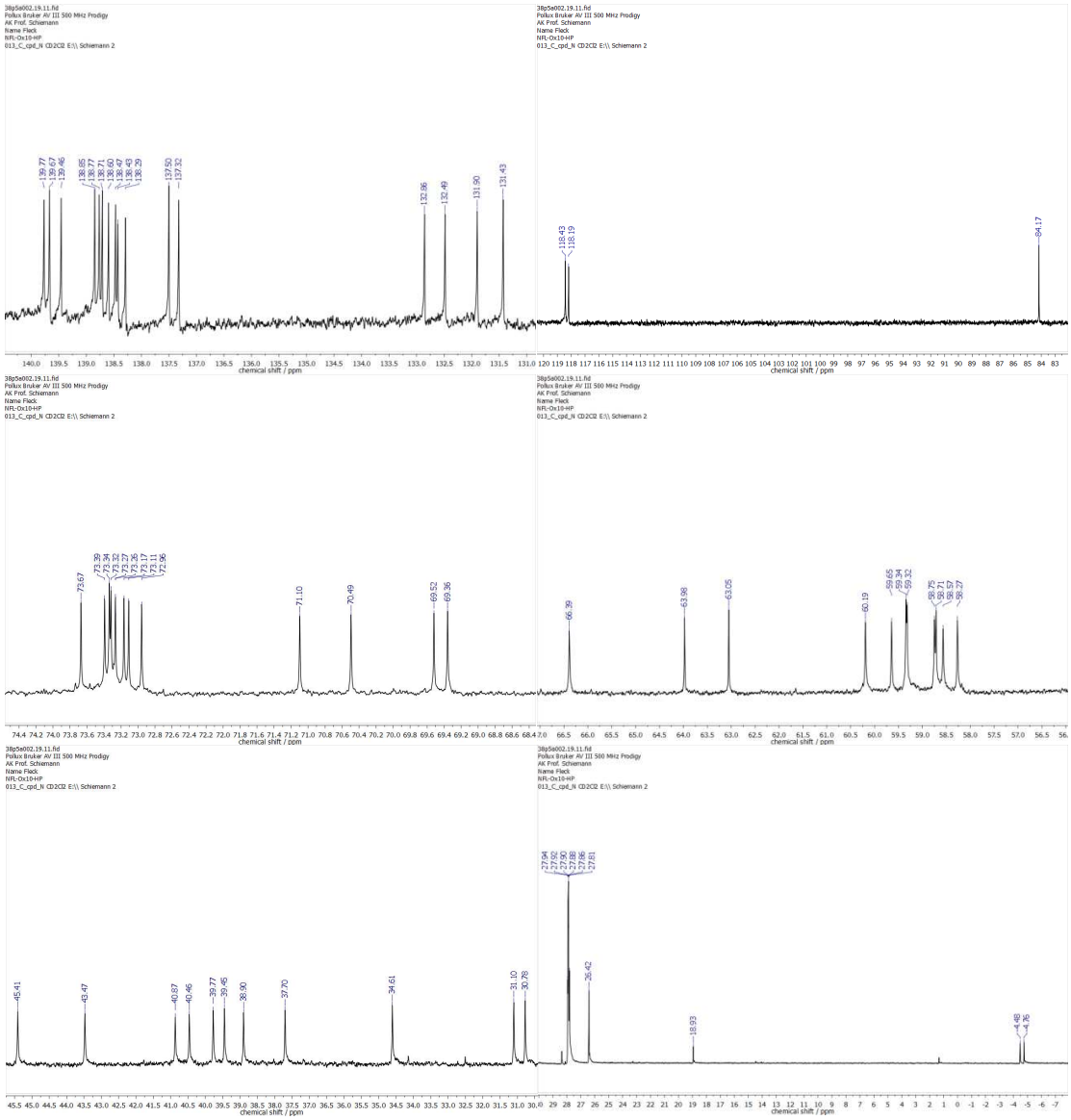

Figure S22: *^{13}C-NMR spectrum (CD_2Cl_2, 125 MHz) of Trityl alcohol* ***21****, close-up views.*

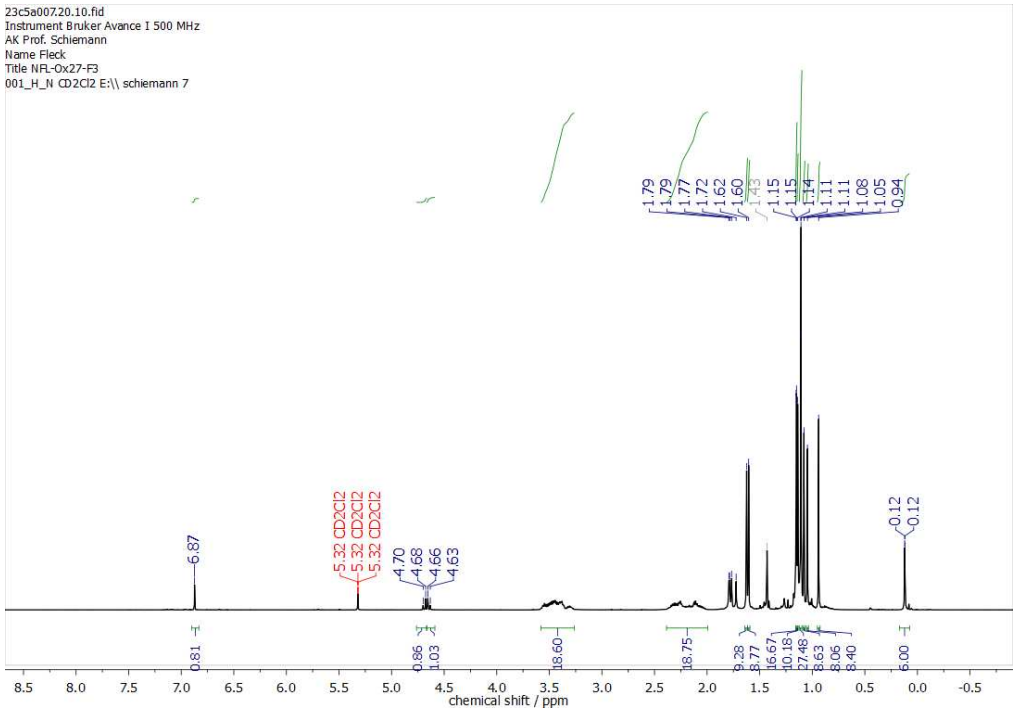

Figure S23: *^{1}H-NMR spectrum (CD_2Cl_2, 500 MHz) of Trityl alcohol* ***22****. The peak at 1.43 ppm belongs to a small impurity of cyclohexane.*

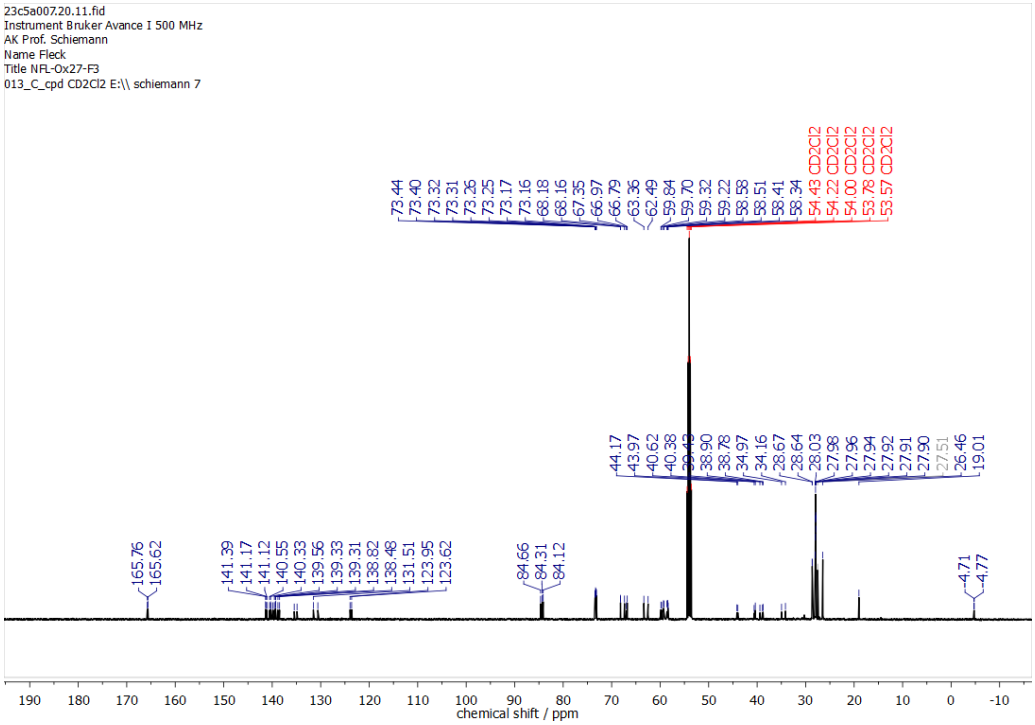

Figure S24: *^{13}C-NMR spectrum (CD_2Cl_2, 125 MHz) of Trityl alcohol* ***22****, full view.*

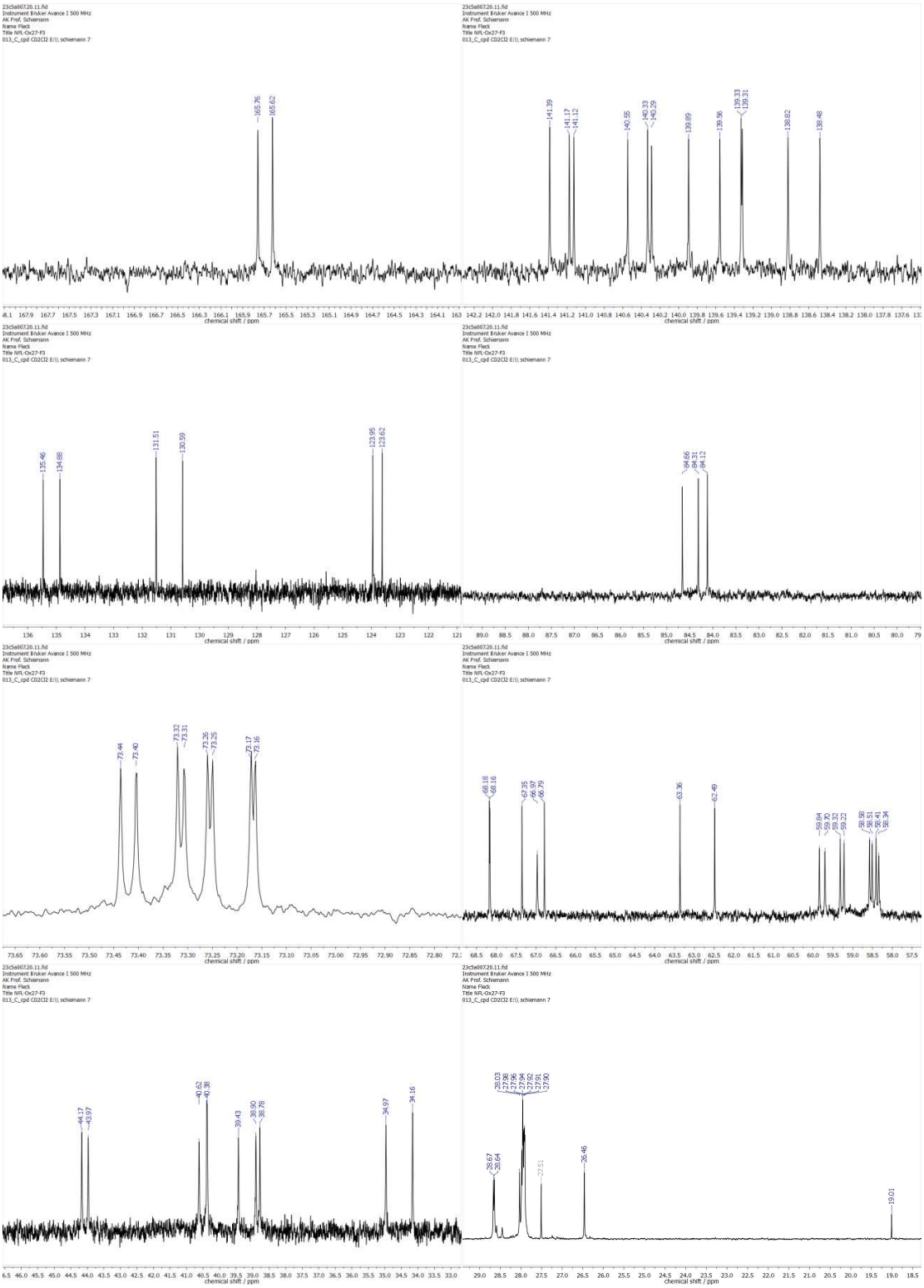

Figure S25: *^{13}C-NMR spectrum (CD_2Cl_2, 125 MHz) of Trityl alcohol* ***22****, close-up views.*

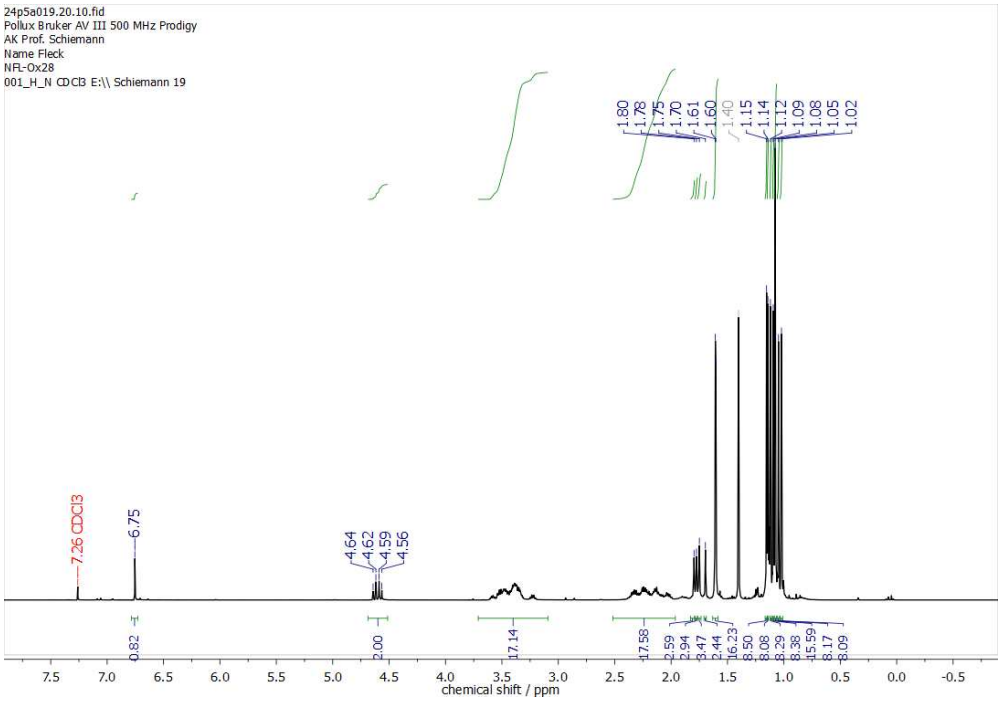

Figure S26: *^{1}H-NMR spectrum ($CDCl_3$, 500 MHz) of Trityl alcohol* ***23****.*

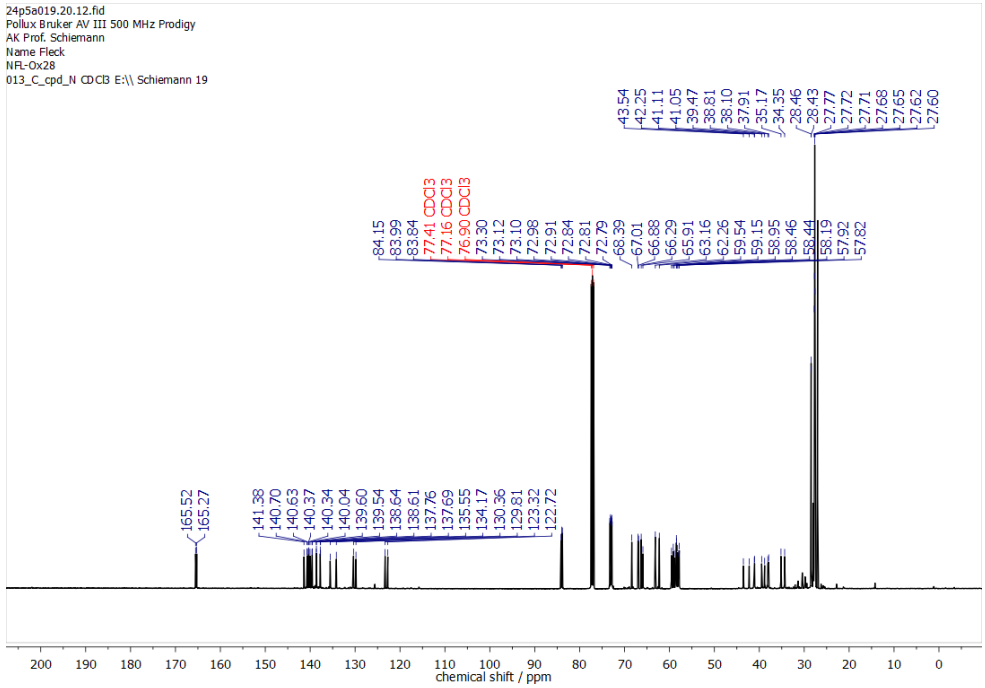

Figure S27: *^{13}C-NMR spectrum ($CDCl_3$, 125 MHz) of Trityl alcohol* ***23****, full view.*

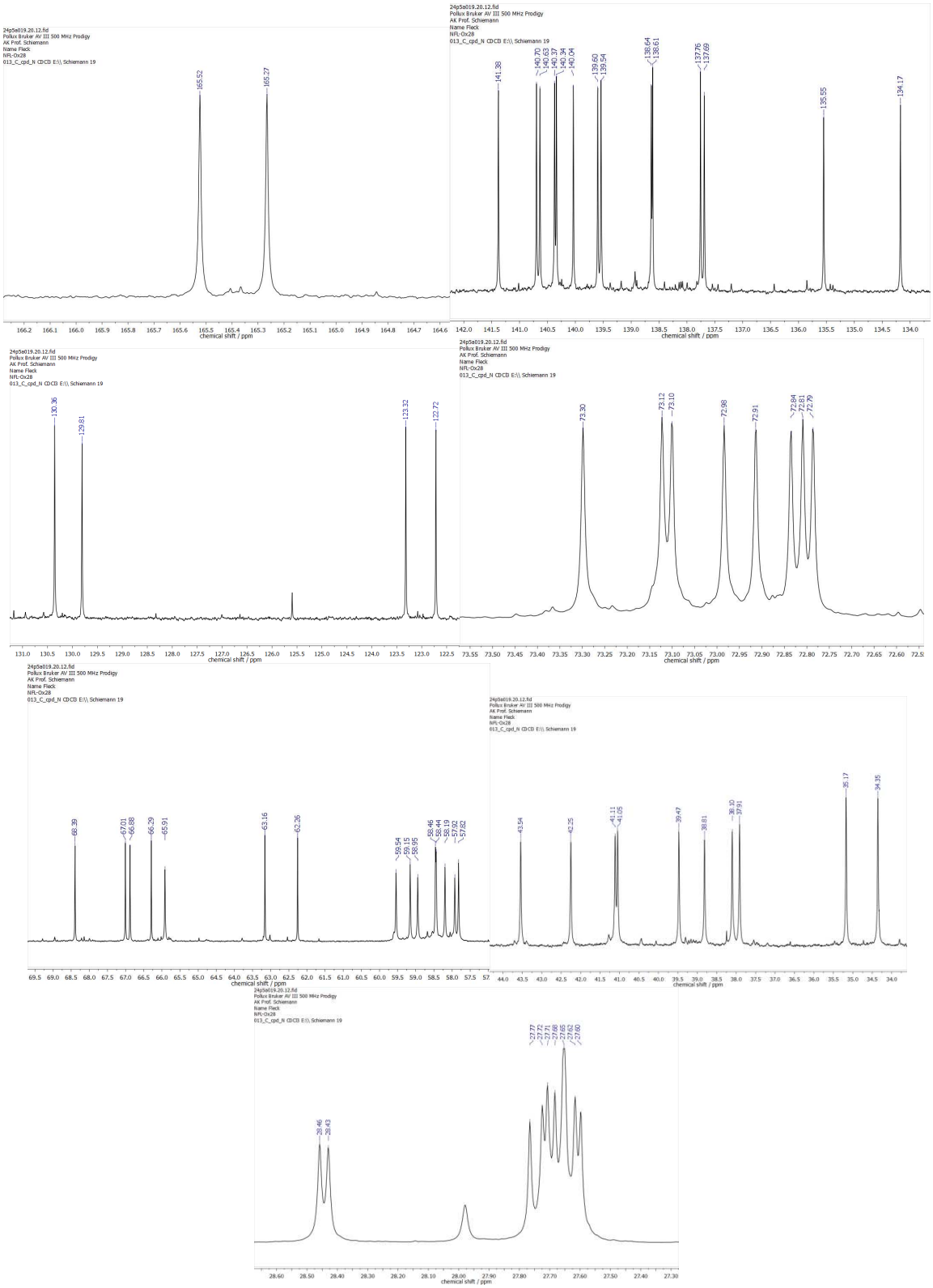

Figure S28: *^{13}C-NMR spectrum (CD_2Cl_2, 125 MHz) of Trityl alcohol* ***23****, close-up views.*

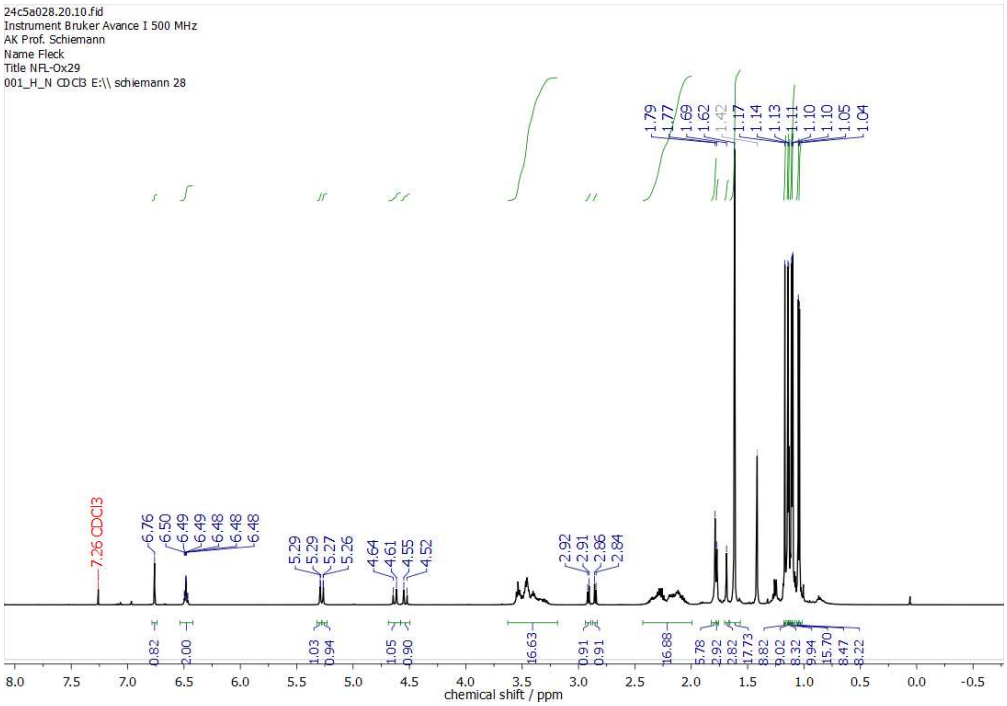

Figure S29: *^{1}H-NMR spectrum ($CDCl_3$, 500 MHz) of Trityl alcohol* ***25****.*

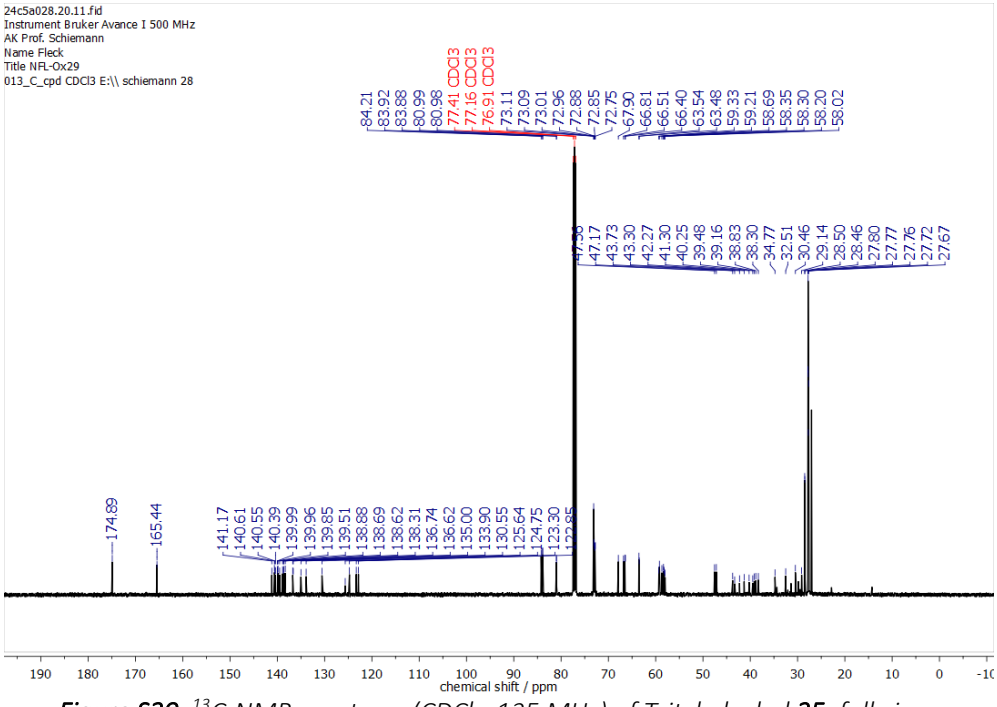

Figure S30: *^{13}C-NMR spectrum ($CDCl_3$, 125 MHz) of Trityl alcohol* ***25****, full view.*

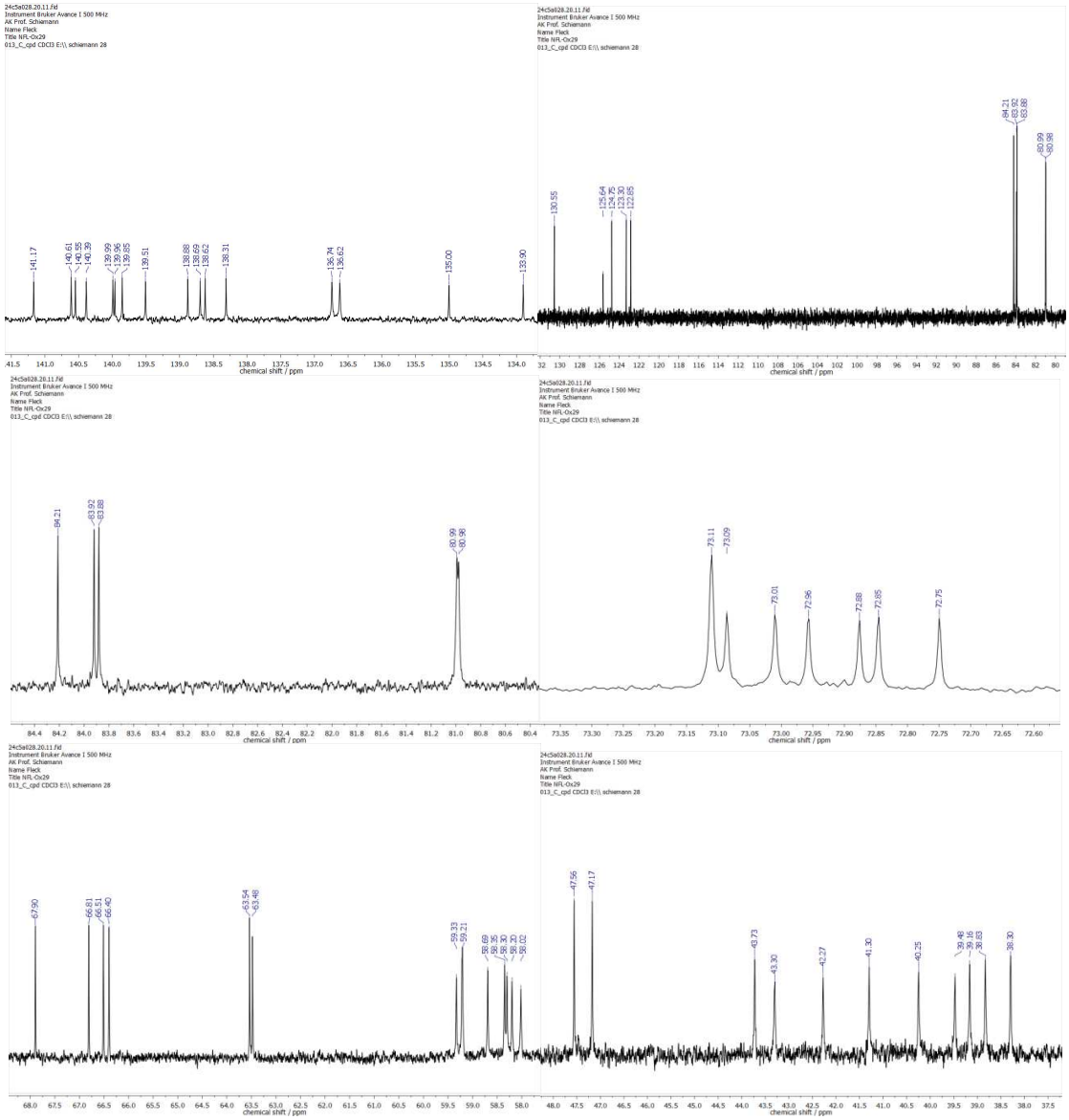

Figure S31: *^{13}C-NMR spectrum ($CDCl_3$, 125 MHz) of Trityl alcohol* ***25****, close-up views.*

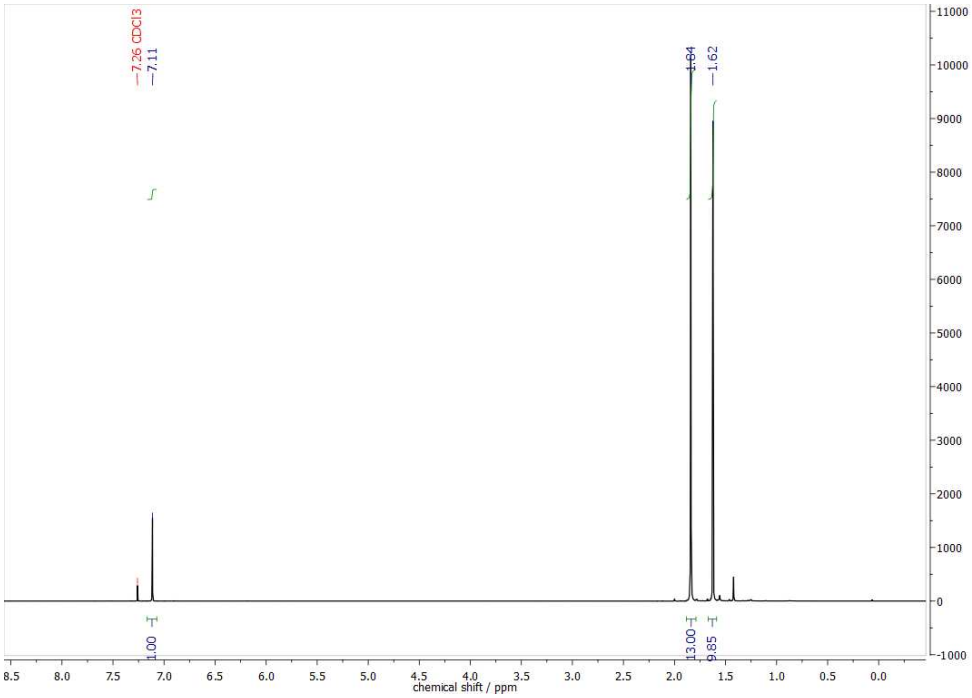

Figure S32: *^{1}H-NMR spectrum ($CDCl_3$, 400 MHz) of Compound **S2**.*

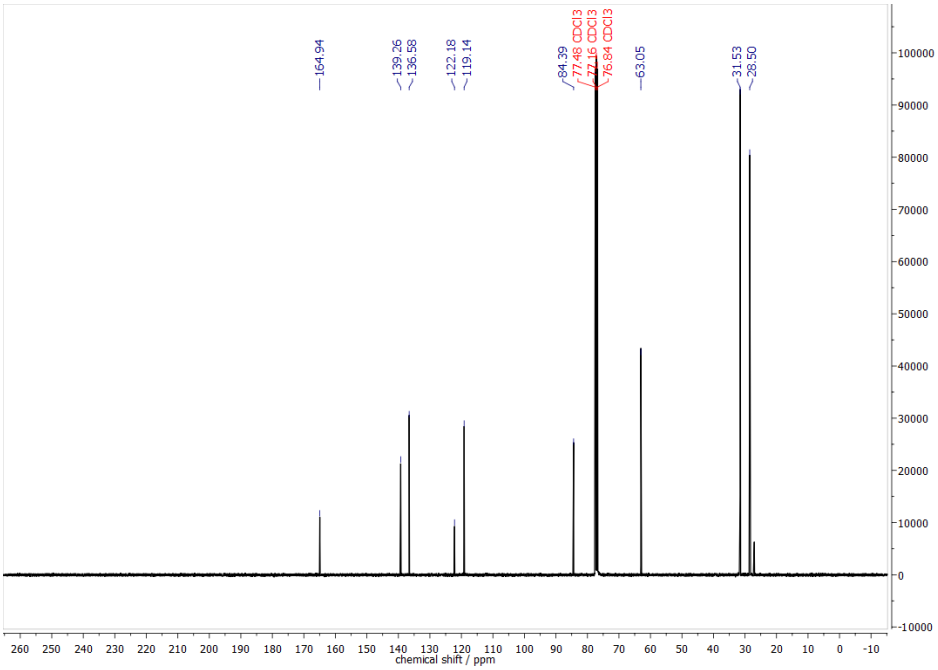

Figure S33: *^{13}C-NMR spectrum ($CDCl_3$, 100 MHz) of Compound **S2**.*

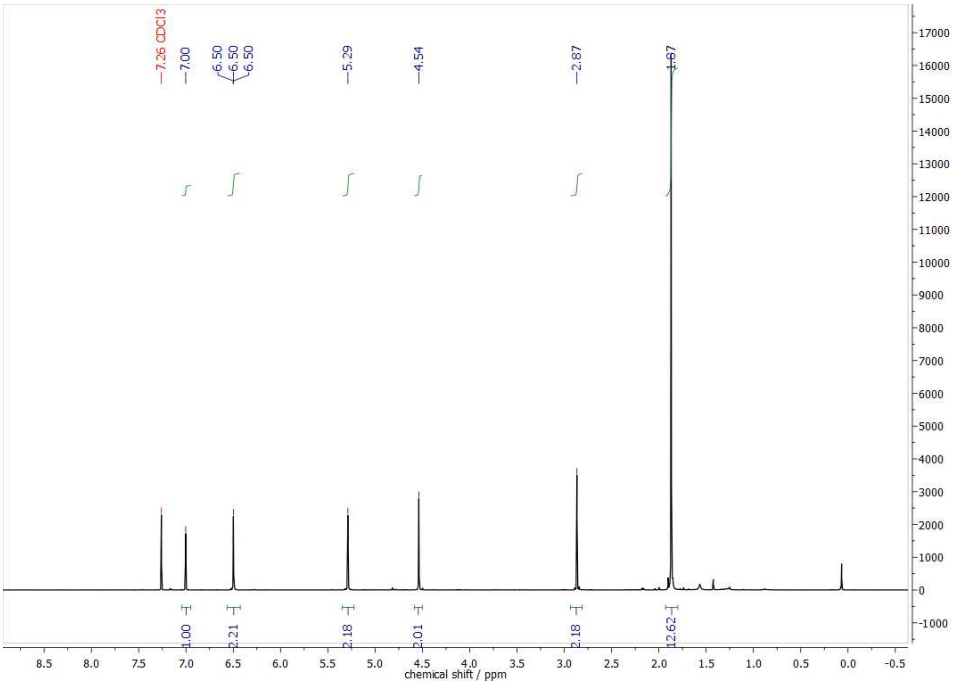

Figure S34: *^{1}H-NMR spectrum ($CDCl_3$, 500 MHz) of Compound* ***S3****.*

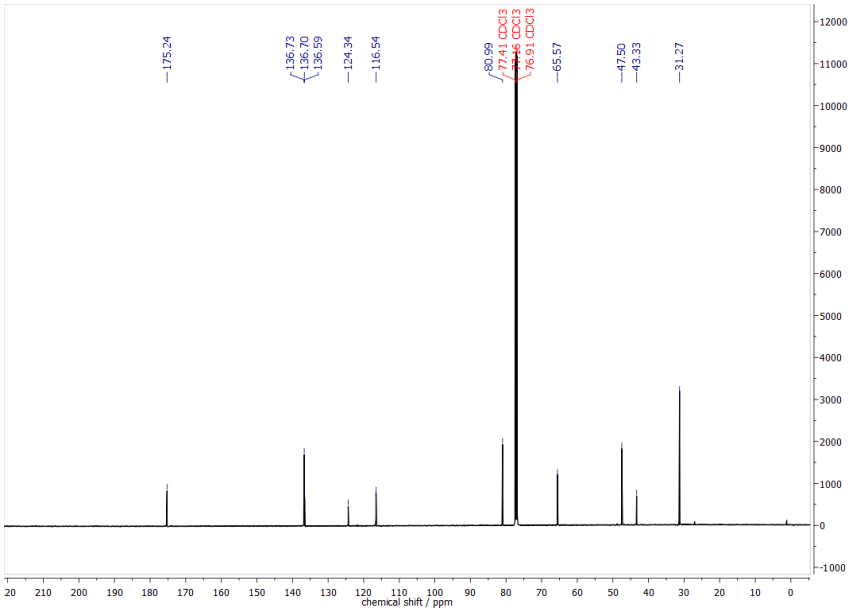

Figure S35: *^{13}C-NMR spectrum ($CDCl_3$, 125 MHz) of Compound* ***S3****.*

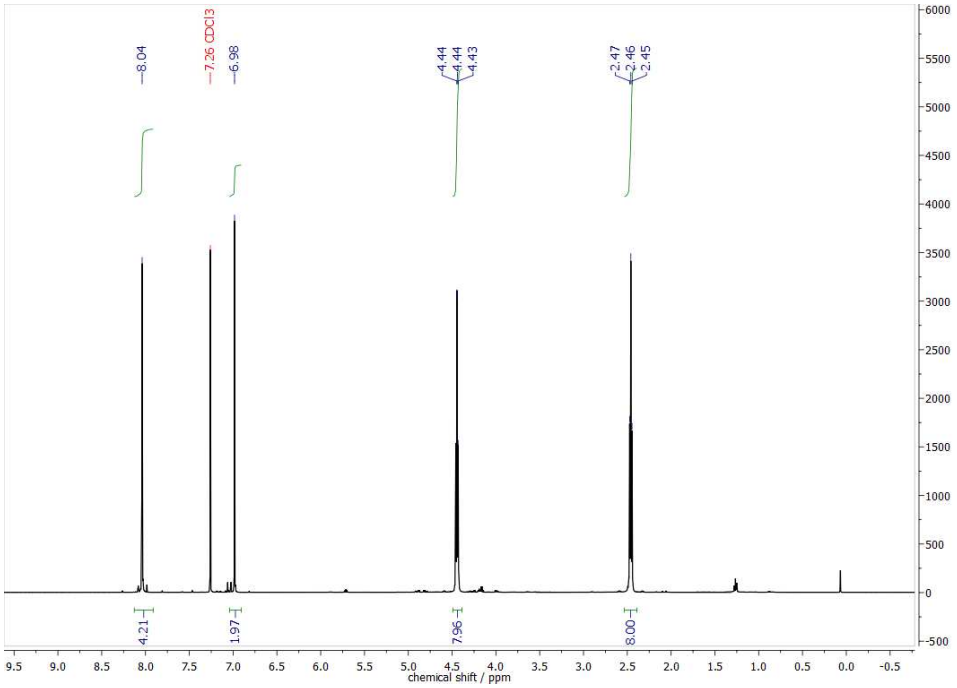

Figure S36: *^{1}H-NMR spectrum ($CDCl_3$, 500 MHz) of Compound* ***S5****.*

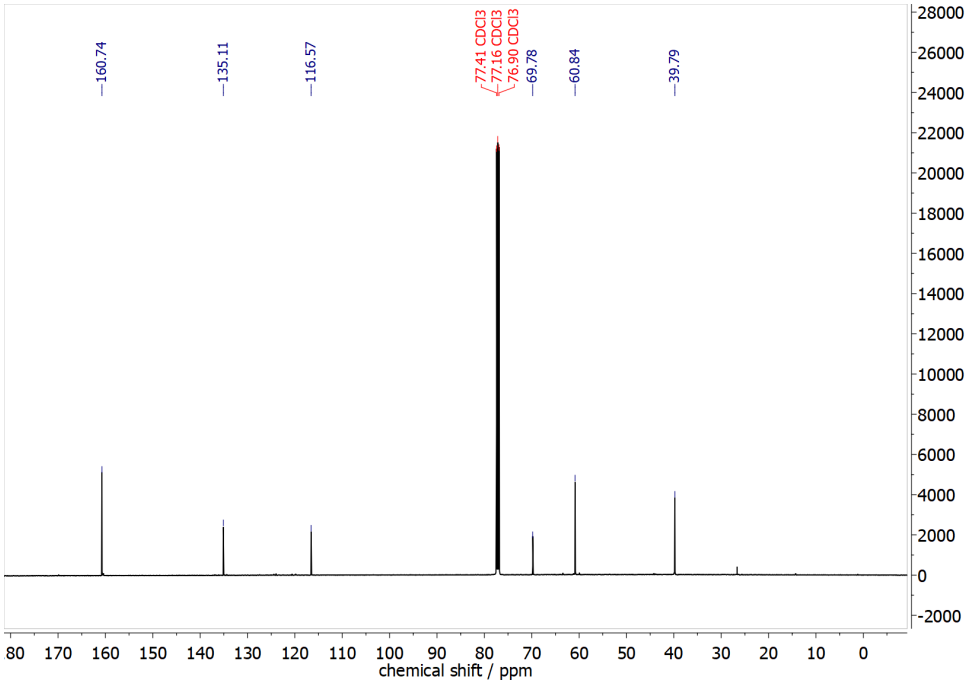

Figure S37: *^{13}C-NMR spectrum ($CDCl_3$, 125 MHz) of Compound* ***S5****.*

4.2 Mass-Spectrometry

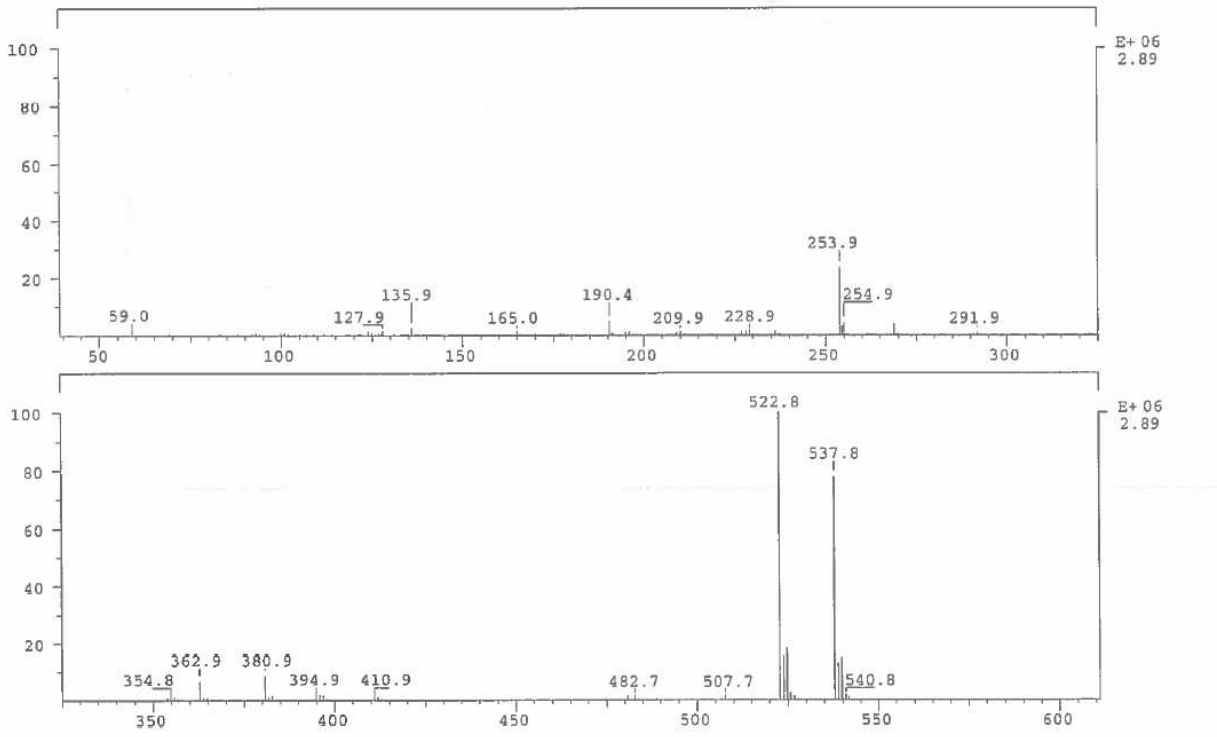

*Figure S38: EI(70 eV) mass spectrum of Thioketal **12**.*

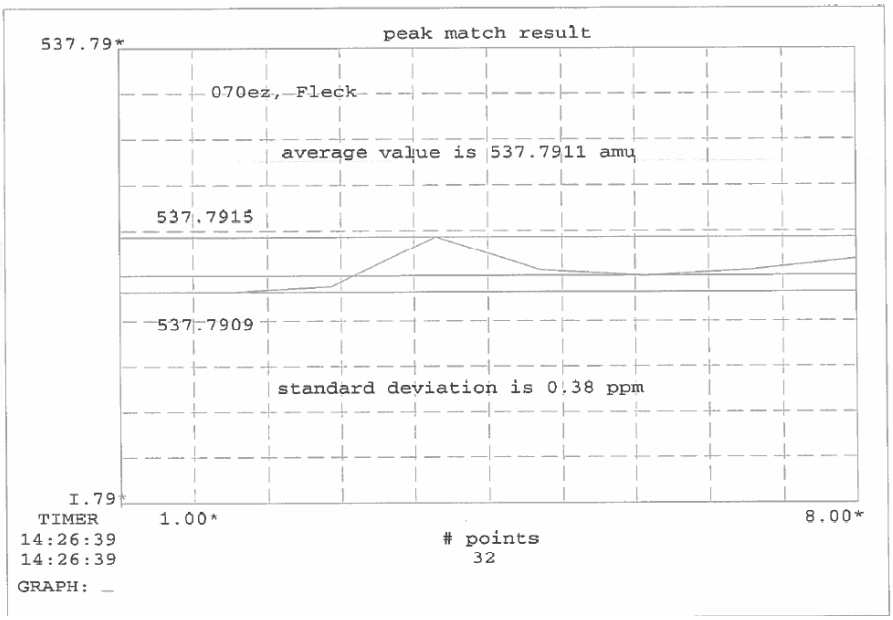

*Figure S39: HRMS result of Thioketal **12** (EI, 70 eV).*

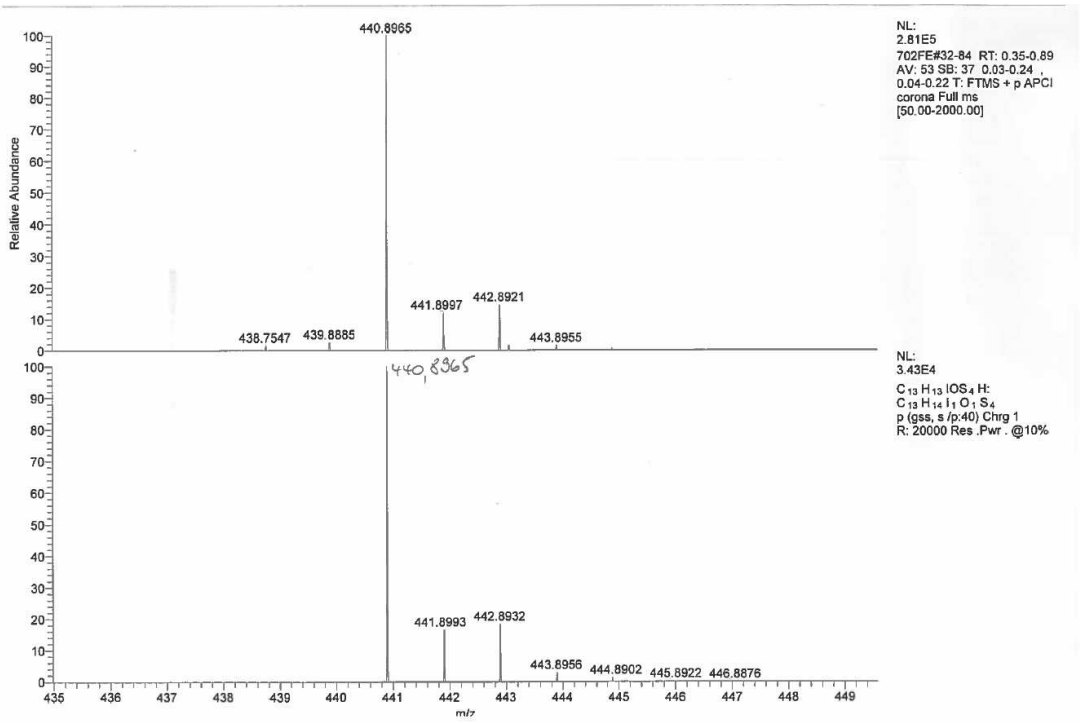

Figure S40: *APCI-HRMS of Aldehyde* ***13****.*

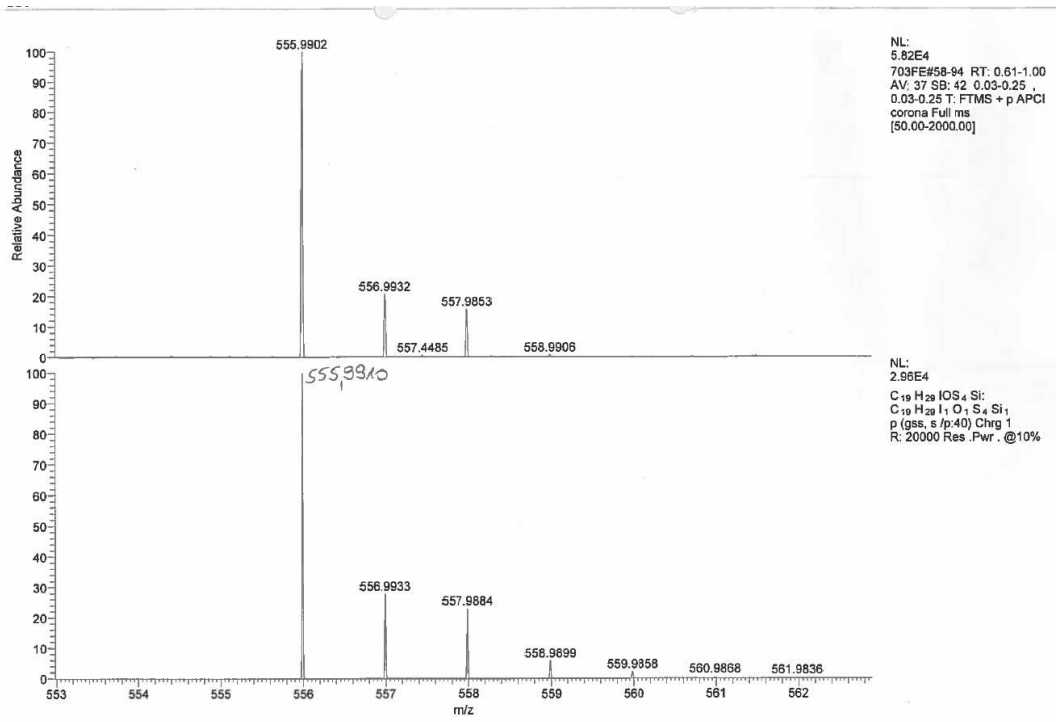

Figure S41: *APCI-HRMS of Thioketal* ***10****.*

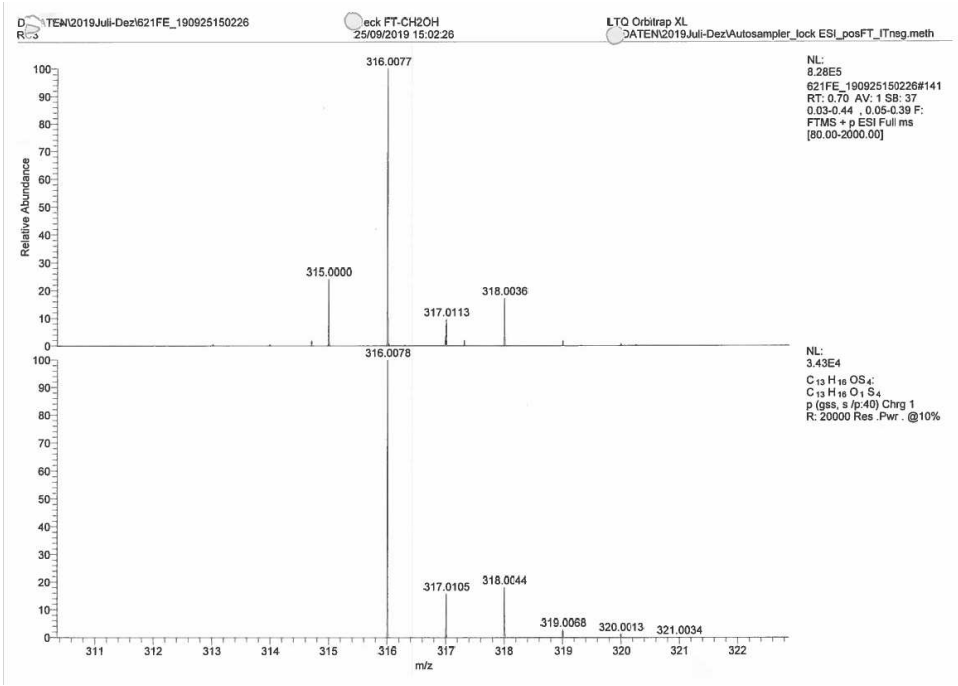

*Figure S42: ESI(+)-HRMS of Alcohol **15**.*

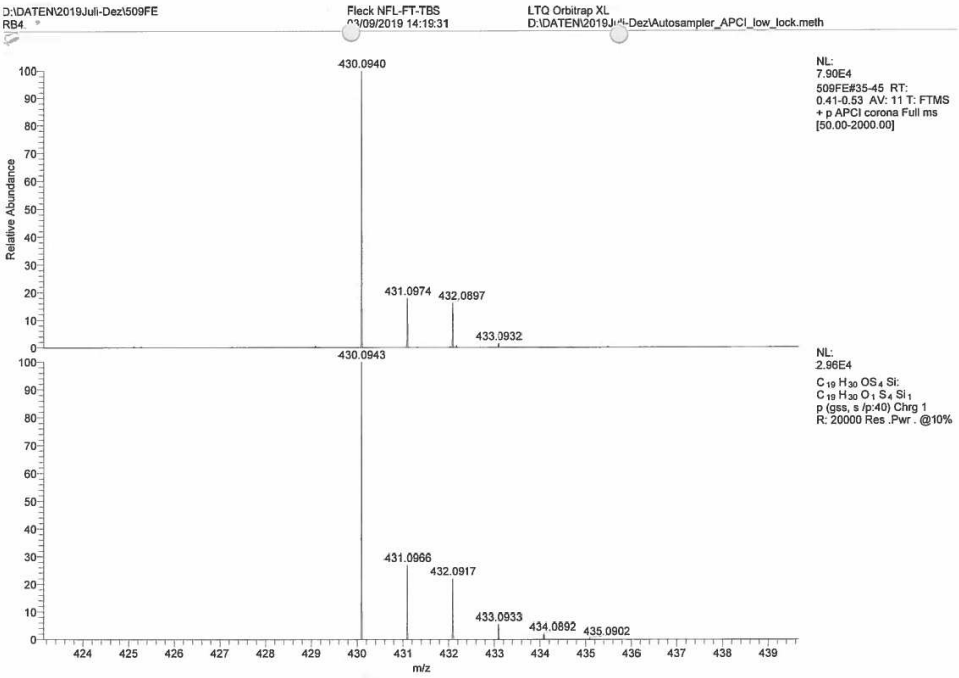

*Figure S43: APCI-HRMS of Thioketal **16**.*

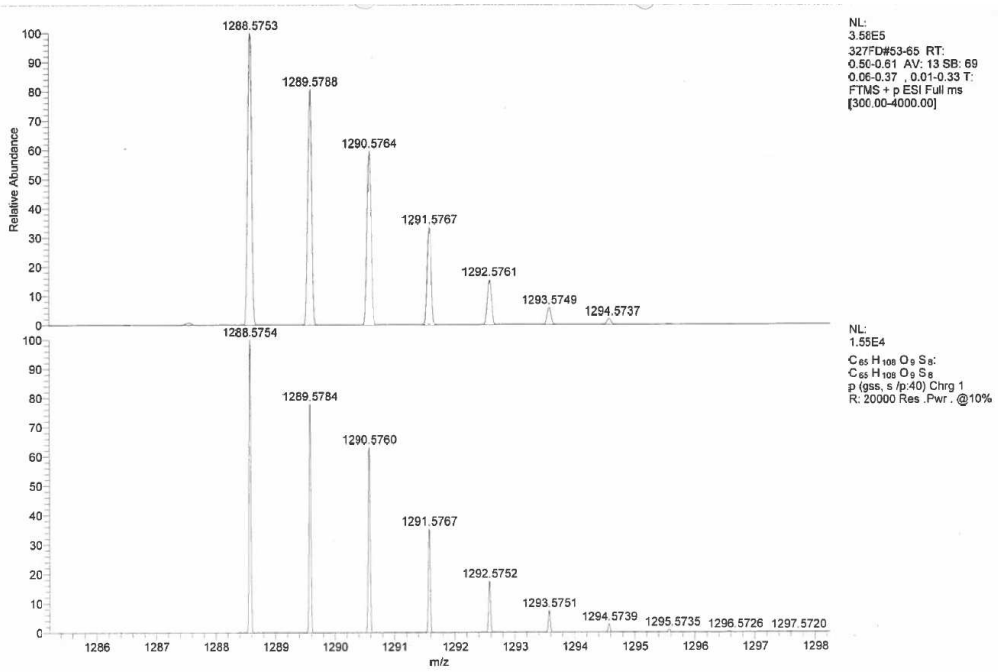

Figure S44: *ESI(+)-HRMS of Diarylmethanol* ***20****.*

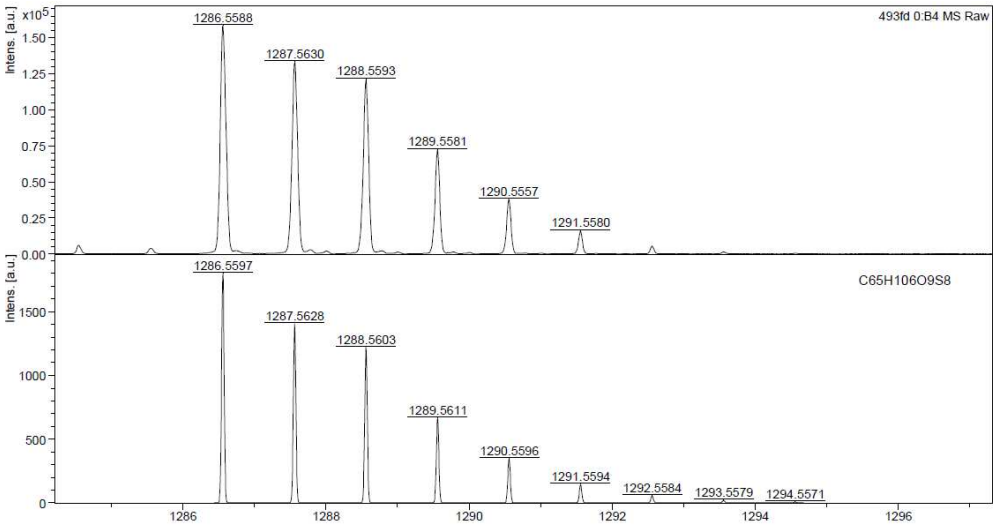

Figure S45: *MALDI(+)-HRMS of Diarylketone* ***17****.*

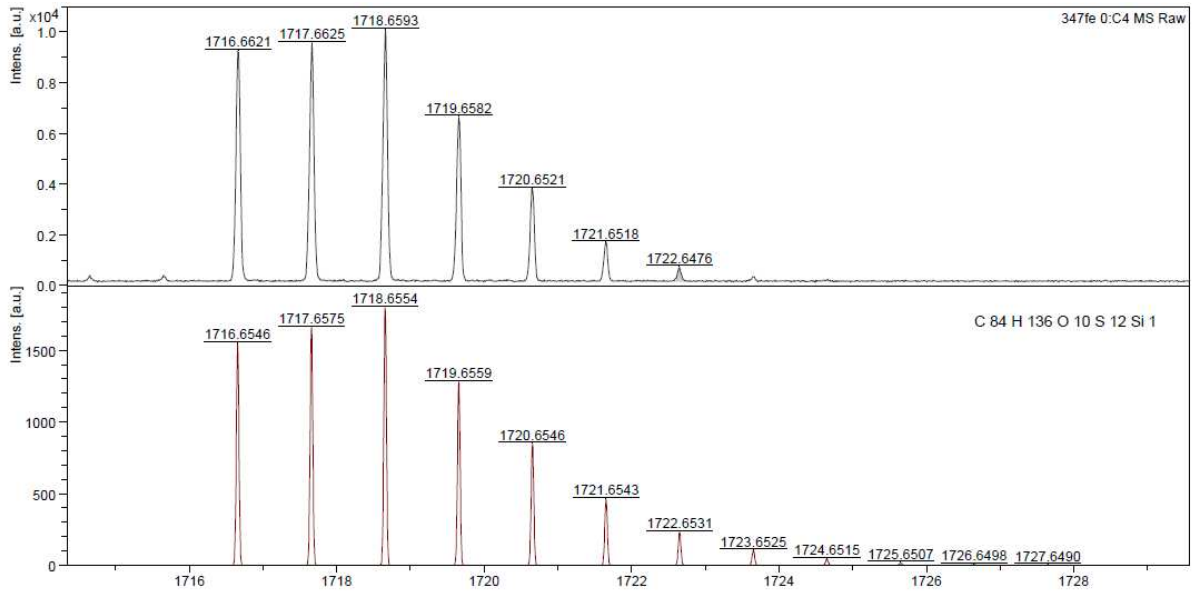

Figure S46: *MALDI(+)-HRMS of Trityl alcohol* ***21****.*

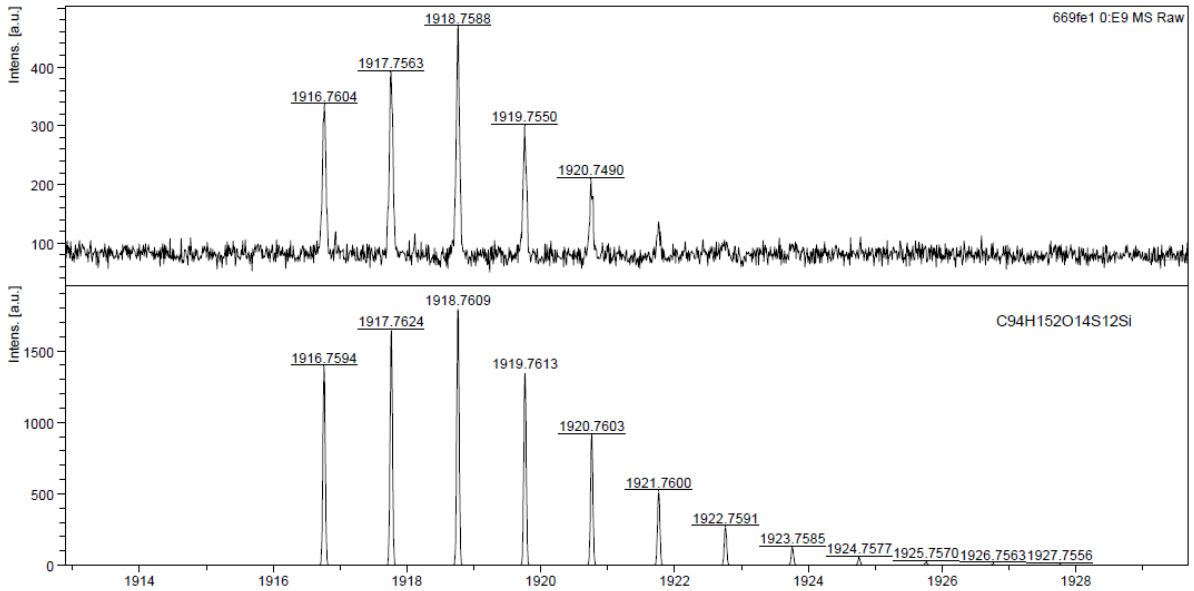

Figure S47: *MALDI(+)-HRMS of Trityl alcohol* ***22****.*

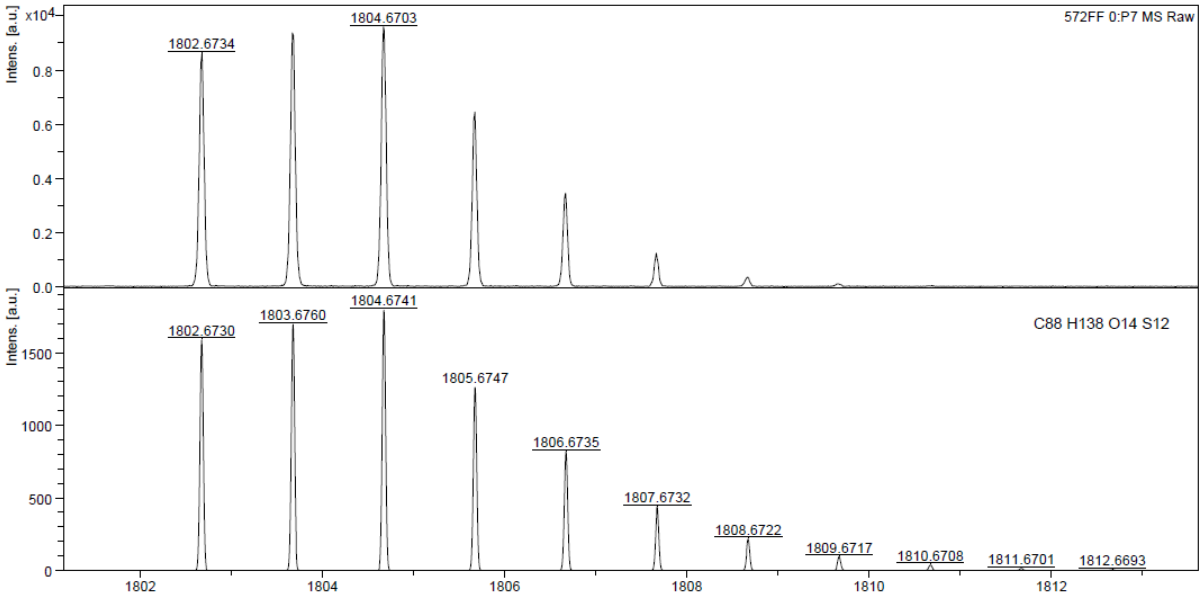

Figure S48: *MALDI(+)-HRMS of Trityl alcohol* ***23****.*

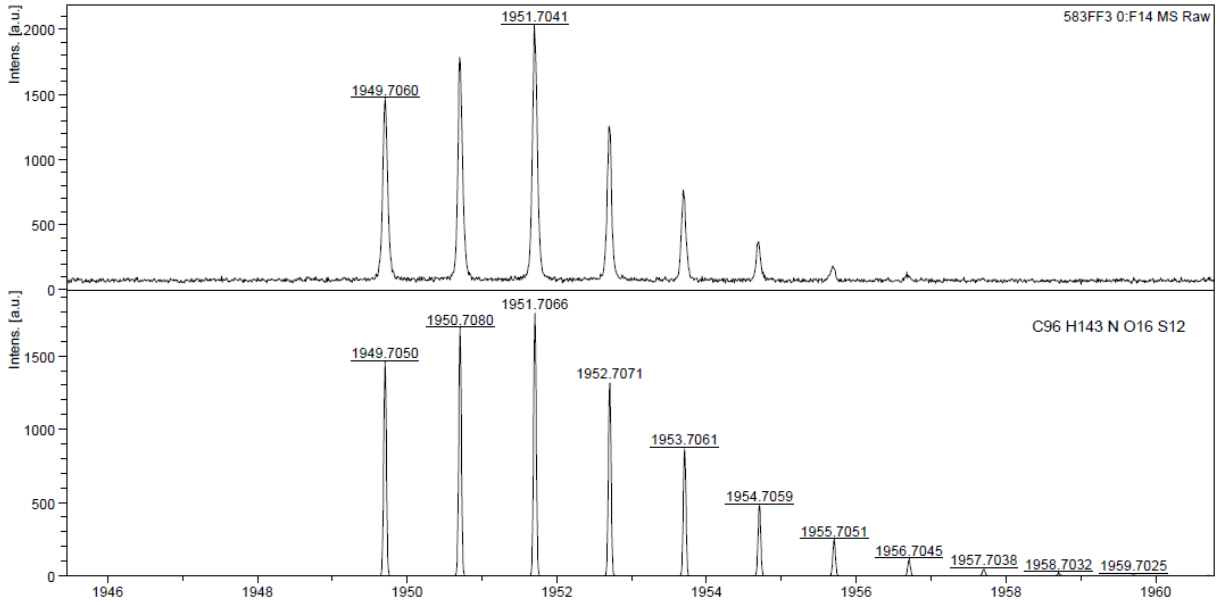

Figure S49: *MALDI(+)-HRMS of Trityl alcohol* ***25****.*

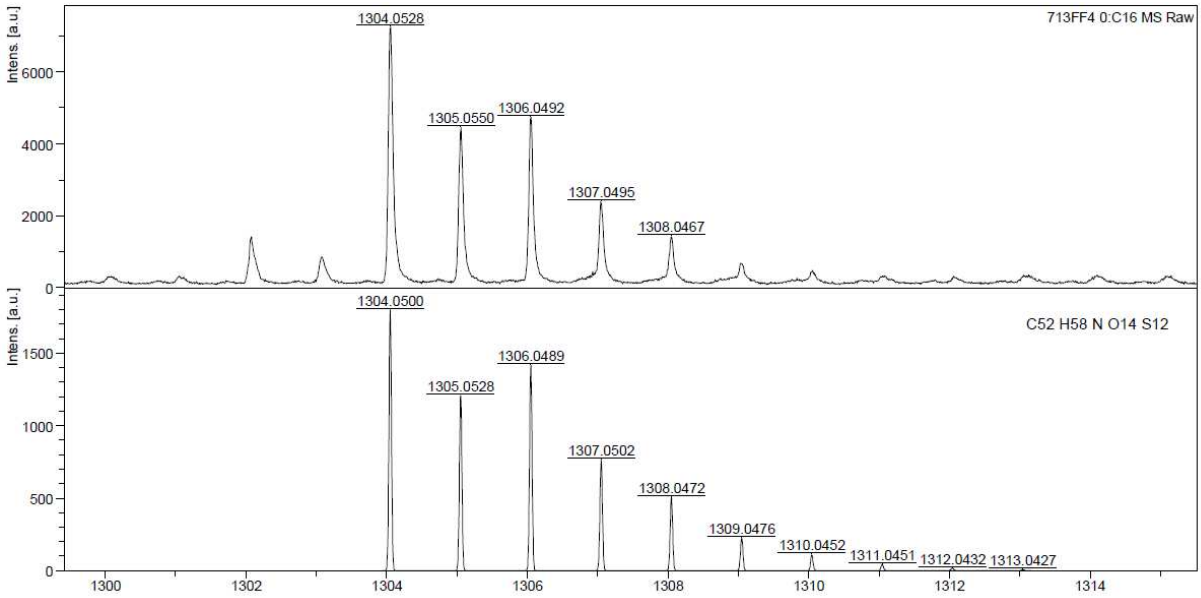

Figure S50: *MALDI(+)-HRMS of* ***9•****.*

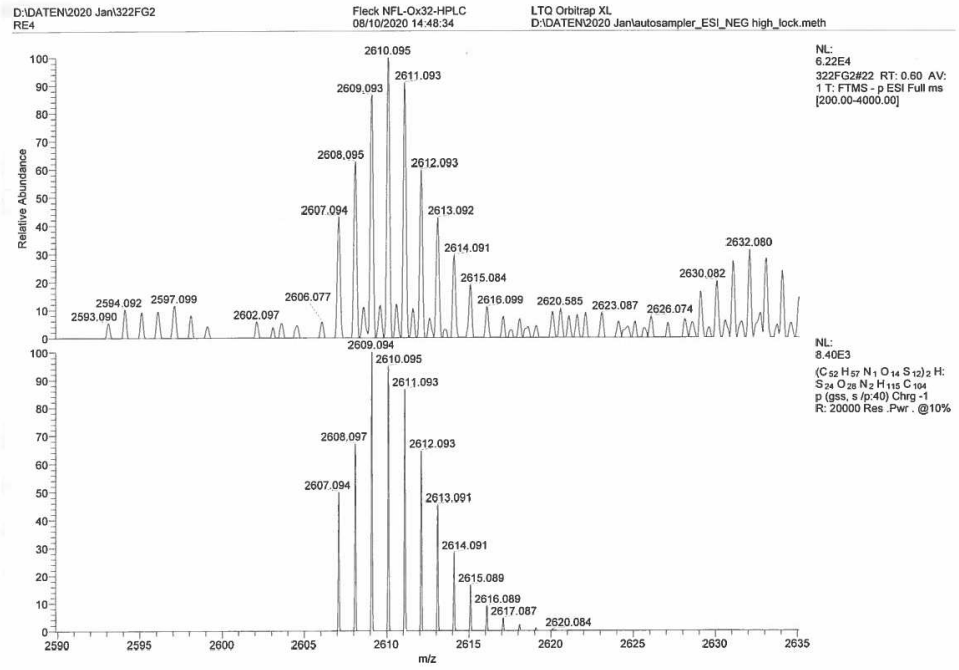

Figure S51: *ESI(-)-HRMS of* $[(\mathbf{9}^{\bullet})_2\text{-H}]^-$.

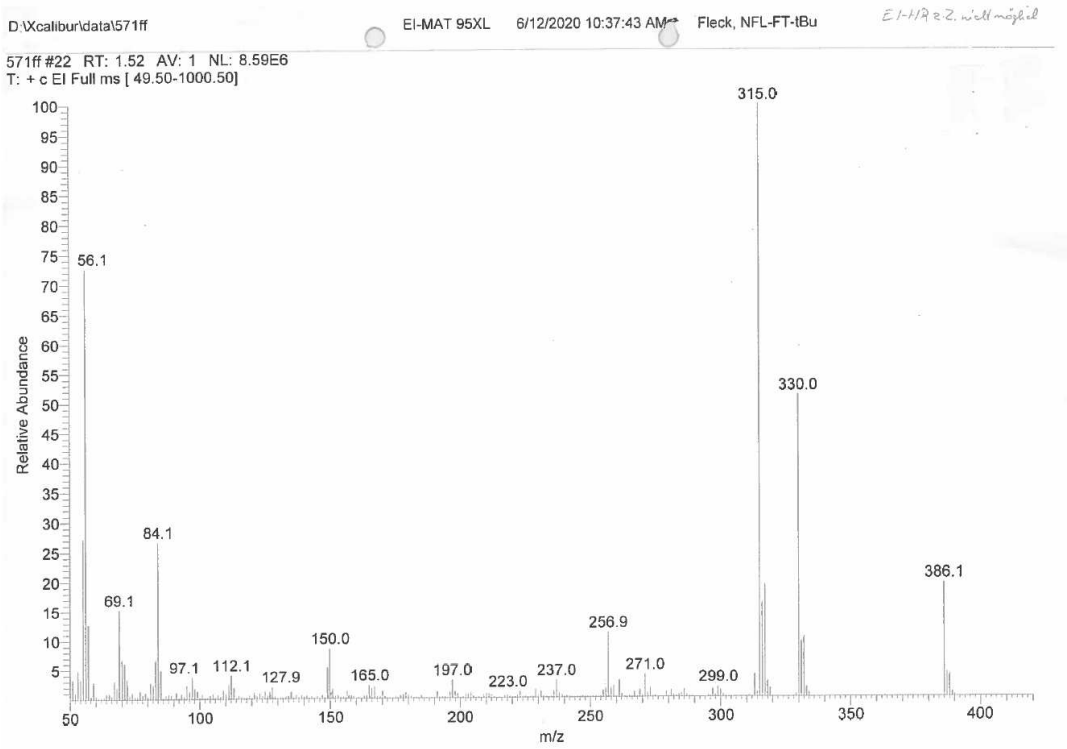

Figure S52: *EI-MS of* ***S2****.*

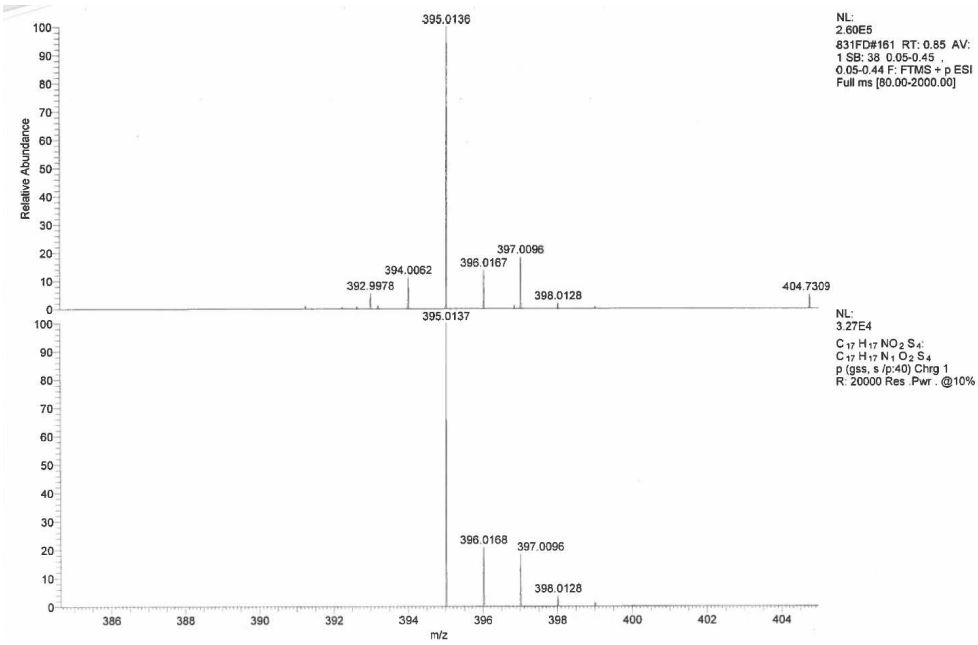

Figure S53: *ESI(+) HRMS of* ***S3*** *[****S3****-furane]*$^{+}$*.*

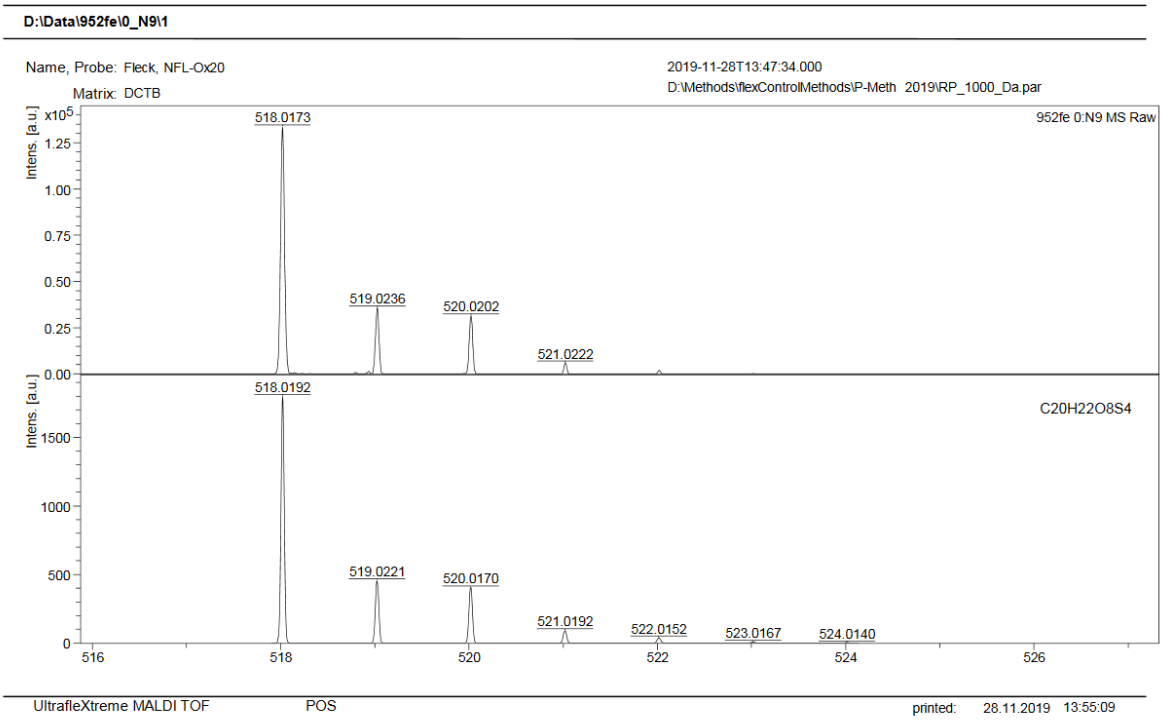

Figure S54: *MALDI(+) HRMS of* ***S5****.*

4.3 Liquid-Chromatography

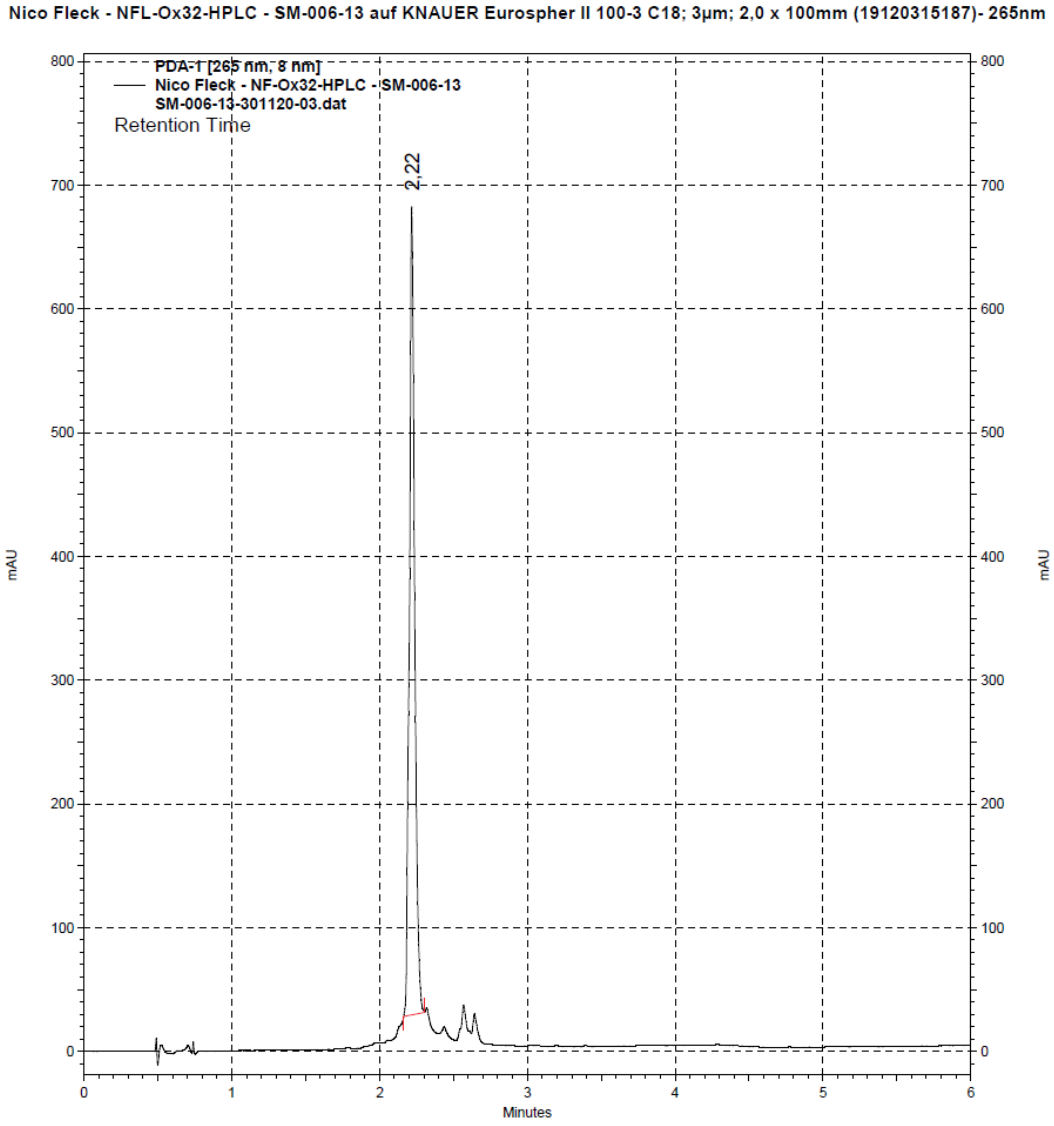

Figure S55: *Analytical UHPLC of* ***9•****.*

UHPLC
Column: Knauer Eurospher II 100-3, C18, 3.0 µm; 2.0 x 100 mm.
A: Acetonitrile + 0.1 % TFA
B: Water + 0.1% TFA

Gradient:
0:00 min 10% A + 90 % B
4:00 min 70% A + 30% B

5. Spin Labelling

5.1 Preparations

In order to create a stock solution of **9•** for labeling, the free label was dissolved in DMSO and three independent dilutions (1:10) in PBS buffer (137 mM NaCl, 2.7 mM KCl, 10 mM Na_2HPO_4, 1.8 mM KH_2PO_4, pH 7.4) were prepared from the DMSO stock solution. CW EPR spectra were recorded of these three samples and the spins counted. Based on the mean value of the EPR spin count experiments, the concentration of the stock solution was determined to be 2.1 mM. Then, the extinction coefficient of **9•** was determined. A 10 µM solution of **9•** was prepared in labeling buffer (20 mM PO_i, 50 mM NaCl, pH 6.8) and an UV-vis spectrum recorded (Cary 100 UV-vis spectrometer from Agilent Technologies, Santa Clara, CA, USA). Using the *Lambert-Beer* equation below, molar extinction coefficients were calculated for **9•** at 457 and 280 nm.

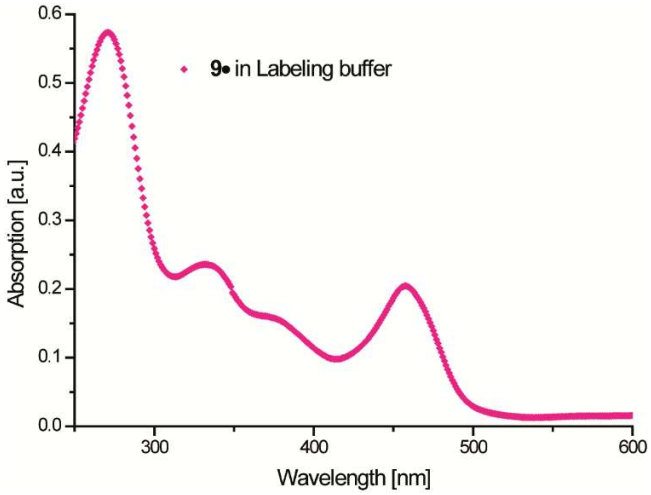

Figure S56: *UV-Vis spectrum of* ***9•*** *in Labeling buffer, recorded at a Cary 100 UV-vis.*

$$\varepsilon_{457} = \frac{A_{457}}{1\ cm * 10\frac{\mu mol}{L}} \quad ; \quad \varepsilon_{280} = \frac{A_{280}}{1cm * 10\frac{\mu mol}{L}}$$

Table S3: *Extinction coefficients of* ***9•***.

Wavelength [nm]	Extinction coefficient ε $[\frac{L}{\mu mol * cm}]$
457	0.0204
280	0.0574

5.2 Labeling of $YopO_{89\text{-}729}$ C219A with 9•

In order to evaluate the site-specifity of **9•** in labeling, the new label was incubated with the cysteine-free mutant $YopO_{89\text{-}729}$ C219*A* (expressed as described previously[8]). 20 nmol of $YopO_{89\text{-}729}$ C219A were incubated with 200 nmol TCEP in 1.5 mL Labeling buffer (20 mM PO_i, 50 mM NaCl, pH 6.8) for 2 h at 4°C followed by removing the reducing agent via a benchtop PD-10 desalting column.

A fivefold excess of **9•** (100 nmol, 47.5µL of a 2.1 mM stock of **9•** in DMSO) was prediluted in 2.5 mL labeling buffer and then added to the 3.5 mL PD10 eluate containing the protein fraction. The reaction mixture was incubated for 16 h at 4 °C., after which excess label was removed via a PD-10 column (4 times 1.5 mL load) and the protein containing eluate concentrated to approximately 2 mL using a VivaSpin 6/50k MWCO (Sartorius, Göttingen, Germany). Any remaining label remnants were removed using a HiPrep 26/10 Desalting column on an Äkta avant system. The fractions showing an absorbance at 280 nm were

pooled and concentrated to 2.0 mL. A UV-vis spectrum was recorded and the molar ratios of YopO and **9•** calculated based on the extinction coefficients of YopO (0.04939 L µmol^{-1} cm^{-1}), **9•** (see SXX) and the method previously described[6]. According to this method, the cysteine-free mutant was labeled to an extent of 7 %. For the PDS measurements, the protein sample was concentrated to 200 µL and rebuffered thrice with deuterated PDS buffer (100 mM TES, 100 mM NaCl, pH 7.4) using a VivaSpin 6/50k MWCO.

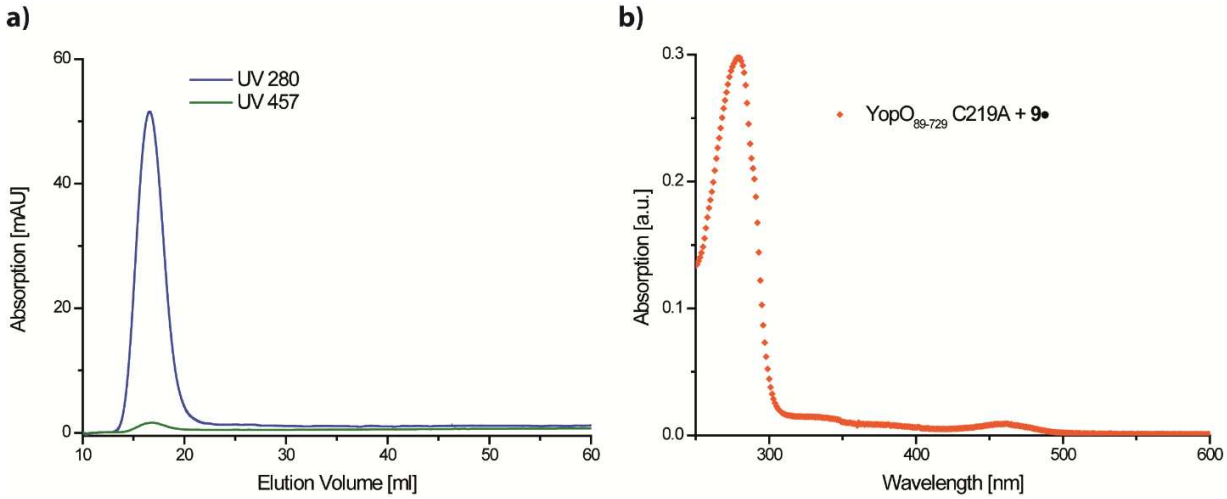

Figure S57: *(a) HiPrep 26/10 Desalting chromatograph of YopO$_{89-729}$ C219A after incubation with* ***9•****. (b) UV-Vis spectrum of cysteine-free YopO after excess label removal recorded at a Cary 100 UV-vis spectrometer.*

Table S4: *Concentrations and molar ratio of YopO and* ***9•*** *after incubation and purification.*

YopO [µM]	9• [µM]	Molar Ratio YopO : 9•
5.4	0.4	1 : 0.07

5.3 Labeling of YopO$_{89-729}$ Y588C/N624C with 9•

The double cysteine mutant YopO$_{89-729}$ Y588C/N624C was obtained from a previous study recently published by us[8]. 20 nmol of the double cysteine construct YopO$_{89-729}$ Y588C/N624C were reduced in a total of 1.5 mL labeling buffer (20 mM POi, 50 mM NaCl, pH 6.8) using a tenfold molar excess of TCEP to cleave any intermolecular disulfide bridges. After an incubation period of 2 h at 4 °C, the reducing agent was removed using a benchtop PD-10 desalting column and the labeling reaction was set up immediately afterwards. To the 3.5 mL PD-10 eluate containing the reduced protein, a 4-fold molar excess of **9•** per cysteine (160 nmol, 76 µL of a 2.1 mM stock of **9•** in DMSO) prediluted in 2.5 mL Labeling buffer was added leading to a final labeling concentrations of 3 µM YopO and 24 µM **9•**, respectively. The labeling reaction was incubated for 16 h at 4 °C. Then excess label was removed using a PD-10 desalting column (4 times 1.5 mL load). The protein containing fractions were pooled and concentrated to 2 mL using a VivaSpin 6/50k MWCO and loaded onto a HiPrep 26/10 Desalting column to remove any remaining free label. The elution peak showing an absorption at 280 nm was pooled and concentrated down to 2.4 mL before recording a UV-vis absorption spectrum.

The molar ratio of YopO to **9•** was calculated as described above for the cysteine-free construct. Based on this, 1.69 equivalents of **9•** per YopO were determined (labeling efficiency of 85 %). For further PDS experiments, the protein sample was concentrated to 200 µL and rebuffered thrice with deuterated PDS buffer (100 mM TES, 100 mM NaCl, pH 7.4) using a VivaSpin 6/50k MWCO.

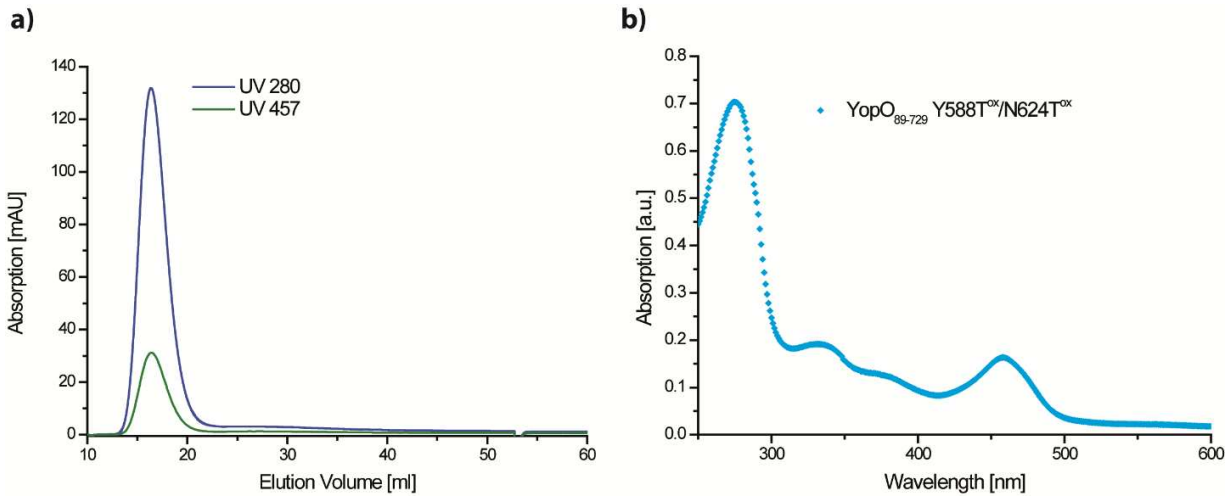

Figure S58: *(a) HiPrep 26/10 Desalting chromatograph of YopO$_{89-729}$ Y588T^{ox}/N624T^{ox} after incubation with* ***9$^{\bullet}$****. (b) UV-Vis spectrum of labeled YopO$_{89-729}$ Y588T^{ox}/N624T^{ox} after removal of excess free* ***9$^{\bullet}$****.*

Table S5: *Concentrations and molar ratio of YopO$_{89-729}$ Y588C/N624C and* ***9$^{\bullet}$*** *after labeling and workup.*

YopO [µM]	9$^{\bullet}$ [µM]	Molar Ratio YopO : 9$^{\bullet}$
4.8	8.1	1 : 1.69

5.4 Protein Mass-Spectrometry

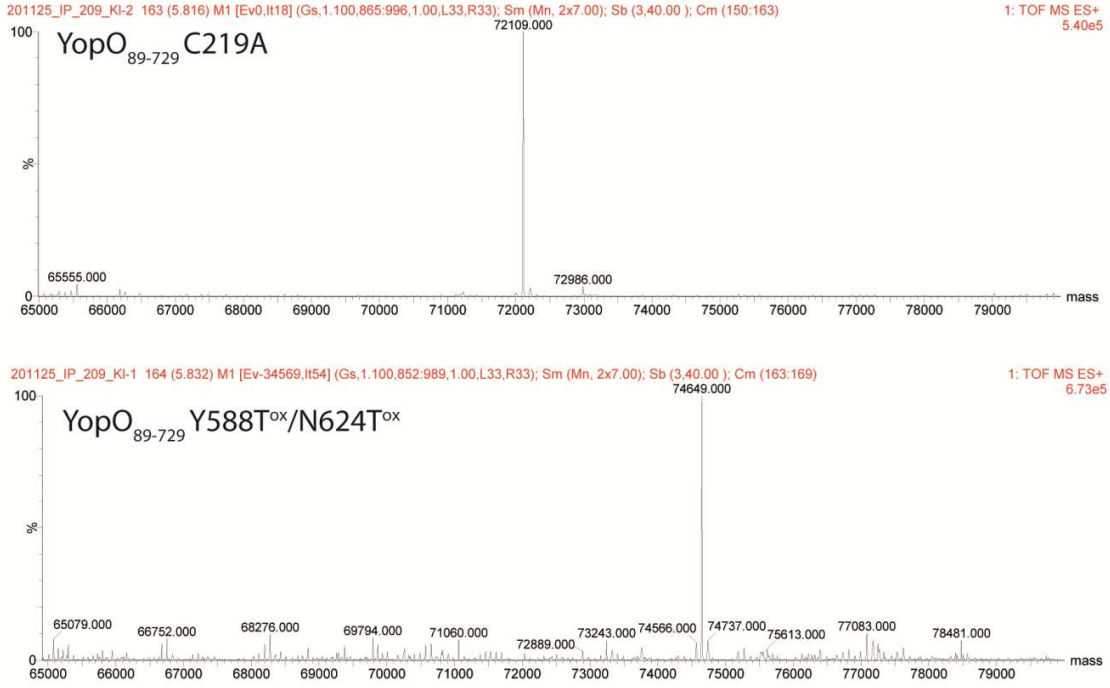

Figure S59: *ESI(+) mass spectra of protein samples. Top: Cysteine-free YopO$_{89-729}$ C219A mutant after incubation with* ***9$^{\bullet}$*** as described in section 5.2, calculated mass: 72108.57 Da ($C_{3176}H_{5085}N_{897}O_{989}S_{14}$). Bottom: Doubly-labelled YopO$_{89-729}$ Y588T^{OX}/N624T^{OX} mutant (section 5.3), calculated mass: 74645.67 Da ($C_{3273}H_{5196}N_{898}O_{1015}S_{40}$).

5.5 Activity Assay

The structural integrity of YopO after labeling with **9•** was evaluated based on the autophosphorylation capability of YopO[9]. Here, 2 µM of YopO Y588T^{ox}/N624T^{ox} and the cysteine-free wild type were incubated with 6 µM G-actin (extracted from rabbit muscle acetone powder) in phosphorylation buffer (50 mM Tris, 10 mM $MgCl_2$, 1 mM ATP, 2 mM $MnCl_2$, pH 8.0) for 1.5 h at 37 °C. Samples without G-actin served as a negative control. After the incubation time, samples were quenched by addition of 8x SDS sample buffer and boiled for 5 min at 95 °C.

An SDS-PAGE was ran (10% gel, 50 min, 175 V, 300 mA) and the acrylamide gel was fixed in 45% MeOH, 10% AcOH (2 times for 30 min, 100 mL each). The gel was washed with MilliQ water (3 times for 10 min, 100 mL each) and stained in the dark with 100 mL Pro-Q Phosphoprotein Diamond Stain (Thermo Fisher Scientific, Waltham, MA, USA) for 90 min. Subsequently, the gel was washed in 20% Acetonitril, 50 mM NaOAc pH 4.0 (3 times for 30 min, 100 mL each) and MilliQ water (2 times for 5 min, 100 mL each). Phosphorylated proteins were detected using an UV-table equipped with a 590 nm longpass emission filter. Afterwards, the gel was stained in Coomassie Brilliant Blue for total protein visualization. As seen in Figure S60, YopO Y588T^{ox}/N624T^{ox} remained active with only marginally reduced activity compared to the wild type.

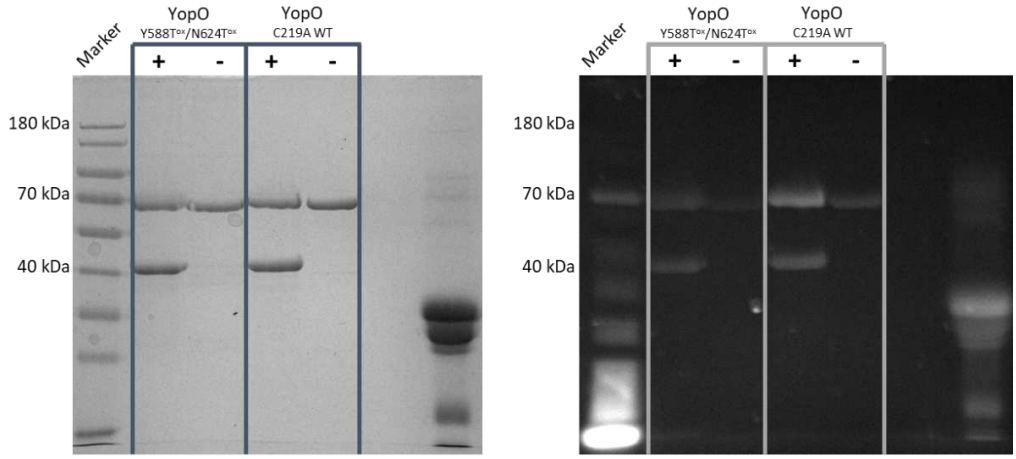

Figure S60: *Coomassie stained SDS gel (left) and the corresponding Pro-Q-stained gel (right). Phosphorylated proteins appear significantly brighter than other proteins in the Pro-Q-stained gel.*

6. CW EPR-Spectroscopy

6.1 Simulation of *CW* EPR Spectra

CW EPR spectra were simulated using the EasySpin[10] toolbox for Matlab (MathWorks, Natick, MA, USA). The spectrum of 50 µM free (i.e. non-bioconjugated) **9•** in PBS buffer at RT was fitted using the "garlic" function of EasySpin (see main text, Figure 1). Appropriate starting values for the "esfit" routine were taken from our study on **6•**.[8] All obtained g-values, hyperfine coupling constants A, and peak-to-peak linewidths (lwpp) are summarized in Table S6; hyperfine coupling constants are correlated with the nuclei by the numbering shown in Figure 61.

Table S6: *Fitting parameters of the cw EPR spectrum of 9• recorded in PBS buffer at RT.*

Fitting result	Value
g	2.0033
A_{N1}	1.48 MHz
A_{H2}	3.02 MHz
A_{H3}	6.09 MHz
A_{C4}	66.32 MHz
A_{C5}	31.60 MHz
A_{C6}	25.82 MHz
A_{C7}	3.59 MHz
A_{C8}	7.02 MHz
lwpp (Gaussian)	0.0116 mT
lwpp (Lorentzian)	0.0256 mT

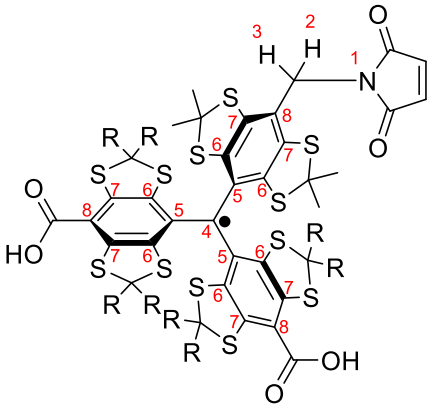

Figure S61: *Structure of **9•** with the atoms labelled according to the nuclei given in Table S6. R = CH_2CH_2OH.*

CW EPR spectra of **9•** recorded at 100 K were simulated with the "pepper" function of EasySpin, appropriate starting values for the fit were taken from [8]. As **9•** exists in an equilibrium between a monomeric and a dimeric form, two spin systems were defined for the simulation. The Pake pattern stemming from the dimer $(\mathbf{9}^{\bullet})_2$ was fitted using a home-written function in EasySpin. Herein, the interspin distance r was transformed into a dipolar coupling constant via D = 52.04 MHz/r³, and r was varied to find the optimal value. The g-values of the monomer and the dimer were assumed to be equal. The parameters of the best fit are collected in Table S7. The weights of the monomer **9•** and the dimer $(\mathbf{9}^{\bullet})_2$ were fitted individually for each spectrum, depending on the glycerol content (Fig. S65).

Table S7: *Fitting parameters of the cw EPR spectrum of 9• obtained at 100 K:*

Fitting result	Value
	Monomer 9•
g	2.0034
A_{N1}	1.31 MHz
A_{H2}	2.75 MHz
A_{H3}	7.03 MHz
A_{C4}	66.45 MHz
A_{C5}	32.66 MHz; 30.96 MHz; 31.81 MHz
A_{C6}	25.63 MHz; 24.17 MHz; 27.54 MHz; 26.14 MHz; 25.92 MHz; 28.89 MHz
A_{C8}	7.22 MHz; 7.26 MHz; 7.10 MHz
lwpp (Lorentzian)	0.1112 mT
lwpp (Gaussian)	0.0807 mT
	Dimer $(\mathbf{9}^{\bullet})_2$
g	2.0034
r	0.987 nm
lwpp (Lorentzian)	0.0114 mT
lwpp (Gaussian)	0.2664 mT

6.2 Reduction Stability

The reduction stability of **9•** was evaluated using the doubly labelled $YopO_{89-729}$ Y588C/N624C construct. Oocytes of the African claw frog *Xenopus laevis* were obtained from EcoCyte Bioscience (Dortmund, Germany) and the lysate was prepared following a protocol of *Karthikeyan et al.*[11]

For HeLa cell lysate, HeLa S3 (ATCC® CCL-2.2, human cervical adenocarcinoma) cells were suspended in PBS buffer (600 µL per 10^8 cells), the suspension was frozen in ethanol/$CO_{2(s)}$ for 5 min, and subsequently thawed in a 37 °C water bath. This procedure was repeated three times, whereupon the cells were lysed with rapid oscillation for 5 minutes. Membranes were separated by centrifugation at 15000 rpm at 4 °C and the lysate was collected as the supernatant. It was separated into several aliquots, immediately shock-frozen in liquid nitrogen, and stored at –80 °C.

Then, $YopO_{89-729}$ $Y588T^{Ox}/N624T^{Ox}$ was diluted to a concentration of 50 µM in the corresponding reductive medium and filled into a 10 µL capillary, which was sealed with superglue and transferred into a 3 mm outer diameter Q-band tube. The EPR-tube was inserted into the spectrometer (EMXmicro) and the spectrometer properly tuned. After this, a *cw* EPR spectrum was recorded every 15 minutes over 15 hours. A home-written bash script was used to monitor the microwave frequency and power throughout the entire measurement. The signal intensities representing the spin concentration were obtained as the double integral over the spectrum for each time point. The dead time, measured from mixing the radical and the respective medium to the beginning of measurement, was kept below 6 minutes.

6.3 Binding of Spin Labels to Cystein-Free YopO C219A

As described in the main text, the extent of non-specific binding of spin labels **4•**, **6•**, and **9•** was studied by addition of a cysteine-free $YopO_{89-729}$ C219A to radical solutions in PBS buffer. The respective protein was obtained from a previous study recently published by us[8] and used as a stock solution in PBS buffer. The protein was added to a solution of the radical in PBS buffer, so that the indicated final concentrations were achieved and then incubated for 20 min at room temperature. The samples were transferred into 10 µL capillaries, which were sealed with glue on both ends and fitted into a 4 mm outer diameter X-band EPR tube. The tube position was pre-adjusted through the tubeholder and not changed throughout the experiment for each radical. X-band *cw* EPR spectra (ModAmp. 0.2G, attenuation 25 dB, 298 K, 10 scans each) were recorded (Figures S62 – S64). In the main text, the respective peak-to-peak intensities are shown (Figure 3a). It is important to note that the double-integral remained constant within a deviation of 10 % for each radical.

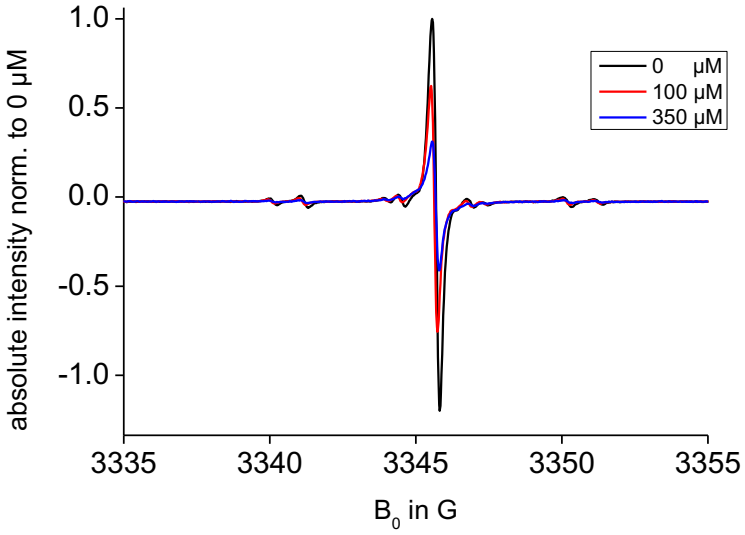

Figure S62: *Measurement for radical* ***4•****.*

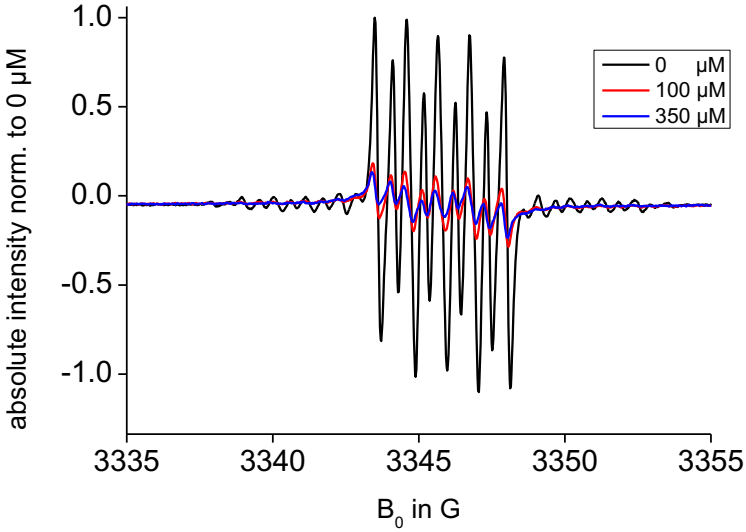

Figure S63: *Measurement for radical* ***6•****.*

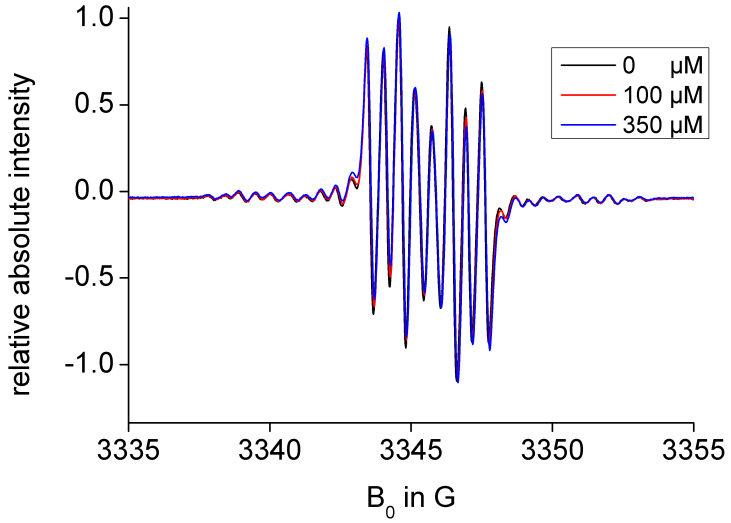

Figure S64: *Measurement for radical* ***9•****.*

6.4 CW EPR on **9•** in Glycerol/Water Mixtures

Dissolving **9•** in mixtures of PBS-buffer and glycerol, the *cw* EPR spectra shown in Figure S65 were recorded at 100 K. A minimum content of 20 % glycerol was required as a cryo-protectant. With rising glycerol content, the features of the Pake pattern arising from homodimerization of **9•** decreased. By simulation of the respective EPR spectra, the monomer/dimer fractions provided in Table S8 were found. Simulation of the EPR spectra was done as described in section 6.1.

Table S8: *Dimer content of the EPR samples.*

Glycerol content [%]	Monomer **9•** [%]	Dimer $(\mathbf{9^{\bullet}})_2$ [%]
20	72	28
60	85	15
85	99	1

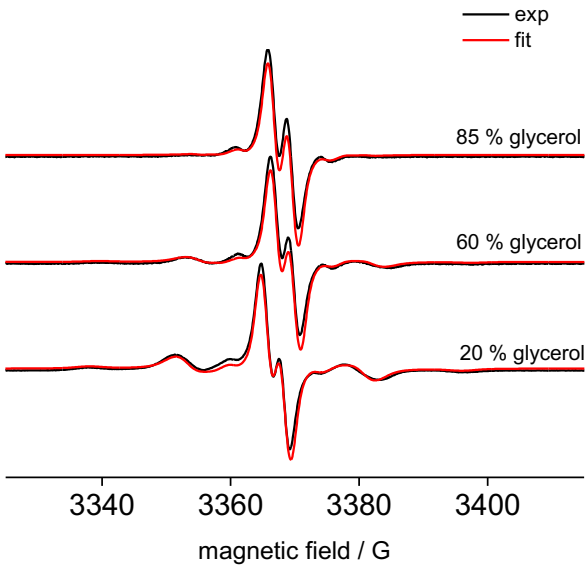

Figure S65: cw EPR spectra of **9•** *at 100 K in glycerol/PBS-buffer mixtures.*

7. Pulsed EPR-spectroscopy

7.1 Sample Preparation

YopO samples in deuterated buffer were diluted 1:1 in ethylene glycol-d_6, transferred into a Q-band EPR tube (O.D. 3 mm, Wilmad LabGlass, Vineland, NJ, USA) and flash-frozen in liquid nitrogen.

7.2 Relaxation Time Measurements

In order to compare the electron spin relaxation behavior of Ox-SLIM **9•** and its predecessor SLIM **6•**, T_1 and T_M relaxation times were measured at 50 K by inversion recovery (Figure S66a) and two-pulse electron spin echo envelope modulation (Figure S66b) experiments, respectively. The pulse sequences were applied at the maximum of the echo-detected field swept EPR spectrum and included phase cycling, two steps for 2pESEEM and four steps for IR. Acquisition parameters are given in Table S9. Measurements were carried out on the constructs YopO Y588T^{ox}/N624T^{ox} and Y588T^{SLIM}/N624T^{SLIM}.

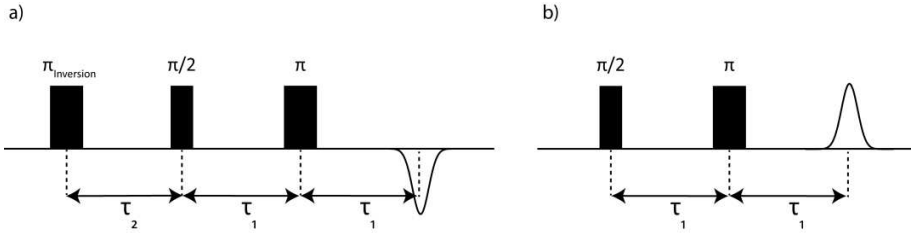

Figure S66: Pulse sequence applied for the inversion recovery (a) and the two-pulse ESEEM (b) experiment.

Table S9: Pulse sequence parameters for relaxation time measurements.

Inversion Recovery		Two-Pulse ESEEM	
Variable	Value	Variable	Value
π/2	12 ns	π/2	12 ns
π	24 ns	π	24 ns
$\pi_{Inversion}$	24 ns	–	–
τ_1	200 ns	τ_1	200 ns
τ_2	400 ns	–	–
τ_2 increment	1 ms	τ_1 increment	8 ns
Shots per Point	1	Shots per Point	10
Shot Repetition Time	500 ms	Shot Repetition Time	15 ms

The results of the relaxation time measurements are shown in Figure S67. Inversion recovery traces were fitted with a single exponential $y = a \cdot exp\left(-\frac{t}{T_1}\right) + c$, with a being the pre-exponential factor, T_1 the transverse relaxation time, and c an offset. Two-pulse ESEEM traces could be fitted with a stretched exponential decay $y = a \cdot exp\left(-\left(\frac{2t}{T_M}\right)^b\right) + c$, wherein T_M is the phase-memory time quantifying the Hahn echo decay. All fit parameters are collected in Table S10.

Table S10: Fit parameters of the relaxation curves.

	Inversion Recovery $y = a \cdot exp\left(-\frac{t}{T_1}\right) + c$	Two-Pulse ESEEM $y = a \cdot exp\left(-\left(\frac{2t}{T_M}\right)^b\right) + c$
Y588T^{ox}/N624T^{ox}	a = –1.552 T_1 = 11 ms c = 0.994	a = 1.171 T_M = 4.00 µs b = 0.783 c = –0.016
Y588T^{SLIM}/N624T^{SLIM}	a = –1.508 T_1 = 7.8 ms c = 0.992	a = 1.574 T_M = 1.45 µs b = 0.621 c = 0.011

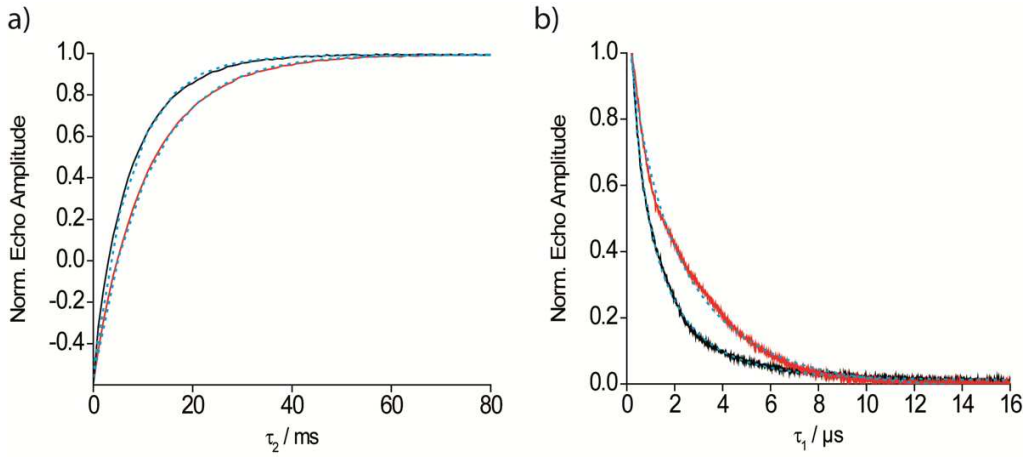

Figure S67: Relaxation experiments on YopO Y588T^{ox}/N624T^{ox} (red) and Y588T^{SLIM}/N624T^{SLIM} (black). Overlay of (a) the Inversion Recovery and b) the Two-Pulse ESEEM time traces. The blue dashed lines are the fits.

7.3 Double Quantum Coherence (DQC) Experiments

The six-pulse Double Quantum Coherence (DQC) sequence (FigureS68) was applied at the maximum of the trityl field-swept EPR spectrum. In the DQC experiment, the interpulse delays τ_1 and τ_2 are incremented and decremented, respectively, and the integral of the DQC echo is recorded as a function of τ_1–τ_2.

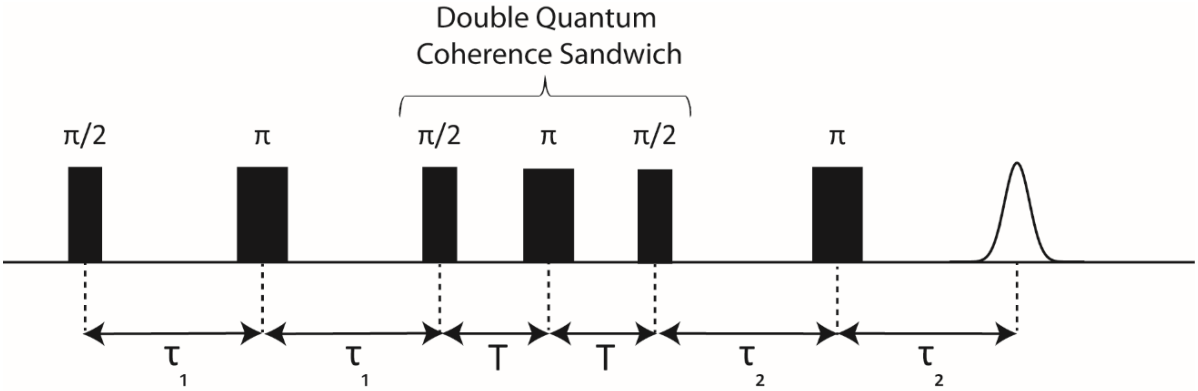

Figure S68: *Schematic representation of the 6-pulse Double Quantum Coherence (DQC) experiment.*

A 64–step phase cycle was applied to remove undesired echoes and thus extract the pure double quantum coherence pathway.[12,13] In order to eliminate deuterium ESEEM from the dipolar time trace, a modulation averaging procedure was applied, i.e. τ_1 and τ_2 were incremented by 8 steps of 16 ns and the respective traces were summed up.[14] All DQC measurements were performed at 50K.

As the pure DQC echo cannot be observed in the transient mode of the spectrometer, the phase of the microwave pulses was adjusted on the Hahn echo sequence to yield a maximally positive amplitude in the real signal channel of the quadrature detector. Proper phase adjustment was checked by summing amplitudes of the Hahn echo obtained from $(\pi/2)_{+x}/(\pi)_{+x}$and $(\pi/2)_{-x}/(\pi)_{-x}$ pulses, which averages out the signal. The same applies to $(\pi/2)_{+y}/(\pi)_{+y}$and $(\pi/2)_{-y}/(\pi)_{-y}$ pulses. Pulse lengths and interpulse delays used for the DQC experiment are given in Table S11.

Table S11: *Parameters for the DQC experiment*

Variable	Value
π/2	12 ns
π	24 ns
τ_1	200 ns
τ_1 increment	4 ns
τ_2	7000 ns ([YopO] = 18.5 µM) 4500 ns ([YopO] = 45 nM)
τ_2 decrement	4 ns
T	50 ns
Shots per Point	3
Shot Repetition Time	15 ms

The symmetric DQC time traces were mirrored at the zero-time. Transformation of the mirrored traces into distance distributions was done with the DeerAnalysis toolbox for Matlab[15]. In order to eliminate the intermolecular background of the primary data, a background correction was performed assuming a homogeneous three-dimensional distribution of background objetcs. The “background start” value was

chosen such that the background-corrected time trace was flat at long dipolar evolution times (last quarter of the time trace); an initial guess of the"background start" value was obtained using the "!" button in DeerAnalysis. The influence of the background correction on the distance distributions was checked by means of the validation tool in DeerAnalysis. Herein, only the "background start" parameter was varied, and the variation ranges were set from the first local minimum of the time trace to the point when the oscillations were entirely damped.

For the sake of comparison, the construct YopO Y588T^{SLIM}/N624T^{SLIM} shown in our previous study[8] was measured again with the same parameters applied to Y588T^{ox}/N624T^{ox}. The time traces before and after background correction, the resulting distance distribution, and the L-curves for Tikhonov-regularization are shown in Figure S69.

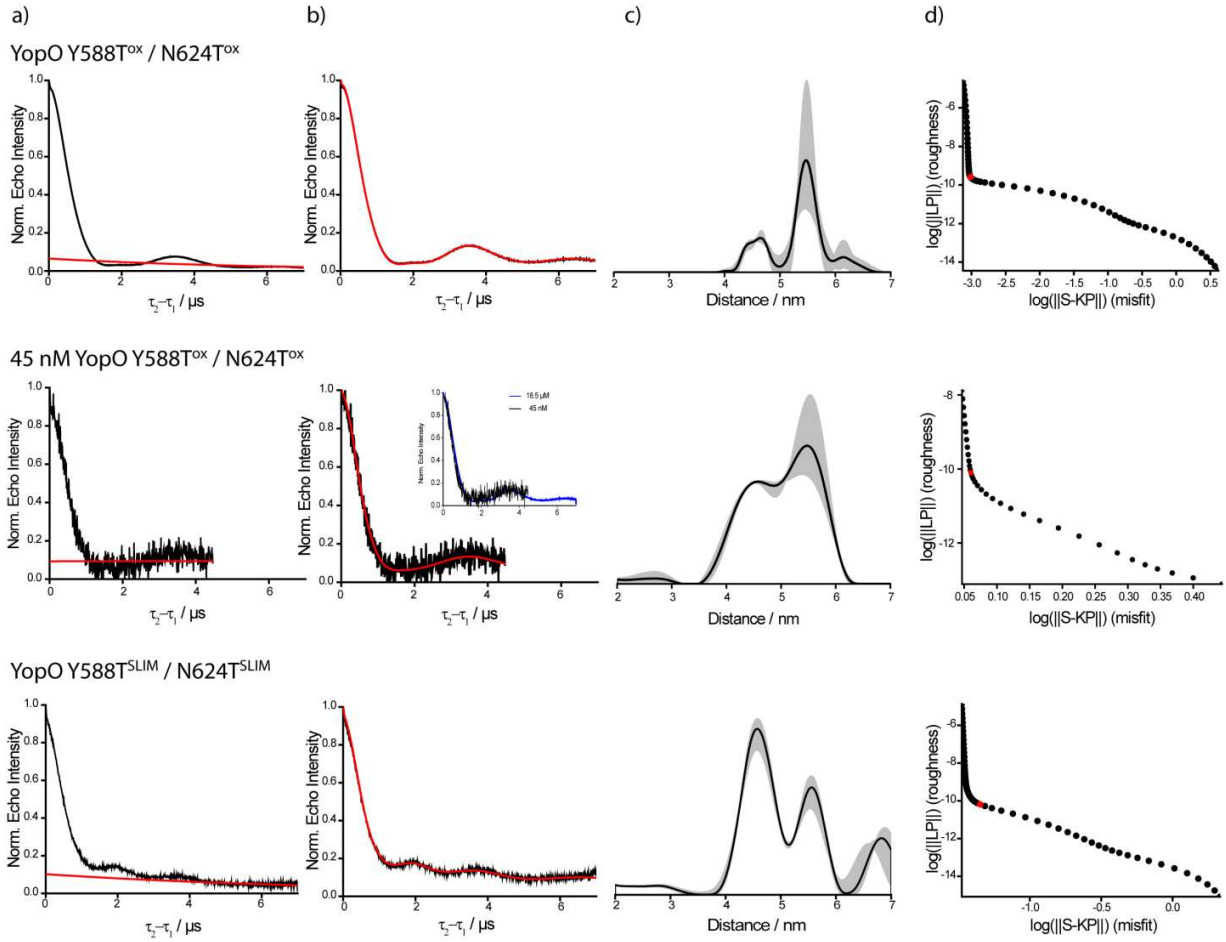

Figure S69: *PDS data obtained for YopO Y588C/N624C labelled with Ox-SLIM* ***9•*** *(18.5 µM in top row, 45 nM in middle row) and SLIM* ***6•*** *(12.5 µM in bottom row). Raw DQC time traces with the background fits shown in red (a). Background-corrected DQC time traces with fits from Tikhonov-regularization in red (b). Distance distributions with the background validation from DeerAnalysis shown as grey shaded area (c). L-curves with the chosen regularization parameter in red (d). For Ox-SLIM, a comparison of the data acquired at 18.5 µM and 45 nM is shown as in inset in part c). The shorter dipolar evolution time chosen for the measurement at 45 nM leads to an artificial broadening of the distance distribution.*

7.4 Determination of the Signal-to-Noise Ratio (SNR)

The SNR of the DQC-traces was determined using the software "SNRcalculator" developed inhouse[16] and available free of charge via github.[17] Table S12 contains the SNR values in reference to the measurement time, and in reference to the measurement time and the spin concentration. As can be seen from the values related to measurement time and concentration, the SNR obtained with $Y588T^{ox}/N624T^{ox}$ exceeds the one obtained with the corresponding SLIM-labelled construct $Y588^{SLIM}/N624T^{SLIM}$ by a factor of 2 (Table S12). With respect to the 45 nM measurement, it should be noted, that the dipolar evolution time was set to 4.5 µs, coming along with an intrinsic increase in SNR.

Table S12: *SNR of the DQC experiments. Note that the given concentrations are protein concentrations.*

SNR related to	$Y588T^{SLIM}/N624T^{SLIM}$ (12.5 µM protein, 7.0 µs trace length)	$Y588T^{ox}/N624T^{ox}$ (18.5 µM protein, 7.0 µs trace length)	$Y588T^{ox}/N624T^{ox}$ (45 nM protein, 4.5 µs trace length)
measurement time	46 $h^{-1/2}$	133 $h^{-1/2}$	1.24 $h^{-1/2}$
measurement time and spin concentration	1.84 μM^{-1} $h^{-1/2}$	3.59 μM^{-1} $h^{-1/2}$	13.8 μM^{-1} $h^{-1/2}$

8. Computational Data

8.1 Homodimer of **9•**

For the input structures, a conformer search was performed applying the Conformer-Rotamer Ensemble Sampling Tool (CREST)[18] at the GFN-FF[19] level of theory. The energetically lowest conformers found for the trityl dimer and monomer were further optimized using the composite method B97-3c.[20] On the optimized geometries free energies were calculated using a multilevel approach. High level single-point energies were calculated with the hybrid density functional PBE0[21] in a large def2-TZVPP[22] basis set. The D4[23] London dispersion correction was applied throughout. Solvation contributions to free energy were calculated with COSMO-RS[24,25] also including the volume work to go from an ideal gas at 1 bar to 1 mol L^{-1} in solution. For the COSMO-RS free energy, two singlepoint calculations with PBE/TZ (one in gas-phase and one in an ideal conductor) were performed. BP86/TZ single-point calculations did not converge, but the effect of the choice of the GGA is rather small for usage with COSMO-RS.S9 The output of these calculations was then processed by the COSMOtherm program.[26] Thermostatistical contributions to the free energy were calculated using GFN2-xTB[26] and the modified RRHO scheme (mRRHO).[28] The total free energies were then calculated as the sum of the single-point energy, dispersion contribution, thermostatistical and solvation contribution according to

$$\Delta G = \Delta E + \Delta\delta G_{solv} + \Delta G_{mRRHO}$$

where Δ indicates the differences between the dimer and the monomers. The respective values are provided in Table S13 below.

Table S13: *Energetic contributions to the dimerization energy for* $(9^{\bullet})_2$

ΔE PBE0-D4/def2-TZVPP	ΔG^{298}_{mRRHO} GFN2-xTB	$\Delta\delta G_{solv}(H_2O)$ COSMO-RS(H_2O)	ΔG
-42.4 kcal/mol	23.1 kcal/mol	4.4 kcal/mol	**-14.8 kcal/mol**

All quantum mechanical calculations were performed with the TURBOMOLE 7.2.[29] (DFT) and xtb 6.3.2 (GFN1-xTB[30] GFN2-xTB[27] GFN-FF[19]) program packages with default convergence criteria 10^{-7} E_h for energies and 10^{-5} E_h $Bohr^1$ for gradients. The resolution-of-identity (RI) approximation for the Coulomb inte-

grals was generally used to speed up the DFT calculations using matching default auxiliary basis sets.[31,32] For the integration of the exchange-correlation contribution, the numerical quadrature grid m4 was employed. All calculations were performed on Intel© Xeon E5-2660 v4 @ 2.00GHz machines.

8.1.1 Coordinates for **9•** in xyz-format

C	-0.4949901	1.9359712	-3.4976828
C	-0.1477457	0.9793283	-2.5434918
C	-0.6799248	0.9976607	-1.2451473
C	-1.7164983	1.9077493	-0.9773188
C	-2.0654557	2.8705192	-1.9210424
C	-1.3896629	2.9726475	-3.1541467
S	0.2924100	1.7729644	-5.0641787
S	0.9917650	-0.2684588	-3.0201439
S	-3.4404255	3.8849796	-1.4405032
S	-2.5508461	1.9567599	0.5721558
C	0.6983481	-0.0333133	-4.8286172
C	-3.1484607	3.7030162	0.3834955
C	-4.4607394	3.8687622	1.1389617
C	-2.0820238	4.7005921	0.8170192
C	-1.6910054	4.6557905	2.2847786
O	-0.7379061	5.6898132	2.5005016
C	-5.6605385	3.0855938	0.6216019
O	-6.7886940	3.2417746	1.4746657
C	1.9382341	-0.3886686	-5.6407140
C	3.2652961	0.1960032	-5.1890224
O	3.8138258	-0.4737529	-4.0460764
C	-0.5278818	-0.8370843	-5.2612706
C	-0.3937229	-2.3419412	-5.1523181
O	-1.7019111	-2.8992838	-5.3331311
C	3.3538100	1.2837811	0.5603033
C	2.0812656	1.2896056	-0.0070677
C	1.2909986	0.1151193	0.0047268
C	1.9553558	-1.0913528	0.3155291
C	3.2663892	-1.1081214	0.8064448
C	3.9307910	0.1055376	1.0750896
S	4.1745343	2.8614927	0.5284518
S	1.5207547	2.8298099	-0.6538619
S	3.9623548	-2.7006122	1.0940016
S	1.1851064	-2.6518899	0.1019937
C	2.6031634	3.8345104	0.4606966
C	2.7922315	-3.5300111	-0.0975256
C	2.5845905	-4.9941313	0.2565815
C	3.3598777	-3.3197685	-1.5014185
C	2.4913694	-3.7608062	-2.6690930
O	3.0570312	-3.3885899	-3.9181029
C	2.2101777	-5.2805551	1.7112736
O	1.4604658	-6.4835519	1.8419809
C	2.8607247	5.2069336	-0.1408003
C	3.3512062	5.2474051	-1.5825978
O	3.7145243	6.5672039	-1.9674405
C	1.9029259	3.8994369	1.8081888
C	2.5277210	4.7599228	2.8880280
O	1.6736736	4.8005900	4.0431354
C	-2.8444682	-2.2736285	0.7911791
C	-2.0830419	-1.3890231	0.0186387
C	-0.9959967	-0.6847147	0.5853994
C	-0.7691305	-0.8465290	1.9723303
C	-1.5468739	-1.7215848	2.7278496
C	-2.5679962	-2.4766684	2.1424664
S	-4.1543532	-3.0984530	-0.0633689
S	-2.5057964	-1.3068409	-1.6880621
S	-1.1317122	-1.8420103	4.4420640
S	0.4899398	0.0172058	2.8596747
C	-3.3363328	-2.9610733	-1.7143625
C	-0.3293579	-0.1801341	4.5030333
C	0.7273471	-0.1761137	5.5874166
C	-1.3742313	0.8985964	4.7054881
C	-4.3790480	-2.9703974	-2.8099415
C	-2.3041914	-4.0558145	-1.8813270
C	-3.3333961	-3.4874185	2.9459433
C	-0.1306619	0.1325251	-0.2269001
N	-2.4658997	-4.4197839	3.6408387
C	-1.4535306	-5.1702668	3.0570080
C	-0.8079302	-5.9360503	4.1621093
C	-1.4524831	-5.6717214	5.2962060
C	-2.5492326	-4.7037690	5.0157694
O	-1.1825680	-5.1926177	1.8700672
O	-3.3644514	-4.2399947	5.7785399
C	-1.4599762	4.1288889	-4.0863355
O	-0.8790799	4.1150833	-5.1532594
O	-2.1140002	5.2457642	-3.7174118
C	5.1355084	0.0334085	1.9433825
O	5.6198828	-1.0305994	2.2704070
O	5.6614924	1.1682803	2.4459212
H	-4.7138427	4.9287144	1.1676041
H	-4.2801643	3.5777201	2.1752072
H	-2.4422657	5.7037996	0.5852560
H	-1.1866847	4.5375103	0.2191855
H	-1.2749460	3.6732449	2.5209452
H	-2.5640610	4.8108205	2.9255809
H	-0.1555781	5.4319789	3.2312119
H	-5.3999414	2.0344222	0.4833762
H	-5.9716801	3.4666074	-0.3476667

H	-6.6430685	2.7144088	2.2670583
H	1.7475702	-0.0804598	-6.6714343
H	2.0465259	-1.4712776	-5.6640142
H	3.1728533	1.2647206	-4.9908377
H	3.9956366	0.0677013	-5.9845949
H	3.3617787	-0.1067087	-3.2728515
H	-0.7673866	-0.5656032	-6.2895777
H	-1.3765911	-0.5289254	-4.6530686
H	0.0052846	-2.6128385	-4.1726797
H	0.2879539	-2.7324609	-5.9090707
H	-1.5944857	-3.8278931	-5.5610259
H	3.4790737	-5.5519050	-0.0210282
H	1.7866368	-5.3808304	-0.3788417
H	4.3252164	-3.8234692	-1.5543511
H	3.5647943	-2.2557260	-1.6211869
H	1.4880696	-3.3399564	-2.5494870
H	2.3915357	-4.8452325	-2.6965481
H	3.3396619	-2.4588878	-3.8733827
H	1.6572107	-4.4340351	2.1223414
H	3.1066577	-5.4021780	2.3151966
H	0.5500188	-6.2581487	1.5959233
H	3.5953491	5.7272266	0.4730028
H	1.9333759	5.7774972	-0.0516458
H	2.6041252	4.8275015	-2.2591898
H	4.2496636	4.6445562	-1.6893162
H	2.9084859	7.0693207	-2.1265971
H	1.7695619	2.8833405	2.1805204
H	0.9102524	4.2966291	1.6167572
H	2.6120969	5.7947935	2.5688890
H	3.5254971	4.4109075	3.1619147
H	1.6886137	3.9278666	4.4514126
H	1.4699505	-0.9499067	5.4204727
H	0.2676872	-0.3328304	6.5614355
H	1.2317904	0.7886879	5.6163965
H	-2.1111302	0.8801995	3.9078396
H	-0.9012671	1.8804810	4.7089367
H	-1.8861065	0.7548238	5.6557099
H	-5.1101329	-2.1797404	-2.6703470
H	-4.8965949	-3.9281006	-2.8232534
H	-3.8930990	-2.8402920	-3.7740590
H	-1.5666116	-4.0263305	-1.0855719
H	-1.7984396	-3.9310115	-2.8361938
H	-2.7902791	-5.0302365	-1.8622619
H	-4.0108769	-4.0395712	2.2994792
H	-3.9269235	-3.0058334	3.7224762
H	-2.5022193	5.1572920	-2.8220476
H	5.1723055	1.9576961	2.1349345
H	0.0407758	-6.5732437	3.9778256
H	-1.2725522	-6.0507625	6.2875859

8.1.2 Coordinates for $(\mathbf{9}^{\bullet})_2$ in xyz-format

C	-3.8936910	-3.0593819	0.8301341
C	-4.7076312	-2.0312016	0.3604217
C	-4.2538562	-0.7014106	0.3185761
C	-2.9596980	-0.4235122	0.8038267
C	-2.1785854	-1.4317538	1.3828504
C	-2.6264648	-2.7698175	1.3768260
S	-4.5552399	-4.6892109	0.6789993
S	-6.3125681	-2.4878821	-0.1996784
S	-0.6404322	-0.8935977	2.0444910
S	-2.2835887	1.1990422	0.7869996
C	-5.8217345	-4.2213794	-0.6115940
C	-1.0903949	0.8920567	2.1683750
C	0.2062325	1.6562876	1.9355244
C	-1.8022589	1.2376556	3.4742436
C	-1.0233866	1.0956550	4.7758208
O	-0.9406597	-0.2461812	5.2603496
C	0.1173095	3.1668107	1.9813561
O	-0.7661439	3.7165485	1.0142404
C	-7.0603958	-5.0944499	-0.4441218
C	-6.8580236	-6.5944346	-0.5017522
O	-6.5180191	-7.0027077	-1.8277042
C	-5.1500816	-4.2855640	-1.9793368
C	-6.0216348	-4.0719059	-3.2095239
O	-6.7746510	-2.8660460	-3.2446710
C	-7.9646900	0.4231058	2.3708455
C	-6.6957868	0.2365277	1.8140127
C	-6.4419892	0.4956083	0.4441687
C	-7.5363028	0.9134116	-0.3466331
C	-8.8089988	1.0394997	0.1945435
C	-9.0650843	0.7595071	1.5514775
S	-8.1116930	0.1732678	4.1093300
S	-5.4407074	-0.3484951	2.8974896
S	-10.0329311	1.6036524	-0.9732293
S	-7.4077125	1.1911794	-2.0876534
C	-6.2781326	0.1194963	4.4586050
C	-9.1945508	0.7933528	-2.4083570

C	-9.5547687	1.5236936	-3.6960071
C	-9.3702870	-0.7380910	-2.4597885
C	-10.5545550	-1.3769322	-1.7762646
O	-11.7976133	-0.9943350	-2.3837031
C	-10.9680978	1.3079407	-4.2124298
O	-11.9556352	1.6708882	-3.2631392
C	-6.0438617	-0.9941819	5.4859210
C	-4.6231413	-1.5112826	5.6549221
O	-3.6706974	-0.5580687	6.1447712
C	-5.8016526	1.4799370	4.9628773
C	-5.9321881	2.6346423	3.9888767
O	-5.4073296	3.8500203	4.5286270
C	-3.2001373	1.7463765	-3.0295172
C	-3.9171584	0.8706724	-2.2222854
C	-4.6209282	1.3206630	-1.0857907
C	-4.6935341	2.7163522	-0.8876693
C	-3.9151543	3.5821439	-1.6687627
C	-3.1128003	3.1051276	-2.7070801
S	-2.4476645	1.0307549	-4.4654265
S	-3.9706043	-0.8114462	-2.7593157
S	-4.0761603	5.3015438	-1.3020658
S	-5.6874304	3.4590495	0.3498891
C	-3.6361673	-0.3897912	-4.5294535
C	-4.7965253	5.0819101	0.3934112
C	-5.8117523	6.1804493	0.6398994
C	-3.7126344	5.0550400	1.4448275
C	-2.9789377	-1.5676965	-5.2153385
C	-4.9198181	0.0314481	-5.2145974
C	-2.2222329	4.0358045	-3.4801776
C	-5.1338506	0.3657471	-0.1276349
N	-0.9192176	3.4781993	-3.7902256
C	-0.3397775	3.4958955	-5.0777766
C	1.0053370	2.8710551	-4.9315140
C	1.1857610	2.5455828	-3.6524804
C	-0.0215389	2.9431380	-2.8775562
O	-0.8653053	3.9466511	-6.0679519
O	-0.2040430	2.8374267	-1.6790302
C	-1.8194984	-3.8909958	1.8712478
O	-2.2643588	-5.0142263	2.0605191
O	-0.5251972	-3.5882125	2.0520564
C	-10.4120613	0.6881302	2.1752669
O	-10.5470624	0.5237193	3.3734242
O	-11.5131628	0.7424468	1.4049605
H	0.6263142	1.3412339	0.9823911
H	0.9192754	1.3439572	2.6942462
H	-2.7174592	0.6518587	3.5370583
H	-2.1304577	2.2746795	3.3897703
H	-1.5006268	1.7299121	5.5273316
H	-0.0002780	1.4441698	4.6749989
H	-1.8255664	-0.4931392	5.5744166
H	1.1266652	3.5696271	1.8609711
H	-0.2379626	3.5154665	2.9480622
H	-0.5526271	3.3492444	0.1440337
H	-7.7959046	-4.8061302	-1.1954299
H	-7.4960064	-4.8687541	0.5278725
H	-7.7922255	-7.0700812	-0.1870123
H	-6.0828943	-6.8977980	0.2090244
H	-6.4284825	-7.9607908	-1.8273484
H	-4.7053097	-5.2740933	-2.0851614
H	-4.3249067	-3.5740230	-1.9770038
H	-6.7414158	-4.8805435	-3.3012696
H	-5.3628919	-4.1391617	-4.0854947
H	-6.2135505	-2.1498088	-2.9110618
H	-8.8575177	1.1897788	-4.4693050
H	-9.3813349	2.5876372	-3.5462196
H	-8.5019199	-1.2016651	-2.0016732
H	-9.3392344	-1.0447564	-3.5047620
H	-10.5567915	-1.1175683	-0.7169204
H	-10.4299961	-2.4600952	-1.8536285
H	-12.5099501	-1.4093497	-1.8865103
H	-11.1064709	0.2734449	-4.5317999
H	-11.1057207	1.9382254	-5.0914354
H	-12.1405033	0.8585652	-2.7656668
H	-6.6433939	-1.8554817	5.1931185
H	-6.4326432	-0.6619777	6.4518246
H	-4.2255338	-1.8468340	4.6997426
H	-4.6483261	-2.3834322	6.3125596
H	-3.8893649	-0.3439335	7.0578694
H	-4.7574991	1.3934010	5.2558736
H	-6.3731399	1.7064088	5.8689105
H	-6.9703311	2.7656168	3.6778621
H	-5.3456959	2.4405410	3.0966733
H	-5.9735129	4.1194175	5.2597678
H	-6.2658872	6.0447065	1.6197646

H	-6.5923219	6.1827426	-0.1141861
H	-5.3181845	7.1508811	0.6407127
H	-4.1563996	4.8987470	2.4266007
H	-3.1808523	6.0064048	1.4515460
H	-2.9889957	4.2721897	1.2558973
H	-2.0606082	-1.8623551	-4.7176151
H	-2.7485234	-1.3173219	-6.2491146
H	-3.6589578	-2.4173540	-5.2280139
H	-5.3752677	0.8737616	-4.7028614
H	-5.6298800	-0.7943684	-5.2134596
H	-4.7154355	0.3208929	-6.2443653
H	-2.0928522	4.9590345	-2.9174692
H	-2.6628968	4.2972251	-4.4423666
H	-0.0142961	-4.4116338	2.1854873
H	-11.2795512	0.8643130	0.4560407
H	1.6762612	2.7413319	-5.7643399
H	2.0366393	2.0859307	-3.1781376
C	8.4096607	1.2813426	-0.7355450
C	7.2196506	0.9817595	-0.0812103
C	6.1289099	0.4259737	-0.7815124
C	6.2594938	0.2943183	-2.1746804
C	7.4582220	0.5739951	-2.8391749
C	8.5741822	1.0390613	-2.1140023
S	9.6515398	2.0046243	0.3138487
S	7.1764016	1.2802985	1.6532430
S	7.4475170	0.3685843	-4.5859918
S	4.8623099	-0.0620310	-3.1638986
C	9.0150020	1.2294056	1.8802580
C	5.8154017	-0.5283325	-4.6673324
C	6.0169036	-2.0407741	-4.7231880
C	5.0288799	-0.0559576	-5.8907268
C	4.7778536	1.4419291	-6.0028051
O	3.7009195	1.7336764	-6.8964893
C	6.6897711	-2.6675606	-3.5224214
O	6.6554897	-4.0843845	-3.6818804
C	9.3849084	2.1547428	3.0355980
C	8.6505326	1.9114135	4.3457558
O	8.9113815	0.6481699	4.9645717
C	9.4863562	-0.2151784	2.0070341
C	10.9087553	-0.4309997	2.5012745
O	11.9127172	0.3500719	1.8662487
C	3.9996554	3.0838026	1.7675573
C	4.3530341	2.2401973	0.7248711
C	4.3070131	0.8248577	0.8730936
C	3.7205878	0.3175538	2.0670016
C	3.3989608	1.1747978	3.1258688
C	3.5737324	2.5604308	3.0006448
S	4.0892771	4.8207839	1.4227285
S	4.8498983	3.0242833	-0.7776855
S	2.7165844	0.4470046	4.5815396
S	3.3777822	-1.3788756	2.3367184
C	3.9816966	4.6140909	-0.4211154
C	3.2098991	-1.2928439	4.1757057
C	2.0678112	-2.2505876	4.5176133
C	4.5142408	-1.6764785	4.8598916
C	5.7397563	-0.8765115	4.4784586
O	6.8725616	-1.4890348	5.0926540
C	1.7212340	-2.3735292	5.9936171
O	1.3878933	-1.1406750	6.5975534
C	4.7463445	5.7557582	-1.0765740
C	4.9847105	5.6306725	-2.5792228
O	3.8259583	5.4819422	-3.3792530
C	2.5158533	4.4816874	-0.8238486
C	1.6378721	5.6937483	-0.6073633
O	1.8536260	6.6427490	-1.6720875
C	4.8728553	-3.7673213	-0.4396349
C	5.3280460	-2.4648828	-0.2309025
C	4.4580456	-1.3724160	-0.3613357
C	3.1369448	-1.6393068	-0.7510285
C	2.6881551	-2.9496612	-0.9716653
C	3.5499307	-4.0354656	-0.7989476
S	6.1043332	-5.0330293	-0.2644313
S	7.0120084	-2.3005959	0.2608504
S	0.9845002	-3.0854309	-1.4235993
S	1.9741832	-0.3454452	-1.0003537
C	7.1399793	-4.0315926	0.8989302
C	0.8476936	-1.3591772	-2.0553879
C	-0.5710129	-0.8946320	-1.8673248
C	1.2974863	-1.3140635	-3.5012475
C	8.5791484	-4.4901915	0.8175745
C	6.5763307	-4.1140432	2.3015741
C	3.1795556	-5.4782234	-1.0310279
C	4.9199523	-0.0153320	-0.1037693
N	1.7787172	-5.8009797	-0.9780962

C	1.0223181	-6.1886377	-2.1041205
C	-0.3585877	-6.4070182	-1.6014305
C	-0.3829657	-6.1858856	-0.2880897
C	0.9851210	-5.7999159	0.1587070
O	1.4587952	-6.3237361	-3.2227759
O	1.3675304	-5.5328594	1.2861701
C	9.8337771	1.2456185	-2.8748130
O	9.8412507	1.3158578	-4.0861545
O	11.0046971	1.3091351	-2.2091810
C	3.2288699	3.4361256	4.1464862
O	2.2560287	3.2774040	4.8445398
O	4.0850610	4.4571185	4.4144014
H	6.5910122	-2.2752624	-5.6216346
H	5.0367741	-2.5069647	-4.8412096
H	4.0595723	-0.5565416	-5.8747801
H	5.5424591	-0.4176227	-6.7839957
H	5.6854431	1.9706177	-6.2966299
H	4.4746792	1.8432539	-5.0399190
H	3.9904673	1.5446720	-7.7949637
H	6.1590442	-2.3802053	-2.6180665
H	7.7192155	-2.3101228	-3.4339149
H	6.7902014	-4.4687845	-2.8055669
H	9.1501880	3.1764664	2.7372779
H	10.4619674	2.1131250	3.1899039
H	7.5745643	1.9425513	4.1856878
H	8.8906527	2.7227618	5.0354483
H	9.7251130	0.7117728	5.4730595
H	9.3379694	-0.7002035	1.0433220
H	8.8257671	-0.7276989	2.7048122
H	11.1365891	-1.5001371	2.4268353
H	10.9748947	-0.1729793	3.5547079
H	11.8825050	0.1730305	0.9198203
H	2.3379547	-3.2433860	4.1478192
H	1.1821422	-1.9409421	3.9692696
H	4.7103727	-2.7283807	4.6417264
H	4.3718433	-1.5972588	5.9369299
H	5.6231068	0.1558075	4.8183280
H	5.8610156	-0.8576742	3.3939283
H	7.5752272	-0.8256091	5.1285220
H	2.5599125	-2.7774954	6.5591177
H	0.9025221	-3.0972768	6.0823824
H	0.5660792	-0.8118957	6.1826069
H	5.7253946	5.8309709	-0.6046741
H	4.2181131	6.6859604	-0.8710425
H	5.6078507	4.7595444	-2.7831941
H	5.5638297	6.5093735	-2.8879220
H	3.1550409	6.0981043	-3.0493950
H	2.0884833	3.6461252	-0.2767086
H	2.4875989	4.2093619	-1.8745669
H	1.8478852	6.1562336	0.3598398
H	0.5958739	5.3778312	-0.5991280
H	1.2398888	7.3738582	-1.5534721
H	-0.6987601	0.1155019	-2.2400822
H	-0.8575867	-0.9146931	-0.8251755
H	-1.2526059	-1.5286776	-2.4253098
H	2.3219829	-1.6591350	-3.6040547
H	1.2298547	-0.2976914	-3.8834255
H	0.6572675	-1.9534880	-4.1070706
H	9.1978613	-3.8806454	1.4738354
H	8.9660651	-4.4182942	-0.1946391
H	8.6644838	-5.5215368	1.1542180
H	5.5413132	-3.7865196	2.3218256
H	7.1425474	-3.4755478	2.9773081
H	6.6228806	-5.1396442	2.6648227
H	3.7062296	-6.0883119	-0.2981488
H	3.5216779	-5.7905719	-2.0180235
H	10.8552958	1.2797253	-1.2408027
H	4.8555411	4.4129332	3.8296794
H	-1.1612756	-6.7050240	-2.2538034
H	-1.2086577	-6.2445693	0.40046

8.2 Ketone **17**

Using the functional PBE0[20] in a def2-TZVP[21]-basis set as implemented in ORCA, structure optimization was carried out for ketone **17** with the results shown in Figures S70 and S71.

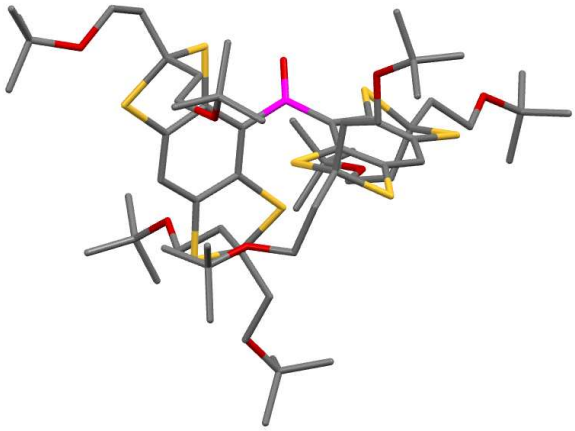

***Figure S70**: DFT optimized structure of ketone **17** with the carbonyl carbon atom highlighted in purple. View along the Bürgi-Dunitz trajectory. Hydrogen atoms were omitted for the sake of clarity.*

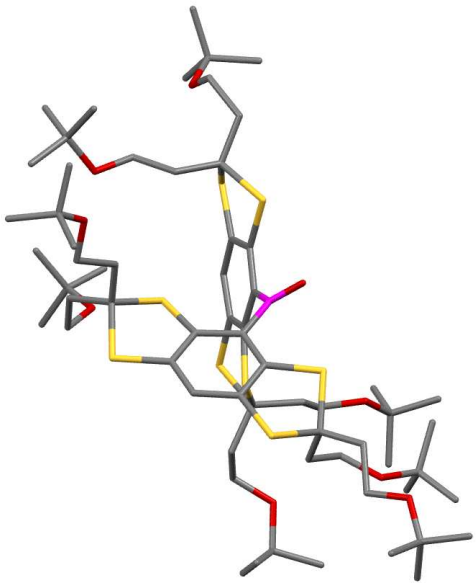

***Figure S71**: DFT optimized structure of ketone **17** with the carbonyl carbon atom highlighted in purple, sideview. Hydrogen atoms were omitted for the sake of clarity.*

8.2.1 Coordinates for **17** in xyz-format

C	-1.5401940	-1.1908634	-1.7527480
C	-1.9758575	-2.3983075	-1.2012024
C	-1.2629327	-2.9971456	-0.1718917
C	-0.1602437	-2.3491369	0.3670176
C	0.2001233	-1.0768192	-0.0851606
C	-0.4781491	-0.5003321	-1.1643035
S	-2.4528852	-0.6097434	-3.1394871
C	-4.0146107	-1.4894271	-2.6416766
S	-3.4387005	-3.0961644	-1.9025299
S	0.7840741	-2.9955940	1.7118124
C	2.2389823	-1.8794974	1.4121585
S	1.4990927	-0.2855722	0.8108895
C	-4.7396625	-0.6071120	-1.6231324
C	-4.7609169	-1.7413885	-3.9498430
C	-6.1648399	-2.3032132	-3.8382592
O	-6.2223815	-3.4451983	-3.0018438
C	-5.8211247	-1.2301508	-0.7524972
O	-6.2722298	-0.2617831	0.1958188
C	2.9029525	-1.5258730	2.7397292
C	3.6369563	-2.6292248	3.4919895
O	4.9774599	-2.8091351	3.0568340
C	3.1444735	-2.4012064	0.3024023
C	3.6631985	-3.8219360	0.3904150
O	4.4155953	-4.0142976	-0.8010867
C	6.0422939	-2.3101655	3.9010128
C	7.2981875	-2.5952629	3.0955419
C	5.9073515	-0.8117092	4.1446736
C	6.0796329	-3.0752590	5.2189856
C	-6.4577218	-4.7384809	-3.6080308
C	-7.8678566	-4.7959195	-4.1829254
C	-6.3245458	-5.7047686	-2.4430771
C	-5.4152646	-5.0519478	-4.6735748
C	-7.6268127	0.2213552	0.0666718
C	-7.7591099	1.2518025	1.1765980
C	-8.6224403	-0.9126526	0.2872517
C	-7.8439416	0.8932976	-1.2839035
C	-0.6908903	3.1709715	1.2558737
C	-0.8219397	2.0728176	0.3968897
C	0.0877164	1.9096921	-0.6614368
C	1.1521200	2.8103501	-0.7944109
C	1.3227036	3.8408437	0.1345195
C	0.3840497	4.0406194	1.1377207
S	-1.8801500	3.2965016	2.5535714
C	-3.1061511	2.1556856	1.7559891
S	-2.0937481	0.9237364	0.8183265
S	2.3959538	2.6856746	-2.0335005
C	3.6867074	3.4703460	-0.9618372
S	2.7768266	4.8253809	-0.0646506
C	-3.9855575	2.8931957	0.7522793
C	-3.9270649	1.4589794	2.8384592
C	-3.2009684	0.4356187	3.6993074
O	-3.0936830	-0.8232059	3.0553177
C	-4.8814010	3.9721188	1.3234705
O	-5.7006203	4.4127300	0.2538540
C	4.7363803	4.0628306	-1.8860349
C	5.8815846	4.7586872	-1.1828512
O	6.7488891	5.2229515	-2.2009642
C	4.1985821	2.4789000	0.0885317
C	4.8086702	1.1892763	-0.4172521
O	6.0596496	1.4611094	-1.0196574
C	7.9259183	5.9509209	-1.7960672
C	8.7694615	5.1447903	-0.8145807
C	7.5443398	7.3027196	-1.2020808
C	8.6845303	6.1470123	-3.0990208
C	6.7014197	0.3903448	-1.7473717
C	7.9919173	1.0276834	-2.2361902
C	7.0044800	-0.7856725	-0.8261195
C	5.8504790	-0.0546035	-2.9307193
C	-3.9305608	-1.9054412	3.5171415
C	-3.5305943	-2.3148138	4.9301842
C	-3.6149847	-3.0283046	2.5434040
C	-5.4113284	-1.5505918	3.4464358
C	-6.4348770	5.6422266	0.4350913
C	-7.2501157	5.6198928	1.7220103
C	-5.4841978	6.8336042	0.4136974
C	-7.3580236	5.6855940	-0.7716640
C	-0.0836696	0.8357121	-1.6654439
O	0.0933731	1.0425816	-2.8570526
C	5.2684686	-5.1733041	-0.8677069
C	4.4740711	-6.4545275	-0.6452512
C	5.8154865	-5.1302450	-2.2856276
C	6.4089191	-5.0593792	0.1386228

H	-1.5790646	-3.9527444	0.2222976
H	-5.1531380	0.2444063	-2.1660970
H	-3.9982989	-0.1935594	-0.9437329
H	-4.1470745	-2.3927764	-4.5681190
H	-4.8384787	-0.7852321	-4.4757800
H	-6.5343463	-2.5152100	-4.8423693
H	-6.8382213	-1.5533404	-3.4193445
H	-5.4043360	-2.0688618	-0.1975713
H	-6.6459838	-1.6292393	-1.3318997
H	2.1262359	-1.1181634	3.3859786
H	3.6109187	-0.7192504	2.5528346
H	3.1228440	-3.5849676	3.3677359
H	3.5996932	-2.4028249	4.5571065
H	3.9938059	-1.7230121	0.2341131
H	2.6082991	-2.3173973	-0.6417294
H	4.2859257	-3.9601800	1.2703538
H	2.8244556	-4.5205776	0.4407173
H	7.2518914	-2.0937692	2.1318144
H	7.4048142	-3.6627126	2.9172806
H	8.1812656	-2.2443939	3.6262955
H	5.8965034	-0.2692772	3.2009995
H	6.7492224	-0.4489470	4.7323018
H	4.9998074	-0.5671079	4.6940470
H	6.1262463	-4.1461740	5.0307542
H	5.2062915	-2.8731437	5.8368401
H	6.9563638	-2.7908805	5.7992013
H	-8.5976500	-4.5407569	-3.4165634
H	-8.0900513	-5.7977777	-4.5475048
H	-7.9971192	-4.1108685	-5.0196599
H	-7.0421080	-5.4589717	-1.6628213
H	-5.3262624	-5.6488738	-2.0158789
H	-6.5068732	-6.7265785	-2.7710810
H	-5.4949656	-4.3860250	-5.5315219
H	-5.5502787	-6.0678244	-5.0418389
H	-4.4120639	-4.9670081	-4.2620789
H	-7.5352782	0.8026823	2.1420359
H	-8.7729811	1.6470755	1.2093893
H	-7.0779388	2.0818907	1.0090255
H	-8.4373694	-1.3944189	1.2458904
H	-8.5604507	-1.6705333	-0.4914954
H	-9.6420745	-0.5295624	0.2869781
H	-7.1285927	1.7010745	-1.4225644
H	-8.8469664	1.3141727	-1.3411429
H	-7.7407353	0.1904928	-2.1091398
H	0.5046475	4.8546241	1.8394255
H	-4.6101755	2.1450997	0.2624322
H	-3.3580802	3.3335973	-0.0206112
H	-4.7698135	0.9749012	2.3493450
H	-4.3474102	2.2311782	3.4854893
H	-3.7128461	0.3512281	4.6588597
H	-2.1878856	0.7815617	3.9092618
H	-4.2727023	4.7808736	1.7345732
H	-5.4990382	3.5779861	2.1358133
H	4.2538074	4.7641377	-2.5641305
H	5.1556995	3.2567197	-2.4835557
H	6.3956107	4.0583739	-0.5247519
H	5.5029462	5.5868988	-0.5723474
H	3.3577245	2.2045010	0.7239052
H	4.9128121	2.9930952	0.7313839
H	4.1165019	0.7086727	-1.1098038
H	4.9277583	0.5141199	0.4394694
H	8.2958362	5.0602551	0.1617393
H	9.7339891	5.6277907	-0.6656287
H	8.9442662	4.1415262	-1.1989034
H	7.0237963	7.1996619	-0.2517193
H	6.8992646	7.8473469	-1.8892169
H	8.4352017	7.9024188	-1.0200931
H	8.9600227	5.1842080	-3.5251627
H	9.5912257	6.7269820	-2.9359340
H	8.0627784	6.6723196	-3.8212781
H	8.5992490	1.3498750	-1.3919079
H	7.7741420	1.9000886	-2.8493449
H	8.5705488	0.3219272	-2.8293303
H	7.5175822	-0.4388781	0.0698245
H	7.6496248	-1.5035248	-1.3305385
H	6.1047145	-1.3207843	-0.5309691
H	5.5744259	0.8001543	-3.5456235
H	4.9411064	-0.5616935	-2.6171995
H	6.4085633	-0.7546269	-3.5503687
H	-2.4654769	-2.5353802	4.9677233
H	-4.0790720	-3.2041176	5.2386303
H	-3.7455458	-1.5331980	5.6572396
H	-2.5536995	-3.2643256	2.5805064
H	-3.8603079	-2.7300436	1.5269045

H	-4.1826911	-3.9240554	2.7902642
H	-5.6723719	-0.7598426	4.1492877
H	-6.0163559	-2.4195801	3.7028575
H	-5.6837948	-1.2269720	2.4445911
H	-6.6158093	5.6454187	2.6063785
H	-7.8715479	4.7268906	1.7670774
H	-7.9034740	6.4898818	1.7657773
H	-4.8163767	6.8384279	1.2732056
H	-6.0435940	7.7680762	0.4326256
H	-4.8785136	6.8144563	-0.4901023
H	-8.0363472	4.8343663	-0.7617914
H	-6.7773501	5.6466118	-1.6911582
H	-7.9484123	6.6001376	-0.7742022
H	3.6237024	-6.4990340	-1.3240694
H	4.1028300	-6.5289330	0.3753607
H	5.1016119	-7.3256058	-0.8279106
H	5.0035982	-5.1916231	-3.0074644
H	6.5010525	-5.9573298	-2.4624591
H	6.3487712	-4.1966282	-2.4548408
H	6.0528870	-5.1137087	1.1649888
H	6.9286228	-4.1115901	0.0114546
H	7.1257641	-5.8669440	-0.0038681

9. References

(1) Fulmer, G. R.; Miller, A. J. M.; Sherden, N. H.; Gottlieb, H. E.; Nudelman, A.; Stoltz, B. M.; Bercaw, J. E.; Goldberg, K. I.; Gan, R.; Apiezon, H., *Organometallics* **2010**, *29*, 2176–2179.

(2) Winkle, M.; Lansinger, J.; Ronald, R. C., *J. Chem. Soc. Chem. Commun.* **1980**, 87–88.

(3) Kopp, K.; Schiemann, O.; Fleck, N., *Molecules* **2020**, *25*, 3666.

(4) Hintz, H.; Vanas, A.; Klose, D.; Jeschke, G.; Godt, A., *J. Org. Chem.* **2019**, *84*, 3304–3320.

(5) Poncelet, M.; Huffman, J. L.; Khramtsov, V. V.; Dhimitruka, I.; Driesschaert, B., *RSC Adv.* **2019**, *9*, 35073–35076.

(6) Graham, B.; Fayter, A. E. R.; Houston, J. E.; Evans, R. C.; Gibson, M. I., *J. Am. Chem. Soc.* **2018**, *140*, 5682–5685.

(7) Wessig, P.; Freyse, D.; Schuster, D.; Kelling, A., *Eur. J. Org. Chem.* **2020**, *2020*, 1732–1744.

(8) Fleck, N.; Heubach, C. A.; Hett, T.; Haege, F. R.; Bawol, P. P.; Baltruschat, H.; Schiemann, O., *Angew. Chem. Int. Ed.* **2020**, *59*, 9767–9772.

(9) Trasak, C.; Zenner, G.; Vogel, A.; Yüksekdag, G.; Rost, R.; Haase, I.; Fischer, M.; Israel, L.; Imhof, A.; Linder, S.; Schleicher, M.; Aepfelbacher, M., *J. Biol. Chem.* **2007**, *282*, 2268–2277.

(10) Stoll, S.; Schweiger, A., *J. Magn. Reson.* **2006**, *178*, 42–55.

(11) Karthikeyan, G.; Bonucci, A.; Casano, G.; Gerbaud, G.; Abel, S.; Thomé, V.; Kodjabachian, L.; Magalon, A.; Guigliarelli, B.; Belle, V.; Ouari, O.; Mileo, E., *Angew. Chem. Int. Ed.* **2018**, *57*, 1366–1370.

(12) Borbat, P. P.; Freed, J. H., *Chem. Phys. Lett.* **1999**, *313*, 145–154.

(13) Saxena, S.; Freed, J. H., *J. Chem. Phys.* **1997**, *107*, 1317–1340.

(14) Akhmetzyanov, D.; Schöps, P.; Marko, A.; Kunjir, N. C.; Sigurdsson, S. T.; Prisner, T. F., *Phys. Chem. Chem. Phys.* **2015**, *17*, 24446–24451.

(15) Jeschke, G.; Chechik, V.; Ionita, P.; Godt, A.; Zimmermann, H.; Banham, J.; Timmel, C.; Hilger, D.; Jung, H., *Appl. Magn. Reson.* **2006**, *30*, 473–498.

(16) Abdullin, D.; Brehm, P.; Fleck, N.; Spicher, S.; Grimme, S.; Schiemann, O., *Chem. Eur. J.* **2019**, *25*, 14388–14398.

(17) https://github.com/dinarabdullin/SnrCalculator

(18) Pracht, P.; Bohle, F.; Grimme, S., *Phys. Chem. Chem. Phys.* **2020**, *22*, 7169–7192.

(19) Spicher, S.; Grimme, S., *Angew. Chem. Int. Ed.* **2020**, *59*, 15665–15673.

(20) Brandenburg, J. G.; Bannwarth, C.; Hansen, A.; Grimme, S., *J. Chem. Phys.* **2018**, *148*, 64104.

(21) Perdew, J. P.; Ernzerhof, M.; Burke, K., *J. Chem. Phys.* **1996**, *105*, 9982–9985.

(22) Schäfer, A.; Huber, C.; Ahlrichs, R., *J. Chem. Phys.* **1994**, *100*, 5829–5835.

(23) Caldeweyher, E.; Ehlert, S.; Hansen, A.; Neugebauer, H.; Spicher, S.; Bannwarth, C.; Grimme, S., *J. Chem. Phys.* 2019, *150*, 154122.
(24) Klamt, A., *J. Phys. Chem.* 1995, *99*, 2224–2235.
(25) Klamt, A.; Jonas, V.; Bürger, T.; Lohrenz, J. C. W., *J. Phys. Chem. A* 1998, *102*, 5074–5085.
(26) Eckert, F.; Klamt, A., *AIChE J.* 2002, *48*, 369–385.
(27) Bannwarth, C.; Ehlert, S.; Grimme, S., *J. Chem. Theory Comput.* 2019, *15*, 1652–1671.
(28) Grimme, S., *Chem. - A Eur. J.* 2012, *18*, 9955–9964.
(29) Furche, F.; Ahlrichs, R.; Hättig, C.; Klopper, W.; Sierka, M.; Weigend, F., *Wiley Interdiscip. Rev. Comput. Mol. Sci.* 2014, *4*, 91–100.
(30) Grimme, S.; Bannwarth, C.; Shushkov, P., *J. Chem. Theory Comput.* 2017, *13*, 1989–2009.
(31) Eichkorn, K.; Treutler, O.; Öhm, H.; Häser, M.; Ahlrichs, R., *Chem. Phys. Lett.* 1995, *240*, 283–290.
(32) Weigend, F., *Phys. Chem. Chem. Phys.* 2006, *8*, 1057–1065.

[P7]: C–C Cross-Coupling Reactions of Trityl Radicals: Spin Density Delocalization, Exchange Coupling, and a Spin Label

Reproduced with permission from

Nico Fleck, Tobias Hett, Jonas Brode, Andreas Meyer, Sabine Richert, Olav Schiemann*, *J. Org. Chem.* **2019**, *84*, 3293-3303.
DOI: https://doi.org/10.1021/acs.joc.8b03229

* Corresponding author.

Contributions

- Performing and analysing the DQC experiment.
- Analysis of the MD simulation.
- Analysis of *cw* EPR spectra.
- Writing of the manuscript in parts.

JOC The Journal of Organic Chemistry
Cite This: J. Org. Chem. 2019, 84, 3293−3303
Article
pubs.acs.org/joc

C−C Cross-Coupling Reactions of Trityl Radicals: Spin Density Delocalization, Exchange Coupling, and a Spin Label

Nico Fleck,[†] Tobias Hett,[†] Jonas Brode,[†] Andreas Meyer,[†,§] Sabine Richert,[‡] and Olav Schiemann*[,†]

[†]Institute of Physical and Theoretical Chemistry, Rheinische Friedrich-Wilhelms-University Bonn, Wegelerstr. 12, 53115 Bonn, Germany

[‡]Institute of Physical Chemistry, University of Freiburg, Albertstraße 21, 79104 Freiburg, Germany

Supporting Information

ABSTRACT: Organic radicals are usually highly reactive and short-lived species. In contrast, tetrathiatriarylmethyl radicals, the so-called trityl- or TAM-radicals, are stable and do survive over longer times even under in-cell conditions. In addition, they show strong EPR signals, have long phase memory times at room temperature, and are reporters on local oxygen and proton concentrations. These properties facilitated their use for magnetic resonance imaging, dynamic nuclear polarization, and spin-labeling EPR under in-cell conditions. Thus, synthetic approaches are required for functionalization of TAM radicals tailored to the desired application. However, most TAM derivatives reported in the literature are based on esterification of the Finland trityl, which is prone to hydrolysis. Here, we report on an approach in which TAM is site-selective iodinated and subsequently C−C cross-coupled to various building blocks in a modular approach. This yields conjugated trityl compounds such as a trityl attached to a porphyrin, an alkinyl functionalized trityl radical, and a strongly exchange-coupled trityl biradical. This synthesis approach thus has implications not only for magnetic resonance spectroscopy but also for the design of molecular magnets or quantum computing devices.

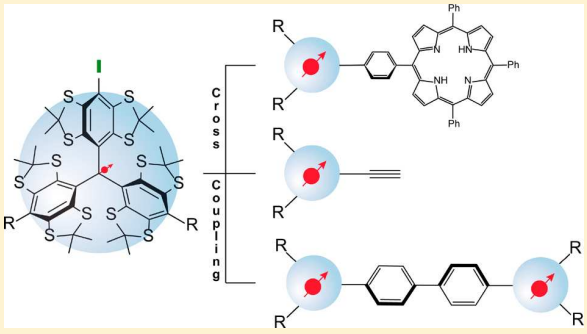

INTRODUCTION

Commonly, organic radicals are associated with low stability and short lifetimes as they are highly reactive open-shell species. Even though this accounts for the majority of organic radicals, this paradigm was disproved by Gomberg already in 1900 by the discovery of the triphenylmethyl radical.[1] Nowadays, numerous stable organic radicals such as carbon-centered phenalenyls[2] and triarylmethyls (trityls)[3,4] as well as nitrogen-centered ones like verdazyls[5,6] or nitroxides[7] are well-known. Techniques like magnetic resonance imaging (MRI),[8−10] dynamic nuclear polarization (DNP),[11,12] and spin labeling electron paramagnetic resonance (EPR) spectroscopy[13−15] have been established as powerful tools in the life sciences, which all depend on the availability of such persistent radicals. Even though nitroxides have been the reliable flagship radicals for these techniques for decades,[16] trityl radicals have emerged as promising alternatives[17] for the following reasons: (1) Trityl radicals derived from the Finland trityl **1**• (Figure 1)[18] are considerably more persistent than the Gomberg radical.[19] For example, trityl derivatives such as the commercially available Oxo63[20] are used to map local oxygen distributions in vivo with MRI.[21] (2) Using trityl radicals, large enhancement factors were achieved in DNP,[22,23] including dissolution DNP experiments.[24] (3) The long lifetime of trityl radicals under *in-cell* conditions,[25] the long phase memory time T_m,[26] and the narrow EPR line width[27] make them promising

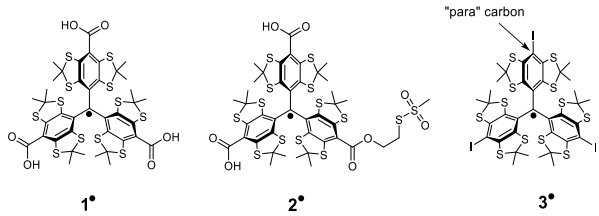

Figure 1. Structure of the Finland trityl radical **1**•, a spin label **2**• derived from it, and the iodinated trityl radical **3**•.

candidates for single-frequency EPR distance measurements[28−30] within cells[25] and at ambient temperature.[31] In particular, the two latter advantages are important for structural biology studies because they enable measurements under truly biological conditions. Compared to nitroxides, trityl radicals can be more or less stable, depending on the type of nitroxide and trityl and the solution conditions used.[32−34] The larger size of the trityl labels as compared to nitroxides and the wider spin density distribution do not impose a broader distance distribution,[29,30] nor do trityl labels per se induce observable structural changes, probably because the

Received: December 20, 2018
Published: February 28, 2019

DOI: 10.1021/acs.joc.8b03229
J. Org. Chem. 2019, 84, 3293−3303

labels have been attached to the biomolecular surface so far.[25,31]

Despite these applications, the reproducible and efficient synthesis of trityl radicals remains challenging, as recent reports show.[35] In addition, the functionalization strategies for trityl radicals are limited. They do involve the nucleophilic quenching of the tritylium cation with various C-, P-, and N-nucleophiles, leading to a monofunctionalization at the para position marked in Figure 1.[36,37] Also, thiol-substituents have been attached to the para positions, and their S_N2 reactivity has been used in the synthesis of, for example, dendrimeric oxygen probes.[38] However, the majority of functionalizations are based on the esterification of **1**$^{\bullet}$, leading to molecules such as **2**$^{\bullet}$.[25] Accordingly, the functionalization is predominantly carried out by reaction with an alcohol or amine carrying further desired functional groups.[39−42] Because the resulting ester linkages are rather nonrigid and can be hydrolyzed under harsh labeling conditions,[43] it is desirable to develop new functionalization strategies for trityl spin labels. Furthermore, the properties of trityl groups make them also interesting candidates for magnetic or electronic materials and quantum computing.[44] Also for these fields, new synthesis approaches are needed that increase the chemical stability and geometric rigidity of the linker groups as well as the electronic conjugation between the spin centers.

In the present work, the site-selective iodine functionalization of trityl radicals in the para position is reported. This iodine derivative **3**$^{\bullet}$ (Figure 1) is then used in C−C cross-coupling reactions of the Suzuki−Miyaura and Sonogashira−Hagihara type. To emphasize the broad scope of this method, we demonstrate the synthesis and characterization of four model compounds with properties that make them interesting for spin labeling, for quantum computing, and as molecular magnets.

RESULTS AND DISCUSSION

Synthesis. *Iodination.* In order to enable the application of C−C cross-coupling strategies, the idea was to derivatize trityl radicals with halogen atoms in the para positions, preferably with iodine, because of its high reactivity in this type of reactions. Instead of the target compound **3**$^{\bullet}$, one could also envision to prepare, for example,the boronic acid derivative; however, **3**$^{\bullet}$ enables a broader scope of different C−C coupling schemes. The synthesis (Scheme 1) of **3**$^{\bullet}$ starts from the

Scheme 1. Synthesis of the Iodine Functionalized Trityl 3$^{\bullet}$[a]

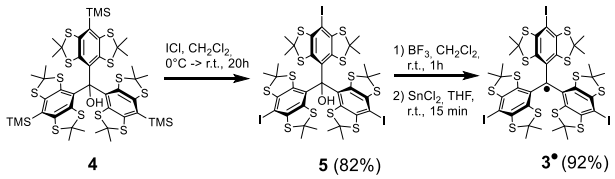

4 **5** (82%) **3**$^{\bullet}$ (92%)

[a]Yields are given in parentheses.

closed-shell trityl alcohol **4**, which was prepared according to the literature.[25,45] The iodine substituent was then introduced by an *ipso*-iododesilylation with iodine monochloride obtaining trityl alcohol **5** as a gray-greenish powder in a yield of 82% on a 5 g scale. The conversion of alcohol **5** into radical **3**$^{\bullet}$ was achieved by abstraction of the central OH-group with BF_3 and reduction of the resulting tritylium cation with $SnCl_2$. The target molecule **3**$^{\bullet}$ is obtained as a deep green powder in a yield of 92% on a 500 mg scale. Proceeding via the silyl-derivative **4** was required as direct approaches for iodination of the unsubstituted trityl alcohol failed.

In the successful reaction sequence depicted in Scheme 1, the radical was generated in the last step of the synthesis, which is more convenient, because it enables NMR monitoring until the last step. Crystallization attempts of the trityl radical derivatives were not successful. However, single crystals of alcohol **5** suitable for X-ray diffraction were obtained by slow evaporation of a diethyl ether solution. The obtained crystal structure (Figure S1, CCDC 1867300) is very similar to the structure of its unsubstituted precursor[46] with respect to the geometric arrangement of the aryl planes showing the typical propeller shaped conformation with dihedral angles of ±68.9°, ±74.4°, and ±81.9° between them. Thus, the molecule is not C_3-symmetric in the solid state. However, this distortion averages out in solution on the NMR time scale, so that the NMR spectra show a C_3-symmetric spectrum (see Figures S48 and S49). Because of the helical structure of the trityl alcohol, the methyl groups become diastereotopic, resulting in four resonances each in the ^{1}H and ^{13}C NMR. The C_{ar}−I bond length of 2.086 Å compares well to typical literature values.[47] Moreover, the structure features a moderate hydrogen bond of the OH-hydrogen to a thioacetal sulfur with a length of d(H···A) = 2.343(5) Å. Although halogen bonding has been studied[48] for tris(4-iodophenyl)methanol,[49] no evidence for this was observed in the crystal structure of **5**, presumably for steric reasons.

C−C Cross-Coupling. The iodine substitution at the aryl ring enables C−C cross-coupling via reactions of the Sonogashira−Hagihara and the Suzuki−Miyaura type, which were both examined on the closed-shell alcohol **5** and the radical compound **3**$^{\bullet}$. Both coupling reactions have a wide scope and do not require the use of organometallic reagents as, for example, for *Negishi* or *Kumada* coupling reactions. This was important, because the reaction of **3**$^{\bullet}$ with, for example, *n*-BuLi led to unselective alkyl-coupling.[50]

Suzuki−Miyaura Coupling. In an exemplary reaction, trityl radical **3**$^{\bullet}$ was reacted with 6 equiv of *p*-tolylboronic acid (Scheme 2), smoothly forming the coupling product **6**$^{\bullet}$ with a

Scheme 2. Suzuki−Miyaura Coupling Reaction with Trityl 3$^{\bullet}$[a]

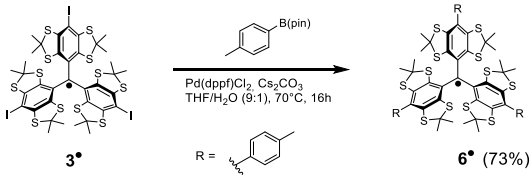

3$^{\bullet}$ **6**$^{\bullet}$ (73%)

[a]Yields are given in parentheses.

yield of 73%. However, it would be useful to be able to perform the C−C cross-coupling reaction in such a way that either only one or two aryl groups are attached in the first step, leaving either two or one iodine positions for further functionalizations. This is for example important for designing trityl spin labels with only one biocompatible group. However, performing the Suzuki coupling in a statistical way using only two equivalents of *p*-tolylboronic acid led to a product mixture, which could not be separated by chromatography. Instead, the

DOI: 10.1021/acs.joc.8b03229
J. Org. Chem. 2019, 84, 3293−3303

statistical coupling of 3• with two equivalents of the more polar 4-methoxycarbonylphenylboronic acid pinacol ester (Scheme 3) enabled the separation of the coupling products by column

Scheme 3. Statistical Suzuki–Miyaura Reaction of 3• and 6[a]

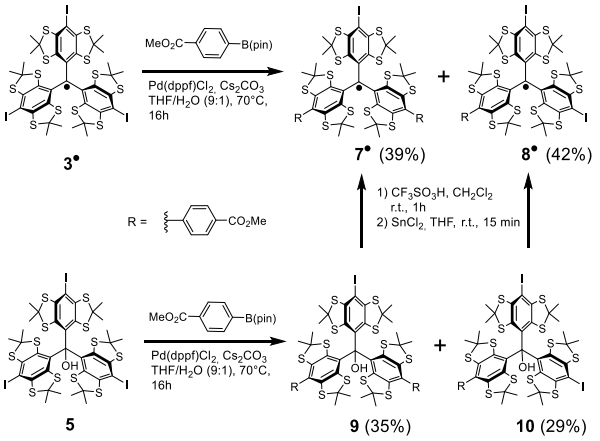

[a]Yields are given in parentheses.

chromatography on silica, providing the mono- and bis-coupled products 7• and 8• in yields of 39% and 42%, respectively.

The analogous reaction with the closed shell trityl alcohol **5** led to coupling products **9** and **10** with yields of 35% and 29%. Protonation of these with CF_3SO_3H in dichloromethane and subsequent reduction with $SnCl_2$ provided 7• and 8• in yields of 86% and 88%, respectively. The use of a Brønsted acid instead of BF_3 was indicated in order to prevent side reactions from the methyl esters.

In both ways, the (mono)functionalization of trityl radicals is feasible in a rather modular approach through subsequent coupling reactions. Regarding the reaction conditions, the solvent mixture THF/H_2O provided sufficient solubility of the trityl species. With respect to the type of catalyst, $Pd(dppf)Cl_2$ proved to be superior over $Pd(OAc)_2/P(t\text{-}Bu)_3$ (only partial coupling products for 6•; see the Supporting Information, p S17) or $Pd(Ph_3P)_2Cl_2$ (no reaction for 6•). Cesium carbonate is well-soluble in organic solvents and therefore the base of choice for Suzuki coupling reactions.[51]

Conjugated Porphyrin-Trityl Model Compound. Having achieved the monofunctionalization, the aim was to attach further groups via C–C cross-coupling that enable different applications. In this line, compounds 12• and 13• are model compounds for the study of exchange-mediated spin polarization transfer from the excited porphyrin to the trityl, which holds promise for applications in the field of molecular spintronics.[52,53] The slow spin relaxation of the trityl might be particularly suitable for the storage of spin information. In addition, the order (low to high field) of absorptive (*a*) and emissive (*e*) transitions in the triplet state EPR spectrum of the porphyrin is reversed in 12• (*eeeaaa*) compared to the otherwise identical compound 13• (*aaaeee*).[54,55] The influence of this initial triplet state spin polarization pattern on spin-information transfer can thus be explored.[56]

Compounds 12• and 13• were synthesized according to Scheme 4 by using 7• as the trityl building block and coupling this via a Suzuki–Miyaura reaction with porphyrin borolan **11**.[57] After purification by column-chromatography, pure 12•

Scheme 4. Synthesis of 12• and 13•[a]

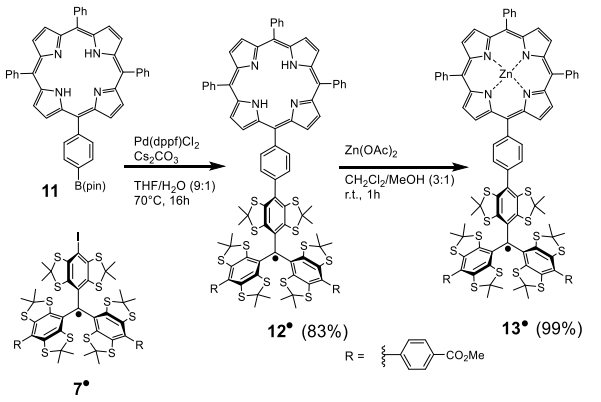

[a]Yields in parentheses.

was obtained in a yield of 83% as a brown-purple solid. In the following step, a zinc(II) ion was incorporated into the porphyrin, yielding 13• quantitatively as a dark reddish solid.

Conjugated Trityl Biradical. Earlier attempts to synthesize trityl containing biradicals led to only very weakly exchange-coupled compounds,[42,58] which may be due to the use of π-conjugation breaking groups for linking the trityls to the molecular bridges. In contrast, the C–C cross-coupling approach presented here enables the connection via conjugated groups. Compound 15•• seemed to be a suitable test system because it enables a direct comparison with related nitroxide[59] and trityl[58] systems.

A Suzuki–Miyaura coupling of trityl alcohol **9** with 4,4′-bis(4,4,5,5-tetramethyl-1,3,2-dioxaborolan-2-yl)biphenyl (Scheme 5) gave **14** in a yield of 48%. The following

Scheme 5. Synthesis of Biradical 15••[a]

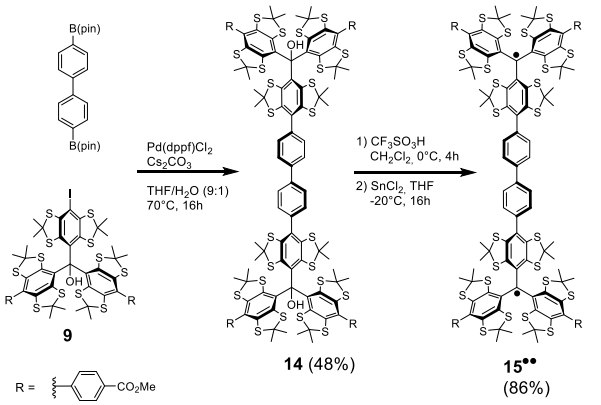

[a]Yields are given in parentheses.

conversion to biradical 15•• was carried out by treatment with CF_3SO_3H and reduction of the resulting cation with $SnCl_2$ in a yield of 86%. It was also possible to obtain 15•• by a Suzuki–Miyaura coupling of 7• with 4,4′-bis(4,4,5,5-tetramethyl-1,3,2-dioxaborolan-2-yl)-biphenyl. However, during column chromatography, 15•• was oxidized to the corresponding trityl alcohols and sulfoxides, presumably because of exposure to air (see the Supporting Information, p S18).

Such an increased sensitivity of exchange-coupled trityl biradicals toward oxygen during chromatography was also

DOI: 10.1021/acs.joc.8b03229
J. Org. Chem. 2019, 84, 3293–3303

reported by Jassoy et al.[58] Therefore, the coupling and column chromatography steps were carried out at the alcohol stage. Earlier reports aiming at building conjugated systems with perchlorinated trityl radicals (PTM-radicals) used Horner–Wadsworth–Emmons reactions,[60,61] which are less versatile then the Suzuki–Miyaura reaction employed here.

Sonogashira–Hagihara Coupling. Ethynyl-substituted stable radicals can be used for spin labeling via *click reaction* with unnatural amino acids containing azides.[62] The Sonogashira–Hagihara coupling reaction is a versatile tool for introducing such terminal alkynes. Current approaches to synthesize ethynyl-substituted trityl radicals use the esterification of **1**$^{\bullet}$[25] with propargyl alcohols. However, as ester groups are rather nonrigid and prone to hydrolysis, it is desired to attach an ethynyl group directly to the para-position of a trityl radical. As an example of such a building block, a Sonogashira–Hagihara coupling of **7**$^{\bullet}$ was performed with triisopropylsilyl acetylene in CH_2Cl_2/Et_3N catalyzed by $Pd(Ph_3P)_2Cl_2$ (Scheme 6). The

Scheme 6. Synthesis of 17$^{\bullet}$[a]

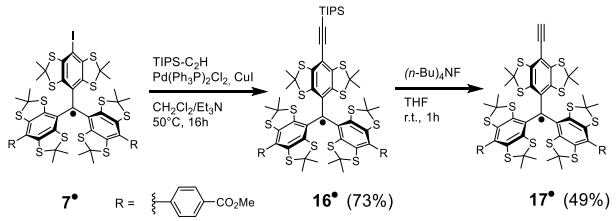

[a]Yields are given in parentheses.

corresponding coupling product **16**$^{\bullet}$ was isolated with a yield of 73%. After removal of the TIPS-protection group with nBu$_4$NF, the ethynyl-trityl radical **17**$^{\bullet}$ was obtained with a yield of 49%. Using less bulky acetylene building blocks such as trimethylsilyl acetylene or 2-methyl-3-butyn-2-ol and common solvents such as THF led to unwanted side reactions. It is presumed that a competitive carbothiolation[63] by insertion of the alkyne into a C–S bond of the cyclic thioacetals takes place. A detailed survey with discussion and additional experimental data is enclosed in the Supporting Information on pages S20–S41. For PTM-radicals, Sonogashira–Hagihara coupling was demonstrated very recently, where obviously no side reactions as in the present case occurred.[64] However, it was shown that spin labels based on PTM-radicals are reduced under in-cell conditions.[65]

Magnetic Resonance Spectroscopy. All paramagnetic compounds in this study were characterized by continuous wave (cw) X-band EPR. They all show an EPR spectrum characteristic for trityl radicals (see the Supporting Information, pp S11–S15). Figure 2a shows the room-temperature spectrum of **7**$^{\bullet}$ as an example and Figure 2b that of **17**$^{\bullet}$, in which an additional $A_{iso}(^1H)$ hyperfine-coupling constant of 3.7 MHz from the ethynylic hydrogen atom could be resolved. The ^{13}C-hyperfine interactions observed are all similar to the values determined for **1**$^{\bullet}$ and its derivates[66] and are reported in Table S2 together with the g-values and line widths. In general, the line widths of the trityl radicals presented here are slightly larger than the corresponding values reported for **1**$^{\bullet}$.[66] This is attributed to unresolved hydrogen hyperfine interactions from the aryl substituents and/or the quadrupole moment of iodine. The latter is supported by the line width of **16**$^{\bullet}$ being significantly smaller than that of its precursor **7**$^{\bullet}$. Additionally,

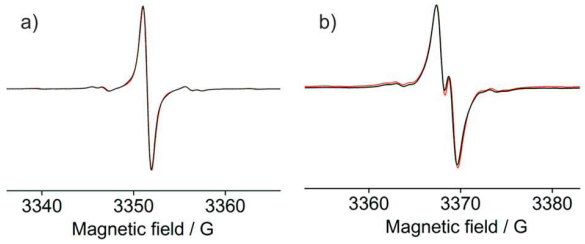

Figure 2. Continuous wave X-band EPR spectra (T = 298 K, c = 50 μM in toluene) of (a) **6**$^{\bullet}$ and (b) **17**$^{\bullet}$. The experimental spectrum is plotted as black solid lines, and the simulation is overlaid as a red lines.

the g_{iso}-value of trityl increases linearly with the number of iodine substituents in the para positions from 2.0032 (**7**$^{\bullet}$ no iodine atom) to 2.0051 (**3**$^{\bullet}$ three iodine atoms), as shown in Figure 3. This is related to spin–orbit coupling, the magnitude

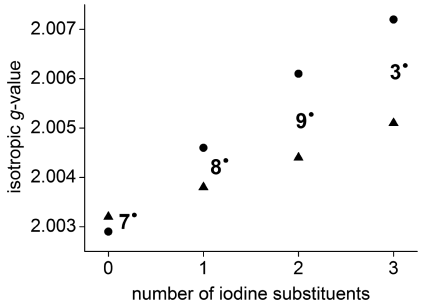

Figure 3. Experimental (▲) g_{iso}-values of iodine containing trityl radicals compared to the calculated values from DFT (●).

of which increases with the atomic number of the involved elements.[67] In the case of aromatic compounds, the shift in g_{iso} (Δg) upon replacing n equivalent hydrogen atoms by n heavy atoms (e.g., iodine) can be approximated by[68] $\Delta g \approx \Sigma_i \lambda_i \rho_i$ (i = 1 to n). Here, λ_i is the spin–orbit coupling constant and ρ_i is the Hückel spin density on the heavy atom. The same trend was observed for the g-values calculated by DFT (PBE, def2-SVP), but the spin density on the iodine substituents seems to be slightly overestimated (Figure 3).

The hyperfine interactions with hydrogen atoms of the porphyrin ring in **12**$^{\bullet}$ and **13**$^{\bullet}$ are not resolved in the cw X-band EPR spectra but can be inferred from ^{1}H NMR spectra. The ^{1}H NMR spectra of **12**$^{\bullet}$ and its diamagnetic analogous trityl alcohol **12-OH** are shown in Figure 4. Both the signals of the bridging phenyl ring (signal 2, Figure 4) and the signals of the aryl groups of the trityl core (signal 3, Figure 4) are broadened beyond visibility in the spectrum of **12**$^{\bullet}$ because of paramagnetic broadening. In contrast, the signals from the pyrrol hydrogen atoms (signal 4, Figure 4) are still present, but they are shifted. The signal marked with an asterisk in Figure 4 exhibits the strongest paramagnetic shift (δ_{para}) and is attributed to the two pyrrol hydrogen atoms in closest proximity to the bridging phenyl ring as they feature the largest spin density according to DFT calculations (Figure S3). Using eq 1, an $A(^1H)$ hyperfine coupling constant of 4 mG can be estimated for these atoms:[69]

$$A(^1\mathrm{H}) = \frac{(\delta - \delta_{dia})\cdot T}{1.16 \times 10^2 \cdot g_{iso}} = 4\ \mathrm{mG} = 11.2\ \mathrm{kHz} \quad (1)$$

DOI: 10.1021/acs.joc.8b03229
J. Org. Chem. 2019, 84, 3293–3303

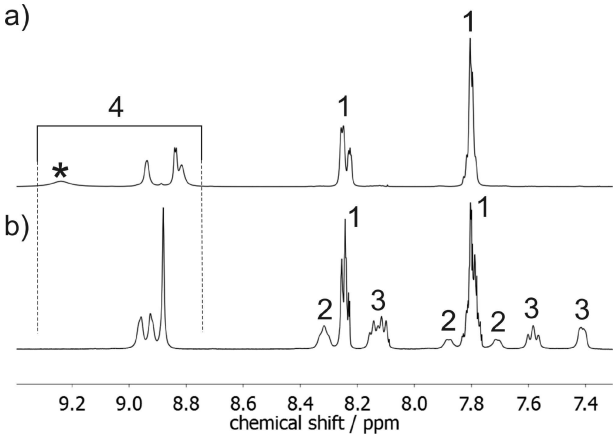

Figure 4. ^{1}H NMR spectra of (a) **12**$^{\bullet}$ and (b) **12-OH** at 298 K in CD_2Cl_2. Signal 1, H_{Ph} (porphyrin); signal 2, H_{Ph} (bridge); signal 3, H_{Ph} (trityl); signal 4, H_{pyrrol} (porphyrin).

Here, δ = 9.28 ppm was extracted from the spectrum of **13**$^{\bullet}$ (Figure 4a), δ_{dia} = 8.96 ppm was taken from the spectrum of **12-OH** (Figure 4b), and g_{iso} was determined to be 2.0032 from the cw X-band EPR spectrum at T = 298 K.

The coupling constant of 4 mG indicates that spin density is distributed into the porphyrin core, which is a key condition to study the interaction of a photoexcited porphyrin spin triplet with the trityl spin doublet. The three terminal phenyl groups of the tetraphenylporphyrin (signal 1, Figure 4) are not affected.

Exchange Coupling in **15**$^{\bullet\bullet}$. Figure 5 shows the room-temperature liquid state cw X-band EPR spectrum of **15**$^{\bullet\bullet}$. The

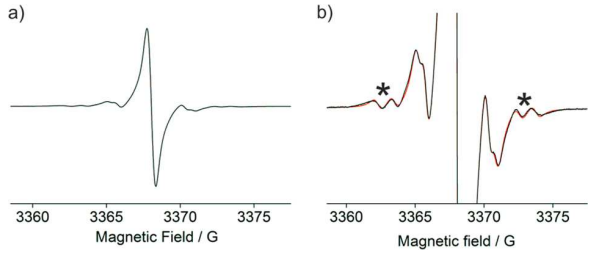

Figure 5. Experimental (black) and simulated (red) cw X-band EPR spectrum of **16**$^{\bullet\bullet}$ at 298 K: (a) full signal range and (b) focused on the ^{13}C-satellites.

intense central line is due to trityl centers carrying no ^{13}C atom. The much less intense lines at lower and higher field of the central line are due to molecules carrying one ^{13}C atom in the *ipso* (A_{iso} = 32 MHz) or *ortho* (A_{iso} = 25 MHz) positions. The corresponding ^{13}C hyperfine splitting is halved as compared to the monotrityl radical because of strong exchange coupling.[70] The four lines of even weaker intensity and marked by asterisks belong to the *ipso* or *ortho* ^{13}C coupling in monotrityl impurities (7%) serving here as an internal standard and highlighting that this coupling is indeed halved in **15**$^{\bullet\bullet}$.

Taking J-coupling into account, the shift of the ^{13}C-hyperfine satellites was simulated using a home-written *EasySpin*[71] script. This yielded a lower limit of 550 MHz for J (Figures 5b and S6). To further investigate the magnetic exchange coupling, measurements in frozen solution were conducted (Figure 6). At cryogenic temperatures between 3.8

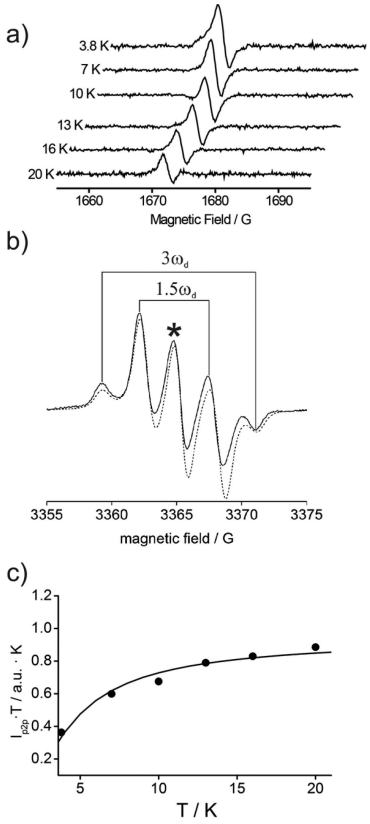

Figure 6. (a) Stacked plot of the half-field spectra of **15**$^{\bullet\bullet}$. (b) cw X-band EPR spectrum of **15**$^{\bullet\bullet}$ at 100 K in CH_2Cl_2/MeOH (2:1). The Pake pattern is indicated by $1.5\omega_d$ and $3\omega_d$. The asterisk indicates the double quantum transition, and the fit is overlaid as a dashed line. (c) Plot of the intensity of the half-field signal I_{p2p} times T versus T (●, experimental data; solid line is the best fit with J = −2.8 cm^{-1}).

and 20 K, the $\Delta m_S = \pm 2$ transition within the triplet state of **15**$^{\bullet\bullet}$ could be observed (Figure 6a). As can be seen from the stack-plot, the peak-to-peak intensity of the half-field signal drops with increasing temperature. Plotting the peak-to-peak intensity I_{p2p} multiplied by the temperature T against T and using the Bleaney−Bowers type equation given in eq 2[72] permit extracting the value of the exchange coupling constant J via least-squares fitting (Figure 6c).

$$I_{p2p}T = C\left(\frac{1}{3 + \exp(-2J/k_BT)}\right) \quad (2)$$

Here, C = 3.8 ± 0.1 K is a spectrometer constant and k_B refers to the Boltzmann constant. The best fit to the experimental data revealed an antiferromagnetic coupling within **15**$^{\bullet\bullet}$ of J = −2.8 ± 0.2 cm^{-1} (see Figure S7) according to the convention of $H_{ex} = -2JS_AS_B$. This value corresponds well to the result of J = −4.4 cm^{-1} obtained from a broken-symmetry DFT (PBE, def2-SVP) calculation. The cw X-band EPR spectrum of **15**$^{\bullet\bullet}$ in the main-field region at 100 K is provided in Figure 6b. This spectrum is a superposition of a dipolar Pake pattern and a double quantum transition,[73] where both show a markedly different saturation behavior (see Figure S8). From the Pake pattern a dipolar coupling constant D of 11 MHz can be read off. Using eq 3 for the strong coupling regime, a distance r of 16.7 Å between both spins can be calculated:[74,75]

DOI: 10.1021/acs.joc.8b03229
J. Org. Chem. 2019, 84, 3293−3303

$$D_{strong} = 1.5 \cdot 52.01\ \text{MHz} \frac{\text{Nm}^3}{r^3} \quad (3)$$

The spectrum was simulated with *EasySpin* by adding a second signal accounting for the 2-photon-transition to the Pake pattern.

This spin−spin distance could be confirmed nicely via a pulsed EPR experiment called Double Quantum Coherence (DQC) experiment[76] (Figure 7), yielding a distance

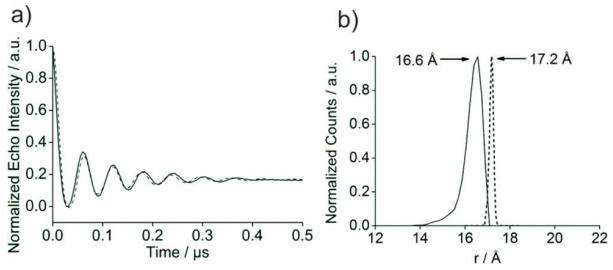

Figure 7. DQC data of **15••**. (a) The background-corrected DQC time trace and (b) the corresponding distance distribution. The experimental distance distribution was corrected by a factor of $\sqrt[3]{1.5}$ in order to account for the strong coupling regime. The distribution expected from MD is overlaid as a dashed line.

distribution peaking at 16.6 Å. From the DFT-derived structure of **15••**, a distance of 18.7 Å between the central carbons can be estimated, which leads to a distance difference between experiment and theory that is on the far side of the error. However, taking spin density delocalization into account[77] (see the Supporting Information, pages S5 and S6) reduces the theoretical spin−spin distance to 17.2 Å, well within the error of the experiment and theory. Because of the large size of *J*, a disentangelment of a distribution in *J* (ΔJ) from the distribution in *r* (Δr) was not attempted.

Comparison. Figure 8 shows four different types of biradicals with comparable interspin distances or radical

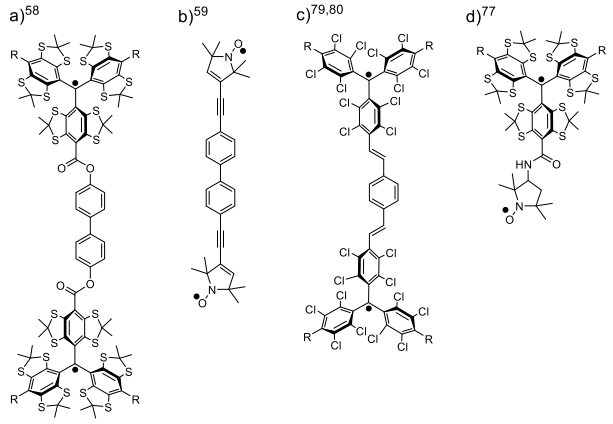

Figure 8. Literature-known biradicals for comparison.

centers as in **15••**. Compared to **15••**, the esterified trityl biradical[58] (Figure 8a) and the conjugated bis-nitroxide[59] (Figure 8b) show a roughly 3 orders of magnitude smaller exchange coupling. Also mixed trityl-nitroxide biradicals display much smaller *J*-values: for the example here, only 0.112 cm^{-1} at a much shorter interspin distance of 10.6 Å (Figure 8d).[78] Perchlorinated trityl radicals (PTM-radicals)[79,80] do show exchange coupling in the same order of magnitude, with the one in Figure 8c exhibiting a *J* of 15 cm^{-1}. Thus, the example of **15••** shows that conjugated trityl radicals of the thioaryl-type can feature strong *J*-coupling in the same order of magnitude as the PTM radicals.

CONCLUSION

In this study, the synthesis of an iodine-substituted trityl radical was shown and its reactivity in Pd-catalyzed C−C cross-coupling reactions was examined. Whereas Suzuki−Miyaura type reactions perform well, an unexpected side reaction was encountered for Sonogashira−Hagihara type reactions. However, both coupling reactions provide an efficient tool to chemists aiming at building novel structures with trityl radicals. Exemplarily, we attached an ethynyl function directly to a trityl radical enabling click-chemistry for, for example, spin labeling of biomolecules. Second, a conjugated trityl biradical with a strong antiferromagnetic exchange coupling of $J = -2.8$ cm^{-1} is described. Exploiting the ease of the coupling reactions further, two trityl-porphyrin conjugates are presented. These enable the study of exchange-mediated spin-polarization transfer between photoexcited chromophore triplet states and trityl radicals. All these examples show that a large diversity of structures involving conjugated trityl radical centers becomes accessible through the presented C−C coupling reactions.

EXPERIMENTAL SECTION

General Procedures. Where indicated, solvents were degassed by applying three freeze−pump−thaw cycles. Thin-layer chromatography was conducted using 250 μm F_{254} silica plates provided by Merck, and spots were visualized with UV light at 254 nm. For column chromatography, silica gel (60 Å pore size, 40−63 μm particle size) purchased from Merck was used. Medium pressure liquid chromatography (MPLC) was performed with a Sepacore X10 system by Büchi (Essen, Germany) using Büchi FlashPure cartrigdes. Solvents were generally removed under reduced pressure by a rotary evaporator, and products were further dried in an oil-pump vacuum at 10^{-3} mbar.

Nuclear Magnetic Resonance Spectroscopy. NMR spectra were recorded on Avance I 300, Avance I 400, Avance III HD 500, or Avance III HD 700 spectrometers from Bruker BioSpin, Rheinstetten, Germany. Chemical shifts are reported referenced to hydrogen residual peaks of the NMR solvent.[81]

Because of the helical chirality of trityl alcohols, a nonsymmetric C_1-structure is expected for **7•**, **8•**, **9**, and **10**. Accordingly, the NMR spectra of **9** and **10** exhibit a distinct resonance for each methyl group at the thioacetals. As the phenyl rings are twisted against each other, their aromatic protons become diastereotopic, leading to four resonances for **9** resolved at 700 MHz and eight resonances for **10**, which however coincide into multipletts even at 700 MHz.

Mass Spectrometry. ESI(+) and APCI-spectra were measured using an OrbitrapXL instrument from Thermo Fisher Scientific, Berlin, Germany. MALDI(+)-spectra were recorded in a Bruker Daltonics autoflex TOF/TOF time-of-flight spectrometer (Bruker, Rheinstetten, Germany) using DCTB as matrix.

EPR Spectroscopy. X-Band cw-EPR spectra were recorded on a Bruker EMX Micro cw X-Band EPR spectrometer (Bruker BioSpin GmbH, Rheinstetten, Germany) using a standard 4119HS resonator. The external magnetic field was modulated with a frequency of 100 kHz and an amplitude of 0.1 G. The microwave power was adjusted to 0.6054 mW, and all measurements were conducted with a time constant of 10.24 ms. The half-field signal for the trityl biradical was measured using a ER4122SHQE resonator with a modulation amplitude of 2.0 G and a microwave power of 54.45 mW. A detailed description of the instrumentation and proceeding for the DQC

DOI: 10.1021/acs.joc.8b03229
J. Org. Chem. 2019, 84, 3293−3303

experiment can be found on in the Supporting Information, pages S7 and S8.

Elemental Analysis. Elemental analysis was conducted on a VarioEL analyzer (Elementar Analysensysteme, Langenselbold, Germany). Elemental analysis of trityl compounds suffers from inaccuracy because of their high sulfur content, which effects the calibration of the instrument.

Computational Methods. For the calculation of *g*-values and spin densities, the structures were preoptimized with GFN-xTB[82] and further refined with DFT using the PBE functional and a def2-SVP basis set with D3BJ dispersion correction as implemented in *ORCA*.[83,84] Both spin densities and *g*-values were obtained from the *ORCA* output files. MD simulations for 298.15 K were carried out using GFN-xTB with a time step of 4 fs.

Syntheses. Tris(8-iodo-2,2,6,6-tetramethylbenzo-[1,2-d;4,5-d′]-bis-[1,3]dithiol-4-yl)-methanol, Trityl Alcohol ***5****.* Tris(8-(trimethylsilyl)-2,2,6,6-tetramethylbenzo-[1,2-d;4,5-d′]-bis-[1,3]dithiol-4-yl)-methanol (5.00 g, 4.55 mmol) was dissolved in 350 mL of dry dichloromethane, and the solution was cooled to 0 °C. Then, iodine monochloride (3.30 g, 1.06 mL, 20.4 mmol, 4.50 equiv) was added to the reaction mixture via a syringe. Iodine monochloride has a mp of approximately 288 °C; therefore, it should be melted in a water bath prior to addition and transferred with a prewarmed syringe. After the mixture was stirred at room temperature overnight, the reaction was quenched by addition of 150 mL of 5% sodium thiosulfate solution and the phases were separated. The dark greenish organic phase was dried over magnesium sulfate, and the solvent was removed under reduced pressure yielding a dark green residue. The crude product was purified by washing with *N*,*N*-dimethylformamide followed by acetone. For that, the residue was suspended in dimethylformamide (35 mL) and sonicated for 10 min. Then, the mixture was centrifuged at 3200*g* (Eppendorf Centrifuge 5810 *R*) for 5 min, whereupon a greyish solid separated. The dark supernatant was discarded, and the procedure was repeated with the precipitated solid three times. Finally, the precipitant was washed with 30 mL of acetone following the procedure above obtaining a greyish/greenish solid with a yield of 4.73 g (3.74 mmol, 82%). Crystals suitable for X-ray diffraction were grown by slow evaporation of a solution of the title compound in Et_2O at 3 °C over 1 week. ^{1}H NMR (500 MHz, CD_2Cl_2, 298 K, δ): 6.20 (s, 1H), 1.85 (s, 9H), 1.82 (s, 9H), 1.77 (s, 9H), 1.68 (s, 9H). $^{13}C\{^1H\}$-NMR (126 MHz, CD_2Cl_2, 298 K, δ): 144.4, 143.7, 136.3, 135.0, 130.9, 85.0, 83.5, 61.4, 60.8, 35.2, 32.2, 29.0, 27.2. HRMS (ESI +) *m*/*z*: $[M]^+$ calcd for $C_{37}H_{37}I_3OS_{12}$, 1261.6621; found, 1261.6636. Elemental analysis [%]: Anal. Calcd for $C_{37}H_{37}I_3OS_{12}$: C, 35.18; H, 2.95; S, 30.46. Found: C, 35.33; H, 3.09; S, 29.42.

Tris(8-(4-methylphenyl)-2,2,6,6-tetramethylbenzo-[1,2-d;4,5-d′]-bis-[1,3]dithiol-4-yl)-methyl Radical, Trityl Radical ***6****•.* Trityl radical **3**• (135 mg, 108 μmol), 4-methylphenylboronic acid (89 mg, 651 μmol, 6.0 equiv), cesium carbonate (210 mg, 651 μmol, 6.0 equiv) and $Pd(dppf)Cl_2$ (5 mg, 5 mol %) were dissolved in a deoxygenated mixture of THF and water (10:1) under argon. The reaction mixture was heated to 70 °C for 16 h and allowed to cool to room temperature. Then, the solvents were removed under reduced pressure. The residue was extracted with dichloromethane, and the organic phase was washed with 0.1 M Na_2EDTA and dried over magnesium sulfate. After removal of the solvents under reduced pressure, the crude product was purified by column chromatography on silica eluting with cyclohexane/ethyl acetate 2:1. Yield: 91 mg (73%). HRMS (APCI) *m*/*z*: $[M]^+$ calcd for $C_{58}H_{57}S_{12}$, 1137.1103; found, 1137.1100.

Tris(8-(4-methylphenyl)-2,2,6,6-tetramethylbenzo-[1,2-d;4,5-d′]-bis-[1,3]dithiol-4-yl)-methanol; Trityl Alcohol ***6-OH****.* (150 mg, 0.119 mmol), *p*-methylphenylboronic acid (97 mg, 0.714 mmol, 6.0 equiv), cesium carbonate (230 mg, 0.714 mmol, 6.0 equiv), and $Pd(dppf)Cl_2$ were placed in a Schlenk flask under argon atmosphere. Then, 20 mL of degassed THF/H_2O (10:1, v/v) was added and the reaction mixture was stirred at 70 °C for 16 h. Afterward, 0.1 M Na_2EDTA solution was added (50 mL), and the aqueous phase was extracted three times with 30 mL of dichloromethane. The unified organic phases were dried over magnesium sulfate, and the solvents were removed under reduced pressure. The product was isolated as a gray/greenish solid after column chromatography on silica eluting with cyclohexane/ethyl acetate 2:1 (v/v). Yield: 104 mg (76%). ^{1}H NMR (500 MHz, CD_2Cl_2, 298 K, δ): 7.33 (d, 2H, $^3J_{H,H}$ = 8 Hz), 7.27 (d, 2H, $^3J_{H,H}$ = 8 Hz), 7.24 (d, 2H, $^3J_{H,H}$ = 7.4 Hz), 7.15 (d, 2H, $^3J_{H,H}$ = 7.4 Hz), 6.54 (s, 1H), 2.41 (s, 3H), 1.87 (s, 9H), 1.78 (s, 9H), 1.72 (s, 9H), 1.65 (s, 9H). $^{13}C\{^1H\}$-NMR (126 MHz, CD_2Cl_2, 298 K, δ): 140.1, 139.3, 139.1, 138.9, 138. 8, 138.6, 133.6, 131.4, 129.8, 129.6, 128.9, 63.3, 62. 7, 54.4, 54.2, 54.0, 53. 8, 53.6, 35.5, 32.7, 29.7, 27.8, 21.7. HRMS (APCI) *m*/*z*: $[M]^+$ calcd for $C_{58}H_{58}OS_{12}$, 1154.1133; found, 1154.1133.

{(8-(4-Carboxylphenyl)-2,2,6,6-tetramethylbenzo-[1,2-d;4,5-d′]-bis-[1,3]dithiol-4-yl)-bis(8-iodo-2,2,6,6-tetramethylbenzo-[1,2-d;4,5-d′]-bis-[1,3]dithiol-4-yl)}-methyl Radical Methyl Ester and {Bis(8-(4-carboxylphenyl)-2,2,6,6-tetramethylbenzo-[1,2-d;4,5-d′]-bis-[1,3]dithiol-4-yl)-(8-iodo-2,2,6,6-tetramethylbenzo-[1,2-d;4,5-d′]-bis-[1,3]dithiol-4-yl)}-methyl Radical Dimethyl Ester; Trityl Radicals ***7****• and* ***8****•.* Trityl radical **3**• (133 mg, 107 μmol), 4-methoxycarbonylphenylboronic acid pinacol ester (56 mg, 214 μmol, 2.0 equiv), cesium carbonate (69 mg, 214 μmol, 2.0 equiv), and $Pd(dppf)Cl_2$ (4 mg, 5.3 μmol, 5 mol %) were dissolved in a deoxygenated mixture of THF and water (20 mL, 10:1) under argon. The reaction mixture was heated to 70 °C for 16 h and allowed to cool to room temperature. Then, the solvents were removed under reduced pressure. The residue was extracted with dichloromethane, and the organic phase was washed with 0.1 M Na_2EDTA and dried over magnesium sulfate. After removal of the solvents under reduced pressure, the crude product was purified by column chromatography on silica eluting with a gradient of cyclohexane/ethyl acetate 9:1 to 2:1.

Trityl radical **8**• yield: 56 mg, 42%. HRMS (APCI) *m*/*z*: $[M]^+$ calcd for $C_{53}H_{50}IO_4S_{12}$, 1260.9397; found, 1260.9418. Trityl radical **9**• yield: 52 mg, 39%. HRMS (ESI+) *m*/*z*: $[M]^+$ calcd for $C_{45}H_{43}I_2O_2S_{12}$, 1252.7995; found, 1258.8099.

{(8-(4-Carboxylphenyl)-2,2,6,6-tetramethylbenzo-[1,2-d;4,5-d′]-bis-[1,3]dithiol-4-yl)-bis(8-iodo-2,2,6,6-tetramethylbenzo-[1,2-d;4,5-d′]-bis-[1,3]dithiol-4-yl)}-methanol Methyl Ester and {Bis(8-(4-carboxylphenyl)-2,2,6,6-tetramethylbenzo-[1,2-d;4,5-d′]-bis-[1,3]dithiol-4-yl)-(8-iodo-2,2,6,6-tetramethylbenzo-[1,2-d;4,5-d′]-bis-[1,3]dithiol-4-yl)}-methanol Dimethyl Ester; Trityl Alcohols ***9*** *and* ***10****.* Trityl alcohol **5** (840 mg, 665 μmol), 4-methoxycarbonylphenylboronic acid pinacol ester (327 mg, 1.33 mmol, 2.00 equiv), cesium carbonate (432 mg, 1.33 mmol, 2.00 equiv), and $Pd(dppf)Cl_2$ (24.3 mg, 33 μmol, 5 mol %) were dissolved in 80 mL of degassed THF/H_2O (9:1, v/v). The reaction mixture was refluxed for 16 h under argon; afterward, the solvents were removed under reduced pressure. The residue was taken up in 100 mL of dichloromethane and washed with water and brine. The organic phase was then dried over $MgSO_4$, and solvents were removed under reduced pressure yielding a greenish crude product. Trityl alcohols **9** and **10** were obtained from MPLC-purification (80 g of SiO_2, CH_2Cl_2/cyclohexane 7:3 (0 → 5 min), CH_2Cl_2/cyclohexane 9:1 (5 → 8 min), CH_2Cl_2/cyclohexane 1:0 (8 → 25 min).

Analytical data for **9**. ^{1}H NMR (700 MHz, CD_2Cl_2, 298 K,δ): 1.64 (s, 3H), 1.66 (s, 3H), 1.71 (s, 3H), 1.71 (s, 3H), 1.72 (s, 3H), 1.76 (s, 3H), 1.78 (s, 3H), 1.81 (s, 3H), 1.83 (s, 3H), 1.85 (s, 3H), 1.86 (s, 3H), 1.91 (s, 3H), 3.92 (s, 3H), 3.92 (s, 3H), 6.43 (s, 1H), 7.33−7.37 (m, 2H), 7.50−7.53 (m, 2H), 8.05−8.12 (m, 4H). ^{13}C-$\{^1H\}$NMR (176 MHz, CD_2Cl_2, 298 K, δ): 27.80, 27.81, 27.82, 29.3, 29.7, 29.8, 32.47, 32.48, 32.49, 33.3, 35.5, 35.6, 35.8, 52. 7, 61.1, 61.7, 63.2, 63.5, 63.86, 63.94, 84.4, 85.5, 129.3, 130.30, 130.33, 130.84, 130.86, 131.41, 131.43, 132.1, 132.66, 132.74, 136.1, 136.7, 138.40, 138.44, 138.83, 138.87, 138.95, 138.98, 140.3, 140.4, 144.2, 144.9, 145.86, 145.90, 166.9, 166.9. HRMS (ESI+) *m*/*z*: $[M]^+$ calcd for $C_{53}H_{51}IO_5S_{12}$, 1277.9424; found, 1277.9447.

Analytical data for **10**. ^{1}H NMR (700 MHz, CD_2Cl_2, 298 K,δ): 1.63 (s, 3H), 1.69 (s, 6H), 1.71 (s, 3H), 1.75 (s, 3H), 1.79 (s, 6H), 1.81 (s, 3H), 1.83 (s, 3H), 1.84 (s, 3H), 1.87 (s, 3H), 1.89 (s, 3H), 3.92 (s, 3H), 6.31 (s, 1H), 7.34 (d, 1H, $^3J_{H,H}$ = 7.9 Hz), 7.50 (d, 1H, $^3J_{H,H}$ = 7.9 Hz), 8.06 (d, 1H, $^3J_{H,H}$ = 7.9 Hz), 8.10 (d, 1H, $^3J_{H,H}$ = 7.9 Hz). $^{13}C\{^1H\}$-NMR (176 MHz, CD_2Cl_2, 298 K, δ): 27.79, 27.82,

DOI: 10.1021/acs.joc.8b03229
J. Org. Chem. 2019, 84, 3293−3303

27.83, 29.4, 29.6, 29.9, 32.2, 33.0, 33.1, 35.5, 35.7, 35.9, 52.7, 61.1, 61.4, 61.79, 61.81, 63.4, 64.0, 84.2, 85.5, 85.6, 125.6, 129.3, 130.27, 130.29, 130.9, 131.2, 131.8, 132.7, 135.8, 135.9, 136.8, 137.0, 138.5, 138.6, 139.0, 140.3, 144.2, 144.3, 144.9, 145.0, 145.8, 166.9. HRMS (ESI+) m/z: $[M]^+$ calcd for $C_{45}H_{44}I_2O_3S_{12}$, 1269.8023; found, 1269.8042.

General Procedure for Generation of Trityl Radicals from Trityl Alcohols. Method A. The trityl alcohol (45 μmol) was dissolved in 5 mL of dry dichloromethane, and boron trifluoride diethyl ether complex (50 mg, 45 μL, 0.352 mmol, 7.80 equiv) was added at 0 °C. The reaction mixture was stirred at room temperature for 90 min. Then, tin(II)-chloride (15 mg, 80 μmol, 1.76 equiv, dissolved in 1 mL of dry THF) was added; the reaction mixture was stirred for additional 20 min and then quenched by addition of 50 mL of water. The organic phase was extracted with dichloromethane twice, after drying over magnesium sulfate; the solvents were removed under reduced pressure, and the radical was obtained as a dark green powder.

Method B. The trityl alcohol (45 μmol) was dissolved in 5 mL of dry dichloromethane, and trifluoromethanesulfonic acid (8.8 mg, 5.2 μL, 58 μmol, 1.30 equiv) was added at 0 °C. The reaction mixture was stirred at room temperature for 1 h. Then, tin(II)-chloride (15 mg, 80 μmol, 1.76 equiv, dissolved in 1 mL of dry THF) was added; the reaction mixture was stirred further for 15 min and then quenched by addition of 50 mL of water. The organic phase was extracted with dichloromethane twice. After drying over magnesium sulfate, the solvents were removed under reduced pressure; the radical was obtained as a dark green powder.

Tris(8-iodo-2,2,6,6-tetramethylbenzo-[1,2-d;4,5-d′]-bis-[1,3]-dithiol-4-yl)-methyl radical, trityl radical **3**$^\bullet$, method A. Yield: 41 mg (90%), dark green solid. HRMS (ESI+) m/z: $[M]^+$ calcd for $C_{37}H_{36}I_3S_{12}$, 1244.6600; found, 1244.6609.

Trityl radical **6**$^\bullet$, method A. Yield: 43 mg (84%), dark green solid. HRMS (ESI+) m/z: $[M]^+$ calcd for $C_{58}H_{57}S_{12}$1137.1103; found, 1137.1100.

Trityl radical **7**$^\bullet$, method B. Yield: 49 mg (86%), dark green solid.

Trityl radical **8**$^\bullet$, method B. Yield: 50 mg (88%), dark green solid.

{Bis(8-(4-carboxylphenyl)-2,2,6,6-tetramethylbenzo-[1,2-d;4,5-d′]-bis-[1,3]dithiol-4-yl)-(8-(5,10,15,20-tetraphenylporphyrin-5-(4-phenyl)-yl)-2,2,6,6-tetramethylbenzo-[1,2-d;4,5-d′]-bis-[1,3]dithiol-4-yl)}-methyl Radical Dimethyl Ester, Trityl Porphyrin ***12***$^\bullet$. Trityl radical **8**$^\bullet$ (22 mg, 17.5 μmol), porphyrin **11** (17.5 μmol, 1.00 equiv), cesium carbonate (6 mg, 18.5 μmol, 1.05 equiv), and Pd(dppf)Cl_2 (1 mg, 1.3 μmol, 7.5 mol %) were dissolved in 10 mL of degassed THF/H_2O (9:1, v/v). The reaction mixture was stirred at 70 °C for 8 h under TLC control (SiO_2, CH_2Cl_2) until the trityl spot (R_f = 0.85) disappeared. After the mixture reached room temperature, the solvents were evaporated in high vacuum. The residue was taken up in 10 mL of dichloromethane and washed with water (20 mL). The organic phase was separated and dried over Na_2SO_4, and the solvents were removed under reduced pressure. Column chromatography on silica eluting with dichloromethane yielded 25 mg (83%) of pure product. ^{1}H NMR (700 MHz, CD_2Cl_2, 298 K, δ): −2.78 (s, 2H), 1.57 (bs, $\Delta_{1/2}$ = 245 Hz), 3.45 (bs, $\nu_{1/2}$ = 750 Hz), 4.49 bs, $\nu_{1/2}$ = 100 Hz), 7.81−7.87 (m, 9H), 8.24−8.31 (m, 6H), 8.83−8.89 (m, 4H), 8.98 (s, 2H), 9.28 (bs, $\nu_{1/2}$ = 53 Hz). HRMS (ESI+) m/z: $[M]^+$ calcd for $C_{97}H_{79}N_4O_4S_{12}$, 1747.2744; found, 1747.2748.

Bis(8-(4-carboxylphenyl)-2,2,6,6-tetramethylbenzo-[1,2-d;4,5-d′]-bis-[1,3]dithiol-4-yl)-(8-(5,10,15,20-tetraphenylporphyrin-5-(4-phenyl)-yl)-2,2,6,6-tetramethylbenzo-[1,2-d;4,5-d′]-bis-[1,3]dithiol-4-yl)}-methanol Dimethyl Ester, Trityl Porphyrin ***12-OH.*** Trityl alcohol **9** (11 mg, 8.6 μmol), porphyrin 11 (6 mg, 8.6 μmol, 1.00 equiv), cesium carbonate (3 mg, 9 μmol, 1.05 equiv), and Pd(dppf)Cl_2 (1 mg, 1.3 μmol, 15 mol %) were dissolved in 10 mL of degassed THF/H_2O (9:1, v/v). The reaction mixture was stirred at 70 °C for 8 h under TLC control (SiO_2, CH_2Cl_2) until the trityl spot (R_f = 0.82) disappeared. After the mixture reached room temperature, the solvents were evaporated in high vacuum. The residue was taken up in 10 mL of dichloromethane and washed with water (20 mL). The organic phase was separated and dried over Na_2SO_4, and the solvents were removed under reduced pressure. Column chromatography on silica eluting with dichloromethane yielded 12 mg (80%) of pure product. ^{1}H NMR (700 MHz, CD_2Cl_2, 298 K, δ): −2.78 (s, 2H), l.71 (s, 3H), 1.74 (s, 3H), 1.80 (s, 6H), 1.82 (s, 3H), 1.84 (s, 3H), 1.84 (s, 3H), 1.91 (s, 3H), 1.92 (s, 3H), 1.96 (s, 3H), 1.97 (s, 3H), 2.03 (s, 3H), 3.93 (s, 3H), 3.94 (s, 3H), 6.64 (s, 1H), 7.39−7.43 (m, 2H), 7.55−7.61 (m, 2H), 7.69−7.72 (m, 1H), 7.76−7.83 (m, 9H), 7.86−7.90 (m, 2H), 8.09−8.16 (m, 4H), 8.22−8.27 (m, 6H), 8.29−8.33 (m, 2H), 8.88 (s, 4H), 8.92 (s, 2H), 8.96 (s, 4H). ^{13}C{^{1}H}-NMR (176 MHz, CD_2Cl_2, 298 K, δ): 166.4, 145.5, 145.4, 142.2, 142.03, 142.02, 140.5, 140.0, 139.8, 139.7, 139.1, 138.70, 138.69, 138.63, 138.4, 138.3, 138.2, 137.8, 137.75, 134.6, 134.5, 133.0, 132.13, 132.10, 131.30, 131.25, 131.0, 130.26, 129.8, 128.8, 127.8, 127.0, 126.74, 126.73, 120.37, 120.32, 119.5, 84.0, 63.21, 63.19, 63.10, 62.64, 62.63, 62.5, 52.1, 35.2, 35.1, 35.0, 32.4, 32.3, 32.1, 29.5, 29.1, 29.0, 27.5, 27.3, 27.2, 26.9. HRMS (ESI+) m/z: $[M]^+$ calcd for $C_{97}H_{81}N_4O_5S_{12}$, 1767.2865; found, 1767.2877.

Bis(8-(4-carboxylphenyl)-2,2,6,6-tetramethylbenzo-[1,2-d;4,5-d′]-bis-[1,3]dithiol-4-yl)-(8-(zinc(II)-5,10,15,20-tetraphenylporphyrin-5-(4-phenyl)-yl)-2,2,6,6-tetramethylbenzo-[1,2-d;4,5-d′]-bis-[1,3]dithiol-4-yl)}-methyl Radical Dimethyl Ester, Trity Porphyrin ***13***$^\bullet$. Trityl porphyrin **12**$^\bullet$(15 mg, 8.6 μmol) was dissolved in 3 mL of dichloromethane, and zinc acetate dihydrate (8 mg, 38.7 μmol, 4.5 equiv) dissolved in 1 mL of methanol was added. The reaction mixture was stirred for 2 h at room temperature and then poured onto 20 mL of water. Extraction with 20 mL of dichloromethane and removal of the solvents under reduced pressure led to a crude product, which was purified by column chromatography on silica eluting with dichloromethane. Compound **13**$^\bullet$ was obtained in a yield of 15 mg (96%) as a dark reddish solid. ^{1}H NMR (400 MHz, CD_2Cl_2, 298 K, δ): 1.57 (bs, $\Delta_{1/2}$ = 260 Hz), 4.49 bs, $\Delta_{1/2}$ = 100 Hz), 7.76−7.83 (m, 9H), 8.20−8.28 (m, 6H), 8.89−8.95 (m, 4H), 9.00 (d, $^3J_{H,H}$ = 4.8 Hz, 2H), 9.34 (bs, $\Delta_{1/2}$ = 53 Hz). HRMS (ESI+) m/z: $[M]^+$ calcd for $C_{97}H_{77}N_4O_4S_{12}Zn$, 1811.1879; found, 1811.1908.

4,4′-Bis[{Bis(8-(4-carboxylphenyl)-2,2,6,6-tetramethylbenzo-[1,2-d;4,5-d′]-bis-[1,3]dithiol-4-yl)-(8-yl-2,2,6,6-tetramethylbenzo-[1,2-d;4,5-d′]-bis-[1,3]dithiol-4-yl)}-methanol]-biphenyl Tetramethyl Ester, Trityl Alcohol ***14***. Trityl alcohol **9** (40 mg, 31.3 μmol, 2.00 equiv), 4,4′-bis(4,4,5,5-tetramethyl-1,3,2-dioxaborolan-2-yl)-biphenyl (6.3 mg, 15.7 μmol, 1.00 equiv), cesium carbonate (10.0 mg, 31.3 μmol, 2.00 equiv), and Pd(dppf)Cl_2 (2 mg, 2.6 μmol, 8.3 mol %) were solved in 10 mL of THF/H_2O (9:1, v/v) previously degassed by three freeze−pump−thaw cycles. The reaction mixture was heated to 70 °C under argon for 16 h. Then, the solvents were removed under reduced pressure and the residue was taken up in 30 mL of degassed dichloromethane and washed with 20 mL of degassed water. The organic phase was separated and dried over $MgSO_4$; after removal of the solvents, a pale-yellow solid was obtained in a yield of 37 mg (48%). ^{1}H NMR (700 MHz, CD_2Cl_2, 298 K, δ): 1.68 (s, 6H), 1.69 (s, 6H), 1.70 (s, 6H), 1.75 (s, 6H), 1.75 (s, 6H), 1.77 (s, 6H), 1.80 (s, 6H), 1.81 (s, 6H), 1.83 (s, 6H), 1.88 (s, 6H), 1.91 (s, 12H), 3.93 (s, 12H), 6.57 (s, 2H), 7.36−7.41 (m, 6H), 7.55 (d, $^3J_{H,H}$ = 7.8 Hz, 4H), 7.58 (d, $^3J_{H,H}$ = 7.5 Hz, 2H), 7.72−7.79 (m, 4H), 8.08 (d, $^3J_{H,H}$ = 7.9 Hz, 4H), 8.12 (d, $^3J_{H,H}$ = 7.9 Hz, 4H). ^{13}C{^{1}H}-NMR (176 MHz, CD_2Cl_2, 298 K, δ): 26.9, 22.2, 27.27, 27.28, 28.9, 29.0, 29.1, 29.2, 29.3, 29.40, 29.43, 29.45, 31.79, 31.80, 31.9, 32.3, 32.4, 33.8, 34.9, 34.97, 35.01, 35.03, 52.1, 62.3, 62.6, 63.0, 63.1, 63.14, 63.15, 83.9, 127.1, 128.78, 128.79, 128.9, 129.1, 129.7, 130.2, 130.9, 131.1, 131.2, 132.05, 132.10, 132.6, 137.68, 137.72, 137.99, 138.00, 138.25, 138.27, 138.28, 138.64, 128.68, 138.77, 139.6, 139.8, 139.9, 140.4, 140.5, 145.39, 145.41, 166.4. HRMS (ESI+) m/z: $[M]^+$ calcd for $C_{118}H_{110}O_{10}S_{24}$, 2456.1400; found, 2456.1560.

4,4′-Bis[{Bis(8-(4-carboxylphenyl)-2,2,6,6-tetramethylbenzo-[1,2-d;4,5-d′]-bis-[1,3]dithiol-4-yl)-(8-yl-2,2,6,6-tetramethylbenzo-[1,2-d;4,5-d′]-bis-[1,3]dithiol-4-yl)}-methyl radical]-biphenyl Tetramethyl Ester, Trityl Biradical ***15***$^{\bullet\bullet}$. Trityl alcohol **14** (20 mg, 8.16 μmol) was dissolved in 5 mL of dry dichloromethane, and triflourmethanesulfonic acid (3 μL, 16.3 μmol, 2.00 equiv) was added at 0 °C, whereupon the color of the reaction mixture turned to a dirty dark green. After 4 h at 0 °C, tin(II)-chloride (3 mg, 13.9 μmol, 1.7 equiv, dissolved in 1 mL of dry THF) was added; the color of the reaction

DOI: 10.1021/acs.joc.8b03229
J. Org. Chem. 2019, 84, 3293−3303

mixture then turned to a clear dark green, and the mixture was stirred for an additional 16 h at room temperature. Subsequently, the solvents were removed in high vacuum, and degassed water (10 mL) and degassed dichloromethane (10 mL) were added under argon. The dark green organic phase was separated, and all solvents were removed in high vacuum (10^{-3} mbar) until a dark green solid was obtained in a yield of 17 mg (86%). HRMS (ESI+) *m/z*: $[M]^+$ calcd for $C_{118}H_{110}O_{10}S_{24}$, 2420.1336; found, 2420.1335.

{Bis(8-(4-carboxylphenyl)-2,2,6,6-tetramethylbenzo-[1,2-d;4,5-d′]-bis-[1,3]dithiol-4-yl)-(8-(2-trimethylsilylethynyl)-2,2,6,6-tetramethylbenzo-[1,2-d;4,5-d′]-bis-[1,3]dithiol-4-yl)}-methyl Radical Dimethyl Ester, Trityl Radical **16•**. Trityl radical **7•** (77 mg, 61 μmol), copper(I)-iodide (1 mg, 10 mol %), and $Pd(Ph_3P)_2Cl_2$ (2 mg, 5 mol %) were dissolved in 25 mL of degassed CH_2Cl_2/Et_3N (1:1, v/v), and TIPS-acetylene (41 μL, 33 mg, 183 μmol, 3.00 equiv) was added under argon. The reaction mixture was stirred at 50 °C for 16 h; then the solvents were removed in high vacuum. The residue was taken up in 20 mL of dichloromethane and washed with water and brine. The organic phase was separated and dried over $MgSO_4$, and solvents were removed under reduced pressure. The crude product was purified by column chromatography on silica eluting with cyclohexane/ethyl acetate (2:1) affording 59 mg (73%) of a deep green solid. HRMS (ESI+) *m/z*: $[M]^+$ calcd for $C_{55}H_{51}O_4S_{12}$, 1315.177; found, 1315.179.

{Bis(8-(4-carboxylphenyl)-2,2,6,6-tetramethylbenzo-[1,2-d;4,5-d′]-bis-[1,3]dithiol-4-yl)-(8-ethynyl-2,2,6,6-tetramethylbenzo-[1,2-d;4,5-d′]-bis-[1,3]dithiol-4-yl)}-methyl Radical Dimethyl Ester, Trityl Radical **17•**. Trityl radical **16•** (30 mg, 22.8 μmol) was dissolved in 2 mL of dry THF, and tetra-*n*-butyl ammonium fluoride (68 μL 1 M in THF, 68 μmol, 3.00 equiv) was added under argon, whereupon the mixture turned turquoise. The reaction mixture was stirred at room temperature for 3 h; then the solvents were removed in high vacuum. The residue was taken up in 20 mL of dichloromethane and washed with water and brine; the organic phase then became ocher. The organic phase was separated and dried over $MgSO_4$, and solvents were removed under reduced pressure. The crude product was purified by column chromatography on silica eluting with dichloromethane, affording 13 mg (49%) of a deep green solid. HRMS (ESI+) *m/z*: $[M]^+$ calcd for $C_{64}H_{71}O_4S_{12}Si$, 1315.1765; found, 1315.1766.

■ ASSOCIATED CONTENT

Supporting Information

The Supporting Information is available free of charge on the ACS Publications website at DOI: 10.1021/acs.joc.8b03229.

X-ray crystallography data; computational details; pulsed/cw EPR data and spectra; reaction details; discussion of the Sonogashira coupling reactions; NMR spectra; mass spectra; MPLC data (PDF)

Structural information for trityl alcohol **5** (CIF)

■ AUTHOR INFORMATION

Corresponding Author

*E-mail: schiemann@pc.uni-bonn.de

ORCID

Olav Schiemann: 0000-0001-6346-9779

Present Address

§A.M.: Max Planck Institute for Biophysical Chemistry, Am Fassberg 11, 37077 Göttingen, Germany.

Notes

The authors declare no competing financial interest.

■ ACKNOWLEDGMENTS

Funding of the Deutsche Forschungsgemeinschaft via the SPP1601 is gratefully acknowledged. The authors thank B.Sc. Leonard Maurer and Prof. Dr. Stefan Grimme, Mulliken Center for Theoretical Chemistry at the University of Bonn, for providing the latest version of the GFN-xTB program and practical advice. The authors also thank Dr. Gregor Schnakenburg, Institute for Inorganic Chemistry at the University of Bonn, for conducting the X-ray diffractometry and the Deutsche Forschungsgemeinschaft (DFG) for funding the diffractometer.

■ REFERENCES

(1) Gomberg, M. An Instance of Trivalent Carbon: Triphenyl Methyl. *J. Am. Chem. Soc.* **1900**, *22*, 757−771.

(2) Hicks, R. G. *Stable Radicals*; Wiley-VCH Verlag GmbH: Weinheim, 2010.

(3) Veciana, J.; Carilla, J.; Miravitlles, C.; Molins, E. Free Radicals as Clathrate Hosts : Crystal and Molecular Structure of 1 : 1 Perchlorotriphenylmethyl Radical - Benzene. *J. Chem. Soc., Chem. Commun.* **1987**, 812−814.

(4) Teruel, L.; Viadel, L.; Carilla, J.; Fajari, L.; et al. A New Constituent of Organic Magnetic Magnetic Materials. *J. Org. Chem.* **1996**, *61*, 6063−6066.

(5) Kuhn, R.; Trischmann, H. Surprisingly Stable Nitrogenous Free Radical. *Angew. Chem., Int. Ed. Engl.* **1963**, *2*, 155.

(6) Schnakenburg, G.; Meyer, A. Syntheses, Spectroscopy, and Crystal Structures of 3-(4-Bromophenyl)-1,5-Diphenylformazan and the 3-(4-Bromophenyl)-1,5-Diphenylverdazyl Radical and the Crystal Structure of the by Product 5-Anilino-3-(4-Bromophenyl)-1-Phenyl-1H-1,2,4-Triazole. *Acta Cryst. E* **2018**, *74*, 292−297.

(7) Likhtenshtein, G. I.; Yamauchi, J.; Nakatsuiji, S. *Nitroxides:Applications in Chemistry, Biomedicine, and Material Science*; Wiley-VCH Verlag GmbH: Weinheim, 2008.

(8) Williams, B. B.; Halpern, H. J. In Vivo EPR Imaging. In *Biomedical EPR, Part A: Free Radicals, Metals, Medicine, and Physiology*; Eaton, S. R., Eaton, G. R., Berliner, L. J., Eds.; Springer US: Boston, MA, 2005; pp 283−319.

(9) Wang, X.; Emoto, M.; Miyake, Y.; Itto, K.; Xu, S.; Fujii, H.; Hirata, H.; Arimoto, H. Novel blood-brain barrier-permeable spin probe for in vivo electron paramagnetic resonance imaging. *Bioorg. Med. Chem. Lett.* **2016**, *26*, 4947−4949.

(10) Epel, B.; Haney, C. R.; Hleihel, D.; Wardrip, C.; et al. Electron Paramagnetic Resonance Oxygen Imaging of a Rabbit Tumor Using Localized Spin Probe Delivery. *Med. Phys.* **2010**, *37*, 2553−2559.

(11) Ni, Q. Z.; Daviso, E.; Can, T. V.; Markhasin, E.; Jawla, S. K.; Swager, T. M.; Temkin, R. J.; Herzfeld, J.; Griffin, R. G. High Frequency Dynamic Nuclear Polarization. *Acc. Chem. Res.* **2013**, *46*, 1933−1941.

(12) Abragam, A.; Goldman, M. Principles of Dynamic Nuclear Polarisation. *Rep. Prog. Phys.* **1978**, *41*, 395−467.

(13) Reginsson, G. W.; Schiemann, O. Studying Biomolecular Complexes with Pulsed Electron-Electron Double Resonance Spectroscopy. *Biochem. Soc. Trans.* **2011**, *39*, 128−139.

(14) Schiemann, O.; Fritscher, J.; Kisseleva, N.; Sigurdsson, S. T.; Prisner, T. F. Structural Investigation of a High-Affinity Mn(II) Binding Site in the Hammerhead Ribozyme by EPR Spectroscopy and DFT Calculations. Effects of Neomycin B on Metal-Ion Binding. *ChemBioChem* **2003**, *4*, 1057−1065.

(15) Klare, J. P.; Steinhoff, H. J. Spin Labeling EPR. *Photosynth. Res.* **2009**, *102*, 377−390.

(16) Berliner, L. J.; Grunwald, J.; Hankovszky, H. O.; Hideg, K. A Novel Reversible Thiol-Specific Spin Label: Papain Active Site Labeling and Inhibition. *Anal. Biochem.* **1982**, *119*, 450−455.

(17) Tidwell, T. Triarylmethyl and Related Radicals. In *Stable Radicals*; Wiley-Blackwell, 2010; pp 1−31.

(18) Andersson, S.; Rydbeck, A.; Mahno, R. S. US Patent 5728370, 1999.

(19) Reddy, T. J.; Iwama, T.; Halpern, H. J.; Rawal, V. H. General Synthesis of Persistent Trityl Radicals for EPR Imaging of Biological Systems. *J. Org. Chem.* **2002**, *67*, 4635−4639.

(20) Günther, U. WO Patent 2012/062975 A1, 2012.

(21) Bobko, A. A.; Dhimitruka, I.; Zweier, J. L.; Khramtsov, V. V. Trityl Radicals as Persistent Dual Function pH and Oxygen Probes for in Vivo Electron Paramagnetic Resonance Spectroscopy and Imaging: Concept and Experiment. *J. Am. Chem. Soc.* **2007**, *129*, 7240−7241.
(22) Mathies, G.; Caporini, M. A.; Michaelis, V. K.; Liu, Y.; Hu, K. N.; Mance, D.; Zweier, J. L.; Rosay, M.; Baldus, M.; Griffin, R. G. Efficient Dynamic Nuclear Polarization at 800 MHz/527 GHz with Trityl-Nitroxide Biradicals. *Angew. Chem., Int. Ed.* **2015**, *54*, 11770−11774.
(23) Mathies, G.; Jain, S.; Reese, M.; Griffin, R. G. Pulsed Dynamic Nuclear Polarization with Trityl Radicals. *J. Phys. Chem. Lett.* **2016**, *7*, 111−116.
(24) Jähnig, F.; Kwiatkowski, G.; Däpp, A.; Hunkeler, A.; Meier, B. H.; Kozerke, S.; Ernst, M. Dissolution DNP Using Trityl Radicals at 7 T Field. *Phys. Chem. Chem. Phys.* **2017**, *19*, 19196−19204.
(25) Jassoy, J. J.; Berndhäuser, A.; Duthie, F.; Kühn, S. P.; Hagelueken, G.; Schiemann, O. Versatile Trityl Spin Labels for Nanometer Distance Measurements on Biomolecules In Vitro and within Cells. *Angew. Chem., Int. Ed.* **2017**, *56*, 177−181.
(26) Owenius, R.; Eaton, G. R.; Eaton, S. S. Frequency (250 MHz to 9.2 GHz) and Viscosity Dependence of Electron Spin Relaxation of Triarylmethyl Radicals at Room Temperature. *J. Magn. Reson.* **2005**, *172*, 168−175.
(27) Bowman, M. K.; Mailer, C.; Halpern, H. J. The Solution Conformation of Triarylmethyl Radicals. *J. Magn. Reson.* **2005**, *172*, 254−267.
(28) Meyer, A.; Jassoy, J. J.; Spicher, S.; Berndhäuser, A.; Schiemann, O. Performance of PELDOR, RIDME, SIFTER, and DQC in Measuring Distances in Trityl Based Bi- and Triradicals: Exchange Coupling, Pseudosecular Coupling and Multi-Spin Effect. *Phys. Chem. Chem. Phys.* **2018**, *20*, 13858−13869.
(29) Kunjir, N. C.; Reginsson, G. W.; Schiemann, O.; Sigurdsson, S. T. Measurements of Short Distances between Trityl Spin Labels with CW EPR, DQC and PELDOR. *Phys. Chem. Chem. Phys.* **2013**, *15*, 19673−19685.
(30) Reginsson, G. W.; Kunjir, N. C.; Sigurdsson, S. T.; Schiemann, O. Trityl Radicals: Spin Labels for Nanometer-Distance Measurements. *Chem. - Eur. J.* **2012**, *18*, 13580−13584.
(31) Shevelev, G. Y.; Krumkacheva, O. A.; Lomzov, A. A.; Kuzhelev, A. A.; Rogozhnikova, O. Y.; Trukhin, D. V.; Troitskaya, T. I.; Tormyshev, V. M.; Fedin, M. V.; Pyshnyi, D. V.; et al. Physiological-Temperature Distance Measurement in Nucleic Acid Using Triarylmethyl-Based Spin Labels and Pulsed Dipolar EPR Spectroscopy. *J. Am. Chem. Soc.* **2014**, *136*, 9874−9877.
(32) Azarkh, M.; Okle, O.; Eyring, P.; Dietrich, D. R.; Drescher, M. Evaluation of spin labels for in-cell EPR by analysis of nitroxide reduction in cell extract of Xenopus laevis oocytes. *J. Magn. Reson.* **2011**, *212*, 450−454.
(33) Jagtap, A. P.; Krstic, I.; Kunjir, N. C.; Hänsel, R.; Prisner, T. F.; Sigurdsson, S. T. Sterically shielded spin labels for in-cell EPR spectroscopy: Analysis of stability in reducing environment. *Free Radical Res.* **2015**, *49*, 78−85.
(34) Karthikeyan, G.; Bonucci, A.; Casano, G.; Gerbaud, G.; Abel, V. T.; Kodjabachian, L.; Magalon, A.; Guigliarelli, B.; Belle, V.; Ouari, O.; Mileo, E. A Bioresistant Nitroxide Spin Label for In-Cell EPR Spectroscopy: In Vitro ad In Oocyted Protein Structural Dynamics Studies. *Angew. Chem., Int. Ed.* **2018**, *57*, 1366−1370.
(35) Rogozhnikova, O. Y.; Vasiliev, V. G.; Troitskaya, T. I.; Trukhin, D. V.; Mikhalina, T. V.; Halpern, H. J.; Tormyshev, V. M. Generation of Trityl Radicals by Nucleophilic Quenching of tris(2,3,5,6-Tetrathiaaryl)methyl Cations and Practical and Convenient Large-Scale Synthesis of Persistent tris(4-Carboxy-2,3,5,6-Tetrathiaaryl)-methyl Radical. *Eur. J. Org. Chem.* **2013**, *2013*, 3347−3355.
(36) Tormyshev, V. M.; Rogozhnikova, O. Y.; Bowman, M. K.; Trukhin, D. V.; Troitskaya, T. I.; Vasiliev, V. G.; Shundrin, L. A.; Halpern, H. J. Preparation of Diversely Substituted Triarylmethyl Radicals by the Quenching of tris(2,3,5,6-Tetrathiaaryl)methyl Cations with C-, N-, P-, and S-Nucleophiles. *Eur. J. Org. Chem.* **2014**, *2014*, 371−380.
(37) Decroos, C.; Prange, T.; Mansuy, D.; Boucher, J.; Li, Y. Unprecedented ipso aromatic nucleophilic substitution upon oxidative decarboxylation of tris(p-carboxytetrathiaaryl)methyl (TAM) radicals: a new access to diversely substituted TAM radicals. *Chem. Commun.* **2011**, *47*, 4805−4807.
(38) Tan, X.; Tao, S.; Liu, W.; Rockenbauer, A.; Villamena, F. A.; Zweier, J. L.; Song, Y.; Liu, Y. Synthesis and Characterization of the Perthiatriarylmethyl Radical and Its Dendritic Derivatives with High Sensitivity and Selectivity to Superoxide Radical. *Chem. - Eur. J.* **2018**, *24*, 6958−6967.
(39) Trukhin, D. V.; Rogozhnikova, O. Y.; Troitskaya, T. I.; Vasiliev, V. G.; Bowman, M. K.; Tormyshev, V. M. Facile and High-Yielding Synthesis of TAM Biradicals and Monofunctional TAM Radicals. *Synlett* **2016**, *27*, 893−899.
(40) Akhmetzyanov, D.; Schöps, P.; Marko, A.; Kunjir, N. C.; Sigurdsson, S. T.; Prisner, T. F. Pulsed EPR Dipolar Spectroscopy at Q- and G-Band on a Trityl Biradical. *Phys. Chem. Chem. Phys.* **2015**, *17*, 24446−24451.
(41) Shevelev, G. Y.; Krumkacheva, O. A.; Lomzov, A. A.; Kuzhelev, A. A.; Trukhin, D. V.; Rogozhnikova, O. Y.; Tormyshev, V. M.; Pyshnyi, D. V.; Fedin, M. V.; Bagryanskaya, E. G. Triarylmethyl Labels: Toward Improving the Accuracy of EPR Nanoscale Distance Measurements in DNAs. *J. Phys. Chem. B* **2015**, *119*, 13641−13648.
(42) (a) Liu, Y.; Song, Y.; Rockenbauer, A.; Sun, J.; Hemann, C.; Villamena, F. A.; Zweier, J. L. Synthesis of Trityl Radical-Conjugated Disulfide Biradicals for Measurement of Thiol Concentration. *J. Org. Chem.* **2011**, *76*, 3853−3860. (b) Liu, Y.; Villamena, F. A.; Song, Y.; Sun, J.; Rockenbauer, A.; Zweier, J. L. Synthesis of ^{14}N- and ^{15}N-Labeled Trityl-Nitroxide Biradicals with Strong Spin-Spin Interaction and Improved Sensitivity to Redox Status and Oxygen. *J. Org. Chem.* **2010**, *75*, 7796−7802.
(43) Yang, Z.; Bridges, M. D.; Lopez, C. J.; Rogozhnikova, O. Y.; Trukhin, D. V.; Brooks, E. K.; Tormyshev, V.; Halpern, H. J.; Hubbell, W. L. A triarylmethyl spin label for long-range distance measurement at physiological temperatures using T_1 relaxation enhancement. *J. Magn. Reson.* **2016**, *269*, 50−54.
(44) Cage, B.; McNeely, H.; Russek, S. E.; Halpern, H. J. Thermomagnetic Properties of the Finland Trityl Radical. *J. Appl. Phys.* **2009**, *105*, 043905.
(45) Fleck, N.; Schnakenburg, G.; Filippou, C.; Schiemann, O. Tris[2,2,6,6-Tetramethyl-8-(Trimethylsilyl)benzo-[1,2-d;4,5-d]bis-(1,3-Dithiol)-4-yl]methanol Diethyl Ether Monosolvate. *Acta Cryst. E* **2018**, *74*, 539−542.
(46) Driesschaert, B.; Robiette, R.; Le Duff, C. S.; Collard, L.; Robeyns, K.; Gallez, B.; Marchand-Brynaert, J. Cofigurationally Stable Tris(tetrathioaryl)methyl Molecular Propellers. *Eur. J. Org. Chem.* **2012**, *33*, 6517−6525.
(47) Allen, F. H.; Kennard, O.; Watson, D. G.; Brammer, L.; Orpen, A. G.; Taylor, R. Tables of bond length determined by X-ray and neutron diffraction. Part 1. Bond lengths in organic compounds. *J. Chem. Soc., Perkin Trans. 2* **1987**, S1−S19.
(48) Shishkin, O. V. Evaluation of True Energy of Halogen Bonding in the Crystals of Halogen Derivatives of Trityl Alcohol. *Chem. Phys. Lett.* **2008**, *458*, 96−100.
(49) Urzua, J.; Torneiro, M. Divergent Synthesis of Porous Tetraphenylmethane Dendrimers. *J. Org. Chem.* **2017**, *82*, 13231−13238.
(50) **3**$^{\bullet}$ reacted with *n*-BuLi under Formation of Alkyl-Coupling Products and not I/H-exchange products (see the Supporting Information, p S17).
(51) Littke, A. F.; Fu, G. C. A Convenient and General Method for Pd-Catalyzed Suzuki Cross-Couplings of Aryl Chlorides and Arylboronic Acids. *Angew. Chem., Int. Ed.* **1998**, *37*, 3387−3388.
(52) Yamauchi, S. Recent Developments in Studies of Electronic Excited States by Means of Electron Paramagnetic Resonance Spectroscopy. *Bull. Chem. Soc. Jpn.* **2004**, *77*, 1255−1268.
(53) Giacobbe, E. M.; Mi, Q.; Colvin, M. T.; Cohen, B.; Ramanan, C.; Scott, A. M.; Yeganeh, S.; Marks, T. J.; Ratner, M. A.; Wasielewski, M. R. Ultrafast Intersystem Crossing and Spin Dynamics of Linked to

DOI: 10.1021/acs.joc.8b03229
J. Org. Chem. 2019, 84, 3293−3303

a Nitroxide Radical at Fixed Distances. *J. Am. Chem. Soc.* **2009**, *131*, 3700−3712.
(54) Clarke, R. H.; Connors, R. E.; Schaafsma, T. J.; Kleibeuker, J. F.; Platenkamp, R. J. The Triplet State of Chlorophylls. *J. Am. Chem. Soc.* **1976**, *98*, 3674−3677.
(55) Van Dorp, W. G.; Schoemaker, W. H.; Soma, M.; Van der Waals, J. H. The lowest triplet state of free base porphyrin. *Mol. Phys.* **1975**, *30*, 1701−1721.
(56) Ishii, K.; Ishizaki, T.; Kobayashi, N. Experimental Evidence of a Selection Rule of Intersystem Crossing to the Excited Quartet States: Metallophthalocyanines Coordinated by 4-Amino-TEMPO. *J. Phys. Chem. A* **1999**, *103*, 6060−6062.
(57) Mani, T.; Niedzwiedzki, D. M.; Vinogradov, S. A. Generation of Phosphorescent Triplet States via Photoinduced Electron Transfer: Energy and Electron Transfer Dynamics in Pt Porphyrin − Rhodamine B Dyads. *J. Phys. Chem. A* **2012**, *116*, 3598−3610.
(58) Jassoy, J. J.; Meyer, A.; Spicher, S.; Wübben, C.; Schiemann, O. Synthesis of Nanometer Sized Bis- and Tris-Trityl Model Compounds with Different Extent of Spin − Spin Coupling. *Molecules* **2018**, *23*, 682.
(59) Weber, A.; Schiemann, O.; Bode, B.; Prisner, T. F. PELDOR at S- and X-Band Frequencies and the Separation of Exchange Coupling from Dipolar Coupling. *J. Magn. Reson.* **2002**, *157*, 277−285.
(60) Souto, M.; Bendixen, D.; Jensen, M.; Díez-Cabanes, V.; Cornil, J.; Jeppesen, J. O.; Ratera, I.; Rovira, C.; Veciana, J. Synthesis and Characterization of Ethylenedithio-MPTTF-PTM Radical Dyad as a Potential Neutral Radical Conductor. *Molecules* **2016**, *2*, 46−56.
(61) Elsner, O.; Ratera, I.; Rovira, C.; Veciana, J. Ferrocene as a Ferromagnetic Coupler. Synthesis and Characterization of a Ferrocene Bridged Polychlorotriphenylmethyl Diradical. *J. Organomet. Chem.* **2001**, *639*, 251−257.
(62) Kucher, S.; Korneev, S.; Tyagi, S.; Apfelbaum, R.; Grohmann, D.; Lemke, E. A.; Klare, J. P.; Steinhoff, H. J.; Klose, D. Orthogonal Spin Labeling Using Click Chemistry for in Vitro and in Vivo Applications. *J. Magn. Reson.* **2017**, *275*, 38−45.
(63) Iovine, V.; Cruciani, F.; Picini, F.; Varrone, M.; Rossi, E.; et al. Competitive Carbothiolation and Sonogashira Cross-Coupling in the Reaction of Trimethylsilylacetylene with Arylthioacetates. *ChemistrySelect* **2016**, *1*, 5201−5205.
(64) Wu, S.; Li, M.; Phan, H.; Wang, D.; Herng, T. S.; Ding, J.; Lu, Z.; Wu, J. Toward Two-Dimensional π-Conjugated Covalent Organic Radical Frameworks Angewandte. *Angew. Chem., Int. Ed.* **2018**, *57*, 8007−8011.
(65) Elewa, M.; Maltar-Strmecki, N.; Said, M.; El Shihawy, H.; El-Sadek, M.; Frank, J.; Drescher, S.; Drescher, M.; Mäder, K.; Hinderberger, D.; Imming, P. Synthesis and EPR-spectroscopic characterization of the perchlorotriarylmethyl tricarboxylic acid radical (PTMTC) and its 13C labelled analogue (13C-PTMTC). *Phys. Chem. Chem. Phys.* **2017**, *19*, 6688−6697.
(66) Kuzhelev, A. A.; Tormyshev, V. M.; Rogozhnikova, O. Y.; Trukhin, D. V.; Troitskaya, T. I.; Strizhakov, R. K.; Krumkacheva, O. A.; Fedin, M. V.; Bagryanskaya, E. G. Triarylmethyl Radicals: An EPR Study of ^{13}C Hyperfine Coupling Constants. *Z. Phys. Chem.* **2017**, *231*, 777−794.
(67) Martin, W. C. Table of Spin-Orbit Energies for p-Electrons in Neutral Atomic (core)np Configurations. *J. Res. Natl. Bur. Stand., Sect. A* **1971**, *75A*, 109−111.
(68) Sinclair, J.; Kivelson, D. Electron Spin Resonance of Substituted Triphenylmethyl Radicals. *J. Am. Chem. Soc.* **1968**, *90*, 5074−5080.
(69) Bertine, I.; Luchinat, C.; Parigi, G.; Ravera, E. *NMR of Paramagnetic Molecules*, 2nd ed.; Elsevier B.V., 2017.
(70) Goldfarb, D.; Stoll, S. *EPR Spectroscopy*, 1st ed.; Wiley, 2018.
(71) Stoll, S.; Schweiger, A. EasySpin, a comprehensive software package for spectral simulation and analysis in EPR. *J. Magn. Reson.* **2006**, *178*, 42−45.
(72) (a) Bencini, A.; Gatteschi, D. *EPR of Exchange Coupled Systems*, 1st ed.; Springer: Heidelberg, 1990. (b) Abrabam, A.; Bleany, B. *Electron Paramagnetic Resonance of Transition Ions*, 1st ed.; Oxford University Press, 1970.
(73) Fritscher, J.; Beyer, M.; Schiemann, O. Synthesis, Crystal Structure and Magnetic Properties of a Novel Nitroxide Biradical. Theoretical Investigation of the Exchange Mechanisms. *Chem. Phys. Lett.* **2002**, *364*, 393−401.
(74) Jeschke, G. Determination of the Nanostructure of Polymer Materials by Electron Paramagnetic Resonance Spectroscopy. *Macromol. Rapid Commun.* **2002**, *23*, 227−246.
(75) Margraf, D.; Cekan, P.; Prisner, T. F.; Sigurdsson, S. T.; Schiemann, O. Ferro- and Antiferromagnetic Exchange Coupling Constants in PELDOR Spectra. *Phys. Chem. Chem. Phys.* **2009**, *11*, 6708−6714.
(76) Saxena, S.; Freed, J. H. Theory of Double Quantum Two-Dimensional Electron Spin Resonance with Application to Distance Measurements Theory of Double Quantum Two-Dimensional Electron Spin Resonance with Application to Distance Measurements. *J. Chem. Phys.* **1997**, *107*, 1317−1340.
(77) Riplinger, C.; Kao, J. P. Y.; Rosen, G. M.; Kathirvelu, V.; Eaton, G. R.; Eaton, S. S.; Kutateladze, A.; Neese, F. Interaction of Radical Pairs Through-Bond and Through-Space : Scope and Limitations of the Point - Dipole Approximation in Electron Paramagnetic Resonance Spectroscopy. *J. Am. Chem. Soc.* **2009**, *131*, 10092−10106.
(78) Liu, Y.; Villamena, F. A.; Rockenbauer, A.; Song, Y.; Zweier, J. L. Structural Factors Controlling the Spin − Spin Exchange Coupling . *J. Am. Chem. Soc.* **2013**, *135*, 2350−2356.
(79) Ballester, M.; Riera, J.; Castañer, J.; Badía, C.; Monsó, J. M. Inert Carbon Free Radicals. Perchlorodiphenylmethyl and Perchlorotriphenylmethyl Radical Series. *J. Am. Chem. Soc.* **1971**, *93*, 2215−2225.
(80) Bonvoisin, J.; Launay, J.-P.; Rovira, C.; Veciana, J. Purely Organic Mixed-Valence Molecules with Nanometric Dimensions Showing Long-Range Electron Transfer. Synthesis, and Optical and EPR Studies of a Radical Anion Derived from a Bis(triarylmethyl)-Diradical. *Angew. Chem., Int. Ed. Engl.* **1994**, *33*, 2106−2109.
(81) Fulmer, G. R.; Miller, A. J. M.; Sherden, N. H.; Gottlieb, H. E.; Nudelman, A.; Stoltz, B. M.; Bercaw, J. E.; Goldberg, K. I. NMR Chemical Shifts of Trace Impurities: Common Laboratory Solvents, Organics, and Gases in Deuterated Solvents Relevant to the Organometallic Chemist. *Organometallics* **2010**, *29*, 2176−2179.
(82) Grimme, S.; Bannwarth, C.; Shushkov, P. A Robust and Accurate Tight-Binding Quantum Chemical Method for Structures, Vibrational Frequencies, and Noncovalent Interactions of Large Molecular Systems Parametrized for all spd-Block Elements (Z = 1−86). *J. Chem. Theory Comput.* **2017**, *13*, 1989−2009.
(83) Neese, F. The ORCA Program System. *WIREs Comput. Mol. Sci.* **2012**, *2*, 73−78.
(84) Neese, F. Software Update : The ORCA Program System, Version 4.0. *WIREs Comput. Mol. Sci.* **2018**, *8*, e1327.

DOI: 10.1021/acs.joc.8b03229
J. Org. Chem. 2019, 84, 3293−3303

Supporting Information

C-C Cross Coupling reactions of Trityl Radicals: Spin Density Delocalization, Exchange Coupling and a Spin Label

Nico Fleck[1], Tobias Hett[1], Jonas Brode[1], Andreas Meyer[1,2], Sabine Richert[3], Olav Schiemann[1,*]

[1]Institute of Physical and Theoretical Chemistry, Rheinische Friedrich-Wilhelms-University Bonn, Wegelerstr. 12, 53115 Bonn, Germany

[2] Current address: Max Planck Institute for Biophysical Chemistry, Am Fassberg 11, 37077 Göttingen, Germany

[3]Institute of Physical Chemistry, University of Freiburg, Albertstraße 21, 79104 Freiburg, Germany

Table of contents

1. Crystallographic Data

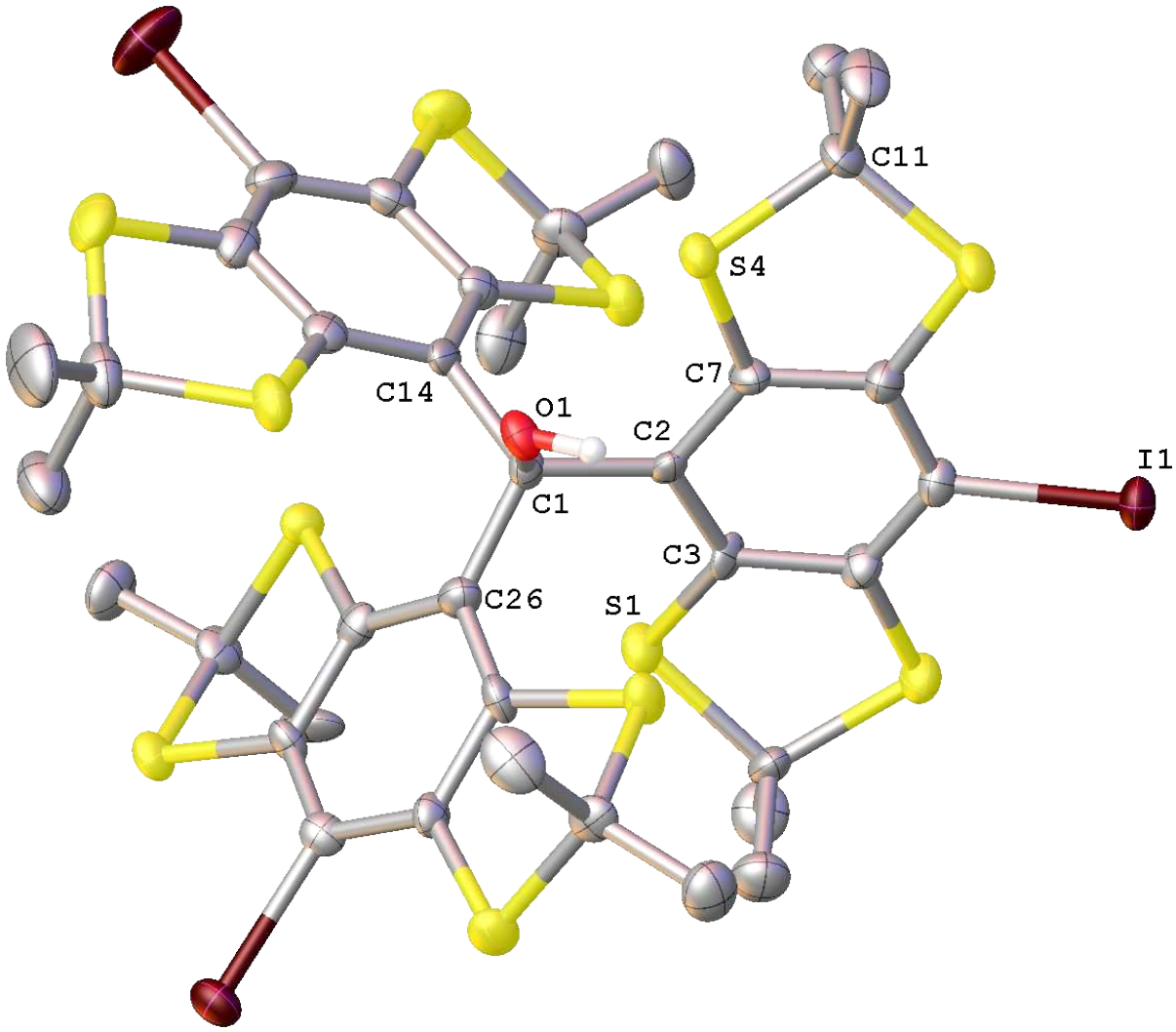

Figure **S1**: Crystal structure of trityl alcohol **5**. The ellipsoid contour was set to 30% probability level.

The CIF-file containing all structural information can be obtained online as additional Supporting Information.

Crystallographic data for **5**

Crystal Habitus	clear greenish yellow plate
Device Type	Bruker X8-KappaApexII
Empirical formula	$C_{41}H_{47}I_3O_2S_{12}$
Moiety formula	$C_{37}H_{37}I_3OS_{12}$, $C_4H_{10}O$
Formula weight	1337.20
Temperature/K	100
Crystal system	orthorhombic
Space group	$Pca2_1$
a/Å	26.4750(8)
b/Å	10.6566(3)
c/Å	18.4500(6)
α/°	90
β/°	90
γ/°	90
Volume/Å^3	5205.4(3)
Z	4
ρ_{calc} / g/cm^3	1.706
μ/mm^{-1}	2.316
F(000)	2640.0
Crystal size/mm^3	0.2 × 0.09 × 0.04
Absorption correction	empirical
T_{min}; T_{max}	0.3729; 0.7460
Radiation	MoKα (λ = 0.71073)
2Θ range for data collection/°	4.674 to 55.996°
Completeness to theta	0.998
Index ranges	$-34 \le h \le 26$, $-14 \le k \le 13$, $-24 \le l \le 24$
Reflections collected	87159
Independent reflections	12545 [R_{int} = 0.1364, R_{sigma} = 0.0917]
Data/restraints/parameters	12545/1/538
Goodness-of-fit on F^2	1.027
Final R indexes [I>=2σ (I)]	R_1 = 0.0653, wR_2 = 0.1403
Final R indexes [all data]	R_1 = 0.0789, wR_2 = 0.1497
Largest diff. peak/hole / e Å^{-3}	1.89/-1.32
Flack parameter	0.068(19)

2. Computational results

2.1 Inclusion of spin density distribution in 16•• for distance calculation

The dipolar coupling constant considering the delocalization of spin density can be described by an extended point-dipole approach[1]:

$$D = \frac{\mu_0 g^2 \beta_e^2}{4\pi h} \sum_{a=1}^{i} \sum_{b=i+1}^{N} \frac{1}{r_{ab}^3} \rho_a \rho_b \; (eq. S1)$$

Here, g equals the trityl g-factor of 2.0032, $ß_e$ is the Bohr magneton, and $\hbar$ the reduced Planck constant. r_{ab} indicates the distance between two atoms bearing the spin densities ρ_a and ρ_b. From this dipolar coupling constant, the effective interspin distance r_{eff} can be determined as:

$$r_{eff} = \sqrt[3]{\frac{\mu_0 g^2 \beta_e^2 \, 1}{4\pi h \;\; D}} \; (eq. S2)$$

Figure S2 shows the distribution of spin density within **15••** schematically. Whereas the central carbon atom of the trityl core exhibit each about 30 % of the spin density, approximately 5 % is delocalized in each phenyl ring (purple) and 0.5 % into each phenyl ring (blue). Note that the spin density on the hydrogen atoms was neglected as only 0.07 % of the spin density was localized on all 108 hydrogen atoms together. The percentage values refer to the entire spin density of 2 electrons. Since the spin density in the phenyl rings decays rapidly with the distance from the central carbon (first phenyl ring: 5 %, second phenyl ring 0.5 %), it was assumed that spin A is not delocalized across the dashed line in Figure S2 and vice versa. By this, only distances across the dashed line contribute to the dipolar coupling constant between spin A and spin B. This yields an effective interspin distance of 1.75 nm for the optimized structure of **15••**, which is in a stretched conformation. Thus, any bending of the structure shortens the distance between the two trityl centers and therefore also the effective interspin distance. In order to account for this, a molecular dynamics (MD) simulation was performed, which was then convoluted with the spin density distribution in order to obtain a distribution of the effective interspin distances. The MD simulation was carried out using the *GFN-xTB*[2] program with a simulation time of 250 ps, a time step of 4 fs and a temperature of 298 K. The DFT-optimized structure was used as an input. Then, a home-written *MATLAB* script was used to calculate the effective interspin distance for each frame of the MD simulation based on the procedure described above. The distance distribution was then obtained as a histogram of these effective interspin distances yielding the plot in Figure 7b in the main text.

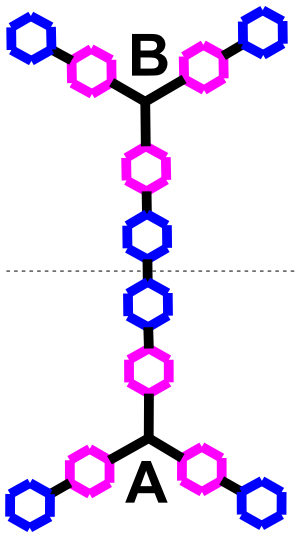

Figure S2: Schematic representation of the spin density distribution in **15••**. The central carbon atoms of the trityl core exhibit each a spin density of 0.58, the phenyl rings in purple of app. 0.10 and the phenyl rings in blue of app. 0.01.

2.2 Spin density distribution in 12•

The Mulliken spin density populations in **12•** were obtained from DFT calculations (PBE, def2-SVP). As shown by the ^{1}H-NMR spectrum in the main text (Figure 4), one signal in the pyrrolic region is strongly shifted compared to the other ones. The spin densities for the hydrogen atoms, which occur in the ^{1}H-NMR of **12•** are provided below in figure S3. Since H_{p1} features the largest spin density among the pyrrolic hydrogens, it was therefore assigned to the most-shifted signal in the NMR-spectrum (Figure 4, main text). The signals, which do not encounter a paramagnetic shift in the ^{1}H-NMR also do not hold spin density according to the DFT calculations.

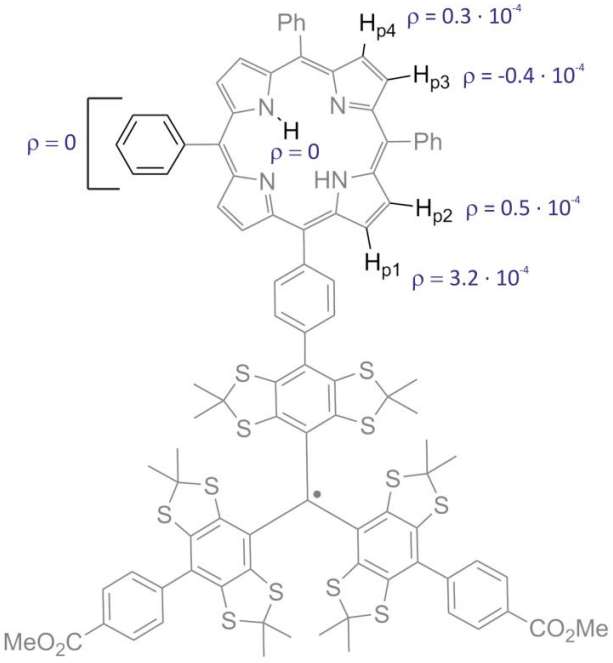

Figure S3: Spin density distribution within **12•** according to DFT.

3. Pulsed EPR

Pulsed EPR measurements were conducted on a Bruker (Bruker BioSpin GmbH, Rheinstetten, Germany) ELEXSYS E580 EPR spectrometer equipped with a CF935 helium gas-flow cryostat (Oxford Instruments, Abington, United Kingdom) and an Oxford Instruments ITC 502 temperature controller. An ER 5106QT-II resonator was used at Q-Band frequencies in combination with a 150 W TWT-amplifier (model: 187 Ka) from Applied Systems Engineering, Texas, USA. All data was acquired using quadrature detection.

Before setting up the DQC experiment, an echo-detected field sweep based on the Hahn echo sequence was conducted. Herein, the π/2 and π pulse lengths were set to 12 ns and 24 ns, respectively. The phase of the microwave was adjusted for subsequent experiments already at the stage of Hahn echo optimization. Care was taken that the full signal intensity was detected in the real channel, whereas signal contributions of the imaginary channel were minimized. By means of the echo-detected field sweep, the resonance field of the trityl signal was determined.

For the DQC-measurement, a 6-pulse sequence[3] was used in conjunction with a 64-step phase cycling in order to filter out single-quantum coherences. All pulse lengths, interpulse delay times and further relevant parameters are given in table S1.

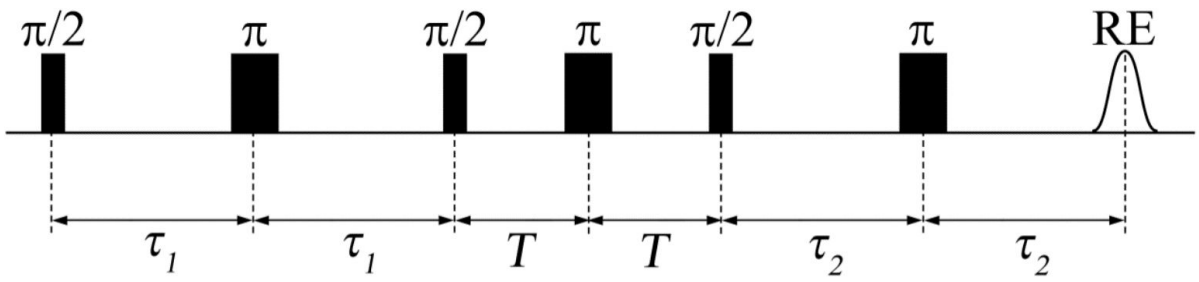

Figure S4: Applied DQC pulse sequence.

Table S1: DQC parameters.

Quantity	Value
π/2-Pulse	12 ns
π-Pulse	24 ns
τ_1, τ_2	350 ns
T	50 ns
SRT	3 ms

Data analysis was performed using the *MATLAB* toolkit *DeerAnalysis*[4,5]. The time trace was pre-processed by applying a background correction. Applying Fast Fourier Transformation as implemented in the *DeerAnalysis* software to the background-corrected time trace yields the Pake pattern shown in Figure S5.

Due to the fast oscillation with a period of 60 ns, a time increment of 4 ns was used for the DQC-experiment. However, *DeerAnalysis 2018* imposes a lower limit of 8 ns as time increment, so that half of the points are discarded prior to analysis, leading to insufficient fits of the time trace. Upon request, the program was modified by its author, *Gunnar Jeschke*, so that time steps of 4 ns could also be handled. Applying a regularization parameter $\alpha = 0.794$ yields the corresponding distance distribution. The regularization parameter was chosen from the L-curve shown in Figure S2 according to the GCV-criterion as implemented in *DeerAnalysis*.

a) **b)**

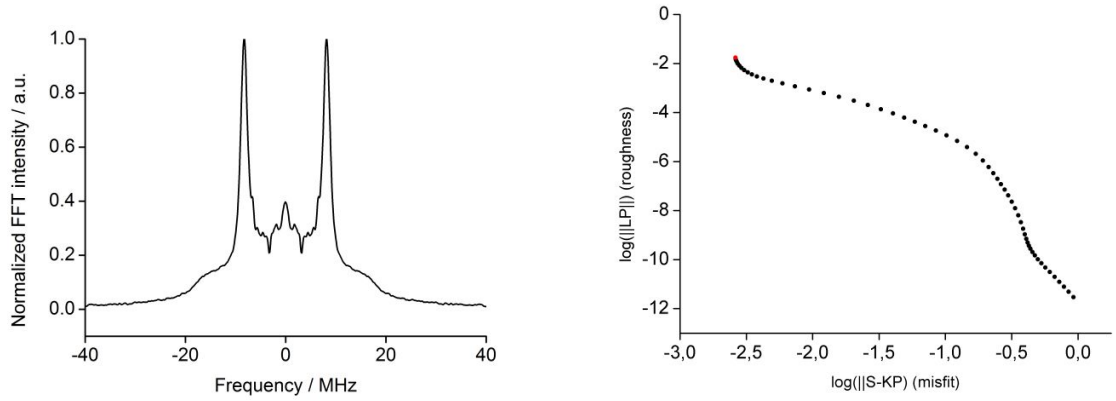

Figure S5: a) Pake pattern obtained from the Fourier Transformation of the DQC time trace. b) L-Curve of the Tikhonov-regularization. The regularization parameter chosen for data analysis is marked in red.

4. cw EPR spectroscopy

4.1 cw-EPR spectroscopy on 15•• in the liquid state

The cw X-band EPR spectrum of **15••** was simulated with *EasySpin*[6] in combination with a home-written *MATLAB* script. The position of the ^{13}C-hyperfine satellites is sensitive to an increasing J up to 550 MHz. While spectra simulated with lower J-values can be distinguished, higher J values do not change the shape of the spectrum further, as the strong coupling regime is accessed as shown in fig. S6.

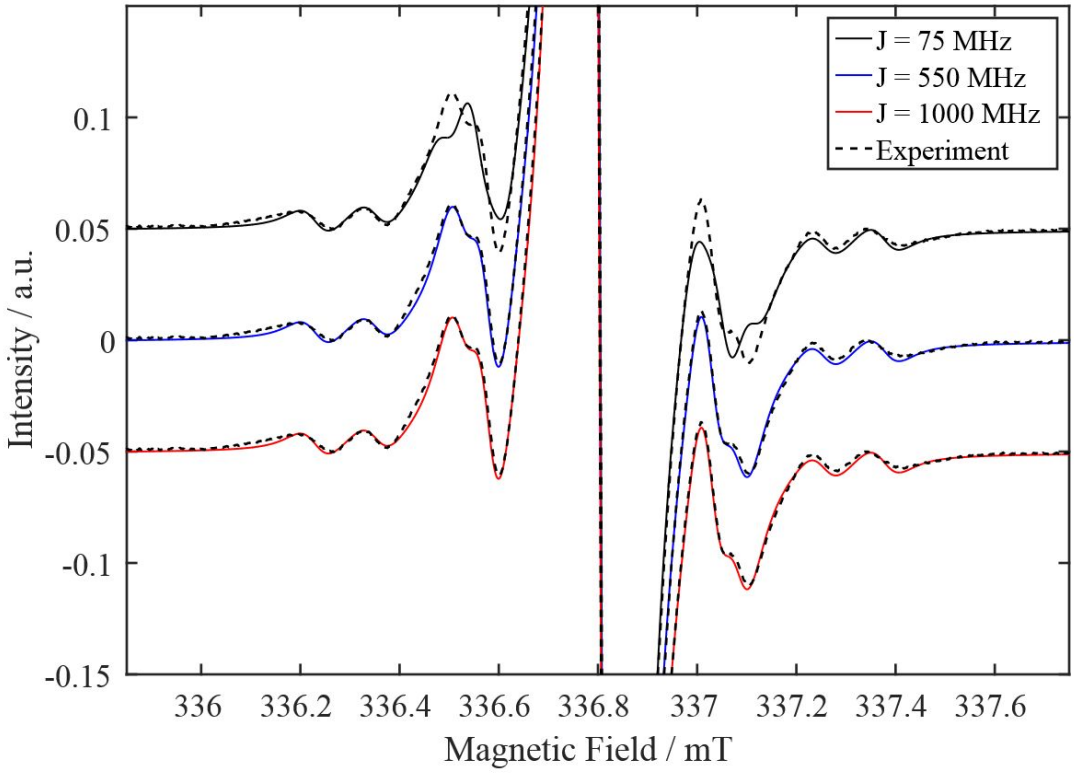

Figure S6: Room temperature *cw*-EPR spectra (X-Band) simulated for **15••** assuming different values of J. The experimental spectrum of **15••** is overlaid as a dotted line.

4.2 cw-EPR spectroscopy on 15•• in the frozen state

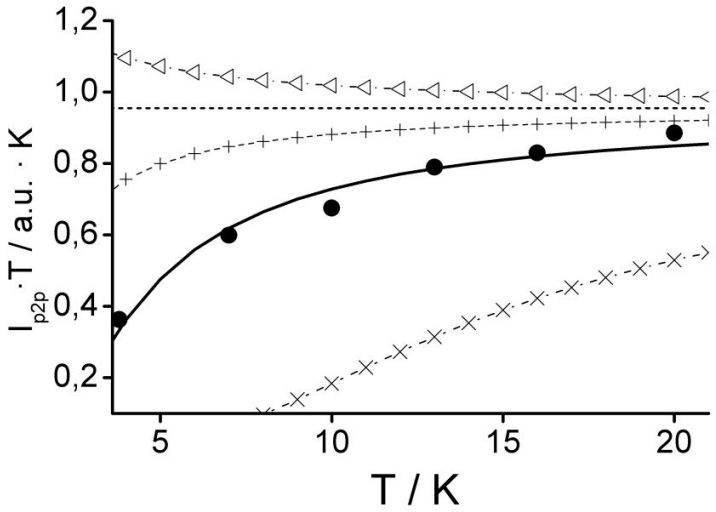

Figure **S7:** Bleany-Bowers fit of the intensity of the half-field signal I_{p2p} versus the temperature T. The best fit for the experimental data provided J = -2.81 cm^{-1}. ● exp. Data; ▬ J = - 2.81 cm^{-1}; Δ J = +1.00 cm^{-1}; + J = -1.00 cm^{-1}; × J = -10.0 cm^{-1}.

The frozen-solution *cw*-EPR spectrum of **15••** was measured as described in the main text. In the main-field region, two transitions occur. One being the $\Delta m_s = 1$ transition and yielding the Pake pattern, the other one is a $\Delta m_s = 2$ double-quantum transition giving the central line. The latter transition requires two coherent photons and therefore its intensity scales differently from the $\Delta m_s = 1$ transition with the microwave power as shown below in figure S78.

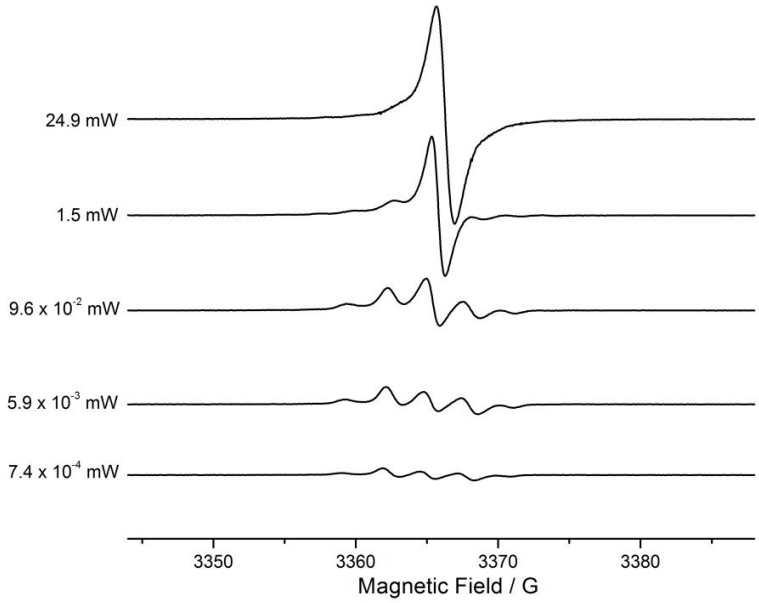

Figure **S8:** *cw*-EPR spectrum of **15••** at 100 K at different microwave power.

4.3 cw-EPR spectra of new compounds

In the section below, *continuous wave (cw) X-band* EPR spectra of the radical compounds presented in the main text are shown together with the respective fits. A summary of hyperfine coupling constants, isotropic g-values and linewidths obtained from the fits is provided in Table S2.

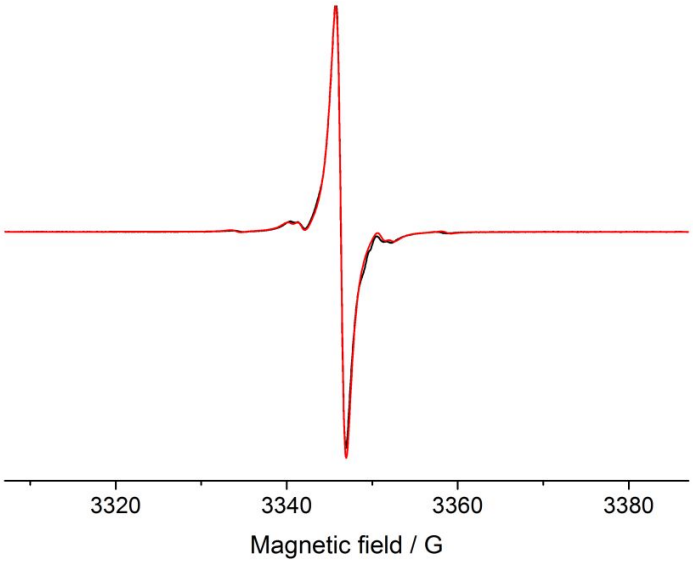

Figure **S9:** Trityl radical **3•** *cw*-EPR, X-Band, 298K.

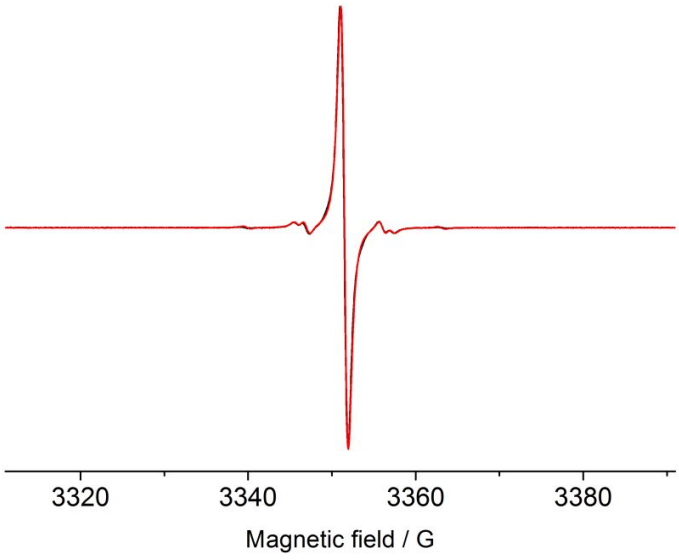

Figure **S10:** Trityl radical **6•** *cw*-EPR, X-Band, 298K.

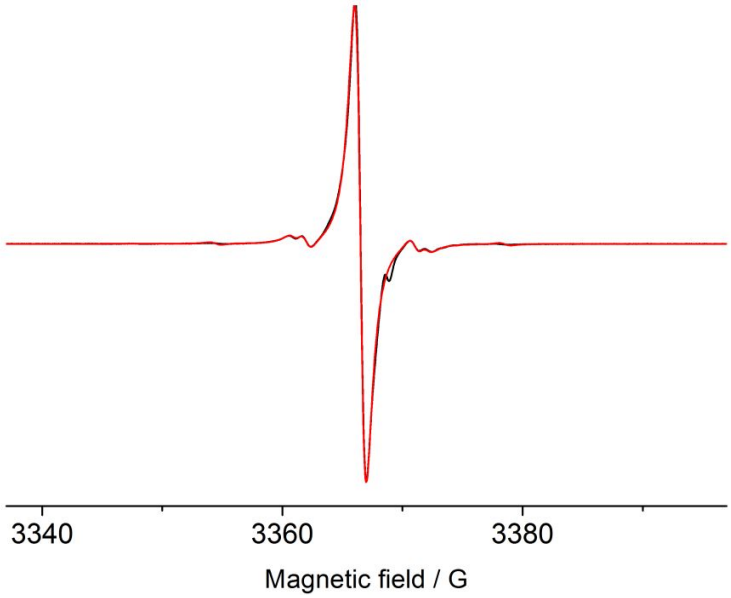

Figure **S11:** Trityl radical **7•** *cw*-EPR, X-Band, 298K.

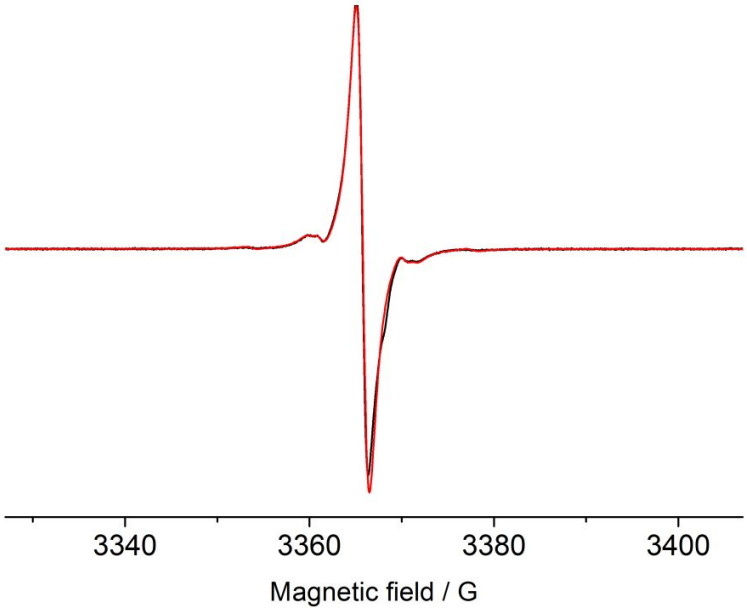

Figure **S12:** Trityl radical **8•** *cw*-EPR, X-Band, 298K.

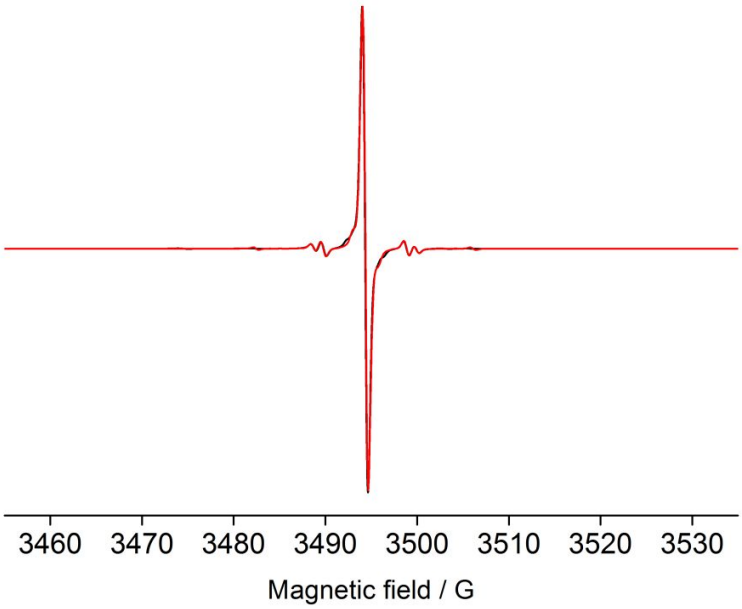

Figure **S13:** Trityl porphyrin **12•** *cw*-EPR, X-Band, 298K.

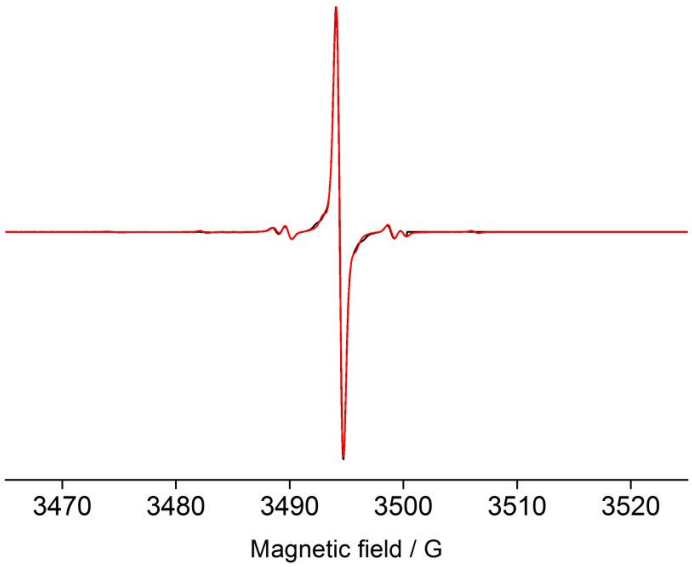

Figure **S14:** Trityl porphyrin **13•** *cw*-EPR, X-Band, 298K.

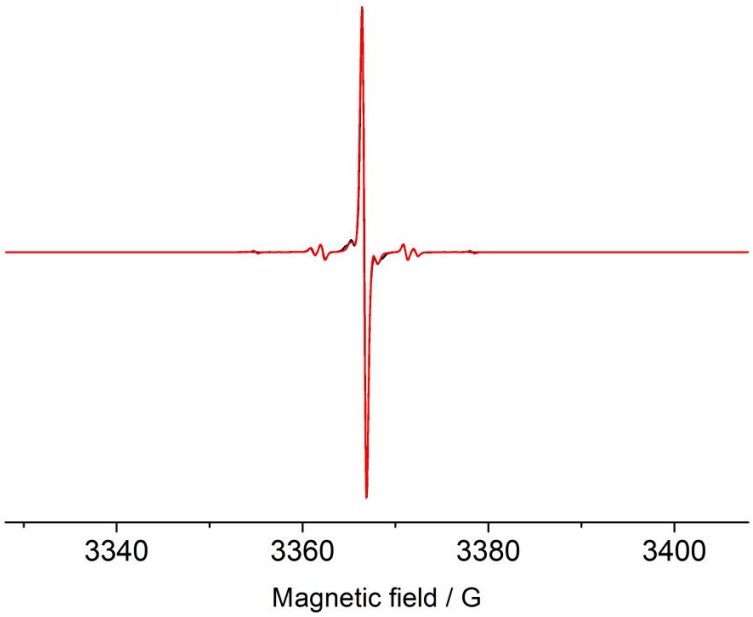

Figure **S15:** Trityl radical **16•** *cw*-EPR, X-Band, 298K.

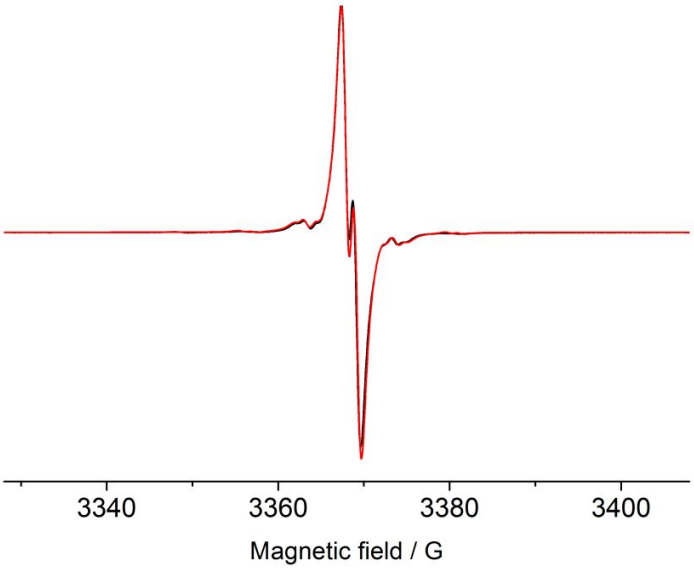

Figure **S16:** Trityl radical **17•** *cw*-EPR, X-Band, 298K.

Table **S2**: EPR parameters obtained from the fit of the *cw*-EPR spectra.

Compound	Isotropic g-value	A / MHz	lwpp Gaussian / mT	lwpp Lorenzian / mT
3•	2.0051	$^{13}C_{central}$: 68.94 $^{13}C_{ipso}$: 32.80 $^{13}C_{ortho}$: 26.08	0.0020	0.1224
6•	2.0032	$^{13}C_{central}$: 65.16 $^{13}C_{ipso}$: 31.56 $^{13}C_{ortho}$:25.56	0.0502	0.0626
7•	2.0038	$^{13}C_{central}$: 67.67 $^{13}C_{ipso}$: 31.56 $^{13}C_{ortho}$:25.56	0	0.0966
8•	2.0044	$^{13}C_{central}$: 67.09 $^{13}C_{ipso}$: 31.80 $^{13}C_{ortho}$:25.20	0	0.1415
12•	2.0032	$^{13}C_{central}$: 66.19 $^{13}C_{ipso}$:31.42 $^{13}C_{ortho}$ 25.38 $^{13}C_{para}$: 6.57 $^{13}C_{meta}$:4.02	0.0482	0.0244
13•	2.0031	$^{13}C_{central}$: 66.75 $^{13}C_{ipso}$: 31.09 $^{13}C_{ortho}$: 25.32 $^{13}C_{para}$: 6.77 $^{13}C_{meta}$:4.50	0.0473	0.0282
15••	2.0036	$^{13}C_{ipso}$: 31.25 $^{13}C_{ortho}$: 25.30	0.0160	0.0551
15•• (100K)	g_{xx} = 2.0036 g_{yy} = 2.0036 g_{zz} = 2.0034	$^{13}C_{ipso}$: 31.25 $^{13}C_{ortho}$: 25.30 D_{ee} = 11.17	0.0787 0.0635 ($2x\Delta m_S = 1$)	0.0402 0.0731 ($2x\Delta m_S = 1$)
16•	2.0032	$^{13}C_{central}$: 66.44 $^{13}C_{ipso}$: 31.01 $^{13}C_{ortho}$: 24.94 $^{13}C_{para}$: 7.87 $^{13}C_{meta}$ 5.74	0.0396	0.0172
17•	2.0032	$^{13}C_{central}$: 67.82 $^{13}C_{ipso}$: 31.93 $^{13}C_{ortho}$: 25.54 $^{1}H_{alkyne}$: 3.72	0.0135	0.1095

5. Reaction of 3• with n-butyl lithium

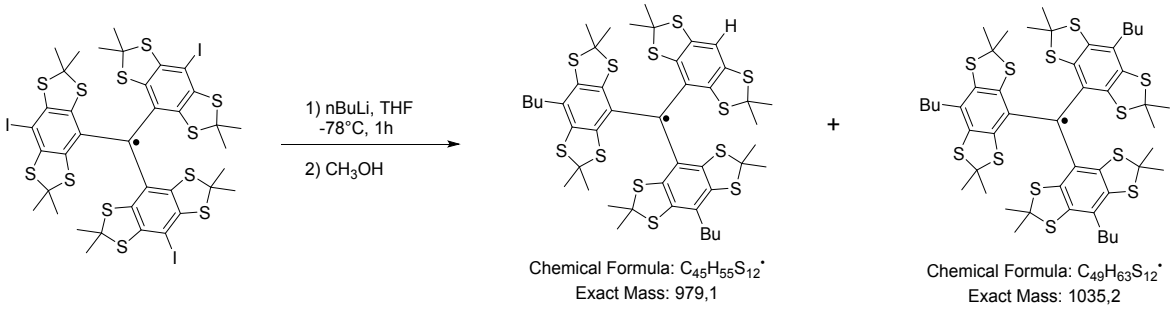

Trityl radical **3•** (100 mg, 79 µmol) was dissolved in 8 mL dry THF and n-butyl lithium (98 µL 2.5 M in hexanes, 3.00 eq.) was added at -78 °C. The deep green solution turns deep purple upon the addition of butyl lithium. After 1 h, 0.5 mL methanol was added and the solution was warmed up to room temperature and stirred for 30 min. Then, solvents were removed under reduced pressure and the crude product was subjected to MALDI(+)-MS analysis, which revealed the product composition displayed above. Interestingly, the main products were coupling products with butyl lithium and not the exchange products.

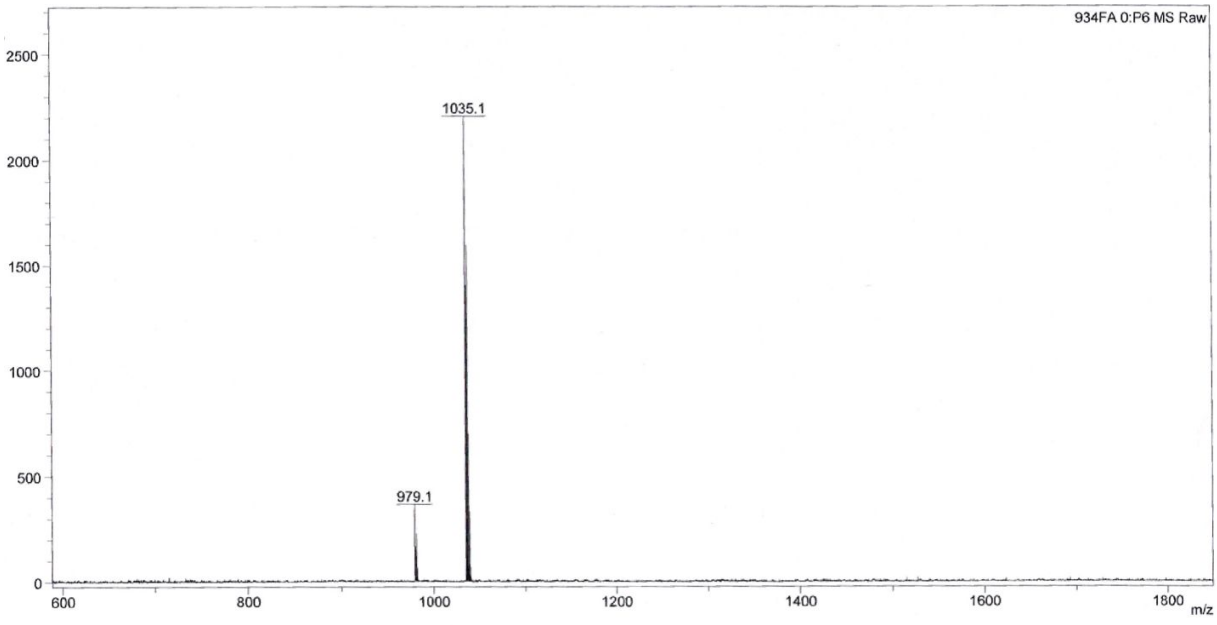

Figure **S17**: MALDI(+)-spectrum of crude product of the reaction of **3•** with *n*BuLi.

6. Catalysts for Suzuki-Coupling

For the reaction of **5** to **6-OH**, the suitability of catalyst $Pd(OAc)_2$ + 2 $^tBu_3P$ was also tested. The aim of this was to test whether the oxidative addition of Pd^0 is inhibited by the steric situation, since the electron-rich $^tBu_3P$ would accelerate this step. However, one sees a decrease in the reaction rate, presumably due to the large cone-angle of $^tBu_3P$ and the steric demand associated with it. The reaction was carried out under the same conditions as described in the synthesis section. ^{1}H-NMR allowed to analyze the product mixture, since the signal of the central OH-group is quite sensitive to para-functionalization.

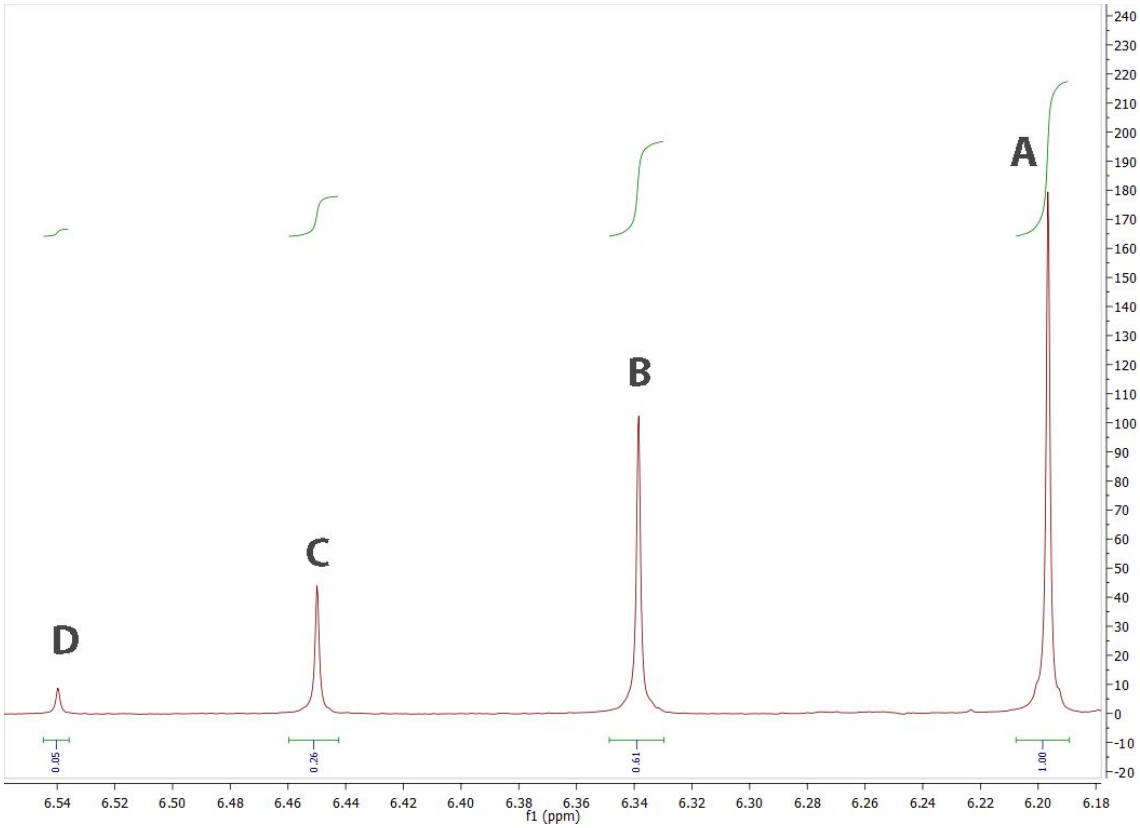

Figure **S18**: ^{1}H-NMR-spectrum (500 MHz) of the crude product. Signal A refers to the starting material **5**, signal D to **6-OH**. Signals C and B are originated from the bis- and mono-coupling product, respectively.

7. Oxygen sensitivity of 15••

During purification of the trityl biradical **15••**, a bleaching of the deep green color during column chromatography was observed. This was attributed to an enhanced sensitivity towards oxygen and partial oxidation, which was also observed for a similar trityl biradical before[7]. This behavior might be explained by the triplet state for **15••**, which is populated by 49.5 % at a *J* of -2.8 cm^{-1} and at 298 K according to the Boltzmann distribution. Since atmospheric oxygen is also a triplet, the kinetic inhibition of the oxidation could be reduced compared to a doublet trityl radical or a singlet trityl alcohol. Figure S19 shows the ESI(+) mass spectrum of **15••** synthesized directly from trityl radical **7•**, the intensity of the $[M+17]^+/[M+16]^+$ peak is remarkable here. Note that both peaks overlap and correspond to the trityl alcohol (**15-OH•**) and the sulfoxide oxidation products. The mass spectrum in figure S20 was recorded from **15••** synthesized via the trityl alcohol approach as described in the main text. Here, the peaks assigned to oxidation products exhibit less intensity. The remaining intensity accounts for the monoradical content as seen in the *cw* EPR spectrum.

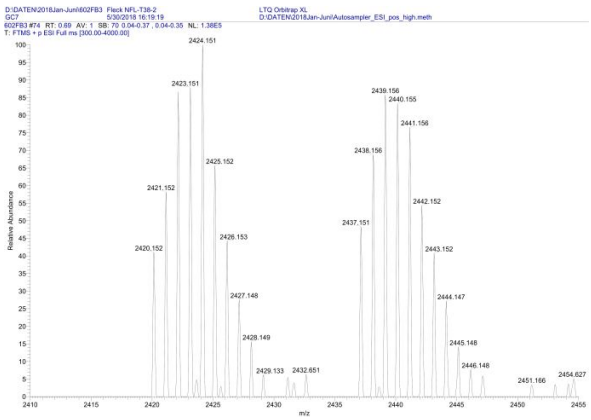

Figure **S19**: ESI(+)-MS of **15••** synthesized from trityl radical **7•** after column chromatography.

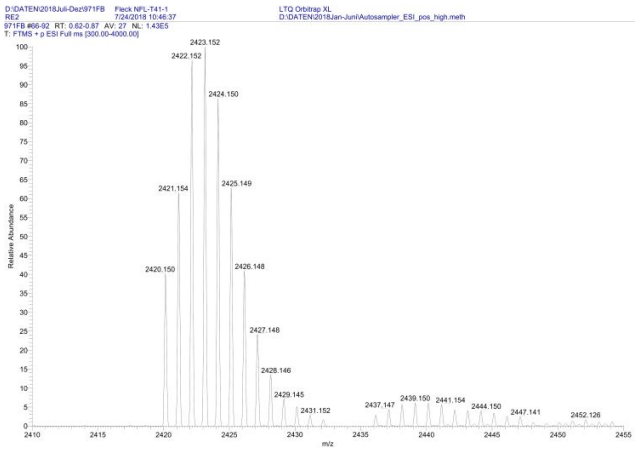

Figure **S20**: ESI(+)-MS of **15••** synthesized from trityl alcohol **9**.

8. Sonogashira reactions

8.1 General procedure for *Sonogashira-Hagihara* reactions

150 mg of **5** (120 µmol), Pd-catalyst (6 µmol, 5 mol%), CuI (12 µmol, 10 mol%) were dissolved in 20 mL of the solvent mixture. Then, the corresponding acetylene (480 µmol, 4 eq.) was added and the reaction mixture was stirred at the corresponding temperature. Solvents were removed under reduced pressure subsequently and the residue was taken up in dichloromethane (30 mL). After washing with 0.1M Na_2EDTA and brine, the organic phase was separated, dried over $MgSO_4$ and the solvents were removed under reduced pressure.

The crude product was then dried in oil-pump vacuum (10^{-3} mbar) and subjected to analysis without further purification.

8.2 General remarks

The C-C cross coupling under *Sonogashira-coupling* conditions was tested on trityl alcohol **5** with 2-methyl-3-butyn-2-ol, trimethylsilyl acetylene (TMS-acetylene), and triisopropylsilyl acetylene (TIPS-acetylene) as alkynes and using common solvents and catalysts (THF/DIPEA or Et_3N, $Pd(Ph_3P)_2Cl_2$, CuI, 70°C, 16h). These reaction conditions showed several side products in the MALDI-MS spectra alongside to the coupling products, as shown in figures S21, S36, and S37. The sum formulas of the side products were obtained via APCI-HRMS (S23-30, S38) and revealed an uptake of alkyne equivalents additional to the desired coupling reaction. Therefore, these side-products are called “insertion products”, as they presumably emerge from an insertion of alkyne into the trityl backbone. It is noteworthy, that this unusual reactivity was observed systematically for all alkynes mentioned above. Using only the copper catalyst led to no reaction at all, whereas the sole use of $Pd(Ph_3P)_2Cl_2$ provided both coupling and insertion products. Other palladium catalysts such as $Pd(OAc)_2$ + $P(^tBu_3P)_3$ or $Pd(dppf)Cl_2$ proved to be inferior both for the coupling and the insertion reaction. Moreover, the choice of either DIPEA or Et_3N as cosolvent did not influence the product composition. Except for the C-I bond, the C-S bonds of the annulated 1,3-dithianes are the only reactive bonds within the molecule. Interestingly, also *Iovine et al.*[8] observed a competitive carbothiolation process *via* alkyne insertion into the C-S bond of phenylthioacetate under palladium catalysis condition. We thus assume an analogous migratory insertion of alkyne into a C-S bond of the trityl moiety.

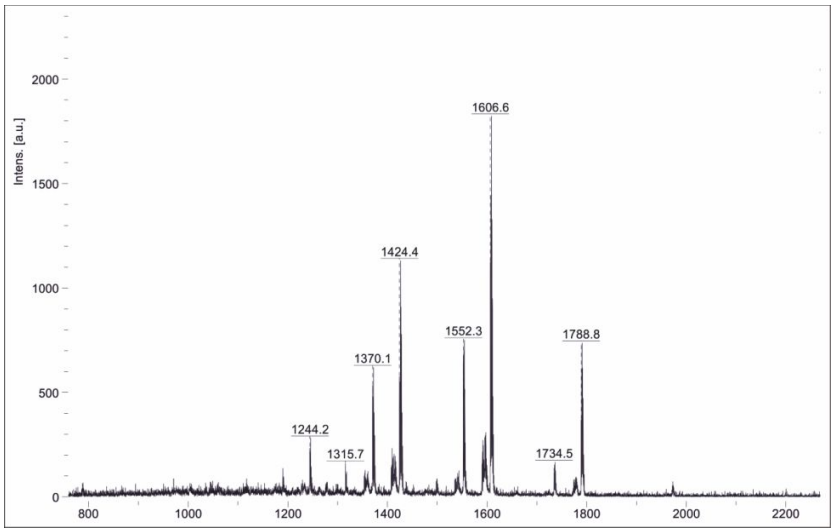

Figure S21: Reaction of **5** with 4 eq. TIPS-acetylene, $Pd(Ph_3P)_2Cl_2$, and CuI in THF/DIPEA (3:1). The MALDI(+)-spectrum of the product mixture obtained is shown. Notation: C_xI_y = x times coupling (x = 1 – 3) and y times insertion of alkyne. Assignment of peaks [*m*/*z*]: 1315.7 (C_1I_0), 1370.1 (C_2I_0), 1424.4 (C_3I_0), 1552.3 (C_2I_1), 1606.6 (C_3I_1), 1734.5 (C_2I_2), 1788.8 (C_3I_2). The peak at 1244.2 corresponds to a C_2-product with a remaining hydrogen instead of iodine.

Whereas the same reactivity was observed for **3•** (Figure S31) and **6**, no insertion reactivity was observed for the unsubstituted parent compound, suggesting that the vicinal iodine seems to be crucial for the insertion reaction. According to the mechanism proposed below in Figure S22, the insertion reaction starts with an oxidative addition of palladium(0) into the C_{ar}-I bond analogous to the coupling reaction. Followed by a 1,2-palladium shift, the insertion reaction runs further through a π-coordination of the alkyne to the palladium and a subsequent migratory insertion into the C-S bond. Such a reaction step would be sensitive to steric demands, which is in agreement with our observation, that the insertion reaction becomes disfavored for the bulky TIPS-acetylene compared to 2-methyl-3-butyn-2-ol and TMS-acetylene.

Moreover, the product with presumably one coupled and one inserted 2-methyl-3-butyn-2-ol (C_1I_1) was isolated by column chromatography and in an amount sufficient for ^{1}H-NMR. As only singlets appeared in the olefin region (Figure S39), a cyclic structure was proposed as given in fig. S22. Surprisingly, the insertion reaction can be suppressed by the use of refluxing CH_2Cl_2/Et_3N as solvent, which is, however, less common for *Sonogashira* couplings. For TIPS-acetylene with $Pd(Ph_3P)_2Cl_2$, this leads solely to coupling products and no insertion (Figure S32), whereas for the sterically less demanding 2-methyl-3-butyl-2-ol, insertion products are observed, again. However, in that case both the insertion and the coupling reaction seem to be equitable,

since they always occurred side by side throughout the entire reaction progress (fig. S42 – S46). Moreover, the use of Pd(dppf)Cl_2 in CH_2Cl_2/Et_3N caused less insertion compared to Pd$(Ph_3P)_2Cl_2$ for 2-methyl-3-butyn-2-ol as coupling substrate (fig. S47).

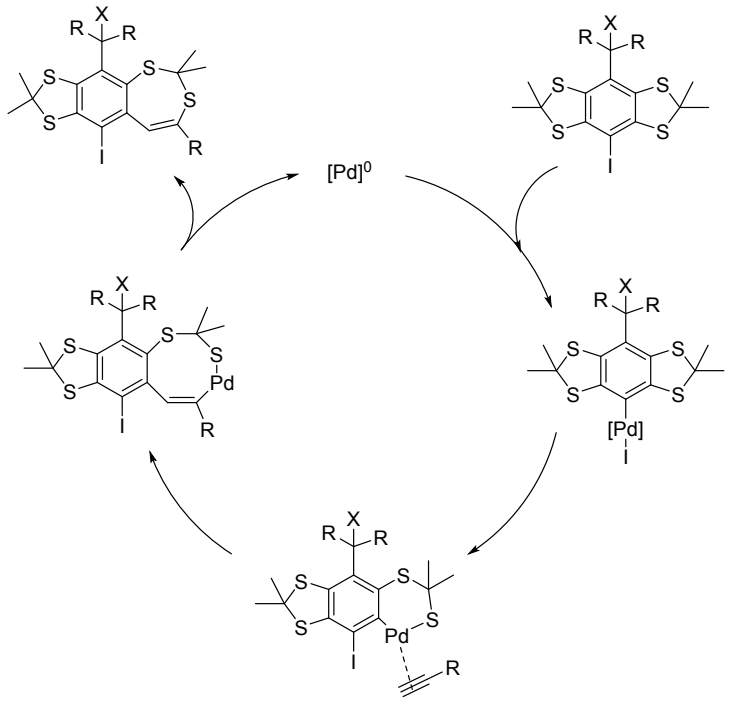

Figure S22: Proposed mechanism of alkyne uptake into the trityl scaffold by a Pd-catalyzed carbothiolation process. Note that X can be either –OH or a radical center and R is a thioaryl-substituent.

All in all, the palladium catalyst is responsible for a presumed migratory insertion of alkyne into the C-S bonds of the thioacetal and which is competing with the *Sonogashira* coupling. By choosing an appropriate solvent, CH_2Cl_2, and a sterically demanding alkyne, TIPS-acetylene, this side reaction can be suppressed. Nonetheless, also the coupling reaction suffers from the steric demand both of the trityl moiety and the TIPS-acetylene, and thus becomes slow. Accordingly, the *Sonogashira-Hagihara* coupling reaction is not versatile with trityl alcohols/radicals and can only be taken into account for bulky acetylenes, such as TIPS-acetylene.

8.3 Reaction with TIPS-acetylene

Following the general procedure, **5** was reacted with triisopropylsilylacetylene in THF/Et_3N 3:1 (v/v) yielding a mixture of insertion and coupling products. An assignment of the peaks to sum formulas and products is presented in table S3. The APCI-spectra are shown below in order of ascending mass is indicated in table S3 (Figures S23-S30).

In the following, products will be denominated with a C_xI_y notation, where *x* indicates the number of coupled alkynes and *y* the number of inserted alkynes according to the sum formula. Note, that APCI-data is presented here. During the ionization process, an α-cleavage at the central carbon is observed leading to an abstraction of the –OH group. Therefore, the $[M-17]^+$ peaks are shown here, whereas the MALDI(+)-spectrum shows $[M]^+$ peaks. The signal intensities in MALDI(+) spectra do not correspond to the sample composition in a quantitative manner, though a qualitative estimate can be obtained from these.

Table S3: Mass spectrometric data for the product mixture obtained with TIPS-acetylene

MALDI(+)-peak $[M]^+$	APCI-peak $[M-17]^+$	sum formula of the corr. trityl alcohol	product type	HRMS figure
1244.2	1227.2450	$C_{59}H_{80}OS_{12}Si_2$	[M-I] C_2I_0	S22
1315.4	1298.9026	$C_{48}H_{58}I_2OS_{12}Si$	C_1I_0	S23
1370.1	1353.1399	$C_{59}H_{79}IOS_{12}Si_2$	C_2I_0	S24
1424.4	1407.3796	$C_{70}H_{100}OS_{12}Si_3$	C_3I_0	S25
1552.3	1535.2886	$C_{70}H_{101}IOS_{12}Si_3$	C_2I_1	S26
1606.6	1589.5247	$C_{81}H_{122}OS_{12}Si_4$	C_3I_1	S27
1734.5	1717.4338	$C_{81}H_{122}IOS_{12}Si_4$	C_2I_2	S28
1788.8	1771.6735	$C_{92}H_{144}OS_{12}Si_5$	C_3I_2	S29

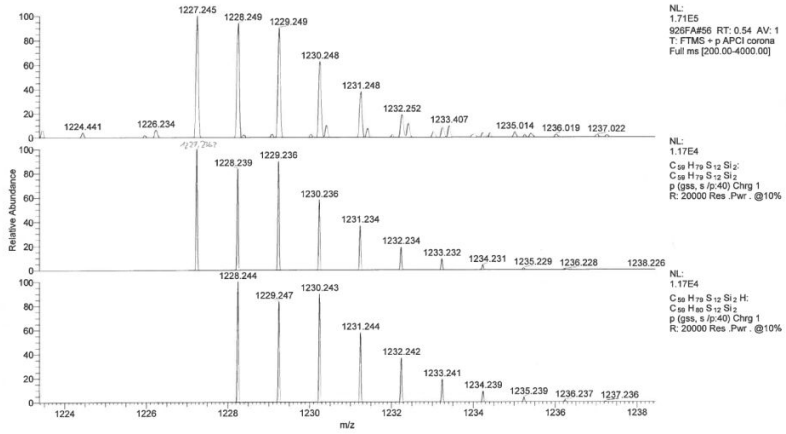

Figure **S23**: APCI-HRMS of the [M-I] C_2I_0 product.

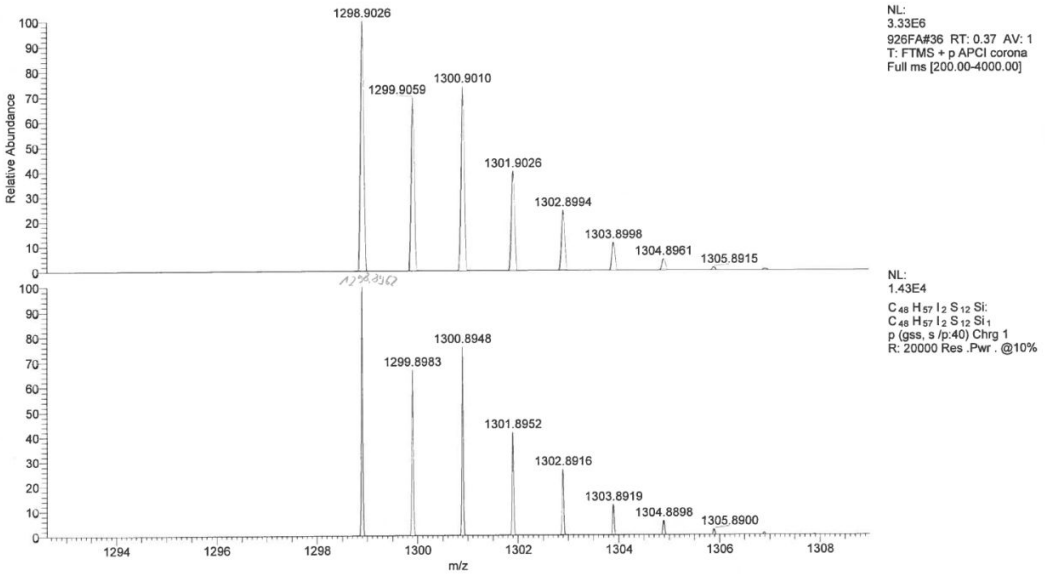

Figure **S24:** APCI-HRMS of the C_1I_0 product

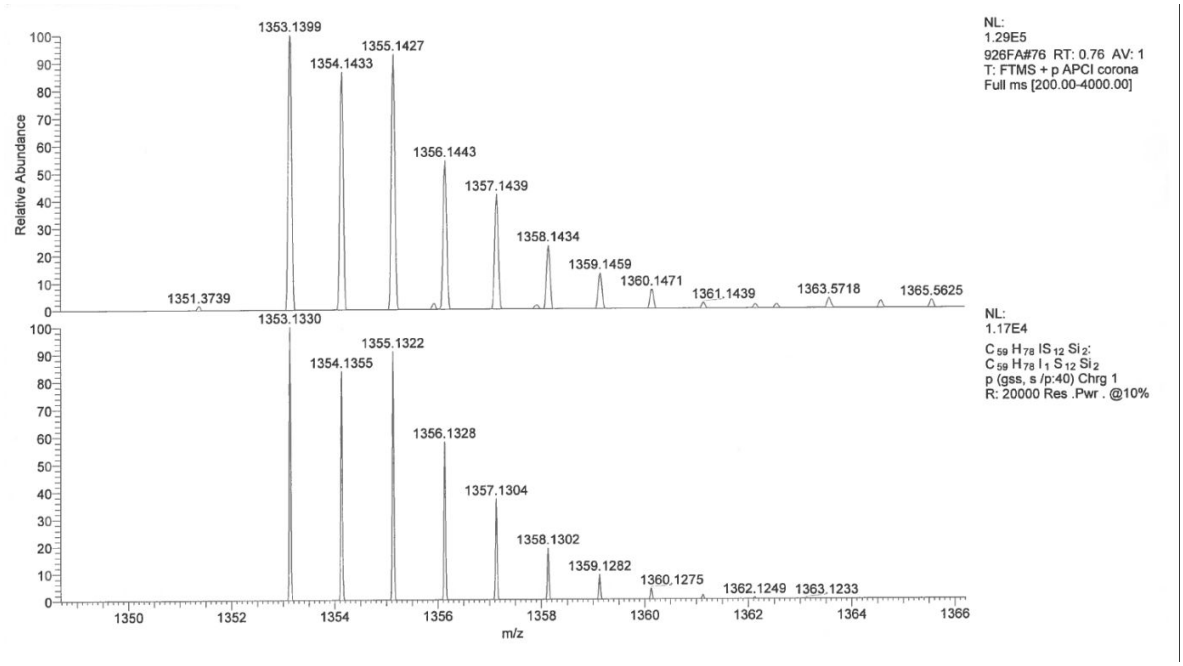

Figure **S25:** APCI-HRMS of the C_2I_0 product

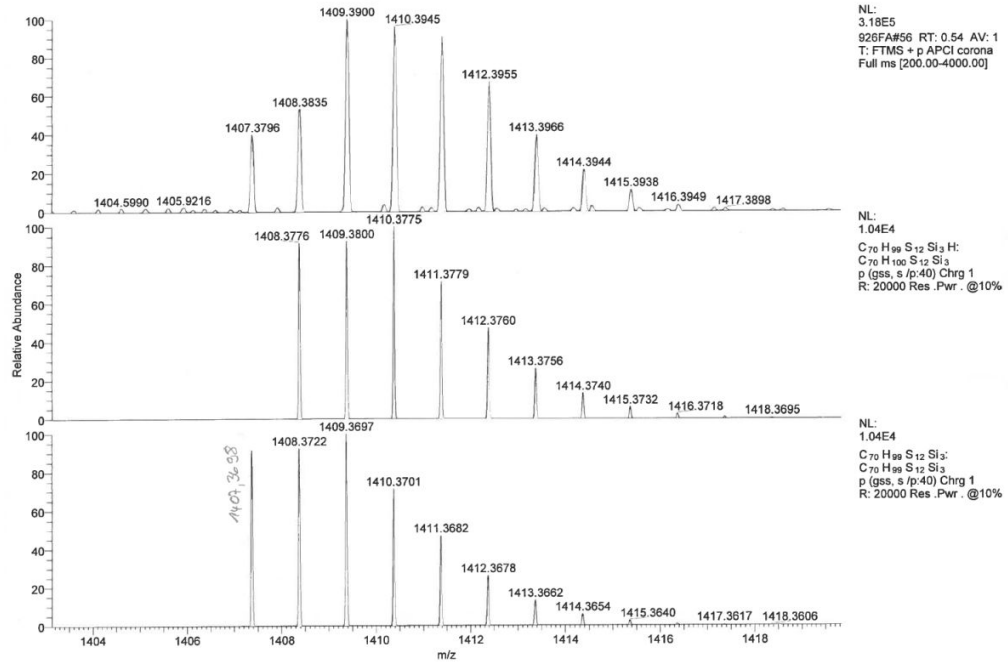

Figure **S26:** APCI-HRMS of the C_3I_0 product

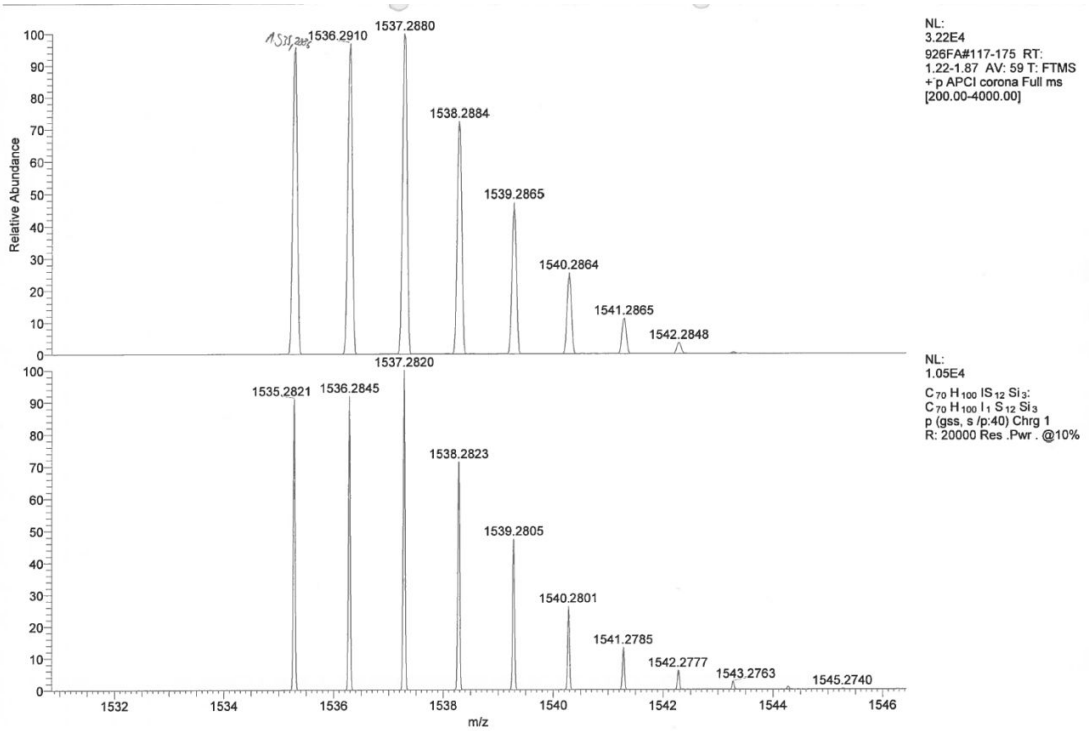

Figure **S27:** APCI-HRMS of the C_2I_1 product

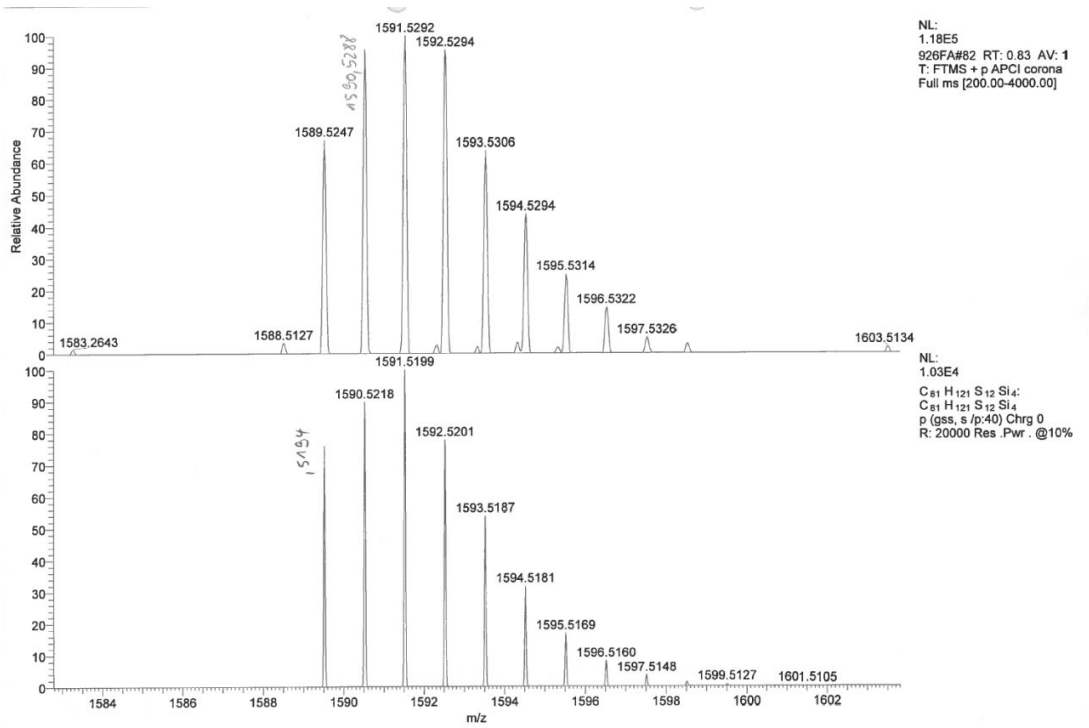

Figure **S28:** APCI-HRMS of the C_3I_1 product

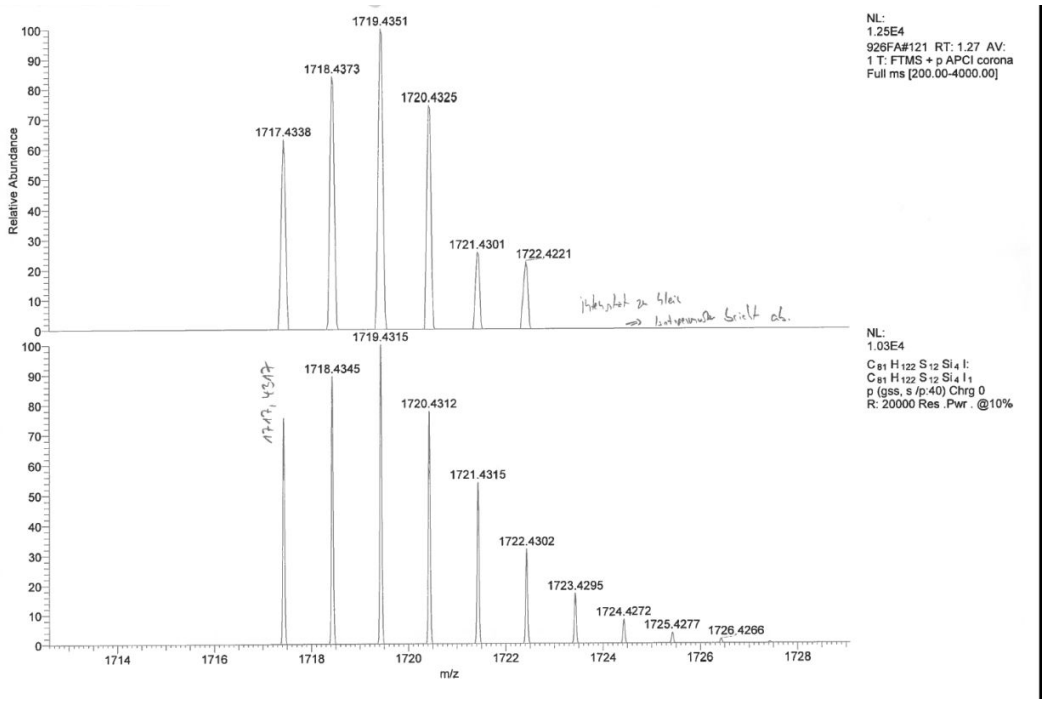

Figure **S29:** APCI-HRMS of the C_2I_2 product

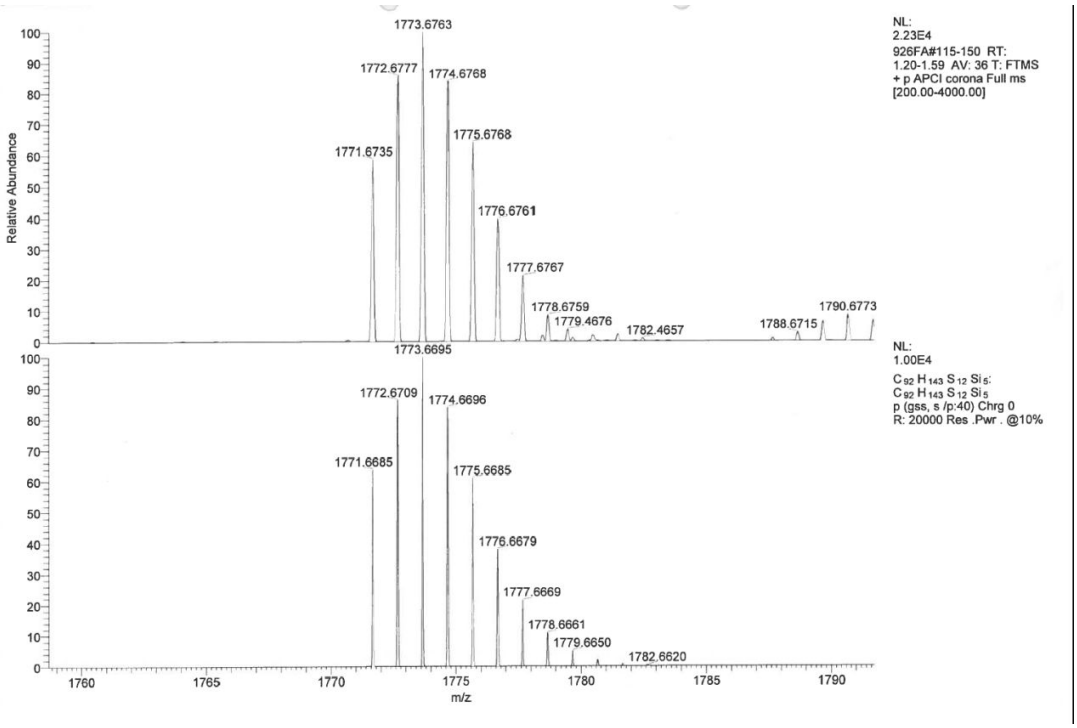

Figure **S30:** APCI-HRMS of the C_3I_2 product

For radical **3•**, an analogous reactivity was observed. However, **3•** is decently less soluble in THF/Et_3N than **5**, leading to unreacted starting material within the product mixture. Nonetheless, insertion products occur here as well.

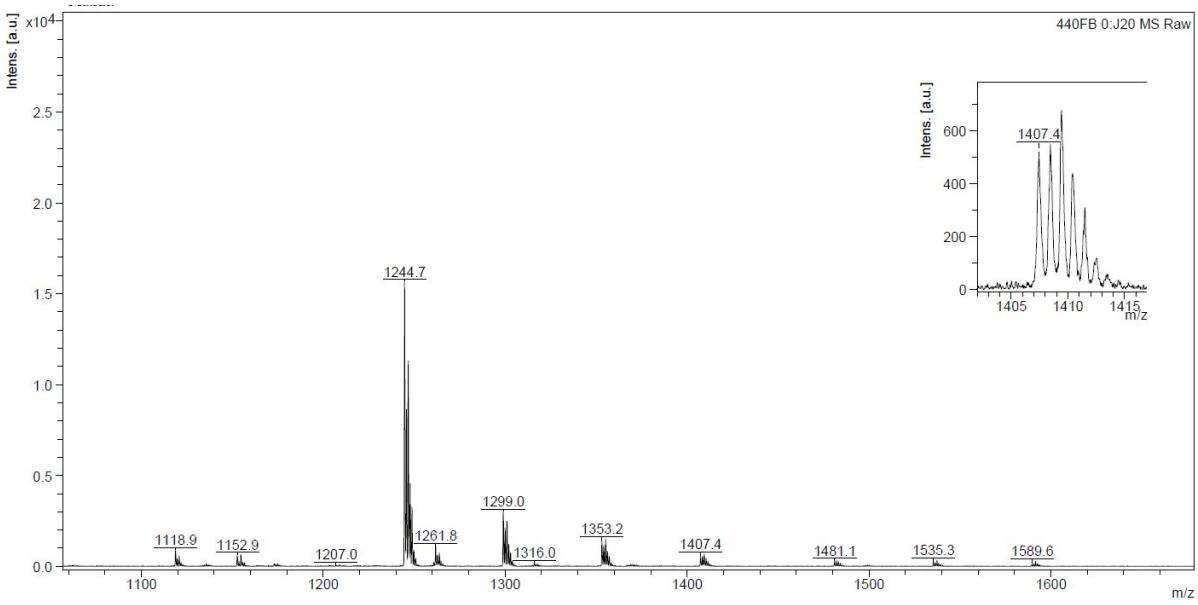

Figure **S31:** MALDI(+)-spectrum of the product mixture.

Table **S4:** Mass spectrometric data for the product mixture obtained from the reaction of **3•** with TIPS-acetylene.

MALDI(+)-peak $[M]^+$	sum formula of the corr. trityl alcohol	product type
1244.7	$C_{37}H_{36}I_3S_{12}$	C_0I_0
1299.0	$C_{48}H_{57}I_2S_{12}Si$	C_1I_0
1353.2	$C_{59}H_{78}IS_{12}Si_2$	C_2I_0
1407.4	$C_{70}H_{99}S_{12}Si_3$	C_3I_0
1481.1	$C_{59}H_{79}I_2S_{12}Si_2$	C_1I_1
1535.3	$C_{70}H_{100}IS_{12}Si_3$	C_2I_1
1589.6	$C_{81}H_{121}S_{12}Si_4$	C_3I_1

In the solvent system CH_2Cl_2/Et_3N 1:1 (v/v), no insertion products were observed as the MALDI(+)-spectrum below shows (Figure S32), even though no quantitative conversion was achieved. The corresponding HRMS-APCI data is provided below in order of ascending mass and indicated in table S5 (Figures S33-35).

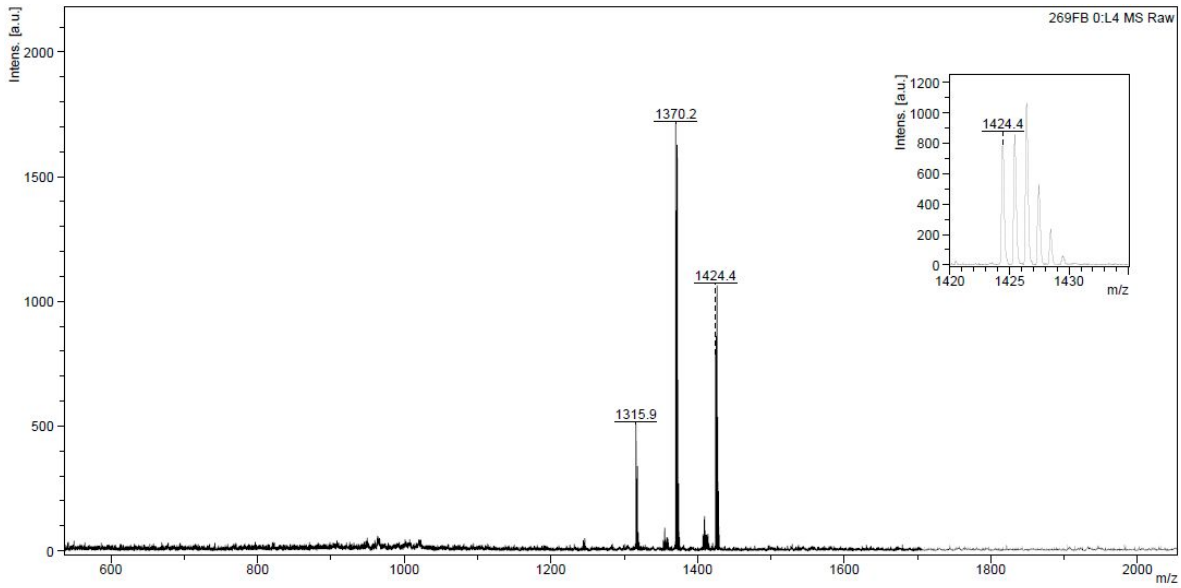

Figure **S32:** MALDI(+)-spectrum of the product mixture.

Table **S5**: Mass spectrometric data for the product mixture obtained from the reaction of **5** with TIPS-acetylene in dichloromethane/triethylamine

MALDI(+)-peak $[M]^+$	APCI-peak $[M-17]^+$	sum formula of the corr. trityl alcohol	product type	HRMS figure
1315.9	1298.8998	$C_{48}H_{58}I_2OS_{12}Si$	C_1I_0	S32
1370.2	1353.1340	$C_{59}H_{79}IOS_{12}Si_2$	C_2I_0	S33
1424.4	1407.3715	$C_{70}H_{100}OS_{12}Si_3$	C_3I_0	S34

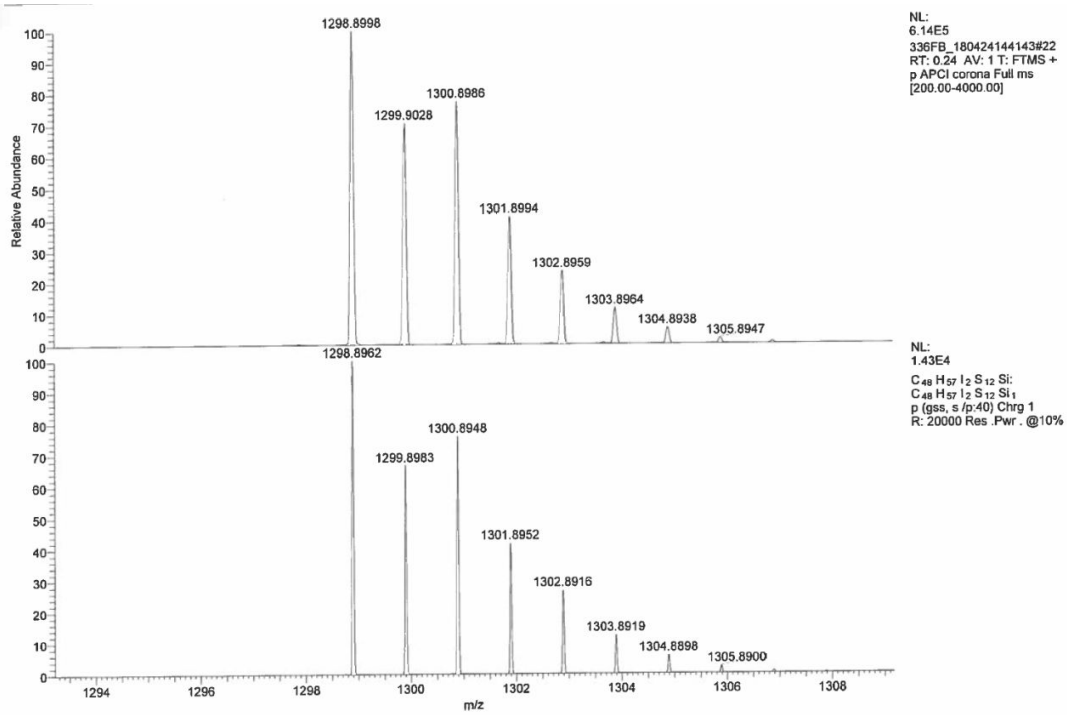

Figure **S33:** APCI-HRMS of the C_1I_0 product

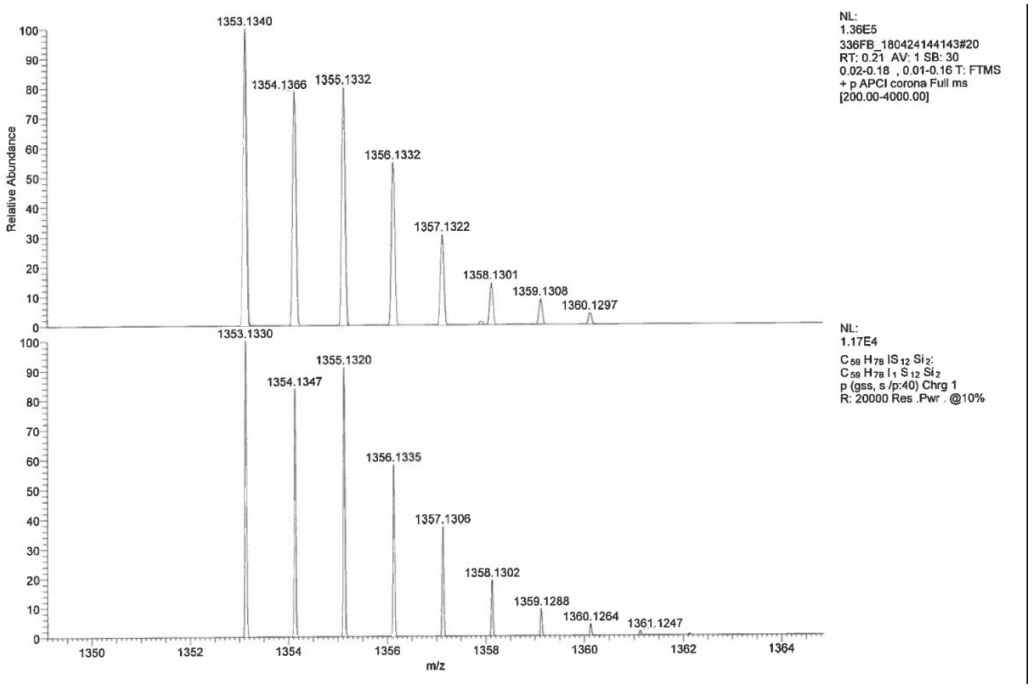

Figure **S34:** APCI-HRMS of the C_2I_0 product

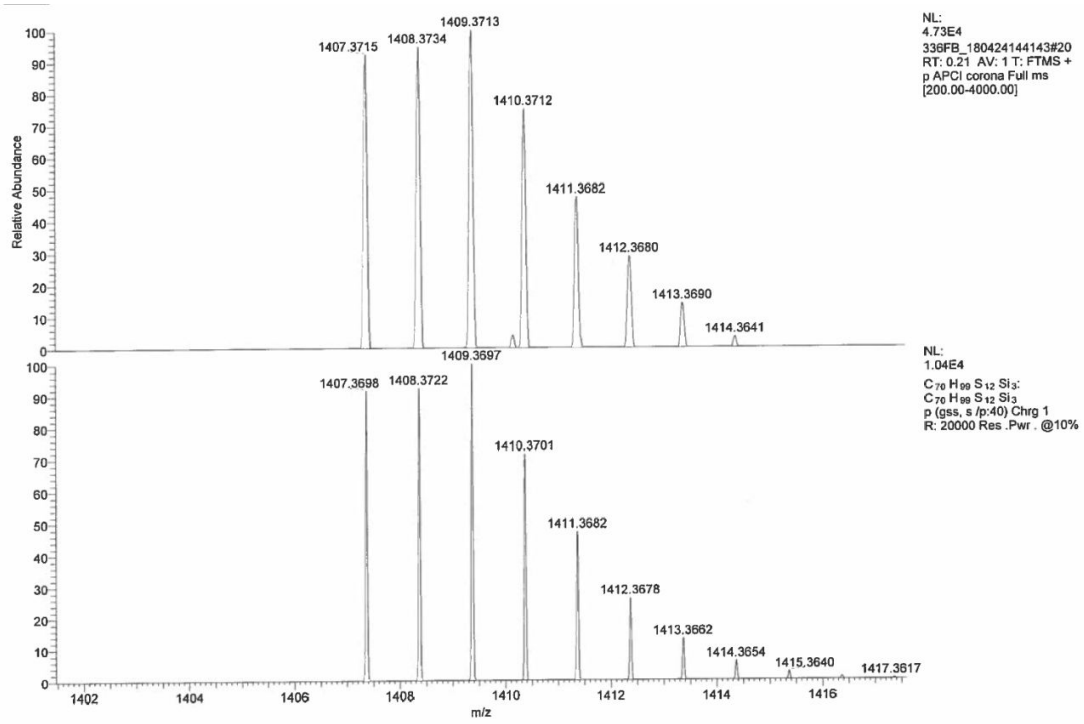

Figure **S35:** APCI-HRMS of the C_3I_0 product

8.4 Reaction with trimethylsilylacetylene

Following the general procedure, **5** was reacted with trimethylsilylacetylene in THF/Et_3N 3:1 (v/v) yielding a mixture of insertion and coupling products as shown by the MALDI spectrum below.

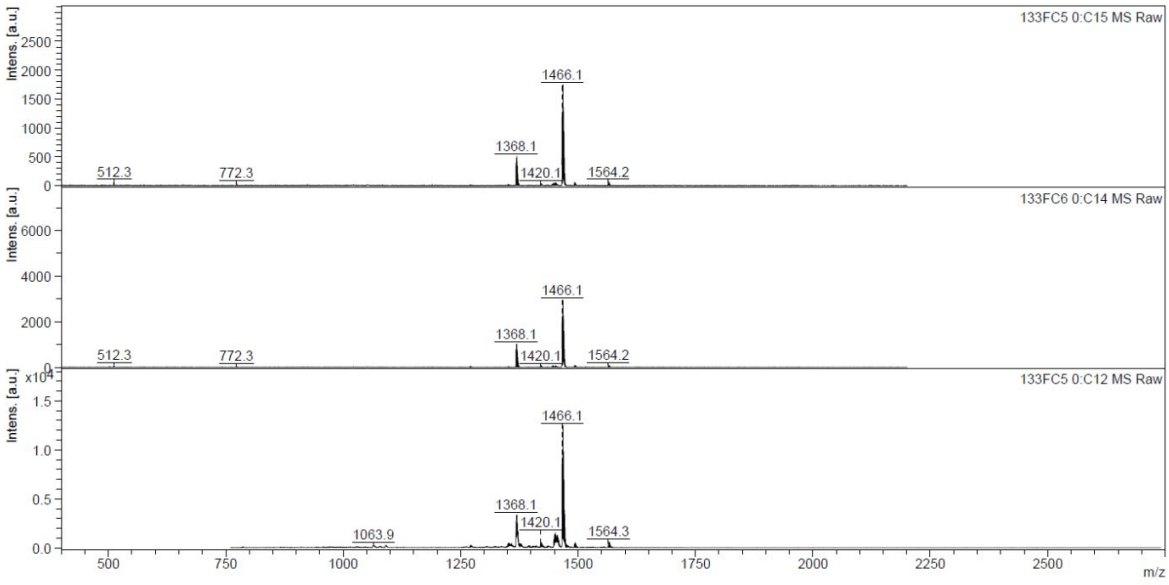

Figure **S36:** MALDI(+)-spectrum of the product mixture

Table **S6:** MALDI data for the product mixture from the reaction of **5** with TMS-acetylene.

MALDI(+)-peak $[M]^+$	sum formula of the corr. trityl alcohol	product type
1368.1	$C_{62}H_{84}OS_{12}Si_5$	C_3I_2
1466.1	$C_{67}H_{94}OS_{12}Si_6$	C_3I_3
1564.2	$C_{72}H_{104}OS_{12}Si_7$	C_3I_4

8.5 Reaction with 2-Methyl-3-butyn-2-ol

Following the general procedure, **5** was reacted with 2-Methyl-3-butyn-2-ol in THF/Et_3N 3:1 (v/v) yielding a mixture of insertion and coupling products as shown by the MALDI spectrum below.

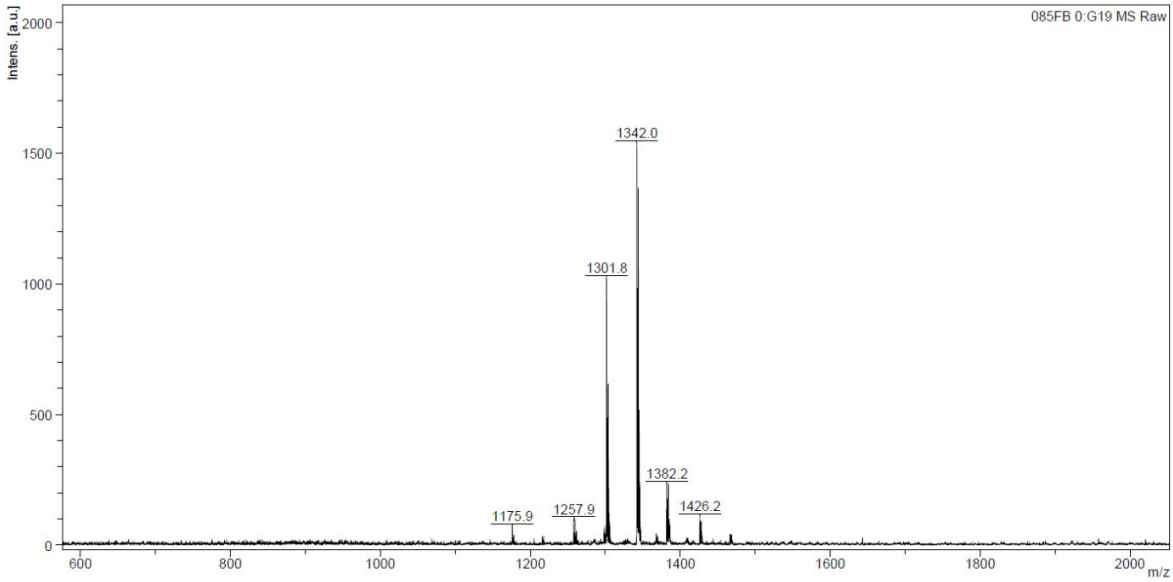

Figure **S37:** MALDI(+)-spectrum of the product mixture

Table **S7**: MALDI-data for the product mixture obtained from the reaction of **5** with 2-Methyl-3-butyn-2-ol.

MALDI(+)-peak $[M]^+$	sum formula of the corr. trityl alcohol	product type
1257.9	$C_{52}H_{59}IO_4S_{12}$	C_2I_1
1301.8	$C_{47}H_{52}I_2O_3S_{12}$	C_1I_1
1342.0	$C_{57}H_{67}IO_5S_{12}$	C_2I_2
1382.2	$C_{67}H_{82}O_7S_{12}$	C_3I_3
1426.2	$C_{62}H_{75}IO_6S_{12}$	C_2I_3

The C_1I_1-product of this batch could be isolated by column chromatography on silica eluting with cyclohexane/ethyl acetate 2:1 (v/v). The HRMS-spectrum shown below confirms the assumed sum formula.

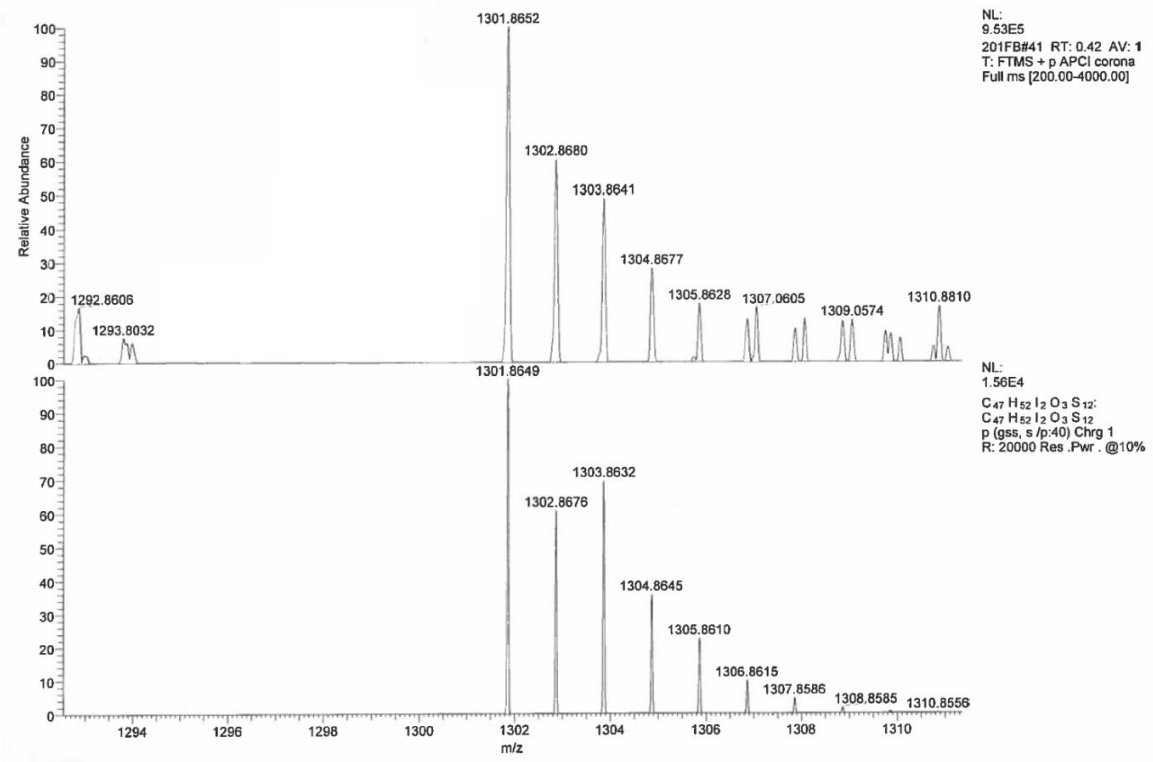

Figure **S38:** APCI-HRMS of the C_1I_1 product

The structure of this C_1I_1 product was then further studied by ^{1}H-NMR at 700 MHz, these spectra are shown below.

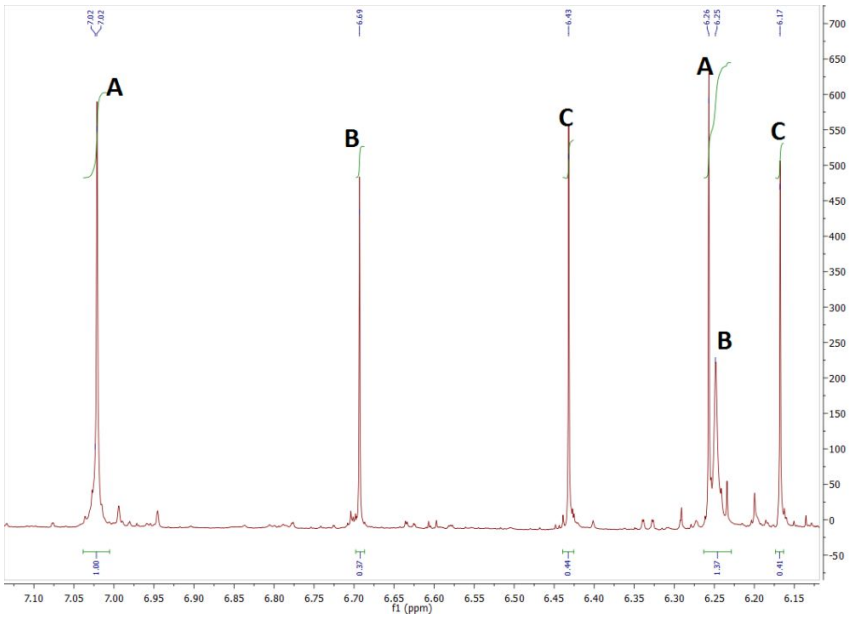

Figure **S39**: ^{1}H-NMR (700 MHz, CD_2Cl_2, 298K) of the C_1I_1 product with 2-methyl-3-butyn-2-ol, olefinic region.

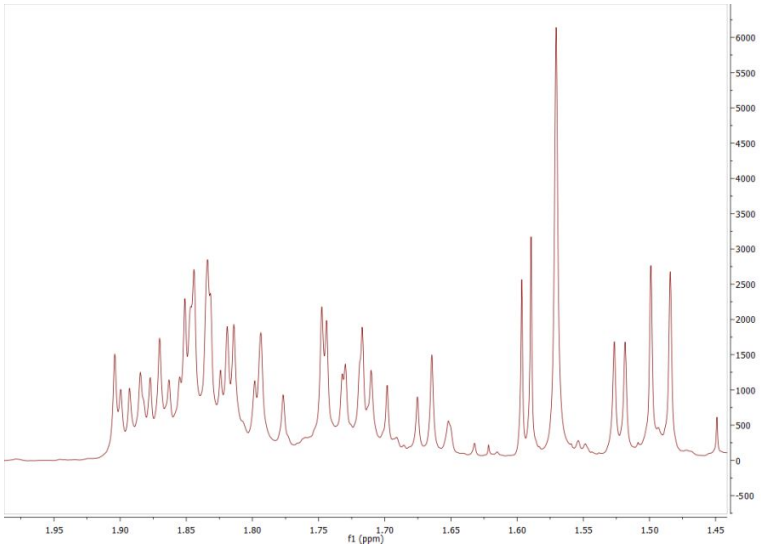

Figure **S40**: ^{1}H-NMR (700 MHz, CD_2Cl_2, 298K) of the C_1I_1 product with 2-methyl-3-butyn-2-ol, aliphatic region.

In the aliphatic region between 1.60 and 1.95 ppm, the methyl protons of the thioacetal give resonances. Cleary, more than 12 peaks – as it would be expected for an asymmetric trityl alcohol – are visible, which means that more than one isomer of the C_1I_1 product exists. According to the mechanism proposed in the main text, six isomers plus their enantiomers can exist:

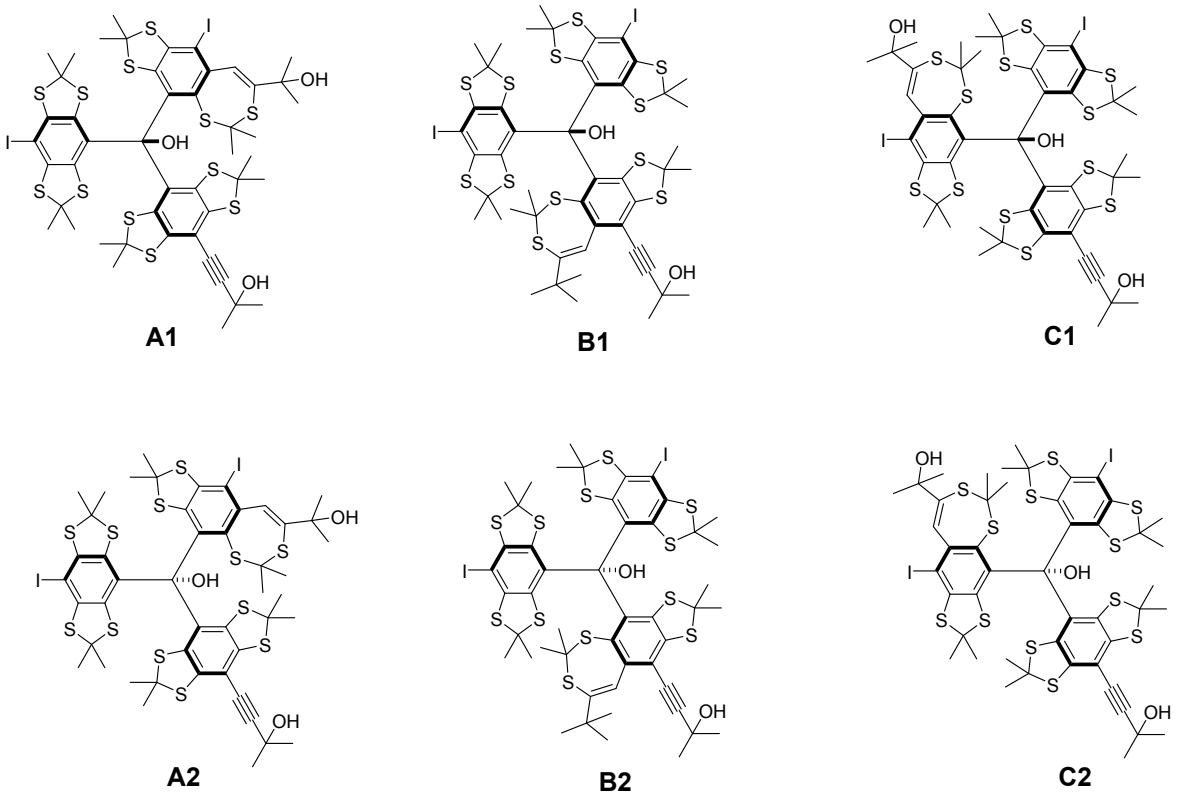

Figure **S41:** Suggested structures of the insertion products.

For the products **A1**, **B1**, and **C1**, a steric clash of the OH-group with the 7-membered ring can be expected, which disfavors the formation of these products. Regarding the NMR-spectra, the olefinic proton of the 7-membered ring and the central OH-proton are expected to give signals between 6 and 7 ppm, both with an equal integral. As shown in the ^{1}H-NMR spectrum, three signal pairs (A, B, C) with equal integrals occur between 6 and 7 ppm, presumably originating from **A2**, **B2**, and **C2**.

For this kind of product structure, no scalar coupling is present, so that only singlets are expected corresponding to the experiment. However, the regioselectivity of the alkyne insertion cannot be determined this way and remains unclear.

In a further experiment, **5** was reacted with 2-methyl-3-butyn-2-ol in CH_2Cl_2/Et_3N and samples for MALDI(+)-analysis were extracted after 2 h (fig. **S42**), 4 h (fig. **S43**), 6 h (fig. **S44**), 8 h (fig. **S45**), and 10 h (fig. **S46**).

This examination revealed that the coupling- and insertion reaction both occur side by side. At no time, only coupling products without insertion products were observed, meaning that neither of both reaction pathways is kinetically strongly preferred.

The corresponding MALDI(+)-spectra are shown below, the following table presents a peak assignment.

Table **S8**: MALDI-data for the product mixtures obtained from the reaction of **5** with 2-methyl-3-butyn-2-ol in dichloromethane/triethylamine.

MALDI(+)-peak $[M]^+$	sum formula of the corr. trityl alcohol	product type
1130.0	$C_{52}H_{58}O_4S_{12}$	C_3I_0
1173.8	$C_{47}H_{51}IO_3S_{12}$	C_2I_0
1217.6	$C_{42}H_{44}I_2O_2S_{12}$	C_1I_0
1257.9	$C_{52}H_{59}IO_4S_{12}$	C_2I_1
1261.5	starting material	
1301.8	$C_{47}H_{52}I_2O_3S_{12}$	C_1I_1
1342.0	$C_{57}H_{67}IO_5S_{12}$	C_2I_2
1382.2	$C_{67}H_{82}O_7S_{12}$	C_3I_3
1426.2	$C_{62}H_{75}IO_6S_{12}$	C_2I_3

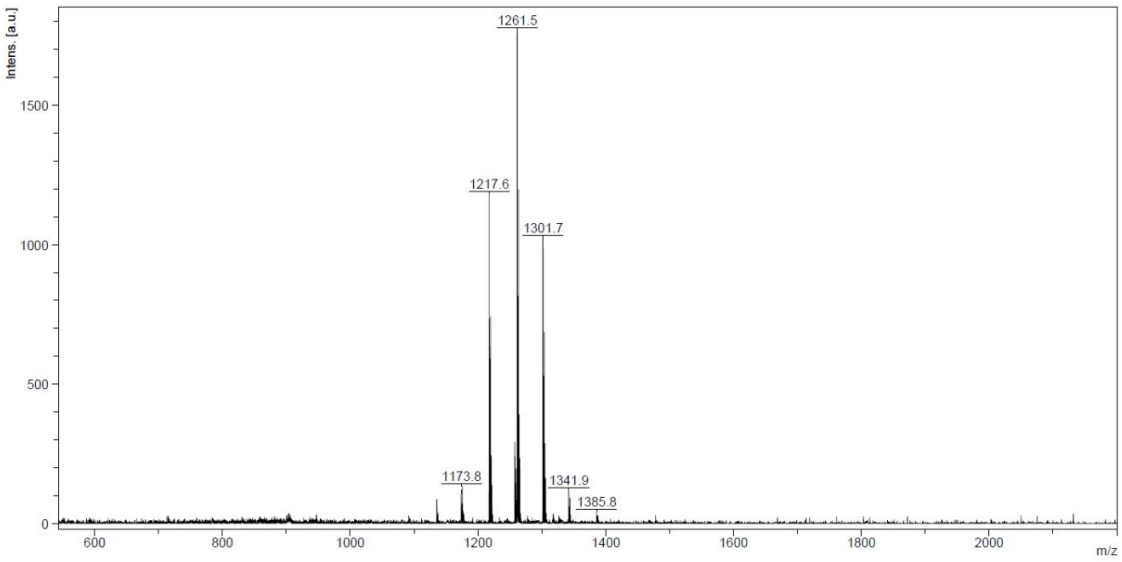

Figure **S42:** MALDI(+) –spectrum after 2 hours reaction time.

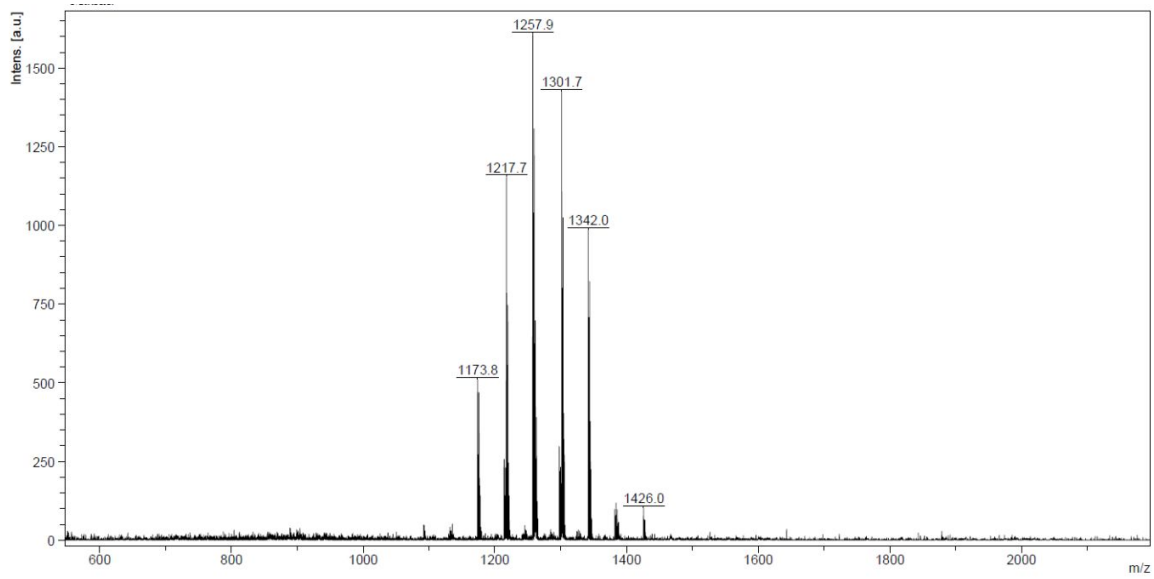

Figure **S43:** MALDI(+) –spectrum after 4 hours reaction time

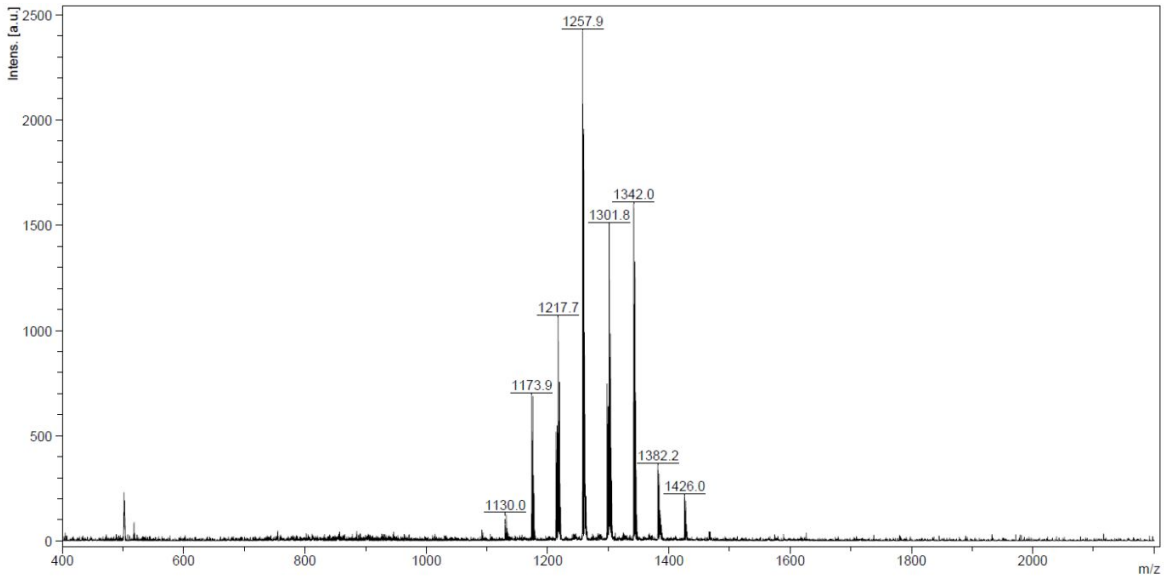

Figure **S44:** MALDI(+) –spectrum after 6 hours reaction time.

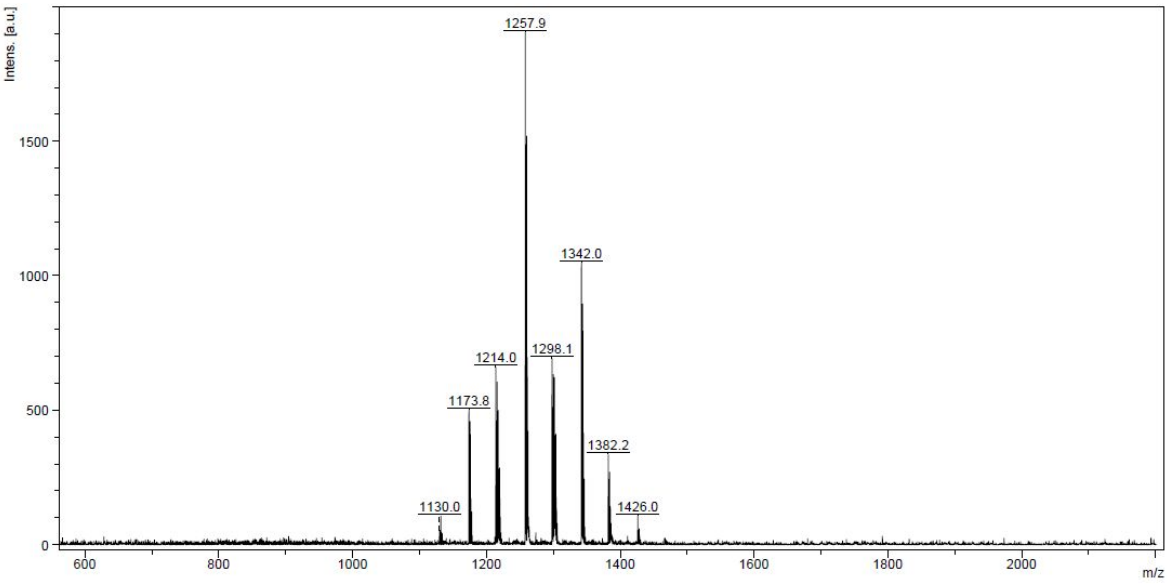

Figure **S45:** MALDI(+) –spectrum after 8 hours reaction time.

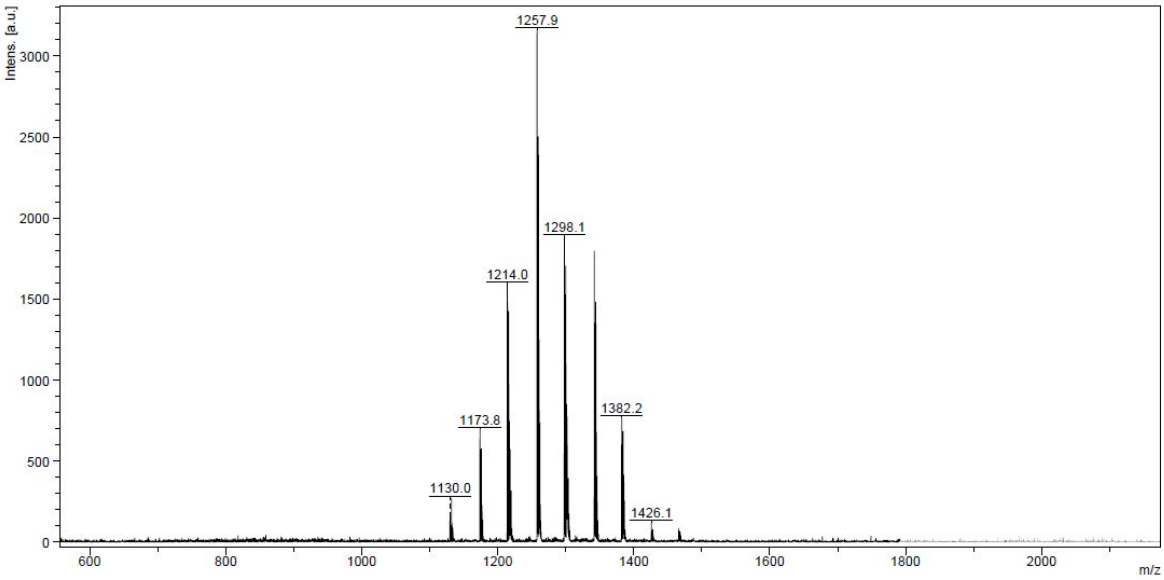

Figure **S46:** MALDI(+) –spectrum after 10 hours reaction time.

Replacing $Pd(Ph_3P)_2Cl_2$ by $Pd(dppf)Cl_2$ in the solvent system CH_2Cl_2/Et_3N (1:1) led to less insertion. Here, a quantitative coupling alongside insertion occurs, so that the coupling reactions seem to be favored here.

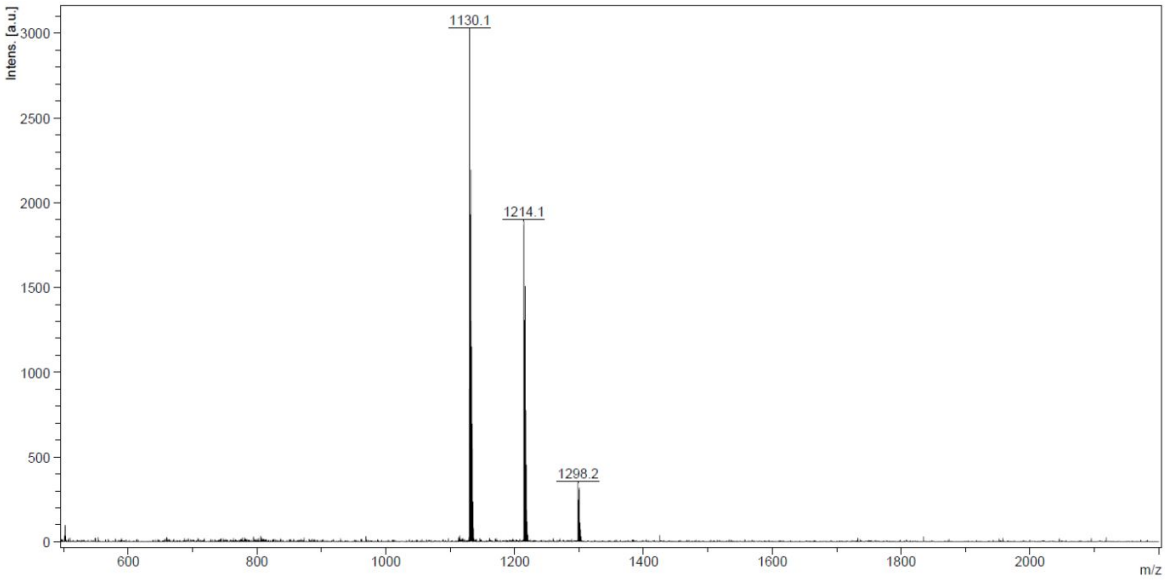

Figure **S47:** MALDI(+) –spectrum of the product mixture

Table **S9:** MALDI data for the reaction of **5** with 2-methyl-3-butyn-2-ol catalyzed with $Pd(dppf)Cl_2$.

MALDI(+)-peak $[M]^+$	sum formula of the corr. trityl alcohol	product type
1130.0	$C_{52}H_{58}O_4S_{12}$	C_3I_0
1214.1	$C_{57}H_{66}O_5S_{12}$	C_3I_1
1298.2	$C_{62}H_{74}O_6S_{12}$	C_3I_2

9. NMR spectra of new compounds

9.1 Trityl alcohol 5

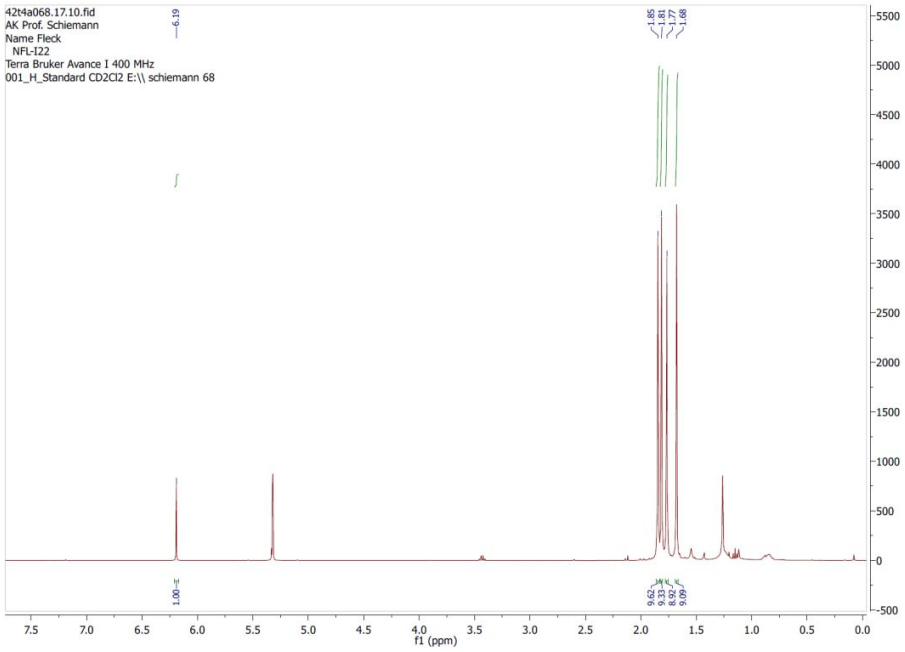

Figure **S48**: ^{1}H-NMR, 400 MHz.

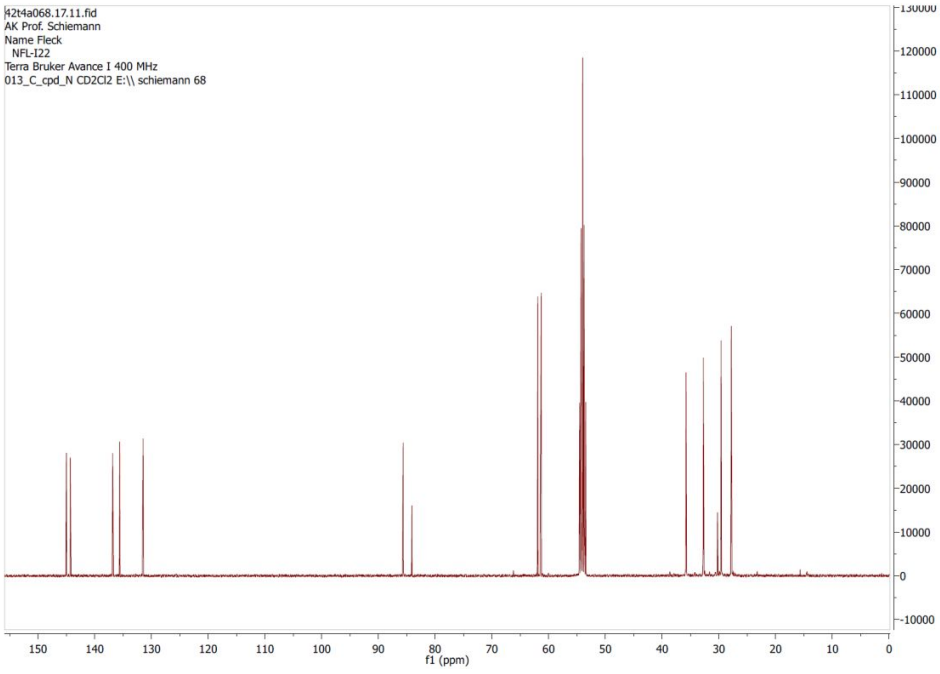

Figure **S49**: ^{13}C{^{1}H}-NMR, 100 MHz.

9.2 Trityl alcohol 6-OH

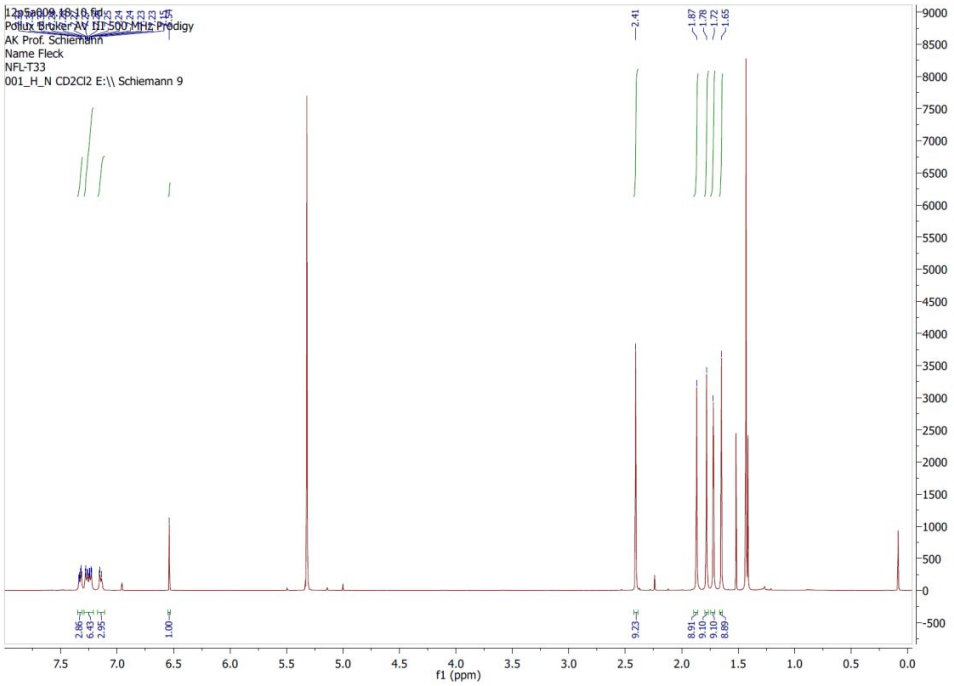

Figure **S50**: ^{1}H-NMR, 500 MHz.

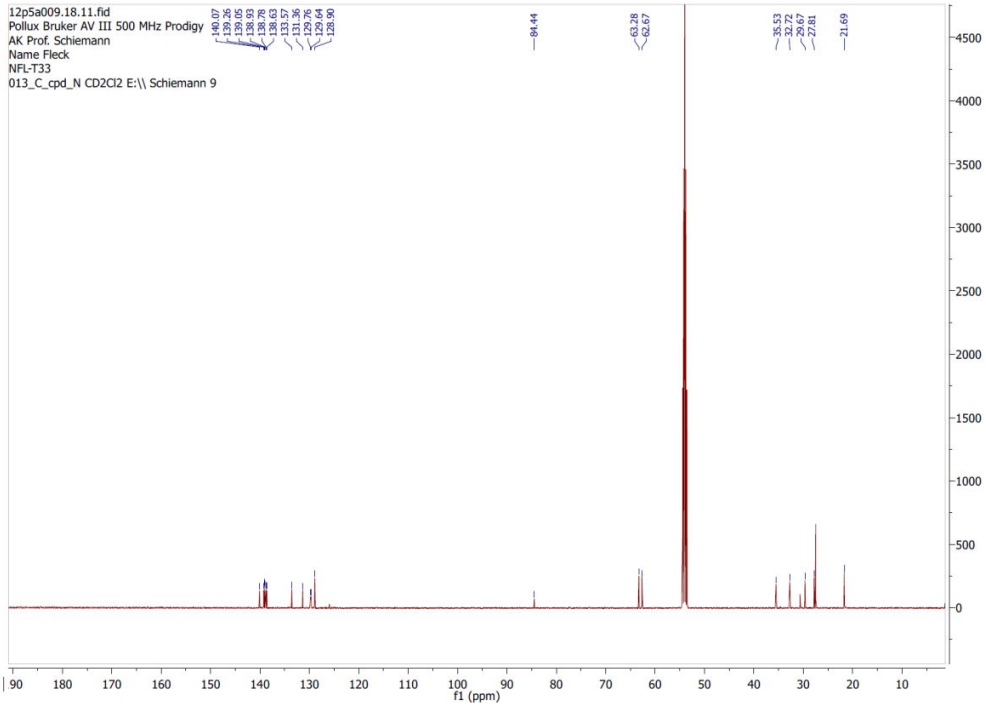

Figure **S51**: ^{13}C{^{1}H}-NMR, 125 MHz.

9.3 Trityl alcohol 9

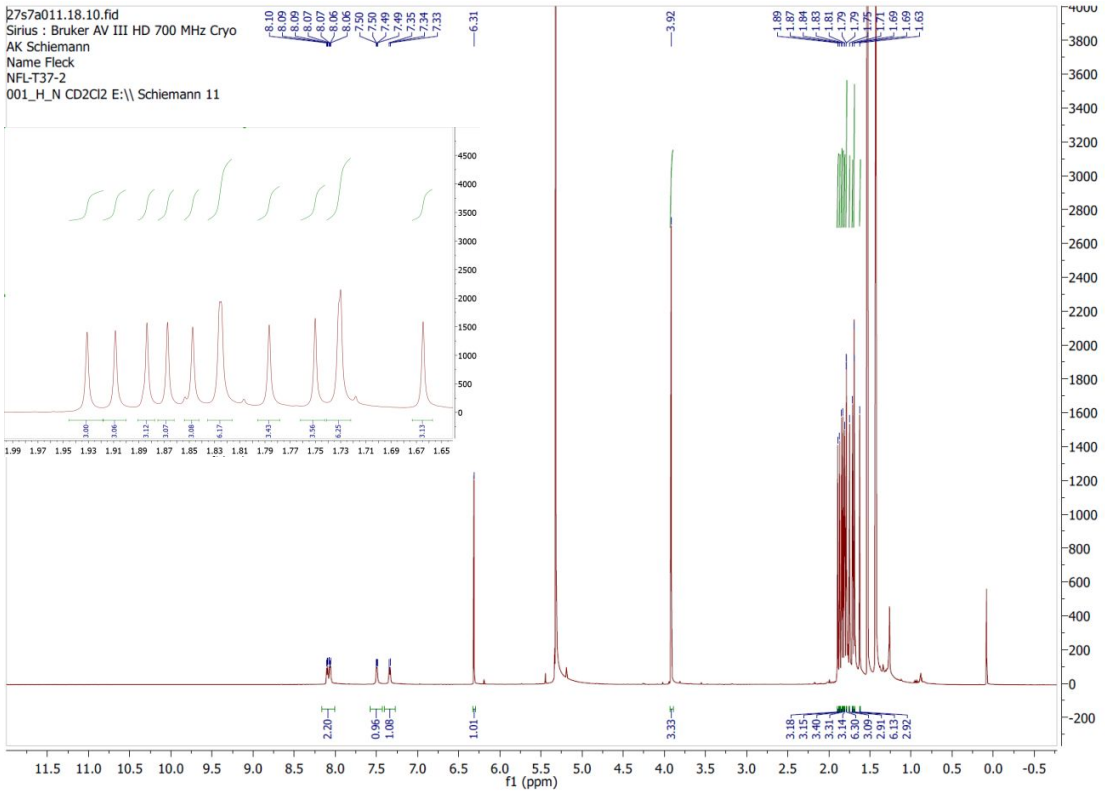

Figure **S52**: ^{1}H-NMR, 700 MHz.

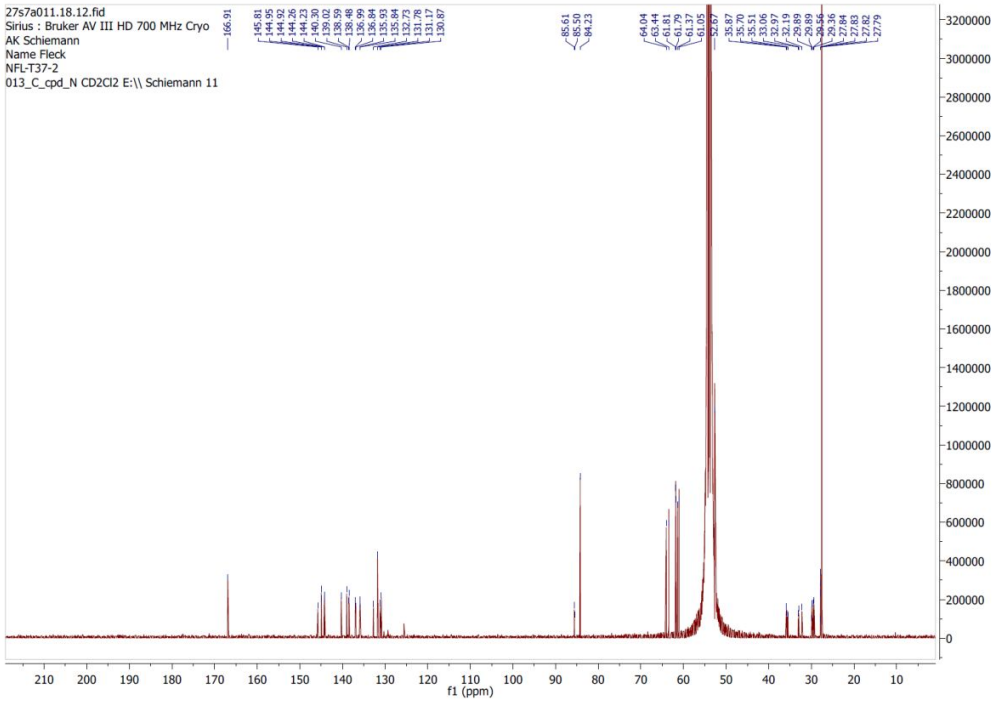

Figure **S53**: $^{13}C\{^{1}H\}$-NMR, 175 MHz.

9.4 Trityl alcohol 10

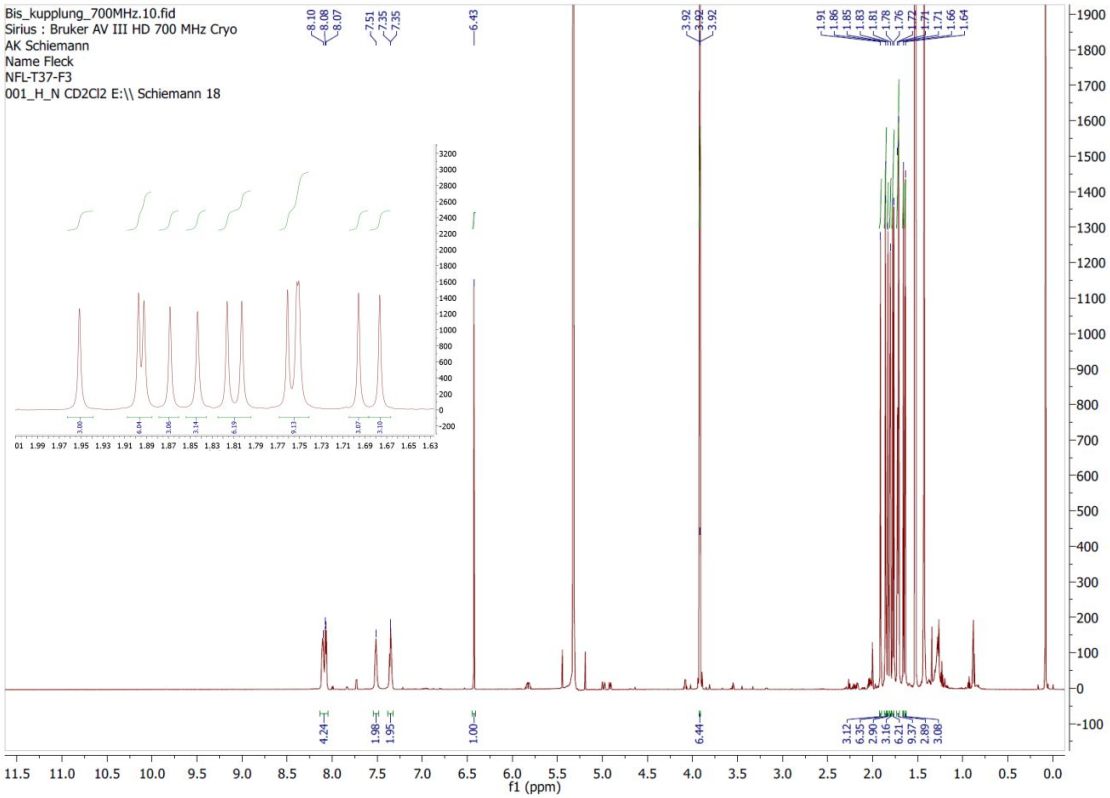

Figure **S54**: ^{1}H-NMR, 700 MHz.

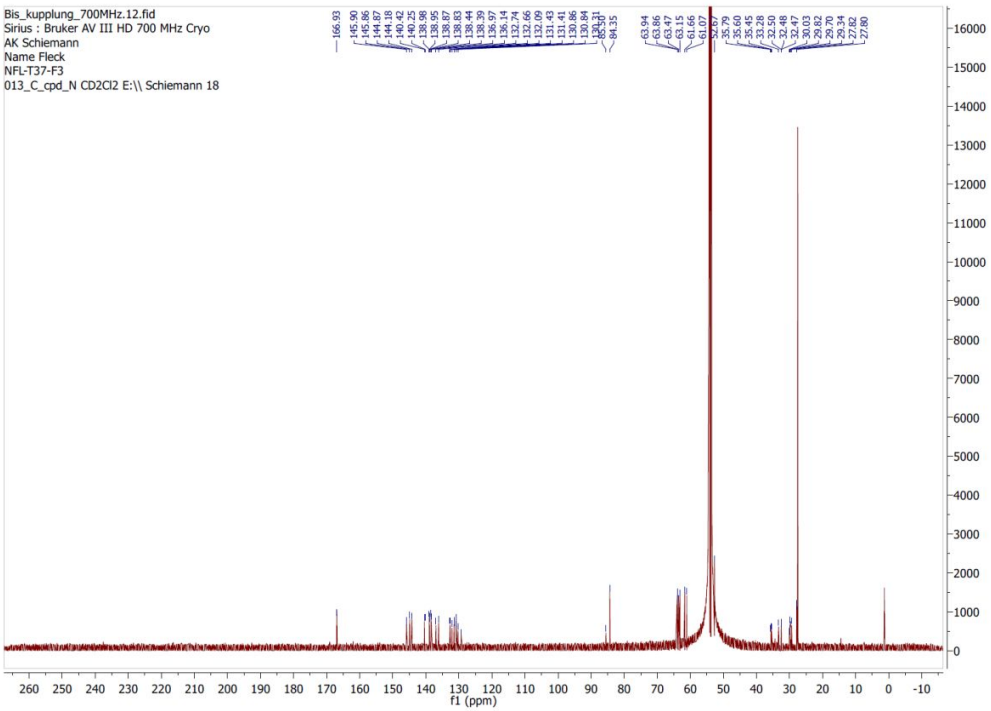

Figure **S55**: $^{13}C\{^{1}H\}$-NMR, 175 MHz.

9.5 Trityl alcohol 14

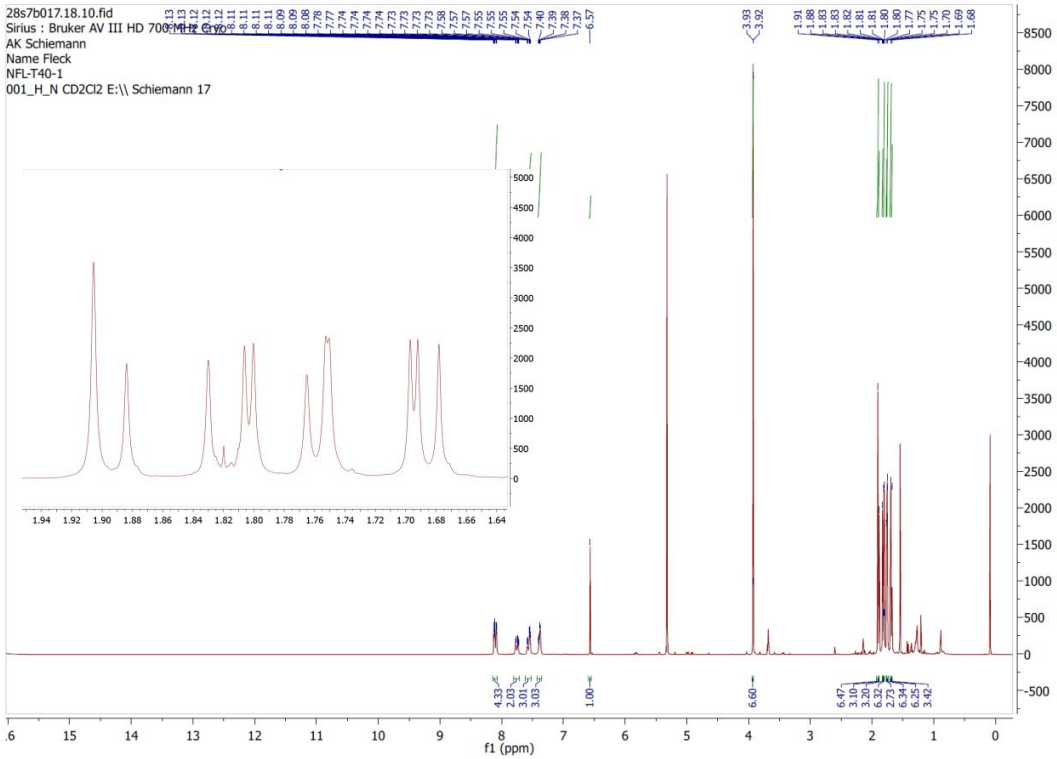

Figure **S56**: ^{1}H-NMR, 700 MHz.

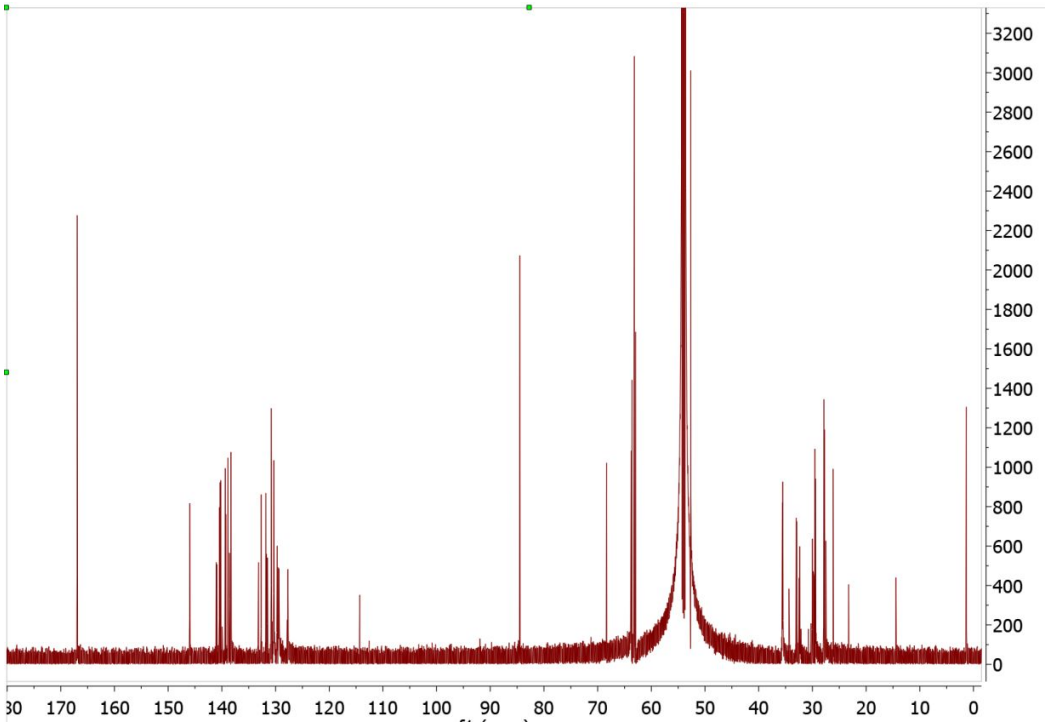

Figure **S57a**: $^{13}C\{^{1}H\}$-NMR, 175 MHz.

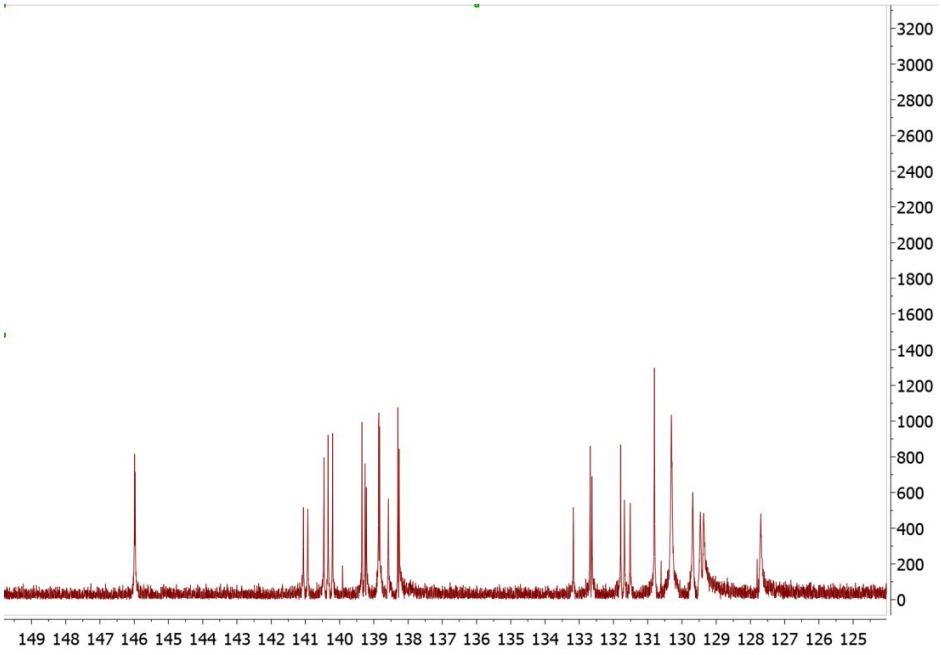

Figure **S57b**: $^{13}C\{^{1}H\}$-NMR, 175 MHz.

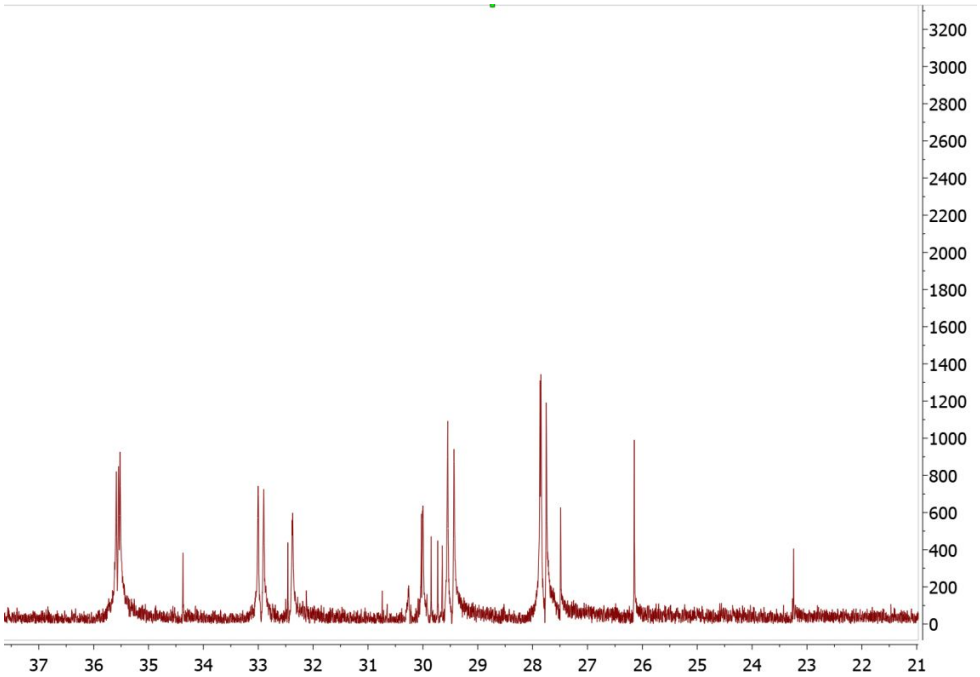

Figure **S57c**: $^{13}C\{^{1}H\}$-NMR, 175 MHz.

9.6 Trityl porphyrin 12-OH

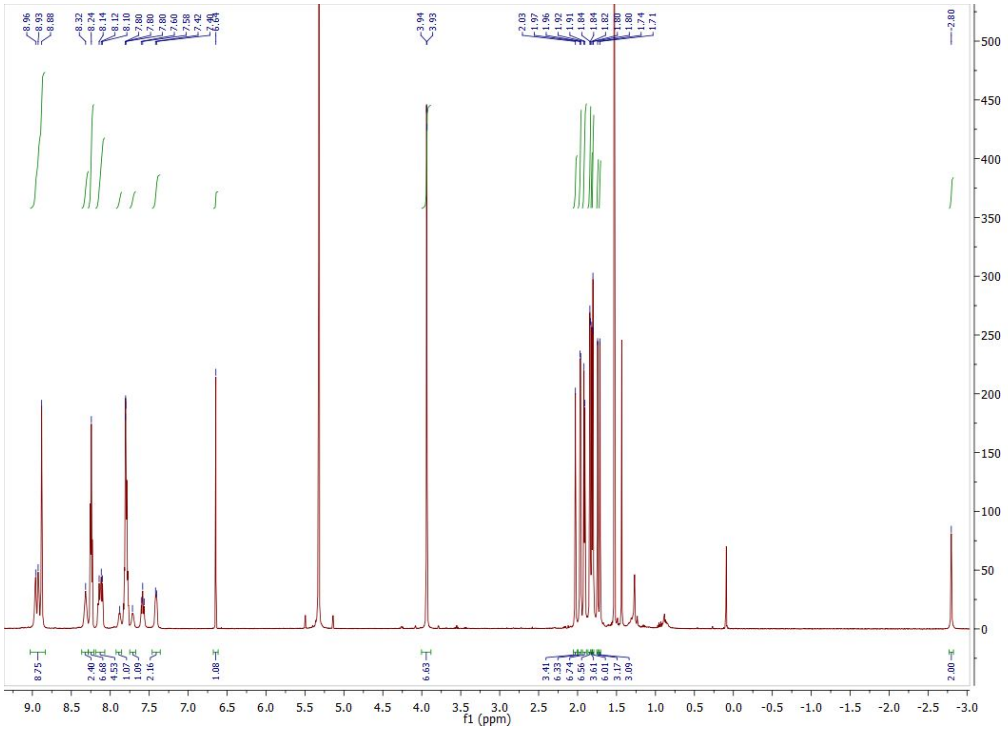

Figure **S58**: ^{1}H-NMR, 700 MHz.

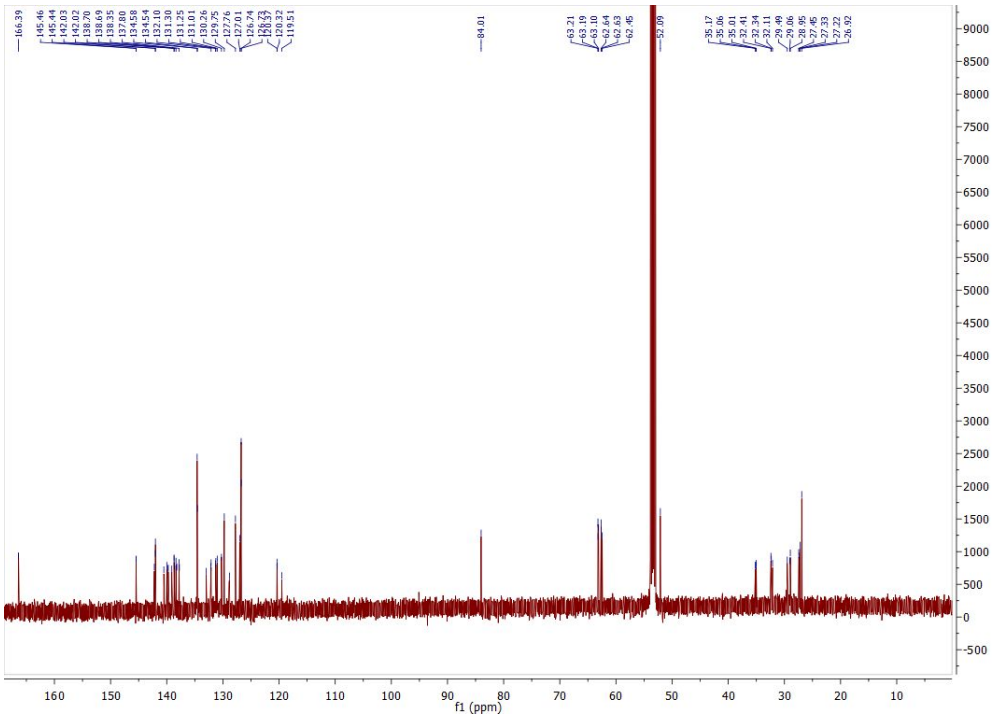

Figure **S59**: $^{13}C\{^{1}H\}$-NMR, 175 MHz.

10. High-Resolution Mass Spectra

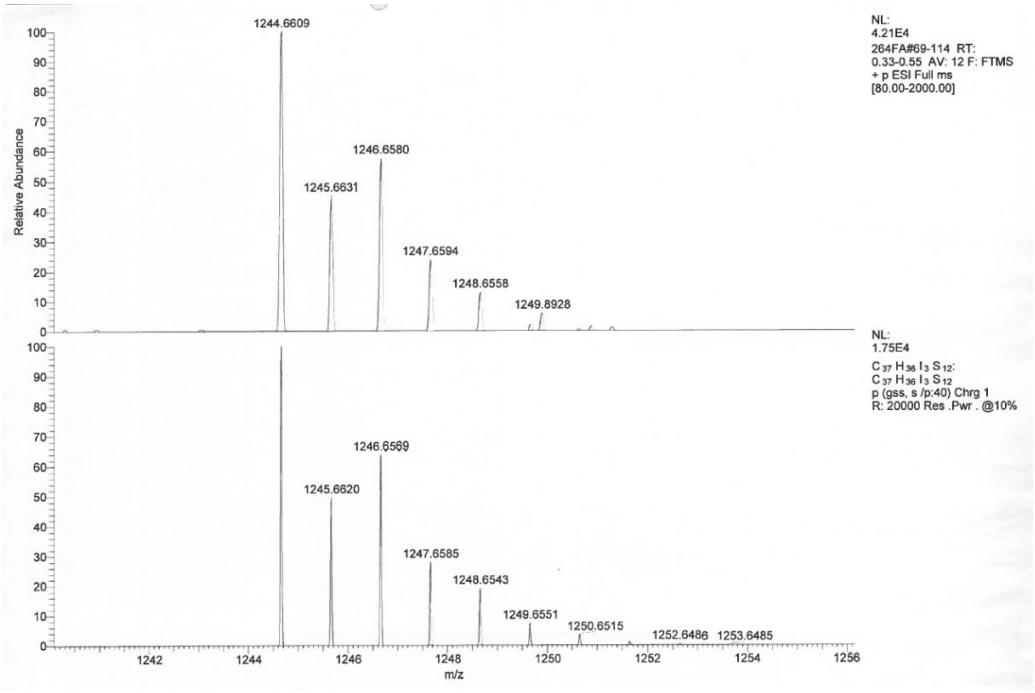

Figure **S60**: ESI(+)-HRMS of trityl radical **3•**.

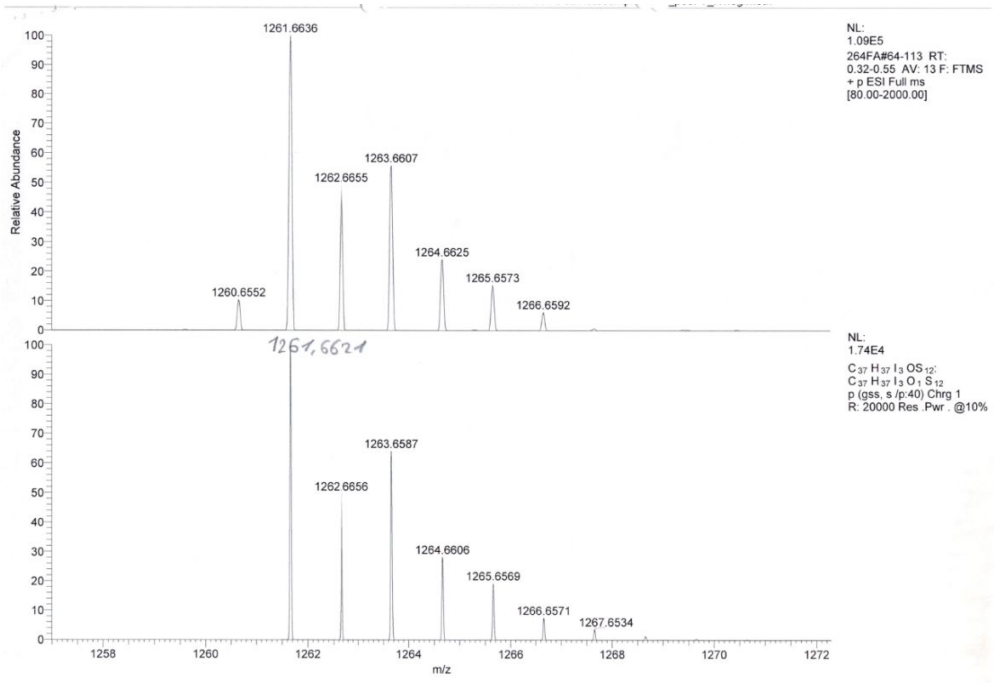

Figure **S61**: ESI(+)-HRMS of trityl alcohol **5**.

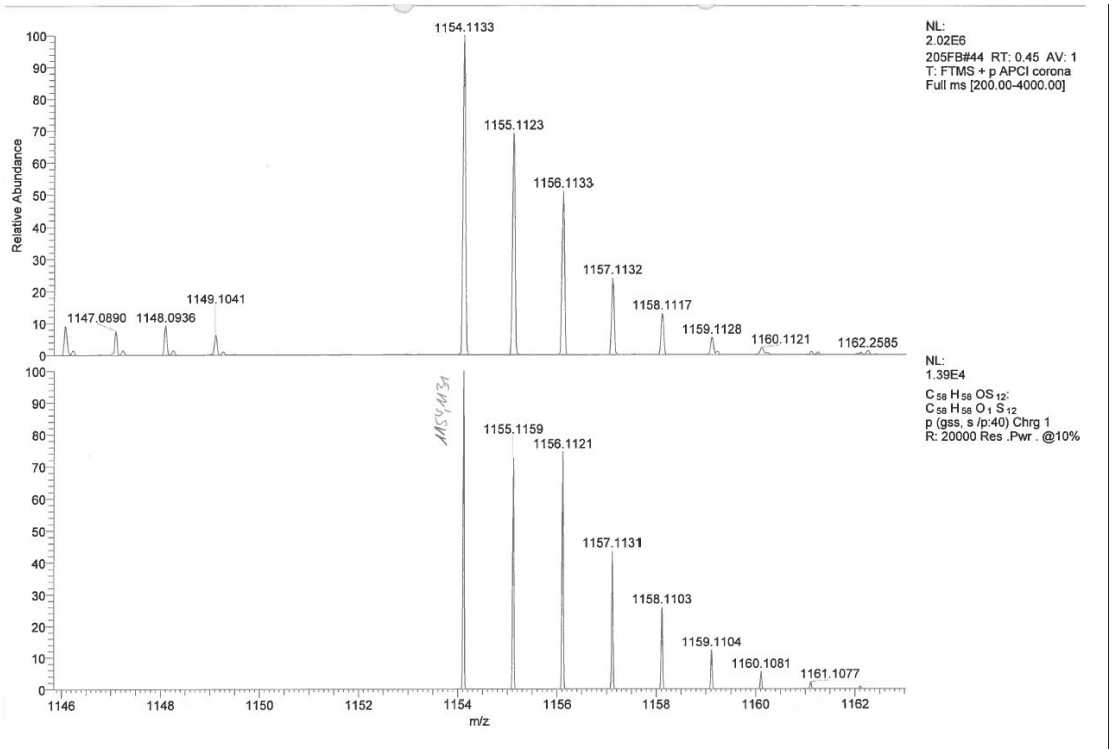

Figure **S62**: APCIHRMS of trityl alcohol **6-OH**.

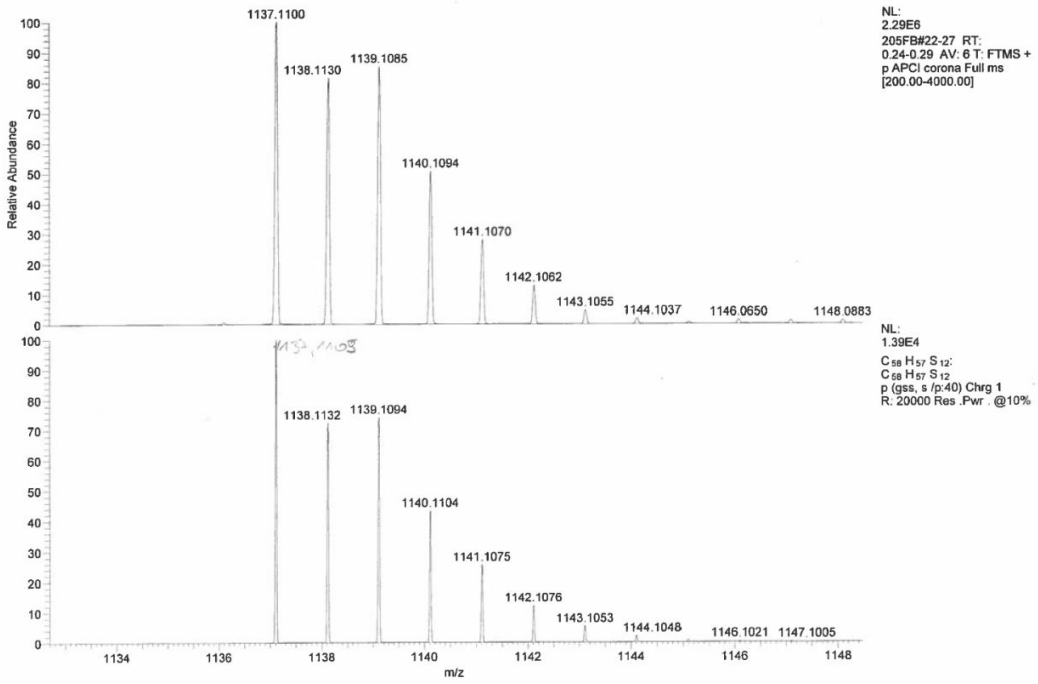

Figure **S63**: APCI-HRMS of trityl radical **6•**.

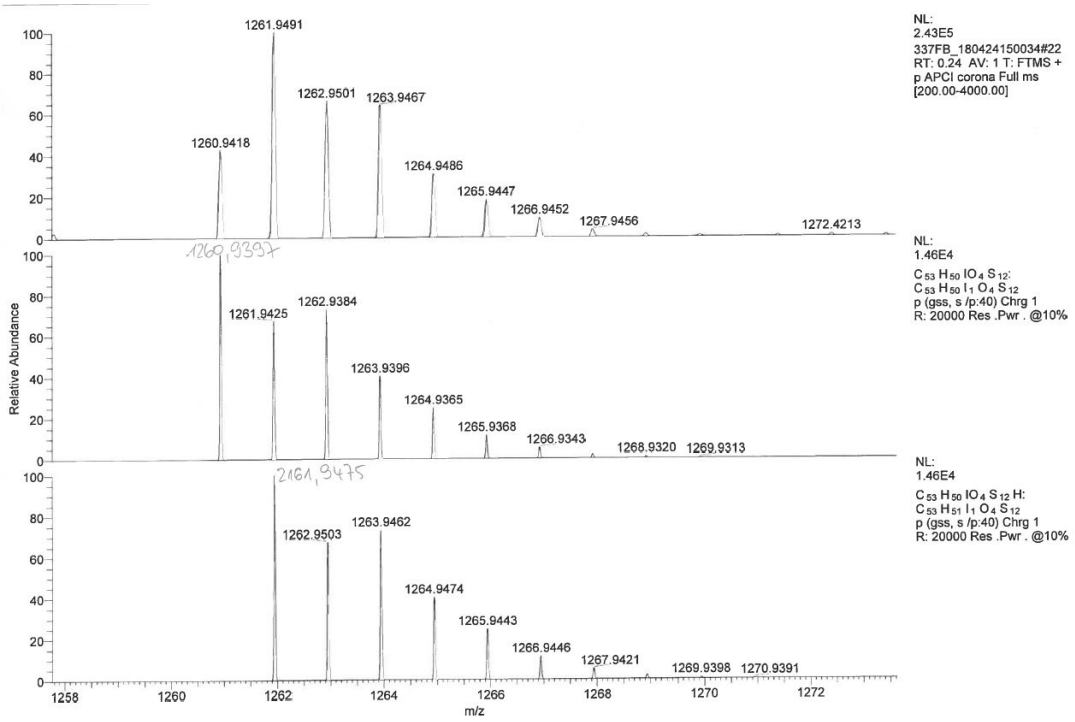

Figure **S64**: APCI-HRMS of trityl radical **7•**.

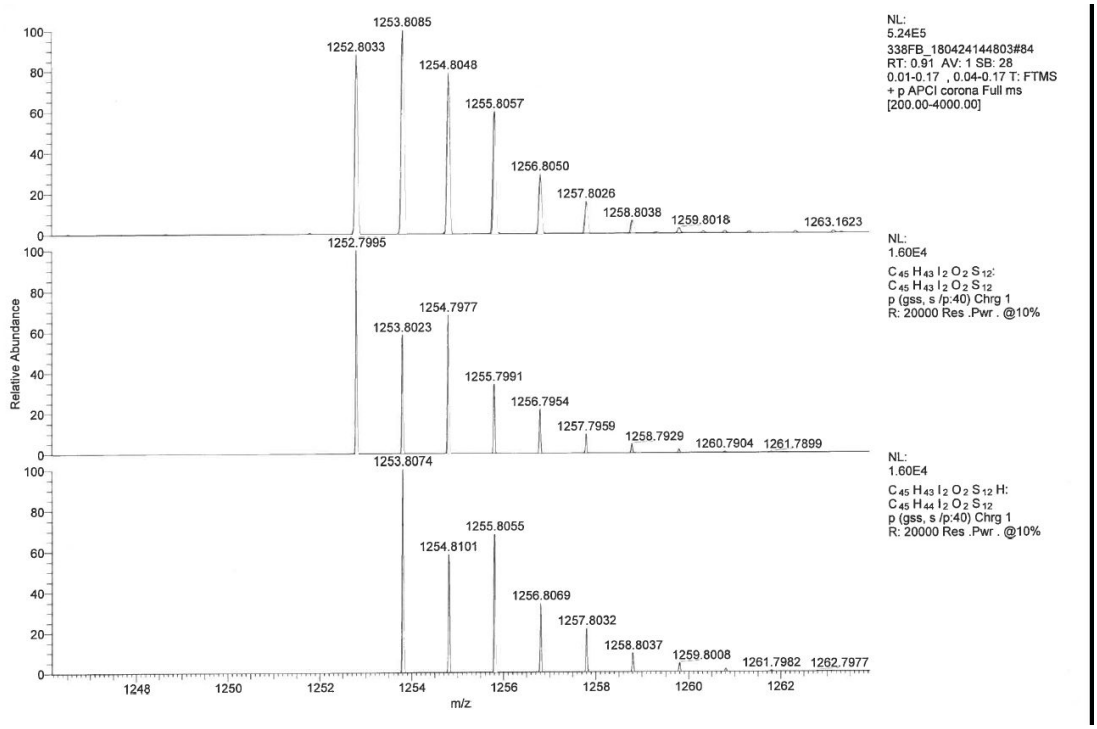

Figure **S65**: APCI-HRMS of trityl radical **8•**.

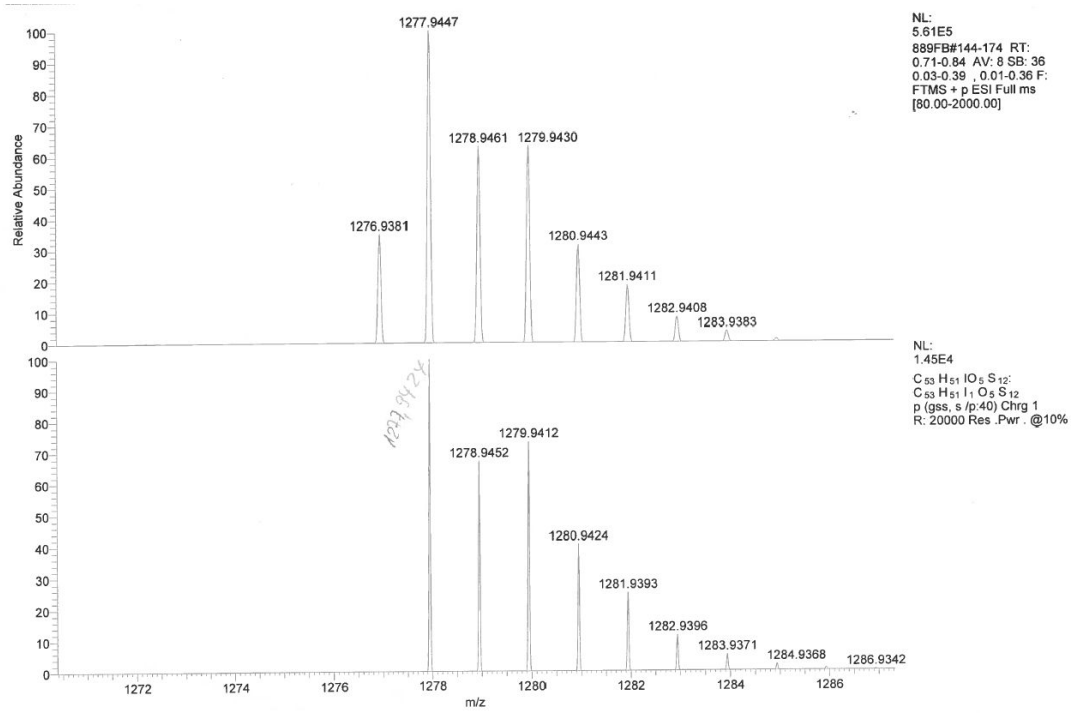

Figure **S66**: ESI(+)-HRMS of trityl alcohol **9**.

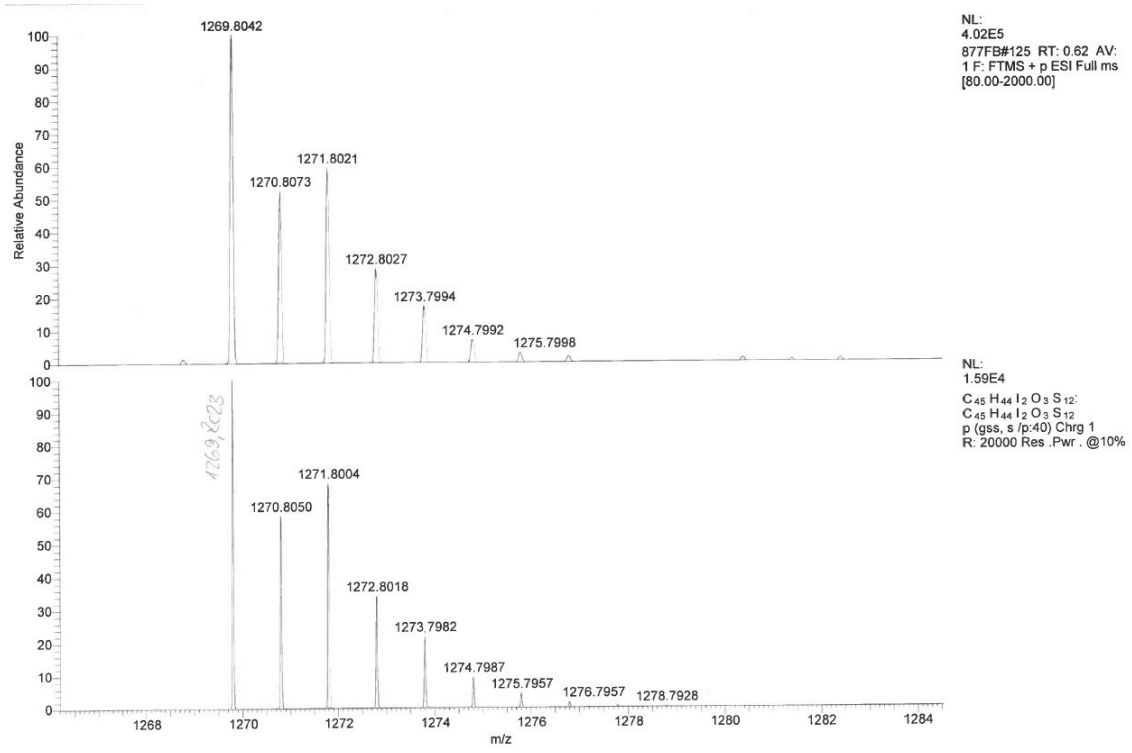

Figure **S67**: ESI(+)-HRMS of trityl alcohol **10** (Figure **S20**) .

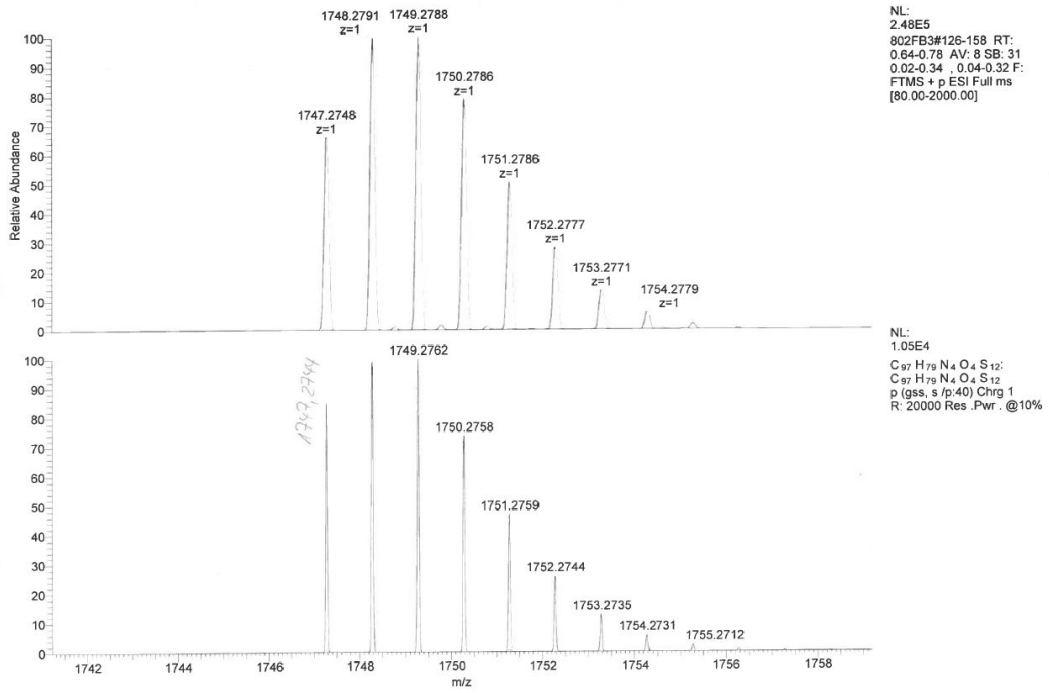

Figure **S68**: ESI(+)-HRMS of trityl porphyrin **12•**.

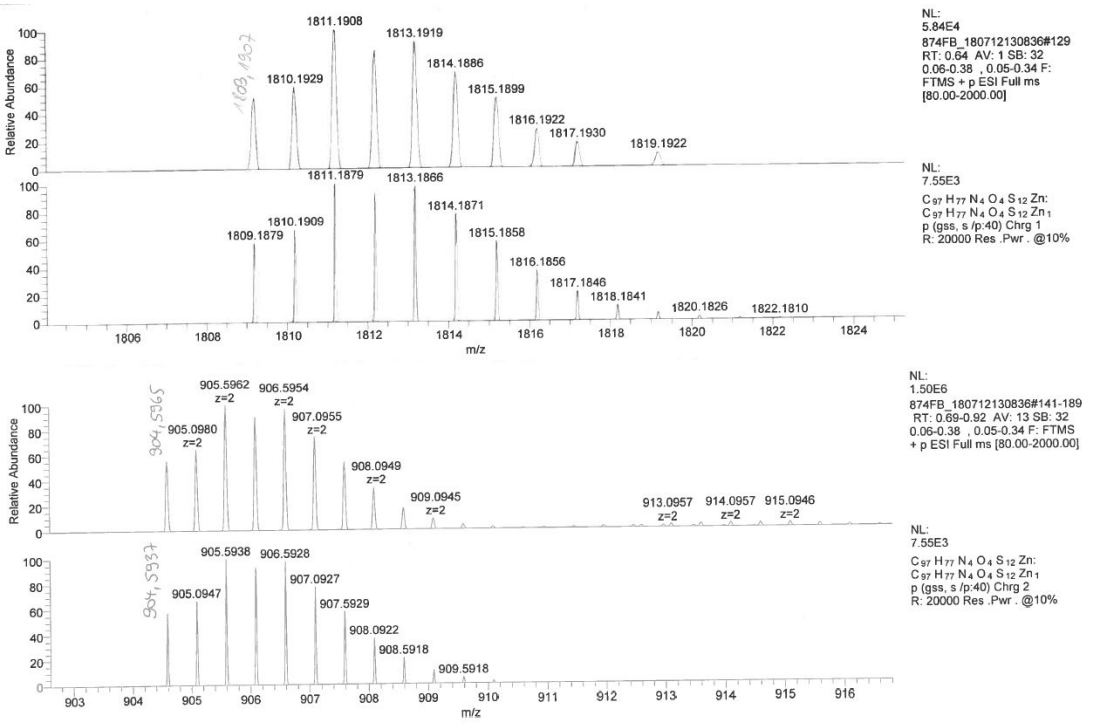

Figure **S69**: ESI(+)-HRMS of trityl porphyrin **13•**.

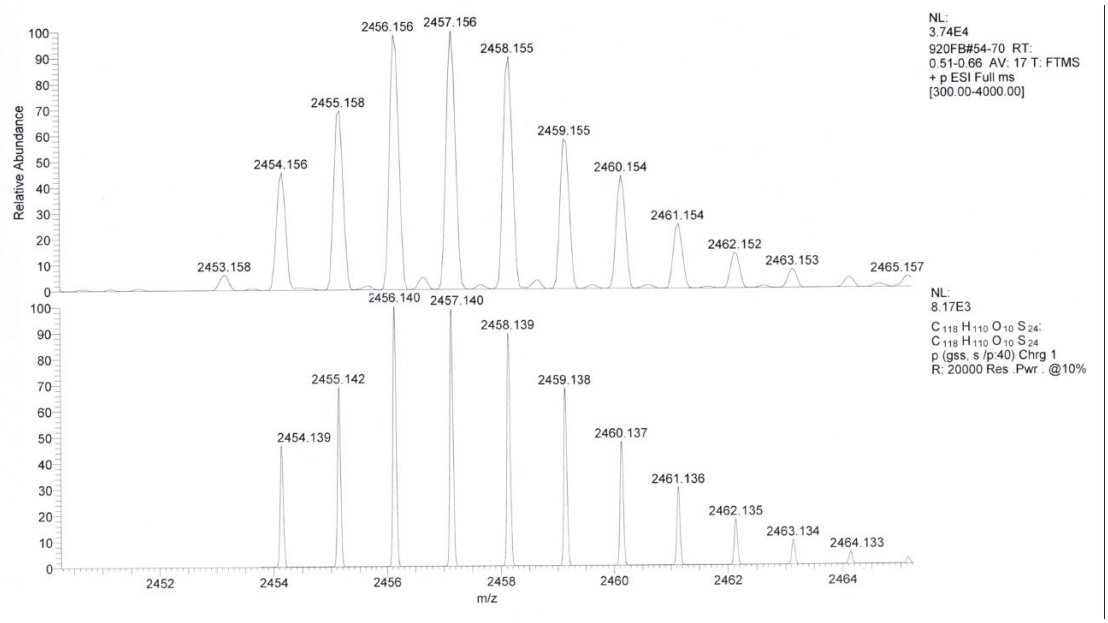

Figure **S70**: ESI(+)-HRMS of trityl alcohol **14**.

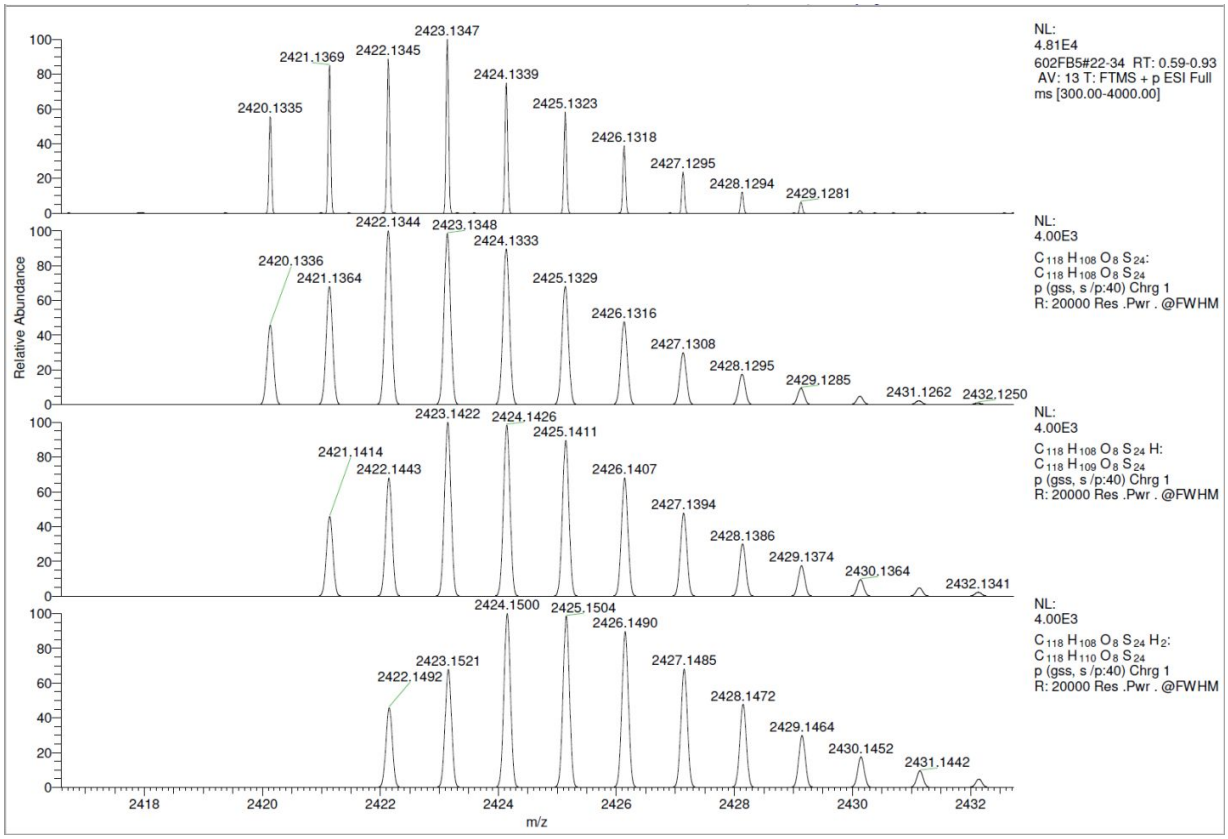

Figure **S71**: ESI(+)-HRMS of trityl biradical **15••**.

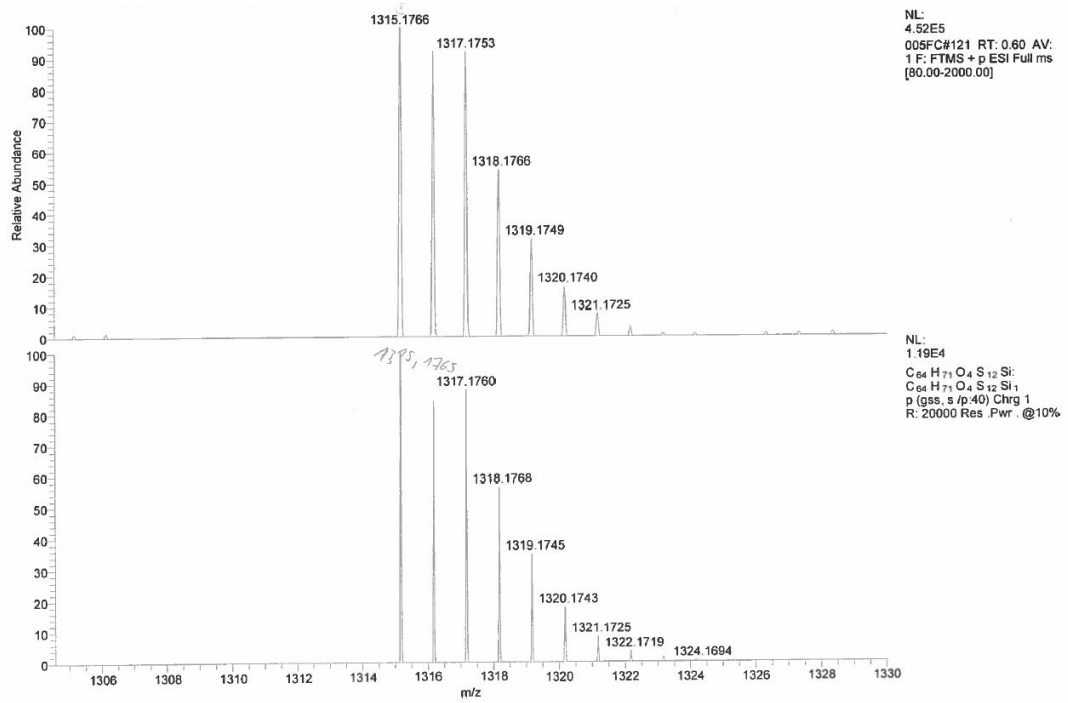

Figure **S72**: ESI(+)-HRMS of trityl radical **16•**.

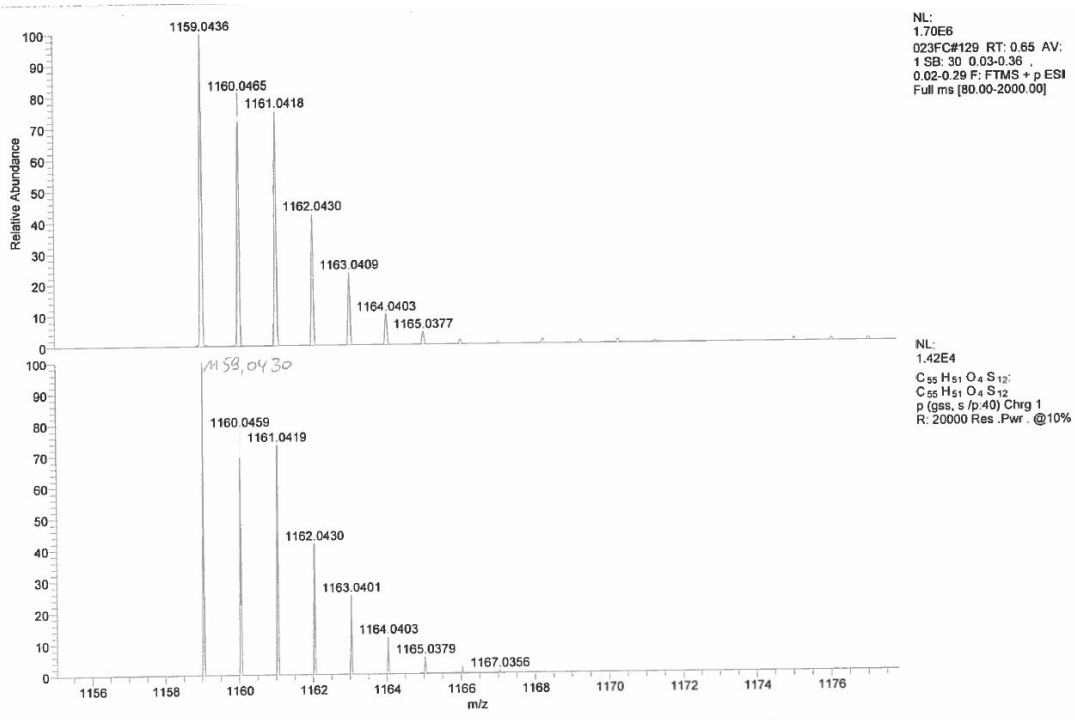

Figure **S73**: ESI(+)-HRMS of trityl radical **17•**.

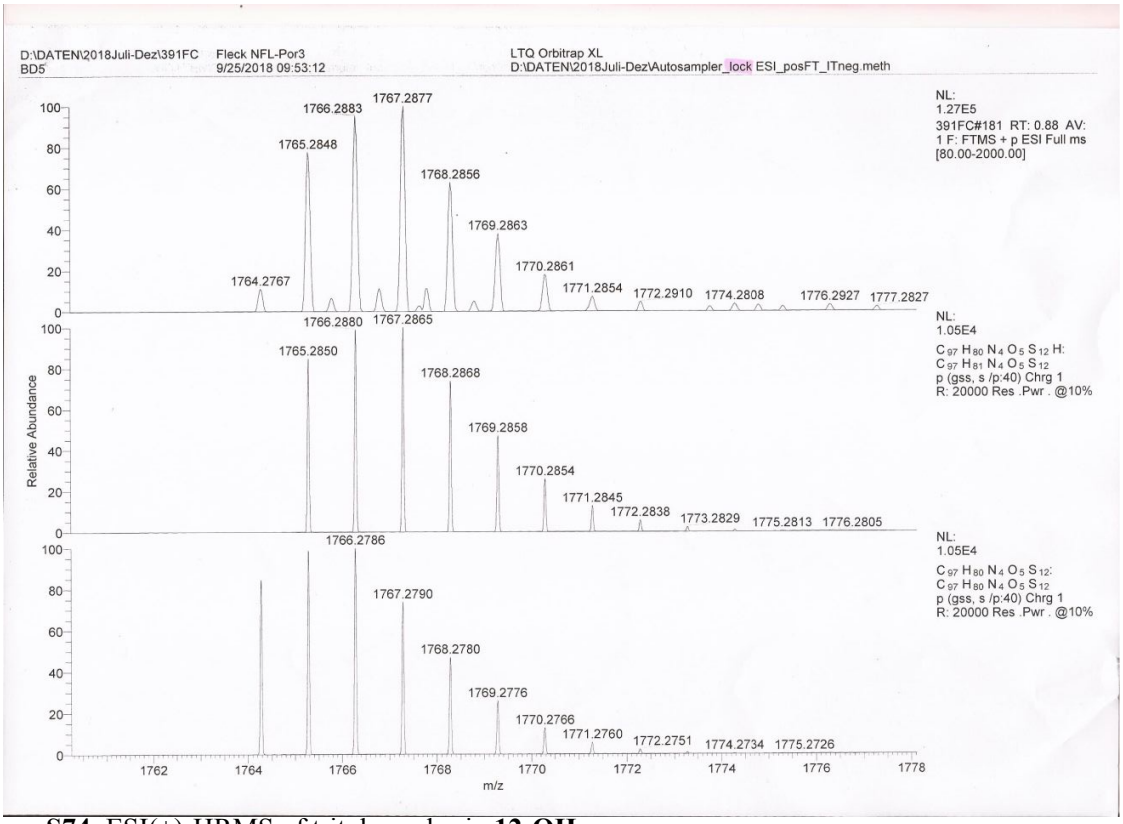

Figure **S74**: ESI(+)-HRMS of trityl porphyrin **12-OH**.

11. MALDI(+) and ESI(+) mass spectra of trityl radicals

In the following, MALDI(+) and ESI(+) mass spectra of all new trityl radicals will be presented serving as an additional purity assessment. Note, that the [M+17]-peak belongs to traces of the corresponding trityl alcohol. Peaks occurring for [M+16] belong to trityl radicals bearing sulfoxide groups due to incorporation of oxygen.

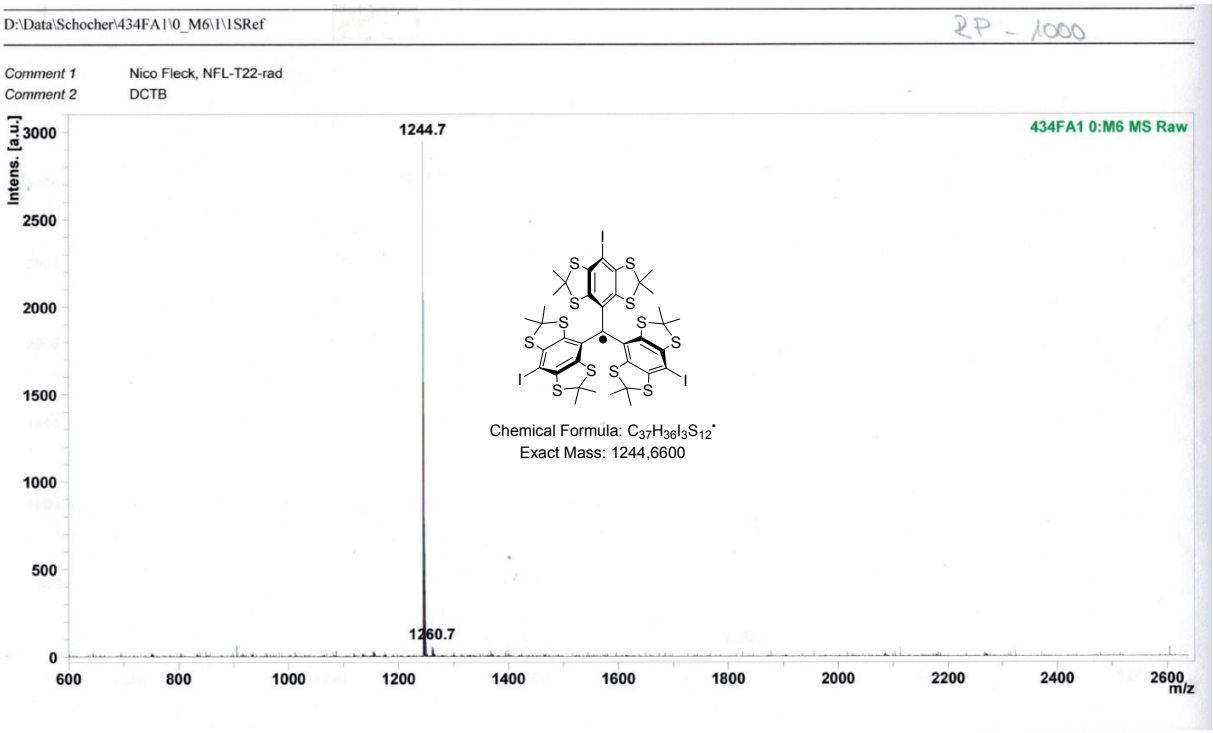

Figure **S75**: MALDI(+) mass spectrum of radical **3•**.

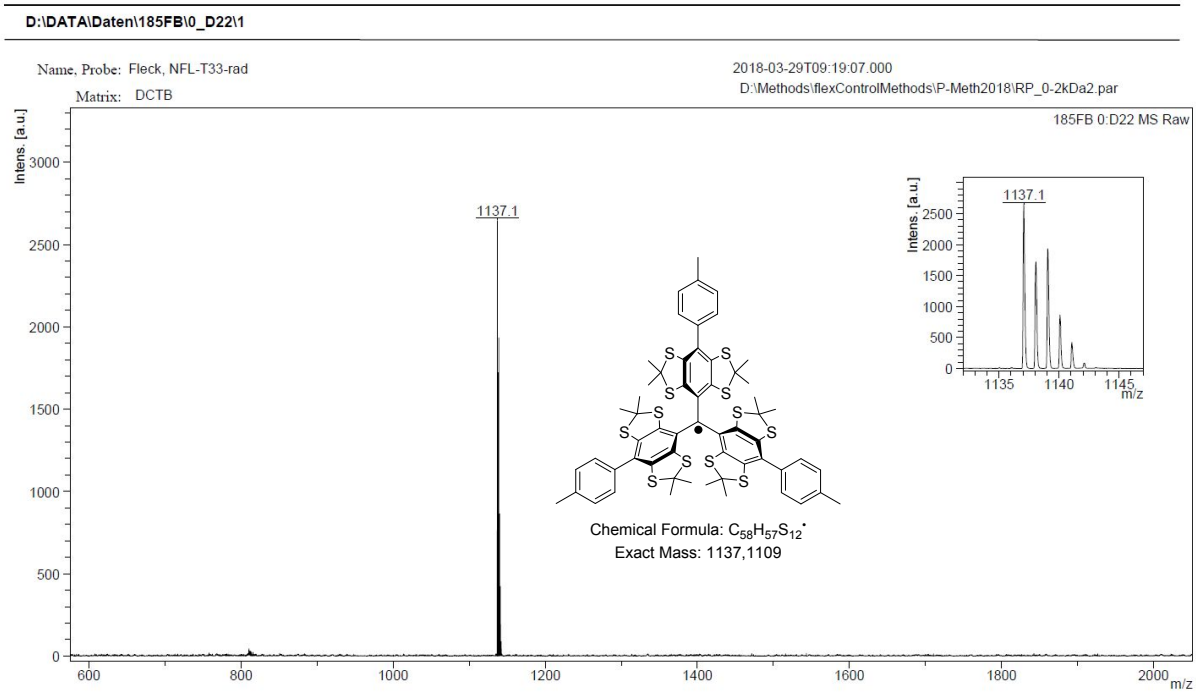

Figure **S76**: MALDI(+) mass spectrum of radical 6•.

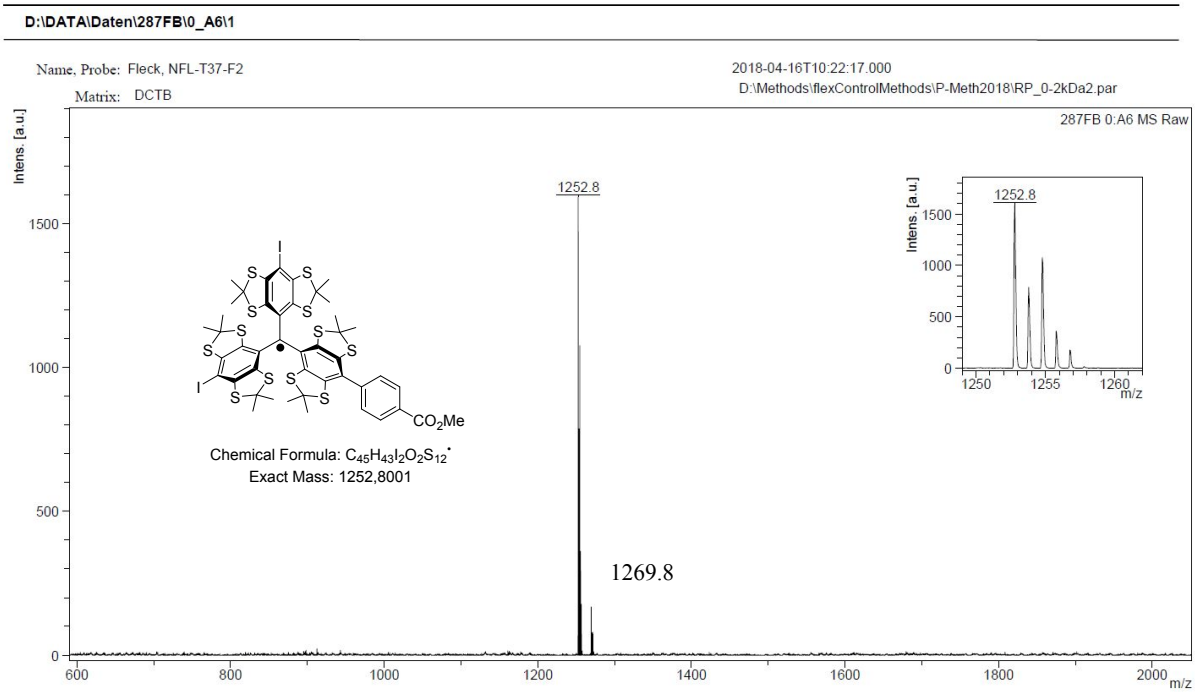

Figure **S77**: MALDI(+) mass spectrum of radical **7**•.

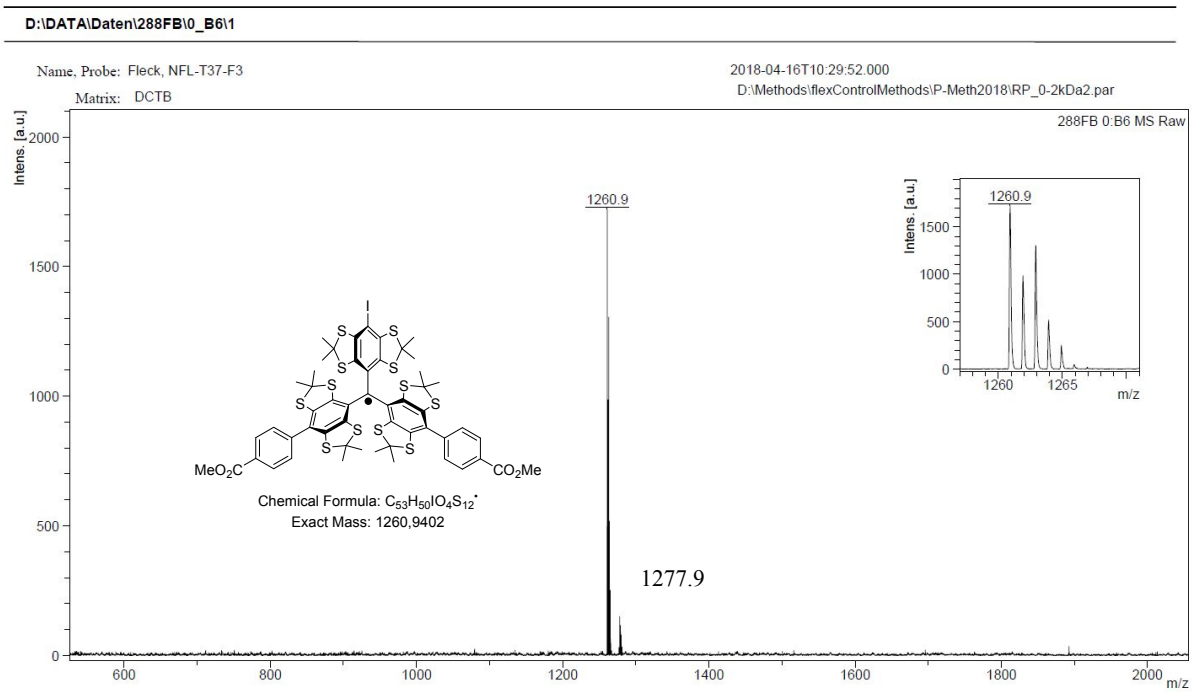

Figure **S78**: MALDI(+) mass spectrum of radical **8•**.

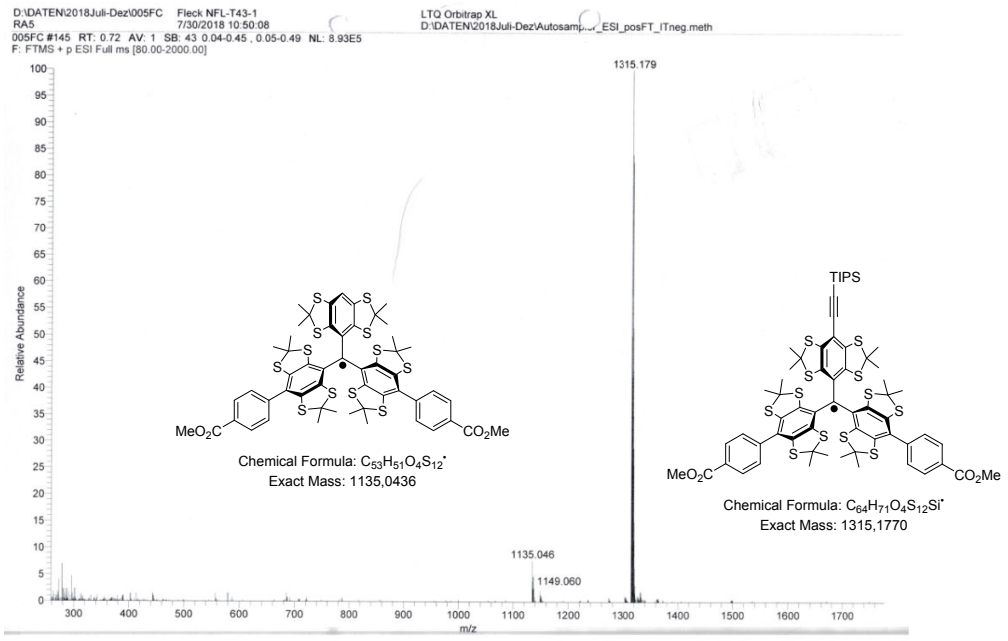

Figure **S79**: ESI(+) mass spectrum of radical **16•**.

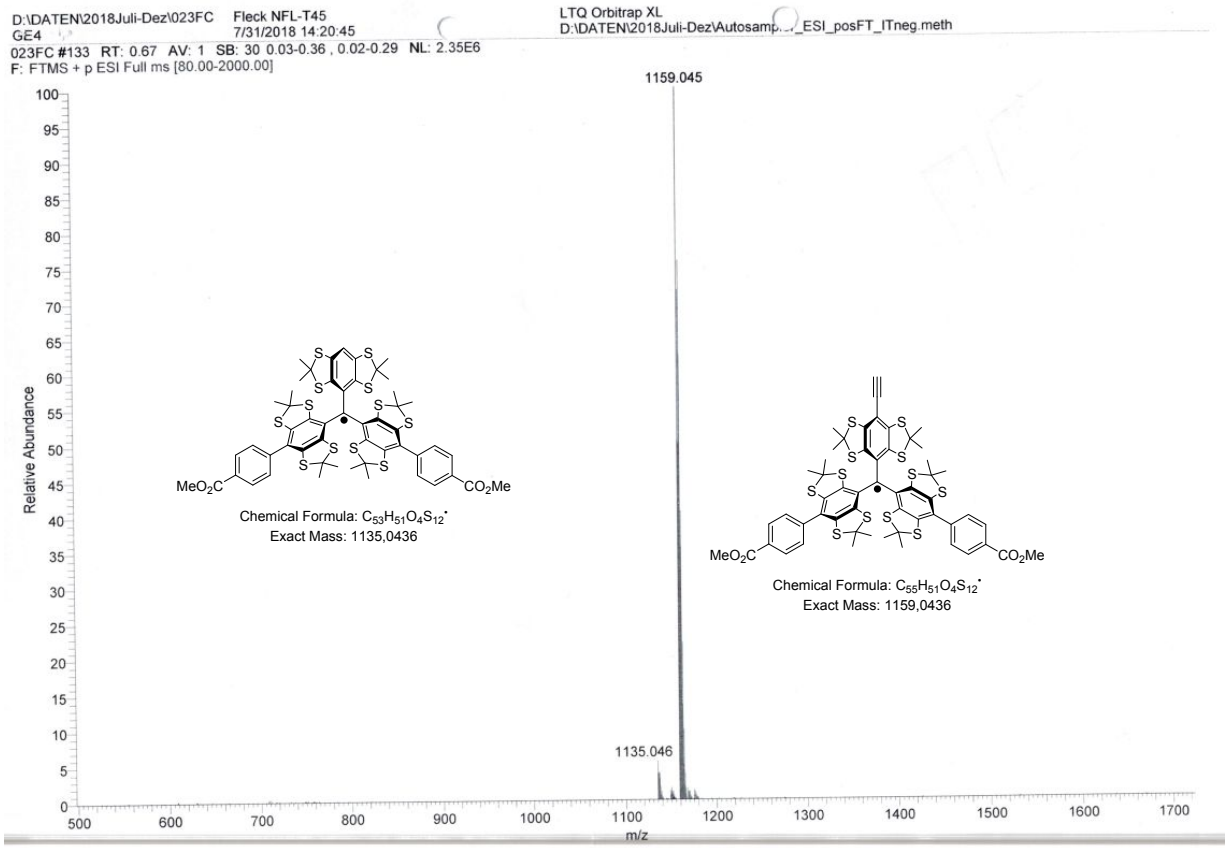

Figure **S80**: ESI(+) mass spectrum of radical **17•**.

12. Medium pressure liquid chromatography

Additionally to mass spectrometry and *cw*-EPR, liquid chromatography (MPLC) was used to examine the purity of all new radical compounds which could not be subjected to NMR analysis. The instrumentation for the MPLC was set up as described in the main text. Besides from this, cyclohexane/ethyl acetate was used as solvent. In the following chromatograms, the green line indicates the ethyl acetate gradient. The initial signal in all chromatograms at a retention time of 00:00 min is artificial and belongs to the automatic zero-adjusting of the detector.

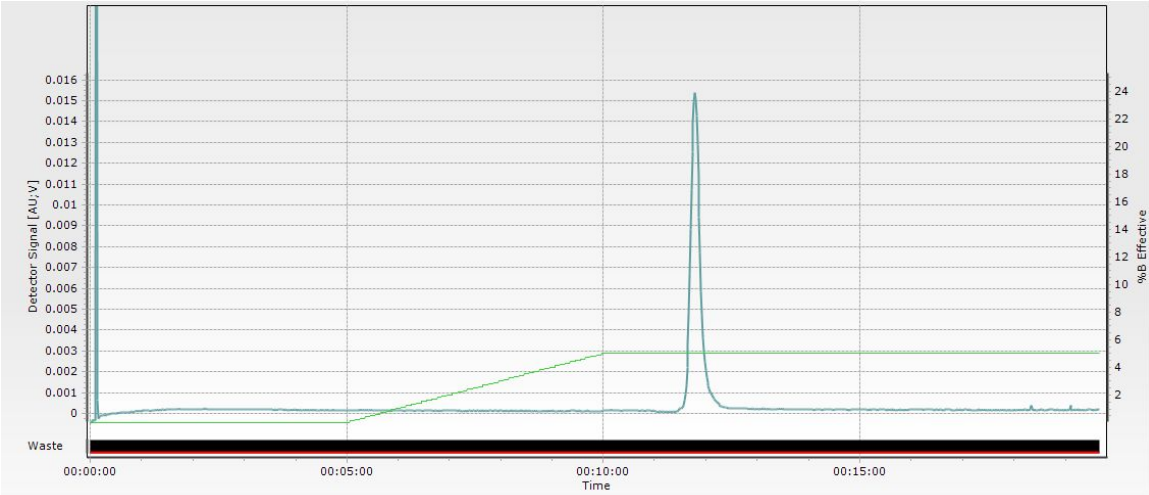

Figure **S81**: MPLC-chromatogram of radical **3•** (t = 11:48 min).

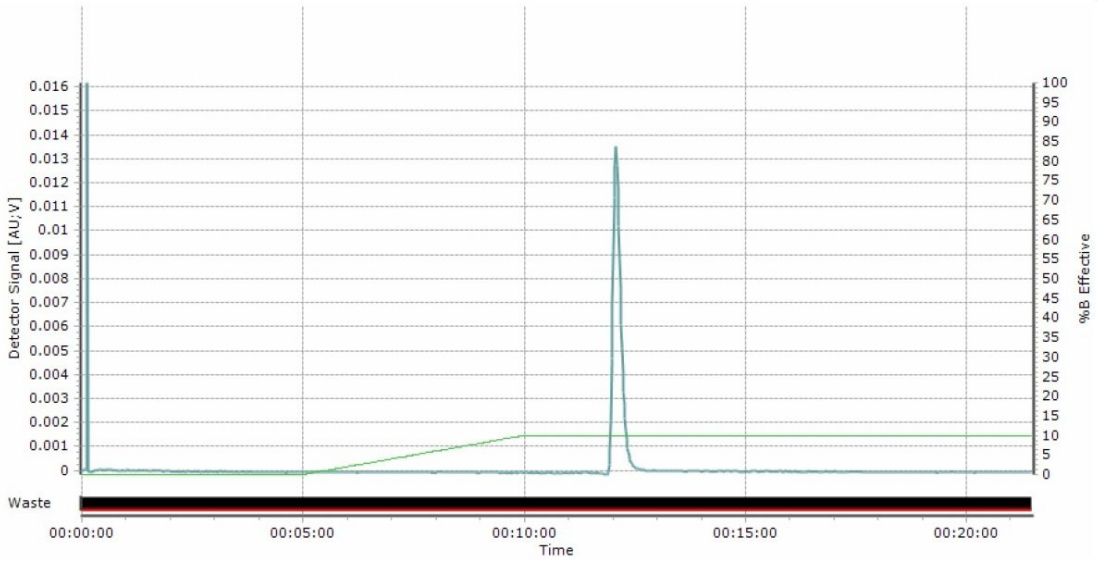

Figure **S82**: MPLC-chromatogram of radical **6•** (t = 12:04 min).

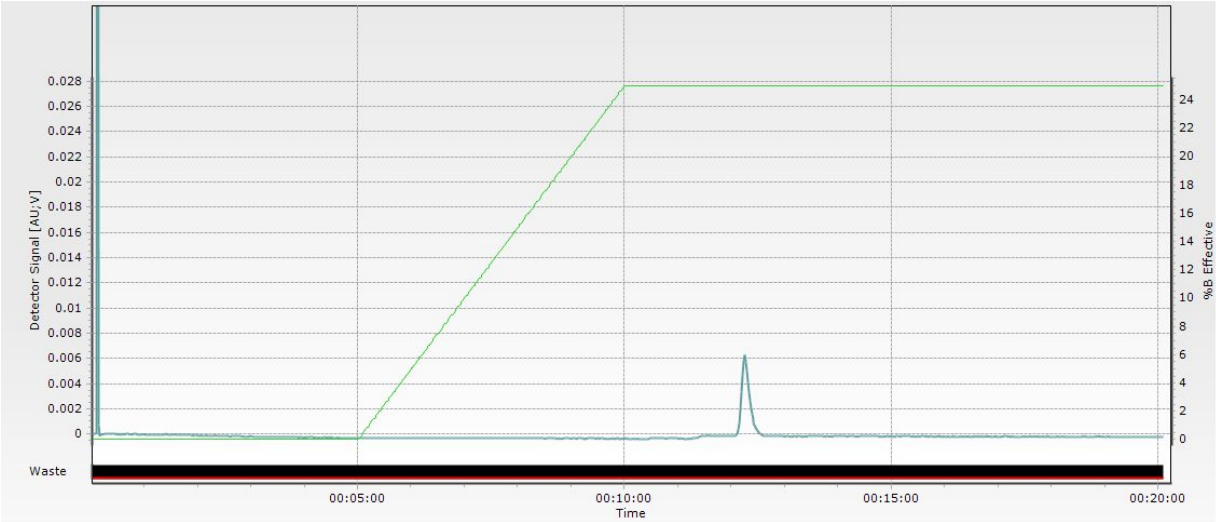

Figure **S83**: MPLC-chromatogram of radical **7•** (t = 12:14 min).

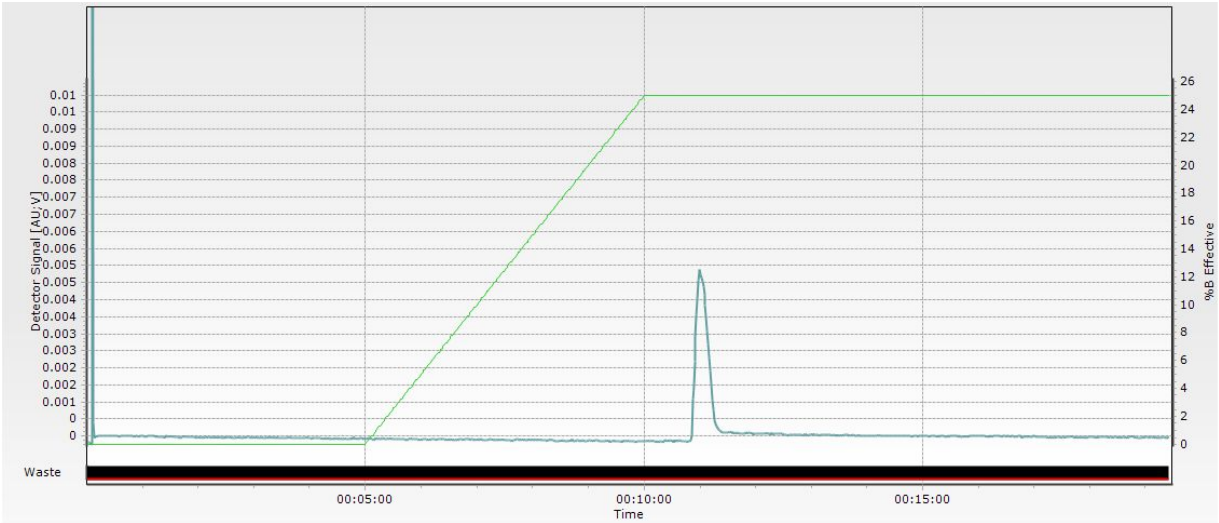

Figure **S84**: MPLC-chromatogram of radical **8•** (t = 11:00)

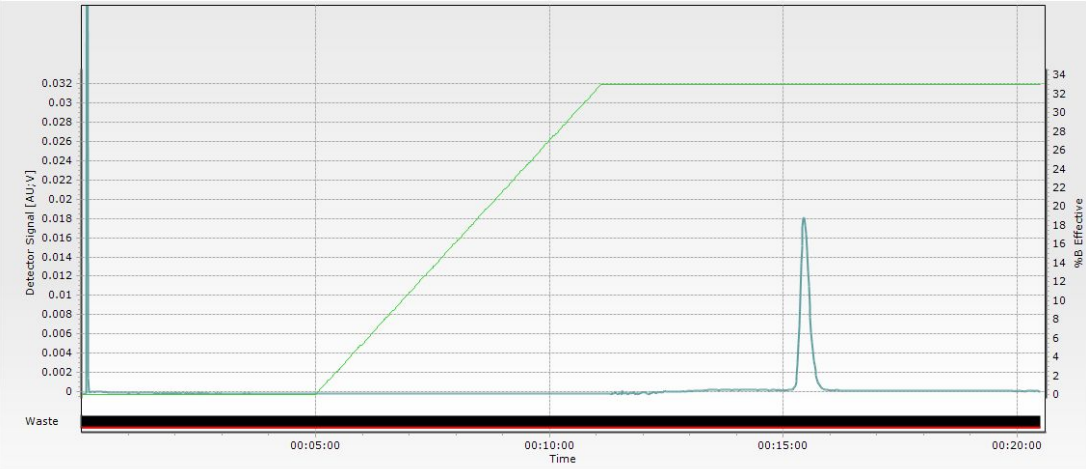

Figure **S85**: MPLC-chromatogram of biradical **15••** (t = 15:26).

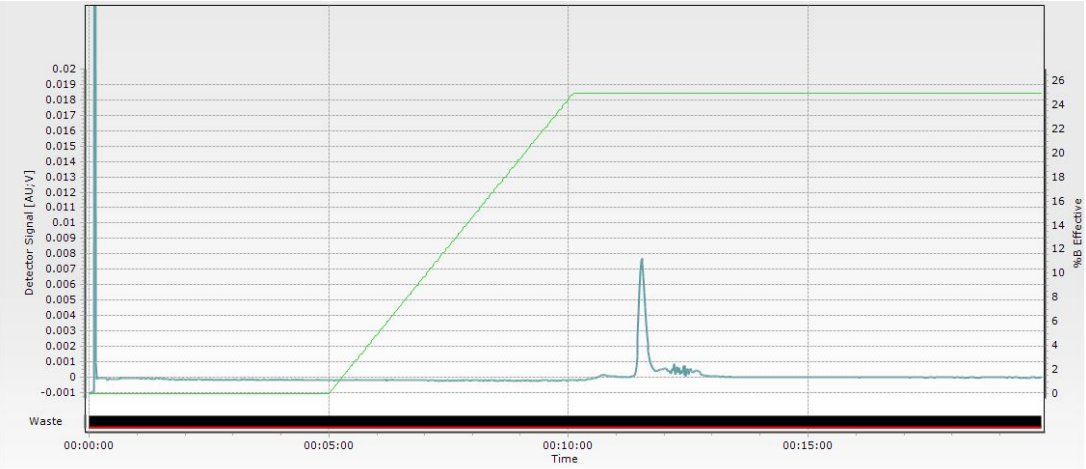

Figure **S86**: MPLC-chromatogram of radical **16•** (t = 11:31 min)

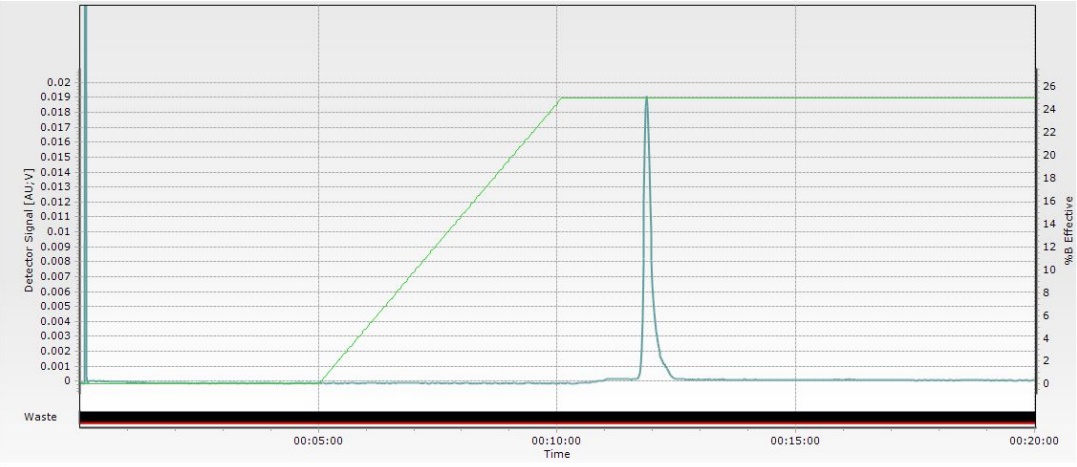

Figure **S87**: MPLC-chromatogram of radical **17•** (t = 11:52 min).

13. References

(1) Elsa, C.; Brecht, M.; Bittl, R. Pulsed Electron − Electron Double Resonance on Multinuclear Metal Clusters : Assignment of Spin Projection Factors Based on the Dipolar Interaction. *J. Am. Chem. Soc.* **2002**, *124*, 12606–12611.

(2) Grimme, S.; Bannwarth, C.; Shushkov, P. A Robust and Accurate Tight-Binding Quantum Chemical Method for Structures , Vibrational Frequencies , and Noncovalent Interactions of Large Molecular Systems Parametrized for all spd-Block Elements (Z = 1−86). *J. Chem. Theory Comput.* **2017**, *13*, 1989–2009.

(3) Saxena, S.; Freed, J. H. Theory of Double Quantum Two–Dimensional Electron Spin Resonance with Application to Distance Measurements Theory of Double Quantum Two-Dimensional Electron Spin Resonance with Application to Distance Measurements. *J. Chem. Phys.* **1997**, *107*, 1317–1340.

(4) Jeschke, G.; Chechik, V.; Ionita, P.; Godt, A.; Zimmermann, H.; Banham, J.; Timmel, C.; Hilger, D.; Jung, H. DeerAnalysis2006 – a Comprehensive Software Package for Analyzing Pulsed ELDOR Data. *Appl. Magn. Reson.* **2006**, *30*, 473–498.

(5) Edwards, T. H.; Stoll, S. Optimal Tikhonov Regularization for DEER Spectroscopy. *J. Magn. Reson.* **2018**, *288*, 58–68.

(6) Stoll, S.; Schweiger, A. EasySpin , a Comprehensive Software Package for Spectral Simulation and Analysis in EPR. *J. Magn. Reson.* **2006**, *178*, 42–55.

(7) Jassoy, J. J.; Meyer, A.; Spicher, S.; Wübben, C.; Schiemann, O. Synthesis of Nanometer Sized Bis- and Tris-Trityl Model Compounds with Different Extent of Spin – Spin Coupling. *Molecules* **2018**, *23*, 682.

(8) Iovine, V.; Cruciani, F.; Picini, F.; Varrone, M.; Rossi, E. Competitive Carbothiolation and Sonogashira Cross-Coupling in the Reaction of Trimethylsilylacetylene with Arylthioacetates. *ChemistrySelect* **2016**, *1*, 5201–5205.

[P8]: Magneto-Structural Correlations in a Mixed Porphyrin(Cu^{2+})/Trityl Spin System: Magnitude, Sign, and Distribution of the Exchange Coupling Constant

Reproduced with permission from

Dinar Abdullin, Tobias Hett, Nico Fleck, Kevin Kopp, Simon Cassidy, Sabine Richert, Olav Schiemann*, *Chem. Eur. J.* **2023**, e202203148.
DOI: https://doi.org/10.1002/chem.202203148

* Corresponding author.

Contributions

- Performing and analysing DFT calculations.

Chemistry–A European Journal
Research Article
doi.org/10.1002/chem.202203148
Chemistry Europe
European Chemical Societies Publishing
www.chemeurj.org

Magneto-Structural Correlations in a Mixed Porphyrin(Cu^{2+})/Trityl Spin System: Magnitude, Sign, and Distribution of the Exchange Coupling Constant

Dinar Abdullin,[a] Tobias Hett,[a] Nico Fleck,[a, b] Kevin Kopp,[a] Simon Cassidy,[c] Sabine Richert,[d] and Olav Schiemann*[a, e]

Abstract: Tetrathiatriarylmethyl radicals (TAM or trityl) are receiving increasing attention in various fields of magnetic resonance such as imaging, dynamic nuclear polarization, spin labeling, and, more recently, molecular magnetism and quantum information technology. Here, a trityl radical attached via a phenyl bridge to a copper(II)tetraphenylporphyrin was synthesized, and its magnetic properties studied by multi-frequency continuous-wave electron paramagnetic resonance (EPR) spectroscopy and magnetic measurements. EPR revealed that the electron spin-spin coupling constant J between the trityl and Cu^{2+} spin centers is ferromagnetic with a magnitude of -2.3 GHz (-0.077 cm^{-1}, $+J\vec{S}_1\vec{S}_2$ convention) and a distribution width of 1.2 GHz (0.040 cm^{-1}). With the help of density functional theory (DFT) calculations, the obtained ferromagnetic exchange coupling, which is unusual for para-substituted phenyl-bridged biradicals, could be related to the almost perpendicular orientation of the phenyl linker with respect to the porphyrin and trityl ring planes in the energy minimum, while the J distribution was rationalized by the temperature weighted rotation of the phenyl bridge about the molecular axis connecting both spin centers. This study exemplifies the importance of molecular dynamics for the homogeneity (or heterogeneity) of the magnetic properties of trityl-based systems.

Introduction

Among the plethora of stable radicals, tetrathiatriarylmethyl radicals (TAM or trityl, for example, **1** in Figure 1) have received increasing attention over the last two decades. Several studies have used the trityl platform to construct new spin labels,[1] polarizing agents for dynamic nuclear polarization (DNP),[2] or functional probes for electron paramagnetic resonance (EPR) based oximetry,[3] pH measurements,[3b,4] viscosimetry,[5] diffusometry,[6] and imaging.[7] The recent application of palladium-catalyzed carbon-carbon cross-coupling reactions increased the chemical diversity of trityl-based radicals and allowed the synthesis of the π-conjugated trityl-biradical **2** (Figure 1) with an exchange coupling constant J of ~168 GHz (5.6 cm^{-1}, $+J\vec{S}_1\vec{S}_2$ convention).[8] The conjugation of trityls to other spin bearing groups thus holds promise for applications in the field of molecular magnetism and quantum information technology.

To exemplify the use of trityl radicals in these latter fields, **1** was conjugated via a phenyl linker to free-base and metalated tetraphenylporphyrins (TPPs) yielding molecules **3**–**5** (Figure 1). These molecules, consisting of a photogenerated triplet spin center and a stable doublet spin center, were studied by transient EPR and optical techniques with respect to the formation of photogenerated quartet spin states.[9] While quartet state formation could be demonstrated, the quartet yield was found to be low and the magnitude of the exchange coupling constant J between the chromophore triplet state and the radical doublet state could not be determined. Since the value of J is not accessible experimentally, the influence of the molecular structure and dynamics on the exchange coupling could not be evaluated in these molecules. To get further insight, we synthesized here the structurally related molecule trityl-phenyl-TPP(Cu^{2+}) **6** (Figure 1) in which the photogener-

[a] Dr. D. Abdullin, T. Hett, Dr. N. Fleck, K. Kopp, Prof. Dr. O. Schiemann
Clausius-Institute of Physical and Theoretical Chemistry
University of Bonn
Wegelerstr. 12, 53115 Bonn (Germany)
E-mail: schiemann@pc.uni-bonn.de
[b] Dr. N. Fleck
Merck KGaA, Q20/001 Frankfurterstr. 250, 64293 Darmstadt (Germany)
[c] Dr. S. Cassidy
Department of Chemistry
University of Oxford
South Parks Road, Oxford OX1 3QR (UK)
[d] Dr. S. Richert
Institute of Physical Chemistry
University of Freiburg
Albertstr. 21, 79104 Freiburg (Germany)
[e] Prof. Dr. O. Schiemann
Department of Chemical and Biological Physics
Weizmann Institute of Science
761001 Rehovot (Israel)

Supporting information for this article is available on the WWW under https://doi.org/10.1002/chem.202203148

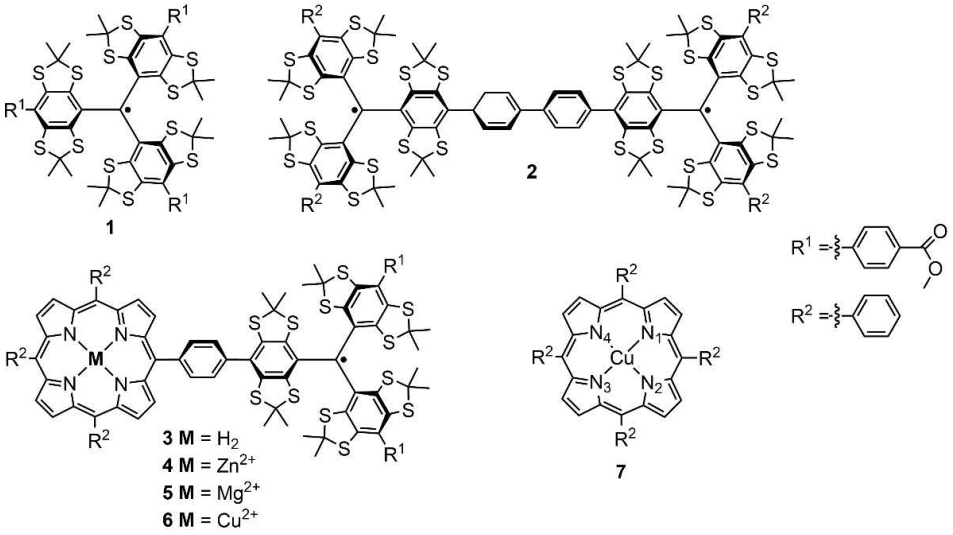

Figure 1. Chemical structures of molecules **1**–**7**.

ated triplet state of the porphyrin is replaced by the ground state doublet **7** (Figure 1). Although the geometric structure of **6** is very similar to that of the photoexcited molecules **3**–**5**, its electronic structure is not; for example, the spin density in the photoexcited triplet states of **3**–**5** is more delocalized than in **7**. Therefore, and although **6** is a good structural model, it can only serve as a model system for the evaluation of the lower boundary of *J* in the photoexcited porphyrin-trityl systems. To measure *J* in **6**, multifrequency EPR and magnetic susceptibility measurements as well as DFT calculations were carried out. Using analytical expressions for the spin Hamiltonian for two different spin-1/2 centers,[10] here trityl and Cu^{2+}, we show that simulation of the frozen solution cw EPR spectra may, under favorable conditions, enable not only the determination of the magnitude[11] but also the sign[11h–m] and the distribution[11d,k,l] of *J*. Further, making use of DFT calculations, the influence of the bridge dynamics on *J* is evaluated.

Theory

The theory of exchange interactions between two chemically dissimilar electron spin centers with $S=1/2$ has been described in several textbooks.[10] Here, we will briefly revisit this theory, focusing on the Cu^{2+}/trityl case and on the sign of *J*. Typically, the EPR theory of exchange interaction is based on the spin Hamiltonian

$$\widehat{\mathcal{H}} = g_1\beta B_0 S_{1z} + g_2\beta B_0 S_{2z} + J\vec{S}_1\vec{S}_2, \quad (1)$$

where β is the Bohr magneton, B_0 is the magnitude of the external static magnetic field $\vec{B}_0$, which is aligned parallel to the *z*-axis of the reference coordinate system, g_1 and g_2 are the *g*-factors of the spins, *J* is the exchange coupling constant, $\vec{S}_1$ and $\vec{S}_2$ are the spin vectors associated with the spins, and S_{1z} and S_{2z} are their projections onto the *z*-axis of the reference coordinate system. The first two terms in Equation (1) describe the Zeeman interaction of spins 1 and 2 with $\vec{B}_0$, and the third term is the Heisenberg exchange interaction between both spins. If $J=0$, the eigenstates of the above Hamiltonian are given by the states $|m_{S1},m_{S2}\rangle$, where m_{S1} and m_{S2} are the eigenvalues of S_{1z} and S_{2z}, equal to either $+1/2$ or $-1/2$. If $J\neq 0$, some of the $|m_{S1},m_{S2}\rangle$ states are mixed, giving rise to new eigenstates, a singlet state *S* and three triplet states T_{-1}, T_0, and T_1 (Table 1). The states T_{-1} and T_1 are identical to the initial states $|-1/2,-1/2\rangle$ and $|+1/2,+1/2\rangle$, respectively, whereas *S* and T_0 are superpositions of the initial states $|+1/2,-1/2\rangle$ and $|-1/2,+1/2\rangle$. The coefficients in the superposition are given by the cosine and sine of an angle α, which is defined as:

Table 1. Spin states of two exchange-coupled electron spin-1/2 centers.

Notation	State	Energy	Energy increment due to $DS_{1z}S_{2z}$
S	$\sin(\alpha)\left\|+\frac{1}{2},-\frac{1}{2}\right\rangle - \cos(\alpha)\left\|-\frac{1}{2},+\frac{1}{2}\right\rangle$	$-\frac{J}{4} - \mathrm{sgn}(J)\sqrt{\left(\frac{\Delta g\beta B_0}{2}\right)^2 + \left(\frac{J}{2}\right)^2}$	$-\frac{D}{4}$
T_{-1}	$\left\|-\frac{1}{2},-\frac{1}{2}\right\rangle$	$\frac{J}{4} - \langle g\rangle\beta B_0$	$+\frac{D}{4}$
T_0	$\cos(\alpha)\left\|+\frac{1}{2},-\frac{1}{2}\right\rangle + \sin(\alpha)\left\|-\frac{1}{2},+\frac{1}{2}\right\rangle$	$-\frac{J}{4} + \mathrm{sgn}(J)\sqrt{\left(\frac{\Delta g\beta B_0}{2}\right)^2 + \left(\frac{J}{2}\right)^2}$	$-\frac{D}{4}$
T_{+1}	$\left\|+\frac{1}{2},+\frac{1}{2}\right\rangle$	$\frac{J}{4} + \langle g\rangle\beta B_0$	$+\frac{D}{4}$

$$\tan(2\alpha) = \frac{J}{\Delta g \beta B_0}, \tag{2}$$

with

$$\Delta g = g_1 - g_2. \tag{3}$$

The energy levels of the four states are given in the third column of Table 1. In addition to Δg, the expressions of the energy levels contain the average g-factor of the two spins, $\langle g \rangle$:

$$\langle g \rangle = \frac{g_1 + g_2}{2}. \tag{4}$$

In the absence of a magnetic field ($B_0 = 0$), the energy levels of the singlet and triplet states are split by J. In the case of a ferromagnetic exchange interaction, J is negative and the triplet states have a lower energy than the singlet state. In the case of an antiferromagnetic exchange interaction, J is positive and the singlet state lies below the triplet states. The EPR transitions between the singlet and triplet states and their energies are listed in Table 2. Importantly, the transition energies and probabilities depend on the ratio x between the magnitude of J and the difference in the Zeeman energies of the two spins:

$$x = \frac{|J|}{\Delta g \beta B_0}. \tag{5}$$

If $x = 0$, the transitions $S \leftrightarrow T_{+1}$ and $T_{-1} \leftrightarrow T_0$ appear at $g = g_1$, and the transitions $T_0 \leftrightarrow T_{+1}$ and $T_{-1} \leftrightarrow S$ at $g = g_2$ yielding two lines in the corresponding EPR spectrum. If x is small, the two lines split into two doublets, one centered at g_1 and the other at g_2, each with a splitting of J at first approximation. As x increases, the transitions $S \leftrightarrow T_{+1}$ and $T_{-1} \leftrightarrow S$ gradually move further apart from each other and lose their intensity, while the transitions $T_0 \leftrightarrow T_{+1}$ and $T_{-1} \leftrightarrow T_0$, converge towards the average g-factor, $\langle g \rangle$, and become more intense. Finally, when x approaches infinity, the energy levels are divided into a triplet (T_{+1}, T_0, T_{-1}), whose states are symmetric, and a singlet S, whose state is asymmetric. In this case, only transitions within the triplet ($T_0 \leftrightarrow T_{+1}$ and $T_{-1} \leftrightarrow T_0$) are allowed and appear at $\langle g \rangle$. Consequently, one can distinguish three different coupling regimes: (1) a weak coupling regime that corresponds to $J \ll \Delta g \beta B_0$, (2) an intermediate coupling regime that corresponds to $J \sim \Delta g \beta B_0$, and (3) a strong coupling regime that corresponds to $J \gg \Delta g \beta B_0$.

Table 2. EPR transitions of two exchange- and dipolar coupled electron spin-1/2 centers.

Transition	Energy	Energy increment due to $DS_{1z}S_{2z}$
$T_{-1} \leftrightarrow T_0$	$\langle g \rangle \beta B_0 - \frac{\Delta g \beta B_0}{2} \mathrm{sgn}(J) \{x - \sqrt{1+x^2}\}$	$-\frac{D}{2}$
$T_0 \leftrightarrow T_{+1}$	$\langle g \rangle \beta B_0 + \frac{\Delta g \beta B_0}{2} \mathrm{sgn}(J) \{x - \sqrt{1+x^2}\}$	$+\frac{D}{2}$
$T_{-1} \leftrightarrow S$	$\langle g \rangle \beta B_0 - \frac{\Delta g \beta B_0}{2} \mathrm{sgn}(J) \{x + \sqrt{1+x^2}\}$	$-\frac{D}{2}$
$S \leftrightarrow T_{+1}$	$\langle g \rangle \beta B_0 + \frac{\Delta g \beta B_0}{2} \mathrm{sgn}(J) \{x + \sqrt{1+x^2}\}$	$+\frac{D}{2}$

Next, the spin Hamiltonian is extended by the dipole-dipole interaction between the electron spins. This is done under the assumption that the dipole-dipole interaction is much weaker than the exchange and Zeeman interactions. In this case, the dipole-dipole interaction can be treated as a perturbation to the initial spin Hamiltonian. Its non-secular component can be neglected in a first approximation, yielding

$$\widehat{\mathcal{H}} = g_1 \beta B_0 S_{1z} + g_2 \beta B_0 S_{2z} + J \vec{S}_1 \vec{S}_2 + D S_{1z} S_{2z}, \tag{6}$$

where D is the dipolar coupling constant, which is by definition positive and can be calculated according to:

$$D = \frac{\mu_0 \beta_e^2 g_1 g_2}{4\pi} \bullet \frac{(1 - 3\cos^2\theta)}{r^3} \tag{7}$$

where μ_0 is the vacuum permeability, β_e is the Bohr magneton, r is the inter-spin distance, and θ is the angle between the inter-spin vector $\vec{r}$ and the applied static magnetic field $\vec{B}_0$. The dipolar term $DS_{1z}S_{2z}$ does not mix different eigenstates of the Hamiltonian given by Equation (1) and, therefore, the eigenstates of the new Hamiltonian are the same as the eigenstates of the initial Hamiltonian (Table 1). However, the energies corresponding to the four eigenstates get an additional increment of $+D/4$ or $-D/4$ (column 4 in Table 1), and the four allowed EPR transitions get an additional increment of $+D/2$ or $-D/2$ (third column in Table 2). Note that in contrast to the exchange interaction term, which determines the separation between the singlet state and triplet states at $B_0 = 0$, the dipolar term results in the separation between T_0 and $T_{+/-1}$ in the triplet state at $B_0 = 0$. This allows determining D and J separately from each other, independently of whether the spin Hamiltonian or quantum chemistry programs like Orca are used. Finally, the spin Hamiltonian is extended by the hyperfine interaction of one of the electron spins (S_1) to a nucleus with an arbitrary spin I. This case is relevant for Cu^{2+}-trityl spin systems, because the electron spin of Cu^{2+} typically has a significant hyperfine interaction with the Cu nuclear spin ($I = 3/2$), while the spin of the trityl core shows only negligible ^{13}C hyperfine coupling. Assuming that the hyperfine interaction is much smaller than the Zeeman and exchange interactions, the non-secular component of the hyperfine interaction can be neglected, yielding

$$\widehat{\mathcal{H}} = g_1 \beta B_0 S_{1z} + g_2 \beta B_0 S_{2z} + J \vec{S}_1 \vec{S}_2 + D S_{1z} S_{2z} + A S_{1z} I_z, \tag{8}$$

where A is the hyperfine coupling constant, and I_z is the projection of the nuclear spin vector $\vec{I}$ onto $\vec{B}_0$. As the hyperfine term $AS_{1z}I_z$ does not mix different nuclear spin states $|m_I\rangle$, where m_I are the eigenvalues of I_z, the eigenstates of the Hamiltonian given by Equation (7) correspond to a product of the electron spin states and the nuclear spin states $|m_I\rangle$ (Table 3). Note that the electron spin states, in particular S and T_0, differ from those given in Table 1. The difference is determined by substituting the angle α by the angle α',

Table 3. Spin states of two exchange- and dipolar coupled electron spin-1/2 centers, one of which shows hyperfine coupling to a nuclear spin.

Notation	State
S	$\left\vert+\frac{1}{2},+\frac{1}{2},m_I\right\rangle$
T_{-1}	$\cos(\alpha')\left\vert+\frac{1}{2},-\frac{1}{2},m_I\right\rangle+\sin(\alpha')\left\vert-\frac{1}{2},+\frac{1}{2},m_I\right\rangle$
T_0	$\sin(\alpha')\left\vert+\frac{1}{2},-\frac{1}{2},m_I\right\rangle-\cos(\alpha')\left\vert-\frac{1}{2},+\frac{1}{2},m_I\right\rangle$
T_{+1}	$\left\vert-\frac{1}{2},-\frac{1}{2},m_I\right\rangle$

$$\tan(2\alpha') = \frac{J}{\Delta g\beta B_0 + Am_I}. \tag{9}$$

Note that α' depends on m_I and is therefore different for each nuclear spin projection.

For the given states, there are $4(2m_I+1)$ different transitions (Table 4). One can show that the energies of these transitions depend on the parameter x' given by

$$x' = \frac{|J|}{\Delta g\beta B_0 + Am_I}. \tag{10}$$

If $x'=0$, the hyperfine coupling splits the spin transition of S_1 into $(2m_I+1)$ hyperfine lines with the spliting constant of A. If x approaches infinity, the two allowed transitions, $|T_0,m_I\rangle \leftrightarrow |T_{+1},m_I\rangle$ and $|T_{-1},m_I\rangle \leftrightarrow |T_0,m_I\rangle$, are also split into $(2m_I+1)$ lines each, but with the splitting constant of $A/2$. Finaly, if $x'\neq 0$ but is finite, the hyperfine splitting has a complex dependence on x'.

Importantly, the analytically derived equations allow predicting the dependence of the EPR spectra on the sign of J. If the electron spins are coupled only via the exchange interaction, changing the sign of J results in interconversion of two allowed transitions, $T_{-1}\leftrightarrow T_0$ and $T_0\leftrightarrow T_{+1}$, and two forbidden transitions, $T_{-1}\leftrightarrow S$ and $S\leftrightarrow T_{+1}$, (second column in Table 2) but it does not change the EPR spectrum (Figure S1). The same result is obtained for the case when one of the electron spins is coupled to a nuclear spin (second column of Table 4, Figure S1). However, when including the dipole-dipole interaction between the electron spins, regardless of whether hyperfine interaction is present or not, the interconversion of the transitions upon changing the sign of J is no longer possible, because the transition energies differ by the dipolar contributions (third column in Tables 2 and 4). In this case, the sign of J affects the shape of the EPR spectrum (Figure S1). The extent of this effect depends on the magnitude of D and on x or, alternatively, x' (Figures S1 and S2). Moreover, in order to be able to determine the sign of J, D must be comparable to or larger than the EPR linewidth (Figure S2).

In the theory part above, the parameters g_1, g_2, D, and A were considered as scalars for the sake of simplicity. In the experiments and simulations below, these parameters are 3×3 tensors. To calculate EPR spectra of anisotropic spin systems, like Cu^{2+}-trityl systems, software packages employing matrix diagonalization can be used such as EasySpin[12] or Spinach.[13]

Results and Discussion

Synthesis and sample characterization. Biradical **6** was obtained from the literature-known precursor **3**[8] by treatment with copper(II)acetate in dichloromethane/methanol (3:2). The identity and purity of the biradical was confirmed by MALDI(+)-HRMS (Figure S3) and EPR spectroscopy. Comparison of the EPR spectrum of **6** with the EPR spectra of references **1** and **7** (Figures S4 and S5) revealed that samples of **6** contained two minor paramagnetic impurities whose EPR spectra are identical to the EPR spectra of the two reference samples. Presumably, these impurities correspond to HO-trityl-phenyl-TPP(Cu^{2+}) (relative amount = 6%, Figure S4), in which the trityl radical is converted to its alcohol form, and to H_2-porphyrin-phenyl-trityl (relative amount = 1%, Figures S5), which did not react with copper(II)acetate. Since the impurities are marginal, the signals belonging to these impurities were subtracted from all EPR spectra of **6**. These spectra are used in the following.

EPR spectroscopy and simulations. The main goal of the EPR measurements was to determine the magnitude, sign, and distribution of J in **6**. EPR measurements of J are often done in solution, because the dipolar coupling constant and the anisotropy of the g- and A- tensors are averaged to zero, thus simplifying the extraction of the magnitude of J from the EPR spectrum.[14] However, the complete averaging of anisotropic interactions is possible only as long as the isotropic tumbling limit is valid.[11] For large, bulky molecules such as **6**, the isotropic tumbling limit is not reached at room temperature (Figure S4), and the liquid-state EPR spectrum is governed by slow molecular motions, which are described by an anisotropic rotational correlation time. In this case, the solid-state EPR spectrum can be described by fewer parameters than the corresponding liquid-state EPR spectrum. Moreover, as was shown in the Theory section, the sign of J can be determined only in the presence of a non-zero dipolar coupling constant D, which can be obtained only in the solid state. For these reasons, the EPR spectra of **6** were measured in frozen toluene solution at 100 K (Figure 2). To test different coupling regimes and to increase the reliability of the subsequent EPR simulations, the EPR measurements were performed at X- (9.4 GHz), Q- (34 GHz), and W-band (94 GHz).

Table 4. EPR transitions of two exchange- and dipolar coupled electron spin-1/2 centers, one of which shows hyperfine coupling to a nuclear spin.

Transition	Energy (without the dipolar contribution)	Dipolar contribution
$\vert T_{-1},m_I\rangle \leftrightarrow \vert T_0,m_I\rangle$	$\langle g\rangle\beta B_0+\frac{Am_I}{2}-\frac{\Delta g\beta B_0+Am_I}{2}\mathrm{sgn}(J)\left\{x'-\sqrt{1+x'^2}\right\}$	$-\frac{D}{2}$
$\vert T_0,m_I\rangle \leftrightarrow \vert T_{+1},m_I\rangle$	$\langle g\rangle\beta B_0+\frac{Am_I}{2}+\frac{\Delta g\beta B_0+Am_I}{2}\mathrm{sgn}(J)\left\{x'-\sqrt{1+x'^2}\right\}$	$+\frac{D}{2}$
$\vert T_{-1},m_I\rangle \leftrightarrow \vert S,m_I\rangle$	$\langle g\rangle\beta B_0+\frac{Am_I}{2}-\frac{\Delta g\beta B_0+Am_I}{2}\mathrm{sgn}(J)\left\{x'+\sqrt{1+x'^2}\right\}$	$-\frac{D}{2}$
$\vert S,m_I\rangle \leftrightarrow \vert T_{+1},m_I\rangle$	$\langle g\rangle\beta B_0+\frac{Am_I}{2}+\frac{\Delta g\beta B_0+Am_I}{2}\mathrm{sgn}(J)\left\{x'+\sqrt{1+x'^2}\right\}$	$+\frac{D}{2}$

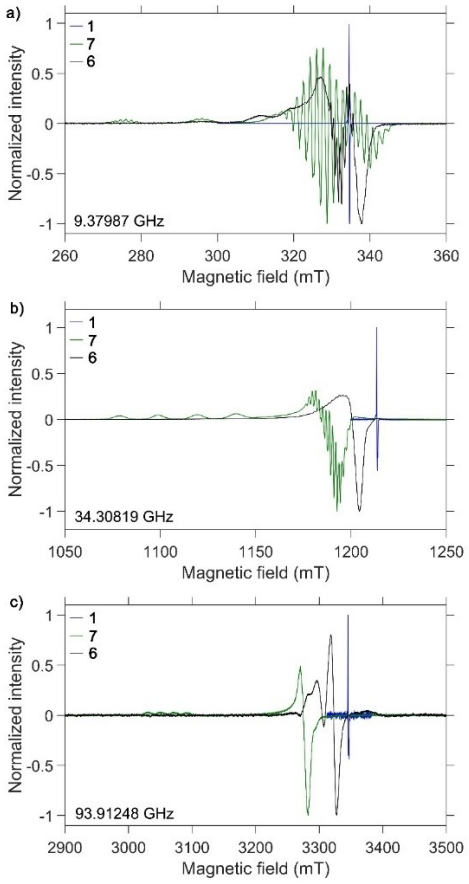

Figure 2. Multifrequency EPR spectra of **1**, **6**, and **7**. The EPR spectra of **6** (black) are overlayed with the EPR spectra of reference molecules **7** (green) and **1** (blue) at **a**) X-, **b**) Q-, and **c**) W-band.

When overlaying the EPR spectra of **6** with those of reference molecules **1** and **7**, one notices that the EPR spectra of **6** are not just the sum of the EPR spectra of the individual Cu^{2+} and trityl spin centers. In particular, the spectra of **6** appear at magnetic fields that lie in between the spectra of **1** and **7** (particularly nicely seen at W-band), indicating at least partial averaging of the trityl and Cu^{2+} *g*-factors. Moreover, the Cu^{2+} hyperfine structure in **6** has an apparent splitting that is about half the hyperfine coupling constant in **7**. All these observations suggest that the trityl and Cu^{2+} spin centers are strongly exchange-coupled in **6**. In addition, an inter-spin distance of 1.3 nm (see DFT calculations below) gives rise to a dipolar coupling constant *D* of 24 MHz (based on Equation (7)).

To determine *J*, all three EPR spectra of **6** were simulated by means of EasySpin. The simulation parameters included the EPR parameters of the individual Cu^{2+} and trityl centers, the dipolar coupling constant *D*, three Euler angles (α_d, β_d, γ_d) describing the orientation of the dipolar frame relative to the laboratory frame, the EPR linewidth, and *J*. The *g*- and hyperfine parameters of the individual trityl and Cu^{2+} centers were assumed to be identical to those in **1** and **7**, respectively, and were determined by simulating their EPR spectra. In agreement with previous reports,[11l,15] the X-band spectrum of **7** was described by an axial *g*-tensor, an axial A(Cu) hyperfine coupling tensor, and four porphyrin ^{14}N nuclei (Table 5), while at Q- and W-band, a small orthorhombicity of the *g*-tensor was resolved (Table S7). The X-band spectrum of **1** was simulated with an isotropic *g*-factor and hyperfine coupling constants corresponding to ^{13}C nuclei in the *ortho*- and *ipso*-positions (Table 5).[8,16] At Q- and W-band, a small axiality of the *g*-tensor of **1** was resolved (Table S8), which is in line with previous reports.[1c,17] *D* was set to the value given above. As the value of *D* is small, its distribution due to the inter-spin distance distribution in **6** was neglected. Since the trityl center is almost isotropic, the orientation of the dipolar tensor is given with respect to the Cu^{2+} center. The laboratory frame was set to coincide with the *g*-tensor of the Cu^{2+} center, where the *z*-axis is perpendicular to the porphyrin ring plane and the *x*- and *y*-axes are in plane and directed along two perpendicular Cu–N bonds (Figure S7).[15b,c] According to the DFT calculations (see below), the inter-spin vector lies almost in the porphyrin plane and is tilted by ~45° from the *x*-axis (Figure S7). This geometry corresponds to α_d, β_d, and γ_d being equal to 45°, 90°, and 0°, respectively. The EPR linewidth of **6** was simulated as an anisotropic, inhomogeneous linewidth. Yet, all attempts to simulate the EPR spectra of **6** with the above parameters were unsuccessful, because the dimension of the spin Hamiltonian matrix was so large that EasySpin could not handle it. This issue has been previously reported for copper bi- and tri-radicals.[11l] In order to make the simulations feasible, all small hyperfine coupling constants, including $A(^{14}N)$ of the Cu^{2+} center and $A(^{13}C)$ of the trityl center, were excluded from consideration. Moreover, all *g*-factors were set to those determined at X-band. With these simplifications, the EasySpin simulations became possible. In Figure 3a, the simulated EPR spectra are plotted as a function of *J* (denoted as $\langle J \rangle$ for the reasons given below). For each microwave band, the simulated spectra were normalized by the maximum intensity, yielding the intensity range of [−1, 1]. Spectral regions with positive and negative intensities were colored red and blue, respectively. For $\langle J \rangle = 0$, the typical features of the Cu^{2+} and trityl spectra can be seen. In the case of $\langle J \rangle \neq 0$, each component of the Cu^{2+} and trityl spectra splits into two, corresponding to one allowed and one forbidden

Table 5. X-band EPR parameters of **1**, **7** and **6**.

Parameter	1	7	6
$g_\perp$, $g_\parallel$(Cu^{2+})		2.048, 2.190	2.048, 2.190
g_{iso} (trityl)	2.003		2.003
$A_\perp$, $A_\parallel$(Cu)/MHz		−64, −615	−64, −615
A_{xx}, A_{yy}, A_{zz} ($N_{1,3}$)/MHz		54, 44, 44	
A_{xx}, A_{yy}, A_{zz} ($N_{2,4}$)/MHz		44, 54, 44	
A_{iso}($^{13}C_{ortho}$)/MHz	25		
A_{iso}($^{13}C_{ipso}$)/MHz	32		
$\langle J \rangle$, σ_J/GHz			−2.3, 1.2
D/MHz			24
α_d, β_d, γ_d/°			45, 90, 0
Linewidth/MHz	2.7[a]	24, 24, 34[b]	120, 120, 70[b]

[a] The linewidth is given as a peak-to-peak linewidth (lwpp) corresponding to homogeneous broadening. [b] The linewidth is given as an anisotropic residual linewidth (Hstrain), [$\Delta\nu_{xx}$, $\Delta\nu_{yy}$, $\Delta\nu_{zz}$], where $\Delta\nu_{xx}$, $\Delta\nu_{yy}$, and $\Delta\nu_{zz}$ are the full widths at half height.

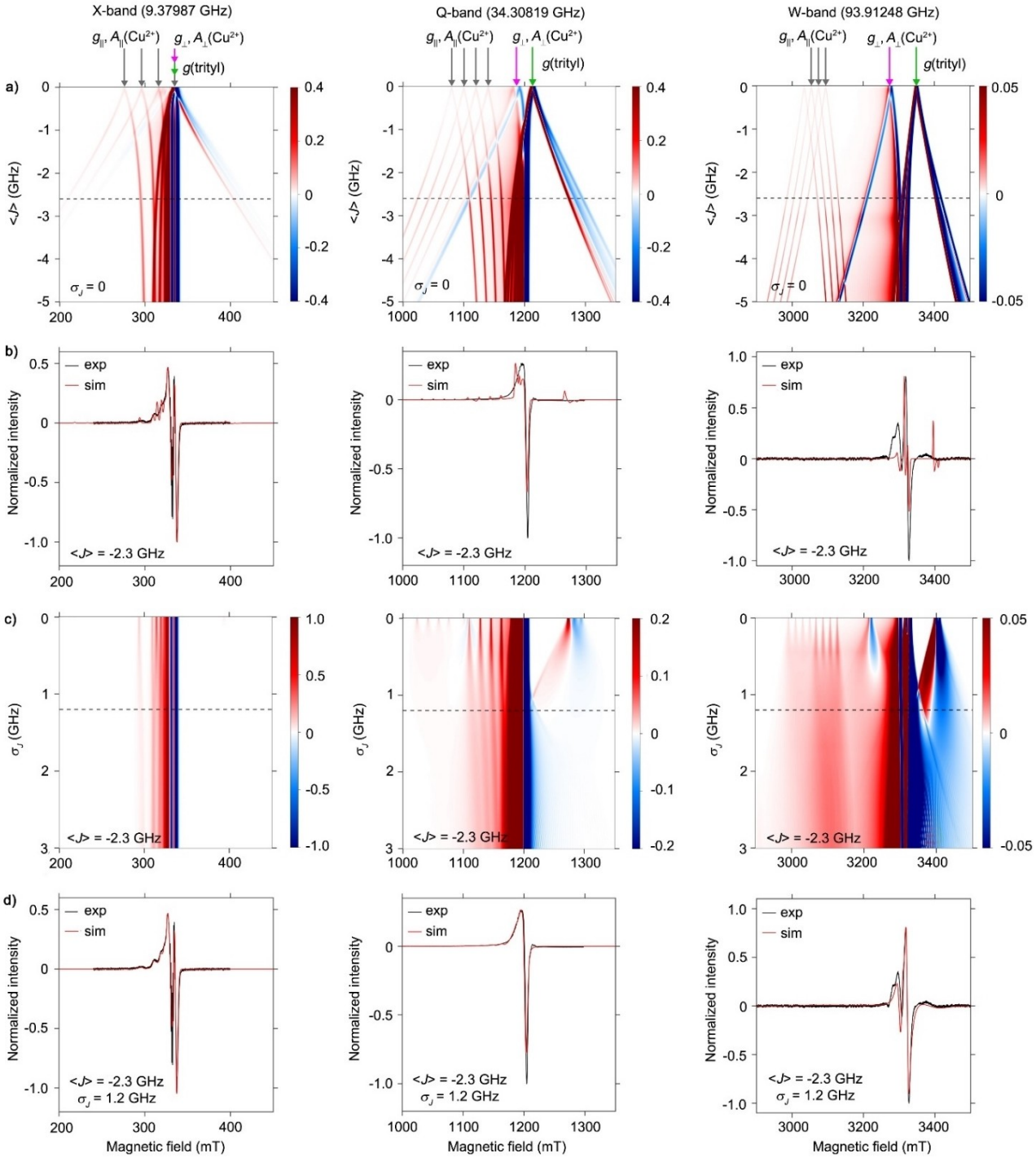

Figure 3. Simulation of the EPR spectra of **6** as a function of $\langle J \rangle$ and σ_J. Left: X-band, middle: Q-band, and right: W-band. **a**) Simulated EPR spectra as a function of $\langle J \rangle$ with σ_J set to 0. All other simulation parameters are set to the values given in the last column of Table 5. The intensity of all simulated spectra is normalized to 1. Spectral features corresponding to Cu^{2+} and trityl are marked by arrows. The best fit for $\langle J \rangle = -2.3$ GHz is marked by a dashed line. **b**) The experimental spectra overlayed with the simulated ones corresponding to $\langle J \rangle = -2.3$ GHz and $\sigma_J = 0$ GHz. **c)** Simulated EPR spectra as a function of σ_J with $\langle J \rangle$ set to -2.3 GHz. All other simulation parameters are set to the values given in the last column of Table 5. The intensity of all simulated spectra is normalized to 1. $\sigma_J = 1.2$ GHz is marked by a dashed line. **d**) The experimental spectra overlayed with the simulated ones corresponding to $\langle J \rangle = -2.3$ GHz and $\sigma_J = 1.2$ GHz.

transition. For $\langle J \rangle = -2.3$ GHz, the positions of the most intense peaks in the simulated and experimental EPR spectra show a reasonable agreement in all three frequency bands. Yet, the widths of these peaks differ largely. In particular, the lines that correspond to the $g_{||}$ component of Cu^{2+} are clearly seen in the simulated Q- and W-band spectra but are absent in the corresponding experimental spectra (Figure 3b). Therefore, it was assumed that J is not a single value but rather has to be

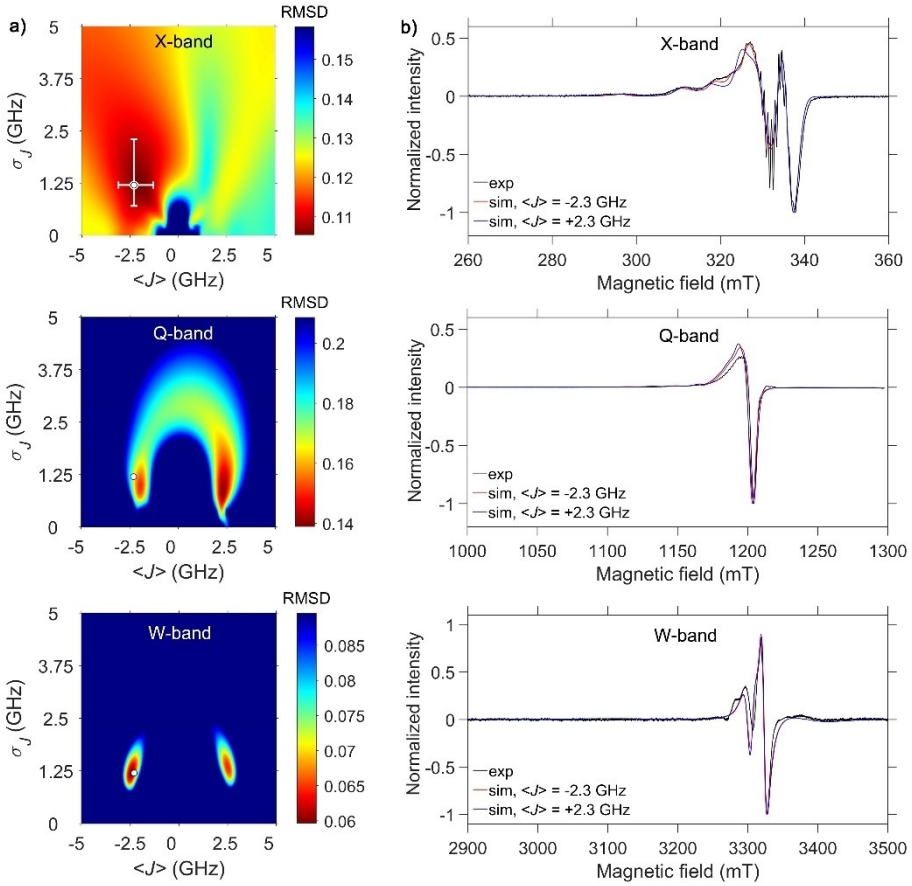

Figure 4. RMSD plots and best solutions for **6** at X- (top), Q- (middle), and W-band (bottom). **a**) RMSD between the simulated and experimental EPR spectra of **6** as a function of simulation parameters $\langle J\rangle$ and σ_J. All other simulation parameters are listed in the last column of Table 5. The optimized values of $\langle J\rangle$ and σ_J are depicted as a white dot. **b)** EPR spectra (black) overlaid with the simulated spectra corresponding to $\langle J\rangle = -2.3$ GHz and $\sigma_J = 1.2$ GHz (red) and to $\langle J\rangle = +2.3$ GHz and $\sigma_J = 1.2$ GHz (blue).

described by a distribution. For simplicity, the distribution of J was approximated by a Gaussian distribution with a mean value $\langle J\rangle$ and a width given by the standard deviation σ_J. In Figure 3c, the influence of σ_J on the spectra is shown for $\langle J\rangle$ set to -2.3 GHz. All and in particular the forbidden transitions broaden with the increase of σ_J, leading to excellent agreement between the simulated and experimental EPR spectra for all three frequency bands at $\langle J\rangle = -2.3$ GHz and $\sigma_J = 1.2$ GHz (Figure 3d). These parameters allow reproducing all features of the corresponding experimental EPR spectra, except for the ^{14}N hyperfine structure, which was excluded from the simulation for the reasons mentioned above (Table 5).

To test whether the obtained $\langle J\rangle$ and σ_J values yield a global fit to the EPR spectra, the root-mean-square-deviation (RMSD) between the simulated and experimental EPR spectra was evaluated on a two-dimensional linear grid of $\langle J\rangle$ and σ_J values with bounds of [−5, 5] GHz and [0, 5] GHz, respectively (Figure 4a). At X-band, the RMSD surface shows one deep minimum at $\langle J\rangle = -2.3$ GHz and $\sigma_J = 1.2$ GHz. At Q- and W-band, the RMSD surfaces show two minima, one at $\langle J\rangle = +2.3$ GHz and another one at $\langle J\rangle = -2.3$ GHz. The minimum at $\langle J\rangle = -2.3$ GHz is slightly deeper at W-band, while at $\langle J\rangle = +2.3$ GHz is slightly deeper at Q-band. According to the theory described

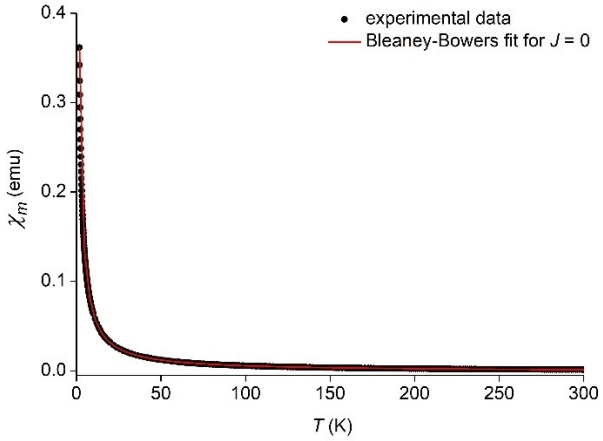

Figure 5. The magnetic susceptibility of **6** as a function of the temperature. The experimental data points (black) are overlaid with the Bleaney-Bowers fit obtained for $J = 0$ (red).

above, the sign of J affects the spectral shape if D is non-zero and the extent of the change depends on the magnitude of D and the ratio $x' = |J|/(\Delta g\beta B_0 + Am_I)$. For **6**, this effect is most

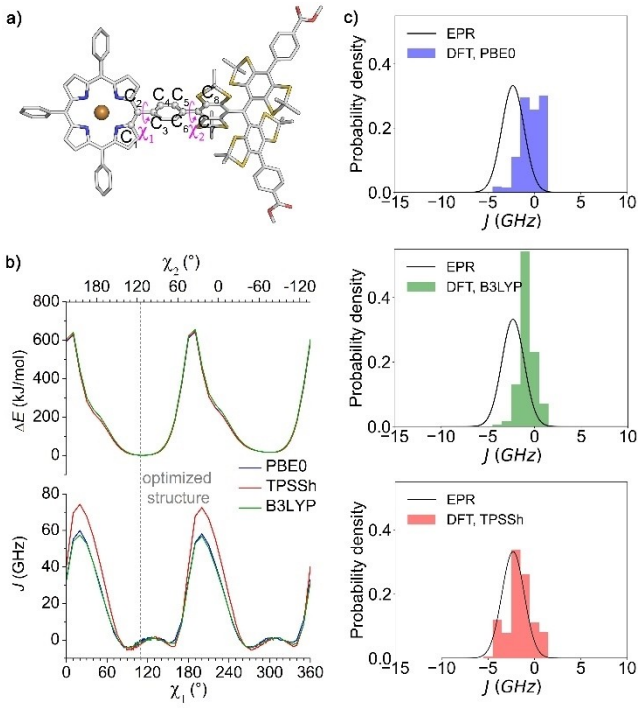

Figure 6. DFT results for **6**. **a**) The structure optimized on the PBE0-D3/def2-TZVP level of theory. The dihedral angles C_1–C_2–C_3–C_4 and C_8–C_7–C_6–C_5 are denoted as χ_1 and χ_2, respectively. The rotation of the phenyl linker is depicted by arrows. **b**) The relative energy (top) and the exchange coupling constant (bottom) as a function of χ_1 and χ_2. **c**) Comparison of the experimentally derived exchange coupling distributions with the DFT-based ones using the functionals PBE0 (top), B3LYP (middle), and TPSSh (bottom).

significant at X-band ($B_0 \sim 0.3$ T), whereas it is too weak for a reliable differentiation between positive and negative J at Q- ($B_0 \sim 1$ T) and W-band ($B_0 \sim 3$ T). This can be seen clearly in Figure 4b, where the spectra simulated with $\langle J \rangle = -2.3$ GHz and $\langle J \rangle = +2.3$ GHz are overlaid and compared to the respective experimental spectrum. At X-band, a positive $\langle J \rangle$ does not reproduce the experimental spectrum as well as a negative $\langle J \rangle$. In contrast, at Q- and W-band, both the negative and positive $\langle J \rangle$ provide similarly good fits to the experimental spectra. Since the X-band spectrum showed the strongest dependence on J, the corresponding RMSD surface was used to estimate the errors of $\langle J \rangle$ and σ_J. By inspecting individual simulated spectra, a reasonable agreement between the simulated and experimental spectra was achieved up to an RMSD value of 0.11 (Figure S8). This value was used as an RMSD threshold to determine the confidence intervals (Figure 4a), which in turn were converted into asymmetric errors, yielding $\langle J \rangle = -2.3^{+1.0}_{-0.8}$ GHz and $\sigma_J = 1.2^{+1.1}_{-0.5}$ GHz. The negative sign of $\langle J \rangle$ means that the Cu^{2+} and trityl spins are ferromagnetically coupled. Considering that a *para*-substituted phenyl bridge between two spin centers usually leads to antiferromagnetic coupling, the obtained ferromagnetic coupling was surprising.

Magnetic susceptibility measurements. As described in the theory section, the exchange interaction between two electron spin centers results in the singlet and triplet energy states split by J. This splitting leads to a temperature-dependent population difference between the singlet and triplet states, which affects the macroscopic magnetization of the sample, a property that can be captured by means of magnetic susceptibility measurements. The temperature dependence of the molar magnetic susceptibility χ_m is described by the Bleaney–Bowers equation[18]

$$\chi_m = \frac{N_A \beta^2 g^2}{k_B T} \frac{2\exp\left(-\frac{J}{k_B T}\right)}{1 + 3\exp\left(-\frac{J}{k_B T}\right)} \tag{11}$$

where N_A is the Avogadro constant, k_B is the Boltzmann constant, T is the temperature, and g is the g-factor of the coupled spin-1/2 centers. Note that Equation (11) corresponds to the $+J\vec{S}_1\vec{S}_2$ convention for the exchange coupling energy, which is used throughout this manuscript. According to Equation (11), a significant difference to a Curie law ($J = 0$) dependence is obtained only if $|J| \geq k_B T$, which sets the lower boundary of $|J|$ that can be determined by magnetic susceptibility measurements. The temperature dependence of the magnetic susceptibility of **6** is depicted in Figure 5. The experimental curve is well reproduced by a Bleaney–Bowers fit obtained with $J = 0$. This implies that $|J|$ does not exceed $k_B T$ even at the lowest temperature measured (1.8 K) and therefore $|J| < 37.5$ GHz (1.25 cm^{-1}) in **6**. This agrees with the J value determined by EPR. Thus, while **6** is in the intermediate to strong coupling regime for EPR (9–94 GHz), it is in the weak coupling regime for the magnetic susceptibility measurement.

DFT calculations. To unravel the reason for the ferromagnetic coupling, the small exchange coupling of **6** compared to **2**, and the distribution in J, DFT calculations were performed. Figure 6a shows the structure of **6** optimized on the PBE0-D3/def2-TZVP level of theory. The distance between the Cu^{2+} atom and the central carbon atom of trityl amounts to 13.5 Å (corresponding to $D = 24$ MHz), and the dihedral angles C_1–C_2–C_3–C_4 (χ_1) and C_5–C_6–C_7–C_8 (χ_2) to 109° and 117°, respectively. J was calculated according to the broken symme-

Table 6. The DFT-based values for $\langle J \rangle$ and σ_J of **6**.

Method	J (optimized structure)	$\langle J \rangle$[a] (rotation of the phenyl linker)	σ_J[b] (rotation of the phenyl linker)
DFT, PBE0	−2.4 GHz (−0.080 cm^{-1})	−0.4 GHz (−0.013 cm^{-1})	1.1 GHz (0.037 cm^{-1})
DFT, TPSSh	−1.2 GHz (−0.040 cm^{-1})	−1.6 GHz (−0.053 cm^{-1})	1.4 GHz (0.046 cm^{-1})
DFT, B3LYP	−0.6 GHz (−0.020 cm^{-1})	−0.8 GHz (−0.027 cm^{-1})	0.8 GHz (0.027 cm^{-1})
EPR	–	−2.3 GHz (−0.077 cm^{-1})	1.2 GHz (0.040 cm^{-1})

[a] These values were extracted from the histograms obtained by rotating the phenyl linker from 0°–360° (see Figure 6c).

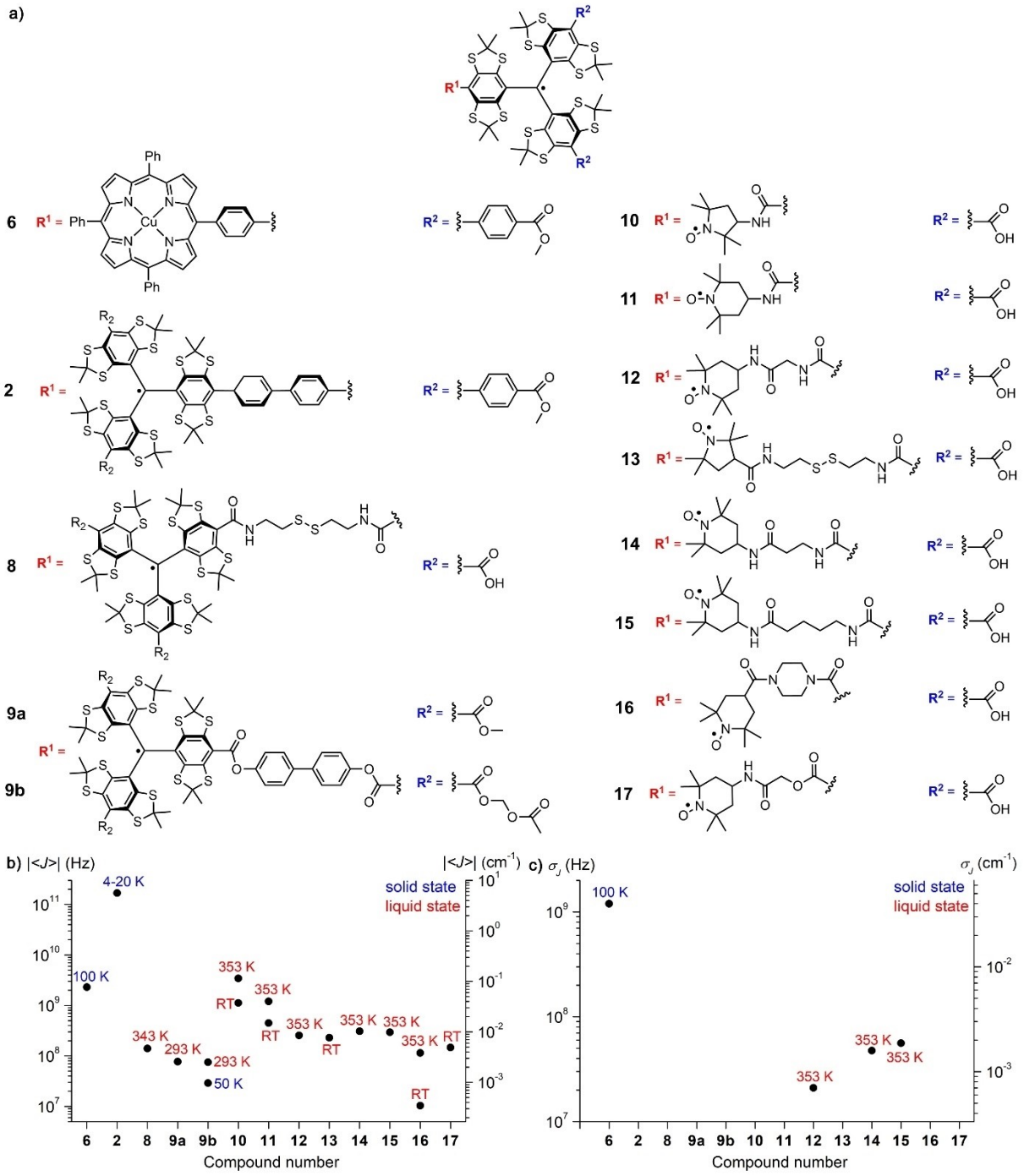

Figure 7. Comparison of $|\langle J\rangle|$ and σ_J for different TAM based biradicals. **a**) Chemical structures of the trityl-based radicals **6**, **2**,[8] and **8**–**17**.[11c,d,f,g] **b**) The absolute values of the mean exchange coupling constant. **c**) The distribution widths of the exchange coupling constant. All values have been measured by means of EPR in either the liquid or solid state. The temperature of the EPR measurements is indicated.

try formalism. Typically, when J is calculated by DFT, hybrid functionals provide the best performance.[19] To avoid bias due to a particular functional, three different hybrid functionals, namely PBE0 (25% Hartree-Fock exchange), B3LYP (20% Hartree-Fock exchange), and TPSSh (10% Hartree-Fock exchange) were used. As can be seen from column 2 in Table 6, all calculated J values are of the same order of magnitude and negative, indicating ferromagnetic exchange coupling and matching the experimentally determined $\langle J\rangle$ value of $-2.3^{+1.0}_{-0.8}$ GHz well.

A geometric parameter that could be the reason for the distribution of J in **6** is the rotation of the phenyl linker about the molecular axis connecting the two spin centers. In order to test this hypothesis, the dependence of J on the orientation of

the phenyl linker described by the dihedral angles χ_1 and χ_2 was evaluated (Figure 6a). In the calculations, the atoms in the TPP(Cu^{2+}) and trityl moieties were fixed at their DFT-optimized positions, while the dihedral angles χ_1 and χ_2 were varied in the range [0°, 360°]. Around the energy minimum, the variation step was 0.5°, while larger steps of 1° to 10° were used outside the energy minimum. For each χ_1 and χ_2 pair, the single-point energy (including the dispersion correction) and J were calculated in the same way as described above. The energies were referenced to the minimum energy, yielding ΔE. The obtained profiles of ΔE and J are shown in Figures 6b and 6c, respectively. Figure 6b reveals that the energy profiles obtained for the three different functionals are very similar and characterized by a rotation barrier of 600 kJ/mol, separating the two symmetry-related minima on the potential surface. The J profiles obtained for the three different functionals are also similar and show a correlation with the corresponding energy profiles (Figure 6c). This shows that the calculated energy and J values are not biased by the choice of the functional. The values of J lie between −5 GHz (ferromagnetic exchange) and +70 GHz (antiferromagnetic exchange) and are highly dependent on χ_1 and χ_2. Interestingly, (χ_1, χ_2) values of about (20°, 200°) and (200°, 20°) yield a strong antiferromagnetic exchange interaction, whereas (110°, 110°) and (290°, 290°) correspond to a weak ferromagnetic exchange interaction. This result may be rationalized based on spin polarization mediated by the overlap of the p_z orbitals between the phenyl bridge and the spin-carrying moieties. If the χ_1 and χ_2 angles are close to 20° or 200°, the phenyl bridge is almost "in plane" with the porphyrin and trityl groups leading to significant π-conjugation between the spin-carrying moieties and, as expected, to a large antiferromagnetic exchange coupling. In contrast, if the χ_1 and χ_2 angles are close to 110° or 290°, the phenyl plane is almost perpendicular to the porphyrin and trityl moieties, drastically reducing the π-conjugation between both spin-carrying moieties, and resulting in a small ferromagnetic exchange coupling. Since the energy minimum of **6** corresponds to $\chi_1 = 109°$ and $\chi_2 = 117°$, a weak ferromagnetic exchange is obtained. This exchange coupling is not mediated through space,[20] as revealed by a DFT calculation on **6** where the phenyl bridge between the (Cu^{2+})TPP and trityl moieties was removed while leaving the geometric arrangement of the two spin centers unchanged (for details see the Supporting Information, Section 6). To calculate the distribution of J based on Figure 6b, the (χ_1, χ_2) and J values that are populated at the freezing point of the solvent (178 K for toluene) were determined by calculation of the Boltzmann weights using the corresponding ΔE values (Figure 6b and Tables S9-S11). Non-zero Boltzmann weights were obtained for the χ_1 and χ_2 angles in the range 95°–130° (Figure S9). The J distribution was then calculated as a histogram of all J values with non-zero Boltzmann weights. The J distributions obtained in this way are depicted in Figure 6c. As can be seen, a good agreement between EPR and DFT is achieved for both $\langle J \rangle$ and σ_J (columns 3 and 4 in Table 6). This indicates that the rotation of the phenyl ring is indeed the main cause for the distribution of J. It should be pointed out here that no active rotation of the phenyl linker is assumed at 100 K, where the frozen-solution EPR spectra were acquired. Instead, it is assumed that the rotamers ensemble of **6**, present at the freezing point of the solvent, here toluene (178 K), is preserved at any temperature below the freezing point.

Comparison to other trityl biradicals. Figure 7 collects the $|\langle J \rangle|$ and σ_J values found for **6** and trityl-based biradicals **2**,[8] and **8**–**17**.[11c,d,f,g] All values are given in accordance with the $+J\vec{S}_1\vec{S}_2$ convention and were measured by means of EPR. Since J is temperature-dependent and may depend on the aggregate state, $|\langle J \rangle|$ and σ_J obtained for different biradicals are compared only qualitatively. Such a comparison reveals that the $|\langle J \rangle|$ value of **6** is one to two orders of magnitude larger than the $|\langle J \rangle|$ value of the amide- and ester-conjugated trityl-nitroxide biradicals (**11**–**16**) as well as the amide- and ester-conjugated bis-trityl biradicals (**8**, **9a**, and **9b**). This shows that the π-conjugation of a trityl radical to the second spin center yields significantly larger $|\langle J \rangle|$ values than non-conjugated bridges. In contrast, the π-conjugated bis-trityl **2** has a $|\langle J \rangle|$ value, which is about two orders of magnitude larger than that of **6** although the trityl groups in **2** are separated by two instead of one phenyl ring. This large difference in J may be due to the spin density of the central carbon atom in the trityl moiety being more delocalized towards the molecular bridge than the spin density of the Cu^{2+} ion in the TPP ring.

Since the distribution width σ_J was rarely reported, its comparison among different biradicals is limited. So far, σ_J was determined only for the trityl-nitroxide biradicals **12**, **14**, and **15** in the liquid state and corresponds to 8%, 15%, and 19% of the respective $|\langle J \rangle|$ values. Interestingly, σ_J of **6**, which was herein determined in the solid state, is as large as 46% of the corresponding $|\langle J \rangle|$. This result reveals that the internal molecular dynamics can have a significant impact on the exchange coupling.

Conclusion

The mixed biradical **6** was synthesized, in which a copper(II)porphyrin and a trityl group are linked via a phenyl bridge. The magnetic properties of this biradical were characterized by means of multi-frequency continuous-wave EPR spectroscopy and magnetic measurements. EPR revealed that the two spin centers are ferromagnetically coupled and that the coupling constant J has a distribution, which can be approximated by a Gaussian distribution with a mean of −2.3 GHz (−0.077 cm^{-1}) and a width of 1.2 GHz (0.040 cm^{-1}). Thus, although the J values of **6** are too small to be determined by magnetic measurements, they fall within the intermediate to strong coupling regime in EPR measurements at microwave frequencies between 9.4 and 94 GHz. Based on DFT calculations, the ferromagnetic coupling, which is unusual for *para*-substituted phenyl-bridged biradicals, was related to the almost perpendicular orientation of the phenyl linker with respect to the porphyrin and trityl moieties (dihedral angles of ~110°). This geometry significantly reduces the overlap of the p_z orbitals and, consequently, the π-conjugation between both spin-carrying groups. Furthermore, the DFT calculations suggest that

the distribution in *J* may be due to the rotation of the phenyl linker about the molecular axis connecting the two spin centers. This study exemplifies the importance of molecular dynamics in addition to magneto-structural correlations. Finally, due to the larger spin density delocalization over the porphyrin system in the photoexcited biradicals **3**–**5** as compared to the ground state biradical **6**, it can be safely assumed that the exchange coupling constants in **3**–**5** are within the strong coupling limit at the usual EPR frequencies.

Experimental Section

Synthesis: Reference molecule **1** and precursor **3** were synthesized as described previously[8] (Supporting Information, Section 2). Reference molecule **7** was purchased from Sigma-Aldrich. For the synthesis of target molecule **6**, 20 mg of **3** (11.4 μmol) were dissolved in 3 mL dichloromethane, followed by addition of 21 mg anhydrous copper(II)acetate (114 mmol) dissolved in 2 mL methanol. The reaction mixture was stirred for 4 h at 40 °C under argon atmosphere. After cooling down to room temperature, the reaction mixture was diluted with 10 mL dichloromethane and washed twice with 0.1 M Na_2EDTA-solution (10 mL) and once with brine (10 mL). The organic phase was separated, dried over Na_2SO_4, and the solvent removed under reduced pressure yielding **6** with minor impurities from **1** and **7**. Column chromatography was not carried out, because the radical center suffers from oxidation on silica, and the sample appeared sufficiently pure for the desired studies.

EPR measurements: For the EPR measurements, 0.5 mM solutions of each radical were prepared in toluene, transferred to quartz EPR tubes, and shock-frozen in liquid nitrogen. Continuous-wave EPR measurements were carried out at two temperatures, 300 K (liquid state) and 100 K (solid state), and at X-, Q-, and W-band, using the spectrometers EMXmicro (Bruker), ELEXSYS E580 (Bruker), and ELEXSYS E680 (Bruker), respectively. Details of the EPR measurements are given in the Supporting Information, Section 3. Note that the magnetic field of each spectrometer was calibrated using MgO:Mn^{2+} (Sigma-Aldrich) as an internal standard.[21]

EPR simulations: Solid-state EPR spectra of **1**, **6**, and **7** were simulated using the "pepper" function of the EasySpin[12] software. The parameters of the simulations are given in the Results and Discussion section.

Magnetic susceptibility measurements: The sample was secured in a gelatin capsule and introduced at the correct height into the SQUID with the aid of a plastic straw. DC measurements were performed using a Quantum Design MPMS-3 SQUID magnetometer. The sample was cooled to 1.8 K in the measuring field of 3000 Oe. The magnetic moment of the sample was measured in the temperature range 1.8–300 K, by stabilizing at each temperature in 0.1 K steps below 10 K, 1 K steps from 11–20 K, and 2 K steps from 22–60 K followed by continuous measurements every 4 seconds while the temperature was swept at 4 K per minute from 62 K to 300 K. Equivalent data was collected having cooled the sample in the absence of field, which showed no discernible difference to the field cooled measurement.

DFT calculations: All unrestricted Kohn–Sham (UKS) DFT calculations were performed with the ORCA[22] quantum chemistry software package (version 4.2.1) on a single node of the Bonna cluster (University of Bonn) using 32 parallel processes and up to 187 GB RAM.

First, the structure of **6** was optimized on the PBE0[23]/def2-TZVP[24] level of theory, using the D3BJ-correction[25] to account for dispersion interactions and the RIJCOSX-approximation for calculation speed-up (def2/J as auxiliary basis). The SCF convergence criterion was set to "TightSCF" ($\sim 7\cdot10^{-7}$ E_h), and the geometry convergence threshold was kept at the default level (keyword "Opt"). Using the optimized structure, further calculations were performed to obtain the value of *J*. These calculations were done on the PBE0-D3/def2-TZVP, TPSSh[26]-D3/def2-TZVP, and B3LYP[27]-D3/def2-TZVP levels of theory with the RIJCOSX approximation[28] (def2/J as auxiliary basis). Here, the SCF convergence criterion was set to "VeryTightSCF" ($2\cdot10^{-8}$ E_h), which was found crucial to obtain values for *J* close to the experiment. *J* was determined according to the broken symmetry formalism (keyword "BrokenSym") following the convention[29]

$$J = -\frac{(E_{HS} - E_{BS})}{\langle S^2\rangle_{HS} - \langle S^2\rangle_{BS}}$$

wherein E_{HS} and E_{BS} correspond to the energy of the high-spin and the broken symmetry state, respectively. The dependence of *J* on the angle of the phenyl linker between the porphyrin and trityl moieties was studied based on the optimized structure and setting the dihedral angle χ to different values between 0° and 360°, leaving the rest of the molecular structure unchanged. Then, the single point energy (including the dispersion correction) and the value of *J* were calculated for each structure obtained.

Acknowledgements

O.S. gratefully acknowledges funding from the Weizmann Institute of Science via a Weston Visiting Professorship and T.H. funding via the Deutsche Forschungsgemeinschaft (DFG, German Research Foundation) – project number 420322655 (Koselleck grant to Benjamin Kaupp). S.R. acknowledges financial support by the Deutsche Forschungsgemeinschaft (DFG, German Research Foundation) – Project number 417643975. Daniella Goldfarb is thanked for critical reading of the manuscript. Dzmitry Firaha is thanked for his suggestions on the DFT calculations. The authors acknowledge access to the Bonna cluster hosted by the University of Bonn. This work is dedicated to Christoph Elschenbroich on the occasion of his 80th birthday. Open Access funding enabled and organized by Projekt DEAL.

Conflict of Interest

The authors declare no conflict of interest.

Data Availability Statement

The data that support the findings of this study are available in the supplementary material of this article.

Keywords: EPR · DFT · molecular magnetism · porphyrin · TAM

[1] a) G. W. Reginsson, N. C. Kunjir, S. T. Sigurdsson, O. Schiemann, *Chem. Eur. J.* **2012**, *18*, 13580–13584; b) Z. Yang, Y. Liu, P. Borbat, J. L. Zweier,

J. H. Freed, W. L. Hubbell, *J. Am. Chem. Soc.* **2012**, *134*, 9950–9952; c) D. Akhmetzyanov, P. Schöps, A. Marko, N. C. Kunjir, S. T. Sigurdsson, T. F. Prisner, *Phys. Chem. Chem. Phys.* **2015**, *17*, 24446–24451; d) B. Joseph, V. M. Tormyshev, O. Y. Rogozhnikova, D. Akhmetzyanov, E. G. Bagryanskaya, T. F. Prisner, *Angew. Chem. Int. Ed.* **2016**, *55*, 11538–11542; *Angew. Chem.* **2016**, *128*, 11710–11714; e) Z. Yang, M. D. Bridges, C. J. López, O. Y. Rogozhnikova, D. V. Trukhin, E. K. Brooks, V. Tormyshev, H. J. Halpern, W. L. Hubbell, *J. Magn. Reson.* **2016**, *269*, 50–54; f) J. J. Jassoy, A. Berndhäuser, F. Duthie, S. P. Kühn, G. Hagelueken, O. Schiemann, *Angew. Chem. Int. Ed.* **2017**, *56*, 177–181; *Angew. Chem.* **2017**, *129*, 183–187; g) J. J. Jassoy, C. A. Heubach, T. Hett, F. Bernhard, F. R. Haege, G. Hagelueken, O. Schiemann, *Molecules* **2019**, *24*, 2735; h) N. Fleck, C. A. Heubach, T. Hett, F. R. Haege, P. P. Bawol, H. Baltruschat, O. Schiemann, *Angew. Chem. Int. Ed.* **2020**, *59*, 9767–9772; *Angew. Chem.* **2020**, *132*, 9854–9859; i) N. Fleck, C. Heubach, T. Hett, S. Spicher, S. Grimme, O. Schiemann, *Chem. Eur. J.* **2021**, *27*, 5292–5297; j) S. Ketter, A. Gopinath, O. Rogozhnikova, D. Trukhin, V. M. Tormyshev, E. G. Bagryanskaya, B. Joseph, *Chem. Eur. J.* **2021**, *27*, 2299–2304.

[2] a) J. H. Ardenkjaer-Larsen, B. Fridlund, A. Gram, G. Hansson, L. Hansson, M. H. Lerche, R. Servin, M. Thaning, K. Golman, *Proc. Natl. Acad. Sci. USA* **2003**, *100*, 10158–10163; b) J. H. Ardenkjaer-Larsen, S. Macholl, H. Jóhannesson, *Appl. Magn. Reson.* **2008**, *34*, 509–522; c) T. Maly, L. B. Andreas, A. A. Smith, R. G. Griffin, *Phys. Chem. Chem. Phys.* **2010**, *12*, 5872–5878; d) B. Corzilius, A. A. Smith, R. G. Griffin, *J. Chem. Phys.* **2012**, *137*, 54201; e) A. A. Smith, B. Corzilius, A. B. Barnes, T. Maly, R. G. Griffin, *J. Chem. Phys.* **2012**, *136*, 15101; f) O. Haze, B. Corzilius, A. A. Smith, R. G. Griffin, T. M. Swager, *J. Am. Chem. Soc.* **2012**, *134*, 14287–14290; g) V. K. Michaelis, A. A. Smith, B. Corzilius, O. Haze, T. M. Swager, R. G. Griffin, *J. Am. Chem. Soc.* **2013**, *135*, 2935–2938; h) V. K. Michaelis, B. Corzilius, A. A. Smith, R. G. Griffin, *J. Phys. Chem. B* **2013**, *117*, 14894–14906; i) G. Mathies, M. A. Caporini, V. K. Michaelis, Y. Liu, K.-N. Hu, D. Mance, J. L. Zweier, M. Rosay, M. Baldus, R. G. Griffin, *Angew. Chem. Int. Ed.* **2015**, *54*, 11770–11774; *Angew. Chem.* **2015**, *127*, 11936–11940; j) G. Mathies, S. Jain, M. Reese, R. G. Griffin, *J. Phys. Chem. Lett.* **2016**, *7*, 111–116.

[3] a) A. A. Bobko, I. Dhimitruka, T. D. Eubank, C. B. Marsh, J. L. Zweier, V. V. Khramtsov, *Free Radical Biol. Med.* **2009**, *47*, 654–658; b) A. A. Bobko, I. Dhimitruka, D. A. Komarov, V. V. Khramtsov, *Anal. Chem.* **2012**, *84*, 6054–6060; c) M. Poncelet, J. L. Huffman, V. V. Khramtsov, I. Dhimitruka, B. Driesschaert, *RSC Adv.* **2019**, *9*, 35073–35076.

[4] I. Dhimitruka, M. Velayutham, A. A. Bobko, V. V. Khramtsov, F. A. Villamena, C. M. Hadad, J. L. Zweier, *Bioorg. Med. Chem. Lett.* **2007**, *17*, 6801–6805.

[5] a) L. Yong, J. Harbridge, R. W. Quine, G. A. Rinard, S. S. Eaton, G. R. Eaton, C. Mailer, E. Barth, H. J. Halpern, *J. Magn. Reson.* **2001**, *152*, 156–161; b) A. A. Kuzhelev, D. V. Trukhin, O. A. Krumkacheva, R. K. Strizhakov, O. Y. Rogozhnikova, T. I. Troitskaya, M. V. Fedin, V. M. Tormyshev, E. G. Bagryanskaya, *J. Phys. Chem. B* **2015**, *119*, 13630–13640.

[6] Y. Talmon, L. Shtirberg, W. Harneit, O. Y. Rogozhnikova, V. Tormyshev, A. Blank, *Phys. Chem. Chem. Phys.* **2010**, *12*, 5998–6007.

[7] a) B. Epel, C. R. Haney, D. Hleihel, C. Wardrip, E. D. Barth, H. J. Halpern, *Med. Phys.* **2010**, *37*, 2553–2559; b) M. Gonet, B. Epel, H. J. Halpern, M. Elas, *Cell Biochem. Biophys.* **2019**, *77*, 187–196.

[8] N. Fleck, T. Hett, J. Brode, A. Meyer, S. Richert, O. Schiemann, *J. Org. Chem.* **2019**, *84*, 3293–3303.

[9] O. Nolden, N. Fleck, E. R. Lorenzo, M. R. Wasielewski, O. Schiemann, P. Gilch, S. Richert, *Chem. Eur. J.* **2021**, *27*, 2683–2691.

[10] a) A. Abragam, B. Bleaney, *Electron paramagnetic resonance of transition ions*; Clarendon Press, Oxford, **2013**; b) D. Goldfarb, S. Stoll, Eds, *Modern EPR spectroscopy: Fundamentals and methods*; Wiley, Chichester, **2018**; c) J. A. Weil, J. R. Bolton, *Electron paramagnetic resonance: Elementary theory and practical applications*; John Wiley, Chichester, **2007**.

[11] a) Y. Liu, F. A. Villamena, A. Rockenbauer, J. L. Zweier, *Chem. Commun.* **2010**, *46*, 628–630; b) Y. Liu, F. A. Villamena, Y. Song, J. Sun, A. Rockenbauer, J. L. Zweier, *J. Org. Chem.* **2010**, *75*, 7796–7802; c) Y. Liu, Y. Song, A. Rockenbauer, J. Sun, C. Hemann, F. A. Villamena, J. L. Zweier, *J. Org. Chem.* **2011**, *76*, 3853–3860; d) Y. Liu, F. A. Villamena, A. Rockenbauer, Y. Song, J. L. Zweier, *J. Am. Chem. Soc.* **2013**, *135*, 2350–2356; e) N. C. Kunjir, G. W. Reginsson, O. Schiemann, S. T. Sigurdsson, *Phys. Chem. Chem. Phys.* **2013**, *15*, 19673–19685; f) J. J. Jassoy, A. Meyer, S. Spicher, C. Wuebben, O. Schiemann, *Molecules* **2018**, *23*, 682; g) A. Meyer, J. J. Jassoy, S. Spicher, A. Berndhäuser, O. Schiemann, *Phys. Chem. Chem. Phys.* **2018**, *20*, 13858–13869; h) G. R. Eaton, S. S. Eaton, *Acc. Chem. Res.* **1988**, *21*, 107–113; i) S. S. Eaton, K. M. More, B. M. Sawant, P. M. Boymel, G. R. Eaton, *J. Magn. Reson.* **1983**, *52*, 435–449; j) R. Calvo, *Appl. Magn. Reson.* **2007**, *31*, 271–299; k) B. E. Bode, J. Plackmeyer, M. Bolte, T. F. Prisner, O. Schiemann, *J. Organomet. Chem.* **2009**, *694*, 1172–1179; l) S. Richert, I. Kuprov, M. D. Peeks, E. A. Suturina, J. Cremers, H. L. Anderson, C. R. Timmel, *Phys. Chem. Chem. Phys.* **2017**, *19*, 16057–16061; m) R. Wang, A. M. Brugh, J. Rawson, M. J. Therien, M. D. E. Forbes, *J. Am. Chem. Soc.* **2017**, *139*, 9759–9762.

[12] S. Stoll, A. Schweiger, *J. Magn. Reson.* **2006**, *178*, 42–55.

[13] H. J. Hogben, M. Krzystyniak, G. T. P. Charnock, P. J. Hore, I. Kuprov, *J. Magn. Reson.* **2011**, *208*, 179–194.

[14] a) T. D. Smith, J. R. Pilbrow, *Coord. Chem. Rev.* **1974**, *13*, 173–278; b) N. Toyama, M. Asano-Someda, T. Ichino, Y. Kaizu, *J. Phys. Chem. A* **2000**, *104*, 4857–4865; c) M. Asano-Someda, N. Toyama, Y. Kaizu, *Mol. Cryst. Liq. Cryst.* **2002**, *379*, 165–170.

[15] a) S. P. Greiner, D. L. Rowlands, R. W. Kreilick, *J. Phys. Chem.* **1992**, *96*, 9132–9139; b) C. Finazzo, C. Calle, S. Stoll, S. van Doorslaer, A. Schweiger, *Phys. Chem. Chem. Phys.* **2006**, *8*, 1942–1953; c) C. Calle, A. Schweiger, G. Mitrikas, *Inorg. Chem.* **2007**, *46*, 1847–1855.

[16] A. A. Kuzhelev, V. M. Tormyshev, O. Y. Rogozhnikova, D. V. Trukhin, T. I. Troitskaya, R. K. Strizhakov, O. A. Krumkacheva, M. V. Fedin, E. G. Bagryanskaya, *Z. Phys. Chem.* **2017**, *231*, 777–794.

[17] A. J. Fielding, P. J. Carl, G. R. Eaton, S. S. Eaton, *Appl. Magn. Reson.* **2005**, *28*, 231–238.

[18] a) B. Bleaney, K. D. Bowers, *The London, Edinburgh, and Dublin Philosophical Magazine and Journal of Science* **1952**, *43*, 372–374; b) C. J. O'Connor, *Prog. Inorg. Chem.* **1982**, *29*, 203–283.

[19] G. Singh, S. Gamboa, M. Orio, D. A. Pantazis, M. Roemelt, *Theor. Chem. Acc.* **2021**, *140*, 139.

[20] J. Fritscher, M. Beyer, O. Schiemann, *Chem. Phys. Lett.* **2002**, *364*, 393–401.

[21] S. Stoll, A. Gunn, M. Brynda, W. Sughrue, A. C. Kohler, A. Ozarowski, A. J. Fisher, J. C. Lagarias, R. D. Britt, *J. Am. Chem. Soc.* **2009**, *131*, 1986–1995.

[22] a) F. Neese, *Wiley Interdiscip. Rev.: Comput. Mol. Sci.* **2012**, *2*, 73–78; b) F. Neese, *Wiley Interdiscip. Rev.: Comput. Mol. Sci.* **2018**, *8*.

[23] a) J. P. Perdew, M. Ernzerhof, K. Burke, *J. Chem. Phys.* **1996**, *105*, 9982–9985; b) C. Adamo, V. Barone, *J. Chem. Phys.* **1999**, *110*, 6158–6170; c) M. Ernzerhof, G. E. Scuseria, *J. Chem. Phys.* **1999**, *110*, 5029–5036.

[24] F. Weigend, R. Ahlrichs, *Phys. Chem. Chem. Phys.* **2005**, *7*, 3297–3305.

[25] a) D. Abdullin, P. Brehm, N. Fleck, S. Spicher, S. Grimme, O. Schiemann, *Chem. Eur. J.* **2019**, *25*, 14388–14398; b) S. Grimme, J. Antony, S. Ehrlich, H. Krieg, *J. Chem. Phys.* **2010**, *132*, 154104.

[26] J. P. Perdew, J. Tao, V. N. Staroverov, G. E. Scuseria, *J. Chem. Phys.* **2004**, *120*, 6898–6911.

[27] a) A. D. Becke, *Phys. Rev. A* **1988**, *38*, 3098–3100; b) C. Lee, W. Yang, R. G. Parr, *Phys. Rev. B* **1988**, *37*, 785–789; c) A. D. Becke, *J. Chem. Phys.* **1993**, *98*, 5648–5652.

[28] F. Neese, F. Wennmohs, A. Hansen, U. Becker, *Chem. Phys.* **2009**, *356*, 98–109.

[29] a) K. Yamaguchi, Y. Takahara, T. Fueno, *in Applied Quantum Chemistry*; (Eds. V. H. Smith, H. F. Schaefer, K. Morokuma), Springer Science + Business Media B.V, Dordrecht, **1986**, 155–184; b) T. Soda, Y. Kitagawa, T. Onishi, Y. Takano, Y. Shigeta, H. Nagao, Y. Yoshioka, K. Yamaguchi, *Chem. Phys. Lett.* **2000**, *319*, 223–230.

Manuscript received: October 9, 2022
Accepted manuscript online: December 15, 2022
Version of record online: ■■, ■■■

Chemistry–A European Journal

Supporting Information

Magneto-Structural Correlations in a Mixed Porphyrin(Cu^{2+})/Trityl Spin System: Magnitude, Sign, and Distribution of the Exchange Coupling Constant

Dinar Abdullin, Tobias Hett, Nico Fleck, Kevin Kopp, Simon Cassidy, Sabine Richert, and Olav Schiemann*

Supporting Information

Magneto-Structural Correlations in a Mixed Porphyrin(Cu^{2+})/Trityl Spin System: Magnitude, Sign, and Distribution of the Exchange Coupling Constant

Dinar Abdullin,[a] Tobias Hett,[a] Nico Fleck,[a,b] Kevin Kopp,[a] Simon Cassidy,[c] Sabine Richert,[d] Olav Schiemann[a,e,*]

[a] Clausius-Institute of Physical and Theoretical Chemistry, University of Bonn, Wegelerstr. 12, 53115 Bonn, Germany.

[b] current address: Merck KGaA, Q20/001, Frankfurter Str. 250, 64293 Darmstadt, Germany

[c] Department of Chemistry, University of Oxford, South Parks Road, Oxford OX1 3QR, United Kingdom.

[d] Institute of Physical Chemistry, University of Freiburg, Albertstr. 21, 79104 Freiburg, Germany.

[e] Weston Visiting Scholar, Department of Chemical and Biological Physics, Weizmann Institute of Science, Rehovot, 761001, Israel

Table of Content

1 General EPR simulations

To investigate the effect of J, and in particular of its sign, on the solid-state EPR spectrum of a biradical consisting of two dissimilar electron spin centers, EPR simulations were performed using EasySpin.[1] All simulations were performed for the X-band (9.5 GHz) using a magnetic field range of [250, 400] mT. The two electron spin centers of an exemplary biradical were assumed to have $S = 1/2$ and isotropic g-factors of $g_1 = 2.0$ and $g_2 = 2.2$, respectively. The EPR linewidths of both spin centers were set to 1 mT.

First, the simulations were performed for the case where the electron spins are coupled only via an exchange interaction. J was set to 11 different positive and 11 different negative values corresponding to $x = 0$, 0.1, 0.2, 0.5, 1, 2, 5, 10, 20, 50, and 100, where $x = |J|/(\Delta g \beta B_0)$ (see Equation 5 in the main text). Figure S1a shows that the simulated spectra are not dependent on the sign of J.

Second, the simulations were performed for the case where the electron spins are again coupled via an exchange interaction, but the first spin is additionally coupled to a nuclear spin with $I = 1/2$ and $A = 100$ MHz. The values of J were identical to those used above and were specified via $x' = |J|/(\Delta g \beta B_0 + A m_I)$ (see Equation 10 in the main text). The simulated spectra are shown in Figure S1b. In line with the theory described in the main text, the obtained positions of the EPR transitions and the hyperfine splittings show the dependence on x', but no dependence on the sign of J.

Third, the simulations were performed for the case where the electron spins are coupled via exchange and dipole-dipole interactions. The values of J were again identical to those used above and D was set to 25 MHz. The simulated spectra are shown in Figure S1c. These spectra show almost the same dependence on x as those in Figure S1a and, importantly, the predicted dependence on the sign of J. Figures S1c and S2 reveal that the extent to which the sign of J changes the shape of the EPR spectrum depends on the magnitude of D, in particular its relative magnitude compared to the linewidth, and on x.

Lastly, the simulations were performed for the case where the electron spins are coupled via exchange and dipole-dipole interactions whereby the first spin is additionally coupled to a nuclear spin with $I = 1/2$ and $A = 100$ MHz. J and D were set to the same values as above. The simulated spectra are shown in Figure S1d. Similar to Figure S1c, the simulated spectra show a dependence on the sign of J due to the non-zero D, and the extent to which the sign of J changes the shape of the EPR spectrum depends on x'.

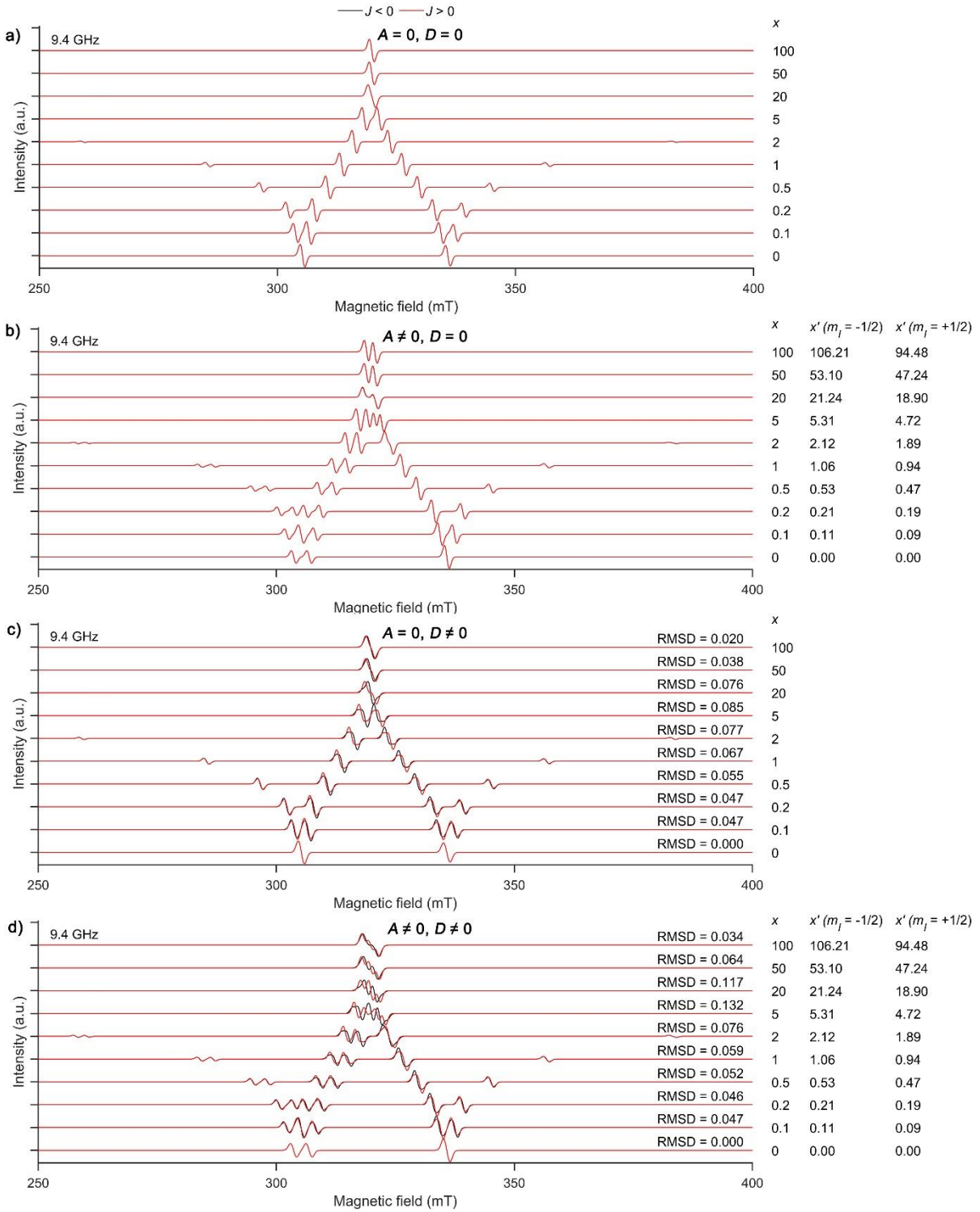

Figure S1. Simulated solid-state EPR spectra of a biradical with $S_1 = S_2 = 1/2$, $g_1 = 2.0$, and $g_2 = 2.2$. **a)** The spins S_1 and S_2 are coupled only via an exchange interaction. **b)** The spins S_1 and S_2 are coupled via an exchange interaction, and S_1 is additionally coupled to the nuclear spin $I = 1/2$ with $A = 100$ MHz. **c)** The spins S_1 and S_2 are coupled via an exchange interaction and a dipole-dipole interaction with $D = 25$ MHz. **d)** The spins S_1 and S_2 are coupled via an exchange interaction and a dipole-dipole interaction with $D = 25$ MHz, whereby S_1 is additionally coupled to the nuclear spin $I = 1/2$ with $A = 100$ MHz. The values of $|J|$ are specified via x (Equation 5 in the main text) or x' (Equation 10 in the main text) and are shown next to each simulated spectrum. Spectra that correspond to positive and negative values of J are colored in black and red, respectively. The RMSD between them are shown for c) and d).

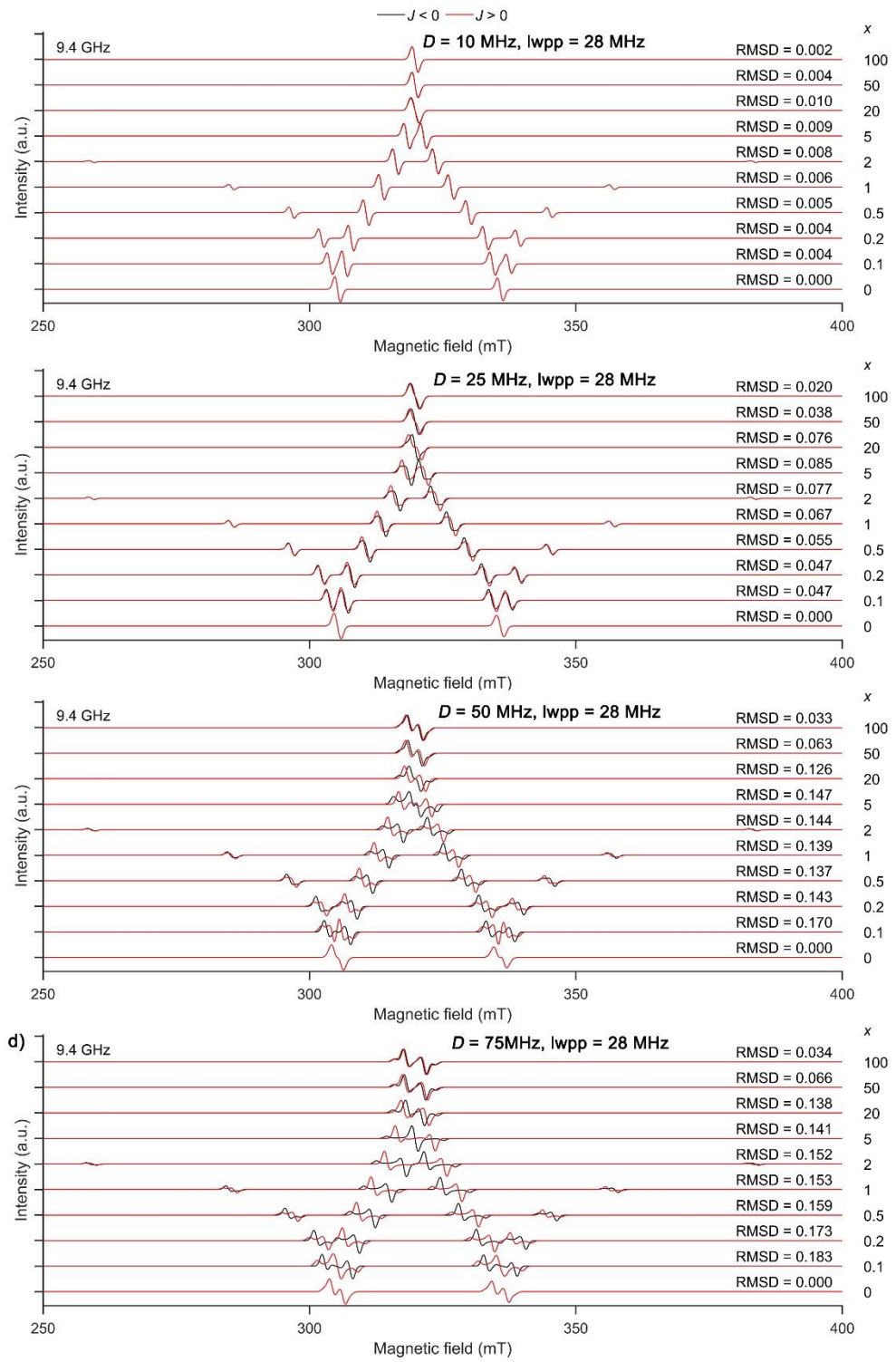

Figure S2. Simulated solid-state EPR spectra of a biradical with $S_1 = S_2 = 1/2$, $g_1 = 2.0$, and $g_2 = 2.2$. The spins S_1 and S_2 are coupled via an exchange interaction and a dipole-dipole interaction. The values of $|J|$ are specified via x (Equation 5 in the main text) and are shown next to each simulated spectrum. Spectra that correspond to positive and negative values of J are colored in black and red, respectively. The RMSD between them are shown on top of each spectrum. The value of D was set to **a)** 10 MHz, **b)** 25 MHz, **c)** 50 MHz, and **d)** 75 MHz. The EPR linewidths (lwpp) of both spin centers were set to 1 mT, i.e., ~28 MHz.

2 Synthesis of 1 and 6

TAM radical **1** (see Figure 1 in the main text) was synthesized in a similar way as described previously.[2] Here, the alcohol precursor of **1** was obtained from the statistical Suzuki-Miyaura cross-coupling reaction of 1500 mg of tris(8-iodo-2,2,6,6-tetramethylbenzo-[1,2-d;4,5-d′]-bis-[1,3]dithiol-4-yl)-methanol (1.19 mmol) with 622 mg of 4-methoxycarbonylphenylboronicacid pinacol ester (2.37 mmol). Furthermore, 43.4 mg of Pd(dppf)Cl_2 (0.0594 mmol) and 772 mg of caesium carbonate (2.37 mmol) were added, and the solids were dissolved in 150 mL of a degassed 9:1 mixture of tetrahydrofuran and water. The reaction mixture was refluxed for 16 h under argon atmosphere. Afterwards, the solvent was removed and the residue was re-dissolved in 100 mL of dichloromethane. The organic phase was washed with water (2x50 mL) and brine (50 mL), and subsequently dried over magnesium sulfate. The solvent was again removed under reduced pressure, resulting in a dark green crude product. The product was purified by column chromatography on silica eluting with *n*-hexane:ethyl acetate (5:1 v:v). This yielded 230 mg (0.178 mmol, 15 %) of the TAM alcohol (R_f = 0.12). **1** was then obtained by dissolving 60 mg of the alcohol precursor (0.047 mmol) in 5 mL of degassed dichloromethane. Subsequently, the mixture was cooled to 0 °C and 6.4 µL of triflic acid (11 mg, 0.073 mmol) were added, whereupon the reaction mixture was allowed to reach room temperature. After 1 h, 13.2 mg of tin(II)chloride (0.0696 mmol) dissolved in 1 mL of tetrahydrofuran were added, and the reaction was stirred for another 16 h at room temperature. The organic phase was washed with water (2x5 mL) and brine (5 mL) and then dried over magnesium sulfate. The solvents were removed under reduced pressure, yielding 43 mg (0.034 mmol, 72 %) of a dark green product. Column chromatography was not carried out as the product was pure.

The synthesis of biradical **6** (see Figure 1 in the main text) is described in the main text. The MALDI(+) high resolution mass spectrometry measurements on **6** were done using a Bruker Daltonics autoflex TOF/TOF time-of-flight spectrometer (Bruker) and DCTB as a matrix. The MALDI(+) spectrum (Figure S3) reveals a single peak at 1808.2 m/z, which is in excellent agreement with the predicted value of 1808.2 m/z (for $C_{97}H_{77}CuN_4O_4S_{12}$).

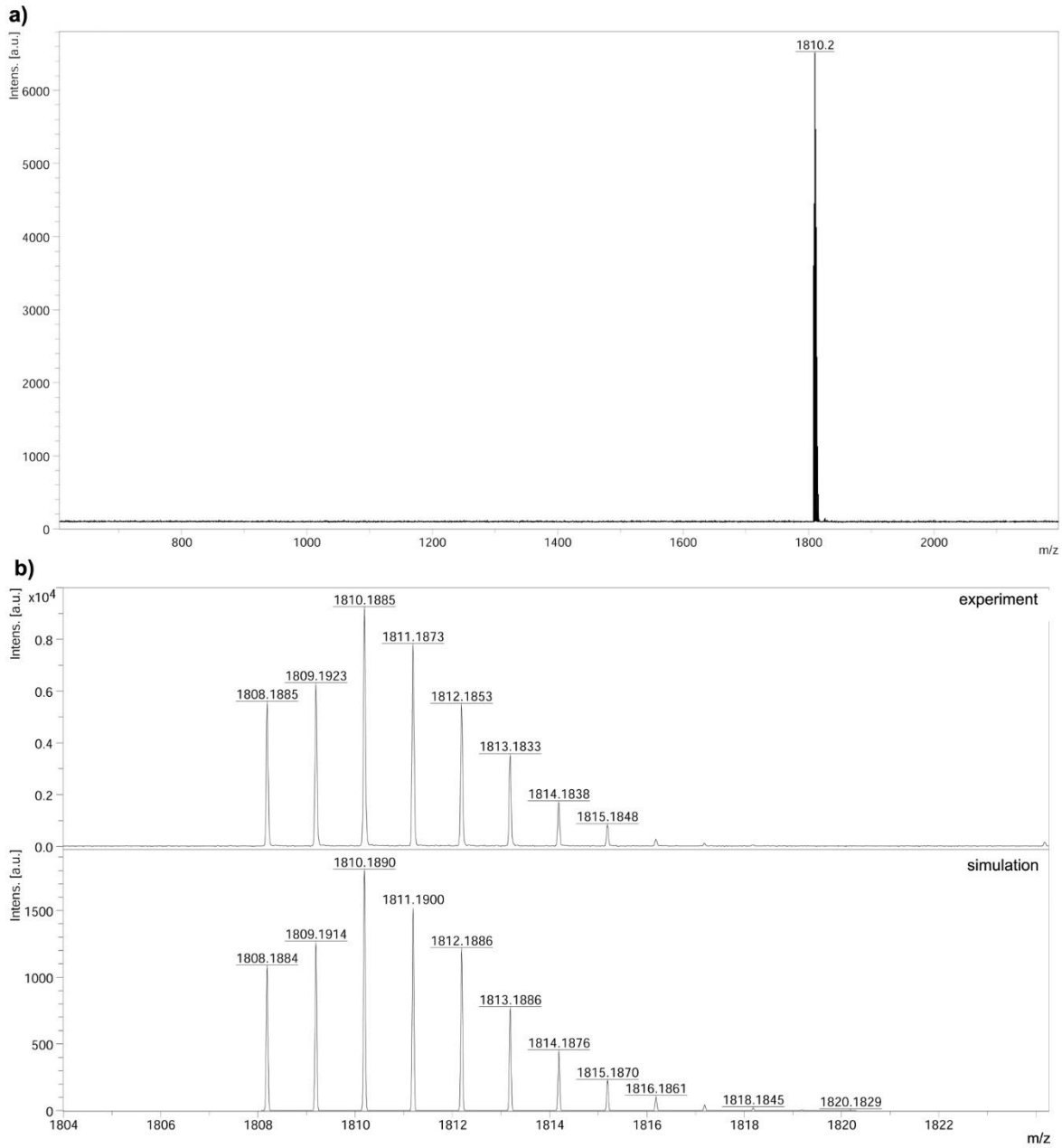

Figure S3. a) MALDI(+) and b) HRMS MALDI(+) spectra of **6**.

3 EPR measurements on 6, 7, and 1

The EPR measurements on **6**, **7**, and **1** were performed at two temperatures, 300 K (liquid state) and 100 K (solid state), and at three microwave bands, X-, Q-, and W-band. For the X-band measurements, an EMXmicro (Bruker) spectrometer was used with the super-high-quality resonator (SHQ) that was mounted inside a continuous flow helium cryostat ER4112HE (Bruker). The temperature of the cryostat was monitored by a Mercury iTC system (Oxford Instruments). The parameters of the X-band EPR measurements are listed in Tables S1 and S2. For the Q-band measurements, the ELEXSYS E580 (Bruker) spectrometer was used with the ER 5106QT/W resonator that was mounted inside a continuous flow helium cryostat CF935 (Bruker). The temperature of the cryostat was monitored by a temperature control system ITC 503 (Oxford Instruments). The parameters of the Q-band EPR measurements are listed in Tables S3 and S4. For the W-band measurements, the ELEXSYS E680 (Bruker) spectrometer was used with the E-680-1021H-TeraFlex® resonator that was mounted inside a continuous flow helium cryostat CF935 (Bruker). The temperature of the cryostat was monitored by a temperature control system ITC 503 (Oxford Instruments). The parameters of the Q-band EPR measurements are listed in Tables S4 and S5. To calibrate the magnetic field of the spectrometers, all EPR spectra were acquired with the internal standard MgO:Mn^{2+} (Sigma-Aldrich).[3]

Table S1. Parameters of the X-band EPR measurements at 300 K.

Parameter	**6**	**7**	**1**
Microwave power / μW	264.9 (25 dB)	563.7 (25 dB)	563.7 (25 dB)
Modulation frequency / kHz	100	100	100
Modulation amplitude / mT	0.2	0.2	0.02
Time constant / ms	40.96	40.96	40.96
Magnetic field range / mT	[230.0, 430.0]	[230.0, 430.0]	[230.0, 430.0]
Magnetic field increment / mT	0.02	0.02	0.02
Number of averages	7	6	1

Table S2. Parameters of the X-band EPR measurements at 100 K.

Parameter	**6**	**7**	**1**
Microwave power / μW	18.1 (40 dB)	18.1 (40 dB)	17.6 (40 dB)
Modulation frequency / kHz	100	100	100
Modulation amplitude / mT	0.2	0.2	0.02
Time constant / ms	20.48	20.48	20.48
Magnetic field range / mT	[240.0, 400.0]	[240.0, 400.0]	[240.0, 400.0]
Magnetic field increment / mT	0.05	0.05	0.02
Number of averages	27	27	1

Table S3. Parameters of the Q-band EPR measurements at 300 K.

Parameter	**6**	**7**	**1**
Microwave power / μW	1300 (10 dB)	1300 (10 dB)	1300 (10 dB)
Modulation frequency / kHz	100	100	100
Modulation amplitude / mT	0.2	0.2	0.05
Time constant / ms	10.24	10.24	10.24
Magnetic field range / mT	[960.0, 1260.0]	[960.0, 1260.0]	[1140.0, 1240.0]
Magnetic field increment / mT	0.1	0.1	0.02
Number of averages	172	535	1

Table S4. Parameters of the Q-band EPR measurements at 100 K.

Parameter	**6**	**7**	**1**
Microwave power / μW	130 (20 dB)	130 (20 dB)	0.13 (50 dB)
Modulation frequency / kHz	100	100	100
Modulation amplitude / mT	0.2	0.2	0.1
Time constant / ms	10.24	10.24	10.24
Magnetic field range / mT	[1000.0, 1300.0]	[1000.0, 1300.0]	[1165.0, 1265.0]
Magnetic field increment / mT	0.1	0.1	0.05
Number of averages	108	513	10

Table S5. Parameters of the W-band EPR measurements at 300 K.

Parameter	**6**	**7**	**1**
Microwave power / μW	650 (10 dB)	650 (10 dB)	650 (10 dB)
Modulation frequency / kHz	100	100	100
Modulation amplitude / mT	0.1	0.1	0.02
Time constant / ms	20.48	20.48	20.48
Magnetic field range / mT	[3000.0, 3900.0]	[2800.0, 3600.0]	[3343.0, 3353.0]
Magnetic field increment / mT	~0.1 (8000/8192)	~0.1 (8000/8192)	~0.01 (100/1024)
Number of averages	1	1	1

Table S6. Parameters of the W-band EPR measurements at 100 K.

Parameter	**6**	**7**	**1**
Microwave power / μW	65 (20 dB)	65 (20 dB)	0.065 (50 dB)
Modulation frequency / kHz	100	100	100
Modulation amplitude / mT	0.2	0.2	0.1
Time constant / ms	20.48	20.48	20.48
Magnetic field range / mT	[2800.0, 3600.0]	[2800.0, 3600.0]	[3315.0, 3385.0]
Magnetic field increment / mT	~0.1 (8000/8192)	~0.1 (8000/8192)	~0.07 (700/1024)
Number of averages	1	1	1

The liquid-state EPR spectra of **6**, **7**, and **1** are shown in Figure S4. The spectra of **6** contain a weak signal, which is identical to the spectra of **1**. Based to the EPR signal intensities, the relative amount of the trityl-based impurity in the sample of **6** was determined to be < 1 %.

The solid-state EPR spectra of **6**, **7**, and **1** are shown in Figure S5. The spectra of **6** contain again a signal, which is identical to the spectra of **1** and is therefore assigned to the trityl-based impurity. Because the trityl signal is saturated much faster than the signal **6** at 100 K, the relative amount of the trityl-based impurity was not evaluated. In addition, the solid-state EPR spectra of **6** revealed another weak signal which is identical to the spectra of **7**. This signal was assigned to a porphyrin(Cu^{2+})-based impurity. Because **6** and **7** were found to have similar EPR

saturation rates, the relative amount of the porphyrin(Cu^{2+})-based impurity was determined from the EPR signal intensities. This yielded 6 %.

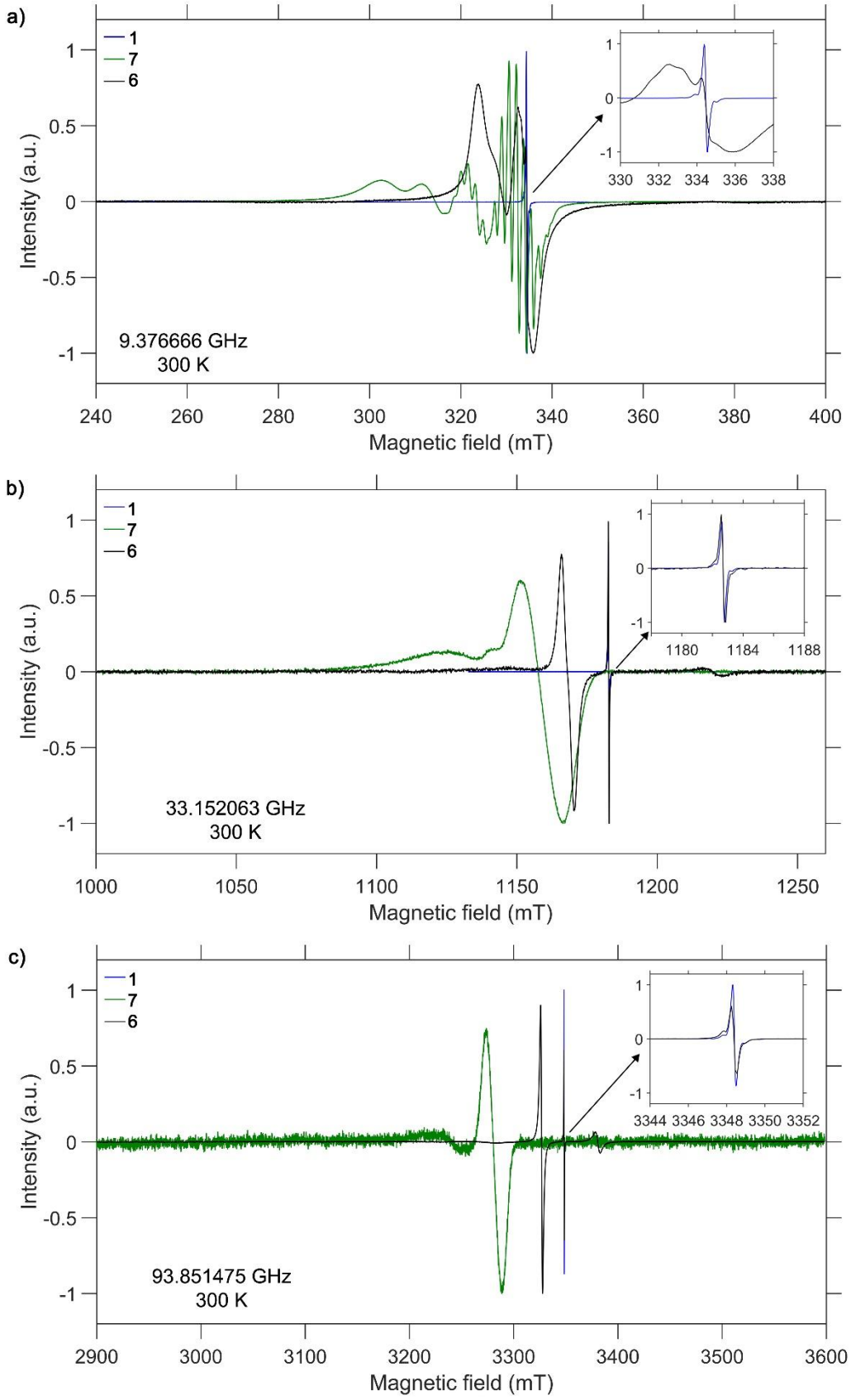

Figure S4. a) X-, **b)** Q-, and **c)** W-band EPR spectra of **6** (black), **7** (green), and **1** (blue). All spectra were acquired at 300 K.

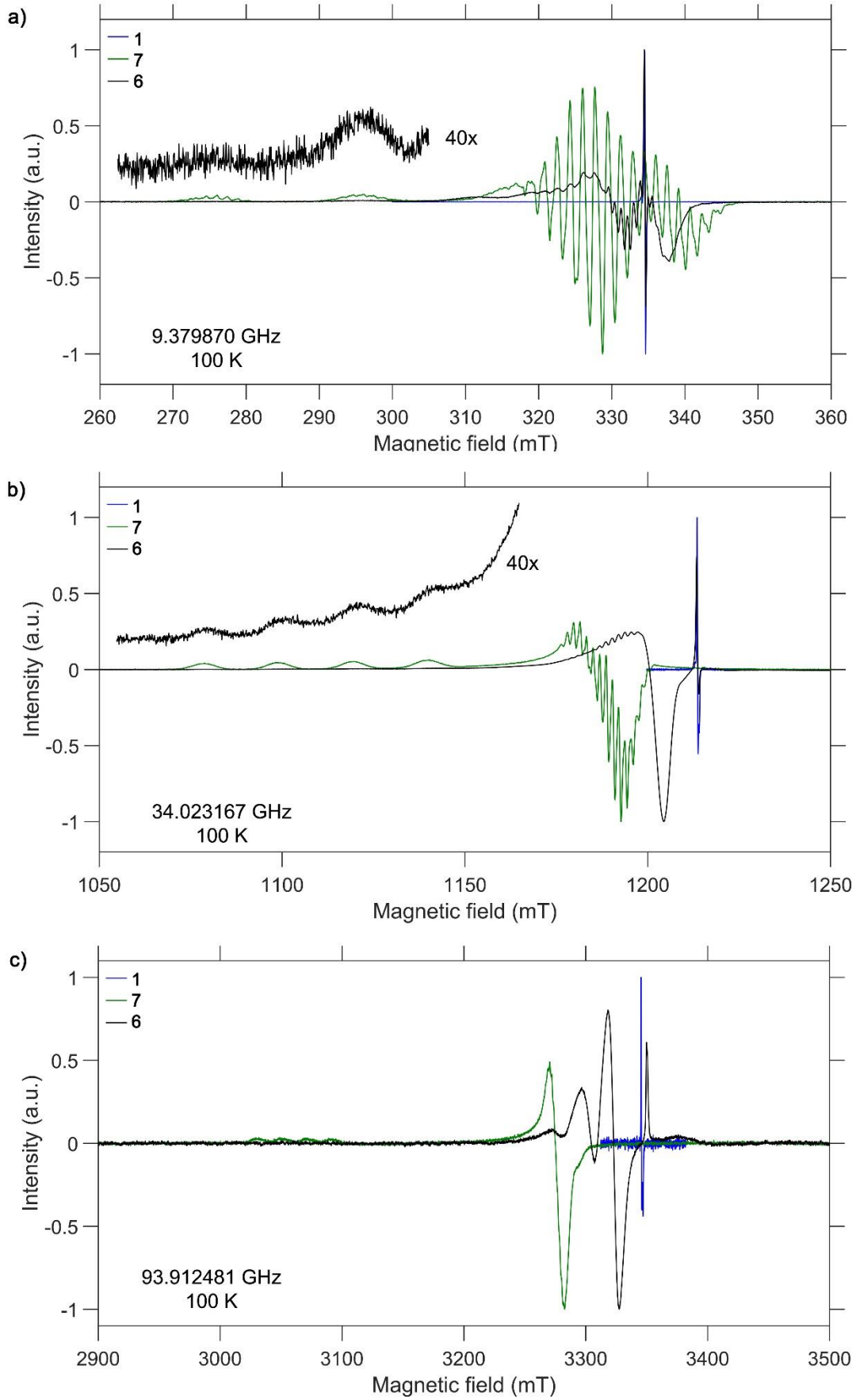

Figure S5. a) X-, **b)** Q-, and **c)** W-band EPR spectra of **6** (black), **7** (green), and **1** (blue). All spectra were acquired at 100 K.

4 EPR simulations for 6, 7, and 1

The solid-state EPR spectra of **6**, **7**, and **1** were simulated using the "pepper" function of EasySpin. For **7** and **1**, the simulation parameters are given in Tables S7 and S8, and the corresponding simulated spectra are shown in Figure S6.

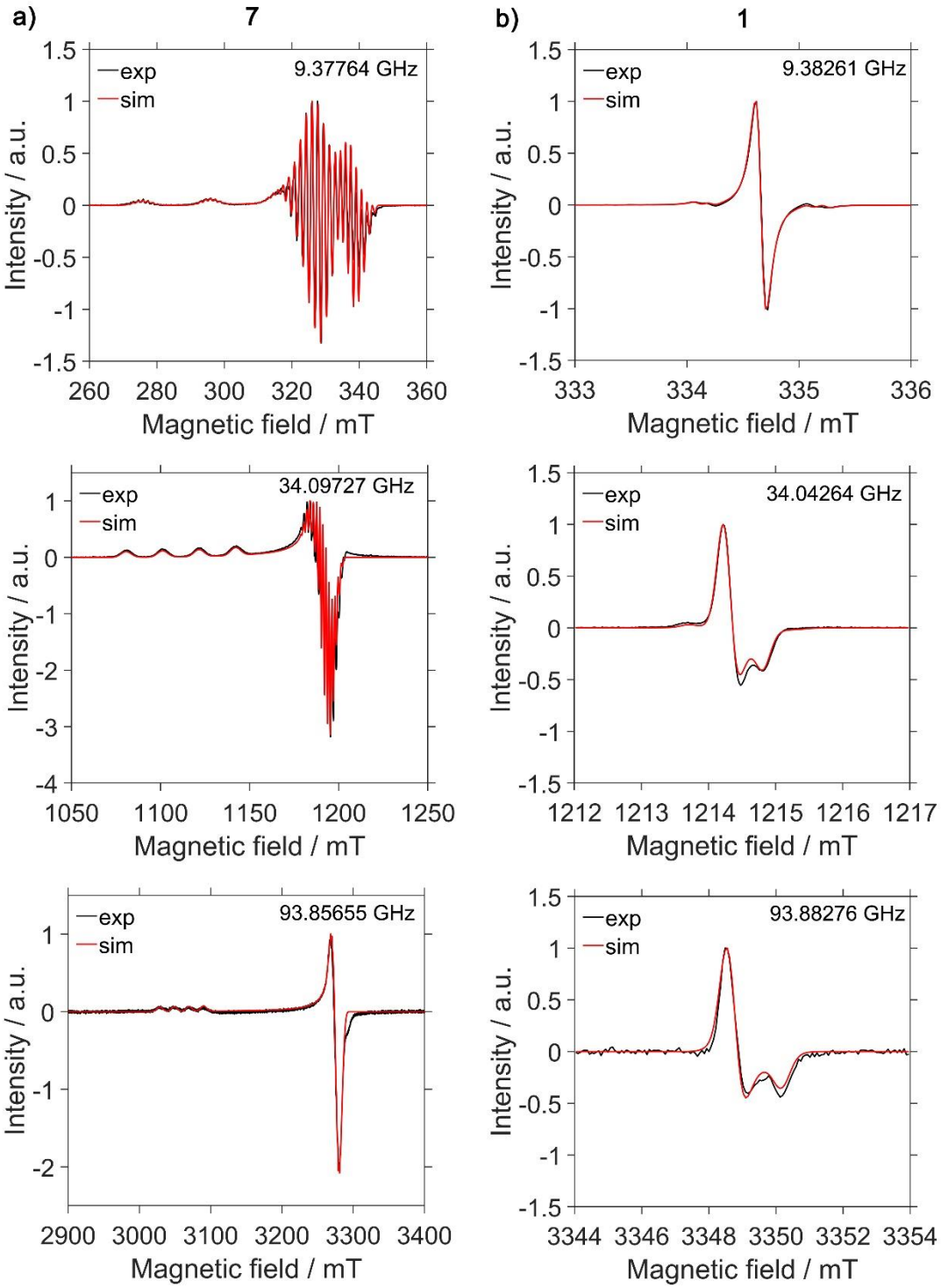

Figure S6. X- (top), Q- (middle), and W-band (bottom) EPR spectra (black) of **a) 7** and **b) 1** together with the simulated spectra (red). The simulation parameters are listed in Tables S7 and S8, respectively.

Table S7. EPR parameters of **7**.

Parameter	X-band	Q-band	W-band
$g_{\perp}, g_{\parallel}$ (± error) or	2.048, 2.190	2.0445, 2.0484, 2.1920	2.0445, 2.0484, 2.1920
g_{xx}, g_{yy}, g_{zz} (± error)	(± 0.001)	(± 0.0004)	(± 0.0002)
$A_{\perp}, A_{\parallel}$ (Cu) / MHz	–64, –615	–64, –628	–64, –628
A_{xx}, A_{yy}, A_{zz} ($N_{1,3}$)[a] / MHz	54, 43, 44	54, 43, 44	54, 43, 44
A_{xx}, A_{yy}, A_{zz} ($N_{2,4}$)[a] / MHz	43, 54, 44	43, 54, 44	43, 54, 44
Linewidth[b] / MHz	24, 24, 34	25, 15, 100	100, 35, 250

[a] The enumeration of N atoms is shown in Figure 1 of the main text.

[b] The linewidth is given as anisotropic residual linewidth (HStrain), [Δv_{xx}, Δv_{yy}, Δv_{zz}], where Δv_{xx}, Δv_{yy}, and Δv_{zz} are the full widths at half height.

Table S8. EPR parameters of **1**.

Parameter	X-band	Q-band	W-band
g_{iso} (± error) or	2.003	2.0030, 2.0022	2.0031, 2.0022
$g_{\perp}, g_{\parallel}$ (± error)	(± 0.001)	(± 0.0002)	(± 0.0001)
$A_{iso}(C_{ortho})$ / MHz	25	25	25
$A_{iso}(C_{ipso})$ / MHz	32	32	32
Linewidth[a] / MHz	0, 0.095	5.6, 0.84	14, 0

[a] The linewidth is given by the peak-to-peak width (lwpp) of a Gaussian and a Lorentzian, which are two contributions to the total linewidth (Voigtian broadening).

For the EasySpin simulations, the laboratory frame was related to the molecular frame of the porphyrin(Cu^{2+}) as shown in Figure S7.[4,5] To simulate the distribution of J in EasySpin, the following procedure was used:

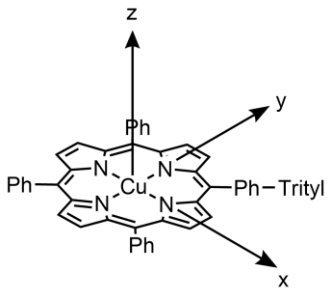

Figure S7. The laboratory frame used in the EasySpin simulations.

1) For the given $\langle J \rangle$ and σ_J, a linear grid of J values, J_i (i = 1–200), within the range [$\langle J \rangle - 3\sigma_J$, $\langle J \rangle + 3\sigma_J$] was generated.
2) For each J_i, the corresponding weight w_i (i = 1–200) was calculated:

$$w_i = \exp\left(-\frac{(J_i - \langle J \rangle)}{2\sigma_J^2}\right).$$

3) EasySpin was used to simulate the EPR spectrum for each J_i.
4) All simulated spectra were added up with the corresponding weights w_i.

The values of $\langle J \rangle$ and σ_J were optimized to minimize the root-mean-square-deviation (RMSD) between the simulated and experimental EPR spectra. For this, the RMSD was evaluated on a two-dimensional linear grid of $\langle J \rangle$ and σ_J values with bounds of [–5, 5] GHz and [0, 5] GHz, respectively. The obtained RMSD surfaces are shown in Figure 3 in the main text. A comparison of the simulated and experimental X-band spectra obtained for several different

516

values of $\langle J \rangle$ and σ_J is shown in Figure S8. Figure S8 reveals that a reasonable agreement between the simulated and experimental spectra is achieved up to an RMSD value of 0.11.

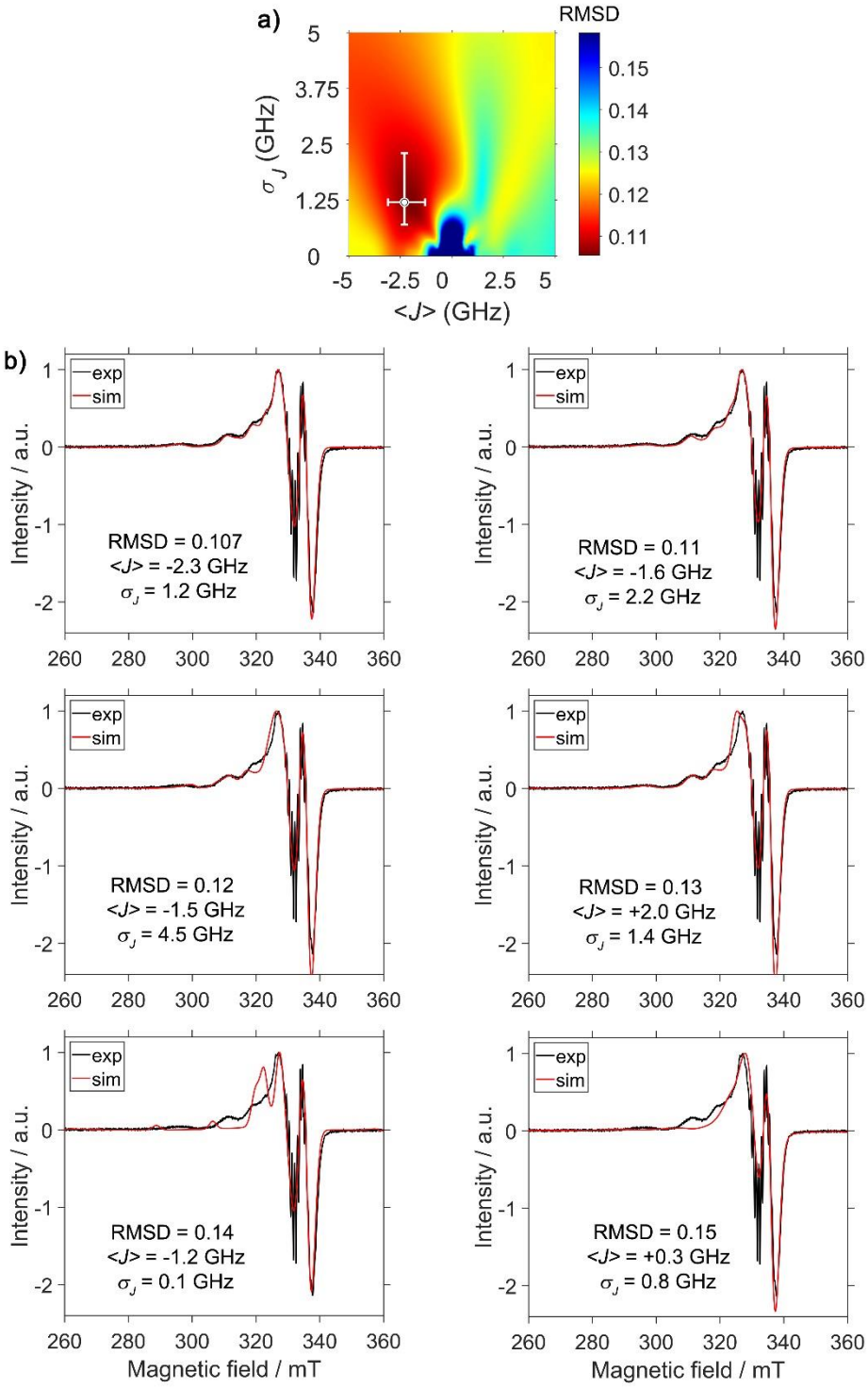

Figure S8. Evaluation of the RMSD. **a)** RMSD between the simulated and experimental X-band EPR spectra of **6** as a function of $\langle J \rangle$ and σ_J. All other simulation parameters are listed in the last column of Table 5 in the main text. The optimized values of $\langle J \rangle$ and σ_J are depicted as a white dot. **b)** The X-band EPR spectrum of **6** is shown together with the simulated spectra corresponding to the RMSD values of 0.107 (global minimum), 0.11, 0.12, 0.13, 0.14, and 0.15. The values of $\langle J \rangle$ and σ_J that result in these RMSD values are also listed.

5 DFT calculations for 6

The atom coordinates of the optimized structure of **6**:

C	0.47840664875415	2.73681424204952	-0.85093962362262
C	0.43615060328312	4.12074744595712	-0.68333079132432
C	-0.51403930423417	4.71811001736554	0.16296942653896
C	-1.38693371629634	3.87065950095378	0.86248237384107
C	-1.31946897537589	2.48593219559677	0.70734702901417
C	-0.39294863670411	1.89771100758742	-0.15457236879257
S	-2.45375075077151	4.44243848731999	2.11915799724534
C	-3.46884519273332	2.92836115774257	2.20638635399171
S	-2.38398160931654	1.54046543068475	1.72342338436589
S	1.73742682041196	2.14013330340245	-1.91308756049976
C	1.89764158289917	3.71346629122066	-2.82460068230149
S	1.62717820143996	5.02425152538975	-1.58840063368896
C	3.30543955101149	3.84752893077758	-3.37269266530262
C	0.84236342843997	3.79297568279711	-3.91353328182472
C	-4.64781310988526	3.04583500382362	1.25517568198851
C	-3.91021326675983	2.71802421285683	3.64544939185940
C	-0.52898137864988	6.16188299409341	0.36595250599694
C	-3.21495830278686	8.70049898273602	1.07795047815371
C	-2.01011552356754	7.99969238151033	1.13389368073257
C	-1.76409855854082	6.89846016168956	0.29025687893760
C	-2.78704131285409	6.53408569586402	-0.60921652024942
C	-3.98312584072926	7.25094141308794	-0.66411984397386
C	-4.22088537718264	8.34273609496180	0.17522116057403
S	-2.66639304286876	5.20660459508922	-1.74563627819788
C	-3.88526947318479	5.90690460408637	-2.90623301068959
S	-5.14265744536659	6.70341433008725	-1.85890291014141
S	-3.37838641204053	10.01705632789290	2.22295367656329
C	-2.15713090202780	9.32482353382022	3.38750845440259
S	-0.87596966997872	8.55872409229854	2.34213429825801
C	-1.53546640730304	10.43946290899451	4.20346025062476
C	-2.80823849136046	8.27761410636379	4.27113544603664
C	-3.22124330938475	6.92795682708796	-3.81131269792497
C	-4.52421578966089	4.78329587368524	-3.69601941616905
C	2.45731745454299	8.45510385115777	0.04909714613355
C	1.16304201136224	7.95295672885888	-0.10734643638942
C	0.74779062864211	6.81424429664315	0.60874620991767
C	1.67020750841704	6.25610562760344	1.51362532419573
C	2.97851867295289	6.72779496463450	1.62124861668190
C	3.39266509875924	7.84630250631198	0.89634976373631
S	1.21393152551415	5.05349244952902	2.68773547986484
C	2.90454893257214	4.42004327543951	2.89723297637850
S	3.98519497890214	5.89339734458016	2.78744554104413
S	2.89296008815999	9.75418948707973	-1.03926573030335
C	1.17146572785901	10.24962067077504	-1.37115164136195
S	0.21511201909210	8.69583529163894	-1.37497634574653
C	1.09619784333732	10.90081109124492	-2.73918097149599
C	0.65888323422262	11.16780406904012	-0.27495909928818

518

C	3.03316018354836	3.79349015231583	4.27311495506250
C	3.23101975836142	3.43371958772727	1.78904435169646
C	-5.48021471950111	9.10554532469391	0.08611501361114
C	2.54749476610880	-6.02087586777333	-0.18087186505322
C	3.22004084189189	-4.75250102175911	-0.23009048951840
C	2.26374428950051	-3.80704719553486	-0.38164019863312
C	1.00566756835037	-4.49560115472819	-0.42511469937745
N	1.20457944631421	-5.84427160267392	-0.34109912326394
C	3.19911073555216	-7.23894649093758	0.00973773630538
C	-0.22551794826110	-3.85403643494252	-0.48297750058969
C	-1.44536781117955	-4.51957517621847	-0.51725711486459
C	-2.71683773127032	-3.85797239431959	-0.44540852650629
C	-3.66278354020737	-4.82474235670240	-0.49230118749930
C	-2.97191647893279	-6.07950180349305	-0.61023465881679
N	-1.62190424339707	-5.87209219704051	-0.59463749361449
C	-3.60930751857877	-7.31128036821937	-0.74280364977194
C	-2.93147099274597	-8.52662821573140	-0.81632569593182
C	-3.57097379654990	-9.78231797129823	-1.09435463345096
C	-2.59571886059423	-10.71794120269867	-1.14411560129820
C	-1.35488955619600	-10.04421465457381	-0.88105128819928
N	-1.58236891751595	-8.70906345242684	-0.69214339847855
C	-0.11718231741593	-10.67988668966451	-0.81791036636986
C	1.07741651934125	-10.01783538781199	-0.53724107145993
C	2.30890464350373	-10.69515095201509	-0.24239933177244
C	3.22498101947728	-9.74001760469806	0.03647180704634
C	2.56694574695588	-8.47315883752343	-0.11765367413502
N	1.25232772480930	-8.66809283883493	-0.44277535685886
C	-5.08643198730043	-7.31952853790642	-0.88030281171682
C	-0.24105370721920	-2.37155306315986	-0.42519874115028
C	-0.03931078271333	-12.13342143550531	-1.09874758554372
C	4.62131755728806	-7.19231232766846	0.42347527773315
C	0.05732414865598	-1.72101119581898	0.76803343871409
C	0.02138275638168	-0.33945428566497	0.84679872093120
C	-0.31443865483272	0.42586027123609	-0.26685772439730
C	-0.59276993637123	-0.22279425585667	-1.46673667016002
C	-0.56388081406950	-1.60546874167422	-1.54126541440949
Cu	-0.18898838017367	-7.27370275458879	-0.52019509071280
C	5.63973276994475	-7.78834656655427	-0.31690905836937
C	6.95668734829902	-7.73033349272315	0.11453424431938
C	7.27657969968171	-7.07078301342396	1.29227555964869
C	6.27241667914402	-6.46617161768385	2.03333624277809
C	4.95768699637793	-6.52869461220718	1.60362081900360
C	-0.71035994435403	-13.07808281118545	-0.32525585736418
C	-0.62938774025074	-14.42838923875060	-0.63326296337569
C	0.12683841312813	-14.85499987669043	-1.71559656160059
C	0.80960706593593	-13.92457330817733	-2.48478596626900
C	0.72595438919454	-12.57635982727967	-2.17743480433593
C	-5.69405955066057	-6.67986007108489	-1.96112761370019
C	-7.07190080444495	-6.68973390223692	-2.10839033954432
C	-7.86713581206769	-7.34548507466992	-1.17968382255348
C	-7.27458444302743	-7.98141372045492	-0.09707728154881

C	-5.89572251588509	-7.96738760540069	0.05079173308733
C	4.76903408290854	8.38154633126939	0.98549237889169
C	-5.45124893431411	10.47923253309758	-0.15178784383462
C	-6.62500512157813	11.19923870765924	-0.27651269561528
C	-7.85430053151865	10.55589155094029	-0.16285265672789
C	-7.89157191740279	9.18861421962204	0.09236320384552
C	-6.71600714623317	8.47069771704120	0.21239673730900
C	5.87216444203147	7.59648799725415	0.65325477719177
C	7.14406447301174	8.14209233324431	0.63791783485775
C	7.33764255122098	9.47981982370264	0.97012979551840
C	6.24570729993451	10.25475910278678	1.34864536244987
C	4.97720769539535	9.71083537692725	1.35587873168920
C	-9.13936614612068	11.27730207982980	-0.33095254592806
O	-10.22890668980355	10.79789111304933	-0.14438966297329
O	-8.95862406012119	12.54146974766507	-0.73812043938712
C	-10.15081557813407	13.28770638171594	-0.94395318665103
C	8.66503886934646	10.13923565057466	0.89850083333198
O	8.88012349965071	11.28040672723279	1.22006631723226
O	9.61420565115335	9.33123628636847	0.40731780031497
C	10.89512896453991	9.92781621200062	0.24155098856829
H	3.50575587565543	3.05683727223070	-4.09932672698448
H	4.04405611125435	3.78897232405241	-2.57287011512241
H	3.41700971084936	4.80578562058645	-3.88581590318921
H	0.98475558681787	2.98769371015286	-4.63873402169583
H	0.91129812480926	4.75449022883451	-4.42824579766679
H	-0.15634515078958	3.70707492015853	-3.48198630071884
H	-4.30309119912887	3.24733269115201	0.23992160991284
H	-5.29528655500008	3.87152067273344	1.56255431208019
H	-5.22907165365192	2.12015103572010	1.25907318642643
H	-4.52141462396999	1.81569174126422	3.72514351677295
H	-4.52242691901369	3.55957173448984	3.97780682066314
H	-3.05022570759841	2.62082939858697	4.30721669505746
H	-1.05917422010477	11.18207426250035	3.56323863356142
H	-0.78716604012248	10.02636726160340	4.88427691993722
H	-2.30173425357899	10.93070327039968	4.80920919556569
H	-3.25870543154522	7.48749549379047	3.66879650598424
H	-3.58733864237269	8.74093067562283	4.88208332053877
H	-2.05756188677391	7.82592148504222	4.92563494484135
H	-2.45187773398618	6.43811916933025	-4.41393652177535
H	-2.74889410918898	7.71717376390568	-3.22459036080368
H	-3.96352446111166	7.38097304745109	-4.47429394842564
H	-3.76377889601910	4.26553480218239	-4.28746756603223
H	-5.26619021170659	5.18844650929239	-4.38840097648691
H	-5.01186357199558	4.06503978943169	-3.03617780298146
H	1.45070307826402	10.22414861846848	-3.51645099343427
H	1.70724622615097	11.80614629984411	-2.75513093170524
H	0.06662836391361	11.19226658047355	-2.95986331183183
H	-0.36820503204925	11.47198874841628	-0.49356218410702
H	1.28865602294961	12.05831748666274	-0.20610959814559
H	0.65698590962907	10.65802130362272	0.68937363961816
H	2.35859481921405	2.93775956022718	4.35259056566349

520

H	2.78771261364419	4.50954382299529	5.05729081574765
H	4.05063158098687	3.42765208875389	4.42956289664990
H	3.16421710882900	3.91008855796410	0.80923492349482
H	2.51939854623109	2.60362022299595	1.80710414734751
H	4.24248589829852	3.04036935319913	1.92097492148360
H	4.28768578487337	-4.61222511519179	-0.17140287215314
H	2.39113180503404	-2.73928785214436	-0.46897712429599
H	-2.85821202706136	-2.79282907095364	-0.34646952923205
H	-4.73327766764762	-4.70610696259398	-0.43830955511794
H	-4.62671794502004	-9.92042807096966	-1.26460574290037
H	-2.70158916198751	-11.76770856403081	-1.36455636674973
H	2.44019824303632	-11.76538136537602	-0.21552944159072
H	4.25030104852188	-9.87727048440493	0.33847959224891
H	0.31604596269571	-2.30922080689122	1.64073128405229
H	0.25337430710344	0.15510823196352	1.78316109419884
H	-0.84671290797873	0.36477630090685	-2.34064263044598
H	-0.79806951406275	-2.10417055854246	-2.47463912222141
H	5.39495026669017	-8.29028497554837	-1.24550743052778
H	7.73575072830173	-8.19935563002648	-0.47496797792403
H	8.30472498566736	-7.02582799786953	1.63298998620642
H	6.51202172375478	-5.94848451536432	2.95485393402241
H	4.17195649943378	-6.06167292853190	2.18571483805671
H	-1.29410857284350	-12.74724379456747	0.52573209294343
H	-1.15811389068960	-15.15060714977858	-0.02209530201048
H	0.18667660747935	-15.90921216182094	-1.96193571351065
H	1.40416502430555	-14.24790953878961	-3.33125495503589
H	1.25235299304890	-11.84604937374242	-2.78107613246971
H	-5.07089179387071	-6.17725036977492	-2.69163386302357
H	-7.52598194672670	-6.18975847305695	-2.95626739680626
H	-8.94421591392361	-7.36229598344968	-1.30308273821203
H	-7.88891011312110	-8.49084257015321	0.63651339644906
H	-5.43316995231624	-8.46129708177763	0.89733527896615
H	-4.49624301669699	10.97875411434783	-0.26923619503084
H	-6.59439333609328	12.26109142329671	-0.48175821204488
H	-8.85531342106589	8.70391342540464	0.18966396990241
H	-6.75130571863792	7.40659368701446	0.41785045481983
H	5.72366320536866	6.55932316226674	0.37899985798488
H	7.99279947587122	7.53617552183004	0.35033946477213
H	6.41277669336748	11.28837900079549	1.62446461264358
H	4.12685339469142	10.31922872348762	1.63663092376510
H	-9.83404725728362	14.24087532983032	-1.36131827574356
H	-10.67800873714808	13.43843571045860	-0.00080445436116
H	-10.81465128209272	12.76632581009239	-1.63419221074336
H	11.54646161291985	9.13579505319083	-0.12121711957811
H	11.26152823381555	10.33023911297055	1.18674400957913
H	10.84669257548993	10.74040022997603	-0.48498035471550

Table S9. Exchange coupling constant J, energy E, relative energy ΔE, and the Boltzmann weight as functions of the dihedral angles χ_1 and χ_2 (see Figure 6a for the definition). Calculated with the PBE0 functional.

χ_1[a] / °	χ_2[a] / °	J / GHz	E / E_h	ΔE / $kJ \cdot mol^{-1}$	$\exp(-\Delta E/RT)$, T = 178 K
0	226.7	33.0	-10676.52936	594.6	0.00
10	216.6	55.2	-10676.51697	627.1	0.00
20	206.4	60.0	-10676.59404	424.8	0.00
30	196.3	53.4	-10676.64885	280.9	0.00
40	186.1	42.0	-10676.67177	220.7	0.00
50	175.9	29.4	-10676.68583	183.8	0.00
60	165.6	15.6	-10676.70596	130.9	0.00
65	160.5	10.2	-10676.71709	101.7	0.00
70	155.4	4.2	-10676.72723	75.1	0.00
75	150.3	0.6	-10676.73573	52.8	0.00
80	145.2	-1.8	-10676.74238	35.3	0.00
85	140.1	-4.2	-10676.74731	22.4	0.00
86	139.1	-3.6	-10676.74811	20.2	0.00
87	138	-4.2	-10676.74886	18.3	0.00
88	137	-4.2	-10676.74955	16.5	0.00
89	136	-3.6	-10676.75020	14.8	0.00
90	135	-4.2	-10676.75079	13.2	0.00
91	134	-4.2	-10676.75133	11.8	0.00
92	132.9	-4.2	-10676.75183	10.5	0.00
93	131.9	-4.2	-10676.75229	9.3	0.00
94	130.9	-3.6	-10676.75272	8.2	0.00
95	129.9	-3.6	-10676.75310	7.1	0.01
96	128.9	-3.6	-10676.75345	6.2	0.01
97	127.8	-3.6	-10676.75377	5.4	0.03
98	126.8	-3.6	-10676.75407	4.6	0.04
98.5	126.3	-3.0	-10676.75420	4.3	0.06
99	125.8	-3.6	-10676.75432	3.9	0.07
99.5	125.3	-4.2	-10676.75445	3.6	0.09
100	124.8	-3.0	-10676.75456	3.3	0.11
100.5	124.3	-4.2	-10676.75467	3.0	0.13
101	123.8	-3.6	-10676.75477	2.8	0.15
101.5	123.3	-1.8	-10676.75487	2.5	0.18
102	122.8	-2.4	-10676.75496	2.3	0.22
102.5	122.2	-1.8	-10676.75505	2.0	0.25
103	121.7	-3.0	-10676.75513	1.8	0.29
103.5	121.2	-2.4	-10676.75521	1.6	0.34
104	120.7	-1.8	-10676.75528	1.4	0.38
104.5	120.2	-1.2	-10676.75535	1.3	0.43
105	119.7	-1.2	-10676.75541	1.1	0.48
105.5	119.2	-2.4	-10676.75547	0.9	0.53
106	118.7	-1.2	-10676.75552	0.8	0.58
106.5	118.2	-1.8	-10676.75557	0.7	0.64
107	117.7	-1.8	-10676.75561	0.6	0.69
107.5	117.2	-1.2	-10676.75565	0.5	0.74
108	116.7	-1.2	-10676.75569	0.4	0.79
108.5	116.2	0.0	-10676.75572	0.3	0.83
109	115.6	-1.2	-10676.75575	0.2	0.87
109.5	115.1	-1.2	-10676.75577	0.1	0.91
110	114.6	-0.6	-10676.75579	0.1	0.94
110.5	114.1	-0.6	-10676.75580	0.1	0.96
111	113.6	0.0	-10676.75581	0.0	0.98
111.5	113.1	-0.6	-10676.75582	0.0	0.99
112	112.6	0.0	-10676.75582	0.0	1.00

112.5	112.1	0.6	-10676.75582	0.0	1.00
113	111.6	0.0	-10676.75582	0.0	0.99
113.5	111.1	0.6	-10676.75581	0.0	0.97
114	110.6	0.0	-10676.75580	0.1	0.95
114.5	110.1	-0.6	-10676.75578	0.1	0.92
115	109.6	0.6	-10676.75576	0.2	0.89
115.5	109.1	0.6	-10676.75574	0.2	0.86
116	108.6	0.6	-10676.75571	0.3	0.81
116.5	108	0.0	-10676.75568	0.4	0.77
117	107.5	0.0	-10676.75564	0.5	0.72
117.5	107	0.0	-10676.75560	0.6	0.67
118	106.5	0.6	-10676.75556	0.7	0.62
118.5	106	0.6	-10676.75551	0.8	0.57
119	105.5	0.0	-10676.75546	1.0	0.52
119.5	105	1.2	-10676.75540	1.1	0.47
120	104.5	0.6	-10676.75534	1.3	0.42
120.5	104	0.6	-10676.75527	1.5	0.37
121	103.5	1.2	-10676.75519	1.7	0.33
121.5	103	0.6	-10676.75511	1.9	0.28
122	102.5	1.2	-10676.75502	2.1	0.24
122.5	102	1.2	-10676.75493	2.3	0.20
123	101.5	1.2	-10676.75483	2.6	0.17
123.5	101	1.2	-10676.75473	2.9	0.14
124	100.5	1.2	-10676.75461	3.2	0.12
124.5	100	1.2	-10676.75449	3.5	0.09
125	99.5	0.0	-10676.75436	3.8	0.07
125.5	99	1.2	-10676.75422	4.2	0.06
126	98.4	1.2	-10676.75408	4.6	0.05
126.5	97.9	0.6	-10676.75393	5.0	0.03
127	97.4	0.6	-10676.75376	5.4	0.03
127.5	96.9	1.2	-10676.75359	5.9	0.02
128	96.4	0.6	-10676.75341	6.3	0.01
128.5	95.9	0.6	-10676.75322	6.8	0.01
129	95.4	0.6	-10676.75302	7.4	0.01
130	94.4	0.6	-10676.75259	8.5	0.00
131	93.4	0.6	-10676.75212	9.7	0.00
132	92.4	0.6	-10676.75159	11.1	0.00
133	91.4	1.2	-10676.75101	12.6	0.00
134	90.4	0.6	-10676.75037	14.3	0.00
135	89.4	0.6	-10676.74967	16.2	0.00
136	88.4	0.0	-10676.74890	18.2	0.00
137	87.4	0.0	-10676.74804	20.4	0.00
138	86.4	0.6	-10676.74710	22.9	0.00
139	85.4	0.0	-10676.74606	25.6	0.00
140	84.4	0.6	-10676.74493	28.6	0.00
145	79.3	0.0	-10676.73744	48.3	0.00
150	74.3	-1.8	-10676.72611	78.0	0.00
155	69.3	-1.2	-10676.70956	121.5	0.00
160	64.4	0.0	-10676.68628	182.6	0.00
170	54.4	10.2	-10676.61499	369.8	0.00
180	44.5	32.4	-10676.52269	612.1	0.00
190	34.6	53.4	-10676.51091	643.0	0.00
200	24.7	58.2	-10676.58635	445.0	0.00
210	14.9	52.2	-10676.63945	305.5	0.00
220	5	41.4	-10676.66159	247.4	0.00
230	355.2	29.4	-10676.67652	208.2	0.00
240	345.4	16.2	-10676.69745	153.3	0.00
245	340.5	9.6	-10676.70847	124.3	0.00
250	335.6	4.8	-10676.71830	98.5	0.00

255	330.7	0.6	-10676.72652	76.9	0.00
260	325.8	-1.8	-10676.73304	59.8	0.00
265	320.9	-3.6	-10676.73801	46.8	0.00
270	316	-4.2	-10676.74169	37.1	0.00
271	315	-3.6	-10676.74230	35.5	0.00
272	314	-4.2	-10676.74287	34.0	0.00
273	313	-3.6	-10676.74340	32.6	0.00
274	312	-3.6	-10676.74390	31.3	0.00
275	311.1	-4.2	-10676.74437	30.1	0.00
276	310.1	-3.6	-10676.74480	28.9	0.00
277	309.1	-3.6	-10676.74521	27.9	0.00
278	308.1	-3.0	-10676.74559	26.9	0.00
279	307.1	-3.6	-10676.74595	25.9	0.00
280	306.2	-3.6	-10676.74630	25.0	0.00
281	305.2	-2.4	-10676.74662	24.2	0.00
282	304.2	-2.4	-10676.74692	23.4	0.00
283	303.2	-2.4	-10676.74720	22.6	0.00
284	302.2	-2.4	-10676.74747	21.9	0.00
285	301.2	-1.8	-10676.74773	21.3	0.00
286	300.3	-1.2	-10676.74797	20.6	0.00
287	299.3	-1.2	-10676.74819	20.0	0.00
288	298.3	-1.2	-10676.74840	19.5	0.00
289	297.3	-0.6	-10676.74859	19.0	0.00
290	296.3	-0.6	-10676.74877	18.5	0.00
291	295.3	0.0	-10676.74893	18.1	0.00
292	294.4	0.0	-10676.74909	17.7	0.00
293	293.4	0.0	-10676.74923	17.3	0.00
294	292.4	0.6	-10676.74935	17.0	0.00
295	291.4	0.6	-10676.74947	16.7	0.00
296	290.4	0.6	-10676.74957	16.4	0.00
297	289.4	0.0	-10676.74966	16.2	0.00
298	288.4	1.2	-10676.74974	16.0	0.00
299	287.5	0.0	-10676.74980	15.8	0.00
300	286.5	1.2	-10676.74985	15.7	0.00
301	285.5	0.6	-10676.74987	15.6	0.00
302	284.5	0.6	-10676.74987	15.6	0.00
303	283.5	1.2	-10676.74985	15.7	0.00
304	282.5	1.2	-10676.74980	15.8	0.00
305	281.5	0.6	-10676.74972	16.0	0.00
306	280.6	0.6	-10676.74961	16.3	0.00
307	279.6	1.2	-10676.74947	16.7	0.00
308	278.6	0.6	-10676.74929	17.1	0.00
309	277.6	1.2	-10676.74908	17.7	0.00
310	276.6	1.2	-10676.74883	18.4	0.00
311	275.6	1.2	-10676.74854	19.1	0.00
315	271.6	0.0	-10676.74685	23.6	0.00
320	266.7	0.0	-10676.74306	33.5	0.00
325	261.7	-0.6	-10676.73658	50.5	0.00
330	256.7	-1.2	-10676.72632	77.5	0.00
335	251.8	-1.2	-10676.71088	118.0	0.00
340	246.8	0.0	-10676.68876	176.1	0.00
350	236.7	10.8	-10676.61992	356.8	0.00
360	226.7	33.0	-10676.52936	594.6	0.00

[a] χ_1 and χ_2 are defined in Figure 6a of the main text.

Table S10. Exchange coupling constant *J*, energy *E*, relative energy Δ*E*, and the Boltzmann weight as functions of the dihedral angles χ_1 and χ_2 (see Figure 6a for the definition). Calculated with the TPSSh functional.

χ_1[a] / °	χ_2[a] / °	*J* / GHz	*E* / E_h	Δ*E* / *kJ·mol*$^{-1}$	exp(-Δ*E*/*RT*), *T* = 178 K
0	226.7	40.2	-10684.02458	599.2	0.00
10	216.6	69.6	-10684.01262	630.6	0.00
20	206.4	74.3	-10684.09018	427.0	0.00
30	196.3	67.8	-10684.14600	280.4	0.00
40	186.1	56.4	-10684.16909	219.8	0.00
50	175.9	41.4	-10684.18304	183.2	0.00
60	165.6	25.2	-10684.20312	130.4	0.00
65	160.5	16.8	-10684.21431	101.0	0.00
70	155.4	9.6	-10684.22455	74.2	0.00
75	150.3	3.0	-10684.23314	51.6	0.00
80	145.2	-0.6	-10684.23981	34.1	0.00
85	140.1	-3.6	-10684.24468	21.3	0.00
86	139.1	-3.6	-10684.24547	19.2	0.00
87	138	-4.2	-10684.24620	17.3	0.00
88	137	-3.6	-10684.24687	15.6	0.00
89	136	-5.4	-10684.24749	13.9	0.00
90	135	-5.4	-10684.24806	12.4	0.00
91	134	-4.8	-10684.24858	11.1	0.00
92	132.9	-5.4	-10684.24906	9.8	0.00
93	131.9	-4.8	-10684.24950	8.7	0.00
94	130.9	-4.8	-10684.24990	7.6	0.01
95	129.9	-5.4	-10684.25026	6.7	0.01
96	128.9	-5.4	-10684.25059	5.8	0.02
97	127.8	-4.2	-10684.25089	5.0	0.03
98	126.8	-4.8	-10684.25116	4.3	0.06
98.5	126.3	-5.4	-10684.25129	4.0	0.07
99	125.8	-4.2	-10684.25140	3.7	0.08
99.5	125.3	-4.2	-10684.25152	3.4	0.10
100	124.8	-3.6	-10684.25162	3.1	0.12
100.5	124.3	-4.2	-10684.25172	2.8	0.15
101	123.8	-4.2	-10684.25182	2.6	0.18
101.5	123.3	-4.2	-10684.25191	2.3	0.21
102	122.8	-4.2	-10684.25199	2.1	0.24
102.5	122.2	-4.2	-10684.25207	1.9	0.28
103	121.7	-4.2	-10684.25215	1.7	0.32
103.5	121.2	-3.6	-10684.25222	1.5	0.36
104	120.7	-4.2	-10684.25228	1.3	0.40
104.5	120.2	-3.6	-10684.25234	1.2	0.45
105	119.7	-3.0	-10684.25240	1.0	0.50
105.5	119.2	-3.0	-10684.25246	0.9	0.55
106	118.7	-3.0	-10684.25251	0.8	0.60
106.5	118.2	-3.6	-10684.25255	0.6	0.65
107	117.7	-3.0	-10684.25260	0.5	0.70
107.5	117.2	-2.4	-10684.25264	0.4	0.75
108	116.7	-2.4	-10684.25267	0.3	0.80
108.5	116.2	-2.4	-10684.25270	0.3	0.84
109	115.6	-2.4	-10684.25273	0.2	0.88
109.5	115.1	-2.4	-10684.25275	0.1	0.92
110	114.6	-2.4	-10684.25277	0.1	0.95
110.5	114.1	-1.8	-10684.25278	0.0	0.97
111	113.6	-1.8	-10684.25279	0.0	0.99
111.5	113.1	-1.8	-10684.25279	0.0	1.00
112	112.6	-1.8	-10684.25280	0.0	1.00

112.5	112.1	-1.8	-10684.25279	0.0	0.99
113	111.6	-1.2	-10684.25279	0.0	0.98
113.5	111.1	-1.2	-10684.25278	0.1	0.97
114	110.6	-0.6	-10684.25276	0.1	0.94
114.5	110.1	-1.2	-10684.25275	0.1	0.91
115	109.6	-1.2	-10684.25273	0.2	0.88
115.5	109.1	-0.6	-10684.25270	0.2	0.85
116	108.6	-0.6	-10684.25268	0.3	0.81
116.5	108	-0.6	-10684.25265	0.4	0.77
117	107.5	-0.6	-10684.25261	0.5	0.72
117.5	107	0.0	-10684.25257	0.6	0.68
118	106.5	0.0	-10684.25253	0.7	0.63
118.5	106	0.0	-10684.25249	0.8	0.58
119	105.5	0.0	-10684.25244	0.9	0.53
119.5	105	0.0	-10684.25239	1.1	0.48
120	104.5	0.0	-10684.25233	1.2	0.44
120.5	104	0.6	-10684.25227	1.4	0.39
121	103.5	0.6	-10684.25220	1.6	0.35
121.5	103	0.6	-10684.25212	1.8	0.30
122	102.5	0.6	-10684.25204	2.0	0.26
122.5	102	0.6	-10684.25196	2.2	0.23
123	101.5	0.6	-10684.25187	2.4	0.19
123.5	101	0.6	-10684.25177	2.7	0.16
124	100.5	0.6	-10684.25166	3.0	0.13
124.5	100	0.6	-10684.25155	3.3	0.11
125	99.5	1.2	-10684.25143	3.6	0.09
125.5	99	1.2	-10684.25131	3.9	0.07
126	98.4	1.8	-10684.25117	4.3	0.06
126.5	97.9	1.2	-10684.25103	4.6	0.04
127	97.4	1.2	-10684.25088	5.0	0.03
127.5	96.9	1.2	-10684.25072	5.5	0.03
128	96.4	1.2	-10684.25055	5.9	0.02
128.5	95.9	0.6	-10684.25038	6.4	0.01
129	95.4	1.2	-10684.25019	6.8	0.01
130	94.4	1.8	-10684.24979	7.9	0.00
131	93.4	1.8	-10684.24934	9.1	0.00
132	92.4	1.8	-10684.24885	10.4	0.00
133	91.4	1.2	-10684.24831	11.8	0.00
134	90.4	1.2	-10684.24770	13.4	0.00
135	89.4	0.6	-10684.24702	15.2	0.00
136	88.4	1.2	-10684.24627	17.1	0.00
137	87.4	1.2	-10684.24544	19.3	0.00
138	86.4	0.6	-10684.24452	21.7	0.00
139	85.4	0.6	-10684.24351	24.4	0.00
140	84.4	0.0	-10684.24239	27.3	0.00
145	79.3	-1.2	-10684.23499	46.7	0.00
150	74.3	-2.4	-10684.22370	76.4	0.00
155	69.3	-3.6	-10684.20702	120.2	0.00
160	64.4	-3.6	-10684.18333	182.4	0.00
170	54.4	8.4	-10684.11056	373.4	0.00
180	44.5	39.6	-10684.01785	616.8	0.00
190	34.6	67.8	-10684.00648	646.7	0.00
200	24.7	72.5	-10684.08243	447.3	0.00
210	14.9	66.6	-10684.13660	305.1	0.00
220	5	55.2	-10684.15908	246.1	0.00
230	355.2	40.2	-10684.17397	207.0	0.00
240	345.4	24.0	-10684.19480	152.3	0.00
245	340.5	16.8	-10684.20587	123.2	0.00
250	335.6	9.0	-10684.21577	97.2	0.00

255	330.7	3.0	-10684.22406	75.5	0.00
260	325.8	-1.2	-10684.23057	58.4	0.00
265	320.9	-3.6	-10684.23546	45.5	0.00
270	316	-4.8	-10684.23904	36.1	0.00
271	315	-4.8	-10684.23962	34.6	0.00
272	314	-5.4	-10684.24017	33.2	0.00
273	313	-5.4	-10684.24068	31.8	0.00
274	312	-5.4	-10684.24115	30.6	0.00
275	311.1	-5.4	-10684.24160	29.4	0.00
276	310.1	-4.8	-10684.24201	28.3	0.00
277	309.1	-4.8	-10684.24240	27.3	0.00
278	308.1	-4.8	-10684.24276	26.4	0.00
279	307.1	-4.8	-10684.24310	25.5	0.00
280	306.2	-4.2	-10684.24342	24.6	0.00
281	305.2	-3.6	-10684.24373	23.8	0.00
282	304.2	-4.2	-10684.24401	23.1	0.00
283	303.2	-4.2	-10684.24429	22.3	0.00
284	302.2	-3.6	-10684.24455	21.7	0.00
285	301.2	-3.6	-10684.24480	21.0	0.00
286	300.3	-2.4	-10684.24503	20.4	0.00
287	299.3	-3.0	-10684.24525	19.8	0.00
288	298.3	-2.4	-10684.24546	19.3	0.00
289	297.3	-2.4	-10684.24565	18.8	0.00
290	296.3	-2.4	-10684.24582	18.3	0.00
291	295.3	-1.8	-10684.24598	17.9	0.00
292	294.4	-1.2	-10684.24613	17.5	0.00
293	293.4	-1.2	-10684.24626	17.2	0.00
294	292.4	-1.8	-10684.24639	16.8	0.00
295	291.4	-1.2	-10684.24650	16.5	0.00
296	290.4	-0.6	-10684.24661	16.3	0.00
297	289.4	-0.6	-10684.24670	16.0	0.00
298	288.4	0.0	-10684.24679	15.8	0.00
299	287.5	0.0	-10684.24686	15.6	0.00
300	286.5	0.0	-10684.24691	15.4	0.00
301	285.5	0.0	-10684.24695	15.3	0.00
302	284.5	0.6	-10684.24697	15.3	0.00
303	283.5	0.6	-10684.24696	15.3	0.00
304	282.5	0.6	-10684.24692	15.4	0.00
305	281.5	0.6	-10684.24686	15.6	0.00
306	280.6	0.6	-10684.24677	15.8	0.00
307	279.6	0.6	-10684.24665	16.1	0.00
308	278.6	1.2	-10684.24650	16.5	0.00
309	277.6	1.2	-10684.24632	17.0	0.00
310	276.6	0.6	-10684.24610	17.6	0.00
311	275.6	1.2	-10684.24584	18.3	0.00
315	271.6	1.2	-10684.24427	22.4	0.00
320	266.7	0.0	-10684.24059	32.0	0.00
325	261.7	-1.2	-10684.23418	48.9	0.00
330	256.7	-2.4	-10684.22397	75.7	0.00
335	251.8	-3.6	-10684.20842	116.5	0.00
340	246.8	-3.0	-10684.18589	175.7	0.00
350	236.7	8.4	-10684.11555	360.3	0.00
360	226.7	40.2	-10684.02458	599.2	0.00

[a] χ_1 and χ_2 are defined in Figure 6a of the main text.

Table S11. Exchange coupling constant *J*, energy *E*, relative energy Δ*E*, and the Boltzmann weight as functions of the dihedral angles χ_1 and χ_2 (see Figure 6a for the definition). Calculated with the B3LYP functional.

χ_1[a] / °	χ_2[a] / °	*J* / GHz	*E* / E_h	Δ*E* / *kJ·mol*$^{-1}$	exp(-Δ*E*/*RT*), *T* = 178 K
0	226.7	32.4	-10680.36787	606.6	0.00
10	216.6	54.0	-10680.35490	640.6	0.00
20	206.4	57.6	-10680.43053	442.1	0.00
30	196.3	52.8	-10680.48495	299.2	0.00
40	186.1	42.0	-10680.50818	238.2	0.00
50	175.9	28.2	-10680.52298	199.3	0.00
60	165.6	16.2	-10680.54421	143.6	0.00
65	160.5	10.2	-10680.55603	112.6	0.00
70	155.4	5.4	-10680.56690	84.0	0.00
75	150.3	1.2	-10680.57611	59.8	0.00
80	145.2	-1.8	-10680.58345	40.6	0.00
85	140.1	-3.6	-10680.58897	26.1	0.00
86	139.1	-4.2	-10680.58988	23.7	0.00
87	138	-4.2	-10680.59072	21.5	0.00
88	137	-4.2	-10680.59151	19.4	0.00
89	136	-4.2	-10680.59224	17.5	0.00
90	135	-4.2	-10680.59292	15.7	0.00
91	134	-4.2	-10680.59355	14.0	0.00
92	132.9	-4.2	-10680.59413	12.5	0.00
93	131.9	-4.2	-10680.59466	11.1	0.00
94	130.9	-3.6	-10680.59516	9.8	0.00
95	129.9	-4.2	-10680.59561	8.6	0.00
96	128.9	-4.2	-10680.59602	7.5	0.01
97	127.8	-3.6	-10680.59640	6.5	0.01
98	126.8	-3.6	-10680.59675	5.6	0.02
98.5	126.3	-3.6	-10680.59691	5.2	0.03
99	125.8	-3.6	-10680.59706	4.8	0.04
99.5	125.3	-3.6	-10680.59721	4.4	0.05
100	124.8	-2.4	-10680.59735	4.1	0.06
100.5	124.3	-3.0	-10680.59748	3.7	0.08
101	123.8	-3.0	-10680.59761	3.4	0.10
101.5	123.3	-3.0	-10680.59772	3.1	0.12
102	122.8	-3.0	-10680.59784	2.8	0.15
102.5	122.2	-2.4	-10680.59794	2.5	0.18
103	121.7	-1.8	-10680.59804	2.2	0.22
103.5	121.2	-2.4	-10680.59814	2.0	0.26
104	120.7	-2.4	-10680.59822	1.8	0.30
104.5	120.2	-1.2	-10680.59830	1.6	0.35
105	119.7	-1.8	-10680.59838	1.4	0.40
105.5	119.2	-1.8	-10680.59845	1.2	0.45
106	118.7	-1.8	-10680.59851	1.0	0.50
106.5	118.2	-2.4	-10680.59857	0.9	0.56
107	117.7	-1.8	-10680.59863	0.7	0.62
107.5	117.2	-1.2	-10680.59867	0.6	0.67
108	116.7	-1.2	-10680.59872	0.5	0.73
108.5	116.2	-1.2	-10680.59876	0.4	0.78
109	115.6	-1.2	-10680.59879	0.3	0.82
109.5	115.1	-1.2	-10680.59882	0.2	0.87
110	114.6	-1.2	-10680.59884	0.1	0.91
110.5	114.1	-0.6	-10680.59886	0.1	0.94
111	113.6	-0.6	-10680.59888	0.1	0.96
111.5	113.1	-1.2	-10680.59889	0.0	0.98
112	112.6	-1.2	-10680.59890	0.0	1.00

112.5	112.1	-1.2	-10680.59890	0.0	1.00
113	111.6	-0.6	-10680.59890	0.0	1.00
113.5	111.1	-0.6	-10680.59889	0.0	0.98
114	110.6	-0.6	-10680.59888	0.1	0.96
114.5	110.1	-0.6	-10680.59886	0.1	0.94
115	109.6	0.0	-10680.59884	0.2	0.90
115.5	109.1	-0.6	-10680.59882	0.2	0.87
116	108.6	0.0	-10680.59879	0.3	0.82
116.5	108	0.0	-10680.59875	0.4	0.77
117	107.5	0.0	-10680.59871	0.5	0.72
117.5	107	0.0	-10680.59867	0.6	0.67
118	106.5	0.6	-10680.59862	0.7	0.61
118.5	106	0.0	-10680.59856	0.9	0.55
119	105.5	0.0	-10680.59851	1.0	0.50
119.5	105	0.0	-10680.59844	1.2	0.44
120	104.5	0.0	-10680.59837	1.4	0.39
120.5	104	0.6	-10680.59829	1.6	0.34
121	103.5	0.6	-10680.59820	1.8	0.29
121.5	103	0.0	-10680.59811	2.1	0.25
122	102.5	0.0	-10680.59801	2.3	0.21
122.5	102	0.6	-10680.59791	2.6	0.17
123	101.5	0.6	-10680.59779	2.9	0.14
123.5	101	0.6	-10680.59767	3.2	0.11
124	100.5	0.0	-10680.59754	3.6	0.09
124.5	100	0.6	-10680.59741	3.9	0.07
125	99.5	0.6	-10680.59726	4.3	0.05
125.5	99	0.6	-10680.59710	4.7	0.04
126	98.4	0.6	-10680.59694	5.1	0.03
126.5	97.9	1.2	-10680.59676	5.6	0.02
127	97.4	1.2	-10680.59658	6.1	0.02
127.5	96.9	1.2	-10680.59639	6.6	0.01
128	96.4	0.6	-10680.59618	7.1	0.01
128.5	95.9	0.6	-10680.59597	7.7	0.01
129	95.4	1.2	-10680.59575	8.3	0.00
130	94.4	0.6	-10680.59527	9.5	0.00
131	93.4	0.6	-10680.59473	10.9	0.00
132	92.4	0.6	-10680.59415	12.5	0.00
133	91.4	0.6	-10680.59352	14.1	0.00
134	90.4	0.0	-10680.59282	16.0	0.00
135	89.4	0.0	-10680.59206	18.0	0.00
136	88.4	0.6	-10680.59122	20.2	0.00
137	87.4	0.6	-10680.59030	22.6	0.00
138	86.4	0.0	-10680.58929	25.2	0.00
139	85.4	0.0	-10680.58818	28.1	0.00
140	84.4	0.0	-10680.58697	31.3	0.00
145	79.3	-0.6	-10680.57906	52.1	0.00
150	74.3	-1.8	-10680.56722	83.2	0.00
155	69.3	-1.8	-10680.55004	128.3	0.00
160	64.4	-1.8	-10680.52608	191.2	0.00
170	54.4	8.4	-10680.45359	381.5	0.00
180	44.5	31.8	-10680.36125	624.0	0.00
190	34.6	52.8	-10680.34887	656.5	0.00
200	24.7	57.0	-10680.42289	462.1	0.00
210	14.9	50.4	-10680.47566	323.6	0.00
220	5	40.2	-10680.49821	264.3	0.00
230	355.2	28.8	-10680.51392	223.1	0.00
240	345.4	16.2	-10680.53596	165.2	0.00
245	340.5	10.2	-10680.54768	134.5	0.00
250	335.6	5.4	-10680.55824	106.8	0.00

255	330.7	1.2	-10680.56717	83.3	0.00
260	325.8	-1.8	-10680.57436	64.4	0.00
265	320.9	-3.6	-10680.57990	49.9	0.00
270	316	-3.6	-10680.58404	39.0	0.00
271	315	-4.2	-10680.58473	37.2	0.00
272	314	-4.2	-10680.58537	35.5	0.00
273	313	-4.2	-10680.58598	33.9	0.00
274	312	-4.2	-10680.58654	32.4	0.00
275	311.1	-3.6	-10680.58707	31.0	0.00
276	310.1	-3.6	-10680.58757	29.7	0.00
277	309.1	-3.6	-10680.58804	28.5	0.00
278	308.1	-3.0	-10680.58847	27.4	0.00
279	307.1	-3.0	-10680.58888	26.3	0.00
280	306.2	-3.0	-10680.58927	25.3	0.00
281	305.2	-3.0	-10680.58963	24.3	0.00
282	304.2	-3.0	-10680.58997	23.4	0.00
283	303.2	-2.4	-10680.59029	22.6	0.00
284	302.2	-2.4	-10680.59058	21.8	0.00
285	301.2	-2.4	-10680.59086	21.1	0.00
286	300.3	-2.4	-10680.59112	20.4	0.00
287	299.3	-1.8	-10680.59136	19.8	0.00
288	298.3	-1.8	-10680.59158	19.2	0.00
289	297.3	-1.2	-10680.59178	18.7	0.00
290	296.3	-1.2	-10680.59197	18.2	0.00
291	295.3	-0.6	-10680.59214	17.7	0.00
292	294.4	-1.2	-10680.59230	17.3	0.00
293	293.4	-0.6	-10680.59244	17.0	0.00
294	292.4	-0.6	-10680.59256	16.6	0.00
295	291.4	-0.6	-10680.59268	16.3	0.00
296	290.4	0.0	-10680.59277	16.1	0.00
297	289.4	0.0	-10680.59285	15.9	0.00
298	288.4	0.6	-10680.59292	15.7	0.00
299	287.5	0.6	-10680.59296	15.6	0.00
300	286.5	1.2	-10680.59298	15.5	0.00
301	285.5	1.2	-10680.59299	15.5	0.00
302	284.5	0.6	-10680.59296	15.6	0.00
303	283.5	0.6	-10680.59291	15.7	0.00
304	282.5	0.6	-10680.59282	15.9	0.00
305	281.5	0.0	-10680.59271	16.2	0.00
306	280.6	0.6	-10680.59256	16.6	0.00
307	279.6	0.6	-10680.59238	17.1	0.00
308	278.6	0.6	-10680.59216	17.7	0.00
309	277.6	1.2	-10680.59189	18.4	0.00
310	276.6	0.6	-10680.59159	19.2	0.00
311	275.6	1.2	-10680.59124	20.1	0.00
315	271.6	1.2	-10680.58930	25.2	0.00
320	266.7	0.0	-10680.58516	36.1	0.00
325	261.7	-0.6	-10680.57824	54.2	0.00
330	256.7	-1.8	-10680.56745	82.6	0.00
335	251.8	-2.4	-10680.55137	124.8	0.00
340	246.8	-1.8	-10680.52856	184.7	0.00
350	236.7	8.4	-10680.45851	368.6	0.00
360	226.7	31.8	-10680.36787	606.6	0.00

[a] χ_1 and χ_2 are defined in Figure 6a of the main text.

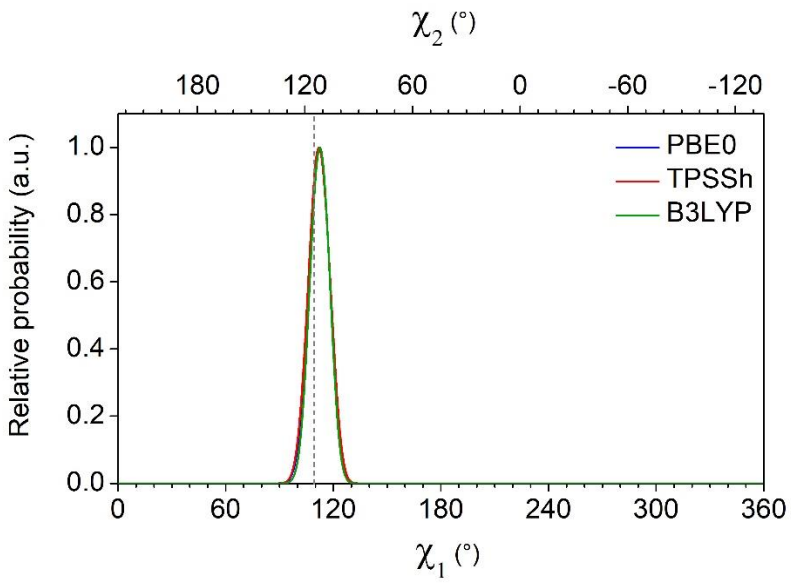

Figure S9. DFT-based distributions of dihedral angles χ_1 and χ_2 (see Figure 6a for the definition) at the freezing point of toluene (178 K). The distributions were obtained with the functionals PBE0 (top), TPSSh (middle), and B3LYP (bottom).

6 DFT calculations for 6 without the phenyl bridge

To test the possibility of a through-space exchange between the electron spin centers in **6**,[6] the phenyl group linking the TPP(Cu^{2+}) and the trityl moieties was removed from the DFT-optimized structure (see the main text), and a hydrogen atom was added on each of the two moieties (Figure S10). Using the obtained structure, the exchange-coupling constant J was calculated by DFT on the PBE0-D3/def2-TZVP level of theory. For further details of the DFT calculations, refer to the Materials and Methods section in the main text. The DFT calculation yielded $J = 0$.

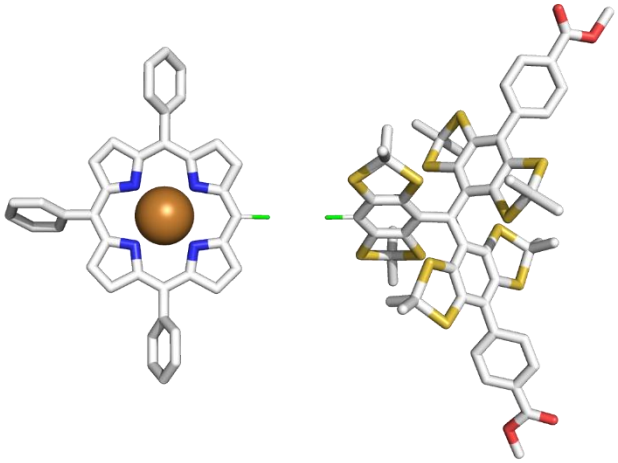

Figure S10. DFT-based structure of the isolated trityl and TPP(Cu^{2+})moieties. The H atoms added to TPP(Cu^{2+}) and trityl are shown in green.

References

[1] S. Stoll, A. Schweiger, *J. Magn. Reson.* **2006**, *178*, 42–55.

[2] N. Fleck, T. Hett, J. Brode, A. Meyer, S. Richert, O. Schiemann, *J. Org. Chem.* **2019**, *84*, 3293–3303.

[3] S. Stoll, A. Gunn, M. Brynda, W. Sughrue, A. C. Kohler, A. Ozarowski, A. J. Fisher, J. C. Lagarias, R. D. Britt, *J. Am. Chem. Soc.* **2009**, *131*, 1986–1995.

[4] C. Calle, A. Schweiger, G. Mitrikas, *Inorg. Chem.* **2007**, *46*, 1847–1855.

[5] C. Finazzo, C. Calle, S. Stoll, S. van Doorslaer, A. Schweiger, *Phys. Chem. Chem. Phys.* **2006**, *8*, 1942–1953.

[6] J. Fritscher, M. Beyer, O. Schiemann, *Chem. Phys. Lett.* **2002**, *364*, 393–401.